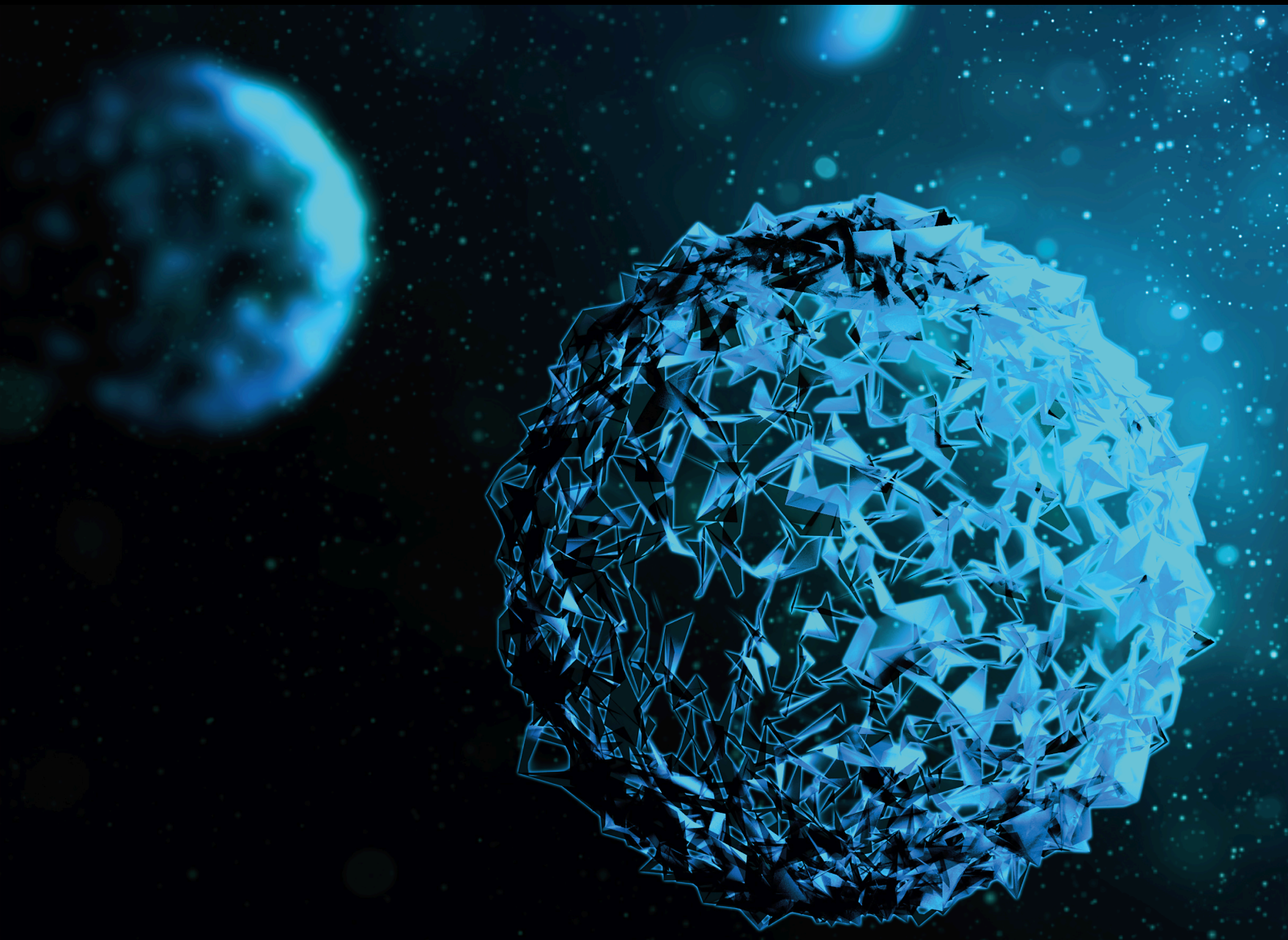


Applications of Bioinformatics and Systems Biology in Precision Medicine and Immuno-Oncology 2021

Lead Guest Editor: Yudong Cai

Guest Editors: Tao Huang, Yu-Hang Zhang, and Taoyang Wu





**Applications of Bioinformatics and Systems
Biology in Precision Medicine and Immuno-
Oncology 2021**

BioMed Research International

**Applications of Bioinformatics and
Systems Biology in Precision Medicine
and Immuno-Oncology 2021**

Lead Guest Editor: Yudong Cai

Guest Editors: Tao Huang, Yu-Hang Zhang, and
Taoyang Wu



Copyright © 2024 Hindawi Limited. All rights reserved.

This is a special issue published in "BioMed Research International." All articles are open access articles distributed under the Creative Commons Attribution License, which permits unrestricted use, distribution, and reproduction in any medium, provided the original work is properly cited.

Section Editors

Penny A. Asbell, USA
David Bernardo , Spain
Gerald Brandacher, USA
Kim Bridle , Australia
Laura Chronopoulou , Italy
Gerald A. Colvin , USA
Aaron S. Dumont, USA
Pierfrancesco Franco , Italy
Raj P. Kandpal , USA
Fabrizio Montecucco , Italy
Mangesh S. Pednekar , India
Letterio S. Politi , USA
Jinsong Ren , China
William B. Rodgers, USA
Harry W. Schroeder , USA
Andrea Scribante , Italy
Germán Vicente-Rodriguez , Spain
Momiao Xiong , USA
Hui Zhang , China

Academic Editors

Bioinformatics

Contents

Retracted: Effects of Pulmonary Surfactant Combined with Noninvasive Positive Pressure Ventilation on KRT-14 and ET-1 Levels in Peripheral Blood and Therapeutic Effects in Neonates with Respiratory Distress Syndrome

BioMed Research International

Retraction (1 page), Article ID 9897420, Volume 2024 (2024)

Retracted: 3D Printed Guides and Preoperative Planning for Uncemented Stem Anteversion Reconstruction during Hip Arthroplasty: A Pilot Study

BioMed Research International

Retraction (1 page), Article ID 9876580, Volume 2024 (2024)

Retracted: A Systematic Analysis on COVID-19 Patients in Inner Mongolia Based on Dynamic Monitoring

BioMed Research International

Retraction (1 page), Article ID 9872914, Volume 2024 (2024)

Retracted: Assembly of 97 Novel Bacterial Genomes in the Microbial Community Affiliated with Polyvinyl Alcohol in Soil of Northern China

BioMed Research International

Retraction (1 page), Article ID 9841978, Volume 2024 (2024)

Retracted: The Early Diagnostic Efficacy of Serum Histone H3 in Rabbit Urosepsis Model

BioMed Research International

Retraction (1 page), Article ID 9835161, Volume 2024 (2024)

Retracted: miR-339-5p Inhibits Autophagy to Reduce the Resistance of Laryngeal Carcinoma on Cisplatin via Targeting TAK1

BioMed Research International

Retraction (1 page), Article ID 9834839, Volume 2024 (2024)

Retracted: Upregulation of miR-29c-3p Hinders Melanoma Progression by Inhibiting CDCA4 Expression

BioMed Research International

Retraction (1 page), Article ID 9813483, Volume 2024 (2024)

Retracted: A Systematic Review and Meta-Analysis of the SuperPATH Approach in Hip Arthroplasty

BioMed Research International

Retraction (1 page), Article ID 9813279, Volume 2024 (2024)

Retracted: Pentoxifylline Can Reduce the Inflammation Caused by LPS after Inhibiting Autophagy in RAW264.7 Macrophage Cells

BioMed Research International

Retraction (1 page), Article ID 9797654, Volume 2024 (2024)

Retracted: Astragalins Protects against Spinal Cord Ischemia Reperfusion Injury through Attenuating Oxidative Stress-Induced Necroptosis

BioMed Research International



Retraction (1 page), Article ID 9764154, Volume 2024 (2024)

Retracted: N-Acetylcysteine Improves Inflammatory Response in COPD Patients by Regulating Th17/Treg Balance through Hypoxia Inducible Factor-1 α Pathway

BioMed Research International

Retraction (1 page), Article ID 9753627, Volume 2024 (2024)

[Retracted] Assembly of 97 Novel Bacterial Genomes in the Microbial Community Affiliated with Polyvinyl Alcohol in Soil of Northern China

Jiaxing Liu, Xun Gu , and Hui Li 


Research Article (14 pages), Article ID 2229147, Volume 2022 (2022)

[Retracted] Effects of Pulmonary Surfactant Combined with Noninvasive Positive Pressure Ventilation on KRT-14 and ET-1 Levels in Peripheral Blood and Therapeutic Effects in Neonates with Respiratory Distress Syndrome

Lihan Huang, Hong Liang, Longbin Liu, Yucong Lin, and Xinzhu Lin 


Research Article (7 pages), Article ID 4117800, Volume 2021 (2021)

[Retracted] Astragalins Protects against Spinal Cord Ischemia Reperfusion Injury through Attenuating Oxidative Stress-Induced Necroptosis

Feng Sun, Haiwei Zhang, Jianhui Shi, Tianwen Huang, and Yansong Wang 


Research Article (8 pages), Article ID 7254708, Volume 2021 (2021)

Identification and Validation of a Dysregulated miRNA-Associated mRNA Network in Temporal Lobe Epilepsy

Xing Li, Yunli Han, Dejun Li, Hai Yuan, Shiqin Huang, Xiaolan Chen, and Yuanhan Qin 


Research Article (12 pages), Article ID 4118216, Volume 2021 (2021)

[Retracted] Upregulation of miR-29c-3p Hinders Melanoma Progression by Inhibiting CDCA4 Expression

Jiazhen Liu, Guilu Tao, Cundi Zhong, and Xiao Liu 










Research Article (15 pages), Article ID 7065963, Volume 2021 (2021)

[Retracted] miR-339-5p Inhibits Autophagy to Reduce the Resistance of Laryngeal Carcinoma on Cisplatin via Targeting TAK1

Guang Li and Zexing Cheng 

Research Article (9 pages), Article ID 9938515, Volume 2021 (2021)


[Retracted] A Systematic Review and Meta-Analysis of the SuperPATH Approach in Hip Arthroplasty

Yanzhi Ge , Zuxiang Chen , Qisong Chen , Yanbin Fu , Mengqiang Fan , Ting Li , Letian Shan , Peijian Tong , and Li Zhou 

Research Article (11 pages), Article ID 5056291, Volume 2021 (2021)


Contents

Study of the G Protein Nucleolar 2 Value in Liver Hepatocellular Carcinoma Treatment and Prognosis

Yiwei Dong, Qianqian Cai, Lisheng Fu, Haojie Liu, Mingzhe Ma, and Xingzhong Wu 


Research Article (12 pages), Article ID 4873678, Volume 2021 (2021)

[Retracted] The Early Diagnostic Efficacy of Serum Histone H3 in Rabbit Urosepsis Model

Xiaolu Zhang, Xiangcheng Zhan, Bisheng Huang, Saiyang Li, and Yunfei Xu 

Research Article (17 pages), Article ID 9969344, Volume 2021 (2021)

Integrative Analysis of Differently Expressed Genes Reveals a 17-Gene Prognosis Signature for Endometrial Carcinoma

Anna Wang, Hongyan Guo, and Zaiqiu Long 

Research Article (18 pages), Article ID 4804694, Volume 2021 (2021)

miR-101-3p Serves as a Tumor Suppressor for Renal Cell Carcinoma and Inhibits Its Invasion and Metastasis by Targeting EZH2

Yunze Dong, Yuchen Gao, Tiancheng Xie, Huan Liu, Xiangcheng Zhan, and Yunfei Xu 


Research Article (12 pages), Article ID 9950749, Volume 2021 (2021)

[Retracted] N-Acetylcysteine Improves Inflammatory Response in COPD Patients by Regulating Th17/Treg Balance through Hypoxia Inducible Factor-1 α Pathway

Xiaopeng Liu, Zhixiong Hu, and Haiying Zhou 



Research Article (7 pages), Article ID 6372128, Volume 2021 (2021)

The Silence of PSMC6 Inhibits Cell Growth and Metastasis in Lung Adenocarcinoma

Jian-Yu Zhang, Ke-Zhi Shi, Xiang-Yu Liao, Shi-Jun Li, Dan Bao, Ying Qian, and Dao-Jun Li 

Research Article (9 pages), Article ID 9922185, Volume 2021 (2021)

PLOD3 Is Associated with Immune Cell Infiltration and Genomic Instability in Colon Adenocarcinoma

Xianyu Deng , Yun Pan, Muqing Yang, Ying Liu, and Jiyu Li 


Research Article (10 pages), Article ID 4714526, Volume 2021 (2021)

FRL: An Integrative Feature Selection Algorithm Based on the Fisher Score, Recursive Feature Elimination, and Logistic Regression to Identify Potential Genomic Biomarkers

Chenyu Ge , Liqun Luo , Jialin Zhang , Xiangbing Meng , and Yun Chen 


Research Article (16 pages), Article ID 4312850, Volume 2021 (2021)

Integrated MicroRNA Expression Profile Reveals Dysregulated miR-20a-5p and miR-200a-3p in Liver Fibrosis

Mu Ye , Sheng Wang , Peilong Sun , and Jingbo Qie 


Research Article (10 pages), Article ID 9583932, Volume 2021 (2021)

Upregulation Mitochondrial Carrier 1 (MTCH1) Is Associated with Cell Proliferation, Invasion, and Migration of Liver Hepatocellular Carcinoma

Guolin Chen , Shanshan Mo, and Di Yuan


Research Article (10 pages), Article ID 9911784, Volume 2021 (2021)

Marker Genes Change of Synovial Fibroblasts in Rheumatoid Arthritis Patients

Lifen Liao, Ke Liang, Lan Lan, Jinheng Wang, and Jun Guo 

Research Article (17 pages), Article ID 5544264, Volume 2021 (2021)

PD-1 Coexpression Gene Analysis and the Regulatory Network in Endometrial Cancer Based on Bioinformatics Analysis

Lina Wang, Zhen Liu, Wenwen Zhang, Aihua Zhang, and Pengpeng Qu 


Research Article (7 pages), Article ID 9923434, Volume 2021 (2021)

Cell Heterogeneity Analysis in Single-Cell RNA-seq Data Using Mixture Exponential Graph and Markov Random Field Model

Yishu Wang , Xuehan Tian, and Dongmei Ai 

Research Article (14 pages), Article ID 9919080, Volume 2021 (2021)

Identification of Molecular Characteristics and New Prognostic Targets for Thymoma by Multiomics Analysis

Dazhong Liu, Pengfei Zhang, Jiaying Zhao, Lei Yang, and Wei Wang 




Research Article (15 pages), Article ID 5587441, Volume 2021 (2021)

PD-L1 and Immune Infiltration of m⁶A RNA Methylation Regulators and Its miRNA Regulators in Hepatocellular Carcinoma

Yingxue Lin, Yinhui Yao , Ying Wang , Lingdi Wang, and Haipeng Cui 

Research Article (16 pages), Article ID 5516100, Volume 2021 (2021)

[Retracted] A Systematic Analysis on COVID-19 Patients in Inner Mongolia Based on Dynamic Monitoring

Lan Yu, Tianbao Li , Li Gao, Bo Wang, Jun Chai, Xiaoli Shi, Rina Su, Geng Tian, Jialiang Yang , and Dejun Sun 

Research Article (8 pages), Article ID 5559187, Volume 2021 (2021)

Identification of Inflammatory Genes, Pathways, and Immune Cells in Necrotizing Enterocolitis of Preterm Infant by Bioinformatics Approaches

Lili Zhang, Lizhen Sun, Mingli Wu, and Jie Huang 


Research Article (9 pages), Article ID 5568724, Volume 2021 (2021)

circRNA circFAT1(e2) Elevates the Development of Non-Small-Cell Lung Cancer by Regulating miR-30e-5p and USP22

Wenmin Dong , Huiqian Zhang , YanCheng Dai , Yi Zhou , Yun Luo , Cheng Zhao , Yiyuan Cao , Yuping Du , and Ying Chen 

Research Article (8 pages), Article ID 6653387, Volume 2021 (2021)




circSLC8A1 Acts as a Tumor Suppressor in Prostate Cancer via Sponging miR-21

Daoyuan Wang, Shuxian Yan, Lihui Wang, Yunlong Li, and Baoping Qiao 

Research Article (9 pages), Article ID 6614591, Volume 2021 (2021)




Contents

[Retracted] Pentoxifylline Can Reduce the Inflammation Caused by LPS after Inhibiting Autophagy in RAW264.7 Macrophage Cells

Danping Ruan , Sinan Deng, Zhonglong Liu , and Jie He 

Research Article (12 pages), Article ID 6698366, Volume 2021 (2021)

Bcl-2 Is Involved in Cardiac Hypertrophy through PI3K-Akt Pathway

Xianwei Meng , Jun Cui , and Guibin He 




Research Article (8 pages), Article ID 6615502, Volume 2021 (2021)

Correlation between TNF- α -308 and +489 Gene Polymorphism and Acute Exacerbation of Chronic Obstructive Pulmonary Diseases

Suyun Yu , Min Xue , Zhijun Yan , Bin Song , Haiping Hong , and Xiwen Gao 



Research Article (8 pages), Article ID 6661281, Volume 2021 (2021)

miR-145-5p Inhibits the Proliferation, Migration, and Invasion of Esophageal Carcinoma Cells by Targeting ABRACL

Shengming Fan , Pei Chen , and Shugang Li 

Research Article (10 pages), Article ID 6692544, Volume 2021 (2021)

[Retracted] 3D Printed Guides and Preoperative Planning for Uncemented Stem Anteversion Reconstruction during Hip Arthroplasty: A Pilot Study

Yingqi Zhang, Zhitao Rao, Jincheng Zhang, Shijie Li, Shimin Chang , and Yeqing Sun 

Research Article (8 pages), Article ID 6621882, Volume 2021 (2021)

Retraction

Retracted: Effects of Pulmonary Surfactant Combined with Noninvasive Positive Pressure Ventilation on KRT-14 and ET-1 Levels in Peripheral Blood and Therapeutic Effects in Neonates with Respiratory Distress Syndrome

BioMed Research International

Received 12 March 2024; Accepted 12 March 2024; Published 20 March 2024

Copyright © 2024 BioMed Research International. This is an open access article distributed under the Creative Commons Attribution License, which permits unrestricted use, distribution, and reproduction in any medium, provided the original work is properly cited.

This article has been retracted by Hindawi following an investigation undertaken by the publisher [1]. This investigation has uncovered evidence of one or more of the following indicators of systematic manipulation of the publication process:

- (1) Discrepancies in scope
- (2) Discrepancies in the description of the research reported
- (3) Discrepancies between the availability of data and the research described
- (4) Inappropriate citations
- (5) Incoherent, meaningless and/or irrelevant content included in the article
- (6) Manipulated or compromised peer review

The presence of these indicators undermines our confidence in the integrity of the article's content and we cannot, therefore, vouch for its reliability. Please note that this notice is intended solely to alert readers that the content of this article is unreliable. We have not investigated whether authors were aware of or involved in the systematic manipulation of the publication process.

Wiley and Hindawi regrets that the usual quality checks did not identify these issues before publication and have since put additional measures in place to safeguard research integrity.

We wish to credit our own Research Integrity and Research Publishing teams and anonymous and named external researchers and research integrity experts for contributing to this investigation.

The corresponding author, as the representative of all authors, has been given the opportunity to register their agreement or disagreement to this retraction. We have kept a record of any response received.

References

- [1] L. Huang, H. Liang, L. Liu, Y. Lin, and X. Lin, "Effects of Pulmonary Surfactant Combined with Noninvasive Positive Pressure Ventilation on KRT-14 and ET-1 Levels in Peripheral Blood and Therapeutic Effects in Neonates with Respiratory Distress Syndrome," *BioMed Research International*, vol. 2021, Article ID 4117800, 7 pages, 2021.

Retraction

Retracted: 3D Printed Guides and Preoperative Planning for Uncemented Stem Anteversion Reconstruction during Hip Arthroplasty: A Pilot Study

BioMed Research International

Received 12 March 2024; Accepted 12 March 2024; Published 20 March 2024

Copyright © 2024 BioMed Research International. This is an open access article distributed under the Creative Commons Attribution License, which permits unrestricted use, distribution, and reproduction in any medium, provided the original work is properly cited.

This article has been retracted by Hindawi following an investigation undertaken by the publisher [1]. This investigation has uncovered evidence of one or more of the following indicators of systematic manipulation of the publication process:

- (1) Discrepancies in scope
- (2) Discrepancies in the description of the research reported
- (3) Discrepancies between the availability of data and the research described
- (4) Inappropriate citations
- (5) Incoherent, meaningless and/or irrelevant content included in the article
- (6) Manipulated or compromised peer review

The presence of these indicators undermines our confidence in the integrity of the article's content and we cannot, therefore, vouch for its reliability. Please note that this notice is intended solely to alert readers that the content of this article is unreliable. We have not investigated whether authors were aware of or involved in the systematic manipulation of the publication process.

Wiley and Hindawi regrets that the usual quality checks did not identify these issues before publication and have since put additional measures in place to safeguard research integrity.

We wish to credit our own Research Integrity and Research Publishing teams and anonymous and named external researchers and research integrity experts for contributing to this investigation.

The corresponding author, as the representative of all authors, has been given the opportunity to register their agreement or disagreement to this retraction. We have kept a record of any response received.

References

- [1] Y. Zhang, Z. Rao, J. Zhang, S. Li, S. Chang, and Y. Sun, "3D Printed Guides and Preoperative Planning for Uncemented Stem Anteversion Reconstruction during Hip Arthroplasty: A Pilot Study," *BioMed Research International*, vol. 2021, Article ID 6621882, 8 pages, 2021.

Retraction

Retracted: A Systematic Analysis on COVID-19 Patients in Inner Mongolia Based on Dynamic Monitoring

BioMed Research International

Received 12 March 2024; Accepted 12 March 2024; Published 20 March 2024

Copyright © 2024 BioMed Research International. This is an open access article distributed under the Creative Commons Attribution License, which permits unrestricted use, distribution, and reproduction in any medium, provided the original work is properly cited.

This article has been retracted by Hindawi following an investigation undertaken by the publisher [1]. This investigation has uncovered evidence of one or more of the following indicators of systematic manipulation of the publication process:

- (1) Discrepancies in scope
- (2) Discrepancies in the description of the research reported
- (3) Discrepancies between the availability of data and the research described
- (4) Inappropriate citations
- (5) Incoherent, meaningless and/or irrelevant content included in the article
- (6) Manipulated or compromised peer review

The presence of these indicators undermines our confidence in the integrity of the article's content and we cannot, therefore, vouch for its reliability. Please note that this notice is intended solely to alert readers that the content of this article is unreliable. We have not investigated whether authors were aware of or involved in the systematic manipulation of the publication process.

Wiley and Hindawi regrets that the usual quality checks did not identify these issues before publication and have since put additional measures in place to safeguard research integrity.

We wish to credit our own Research Integrity and Research Publishing teams and anonymous and named external researchers and research integrity experts for contributing to this investigation.

The corresponding author, as the representative of all authors, has been given the opportunity to register their agreement or disagreement to this retraction. We have kept a record of any response received.

References

- [1] L. Yu, T. Li, L. Gao et al., "A Systematic Analysis on COVID-19 Patients in Inner Mongolia Based on Dynamic Monitoring," *BioMed Research International*, vol. 2021, Article ID 5559187, 8 pages, 2021.

Retraction

Retracted: Assembly of 97 Novel Bacterial Genomes in the Microbial Community Affiliated with Polyvinyl Alcohol in Soil of Northern China

BioMed Research International

Received 12 March 2024; Accepted 12 March 2024; Published 20 March 2024

Copyright © 2024 BioMed Research International. This is an open access article distributed under the Creative Commons Attribution License, which permits unrestricted use, distribution, and reproduction in any medium, provided the original work is properly cited.

This article has been retracted by Hindawi following an investigation undertaken by the publisher [1]. This investigation has uncovered evidence of one or more of the following indicators of systematic manipulation of the publication process:

- (1) Discrepancies in scope
- (2) Discrepancies in the description of the research reported
- (3) Discrepancies between the availability of data and the research described
- (4) Inappropriate citations
- (5) Incoherent, meaningless and/or irrelevant content included in the article
- (6) Manipulated or compromised peer review

The presence of these indicators undermines our confidence in the integrity of the article's content and we cannot, therefore, vouch for its reliability. Please note that this notice is intended solely to alert readers that the content of this article is unreliable. We have not investigated whether authors were aware of or involved in the systematic manipulation of the publication process.

Wiley and Hindawi regrets that the usual quality checks did not identify these issues before publication and have since put additional measures in place to safeguard research integrity.

We wish to credit our own Research Integrity and Research Publishing teams and anonymous and named

external researchers and research integrity experts for contributing to this investigation.

The corresponding author, as the representative of all authors, has been given the opportunity to register their agreement or disagreement to this retraction. We have kept a record of any response received.

References

- [1] J. Liu, X. Gu, and H. Li, "Assembly of 97 Novel Bacterial Genomes in the Microbial Community Affiliated with Polyvinyl Alcohol in Soil of Northern China," *BioMed Research International*, vol. 2022, Article ID 2229147, 14 pages, 2022.

Retraction

Retracted: The Early Diagnostic Efficacy of Serum Histone H3 in Rabbit Urosepsis Model

BioMed Research International

Received 12 March 2024; Accepted 12 March 2024; Published 20 March 2024

Copyright © 2024 BioMed Research International. This is an open access article distributed under the Creative Commons Attribution License, which permits unrestricted use, distribution, and reproduction in any medium, provided the original work is properly cited.

This article has been retracted by Hindawi following an investigation undertaken by the publisher [1]. This investigation has uncovered evidence of one or more of the following indicators of systematic manipulation of the publication process:

- (1) Discrepancies in scope
- (2) Discrepancies in the description of the research reported
- (3) Discrepancies between the availability of data and the research described
- (4) Inappropriate citations
- (5) Incoherent, meaningless and/or irrelevant content included in the article
- (6) Manipulated or compromised peer review

The presence of these indicators undermines our confidence in the integrity of the article's content and we cannot, therefore, vouch for its reliability. Please note that this notice is intended solely to alert readers that the content of this article is unreliable. We have not investigated whether authors were aware of or involved in the systematic manipulation of the publication process.

Wiley and Hindawi regrets that the usual quality checks did not identify these issues before publication and have since put additional measures in place to safeguard research integrity.

We wish to credit our own Research Integrity and Research Publishing teams and anonymous and named external researchers and research integrity experts for contributing to this investigation.

The corresponding author, as the representative of all authors, has been given the opportunity to register their agreement or disagreement to this retraction. We have kept a record of any response received.

References

- [1] X. Zhang, X. Zhan, B. Huang, S. Li, and Y. Xu, "The Early Diagnostic Efficacy of Serum Histone H3 in Rabbit Urosepsis Model," *BioMed Research International*, vol. 2021, Article ID 9969344, 17 pages, 2021.

Retraction

Retracted: miR-339-5p Inhibits Autophagy to Reduce the Resistance of Laryngeal Carcinoma on Cisplatin via Targeting TAK1

BioMed Research International

Received 12 March 2024; Accepted 12 March 2024; Published 20 March 2024

Copyright © 2024 BioMed Research International. This is an open access article distributed under the Creative Commons Attribution License, which permits unrestricted use, distribution, and reproduction in any medium, provided the original work is properly cited.

This article has been retracted by Hindawi following an investigation undertaken by the publisher [1]. This investigation has uncovered evidence of one or more of the following indicators of systematic manipulation of the publication process:

- (1) Discrepancies in scope
- (2) Discrepancies in the description of the research reported
- (3) Discrepancies between the availability of data and the research described
- (4) Inappropriate citations
- (5) Incoherent, meaningless and/or irrelevant content included in the article
- (6) Manipulated or compromised peer review

The presence of these indicators undermines our confidence in the integrity of the article's content and we cannot, therefore, vouch for its reliability. Please note that this notice is intended solely to alert readers that the content of this article is unreliable. We have not investigated whether authors were aware of or involved in the systematic manipulation of the publication process.

Wiley and Hindawi regrets that the usual quality checks did not identify these issues before publication and have since put additional measures in place to safeguard research integrity.

We wish to credit our own Research Integrity and Research Publishing teams and anonymous and named external researchers and research integrity experts for contributing to this investigation.

The corresponding author, as the representative of all authors, has been given the opportunity to register their agreement or disagreement to this retraction. We have kept a record of any response received.

References

- [1] G. Li and Z. Cheng, "miR-339-5p Inhibits Autophagy to Reduce the Resistance of Laryngeal Carcinoma on Cisplatin via Targeting TAK1," *BioMed Research International*, vol. 2021, Article ID 9938515, 9 pages, 2021.

Retraction

Retracted: Upregulation of miR-29c-3p Hinders Melanoma Progression by Inhibiting CDCA4 Expression

BioMed Research International

Received 12 March 2024; Accepted 12 March 2024; Published 20 March 2024

Copyright © 2024 BioMed Research International. This is an open access article distributed under the Creative Commons Attribution License, which permits unrestricted use, distribution, and reproduction in any medium, provided the original work is properly cited.

This article has been retracted by Hindawi following an investigation undertaken by the publisher [1]. This investigation has uncovered evidence of one or more of the following indicators of systematic manipulation of the publication process:

- (1) Discrepancies in scope
- (2) Discrepancies in the description of the research reported
- (3) Discrepancies between the availability of data and the research described
- (4) Inappropriate citations
- (5) Incoherent, meaningless and/or irrelevant content included in the article
- (6) Manipulated or compromised peer review

The presence of these indicators undermines our confidence in the integrity of the article's content and we cannot, therefore, vouch for its reliability. Please note that this notice is intended solely to alert readers that the content of this article is unreliable. We have not investigated whether authors were aware of or involved in the systematic manipulation of the publication process.

Wiley and Hindawi regrets that the usual quality checks did not identify these issues before publication and have since put additional measures in place to safeguard research integrity.

We wish to credit our own Research Integrity and Research Publishing teams and anonymous and named external researchers and research integrity experts for contributing to this investigation.

The corresponding author, as the representative of all authors, has been given the opportunity to register their agreement or disagreement to this retraction. We have kept a record of any response received.

References

- [1] J. Liu, G. Tao, C. Zhong, and X. Liu, "Upregulation of miR-29c-3p Hinders Melanoma Progression by Inhibiting CDCA4 Expression," *BioMed Research International*, vol. 2021, Article ID 7065963, 15 pages, 2021.

Retraction

Retracted: A Systematic Review and Meta-Analysis of the SuperPATH Approach in Hip Arthroplasty

BioMed Research International

Received 12 March 2024; Accepted 12 March 2024; Published 20 March 2024

Copyright © 2024 BioMed Research International. This is an open access article distributed under the Creative Commons Attribution License, which permits unrestricted use, distribution, and reproduction in any medium, provided the original work is properly cited.

This article has been retracted by Hindawi following an investigation undertaken by the publisher [1]. This investigation has uncovered evidence of one or more of the following indicators of systematic manipulation of the publication process:

- (1) Discrepancies in scope
- (2) Discrepancies in the description of the research reported
- (3) Discrepancies between the availability of data and the research described
- (4) Inappropriate citations
- (5) Incoherent, meaningless and/or irrelevant content included in the article
- (6) Manipulated or compromised peer review

The presence of these indicators undermines our confidence in the integrity of the article's content and we cannot, therefore, vouch for its reliability. Please note that this notice is intended solely to alert readers that the content of this article is unreliable. We have not investigated whether authors were aware of or involved in the systematic manipulation of the publication process.

Wiley and Hindawi regrets that the usual quality checks did not identify these issues before publication and have since put additional measures in place to safeguard research integrity.

We wish to credit our own Research Integrity and Research Publishing teams and anonymous and named external researchers and research integrity experts for contributing to this investigation.

The corresponding author, as the representative of all authors, has been given the opportunity to register their agreement or disagreement to this retraction. We have kept a record of any response received.

References

- [1] Y. Ge, Z. Chen, Q. Chen et al., "A Systematic Review and Meta-Analysis of the SuperPATH Approach in Hip Arthroplasty," *BioMed Research International*, vol. 2021, Article ID 5056291, 11 pages, 2021.

Retraction

Retracted: Pentoxifylline Can Reduce the Inflammation Caused by LPS after Inhibiting Autophagy in RAW264.7 Macrophage Cells

BioMed Research International

Received 12 March 2024; Accepted 12 March 2024; Published 20 March 2024

Copyright © 2024 BioMed Research International. This is an open access article distributed under the Creative Commons Attribution License, which permits unrestricted use, distribution, and reproduction in any medium, provided the original work is properly cited.

This article has been retracted by Hindawi following an investigation undertaken by the publisher [1]. This investigation has uncovered evidence of one or more of the following indicators of systematic manipulation of the publication process:

- (1) Discrepancies in scope
- (2) Discrepancies in the description of the research reported
- (3) Discrepancies between the availability of data and the research described
- (4) Inappropriate citations
- (5) Incoherent, meaningless and/or irrelevant content included in the article
- (6) Manipulated or compromised peer review

The presence of these indicators undermines our confidence in the integrity of the article's content and we cannot, therefore, vouch for its reliability. Please note that this notice is intended solely to alert readers that the content of this article is unreliable. We have not investigated whether authors were aware of or involved in the systematic manipulation of the publication process.

Wiley and Hindawi regrets that the usual quality checks did not identify these issues before publication and have since put additional measures in place to safeguard research integrity.

We wish to credit our own Research Integrity and Research Publishing teams and anonymous and named external researchers and research integrity experts for contributing to this investigation.

The corresponding author, as the representative of all authors, has been given the opportunity to register their agreement or disagreement to this retraction. We have kept a record of any response received.

References

- [1] D. Ruan, S. Deng, Z. Liu, and J. He, "Pentoxifylline Can Reduce the Inflammation Caused by LPS after Inhibiting Autophagy in RAW264.7 Macrophage Cells," *BioMed Research International*, vol. 2021, Article ID 6698366, 12 pages, 2021.

Retraction

Retracted: Astragalin Protects against Spinal Cord Ischemia Reperfusion Injury through Attenuating Oxidative Stress-Induced Necroptosis

BioMed Research International

Received 12 March 2024; Accepted 12 March 2024; Published 20 March 2024

Copyright © 2024 BioMed Research International. This is an open access article distributed under the Creative Commons Attribution License, which permits unrestricted use, distribution, and reproduction in any medium, provided the original work is properly cited.

This article has been retracted by Hindawi following an investigation undertaken by the publisher [1]. This investigation has uncovered evidence of one or more of the following indicators of systematic manipulation of the publication process:

- (1) Discrepancies in scope
- (2) Discrepancies in the description of the research reported
- (3) Discrepancies between the availability of data and the research described
- (4) Inappropriate citations
- (5) Incoherent, meaningless and/or irrelevant content included in the article
- (6) Manipulated or compromised peer review

The presence of these indicators undermines our confidence in the integrity of the article's content and we cannot, therefore, vouch for its reliability. Please note that this notice is intended solely to alert readers that the content of this article is unreliable. We have not investigated whether authors were aware of or involved in the systematic manipulation of the publication process.

Wiley and Hindawi regrets that the usual quality checks did not identify these issues before publication and have since put additional measures in place to safeguard research integrity.

We wish to credit our own Research Integrity and Research Publishing teams and anonymous and named

external researchers and research integrity experts for contributing to this investigation.

The corresponding author, as the representative of all authors, has been given the opportunity to register their agreement or disagreement to this retraction. We have kept a record of any response received.

References

- [1] F. Sun, H. Zhang, J. Shi, T. Huang, and Y. Wang, "Astragalin Protects against Spinal Cord Ischemia Reperfusion Injury through Attenuating Oxidative Stress-Induced Necroptosis," *BioMed Research International*, vol. 2021, Article ID 7254708, 8 pages, 2021.

Retraction

Retracted: N-Acetylcysteine Improves Inflammatory Response in COPD Patients by Regulating Th17/Treg Balance through Hypoxia Inducible Factor-1 α Pathway

BioMed Research International

Received 12 March 2024; Accepted 12 March 2024; Published 20 March 2024

Copyright © 2024 BioMed Research International. This is an open access article distributed under the Creative Commons Attribution License, which permits unrestricted use, distribution, and reproduction in any medium, provided the original work is properly cited.

This article has been retracted by Hindawi following an investigation undertaken by the publisher [1]. This investigation has uncovered evidence of one or more of the following indicators of systematic manipulation of the publication process:

- (1) Discrepancies in scope
- (2) Discrepancies in the description of the research reported
- (3) Discrepancies between the availability of data and the research described
- (4) Inappropriate citations
- (5) Incoherent, meaningless and/or irrelevant content included in the article
- (6) Manipulated or compromised peer review

The presence of these indicators undermines our confidence in the integrity of the article's content and we cannot, therefore, vouch for its reliability. Please note that this notice is intended solely to alert readers that the content of this article is unreliable. We have not investigated whether authors were aware of or involved in the systematic manipulation of the publication process.

Wiley and Hindawi regrets that the usual quality checks did not identify these issues before publication and have since put additional measures in place to safeguard research integrity.

We wish to credit our own Research Integrity and Research Publishing teams and anonymous and named external researchers and research integrity experts for contributing to this investigation.

The corresponding author, as the representative of all authors, has been given the opportunity to register their agreement or disagreement to this retraction. We have kept a record of any response received.

References

- [1] X. Liu, Z. Hu, and H. Zhou, "N-Acetylcysteine Improves Inflammatory Response in COPD Patients by Regulating Th17/Treg Balance through Hypoxia Inducible Factor-1 α Pathway," *BioMed Research International*, vol. 2021, Article ID 6372128, 7 pages, 2021.

Retraction

Retracted: Assembly of 97 Novel Bacterial Genomes in the Microbial Community Affiliated with Polyvinyl Alcohol in Soil of Northern China

BioMed Research International

Received 12 March 2024; Accepted 12 March 2024; Published 20 March 2024

Copyright © 2024 BioMed Research International. This is an open access article distributed under the Creative Commons Attribution License, which permits unrestricted use, distribution, and reproduction in any medium, provided the original work is properly cited.

This article has been retracted by Hindawi following an investigation undertaken by the publisher [1]. This investigation has uncovered evidence of one or more of the following indicators of systematic manipulation of the publication process:

- (1) Discrepancies in scope
- (2) Discrepancies in the description of the research reported
- (3) Discrepancies between the availability of data and the research described
- (4) Inappropriate citations
- (5) Incoherent, meaningless and/or irrelevant content included in the article
- (6) Manipulated or compromised peer review

The presence of these indicators undermines our confidence in the integrity of the article's content and we cannot, therefore, vouch for its reliability. Please note that this notice is intended solely to alert readers that the content of this article is unreliable. We have not investigated whether authors were aware of or involved in the systematic manipulation of the publication process.

Wiley and Hindawi regrets that the usual quality checks did not identify these issues before publication and have since put additional measures in place to safeguard research integrity.

We wish to credit our own Research Integrity and Research Publishing teams and anonymous and named

external researchers and research integrity experts for contributing to this investigation.

The corresponding author, as the representative of all authors, has been given the opportunity to register their agreement or disagreement to this retraction. We have kept a record of any response received.

References

- [1] J. Liu, X. Gu, and H. Li, "Assembly of 97 Novel Bacterial Genomes in the Microbial Community Affiliated with Polyvinyl Alcohol in Soil of Northern China," *BioMed Research International*, vol. 2022, Article ID 2229147, 14 pages, 2022.

Research Article

Assembly of 97 Novel Bacterial Genomes in the Microbial Community Affiliated with Polyvinyl Alcohol in Soil of Northern China

Jiaying Liu,¹ Xun Gu^{1,2} and Hui Li¹

¹MOE Key Laboratory of Contemporary Anthropology, School of Life Sciences, Fudan University, Shanghai 200438, China

²Department of GDC Biology, Iowa State University, Ames, IA 50014, USA

Correspondence should be addressed to Xun Gu; xgu@iastate.edu and Hui Li; leilyn102@88.com

Received 28 May 2021; Revised 5 October 2021; Accepted 7 October 2021; Published 18 January 2022

Academic Editor: Yu-Hang Zhang

Copyright © 2022 Jiaying Liu et al. This is an open access article distributed under the Creative Commons Attribution License, which permits unrestricted use, distribution, and reproduction in any medium, provided the original work is properly cited.

Background. Undeveloped ecosystems belong to rich source of microbial population, of which resources remain unearthed. A kind of polymeric compound system with high polyvinyl alcohol (PVA) content has been reported and named *Taisui*. Marker gene amplification showed that *Taisui* harbored little-explored microbial communities. **Aim.** To address this issue, our study attempted to recover draft genomes and functional potential from microbial communities in *Taisui* using the metagenomic approach. **Material and Methods.** *Taisui* communities provided 97 novel bacterial genomes from 13 bacterial phyla, including bacteria candidate phylum. Two novel genus-level lineages were recovered from Planctomycetes and Chloroflexi. Based on the draft genomes, we expanded the number of taxa with potential productions of PKS and NRPS in phyla including Candidatus Dadabacteria, Chloroflexi, and Planctomycetes. **Results.** A rich diversity of PVA dehydrogenase genes from 4 phyla, involving Proteobacteria, Acidobacteria, Acitinobacteria, and Planctomycetes, were identified. The phylogenetic tree of PVA dehydrogenase showed the possibility of horizontal gene transfer between microbes. **Conclusion.** Our study underscores the substantial microbial diversity and PVA degradation potential in the previously unexplored *Taisui* system.

1. Introduction

Polyvinyl alcohol (PVA) is a common water-soluble polymer for farming, packing, fiber coating, etc. Due to the high mass of production and utilization, PVA pollution in the environment was considerable, especially in the major production regions: China, the USA, Western Europe, and Japan [1, 2]. For PVA degradation with less cost and sludge generation, bacterial PVA-degraders were isolated from PVA-containing systems [2]. However, symbiotic behaviors of PVA degrading microbes make the study of microbial community in PVA-containing systems be needed. A kind of underground polymeric compound (named “*Taisui*”) system has been reported recently [3]. Chemical analysis showed that this system can be characterized by high level of PVA or a mixture of PVA and polyacrylic acid [3]. The distribution of *Taisui* has been analysed through finding reports from 1992 to 2015. More

than 60% of *Taisuis* existed in soil layers, and more than 60% of them were in northern China [4].

The PVA-containing system of *Taisui* can be a valuable object of metagenomic analysis. First, *Taisui* has stable morphological characteristics and internal structures [3]. Like a bioreactor, the structure of *Taisui* (Figure S1) separates microbial populations from surrounding environments. Second, *Taisui* has stable chemical compositions [3], which indicates stable microbial pattern. Third, *Taisui* systems harboring little-explored microbial communities. Previous research has shown that *Taisui* hosts a rich diversity of novel microbes [3]. More than 40% bacterial OTUs in 2 samples were unclassified at the phylum level, and more than 75% fungal OTUs in 8 samples were unclassified. Metagenomic sequencing can bypass the cultivation bottleneck by obtaining metagenome-assembled genomes (MAGs), leading to the discovery of novel microbial diversity and new metabolisms

from challenging systems [5, 6]. Based on these prior observations, we inferred that *Taisui* systems offered an opportunity for expand microbial diversity and PVA biodegradation. In this study, we reconstructed MAGs from metagenome of *Taisui* samples and investigated PVA degradation potential of *Taisui* microbiota. The results show the wealth of evolutionary diversity in unexplored systems, markedly expand the diversity of PVA dehydrogenase, and will contribute to future comparative studies of PVA polluted environments.

2. Material and Methods

2.1. Sample Collection. Four *Taisui* samples included in this study were collected from Jinzhou (Liaoning province), Baotou (Inner Mongolia), and Aksu (Xinjiang Province, Figure 1(a)). The *Taisui* individuals were washed using fresh water after being dug out from the soil layer, and the entire of them were delivered at room temperature (about 15°C). For each *Taisui* individual, four samples were collected in the meantime. The samples were collected both from the outside (the surface of *Taisui*) and the inside (about 5 cm depth from the outside) in equal quantity (2 * 2 * 2 cm of each). The samples, belonging to one *Taisui* individual, were pooled as one sample for future investigation. To observe the structure of *Taisui*, the TS.JZ1 sample was used as a representative sample for microscopic observations. Photographs were taken using a digital camera mounted on a light microscope.

2.2. DNA Extraction and Sequencing. Before DNA extraction, we used 1% dimethyl sulphoxide and dry bath to remove polyvinyl alcohol. DNA extraction referred to the phenol-chloroform extraction [7] was described in the supplement. After DNA purification, equal volumes of isopropanol at +4°C (100%) were added to the upper phase previously transferred into a clean 1.5 ml tube, then tubes were slowly mixed by inversion and kept overnight at -20°C, before another centrifugation (15 min at 16000 × g). Following removal of the supernatant, 1 ml of 70% ethanol at +4°C was added to the DNA pellets. These pellets were suspended by flicking the tubes, followed by inversion and centrifugation (15 min at 16000 × g), then pellets were dried for 10 min (V-AQ mode, Vacufuge plus, Eppendorf), and 50 µl of nuclease-free water was added. Samples were shotgun-sequenced for metagenomics on the Illumina HiSeq platform at Novogene (Tianjin, China), and paired-end reads were generated. For HiSeq sequencing, each sample can be barcoded (added during library preparation), and equal quantities of barcoded libraries can be multiplexed during sequencing. HiSeq reads are aligned to a cohort of nonredundant National Center for Biotechnology Information (NCBI) complete genomes using the Short Oligonucleotide Analysis Package (SOAP) alignment tool29, which is typically faster to run than the Basic Local Alignment Search Tool (BLAST) or the BLAST-like Alignment Tool (BLAT). Genome coverage is calculated using the SOAP.coverage package.

2.3. De Novo Assembly and Analysis. The quality control of the metagenomic reads was performed using FastQC [8]

and MultiQC [9]. Adapters and low-quality reads were removed. We set the minimum base quality score of 38. Bases with quality score < 38 were treated as low-quality bases. Reads were filtered as long as they contained more than 40 bp of low-quality bases. We also removed reads that contained more than 10 bp of N and reads that overlapped more than 15 bp with adapters to generate clean data. The high-quality reads were de novo assembled into contigs by using MEGAHIT [10] with default settings. We used QUAST [11] to evaluate metagenomic assemblies.

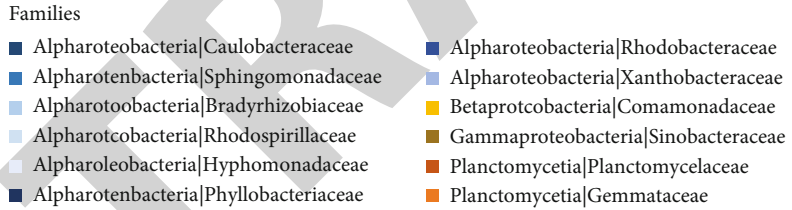
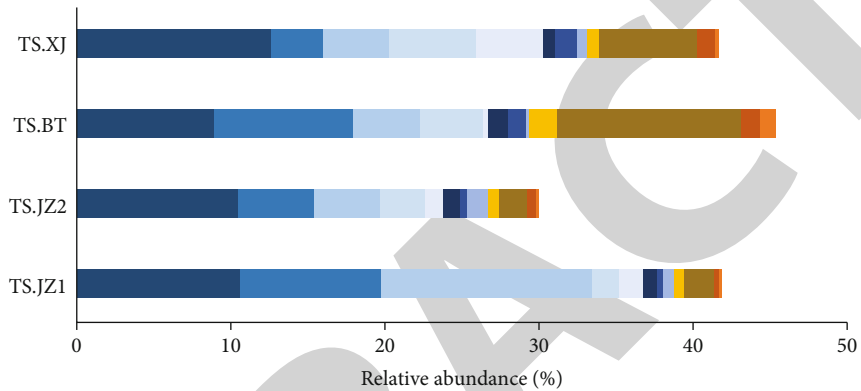
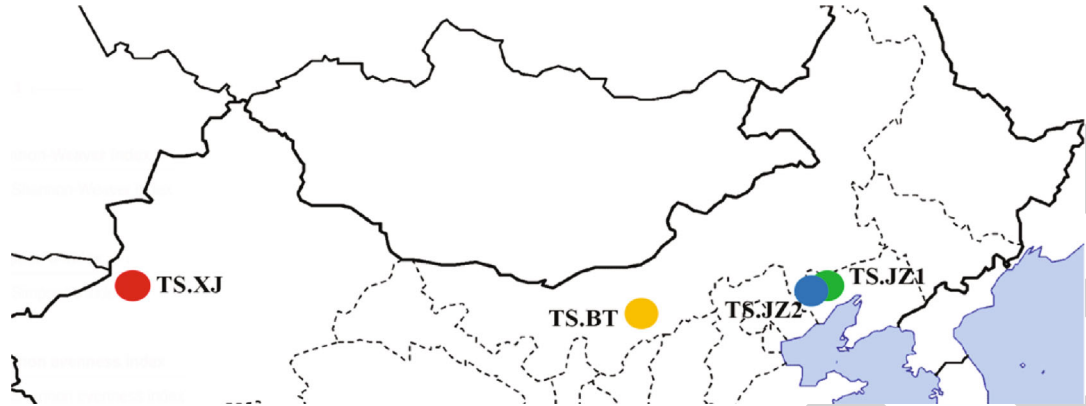
Assembled contigs were used to predict open reading frames (ORFs) using Prokka [12] with annotation mode included archaea, bacteria, mitochondria, and viruses. To get the nonredundant ORF dataset, the ORFs of four samples were merged, and the redundant ORFs were removed using CD-HIT [13, 14]. The abundance of ORFs in each sample was calculated using Salmon [15]. The ORFs were taxonomically annotated against the NCBI GenBank nonredundant protein sequence (nr) database using DIAMOND (*E*-value 1e-5) [16]. Taxonomic annotations were generated using MEGAN6 [17], with the maximum *e*-value cutoff as 1e-5. For KEGG and COG annotation, the ORFs were searched against eggNOG database using eggNOG-mapper [18]. Besides, the ORFs that encode carbohydrate-active enzyme (CAZyme) domain were profiled by mapping against CAZY database [19] using DIAMOND (*E*-value 1e-5).

Shannon-Weaver index, Simpson's index, Shannon evenness index, and Bray-Curtis index of all taxa at the species level were estimated using Vegan. UPGMA clustering of samples was obtained using SplitsTree4 [20]. The clustering tree and bar plots were edited in iTOL [21].

2.4. Meta-Pathway Reconstruction. The meta-pathways were the combination of metabolic pathways of multiple bacteria in the metagenomic dataset. The meta-pathways were reconstructed based on the functional annotation of ORFs (generated using eggNOG database and CAZy database). Also, the KEGG pathways were profiled using Pathview [22] for reconstruction. To evaluate the contribution of bacteria to a given enzyme in the metabolic pathways, the taxonomic annotation of ORFs (generated using NCBI-NR database) was combined with the functional annotation.

2.5. Metagenomic-Assembled Genome. Coassemblies were binned using MetaWRAP (parameters: -c 70 -x 5) [23], which called concoct, maxbin2, and metabat2 for binning at the same time. Bin refinement was performed based on the results of these binning software packages using "bin_refinement." Reads were aligned to contigs using BWA to generate separate files for each cluster. Separated reads were then reassembled using "reassemble_bins," and final beat bins were obtained based on the results of CheckM [24], which resulted in a final set of 97 bins.

Using CheckM, bins were filtered for completeness ≥ 70% and contamination ≤ 5%. Taxonomy was assigned to genome bins using GTDB-Tk [25]. The amino acid identity (AAI) between MAGs was calculated by CompareM v. 0.1.1 [26]. The replication of MAGs was checked at 95% average nucleotide identity (ANI) to generate the species number



(b)

FIGURE 1: Continued.

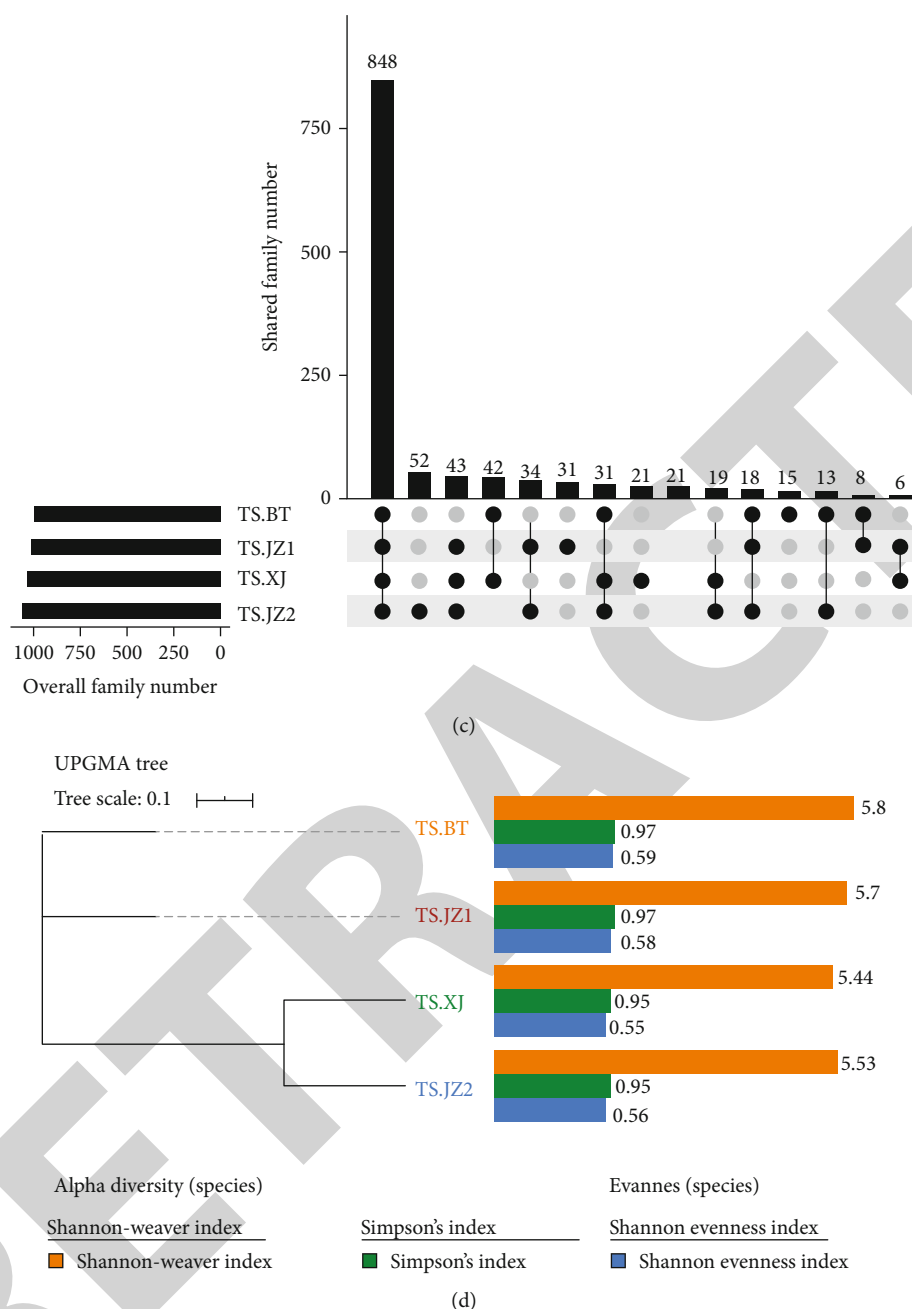


FIGURE 1: Taxonomic analysis of Taisui metagenome: (a) sample locations in northern China, (b) the relative abundance (%) of major families in Taisui samples, (c) the upset plot of the family count in each sample, and (d) alpha and beta diversities of Taisui metagenomes (the UPGMA clustering based on Bray-Curtis distances of species richness).

using pyani [27, 28]. According to the standards suggested by Glendinning et al. [29], genomes were defined as novel strains (GTDB-Tk ANI output < 99%), novel species (GTDB-Tk ANI output < 95%), and novel genera (all MAGs clustered at 60% AAI [30] without a genus GTDB-Tk assignment).

For MAG phylogenetic analysis, the concatenated sequence alignment of core marker genes was built by Up-to-date Bacterial Core Gene pipeline (UBCG) [31]. Conserved blocks were selected from multiple alignments by Gblocks (parameters: -b5 h) [32] for further analysis. The best-fit evolutionary model was selected using

ModelTest-NG [33]. The phylogenetic tree was inferred using RAXML-NG [34] with the GTR+I+G4 model. Node support was generated through 500 bootstrap replicates. The phylogenetic tree was finalized for publication using iTOL website [21].

For the phylogenetic placement analysis, the MAGs and reference genomes from NCBI database belonging to the phyla Planctomycetes and Chloroflexi were selected. To build the tree of Chloroflexi, we selected 15 genomes involving complete genomes of Anaerolineae, Ardenticatenia, and Dehalococcidia (part of Dehalococcidia complete

genomes were selected according to the results of GTDB-Tk), and closely related genome (UBA2991) of MAGs according to GTDB-Tk. And for the tree of Planctomycetes, we selected 48 genomes involving complete genomes of Planctomycetia, Phycisphaerales, and genomes of UBA1135, UBA1845, and UBA966 according to GTDB-Tk. All genomes used in phylogeny were evaluated by CheckM to confirm completeness $\geq 70\%$. The concatenated core gene alignments were also performed through UBCG and were selected using Gblocks. Model selecting and phylogenetic tree building were performed as before with the GTR+I+G4 model and 100 bootstrap replicates.

2.6. The Phylogenetic Tree of PVA Dehydrogenase. We used our nonredundant protein sequences of PVA dehydrogenase and all known protein sequences of PVA dehydrogenase (AMG75031.1, Q588Z1.3, and P77931.1) from NCBI to build the phylogenetic tree. Only sequences with length more than 500 bp were involved. Sequences were aligned using MAFFT [35] and were trimmed using trimAL [36]. The best-fit evolutionary model was selected using ModelTest-NG [33]. A multiple sequence alignment program, MAFFT, includes two novel techniques: the progressive method (FFT-NS-2) and the iterative refinement method (FFT-NS-i). The MAFFT program package is freely available at <http://www.biophys.kyoto-u.ac.jp/~kato/programs/align/mafft.trimAL>, a tool for automated alignment trimming in large-scale phylogenetic analyses, is freely available for download (<http://trimal.cgenomics.org>) and can be used online through the Phylemon web server (<http://phylemon2.bioinfo.cipf.es/>). ModelTest-NG is a reimplement from scratch of jModelTest and ProtTest, two popular tools for selecting the best-fit nucleotide and amino acid substitution models, respectively. ModelTest-NG is available under a GNU GPL3 license at <https://github.com/ddarriba/modeltest>. The phylogenetic tree was inferred using RAXML-NG [34] with the LG+G4 model. RAXML-NG is a from-scratch reimplement of the established greedy tree search algorithm of RAXML/ExaML. RAXML-NG offers improved accuracy, flexibility, speed, scalability, and usability compared with RAXML/ExaML. AxML-NG web service (maintained by Vital-IT) is available at <https://raxml-ng.vital-it.ch/>. Node support was generated through 100 bootstrap replicates. The phylogenetic tree was finalized for publication using iTOL website [21].

3. Results

We obtained shotgun metagenome sequence from four *Taisui* samples (located in Liaoning, Inner Mongolia, and Xinjiang province, Figure 1(a)). The metagenomic database provided 27.3 Gb clean data and 178 million high-quality reads in total for de novo assembling and binning (Table 1).

3.1. Taxonomic Annotation. The taxonomic annotation indicates the stabilization of four *Taisui* microbial communities. Proteobacteria was the dominant phylum with relative abundances from 59.55% to 71.82%. Five phyla, Planctomycetes, Acidobacteria, Chloroflexi, Actinobacteria, and

Bacteroidetes, were subdominant populations (with abundances from 1% to 10%). The stabilization of *Taisui* communities was also found at other taxonomic levels. At the family level, most taxa (>80%) were common in all samples (Figure 1(c)). Twelve families—containing Caulobacteraceae, Sphingomonadaceae, Bradyrhizobiaceae, etc.—were enriched in samples with more than 1% relative abundance in at least one sample (Figure 1(b)). However, diversities emerged in family distribution. For example, TS.JZ1 had more than 2 fold abundance of Bradyrhizobiaceae compared with other samples; TS.BT and TS.XJ had more than 2 fold abundance of Sinobacteraceae compared with samples from Liaoning (Figure 1(b)).

Taisui from the same location (TS.JZ1 and TS.JZ2) had similar microbial composition. Simpson index in TS.JZ1 was the same as TS.JZ2, while Simpson index in TS.BT was the same as TS.XJ. Shannon index shows more diversity among samples, but indicates the same trend as Simpson index (Figure 1(d)). Besides, the UPGMA tree based on beta diversity illustrates TS.JZ1 and TS.JZ2 as one clade (Figure 1(d)).

3.2. Metagenome-Assembled Genomes

3.2.1. Assembly of 97 Draft Genomes. We generated 97 metagenome-assembled genomes (MAGs) with completeness $\geq 70\%$ and contamination $\leq 5\%$. According to Bowers et al. [37], 65 MAGs were high-quality drafts. Among them, 43 bins were preferable with >95% completeness and <5% contamination, and 2 bins were almost complete with >97% completeness and 0% contamination. All MAGs had at least 6 \times average coverage depth, and 6 Proteobacteria MAGs had more than 100 \times coverage (Figure 2). Our MAGs were taxonomically assigned to 13 microbial phyla by GTDB-Tk (Figure 2). Notably, 2 MAGs belonged to the bacteria candidate phylum.

We obtained 95 putative novel species (ANI between MAG vs. reference genome < 95% and 67 MAGs without closest placement ANI), and 97 putative novel strains (ANI < 99%), according to the standard suggested by Glendinning et al. [29]. Besides, metagenomic databases provided 39 putative novel genera from 43 MAGs (MAGs which clustered at 60% mean AAI (amino acid identity) did not have a genus assignment by GTDB-Tk [30]). Putative novel genera belonged to 8 phyla involving Proteobacteria, Planctomycetes, Chloroflexi, Acidobacteria, Bacteroidota, Bdellovibrionota, Gemmatimonadota, and Verrucomicrobiota.

3.2.2. Novel Genus-Level Lineages. Two novel genus-level lineages were found in *Taisui* database, based on the standards: (1) they formed monophyletic lineages in the phylogeny, and (2) the average AAI was 60-80% between the genomes of such lineages and was <55% compared with known genera [30, 38].

In the tree of Planctomycetes members, we defined one genus-level novel lineage within the Planctomycetia class (Figure 3(a)). This lineage involved TS_28 (average coverage depth 24 \times) and Planctomycetiales bacterium (GCF_009177095), with 66.4% AAI between members of it. The

TABLE 1: Summary of shotgun sequencing and assembly statistics.

	TS.JZ1	TS.JZ2	TS.BT	TS.XJ
Clean data size (Gb)	6.4	6.7	7.1	7.1
Clean_Q20	98.66	97.48	97.09	97.52
Clean_Q30	96.55	93.37	92.36	93.41
Number of high quality paired-end reads	45,183,937	43,169,867	44,363,607	45,284,710
Total number of bases	6,777,590,550	6,475,480,050	6,654,541,050	6,792,706,500
Number of contigs (≥ 500 bp)	391,852	533,634	419,397	479,713
Total contig length (bp)	472,635,294	637,814,029	686,512,143	702,537,509
Average contig size (bp)	1206	1195	1637	1464
Contig N50 (bp)	1339	1287	2465	1910
Largest contig size (bp)	290,257	1,977,463	851,561	1,021,402
Number of transcripts (Prokka)	711,761	820,620	776,716	824,658
Average transcripts length (bp)	473	514	624	585

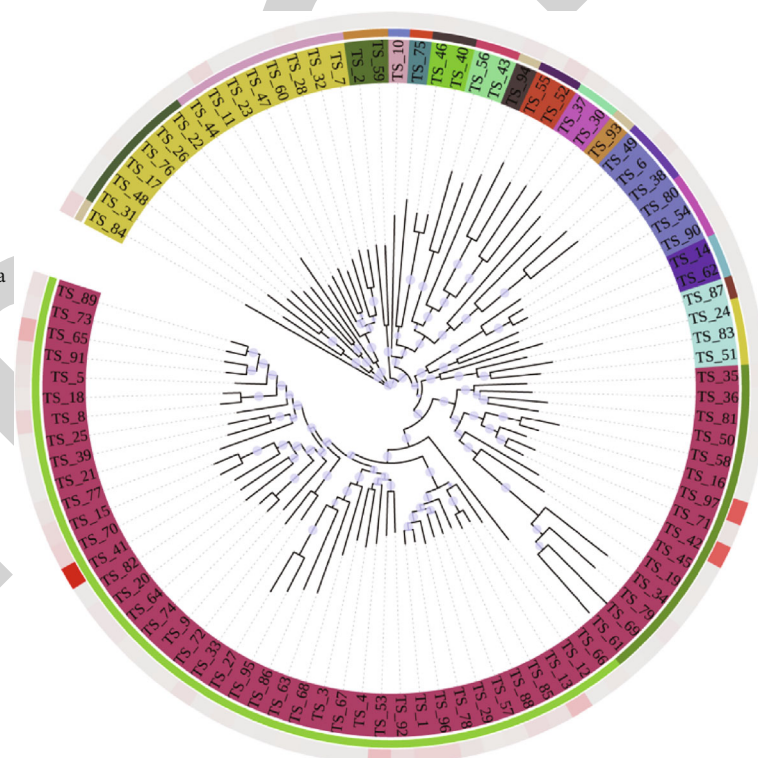
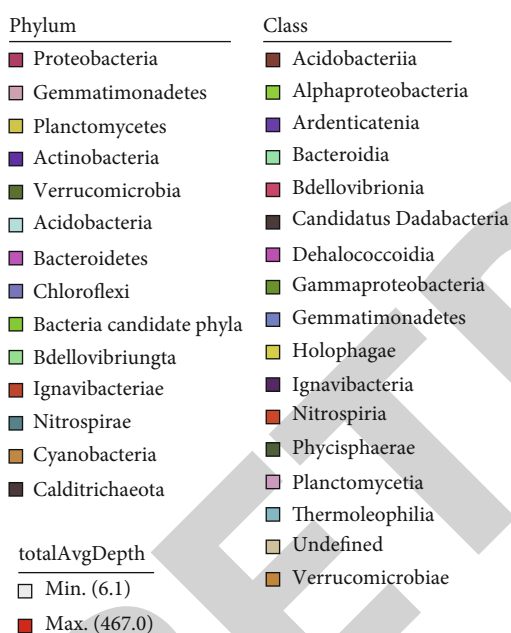


FIGURE 2: The maximum-likelihood tree among genomes recovered from Taisui samples. The MAGs were labelled by phylum and class, as assigned by GTDB-Tk. MAGs with “undefined” label were only able to be defined at phylum level. Branches with bootstrap that support more than 50% were denoted with a purple circle, which became larger as the bootstrap support value increases. The average coverage depth of all contigs in a bin was shown as heat map.

lineage—containing TS_28, GCF_009177095, TS_23 (7x), TS_47 (7x), and TS_60 (9x)—was a novel lineage at a higher taxonomic rank, because AAI between members ranged from 54.9% to 59.8%. Besides, the TS_84 (64x) may belong to a candidate novel class of Planctomycetes, which has shown AAI < 45% with other members of the Planctomycetes tree.

In the tree of Chloroflexi members, we defined one genus-level novel lineage within the Dehalococcoidia class (Figure 3(b)). It contained TS_80 (10x), TS_54 (13x), TS_

90 (17x), and Dehalococcoidia bacterium UBA2991. The UBA2991 was identified in saline water as the unclassified Dehalococcoidia bacterium [39]. Members of this lineage show < 49% AAI with genomes of Dehalococcoidales order and Dehalogenimonas order, which suggests this lineage was at least genus-level [30].

3.2.3. *Novel Gene Clusters for Secondary Metabolite Biosynthesis.* Among our MAGs, 503 biosynthetic gene clusters (BGCs) were identified from 12 microbial phyla

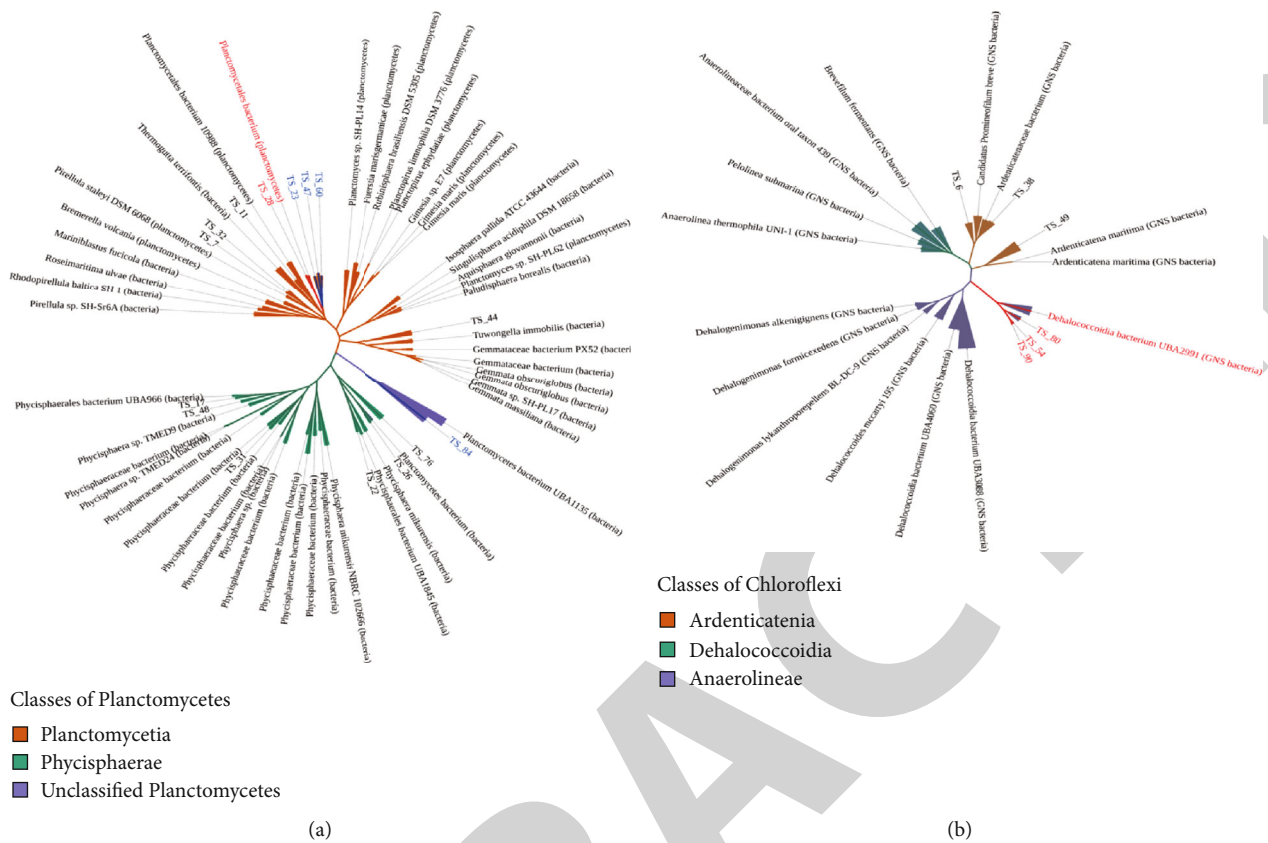


FIGURE 3: Placement of the Planctomycetes (a) and Chloroflexi (b) MAGs into their phylogenetic context. The trees included MAGs and published genomes with the completeness $\geq 70\%$ and were inferred using RAXML-NG with 100 bootstrap replicates. Only branches with bootstrap support values $\geq 50\%$ were shown. The MAGs were labelled at the class level. Genus-level novel branches were shown in red. Novel branches at higher level than genus were shown in purple.

(Figure 4(a)). Our BGCs included 22 kinds of types, containing polyketide synthases (PKSs), nonribosomal peptide synthases (NRPSs), synthases of linear azole-containing peptides (LAP), etc. Proteobacteria are linked with most types of BGCs ($n = 18$), followed by Planctomycetes ($n = 12$), Chloroflexi ($n = 10$), and Acidobacteria ($n = 10$).

MAGs provided BGCs that relate to new drug development. We identified 167 PKS (types I and III), NRPS, NRPS-like, and NRPS-PKS gene clusters from 8 phyla. Searching against the MIBiG database, 149 NRPS, NRPS-like, and PKS gene clusters had the potential structural divergence of their products with known biosynthetic genes, because these BGCs showed $<60\%$ similarity with known clusters [40].

In the Chloroflexi phylum, *Candidatus Promineofilum* sp. TS_38 had unusually large repertoires of NRPS (include NRPS-like clusters) or PKS regions. TS_38 contained 14 targeted biosynthetic loci (754.9 kbp in total length) in 7.3 Mbp contigs. The largest interested region was 108.2 kbp. Seven regions were complex NRPS-type I PKS systems (involving hybrid, neighboring, or interleaved) in TS_38 (Figure 4(b)).

In the Planctomycetes phylum, MAGs of novel lineage—including TS_28, TS_23, TS_47, and TS_60—were identified with PKS or NRPS loci. The phylogenetic tree reveals that the NRPS-like and T3PKS gene clusters were commonly observed in the closest reference genomes, but

the NRPS and T1PKS gene clusters were only observed in the *Taisui* MAGs (Figure 4(c)).

3.3. PVA Degradation

3.3.1. Novel Putative PVA Dehydrogenase Genes. *Taisui* metagenomic database provided 264 putative PVA dehydrogenase gene based on the KEGG database. Most of PVA dehydrogenase genes were derived from Proteobacteria (208), followed by Acidobacteria (29) and Actinobacteria (21). To understand the evolution of the PVA dehydrogenase genes, we built the phylogenetic tree using protein sequences of our putative genes (length > 500 bp) and all 3 PVA dehydrogenase sequences from NCBI. The phylogenetic tree shows that PVA dehydrogenase may have been ancestral in Proteobacteria, Acidobacteria, and Actinobacteria phyla (Figure 5). PVA dehydrogenase in Deltaproteobacteria members (including Deltaproteobacteria bacterium and *Phenylobacterium* sp.) may be gained via horizontal gene transfer from members of Actinobacteria. One species of Planctomycetes had PVA dehydrogenase, which was placed between clades of Actinobacteria.

3.3.2. Putative Pyrroloquinoline-Quinone Synthase Genes. In PVA degradation, pyrroloquinoline quinone (PQQ) is presumed to be needed for PVA dehydrogenase [2]. To identify

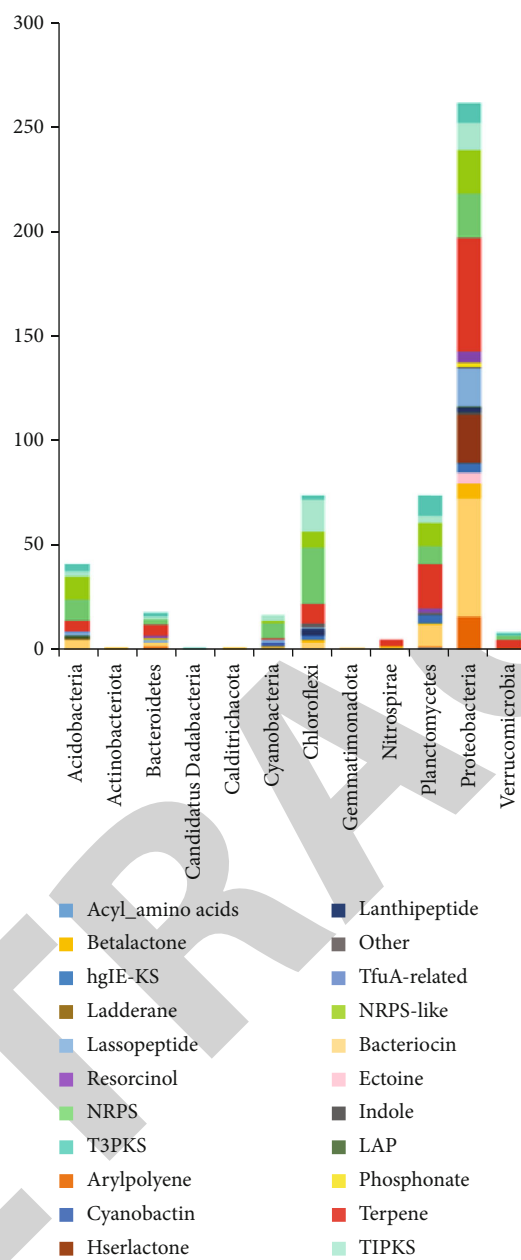


FIGURE 4: Continued.

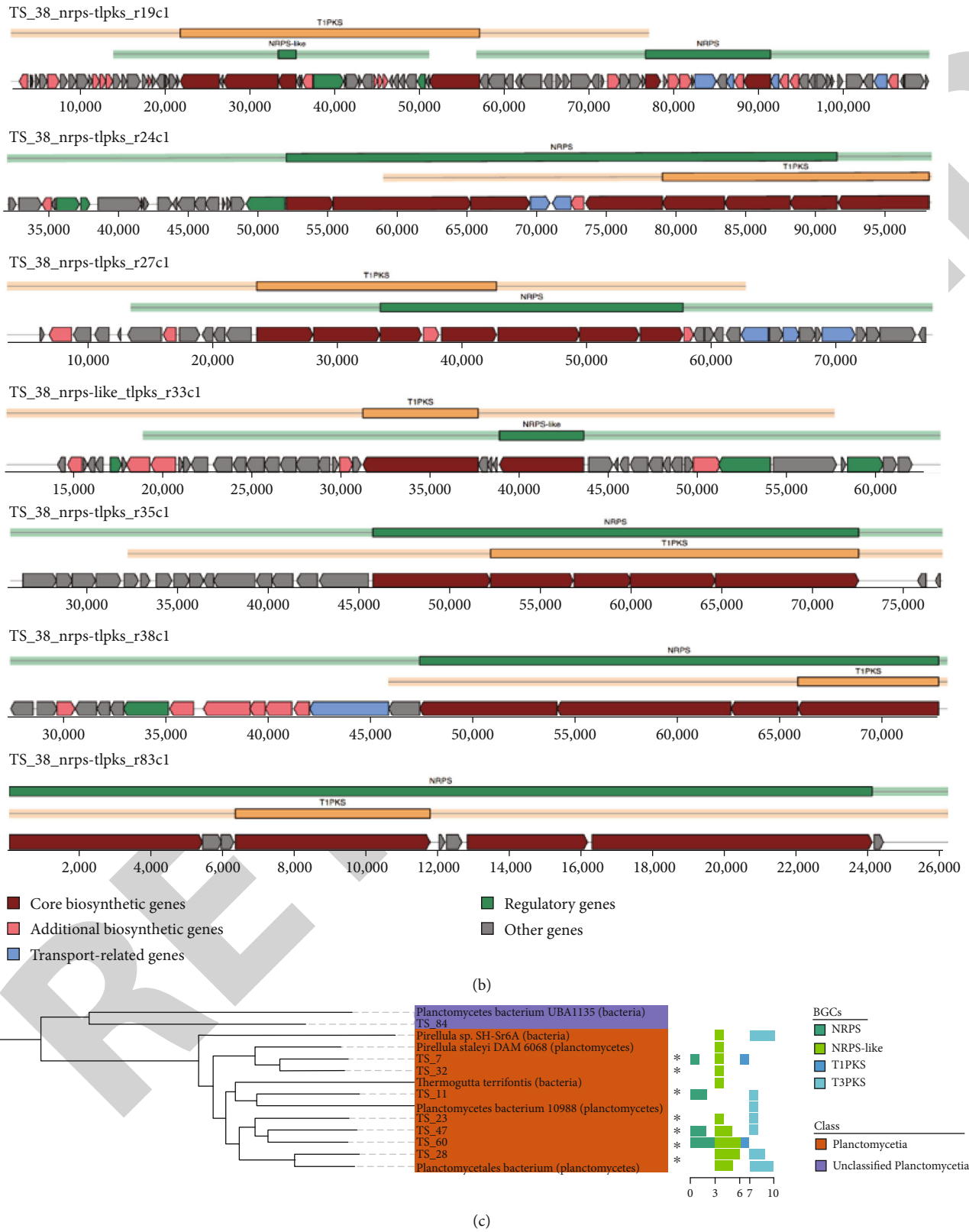


FIGURE 4: Predicted biosynthetic gene clusters from the Taisui MAGs: (a) biosynthetic gene clusters (BGCs) identified on MAG sequences were summed as phyla on the y axis and were colored by product types as the results of antiSMASH, (b) seven large PKS-NRPS hybrid or neighboring or interleaved gene clusters in the Candidatus Promineofilum sp. TS_38 genome were shown, and (c) phylogenetic tree of Planctomycetia MAGs with predicted PKS or NRPS clusters (*) and closest reference genomes of them (counts of PKS or NRPS clusters was shown in the bar plot).

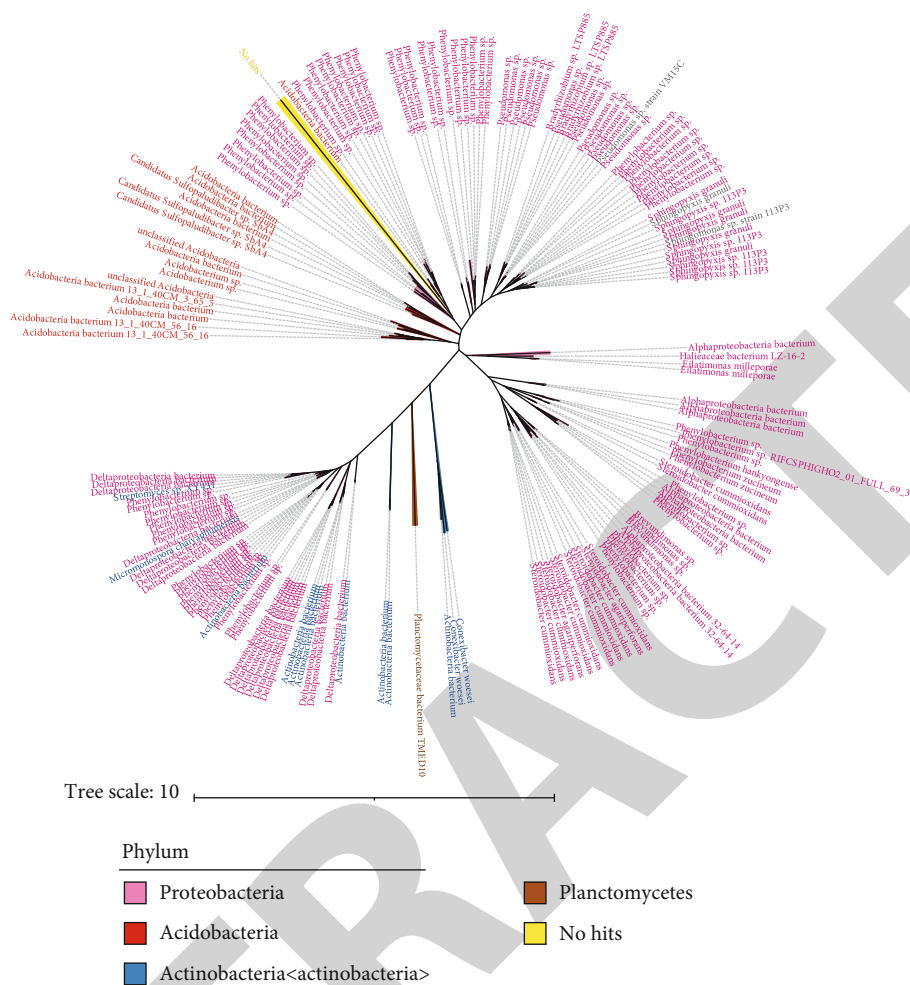


FIGURE 5: The maximum-likelihood tree of protein sequences of PVA dehydrogenase. Sequences from NCBI were shown in gray.

microbial symbiotic during PVA degradation, we assigned putative PQQ synthase genes to taxon. More than half of PQQ synthase genes were derived from Proteobacteria. *Bradyrhizobium icene* provided most amount of PQQ synthase (387), followed by *Chlorobi bacterium* OLB5 (164) and *Novosphingobium nitrogenifigens* (137). The result shows the difference of providers for PVA dehydrogenase and PQQ synthase in *Taisui* systems.

4. Discussion

4.1. *The Relative Stable Microbial System in Taisui.* In the present work, we gave the first standard of *Taisui* metagenome through shotgun sequencing of four samples. According to the analysis of 228 *Taisui* finding-reports, *Taisui* mainly exists in the soil layer of northern China [4]. Therefore, we chose four soil existed *Taisui* samples from northern China with stable morphology for better representation (microscopic observations in Figure S1). The taxonomic analysis illustrates a relatively consistent microbial community structure in different *Taisui* samples. *Taisui* samples from the same location had closer community structures. Biogeographic patterns of bacteria had been identified in soil metagenomes, which are more related to

environmental variation [41]. The taxonomic variation between *Taisui* samples may also be influenced by environmental variations, for example, precipitation (TS.JZ1 and TS.JZ2 were from subhumid regions; TS.BT was from the semiarid region; TS.XJ was from the arid region). Besides, dominant taxa in *Taisui* were common taxa in soil metagenomes. Marker gene amplification of *Taisui* also illustrates the same phenomenon [3]. It is reasonable because we used soil existed *Taisui*.

The functional annotation shows almost the same relative abundances of functional classifications of *Taisui* samples (Figure S2 and S3). The functional stability was also identified in human gut microbiota, which indicates the existence of a relatively stable ecological system [42]. Reconstruction of meta-pathway illustrated *Taisui* communities as carbon fixation, nitrogen fixation, and biosynthesis (Figure 6). At the family level, Caulobacteraceae, Sinobacteraceae, and Sphingomonadaceae contributed more than 30% related genes of the reductive citric acid cycle (rTCA cycle), while Burkholderiales, Xanthobacteraceae, Sphingomonadaceae, and Bradyrhizobiaceae contributed almost half of the N-fixation enzymes on average. The difference between functional providers of carbon fixation and nitrogen fixation may suggest the symbiosis between microbes

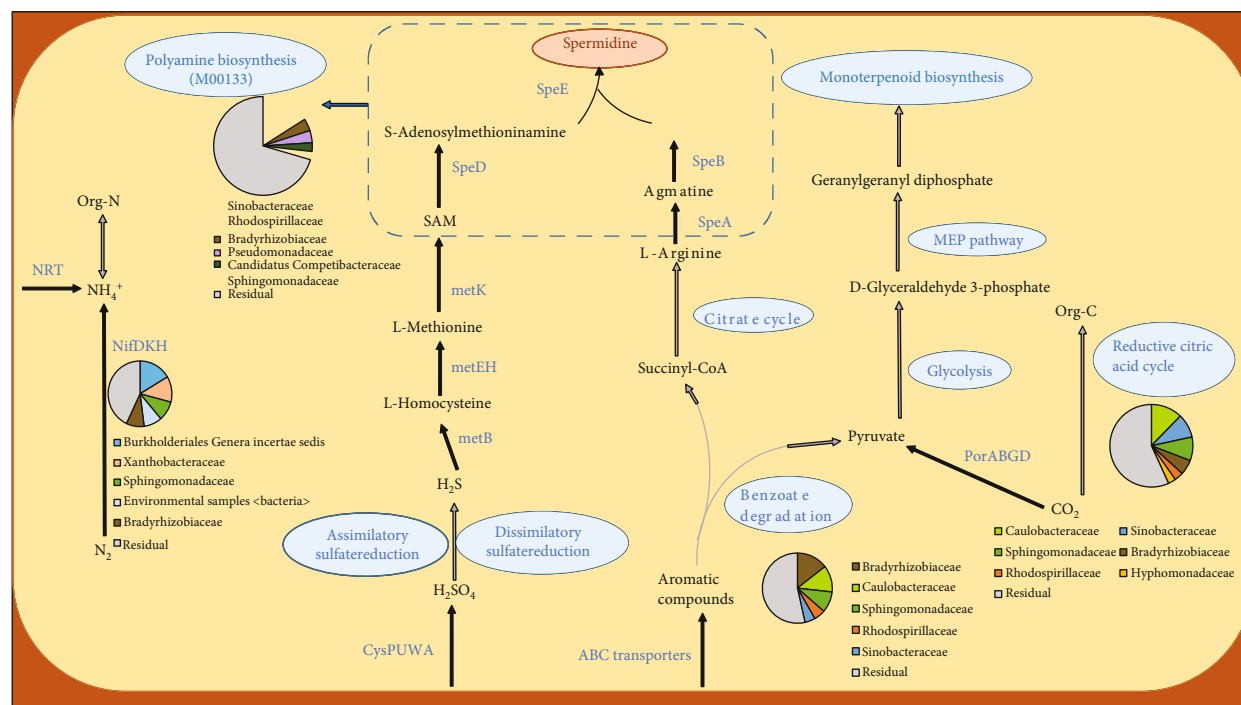


FIGURE 6: The sketch map of the metabolic pathways reconstructed from genes of Taisui samples (based on Figure S4–S7). The pie charts, which beside the names of enzymes or pathways, show the contribution ratio of taxa at family level. Abbreviations: NRT: ammonium transporter; NifDKH: nitrogenase; metB: cystathionine gamma-synthase; metE: 5-methyltetrahydropteroyltriglutamate-homocysteine methyltransferase; metH: 5-methyltetrahydrofolate-homocysteine methyltransferase; metK: S-adenosylmethionine synthetase; SepD: S-adenosylmethionine decarboxylase; SepA: arginine decarboxylase; SepB: agmatinase; SepE: spermidine synthase; PorABGD: pyruvate ferredoxin oxidoreductase; SAM: S-Adenosylmethionine; CysPUWA: sulfate transporters; ABC transporters: ATP-binding cassette transporters; MEP: 2-C-methyl-D-erythritol-4-phosphate.

in the *Taisui* community. However, more samples are needed for reliable cooccurrence network analysis [43].

4.2. Expanded Diversity of Microbial Genome and Biosynthetic Gene Cluster. Historical changes in population size, such as those caused by demographic range expansions, can produce nonadaptive changes in genomic diversity through mechanisms such as gene surfing. Microbial species and their populations exhibit remarkable genomic diversity [44]. While mutation and recombination promote genetic variation in all forms of life, the genomic diversity of Bacteria and Archaea is enhanced dramatically by their proclivity for Horizontal Gene Transfer (HGT). Genomic analyses of diverse microbes provide similar results and it seems that a majority of genes in any pan-genome will be comprised of either high-frequency core genes or low-frequency strain-specific genes. These patterns of genomic diversity reveal the fundamental impact of HGT on evolution, and they suggest that bacterial and archaeal genomes comprise a dynamic mosaic of horizontally acquired genes whose frequency fluctuates in the population in response to both selection and genetic drift.

Our MAGs filled in some phylogenetic gaps and could be valuable in the detail inferring of phylogenetic relationships in bacterial. The MAGs for novel genera include taxa with very little genomic information published. One novel genus belonging to Proteobacteria was assigned to the Steroidobacteraceae family, and this family has only 9 published

genomes in NCBI. In the Chloroflexi phylum, we identified one novel genus in each of the classes Dehalococcoidia and Ardenticatenia. The Dehalococcoidia contain only 2 formally published genera, involving Dehalococcoides and Dehalogenimonas [45]. And the Ardenticatenia class only had been identified in sludge and hydrothermal field [46–49] with 8 published genome on NCBI. In the Acidobacteria phylum, 3 novel genera of the Holophagales order were identified. The Holophagales order only contains the genera *Holophaga* and *Geotes* with a wide range of uncultured bacteria mainly from marine and soil [50].

Our MAGs also included novel gene clusters of NRPS, NRPS-like, and PKS (89.2% gene clusters < 60% similarity with known BGCs). Most of identified BGCs were linked with Proteobacteria, which is a common producer of wide bacterial natural products [51–53]. But few BGCs were reported in the published genomes of bacteria candidate phyla [54, 55]. We expand the number of taxa in Candidatus Dadabacteria phylum encoding BGCs. Besides, 2 MAGs of the Ardenticatenaceae family (belonging to Chloroflexi phylum) were detected with large NRPS or PKS loci, which were referred to as “*Candidatus Promineofilum* sp. TS_6” and “*Candidatus Promineofilum* sp. TS_38.” The BGCs linked to Ardenticatenaceae were few (6 linked clusters in total), according to the IMG database [54]. We expand Ardenticatenaceae with potential productions of PKS and NRPS. The large NRPS and PKS loci may provide source for new drug finding.

According to the phylogenetic tree of Planctomycetes members, NRPS and T1PKS were only observed in *Taisui* MAGs (novel lineage including TS_23, TS_47, TS_60, and TS_28). This result suggests that these two types of BGCs were acquired independently in evolutionary time in these taxa. The products of BGCs were used for the competition or communication with the producers' environment, and the abundance of NRPS and PKS domains was influenced by environmental conditions, involving soil depth, latitude, moisture, etc. [55, 56]. Therefore, the unconventional environment offered by *Taisui* may cause the encoding of NRPS and T1PKS gene clusters in these MAGs.

4.3. Rich Diversity of PVA Dehydrogenase Genes in the *Taisui* Microbial Community. PVA degradation includes two steps: first, the conversion from the 1,3-glycol structure of two successive repeating units to the beta-diketone; second, the broken of the carbon-carbon bond and the conversion of ketone group to carboxylic group [57]. In *Taisui* systems, the first step may begin with PQQ and PVA dehydrogenase, according to the functional annotation. *Taisui* has high water content, so the carbon-carbon bond may be cleavage by oxidized PVA hydrolase with H₂O participation, like the model illustrated in methylotrophic yeast [58].

Microbes with PVA degradation ability are rare. Most PVA-degraders belong to the *Pseudomonas* and *Sphingomonas* genera. Although with novel degraders identified from grapes and marine bacterium [2], the taxonomic survey of PVA-degraders is not fruitful. Our results of putative PVA-degraders from 4 phyla can be a markable expansion for PVA biodegradation. Genera involving *Phenylobacterium*, *Conexibacter*, *Steroidobacter*, *Brevundimonas*, *Eilatimonas*, *Sphingopyxis*, and *Acidobacterium* may also be the source of PVA-degraders.

For PQQ-dependent PVA dehydrogenase, PVA degradation begins with the action of PQQ [2]. The production of PQQ by microbes (involving *Bradyrhizobium*, *Novosphingobium*, *Rhodopseudomonas*, etc.) can enhance the rate of PVA degradation. Besides, PVA dehydrogenase and PQQ synthase were abundant in different species, which suggests the microbial dependency on PVA degradation in *Taisui*.

5. Conclusion

According to metagenomic analysis, we concluded that the community structure of polymeric compound *Taisui* was relatively stable. The high abundances of Proteobacteria, Acidobacteria, Chloroflexi, Actinobacteria, and Bacteroidetes in *Taisui* can also be identified in the soil microbial community, suggesting the close relationship of *Taisui* and soil. As a unexplored system, *Taisui* communities provide genomes of previously poorly sampled microbial lineages, which is a valuable step for a comprehensive picture of the evolutionary history of life. For new drug development, BGCs of PKS and NRPS were expanded in phyla including Candidatus Dadabacteria, Chloroflexi, and Planctomycetes. The substantial putative PVA dehydrogenase genes were identified in 4 phyla, suggesting rich diversity of PVA dehydrogenase genes in *Taisui* communities. The gene of PVA

degradation in microbes may acquire independently or from horizontal gene transfer. And the PQQ providers may enhance the PVA degradation rate in *Taisui*.

Data Availability

Sequences in this paper have been submitted to NCBI with SRA accession numbers SRR8569139-SRR8569142.

Conflicts of Interest

The authors declare that they have no conflicts of interest.

Authors' Contributions

Jiaxing Liu did the conceptualization, methodology, investigation, writing—original draft, and funding acquisition. Jiaxing Liu did the validation, writing—review and editing. Jiaxing Liu did the visualization. Jiaxing Liu did the supervision and writing—review and editing. Xun Gu did the conceptualization, supervision, and writing—review and editing. Hui Li did the conceptualization, writing—review and editing, supervision, and funding acquisition.

Acknowledgments

We thank Mr. Cao Dongsheng for the collection of *Taisui* samples. This work was supported by the Shanghai Ziraner-nan Natural Medicine Development Foundation (ZRER201501), B&R Joint Laboratory of Eurasian Anthropology (18490750300), and the National Key R&D Program of China (2020YFE0201600).

Supplementary Materials

Figure S1: microscopic observations of *Taisui* tissues. (a) The histological imprints of a piece of *Taisui* tissue. (b) The histological sections stained with hematoxylin and eosin (HE) of *Taisui* tissues. Figure S2: the relative abundance (%) of KEGG based annotations in *Taisui* samples. The relative abundances of the level 1 classification of KEGG in four samples. (b) The relative abundances of the level 2 classification of KEGG in four samples (classifications with relative abundance above 1% are shown). Figure S3: the relative abundance (%) of COG-based annotations in *Taisui* samples. The relative abundances of the level 1 classification of COG in four samples. (b) The relative abundances of the level 2 classification of COG in four samples. Figure S4: the enrichment of carbon fixation pathways in four *Taisui* samples. Each node was divided into four blocks vertically, representing TS.JZ1, TS.JZ2, TS.BT, and TS.XJ in order from left to right. The colors of blocks represent the count of transcripts that annotated to this function, and the red block represents the transcripts number ≥ 500 . Figure S5: the enrichment of benzoate degradation pathways in four *Taisui* samples. Each node was divided into four blocks vertically, representing TS.JZ1, TS.JZ2, TS.BT, and TS.XJ in order from left to right. The colors of blocks represent the count of transcripts that annotated to this function, and the red block represents the transcripts number ≥ 500 . Figure S6: the enrichment of nitrogen metabolism pathways in four *Taisui*

samples. Each node was divided into four blocks vertically, representing TS.JZ1, TS.JZ2, TS.BT, and TS.XJ in order from left to right. The colors of blocks represent the count of transcripts that annotated to this function, and the red block represents the transcripts number ≥ 500 . Figure S7: the enrichment of terpenoid backbone biosynthesis pathways in four *Taisui* samples. Each node was divided into four blocks vertically, representing TS.JZ1, TS.JZ2, TS.BT, and TS.XJ in order from left to right. The colors of blocks represent the count of transcripts that annotated to this function, and the red block represents the transcripts number ≥ 500 . (*Supplementary Materials*)

References

- [1] M. Amann and O. Minge, "Biodegradability of poly(vinyl acetate) and related polymers," in *Synthetic Biodegradable Polymers*, *Advances in Polymer Science*, B. Rieger, A. Künkel, G. W. Coates, R. Reichardt, E. Dinjus, and T. A. Zevaco, Eds., pp. 137–172, Springer, Berlin, Heidelberg, 2011.
- [2] N. B. Halima, "Poly(vinyl alcohol): review of its promising applications and insights into biodegradation," *RSC Advances*, vol. 6, no. 46, pp. 39823–39832, 2016.
- [3] E. Li, J. Ren, Q. Chen et al., "Uncovering the mysterious identity of Taisui—an old Chinese folk legend," *Science China. Life Sciences*, vol. 63, no. 12, pp. 1942–1945, 2020.
- [4] C. Wang and S. Wang, "A research of the finding and distribution law of Taisui in modern China," *Agricultural Sciences*, vol. 6, no. 4, pp. 407–414, 2015.
- [5] M. Albertsen, P. Hugenholtz, A. Skarshewski, K. L. Nielsen, G. W. Tyson, and P. H. Nielsen, "Genome sequences of rare, uncultured bacteria obtained by differential coverage binning of multiple metagenomes," *Nature Biotechnology*, vol. 31, no. 6, pp. 533–538, 2013.
- [6] L.-X. Chen, K. Anantharaman, A. Shaiber, A. M. Eren, and J. F. Banfield, "Accurate and complete genomes from metagenomes," *Genome Research*, vol. 30, no. 3, pp. 315–333, 2020.
- [7] M. R. Green and J. Sambrook, "Isolation of high-molecular-weight DNA using organic solvents," *Cold Spring Harbor Protocols*, vol. 2017, no. 4, 2017.
- [8] R. K. Patel and M. Jain, "NGS QC toolkit: a toolkit for quality control of next generation sequencing data," *PLoS One*, vol. 7, no. 2, article e30619, 2012.
- [9] P. Ewels, M. Magnusson, S. Lundin, and M. Käller, "MultiQC: summarize analysis results for multiple tools and samples in a single report," *Bioinformatics*, vol. 32, no. 19, pp. 3047–3048, 2016.
- [10] D. Li, C.-M. Liu, R. Luo, K. Sadakane, and T.-W. Lam, "MEGAHIT: an ultra-fast single-node solution for large and complex metagenomics assembly via succinct de Bruijn graph," *Bioinformatics*, vol. 31, no. 10, pp. 1674–1676, 2015.
- [11] A. Gurevich, V. Saveliev, N. Vyahhi, and G. Tesler, "QUAST: quality assessment tool for genome assemblies," *Bioinformatics*, vol. 29, no. 8, pp. 1072–1075, 2013.
- [12] T. Seemann, "Prokka: rapid prokaryotic genome annotation," *Bioinformatics*, vol. 30, no. 14, pp. 2068–2069, 2014.
- [13] L. Fu, B. Niu, Z. Zhu, S. Wu, and W. Li, "CD-HIT: accelerated for clustering the next-generation sequencing data," *Bioinformatics*, vol. 28, no. 23, pp. 3150–3152, 2012.
- [14] W. Li and A. Godzik, "Cd-hit: a fast program for clustering and comparing large sets of protein or nucleotide sequences," *Bioinformatics*, vol. 22, no. 13, pp. 1658–1659, 2006.
- [15] R. Patro, G. Duggal, M. I. Love, R. A. Irizarry, and C. Kingsford, "Salmon provides fast and bias-aware quantification of transcript expression," *Nature Methods*, vol. 14, no. 4, pp. 417–419, 2017.
- [16] B. Buchfink, C. Xie, and D. H. Huson, "Fast and sensitive protein alignment using DIAMOND," *Nature Methods*, vol. 12, no. 1, pp. 59–60, 2015.
- [17] D. H. Huson, S. Beier, I. Flade et al., "MEGAN community edition - interactive exploration and analysis of large-scale microbiome sequencing data," *PLoS Computational Biology*, vol. 12, no. 6, article e1004957, 2016.
- [18] J. Huerta-Cepas, D. Szklarczyk, K. Forslund et al., "eggNOG 4.5: a hierarchical orthology framework with improved functional annotations for eukaryotic, prokaryotic and viral sequences," *Nucleic Acids Research*, vol. 44, no. D1, pp. D286–D293, 2016.
- [19] B. L. Cantarel, P. M. Coutinho, C. Rancurel, T. Bernard, V. Lombard, and B. Henrissat, "The carbohydrate-active enzymes database (CAZy): an expert resource for glycogenomics," *Nucleic Acids Research*, vol. 37, no. Database, pp. D233–D238, 2009.
- [20] D. H. Huson and D. Bryant, "Application of phylogenetic networks in evolutionary studies," *Molecular Biology and Evolution*, vol. 23, no. 2, pp. 254–267, 2006.
- [21] I. Letunic and P. Bork, "Interactive tree of life (iTOL) v3: an online tool for the display and annotation of phylogenetic and other trees," *Nucleic Acids Research*, vol. 44, no. W1, pp. W242–W245, 2016.
- [22] W. Luo and C. Brouwer, "Pathview: an R/Bioconductor package for pathway-based data integration and visualization," *Bioinformatics*, vol. 29, no. 14, pp. 1830–1831, 2013.
- [23] G. V. Urutskiy, J. DiRuggiero, and J. Taylor, "MetaWRAP—a flexible pipeline for genome-resolved metagenomic data analysis," *Microbiome*, vol. 6, no. 1, p. 158, 2018.
- [24] D. H. Parks, M. Imelfort, C. T. Skennerton, P. Hugenholtz, and G. W. Tyson, "CheckM: assessing the quality of microbial genomes recovered from isolates, single cells, and metagenomes," *Genome Research*, vol. 25, no. 7, pp. 1043–1055, 2015.
- [25] P.-A. Chaumeil, A. J. Mussig, P. Hugenholtz, and D. H. Parks, "GTDB-Tk: a toolkit to classify genomes with the genome taxonomy database," *Bioinformatics*, vol. 36, pp. 1925–1927, 2019.
- [26] D. Parks, "CompareM," 2016, <https://github.com/dparks1134/CompareM>.
- [27] R. A. Barco, G. M. Garrity, J. J. Scott, J. P. Amend, K. H. Nealson, and D. Emerson, "A genus definition for Bacteria and Archaea based on a standard genome relatedness index," *mBio*, vol. 11, no. 1, 2020.
- [28] L. Pritchard, R. H. Glover, S. Humphris, J. G. Elphinstone, and I. K. Toth, "Genomics and taxonomy in diagnostics for food security: soft-rotting enterobacterial plant pathogens," *Analytical Methods*, vol. 8, no. 1, pp. 12–24, 2015.
- [29] L. Glendinning, R. D. Stewart, M. J. Pallen, K. A. Watson, and M. Watson, "Assembly of hundreds of novel bacterial genomes from the chicken caecum," *Genome Biology*, vol. 21, no. 1, p. 34, 2020.
- [30] C. Luo, L. M. Rodriguez-R, and K. T. Konstantinidis, "MyTaxa: an advanced taxonomic classifier for genomic and

Retraction

Retracted: Effects of Pulmonary Surfactant Combined with Noninvasive Positive Pressure Ventilation on KRT-14 and ET-1 Levels in Peripheral Blood and Therapeutic Effects in Neonates with Respiratory Distress Syndrome

BioMed Research International

Received 12 March 2024; Accepted 12 March 2024; Published 20 March 2024

Copyright © 2024 BioMed Research International. This is an open access article distributed under the Creative Commons Attribution License, which permits unrestricted use, distribution, and reproduction in any medium, provided the original work is properly cited.

This article has been retracted by Hindawi following an investigation undertaken by the publisher [1]. This investigation has uncovered evidence of one or more of the following indicators of systematic manipulation of the publication process:

- (1) Discrepancies in scope
- (2) Discrepancies in the description of the research reported
- (3) Discrepancies between the availability of data and the research described
- (4) Inappropriate citations
- (5) Incoherent, meaningless and/or irrelevant content included in the article
- (6) Manipulated or compromised peer review

The presence of these indicators undermines our confidence in the integrity of the article's content and we cannot, therefore, vouch for its reliability. Please note that this notice is intended solely to alert readers that the content of this article is unreliable. We have not investigated whether authors were aware of or involved in the systematic manipulation of the publication process.

Wiley and Hindawi regrets that the usual quality checks did not identify these issues before publication and have since put additional measures in place to safeguard research integrity.

We wish to credit our own Research Integrity and Research Publishing teams and anonymous and named external researchers and research integrity experts for contributing to this investigation.

The corresponding author, as the representative of all authors, has been given the opportunity to register their agreement or disagreement to this retraction. We have kept a record of any response received.

References

- [1] L. Huang, H. Liang, L. Liu, Y. Lin, and X. Lin, "Effects of Pulmonary Surfactant Combined with Noninvasive Positive Pressure Ventilation on KRT-14 and ET-1 Levels in Peripheral Blood and Therapeutic Effects in Neonates with Respiratory Distress Syndrome," *BioMed Research International*, vol. 2021, Article ID 4117800, 7 pages, 2021.

Research Article

Effects of Pulmonary Surfactant Combined with Noninvasive Positive Pressure Ventilation on KRT-14 and ET-1 Levels in Peripheral Blood and Therapeutic Effects in Neonates with Respiratory Distress Syndrome

Lihan Huang,^{1,2} Hong Liang,^{1,2} Longbin Liu,^{1,2} Yucong Lin,^{1,2} and Xinzhu Lin ^{1,2}

¹Department of Neonatology, Women and Children's Hospital, School of Medicine, Xiamen University, Xiamen 361003, China

²Xiamen Key Laboratory of Perinatal-Neonatal Infection, Xiamen, 361003 Fujian Province, China

Correspondence should be addressed to Xinzhu Lin; zhutu313959@163.com

Received 21 April 2021; Revised 24 July 2021; Accepted 26 July 2021; Published 31 October 2021

Academic Editor: Tao Huang

Copyright © 2021 Lihan Huang et al. This is an open access article distributed under the Creative Commons Attribution License, which permits unrestricted use, distribution, and reproduction in any medium, provided the original work is properly cited.

This study is aimed at exploring the effect of pulmonary surfactant (PS) combined with noninvasive positive pressure ventilation on the levels of Keratin-14 (KRT-14) and Endothelin-1 (ET-1) in peripheral blood and the therapeutic effect of neonatal respiratory distress syndrome (NRDS). Altogether 137 cases of neonates with respiratory distress syndrome treated in our hospital from April 2016 to July 2018 were collected. Among them, 64 cases treated with noninvasive positive pressure ventilation were considered as the control group, and 73 cases treated with PS combined with noninvasive positive pressure ventilation were considered as the observation group. The expression of KRT-14 and ET-1 in the two groups was compared. The therapeutic effect, death, complications, and blood gas indexes PaO₂, PaCO₂, and PaO₂/FiO₂ in the two groups were compared. Receiver operating characteristic curve (ROC) was applied to analyze the diagnostic value of KRT-14 and ET-1 in the therapeutic effect of NRDS. The effective rate of the observation group was higher than that of the control group. After treatment, PaO₂ and PaO₂/FiO₂ in both groups were notably higher than that before treatment, while PaCO₂ was notably lower than that before treatment. And after treatment, the levels of PaO₂ and PaO₂/FiO₂ in the observation group were remarkably higher than that in the control group; PaCO₂ was notably lower than that in the control group. After treatment, the levels of KRT-14 and ET-1 in the two groups were remarkably lower than those before treatment, and the levels of KRT-14 and ET-1 in the observation group were considerably lower than those in the control group after treatment. ROC curve showed that the area under the curve (AUC) of KRT-14 was 0.791, and the AUC of ET-1 was 0.816. PS combined with noninvasive positive pressure ventilation can notably improve the therapeutic effect of NRDS. KRT-14 and ET-1 levels may be potential therapeutic diagnostic indicators.

1. Introduction

Neonatal respiratory distress syndrome (NRDS) is one of the most common diseases in neonatal intensive care unit, the incidence rate of which is about 7% among infants, and it is also one of the main causes of neonatal death in hospital in China [1, 2]. The main mechanism of the disease is hypoxemia and hypercapnia caused by lack of surfactant. The diffusion efficiency of oxygen through the alveolar-capillary exchange barrier is disturbed due to various factors, and lung injury in neonates will lead to asthma, septicemia, pneumo-

nia, and other complicated symptoms [3]. Premature delivery of pregnant women and pregnancy diseases may lead to morbidity. Only early diagnosis and treatment can improve the quality of life of neonates [4, 5].

Since the pathogenesis of NRDS is the lack of pulmonary surfactant, exogenous pulmonary surfactant (PS) replacement therapy is also found to be an effective treatment [6]. When neonates suffer from respiratory failure, respiratory support for them can also improve their condition. But invasive ventilation is easy to cause a series of complications such as lung infection, ventilator-associated lung injury, etc.,

which makes people pay wide attention to the clinical application of noninvasive ventilation [7]. It has been found in lots of studies that noninvasive positive pressure ventilation can significantly improve the condition of NRDS neonates and has good safety [8, 9]. At the same time, some studies also reveal that PS combined with noninvasive positive pressure ventilation can further improve the clinical efficacy [10].

Keratin-14 (KRT-14) is a cytoskeleton protein that has good diagnostic value for lung tissue injury [11]. A study by team of Confalonieri et al. [12] reported that KRT14 is a viable biomarker for activation and repair/regeneration of lung cells. It participates in the repair and regeneration of alveoli, and the alveoli collapsed, and lung cells were severely damaged in neonates with NRDS, so KRT14 may be used as an indicator of the improvement of the condition of neonates with RDS. Endothelin-1 (ET-1) is a vasoactive substance, which is mainly produced in lung tissue. It promotes the gradual change of pulmonary vascular reactivity through angiogenesis. It involves vascular regulation, bronchoconstriction, and inflammatory reaction in respiratory system. Endothelium and epithelial dysfunction in RDS patients can be caused by induction of proinflammatory mechanism. The use of endothelin receptor antagonist can regulate lung injury [13, 14]. The study of El's team [15] examined the plasma ET-1 concentration of 69 premature neonates aged 28 weeks to 34 weeks and diagnosed with NRDS. It is found that the ET-1 concentration on the 3rd day of birth increases significantly, and it has predictive value for whether the infant would develop bronchopulmonary dysplasia. At present, there is little research on the correlation of KRT-14 and ET-1 with curative effect of NRDS neonates.

Therefore, this study is aimed at providing the basis and direction for clinical research through PS combined with noninvasive positive pressure ventilation to treat NRDS neonates and observing the levels of KRT-14 and ET-1 in peripheral blood.

2. Materials and Methods

Totally 137 neonates with NRDS treated in our hospital from April 2016 to July 2018 were collected. All neonates were admitted to hospital for basic treatment such as keeping breathing smooth, anti-infection, and maintaining water and electrolyte balance. Among them, 64 infants were included in the control group, who received treatment of noninvasive positive pressure ventilation on the basis of basic treatment, including 37 males and 27 females. The other 73 infants received treatment of PS combined with noninvasive positive pressure ventilation on the basis of basic treatment were considered as the observation group, including 38 males and 35 females. The study was approved by the Medical Ethics Committee, and all parents of the infants were informed and signed the informed consent form.

2.1. Inclusion and Exclusion Criteria. For inclusion criteria, all neonates were diagnosed as NRDS by imaging, and the

diagnostic criteria were based on the European consensus guidelines on the management of respiratory distress syndrome-2016 update [16]. Newborns with complete clinical data and treatment.

For exclusion criteria, neonates had congenital immune defects. Neonates complicated with other respiratory diseases, acute infectious diseases, or liver and kidney insufficiency. Neonates were allergy to therapeutic drugs or methods.

2.2. Therapies. After admission, the two groups of neonates were treated with 21%-80% oxygen concentration, 6-8 L/min gas flow rate, and 4-7 CMH pressure. When CPAP decreased to 2-3 cmH₂O and oxygen concentration decreased to 25%, dyspnea was significantly relieved or disappeared; the treatment was terminated. If the oxygen concentration was >80%, the pressure was >6-7 cmH₂O, and the oxygen saturation was still <85% after 6-8 hours of treatment, or type II respiratory failure occurred, the treatment method was changed to mechanical ventilation. On the basis of the above, neonates in the observation group were injected with exogenous PS [17] into trachea as soon as possible.

2.3. Sample Collection and ELISA Detection. After the patient was admitted to hospital and at 7: 00 a.m. the next morning after treatment, 5 mL of sterile venous blood was collected and loaded into the coagulation tube. The serum was collected by centrifuge (3000 x g at 4°C for 10 min) and stored in the refrigerator at -80°C. The levels of KRT-14 and ET-1 were detected by ELISA. Blank well, standard sample well, and sample to be tested well were set up. S0 standard substance with the concentration of 0 was added into the blank well, and 50 μL of standard substance with different concentrations was added to the standard well. In the sample well, 10 μL of sample to be tested was firstly added to it and then added with sample diluent 40 μL. Nothing was added to the blank well. In addition to the blank wells, 100 μL of HRP labeled detection antibody was added to each of the standard wells and the sample wells. The reaction wells were sealed with a sealing plate membrane and incubated in a water bath at 37°C for 65 min. The liquid was discarded, and the absorbent paper was patted dry. Each well was filled with washing liquid and allowed to stand for 2 min. The washing liquid was thrown off, and the absorbent paper was patted dry. This procedure was repeated 6 times. Substrates A and B were added to each well, 50 μL each, and incubated at 37°C in the dark for 10 min. The OD value of each well was measured at 450 nm wavelength within 15 min after adding 50 μL of stop solution to each well. Calculate the concentration.

2.4. Efficacy Evaluation. For effective, after treatment, the clinical symptoms of the neonates disappeared or relieved, X-ray films showed that abnormal shadow areas of the lungs disappeared or improved, and blood gas indexes were normal or improved. For ineffective, after treatment, the clinical symptoms of the neonates became worse or did not improve or even died, X-ray films showed enlarged or not improved

TABLE 1: Clinical data.

	Observation group (n = 73)	Control group (n = 64)	X ² /t	p
Gender				
Male	38 (52.05)	37 (57.81)		
Female	35 (47.95)	27 (42.19)	0.456	0.499
Gestational age (weeks)	33.37 ± 2.12	32.87 ± 2.05	1.399	0.164
Body mass (kg)	2.82 ± 0.69	2.71 ± 0.58	1.002	0.318
Apgar score	8.47 ± 1.31	8.28 ± 1.26	0.862	0.390
Age of pregnant woman (years)	27.3 ± 4.8	26.5 ± 4.1	1.041	0.230
Hypertension of pregnant women	9 (12.33)	5 (7.81)	0.758	0.384
Diabetes of pregnant women	11 (15.07)	7 (10.94)	0.510	0.475
Premature rupture of membranes	9 (12.33)	10 (15.63)	0.310	0.578
Delivery mode				
Eutocia	41 (56.16)	40 (62.50)	0.566	0.452
Cesarean section	32 (43.84)	24 (37.50)		
Premature delivery				
Yes	52 (71.23)	41 (64.06)	0.804	0.370
No	21 (28.77)	23 (35.94)		
Delivery history				
Primiparity	50 (68.49)	43 (67.19)	0.027	0.870
Multiparity	23 (31.51)	21 (32.81)		

shadow areas, and blood gas indexes deteriorated or did not improve.

2.5. Outcome Measures. For main outcome measures, the expression of KRT-14 and ET-1 in the observation group and the control group was compared, and the therapeutic effect, death, and complications of the two groups were compared.

For secondary outcome measures, the clinical data of the two groups of neonates were compared. The blood gas indexes PaO₂, PaO₂, and PaO₂/FiO₂ of the two groups of neonates were compared. The diagnostic value of KRT-14 and ET-1 in the therapeutic effect of NRDS neonates was analyzed by using receiver operating characteristic curve (ROC).

2.6. Statistical Analysis. SPSS20.0 (SPSS, Chicago, USA) was utilized to carry out statistical analysis on the collected data. GraphPad Prism 7 (GraphPad, San Diego, USA) was adopted for pictures drawing of the collected data. Enumeration data were expressed as (%), qualified by chi-square test, and expressed by x². Measurement data were expressed by mean standard deviation (Means ± SD). All measurement data were in accordance with normal distribution. Independent sample *t*-test was used for comparison between the two groups. ROC was used to evaluate the diagnostic value of KRT-14 and ET-1 in the therapeutic effect of NRDS neonates. *p* < 0.05 was regarded as statistically significant.

3. Results

3.1. Clinical Data. By comparing the clinical data of the two groups of neonates, we found that there was no remarkable difference between the two groups in gender, gestational

TABLE 2: Therapeutic effect and adverse reactions.

	Observation group (n = 73)	Control group (n = 64)	t	p
Effective curative effect	67 (91.78)	51 (79.69)	4.175	0.041
Ineffective curative effect	6 (8.22)	13 (20.31)		
Death	3 (4.11)	6 (9.38)	1.540	0.215
Bronchial dysplasia	6 (8.22)	11 (17.19)	2.514	0.112
Cyanopathy	8 (10.96)	10 (15.63)	0.651	0.420
Shortness of breath	9 (12.33)	14 (21.88)	2.225	0.136

age, body mass, Apgar score, age of pregnant women, hypertension of pregnant women, diabetes of pregnant women, premature rupture of membranes, delivery mode, premature delivery, and delivery history, as shown in Table 1.

Comparison of therapeutic effects and adverse reactions between the two groups

We observed and compared the therapeutic effects of the two groups of neonates after treatment. It was found that the effective rate of the observation group was considerably higher than that of the control group. There was no remarkable difference between the two groups in death, bronchial dysplasia, cyanosis, and shortness of breath, as shown in Table 2.

3.2. Blood Gas Index of Two Groups. By comparing the blood gas indexes PaO₂, PaCO₂, and PaO₂/FiO₂ before and after treatment, we found that there was no remarkable difference

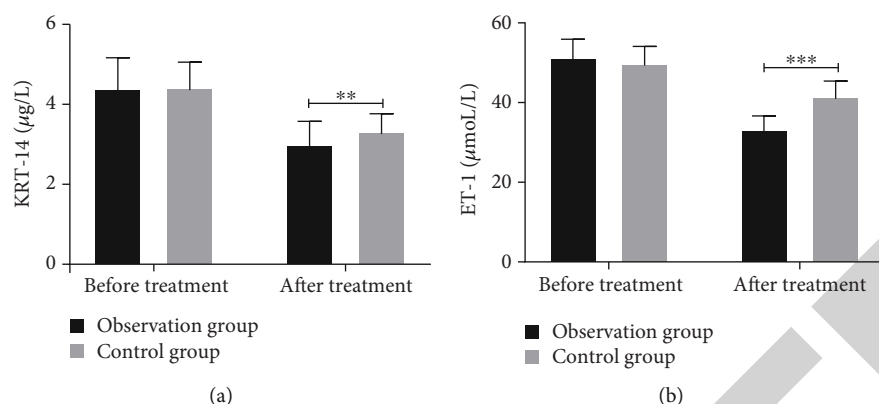


FIGURE 1: Changes of blood gas indexes before and after treatment. (a) There was no significant difference in PaO_2 between the observation group (42.39 ± 6.14) and the control group (41.01 ± 5.89) ($t = 1.338$, $p = 0.183$). PaO_2 in both groups was significantly increased after treatment ($p < 0.05$), and it in the observation group (76.92 ± 5.94) was significantly higher than the control group (68.54 ± 5.96) ($t = 8.226$, $p < 0.001$). (b) There was no significant difference in PaCO_2 between the observation group (51.38 ± 4.57) and the control group (52.64 ± 3.89) ($t = 1.725$, $p = 0.087$). PaCO_2 in both groups was significantly decreased after treatment ($p < 0.05$), and it in the observation group (35.58 ± 3.10) was significantly lower than the control group (43.08 ± 3.83) ($t = 12.659$, $p < 0.001$). (b) There was no significant difference in $\text{PaO}_2/\text{FiO}_2$ between the observation group (189.19 ± 10.95) and the control group (192.05 ± 11.55) ($t = 1.487$, $p = 0.139$). $\text{PaO}_2/\text{FiO}_2$ in both groups was significantly increased after treatment ($p < 0.05$), and it in the observation group (426.97 ± 41.39) was significantly higher than the control group (387.18 ± 28.86) ($t = 6.115$, $p < 0.001$). ** denotes $p < 0.01$; *** denotes $p < 0.001$.

between the observation group and the control group in the three before treatment. After treatment, PaO_2 and $\text{PaO}_2/\text{FiO}_2$ in both groups were notably higher than before treatment, while PaCO_2 was notably lower than before treatment. The levels of PaO_2 and $\text{PaO}_2/\text{FiO}_2$ in the observation group were considerably higher than the control group, while PaCO_2 was considerably lower than the control group, as shown in Figure 1.

Changes and contents of krt-14 and ET-1 before and after treatment

Comparison of the levels of KRT-14 and ET-1 before and after treatment in the two groups revealed that the levels of them in the observation group were not considerably different from those in the control group before treatment. After treatment, the levels of the two in both groups were notably lower than those before treatment, and the levels of the two in the observation group were considerably lower than those in the control group, as shown in Figure 2.

3.3. Diagnostic Value of Therapeutic Effects of KRT-14 and ET-1. By comparing the levels of KRT-14 and ET-1 in neonates with effective and ineffective curative effects, we found that the levels of the two in neonates with ineffective curative effects were considerably higher than those in neonates with effective curative effects ($p < 0.05$). Through ROC, we detected the diagnostic value of KRT-14 and ET-1 in the curative effects of NRDS neonates and found that the area under the curve (AUC) of KRT-14 was 0.791, and the AUC of ET-1 was 0.816, as shown in Table 3 and Figure 3.

4. Discussion

The basic pathogenesis of NRDS is acute diffuse alveolar capillary injury, which leads to increase pulmonary capillary

permeability, alveolar, and interstitial edema and ultimately gives rise to type II alveolar cells damage. This kind of damage will reduce pulmonary surfactant, thus leading to a decrease in alveolar surface tension, contraction of alveolar groups, and abnormal pulmonary ventilation/blood flow ratio, eventually triggering severe hypoxemia [18, 19]. Non-invasive positive pressure ventilation can relax the alveoli of neonates, improve the compliance of neonates' lungs, maintain the pressure in alveoli, and keep smooth breathing of neonates. Exogenous PS can supplement the lack of PS in neonates, thus reducing the tension of alveoli in neonates, preventing alveoli atrophy, improving lung respiratory function and lung compliance, and increasing blood oxygen saturation in NRDS, thus to reduce the mechanical ventilation time of neonates [20, 21].

First of all, we compared the therapeutic effect and adverse reactions of the two groups after treatment and found that the therapeutic effect of PS combined with non-invasive positive pressure ventilation was much better than that of noninvasive positive pressure ventilation alone, but there was no statistical difference in mortality rate between the two groups. Then, we compared the blood gas indexes PaO_2 , PaCO_2 , and $\text{PaO}_2/\text{FiO}_2$ of the two groups before and after treatment. After treatment, PaO_2 and $\text{PaO}_2/\text{FiO}_2$ increased in both groups, and PaCO_2 decreased significantly. After treatment, the levels of PaO_2 and $\text{PaO}_2/\text{FiO}_2$ in the observation group were remarkably higher than those in the control group, while PaCO_2 was remarkably lower than that in the control group. The blood gas status of NRDS neonates will be remarkably worse than that of normal newborns due to the oxygenation status of the lungs and the respiratory function of the neonates. Once the symptoms of the neonates are controlled and the pulmonary function and respiratory function are improved, the blood gas index

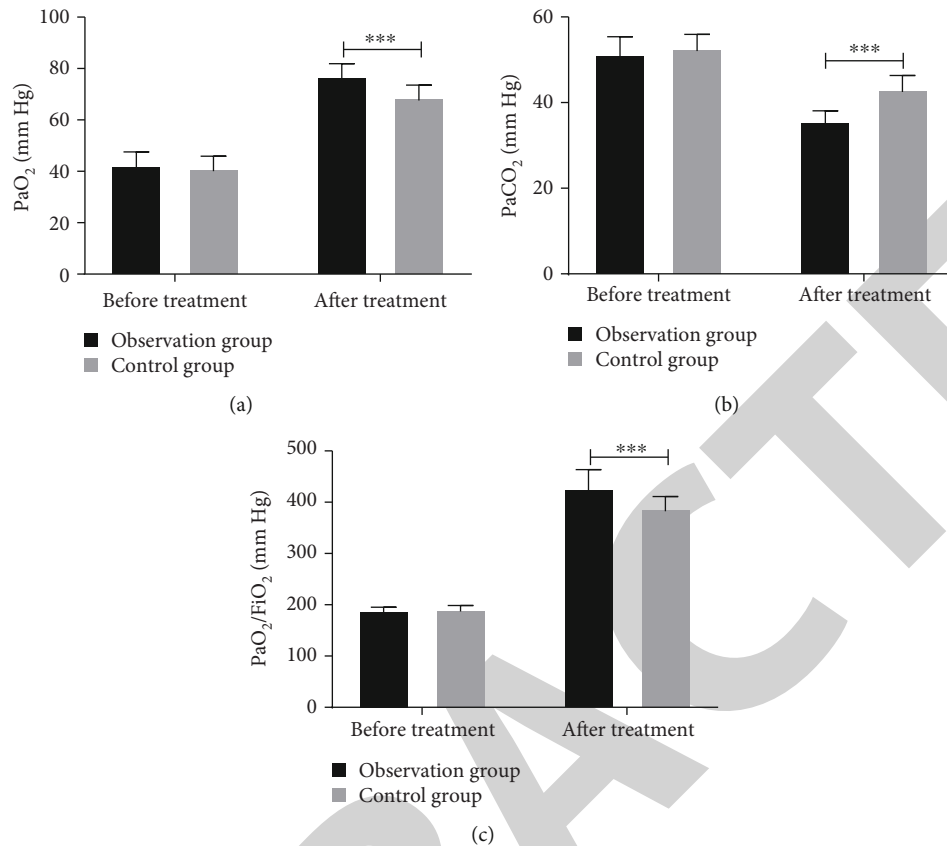


FIGURE 2: Levels of KRT-14 and ET-1 before and after treatment. (a) There was no significant difference in KRT-14 between the observation group (4.38 ± 0.84) and the control group (4.41 ± 0.70) ($t = 0.822, p = 0.225$). KRT-14 in both groups was significantly decreased after treatment ($p < 0.05$), and it in the observation group (2.99 ± 0.64) was significantly lower than the control group (3.31 ± 0.51) ($t = 3.206, p < 0.002$). (b) There was no significant difference in ET-1 between the observation group (51.34 ± 5.13) and the control group (49.90 ± 4.75) ($t = 1.697, p = 0.092$). ET-1 in both groups was significantly decreased after treatment ($p < 0.05$), and it in the observation group (33.29 ± 3.93) was significantly lower than the control group (41.51 ± 4.48) ($t = 11.441, p < 0.001$). *** denotes $p < 0.001$.

TABLE 3: ROC.

Index	AUC	95% CI	Specificity	Sensitivity	Youden index	Cut-off
KRT-14	0.791	0.665~0.917	85.47%	60.00%	45.47%	>3.645
ET-1	0.816	0.726~0.907	76.07%	70.00%	46.07%	>40.060

of the neonates will return to normal [22]. This also shows that the combined treatment is more effective.

Then, we detected the levels of KRT-14 and ET-1 of neonates in both groups. KRT-14 and ET-1 are two factors related to lung tissue [23, 24]. We found that the levels of KRT-14 and ET-1 in the two groups after treatment were notably lower than those before treatment, and the levels of the two in the observation group after treatment were notably lower than those in the control group. Moreover, we also found that KRT-14 and ET-1 in neonates with ineffective therapeutic effects were remarkably higher than those in neonates with effective therapeutic effects, which further suggests that KRT-14 and ET-1 may be used as therapeutic diagnostic indicators for NRDS neonates. Therefore, we evaluated the diagnostic value of therapeutic effect of KRT-

14 and ET-1 by ROC and found that the AUC of KRT-14 was, specificity and sensitivity was, and the AUC of ET-1 curve was, specificity and sensitivity was. Both of them have certain diagnostic value in the diagnosis of curative effect of NRDS neonates and may become the diagnostic index of curative effect of potential NRDS neonates.

However, there are still some deficiencies in our study. The subjects included in our study are all sick neonates, and healthy newborns are not included for comparison. We did not explore differences between the measures tested in this study and healthy newborns. Secondly, there are different types of PS available for treatment [25, 26], so it is hoped that corresponding research can be added in the follow-up for the differences in therapeutic effects of different PS. At last, we found that some complications occurred

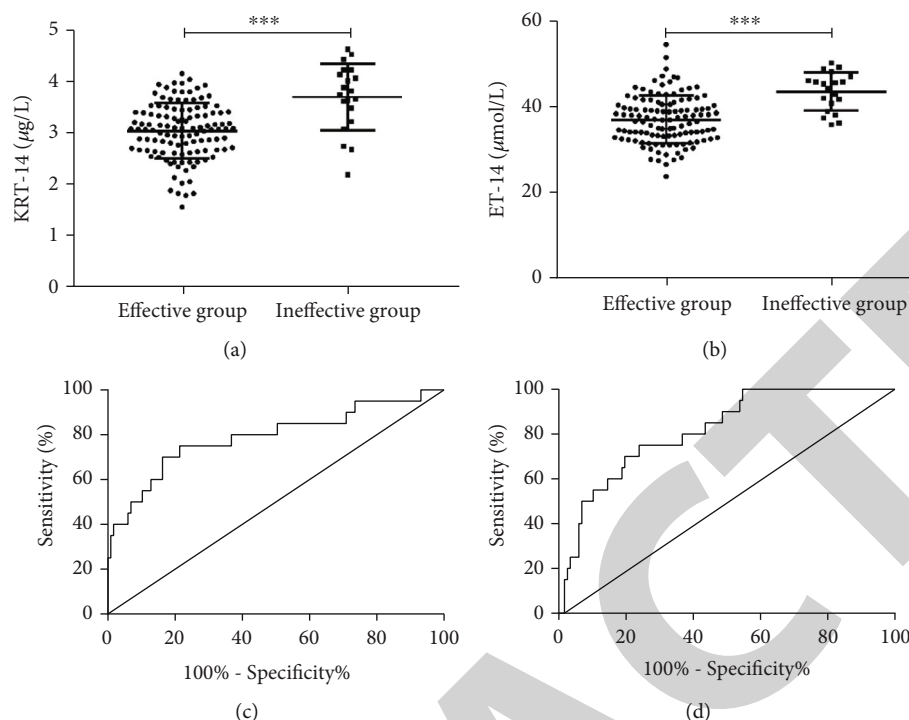


FIGURE 3: Diagnostic value of curative effect of KRTt-14 and ET-1. (a) KRT-14 in neonates with effective therapeutic effect (2.94 ± 0.56) was significantly lower than that in neonates with ineffective efficacy (3.70 ± 0.65) ($t = 5.472$, $p < 0.001$). (b) ET-1 in neonates with effective therapeutic effect (33.80 ± 5.36) was significantly lower than that in neonates with ineffective efficacy (42.68 ± 4.48) ($t = 6.997$, $p < 0.001$). (c) ROC of KRT-14 in diagnosis of therapeutic effect after treatment. (d) ROC of ET-1 in diagnosis of therapeutic effect after treatment. *** denotes $p < 0.001$.

in the treatment of neonates, but we did not explore the risk factors of these complications. We hope to supplement the corresponding discussion in the follow-up study to improve our point of view.

5. Conclusion

PS combined with noninvasive positive pressure ventilation can significantly improve the therapeutic effect of NRDS. KRT-14 and ET-1 levels may be potential therapeutic diagnostic indicators.

Data Availability

The datasets used and/or analyzed during the current study are available from the corresponding author on reasonable request.

Ethical Approval

This study was approved by the ethics committee of Women and Children's Hospital. Patients who participated in this research had complete clinical data.

Consent

Signed written informed consents were obtained from the guardians.

Conflicts of Interest

The authors declare that they have no competing interests.

Authors' Contributions

LH conceived the study and drafted the manuscript. HL and LL collected the samples and treated neonates. YL and XL were responsible for ELISA detection and efficacy evaluation. All authors read and approved the final manuscript. Lihan Huang and Hong Liang contributed equally to this work.

Acknowledgments

The project was supported by a funding from the Science and Technology Planning Project of Xiamen (3502Z20171006).

References

- [1] B. Zhang, Y. Dai, H. Chen, and C. Yang, "Neonatal mortality in hospitalized Chinese population: a meta-analysis," *BioMed Research International*, vol. 2019, Article ID 7919501, 7 pages, 2019.
- [2] J. Luo, J. Chen, Q. Li, and Z. Feng, "Differences in clinical characteristics and therapy of neonatal acute respiratory distress syndrome (ARDS) and respiratory distress syndrome (RDS):

Retraction

Retracted: Astragalin Protects against Spinal Cord Ischemia Reperfusion Injury through Attenuating Oxidative Stress-Induced Necroptosis

BioMed Research International

Received 12 March 2024; Accepted 12 March 2024; Published 20 March 2024

Copyright © 2024 BioMed Research International. This is an open access article distributed under the Creative Commons Attribution License, which permits unrestricted use, distribution, and reproduction in any medium, provided the original work is properly cited.

This article has been retracted by Hindawi following an investigation undertaken by the publisher [1]. This investigation has uncovered evidence of one or more of the following indicators of systematic manipulation of the publication process:

- (1) Discrepancies in scope
- (2) Discrepancies in the description of the research reported
- (3) Discrepancies between the availability of data and the research described
- (4) Inappropriate citations
- (5) Incoherent, meaningless and/or irrelevant content included in the article
- (6) Manipulated or compromised peer review

The presence of these indicators undermines our confidence in the integrity of the article's content and we cannot, therefore, vouch for its reliability. Please note that this notice is intended solely to alert readers that the content of this article is unreliable. We have not investigated whether authors were aware of or involved in the systematic manipulation of the publication process.

Wiley and Hindawi regrets that the usual quality checks did not identify these issues before publication and have since put additional measures in place to safeguard research integrity.

We wish to credit our own Research Integrity and Research Publishing teams and anonymous and named

external researchers and research integrity experts for contributing to this investigation.


The corresponding author, as the representative of all authors, has been given the opportunity to register their agreement or disagreement to this retraction. We have kept a record of any response received.

References

- [1] F. Sun, H. Zhang, J. Shi, T. Huang, and Y. Wang, "Astragalin Protects against Spinal Cord Ischemia Reperfusion Injury through Attenuating Oxidative Stress-Induced Necroptosis," *BioMed Research International*, vol. 2021, Article ID 7254708, 8 pages, 2021.

Research Article

Astragalins Protects against Spinal Cord Ischemia Reperfusion Injury through Attenuating Oxidative Stress-Induced Necroptosis

Feng Sun,¹ Haiwei Zhang,² Jianhui Shi,³ Tianwen Huang,⁴ and Yansong Wang⁵ 

¹Heilongjiang Beidahuang Group General Hospital, No.235 Hasuang Road, Harbin, Heilongjiang Province, China

²Department of Imaging, General Hospital of General Administration of Agriculture and Reclamation, Harbin 150088, China

³Department of Orthopedic Surgery, Heilongjiang Provincial Hospital, Harbin 150036, China

⁴Department of Orthopedic Surgery, General Hospital of General Administration of Agriculture and Reclamation, Harbin 150088, China

⁵Department of Spine Surgery, The First Affiliated Hospital of Harbin Medical University, Harbin 150001, China

Correspondence should be addressed to Yansong Wang; you26724890@163.com

Received 21 April 2021; Revised 1 September 2021; Accepted 3 September 2021; Published 28 October 2021

Academic Editor: Tao Huang

Copyright © 2021 Feng Sun et al. This is an open access article distributed under the Creative Commons Attribution License, which permits unrestricted use, distribution, and reproduction in any medium, provided the original work is properly cited.

Spinal cord ischemia/reperfusion (SCI/R) injury is a devastating complication usually occurring after thoracoabdominal aortic surgery. However, it remains unsatisfactory for its intervention by using pharmacological strategies. Oxidative stress is a main pharmacological process involved in SCI/R, which will elicit downstream programmed cell death such as the novel defined necroptosis. Astragalins is a bioactive natural flavonoid with a wide spectrum of pharmacological activities. Herein, we firstly evaluated the effect of astragalins to oxidative stress as well as the possible downstream necroptosis after SCI/R in mice. Our results demonstrated that astragalins improves the ethological score and histopathological deterioration of SCI/R mice. Astragalins mitigates oxidative stress and ameliorates inflammation after SCI/R. Astragalins blocks necroptosis induced by SCI/R. That is, the amelioration of astragalins to the motoneuron injury and histopathological changes. Indicators of oxidative stress, inflammation, and necroptosis after SCI/R were significantly blocked. Summarily, we firstly illustrated the protection of astragalins against SCI/R through its blockage to the necroptosis at downstream of oxidative stress.

1. Introduction

Ischemia reperfusion injury is a secondary pathological condition caused by restoration of blood perfusion to the primary ischemic tissues [1]. In clinical surgery, before vascular and general surgery, transient clamping to the related arterial vessels is usually imperative. However, occurrence of secondary reperfusion injury after surgery is still inevitable, especially in thoracoabdominal aortic surgery. Spinal cord ischemia/reperfusion (SCI/R) injury is mainly such a devastating complication of thoracoabdominal aortic surgery, which will in different degree threaten the patients with risk of quadriplegia or paraplegia [2–4]. Although treatments according to the etiology of SCI/R and surgical strategies have been advanced, effective and ideal pharmacological therapeutics for SCI/R are still insufficient.

In pathology, excessive reactive oxygen species elicited by ischemia and reperfusion overwhelms the redox balance of cells thus leading to oxidative stress. It has been recognized that oxidative stress as a pivotal pathological mediator for ischemia reperfusion and prevention to oxidative stress can effectively protect against ischemia reperfusion injury [5–7]. Cell necrosis is one of the downstream events of oxidative stress and catastrophic consequence of ischemia reperfusion [1]. Died cells, especially necrotic cells, will release damage-associated molecular patterns (DAMPs), for example, high-mobility group box 1 (HMGB1), to mobilize and stimulate sterile inflammation response, which mainly presents as an excess of proinflammatory factor upregulation, for example, interleukin-6 (IL-6) and tumor necrosis factor- α (TNF- α) [8, 9]. In turn, the triggered

inflammation will lead to further cell necrosis. Therefore, inhibition of oxidative stress and its downstream cell death as well as inflammation demonstrates a great therapeutic potential after SCI/R [5, 6, 10–13].

Recently, a novel modality of programmed cell death has been discovered, namely, necroptosis, which is similar with passive necrosis in morphology but is regulated by genes like apoptosis [14]. Studies have been reported that necroptosis plays an important pathological role in ischemia reperfusion injury, and block to necroptotic signaling pathway receptor-interacting protein 1- (RIP1-) RIP3-mixed lineage kinase domain-like protein (MLKL) can apparently ameliorates ischemia and reperfusion injury [15–18]. Like passive necrosis, necroptosis can also trigger inflammation; thus, downregulation to necroptosis is meaningful to alleviate inflammation after ischemia reperfusion injury [19–21]. Besides, in Liu's research, they revealed the pathological role of necroptosis in mouse spinal cord injury model, which could be ameliorated by the RIP1 specific inhibitor necrostatin-1 [22]. However, in SCI/R, whether necroptosis is triggered still remains unverified.

Astragalin is a bioactive natural flavonoid extracted from a number of plants [23]. Extensive pharmacological effects of astragalin have been reported recent years. Astragalin has been demonstrated to mitigate lipopolysaccharide, IL-1 β , and collagen-induced inflammation as well as allergic inflammation [24–28]. Meanwhile, astragalin has potential of antioxidative stress and antiapoptosis [29–31]; in myocardial ischemia reperfusion injury, astragalin played cardioprotective role through its pharmacological activities of antioxidative, antiapoptotic, and anti-inflammatory [32]. Based on these studies, considering the pathological characteristic of SCI/R, the present work firstly revealed the antioxidative stress and anti-inflammation role of astragalin to reduce neuro-necroptosis in SCI/R.

2. Materials and Methods

2.1. Spinal Cord Ischemia Reperfusion Injury Model and Drug Administration. Adult male C57BL/6 mice weight about 25 g were randomly divided into four groups: the sham group, the SCI/R group, the SCI/R with astragalin administration group, and the SCI/R with necrostatin-1 treatment group ($n = 6$ in each group). Animal experiments were approved by the Ethics Committee of Experimental Research, Harbin Medical University, and performed according to the Guide for the Care and Use of Laboratory Animals published by the National Institutes of Health. Procedures of SCI/R were operated according to the previous studies [33, 34]. In brief, mice were firstly intubated and ventilated by inhalation of 1.5% isoflurane to induce anesthetization before fixed on the mouse pad in supine position. Then, heparin with concentration of 200 IU/kg was injected subcutaneously. The cervicothoracic hair was cleared by hair removal cream to expose the surgical region. A cervicothoracic incision along with the ventral midline was made, and the chest wall was opened from the top of the manubrium caudad to the second rib. Then, the aortic arch and left subclavian artery were exposed and occluded by mouse artery clamps for 8 minutes. Finally, the chest was closed, and mice

were maintained body temperature on an electric blanket. Bladder evacuation was expressed manually twice daily during the reperfusion period. Mice in astragalin and necrostatin-1 treatment groups were administrated with 1 mg/kg astragalin and 2 mg/kg necrostatin-1 by intrathecal injection according to the designed procedure as shown in Figure 1(a).

2.2. Neurobehavioral Evaluation. Motor neuron deficit after SCI/R was evaluated according to Basso's score of locomotion at 1 h, 12 h, 24 h, 48 h, and 72 h [35]. The evaluated grades range from 0 to 9, which, respectively, means from totally no ankle movements to normal movements.

2.2.1. Histopathological Observation. After 72 h of SCI/R, mice were anesthetized by isoflurane before decollation to flense the spinal cord tissues. The T6 to L5 segments of the spinal cord tissues were fixed in paraformaldehyde (4%, w/v) at room temperature for 24 h. Then, the tissues were embedded in paraffin and cut transversely into serial sections with a thickness of 6 μ m. Standard hematoxylin and eosin (HE) staining of tissue slides was performed followed by the manufacturer's suggestion of HE commercial kit (C0105, Beyotime Institute of Biotechnology, China).

2.3. Serum SOD, GSH, and MDA Assay. Superoxide dismutase (SOD), which catalyzes the dismutation of the superoxide anion into hydrogen peroxide and molecular oxygen, is one of the most important antioxidant enzymes. Glutathione (gamma-glutamyl-cysteinyl-glycine; GSH) is the most abundant low-molecular-weight thiol, and GSH/glutathione disulfide is the major redox couple in animal cells. Malondialdehyde (MDA) is one of the final products of polyunsaturated fatty acid peroxidation in the cells. An increase in free radicals causes overproduction of MDA. Malondialdehyde level is commonly known as a marker of oxidative stress. After 72 h reperfusion, blood was harvested from the eyeballs of mice before separation to gain serum. The serum SOD activity, GSH concentration, and MDA content were measured in accordance with the manufacturers' direction for commercial SOD, GSH and MDA kits (S0101, S0053 and S0131, respectively, Beyotime Institute of Biotechnology, China).

2.4. Tissue Enzyme-Linked Immunosorbent Assay of IL-6 and TNF- α . IL-6 is a pleiotropic proinflammatory cytokine that is mainly secreted by monocytes, and TNF- α is predominantly produced by macrophages. The two markers are associated with apoptosis. The spinal cord tissues harvested after 72 h reperfusion were homogenized in cold PBS using a manual homogenizer; then, the spinal cord homogenated lysis was gained after cryogenic ultracentrifugation to subsequently detect the IL-6 and TNF- α . Commercial enzyme linked immunosorbent assay kits of IL-6 and TNF- α were purchased from R&D Systems, Inc. (M6000B and MTA00B, respectively). Measurement protocol of IL-6 and TNF- α was according to the manufacturers' instructions.

2.5. Western Blotting. Spinal cord tissue protein was extracted using RIPA lysis (P0013K, Beyotime Institute of Biotechnology, China) added with phosphatase and protease

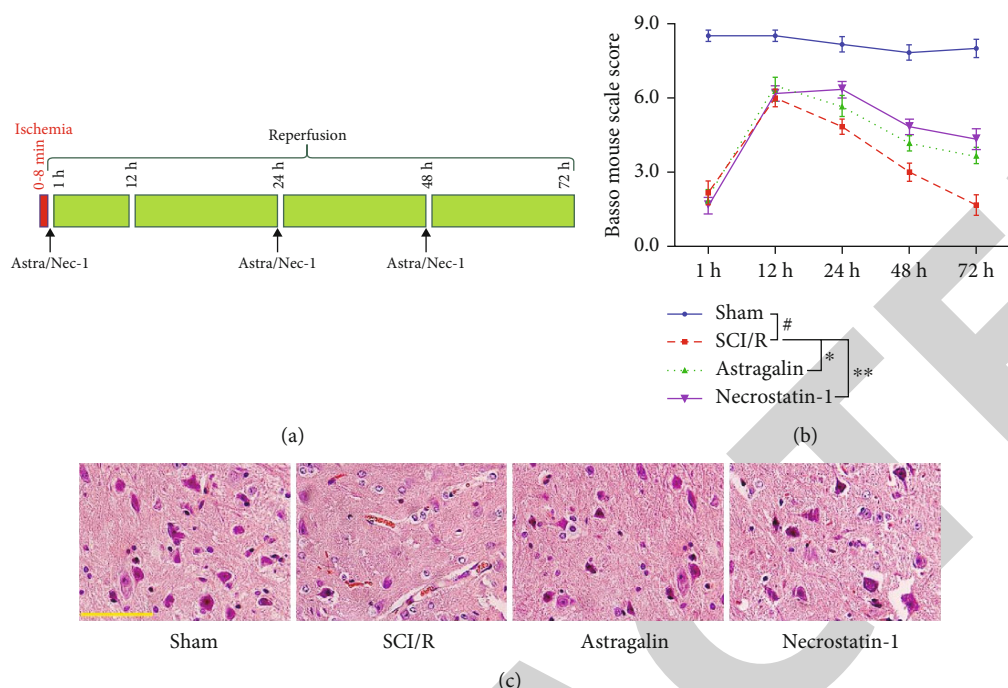


FIGURE 1: The behavioral score and histopathology were improved by astragalin administration. Mice were suffered from spinal cord ischemia before 1 h, 12 h, 24 h, 48 h, and 72 h reperfusion. (a) Procedure of astragalin and necrostatin-1 treatment and the time course of neurobehavioral evaluation. (b) Basso mouse score of each experimental mouse, $n = 6$ per group. Data are presented as mean \pm SEM, one-way ANOVA, compared to the SCI/R group, $\#P < 0.001$, $*P < 0.05$, $**P < 0.01$. (c) Histopathological changes of spinal cord grey matter in different groups. Scale bar (yellow): 100 μm .

inhibitor cocktail (Thermo Scientific, USA). Protein quantification was determined by the Bradford method. Tissue protein extracts were denatured in boiled water bath and then loaded into the lane of sodium dodecyl sulfate polyacrylamide gels. After electrophoresis, the protein was separated and then transferred onto nitrocellulose membranes (HATF00010, Merck Millipore, Germany). The membranes loaded with target proteins were blocked in 5% nonfat milk for 2 h and incubated in primary antibody buffer at 4°C overnight. After primary antibody incubation, the membranes were incubated in HRP-conjugated secondary antibody buffer for 2 h at room temperature. Final protein bands were visualized with the Immobilon Western Chemiluminescent HRP Substrate (Millipore, Billerica, MA, USA).

2.6. Reagents and Antibodies. Astragalin was purchased from Chengdu Pulis Biotech Co., Ltd. (480-10-4). Necrostatin-1 was from Sigma (St. Louis, MO, USA). Antibodies to HMGB1 were purchased from Cell Signaling Technology (Beverly, MA, USA). Antibody to RIP1 was purchased from Proteintech (Rosemont, IL, USA). Antibody to RIP3 was purchased from Santa Cruz Biotechnology (Santa Cruz, CA, USA). Antibody to MLKL was purchased from Signalway Antibody (College Park, MD, USA). Secondary antibodies conjugated with HRP were from Jackson Laboratories (West Grove, PA, USA).

2.7. Statistical Analysis. The density of protein blots assayed by western blotting was semiquantified by the ImageJ software (National Institutes of Health, Bethesda, MD, USA). Softwares of Microsoft Excel (The Microsoft, USA) and

GraphPad Prism v.5.01 (GraphPad Software, La Jolla, CA, USA) were used to analyze the experimental results. Data are expressed as mean \pm SEM. Variance comparison among multiple groups was determined using one-way ANOVA with Bonferroni post hoc analysis. $*P < 0.05$ was defined as significantly statistical difference.

3. Results

3.1. Astragalin Improves the Ethological Score and Histopathological Deterioration of SCI/R Mice. In order to evaluate the pharmacological effect and cellular mechanism of astragalin to SCI/R, according to the preexperiments, mice were treated with astragalin and necrostatin-1 after the operation of descending thoracic aorta and left subclavian artery occlusion, and the procedure of astragalin and necrostatin-1 administration is showed in Figure 1(a). Observation to the ethology was assessed using Basso mouse score system. As the results shown in Figure 1(b), movement of mouse hind limb in the Sham group showed no apparent abnormal change from 1 h to 72 h after SCI/R, while in the SCI/R group, mouse ethological score was remarkably decreased, and significant difference was presented when compared with the Sham group, suggesting serious injury to the motor neurons had been caused by ischemia reperfusion ($\#P < 0.001$). However, astragalin treatment could increase the Basso mouse score from 12 h to 72 h after SCI/R compared to the SCI/R group, which was similar to the necrostatin-1 group, indicating an improvement to the motor function ($*P < 0.05$). Similarly, results from HE

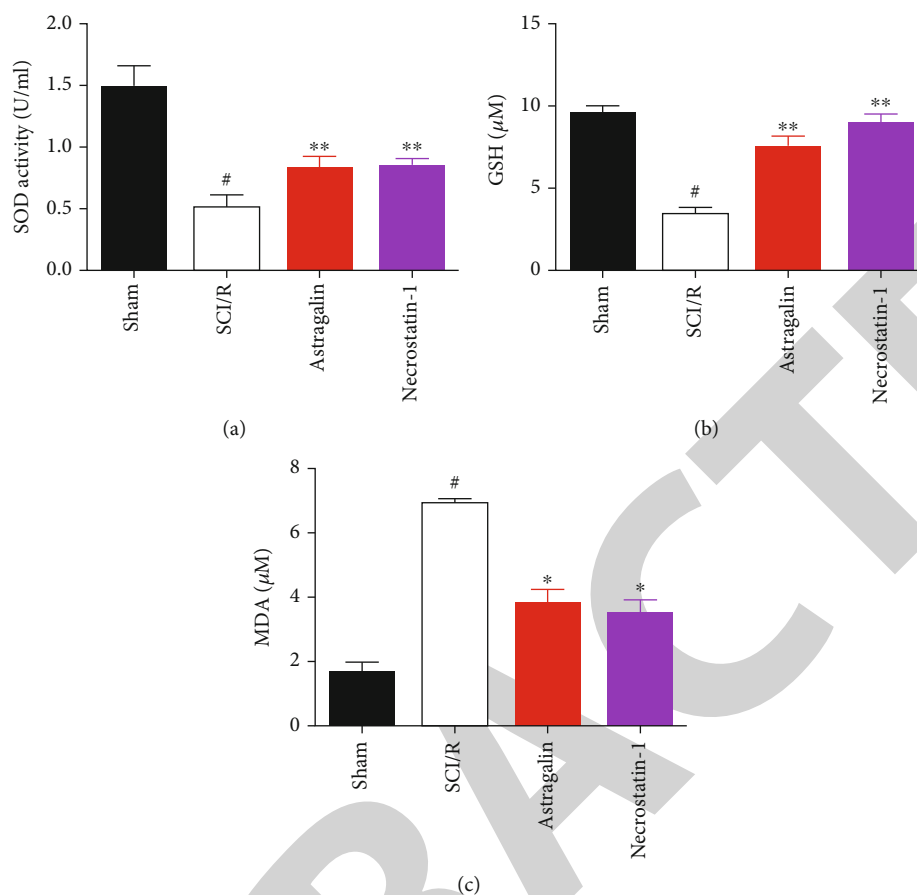


FIGURE 2: Astragalin administration reduced the level of SOD, GSH, and MDA. Mouse serum was harvested after 72 h SCI/R and assayed by related commercial kits: (a) SOD activity; (b) GSH content; (c) MDA concentration in serum from each experimental group. $n = 6$ independent experiments. Data are presented as mean \pm SEM, one-way ANOVA, compared to the SCI/R group, # $P < 0.001$, * $P < 0.05$, ** $P < 0.01$.

staining in Figure 1(c) also showed such tendency. In the Sham group, cellular and nuclear staining was legible, and motor neurons were rich in the spinal cord grey matter, while the motor neurons were significantly injured, and the number was largely reduced in the SCI/R group, which could be salvaged by astragalin and necrostatin-1 treatment. These data suggested that astragalin treatment had the potential to alleviate SCI/R injury like necrostatin-1.

3.2. Astragalin Mitigates Oxidative Stress after SCI/R. As abovementioned, oxidative stress is an important pathological process involved in SCI/R. Therefore, to determine the mechanism underlying the protection of astragalin to SCI/R, we detected the serum indicators of oxidative stress. As shown in Figures 2(a)–2(c), compared to the Sham group, the serum SOD and GSH levels in the SCI/R group were significantly decreased, while the MDA concentration was apparently increased (# $P < 0.001$). However, when compared to the SCI/R group, after astragalin administration, the SOD activity and GSH level were remarkably salvaged and increased (** $P < 0.01$), and MDA was significantly reduced (* $P < 0.05$). The results in the necrostatin-1 group was parallel to the astragalin group (Figures 2(a)–2(c)).

These data suggested the mitigation of astragalin to oxidative stress after SCI/R, which is similar to the RIP1 inhibitor necrostatin-1.

3.3. Astragalin Ameliorates Inflammation after SCI/R. Since inflammation is a pivotal phenomenon triggered by cell necrosis after ischemia reperfusion injury, we further evaluated the changes of proinflammatory factors TNF- α and IL-6. Data in Figure 3(a) showed that TNF- α in spinal cord tissues was largely raised in the SCI/R group when compared to the Sham group (# $P < 0.001$) but was significantly reduced by astragalin and necrostatin-1 administration (* $P < 0.05$). At the same time, compared to the Sham group, the level of IL-6 was also apparently increased in the SCI/R group (# $P < 0.001$), and astragalin as well as necrostatin-1 decreased the IL-6 after SCI/R (* $P < 0.05$). These data indicated alleviation of astragalin to the inflammation after SCI/R.

3.4. Astragalin Blocks Necroptosis Induced by SCI/R. Necroptosis has been recognized as a novel pharmacological target after ischemia reperfusion injury [15]. In order to investigate whether necroptosis was induced in SCI/R as well as the effect of astragalin administration, we evaluated the classical protein markers of necroptosis by western blotting. Data in Figure 4

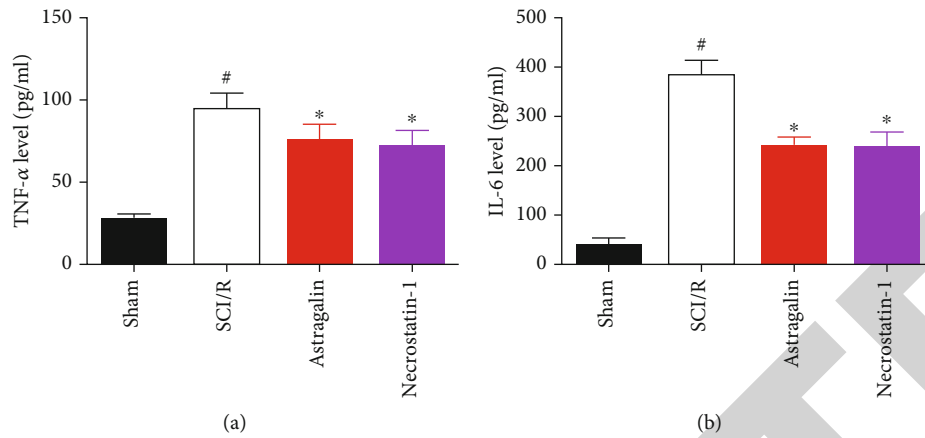


FIGURE 3: Astragal and necrostatin-1 administration decreased the level of TNF-α and IL-6 after SCI/R. Mouse tissue homogenate was harvested after 72h SCI/R and assayed by related commercial kits. (a) TNF-α level in spinal cord tissues. (b) IL-6 level in spinal cord tissues after SCI/R. *n* = 6 independent experiments. Data are presented as mean ± SEM, one-way ANOVA, compared to the SCI/R group, [#]*P* < 0.001, ^{*}*P* < 0.05.

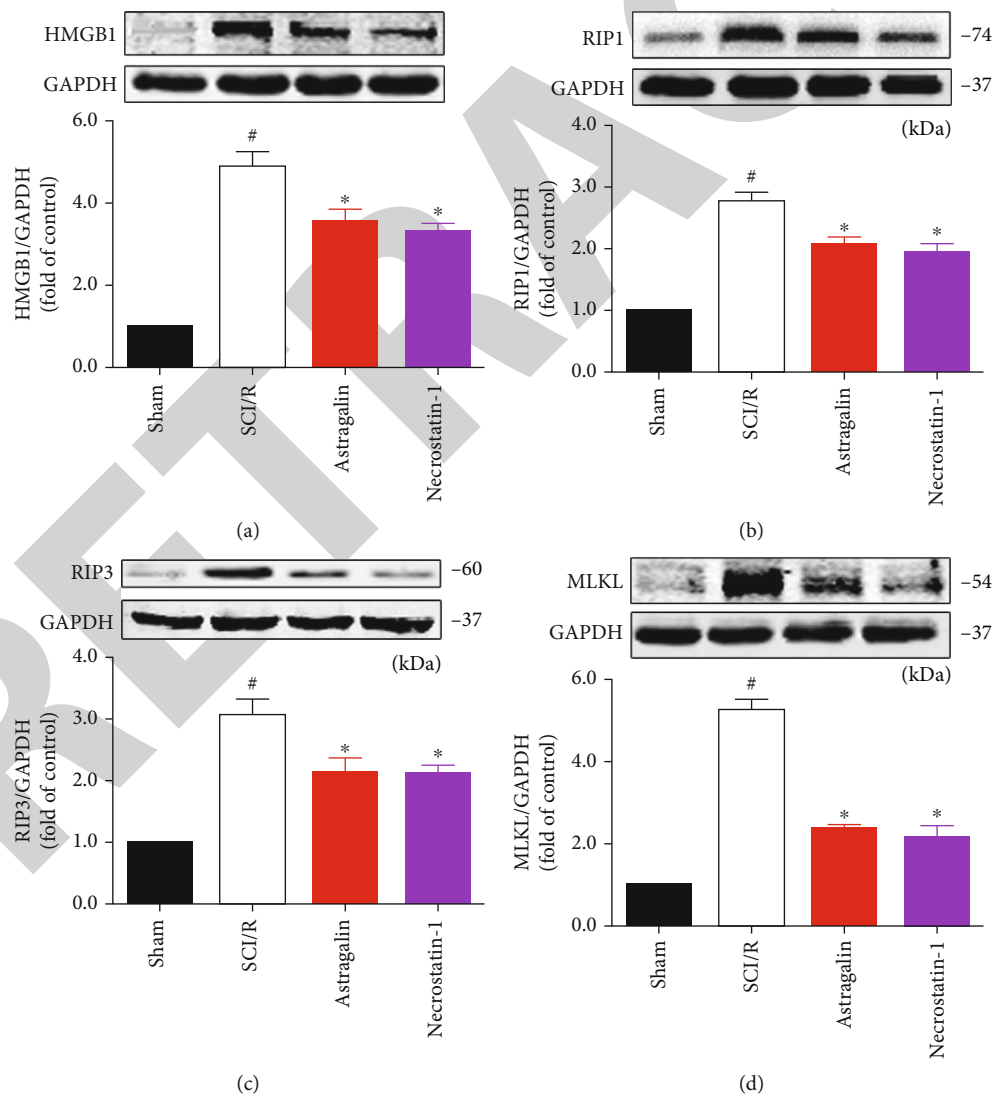


FIGURE 4: Astragal and necrostatin-1 administration blocked the protein levels of necroptosis after SCI/R. Protein markers were evaluated by western blotting: (a) protein HMGB1; (b) RIP1; (c) RIP3; (d) MLKL expression in spinal cord tissues from different group mouse. *n* = 3 independent experiments. Data are presented as mean ± SEM, one-way ANOVA, compared to the SCI/R group, [#]*P* < 0.001, ^{**}*P* < 0.01.

showed that HMGB1 (Figure 4(a)), RIP1 (Figure 4(b)), RIP3 (Figure 4(c)), and MLKL (Figure 4(d)) in the spinal cord tissues from SCI/R mice were significantly upregulated compared to the Sham group ($\#P < 0.001$). Nevertheless, the administration of astragalín could effectively block these aberrant upregulation of these proteins ($*P < 0.05$, $**P < 0.01$), which was parallel with the RIP1 inhibitor necrostatin-1, demonstrating that necroptosis was truly induced in SCI/R and could be inhibited by astragalín administration.

4. Discussion

Our present results show that the dyskinesia and histopathological deterioration after SCI/R are apparently alleviated by the natural flavonoid astragalín, and we have also verified amelioration of astragalín administration to oxidative stress and inflammation, which are similar to the effects of RIP1 inhibitor necrostatin-1. Besides, it has been illustrated the obvious necroptosis after SCI/R and the inhibition of astragalín to necroptosis. Therefore, we conclude that astragalín is a protective agent to SCI/R, and the potential cellular mechanism is based on its alleviation to oxidative stress-induced necroptosis.

Restoration of blood flow after ischemia triggers reactive oxygen species redundancy; thus, the cellular antioxidant defenses are overwhelmed, and cells are stuck in a state of oxidative stress, which has been seen as a key pathological process induced by ischemia reperfusion injury [36]. SOD and glutathione peroxidases are two typical antioxidant enzymes; therefore, the activity of SOD and the level of GSH are usually recognized as biomarkers of oxidative stress [37]. On the other hand, biomolecules of cells are overoxidized by the reactive oxygen species and generate a lot of byproduct, for example, MDA, which is also looked as a classical indicator of oxidative stress injury [38]. Previous studies have revealed that salvation to the activity of SOD and level of GSH after SCI/R could effectively mitigated neuronal injury [5, 11, 39]. In our research, we also found apparently oxidative stress indicated by decreased SOD activity and GSH level as well as increased MDA concentration after SCI/R, but astragalín administration during reperfusion for 3 days could ameliorate this oxidative stress significantly (Figures 2(a)–2(c)). This antioxidant feature of astragalín is similar with the previous work in other disease models [31, 40, 41].

Activation of native innate immune cells and infiltrating leukocytes after SCI/R gives rise to inflammation, which is another pivotal pathological factor of SCI/R injury [8]. Release of proinflammatory cytokines such as IL-6 and TNF- α from inflammatory cells manifests inflammatory cascades, and reduce of these factors in tissues or serum after SCI/R reflects a potential anti-inflammatory effect [42, 43]. Similarly, in our work, though there was high increase of proinflammatory cytokines TNF- α and IL-6 in spinal cord tissue homogenate after SCI/R, astragalín treatment generated apparent anti-inflammatory effect by reduce to these two classical inflammatory factors (Figures 3(a) and 3(b)), in line with its anti-inflammation potential in other diseases [27, 44, 45].

The recently illustrated necroptosis is a serious cellular endpoint after ischemia reperfusion injury [17, 46]. Oxidative stress is a key inducement factor of cell death, because

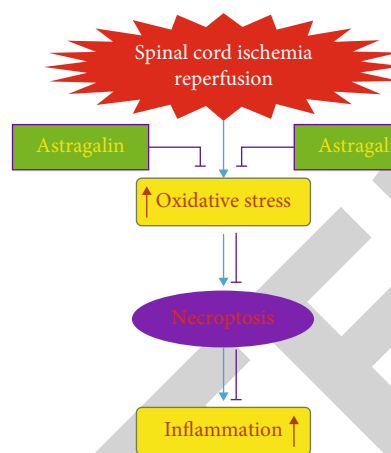


FIGURE 5: Schematic diagram for the protective effect and cellular mechanisms of astragalín in SCI/R. Oxidative stress is triggered after spinal cord ischemia reperfusion injury, thus leading to the devastating cellular endpoints: necroptosis, which stimulates the inflammation. However, astragalín administration, like necrostatin-1, could reduce oxidative stress and the downstream cellular necroptosis, resulting in relief to the inflammation.

overoxidized biomolecules such as proteins and lipids after ischemia reperfusion not only leads to directly cellular collapse but also triggers programmed signaling pathways of necroptosis. Therefore, it is undoubtedly protective against SCI/R injury through inhibition to the necroptosis. In the present work, we demonstrated the upregulation of necroptosis signaling RIP1-RIP3 and the blockage of necrostatin-1 and astragalín to the signaling after SCI/R (Figure 4), thus illustrating the pathological role of necroptosis and the cellular mechanisms for the protection of astragalín against SCI/R. Of note, it is very interesting that we also revealed the generation of necroptosis, another novel form of programmed cell death in SCI/R, because RIP1 specific inhibitor necrostatin-1 could remarkably block RIP1-RIP3 signaling and result in the protection against SCI/R.

In summary, our work firstly proved the protection of the natural flavonoid astragalín against SCI/R, and the cellular mechanisms of its downregulation to oxidative stress stimulated necroptosis (Figure 5), thus provides a valuable new pharmacological strategy for clinical SCI/R intervention especially after thoracoabdominal aortic surgeries. Furthermore, the rudimentary reveal of necroptosis in SCI/R injury provokes an interesting work about the further mechanisms of inhibitors to necroptosis after SCI/R in the future.

Data Availability

The datasets used and/or analyzed during the current study are available from the corresponding author on reasonable request.

Ethical Approval

The current study was approved by the Ethics Committee of Experimental Research, Harbin Medical University.

Consent

No consent was necessary.

Conflicts of Interest

The authors declare no competing interests.

Authors' Contributions

FS designed the study, collected the data, and performed the statistical analysis and drafted the manuscript. HWZ, JHS, and TWH were responsible for collecting the data, performing the statistical analysis, and conducting the literature search. YSW supervised the project, designed the study, and helped to analyze the data and write the manuscript. All authors read and approved the final manuscript.

Acknowledgments

This work was supported by grants from the National Natural Science Foundation of China (No. 81871781) and the Project of Shanghai Municipal Science and Technology Commission (No. 20Y21903200).

References

- [1] H. K. Eltzschig and T. Eckle, "Ischemia and reperfusion—from mechanism to translation," *Nature Medicine*, vol. 17, no. 11, pp. 1391–1401, 2011.
- [2] T. Bisdas, G. Panuccio, M. Sugimoto, G. Torsello, and M. Austermann, "Risk factors for spinal cord ischemia after endovascular repair of thoracoabdominal aortic aneurysms," *Journal of Vascular Surgery*, vol. 61, no. 6, pp. 1408–1416, 2015.
- [3] F. Romi and H. Naess, "Spinal cord infarction in clinical neurology: a review of characteristics and long-term prognosis in comparison to cerebral infarction," *European Neurology*, vol. 76, no. 3–4, pp. 95–98, 2016.
- [4] H. Awad, M. E. Ramadan, H. F. El Sayed, D. A. Tolpin, E. Tili, and C. D. Collard, "Spinal cord injury after thoracic endovascular aortic aneurysm repair," *Canadian Journal of Anaesthesia*, vol. 64, no. 12, pp. 1218–1235, 2017.
- [5] S. Yu, L. Xie, Z. Liu, C. Li, and Y. Liang, "MLN4924 exerts a neuroprotective effect against oxidative stress via Sirt1 in spinal cord ischemia-reperfusion injury," *Oxidative Medicine and Cellular Longevity*, vol. 2019, Article ID 7283639, 14 pages, 2019.
- [6] L. Xie, Z. Wang, C. Li, K. Yang, and Y. Liang, "Protective effect of nicotinamide adenine dinucleotide (NAD⁺) against spinal cord ischemia-reperfusion injury via reducing oxidative stress-induced neuronal apoptosis," *Journal of Clinical Neuroscience*, vol. 36, pp. 114–119, 2017.
- [7] G. A. Kurian, R. Rajagopal, S. Vedantham, and M. Rajesh, "The role of oxidative stress in myocardial ischemia and reperfusion injury and remodeling: revisited," *Oxidative Medicine and Cellular Longevity*, vol. 2016, Article ID 1656450, 14 pages, 2016.
- [8] M. A. Anwar, T. S. Al Shehabi, and A. H. Eid, "Inflammogenesis of secondary spinal cord injury," *Frontiers in Cellular Neuroscience*, vol. 10, p. 98, 2016.
- [9] S. Amor, L. A. Peferoen, D. Y. Vogel et al., "Inflammation in neurodegenerative diseases—an update," *Immunology*, vol. 142, no. 2, pp. 151–166, 2014.
- [10] G. Stokman, L. Kors, P. J. Bakker et al., "NLRX1 dampens oxidative stress and apoptosis in tissue injury via control of mitochondrial activity," *The Journal of Experimental Medicine*, vol. 214, no. 8, pp. 2405–2420, 2017.
- [11] J. Fu, H. Sun, Y. Zhang et al., "Neuroprotective effects of luteolin against spinal cord ischemia-reperfusion injury by attenuation of oxidative stress, inflammation, and apoptosis," *Journal of Medicinal Food*, vol. 21, no. 1, pp. 13–20, 2018.
- [12] B. Ni, Z. Cao, and Y. Liu, "Glycyrrhizin protects spinal cord and reduces inflammation in spinal cord ischemia-reperfusion injury," *The International Journal of Neuroscience*, vol. 123, no. 11, pp. 745–751, 2013.
- [13] S. G. Liu, Y. M. Wang, Y. J. Zhang et al., "ZL006 protects spinal cord neurons against ischemia-induced oxidative stress through AMPK-PGC-1 α -Sirt3 pathway," *Neurochemistry International*, vol. 108, pp. 230–237, 2017.
- [14] A. Linkermann and D. R. Green, "Necroptosis," *The New England Journal of Medicine*, vol. 370, no. 5, pp. 455–465, 2014.
- [15] T. Zhang, Y. Zhang, M. Cui et al., "CaMKII is a RIP3 substrate mediating ischemia- and oxidative stress-induced myocardial necroptosis," *Nature Medicine*, vol. 22, no. 2, pp. 175–182, 2016.
- [16] C. R. Kim, J. H. Kim, H. L. Park, and C. K. Park, "Ischemia reperfusion injury triggers TNF α induced-necroptosis in rat retina," *Current Eye Research*, vol. 42, no. 5, pp. 771–779, 2017.
- [17] A. Linkermann, M. J. Hackl, U. Kunzendorf, H. Walczak, S. Krautwald, and A. M. Jevnikar, "Necroptosis in immunity and ischemia-reperfusion injury," *American Journal of Transplantation*, vol. 13, no. 11, pp. 2797–2804, 2013.
- [18] H. M. Ni, X. Chao, J. Kaseff et al., "Receptor-interacting serine/threonine-protein kinase 3 (RIPK3)-mixed lineage kinase domain-like protein (MLKL)-mediated necroptosis contributes to ischemia-reperfusion injury of steatotic livers," *The American Journal of Pathology*, vol. 189, no. 7, pp. 1363–1374, 2019.
- [19] F. Yang, L. Shang, S. Wang et al., "TNF α -Mediated Necroptosis Aggravates Ischemia-Reperfusion Injury in the Fatty Liver by Regulating the Inflammatory Response," *Oxidative Medicine and Cellular Longevity*, vol. 2019, Article ID 2301903, 14 pages, 2019.
- [20] J. Chen, Z. Jiang, X. Zhou et al., "Dexmedetomidine preconditioning protects cardiomyocytes against hypoxia/reoxygenation-induced necroptosis by inhibiting HMGB1-mediated inflammation," *Cardiovascular Drugs and Therapy*, vol. 33, no. 1, pp. 45–54, 2019.
- [21] M. Yang, Y. Lv, X. Tian et al., "Neuroprotective effect of β -Carophyllene on cerebral ischemia-reperfusion injury via regulation of necroptotic neuronal death and inflammation: in vivo and in vitro," *Frontiers in Neuroscience*, vol. 11, p. 583, 2017.
- [22] M. Liu, W. Wu, H. Li et al., "Necroptosis, a novel type of programmed cell death, contributes to early neural cells damage after spinal cord injury in adult mice," *The Journal of Spinal Cord Medicine*, vol. 38, no. 6, pp. 745–753, 2015.
- [23] A. Riaz, A. Rasul, G. Hussain et al., "Astragaloside: a bioactive phytochemical with potential therapeutic activities," *Advances in Pharmacological Sciences*, vol. 2018, Article ID 9794625, 15 pages, 2018.

Research Article

Identification and Validation of a Dysregulated miRNA-Associated mRNA Network in Temporal Lobe Epilepsy

Xing Li,¹ Yunli Han,¹ Dejun Li,² Hai Yuan,¹ Shiqin Huang,¹ Xiaolan Chen,¹ and Yuanhan Qin ¹

¹Departments of Pediatrics, The First Affiliated Hospital of Guangxi Medical University, Nanning, 530021 Guangxi Zhuang Autonomous Region, China

²Departments of Pediatrics, Wuzhou Workers' Hospital, Wuzhou, 543000 Guangxi Zhuang Autonomous Region, China

Correspondence should be addressed to Yuanhan Qin; yuyou4090830@163.com

Received 23 April 2021; Revised 26 September 2021; Accepted 28 September 2021; Published 22 October 2021

Academic Editor: Tao Huang

Copyright © 2021 Xing Li et al. This is an open access article distributed under the Creative Commons Attribution License, which permits unrestricted use, distribution, and reproduction in any medium, provided the original work is properly cited.

Objectives. This study is aimed at exploring the relationships between miRNAs and mRNAs and to characterize their biological functions in temporal lobe epilepsy (TLE). **Methods.** Novel clinical significant miRNAs and target genes and their potential underlying mechanisms have been discovered and explored by mining miRNAs and mRNA expression data of TLE patients using various bioinformatics methods. Reverse transcription-quantitative polymerase chain reaction (RT-qPCR) was used to validate the bioinformatic analysis results. **Results.** A total of 6 dysregulated miRNAs and 442 differentially expressed genes (DEGs) related to TLE were obtained from GEO database (GSE114701 and GSE127871 datasets). A protein-protein interaction (PPI) network containing the 442 DEGs was established. mRNA response elements from the 6 dysregulated miRNAs were predicted using the miRDB and TargetScan bioinformatic tools. By merging the identified targets of the dysregulated miRNAs and the 247 downregulated DEGs, a miRNA-mRNA network was constructed revealing the interaction of miR-484 with eight mRNAs (*ABLIM2*, *CEP170B*, *CTD-3193O13.9*, *EFNA5*, *GAP43*, *PRKCB*, *FXYD7*, and *NCAN*). A weighted correlation network analysis (WGCNA) based on the eight genes was established and demonstrated that these mRNAs, except *FXYD7* and *NCAN*, were hub genes in the network. Gene Oncology (GO) annotation and Kyoto Encyclopedia of Genes and Genomes (KEGG) pathway enrichment analysis revealed that the six hub genes were mainly involved in cellular-related biological functions and the neurotransmitter synapse pathway. The differences in expression levels of the miR-484 and the three hub genes (*CTD-3193O13.9*, *EFNA5*, and *PRKCB*) observed experimentally in TLE patients compared to those of healthy controls were consistent with the WGCNA prediction. **Conclusion.** Our study suggests that understanding the miRNA-mRNA interactions will provide insights into the epilepsy pathogenesis. In addition, our results indicate that miR-484 may be a promising novel biomarker for TLE.

1. Introduction

Temporal lobe epilepsy (TLE) is the refractory epilepsy marked by spontaneous recurrent seizures and the leading cause of hippocampal sclerosis. TLE is accountable for 50–80% of all diagnosed refractory epilepsy cases and is divided mainly into medial temporal lobe epilepsy (MTLE) and lateral temporal lobe epilepsy (LTLE) [1]. TLE neuropsychiatric complications have been reported to affect 30–70% of

patients, the most common of which are memory deficits [2] and cognitive impairment [3]. Although neurostimulation, epileptogenic zone surgery, and antiepileptic drugs have been applied for TLE therapy, the drug-resistant rate and neuropsychological impairment of TLE patients are still high [4]. Recent studies have shown some new insights about genetic and regulatory changes in the biological processes underlying TLE. However, the precise pathogenesis and effective biomarkers involved in the TLE epileptogenesis

still remain unclear. Thus, recognizing TLE-related molecules for early diagnosis and treatment is currently an urgent need.

MicroRNAs (miRNA) are a group of small noncoding RNAs (approximately 20 nucleotides) that modulate the posttranscriptional expression of the target gene. They specifically bind to target mRNAs in the untranslated region, which results in transcript degradation or translation inhibition. miRNAs have been continuously reported to participate in numerous biological processes in recent years, including several neurological diseases. In particular, different evidence has identified miRNA expression changes in epilepsy [5, 6]. For example, several studies have shown that miRNA can be manipulated to reduce spontaneous seizure and be a potential therapeutic target for TLE. A recent study reported a positive correlation between miRNA-145-5p and clinical evaluation of refractory epilepsy [7]. In addition, the miR-23a up-regulation can aggravate the hippocampal neuronal injuries and memory impairment in the mouse TLE model [8]. Therefore, the miRNA molecular functions on epileptogenesis and its progression have received considerable attention.

In this study, we analyzed miRNAs and mRNA expression profiles of TLE patients available in the GEO database and identified a set of differentially expressed genes (DEGs) and miRNAs. In addition, we collected miRNA-target interactions to construct a miRNA-mRNA network and acquired key TLE-related genes. By weighted correlation network analysis (WGCNA), we identified the key genes that are significantly associated with TLE clinical features. GO annotation and KEGG enrichment analysis were performed to unravel the biological mechanisms underlying TLE.

2. Materials and Methods

2.1. Microarray Data Collection. miRNA expression profiles of temporal lobe epilepsy (TLE) patients were collected from the NCBI GEO database (<https://www.ncbi.nlm.nih.gov/geo/>) using accession number GSE114701. In total, 40 samples (20 TLE patients after seizure and 20 healthy controls) analyzed on the TaqMan OpenArray Human microRNA Panel platform were included in each subseries datasets (GSE114697 Marburg and GSE114700 Beaumont). The miRNA expression file of normalized RT-qPCR data was downloaded and further processed. As for GSE114697 and GSE114700, microRNA expression in the plasma of 16 patients with epilepsy, before and after seizure, and 16 controls was measured by the TaqMan OpenArray Human microRNA Panel.

RNA-seq data of mRNA expression for hippocampal lesions in TLE were obtained from the GEO database using accession number GSE127871, which contains hippocampal tissue resected from 12 medically intractable TLE patients with presurgery seizure frequencies ranging from 0.33 to 120 seizures per month. Clinical data features, such as high seizure frequency (HSF) vs low seizure frequency (LSF) per month, were also collected on the same dataset. Data from 12 hippocampus samples that were analyzed on an Illumina HiSeq 2500 platform were also included. These samples con-

tain 4 HSF patients (mean = 4 seizures/month) and 8 LSF patients (mean = 60 seizures/month).

2.2. Measures

2.2.1. Identification of Differentially Expressed Genes (DEGs) and miRNAs. Human miRNAs were obtained from GSE114697 and GSE114700 datasets, and differentially expressed miRNAs were identified using the $2^{-\Delta\Delta Ct}$ method. The significant differences between groups (HSF and LSF patients) were analyzed using the paired *t*-test. The miRNAs that met both criteria of adjusted $P < 0.05$ and $|\log_2(\text{FC})| > 1$ were considered as TLE-related differentially expressed miRNAs. All differentially expressed miRNAs were integrated in the Marburg and Beaumont centers.

Differentially expressed genes (DEGs) in the GSE127871 dataset were identified using edge R, a Bioconductor package that employs the empirical analysis method. Significant DEGs between the HSF and LSF groups met both criteria of a P value < 0.05 and $|\log_2(\text{FC})| > 1.5$.

2.3. Functional and Pathway Enrichment Analysis. The DEGs identified in the GSE127871 dataset were classified by the related terms of gene ontology (GO) analysis, including cellular components (CC), molecular function (MF), and biological processes (BP). Kyoto Encyclopedia of Genes and Genomes (KEGG) is considered an advanced database that integrates genomic information, biological functions, disease development, and several bioinformatics studies. Based on the GO and KEGG databases, Fisher's exact test was used to identify relevance of DEGs and their functional items, especially the BP terms and functionally enriched KEGG pathways. A P value < 0.05 was considered a statistically significant enrichment.

2.4. Establishment of the Protein-Protein Interaction (PPI) Network and Identification of Hub Genes. The Search Tool for the Retrieval of Interacting Genes (STRING) database (<https://string-db.org/>) was used to analyze protein-protein interaction (PPI) information [9]. The PPI pairs were extracted using an interaction score > 0.9 and were applied for the PPI network construction. Subsequently, the Cytoscape software (version 3.6.1; <http://cytoscape.org/>) was used to visualize the PPI network [10]. Nodes with a higher degree of connectivity represented the highly interacting genes or proteins in the network. CytoHubba is a common useful plugin for calculating the degree of each node in Cytoscape. In this study, nodes with a degree greater than 5 were identified as central genes in the network.

2.5. Construction of the miRNA-mRNA Network. The miRNA-mRNA interactions were predicted by miRDB and TargetScan, two algorithms for miRNA target prediction. After obtaining miRNA-mRNA regulatory data, the network of association between miRNA and mRNA networks in TLE was generated through the intersection of the predicted miRNA target genes and the identified DEGs. The Cytoscape software was employed to visualize the regulatory network.

TABLE 1: Primer sequences of PCR.

Gene ID	Forward primer (5'-3')	Reverse primer (3'-5')
hsa_miRNA_484	TCAGGCTCAGTCCCCTCC	CAGTGCCTGTCGTGGAGT
ABLIM2	GGGAGGATGGAAGCTTGGAC	GTCCTGGGAGAGGGTCAGAT
CEP170B	AAGATGAGTGCCACGTCCTG	CAGCGTGACGTACTTCTGGT
CTD-3193O13.9	CCGAGAGGAACTACAGCGTC	CACCTCCATCGCGGACAG
EFNA5	GCACGCTTCTCCATCTTGTG	AATGAAAGTGGGCGAGAAAGGA
GAP43	GCTGTGCTGTATGAGAAGAACC	AGGACTTTGTCATCGCCAGT
PRKCB	CGATTTTTCACCCGCCATCC	CACCACAATAGCCGTTGAGC

2.6. Screening of Related Modules to Seizure Risk by Weighted Correlation Network Analysis (WGCNA). WGCNA is a data mining approach used to screen biomarkers and pathways implicated in the pathogenesis, progression, and prognosis of various diseases. WGCNA can be used for finding clusters (modules) of highly correlated genes, for summarizing such clusters using the module eigengene or an intramodular hub gene, for relating modules to one another and to external sample traits (using eigengene network methodology), and for calculating module membership measures [11, 12]. The WGCNA algorithm was used to analyze the correlation between the modules and clinical parameters in TLE. The coexpression network was constructed using the WGCNA R package and visualized by the Cytoscape software. Then, seizure risk-related modules were identified using the WGCNA algorithm. Briefly, Person's correlation coefficients were performed to calculate the counts per million (CPM) in selected genes. The CPM matrix was used as the input of the expression value for the hierarchical clustering analysis. Subsequently, the gene modules that were significantly associated with clinical traits of seizure frequency were identified. The gene information in the most relevant module was extracted, and the potential biological terms and pathways were investigated by GO annotation and KEGG pathway enrichment analysis.

2.7. miRNA-484 and Hub Gene Validation. Plasma samples were obtained from 20 patients diagnosed with TLE and 20 healthy controls at the First Affiliated Hospital of Guangxi Medical University. Total RNA was isolated from samples using Trio (Invitrogen) according to the manufacturers' protocol. The total RNA was measured using a Nanodrop 2000 microvolume spectrophotometer (LifeReal, China) by absorbance measurements at a 260 nm wavelength. RNA integrity was analyzed by 2% agarose gel electrophoresis stained with ethidium bromide. Complementary DNA (cDNA) was synthesized from 1 μ g of total RNA using the TransScript® Uni One-Step gDNA Removal and cDNA Synthesis SuperMix (TransGen Biotech, China) according to the manufacturer's guidelines. The reverse transcription-PCR (RT-PCR) reactions were carried out on an Agilent AriaMx Real-Time PCR system with a 20 μ L reaction volume. The PCR primer sequences of miRNA-484 and its target genes are shown in Table 1. To create the RT-PCR normalization, U6 RNA and GAPDH were chosen as the endogenous control for miRNA and

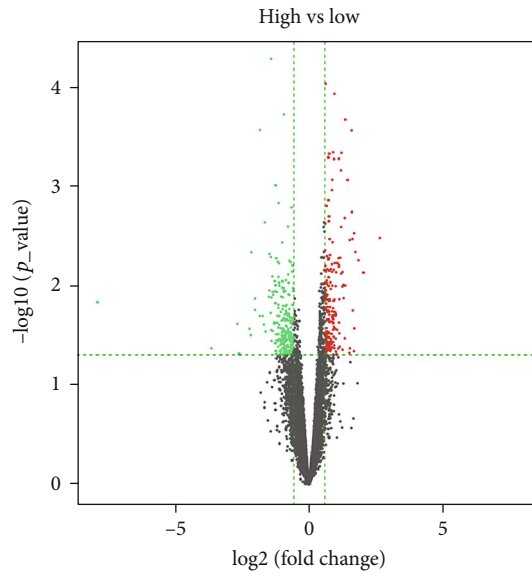
mRNA, respectively. miRNA-484 and six DEG expression were determined using the $2^{-\Delta\Delta Ct}$ method. All RT-PCR procedures were performed in triplicates. The results were analyzed by Mx3000P real-time PCR software version 2.00.

3. Results

3.1. Identification of Differentially Expressed Genes (DEGs) and miRNAs. A total of 442 DEGs were identified by comparing HSF and LSF hippocampus tissues from the GSE127871 dataset, with 195 and 247 DEGs being up- and downregulated, respectively. As shown in Figure 1(a), the expression of the identified DEGs potentially distinguishes the HSF group from the LSF group by a volcano plot. The volcano plot was generated by the R package "ggplot2." The red and green dots represent the up- and downregulated DEGs, respectively. In addition, 51 dysregulated miRNAs were identified in the GSE114697 and GSE114700 datasets, among which 6 (has-miR-133a, has-miR-17, has-miR-191, has-miR-223, has-miR-328, and has-miR-484; Table 2) showed to have a significant differential expression, being upregulated in TLE patients ($|\log_2(FC)| > 1$, P value < 0.05).

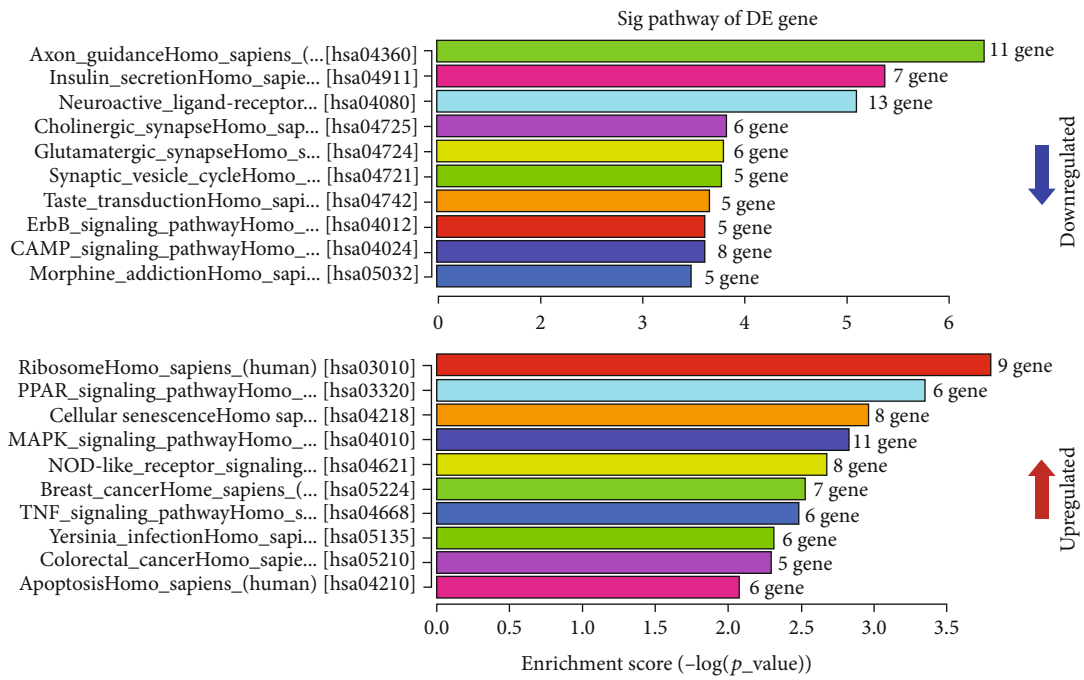
3.2. Functional Enrichment Analysis of DEGs. GO and KEGG analyzes were performed at the DAVID server to understand the function of DEGs. According to the results of the GO term analysis, the most enriched BP terms of the upregulated DEGs were mainly related to the response to external stimulus, response to organic substance, and regulation of the developmental process. However, nervous system development, chemical synaptic transmission, and regulation of membrane potential were the most enriched items of the downregulated DEGs. KEGG analysis results revealed 35 pathways related to the upregulated DEGs and 64 associated with the downregulated DEGs. The upregulated DEGs were mainly involved in ribosome biogenesis, PPAR signaling, and cellular senescence pathways. The downregulated DEGs, in turn, were mainly associated with axon guidance, insulin secretion, and neuroactive ligand-receptor interaction pathways. Figure 1(b) shows the top 10 most enriched pathways for up- and downregulated DEGs.

3.3. PPI Network Analysis of DEGs. Based on the STRING database, a PPI network was constructed containing all 442 identified DEGs and that included 268 interactions



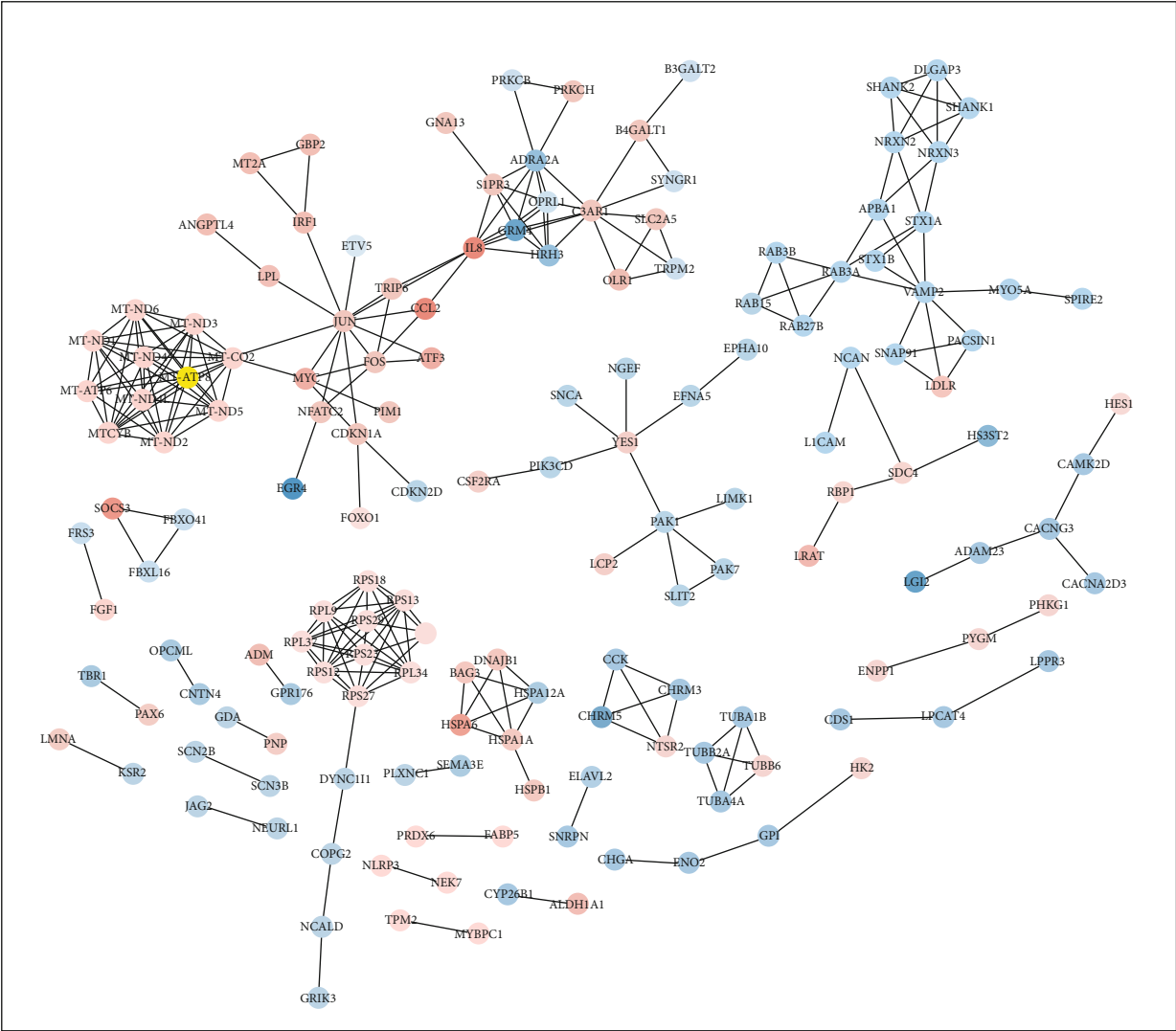
- Upregulated genes (195)
- Not differential expressed (10348)
- Downregulated genes (247)

(a)



(b)

FIGURE 1: Continued.



TLE_diff_exp_gene_ppinteractions

(c)

FIGURE 1: Continued.

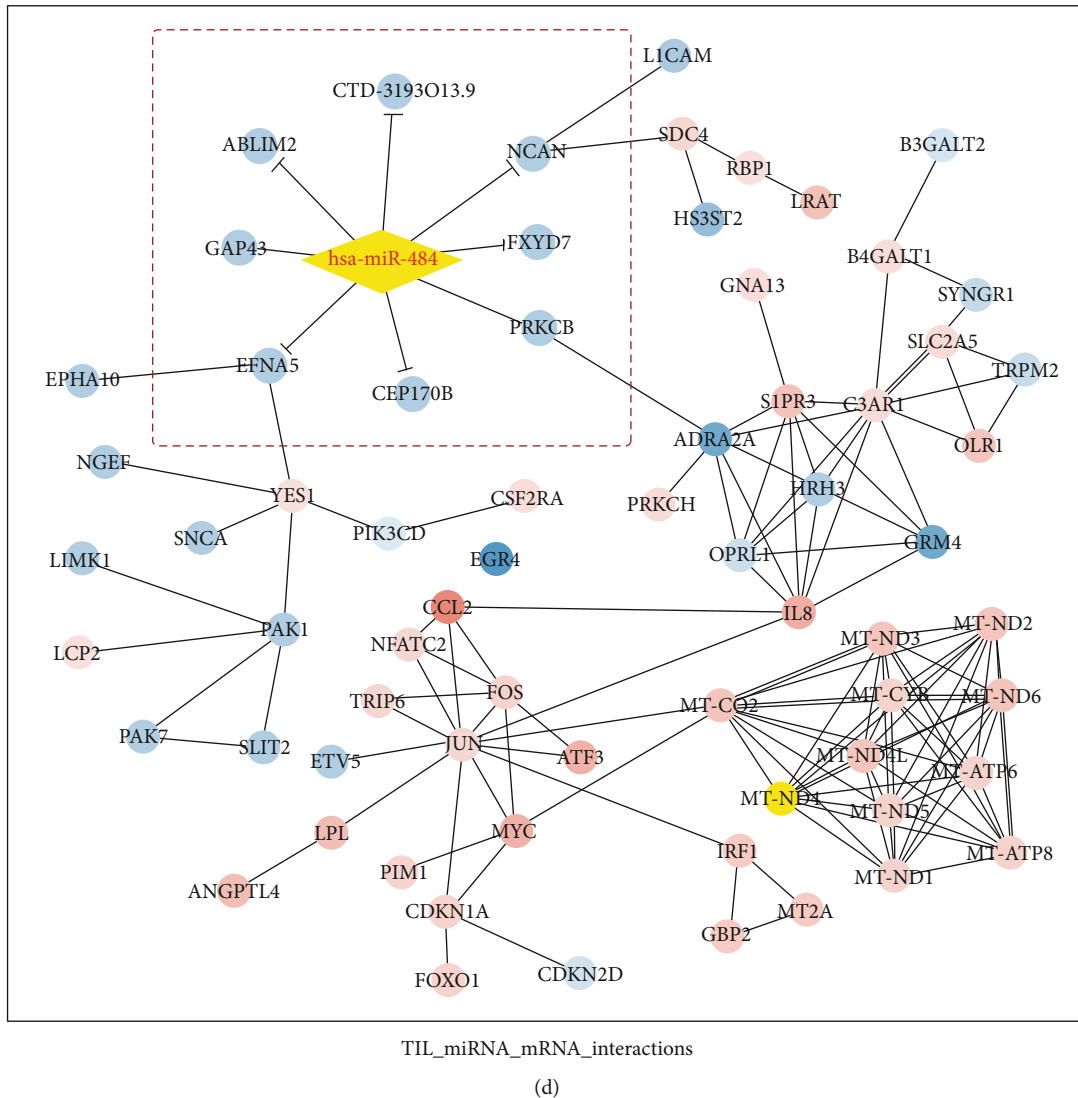


FIGURE 1: (a) The volcano plot of DGEs in TLE based on data from GEO. (b) Biological pathway enrichment analysis of up- and downregulated DEGs with the top 10 enrichment scores. (c) Protein-protein interaction network constructed with the DEGs. Red nodes represent upregulated genes, and blue nodes represent downregulated genes. (d) An integration network of the miRNA regulatory network and PPI network. The network consisting of has-miRNA-484, 76 upregulated DEGs, and 80 downregulated DEGs was generated by Cytoscape. The yellow diamond represents has-miRNA-484, red nodes represent upregulated genes, blue nodes represent downregulated genes, and the T-arrow edge represents miRNA-mRNA interactions.

TABLE 2: Information of the six differentially expressed miRNAs in TLE.

miRNA	log2FC	P value	q value	Regulation
hsa-miR-133a	1.00434	0.0428	0.9061	Up
hsa-miR-17	1.33481	0.0063	0.0644	Up
hsa-miR-191	1.53602	0.0091	0.0666	Up
hsa-miR-223	1.08246	0.0057	0.0644	Up
hsa-miR-328	1.64252	0.0018	0.0435	Up
hsa-miR-484	1.66121	0.0016	0.0435	Up

according to the highest confidence score and using a combined score > 9 as the cutoff. After calculating the connectivity degree, the PPI network was built comprising 156 nodes

and 268 edges and the interactions between the DEGs were visualized using the Cytoscape software (Figure 1(c)). Based on the CytoHubba plugin calculation, DEGs with a degree > 6 were considered central genes in the PPI network. The top 28 central genes are shown in Table 3. Among them, VAMP2 and ADRA2A were downregulated genes, while others were all upregulated in TLE samples.

3.4. Identification of Eight miRNA-mRNA Interactions. The miRNA-mRNA interactions were predicted with the miRDB and TargetScan algorithms. Following the collection of overlapping genes between the target genes of the six upregulated miRNAs and the 247 downregulated DEGs, the miRNA-mRNA network of TLE was constructed. miR-484 was found to have the highest overlapping target

TABLE 3: The top 28 differentially expressed genes in TLE.

Gene	Degree	Gene	Degree	Gene	Degree	Gene	Degree
JUN	12	MT-ND6	10	RPS18	9	RPL37	8
MT-CO2	11	MT-ND2	10	RPS13	9	VAMP2	8
C3AR1	11	MT-ND3	10	RPS29	9	IL8	8
MT-ND1	10	MT-ND5	10	RPS12	9	ADRA2A	8
MT-CYB	10	MT-ND4L	10	RPL9	9	TPT1	7
MT-ND4	10	RPS27	10	MT-ATP8	9	S1PR3	7
MT-ATP6	10	RPS23	9	RPL34	8	FOS	6

number with DEGs. The intersection between the miRNA-mRNA network and the DEG PPI network provided a preliminary view of the connections between miR-484 and DEGs. Moreover, eight miRNA-mRNA regulatory modules, including the miR-484/FXYD7 regulatory axis, miR-484/NCAN regulatory axis, miR-484/ABLIM2 regulatory axis, miR-484/CEP170B regulatory axis, miR-484/CTD-3193O13.9 regulatory axis, miR-484/EFNA5 regulatory axis, miR-484/GAP43 regulatory axis, and miR-484/PRKCB regulatory axis, were found in the intersected network (Figure 1(d)).

3.5. Coexpression Module Identification Based on WGCNA Analysis. The GSE127871 dataset containing 12 TLE samples was used for hierarchical clustering with the R WGCNA package. As shown in Figure 2(a), a total of 20 coexpression modules with a comfortable scale-free topology fit index (value = 0.8) were identified in the hierarchical clustering dendrogram. The gene counts varied for each module from 48 to 3127 genes.

To analyze the interaction association between the different modules, a heat map was generated using the “heat map tool” package in R. Figure 2(b) revealed that a light color density in the middle of the figure represents a high correlation of different modules. In addition, the module-trait relationship analysis results showed that the turquoise and magenta modules were strongly related to TLE seizures, as suggested in Figure 2(c).

To screen for genes associated with the upregulated miRNA-484 in TLE, the turquoise module was selected for subsequent analysis. It was found that six genes (*ABLIM2*, *CEP170B*, *CTD-3193O13.9*, *EFNA5*, *GAP43*, and *PRKCB*) were enriched in the turquoise module according to their degree of connectivity ($R^2 = 0.44$). Thus, these six genes were recognized as the most significant genes related to the TLE illness status and then selected as hub genes.

3.6. GO Annotation and KEGG Pathway Analyzes of Hub Genes. To further elucidate the TLE biological mechanism and identify potential biomarkers, GO annotation and KEGG pathway analyzes of the six hub genes were performed. The enrichment and *P* value analyses revealed the top ten highly enriched BP, CC, and MF terms, which are shown in Figure 3. It was observed that the most significantly modulated GO terms in BP were cellular process ($P = 3.31e - 181$), response to stimulus ($P = 1.34e - 113$),

and regulation of signaling ($P = 1.74e - 102$). The CC enriched in TLE were primarily associated with the membrane ($P = 2.36e - 252$), cytosol ($P = 4.56e - 201$), and membrane-bounded organelle ($9.30e - 191$), while the enriched MF were primarily those associated with protein binding ($P = 3.17e - 252$), catalytic activity ($P = 3.45e - 82$), and enzyme binding ($P = 4.52e - 61$). In addition, these hub genes also participate in the regulation of many KEGG pathways. A total of 110 significantly enriched pathways were obtained (*P* value < 0.05). The top 10 *P* values of enriched pathways are also shown in Figure 3. Among them, the synaptic vesicle (SV) cycle ($P = 2.32e - 8210$), dopaminergic synapse ($P = 6.97e - 8209$), and glutamatergic synapse ($P = 2.10e - 8208$) were most strongly associated pathways with TLE.

3.7. Experimental Validation of miRNA-484 and Hub Genes.

To confirm the results obtained by the bioinformatics tools, the expression levels of the miRNA-484 and the six hub genes were verified in the plasma of 20 TLE patients and compared to those of 20 healthy controls by RT-qPCR. The results showed that the miRNA-484 expression level was significantly increased in TLE patients compared to controls (Figure 4(a)). Moreover, the expression level of the *CTD-3193O13.9*, *EFNA5*, and *PRKCB* genes decreased significantly in TLE patients (Figures 4(b)–4(d)). The differences in the expression level of the *ABLIM2*, *GAP43*, and *CEP170B* genes between the two groups were not significant. These results revealed that the increased levels of miRNA-484 expression and decreased levels of hub gene expression (*CTD-3193O13.9*, *EFNA5*, and *PRKCB*) were consistent with the data obtained by the WGCNA analysis.

4. Discussion

TLE is a heterogeneous disease and a unique subtype of refractory epilepsy with poor prognosis. TLE patients are more likely to have drug resistance and underwent cognitive impairment. As the molecular mechanisms underlying therapy resistance and pathological process of TLE have not been fully elucidated, there is still no specific therapeutic target and an effective prognostic factor. Therefore, more studies are needed to discover and explore new TLE-related molecules.

MicroRNAs are a group of small noncoding RNAs with abundant biological information that have been shown to be

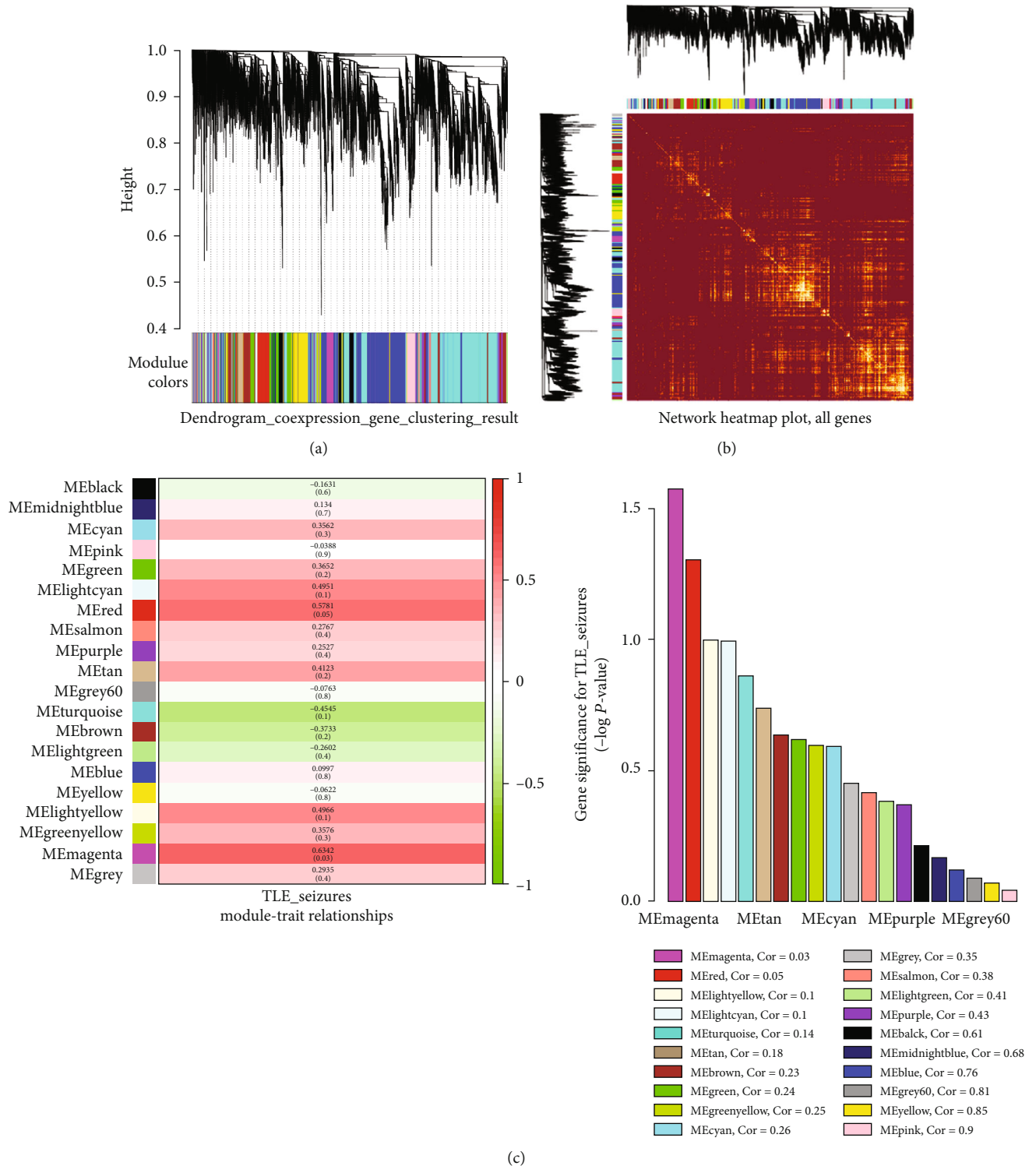


FIGURE 2: Construction of coexpression modules by WGCNA package in R. (a) The cluster dendrogram of coexpression genes in GSE127871. Each color row represents one coexpression module and gray represents genes that cannot be categorized into any module. (b) Heat map plot of genes in the weighted correlation network. Each colored row represents a color-coded module which contains a group of highly connected genes. (c) Heat map of the module-trait relationship. The module name is shown on the left side of each cell. The intensity of correlations of TLE is indicated on the right side of the heat map. Red represents the negative correlation between modules and the seizure frequency of TLE, and green represents negative correlation.

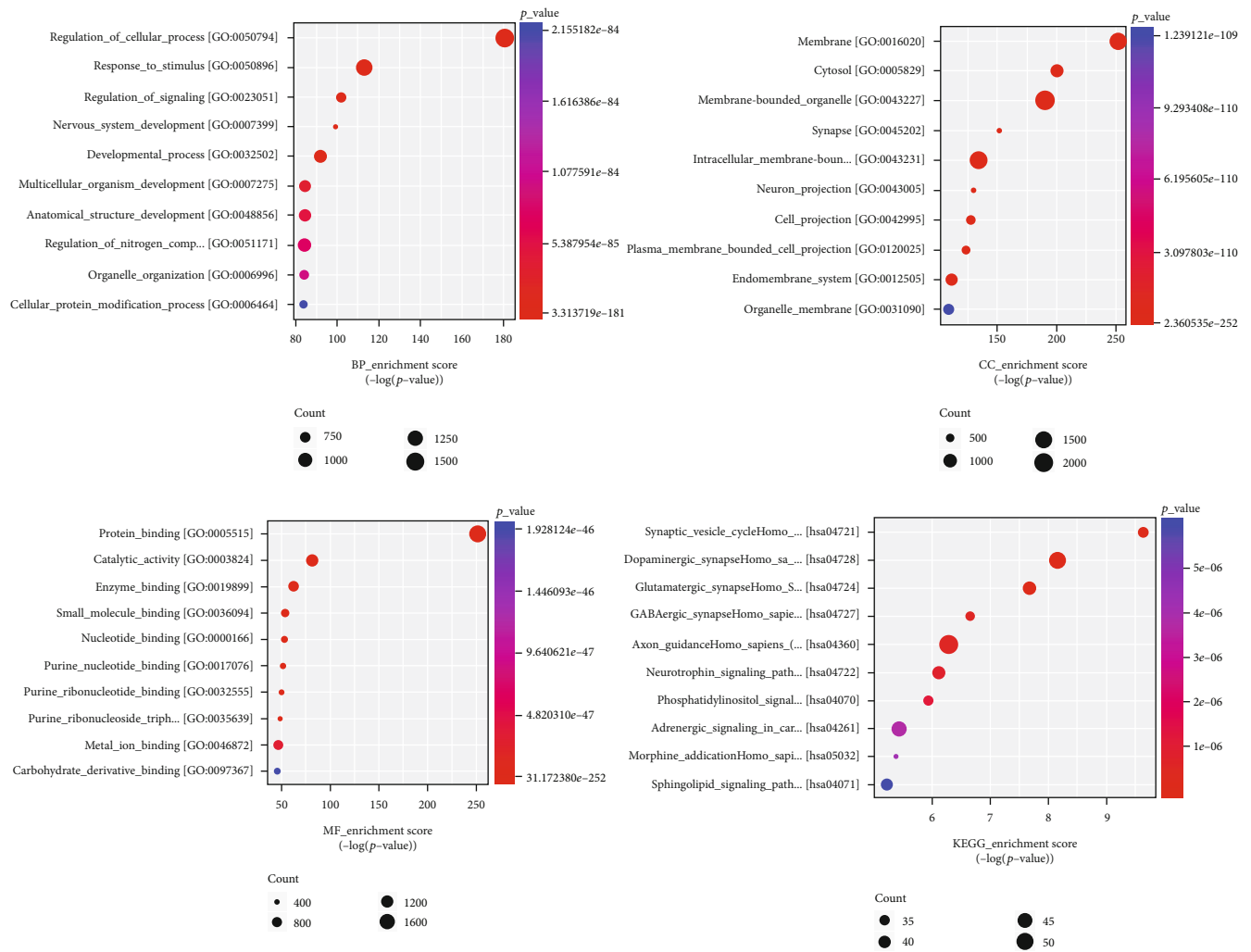


FIGURE 3: Top ten GO and KEGG enrichment annotations of the turquoise module. BP, CC, and MF terms and KEGG pathway enrichment analysis. The sizes of the circle dots represent the counts of enriched DEGs, and the intensity of circle color represents the P value.

involved in a myriad of human disorders, including seizure disorders. Early functional studies on TLE indicated that miRNA usually serves as diagnostic and therapeutic targets to influence seizures or hippocampal pathology. For example, miRNA-124, which is related to neuronal differentiation, can inhibit neuronal excitability by targeting cAMP-response element-binding protein1 (CREB1) [13]. Moreover, miR-199a-5p silencing inhibits the hippocampal neuron loss and apoptosis by targeting the antiapoptotic protein silent information regulator 1 (SIRT1) [14]. Emerging studies on the multitargeting effects of miRNAs and the coordinating gene networks have also revealed that miRNAs are crucial TLE regulators. However, the mechanism of miRNA in TLE remains unclear. There is still a need for future identification of new dysregulated miRNAs and miRNA targets in TLE.

In the present study, we identified a group of differentially expressed molecules correlated to TLE in the publicly available databases using different bioinformatics tools. In the identified molecules, 6 miRNAs (has-miR-133a, has-miR-17, has-miR-191, has-miR-223, has-miR-328, and has-

miR-484) were upregulated, 195 DEGs were upregulated, and 247 were downregulated. After the construction of a miRNA-mRNA regulatory network, we found that the upregulated miR-484 is able to regulate the expression of eight downregulated DEGs, including *ABLIM2*, *CEP170B*, *CTD-3193O13.9*, *EFNA5*, *GAP43*, *PRKCB*, *FXYD7*, and *NCAN*. These data suggest that miR-484 may be a potential targeted marker for TLE. This is the first report in the literature indicating that miR-484 plays a role in epilepsy.

To ascertain whether hsa-miR-484 performs functions and influences the clinical phenotypic effects in TLE, we carried out a WGCNA analysis and found that the eight identified DEGs enriched the turquoise, brown, and black modules associated with TLE. Among them, the turquoise module was the most strongly related to the TLE seizure phenotype according to the module-trait relationship analysis. Remarkably, we found that, except *FXYD7* and *NCAN*, all six other downregulated DEGs that are modulated by miR-484 were mostly enriched in the significant turquoise module and can function as hub markers for TLE. Finally, GO functional annotations and KEGG pathway analysis of these six hub

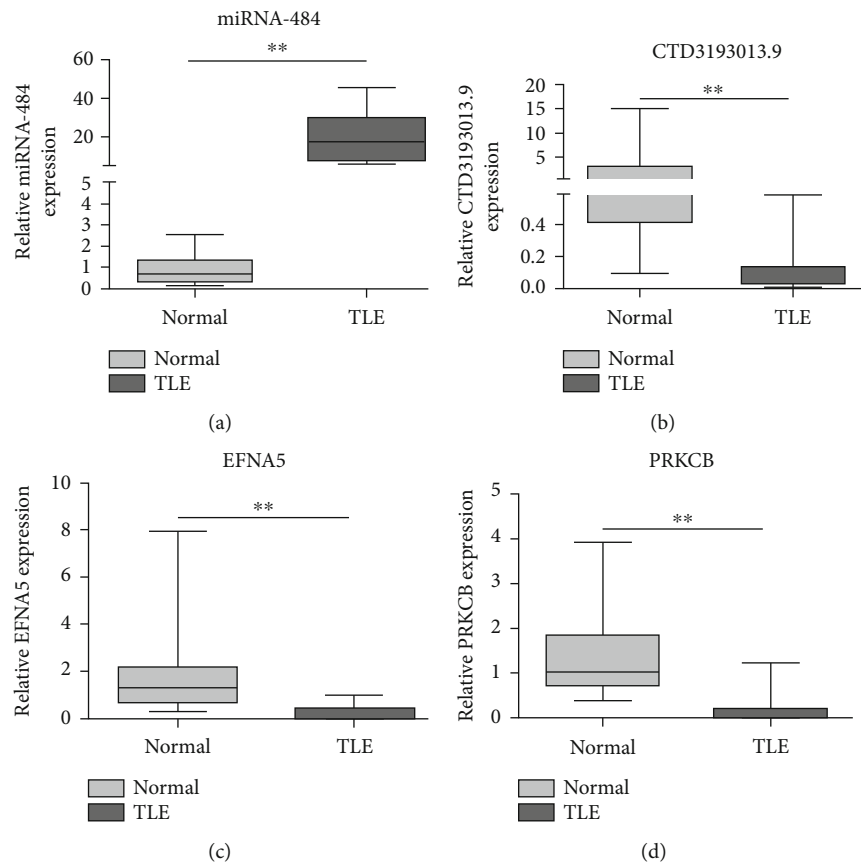


FIGURE 4: Expression levels of miRNA-484 and six genes in TLE: (a) miRNA-484, (b) *CTD-3193013.9*, (c) *EFNA5*, and (d) *PRKCB*. The mark ** means that there was significant difference between TLE and controls.

genes in the turquoise module were performed to understand the mechanisms underlying epileptogenesis. The results showed that these hub genes were involved in multiple GO BP terms such as the cellular process, multicellular organism development, and cellular protein modification process. In addition, these hub genes also participate in the regulation of many KEGG pathways, such as the SV cycle, dopaminergic synapse, GABAergic synapse, axon guidance, glutamatergic synapse, neurotrophic signaling, phosphatidylinositol signaling system, and sphingolipid signaling. As an example, animal model experiments reported that the SV cycle was targeted with some pathogenic genes, which then derived neurotransmitters release—monoamines, glutamate, GABA, etc.—and participated in the pathophysiology of seizures and epilepsy [15, 16]. Evidence has indicated that dopamine can aggravate epileptiform activity by decreasing the Mg^{2+} concentration in the newborn mouse hippocampus in vitro. Furthermore, the induction of changes in the GABAergic and glutamatergic systems leads to increased neuron excitability and the involvement of these dysregulated systems in epileptogenesis [17]. Glutamate receptors, including AMPA receptors, are characterized by influencing the alternation of Ca^{2+} concentrations, thus causing neuronal death and becoming involved in the epilepsy pathophysiology [18, 19]. Experiments using the KA-induced TLE mouse model have found that a reduction in

AMPA receptors leads to a decrease in glutamatergic transmission and therefore increases the neuron excitotoxicity and compromises the hippocampal cognitive functions [19]. These findings provide important evidence for the regulatory mechanism of miRNA-484 and the six hub genes (*ABLIM2*, *CEP170B*, *CTD-3193013.9*, *EFNA5*, *GAP43*, and *PRKCB*) in TLE.

Previous studies have shown that three of the six hub genes identified here play key roles in epilepsy. Shu et al. suggested that ephrin-A5 (*EFNA5*) is upregulated in hippocampus tissue of a TLE mouse model, and that modulates neuron generation and microvessel remodeling by inhibiting the ERK and Akt signaling pathways [20]. Ying et al. found that *GAP43* expression is higher in the epileptic area compared to the nonepileptic area. They also showed that patients with higher *GAP43* scores are associated with longer epilepsy duration and poor surgical outcome in focal cortical dysplasia IIA/B [21]. Danis et al. reported that the *PRKCB* expression is reduced by miR-184 in the 3'UTR luciferase reporter assay and that this effect may be involved in the TLE translational regulation [22]. Although the involvement of the *ABLIM2* gene in epilepsy has never been previously reported, it has been associated with neuron guidance processes [23]. Furthermore, bioinformatics analyzes have shown that *ABLIM2* is a hub gene and plays an important role in neurodegenerative diseases [24]. However, in relation

to the other two identified hub genes (CEP170B and CTD-3193O13.9), their involvement in epilepsy and other neurological disorders had not been pointed out so far.

RT-qPCR analysis of the miRNA-484 and the six hub gene expression levels in the plasma of TLE patients confirmed the results obtained by bioinformatic analyzes. The data revealed that the miRNA-484 expression was significantly increased in TLE patients. The results also revealed that three of the six hub genes (CTD-3193O13.9, EFNA5, and PRKCB) were associated with TLE and had a significant decrease in their expression level compared to the controls. These results indicate that miRNA-484 can inhibit seizure frequency in TLE by targeting CTD-3193O13.9, EFNA5, and PRKCB, which suggests that miRNA-484 may be a promising diagnostic marker for epileptogenesis. Although the experimental verification of the expression levels of miR-484 and the three hub genes in TLE patients corroborates the bioinformatics data and indicates their involvement in the TLE pathogenesis, further studies should be performed to confirm our findings in vitro and in vivo.

5. Conclusions

We identified six hub genes, the majority of which were associated with the seizure development and enrichment of the synaptic structure and neurotransmitter signaling pathways. In addition, we found that miR-484 upregulation is accompanied by the epilepsy progression via inhibition of the three hub gene expression (CTD-3193O13.9, EFNA5, and PRKCB). Our results highlight the possibility that miR-484 may be indicated as a promising novel biomarker for TLE.

Data Availability

The datasets generated and analyzed during the current study are publicly available in the GEO database (under accession code: GSE114701 and GSE127871). All the other raw data could be accessed by contacting the corresponding author if any qualified researcher needs it.

Conflicts of Interest

The authors declare that there are no conflicts of interest regarding the publication of this paper.

Acknowledgments

The authors thank Yuanhan Qin, research coordinator, for her contribution to this study. This study was funded by the 139 Plan for training high-level key medical talents in Guangxi of health.

References

- [1] F. L. Vale, E. Effio, N. Arredondo et al., "Efficacy of temporal lobe surgery for epilepsy in patients with negative MRI for mesial temporal lobe sclerosis," *Journal of Clinical Neuroscience*, vol. 19, no. 1, pp. 101–106, 2012.
- [2] R. A. Machado, V. Benjumea-Cuartas, J. F. Zapata Berruecos, P. M. Agudelo-Flóres, and L. M. Salazar-Peláez, "Reelin, tau phosphorylation and psychiatric complications in patients with hippocampal sclerosis and structural abnormalities in temporal lobe epilepsy," *Epilepsy & Behavior*, vol. 96, pp. 192–199, 2019.
- [3] V. L. Ives-Deliperi and H. Jokeit, "Impaired social cognition in epilepsy: a review of what we have learnt from neuroimaging studies," *Frontiers in Neurology*, vol. 10, p. 940, 2019.
- [4] E. Tramonì-Negre, I. Lambert, F. Bartolomei, and O. Felician, "Long-term memory deficits in temporal lobe epilepsy," *Revue Neurologique (Paris)*, vol. 173, no. 7-8, pp. 490–497, 2017.
- [5] L. G. L. Antônio, P. Freitas-Lima, G. Pereira-da-Silva et al., "Expression of microRNAs miR-145, miR-181c, miR-199a and miR-1183 in the blood and hippocampus of patients with mesial temporal lobe epilepsy," *Journal of Molecular Neuroscience*, vol. 69, no. 4, pp. 580–587, 2019.
- [6] E. Aronica, K. Fluiter, A. Iyer et al., "Expression pattern of miR-146a, an inflammation-associated microRNA, in experimental and human temporal lobe epilepsy," *The European Journal of Neuroscience*, vol. 31, no. 6, pp. 1100–1107, 2010.
- [7] C. H. Shen, Y. X. Zhang, Y. Zheng et al., "Expression of plasma microRNA-145-5p and its correlation with clinical features in patients with refractory epilepsy," *Epilepsy Research*, vol. 154, pp. 21–25, 2019.
- [8] X. Zhu, A. Zhang, J. Dong et al., "MicroRNA-23a contributes to hippocampal neuronal injuries and spatial memory impairment in an experimental model of temporal lobe epilepsy," *Brain Research Bulletin*, vol. 152, pp. 175–183, 2019.
- [9] C. von Mering, M. Huynen, D. Jaeggi, S. Schmidt, P. Bork, and B. Snel, "STRING: a database of predicted functional associations between proteins," *Nucleic Acids Research*, vol. 31, no. 1, pp. 258–261, 2003.
- [10] P. Shannon, A. Markiel, O. Ozier et al., "Cytoscape: a software environment for integrated models of biomolecular interaction networks," *Genome Research*, vol. 13, no. 11, pp. 2498–2504, 2003.
- [11] M. Shao, W. Li, S. Wang, and Z. Liu, "Identification of key genes and pathways associated with esophageal squamous cell carcinoma development based on weighted gene correlation network analysis," *Journal of Cancer*, vol. 11, no. 6, pp. 1393–1402, 2020.
- [12] P. Langfelder and S. Horvath, "WGCNA: an R package for weighted correlation network analysis," *BMC Bioinformatics*, vol. 9, no. 1, p. 559, 2008.
- [13] W. Wang, X. Wang, L. Chen et al., "The microRNA miR-124 suppresses seizure activity and regulates CREB1 activity," *Expert Reviews in Molecular Medicine*, vol. 18, article e4, 2016.
- [14] G. Jiang, R. Zhou, X. He et al., "Expression levels of microRNA-199 and hypoxia-inducible factor-1 alpha in brain tissue of patients with intractable epilepsy," *The International Journal of Neuroscience*, vol. 126, no. 4, pp. 326–334, 2016.
- [15] E. Cortès-Saladefont, A. Tristán-Noguero, R. Artuch, X. Altafaj, A. Bayès, and A. Garcia-Cazorla, "Diseases of the synaptic vesicle: a potential new group of neurometabolic disorders affecting neurotransmission," *Seminars in Pediatric Neurology*, vol. 23, no. 4, pp. 306–320, 2016.
- [16] H. Stamberger, M. Nikanorova, M. H. Willemsen et al., "STXBP1 encephalopathy: a neurodevelopmental disorder including epilepsy," *Neurology*, vol. 86, no. 10, pp. 954–962, 2016.

- [17] S. Sharopov, J. Moser, R. Chen et al., "Dopaminergic modulation of low-Mg²⁺-induced epileptiform activity in the intact hippocampus of the newborn mouse in vitro," *Journal of Neuroscience Research*, vol. 90, no. 10, pp. 2020–2033, 2012.
- [18] B. K. Siesjö and F. Bengtsson, "Calcium fluxes, calcium antagonists, and calcium-related pathology in brain ischemia, hypoglycemia, and spreading depression: a unifying hypothesis," *Journal of Cerebral Blood Flow and Metabolism*, vol. 9, no. 2, pp. 127–140, 1989.
- [19] D. E. Pellegrini-Giampietro, J. A. Gorter, M. V. Bennett, and R. S. Zukin, "The GluR2 (GluR-B) hypothesis: Ca(2+)-permeable AMPA receptors in neurological disorders," *Trends in Neurosciences*, vol. 20, no. 10, pp. 464–470, 1997.
- [20] Y. Shu, B. Xiao, Q. Wu et al., "The Ephrin-A5/EphA4 interaction modulates neurogenesis and angiogenesis by the p-Akt and p-ERK pathways in a mouse model of TLE," *Molecular Neurobiology*, vol. 53, no. 1, pp. 561–576, 2016.
- [21] Z. Ying, I. Najm, A. Nemes et al., "Growth-associated protein 43 and progressive epilepsy in cortical dysplasia," *Annals of Clinical Translational Neurology*, vol. 1, no. 7, pp. 453–461, 2014.
- [22] B. Danis, M. van Rikxoort, A. Kretschmann et al. et al., "Differential expression of miR-184 in temporal lobe epilepsy patients with and without hippocampal sclerosis - influence on microglial function," *Scientific Reports*, vol. 6, p. 33943, 2016.
- [23] J. Li, F. Chen, Q. Zhang et al., "Genome-wide network-assisted association and enrichment study of amyloid imaging phenotype in Alzheimer's disease," *Current Alzheimer Research*, vol. 16, no. 13, pp. 1163–1174, 2019.
- [24] E. De Braekeleer, J. C. Ianotto, N. Douet-Guilbert et al., "A second case of secondary acute myeloblastic leukemia associated with the MLL-KIAA0284 fusion gene," *Blood Cells, Molecules & Diseases*, vol. 42, no. 3, pp. 292–293, 2009.

Retraction

Retracted: Upregulation of miR-29c-3p Hinders Melanoma Progression by Inhibiting CDCA4 Expression

BioMed Research International

Received 12 March 2024; Accepted 12 March 2024; Published 20 March 2024

Copyright © 2024 BioMed Research International. This is an open access article distributed under the Creative Commons Attribution License, which permits unrestricted use, distribution, and reproduction in any medium, provided the original work is properly cited.

This article has been retracted by Hindawi following an investigation undertaken by the publisher [1]. This investigation has uncovered evidence of one or more of the following indicators of systematic manipulation of the publication process:

- (1) Discrepancies in scope
- (2) Discrepancies in the description of the research reported
- (3) Discrepancies between the availability of data and the research described
- (4) Inappropriate citations
- (5) Incoherent, meaningless and/or irrelevant content included in the article
- (6) Manipulated or compromised peer review

The presence of these indicators undermines our confidence in the integrity of the article's content and we cannot, therefore, vouch for its reliability. Please note that this notice is intended solely to alert readers that the content of this article is unreliable. We have not investigated whether authors were aware of or involved in the systematic manipulation of the publication process.

Wiley and Hindawi regrets that the usual quality checks did not identify these issues before publication and have since put additional measures in place to safeguard research integrity.

We wish to credit our own Research Integrity and Research Publishing teams and anonymous and named external researchers and research integrity experts for contributing to this investigation.

The corresponding author, as the representative of all authors, has been given the opportunity to register their agreement or disagreement to this retraction. We have kept a record of any response received.

References

- [1] J. Liu, G. Tao, C. Zhong, and X. Liu, "Upregulation of miR-29c-3p Hinders Melanoma Progression by Inhibiting CDCA4 Expression," *BioMed Research International*, vol. 2021, Article ID 7065963, 15 pages, 2021.

Research Article

Upregulation of miR-29c-3p Hinders Melanoma Progression by Inhibiting CDCA4 Expression

Jiazheng Liu,¹ Guilu Tao,² Cundi Zhong,¹ and Xiao Liu¹ 

¹Department of Laboratory, Second Affiliated Hospital of Dalian Medical University, Dalian, Liaoning Province, China

²Department of Wound Repairment, Second Affiliated Hospital of Dalian Medical University, Dalian, Liaoning Province, China

Correspondence should be addressed to Xiao Liu; lutou489@163.com

Received 11 April 2021; Accepted 16 August 2021; Published 29 August 2021

Academic Editor: Tao Huang

Copyright © 2021 Jiazheng Liu et al. This is an open access article distributed under the Creative Commons Attribution License, which permits unrestricted use, distribution, and reproduction in any medium, provided the original work is properly cited.

Objective. To investigate the expression and regulation mechanism of miR-29c-3p and cell division cycle associated 4 (CDCA4) in melanoma (MM). **Data and Methods.** Fifty-nine patients with MM admitted to our hospital were enrolled as the MM group. They were followed up for 3 years to analyze the prognostic factors; meanwhile, 51 healthy subjects were allocated into a normal group. MM cell lines (M21 and C8161) were transfected with miR-29c-3p-mimics, miR-29c-3p-inhibitor, miR-NC, si-CDCA4, and sh-CDCA4. The expression of miR-29c-3p, CDCA4, Bax, Caspase3, Bcl-2, N-cadherin, vimentin, and E-cadherin was quantified, and cell proliferation, migration, invasion, and apoptosis, as well as epithelial-mesenchymal transition (EMT), were determined. **Results.** Serum miR-29c-3p was lowly expressed and CDCA4 was highly expressed in the MM group. The area under the curve (AUC) of both for diagnosing MM was greater than 0.9. miR-29c-3p and CDCA4 were related to regional lymph node staging (N staging), distant metastasis (M staging), tumor diameter, and pathological differentiation. Low miR-29c-3p and high CDCA4 were associated with poor prognosis of MM. Overexpression of miR-29c-3p and suppression of CDCA4 hindered cell proliferation, migration, invasion, and expression of Bax, Caspase3, N-cadherin, and vimentin, but cell apoptosis and expression of Bcl-2 and E-cadherin were enhanced. Dual-luciferase reporter (DLR) assay confirmed the targeted relationship between miR-29c-3p and CDCA4. After miR-29c-3p-mimics+sh-CDCA4 was transfected into M21 and C8161 cells, the proliferation, invasion, and apoptosis were not different from those in the miR-NC group transfected with unrelated sequences. **Conclusion.** Overexpression of miR-29c-3p suppresses CDCA4 expression and decreases proliferation, migration, invasion, apoptosis, and EMT of MM cells, thus hindering MM progression.

1. Introduction

Melanoma (MM) is a prevalent malignant tumor in western countries with a highly heterogeneous prognosis in advanced patients and a rising incidence [1, 2]. According to epidemiological statistics, the 10-year survival is less than 30%, with 232,000 new cases and 55,000 deaths worldwide [3, 4]. The treatment mostly depends on clinical stages, tumor diameter, gene mutation, and other pathological data. Resection operation is the preferred choice for early-stage patients, and interferon- α - (INF- α -) based adjuvant therapy and systemic therapy were generally applied to middle- and advanced-stage patients, respectively. However, those treatment regimens are more or less potentially dangerous [5]. Progression to advanced MM leads to greatly reduced therapeutic effec-

tiveness and high cost, and the best way to prevent the progression is early diagnosis [6]. At present, the diagnosis of MM mainly relies on pathological biopsy and computer-assisted imaging techniques which have the limitations of low acceptability, high cost, and complicated operation [7]. Therefore, it is of great significance to find reliable, convenient, and cost-effective biological diagnostic indicators for prevention, early diagnosis, and treatment of MM.

MicroRNAs (miRNAs) regulate gene expression through a variety of biological mechanisms and have excellent pathological regulation functions in cancer cells and the tumor microenvironment [8–10]. The abnormal expression of miRNAs in the serum of MM patients provides a new insight for serum-based noninvasive diagnosis of MM, and a number of miRNAs have been reported to be available

for the early diagnosis of this disease [11, 12]. miR-29c-3p is a member of the miRNA family and miR-29 family. miR-29a/b functions as a cytokine signal transducer in the IFN- γ -related MM regulation mechanism, while miR-29c-3p is involved in MM progression by mediating methylation of relevant genes, which is valuable for evaluating the prognosis of the patients [13, 14]. Cell division cycle associated 4 (CDCA4) is a functional protein that interferes with the cell cycle by participating in the transcriptional activation of transcription factor E2F, and its expression in cancer cells is capable of regulating cell growth and DNA synthesis [15]. As a direct target for miR-15a, CDCA4 affects growth and invasion of mouse MM cells, playing an essential role in the regulatory mechanism of MM [16].

In this study, online target gene prediction software (http://www.targetscan.org/vert_72/) demonstrated that CDCA4 shared target loci with miR-29c-3p, so we speculated that miR-29c-3p affected the biological function of MM cells by targeting CDCA4. We aimed to investigate the expression and regulation mechanism of miR-29c-3p and cell division cycle associated 4 (CDCA4) in melanoma (MM).

2. Data and Methods

2.1. Clinical Data. Fifty-nine patients (33 males and 26 females, average age: 58.65 ± 7.33 years) with MM who were admitted to our hospital from March 2014 to March 2016 being enrolled as the MM group. Another 51 healthy individuals (29 males and 22 females, average age: 58.43 ± 7.18 years) were enrolled. There was no significant difference in sex and age between the two groups ($P > 0.05$), indicating a comparability.

2.2. Inclusion Criteria. Patients diagnosed with MM by pathology or laboratory indicators [17] and meeting tumor-node-metastasis (TNM) staging criteria [18], patients treated for the first time, and patients who received no drugs that affected the indicators of this study within half a year were included. Exclusion criteria are as follows: patients with other malignant tumors, organ dysfunction, other skin diseases, or infectious and autoimmune diseases. All patients and their families agreed to participate in the study and signed the informed consent form. Hospital Ethics Committee approval was obtained.

2.3. Experimental Reagents and Materials. Human MM cell lines M21, MV3, C8161, and FM88 and normal skin cell line HFF (C0815, C0922, GD-C0038632A66388, GD-C0038632A67230, GD-C0038632A65580, Guandao Bioengineering Co., Ltd., Shanghai, China); Lipofectamine™ 2000 Kit (11668019, Woosen Biological Technology Co., Ltd., Hangzhou, Zhejiang, China); TransScript Green miRNA Two-Step qRT-PCR SuperMix and TransScript II Green Two-Step qRT-PCR SuperMix (abx098036, abx098035, QW Biotechnology Co., Ltd., Beijing, China); methyl thiazolyl tetrazolium (MTT) kit, radioimmunoprecipitation assay (RIPA), and TRIzol (111105-500, 9806S, KGA1201, Winter Song Boye Biotechnology Co. Ltd., Bei-

jing, China); dual-luciferase reporter (DLR) assay kit, goat anti-rabbit (IgG) secondary antibody, fetal bovine serum (FBS), and enhanced chemiluminescence (ECL) developer (KFS303-TFX, WK363-BXY, QS071, GL1055-LIE, Baiao Laibo Technology Co., Ltd., Beijing, China); and phosphate buffer saline (PBS) and bicinchoninic acid (BCA) protein kit (120830, 120982, ChreaGen Biotechnology Co., Ltd., Beijing, China). CDCA4, Bax, Caspase3, Bcl-2, N-cadherin, vimentin, E-cadherin, and β -actin antibody (Kemin Biotechnology Co., Ltd., Shanghai, China); a polymerase chain reaction (PCR) instrument and flow cytometer (DLK0003730, DLK0002051, DERICA Biotechnology Co., Ltd., Beijing, China); an ultraviolet (UV) spectrophotometer (UV-1100, Peking University Care Industrial Park, Beijing, China); and primers (Beijing Future Biotechnology Co., Ltd.) were used.

2.4. Cell Culture, Passage, and Transfection. MM cell lines were cultured in Dulbecco's modified Eagle medium (DMEM) comprising 10% FBS at 37°C and 5% CO₂. When reaching 85% confluence, the cells were digested with 25% Trypsin, then placed in the medium for continuous culture to complete passage, and, finally, transfected with miR-29c-3p-mimics (overexpression sequence) and miR-29c-3p-inhibitor (inhibition sequence), negative control miR (miR-NC), targeted inhibition of CDCA4 RNA (si-CDCA4), targeted overexpression of CDCA4 RNA (sh-CDCA4), and negative control RNA (si-NC) separately with a Lipofectamine™ 2000 kit.

2.5. Detection Methods

2.5.1. Quantitative Real-Time PCR (qRT-PCR). A TRIzol kit was employed to extract the total RNA from the collected serum and cells, and the purity and concentration were read with an UV spectrophotometer. Total RNA (5 μ g) was taken for reverse transcription, and 1 μ L of synthesized cDNA was served for amplification. The miR-29c-3p amplification system consists of the following: cDNA 1 μ L, upstream and downstream primers 0.4 μ L each, 2x TransTaq® Tip Green qPCR SuperMix 10 μ L, Passive Reference Dye (50x) 0.4 μ L, and finally made up to 20 μ L with ddH₂O. Amplification conditions are as follows: PCR conditions: 94°C for 30 s, 40 cycles of 94°C for 5 s and 60°C for 30 s. The CDCA4 amplification system consists of the following: cDNA 1 μ L, upstream and downstream primers 0.4 μ L each, 2x TransScript® Tip Green qPCR SuperMix 10 μ L, Passive Reference Dye (50x) 0.4 μ L, and finally made up to 20 μ L with nuclease-free water. Amplification conditions consist of the following: 95°C for 30 s, 40 cycles of 95°C for 10 s and 60°C for 30 s. Each sample was provided with 3 repeated wells, and the test was conducted for 3 times. U6 and β -actin were served as an internal reference of miR-29c-3p and CDCA4, and $2^{-\Delta\Delta ct}$ was employed to analyze the data [19].

2.5.2. Western Blot. Cultured cells were added with RIPA to extract the total protein, and the concentration was detected by BCA. The protein with a density of 4 μ g/ μ L was separated by 12% sodium dodecylsulphate-polyacrylamide gel electrophoresis (SDS-PAGE) and grafted to a polyvinylidene

difluoride (PVDF) membrane. The membrane was sealed with 5% defatted milk powder for 2 h, then added with CDCA4, Bax, Caspase3, Bcl-2, E-cadherin, N-cadherin, vimentin, and β -actin antibody (1:1000), and sealed overnight at 4°C. After removal of the β -actin antibody, a goat anti-rabbit secondary antibody (1:1000, HRP) was added; the membrane was incubated at 37°C for 1 h and rinsed with PBS for 3 times, 5 min each. Afterwards, the liquid was dried with filter paper. Development was carried out in a dark-room with an ECL developer. The protein bands were scanned to analyze the gray value in Quantity One software. Relative expression of protein = target protein band gray value/ β -actin protein band gray value.

2.5.3. MTT Assay for Cell Viability. MM cells harvested 24 hours after transfection (5×10^3 cells/well) were inoculated in 96-well plates at 37°C for 24, 48, and 72 hours, and 20 μ L MTT solution (5 μ g/mL) was added at each time point. After inoculating at 37°C for 4 h, 200 μ L dimethyl sulfoxide (DMSO) was added to each well. The optical density (OD) value was read by a spectrophotometer at the 490 nm wavelength.

2.5.4. Wound Healing Assay for In Vitro Cell Migration. Cells diluted to 3×10^5 cells/mL were inoculated in 6-well plates. After reaching 85% confluence, a scratch was made artificially in monolayer cells using 200 μ L sterile pipette tips. The scratched cells were washed with PBS and cultured in a new medium. At 0 h (W0) and 24 h (W24) after scratching, cell migration was evaluated by a microscope through three scratches.

2.5.5. Transwell for Cell Invasion. MM cells harvested 24 hours after transfection (3×10^3 cells/well) were inoculated in 24-well plates, then trypsinized and transferred to the apical chamber. RPMI 1640 solution (200 μ L) was added to the upper apical while RPMI 1640 (500 mL containing 10% FBS) to the basolateral chamber. After a 48 h culture at 37°C, substrates and cells in the apical chamber were removed. The membrane was washed 3 times with PBS, immobilized for 10 min with paraformaldehyde, washed another 3 times with double distilled water, and stained with 0.5% crystal violet after drying. Cell invasion was determined with a microscope.

2.5.6. Flow Cytometry for Cell Apoptosis. Transfected cells were digested with 0.25% trypsin, washed twice with PBS, added with 100 μ L of binding buffer, and then prepared into 1×10^6 /mL suspension. Annexin V-FITC and propidium iodide (PI) were added sequentially, and the suspension was incubated at room temperature in the dark for 5 min. Cell apoptosis was detected with a flow cytometer, and the test was repeated 3 times to take the average.

2.5.7. DLR Assay. TargetScan7.2 predicted downstream target genes of miR-29c-3p. CDCA4 3'-untranslated region-wild type (3'UTR-Wt), CDCA4 3'UTR-mutant (Mut), miR-29c-3p-mimics, and miR-NC were transferred into M21 and C8161 cells using a Lipofectamine™ 2000 kit, and luciferase activity was determined in a DLR assay system.

2.6. Statistical Analysis. In our study, GraphPad 6 was employed for building graphs and processing data. Inter-group comparison was conducted with independent sample *t*-test and multigroup comparison with one-way analysis of variance (ANOVA) (denoted by *F*). The post hoc pairwise comparison was conducted with Fisher's least significant difference *t*-test, expression at multiple time points was analyzed with repeated measurement ANOVA (denoted by *F*), and the post hoc test was carried out with Bonferroni [20, 21]. The diagnostic value of miR-29c-3p and CDCA4 in MM was visualized with a receiver operating characteristic (ROC) curve [22]. Pearson's test identified the correlation of miR-29c-3p with CDCA4 in the serum, and the Cox analysis analyzed the independent prognostic factors of MM. A value of $P < 0.05$ indicated statistically significant difference [23–25].

3. Results

3.1. Expression and Diagnostic Value of Sera miR-29c-3p and CDCA4. The MM group exhibited remarkably lower serum miR-29c-3p and higher serum CDCA4 than the normal group ($P < 0.05$). The areas under the curve (AUC) of miR-29c-3p and CDCA4 for diagnosing MM were 0.912 and 0.939, respectively. Pearson's test revealed the negative correlation between the expressions of miR-29c-3p and CDCA4 ($r = -0.671$, $P < 0.001$). Both miR-29c-3p and CDCA4 were associated with regional lymph node staging (N staging), distant metastasis (M staging), tumor diameter, and pathological differentiation ($P < 0.05$), and miR-29c-3p is also closely correlated with tumor invasion staging (T staging) ($P < 0.05$) (see Figure 1 and Table 1).

3.2. Prognostic Value of Sera miR-29c-3p and CDCA4 in MM. All 59 patients with MM were followed up successfully for 3 years, and the 3-year overall survival (OS) was 27.12% (16/59). Among them, 16 dead patients were regarded as the poor prognosis group and 43 surviving patients as the good prognosis group. It turned out that patients in the poor prognosis group had remarkably lower serum miR-29c-3p and higher serum CDCA4 than those in the good prognosis group ($P < 0.05$). The AUC of miR-29c-3p and CDCA4 for predicting the poor prognosis of MM were 0.830 and 0.842, respectively. Low miR-29c-3p and high CDCA4 were correlated with lower OS. Cox regression revealed that TNM staging, tumor diameter, pathological differentiation, miR-29c-3p, and CDCA4 were independent prognostic factors of MM (see Figure 2 and Table 2).

3.3. Effects of miR-29c-3p on Biological Functions of MM Cells and Epithelial-Mesenchymal Transition- (EMT-) Related Proteins. miR-29c-3p showed suppressed expression in M21, MV3, C8161, and FM88 cells. After M21 and C8161 cells were transfected with miR-29c-3p-mimics, not only the miR-29c-3p-3p protein expression but also Bax, Caspase3, and E-cadherin expressions were elevated markedly, but the proliferation, migration, invasion, and protein expression of Bcl-2, N-cadherin, and vimentin were remarkably inhibited. However, opposite results were acquired when

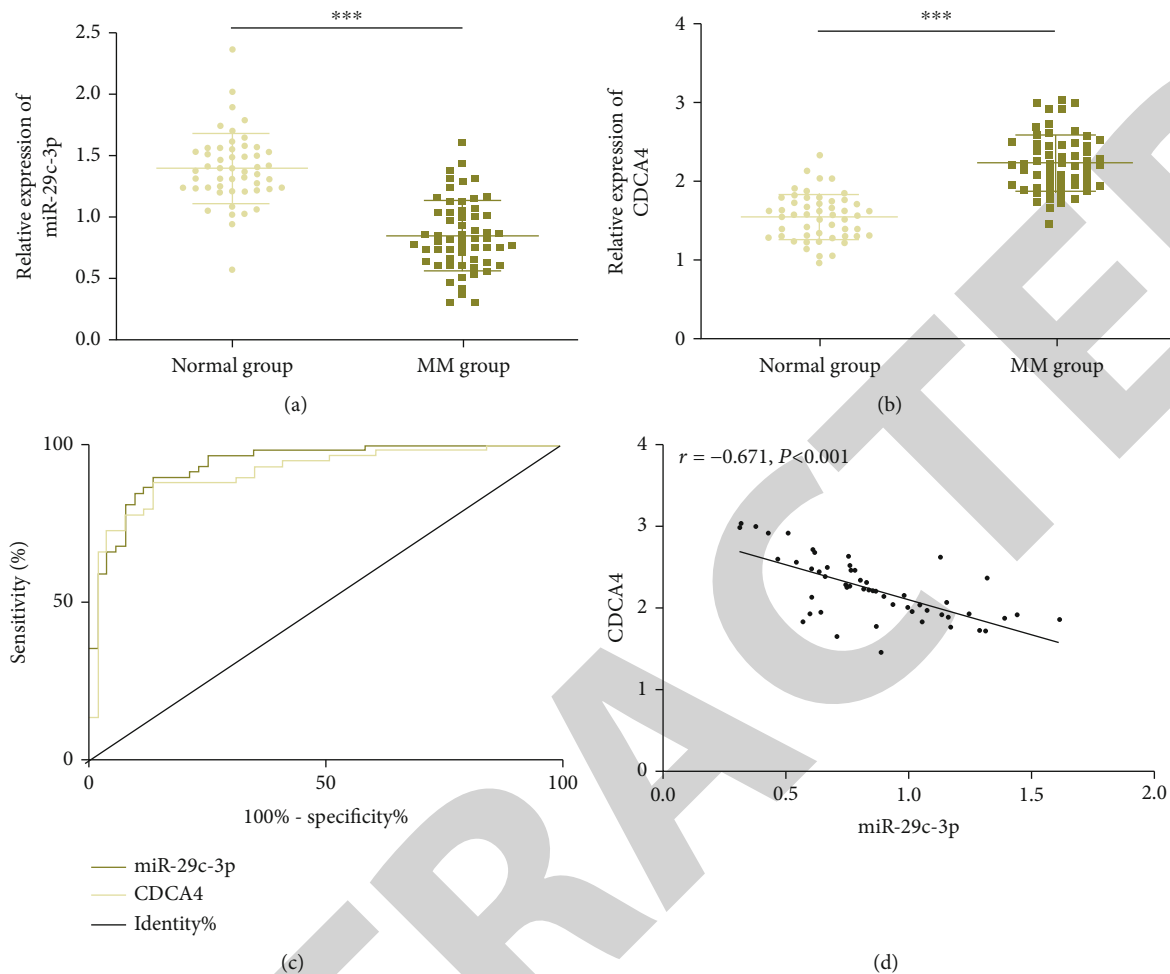


FIGURE 1: Expression and diagnostic value of sera miR-29c-3p and CDCA4. (a) Expression of serum miR-29c-3p in the MM group is remarkably lower than that in the normal group. (b) Expression of serum CDCA4 in the MM group is remarkably higher than that in the normal group. (c) AUC of miR-29c-3p and CDCA4 for diagnosing MM are 0.912 and 0.939, respectively. (d) Serum miR-29c-3p is closely negatively correlated with CDCA4 expression ($r = -0.671$, $P < 0.001$). Note: *** $P < 0.001$.

cells were transfected with miR-29c-3p-inhibitor ($P < 0.05$) (see Figure 3).

3.4. Effects of CDCA4 on Biological Functions of MM Cells and EMT-Related Proteins. CDCA4 showed elevated expression in M21, MV3, C8161, and FM88 cells. After M21 and C8161 cells were transfected with si-CDCA4, not only CDCA4 expression but also proliferation, migration, and invasion, as well as the Bcl-2, N-cadherin, and vimentin expressions, were inhibited, but the expressions of Bax, Caspase3, and E-cadherin were remarkably elevated. However, opposite results were acquired in cells transfected with sh-CDCA4 ($P < 0.05$) (see Figure 4).

3.5. Identification of miR-29c-3p Target Genes. Targeted binding loci between CDCA4 and miR-29c-3p were discovered by TargetScan7.2. Therefore, we conducted a DLR assay and found that the luciferase activity of pmirGLO-CDCA4-3'UTR-Wt decreased significantly after upregulating miR-29c-3p ($P < 0.05$), but that of pmirGLO-CDCA4-3'UTR-Mut showed no changes ($P > 0.05$). Western blot demon-

strated that the expression of the CDCA4 protein in M21 and C8161 cells was remarkably suppressed after miR-29c-3p-mimics transfection ($P < 0.05$) (see Figure 5).

3.6. Cell Cotransfection. After transfecting miR-29c-3p-mimics+sh-CDCA4 and miR-29c-3p-inhibitor+si-CDCA4, M21 and C8161 cells showed no significant difference in proliferation, invasion, and expression of proteins compared with miR-NC ($P > 0.05$). However, compared with the cells transfected with miR-29c-3p-mimics, the proliferation, migration, and invasion and the expression of Bcl-2, N-cadherin, and vimentin proteins were remarkably enhanced, but the apoptosis and the expression of Bax, Caspase3, and E-cadherin proteins were remarkably inhibited. Compared with those transfected with the miR-29c-3p-inhibitor, all the results were reversed ($P < 0.05$) (see Figure 6).

4. Discussion

In this study, we found that miR-29c-3p hinders the progression of MM through the targeted inhibition of CDCA4.

TABLE 1: Association between miR-29c-3p, CDCA4, and pathological data (*n* (%), mean \pm SD).

Factor	<i>n</i> = 59	miR-29c-3p	<i>T</i>	<i>P</i>	CDCA4	<i>T</i>	<i>P</i>
Sex			0.824	0.414		0.569	0.572
Male	33	0.83 \pm 0.24			2.18 \pm 0.36		
Female	26	0.88 \pm 0.22			2.13 \pm 0.30		
Age (years)			0.893	0.376		0.768	0.446
<60	31	0.86 \pm 0.20			2.11 \pm 0.29		
\geq 60	28	0.81 \pm 0.23			2.17 \pm 0.31		
T staging			2.885	0.006		1.903	0.062
T2/T3	45	0.94 \pm 0.27			2.06 \pm 0.31		
T4	14	0.72 \pm 0.16			2.23 \pm 0.22		
N staging			3.112	0.003		3.033	0.004
N0	17	0.96 \pm 0.19			2.04 \pm 0.20		
N1	42	0.75 \pm 0.25			2.26 \pm 0.27		
M staging			3.178	0.002		3.265	0.002
M0	48	0.98 \pm 0.27			2.02 \pm 0.22		
M1	11	0.71 \pm 0.16			2.25 \pm 0.16		
Tumor diameter (cm)			3.529	<0.001		2.970	0.004
<5	34	0.95 \pm 0.23			2.05 \pm 0.19		
\geq 5	25	0.74 \pm 0.22			2.22 \pm 0.25		
Pathological differentiation			3.965	<0.001		3.246	0.002
Poorly differentiated	35	0.70 \pm 0.24			2.28 \pm 0.36		
Moderately and highly differentiated	24	0.94 \pm 0.21			1.99 \pm 0.30		

More and more scholars have shown great enthusiasm for the clinical value and regulation of miR-29c-3p and CDCA4 in human diseases; accordingly, numerous related researches emerged. For example, Licholai and Szczeklik stated that miR-29c-3p is a potential diagnostic indicator for patients with abdominal aortic aneurysm; it also inhibits the synthesis of the extracellular matrix by inhibiting related transcripts [26]. Besides, Chen et al. indicated that miR-29c-3p, a tumor suppressor, hinders invasion and migration of colon cancer cells by targeting the Pleckstrin homology-like domain family B member 2 (PHLDB2) [27]. In addition, according to Shi et al., silencing CDCA4 effectively inhibits the proliferation and accelerates the apoptosis of breast cancer cells [28].

The above findings remind us of the potential value of miR-29c-3p and CDCA4 in human diseases, so we explored their effects on MM in this study. It turned out that miR-29c-3p and CDCA4 showed low expression and high expression in the serum of MM patients, respectively, which made them available to distinguish the patients from healthy individuals. Therefore, we assessed the diagnostic value of miR-29c-3p and CDCA4 for MM. Surprisingly, the AUC of the two were 0.912 and 0.939, respectively, indicating their excellent diagnostic value for MM. We also analyzed the potential clinical value of miR-29c-3p and CDCA4. The results revealed that both were closely related to N staging, M staging, tumor diameter, and pathological differentiation, and miR-29c-3p was also related to T staging. Therefore, both miR-29c-3p and CDCA4 participate in the pathological

process of MM and have a potential value in predicting pathological parameters of patients. We also found that low miR-29c-3p and high CDCA4 in serum were associated with poor prognosis and low 3-year OS of MM patients. Cox regression confirmed that both were independent prognostic factors of MM and so were TNM staging, tumor diameter, and pathological differentiation. In the study of Mirili, it was also pointed out that TNM staging, ulcer, and prognostic nutritional index (PNI) are independent predictors of OS of patients with MM [29], which indicates that PNI may also be a prognostic indicator of MM.

The above is our exploration on the potential clinical value of miR-29c-3p and CDCA4; next, the biological function analysis has been carried out. The expression of miR-29c-3p and CDCA4 in MM cell lines was consistent with that in the serum. We transfected M21 and C8161 cells with the most significant expression in cell lines. Cells transfected with miR-29c-3p-mimics or si-CDCA4 showed not only lower proliferation, migration, and invasion but also higher apoptosis. However, opposite results were achieved in the cells transfected with the miR-29c-3p-inhibitor or sh-CDCA4. The above results suggested that overexpression of miR-29c-3p or knockdown of CDCA4 may play a role in hindering MM progression. In addition, the DLR assay showed that overexpressed miR-29c-3p remarkably reduced luciferase activity of pmirGLO-CDCA4-3'UTR-Wt, but it had no effect on pmirGLO-CDCA4-3'UTR-Mut. Furthermore, miR-29c-3p-mimics suppressed the expression of

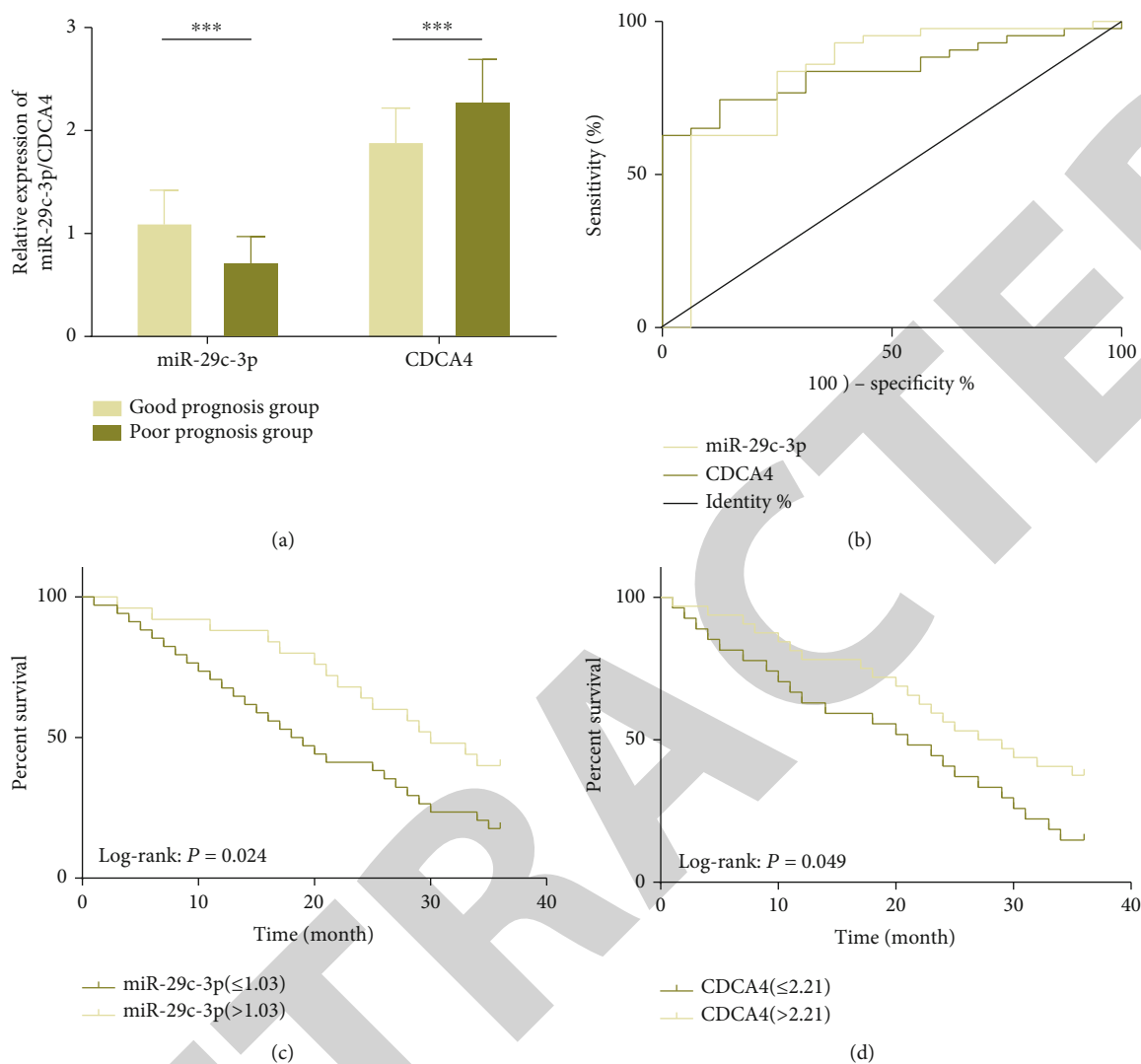


FIGURE 2: Prognostic value of sera miR-29c-3p and CDCA4 in MM. (a) Low miR-29c-3p and high CDCA4 are significantly correlated with poor prognosis of MM patients. (b) AUC of sera miR-29c-3p and CDCA4 for predicting poor prognosis of MM are 0.830 and 0.842, respectively. (c) Low miR-29c-3p is significantly correlated with the lower 3-year OS of MM patients. (d) High CDCA4 is significantly correlated with the lower 3-year OS of MM patients. Note: *** $P < 0.001$.

TABLE 2: Univariate and multivariate Cox regression analyses.

Indicator	Univariate		Multivariate	
	HR (95% CI)	<i>P</i>	HR (95% CI)	<i>P</i>
Sex	1.209 (0.789-2.173)	0.216		
Age	1.105 (0.890-1.542)	0.099		
T staging	1.957 (2.016-2.163)	0.016	1.646 (1.446-2.971)	0.012
N staging	3.869 (1.485-3.420)	<0.001	3.365 (2.329-4.122)	0.001
M staging	2.224 (1.196-3.775)	0.009	2.531 (0.817-3.924)	0.002
Tumor diameter	1.563 (1.017-2.491)	0.043	1.768 (0.465-2.354)	0.001
Pathological differentiation	2.832 (1.334-11.365)	0.001	3.665 (0.845-9.954)	0.005
miR-29c-3p	7.036 (1.564-9.254)	0.004	6.174 (1.341-28.315)	0.020
CDCA4	5.111 (1.021-21.708)	0.011	7.033 (1.562-9.246)	0.003

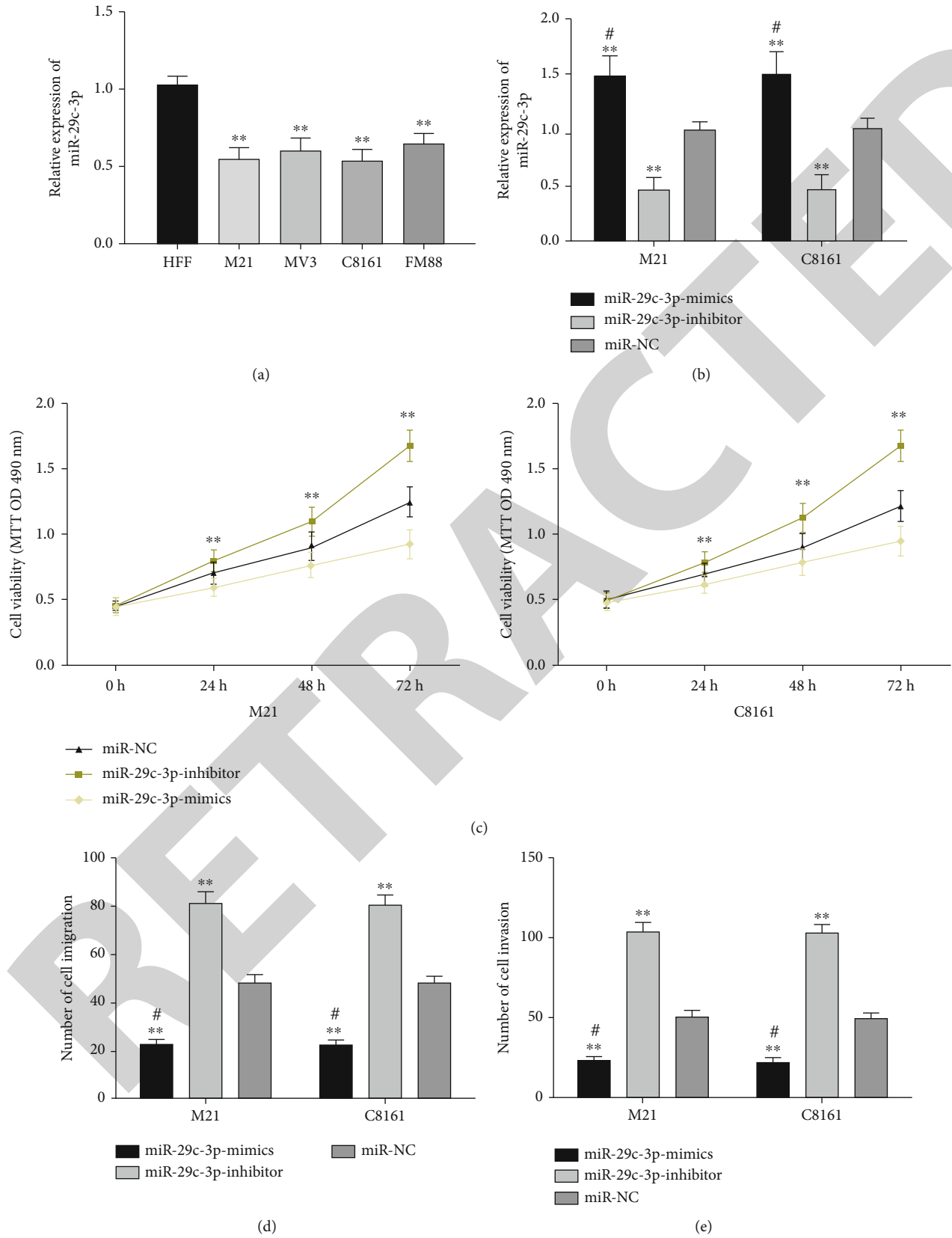


FIGURE 3: Continued.

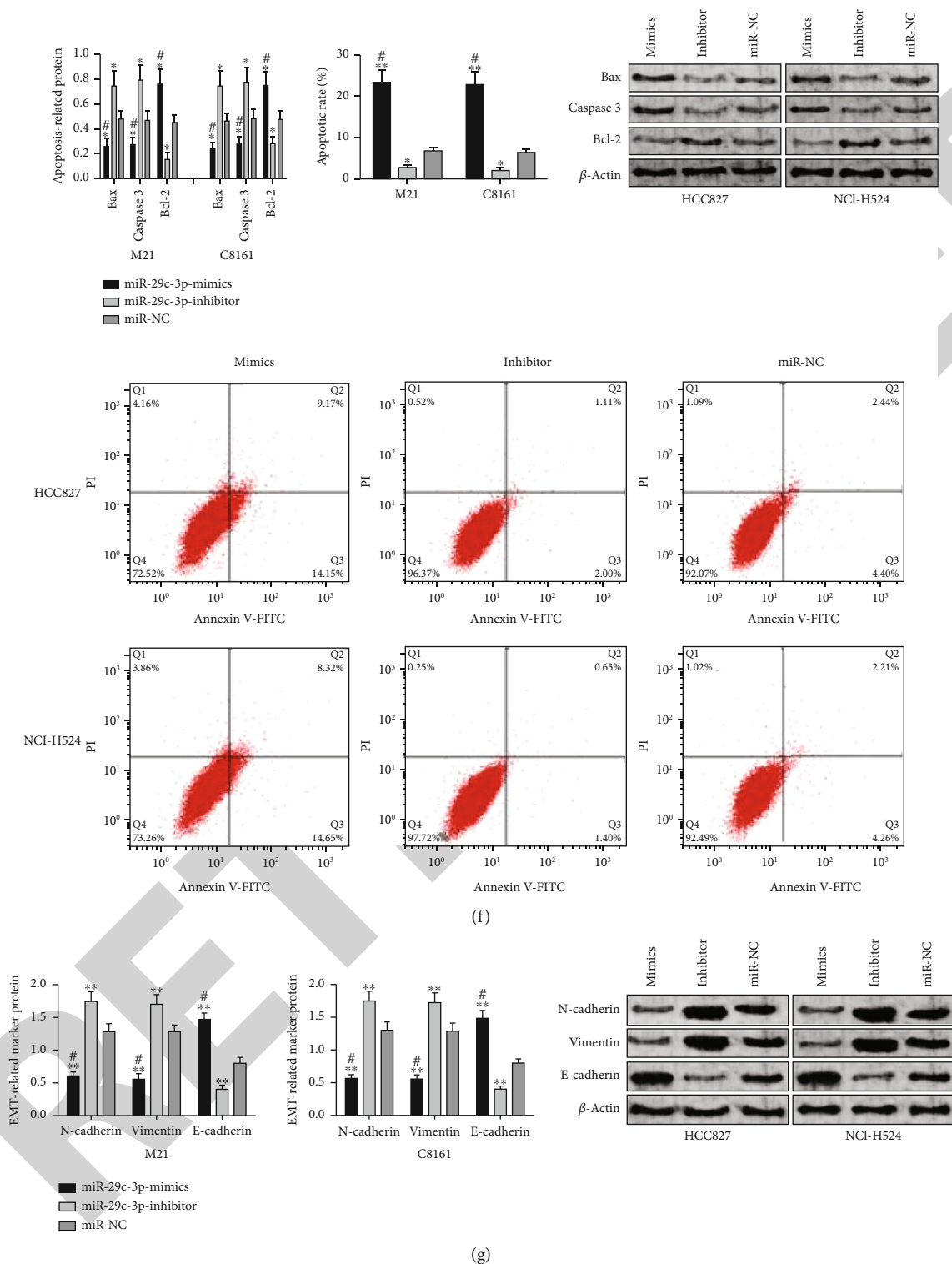


FIGURE 3: Effects of miR-29c-3p on biological functions of MM cells and EMT-related proteins. (a) miR-29c-3p is lowly expressed in MM cells, especially in M21 and C8161 cells. (b) Expression of miR-29c-3p is elevated markedly in cells transfected with miR-29c-3p-mimics. (c) Proliferation of cells transfected with miR-29c-3p-mimics is hindered markedly. (d) Migration of cells transfected with miR-29c-3p-mimics is hindered markedly. (e) Invasion of cells transfected with miR-29c-3p-mimics is hindered markedly. (f) Expression of Bcl-2 protein in the cells transfected with miR-29c-3p-mimics is remarkably suppressed, while those of Bax and Caspase3 proteins are remarkably elevated. Apoptosis of cells transfected with miR-29c-3p-mimics is significantly enhanced. The protein map and flow cytometry diagram are provided. (g) Expression of N-cadherin and vimentin proteins in the cells transfected with miR-29c-3p-mimics is remarkably suppressed, while that of E-cadherin protein is remarkably elevated. The protein map is provided. Note: * $P < 0.05$, ** $P < 0.01$ vs. the miR-NC group or HFF cells; # $P < 0.05$ vs. the miR-29c-3p-inhibitor group.

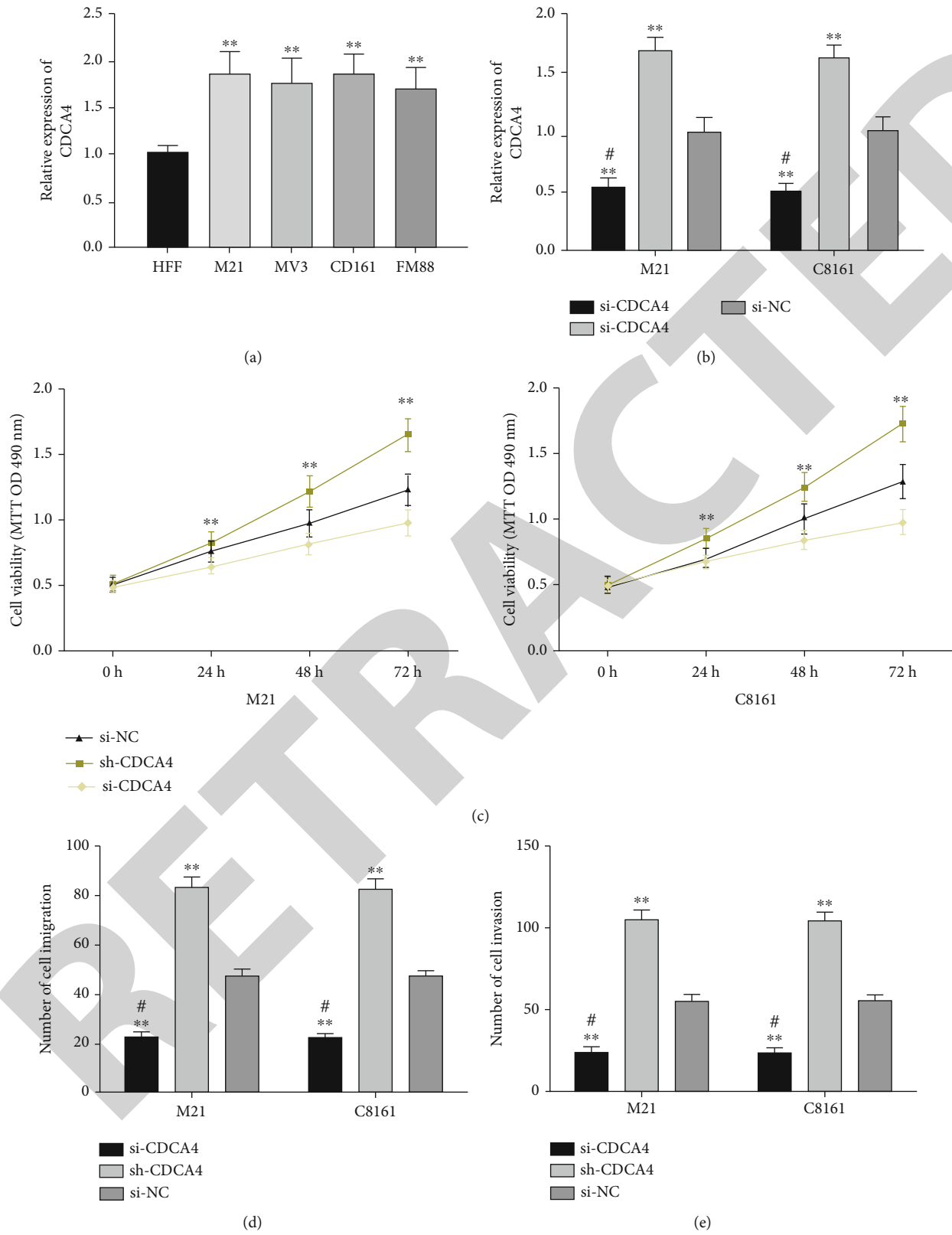


FIGURE 4: Continued.

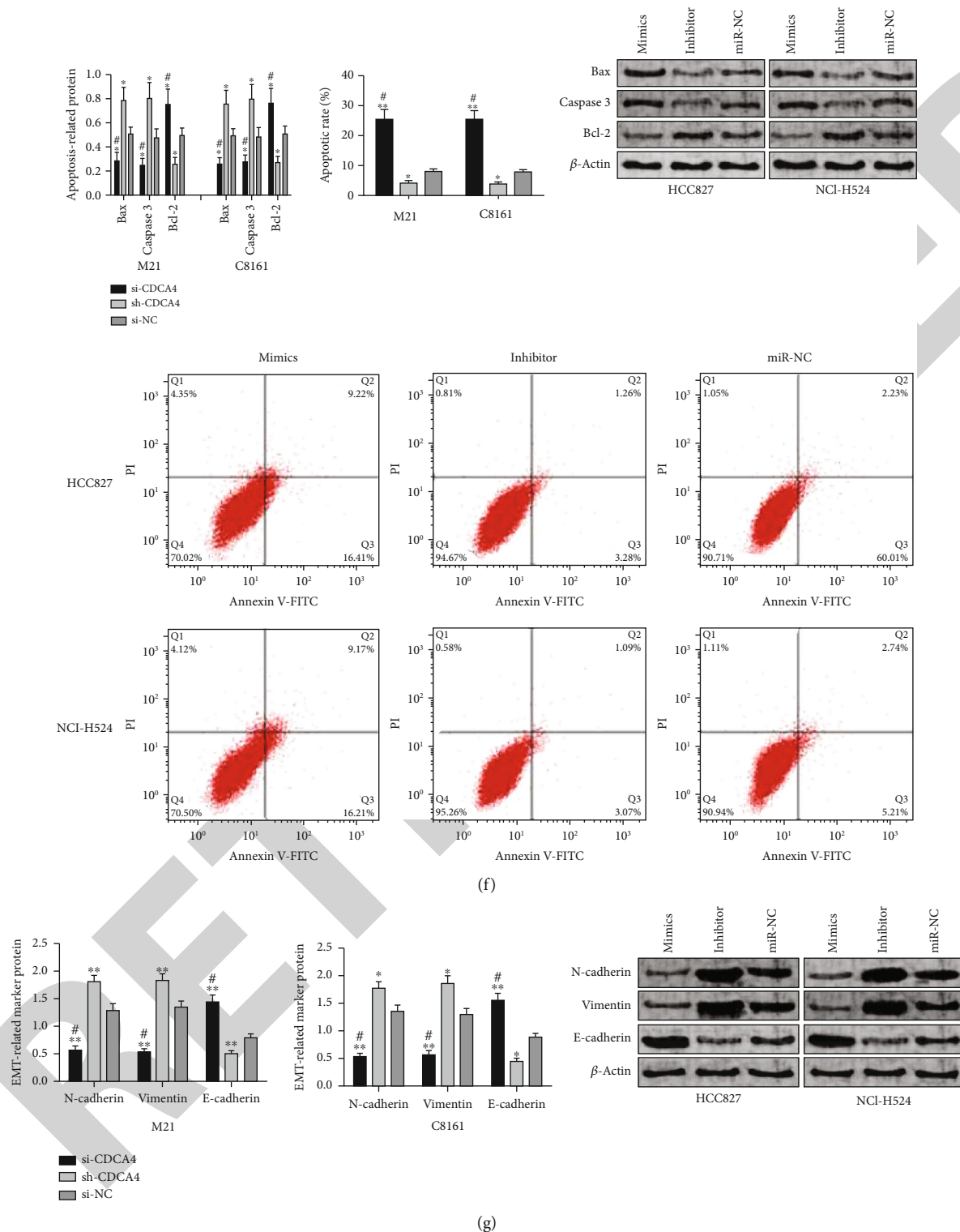


FIGURE 4: Effects of CDCA4 on biological functions of MM cells and EMT-related proteins. (a) CDCA4 is highly expressed in MM cells, especially in M21 and C8161 cells. (b) Expression of CDCA4 is suppressed markedly in cells transfected with si-CDCA4. (c) Proliferation of cells transfected with si-CDCA4 is hindered markedly. (d) Migration of cells transfected with si-CDCA4 is hindered markedly. (e) Invasion of cells transfected with si-CDCA4 is hindered markedly. (f) Expression of Bcl-2 protein in cells transfected with si-CDCA4 is remarkably suppressed, while those of Bax and Caspase3 proteins are remarkably elevated. Apoptosis of cells transfected with si-CDCA4 is significantly enhanced. The protein map and flow cytometry diagram are provided. (g) Expression of N-cadherin and vimentin proteins in the cells transfected with si-CDCA4 is remarkably suppressed, while that of E-cadherin protein is remarkably elevated. The protein map is provided. Note: * $P < 0.05$, ** $P < 0.01$ vs. the miR-NC group or HFF cells; # $P < 0.05$ vs. the miR-29c-3p-inhibitor group.

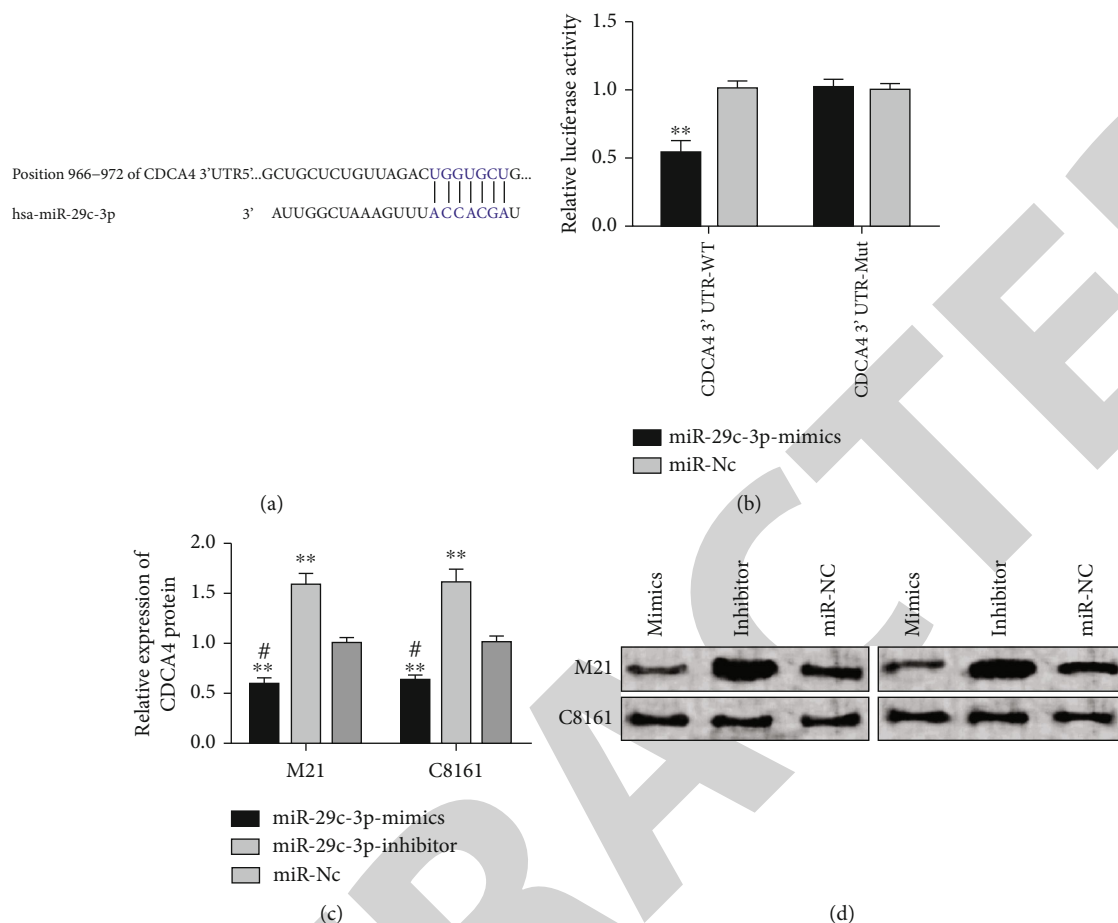
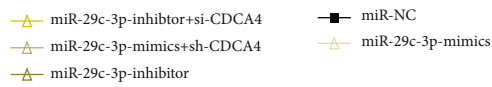
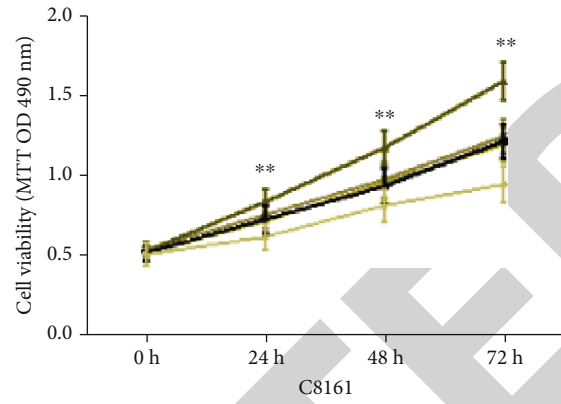
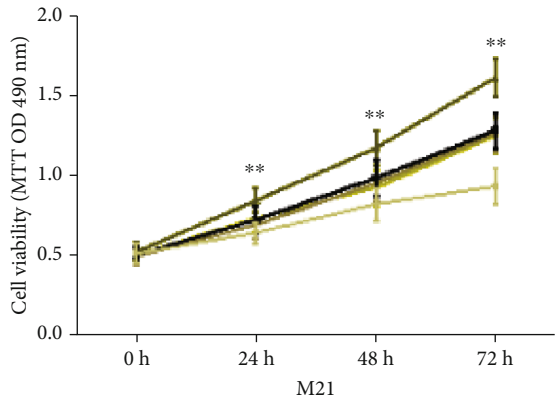


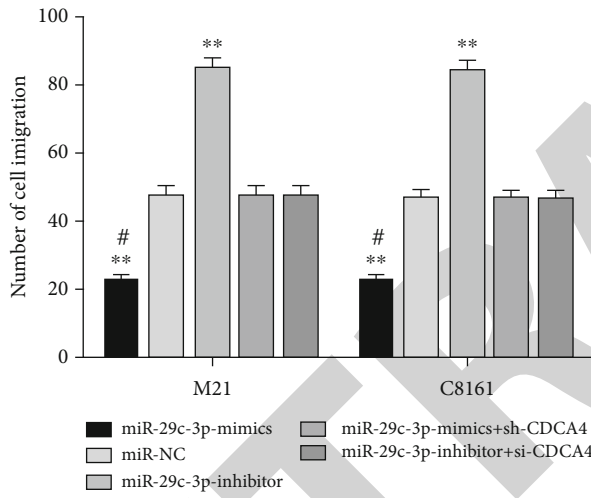
FIGURE 5: Detection of luciferase activity. (a) There are targeted binding loci between miR-29c-3p and CDCA4. (b) Relative luciferase activity-DLR assay. (c) Expression of CDCA4 protein in transfected M21 and C8161 cells. (d) Protein map. Note: $**P < 0.01$.

CDCA4 protein, and the miR-29c-3p-inhibitor increased it remarkably. Therefore, there was a targeted regulatory relationship between miR-29c-3p and CDCA4. A cotransfection experiment demonstrated that after transfecting miR-29c-3p-mimics+sh-CDCA4 or miR-29c-3p-inhibitor+si-CDCA4 to M21 and C8161 cells, the biological functions of cells showed no significant difference compared with the miR-NC group. However, compared with the cells transfected with miR-29c-3p-mimics, the cells showed enhanced proliferation, migration, invasion, and weakened apoptosis, while compared with miR-29c-3p-inhibitor, all the results were reversed. So the targeted regulatory relationship between miR-29c-3p and CDCA4 was confirmed. Through the above tests, we initially proved that upregulation of miR-29c-3p inhibited CDCA4 expression, thus preventing malignant biological progress of MM. In the study by Wang et al., taurine-upregulated gene 1 (TUG1) regulates proliferation, invasion, and apoptosis of MM cells by mediating miR-29c-3p, suggesting that miR-29c-3p may be a therapeutic target in the pathological mechanism of MM [30]. Furthermore, Alderman and Yang [31] reported that CDCA4, targeted by miR-15a, regulates the proliferation, cycle, and migration of MM cells, suggesting that CDCA4 is also a potential novel therapeutic target for MM.

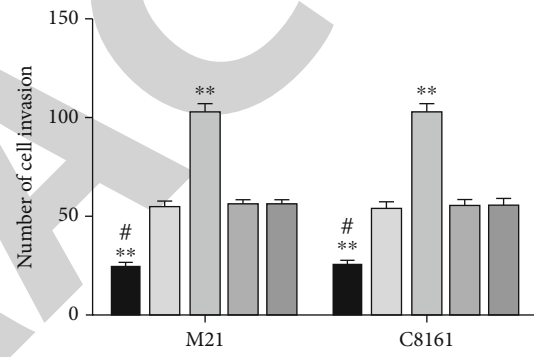
The apoptosis and EMT of MM cells are closely related to the malignant progression of tumors [32, 33], so studying these two biological processes would help us to further understand the regulatory mechanism of MM. Therefore, we measured the expression of apoptosis-related proteins (Bax, Caspase3, and Bcl-2) and EMT-related proteins (N-cadherin, vimentin, and E-cadherin) in MM cells under different transfection backgrounds. Bax and Caspase3 are well-known proapoptotic proteins, and Bcl-2 is an antiapoptotic protein, all of which are involved in the apoptosis mechanism of MM cells [34, 35]. N-cadherin, vimentin, and E-cadherin are important proteins involved in the EMT of MM cells. The decrease of N-cadherin and vimentin and the increase of E-cadherin generally portend the suppressed EMT, which is one of the positive manifestations of the inhibition of MM invasion and metastasis [36]. In our study, MM cells transfected with miR-29c-3p-mimics or si-CDCA4 exhibited protein expression unfavorable to MM progression, that is, the expressions of Bax, Caspase3, and E-cadherin proteins were remarkably elevated and those of Bcl-2, N-cadherin, and vimentin were remarkably suppressed. However, miR-29c-3p-mimics+sh-CDCA4, miR-29c-3p-inhibitor+si-CDCA4, and miR-NC transfection induced little difference in the expression of related



(a)

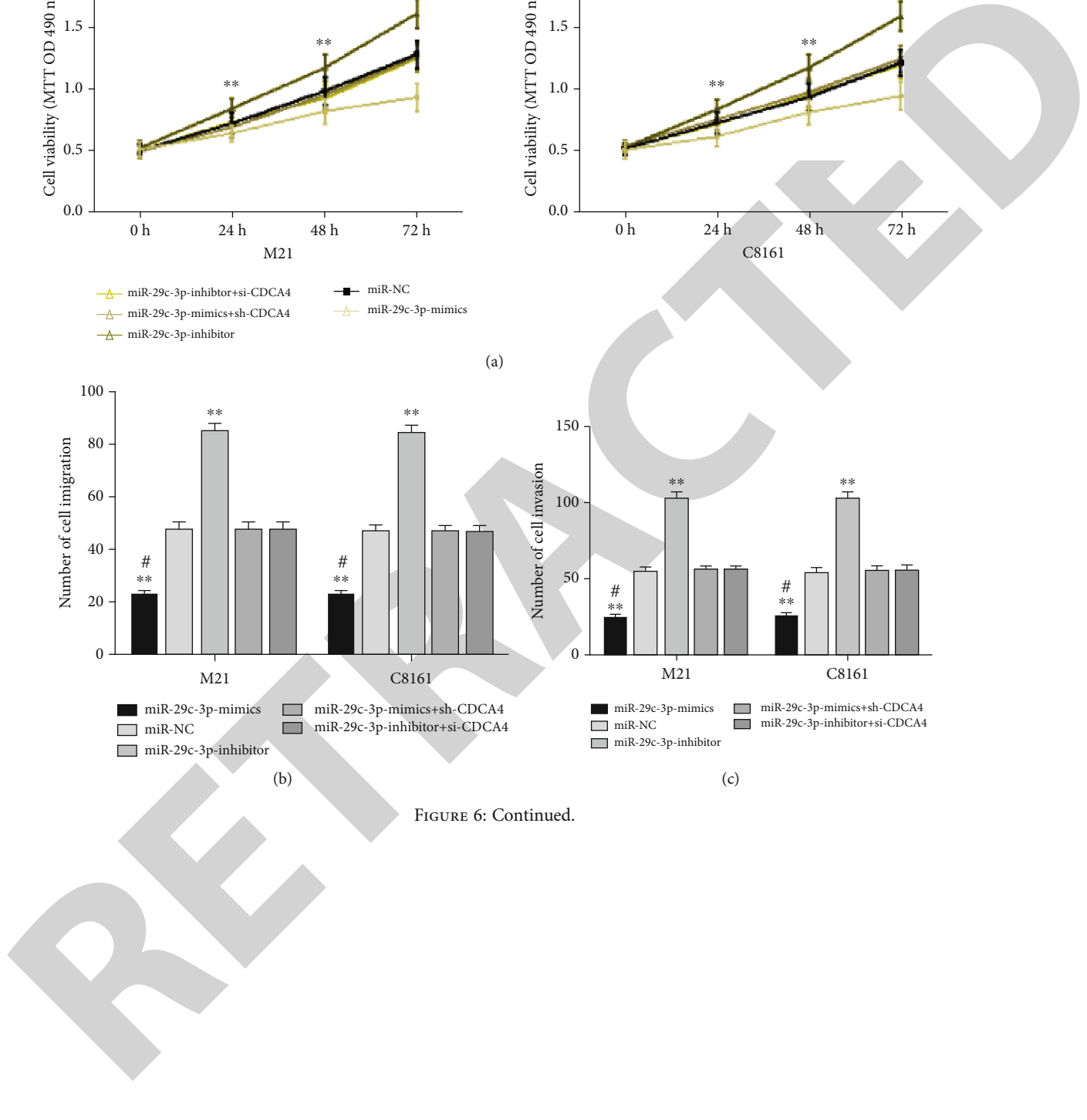


(b)



(c)

FIGURE 6: Continued.



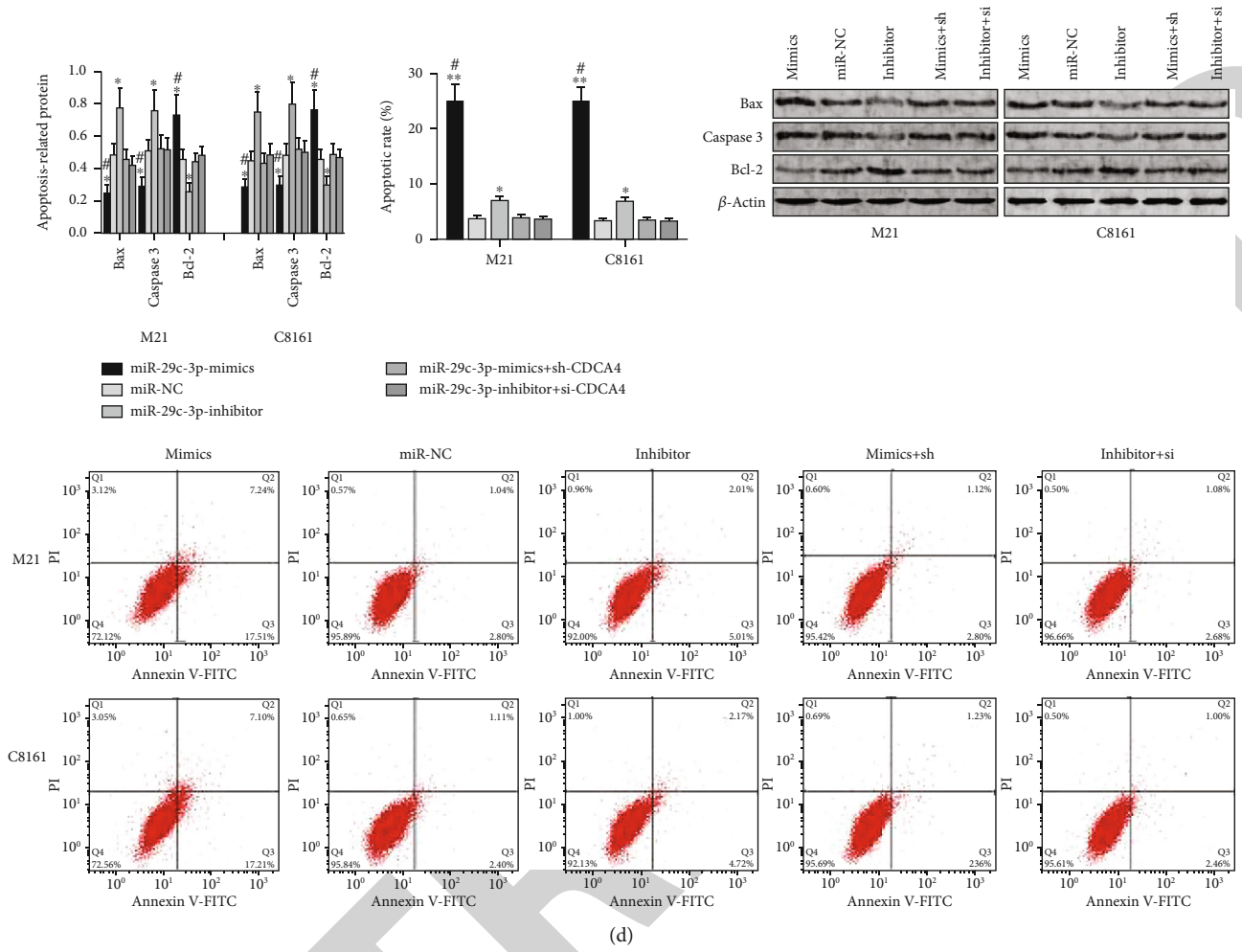


FIGURE 6: Continued.

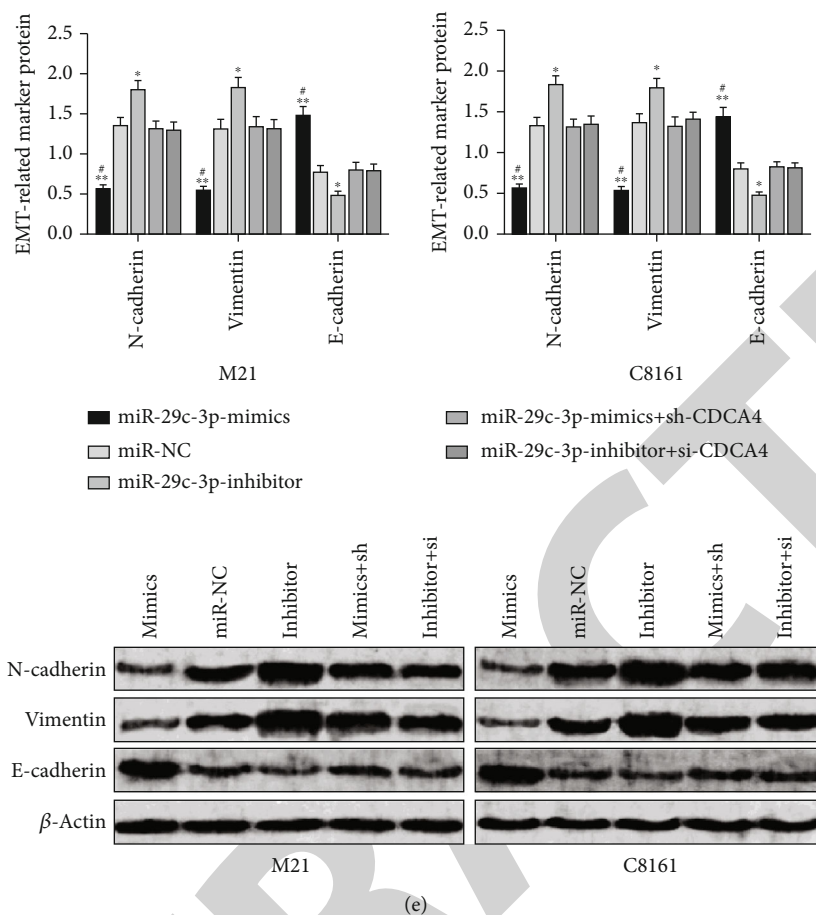


FIGURE 6: Cell cotransfection. (a) Cell proliferation after transfecting miR-29c-3p-mimics+sh-CDCA4. (b) Cell migration after transfecting miR-29c-3p-mimics+sh-CDCA4. (c) Cell invasion after transfecting miR-29c-3p-mimics+sh-CDCA4. (d) Expression of Bax, Caspase3, Bcl-2, and other apoptosis-related proteins and apoptosis after transfecting miR-29c-3p-mimics+sh-CDCA4. The protein map and flow cytometry diagram are provided. (e) Expression of EMT-related proteins after transfecting miR-29c-3p-mimics+sh-CDCA4. The protein map is provided. Note: * $P < 0.05$, ** $P < 0.01$ vs. the miR-NC group or HFF cells; # $P < 0.05$ vs. the miR-29c-3p-inhibitor group.

proteins. So it was inferred that upregulation of miR-29c-3p suppressed CDCA4 in a targeted manner, as well as hindered malignant progression of MM cells by promoting the antiapoptosis mechanism and inhibiting EMT of MM cells.

To sum up, miR-29c-3p hinders progression of MM through targeted inhibition of CDCA4. However, there is still room for improvement in this study. Firstly, it is necessary to analyze the relevant regulatory mechanisms in depth so as to investigate the potential mechanisms in this targeted relationship. Secondly, we should assess the value of sera miR-29c-3p and CDCA4 for predicting the efficacy in MM and find out whether there are dynamic changes in patients before and after treatment, thus exploring the potential clinical application value of the two.

Data Availability

All the raw data could be accessed by contacting the corresponding author on reasonable request.

Conflicts of Interest

The authors have no conflict of interest to declare.

References

- [1] D. Schadendorf, D. E. Fisher, C. Garbe et al., "Melanoma," *Nature Reviews. Disease Primers*, vol. 1, no. 1, p. 15003, 2015.
- [2] C. Gu, X. Shi, C. Dai et al., "RNA m⁶A modification in cancers: molecular mechanisms and potential clinical applications," *The Innovation*, vol. 1, no. 3, p. 100066, 2020.
- [3] R. L. Read, L. Haydu, R. P. Saw et al., "In-transit melanoma metastases: incidence, prognosis, and the role of lymphadenectomy," *Annals of Surgical Oncology*, vol. 22, no. 2, pp. 475–481, 2015.
- [4] J. Guo, S. Qin, J. Liang et al., "Chinese guidelines on the diagnosis and treatment of melanoma (2015 edition)," *Annals of translational medicine*, vol. 3, no. 21, p. 322, 2015.
- [5] C. Garbe, K. Peris, A. Hauschild et al., "Diagnosis and treatment of melanoma. European consensus-based interdisciplinary guideline - update 2016," *European Journal of Cancer*, vol. 63, pp. 201–217, 2016.

Retraction

Retracted: miR-339-5p Inhibits Autophagy to Reduce the Resistance of Laryngeal Carcinoma on Cisplatin via Targeting TAK1

BioMed Research International

Received 12 March 2024; Accepted 12 March 2024; Published 20 March 2024

Copyright © 2024 BioMed Research International. This is an open access article distributed under the Creative Commons Attribution License, which permits unrestricted use, distribution, and reproduction in any medium, provided the original work is properly cited.

This article has been retracted by Hindawi following an investigation undertaken by the publisher [1]. This investigation has uncovered evidence of one or more of the following indicators of systematic manipulation of the publication process:

- (1) Discrepancies in scope
- (2) Discrepancies in the description of the research reported
- (3) Discrepancies between the availability of data and the research described
- (4) Inappropriate citations
- (5) Incoherent, meaningless and/or irrelevant content included in the article
- (6) Manipulated or compromised peer review

The presence of these indicators undermines our confidence in the integrity of the article's content and we cannot, therefore, vouch for its reliability. Please note that this notice is intended solely to alert readers that the content of this article is unreliable. We have not investigated whether authors were aware of or involved in the systematic manipulation of the publication process.

Wiley and Hindawi regrets that the usual quality checks did not identify these issues before publication and have since put additional measures in place to safeguard research integrity.

We wish to credit our own Research Integrity and Research Publishing teams and anonymous and named external researchers and research integrity experts for contributing to this investigation.

The corresponding author, as the representative of all authors, has been given the opportunity to register their agreement or disagreement to this retraction. We have kept a record of any response received.

References

- [1] G. Li and Z. Cheng, "miR-339-5p Inhibits Autophagy to Reduce the Resistance of Laryngeal Carcinoma on Cisplatin via Targeting TAK1," *BioMed Research International*, vol. 2021, Article ID 9938515, 9 pages, 2021.

Research Article

miR-339-5p Inhibits Autophagy to Reduce the Resistance of Laryngeal Carcinoma on Cisplatin via Targeting TAK1

Guang Li and Zexing Cheng 

Department of Otorhinolaryngology-Head and Neck Surgery, The Affiliated Hospital of Yangzhou University, Yangzhou, Jiangsu 225001, China

Correspondence should be addressed to Zexing Cheng; chenpinjie0108655@163.com

Received 27 March 2021; Revised 25 June 2021; Accepted 7 July 2021; Published 4 August 2021

Academic Editor: Tao Huang

Copyright © 2021 Guang Li and Zexing Cheng. This is an open access article distributed under the Creative Commons Attribution License, which permits unrestricted use, distribution, and reproduction in any medium, provided the original work is properly cited.

Laryngeal carcinoma is a malignant disease with high morbidity and mortality. Several studies have indicated that miRNA dysfunction involves in the development of laryngeal carcinoma. In this study, the connection of miR-339-5p and laryngeal carcinoma was investigated, and qRT-PCR, CCK-8, and flow cytometry assay were used to observe the function of miR-339-5p on laryngeal carcinoma. Besides, the target database, dual-luciferase reporter assay, and western blot were used to explore the regulation mechanism of miR-339-5p on the progression of laryngeal carcinoma. The results showed that miR-339-5p was significantly downregulated in cisplatin-resistant cells of laryngeal carcinoma, and miR-339-5p upregulation could weaken the resistance of laryngeal carcinoma cells on cisplatin. Moreover, miR-339-5p could directly react with 3'-UTR of TAK1, and TAK1 could reverse the effects of miR-339-5p on the progression of autophagy. In conclusion, this study suggests that miR-339-5p can inhibit the autophagy to decrease the cisplatin resistance of laryngeal carcinoma via targeting TAK1.

1. Introduction

Laryngeal carcinoma is the second most prevalent malignancy of the upper aerodigestive tract, which is associated with several factors such as tobacco and alcohol consumption [1, 2]. Statistically, there are more than 13,360 new cases and 3660 deaths every year in the United States. Even with current strategies, the overall 5-year survival rate of the patients with laryngeal carcinoma is only 64.2% [3]. Moreover, more than 60% of the patients are diagnosed with advanced stage of laryngeal carcinoma when they firstly accept the diagnosis [4]. Cisplatin (DDP), an effective chemotherapy drug, has been widely used for cancer treatment in clinical practice [5]. However, the drug resistance of cancer limits the lethal effect of cisplatin on tumors [6]. Autophagy is an important tactic of cells to keep from the damages induced by starvation, oxidative stress, and poisonous substance, and increasing studies have indicated that cell autophagy is involved in the drug-resistant formation of tumor cells [7, 8].

MicroRNAs (miRNAs), a class of noncoding RNA with short chain, are responsible for transcriptional inhibition of mRNAs to regulate the expression of the related proteins in various eukaryotic cells [9, 10]. These small RNAs have been accepted as important molecular regulators in cellular life activities by many researchers [11, 12]. Many studies have demonstrated that the dysfunction of miRNAs can facilitate tumor growth, invasion, migration, and drug resistance [13]. For instance, miR-337-3p could modulate the proliferation, invasion, migration, and apoptosis of cervical cancer cells via targeting Rap1A [14]. Considering the mechanism of miRNAs, the novel therapeutic strategies have been widely used for the treatment and research of human diseases [15]. miR-339-5p has been found as a tumor suppressor to inhibit the growth of various tumors while its role in laryngeal carcinoma remains unclear [16].

In this study, we investigate the connection of miR-339-5p and laryngeal carcinoma and aimed to provide some reference for laryngeal carcinoma treatment.

2. Materials and Methods

2.1. Cell Lines and Cell Culture. Human epithelial type 2 (Hep-2) was purchased from BeNa Culture Collection Co., Ltd. (Beijing, China), and the cells were cultured with Dulbecco's modified Eagle's medium (DMEM) including 10% fetal bovine serum (FBS) purchased from Procell Life Science&Technology Co., Ltd. (Wuhan, China). The cells were cultured at 37°C in a humidified incubator with 5% CO₂. Trypsinase solution (0.25%) (HyClone Logan, State of Utah, USA) was used to obtain adherent cells. Hep-2 cells were cultured; the cells in the culture medium contained cisplatin to establish cisplatin-resistant cells. The concentration of cisplatin was gradually increased (0.5, 1, 1.5, and 2 μM). The cells were maintained in each concentration of cisplatin for a period of 3 months.

2.2. Cell Transfection. The miR-339-5p mimics and control miRNA were purchased from Generay Biotech (Shanghai, China). pcDNA-TAK1 and control pcDNA were also designed and purified by Generay Biotech (Shanghai, China). The cisplatin-resistant cells were seeded and cultured in 6-well plates. 4 μg of DNA, 100 pmol RNA, or 10 μl Lipofectamine 2000 was diluted and incubated with 250 μl serum-free medium for 5 min, respectively. After that, the diluted transfectants were mixed with diluted Lipofectamine 2000 at equal proportion. The mixtures were incubated at 25°C for 20 min. The 500 μl of mixtures was added in each well, and then, the cells were cultured for 24 hours.

2.3. RNA Extraction and RT-qPCR Analysis. The cultured cells were subjected to total RNA extraction with Trizol reagent (ThermoFisher, Massachusetts, USA). 2 μg of total RNA was reverse transcribed to cDNA by the Revert Aid First Strand cDNA Synthesis Kit (Thermo Fisher, Massachusetts, USA). qRT-PCR were performed with the 7300 Real-Time PCR System (Applied Biosystems, Waltham, MA, USA). The following conditions were used: denaturation at 95°C for 3 min, followed by amplification for 40 cycles at 95°C for 12 s, at 62°C for 40 s, and at 70°C for 30 s. The relative expression levels of miRNAs were calculated with the $2^{-(\Delta\Delta Ct)}$ method [17, 18]. The primers of miR-339-5p and TAK1 were synthesized and purified by RiboBio (Guangzhou, China). U6 was used as the endogenous controls. The primer sequences of miR-339-5p and U6 are listed in Table 1.

2.4. Western Blot. The total proteins of cells were extracted with RIPA buffer and 1% PMSF (Beyotime, Shanghai, China) for western blot. The concentration of the proteins was measured using a Pierce BCA protein assay kit (Beyotime, Shanghai, China). The proteins in the extracts were separated by 15% SDS-PAGE gels and then were transferred from SDS-PAGE onto PVDF membranes. After that, the membranes were immersed into 5% fat-free milk and cultured for 1 hour. The membranes were incubated with the related first antibody of the protein at 4°C for 24 hours. Subsequently, the membranes were incubated with the second antibody for 1 hour. Finally, the relative expression levels of the proteins were observed by a chemiluminescence

TABLE 1: Primer sequences of miR-339-5p and U6.

Name of primer	Sequences
miR-339-5p-F	5'-GGGTCCCTGTCCTCCA-3'
miR-339-5p-R	5'-TGCGTGTCTGGAGTC-3'
U6-F	5'-CTCGCTTCGGCAGCAC-3'
U6-R	5'-AACGCTTCACGAATTGCGT-3'

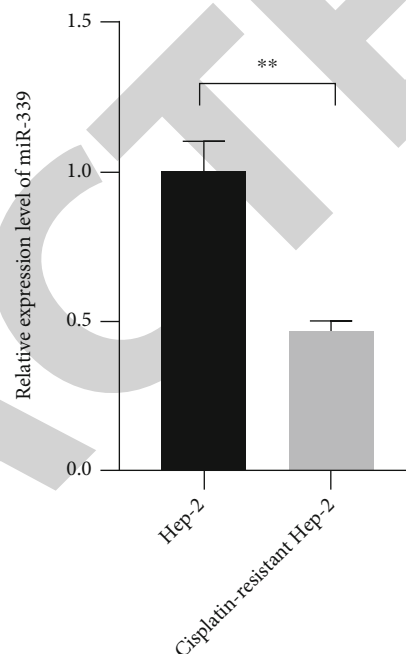


FIGURE 1: miR-339-5p was downregulated in cisplatin-resistant Hep-2 cells. The relative expression level of miR-339-5p was measured by qRT-PCR. ** meant $P < 0.05$.

detection system. The antibodies were used as follow: anti-TAK1 (1:1000, ab10979591, ThermoFisher, Massachusetts, USA); anti-LC3B (1:1000, ab2234770, ThermoFisher, Massachusetts, USA); anti-p-AMPK (1:2000, ab2533585, ThermoFisher, Massachusetts, USA); anti-β-actin (1:1000, sc-47,778, Santa Cruz).

2.5. Dual-Luciferase Reporter Gene Assay. The 3'-UTR-mutant sequence and 3'-UTR-wild sequence of TAK1 were inserted into the pmirGLO luciferase reporter vectors, respectively. The vectors containing the mutant sequence and wild sequence of TAK1 were named as TAK1-mutant type (TAK1-mut) and TAK1-wild type (TAK1-wt). TAK1-mut and TAK1-wt were, respectively, cotransfected with miR-339-5p mimics or miR-NC into HEK-293T for 48 hours. Finally, the luciferase activity of HEK-293T was observed by a dual-luciferase reporter assay system.

2.6. Flow Cytometry Assay. The cisplatin-resistant cells were treated with trypsinase (0.25%, EDTA-free) and harvested. After washing three times with ice phosphate-buffered saline (PBS), 2×10^3 cells were diluted in ice Annexin V-FITC

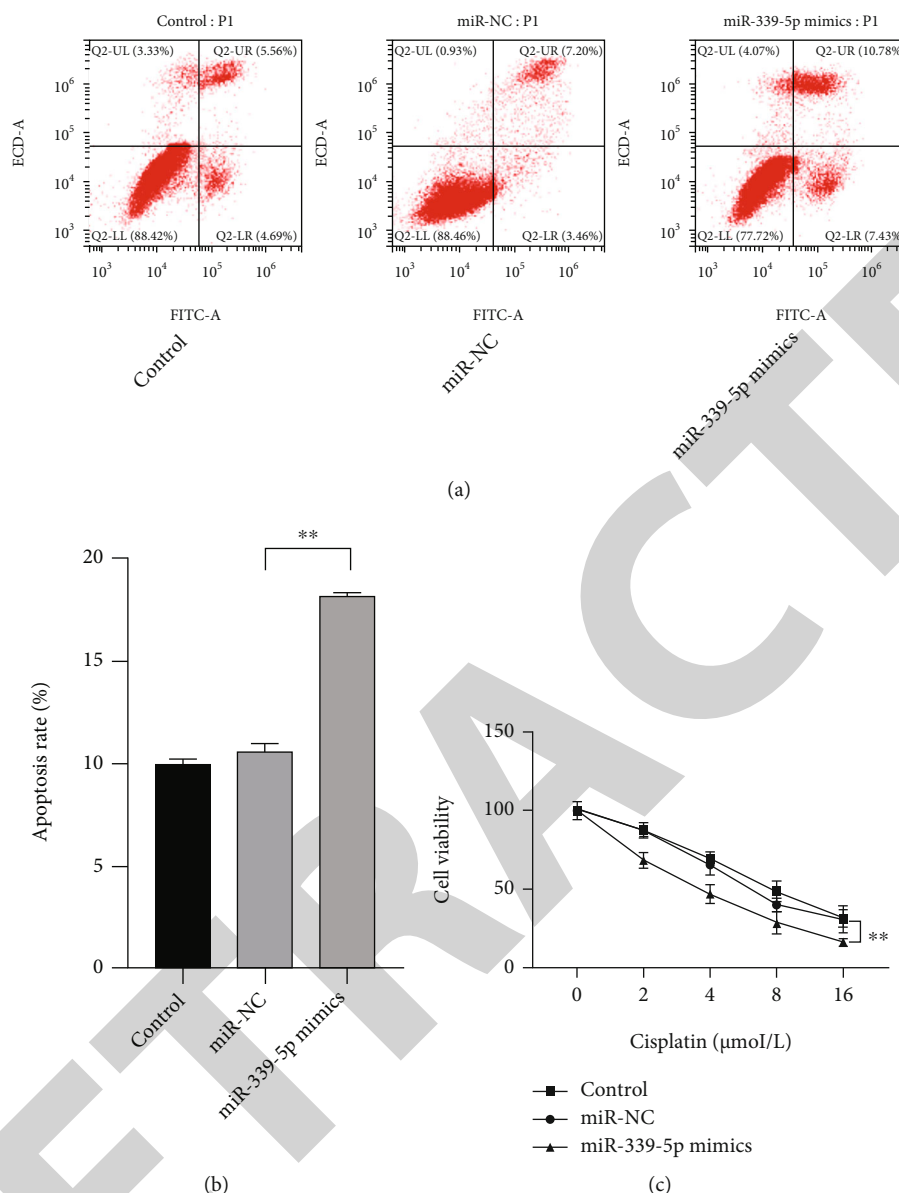


FIGURE 2: miR-339-5p upregulation reduced the cisplatin resistance and promotes the apoptosis of cisplatin-resistant Hep-2 cells. (a, b) The effect of miR-339-5p on the apoptosis rate of cisplatin-resistant Hep-2 cells was observed by flow cytometry assay. (c) The effect of miR-339-5p on the viability of cisplatin-resistant Hep-2 cells was observed by the CCK-8 assay. ** meant $P < 0.01$.

binding buffer. Subsequently, the cells were incubated with 5 μl Annexin V-FITC (10 μg/ml) in the dark for 10 min. After that, 10 μl of propidium iodide (PI 20 μg/ml) was added into the cells. Finally, the apoptosis level of the cells was instantly observed by a flow cytometry equipment (BD Biosciences, State of New Jersey, USA).

2.7. CCK-8 Assay. The cisplatin-resistant cells were seeded into 96-well plates at 5×10^4 cells/well. After transfection, then miR-339-5p mimic, miR-NC, TAK1 overexpression plasmid (pCMV-TAK1), and empty pCMV plasmid (NC) were transfected into the cells when their density is at 70%, and the cells were incubated for 48 hours. After that, 10 μl of CCK-8 solution (Amyjet, Wuhan, China) was added to each well, and the cells were incubated for 2 hours at 37°C.

Finally, a microplate reader (Flash, Shanghai, China) was used to observe the absorbance of each well at 450 nm.

2.8. Statistical Analysis. All assays were performed at least 3 times, independently. The results were analyzed by SPSS 20.0, and the figures were drawn by GraphPad Prism 8.0. The difference of all groups was calculated through the Chi-squared test or ANOVA with Tukey's post hoc test [19]. $P < 0.05$ meant that the difference was statistically significant [20, 21].

3. Results

3.1. miR-339-5p Was Significantly Downregulated in Hep-2 Treated with Cisplatin. To illustrate the connection of miR-

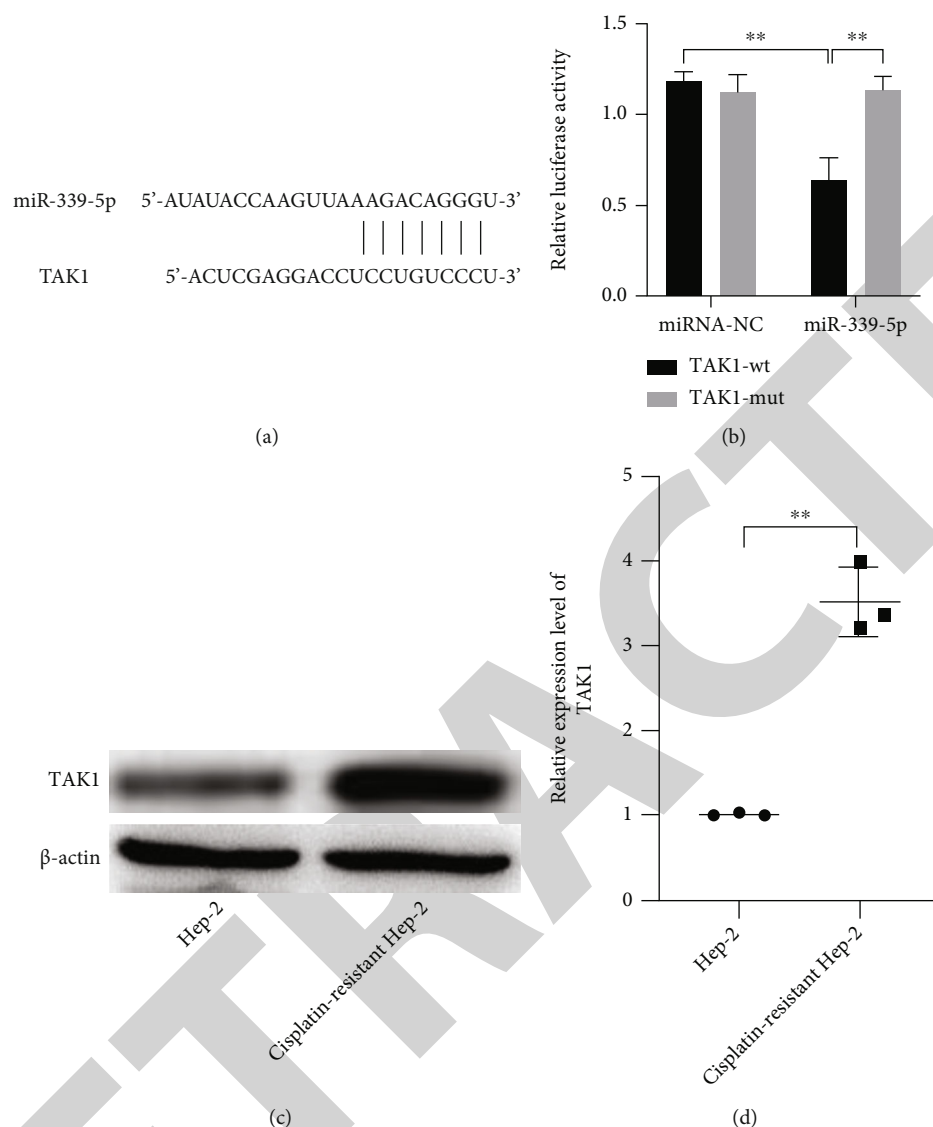


FIGURE 3: miR-339-5p directly targeted the 3'-UTR of TAK1, and TAK1 was upregulated in cisplatin-resistant Hep-2 cells. (a) The binding effect of miR-339-5p and TAK1 was predicted by TargetScan. (b) The binding effects of miR-339-5p on 3'-UTR of TAK1 were observed by dual-luciferase reporter assay. (c, d) The relative expression levels of TAK1 in Hep-2 and cisplatin-resistant Hep-2 cells were observed by western blot. ** meant $P < 0.01$.

339-5p and laryngeal carcinoma, the Hep-2 cells were treated with cisplatin to establish cisplatin-resistant Hep-2, and the qRT-PCR was used to observe the levels of miR-339-5p in Hep-2 and resistant cells. The qRT-PCR assay reflected that the expression level of miR-339-5p was significantly downregulated in cisplatin-resistant Hep-2 cells compared with Hep-2 cells (Figure 1, $P < 0.01$).

3.2. miR-339-5p Upregulation Reduced the Resistance of Hep-2 Cells on Cisplatin. To further explore the functions of miR-339-5p on the progression of laryngeal carcinoma cells, the miR-339-5p mimics were transfected into cisplatin-resistant Hep-2 cells, and CCK-8, transwell, and cytometry assays were used to observe the changes of the cells. The CCK-8 assay showed that the viability of the cancer

cells was effectively suppressed when transfected with miR-339-5p mimics (Figure 2(c)), $P < 0.01$). Compared with the cells in negative control groups, the apoptosis level of the cells visibly increased when miR-339-5p was downregulated (Figures 2(a) and 2(b), $P < 0.01$). Those observations suggested that the resistance of Hep-2 cells on cisplatin was inhibited when miR-339-5p was upregulated.

3.3. miR-339-5p Directly Target the 3'-UTR of TAK1. The databases such as miRWalk and TargetScan were used to search the potential targets of miR-339-5p. The results showed that TAK1 was a possible target of miR-339-5p (Figure 3(a)). The dual-luciferase reporter assay was used to confirm whether miR-339-5p could act with TAK1. The results showed that the luciferase activities of the cells

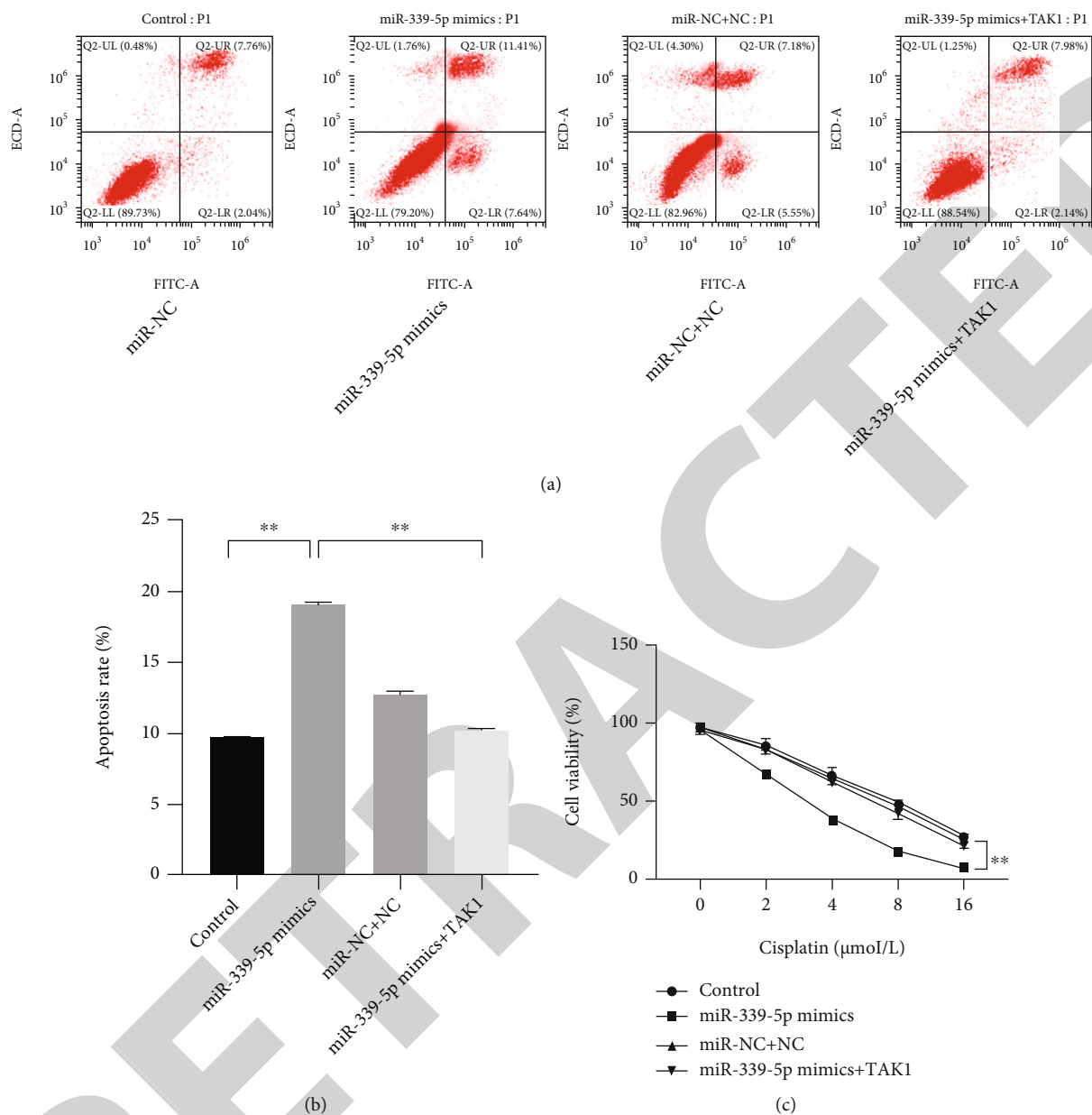


FIGURE 4: TAK1 reversed the effects of miR-339-5p on cisplatin-resistant Hep-2 cells. (a, b) The effect of TAK1 on the regulation of miR-339-5p on the apoptosis rate of cisplatin-resistant Hep-2 cells was observed by flow cytometry assay. (c) The effect of TAK1 on the regulation of miR-339-5p on the viability of cisplatin-resistant Hep-2 cells was observed by the CCK-8 assay. ** meant $P < 0.01$.

cotransfected miR-339-5p and the wild type of TAK1 reduced significantly compared with the cells cotransfected miR-339-5p and the mutant type of TAK1 (Figure 3(b), $P < 0.01$). The luciferase activities of the cells transfected with miR-NC did not show remarkable changes. Besides, the increased expression level of TAK1 was also observed in the pathological tissues and cancer cells compared with Hep-2 cells (Figures 3(c) and 3(d), $P < 0.01$).

3.4. TAK1 Upregulation Reversed the Effects of miR-339-5p on Hep-2 Cells. The inhibited effect of miR-339-5p on TAK1 was proved in this study, and it was hypothesized that TAK1 is involved in the regulation of miR-339-5p on laryngeal carci-

noma cells. The miR-339-5p mimics and TAK1 were cotransfected into the laryngeal carcinoma cells, and the CCK-8 and flow cytometry assay were used to observe the phenotypic changes of Hep-2 cells. The CCK-8 showed that the weakened viability of Hep-2 induced by miR-339-5p and cisplatin was reversed by TAK1 upregulation compared with the cell negative control (Figure 4(a), $P < 0.01$). Besides, the increased apoptosis level of cisplatin-resistant Hep-2 cells enhanced by miR-339-5p and was also reversed by TAK1 (Figures 4(b) and 4(c), $P < 0.01$).

3.5. miR-339-5p Inhibited the Autophagy Level to Reduce the Resistance of Hep-2 Cells on Cisplatin. Considering the effects

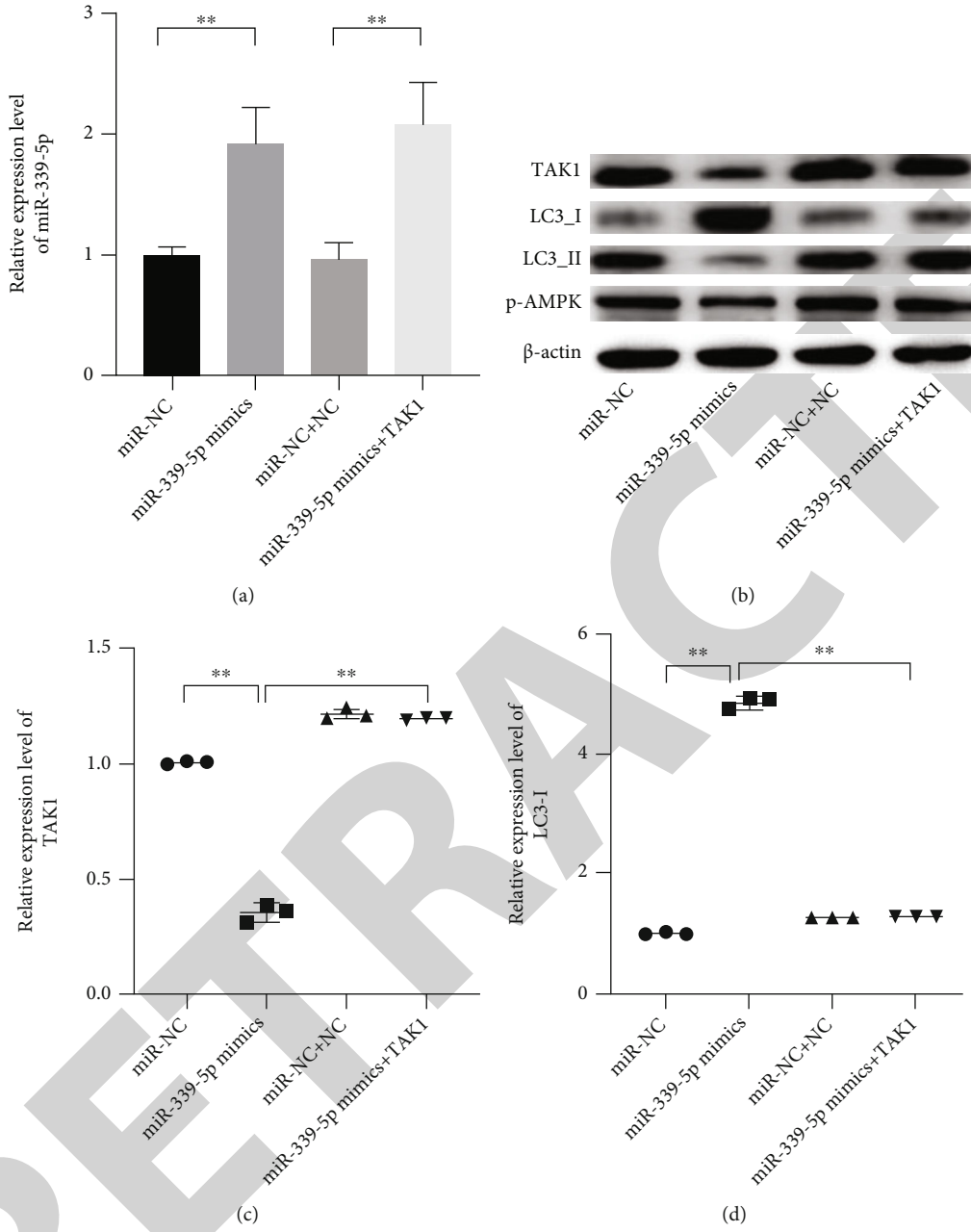


FIGURE 5: Continued.

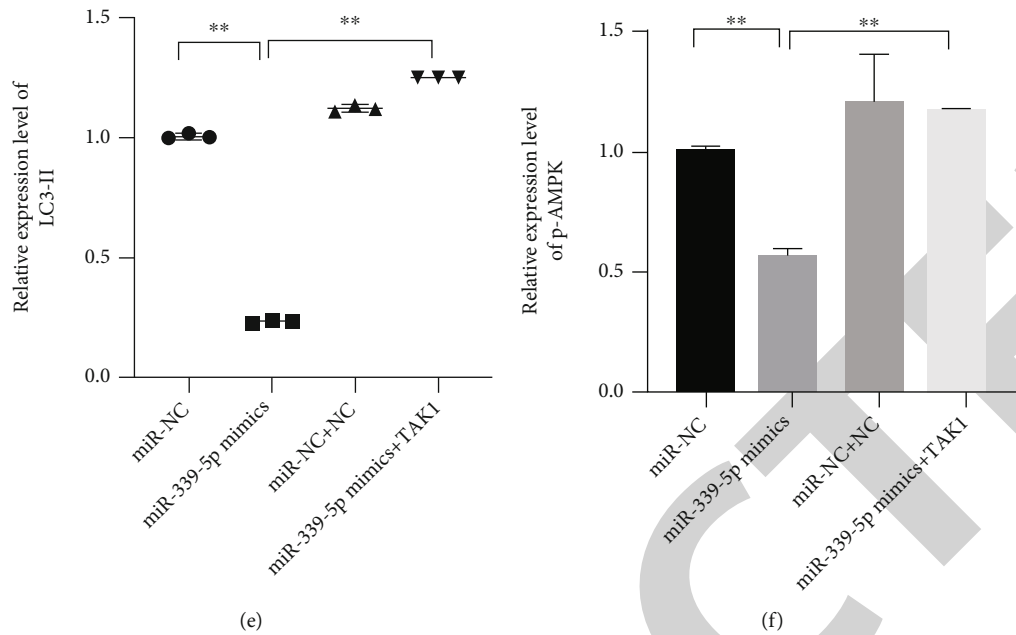


FIGURE 5: miR-339-5p inhibited the autophagy of cisplatin-resistant Hep-2 cells, and the TAK1 could reverse the effects of miR-339-5p on the cells. (a) The relative expression level of miR-339-5p was measured by qRT-PCR. (b–f) The relative expression levels of TAK1, LC3-I, LC3-II, and pAMPK were observed by western blot assay. ** meant $P < 0.05$.

of miR-339-5p on the resistance of laryngeal carcinoma, the changes of the autophagy pathway in laryngeal carcinoma cells were observed. The miR-339-5p mimics and TAK1 expressed vectors were transfected into the cells, and the western blot was used to measure the expression levels of some autophagy-related proteins in Hep-2 cells. The result showed that the increased LC3-I and reduced LC3-II in Hep-2 cells induced by miR-339-5p upregulation could be reversed by TAK1 (Figures 5(a)–5(e), $P < 0.01$). Besides, it was also found that increased miR-339-5p significantly inhibited the expression of p-AMPK when the cells suffered the impairment from cisplatin (Figure 5(f), $P < 0.01$).

4. Discussion

Laryngeal carcinoma poses a serious threat to the health of human. The major lethal effects of chemotherapy drugs on tumors depend on inducing the apoptosis of pathological cells [22]. Recently, increasing studies have revealed that some tumor cells can form the resistance on some antitumor drugs through the autophagy pathway [23, 24]. In this study, we illustrated the functions of miR-339-5p on laryngeal carcinoma and revealed the regulation mechanism of miR-339-5p on improving the resistance of laryngeal carcinoma on cisplatin.

Many studies have demonstrated that the dysfunction of some miRNAs contributes to the progression of tumors such as the malignant proliferation and formation of the drug resistance [25, 26]. Xu et al. [27] have found that miR-1265 was significantly downregulated in gastric cancer cells, and miR-1265 upregulation could inhibit the proliferation and induce apoptosis of the tumor cells via impairing the autophagy pathway.

In this study, we found that miR-339-5p played an important role in decreasing the resistance of laryngeal carcinoma cells on cisplatin. miR-339-5p has been confirmed as a tumor inhibitor to suppress the formation and development of the tumors. Liang and Tang [28] have suggested that miR-339-5p could be negatively regulated by LINC00467, and miR-339-5p could play a tumor inhibitor role to induce the apoptosis of glioblastoma. Cisplatin, an inorganic molecular drug, has been widely used for the treatment of various cancers. It can trigger the damage of DNA via combining the nitrogen atoms of DNA base and further activate the apoptosis of tumor cells [29]. Cisplatin is one of the most effective agents, and the researches have proved that cisplatin could significantly improve the overall survival rates of the patients with cancer [30]. However, even with the satisfactory effects on tumors at the beginning of chemotherapy, the cell resistance still limits the long-term lethal effect of cisplatin in cancer treatment [31]. The program of apoptosis acts as the major mechanism on regulating the death of cells, and resistance to apoptosis is an important strategy of tumor cells away from the injury of drugs [32].

miRNAs are characterized by regulating the expression of some proteins via targeting the related mRNAs [33]. In this study, we found that miR-339-5p could directly target the 3'-UTR of TAK1, and the increased TAK1 was also observed in cisplatin-resistant cells of laryngeal carcinoma. TAK1 is a pivotal signal transducer critical for TGF- β functions in EMT and apoptosis via regulating the activation of the c-Jun N-terminal kinase (JNK) and p38 MAPK cascade [34]. Multiple studies have confirmed that TAK1 is related to the progressions of some tumors. TAK1 can promote the metastasis, invasion, and proliferation of tumors [35]. Iriondo et al.

[36] have indicated that the abnormal expression of TAK1 is a major cause of the metastasis of triple-negative breast cancer to the lung. Besides, it has been found that TAK1 plays a key role in the drug resistance of some tumors. The results in this study showed that TAK1 upregulation could reverse the effects of miR-339-5p on depressing the cisplatin resistance of laryngeal carcinoma cells. Piro et al. have suggested that TAK1 is associated with the resistance to preoperative chemoradiotherapy of the patients with esophageal adenocarcinoma, and TAK1 can significantly reduce the apoptosis level of the tumor cells via promoting the expression of BIRC3 [37]. Moreover, we also found that miR-339-5p and TAK1 are related to the autophagy of laryngeal carcinoma cells, and miR-339-5p could inhibit the autophagy pathway way to decrease the resistance of laryngeal carcinoma on cisplatin via targeting TAK1. Autophagy is a common tactic of cells to counter the adverse factors such as starvation and poison attack. Cell autophagy is usually associated with the elevated ratio of LC3-II to LC3-I [38]. Our results showed that miR-339-5p upregulation effectively inhibits the increased ratio of LC3-II to LC3-I in cisplatin-resistant cells of laryngeal carcinoma, and the effects of miR-339-5p could be reversed by TAK1. Besides, the decreased AMPK and mTOR induced by miR-339-5p were also observed in cisplatin-resistant cells, and those phenomena could be rescued by STAK1. Therefore, this study suggests that miR-339-5p can inhibit the autophagy to improve the cisplatin resistance of laryngeal carcinoma cells via targeting TAK1.

5. Conclusion

In conclusion, this study suggests that miR-339-5p inhibits autophagy to reduce the resistance of laryngeal carcinoma on cisplatin via targeting TAK1.

Data Availability

The raw data can be provided if any other qualified authors need it.

Conflicts of Interest

The authors declare that they have no conflicts of interest.

Acknowledgments

This work is supported by the Science and Technology Commission of Sichuan Municipality, Science and Technology Innovation Action Plan (No. 175111300).

References

- [1] S. A. Patel, M. M. Qureshi, M. A. Dyer, S. Jalisi, G. Grillone, and M. T. Truong, "Comparing surgical and nonsurgical larynx-preserving treatments with total laryngectomy for locally advanced laryngeal cancer," *Cancer*, vol. 125, no. 19, pp. 3367–3377, 2019.
- [2] R. T. Hughes, W. J. Beuerlein, S. S. O'Neill et al., "Human papillomavirus-associated squamous cell carcinoma of the larynx or hypopharynx: clinical outcomes and implications for laryngeal preservation," *Oral Oncology*, vol. 98, pp. 20–27, 2019.
- [3] B. Liu, C. Gu, Y. Wang et al., "Feasibility and efficacy of simultaneous off-pump coronary artery bypass grafting and esophagectomy in elderly patients," *Oncotarget*, vol. 8, no. 28, pp. 46498–46505, 2017.
- [4] P. Y. Fong, S. H. Tan, D. W. T. Lim et al., "Association of clinical factors with survival outcomes in laryngeal squamous cell carcinoma (LSCC)," *PLoS One*, vol. 14, no. 11, article e0224665, 2019.
- [5] X. Shen, X. Gao, H. Li, Y. Gu, and J. Wang, "TIMP-3 increases the chemosensitivity of laryngeal carcinoma to cisplatin via facilitating mitochondria-dependent apoptosis," *Oncology Research*, vol. 27, no. 1, pp. 73–80, 2018.
- [6] R. Li, S. Chen, J. Zhan et al., "Long noncoding RNA *FOXD2-AS1* enhances chemotherapeutic resistance of laryngeal squamous cell carcinoma via STAT3 activation," *Cell Death & Disease*, vol. 11, no. 1, p. 41, 2020.
- [7] X. Huang, G. Gan, X. Wang, T. Xu, and W. Xie, "The HGF-MET axis coordinates liver cancer metabolism and autophagy for chemotherapeutic resistance," *Autophagy*, vol. 15, no. 7, pp. 1258–1279, 2019.
- [8] M. H. Lee, D. Koh, H. Na et al., "MTA1 is a novel regulator of autophagy that induces tamoxifen resistance in breast cancer cells," *Autophagy*, vol. 14, no. 5, pp. 812–824, 2018.
- [9] J. L. Gomez, A. Chen, M. P. Diaz et al., "A network of sputum microRNAs is associated with neutrophilic airway inflammation in asthma," *American Journal of Respiratory and Critical Care Medicine*, vol. 202, no. 1, pp. 51–64, 2020.
- [10] C. Gu, X. Shi, Z. Huang et al., "A comprehensive study of construction and analysis of competitive endogenous RNA networks in lung adenocarcinoma," *Biochim Biophys Acta Proteins Proteom*, vol. 1868, no. 8, 2020.
- [11] C. Gu, X. Shi, W. Qiu et al., "Comprehensive analysis of the prognostic role and mutational characteristics of m6A-related genes in lung squamous cell carcinoma," *Frontiers in Cell and Development Biology*, vol. 9, p. 661792, 2021.
- [12] C. Gu, X. Shi, C. Dai et al., "RNA m⁶A modification in cancers: molecular mechanisms and potential clinical applications," *The Innovation*, vol. 1, no. 3, p. 100066, 2020.
- [13] S. Shirjang, B. Mansoori, S. Asghari et al., "MicroRNAs in cancer cell death pathways: apoptosis and necroptosis," *Free Radical Biology & Medicine*, vol. 139, pp. 1–15, 2019.
- [14] X. M. Cao, "Role of miR-337-3p and its target Rap1A in modulating proliferation, invasion, migration and apoptosis of cervical cancer cells," *Cancer Biomarkers*, vol. 24, no. 3, pp. 257–267, 2019.
- [15] X. Lai, M. Eberhardt, U. Schmitz, and J. Vera, "Systems biology-based investigation of cooperating microRNAs as monotherapy or adjuvant therapy in cancer," *Nucleic Acids Research*, vol. 47, no. 15, pp. 7753–7766, 2019.
- [16] C. Z. Gan, G. Li, Q. S. Luo, and H. M. Li, "miR-339-5p down-regulation contributes to Taxol resistance in small-cell lung cancer by targeting α 1,2-fucosyltransferase 1," *IUBMB Life*, vol. 69, no. 11, pp. 841–849, 2017.
- [17] C. Gu, Z. Huang, X. Chen et al., "TEAD4 promotes tumor development in patients with lung adenocarcinoma via ERK signaling pathway," *Biochimica et Biophysica Acta - Molecular Basis of Disease*, vol. 1866, no. 12, p. 165921, 2020.

Retraction

Retracted: A Systematic Review and Meta-Analysis of the SuperPATH Approach in Hip Arthroplasty

BioMed Research International

Received 12 March 2024; Accepted 12 March 2024; Published 20 March 2024

Copyright © 2024 BioMed Research International. This is an open access article distributed under the Creative Commons Attribution License, which permits unrestricted use, distribution, and reproduction in any medium, provided the original work is properly cited.

This article has been retracted by Hindawi following an investigation undertaken by the publisher [1]. This investigation has uncovered evidence of one or more of the following indicators of systematic manipulation of the publication process:

- (1) Discrepancies in scope
- (2) Discrepancies in the description of the research reported
- (3) Discrepancies between the availability of data and the research described
- (4) Inappropriate citations
- (5) Incoherent, meaningless and/or irrelevant content included in the article
- (6) Manipulated or compromised peer review

The presence of these indicators undermines our confidence in the integrity of the article's content and we cannot, therefore, vouch for its reliability. Please note that this notice is intended solely to alert readers that the content of this article is unreliable. We have not investigated whether authors were aware of or involved in the systematic manipulation of the publication process.

Wiley and Hindawi regrets that the usual quality checks did not identify these issues before publication and have since put additional measures in place to safeguard research integrity.

We wish to credit our own Research Integrity and Research Publishing teams and anonymous and named external researchers and research integrity experts for contributing to this investigation.









The corresponding author, as the representative of all authors, has been given the opportunity to register their agreement or disagreement to this retraction. We have kept a record of any response received.

References

- [1] Y. Ge, Z. Chen, Q. Chen et al., "A Systematic Review and Meta-Analysis of the SuperPATH Approach in Hip Arthroplasty," *BioMed Research International*, vol. 2021, Article ID 5056291, 11 pages, 2021.

Research Article

A Systematic Review and Meta-Analysis of the SuperPATH Approach in Hip Arthroplasty

Yanzhi Ge ¹, Zuxiang Chen ¹, Qisong Chen ², Yanbin Fu ³, Mengqiang Fan ¹,
Ting Li ⁴, Letian Shan ¹, Peijian Tong ¹, and Li Zhou ¹

¹The First Affiliated Hospital, Zhejiang Chinese Medical University, Hangzhou, 310053 Zhejiang, China

²Department of Clinical Pharmacy, Ningbo Yinzhou No.2 Hospital, Ningbo, 315400 Zhejiang, China

³Guangdong Provincial People's Hospital, Guangdong Academy of Medical Sciences, School of Medicine, South China University of Technology, Guangzhou, 510080 Guangdong, China

⁴The First Affiliated Hospital, College of Medicine, Zhejiang University, Hangzhou, 310003 Zhejiang, China

Correspondence should be addressed to Letian Shan; letian.shan@zcmu.edu.cn, Peijian Tong; tongpeijian@163.com, and Li Zhou; zhouli0117@foxmail.com

Received 8 April 2021; Accepted 6 July 2021; Published 22 July 2021

Academic Editor: Tao Huang

Copyright © 2021 Yanzhi Ge et al. This is an open access article distributed under the Creative Commons Attribution License, which permits unrestricted use, distribution, and reproduction in any medium, provided the original work is properly cited.

Objective. To compare the clinical and radiographic results of the supercapsular percutaneously assisted total hip (SuperPATH) approach and the conventional approach in hip arthroplasty. **Design.** Based on a prepublished protocol (PROSPERO: CRD42020177717), we searched PubMed, Embase, and Cochrane for relevant literatures up to January 30, 2021. The methodological qualities were assessed using the guidelines provided by the Cochrane Collaboration for Systematic Reviews. Randomized- or fixed-effect models were used to calculate the weighted mean difference (WMD) or odds ratio (OR), respectively, for continuous and dichotomous variables. **Results.** 6 articles were included in the study, and 526 patients were selected, which included 233 cases in the SuperPATH groups and 279 cases in the conventional groups, and 4 cases performed two surgeries in succession. The SuperPATH group demonstrated shorter incision length (WMD = -7.87, 95% CI (-10.05, -5.69), $P < 0.00001$), decreased blood transfusion rate (OR = 0.48, 95% CI (0.25, 0.89), $P = 0.02$), decreased visual analogue scale (VAS) (WMD = -0.40, 95% CI (-0.72, -0.08), $P = 0.02$), and higher Harris hip score (HHS) (WMD = 1.98, 95% CI (0.18, 3.77), $P = 0.03$) than the conventional group. However, there was no difference in VAS ($P = 0.14$) and HHS ($P = 0.86$) between the two groups 3 months later, nor in the acetabular abduction angle ($P = 0.32$) in either group. **Conclusions.** SuperPATH, as a minimally invasive approach with its reduced tissue damage, quick postoperative recovery, and early rehabilitation, demonstrates the short-term advantages of hip arthroplasty. As the evidences in favor of the SuperPATH technique were limited in a small number of studies and short duration of follow-up, more research is required to further analyze its long-term effect.

1. Introduction

Hip arthroplasty is an effective method to manage various hip diseases. This operation is increasingly favored by surgeons because it relieves pain effectively and is associated with early mobilization and improved life quality among patients. In recent years, artificial joint replacement and surgical instruments have evolved rapidly. However, previous studies reported high risks of trauma, blood loss, and postoperative complications during the process of traditional approach [1]. The advancement in minimally invasive sur-

gery technology has improved the surgical results and reduced the possibility of surgical injury. An increasing number of researchers are proposing and developing minimally invasive techniques as the trend of future surgical management [2–4].

The supercapsular percutaneously assisted total hip (SuperPATH) technology, first reported by Dr. Chow in September 2011, runs between the gluteus minimus and piriformis [5] without cutting off any hip muscles and therefore preserves the integrity of muscles surrounding the joint capsule [6]. As a minimally invasive technique, SuperPATH

is conducive to rapid postsurgery rehabilitation of patients. Compared to the conventional approach, the SuperPATH technology is appreciated by surgeons for its small surgical incision, less soft tissue damage, and fast postoperative rehabilitation. Contrarily, Rasuli and Gofton [7] reported that SuperPATH demonstrated a longer learning curve and the proficiency continued to decrease beyond the first 50 cases, which potentially prolonged the operation time.

Herein, we performed several randomized controlled trials (RCTs) and clinical controlled trials (CCTs) to compare the SuperPATH approach with the conventional approach for hip arthroplasty. Through this systemic review and meta-analysis, we further explored the short-term curative outcomes of the SuperPATH approach.

2. Methods

Literature selection, assessments of eligibility criteria, and data extraction and analyses were performed based on the protocol registered in (PROSPERO: CRD42020177717).

2.1. Search Strategies. A computerized retrieval of relevant literatures from PubMed, Embase and Cochrane library were performed up to January 30, 2021 to identify qualified trials and studies regarding SuperPATH. All aspects of the international systematic review were followed using the Cochrane handbook and the study was written according to the Preferred Reporting Items for Systematic Reviews and Meta-Analyses (PRISMA) statement [8]. Keywords related to SuperPATH and the medical subject headings (MeSH) related to hip osteoarthritis, femoral neck fractures, femoral head necrosis and hip arthroplasty were used. The search strategy in PubMed was shown in Table 1, and the search strategy for the other two databases was omitted due to the similar steps.

2.2. Inclusion and Exclusion Criteria. Only RCTs, prospective or retrospective comparative studies, were enrolled. Inclusion criteria were (1) degenerative hip arthritis, avascular necrosis of the femoral head, or fresh femoral neck fractures; (2) SuperPATH approach or conventional approach (posterior approach, posterolateral approach, and direct anterior approach); and (3) having at least one of the following items reported: skin-to-skin operation time, length of incision, blood loss, blood transfusion rate, hospitalization time, visual analogue score (VAS), Harris hip score (HHS), and imaging measurements (acetabular anteversion angle and acetabular abduction angle).

Patients were removed for any of the following conditions: (1) revision of artificial total hip joint, severe osteoporosis, bone tumors, and muscle or nervous system diseases; (2) no comparison of the two approaches; (3) follow-up period of less than a year; and (4) republished literature, case reports, and reviews.

2.3. Data Extraction and Quality Assessment. Two reviewers were independently in accordance with the inclusion criteria for the quality of the literature evaluation and data extraction and then cross-checked. If there were any disagreements between them, a senior (Peijian Tong) would make a decision. RCTs were evaluated for quality using

TABLE 1: PubMed search strategy.

Sequence	Command search
1	#1 "clinical trial"[PT] OR "follow up study"[PT] OR "randomized controlled trial"[PT] OR "cohort study"[PT]
2	#2 (((cohort[TIAB]) OR randomized[TIAB]) OR randomly[TIAB]) OR trial*[TIAB]) OR placebo[TIAB]
3	#3 #1 OR #2
4	#4 gonarthrosis[TIAB]
5	#5 "Osteoarthritis, Hip"[Mesh]
6	#6 "Femoral Neck Fractures"[Mesh]
7	#7 "Femur Head Necrosis"[Mesh]
8	#8 #4 OR #5 OR #6 OR #7
9	#9 approach*[TIAB]
10	#10 SuperPATH[TIAB]
11	#11 supercapsular percutaneously assisted total hip[TIAB]
12	#12 #9 OR #10 OR #11
13	#13 "Arthroplasty, Replacement, Hip"[Mesh]
14	#14 #3 AND #8 AND #12 AND #13

the Cochrane risk assessment tool [9]. The Newcastle-Ottawa Scale (NOS) [10] was used for the quality assessment of cohort studies. This scale includes three major parts, being the selection of study groups, ascertainment of exposure, and outcome as well as group comparability. The general scores greater than or equal to 7 were considered low risk of bias.

The following information was extracted from the study: (1) characteristics of the studies (author, published time, disease, surgery, type of study, case characteristics, etc.); (2) outcome indicators: skin-to-skin operation time, length of incision, blood loss, blood transfusion rate, hospitalization time, imaging measurements (acetabular anteversion angle and acetabular abduction angle), postoperative VAS, and HHS at 1 week, 1 month, 3 months, 6 months, and 1 year after surgery.

2.4. Statistical Analyses. Meta-analysis was performed with Revman5.3 (Cochrane Collaboration, Copenhagen, Denmark) software for the available indicators. For the dichotomous variable, the odds ratios (ORs) and 95% confidence interval (95% CI) were used as the effect indicators. For the continuous variables, the weighted mean difference (WMD) and 95% CI were used as the effect indicator. When statistical heterogeneity of the study did not exist ($P \geq 0.1$ or $I^2 < 50\%$), the fixed-effect model was used. When statistical heterogeneity existed ($P < 0.1$ or $I^2 > 50\%$), the random-effect model was used for data synthesis. The results of this meta-analysis were shown in the forest plot, and $P < 0.05$ was considered as statistically significant.

3. Results

3.1. Literature Search Results. A total of 392 articles were initially obtained, of which 127 articles were excluded for

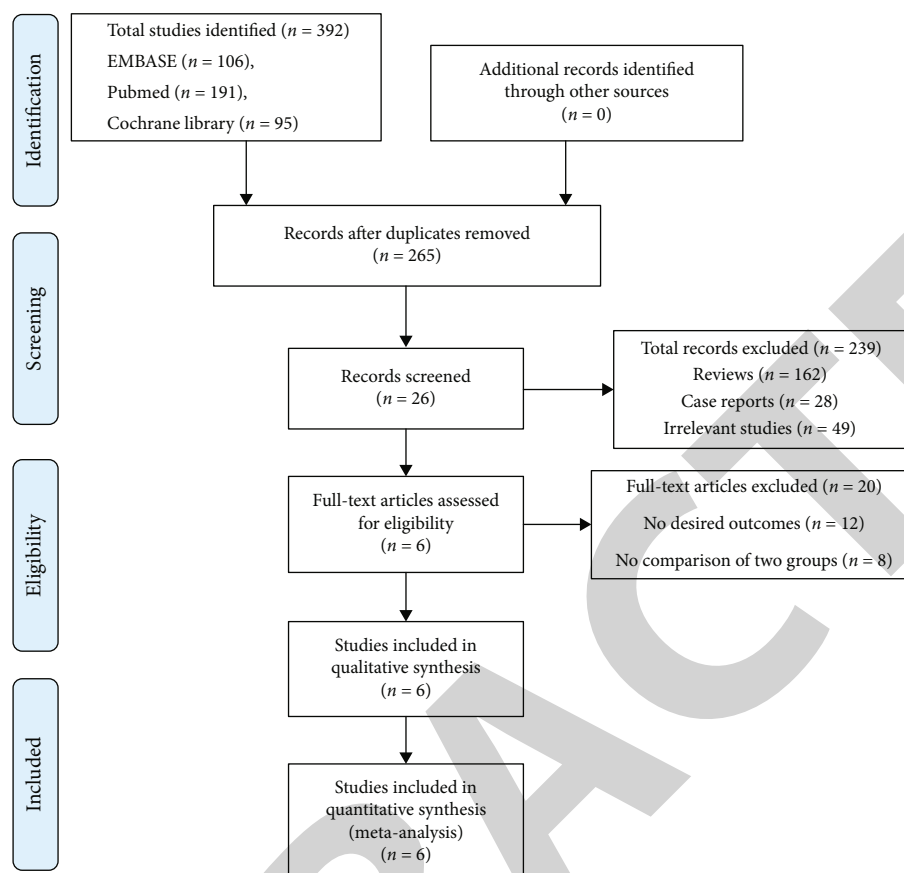


FIGURE 1: PRISMA study flow diagram.

repeated publishing. By reading titles and abstracts, 239 articles were excluded from reviews, case reports, and irrelevant studies. For no comparison of two approaches and literature that was not related to the purpose of the study, 8 documents were screened out. Further checking the context led to the exclusion of 9 articles lacking required data and 3 articles including other irrelevant interventions. Finally, 6 qualified articles [11–16] were selected. The literature inclusion and exclusion processes were shown in Figure 1, following the PRISMA statement.

3.2. The Basic Characteristics and Quality Evaluation of Included Studies. The basic characteristics of the 526 patients were shown in Table 2. Concerning the body mass index, one of the studies [16] was not mentioned. Regarding RCTs, there were a total of 3 studies [11, 12, 16] enrolled in this article. Due to the particularity of surgery, all RCT studies did not report the methods of binding to participants and/or operators. Besides, one paper [11] explained the randomization but no randomized paired design was mentioned. None of the 3 RCTs had incomplete outcome or detection bias. The risk of bias graph and summary for the RCT studies were all shown in Figures 2 and 3. As shown in Table 3, the NOS scores of these three cohort studies [13–15] were 8, 8, and 8. In general, all of the 6 articles included in this study were of good quality, with standardized research design and good

research value. The number of studies enrolled was less than 10; therefore, no publication bias was conducted.

3.3. Surgical Outcomes

3.3.1. Operation Time. Operation time (Figure 4(a)) was recorded in 6 studies [11–16] and random effects models were used because of the statistical heterogeneity of the results ($\chi^2 = 44.29$, $df = 5$, $I^2 = 89\%$, $P < 0.00001$). The results showed that there was no significant difference between the two groups (WMD = 6.81, 95% CI (-1.47, 15.09), $P = 0.11$).

3.3.2. Incision Length. Based on the available data from 4 studies [11, 12, 15, 16], we found significant heterogeneity ($\chi^2 = 111.20$, $df = 3$, $I^2 = 97\%$, $P < 0.00001$). As was shown in Figure 4(b), the pooled results were statistically different between the two groups based on the random-effect model (WMD = -7.87, 95% CI (-10.05, -5.69), $P < 0.00001$).

3.3.3. Intraoperative Blood Loss. 6 studies [11–16] recorded intraoperative blood loss. Because of statistical heterogeneity ($\chi^2 = 402.99$, $df = 5$, $I^2 = 99\%$, $P < 0.00001$), random-effect models were applied. The results in Figure 4(c) showed no significant difference between the two groups (WMD = 41.74, 95% CI (-53.22, 136.70), $P = 0.39$).

TABLE 2: Characteristics of included studies.

Study	Disease	Surgery	Type of study	Sex (F/M)		Age (years)		BMI (kg/m ²)		Follow-up (months)
				SuperPATH group	Conventional group	SuperPATH group	Conventional group	SuperPATH group	Conventional group	
Xie et al., 2017	Hip osteoarthritis	THA	RCT	12/34	19/27	66.6 ± 11.88	64.47 ± 12.09	23.62 ± 1.63	24.06 ± 2.72	12
Xu et al., 2019	Femoral neck fractures	Hip hemiarthroplasty	CCT	33/19	53/25	80.8 ± 4.4	80 ± 7.7	36.6 ± 4.4	36.0 ± 6.3	12
Wang et al., 2019	Femoral neck fractures	THA	RCT	28/27	30/25	69.03 ± 3.01	70.13 ± 3.35	NS	NS	12
Martínez et al., 2019	Hip osteoarthritis	THA	CCT	10/20	20/40	56.0 ± 14.2	60.0 ± 8.6	27.5 ± 4.8	27.9 ± 4.1	12
Jia et al., 2019	Femoral neck fractures	Hip hemiarthroplasty	RCT	19/31	21/29	78.1 ± 2.3	79.5 ± 2.6	23.82 ± 1.53	24.06 ± 1.72	12
Meng et al., 2019	Hip osteoarthritis	Bilateral THA	CCT		4/0	51.0 ± 4.54		21.49 ± 1.73		12

SuperPATH: supercapsular percutaneously assisted total hip; BMI: body mass index; THA: total hip arthroplasty; RCT: randomized controlled trial; CCT: case-controlled trial; NS: not stated.

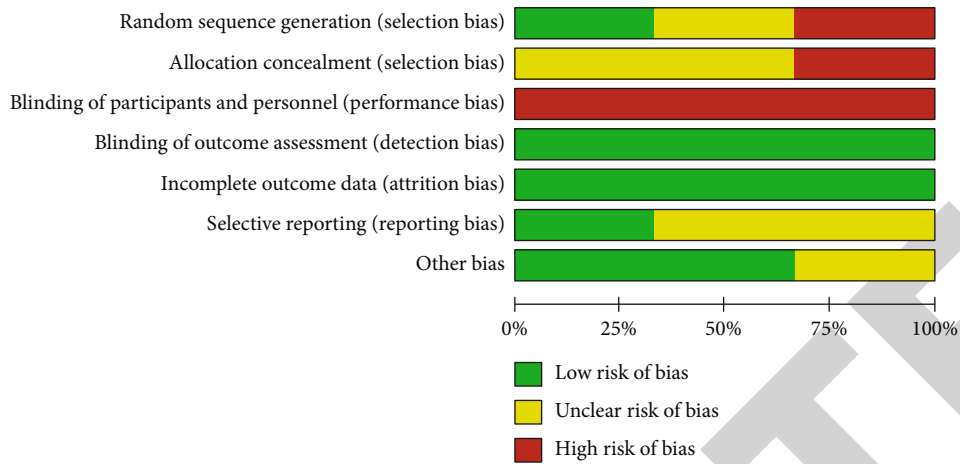


FIGURE 2: Risk of bias graph. Each risk of bias item is presented as percentages across all included studies.

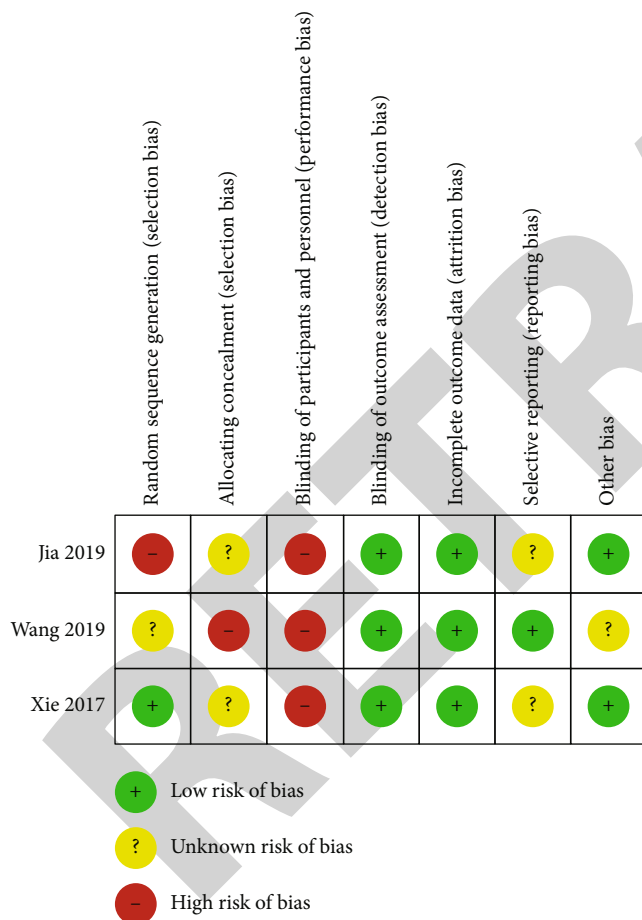


FIGURE 3: Risk of bias summary.

3.3.4. *Blood Transfusion Rate.* Data extracted from 4 studies [11, 12, 14, 15], including 326 participants, showed a postoperative transfusion rate (Figure 4(d)). Due to no significant differences in heterogeneity ($\chi^2 = 2.05$, $df = 2$, $I^2 = 2\%$, $P = 0.36$), data was summarized using the fixed-effect model. The pooled results showed statistically significant difference

between the two groups (OR = 0.48, 95% CI (0.25, 0.89), $P = 0.01$).

3.3.5. *Hospitalization Time.* A total of 206 participants (Figure 4(e)) referred to the length of stay [11, 15, 16]. Due to no significant differences in heterogeneity ($\chi^2 = 45.28$, $df = 2$, $I^2 = 96\%$, $P < 0.00001$), data was summarized using random-effect models. The pooled results showed no statistically significant difference between the two groups (WMD = -1.94, 95% CI (-4.69, 0.82), $P = 0.17$).

3.4. *Radiological Outcomes (Acetabular Anteversion Angle and Acetabular Abduction Angle).* As was shown in Figure 4(f), two studies [11, 15] showed significant heterogeneity of the acetabular anteversion angle. The fixed-effect model was adopted ($\chi^2 = 1.70$, $df = 1$, $I^2 = 41\%$, $P = 0.19$). There was significant difference between the two groups (WMD = -0.98, 95% CI (-1.6, -0.31), $P = 0.004$).

As was shown in Figure 4(g), the results of two studies [11, 15] showed no statistically significant heterogeneity in the acetabular abduction angle ($\chi^2 = 1.06$, $df = 1$, $I^2 = 6\%$, $P = 0.30$). The difference between the two groups was not statistically significant (WMD = -1.32, 95% CI (-3.92, 1.27), $P = 0.32$).

3.5. *Functional Outcomes*

3.5.1. *VAS.* 4 articles [11, 12, 15, 16] mentioned VAS (Figure 5(a)). We found significant heterogeneity in pooled results, so we used the random-effect model ($\chi^2 = 282.54$, $df = 13$, $I^2 = 95\%$, $P < 0.00001$). The pooled follow-up results showed a statistically significant difference between the two groups (WMD = -0.40, 95% CI (-0.72, -0.08), $P = 0.02$).

The subgroup analysis of VAS at 1 week and 1, 3, 6, and 12 months after operation showed that week 1 (WMD = -1.33, 95% CI (-2.16, -0.51), $P = 0.02$) was statistically significant but indicated no statistical significance at one month (WMD = -0.46, 95% CI (-1.12, 0.20), $P = 0.17$), three months (WMD = -0.17, 95% CI (-0.41, 0.06), $P = 0.14$), six months (WMD = -0.05, 95% CI (-0.23, 0.14),

TABLE 3: Newcastle-Ottawa Scale for risk of bias assessment of cohort studies included in the meta-analysis.

Study	Selection			Comparability	Outcome			Overall scores	
	1	2	3		4	5	6		7
Martínez et al.	★	★	★	★	★★	☆	★	★	8
Xu et al.	★	★	★	★	★★	★	★	☆	8
Meng et al.	☆	★	★	★	★★	★	★	★	8

1: representativeness of exposed cohort; 2: selection of nonexposed; 3: ascertainment of exposure; 4: outcome not present at start; 5: assessment of outcome; 6: adequate follow-up length; 7: adequacy of follow-up. ☆ score of 0, ★ score of 1, ★★ score of 2.

$P = 0.62$), and a year (WMD = -0.09 , 95% CI (-0.21 , 0.02), $P = 0.12$) after surgery.

3.5.2. HHS. As was shown in Figure 5(b), the statistical analysis of 5 studies [11–13, 15, 16] showed statistically significant heterogeneity ($\chi^2 = 368.59$, $df = 16$, $I^2 = 96\%$, $P < 0.00001$). The difference of pooled follow-up results between two groups was statistically significant (WMD = 1.98 , 95% CI (0.18 , 3.77), $P = 0.03$).

The meta-analysis of HHS showed that the two groups were significantly different at 1 week after surgery (WMD = 7.96 , 95% CI (3.63 , 12.28), $P = 0.0003$), 1 month after operation (WMD = 3.76 , 95% CI (2.09 , 5.42), $P < 0.00001$), and a year after operation (WMD = 0.84 , 95% CI (0.17 , 1.51), $P = 0.01$), but not at three months (WMD = -0.33 , 95% CI (-4.15 , 3.49), $P = 0.86$) nor six months (WMD = -0.09 , 95% CI (-1.73 , 1.55), $P = 0.91$) after surgery.

4. Discussion

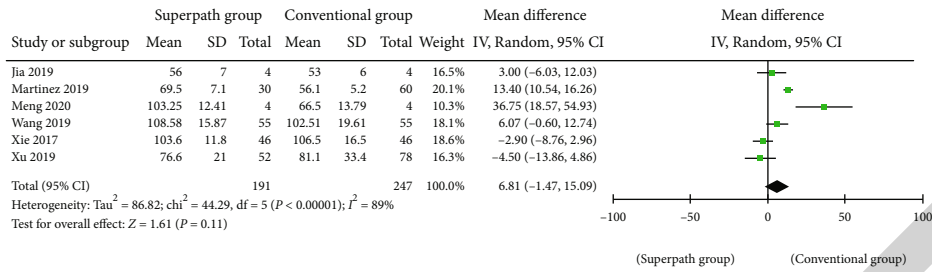
The SuperPATH technology is a combination of the Super-Cap technique [5] and PATH technique [17] and has become a revolutionary approach with minimal invasion. It is consistent with the anatomical landmarks of the conventional posterolateral approach, as it preserves all the benefits of the standard posterolateral technique, such as the clearly exposed vision and precision of prosthesis installation. Also, the SuperPATH technology does not require special operative tables and can be easily converted to a standard posterior approach. During soft tissue separation, the SuperPATH technology does not transversely cutoff muscles and tendons, which preserves the integrity of the adjacent external rotators to the joint capsule. Furthermore, acetabular preparation is straightforward, aided by the percutaneous incision, thereby providing a rapid postoperative recovery as the muscles remain intact. A previous meta-analysis [18] revealed the advantage of SuperPATH approach sourcing mostly from Chinese database and literatures, which was quite different from our study.

In the current study, we performed a systematic review and meta-analysis that compared the SuperPATH approach with the conventional approach in hip arthroplasty. 6 studies (3 RCTs and 3 CCTs) met our inclusion criteria. In terms of incision length, four studies reported a shorter average length of the surgical incision in the SuperPATH group than that in the conventional group. Unlike the great trauma caused by the conventional approach, minimally invasive surgery brings a series of advantages which cannot be defined by

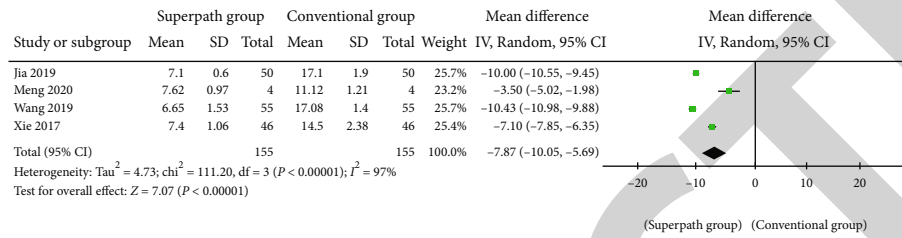
short incision only. For instance, direct anterior access may cause lateral femoral cutaneous nerve injury [19], whereas the lateral approach may cause the superior gluteal nerve injury and cutoff the insertion of the gluteus minimus [20]. Furthermore, the posterior lateral approach requires incising the piriformis muscle to expose the joint capsule [21]. As a minimally invasive surgery, SuperPATH is a satisfactory approach not only for its minimal incision but also for its protection of the external muscles and ligaments without cutting them off. We found that violent pulling of the distal or proximal soft tissue during surgery potentially reduced post-operative incision necrosis, subcutaneous fat liquefaction, and other complications associated with other minimally invasive THAs. Thus, obesity and stiffness of muscles are contraindications for conventional surgical options. On account of a short incision, mini-invasive surgery may be linked to the inaccuracy of prosthesis placement due to the missing field of vision and unclear anatomical landmarks. However, SuperPATH is not a contraindication to obesity and stiffness of muscles. This further broadens the indications for the resolution of intraoperative joint capsule exposures and anatomic landmarks [3]. In another study, Eskelinen [22] suggested that more attention should be given to tissue protection and placement of the prosthesis and the short incision (≤ 10 cm) should be made into the secondary site simultaneously. Elsewhere, Han et al. [23] found that intraoperative protection of the external rotation muscles could lower the postoperative dislocation rate from 1.8% to 6.2%.

In the present study, 6 articles documented the operation time. The results revealed no difference in the operating time between the two groups, which may be closely associated with the learning curve of the new SuperPATH technology. For instance, Rasuli and Gofton [7] reported 50 cases and 49 cases adopting SuperPATH and PATH, respectively, as minimally invasive approaches for total hip arthroplasty. In their study, the operation time of the SuperPATH group exhibited a decreasing trend, suggesting that the learning curve may be associated with prolonged operation time. Besides, the incision suturing step was, in most cases, performed by junior physicians at the end of the surgery and may impact the overall operation time.

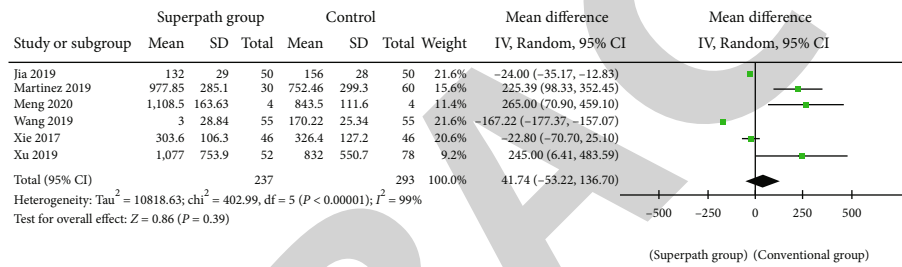
Blood loss and transfusion rates in prosthetic hip operations were closely associated with the bleeding during osteotomy, intramedullary reaming of the medullary cavity, and muscle excision. With the SuperPATH approach, smaller soft tissue dissection was associated with less bleeding and lower transfusions rates. In our analysis, 6 studies and 4



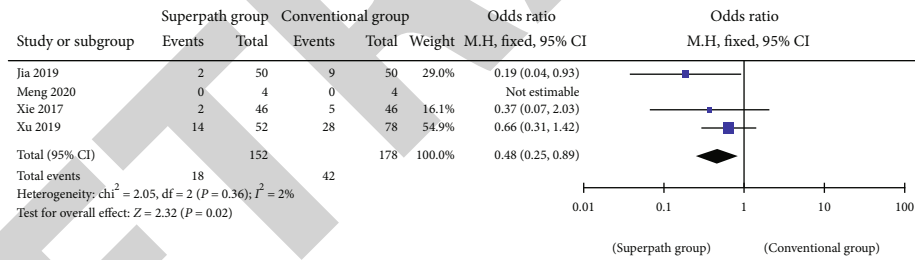
(a)



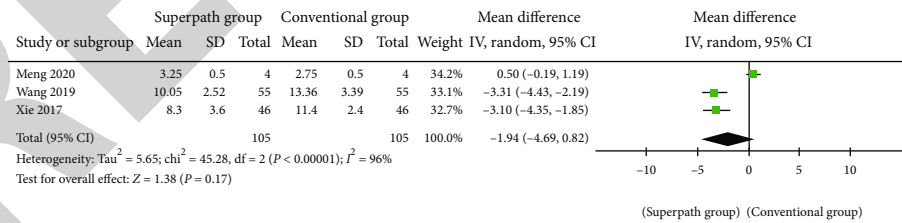
(b)



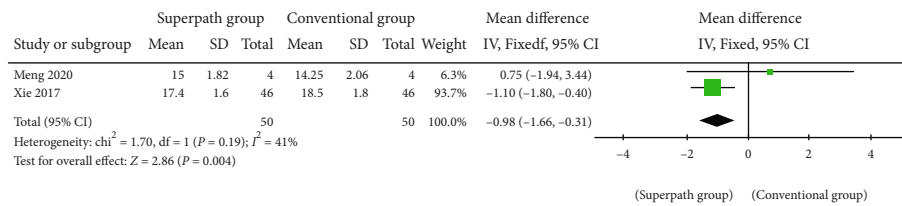
(c)



(d)

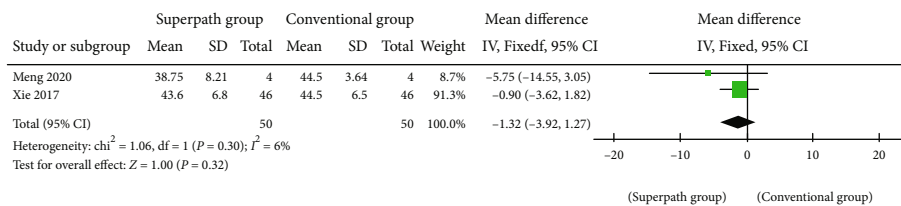


(e)



(f)

FIGURE 4: Continued.



(g)

FIGURE 4: Forest plot analysis comparing the SuperPATH group vs the conventional group. (a) Operation time. (b) Incision length. (c) Blood loss. (d) Transfusion rate. Blood loss. (e) Hospitalization time. (f) Anteversion angle. (g) Abduction angle.

studies mentioned intraoperative blood loss and blood transfusion rates, respectively. Although no significant difference was found in intraoperative blood loss, blood transfusion rates were significantly lower with the SuperPATH technique, which is most likely because the SuperPATH technique can result in less trauma by protecting the joint capsule and external rotation muscles. As a new technique, surgeons may prolong the operation time and have increased blood loss risks for unskilled operation. Gofton et al. [6] and Rasuli and Gofton [7] found that the transfusion rates of SuperPATH minimally invasive surgery were 3.3% and 4.0%, respectively, lower compared to those with conventional approaches.

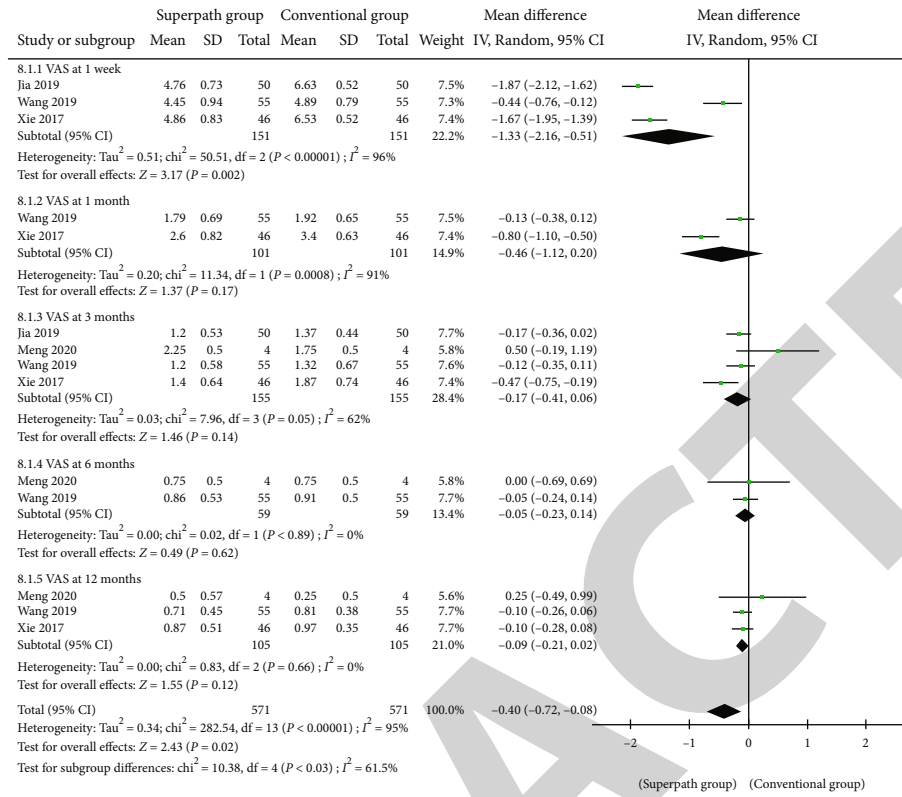
3 studies reported on the hospitalization time but exhibited no significant difference. Cardenas-Nylander et al. [24] found that the average length of stay for patients who underwent SuperPATH surgery was 1.4 days, less than that of the conventional THA. Gofton and Fitch [25] explored the 30-day readmission rates for 479 patients who underwent THA and found that the 30-day readmission rate for the SuperPATH minimally invasive total hip arthroplasty ranged from 4.3% to 2.3% compared to conventional procedures. The same research team investigated 99 patients between April 2013 and January 2014 and reported that the overall costs of hospitalization of the SuperPATH approach were 28.4% lower than those of the conventional lateral approach [6]. Thus, SuperPATH significantly reduced postoperative costs. Meng et al. [15] in their study performed bilateral hip arthroplasty in succession, demonstrating that the SuperPATH approach could reduce the whole length of stay and enhance the postsurgery recovery.

4 studies mentioned VAS as well as the subgroup analysis revealed that 1 week after surgery, pain relief was significantly improved in the SuperPATH group than that in the conventional surgery group. However, there was no difference between the two groups during the 1 to 12 months follow-up. Based on the above discussion, the SuperPATH technology improved patient satisfaction in the early postoperative period. Bodrogi et al. [26] performed the SuperPATH technique in 17 patients with femoral neck fractures, and the clinical follow-up found that postoperative analgesia dosage was reduced and the hospital stays were shortened. Jiang [27] measured the circumference of the thigh after the SuperPATH surgery and found that the postoperative degree of edema was significantly lower than other small incision surgeries, thus reducing the patient pain and other constrained symptoms.

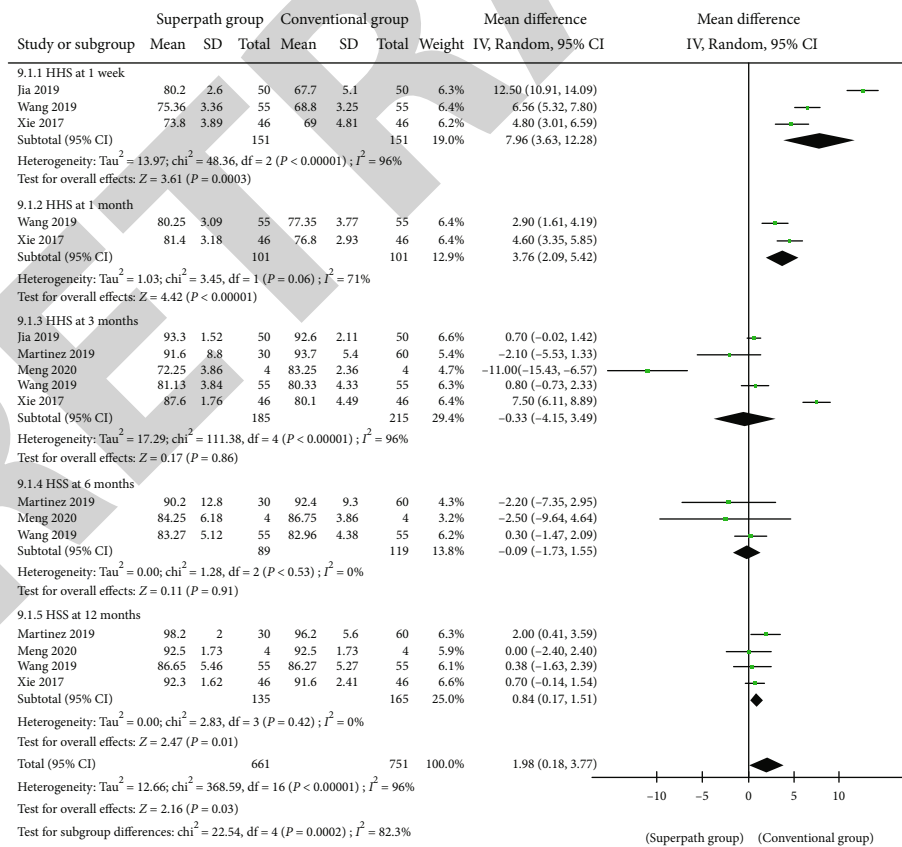
HHS is a widely used synthetical mark to evaluate the hip function and assess the effect of hip replacement. In this meta-analysis, the HHS at week 1 and one month postoperatively in the SuperPATH group was higher than that in the conventional replacement group. However, we found no significant difference after 3 months. None of the included articles mentioned specific details of the HHS. The author believed that HHS in the initial period was low in the SuperPATH replacement group, demonstrating a nearly functional recovery. The difference in the middle period was not significant, but the overall follow-up was shorter. And the long-term efficacy still needed a follow-up assessment. Della et al. [3] collected postoperative imaging measurements in 66 patients and found that the early results in the SuperPATH group were superior to the conventional group. However, the long-term results needed further investigation.

Moreover, Lewinnek et al. [28] found that the dislocation rate for cup orientation with anteversion of 15 ± 10 degrees and lateral opening of 40 ± 10 degrees was 1.5%, with respect to minimal risks of dislocation in the postoperative period. Herein, following the analysis of 2 studies, we found no difference in acetabular abduction angles by comparing the SuperPATH group to the conventional group. Simultaneously, the two groups showed significant differences in acetabular anteversion angles. In a previous study by Williams et al. [29], the transverse acetabular ligament was applied to establish the position of the acetabular locator. This method was suitable for both conventional and minimally invasive procedures. Therefore, reaming and placement of the acetabular component referring to the transverse acetabular ligament can significantly improve the accuracy of the prosthesis position. Rasuli and Gofton [7] also revealed that the reference to acetabular transverse ligament during operation could increase the accuracy of the prosthesis and reduce the rate of dislocation. In our review, only two studies and 50 patients were enrolled for analysis, which may restrain the accuracy of our judgment.

This article had some limitations: (1) the follow-up of each study and some of the evaluation indicators were inconsistent, (2) the analysis lacks detailed score data and the incidence of complications was not assessed, (3) only published papers were identified; thus, unpublished articles might influence the ultimate result, and (4) the SuperPATH technology was first reported in 2011, and multicenters, larger samples, and follow-up assessments are still needed to determine its long-term efficacy and complications.



(a)



(b)

FIGURE 5: Forest plot analysis from 5 times comparing the SuperPATH group vs the conventional group. (a) VAS. (b) HHS.

Our meta-analysis demonstrated that the short- and medium-term postoperative hip-related scores of the SuperPATH approach were not significantly different from those of the conventional approach. However, the SuperPATH approach, on account of shorter incision length, lower postoperative transfusion rate, preferable early postoperative VAS, and HHS, is superior to the conventional approach. Furthermore, it has potential benefits, including low tissue damage and rapid postoperative recovery, which can significantly improve the quality of life and satisfaction of patients.

5. Conclusions

Our study suggested that SuperPATH was associated with shorter incision length, less blood transfusion rate, better functional recovery, and lower pain scores. Due to the limited number of studies and insufficient sample sizes, the conclusion should be treated cautiously. And larger sample sizes with well-designed RCTs are required to confirm our conclusion.

Data Availability

All data can be obtained from corresponding author Li Zhou or the first author Yanzhi Ge.

Disclosure

This manuscript has been preprinted in Research Square (10.21203/rs.3.rs-41289/v1).

Conflicts of Interest

The authors declare that they have no conflicts of interest.

Authors' Contributions

The following authors designed the study (Yanzhi Ge, Peijian Tong), collected the data (Yanzhi Ge, Zuxiang Chen, and Yanbin Fu), analyzed the data (Li Zhou, Mengqiang Fan, and Ting Li), wrote the initial drafts (Yanzhi Ge), and ensured the accuracy of the data and analysis (Peijian Tong, Letian Shan, Li Zhou). Yanzhi Ge, Li Zhou, Qisong Chen, and Letian Shan revised the manuscript. All authors read and approved the manuscript. Yanzhi Ge and Zuxiang Chen contributed equally to this work.

Acknowledgments

The authors want to thank all patients and subjects for their participation. This work was supported by the scientific research project of the Zhejiang Education Commission (grant number Y202044541 to author Yanzhi Ge), Zhejiang Natural Science Foundation Young Scholars (grant number LQ20H270009 to author Li Zhou), Zhejiang Traditional Chinese Medical Science Foundation (grant number 2020ZA039 to author Li Zhou), and Natural Science Foundation of Zhejiang Chinese Medical University (grant number 2020ZG42 to author Li Zhou).

References

- [1] X. Li, L. Ma, Q. Wang, and K. Rong, "Comparison of total hip arthroplasty with minimally invasive SuperPath approach vs. conventional posterolateral approach in elderly patients: a one-year follow-up randomized controlled research," *Asian Journal of Surgery*, vol. 44, no. 3, pp. 531–536, 2021.
- [2] D. J. Roger and D. Hill, "Minimally invasive total hip arthroplasty using a transpiriformis approach: a preliminary report," *Clinical Orthopaedics and Related Research*, vol. 470, no. 8, pp. 2227–2234, 2012.
- [3] P. K. Della Torre, D. A. Fitch, and J. C. Chow, "Supercapsular percutaneously-assisted total hip arthroplasty: radiographic outcomes and surgical technique," *Ann Transl Med*, vol. 3, no. 13, 2015.
- [4] N. Capuano, A. Del Buono, and N. Maffulli, "Tissue preserving total hip arthroplasty using superior capsulotomy," *Operative Orthopädie und Traumatologie*, vol. 27, no. 4, pp. 334–341, 2015.
- [5] J. Chow, B. Penenberg, and S. Murphy, "Modified micro-superior percutaneously-assisted total hip: early experiences & case reports," *Current Reviews in Musculoskeletal Medicine*, vol. 4, no. 3, pp. 146–150, 2011.
- [6] W. Gofton, J. Chow, K. D. Olsen, and D. A. Fitch, "Thirty-day readmission rate and discharge status following total hip arthroplasty using the supercapsular percutaneously-assisted total hip surgical technique," *International Orthopaedics*, vol. 39, no. 5, pp. 847–851, 2015.
- [7] K. J. Rasuli and W. Gofton, "Percutaneously assisted total hip (PATH) and Supercapsular percutaneously assisted total hip (SuperPATH) arthroplasty: learning curves and early outcomes," *Ann Transl Med*, vol. 3, no. 13, p. 179, 2015.
- [8] M. D. F. McInnes, D. Moher, B. D. Thombs et al., "Preferred reporting items for a systematic review and meta-analysis of diagnostic test accuracy studies: the PRISMA-DTA statement," *JAMA*, vol. 319, no. 4, pp. 388–396, 2018.
- [9] J. P. T. Higgins, D. G. Altman, P. C. Gotzsche et al., "The Cochrane Collaboration's tool for assessing risk of bias in randomised trials," *BMJ*, vol. 343, no. oct18 2, p. d5928, 2011.
- [10] A. Stang, S. Jonas, and C. Poole, "Case study in major quotation errors: a critical commentary on the Newcastle-Ottawa scale," *European Journal of Epidemiology*, vol. 33, no. 11, pp. 1025–1031, 2018.
- [11] J. Xie, H. Zhang, L. Wang, X. Yao, Z. Pan, and Q. Jiang, "Comparison of supercapsular percutaneously assisted approach total hip versus conventional posterior approach for total hip arthroplasty: a prospective, randomized controlled trial," *Journal of Orthopaedic Surgery and Research*, vol. 12, no. 1, p. 138, 2017.
- [12] J. Jianbo, J. Ying, L. Xinxin, W. Lianghao, Y. Baoqing, and A. Rongguang, "Hip hemiarthroplasty for senile femoral neck fractures: minimally invasive SuperPath approach versus traditional posterior approach," *Injury*, vol. 50, no. 8, pp. 1452–1459, 2019.
- [13] J. Más Martínez, J. Sanz-Reig, M. Morales-Santías, D. Bustamante Suarez de Puga, C. Verdu Roman, and E. Martinez Gimenez, "Comparative cohort study of the SuperPath approach and the conventional posterior approach in primary cementless hip replacement surgery," *Rev Esp Cir Ortop Traumatol (Engl Ed)*, vol. 63, no. 5, pp. 346–354, 2019.
- [14] K. Xu, D. Anwaier, R. He et al., "Hidden blood loss after hip hemiarthroplasty using the superPATH approach: a retrospective study," *Injury*, vol. 50, no. 12, pp. 2282–2286, 2019.

Research Article

Study of the G Protein Nucleolar 2 Value in Liver Hepatocellular Carcinoma Treatment and Prognosis

Yiwei Dong,¹ Qianqian Cai,² Lisheng Fu,¹ Haojie Liu,¹ Mingzhe Ma,³ and Xingzhong Wu¹ 

¹Department of Biochemistry and Molecular Biology, School of Basic Medical Sciences, Fudan University, Key Lab of Glycoconjugate Research, Ministry of Public Health, Shanghai 200032, China

²Shanghai Key Laboratory of Molecular Imaging, Shanghai University of Medicine and Health Sciences, Shanghai 201318, China

³Department of Gastric Surgery, Fudan University Shanghai Cancer Center, Shanghai 200025, China

Correspondence should be addressed to Xingzhong Wu; xz_wu@shmu.edu.cn

Received 10 May 2021; Accepted 29 June 2021; Published 20 July 2021

Academic Editor: Tao Huang

Copyright © 2021 Yiwei Dong et al. This is an open access article distributed under the Creative Commons Attribution License, which permits unrestricted use, distribution, and reproduction in any medium, provided the original work is properly cited.

LIHC (liver hepatocellular carcinoma) mostly occurs in patients with chronic liver disease. It is primarily induced by a vicious cycle of liver injury, inflammation, and regeneration that usually last for decades. The G protein nucleolar 2 (GNL2), as a protein-encoding gene, is also known as NGP1, Nog2, Nug2, Ngp-1, and HUMAUANTIG. Few reports are shown towards the specific biological function of GNL2. Meanwhile, it is still unclear whether it is related to the pathogenesis of carcinoma up to date. Here, our study attempts to validate the role and function of GNL2 in LIHC via multiple databases and functional assays. After analysis of gene expression profile from The Cancer Genome Atlas (TCGA) database, GNL2 was largely heightened in LIHC, and its overexpression displayed a close relationship with different stages and poor prognosis of carcinoma. After enrichment analysis, the data revealed that the genes coexpressed with GNL2 probably participated in ribosome biosynthesis which was essential for unrestricted growth of carcinoma. Cell functional assays presented that GNL2 knockdown by siRNA in LIHC cells MHCC97-H and SMCC-7721 greatly reduced cell proliferation, migration, and invasion ability. All in all, these findings capitulated that GNL2 could be a promising treatment target and prognosis biomarker for LIHC.

1. Background

Liver cancer is composed of primary carcinoma and metastatic carcinoma [1, 2]. As far as the most common inducers of carcinoma-associated mortality in the world, primary liver carcinoma ranks second, thus becoming a great public health challenge [3–5]. Primary liver carcinoma consists of liver hepatocellular carcinoma (LIHC), intrahepatic cholangiocarcinoma (iCCA), and other rarely seen neoplasms [6, 7]. Mostly, LIHC occurs in patients with chronic liver disease, and it is generally caused by a vicious cycle of liver damage, inflammation, and regeneration that usually span several decades [8–11]. Like other malignant neoplasms, the widely generated biological alteration in LIHC pathogenesis comprises activated oncogene and inactivated neoplasm inhibitor genes [12]. Since its discovery over 60 years ago, alpha-fetoprotein (AFP) has

been the most commonly used biomarker in LIHC management [4, 13, 14]. However, LIHC is classified as a complicated disease accompanied by several risk factors caused pathogenic mechanisms. Thus, to characterize LIHC only by a single biomarker is not feasible. To explore the pathogenesis of LIHC and uncover the candidate biomarkers become urgently needed.

As a protein-encoding gene, the G protein nucleolar 2 (GNL2) is also named by nucleostemin (NS), which is essential for stem cell growth and development [15, 16]. GNL2 is highly expressed in tissues, such as testis and bone marrow [17, 18]. Presently, there are no researches on the particular biological function of GNL2, and little is known about its relationship with carcinoma pathogenesis.

Here, our study is aimed at investigating whether there is an association of GNL2 expression with the prognosis in LIHC patients. In addition, our study also wants to validate

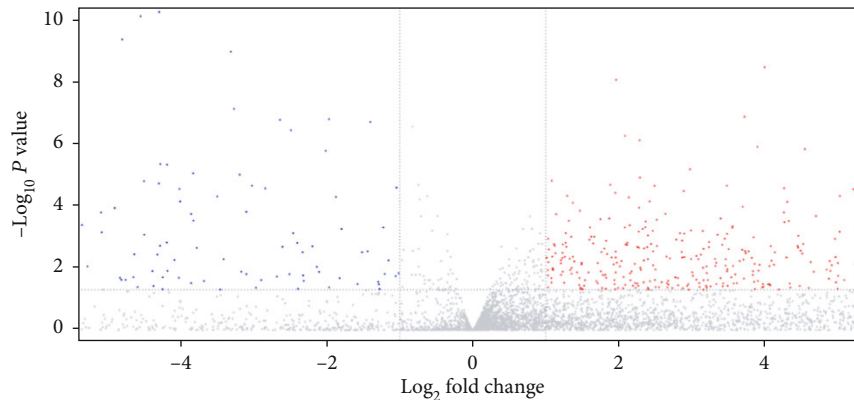


FIGURE 1: Volcano plot illustrated the DEGs existing in liver carcinoma samples and normal ones based on TCGA dataset. Genes with upregulation were presented as the red dot, while those with downregulation were shown as the blue dot.

its inhibitory effect on LIHC cell proliferation, migration, and invasion by *in vitro* experiments.

2. Material and Methods

2.1. Identification of the Differentially Expressed Genes (DEGs) in TCGA Database. The Cancer Genome Atlas (TCGA) database, as the National Cancer Institute (NCI) and the National Human Genome Institute (NHGRI) supported the project, was employed to obtain mRNA expression profile of liver carcinoma and normal samples. It could offer all-inclusive maps of the main alterations of genomic in multiple sorts of carcinomas. $|\log_2 \text{fold change (FC)}| > 1$ and $P \text{ value} < 0.05$ were considered to be parameters for identifying the DEGs. The protein-protein network (PPI) of the selected DEGs was constructed by the Search Tool for the Retrieval of Interacting Genes (STRING) database.

2.2. Gene Expression Profiling Interactive Analysis (GEPIA) Database. GEPIA is an interacting online server for the analysis of RNA sequencing data of tumorous and healthy samples from the Genotype-Tissue Expression (GTEx) and TCGA datasets. The URL of GEPIA is <http://gepia.cancer-pku.cn>. In this study, we used GEPIA to determine GNL2 expression in different stages of liver carcinoma and then perform patient survival analysis and identify similar genes.

2.3. Kaplan-Meier Plotter Database. The Kaplan-Meier plotter (<https://kmplot.com/analysis/>), functioning as a web tool, is used to validate survival biomarkers in the light of meta-analysis. The information of gene expression profile and various survival data comprising overall survival (OS), relapse-free survival (RFS), and disease-specific survival (DSS) come from the well-known public databases, including GEO (only Affymetrix microarrays), EGA, and TCGA. Kaplan-Meier plotter was taken to generate the survival curves of GNL2, and log rank P values, as well as hazard ratio (HR) with 95% confidence intervals, were calculated.

2.4. Biological Process and Pathway Enrichment Analysis. The top 1000 genes coexpressed with GNL2 (sorted by Pearson correlation coefficient) in LIHC-tumor and LIHC-normal dataset were identified by GEPIA. To assess the gene-

annotation enrichment, we utilized the online tool Enrichr (<https://maayanlab.cloud/Enrichr/>). Enrichment annotations were presented as Kyoto Encyclopedia of Genes and Genomes (KEGG) pathway and Gene Ontology (GO) biological process. Data were plotted and visualized using an online platform <http://www.bioinformatics.com.cn>.

2.5. Cell Culture and Transfection. The human LIHC cell lines MHCC97-H and SMCC-7721 were obtained from the China Center for Type Culture Collection in 2020 and authenticated by short tandem repeat analysis. All cells were routinely cultured in DMEM medium (Thermo Fisher Scientific, Inc., USA) supplemented with 10% FBS (Thermo Fisher Scientific, Inc., USA) in an incubator with 5% CO_2 at 37°C. SiRNA targeting GNL2 (si-GNL2) and a negative control siRNA (si-NC) were acquired from GeneCopoeia, Inc. (USA). When MHCC97-H and SMCC-7721 cells confluence reached up to 80% on the following day, they were transfected with indicated siRNAs utilizing Lipofectamine 2000 (Invitrogen, USA) as the manual described. Reduced efficiency of GNL2 was determined by qRT-PCR at 48 h post-transfection. The siRNAs used were as follows: si-GNL2-1, 5'-CACGTGTGATTAAGCAGTCATCATT-3'; si-GNL2-2, 5'-CCATACAAAGTTGTCATGAAGCAAA-3'; si-NC, 5'-UUCUCCGAACGUGUCACGUTT-3'.

2.6. Quantitative Reverse-Transcription PCR (qRT-PCR) Assay. Overall RNA was harvested from indicated cells utilizing TRIzol reagent (Invitrogen, USA). qRT-PCR was carried out on a Bio-Rad Single Color Real-Time PCR system (Bio-Rad Laboratories, Inc., USA) with SYBR-Green Real-Time PCR Master Mix (Toyobo Life Science, Japan). β -Actin was used as an internal control.

2.7. Cell Proliferation Assay. 2,000 of si-NC- and si-GNL2-transfected cells were plated in per well of 96-well plates, followed by maintaining 0, 24, 48, and 72 h at 37°C. 10 μl of CCK-8 reagent was added into each well at the indicated time, followed by another 2 h incubation. The wavelength at 450 nm was read in a Varioskan Flash spectrophotometer (Thermo Fisher Scientific, Inc., USA).

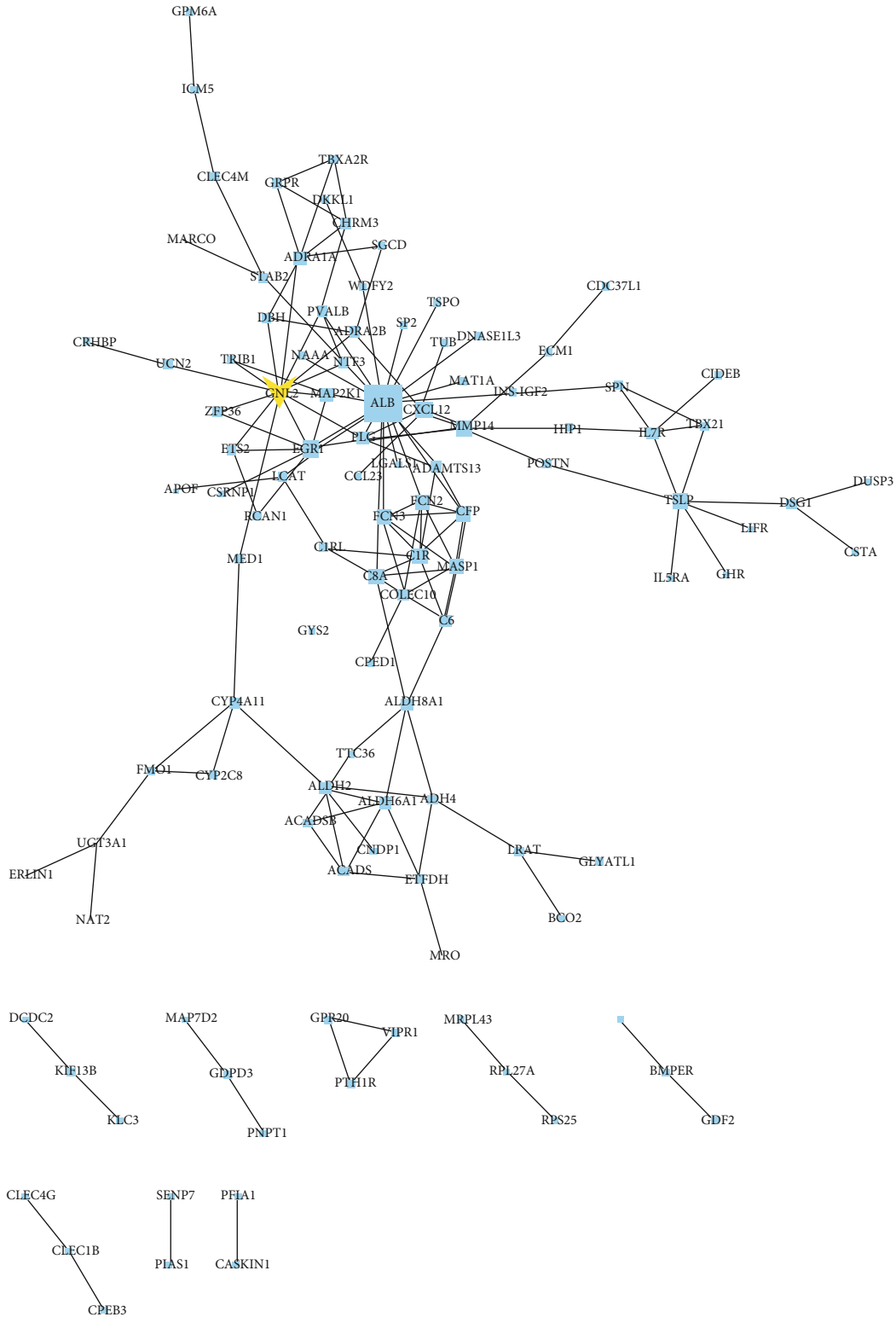


FIGURE 2: PPI network of the DEGs. Nodes displayed proteins, and edges exhibited the interactions between proteins.

2.8. *Transwell Assay.* For cell migration assay, Matrigel needed not to be precoated in the Transwell chamber (Corning, NY). The Transwell upper chamber was added 50,000 si-NC- or si-GNL2-transfected cells suspended in serum-free DMEM medium, and the lower chamber was added DMEM medium

with 10% FBS, followed by maintaining 24h at 37°C. Then, migrated cells underside were rinsed by PBS, fixed by methanol, and stained by DAPI. Positive cells were photographed and counted under a microscope. Five random fields were selected and counted the average. For cell invasion assay,

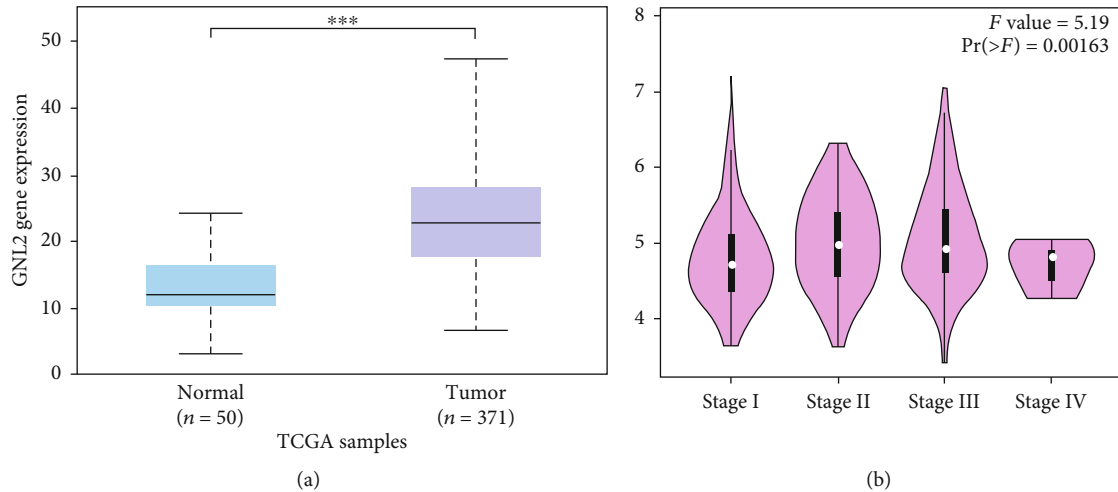


FIGURE 3: Highly expressed GNL2 was in LIHC, and its higher expression was associated with carcinoma stages. (a) To analyze GNL2 expression level in normal and tumor tissues of the liver based on TCGA dataset. *** $P < 0.001$. (b) Analysis of GNL2 expression level in different liver carcinoma stages based on GEPIA dataset.

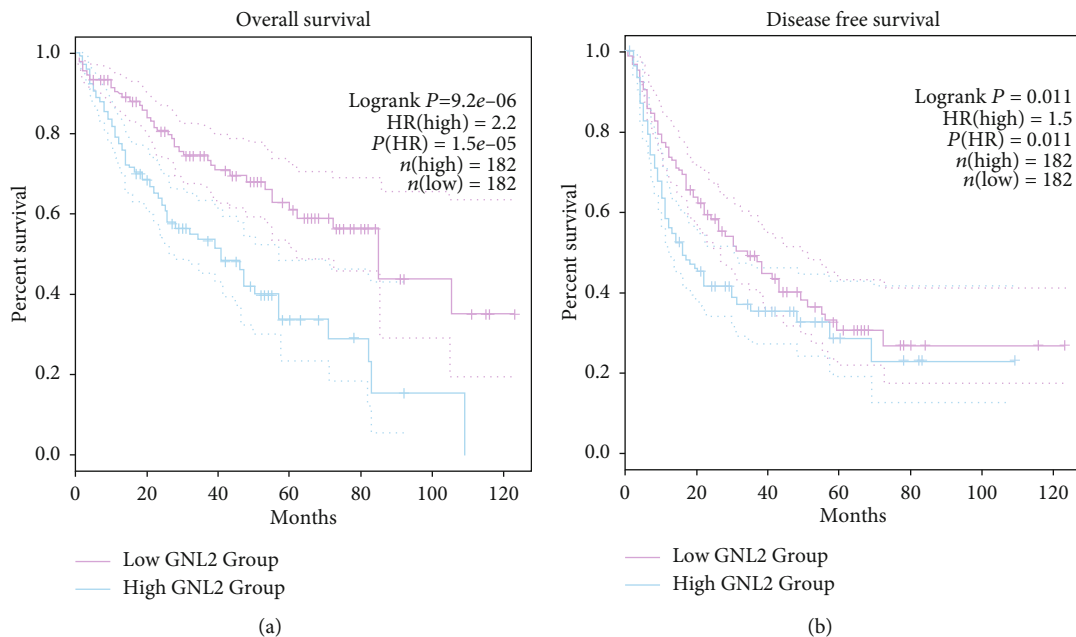


FIGURE 4: GNL2 high expression was a poor prognosis factor for LIHC. (a) GEPIA analysis of the OS curves of LIHC patients with highly expressed or lowly expressed GNL2. (b) GEPIA analysis of the DFS curves of LIHC patients with highly expressed or lowly expressed GNL2.

2 mg/mL Matrigel was precoated in the upper chamber. The remaining procedures were the same as the cell migration assay.

2.9. Statistical Analysis. Our data were analyzed by the SPSS software (IBM Corp., USA) and were represented as the mean \pm SD. The Student *t*-test was employed to analyze the difference in mRNA expression from TCGA database. The correlation existing in expression and pathological stage of carcinoma was assessed by one-way ANOVA. The differences in survival ratio between highly expressed GNL2 and lowly expressed GNL2 groups were detected by Kaplan-

Meier analysis and log-rank test. The Student *t*-test was employed to compare the difference of the si-GNL2-transfected group with the si-NC-transfected group. The great statistical difference indicated $P < 0.05$.

3. Results

3.1. Identification of the DEGs and Overexpressed Gene GNL2 in LIHC. As indicated before, to define the DEGs in liver carcinoma and normal samples, we obtained gene expression information from TCGA database. Totally, 361 DEGs were selected, comprising 283 genes with increased expression

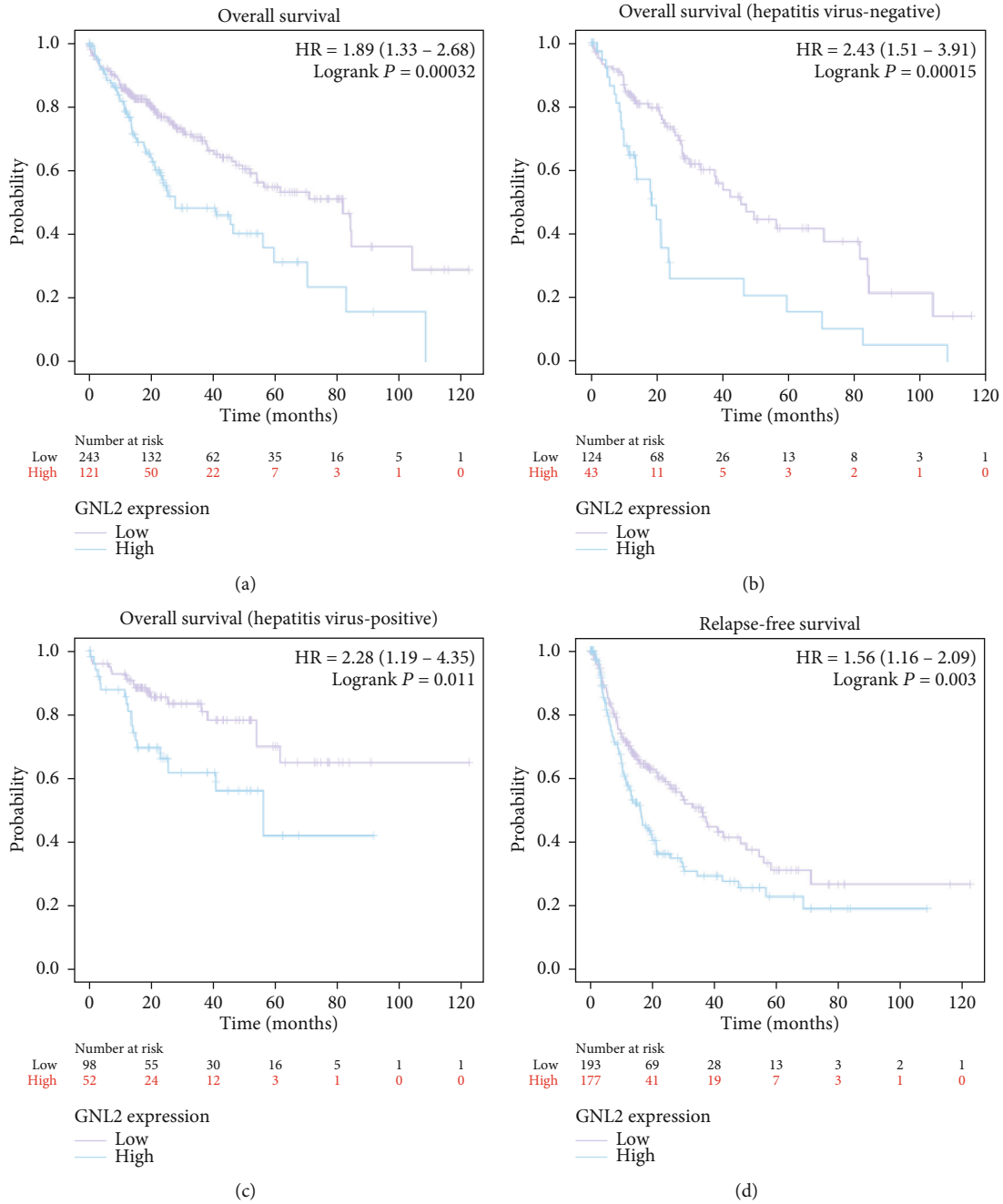


FIGURE 5: Continued.

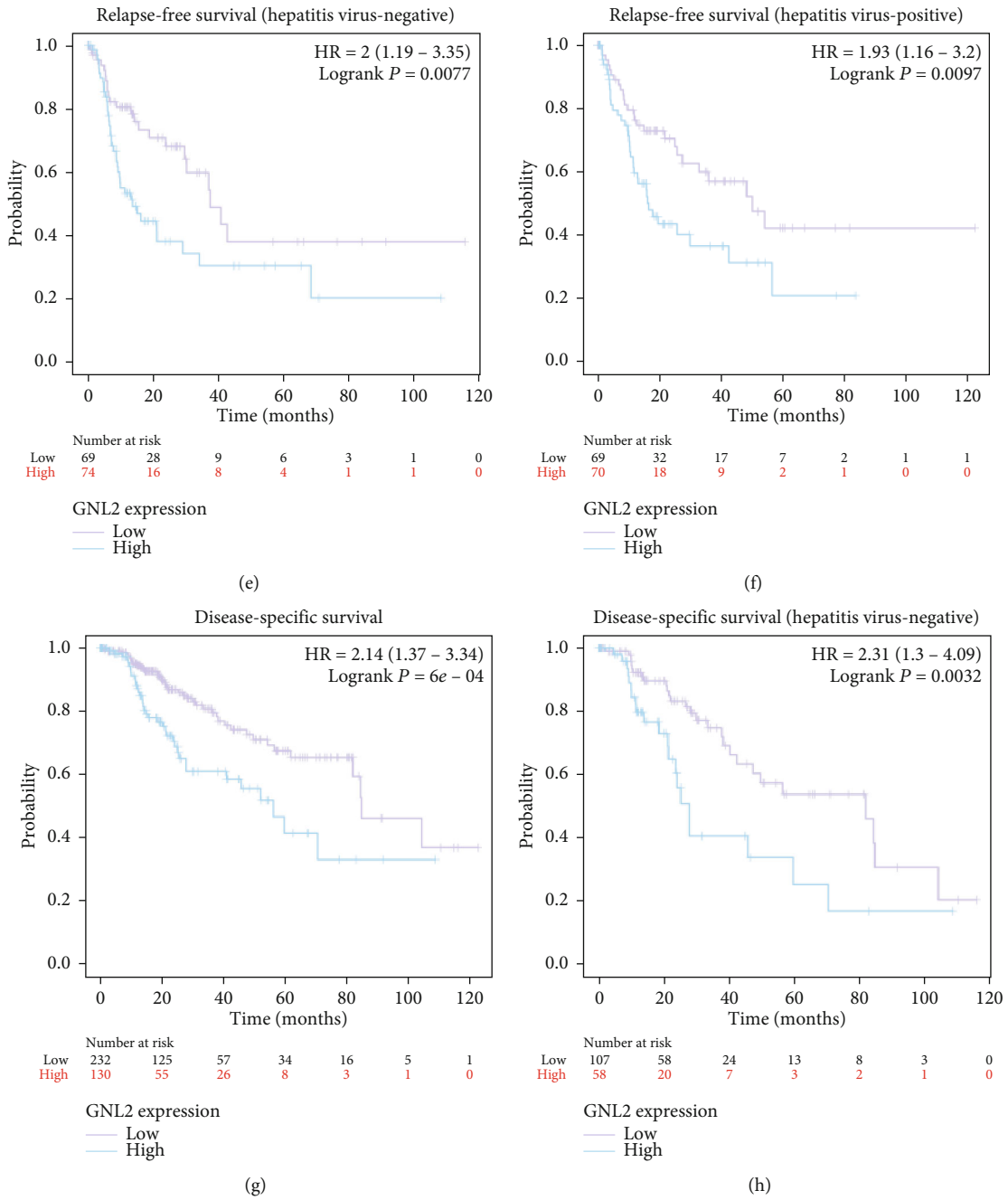
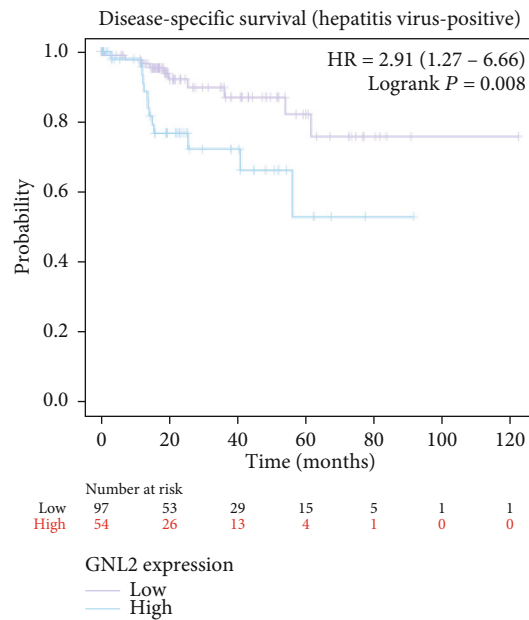


FIGURE 5: Continued.



(i)

FIGURE 5: Prognosis value of GNL2 in LIHC was confirmed by the Kaplan-Meier plotter dataset. The impacts of GNL2 expression levels on the (a) OS, (d) RFS, and (g) DSS of LIHC patients. The impacts of GNL2 expression levels on the (b) OS, (e) RFS, and (h) DSS of LIHC patients without hepatitis virus infection. The impacts of GNL2 expression levels on the (c) OS, (f) RFS, and (i) DSS of LIHC patients with hepatitis virus infection.

and 78 genes with decreasing expression (Figure 1 volcano plot). Figure 2 displayed the PPI network, 110 nodes (proteins) and 159 edges (proteins interactions). Besides, it was observed that the degree of GNL2 was high which partly revealed the potential role of GNL2 as a candidate biomarker for LIHC.

3.2. Validation of the Relationship between the Stages of Liver Carcinoma and the Expression of GNL2. TCGA database analysis showed that LIHC tumor tissues highly expressed GNL2 in comparison with normal tissues (Figure 3(a)). Then, GEPIA analysis discovered the associations between various pathological carcinoma stages of LIHC patients and GNL2 expression level. It was found that GNL2 expression was significantly associated with the pathological carcinoma stages of LIHC (Figure 3(b), $P = 0.00163$). Our results demonstrated that GNL2 exhibited an important part in clinical practice.

3.3. Prognostic Value of GNL2 for LIHC Patients. Subsequently, we employed GEPIA to investigate the relationship of GNL2 expression with LIHC patient's prognosis. Figures 4(a) and 4(b) demonstrated the OS and DFS curves of LIHC patients with different GNL2 expression levels. Kaplan-Meier analysis plus the log-rank test was taken to assess the impacts of the expression of GNL2 on OS and DFS. Compared to the lowly expressed GNL2 group, the highly expressed GNL2 group exhibited a shorter OS and DFS (log rank $P = 9.2e - 06$ and 0.011 , respectively). Additionally, we further verified that high expression of GNL2 led to poor prognosis in LIHC patients by Kaplan-Meier plotter database analysis. Figures 5(a), 5(d), and 5(g) showed that LIHC patients with highly expressed

GNL2 had shorter OS, RFS, and DSS compared to those with the lowly expressed group, in line with the GEPIA analysis. Given the high incidence of hepatocellular carcinoma was mainly due to the prevalence of hepatitis virus infection, we further evaluated the prognosis of LIHC patients stratified according to hepatitis virus infection. The results showed that the hepatitis virus did not affect the prognosis of GNL2 (Figures 5(b), 5(c), 5(e), 5(f), 5(h), and 5(i)).

3.4. Biological Process and Pathway Enrichment Analysis. We conducted KEGG and GO enrichment analyses of genes coexpressed with GNL2 in LIHC tumor and normal tissues to validate the function of GNL2 in liver carcinoma. Figure 6(a) displayed the results of KEGG pathway enrichment, including cell cycle, mRNA surveillance pathway, proteasome, ribosome, RNA transport, DNA replication, Fanconi anemia pathway, ribosome biogenesis in eukaryotes, spliceosome, and homologous recombination. Figure 6(b) showed the enriched biological processes of the genes coexpressed with GNL2 as the following: rRNA processing (GO:0006364), rRNA metabolic process (GO:0016072), ribosome biogenesis (GO:0042254), mRNA processing (GO:0006397), translation (GO:0006412), RNA splicing via transesterification reactions with bulged adenosine as nucleophile (GO:0000377), mRNA splicing via spliceosome (GO:0000398), gene expression (GO:0010467), cellular macromolecule biosynthetic process (GO:0034645), and ncRNA processing (GO:0034470).

3.5. Cell Functional Results of GNL2 Downregulation in LIHC Cells. We transfected siRNAs into MHCC97-H and SMCC-7721 cells to evaluate the effects of ablated GNL2 on cell

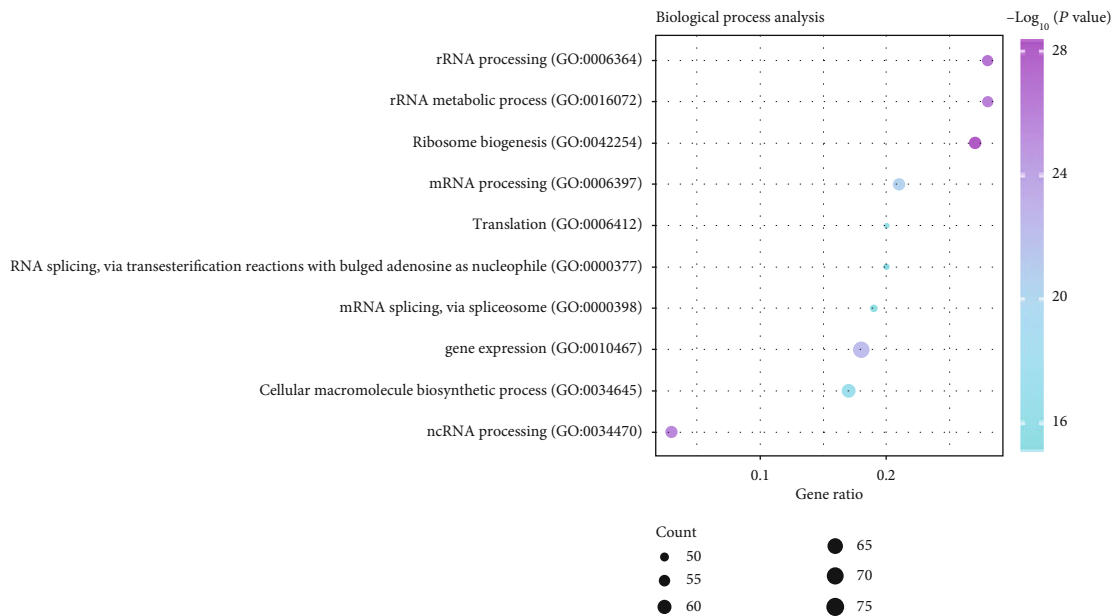
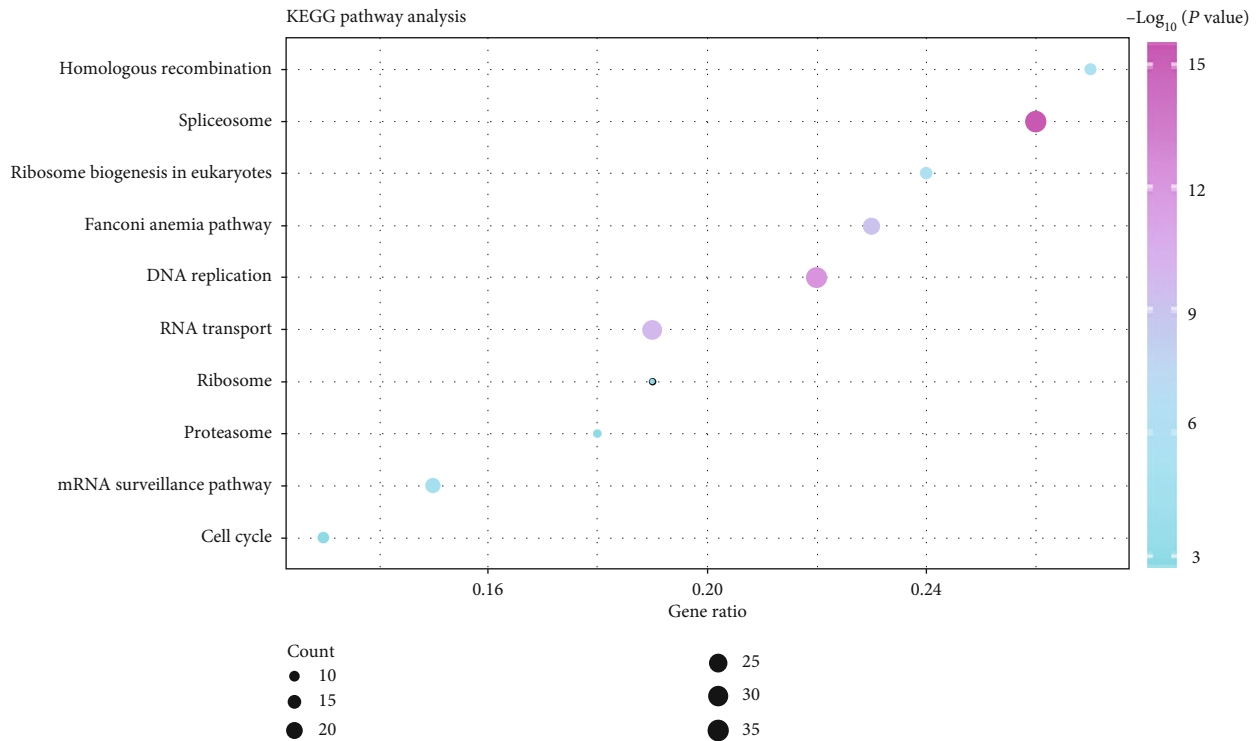


FIGURE 6: KEGG and GO analyses of genes coexpressed with GNL2 in LIHC. (a) Dot bubble chart of enriched GO biological process terms. (b) Dot bubble chart of enriched KEGG pathways.

function (Figures 7(a) and 7(b)). CCK-8 assay data showed that si-GNL2-transfected cell proliferation was significantly hindered in comparison with control si-NC-transfected cells after 24, 48, and 72 h treatment (Figures 7(c) and 7(d)). In addition, Transwell assay data revealed that transfection of si-GNL2 in LIHC cells could suppress invasion and migration abilities (Figures 8(a)–8(d)). Therefore, GNL2 knock-

down largely curbed MHCC97-H and SMCC-7721 cell proliferation, invasion, and migration.

4. Discussion

LIHC is a malignant neoplasm that often occurs in the liver, which is related to drinking, viral hepatitis, eating moldy

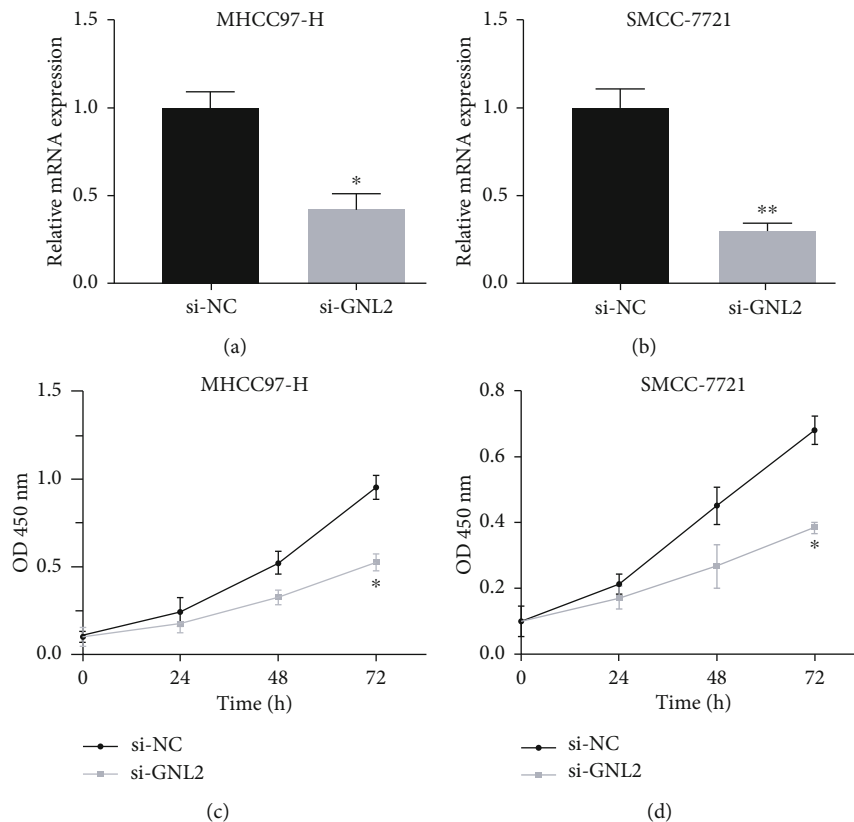


FIGURE 7: Evaluation of cell proliferation in si-GNL2-transfected LIHC cells. GNL2 expression was reduced in (a) MHCC97-H and (b) SMCC-7721 by si-GNL2. * $P < 0.05$; ** $P < 0.01$. Detection of cell proliferation ability in si-GNL2-transfected (c) MHCC97-H and (d) SMCC-7721 cells by CCK-8 assay. * $P < 0.05$.

food, genetics, etc. [19]. Currently, the studies about LIHC are few. As for LIHC treatment, Kim et al. summarized and discussed clinical researches towards systematical chemical therapy for advanced cancer [20]. Zhang and Zhang found FoxP4 functioned as a tumor promoter in LIHC cells by transcriptionally regulating Slug and highlighted the potential effects of FoxP4 on the prognosis and treatment of LIHC [21]. The early stage is often asymptomatic, and obvious symptoms like liver area pain, fever, and fatigue usually appear in the advanced stage [22]. It is possible to cure LIHC in its early stage, but the treatment is complicated in the middle and advanced stages [23, 24]. Therefore, it is necessary to have a better understanding of the molecular mechanism involved in liver carcinoma initiation and to screen novel biomarkers. In this study, we screened 361 DEGs and GNL2 was one of the significantly upregulated genes. Besides, GNL2 was observed to have a high degree in the PPI network. Thus, we considered GNL2 as candidate biomarkers for LIHC.

NS or GNL3 (nucleostemin) and GNL3-like (GNL3L) are two members of the GNL2 family [25]. The two both comprise an MMR_HSR1 domain, depicted by five GTP binding motifs formed as a cyclic order. The two have a common Grnlp homologous sequence in yeast, highly similar to the sequence in vertebrates. GNL3L is the vertebrate aileron of NS, while GNL2 is single both in vertebrates and invertebrates. NS is a protein playing essentially in stem cell growth

and maintenance [15]. However, few pieces of research are conducted to explore the relation between GNL2 and disease. Herein, our study plans to explore the role and function of GNL2 in LIHC.

As far as gene expression information from the TCGA database, GNL2 was highly expressed in LIHC tumor samples compared to that in normal samples, implying GNL2 was a possible oncogene in LIHC. After analysis of the associations between various pathological carcinoma stages of LIHC patients and GNL2 expression, the data revealed that high expression of GNL2 was significantly associated with advanced cancer stages. Kaplan-Meier analysis based on GEPIA and Kaplan-Meier plotter datasets consistently verified that LIHC patients with highly expressed GNL2 exhibited a shorter survival ratio. What was more, *in vitro* knockdown functional experiments demonstrated that reducing GNL2 by siRNA impeded LIHC cell proliferation, migration, and invasion abilities. Based on the above findings, GNL2 was probably considered as a treatment target and a biomarker for LIHC patients' prognosis.

The alteration of ribosome biogenesis often occurs in carcinoma cells due to the rising need for protein synthesis in unrestricted cancer growth [26]. Ribosome biosynthesis is a complicated biological process required for the coordination of multiple factors and a huge cellular energy investment. The ribosome is essential for protein production and therefore is essential for cell survival, growth, and proliferation.

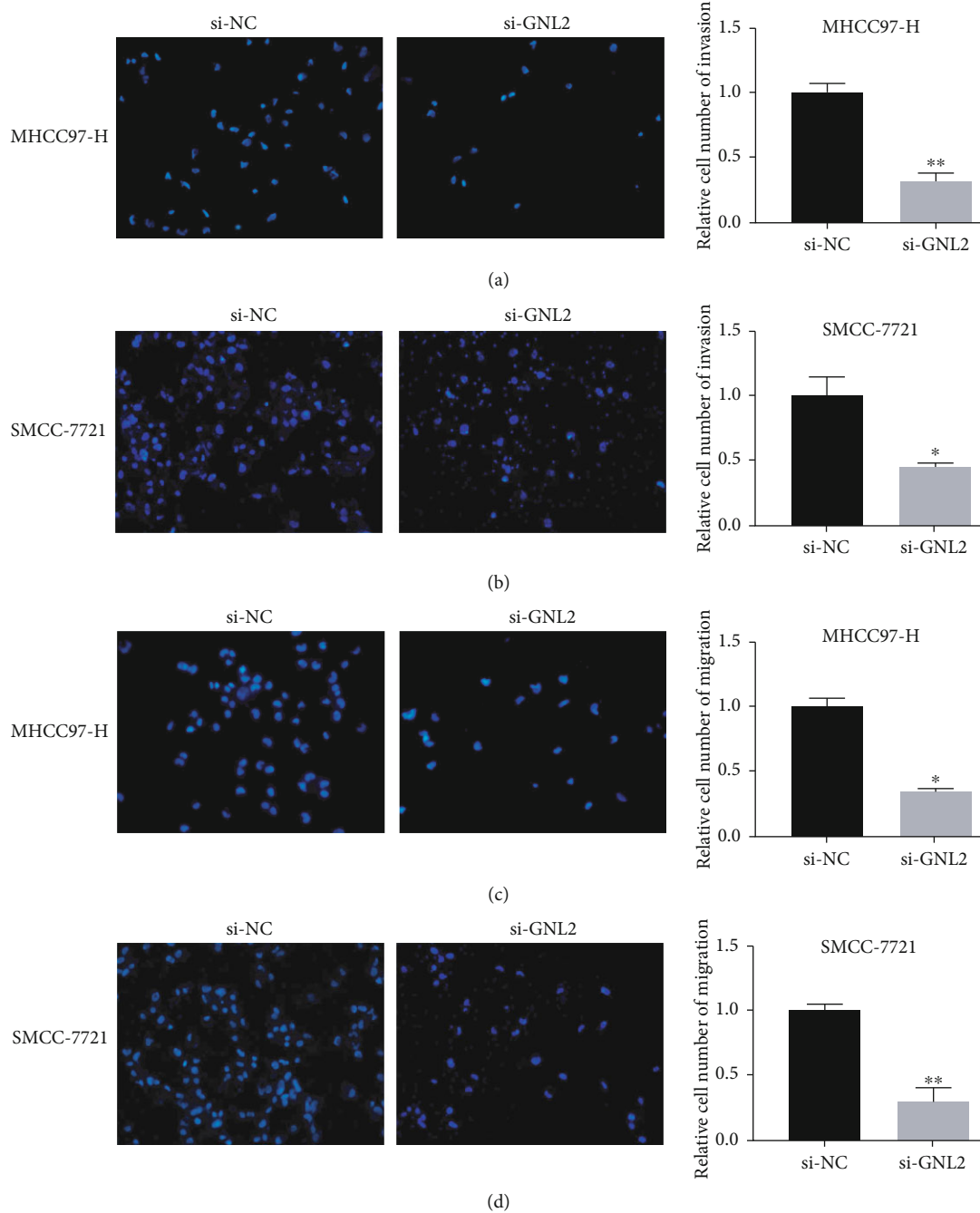


FIGURE 8: Cell functional results of GNL2 downregulation in LIHC cells. Validation of cell invasion capability in si-GNL2-transfected (a) MHCC97-H and (b) SMCC-7721 cells by Transwell assay. * $P < 0.05$; ** $P < 0.01$. Validation of cell migration capability in si-GNL2-transfected (c) MHCC97-H and (d) SMCC-7721 cells by Transwell assay. * $P < 0.05$; ** $P < 0.01$.

Ribosomal biogenesis begins in the nucleolus, including ribosomal RNA synthesis and processing, ribosomal protein assembly, and transport to the cytoplasm [27]. Interference in ribosome biogenesis can promote cell cycle arrest, apoptosis, or senescence and thus is usually associated with carcinoma, aging, and some other related degenerative diseases [28]. The hyperactivation of ribosome biogenesis usually occurs in tumor cells to cope with a rising need in protein synthesis and maintain unrestricted growth [29]. Importantly, the hyperactivation of ribosome biogenesis can be ini-

tiated by overexpressing oncogenes or eliminating neoplasm suppressing genes. In our study, we found that GNL2 was largely associated with altered ribosome biogenesis in cancer cells through KEGG and GO enrichment analyses, thereby playing a vital role in carcinoma initiation and progression.

This study has some limitations. First, we did not construct an overexpression vector of GNL2, and we further explored the regulation of GNL2 overexpression on the proliferation, invasion, and migration of LIHC cells. Secondly, we have not used clinical samples to analyze GNL2 mRNA

and protein levels. In future studies, we will collect more clinical samples for analysis of GNL2 mRNA and protein levels.

5. Conclusion

To our knowledge, this study reported the function of GNL2 in LIHC for the first time, and the results showed that GNL2 was a new biomarker for predicting the prognosis of LIHC patients. Bioinformatics analysis showed that GNL2 was greatly raised in LIHC, and its overexpression was closely related to cancer stage and poor prognosis. Enrichment analysis suggested that GNL2 was largely related to ribosome biosynthesis which was essential for cancer unrestricted growth. Ablating GNL2 resulted in the reduction of cell proliferation, migration, and invasion abilities. These findings demonstrated that GNL2 could be a promising treatment target for LIHC.

Data Availability

The datasets used and/or analyzed during the current study are available from the corresponding author on reasonable request.

Conflicts of Interest

The authors have declared that no conflict of interest exists.

Authors' Contributions

Study concept and design was done by Yiwei Dong, Qianqian Cai, and Xingzhong Wu. Drafting of the manuscript was done by Yiwei Dong, Qianqian Cai, and Lisheng Fu. Acquisition of data, analysis, and interpretation of data were done by Yiwei Dong, Haojie Liu, and Mingzhe Ma. Statistical analysis was done by Yiwei Dong and Qianqian Cai. Critical revision of the manuscript was done by Yiwei Dong and Xingzhong Wu. All authors read and approved the final manuscript. Yiwei Dong and Qianqian Cai contributed equally to this work.

Acknowledgments

This study was supported by the grants from the National Natural Science Foundation of China (82003101, 31570800, and 81571359).

References

- [1] K. Memon, R. J. Lewandowski, L. Kulik, A. Riaz, M. F. Mulcahy, and R. Salem, "Radioembolization for primary and metastatic liver cancer," *Seminars in Radiation Oncology*, vol. 21, no. 4, pp. 294–302, 2011.
- [2] E. Hoti and R. Adam, "Liver transplantation for primary and metastatic liver cancers," *Transplant International*, vol. 21, no. 12, pp. 1107–1117, 2008.
- [3] M. K. Yung, C. W. Yip, G. T. Y. Chung et al., "Copy number gain of granulins-epithelin precursor (GEP) at chromosome 17q21 associates with overexpression in human liver cancer," *BMC Cancer*, vol. 15, no. 1, 2015.
- [4] S. Parpart, S. Roessler, F. Dong et al., "Modulation of miR-29 expression by alpha-fetoprotein is linked to the hepatocellular carcinoma epigenome," *Hepatology*, vol. 60, no. 3, pp. 872–883, 2014.
- [5] V. Mazzaferro, Y. S. Chun, R. T. P. Poon et al., "Liver transplantation for hepatocellular carcinoma," *Annals of Surgical Oncology*, vol. 15, no. 4, pp. 1001–1007, 2008.
- [6] Y. Tang, Y. Zhang, and X. Hu, "Identification of potential hub genes related to diagnosis and prognosis of hepatitis B virus-related hepatocellular carcinoma via integrated bioinformatics analysis," *BioMed Research International*, vol. 2020, Article ID 4251761, 19 pages, 2020.
- [7] E. C. Lo, A. N. Rucker, and M. P. Federle, "Hepatocellular carcinoma and intrahepatic cholangiocarcinoma: imaging for diagnosis, tumor response to treatment and liver response to radiation," *Seminars in Radiation Oncology*, vol. 28, no. 4, pp. 267–276, 2018.
- [8] J. Y. Zhang, W. Zhu, H. Imai, K. Kiyosawa, E. K. L. Chan, and E. M. Tan, "De-novo humoral immune responses to cancer-associated autoantigens during transition from chronic liver disease to hepatocellular carcinoma," *Clinical and Experimental Immunology*, vol. 125, no. 1, pp. 3–9, 2001.
- [9] A. Nicoletti, F. R. Ponziani, M. Biolato et al., "Intestinal permeability in the pathogenesis of liver damage: from non-alcoholic fatty liver disease to liver transplantation," *World Journal of Gastroenterology*, vol. 25, no. 33, pp. 4814–4834, 2019.
- [10] M. R. Alison, L. J. Nicholson, and W. R. Lin, "Chronic inflammation and hepatocellular carcinoma," *Recent Results in Cancer Research*, vol. 185, pp. 135–148, 2011.
- [11] R. Dayoub, H. Wagner, F. Bataille et al., "Liver regeneration associated protein (ALR) exhibits antimetastatic potential in hepatocellular carcinoma," *Molecular Medicine*, vol. 17, no. 3-4, pp. 221–228, 2011.
- [12] T. Tu, M. Budzinska, A. Maczurek et al., "Novel aspects of the liver microenvironment in hepatocellular carcinoma pathogenesis and development," *International Journal of Molecular Sciences*, vol. 15, no. 6, pp. 9422–9458, 2014.
- [13] G. L. Wong, H. L. Y. Chan, Y. K. Tse et al., "On-treatment alpha-fetoprotein is a specific tumor marker for hepatocellular carcinoma in patients with chronic hepatitis B receiving entecavir," *Hepatology*, vol. 59, no. 3, pp. 986–995, 2014.
- [14] V. V. Khien, H. V. Mao, T. T. Chinh et al., "Clinical evaluation of lentil lectin-reactive alpha-fetoprotein-L3 in histology-proven hepatocellular carcinoma," *The International Journal of Biological Markers*, vol. 16, no. 2, pp. 105–111, 2001.
- [15] P. B. Essers, T. C. Pereboom, Y. J. Goos, J. T. Paridaen, and A. W. MacInnes, "A comparative study of nucleostemin family members in zebrafish reveals specific roles in ribosome biogenesis," *Developmental Biology*, vol. 385, no. 2, pp. 304–315, 2014.
- [16] Z. Wang, X. Wang, B. Xie, Z. Hong, and Q. Yang, "Arabidopsis Nucleostemin-like 1 (NSN1) regulates cell cycling potentially by cooperating with nucleosome assembly protein AtNAP1;1," *BMC Plant Biology*, vol. 18, no. 1, p. 99, 2018.
- [17] M. M. Yaghoobi, S. J. Mowla, and T. Tiraihi, "Nucleostemin, a coordinator of self-renewal, is expressed in rat marrow stromal cells and turns off after induction of neural differentiation," *Neuroscience Letters*, vol. 390, no. 2, pp. 81–86, 2005.
- [18] C. Han, X. Zhang, W. Xu, W. Wang, H. Qian, and Y. Chen, "Cloning of the nucleostemin gene and its function in transforming human embryonic bone marrow mesenchymal stem

- cells into F6 tumor cells,” *International Journal of Molecular Medicine*, vol. 16, no. 2, pp. 205–213, 2005.
- [19] G. Li, G. Cai, D. Li, and W. Yin, “MicroRNAs and liver disease: viral hepatitis, liver fibrosis and hepatocellular carcinoma,” *Postgraduate Medical Journal*, vol. 90, no. 1060, pp. 106–112, 2014.
- [20] D. W. Kim, C. Talati, and R. Kim, “Hepatocellular carcinoma (HCC): beyond sorafenib-chemotherapy,” *Journal of Gastrointestinal Oncology*, vol. 8, no. 2, pp. 256–265, 2017.
- [21] G. Zhang and G. Zhang, “Upregulation of FoxP4 in HCC promotes migration and invasion through regulation of EMT,” *Oncology Letters*, vol. 17, no. 4, pp. 3944–3951, 2019.
- [22] R. Sacco, L. Giorgi, L. Fornaro, and I. Bargellini, “Trans-arterial radioembolization for hepatocellular carcinoma,” *Digestive Diseases*, vol. 33, no. 5, pp. 661–667, 2015.
- [23] A. S. Befeler and A. M. Di Bisceglie, “Hepatocellular carcinoma: diagnosis and treatment,” *Gastroenterology*, vol. 122, no. 6, pp. 1609–1619, 2002.
- [24] Z. Morise, N. Kawabe, H. Tomishige et al., “Recent advances in the surgical treatment of hepatocellular carcinoma,” *World Journal of Gastroenterology*, vol. 20, no. 39, pp. 14381–14392, 2014.
- [25] J. T. Paridaen, E. Janson, K. H. Utami et al., “The nucleolar GTP-binding proteins Gnl2 and nucleostemin are required for retinal neurogenesis in developing zebrafish,” *Developmental Biology*, vol. 355, no. 2, pp. 286–301, 2011.
- [26] F. Catez, N. Dalla Venezia, V. Marcel, C. Zorbas, D. L. J. Lafontaine, and J. J. Diaz, “Ribosome biogenesis: an emerging drug-gable pathway for cancer therapeutics,” *Biochemical Pharmacology*, vol. 159, pp. 74–81, 2019.
- [27] J. L. Woolford Jr. and S. J. Baserga, “Ribosome biogenesis in the yeast *Saccharomyces cerevisiae*,” *Genetics*, vol. 195, no. 3, pp. 643–681, 2013.
- [28] Z. Turi, M. Lacey, M. Mistrik, and P. Moudry, “Impaired ribosome biogenesis: mechanisms and relevance to cancer and aging,” *Aging*, vol. 11, no. 8, pp. 2512–2540, 2019.
- [29] S. Bursac, M. C. Brdovcak, G. Donati, and S. Volarevic, “Activation of the tumor suppressor p53 upon impairment of ribosome biogenesis,” *Biochimica et Biophysica Acta*, vol. 1842, no. 6, pp. 817–830, 2014.

Retraction

Retracted: The Early Diagnostic Efficacy of Serum Histone H3 in Rabbit Urosepsis Model

BioMed Research International

Received 12 March 2024; Accepted 12 March 2024; Published 20 March 2024

Copyright © 2024 BioMed Research International. This is an open access article distributed under the Creative Commons Attribution License, which permits unrestricted use, distribution, and reproduction in any medium, provided the original work is properly cited.

This article has been retracted by Hindawi following an investigation undertaken by the publisher [1]. This investigation has uncovered evidence of one or more of the following indicators of systematic manipulation of the publication process:

- (1) Discrepancies in scope
- (2) Discrepancies in the description of the research reported
- (3) Discrepancies between the availability of data and the research described
- (4) Inappropriate citations
- (5) Incoherent, meaningless and/or irrelevant content included in the article
- (6) Manipulated or compromised peer review

The presence of these indicators undermines our confidence in the integrity of the article's content and we cannot, therefore, vouch for its reliability. Please note that this notice is intended solely to alert readers that the content of this article is unreliable. We have not investigated whether authors were aware of or involved in the systematic manipulation of the publication process.

Wiley and Hindawi regrets that the usual quality checks did not identify these issues before publication and have since put additional measures in place to safeguard research integrity.

We wish to credit our own Research Integrity and Research Publishing teams and anonymous and named external researchers and research integrity experts for contributing to this investigation.

The corresponding author, as the representative of all authors, has been given the opportunity to register their agreement or disagreement to this retraction. We have kept a record of any response received.

References

- [1] X. Zhang, X. Zhan, B. Huang, S. Li, and Y. Xu, "The Early Diagnostic Efficacy of Serum Histone H3 in Rabbit Urosepsis Model," *BioMed Research International*, vol. 2021, Article ID 9969344, 17 pages, 2021.

Research Article

The Early Diagnostic Efficacy of Serum Histone H3 in Rabbit Urosepsis Model

Xiaolu Zhang,¹ Xiangcheng Zhan,¹ Bisheng Huang,² Saiyang Li,³ and Yunfei Xu¹ 

¹Department of Urology, Shanghai Tenth People's Hospital, Tongji University School of Medicine, Shanghai 200072, China

²Department of Urology, Changhai Hospital Affiliated to the Second Military Medical University/Naval Medical University, Shanghai 200433, China

³Department of Urology, The Third Affiliated Hospital of Soochow University, Jiangsu 213003, China

Correspondence should be addressed to Yunfei Xu; xujiaoyao17570612@163.com

Received 28 March 2021; Revised 9 June 2021; Accepted 5 July 2021; Published 17 July 2021

Academic Editor: Tao Huang

Copyright © 2021 Xiaolu Zhang et al. This is an open access article distributed under the Creative Commons Attribution License, which permits unrestricted use, distribution, and reproduction in any medium, provided the original work is properly cited.

Objective. We want to explore the changing law of circulating histones in the acute stage of urosepsis and to find more sensitive and specific biomarkers for diagnosing urosepsis as early as possible. **Methods.** Twenty healthy male New Zealand rabbits were randomly divided into 4 groups ($N = 5$): the control group, sham group, model group of LPS 600 $\mu\text{g}/\text{kg}$, and model group of LPS 1000 $\mu\text{g}/\text{kg}$. Heart rate (HR), respiration rate (RR), rectal temperature (T), and mean arterial pressure (MAP) were examined at 1, 3, 6, 12, and 24 hours after operation. Besides, peripheral blood cell counts (RBC, WBC, PLT, and Hb) and C reaction protein (CRP) were tested at 1, 3, and 6 hours after operation, while the levels of histone H3, MMP-9, TIMP-1, and procalcitonin (PCT) in the serum were tested at 1, 3, and 6 hours after operation by ELISA. The heart, left lung, liver, and left kidney were harvested for HE stain and observed to research the pathological change of these tissues. **Results.** (1) The general status of rabbits: rabbits in the control and sham groups came out in 2h after operation and regain to drink and eat in 12-24h after operation. State of the rabbits in the control group was better than that in the sham group. Rabbits in the model groups were languid after operation and stopped to drink and eat. (2) Vital signs of rabbits: there was no statistic difference in HR ($P = 0.238$) and RR ($P = 0.813$) among all groups. MAP of the model groups decreased at 3h postoperative, but transient ($P < 0.001$). The T of the LPS 1000 group decreased at 6h postoperative ($P = 0.003$). (3) The change of biomarkers: H3 level of the LPS groups in the serum increased at 1h postoperative ($P < 0.01$); MMP-9 of the LPS 1000 group increased at 1h postoperative ($P < 0.01$); WBC of the model groups decreased at 3h postoperative ($P < 0.05$); PLT of the LPS 1000 group is significantly increased at 1h postoperative ($P < 0.05$); no statistic difference was found in CRP, PCT, and TIMP-1 among all groups. (4) Pathological sections: no abnormal performance was found in the control and sham groups. Glomerulus of the model groups was out of shape and necrosis with obvious renal tubule expansion. Pulmonary pathology showed alveolar septum diffuse increased and inflammatory infiltrate. Change of the LPS 1000 group was more serious than that of the LPS 600 group. **Conclusions.** Ligating the ureter after an injection of 1000 $\mu\text{g}/\text{kg}$ LPS into the ureter of the rabbit can establish the animal model of urosepsis. Histone H3 increase immediately at 1h postoperative and are promised to be biomarkers of urosepsis, which are more effective than WBC, CRP, and PCT.

1. Introduction

Urinary stone disease (USD) is a common disease of urology with 1-5% morbidity while still on the rise in recent years. With the development of endoscopic urology, the main treatment of USD has changed from open operation to intracavitary lithotripsy [1]. At the same time, the incidence of

postoperative complications has increased, including urosepsis. Urosepsis refers to sepsis caused by urinary tract or male reproductive organ infection, which accounts for about 5% of all sepsis. Previous reports indicated low incidence of urosepsis while the incidence of systemic inflammatory response syndrome (SIRS) and severe septic shock can be as high as 11.2-22% and 0.3-4.7% after intracavitary lithotripsy [2-6].

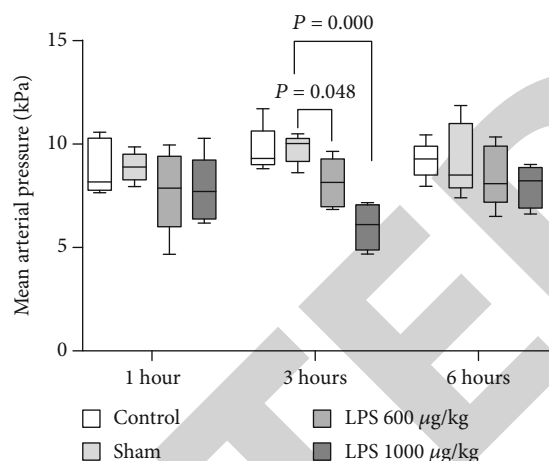
Moreover, asymptomatic urinary tract infections can be rapidly progressing to urosepsis in a short period of time; the mortality of the patients reaches 20-63%, which is a serious threat to the life and health of the patients. Although strengthening aseptic operation standard, shortening operation time, and placing ureteral stent can reduce the occurrence of postoperative infection, some high-risk factors such as complex stone, solitary kidney, and immune dysfunction cannot be avoided; urosepsis is still a difficult clinical problem to be solved.

Kumar et al. have shown that when sepsis occurs, the survival rate of the patients decreased by 8% per hour without sensitive antibiotics, and it is recommended to complete the bacterial culture and use of antibiotics within 1 h of onset [7]. According to the current diagnostic criteria, both infection evidence and signs of organ failure are needed, missing the window of early treatment [8–11]. Therefore, finding sensitive biomarkers in the early stage of sepsis is an effective way to improve the survival rate of the patient.

Histones are basic structural components of chromatin. The circulating histone in human body mainly comes from the passive release of dead or apoptotic cells and the active secretion of activated inflammatory cells [12]. Normally, histones released by chromatin collapse of dead cells are quickly cleared by monocytes, but in pathology cases, chromatin in the blood exceeds the metabolic capacity of the body; circulating histone level increases significantly [13–16]. Meanwhile, at the time of pathogen invasion, histone is secreted actively by activated inflammatory cells as neutrophil extracellular traps (NETs) and participates in the inflammatory response [17–19]. Among the five subtypes of histone, H3 and H4 are proved to be associated with this process [13].

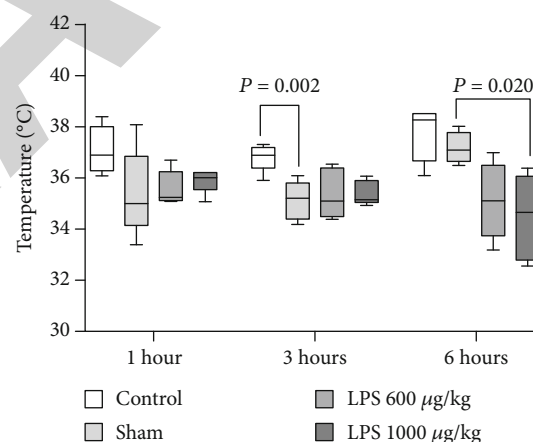
H3 combines Toll-like receptor-2 (TLR2) and Toll-like receptor-4 (TLR4), taking part in various physiological and pathological processes [20]. In the previous study, Xu et al. demonstrated that H3 can directly damage endothelial cells and activate inflammatory signal pathway, promoting the release of cytokines such as tumor necrosis factor (TNF), leukocyte mediator (IL), and tissue factor (TF). In patients with sepsis, the median level of circulating H3 in the death group is significantly higher than that in the survival group; detecting nucleosome levels in the peripheral circulation helps evaluate the patients' prognosis [13]. In mouse sepsis model established by cecum puncture and ligation, histone antagonist reduces the damage of cardiac function [21]. Other researches also show that neutralizing H3 can improve the survival rate of sepsis mice [22], which prove that H3 plays an important role in the development of sepsis.

Sepsis model is commonly established by cecum puncture and ligation, or intra-abdominal injection of lipopolysaccharide (LPS) solution. However, the method of constructing uremic sepsis model is not clear [23]. In this study, we established the rabbit urosepsis model by ligating the ureter after injecting different concentrations of LPS solution into the ureter. Serum H3 level is detected compared with traditional diagnostic indexes of urosepsis such as PCT, CRP, and blood routine examination, so as to explore the sensitive and effective biomarkers for the early diagnosis of urosepsis.



Notes: MAP of LPS600 group was significantly lower than sham group ($P = 0.048$); MAP of LPS1000 group was significantly lower than sham group ($P < 0.001$).

FIGURE 1: Changes of MAP postoperation. MAP of the LPS 600 group was significantly lower than the sham group ($P = 0.048$). MAP of the LPS 1000 group was significantly lower than the sham group ($P < 0.001$).



Notes: Rectal temperature of sham group significantly decreased compared with control group ($P = 0.002$); temperature of LPS1000 group significantly decreased at 6 h post operation compared with sham group ($P = 0.006$).

FIGURE 2: Changes of rectal temperature postoperation. Rectal temperature of the sham group significantly decreased compared with the control group ($P = 0.002$); temperature of the LPS 1000 group significantly decreased at 6 h postoperation compared with the sham group ($P = 0.006$).

2. Material and Methods

2.1. Material and Supplies. 20 healthy male New Zealand rabbits provided from central laboratory of Shanghai Tenth People's Hospital were used. 4% paraformaldehyde solution was provided by central laboratory of Shanghai Tenth People's Hospital. Lipopolysaccharide (LPS, Sigma L6386-100MG),

TABLE 1: Comparison of vital signs among groups immediately after operation ($\bar{x} \pm s$).

Parameters	Groups				F	P	Multiple comparison	
	Control (n = 5)	Sham (n = 5)	LPS 600 (n = 5)	LPS 1000 (n = 5)			LSD test ^a	Dunnnett t-test ^b
Cardiac rate (times/minute)	168.80 ± 71.89	223.60 ± 68.04	213.80 ± 51.89	155.40 ± 26.06	1.691	0.209	—	—
Respiratory rate (times/minute)	26.80 ± 10.18	28.00 ± 10.00	27.20 ± 10.52	37.40 ± 17.33	0.832	0.495	—	—
Rectal temperature (°C)	37.56 ± 0.86	35.18 ± 1.14	35.98 ± 0.93	36.06 ± 0.70	5.808	0.007 ^c	0.001 0.189 0.150	-0.333 0.274
MAP (kPa)	7.91 ± 1.03	7.93 ± 1.29	7.96 ± 1.69	7.75 ± 0.78	0.029	0.993	—	—

^aLSD test was between the control group vs. sham group, sham group vs. LPS 600 group, and sham group vs. LPS 1000 group, respectively, and same as what follows. ^bDunnnett t-test was between the LPS 600 group vs. sham group and LPS 1000 group vs. sham group, and same as what follows. ^cFor rectal temperature, significant difference exists among groups ($P < 0.01$), which just comes from difference between the control group and sham group ($P < 0.005$).

TABLE 2: Comparison of vital signs among groups 1 h postoperation ($\bar{x} \pm s$).

Parameters	Groups				F	P	Multiple comparison	
	Control (n = 5)	Sham (n = 5)	LPS 600 (n = 5)	LPS 1000 (n = 5)			LSD test	Dunnnett t-test
Cardiac rate (times/minute)	160.60 ± 52.86	224.80 ± 50.66	185.00 ± 55.11	175.00 ± 36.28	1.559	0.238	—	—
Respiratory rate (times/minute)	28.20 ± 5.81	36.60 ± 15.96	37.60 ± 28.43	39.00 ± 19.96	0.317	0.813	—	—
Rectal temperature (°C)	37.10 ± 0.91	35.40 ± 1.71	35.58 ± 0.69	35.90 ± 0.46	2.627	0.086	—	—
MAP (kPa)	8.86 ± 1.32	8.89 ± 0.70	7.74 ± 1.98	7.78 ± 1.60	0.949	0.440	—	—

No significant difference was found in parameters above.

TABLE 3: Comparison of vital signs among groups 3 h postoperation ($\bar{x} \pm s$).

Parameters	Groups				F	P	Multiple comparison	
	Control (n = 5)	Sham (n = 5)	LPS 600 (n = 5)	LPS 1000 (n = 5)			LSD test	Dunnnett t-test
Cardiac rate (times/minute)	186.40 ± 92.09	223.30 ± 58.65	227.40 ± 45.48	163.00 ± 24.67	1.321	0.304	—	—
Respiratory rate (times/minute)	40.00 ± 9.49	46.60 ± 12.24	44.60 ± 31.99	55.25 ± 20.61	0.421	0.421	—	—
Rectal temperature (°C)	36.82 ± 0.54	35.12 ± 0.75	35.38 ± 0.97	35.35 ± 0.51	5.655	0.009 ^a	0.002 0.580 0.644	-0.826 0.874
MAP (kPa)	9.71 ± 1.13	9.77 ± 0.71	8.12 ± 1.18	6.01 ± 1.13	12.405	<0.001 ^b	0.932 0.025 <0.001	0.048 <0.001

^aSignificant difference of rectal temperature exists among groups ($P < 0.01$), which just comes from difference between the control group and sham group ($P = 0.002 < 0.005$). ^bSignificant difference of MAP exists among groups ($P \leq 0.001$), which comes from difference between the LPS 600 group and sham group ($P = 0.05$) and between the LPS 1000 group and sham group ($P < 0.001$).

sodium heparin (Sigma H3149-500KU-9), chloral hydrate, xylazine hydrochloride injection, and the rabbit histone H3, matrix metalloproteinases-9 (MMP-9), procalcitonin (PCT), and tissue inhibitor of metalloproteinase-1 (TIMP-1) enzyme-linked immunosorbent assay (ELISA) kits were purchased commercially.

In animal model, rabbits were 2-3 months old and weighed between 1.61 and 3.30 (2.54 ± 0.45) kg. 20 rabbits were randomly assigned into the control group, sham group,

experimental group of LPS 600 $\mu\text{g}/\text{kg}$ (LPS 600 group), and experimental group of LPS 1000 $\mu\text{g}/\text{kg}$ (LPS 1000 group). Each group had 5 rabbits. All rabbits were anesthetized using xylazine hydrochloride intramuscular injection at 1 mg/kg and 10% chloral hydrate intraperitoneal injection at 3 mL/kg. The distal segment of femoral artery was ligated, and the proximal segment was cannulated for measuring blood pressure and collecting blood. For rabbits of the sham group, the left ureter was identified and abdominal cavity was washed

TABLE 4: Comparison of vital signs among groups 6 h postoperation ($\bar{x} \pm s$).

Parameters	Groups				F	P	Multiple comparison	
	Control (n = 5)	Sham (n = 5)	LPS 600 (n = 5)	LPS 1000 (n = 4)			LSD test	Dunnnett t-test
Cardiac rate (times/minute)	221.40 ± 134.20	225.40 ± 128.19	223.80 ± 74.32	130.0 ± 11.80	0.863	0.482	—	—
Respiratory rate (times/minute)	53.60 ± 24.43	50.80 ± 14.04	45.00 ± 17.07	33.25 ± 15.78	1.039	0.404	—	—
Rectal temperature (°C)	37.74 ± 1.04	37.20 ± 0.60	35.12 ± 1.47	34.50 ± 1.71	7.372	0.003 ^a	0.503 0.018 0.006	-0.052 0.020
MAP (kPa)	9.22 ± 0.89	9.25 ± 1.76	8.44 ± 1.48	8.00 ± 1.05	0.921	0.454	—	—

^aSignificant difference of rectal temperature exists among groups ($P < 0.05$), which just comes from difference between the LPS 1000 group and sham group ($P = 0.002 < 0.005$). ^bSignificant difference of MAP exists among groups ($P \leq 0.05$).

TABLE 5: Comparison of vital signs among groups 12 h postoperation ($\bar{x} \pm s$).

Parameters	Groups				F	P	Multiple comparison	
	Control (n = 5)	Sham (n = 5)	LPS 600 (n = 5)	LPS 1000 (n = 4)			LSD test	Dunnnett t-test
Cardiac rate (times/minute)	238.20 ± 88.65	220.80 ± 75.64	227.40 ± 86.39	143.00 ± 34.86	1.367	0.291	—	—
Respiratory rate (times/minute)	60.20 ± 18.74	54.40 ± 17.18	49.20 ± 19.97	49.00 ± 22.18	0.355	0.786	—	—
Rectal temperature (°C)	39.02 ± 0.62	38.34 ± 0.59	35.34 ± 2.40	34.93 ± 1.77	8.523	0.002 ^a	0.495 0.008 0.005	-0.037 0.026
MAP (kPa)	9.68 ± 1.81	9.08 ± 1.29	7.48 ± 1.68	9.73 ± 1.00	2.334	0.115	—	—

^aSignificant difference of rectal temperature exists among groups ($P < 0.005$), which comes from difference between the LPS 600 group and sham group ($P \leq 0.05$) and between the LPS 1000 group and sham group ($P \leq 0.05$).

TABLE 6: Comparison of vital signs among groups 24 h postoperation ($\bar{x} \pm s$).

Parameters	Groups				F	P	Multiple comparison	
	Control (n = 5)	Sham (n = 5)	LPS 600 (n = 4)	LPS 1000 (n = 4)			LSD test	Dunnnett t-test
Cardiac rate (times/minute)	256.80 ± 86.90	209.60 ± 64.90	176.75 ± 98.21	154.75 ± 50.91	1.491	0.260	—	—
Respiratory rate (times/minute)	58.00 ± 22.51	45.60 ± 11.93	42.00 ± 13.00	55.00 ± 13.71	0.982	0.429	—	—
Rectal temperature (°C)	38.84 ± 0.57	39.02 ± 0.55	35.48 ± 3.56	37.20 ± 2.20	3.046	0.064	—	—
MAP (kPa)	9.71 ± 1.49	8.74 ± 1.05	6.09 ± 3.50	8.57 ± 1.42	2.453	0.110	—	—

No significant difference was found in parameters above.

using 5 mL normal saline. For rabbits of the experimental groups, the distal segment of the left ureter was ligated and the proximal segment was cannulated and injected LPS solution. All the survived animals were sacrificed at 24 h after surgery.

2.2. Sample Collection and Measure. Cardiac rate, respiratory rate, and rectal temperature were measured at immediately, 1 h, 3 h, 6 h, 12 h, and 24 h after surgery. Blood samples were obtained at 1 h, 3 h, and 6 h after surgery. Fresh samples were used for routine blood and CRP test. Others were preserved at 4°C and centrifuged at 3000 rpm for 10 min. Supernatants

were preserved at -80°C and used to test histone H3, MMP-9, TIMP-1, and PCT using enzyme-linked immunosorbent assay kit. Organization of the cardiac, lung, liver, and left kidney was obtained for pathological examination.

2.3. Statistical Analysis. One-way ANOVA test was used for comparison among all the groups. LSD test and Dunnnett t-test were both used and take the major P value to compare the intergroup difference. P value < 0.05 was considered statistically significant. ROC curves were made using data of 1 h, 3 h, and 6 h to evaluate the predicting value of each parameter. IBM SPSS Statistics 25 software was employed for the analysis.

TABLE 7: Comparison of routine blood and CRP among groups 1 h postoperation ($\bar{x} \pm s$).

Parameters	Groups				F	P	Multiple comparison	
	Control (n = 5)	Sham (n = 5)	LPS 600 (n = 5)	LPS 1000 (n = 5)			LSD test	Dunnnett t-test
Erythrocyte count ($10^{12}/L$)	6.39 ± 0.71	6.84 ± 1.17	6.68 ± 0.83	6.66 ± 0.53	0.246	0.863	—	—
Leukocyte count ($10^9/L$)	6.36 ± 1.31	6.60 ± 4.18	5.90 ± 7.24	2.30 ± 1.06	1.117	0.372	—	—
Neutrophil count ($10^9/L$)	2.32 ± 1.19	2.10 ± 1.89	1.61 ± 2.82	0.26 ± 0.13	1.317	0.304	—	—
Hemoglobin (g/L)	129.80 ± 15.07	135.20 ± 14.10	139.40 ± 23.78	123.80 ± 11.08	0.820	0.501	—	—
Platelet count ($10^9/L$)	180.00 ± 70.06	257.20 ± 136.34	456.80 ± 231.59	685.80 ± 150.52	10.340	0.001 ^a	0.451 0.053 0.001	0.153 0.005
CRP (mg/L)	75.49 ± 1.56	75.63 ± 2.52	77.98 ± 4.57	78.20 ± 0.86	1.413	0.276	—	—

^aSignificant difference of platelet count exists among groups ($P < 0.005$), which just comes from difference between the LPS 1000 group and sham group ($P \leq 0.01$).

TABLE 8: Comparison of routine blood and CRP among groups 3 h postoperation ($\bar{x} \pm s$).

Parameters	Groups				F	P	Multiple comparison	
	Control (n = 5)	Sham (n = 5)	LPS 600 (n = 5)	LPS 1000 (n = 5)			LSD test	Dunnnett t-test
Erythrocyte count ($10^{12}/L$)	6.00 ± 0.59	6.78 ± 1.18	7.21 ± 1.07	6.39 ± 0.99	1.383	0.284	—	—
Leukocyte count ($10^9/L$)	10.84 ± 2.71	9.84 ± 3.86	3.86 ± 4.74	1.74 ± 0.40	8.847	0.001 ^a	0.643 0.012 0.002	0.037 0.007
Neutrophil count ($10^9/L$)	4.10 ± 3.54	2.26 ± 2.48	0.90 ± 1.03	0.32 ± 0.04	2.858	0.07	—	—
Hemoglobin (g/L)	121.20 ± 9.93	131.40 ± 16.59	136.20 ± 23.49	117.40 ± 20.96	1.118	0.371	—	—
Platelet count ($10^9/L$)	251.60 ± 74.59	187.80 ± 108.62	402.80 ± 171.26	633.60 ± 206.74	8.779	0.001 ^b	0.510 0.037 <0.001	0.113 0.002
CRP (mg/L)	74.80 ± 1.26	75.49 ± 3.23	77.64 ± 2.96	77.67 ± 1.23	1.958	0.161	—	—

^aSignificant difference of leukocyte count exists among groups ($P = 0.001$), which comes from difference between the LPS 600 group and sham group ($P \leq 0.05$) and between the LPS 1000 group and sham group ($P < 0.01$). ^bSignificant difference of platelet count exists among groups ($P = 0.001$), which just comes from difference between the LPS 1000 group and sham group ($P \leq 0.005$).

TABLE 9: Comparison of routine blood and CRP among groups 6 h postoperation ($\bar{x} \pm s$).

Parameters	Groups				F	P	Multiple comparison	
	Control (n = 5)	Sham (n = 5)	LPS 600 (n = 5)	LPS 1000 (n = 4)			LSD test	Dunnnett t-test
Erythrocyte count ($10^{12}/L$)	5.49 ± 1.78	5.86 ± 0.86	7.11 ± 1.25	5.64 ± 1.37	1.464	0.264	—	—
Leukocyte count ($10^9/L$)	10.26 ± 5.42	11.36 ± 5.24	4.76 ± 4.06	2.83 ± 0.96	4.013	0.028 ^a	0.701 0.033 0.012	0.045 0.017
Neutrophil count ($10^9/L$)	4.76 ± 4.00	4.42 ± 3.58	1.18 ± 0.90	1.08 ± 0.51	18.971	0.11	—	—
Hemoglobin (g/L)	108.80 ± 26.41	110.80 ± 14.96	138.20 ± 25.17	105.75 ± 30.45	1.819	0.187	—	—
Platelet count ($10^9/L$)	206.00 ± 92.80	234.20 ± 128.75	379.40 ± 231.25	594.75 ± 240.02	4.237	0.023 ^b	0.808 0.222 0.009	0.449 0.041
CRP (mg/L)	75.86 ± 1.35	76.75 ± 2.01	77.64 ± 2.63	78.08 ± 0.79	1.108	0.379	—	—

^aSignificant difference of leukocyte count exists among groups ($P = 0.028$), which comes from difference between the LPS 600 group and sham group ($P < 0.05$) and between the LPS 1000 group and sham group ($P < 0.05$). ^bSignificant difference of platelet count exists among groups ($P = 0.023$), which just comes from difference between the LPS 1000 group and sham group ($P < 0.005$).

3. Results

3.1. Postoperation Reactions of Rabbits

3.1.1. Control Group. All 5 rabbits wake up in 2 h after the operation and begin to eat and drink within 12 h. The form of excrement is normal, is sensitive to stimulations, quickly escapes from capture, and no mouth and nasal discharge were found. All rabbits are alive after 24 h.

3.1.2. Sham Operation Group. All 5 rabbits wake up in 2 h and begin to eat within 12 h but the food intake is slightly less than that of the control. The form of excrement is normal, is sensitive to stimulations, capture is evasive, is slightly duller than the control group, and no eyes and nasal discharge were found. All rabbits survived 24 h after the operation.

3.1.3. LPS 600 $\mu\text{g}/\text{kg}$ Group. We find that postoperative rabbits are somnolent, stop eating, slightly escape, and struggle when captured. They all have conjunctival congestion, with a small amount of yellow secretion in the mouth and nose. One rabbit dies 24 h after the operation, and the remaining 4 survived. The survived rabbits gradually return to autonomous gesture, and the conjunctival congestion recedes.

3.1.4. LPS 1000 $\mu\text{g}/\text{kg}$ Group. One rabbit dies 3 h after the operation; others survive but are all in coma for the next 24 h, accompanied with severe conjunctival congestion and more mouth and nasal secretions. Two surviving rabbits are found with thrombosis in arterial catheterization.

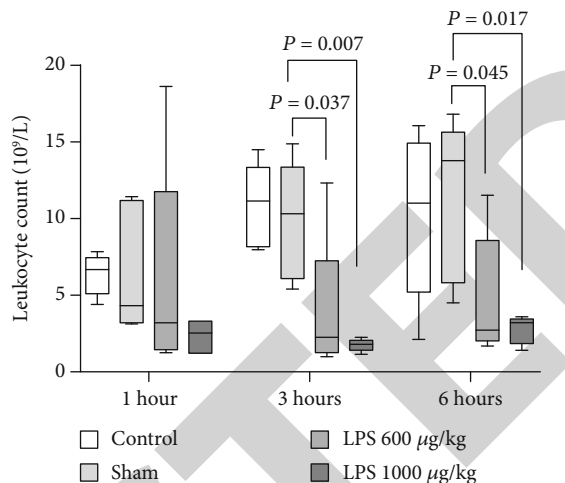
3.2. Changes of Vital Signs of Rabbits

3.2.1. Postoperation. There is no significant difference in heart rate, respiratory rate, and mean arterial pressure (MAP) among the groups (Figure 1). The anal temperature in the control group is 1°C higher than that in the rest groups ($P = 0.007$) (Figure 2). However, there is no difference in the postoperative groups indicating that the rise of the anal temperature is due to the operation (Table 1).

3.2.2. 1 h after Operation. There is no significant difference in heart rate, respiratory rate, anal temperature, and MAP among the groups (Table 2).

3.2.3. 3 h after Operation. There is no significant difference in heart rate and respiratory rate among the groups. The anal temperature in the sham group is lower than that in the control group ($P = 0.002$), but no significant difference was found among the LPS group and sham group. MAP in both the experimental groups was lower than that in the sham group, and no significant difference was found between the sham and control groups (Table 3).

3.2.4. 6 h after Operation. Anal temperature of the LPS 1000 group is lower than that in the sham group. There is no significant difference between the LPS 600 and sham groups because the results of LSD test ($P = 0.018$) and Dunnett *t*-test ($P = 0.052$) disagree. No difference was found in other parameters (Table 4).



Notes: Leukocyte count of LPS600 ($P = 0.037$) and LPS1000 group ($P = 0.007$) were significantly decreased at 3 h post operation compared with the sham group; similar change was observed at 6 h post operation in the 2 group ($P = 0.045$ and $P = 0.017$).

FIGURE 3: Changes of leukocyte count postoperation. Leukocyte counts of the LPS 600 ($P = 0.037$) and the LPS 1000 group ($P = 0.007$) were significantly decreased at 3 h postoperation compared with the sham group; similar change was observed at 6 h postoperation in the 2 groups ($P = 0.045$ and $P = 0.017$).

3.2.5. 12 h after Operation. Anal temperature in two experimental groups was lower than that in the sham group. No difference was found in other parameters (Table 5).

3.2.6. 24 h after Operation. No difference was found in all parameters (Table 6).

3.3. Changes of Blood Routine and CRP. Platelet count 1 h after operation in the LPS 1000 group is $(685.80 \pm 150.52) \times 10^9/\text{L}$, which is higher than $(180.00 \pm 70.06) \times 10^9/\text{L}$ in the sham group. And the increase of platelet continued to 6 h (Tables 7–9). But no similar change was found in the LPS 600 group. Leukocyte count 3 h after operation of the LPS 600 and LPS 1000 group is $(3.86 \pm 4.74) \times 10^9/\text{L}$ and $(1.74 \pm 0.40) \times 10^9/\text{L}$, respectively, and both were significantly lower than that of the sham group (Table 8). Leukocyte count in the LPS 600 group at 6 h increased to $(4.76 \pm 4.06) \times 10^9/\text{L}$, and that in LPS 1000 increased to $(2.83 \pm 0.96) \times 10^9/\text{L}$ (Figure 3). Both were lower than the sham group (Table 9). No significant difference was found in neutrophil count, erythrocyte, hemoglobin, and CRP (Tables 7–9).

3.4. Changes of Serum Histone, PCT, MMP-9, and TIMP-1. Concentration of histone H3 and H4 of the LPS 600 group at 1 h after operation was $5.71 \pm 0.32 \text{ ng/mL}$ and $2.89 \pm 0.30 \text{ ng/mL}$, respectively. Histone H3 and H4 of the LPS 1000 group at 1 h after operation were $6.22 \pm 0.57 \text{ ng/mL}$ and $3.32 \pm 0.26 \text{ ng/mL}$, respectively. All those parameters were significantly increased at 1 h after operation and stay to 6 h

TABLE 10: Comparison of results of ELISA among groups 3 h postoperation ($\bar{x} \pm s$).

Parameters	Groups				F	P	Multiple comparison	
	Control (n = 5)	Sham (n = 5)	LPS 600 (n = 5)	LPS 1000 (n = 5)			LSD test	Dunnnett t-test
PCT (pg/mL)	10.72 ± 2.13	13.98 ± 1.29	11.99 ± 2.68	11.21 ± 1.46	2.653	0.084	—	—
Histone H3 (ng/mL)	4.10 ± 0.49	4.13 ± 0.42	6.04 ± 0.21	6.49 ± 0.38	51.975	<0.001 ^a	0.880 <0.001 <0.001	<0.001 <0.001
Histone H4 (ng/mL)	2.24 ± 0.26	2.49 ± 0.25	3.19 ± 0.24	3.46 ± 0.31	23.052	<0.001 ^b	0.159 0.001 <0.001	0.003 <0.001
MMP-9 (ng/mL)	51.38 ± 3.94	59.11 ± 23.57	47.88 ± 20.41	136.10 ± 41.61	12.925	<0.001 ^c	0.646 0.506 <0.001	0.783 0.003
TIMP-1 (ng/mL)	70.06 ± 12.93	82.10 ± 28.99	67.54 ± 15.39	52.93 ± 8.10	2.190	0.129	—	—

^aSignificant difference of concentration of H3 exists among groups ($P < 0.001$), which comes from difference between the LPS 600 group and sham group ($P < 0.001$) and between the LPS 1000 group and sham group ($P < 0.001$). ^bSignificant difference of concentration of H4 exists among groups ($P < 0.001$), which comes from difference between the LPS 600 group and sham group ($P < 0.005$) and between the LPS 1000 group and sham group ($P < 0.001$). ^cSignificant difference of concentration of MMP-9 exists among groups ($P < 0.001$), which just comes from difference between the LPS 1000 group and sham group ($P < 0.005$).

TABLE 11: Comparison of results of ELISA among groups 6 h postoperation ($\bar{x} \pm s$).

Parameters	Groups				F	P	Multiple comparison	
	Control (n = 5)	Sham (n = 5)	LPS 600 (n = 5)	LPS 1000 (n = 4)			LSD test	Dunnnett t-test
PCT (pg/mL)	14.37 ± 5.55	15.08 ± 5.19	11.94 ± 1.61	10.62 ± 3.39	1.093	0.384	—	—
Histone H3 (ng/mL)	4.57 ± 0.42	4.32 ± 0.39	6.92 ± 0.55	7.45 ± 0.45	57.107	<0.001 ^a	0.384 <0.001 <0.001	0.001 <0.001
Histone H4 (ng/mL)	2.49 ± 0.19	2.59 ± 0.18	3.74 ± 0.30	3.68 ± 0.18	44.475	<0.001 ^b	0.501 <0.001 <0.001	<0.001 <0.001
MMP-9 (ng/mL)	64.10 ± 25.71	48.92 ± 14.78	63.83 ± 25.53	111.55 ± 12.21	7.463	0.003 ^c	0.290 0.271 <0.001	0.387 0.001
TIMP-1 (ng/mL)	87.59 ± 24.59	80.64 ± 26.89	79.11 ± 18.89	49.54 ± 11.52	2.479	0.104	—	—

^aSignificant difference of concentration of H3 exists among groups ($P < 0.001$), which comes from difference between the LPS 600 group and sham group ($P < 0.001$) and between the LPS 1000 group and sham group ($P < 0.001$). ^bSignificant difference of concentration of H4 exists among groups ($P < 0.001$), which comes from difference between the LPS 600 group and sham group ($P < 0.05$) and between the LPS 1000 group and sham group ($P < 0.001$). ^cSignificant difference of concentration of MMP-9 exists among groups ($P < 0.001$), which just comes from difference between the LPS 1000 group and sham group ($P < 0.005$).

TABLE 12: Comparison of results of ELISA among groups 1 h postoperation ($\bar{x} \pm s$).

Parameters	Groups				F	P	Multiple comparison	
	Control (n = 5)	Sham (n = 5)	LPS 600 (n = 5)	LPS 1000 (n = 5)			LSD test	Dunnnett t-test
PCT (pg/mL)	9.46 ± 2.09	15.56 ± 9.81	11.40 ± 1.67	12.59 ± 2.79	1.176	0.350	—	—
Histone H3 (ng/mL)	3.89 ± 0.50	4.18 ± 0.60	5.71 ± 0.32	6.22 ± 0.57	25.031	<0.001 ^a	0.385 <0.001 <0.001	0.001 <0.001
Histone H4 (ng/mL)	2.32 ± 0.18	2.39 ± 0.30	2.89 ± 0.29	3.32 ± 0.26	15.747	<0.001 ^b	0.676 0.008 <0.001	0.030 <0.001
MMP-9 (ng/mL)	57.71 ± 19.22	42.79 ± 9.53	47.00 ± 20.91	120.18 ± 18.46	20.997	<0.001 ^c	0.199 0.710 <0.001	0.896 <0.001
TIMP-1 (ng/mL)	76.14 ± 15.07	80.36 ± 20.65	62.24 ± 26.40	50.91 ± 6.18	2.606	0.088	—	—

^aSignificant difference of concentration of H3 exists among groups ($P < 0.001$), which comes from difference between the LPS 600 group and sham group ($P < 0.005$) and between the LPS 1000 group and sham group ($P < 0.001$). ^bSignificant difference of concentration of H4 exists among groups ($P < 0.001$), which comes from difference between the LPS 600 group and sham group ($P < 0.05$) and between the LPS 1000 group and sham group ($P < 0.001$). ^cSignificant difference of concentration of MMP-9 exists among groups ($P < 0.001$), which just comes from difference between the LPS 1000 group and sham group ($P < 0.001$).

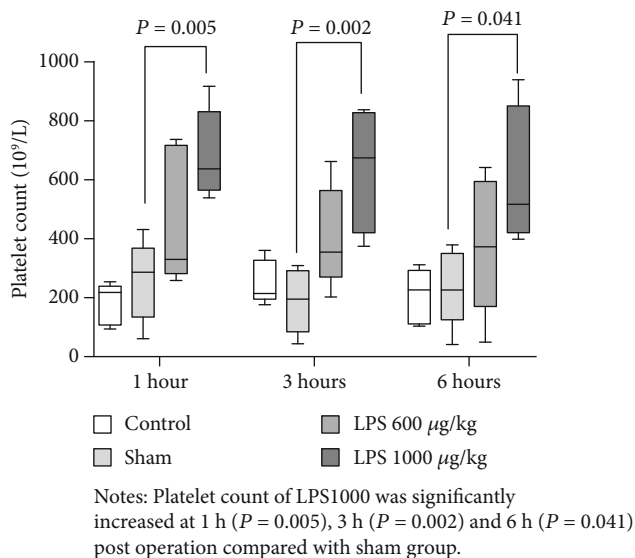


FIGURE 4: Changes of platelet count postoperation. Platelet count of LPS 1000 was significantly increased at 1 h ($P = 0.005$), 3 h ($P = 0.002$), and 6 h ($P = 0.041$) postoperation compared with the sham group.

(Tables 10 and 11). Concentration of MMP-9 of the LPS 1000 group at 1 h after operation was 120.18 ± 18.46 ng/mL, which was significantly higher than the sham group (Table 12). Higher concentration of MMP-9 stayed to 3 h (136.10 ± 41.61 ng/mL) and 6 h (111.55 ± 12.21 ng/mL) after operation (Tables 10 and 11). For concentration of MMP-9, no similar change was found in the LPS 600 group. The change of concentration of PCT and TIMP-1 in the experimental groups had no statistical significance.

3.5. Comparison of Diagnostic Capability of Parameters

3.5.1. Early Diagnostic. Serum histone H3/H4 and blood platelet count are earliest rising indicators among postoperative parameters (Figures 4–6). However, for MMP-9 and platelet count, only in the LPS 1000 group had statistical significance, which may mean these parameters just change in severe sepsis. At 3 h postoperation, MAP and leukocyte count significantly decreased, and concentration of H3, H4, MMP-9, and platelet count significantly increased. Similarly, only MMP-9 and platelet in the LPS 1000 group had statistical significance. MAP at 6 h postoperation increased to normal level; this could mean the change of blood pressure was transient so it could not be used for diagnosis. No significant difference was found in other parameters including heart rate, respiratory rate, CRP, PCT, and TIMP-1, so these parameters have no early diagnosis value.

3.5.2. Sensibility and Specificity. The order of area under the curve (AUC) at 1 h postoperation was H3 (1.000) > H4 (0.970) > platelet count (0.950) > MMP-9 (0.680). All these parameters had a diagnosis value except MMP-9 ($P = 0.174 > 0.05$), and the diagnosis value of H3 and H4 was better than others. The sensibility and specificity of H3

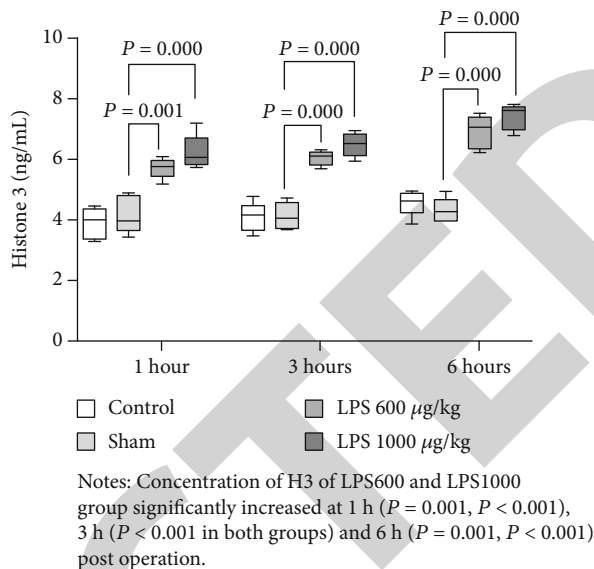


FIGURE 5: Changes of concentration of H3 postoperation. Concentration of H3 of the LPS 600 and the LPS 1000 groups significantly increased at 1 h ($P = 0.001$, $P < 0.001$), 3 h ($P < 0.001$ in both groups), and 6 h ($P = 0.001$, $P < 0.001$) postoperation.

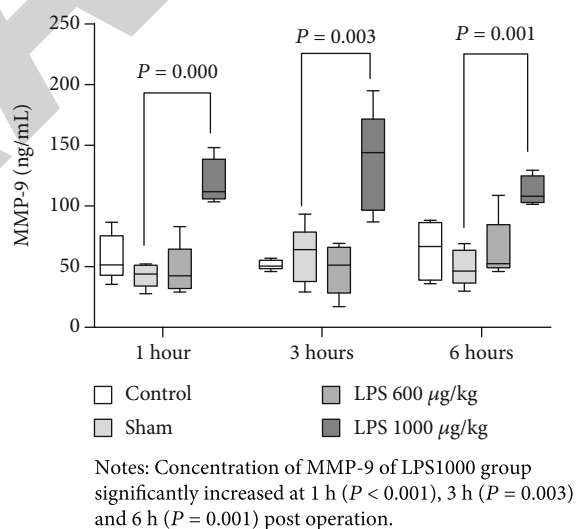


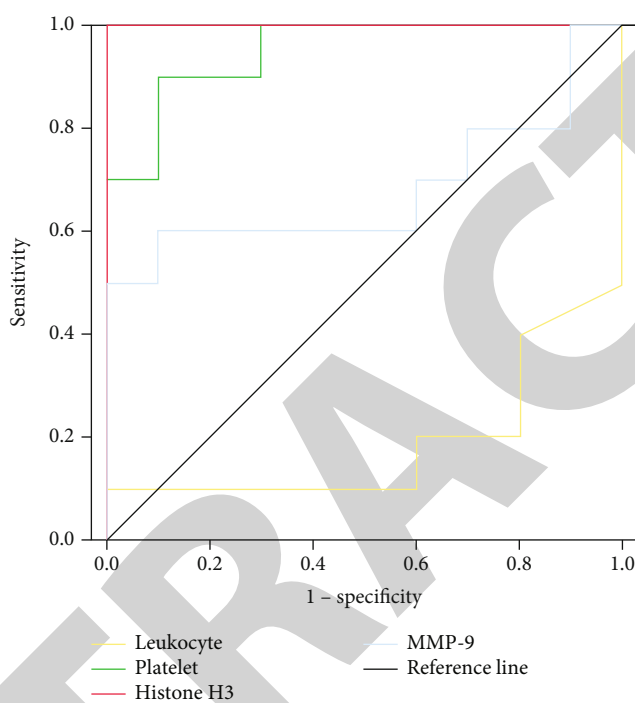
FIGURE 6: Changes of MMP-9 postoperation. Concentration of MMP-9 of the LPS 1000 group significantly increased at 1 h ($P < 0.001$), 3 h ($P = 0.003$), and 6 h ($P = 0.001$) postoperation.

were both 100% when the cut-off is 5.04 ng/mL. The sensibility and specificity of H4 were 100% and 90%, respectively, when the cut-off is 2.62 ng/mL (Table 13, Figure 7).

The order of AUC at 3 h postoperation was H3 (1.000) = H4 (1.000) > platelet count (0.920) = leukocyte count (0.920) > MMP-9 (0.710). MAP of experimental decreased transiently at 3 h postoperation so it has no diagnosis value. The sensibility and specificity of H3 and H4 were both 100% when the cut-off was 5.27 ng/mL and 2.87 ng/mL, respectively (Table 14, Figure 8).

TABLE 13: Comparison of diagnostic capability of parameters at 1 h postoperation.

Parameter	Cut-off	AUC	Standard error	95% CI	P^a	Sensibility (%)	Specificity (%)
Leukocyte count ($10^9/L$)	3.8	0.810	0.106	0.602-1.000	0.019	80.0	80.0
Platelet count ($10^9/L$)	305.5	0.950	0.045	0.862-1.000	0.001	90.0	90.0
H3 (ng/mL)	5.04	1.000	<0.001	1.000-1.000	<0.001	100.0 ^b	100.0 ^b
MMP-9 (ng/mL)	73.89	0.680	0.131	0.424-0.936	0.174	60.0	90.0



Notes: All parameters above but MMP-9 ($P = 0.174$) had diagnosis value ($P < 0.05$). AUC of H3, Leucocyte and platelet was 1.000, 0.810 and 0.950 respectively.

FIGURE 7: Postoperative 1 h ROC curve of indexes. All parameters above but MMP-9 ($P = 0.174$) had a diagnosis value ($P < 0.05$). AUC of H3, leukocyte, and platelet was 1.000, 0.810, and 0.950, respectively.

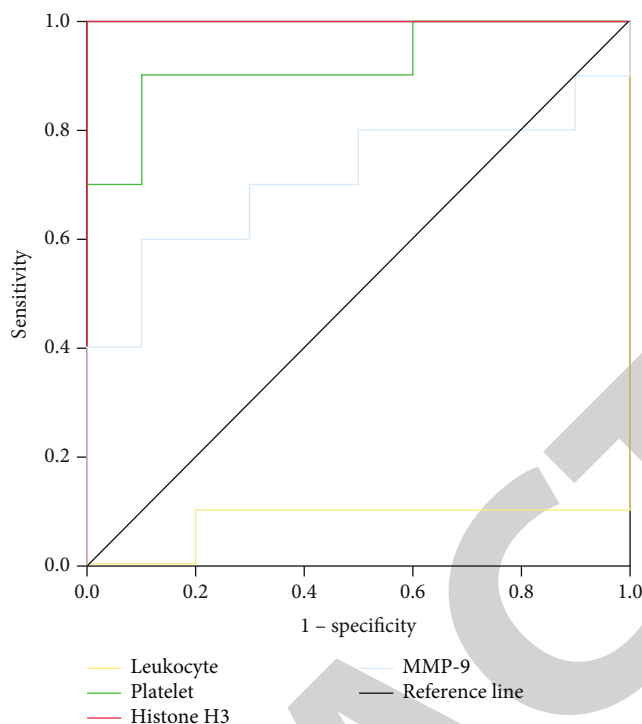
TABLE 14: Comparison of diagnostic capability of parameters at 3 h postoperation.

Parameter	Cut-off	AUC	Standard error	95% CI	P^a	Sensibility (%)	Specificity (%)
Leukocyte count ($10^9/L$)	3.8	0.920	0.078	0.767-1.000	0.001	90.0	100.0
Platelet count ($10^9/L$)	305.5	0.920	0.065	0.792-1.000	0.001	90.0	90.0
H3 (ng/mL)	5.04	1.000	<0.001	1.000-1.000	<0.001	100.0 ^b	100.0 ^b
MMP-9 (ng/mL)	73.89	0.710	0.125	0.464-0.956	0.112	60.0	90.0

The order of AUC at 6 h postoperation was H3 (1.000) = H4 (1.000) > leukocyte count (0.867) > platelet count (0.856) > MMP - 9 (0.822). All these parameters are diagnostic efficient and histone H3 and H4 have more advantages in specificity and sensitivity (Table 15, Figure 9).

3.6. Pathology at 24 h Postoperation. In the control group, no necrosis, hemorrhage, or inflammatory infiltration was

observed in myocardial cells (Figure 10). Structure of alveoli was clear (Figure 11). Several minor bleeders were observed in pulmonary tissue. Structure of liver lobule and glomerulus was clear (Figure 12). What we observed in the sham group was similar to the control group. In the experimental groups, we observed karyopyknosis and breakage of the cardiomyocyte nucleus. We found necrosis of myocardial cells and inflammatory infiltration and hemorrhage in necrosis



Notes: All parameters above but MMP-9 ($P = 0.112$) had diagnosis value ($P < 0.05$). AUC of H3, platelet and leucocyte was 1.000, 0.920 and 0.911 respectively.

FIGURE 8: Postoperative 3 h ROC curve of indexes. All parameters above but MMP-9 ($P = 0.112$) had a diagnosis value ($P < 0.05$). AUC of H3, platelet, and leucocyte was 1.000, 0.920, and 0.911, respectively.

TABLE 15: Comparison of diagnostic capability of parameters at 6 h postoperation.

Parameter	Cut-off	AUC	Standard error	95% CI	P^a	Sensibility (%)	Specificity (%)
Leukocyte count ($10^9/L$)	6.4	0.867	0.089	0.693-1.000	0.007	88.9	80.0
Platelet count ($10^9/L$)	345.5	0.856	0.100	0.659-1.000	0.009	90.0	90.0
H3 (ng/mL)	5.6	1.000	<0.001	1.000-1.000	<0.001	100.0 ^b	100.0 ^b
MMP-9 (ng/mL)	94.35	0.822	0.097	0.633-1.000	0.018	55.6	100.0

^a $P < 0.05$ means the parameter had a diagnosis value. ^bFor data of histone H3 and H4, the minimum in the experimental group was greater than maximum in the sham and control groups, so the sensibility and specificity were 100%.

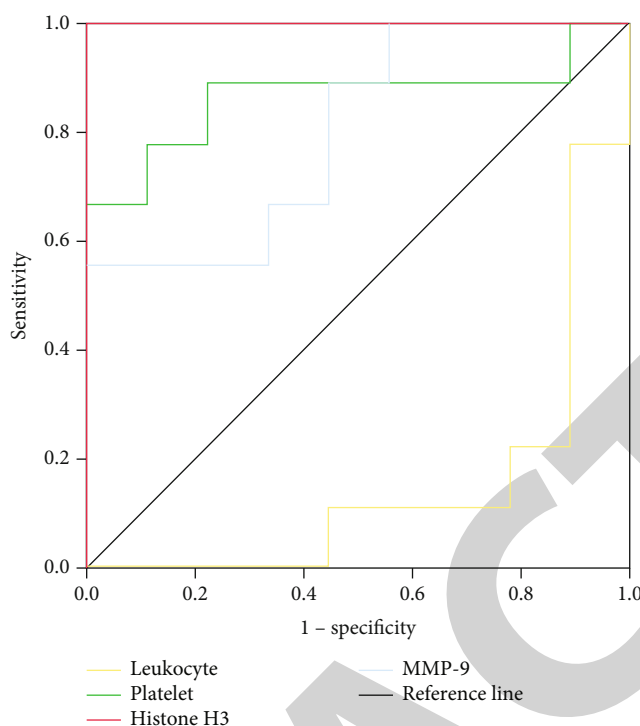
sections. No normal alveoli structure was observed in the experimental groups. And widespread bleeding and inflammation infiltration was found in the alveoli. Most liver cells in the experimental groups were edema and ballooning degeneration, and local inflammation was observed. Widespread renal tubular epithelial cell necrosis and glomerulus were severely out of shape (Figure 13). Casts were observed in enlarged lumen. All the changes above were more obvious in the LPS 1000 group.

4. Discussion

Millions of people suffer from sepsis worldwide every year, and the mortality rate can exceed 25%, which seriously

threatens the life and health of human beings [9, 10]. Urosepsis accounts for about 5% of all sepsis, which is an important cause of death in urology patients, especially after urolithiasis surgery. The early diagnosis and treatment of sepsis have always been a vital but difficult point in the field of medicine. At present, two conditions should be met for the diagnosis of sepsis at the same time: (1) evidence of infection and (2) sequential organ failure score (SOFA) ≥ 2 . The SOFA score included objective criteria for respiratory failure, coagulation dysfunction, elevated bilirubin, decreased blood pressure, disturbance of consciousness, and renal failure, lacking effective biomarkers for early diagnosis.

To explore the mechanism of the urosepsis occurrence and development, rational animal model is needed. Five



Notes: All parameters above had diagnosis value ($P < 0.05$).
 AUC of H3, leucocyte, platelet and MMP-9 was 1.000, 0.852, 0.864 and 0.802 respectively.

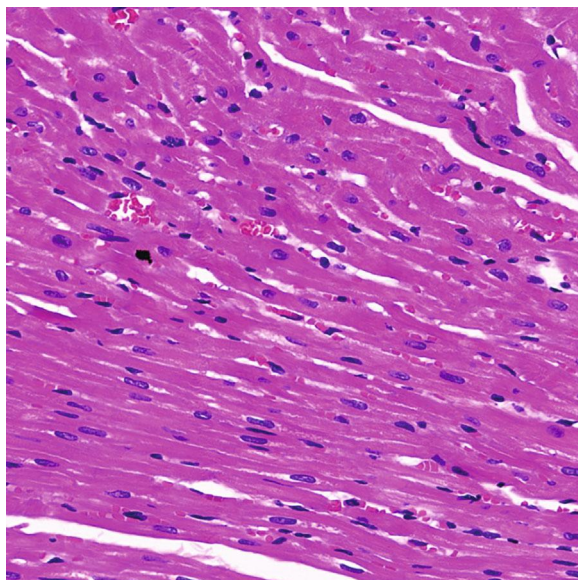
FIGURE 9: Postoperative 6 h ROC curve of indexes. All parameters above had a diagnosis value ($P < 0.05$). AUC of H3, leucocyte, platelet, and MMP-9 was 1.000, 0.852, 0.864, and 0.802, respectively.

kinds of modeling method are commonly used: (1) intravenous injection of exogenous toxin (commonly used LPS); (2) intravenous injection of bacterial suspension; (3) destruction of biological protection barrier of experimental animals; (4) manufacture of local soft tissue infection; and (5) pneumonia, meningitis model, etc. The method of constructing urosepsis remains unclear [21]. Patients undergoing intracavitary lithotripsy are susceptible to postoperative urinary sepsis and are now considered to be related to the interaction between the obstruction caused by urinary calculi and the infection [24]. In urinary tract obstruction combined with a sharp increase in intrarenal pressure during intracavitary lithotripsy, the toxin retrogrades into the blood circulation and eventually develops into urosepsis [25, 26]. We intend to simulate the nosogenesis by injecting the LPS solution into the ureter to induce urinary tract infection and ligating ureter to make ureteral obstruction. Given the difficulty of operation and postoperative evaluation, we selected New Zealand rabbits aged 2-3 months.

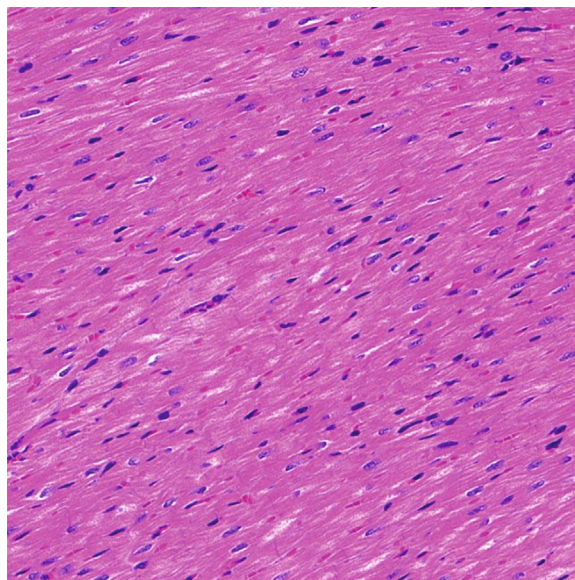
According to previous study, two LPS concentration gradients were set up in the experimental group, which were $600 \mu\text{g}/\text{kg}$ and $1000 \mu\text{g}/\text{kg}$, respectively, in order to find out the suitable concentration of the model and simulate the different severity of infection. Histological and pathological examination was performed 24 hours after operation to confirm the establishment of the model. We set up the sham-

operation group to exclude the influence of the operation on the result. All rabbits in the control group and sham operation group survive after the operation. Except for the transient hypothermia at a 3-hour postoperative time in the sham operation group (considering to be surgical factors), no infection-related clinical symptoms and signs are detected. Pathological results showed that the morphology of the heart, lung, liver, and kidney is basically normal, which proved that the operation itself would not cause urosepsis. On the contrary, in the LPS-treated groups, diffuse thickening of alveolar septum, massive infiltration of inflammatory cells in the alveoli, destruction of nephron, and disintegration of glomerular structure are found, indicating multiple organ failures of the rabbits; urosepsis model is successfully established. Thus, ligating the ureter after injection of LPS solution into the ureter can trigger urosepsis in rabbits.

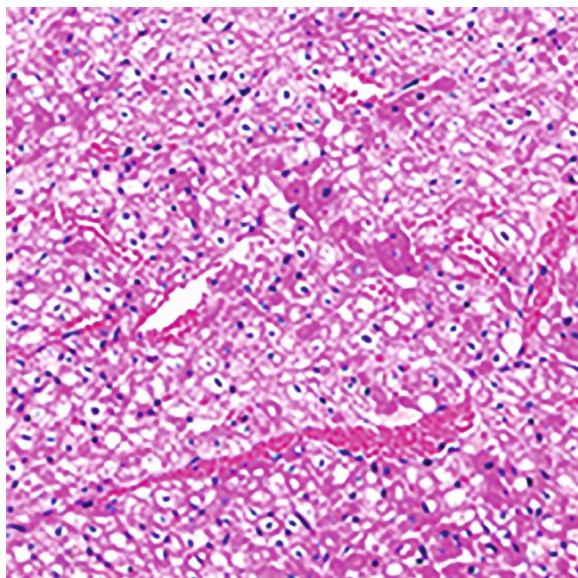
Comparing the experimental group with the sham operation group, there is no significant change in postoperative heart and respiratory rate; anal temperature decreases significantly after 6 hours; mean arterial pressure returned to normal after a transient decrease at 3 hours after operation and remained at normal level until 24 hours. Therefore, the urosepsis cannot be diagnosed with these clinical indexes, but pathology confirms that the rabbits in the experimental groups have entered the early stage of sepsis. Peripheral blood WBC count $(3.86 \pm 4.74) \times 10^9/\text{L}$ in the LPS 600 group



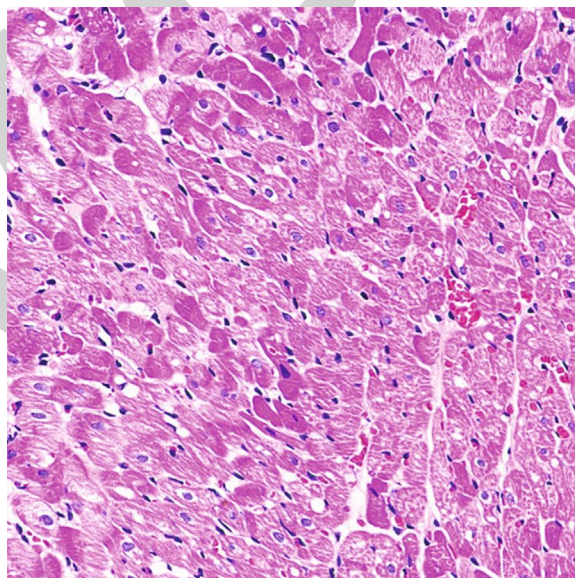
(a) Myocardial cells of the control group (HE, 20x)



(b) Myocardial cells of the sham group (HE, 20x)



(c) Myocardial cells of the LPS 600 group (HE, 20x)



(d) Myocardial cells of the LPS 1000 group (HE, 20x)

FIGURE 10: Pathology of myocardial at 24 h postoperation (HE, 20x).

and $(1.74 \pm 0.40) \times 10^9/L$ in the LPS 1000 group is significantly lower than that in the sham group $(9.84 \pm 3.86) \times 10^9/L$ 3 hours after the operation. When it comes to 6 hours after the operation, the WBC count rises up to $(4.76 \pm 4.06) \times 10^9/L$ and $(2.83 \pm 0.96) \times 10^9/L$; this result is consistent with the findings of Wu et al. that in the early stage of sepsis, peripheral blood WBC trend decreases at first and then increases. Hence, for postoperative patients with dynamic monitoring of WBC, if the changes show a downward trend, urosepsis should be considered rather than waiting for the WBC to rise significantly. It should be noticed that in the LPS 1000 group, the platelet count increases significantly and reaches $(685.80 \pm 150.52) \times 10^9/L$ at 1 hour after opera-

tion, which is much higher than that in the sham group, and the platelet level is maintained until 6 hours after the operation $((594.75 \pm 240.02) \times 10^9/L)$. However, according to sepsis guideline, the lower the platelet count, the higher the SOFA score, that is, the more evidence for the diagnosis of sepsis. Thiery-Antier et al. also reported that decrease of platelet within 24 hours after the diagnosis of sepsis indicates a higher 28-day mortality rate [27]. Considering the changing trend of WBC in urosepsis, we give the hypothesis that in the early stage of urosepsis, the peripheral blood platelet count may increase first and then decrease and the increase of platelet count has a greater value in the early diagnosis of urosepsis.

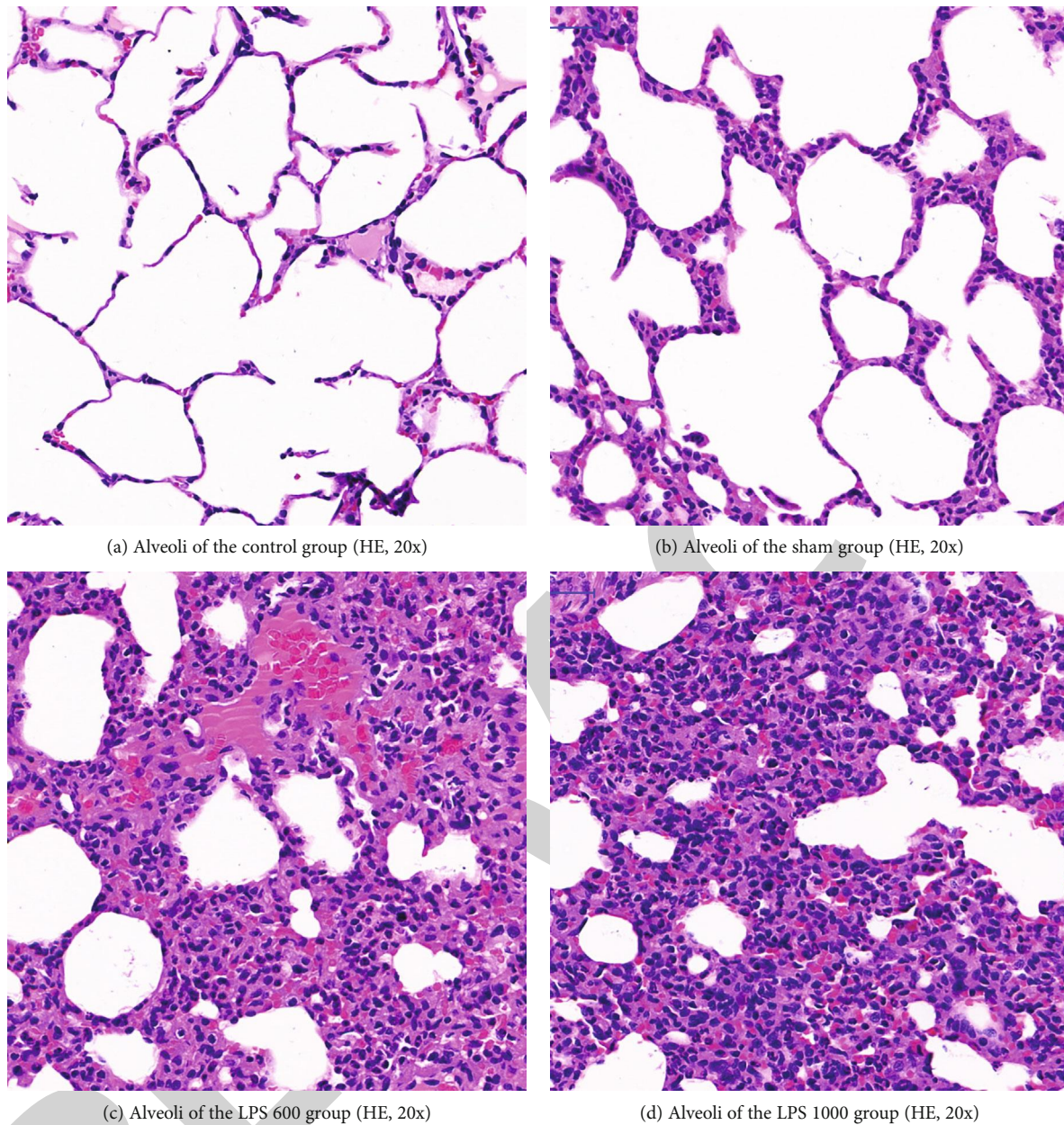


FIGURE 11: Pathology of alveoli at 24 h postoperation (HE, 20x).

In addition to platelet, serum histone H3 also increases significantly at 1 hour after operation. In the LPS 600 group, serum histone H3 reaches $(5.71 \pm 0.32) \times 10^9/L$ which is higher than that in the sham group and the gap grows over time. 6 hours after the operation, H3 level in the LPS 600 and LPS 1000 groups is $(6.92 \pm 0.55) \times 10^9/L$ and $(7.45 \pm 0.45) \times 10^9/L$, respectively. ROC curve analysis finds that H3 can predict urosepsis with an AUC of 1.00. When setting 5.04 as the cut-off value by the Youden index, we find that serum $H3 \geq 5.04$ has a sensitivity of 100% and specificity of 100% (Youden index: 1), which is higher than platelet and MMP-9. After analyzing ELISA data, we find that the serum H3 contents in the noninfected groups (control and sham

group) and the LPS-treated groups have almost no crossover. 1 hour after the operation, serum H3 level in the noninfected groups is lower than 4.9 ng/mL while in the LPS-treated groups is all higher than 5.1 ng/mL. Thus, when using any concentration between 4.9 and 5.1 ng/mL as a critical threshold to distinguish infection, the extreme case of sensitivity and specificity of 100% occurs. This may due to insufficient sample size but we can still consider histone H3 as a potential biomarker for early diagnosis of urosepsis. Histone H3 as the main cytotoxic protein in the five subtypes of histone can directly damage endothelia cells, activate the inflammatory signaling pathway, and cause the mass release of inflammatory cytokines. H3 interacts with the phospholipid

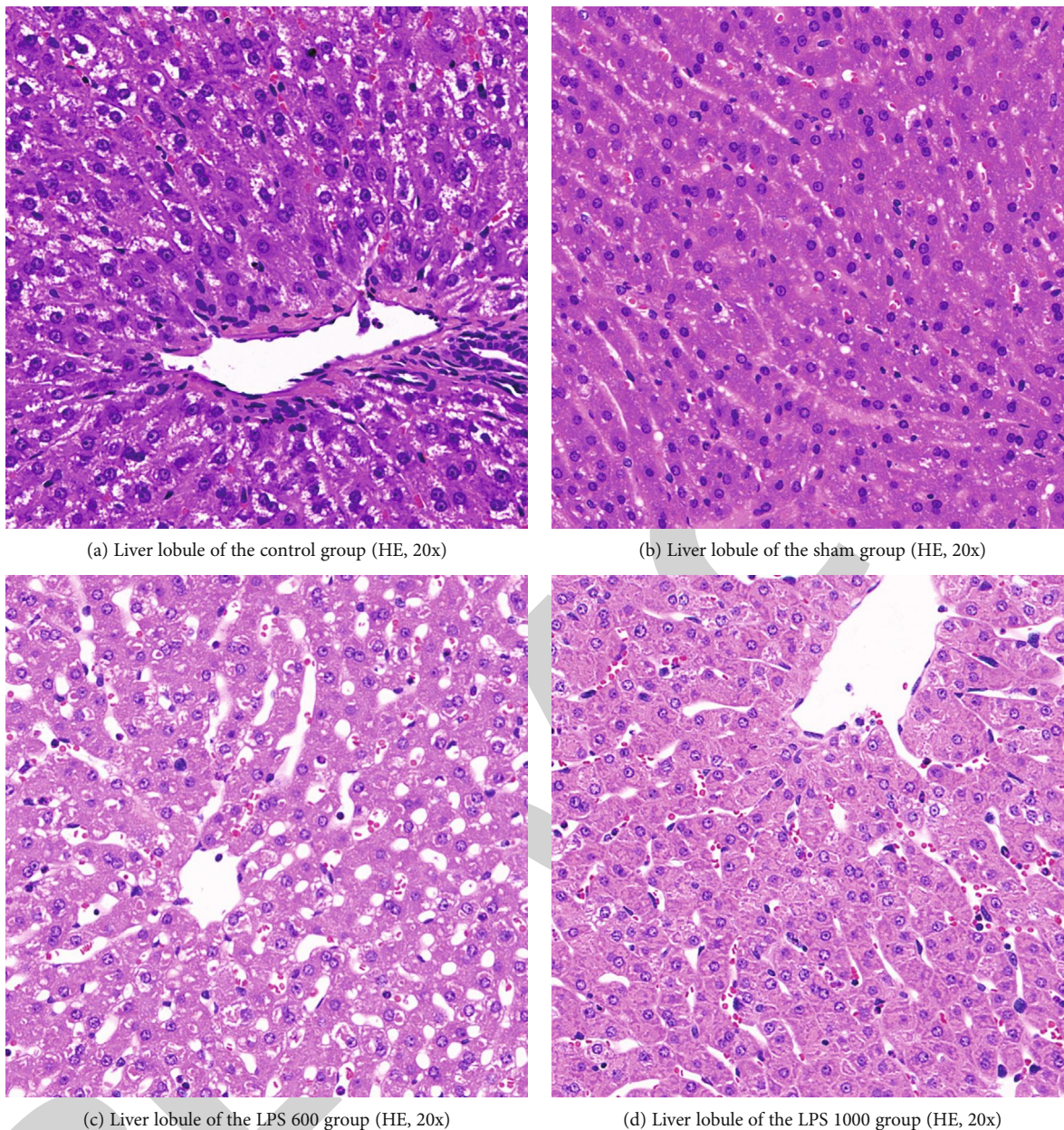


FIGURE 12: Pathology of liver lobule at 24 h postoperation (HE, 20x).

bimolecular layer of the cell membrane to promote the formation of channels and destroy the barrier structure of the cell membrane. As an important component of the neutrophil extracellular trap (NETs), histone is secreted by activated neutrophils when inflammation occurs, and Toll-like receptors-2/4 (TLR-2/4) triggered NF- κ B depended inflammatory signaling pathway which promotes the recruitment of WBCs in the microvasculature, thus mediating the occurrence of inflammation and tissue damage [13–15, 18, 19, 28]. This suggests that H3 plays an important role in the development of inflammatory process in the body. In addition to having great early diagnostic potential, antagonizing H3 may also become a viable treatment for urosepsis.

We find H3 levels in 1, 3, and 6 hours after the operation are significantly increased, but there is no significant change in peripheral blood neutrophils between groups after the operation (Tables 7–9). There may be two reasons behind the change: (1) When inflammation is induced, neutrophils are more efficiently active in H3 secretion, which occurs before the number of neutrophils rises. (2) Mass production of H3 in peripheral blood is derived from apoptotic or dead cells in the inflammatory process. Hence, uncovering the source of H3 in the early stage of urosepsis with massive blood intake still needs further study. Matrix metalloproteinases (MMP-9) and tissue inhibitor of metalloproteinase-1 (TIMP-1) are newly discovered inflammatory cytokines.

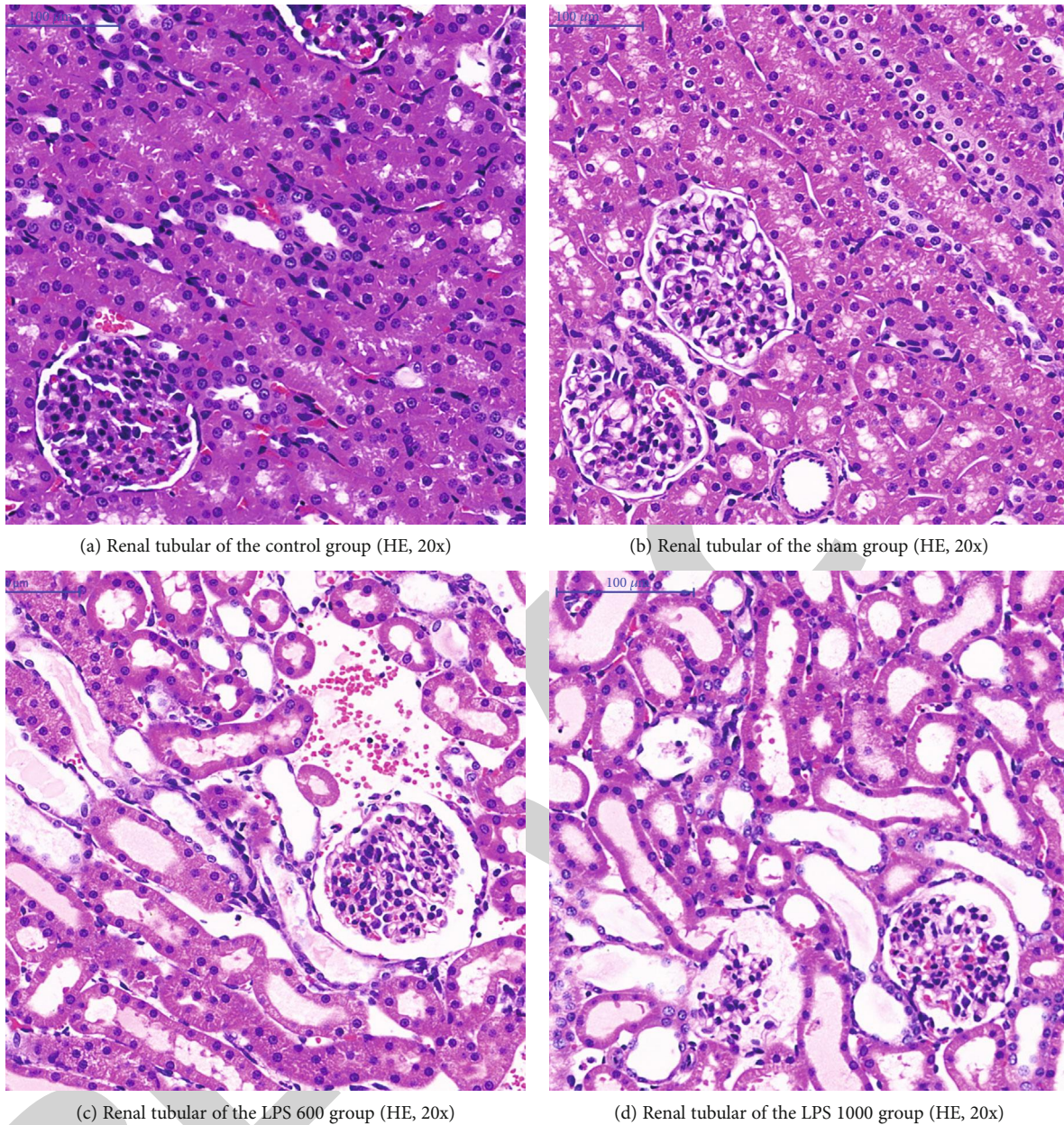


FIGURE 13: Pathology of renal tubular at 24 h postoperation (HE, 20x).

Clinical trials have confirmed that the serum levels of MMP-9 and TIMP-1 increased significantly on the first day of sepsis occurrence, beginning to decrease on the third day, and the increase of concentration is especially evident in the serum of deceased patients [29, 30]. We find that TIMP-1 has no significant change in the early stage of urosepsis; MMP-9 increases significantly 1 hour after the operation but only in the LPS 1000 group. When the diagnostic point is 73.89 ng/mL, the diagnostic sensitivity is 60% and the specificity is 90%, which have certain diagnostic significance but are not as good as that of histone H3. Therefore, the diagnostic capacity of MMP-9 in the early stage of urosepsis is yet to be verified.

To sum up, ligating the ureter after an injection of 1000 $\mu\text{g}/\text{kg}$ LPS into the ureter of the rabbit can establish the animal model of urosepsis. On the basis of a realistic simulation of the pathogenesis of urosepsis, this method ensures a long enough survival time to collect clinical data and specimens. The increase of serum histone H3 can be detected within 1 hour of the infection with high diagnostic sensitivity and specificity of urosepsis as well, which is a sufficient biomarker for the early diagnosis of urosepsis. Furthermore, peripheral platelet count and serum MMP-9 concentration are also potential indexes. Whether these indexes can be used as biomarkers in clinical diagnosis needs to be further verified by clinical trials in the future.

Data Availability

All the data would be provided if required.

Conflicts of Interest

The authors declare that they have no conflicts of interest.

Authors' Contributions

Xiaolu Zhang and Xiangcheng Zhan contributed equally to this work.

Acknowledgments

This work was supported by the Foundation of Shanghai Municipal Health Commission (No. 201940105) and the National Natural Science Foundation of China (No. 81971371).

Supplementary Materials

Supplemental Figure S1: postoperative changes of heart rate. Supplemental Figure S2: postoperative changes of respiratory rate. Supplemental Figure S3: postoperative changes of CRP level. Supplemental Figure S4: postoperative changes of PCT level. Supplemental Figure S5: postoperative changes of TIMP-1 level. (*Supplementary Materials*)

References

- [1] E. Rivers, B. Nguyen, S. Havstad et al., "Early goal-directed therapy in the treatment of severe sepsis and septic shock," *The New England Journal of Medicine*, vol. 345, no. 19, pp. 1368–1377, 2001.
- [2] R. O. Draga, E. T. Kok, M. R. Sorel, R. J. Bosch, and T. M. Lock, "Percutaneous nephrolithotomy: factors associated with fever after the first postoperative day and systemic inflammatory response syndrome," *Journal of Endourology*, vol. 23, no. 6, pp. 921–927, 2009.
- [3] B. Sanand, S. Kumar, N. Taneja, V. Sharma, A. K. Mandal, and S. K. Singh, "One week of nitrofurantoin before percutaneous nephrolithotomy significantly reduces upper tract infection and urosepsis: a prospective controlled study," *Urology*, vol. 77, no. 1, 2011.
- [4] M. S. Michel, L. Trojan, and J. J. Rassweiler, "Complications in percutaneous nephrolithotomy," *European Urology*, vol. 51, no. 4, pp. 899–906, 2007.
- [5] F. Sharifi Aghdas, H. Akhavadegan, A. Aryanpoor, H. Inanloo, and M. Karbakhsh, "Fever after percutaneous nephrolithotomy: contributing factors," *Surgical Infections*, vol. 7, no. 4, pp. 367–371, 2006.
- [6] D. Margel, Y. Ehrlich, N. Brown, D. Lask, P. M. Livne, and D. A. Lifshitz, "Clinical implication of routine stone culture in percutaneous nephrolithotomy—a prospective study," *Urology*, vol. 67, no. 1, pp. 26–29, 2006.
- [7] A. Kumar, D. Roberts, K. E. Wood et al., "Duration of hypotension before initiation of effective antimicrobial therapy is the critical determinant of survival in human septic shock," *Critical Care Medicine*, vol. 34, no. 6, pp. 1589–1596, 2006.
- [8] S. Oda, M. Aibiki, T. Ikeda et al., "The Japanese guidelines for the management of sepsis," *Journal of Intensive Care*, vol. 2, no. 1, p. 55, 2014.
- [9] A. Rhodes, L. E. Evans, W. Alhazzani et al., "Surviving Sepsis Campaign: International Guidelines for Management of Sepsis and Septic Shock: 2016," *Critical Care Medicine*, vol. 45, no. 3, pp. 486–552, 2017.
- [10] C. W. Seymour, V. X. Liu, T. J. Iwashyna et al., "Assessment of Clinical Criteria for Sepsis: for the Third International Consensus Definitions for Sepsis and Septic Shock (Sepsis-3)," *JAMA*, vol. 315, no. 8, pp. 762–774, 2016.
- [11] M. Singer, C. S. Deutschman, C. W. Seymour et al., "The Third International Consensus Definitions for Sepsis and Septic Shock (Sepsis-3)," *JAMA*, vol. 315, no. 8, pp. 801–810, 2016.
- [12] K. Luger, A. W. Mader, R. K. Richmond, D. F. Sargent, and T. J. Richmond, "Crystal structure of the nucleosome core particle at 2.8 Å resolution," *Nature*, vol. 389, no. 6648, pp. 251–260, 1997.
- [13] J. Xu, X. Zhang, R. Pelayo et al., "Extracellular histones are major mediators of death in sepsis," *Nature Medicine*, vol. 15, no. 11, pp. 1318–1321, 2009.
- [14] S. Denk, M. Perl, and M. Huber-Lang, "Damage- and pathogen-associated molecular patterns and alarmins: keys to sepsis?," *European Surgical Research*, vol. 48, no. 4, pp. 171–179, 2012.
- [15] S. Holdenrieder and P. Stieber, "Clinical use of circulating nucleosomes," *Critical Reviews in Clinical Laboratory Sciences*, vol. 46, no. 1, pp. 1–24, 2009.
- [16] S. R. Clark, A. C. Ma, S. A. Tavener et al., "Platelet TLR4 activates neutrophil extracellular traps to ensnare bacteria in septic blood," *Nature Medicine*, vol. 13, no. 4, pp. 463–469, 2007.
- [17] S. Jahr, H. Hentze, S. Englisch et al., "DNA fragments in the blood plasma of cancer patients: quantitations and evidence for their origin from apoptotic and necrotic cells," *Cancer Research*, vol. 61, no. 4, pp. 1659–1665, 2001.
- [18] V. Brinkmann, U. Reichard, C. Goosmann et al., "Neutrophil extracellular traps kill bacteria," *Science*, vol. 303, no. 5663, pp. 1532–1535, 2004.
- [19] X. Yang, L. Li, J. Liu, B. Lv, and F. Chen, "Extracellular histones induce tissue factor expression in vascular endothelial cells via TLR and activation of NF- κ B and AP-1," *Thrombosis Research*, vol. 137, pp. 211–218, 2016.
- [20] D. Tang, R. Kang, C. B. Coyne, H. J. Zeh, and M. T. Lotze, "PAMPs and DAMPs: signal 0s that spur autophagy and immunity," *Immunological Reviews*, vol. 249, no. 1, pp. 158–175, 2012.
- [21] M. Kalbitz, J. J. Grailer, F. Fattahi et al., "Role of extracellular histones in the cardiomyopathy of sepsis," *The FASEB Journal*, vol. 29, no. 5, pp. 2185–2193, 2015.
- [22] Y. Li, Z. Liu, B. Liu et al., "Citruinated histone H3: a novel target for the treatment of sepsis," *Surgery*, vol. 156, no. 2, pp. 229–234, 2014.
- [23] H. Wu, S. Zhu, S. Yu et al., "Early drastic decrease in white blood count can predict uroseptic shock induced by upper urinary tract endoscopic lithotripsy: a translational study," *The Journal of Urology*, vol. 193, no. 6, pp. 2116–2122, 2015.
- [24] D. Volkin and O. Shah, "Complications of ureteroscopy for stone disease," *The Italian Journal of Urology and Nephrology*, vol. 68, no. 6, pp. 570–585, 2016.
- [25] S. A. Troxel and R. K. Low, "Renal intrapelvic pressure during percutaneous nephrolithotomy and its correlation with the

Research Article

Integrative Analysis of Differently Expressed Genes Reveals a 17- Gene Prognosis Signature for Endometrial Carcinoma

Anna Wang,¹ Hongyan Guo,² and Zaiqiu Long¹ 

¹Department of Gynecology, Cancer Hospital of China Medical University, Liaoning Cancer Hospital & Institute, Liaoning, China

²Department of Information Engineering, Shenyang Polytechnic College, Liaoning, China

Correspondence should be addressed to Zaiqiu Long; longzaiqiu@cancerhosp-ln-cmu.com

Received 15 May 2021; Revised 28 June 2021; Accepted 3 July 2021; Published 15 July 2021

Academic Editor: Tao Huang

Copyright © 2021 Anna Wang et al. This is an open access article distributed under the Creative Commons Attribution License, which permits unrestricted use, distribution, and reproduction in any medium, provided the original work is properly cited.

Endometrial carcinoma (EC) is the fifth widely occurring malignant neoplasm among women all over the world. However, there is still lacking efficacy indicators for EC's prognosis. Here, we analyzed two databases including an RNA-sequencing-based TCGA dataset and a microarray-based GSE106191. After normalizing the raw data, we identified 114 common genes with upregulation and 308 common genes with downregulation in both the TCGA and GSE106191 databases. Bioinformatics analysis showed that the differently expressed genes in EC were related to the IL17 signaling pathway, PI3K-Akt signaling pathway, and cGMP-PKG signaling pathway. Furthermore, we performed the least absolute shrinkage and selection operator (LASSO) Cox regression analysis and generated a signature featuring 17 prognosis-related genes (MAL2, ANKRD22, METTL7B, IL32, ERFE, OAS1, TRPC1, SRPX, RAPGEF4, PSD3, SIMC1, TRPC6, WFS1, PGR, PAMR1, KCNK6, and FAM189A2) and found that it could predict OS in EC patients. The further analysis showed that OAS1, MAL2, ANKRD22, METTL7B, and IL32 were significantly upregulated in EC samples after comparison with normal samples. However, TRPC1, SRPX, RAPGEF4, PSD3, SIMC1, TRPC6, WFS1, PGR, PAMR1, KCNK6, and FAM189A2 were significantly downregulated in EC samples in comparison with normal samples. And correlation analysis showed that our results showed that the expressions of 17 prognosis-related hub genes were significantly correlated based on Pearson correlation. We here offer a newly genetic biomarker for the prediction of EC patients' prognosis.

1. Introduction

Endometrial carcinoma (EC) is the fifth commonly occurring malignant neoplasm among women all over the world, with an estimated 382,000 new EC cases and nearly 90,000 deaths in 2018 [1, 2]. Especially in the United States, it is speculated that the number of newly diagnosed ECs will be increasing over time. It is estimated that the occurrence rate is still rising with increasing risk factors for certain ECs, including obesity rate and the aging of the US population [3]. The incidence rate of EC increases after the age of 30, and the peak incidence is within 60 to 69 years. 20% to 30% of patients with EC are diagnosed in the advanced stage during surgery. In the clinic, the five-year survival rate of patients in stage III ranged from 40% to 70% and in stage IV was within 0 to 10% [1, 4]. Despite therapeutic advances having been made, high recurrence rate and metastasis remain to be big chal-

lenges [4]. To determine effective therapeutic strategies in ameliorating the prognostic status of EC patients is thus essential.

Presently, as per the World Health Organization (WHO) classification system classification, EC comprises two sorts on the basis of histological features [5]. Endometrioid adenocarcinoma or well-differentiated endometrioid subtypes accounted for 80% over EC cases and was considered as estrogen-dependent type I of EC [1, 4, 6]. Approximately 10% of EC cases were type II, manifested as nonendometrial or poorly differentiated EC. Difference existed in the molecular changes of the two EC types [1, 4, 7]. In general, in the activated oncogene and inactivated tumor suppressor gene, defective DNA repair contributed mainly to the occurrence of neoplasms [1, 8]. For instance, the inactivated tumor suppressor gene *PTEN* accompanied by DNA mismatch repair gene defects manifested as the microsatellite instability

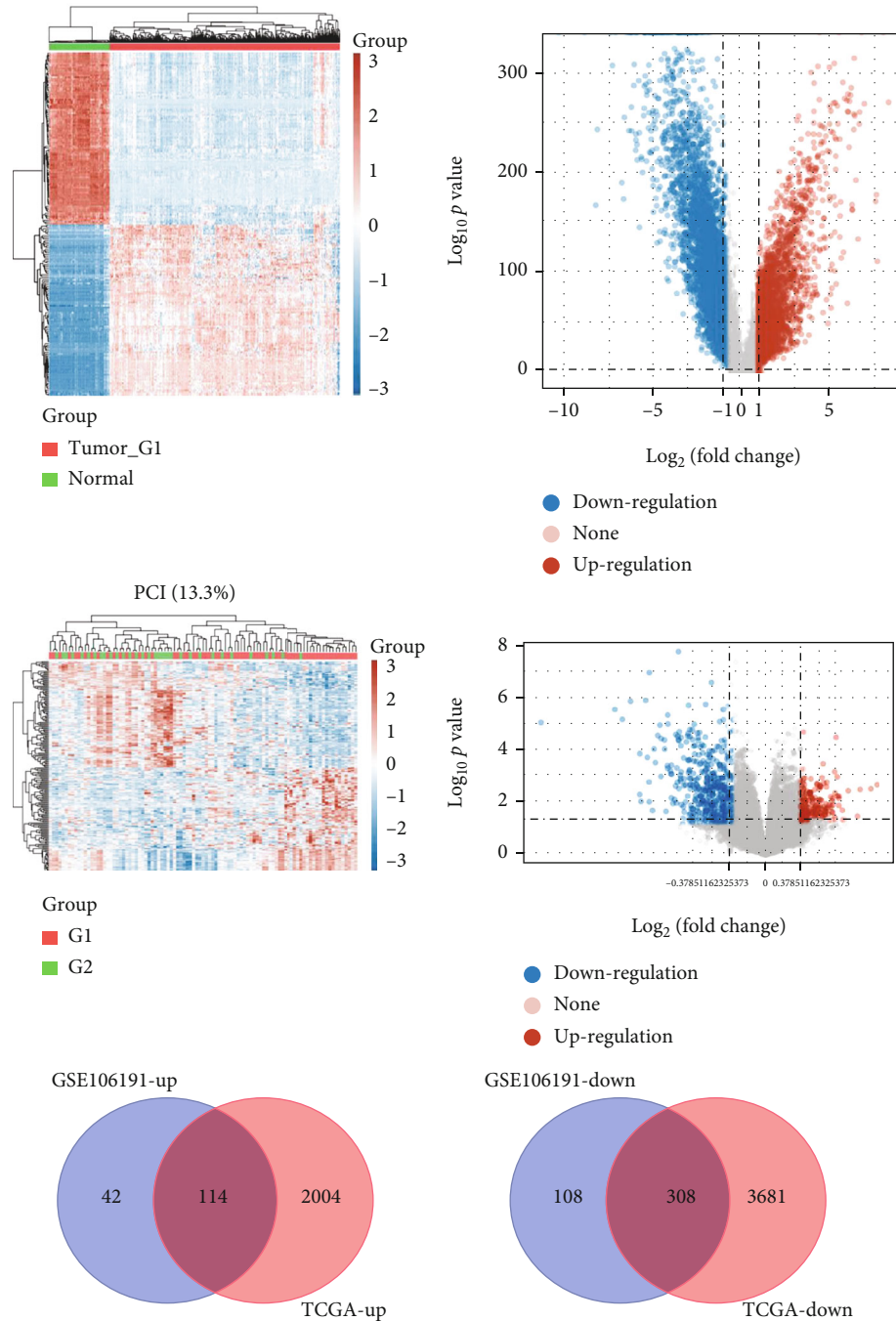


FIGURE 1: Screening of DEGs in EC. (a, b) Heat map (a) and volcano map (b) identified 2118 genes with upregulation and 3989 genes with downregulation by analyzing the TCGA database. (c, d) Heat map (c) and volcano map (d) showed 156 genes with upregulation and 416 genes with downregulation by analyzing the GSE106191 database. (e, f) Venn map analysis of common upregulated and downregulated genes in EC by analyzing the TCGA and GSE106191 databases.

phenotype, or activated KRAS2 and/or adhesion molecules genes were detected in the early stage of type I EC [9]. Previous studies have shown that mutated TP53 and Her-2 occurred in type II EC, which was probably caused by the background of the atrophic endometrium. It seems that these molecular changes were specific in type I and type II of ECs [10, 11]. Although many efforts have been made to set up a molecularly based histological classification, it is still urgently

needed to identify the gene expression profiles between different histological types of ECs that distinguish normal cells from cancer cells. There have been public reports showing that the differentially expressed genes existed in different histological sorts of EC [12, 13]. However, a limited set of genes were reported in these studies. More and more researches are thus needed to characterize EC and unearth the genes functioning importantly in the mechanisms of EC.

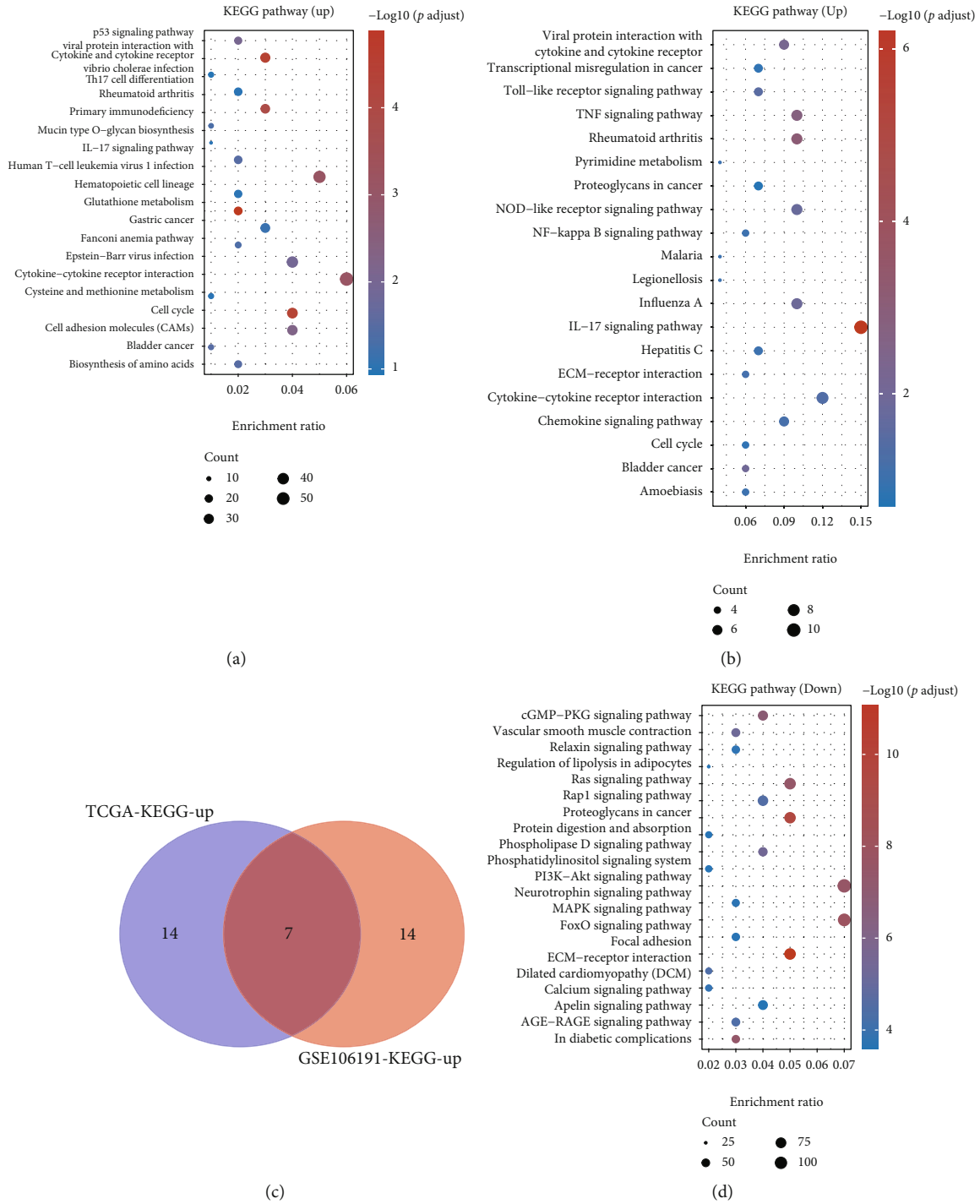


FIGURE 2: Continued.

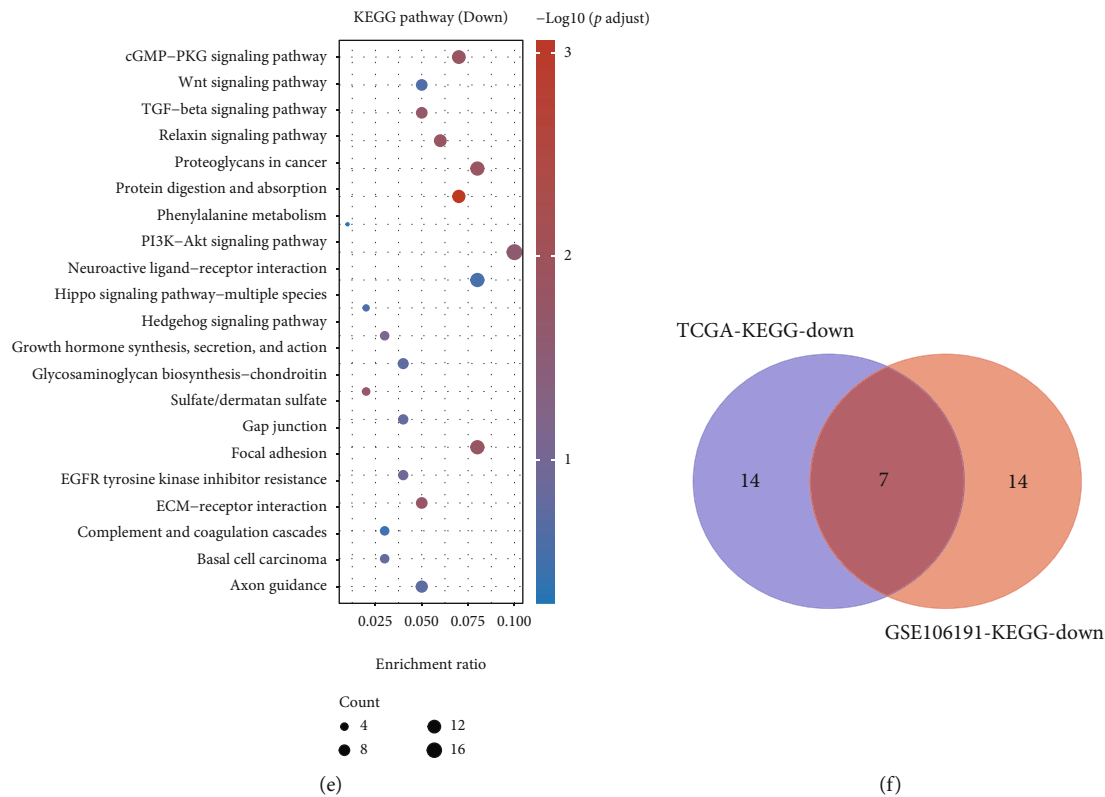


FIGURE 2: KEGG pathway analysis of DEGs in EC. (a) KEGG pathway analysis of upregulated genes by analyzing the TCGA database. (b) KEGG pathway analysis of upregulated genes by analyzing the GSE106191 database. (c) Venn map analysis of upregulated gene-related pathways. (d) KEGG pathway analysis of downregulated genes by analyzing the TCGA database. (e) KEGG pathway analysis of downregulated genes by analyzing the GSE106191 database. (f) Venn map analysis of downregulated gene-related pathways.

Herein, we attempted to systematically screen more novel differentially expressed genes and related molecular pathways and the clinical significance of the identified genes in EC. To sum up, identification of EC-related genes and gene pathways as well as the clinical implication is conducive to understanding the pathophysiology of this cancer and uncovering the potential diagnostic biomarkers of EC.

2. Materials and Methods

2.1. Establishment and Verification of Gene Prognostic Model. We carried out the LASSO Cox regression model (R package “glmnet”) to select the candidate genes and subsequently established the prognostic model [14, 15]. We ultimately retained 17 genes and their coefficients and utilized the minimum criteria to determine the penalty parameter (λ). We calculated the risk score after centralizing and standardizing (applying the “scale” function in R) the TCGA expression data. The risk score formula was shown as follows: risk score = $\sum 7iX_i \times Y_i$ (X_i : coefficients, Y_i : gene expression level).

2.2. Identification of Differentially Expressed Genes (DEGs). We obtained expression matrixes and platform information from Gene Expression Omnibus (GEO) datasets. The dataset GSE106191 was used, which includes the primary tumor of 66 endometrial cancer patients (64 carcinoma samples and

33 hyperplasia samples). Then, Software R (version 3.5.1, <https://www.r-project.org>) and “limma” packages (<http://www.bioconductor.org/>) [16] were applied to select the DEGs existing in the EC samples and control samples. These selection criteria were adjusted p value < 0.05 and fold change (FC) ≥ 2 or fold change (FC) ≤ 0.5 .

2.3. Functional Enrichment Analysis. We usually applied Gene Ontology (GO) functional enrichment analysis to describe gene functions, consisting of molecular function (MF), biological process (BP), or cellular component (CC) [17, 18]. And we then utilized the Kyoto Encyclopedia of Genes and Genomes (KEGG) pathway enrichment analysis to identify molecular interaction and relation networks. p value < 0.05 was thought to be statistically significant. Based on the DEGs in the GEO datasets, we conducted GO and KEGG enrichment analyses by the online tool DAVID (<https://david.ncifcrf.gov/home.jsp>) [19, 20]. The top significantly enriched analysis results were shown.

2.4. Survival Analysis. For identification of prognosis-predicting genes, we integrated the clinical data of EC patients in The Cancer Genome Atlas (TCGA) and carried out Kaplan-Meier curve analysis [21, 22]. The survival curves of DEGs were drew by “survival” package in R. p value < 0.05 was denoted as a significantly statistical difference.

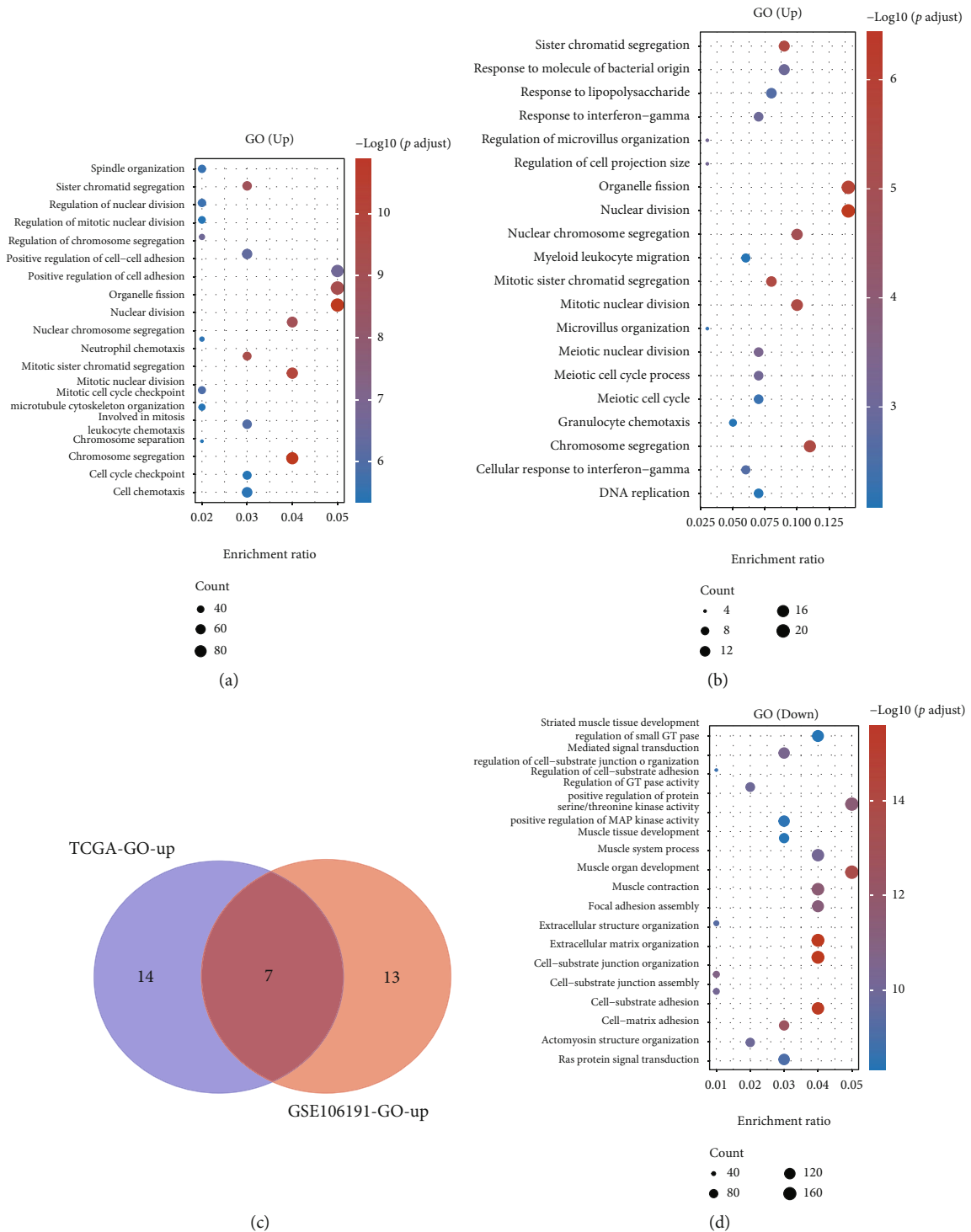


FIGURE 3: Continued.

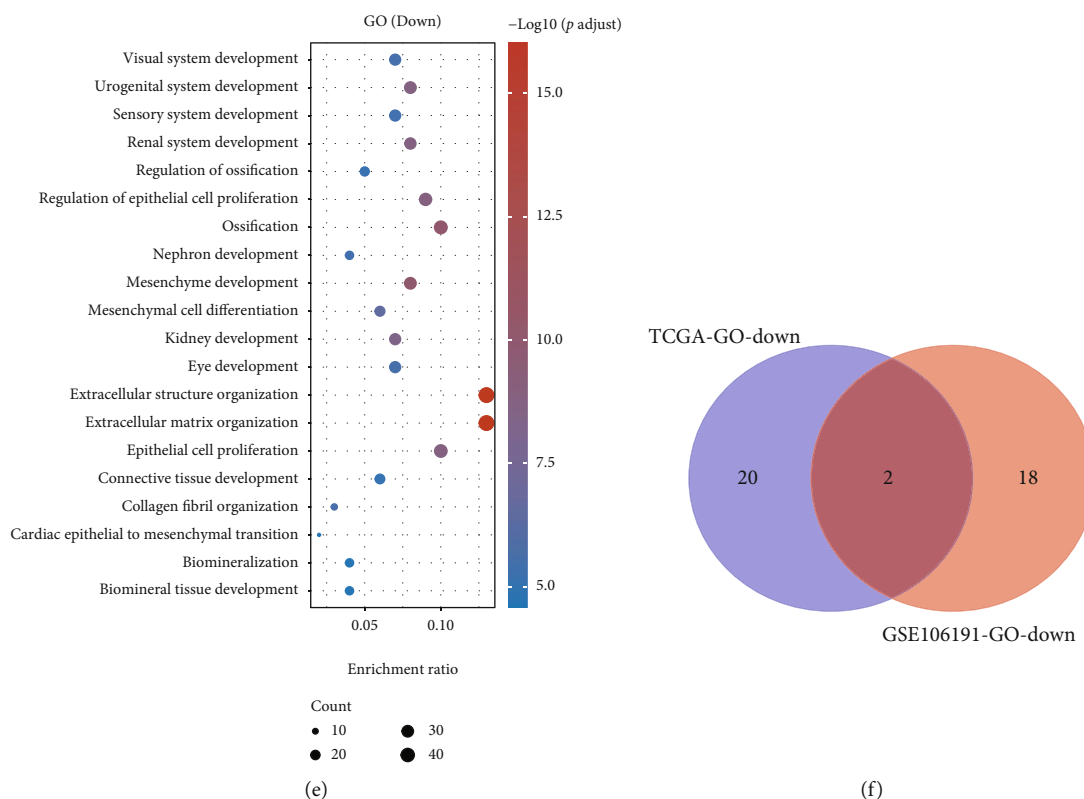


FIGURE 3: GO analysis of DEGs in EC. (a) GO analysis of upregulated genes by analyzing the TCGA database. (b) GO analysis of upregulated genes by analyzing the GSE106191 database. (c) Venn map analysis of upregulated gene-related pathways. (d) GO analysis of downregulated genes by analyzing the TCGA database. (e) GO analysis of downregulated genes by analyzing the GSE106191 database. (f) Venn map analysis of downregulated gene-related pathways.

2.5. Statistical Analysis. SPSS 22.0 software (Chicago, USA) was employed to analyze the data. All representative data were shown as the mean \pm standard deviation (SD) [23–25]. We carried out the Students' *t*-test and one-way ANOVA to separately determine the difference existing in two groups and multiple groups. *p* value < 0.05 was denoted as a significantly statistical difference [26–28]. All experiments were performed in three independent times in replicates at one time.

3. Results

3.1. Screening of DEGs in EC. To identify the DEGs in EC, we analyzed two databases including the RNA-sequencing-based TCGA dataset and microarray-based GSE106191. After normalizing the raw data, we identified 2118 genes with upregulation and 3989 genes with downregulation by analyzing the TCGA database (Figures 1(a) and 1(b)). Meanwhile, we found 156 genes with upregulation and 416 genes with downregulation by analyzing the GSE106191 database (Figures 1(c) and 1(d)). Among the DEGs, 114 common genes with upregulation and 308 common genes with downregulation were identified in both the TCGA and GSE106191 databases (Figures 1(e) and 1(f)).

3.2. Bioinformatics Analysis of DEGs in EC. Next, we performed KEGG and GO analyses of DEGs in endometrial car-

cinoma using TCGA and GSE106191, respectively. As presented in Figure 2, the KEGG analysis showed that the pathways related to DEGs were similar by analyzing either TCGA or GSE106191 (Figures 2(a), 2(b), 2(d), and 2(e)). The KEGG analyses of upregulated genes were related to bladder cancer, cell cycle, cytokine-cytokine receptor interaction, IL17 signaling pathway, cytokine, and cytokine receptor (Figure 2(c)). The KEGG analyses of downregulated genes were related to ECM-receptor interaction, focal adhesion, PI3K-Akt signaling pathway, protein digestion and absorption, proteoglycans in carcinoma, relaxin signaling pathway, and cGMP-PKG signaling pathway (Figure 2(f)).

Furthermore, the GO analysis also showed that the biological processes related to DEGs were similar by analyzing either TCGA or GSE106191 (Figures 3(a), 3(b), 3(d), and 3(e)). The GO analyses of upregulated genes were related to chromosome segregation, mitotic nuclear division, mitotic sister chromatid segregation, nuclear chromosome segregation, nuclear division, organelle fission, and sister chromatid segregation (Figure 3(c)). The GO analysis of downregulated genes exhibited a relationship to extracellular matrix organization and structure organization (Figure 3(f)).

3.3. Identification of Prognosis-Related DEGs in EC. In the above analysis, we identified 572 DEGs in EC. In order to identify prognosis-related DEGs in ECs, we carried out the Kaplan-Meier Plotter to determine the correlation of

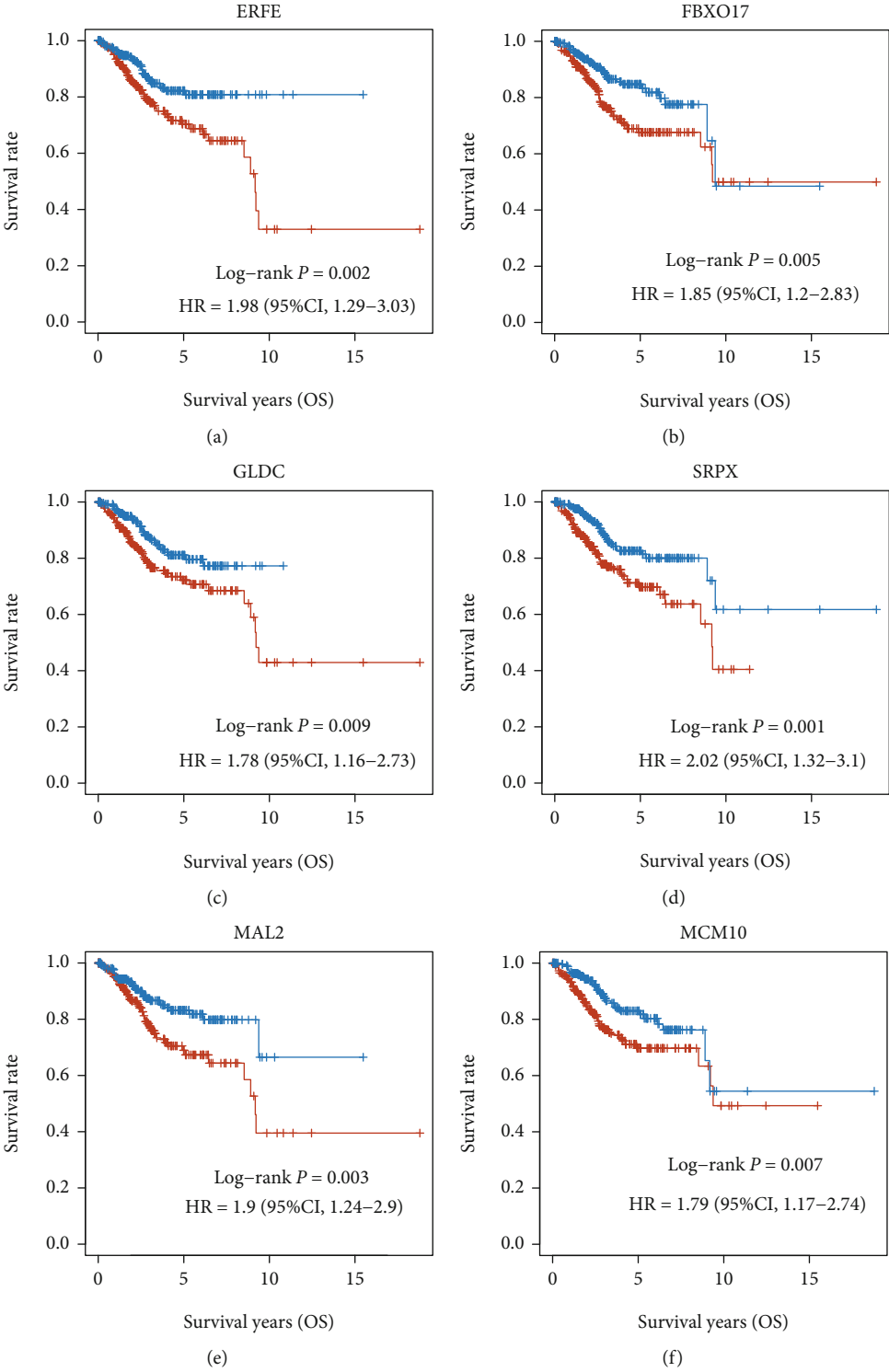


FIGURE 4: Continued.

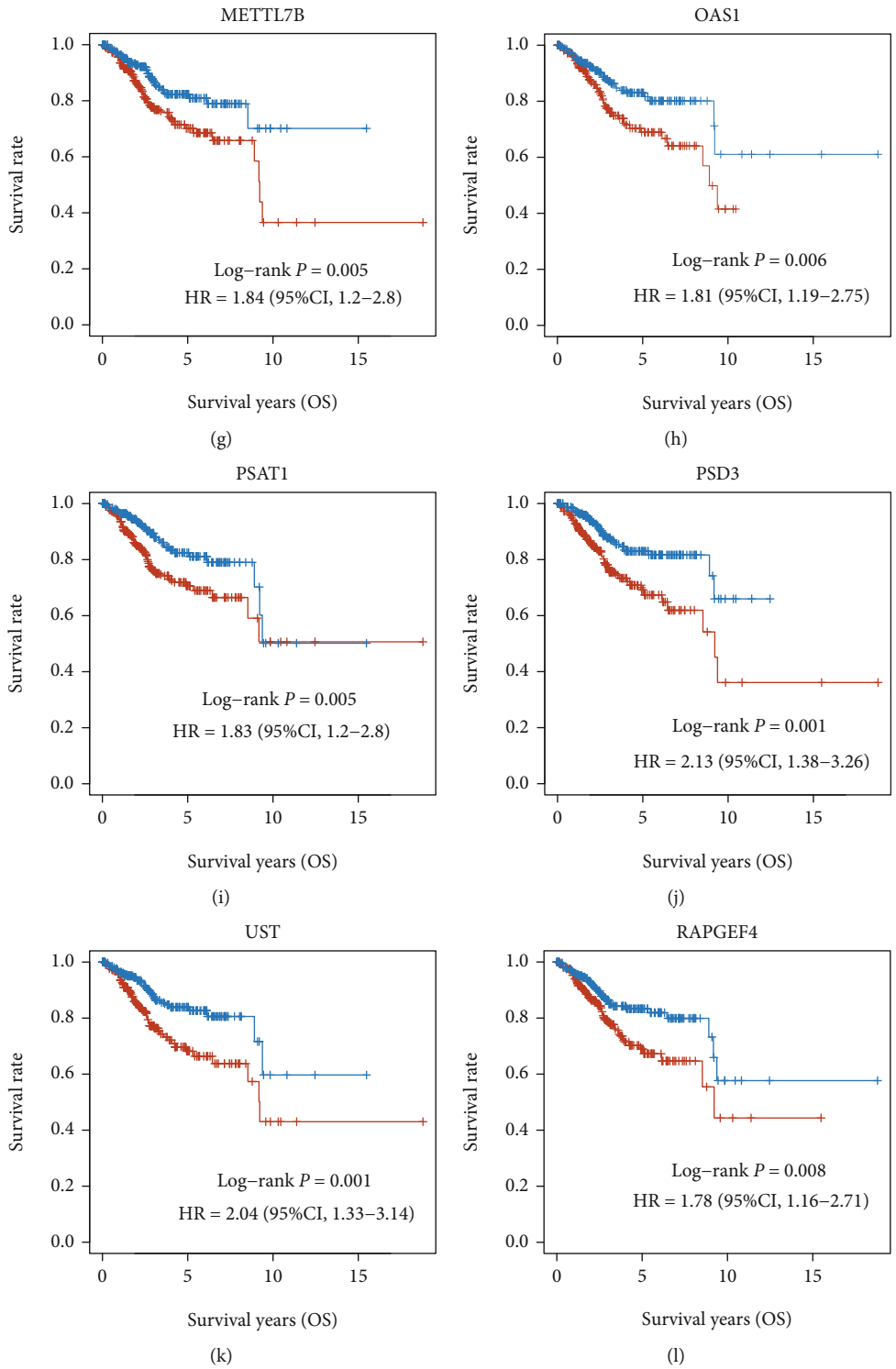


FIGURE 4: Continued.

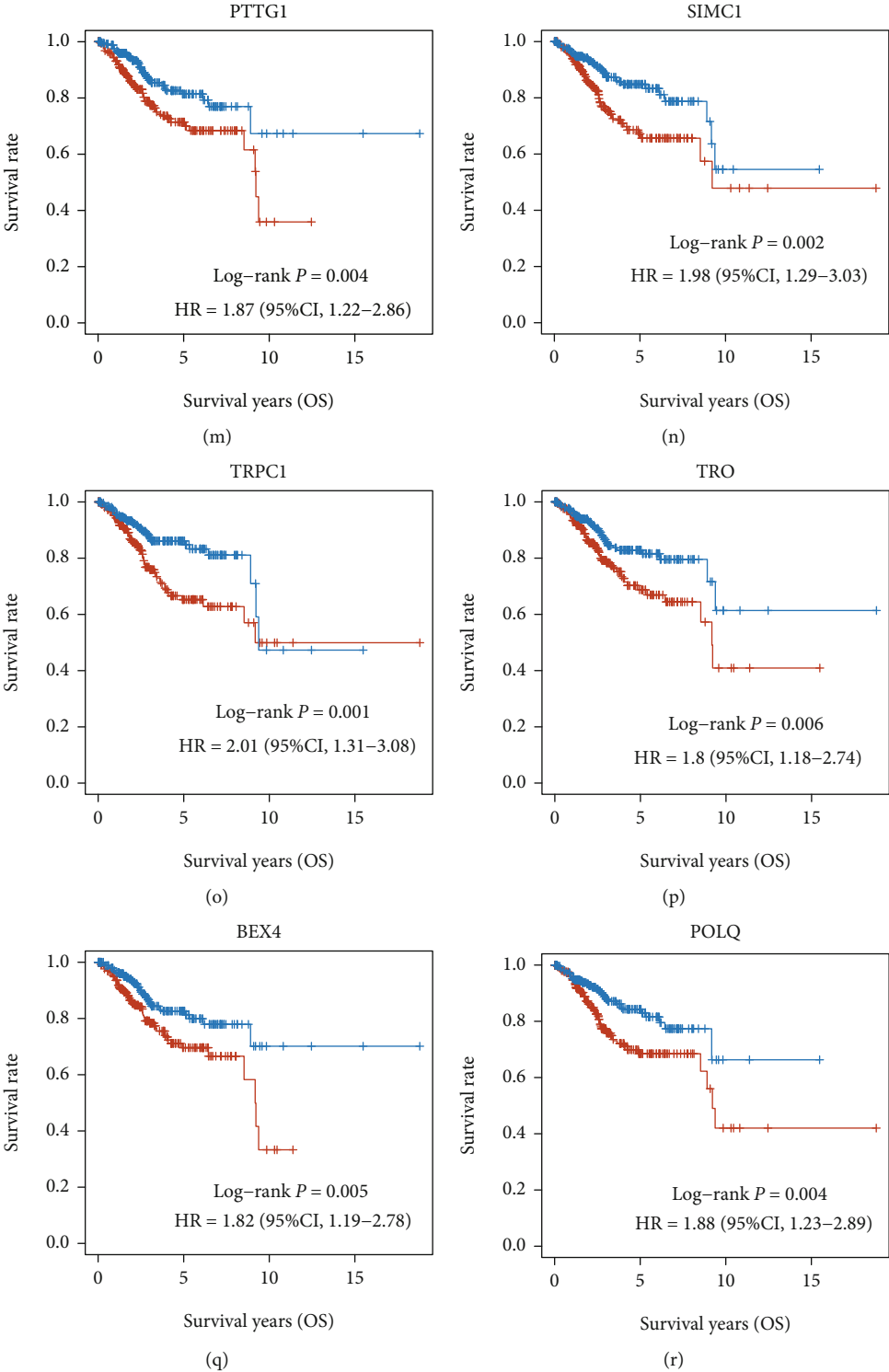


FIGURE 4: Continued.

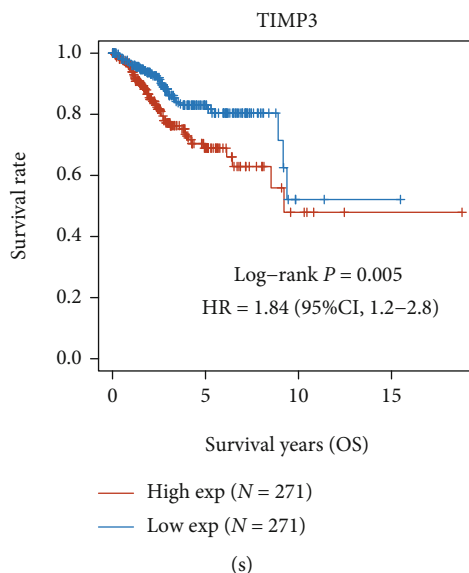


FIGURE 4: Identification of DEGs related to poor prognosis in EC. (a–s) Among these genes, higher expressions of BEX4, ERFE, FBXO17, GLDC, MAL2, MCM10, METTL7B, OAS1, POLQ, PSAT1, PSD3, PTTG1, RAPGEF4, SIMC1, SRPX, TIMP3, TRO, TRPC1, and UST were correlated to shorter OS time in patients with EC.

the DEG expression with the overall survival (OS) time in EC. Finally, we identified 30 DEGs that were related to the prognosis of EC, including KCNK6, IL32, FAM189A2, WFS1, GREB1, WFDC1, PGR, PAMR1, TRPC6, ADAM28, ANKRD22, GLDC, RAPGEF4, MCM10, TRO, OAS1, BEX4, PSAT1, METTL7B, TIMP3, FBXO17, PTTG1, POLQ, MAL2, SIMC1, ERFE, TRPC1, SRPX, UST, and PSD3. Among these genes, higher expressions of BEX4, ERFE, FBXO17, GLDC, MAL2, MCM10, METTL7B, OAS1, POLQ, PSAT1, PSD3, PTTG1, RAPGEF4, SIMC1, SRPX, TIMP3, TRO, TRPC1, and UST were correlated to shorter OS time in patients with EC (Figures 4(a)–4(s)). However, higher expressions of WFS1, GREB1, FAM189A2, ANKRD22, WFDC1, TRPC6, KCNK6, IL32, PGR, PAMR1, and ADAM28 were correlated to longer OS time in patients with EC (Figures 5(a)–5(k)).

3.4. Establishing a Prognostic Gene Model in the TCGA Cohort. We utilized the least absolute shrinkage and selection operator (LASSO) Cox regression analysis to establish the prognostic gene model. Figures 6(a) and 6(b) revealed a 17-gene signature constructed in the light of the optimum λ value. We calculated the risk score as follows: risk score = $(4e - 04) * MAL2 + (-0.0263) * ANKRD22 + (0.0493) * METTL7B + (0.0688) * IL32 + (0.0022) * ERFE + (0.01) * OAS1 + (0.0745) * TRPC1 + (0.1564) * SRPX + (0.4778) * RAPGEF4 + (0.0496) * PSD3 + (0.0383) * SIMC1 + (-0.3016) * TRPC6 + (-0.2001) * WFS1 + (-0.0341) * PGR + (-0.0821) * PAMR1 + (-0.0912) * KCNK6 + (-0.0813) * FAM189A2$. 543 patients with EC were divided equally into the low-risk group and the high-risk group on the basis of the median score calculated by the risk score formula. Compared to patients in the low-risk group, those in the high-risk group displayed a larger death toll and a shorter survival time (Figure 6(c)). Our data revealed that an obviously lower OS time was observed

in the high-risk group of EC patients, in comparison with the low-risk group of EC patients by Kaplan-Meier Plotter analysis (Figure 6(d)). We applied time-dependent receiver operating characteristic (ROC) analysis to assess the sensitivity and specificity of the prognostic model. And our results indicated that the area under the ROC curve (AUC) was 0.757 for 1-year, 0.758 for 3-year, 0.798 for 5-year, and 0.735 for 10-year survival (Figure 6(e)).

3.5. Genetic Alteration Differences of Prognostic Genes in EC Patients. Furthermore, genetic alteration of prognostic genes in EC was analyzed using the cBioPortal database, which included 726 patients from seven related studies. We observed that the mutation rates of prognostic genes for EC ranged from 0.8% to 10% for individual genes (MAL2, 5%; ANKRD22, 4%; METTL7B, 2.5%; IL32, 2.6%; ERFE, 0.8%; OAS1, 3%; TRPC1, 9%; SRPX, 6%; RAPGEF4, 10%; PSD3, 10%; SIMC1, 7%; TRPC6, 7%; WFS1, 6%; PGR, 7%; PAMR1, 7%; KCNK6, 4%; and FAM189A2, 5%). Among these genes, RAPGEF4 and PSD3 were found to have the highest mutation rate in EC, which are mutated in about 10% EC cases (Figure 7).

3.6. Validation of 17 Prognosis-Related Hub Gene Expressions in EC. For verification of the bioinformatics analysis data in-depth, UALCAN databases were used to confirm our findings. As presented in Figure 7, compared to normal samples, OAS1, MAL2, ANKRD22, METTL7B, and IL32 were dramatically upregulated in EC samples, whereas TRPC1, SRPX, RAPGEF4, PSD3, SIMC1, TRPC6, WFS1, PGR, PAMR1, KCNK6, and FAM189A2 were greatly downregulated in EC samples (Figures 8(a)–8(o)).

We also analyzed the correlation among these 17 prognosis-related hub genes in EC. Our results showed that the expressions of the 17 prognosis-related hub genes were

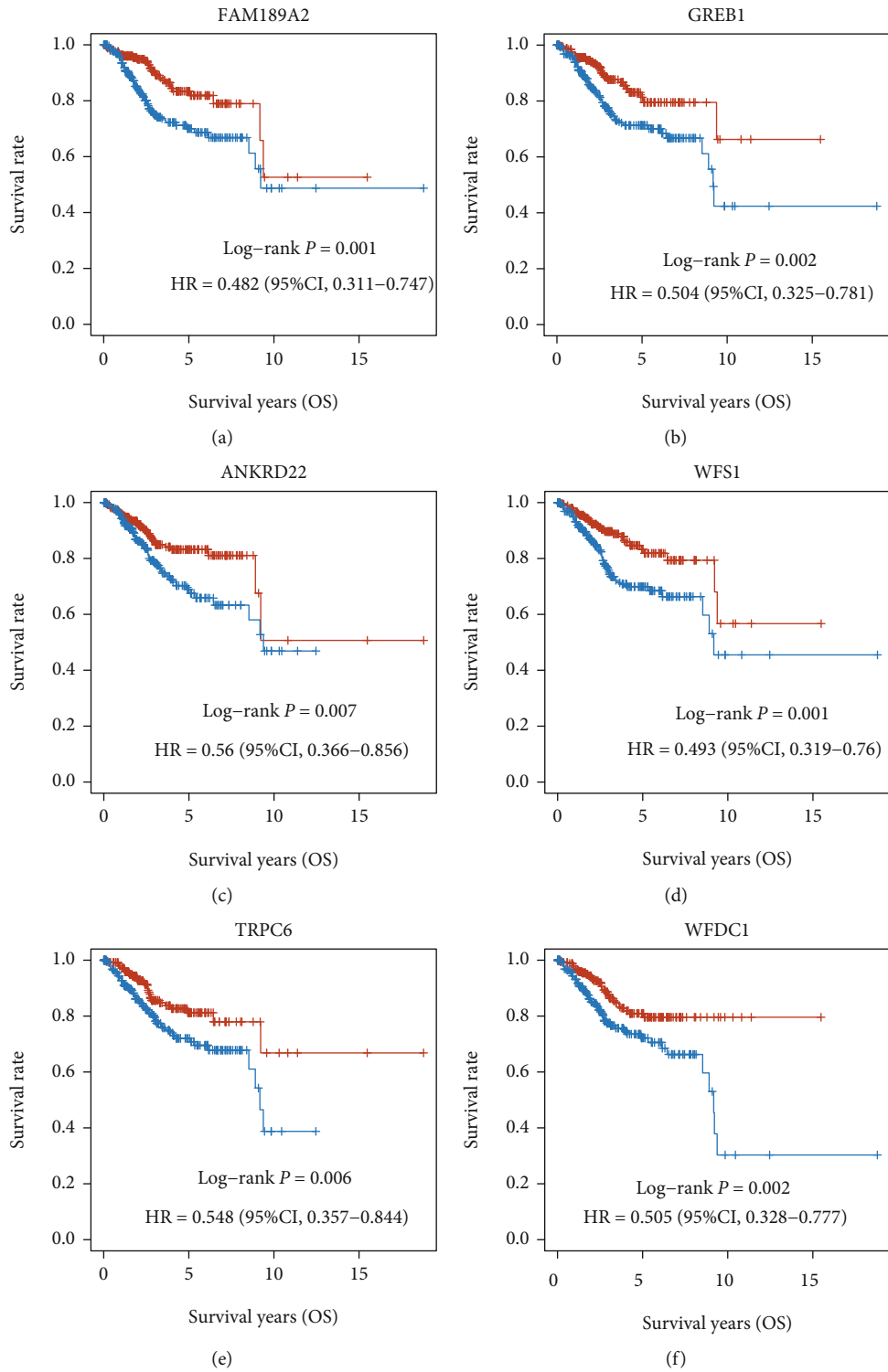


FIGURE 5: Continued.

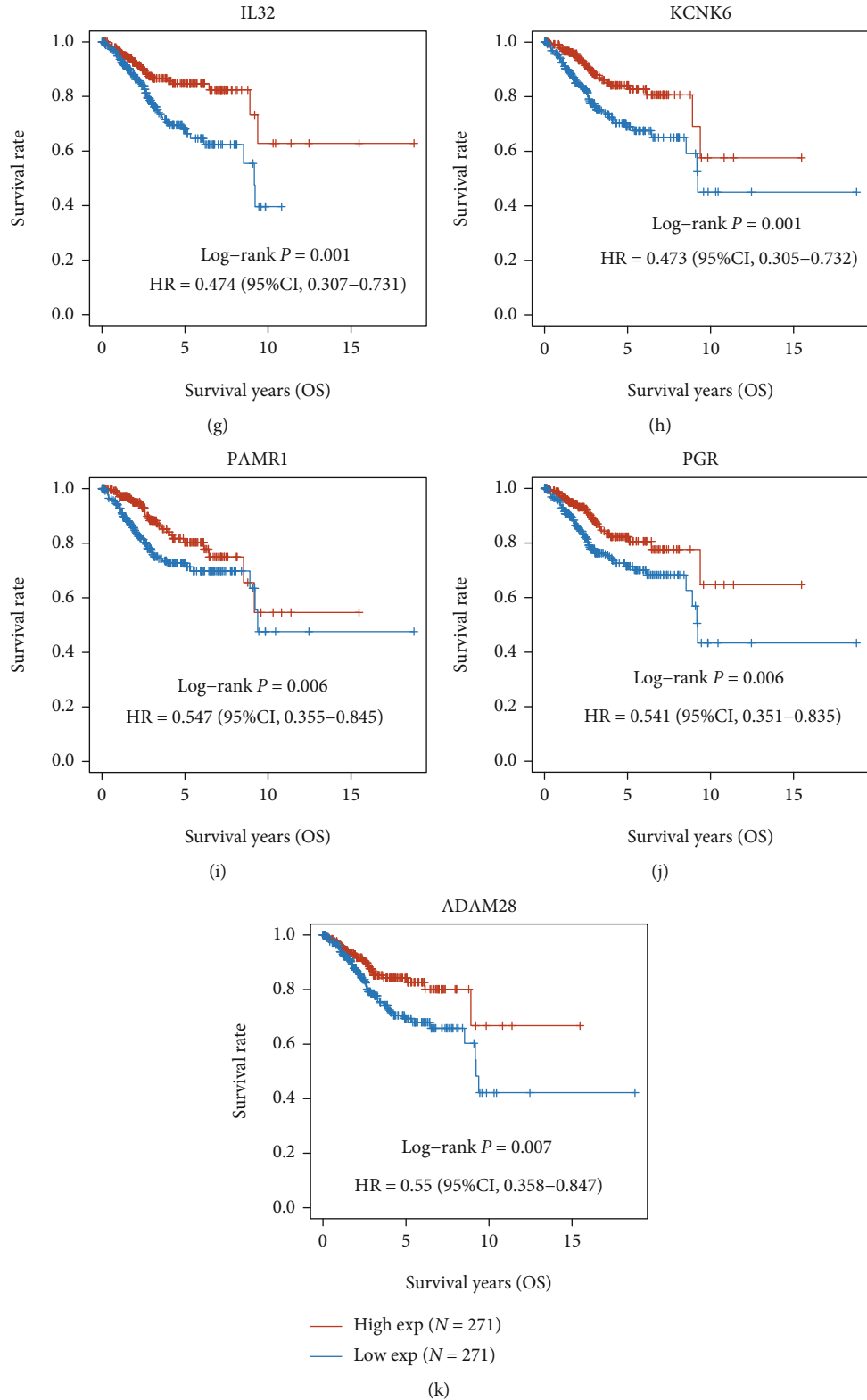


FIGURE 5: Identification of DEGs related to good prognosis in EC. (a–k) Higher expressions of WFS1, GREB1, FAM189A2, ANKRD22, WFDC1, TRPC6, KCNK6, IL32, PGR, PAMR1, and ADAM28 were correlated to longer OS time in patients with EC.

significantly correlated based on Pearson correlation. The most significantly negatively correlated gene pairs included FAM189A2-MAL2, MAL2-FAM189A2, TRPC6-OAS1,

OAS1-TRPC6, WFS1-ANKRD22, and ANKRD22-WFS1. And the most significantly positively correlated gene pairs included SIMC1-MAL2, MAL2-SIMC1, PGR-WFS1, WFS1-

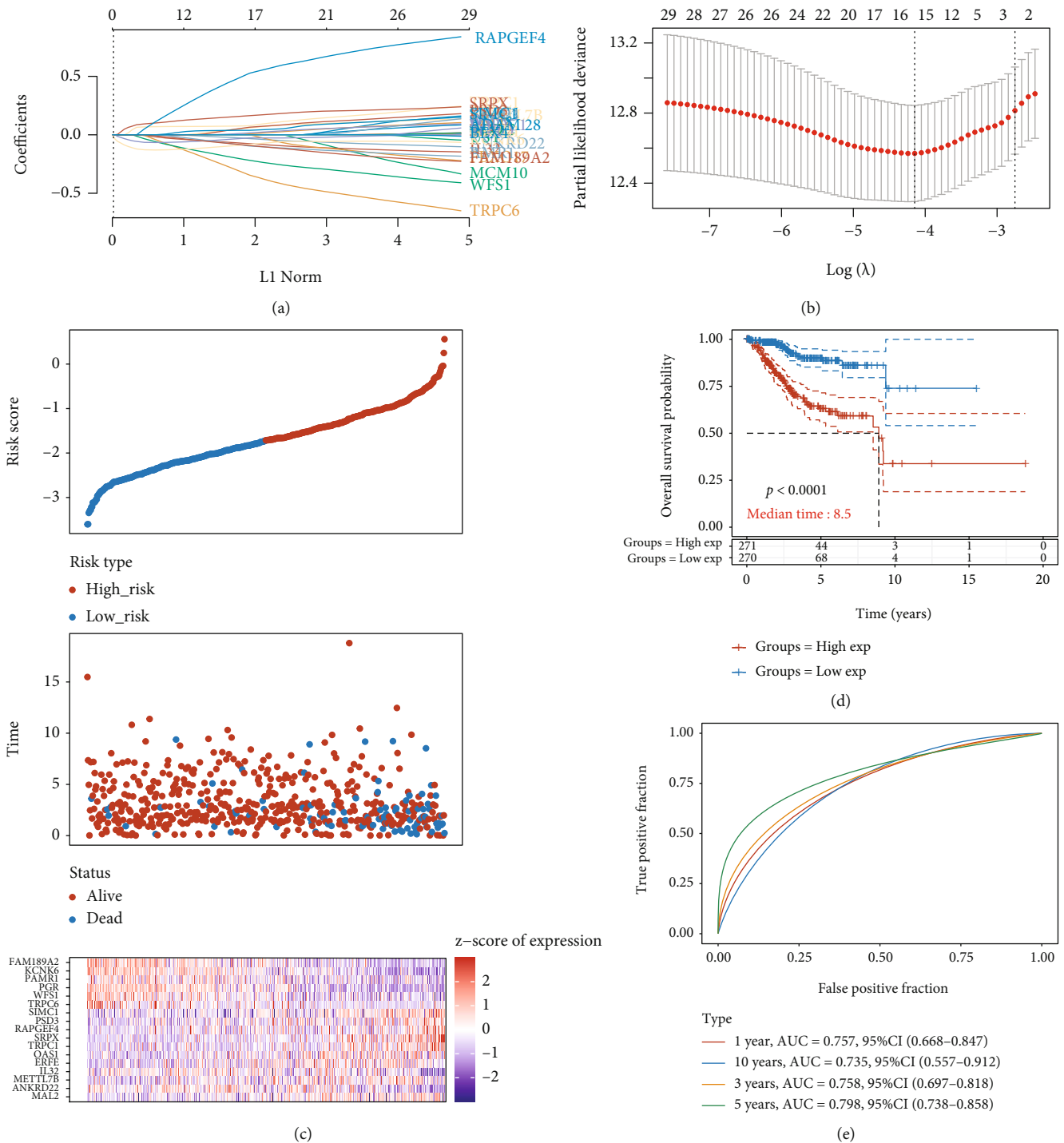


FIGURE 6: Establishing a prognostic gene model in the TCGA cohort. (a) LASSO coefficients profiles of 30 prognostic genes in EC. (b) LASSO regression with tenfold cross-validation obtained 17 prognostic genes using minimum lambda value. (c) 543 patients with EC were divided equally into low-risk group and high-risk group on the basis of the median score calculated by the risk score formula. (d) Lower OS time was observed in the high-risk group of EC patients, in comparison with the low-risk group of EC patients by Kaplan-Meier Plotter analysis. (e) Time-dependent receiver operating characteristic (ROC) analysis to assess the sensitivity and specificity of the prognostic model.

PGR, RAPGEF4-TRPC1, TRPC1-RAPGEF4, RAPGEF4-SRPX, SRPX-RAPGEF4, IL32-ANKRD22, ANKRD22-IL32, FAM189A2-PGR, PGR-FAM189A2, FAM189A2-KCNK6, KCNK6-FAM189A2, SRPX-TRPC1, TRPC1-SRPX, TRPC6-

SRPX, SRPX-TRPC6, PAMR1-RAPGEF4, RAPGEF4-PAMR1, ERFE-METTL7B, METTL7B-ERFE, FAM189A2-WFS1, WFS1-FAM189A2, PSD3-RAPGEF4, RAPGEF4-PSD3, OAS1-MAL2, and MAL2-OAS1 (Figure 9).

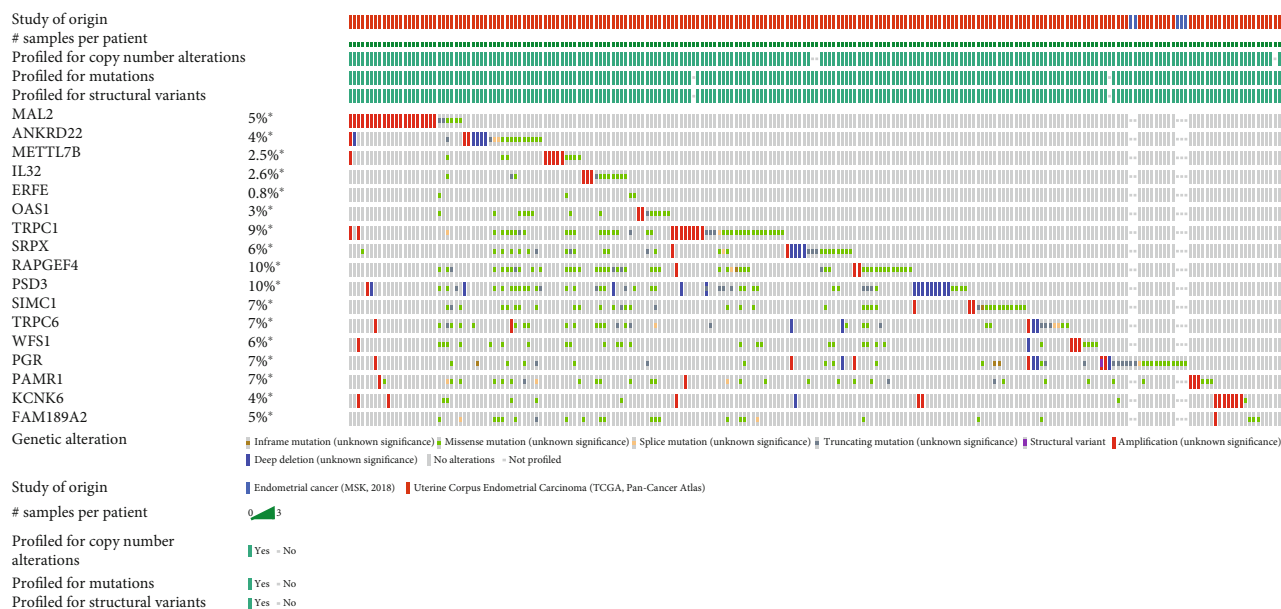


FIGURE 7: Genetic alteration differences of prognostic genes in EC patients. The mutation rates of prognostic genes for EC ranged from 0.8% to 10% for individual genes (MAL2, 5%; ANKRD22, 4%; METTL7B, 2.5%; IL32, 2.6%; ERFE, 0.8%; OAS1, 3%; TRPC1, 9%; SRPX, 6%; RAPGEF4, 10%; PSD3, 10%; SIMC1, 7%; TRPC6, 7%; WFS1, 6%; PGR, 7%; PAMR1, 7%; KCNK6, 4%; and FAM189A2, 5%).

4. Discussion

Emerging studies revealed that the occurrence of EC resulted from the abnormally expressed multiple carcinoma-related genes [29, 30], amid which have been shown to display a relationship to EC's susceptibility and progression [29, 30]. Many molecular biology methods have been used to identify biomarkers of cancers [31–34]. Nevertheless, the majority of them merely concentrated on a single genetic factor, limiting these biomarkers' reliability.

Our current study discovered more EC-related genes with differential expression than previous researches, indicating they may play importantly in the mechanism of EC. Our data revealed 114 common genes with upregulation and 308 common genes with downregulation in EC samples in comparison with normal samples. Bioinformatics analysis showed that these genes were significantly correlated to multiple key signaling in EC, such as the cGMP-PKG signaling pathway. Furthermore, we identified that 30 DEGs were related to the prognosis of EC, comprising KCNK6, IL32, FAM189A2, WFS1, GREB1, WFDC1, PGR, PAMR1, TRPC6, ADAM28, ANKRD22, GLDC, RAPGEF4, MCM10, TRO, OAS1, BEX4, PSAT1, METTL7B, TIMP3, FBXO17, PTTG1, POLQ, MAL2, SIMC1, ERFE, TRPC1, SRPX, UST, and PSD3.

Here, we conducted GO and KEGG analyses of the involved biological processes and pathways related to these DEGs in EC's progression. The pathway analysis of these DEGs showed that the interconnected network of genes participated in the cyclic guanosine monophosphate- (cGMP-) protein kinase G (PKG) signaling pathway. As previously described, the contractility of the uterine smooth muscle is of importance for the periodic shedding of the endometrial lining and the expulsion of the fetus during parturition. There was one study showing that the nitric oxide- (NO-)

cGMP signaling pathway participates in the relaxation of the smooth muscle. cGMP-dependent PKG, which is essential for reducing cytoplasmic calcium and muscle tension, was the downstream target of the NO-cGMP pathway [35]. PKG was responsible for controlling the uterine smooth muscle tone which produced force near menstruation and regulated blood flow to the endometrial lining. The above data together confirmed that PKG functioned crucially in controlling the contraction of the uterine and vascular smooth muscle during the periodical menstruation [35]. PI3K-AKT signaling is one of the most important pathways in our study. PI3K-AKT signaling could be antagonized by the tumor suppressor phosphatase and tensin homolog (PTEN) which was reported to be usually mutated in several sorts of neoplasms, such as the endometrium, skin, brain, and prostate cancers [36–38]. PTEN has a powerful phosphatase activity, which is the best characterized physiological function leading to the tumor suppressor function of PTEN.

The IL17 signaling pathway was also one of the important pathways detected here. In inflammatory mediators, more and more evidence emphasizes the role of the interleukin-17 (IL17) cytokine family in malignant diseases. IL17 is becoming a crucial cytokine to promote and develop carcinomas by maintaining a chronic inflammatory microenvironment which is conducive to tumor formation [39, 40]. While IL17 may regulate chemokines and cytokines in gynecologic cancers, Toll-like receptors may function importantly in the gynecologic carcinomas' development via triggering an inflammatory response and cell survival in the microenvironment of the tumor [41].

Our study generated a signature featuring 17 prognosis-related genes (MAL2, ANKRD22, METTL7B, IL32, ERFE, OAS1, TRPC1, SRPX, RAPGEF4, PSD3, SIMC1, TRPC6, WFS1, PGR, PAMR1, KCNK6, and FAM189A2) and

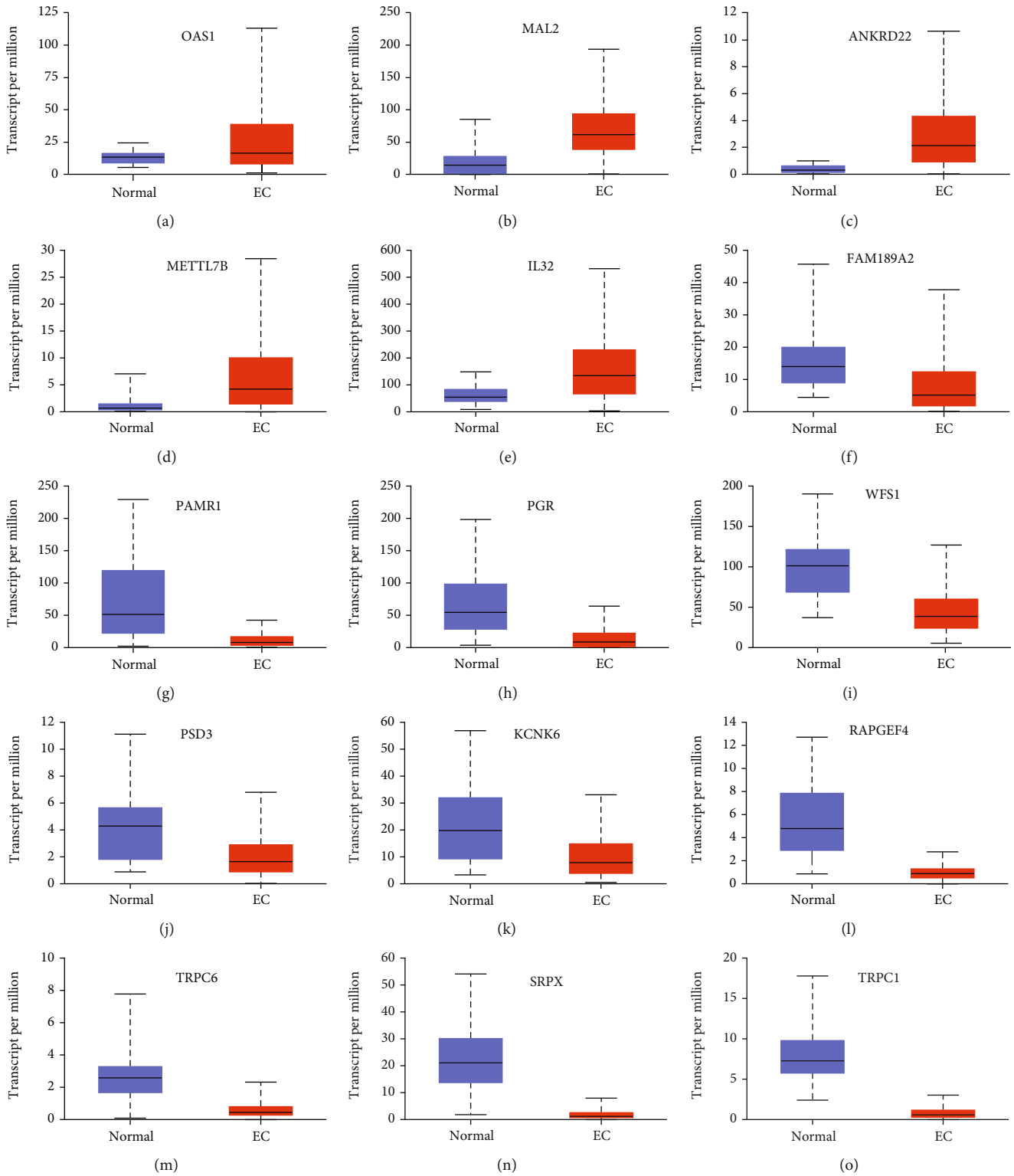


FIGURE 8: Validation of 17 prognosis-related hub gene expressions in EC.

demonstrated that they were utilized as predictors of OS in EC patients. We obtained many genes that were previously reported to be involved in endometriosis patients or endometrial stromal cells. For instance, the members of the transient receptor potential (TRP) ion channel superfamily, known as having the calcium permeability, has become pivotal modu-

lators in the endometrium. Previous studies have shown that TRPC1 and TRPC6 were highly expressed in the entire endometrium during the periodical menstruation. Additionally, TRPV2, TRPV4, TRPC1/4, and TRPC6 were found in human endometrial stromal cells (hESCs) from patients with endometriosis [25]. Previous reports suggested that

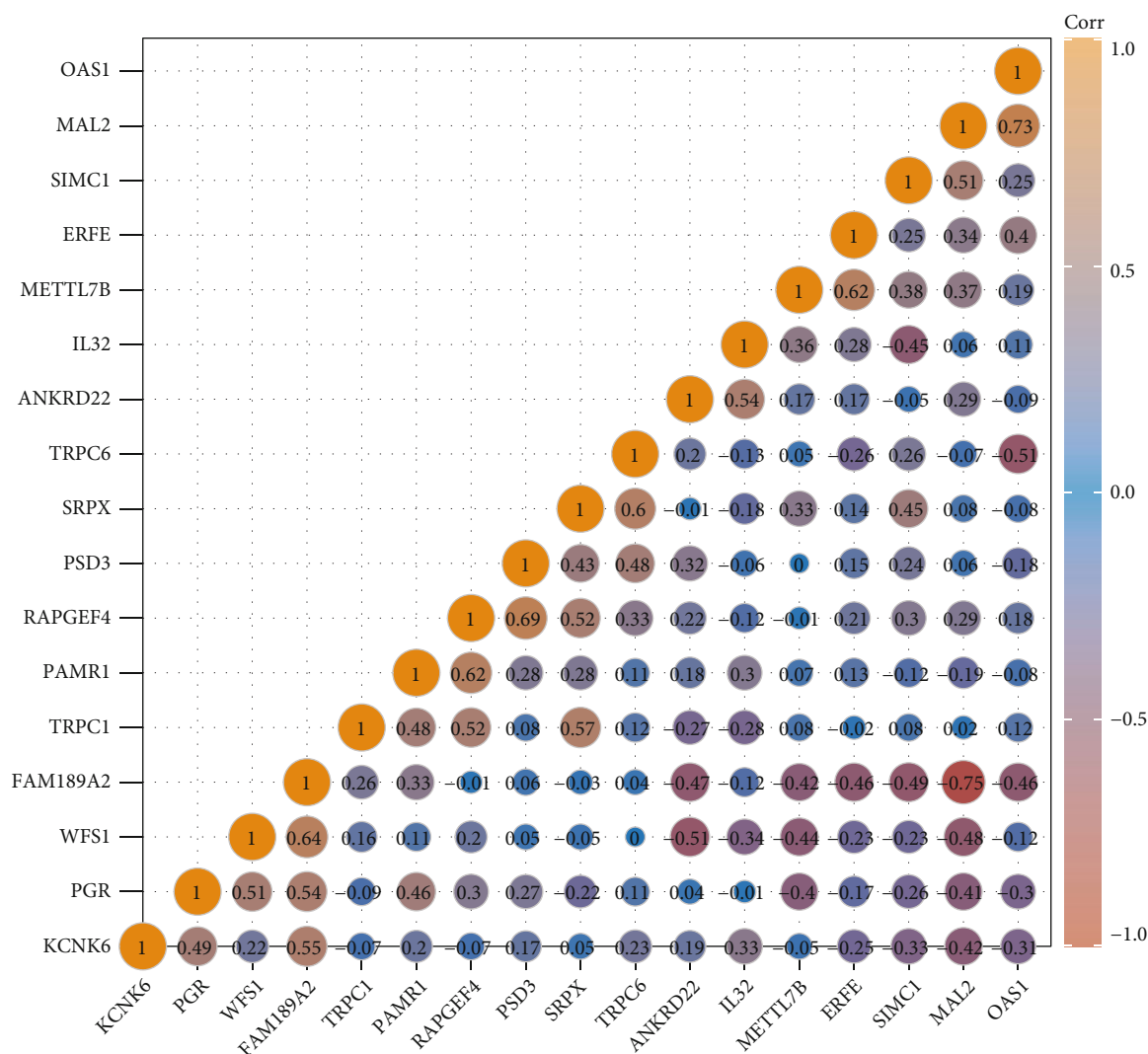


FIGURE 9: 17 prognosis-related hub gene expressions were correlated to each other in EC. The expressions of 17 prognosis-related hub genes were significantly correlated based on Pearson correlation.

the cAMP2-activated exchange protein (EPAC2, RAPGEF4), another cAMP mediator, took part in endometrial stromal cell differentiation via regulating calreticulin (CALR) expression [42]. Compared with the control group, the level of interleukin-32 (IL32) in peritoneal fluid (PF) in women with endometriosis was significantly higher. The endometrial cells treated with IL32 in vitro significantly enhanced cell viability, proliferation, and invasion capabilities [43]. In silico methods can distinguish many key genes related to the maintenance of telomeres, which were unknown to the occurrence and prognosis of EC before, including WFS1. Prognostic biomarkers of EC are essential for ameliorating risk assessment before and after surgery and making guided- treatment decisions. PGR and PTEN were one of the most clinically valuable EC prognostic biomarkers. In our research, we showed that significant genes with upregulation in EC samples included OAS1, MAL2, ANKRD22, METTL7B, and IL32 after comparison with normal samples. Obvious genes with downregulation in EC samples comprised TRPC1, SRPX, RAPGEF4, PSD3, SIMC1,

TRPC6, WFS1, PGR, PAMR1, KCN6, and FAM189A2. And correlation analysis showed that our results showed that the expressions of 17 prognosis-related hub genes were significantly correlated based on Pearson correlation.

However, there are still several limitations in our literature. Firstly, the number of samples is limited, which should be enlarged in the following study, and all the samples are from public datasets; our own data is also very important. Secondly, we need to conduct more researches to expound the function and potential mechanisms of these promising biomarkers in the progression of EC.

5. Conclusion

In summary, our findings revealed 114 common genes with upregulation and 308 common genes with downregulation in EC samples relative to normal ones. Bioinformatics analysis showed these genes exhibited a significant relationship to multiple signaling and biological processes, such as the cGMP-PKG signaling pathway and PI3K-AKT signaling.

Moreover, we constructed a 17-gene signature to make a prediction of OS in EC patients using the TCGA cohorts. We collectively supplied a potential gene signature for the prediction of EC patients' prognosis.

Data Availability

All the data and material were presented in GSE106191 and TCGA (<https://portal.gdc.cancer.gov/>).

Conflicts of Interest

The authors declare that there is no conflict of interests.

Authors' Contributions

Anna Wang is a co-first author.

References

- [1] D. W. Bell and L. H. Ellenson, "Molecular genetics of endometrial carcinoma," *Annual Review of Pathology*, vol. 14, no. 1, pp. 339–367, 2019.
- [2] C. Gu, X. Shi, C. Dai et al., "RNA m⁶A modification in cancers: molecular mechanisms and potential clinical applications," *The Innovation*, vol. 1, no. 3, p. 100066, 2020.
- [3] C. Gaber, R. Meza, J. J. Ruterbusch, and M. L. Cote, "Endometrial cancer trends by race and histology in the USA: projecting the number of new cases from 2015 to 2040," *Journal of racial and ethnic health disparities*, vol. 4, no. 5, pp. 895–903, 2016.
- [4] F. S. Saghir, I. M. Rose, A. Z. Dali, Z. Shamsuddin, A. R. Jamal, and N. M. Mokhtar, "Gene expression profiling and cancer-related pathways in type I endometrial carcinoma," *International Journal of Gynecological Cancer*, vol. 20, no. 5, pp. 724–731, 2010.
- [5] T. M. Kim, P. W. Laird, and P. J. Park, "The landscape of microsatellite instability in colorectal and endometrial cancer genomes," *Cell*, vol. 155, no. 4, pp. 858–868, 2013.
- [6] F. Amant, P. Moerman, P. Neven, D. Timmerman, E. van Limbergen, and I. Vergote, "Endometrial cancer," *Lancet*, vol. 366, no. 9484, pp. 491–505, 2005.
- [7] S. F. Lax, "Molecular genetic pathways in various types of endometrial carcinoma: from a phenotypical to a molecular-based classification," *Virchows Archiv*, vol. 444, no. 3, pp. 213–223, 2004.
- [8] D. Black, R. A. Soslow, D. A. Levine et al., "Clinicopathologic significance of defective DNA mismatch repair in endometrial carcinoma," *Journal of Clinical Oncology*, vol. 24, no. 11, pp. 1745–1753, 2006.
- [9] M. P. Hayes, H. Wang, R. Espinal-Witter et al., "PIK3CA and PTEN mutations in uterine endometrioid carcinoma and complex atypical hyperplasia," *Clinical Cancer Research*, vol. 12, no. 20, pp. 5932–5935, 2006.
- [10] S. F. Lax, B. Kendall, H. Tashiro, R. J. C. Slebos, and L. H. Ellenson, "The frequency of p53, K-ras mutations, and microsatellite instability differs in uterine endometrioid and serous carcinoma: evidence of distinct molecular genetic pathways," *Cancer*, vol. 88, no. 4, pp. 814–824, 2000.
- [11] P. W. Schlosshauer, L. H. Ellenson, and R. A. Soslow, "β-Catenin and E-cadherin expression patterns in high-grade endometrial carcinoma are associated with histological subtype," *Modern Pathology*, vol. 15, no. 10, pp. 1032–1037, 2002.
- [12] S. A. Saidi, C. M. Holland, D. P. Kreil et al., "Independent component analysis of microarray data in the study of endometrial cancer," *Oncogene*, vol. 23, no. 39, pp. 6677–6683, 2004.
- [13] J. I. Risinger, G. L. Maxwell, G. V. Chandramouli et al., "Microarray analysis reveals distinct gene expression profiles among different histologic types of endometrial cancer," *Cancer Research*, vol. 63, no. 1, pp. 6–11, 2003.
- [14] S. Engebretsen and J. Bohlin, "Statistical predictions with glmnet," *Clinical Epigenetics*, vol. 11, no. 1, p. 123, 2019.
- [15] C. Gu, X. Shi, W. Qiu et al., "Comprehensive analysis of the prognostic role and mutational characteristics of m6A-related genes in lung squamous cell carcinoma," *Frontiers in Cell and Development Biology*, vol. 9, p. 661792, 2021.
- [16] I. Diboun, L. Wernisch, C. A. Orengo, and M. Koltzenburg, "Microarray analysis after RNA amplification can detect pronounced differences in gene expression using limma," *BMC Genomics*, vol. 7, no. 1, p. 252, 2006.
- [17] C. Gu, J. Chen, X. Dang et al., "Hippo pathway core genes based prognostic signature and immune infiltration patterns in lung squamous cell carcinoma," *Frontiers in oncology*, vol. 11, no. 1486, 2021.
- [18] C. Gu, X. Shi, Z. Huang et al., "A comprehensive study of construction and analysis of competitive endogenous RNA networks in lung adenocarcinoma," *Biochimica et Biophysica Acta (BBA)-Proteins and Proteomics*, vol. 1868, no. 8, p. 140444, 2020.
- [19] B. T. Sherman and R. A. Lempicki, "Systematic and integrative analysis of large gene lists using DAVID bioinformatics resources," *Nature Protocols*, vol. 4, no. 1, pp. 44–57, 2009.
- [20] X. Shi, T. Huang, J. Wang et al., "Next-generation sequencing identifies novel genes with rare variants in total anomalous pulmonary venous connection," *eBioMedicine*, vol. 38, pp. 217–227, 2018.
- [21] J. Liu, S. Nie, J. Liang et al., "Competing endogenous RNA network of endometrial carcinoma: a comprehensive analysis," *Journal of Cellular Biochemistry*, vol. 120, no. 9, pp. 15648–15660, 2019.
- [22] C. Gu, Z. Huang, X. Chen et al., "TEAD4 promotes tumor development in patients with lung adenocarcinoma via ERK signaling pathway," *Biochimica et Biophysica Acta - Molecular Basis of Disease*, vol. 1866, no. 12, p. 165921, 2020.
- [23] X. Pan, C. Gu, R. Wang, H. Zhao, J. Yang, and J. Shi, "Transmanubrial osteomuscular sparing approach for resection of cervico-thoracic lesions," *Journal of Thoracic Disease*, vol. 9, no. 9, pp. 3062–3068, 2017.
- [24] C. Gu, R. Wang, X. Pan et al., "Comprehensive study of prognostic risk factors of patients underwent pneumonectomy," *Journal of Cancer*, vol. 8, no. 11, pp. 2097–2103, 2017.
- [25] Y. Sun, C. Gu, J. Shi et al., "Reconstruction of mediastinal vessels for invasive thymoma: a retrospective analysis of 25 cases," *Journal of Thoracic Disease*, vol. 9, no. 3, pp. 725–733, 2017.
- [26] C. Chen, X. Zhang, C. Gu et al., "Surgery performed at night by continuously working surgeons contributes to a higher incidence of intraoperative complications in video-assisted thoracoscopic pulmonary resection: a large monocentric retrospective study," *European Journal of Cardio-Thoracic Surgery*, vol. 57, no. 3, pp. 447–454, 2020.
- [27] C. Gu, X. Pan, R. Wang et al., "Analysis of mutational and clinicopathologic characteristics of lung adenocarcinoma with

- clear cell component,” *Oncotarget*, vol. 7, no. 17, pp. 24596–24603, 2016.
- [28] J. Chen, C. Gu, X. Chen et al., “Clinicopathological and prognostic analyses of 86 resected pulmonary lymphoepithelioma-like carcinomas,” *Journal of Surgical Oncology*, vol. 123, no. 2, pp. 544–552, 2021.
- [29] J. Liu, M. A. Eckert, B. T. Harada et al., “m⁶A mRNA methylation regulates AKT activity to promote the proliferation and tumorigenicity of endometrial cancer,” *Nature Cell Biology*, vol. 20, no. 9, pp. 1074–1083, 2018.
- [30] Y. Xiao, L. Jin, C. Deng et al., “Inhibition of PFKFB3 induces cell death and synergistically enhances chemosensitivity in endometrial cancer,” *Oncogene*, vol. 40, no. 8, pp. 1409–1424, 2021.
- [31] R. C. Arend, B. A. Jones, A. Martinez, and P. Goodfellow, “Endometrial cancer: molecular markers and management of advanced stage disease,” *Gynecologic Oncology*, vol. 150, no. 3, pp. 569–580, 2018.
- [32] C. Gu and C. Chen, “Methylation in lung cancer: a brief review,” *Methods in Molecular Biology*, vol. 2204, pp. 91–97, 2020.
- [33] Y. Bao, C. Gu, H. Xie et al., “Comprehensive study of neoadjuvant targeted therapy for resectable non-small cell lung cancer,” *Annals of Translational Medicine*, vol. 9, no. 6, p. 493, 2021.
- [34] Y. Yuan, Q. Huang, C. Gu, and H. Chen, “Disease-free survival improved by use of adjuvant EGFR tyrosine kinase inhibitors in resectable non-small cell lung cancer: an updated meta-analysis,” *Journal of Thoracic Disease*, vol. 9, no. 12, pp. 5314–5321, 2017.
- [35] S. H. Francis, J. L. Busch, J. D. Corbin, and D. Sibley, “cGMP-dependent protein kinases and cGMP phosphodiesterases in nitric oxide and cGMP action,” *Pharmacological Reviews*, vol. 62, no. 3, pp. 525–563, 2010.
- [36] H. Koike, M. Nozawa, M. A. de Velasco et al., “Conditional PTEN-deficient mice as a prostate cancer chemoprevention model,” *Asian Pacific Journal of Cancer Prevention*, vol. 16, no. 5, pp. 1827–1831, 2015.
- [37] M. Shi, X. Zhou, Z. Zhang et al., “A novel PI3K inhibitor displays potent preclinical activity against an androgen-independent and PTEN-deficient prostate cancer model established from the cell line PC3,” *Toxicology Letters*, vol. 228, no. 3, pp. 133–139, 2014.
- [38] X. Jiang, S. Chen, J. M. Asara, and S. P. Balk, “Phosphoinositide 3-kinase pathway activation in phosphate and tensin homolog (PTEN)-deficient prostate cancer cells is independent of receptor tyrosine kinases and mediated by the p110 β and p110 δ catalytic subunits,” *The Journal of Biological Chemistry*, vol. 285, no. 20, pp. 14980–14989, 2010.
- [39] L. Liu, F. Chen, A. Xiu, B. du, H. Ai, and W. Xie, “Identification of key candidate genes and pathways in endometrial cancer by integrated bioinformatical analysis,” *Asian Pacific Journal of Cancer Prevention*, vol. 19, no. 4, pp. 969–975, 2018.
- [40] H. A. Alshaker and K. Z. Matalka, “IFN- γ , IL-17 and TGF- β involvement in shaping the tumor microenvironment: the significance of modulating such cytokines in treating malignant solid tumors,” *Cancer Cell International*, vol. 11, no. 1, p. 33, 2011.
- [41] N. Hussein-zadeh and S. M. Davenport, “Role of toll-like receptors in cervical, endometrial and ovarian cancers: a review,” *Gynecologic Oncology*, vol. 135, no. 2, pp. 359–363, 2014.
- [42] K. Kusama, M. Yoshie, K. Tamura, K. Imakawa, and E. Tachikawa, “EPAC2-mediated calreticulin regulates LIF and COX2 expression in human endometrial glandular cells,” *Journal of Molecular Endocrinology*, vol. 54, no. 1, pp. 17–24, 2015.
- [43] M. Y. Lee, S. H. Kim, Y. S. Oh et al., “Role of interleukin-32 in the pathogenesis of endometriosis: in vitro, human and transgenic mouse data,” *Human Reproduction*, vol. 33, no. 5, pp. 807–816, 2018.

Research Article

miR-101-3p Serves as a Tumor Suppressor for Renal Cell Carcinoma and Inhibits Its Invasion and Metastasis by Targeting EZH2

Yunze Dong, Yuchen Gao, Tiancheng Xie, Huan Liu, Xiangcheng Zhan, and Yunfei Xu 

Department of Urology, Shanghai Tenth People's Hospital, School of Medicine in Tongji University, 301 Yanchang Road, Jing'an District, Shanghai 200072, China

Correspondence should be addressed to Yunfei Xu; xujiaoyao17570612@163.com

Received 31 March 2021; Accepted 24 June 2021; Published 8 July 2021

Academic Editor: Tao Huang

Copyright © 2021 Yunze Dong et al. This is an open access article distributed under the Creative Commons Attribution License, which permits unrestricted use, distribution, and reproduction in any medium, provided the original work is properly cited.

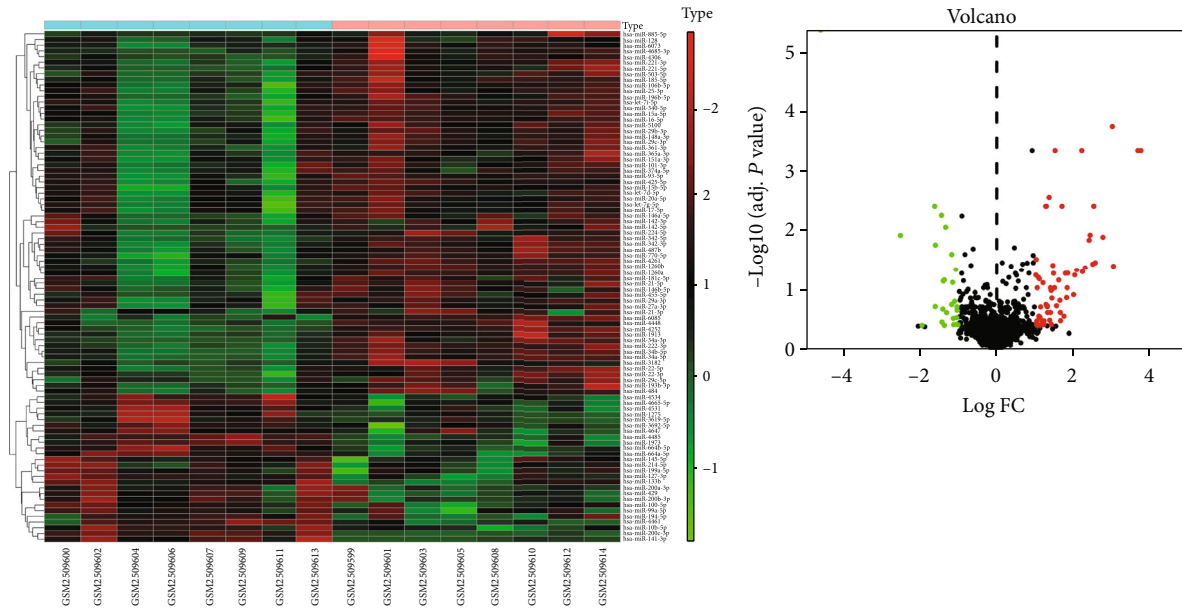
Background. The role of miRNAs in renal cell carcinoma (RCC) is not certain. We wanted to study the biological functions and potential mechanisms of miR-101-3p in RCC. **Methods.** miR-101-3p was inhibited in A498 and OSRC-2 (two RCC cell lines). We studied its effect on cell invasion and proliferation. Target EZH2 of miR-101-3p was designated by different methods, including luciferase functional analysis and Western blotting. The expression level of the target gene in treated cells was quantitatively analyzed by quantitative real-time polymerase chain reaction. In addition, induction of miR-101-3p to prevent tumor formation of A498 cells in mice was further studied. **Results.** The overexpression of miR-101-3p significantly inhibited the proliferation, migration, and invasion in two RCC cells. Western blotting and luciferase functional analysis indicated that miR-101-3p regulated the expression of EZH2 in two cell lines. Mice inoculated with A498 and OSRC-2 cells transfected with miR-101-3p mimics showed significantly smaller xenografts and weaker EZH2 expression levels than the control group. **Conclusions.** miR-101-3p inhibited RCC cell proliferation, migration, and invasion by targeting EZH2.

1. Introduction

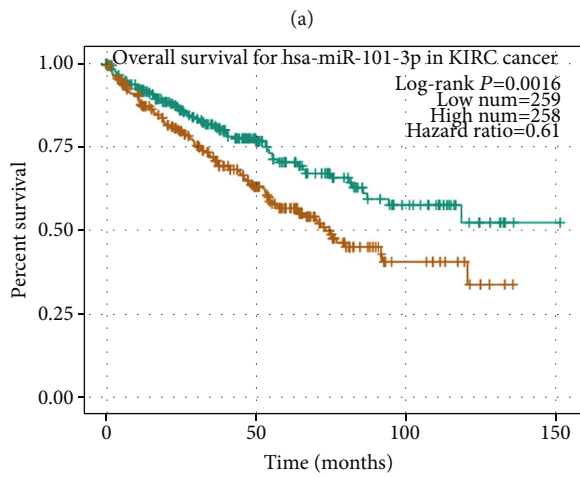
RCC is one of the most common malignancies of the urinary system [1], accounting for about 2%~3% of adult malignancies [2]. For localized and early-stage RCC, the best treatment is radical and partial nephrectomy, which has a 92.6% 5-year survival rate [3]. However, for metastatic RCC, the 5-year survival rate is expected to be very poor due to its resistance to radiotherapy and chemotherapy [4]. Although the advent of antiangiogenic drugs with tyrosine kinase inhibitors (TKI) has improved the prognosis of RCC, the associated resistance remains elusive [5]. It is important to uncover the mechanism of renal cancer and find potential prognostic biomarkers and therapeutic targets for renal cancer. Thus, we sought to find the molecular mechanism underlying RCC pathogenesis.

miRNA is a small nontranslated RNA that inhibits the expression of target genes through translation inhibition or transcriptional silencing [6]. Current studies have shown that

miRNAs can act on at least 30% of protein-coding genes [7]. With the continuous development of technology, various miRNAs have been identified and have been widely proven to play an important role in tumorigenesis. Among them, miR-101-3p has been declared to regulate cancer development by acting as a tumor suppressor or an oncogene in tumorigenesis. For example, Wang et al. found that miR-101-3p promotes apoptosis of oral cancer cells by targeting BICC1 [8]. Wu et al. reported that it diametrically targets SRF to inhibit HOX transcript antisense RNA- (HOTAIR-) induced proliferation of gastric cancer cells [9]. In hepatocellular carcinoma, the LINC00052/miR-101-3p axis inhibited cell proliferation and metastasis by targeting SOX9 [10]. In non-small-cell lung cancer (NSCLC), it inhibits the growth and metastasis of NSCLC by blocking the PI3K/Akt signaling pathway by targeting MALAT-1 [11]. However, until now, its roles and underlying molecular mechanisms in RCC progression still remain unknown and need to be elucidated.

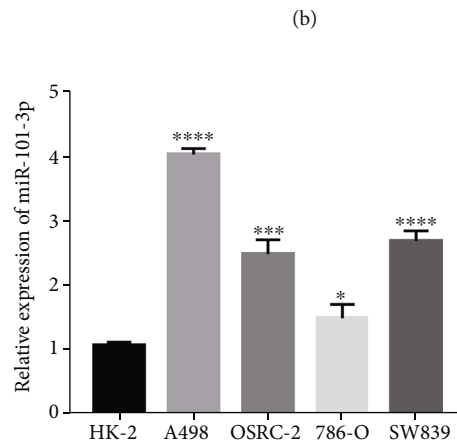


■ N
■ T



Group
 — High + (High, 1)
 — Low + (Low, 1)

(c)



(d)

FIGURE 1: Continued.

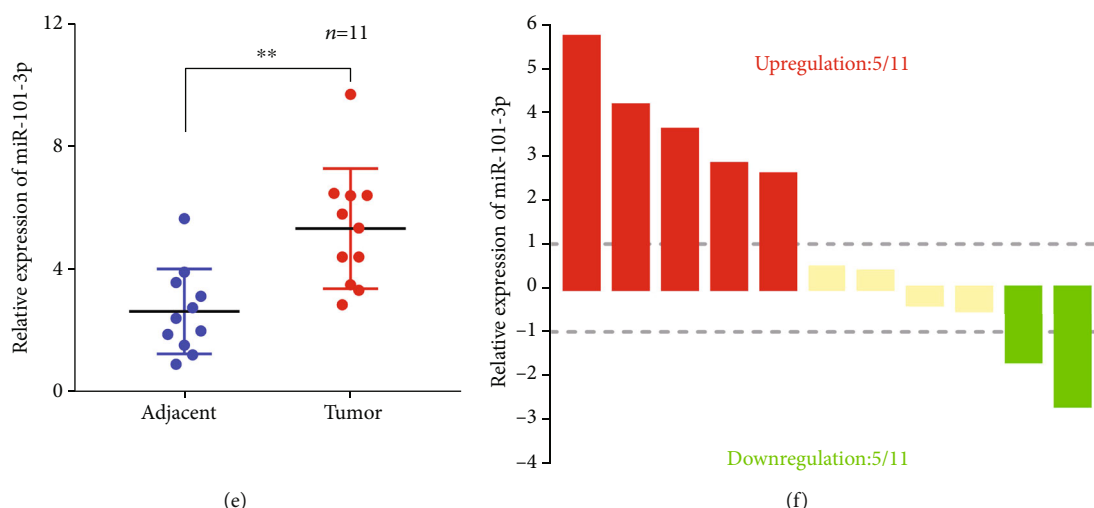


FIGURE 1: miR-101-3p was upregulated in RCC tissues and cell lines. (a, b) Expression level of miR-454 in the miRNA expression profiling array was presented by the clustered heat map and volcano plot. (c) Kaplan-Meier survival analyses indicated that high miR-101-3p expression was closely related to poor survival. (d) miR-101-3p was highly expressed in RCC samples and cell lines when compared with normal tissues and HK-2. (e, f) The expression of miR-101-3p in RCC cell lines and 11 paired clinical specimens ($*P < 0.05$, $**P < 0.01$, $***P < 0.001$, and $****P < 0.0001$).

Thus, we focused on the role of miR-101-3p in RCC and found its low expression in RCC tissue based on the starBase database and clinical tumor specimen analysis. Its overexpression inhibited the proliferation, invasion, and migration of RCC cells. In addition, we found that the enhancer of zeste 2 polycomb repressive complex 2 subunit (EZH2) is a direct downstream target of miR-101-3p. Then, this miRNA in RCC was studied using A498 and OSRC-2 cells as models. These two cell lines have been widely used in the study of RCC. Therefore, we used the functional gain/loss method to demonstrate that it affected the proliferation and invasion of RCC cells in vitro and in vivo, respectively. Our findings suggest the oncogenic role of miR-101-3p in RCC and may provide a new potential target for RCC therapy.

2. Materials and Methods

2.1. RCC Tissue Samples. Between January 2019 and June 2020, 11 RCC samples and normal samples were collected from Shanghai Tenth People's Hospital. Fresh tumor tissue was stored in liquid nitrogen to avoid RNA degradation. The specimens were used with the consent of all patients and approved by the Ethics Committee of Shanghai Tenth People's Hospital of Tongji University.

All procedures in this study were performed in accordance with the ethical standards of the institutional and/or national research committee and with the World Medical Association's Declaration of Helsinki.

2.2. Bioinformatics Analysis. The GEO dataset GSE16441 was used for analysis. In this dataset, microRNAs from 17 RCC tumors and 17 corresponding nontumor samples were hybridized on a single-channel platform for miRNA expression analysis. Differentially expressed miRNAs were identified and presented by a clustered heat map and volcano plot [12, 13]. The expression of miR-101-3p and EZH2 was

evaluated based on the starBase database (<http://starbase.sysu.edu.cn/>). The potential target genes of miR-101-3p were predicted using TargetScan (<http://www.targetscan.org/>), miRTarBase (<http://mirtarbase.cuhk.edu.cn/>), and miRDB (<http://mirdb.org/>) [14].

2.3. Cell Culture. Human RCC cell lines A498, OSRC-2, 786-O, and SW839 and human normal kidney tubular epithelial cell line (HK-2) were purchased from the Cell Bank of the Chinese Academy of Sciences (Shanghai, China) and were cultured, respectively, in DMEM (Invitrogen, Carlsbad, CA) supplemented with 10% fetal bovine serum (FBS), 50 U/ml of penicillin, and 50 μ g/ml of streptomycin (Invitrogen).

2.4. RNA Extraction, Reverse Transcription, and Quantitative Real-Time PCR (qRT-PCR) Analyses. Total RNA was measured using a rapid RNA extraction kit (Epizyme, Shanghai). The purity and concentration of RNA were measured using a NanoDrop 2000 spectrophotometer. The cDNA was synthesized using a Bulge Loop™ miRNA RT primer kit (RiboBio, China). An SYBR green qPCR kit (Yeason, Guangzhou, China) was used for qRT-PCR. Expressions of miR-101-3p and EZH2 were normalized to GAPDH or U6 applying the $2^{-\Delta\Delta C_t}$ method.

2.5. Western Blotting Analysis. The sample is lysed on ice for 30 minutes with a RIPA buffer (1:100 protease inhibitors). After measuring the protein content, calculate the sample amount. After adding enough electrophoresis solution, start to prepare for loading. After electrophoresis, the electrophoresis can be stopped just after the bromophenol blue runs out, and the membrane is transferred. The hybridization was carried out overnight at 4°C (1:10000 for GAPDH, 1:1000 for EZH2). Then, it was extensively washed and incubated in a blocking buffer for 1 h at room temperature with appropriate horseradish peroxidase combined with a

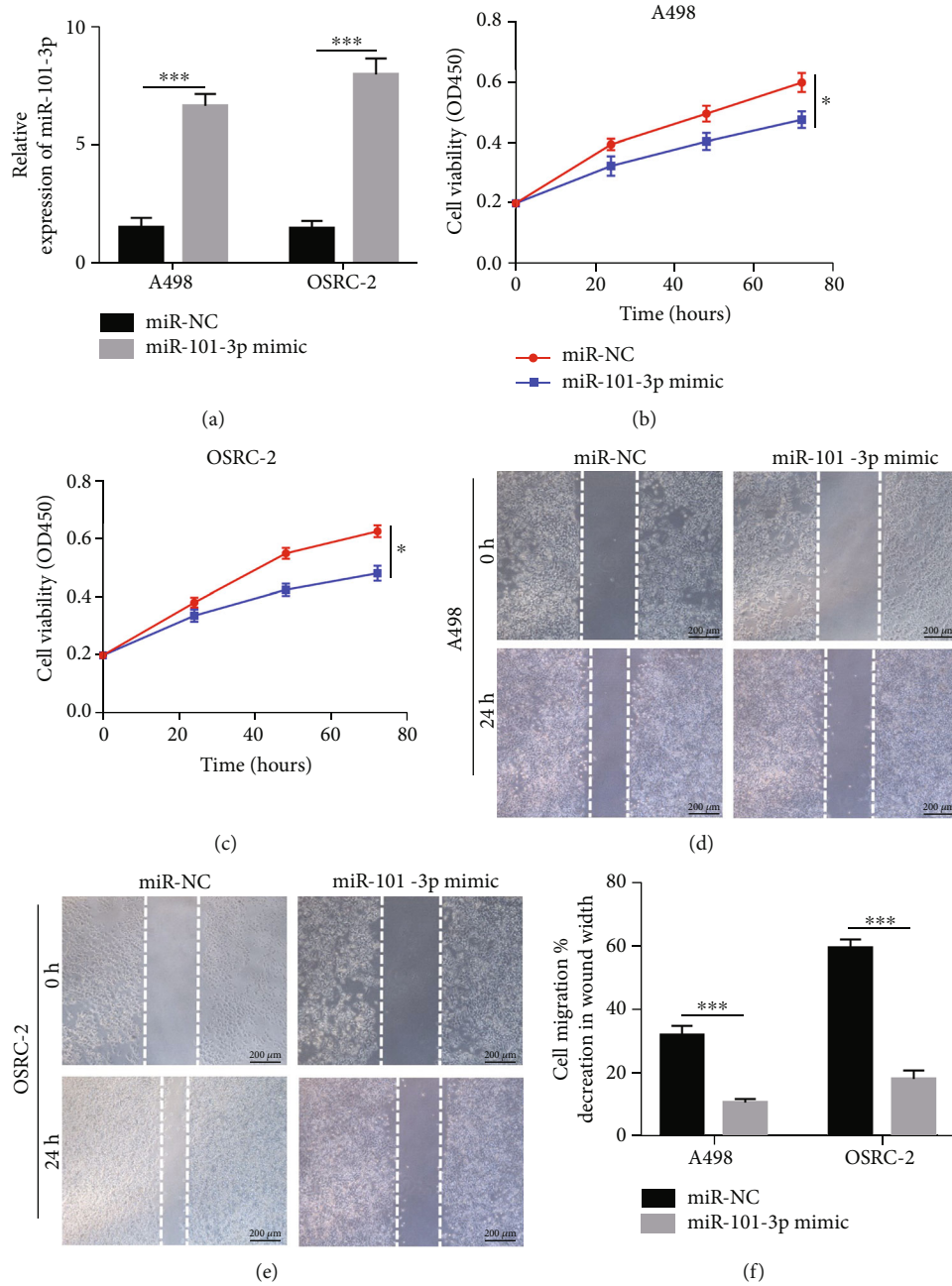


FIGURE 2: Continued.

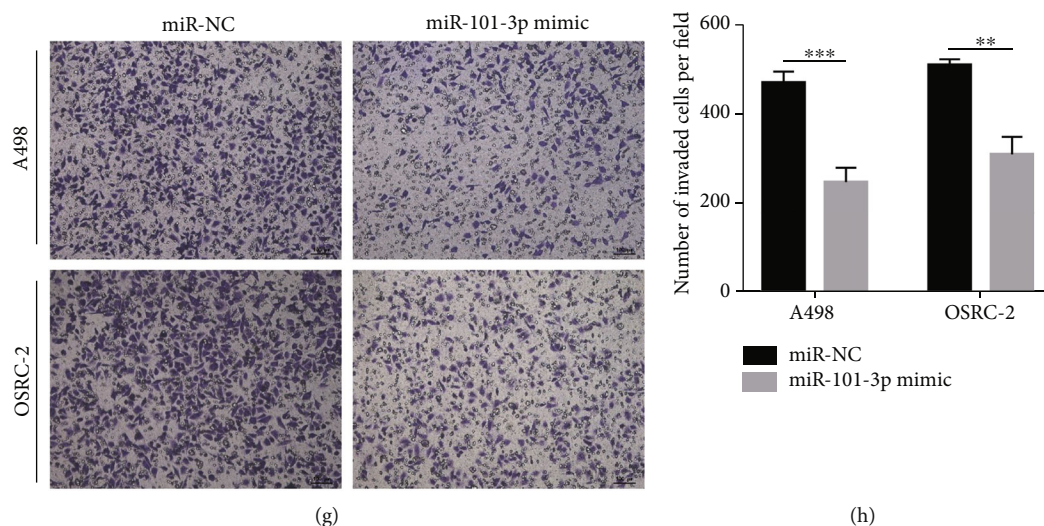


FIGURE 2: Overexpressing miR-101-3p attenuated proliferation, migration, and invasion of RCC cells. (a) miR-101-3p mimics' expression efficiency was detected by qRT-PCR in OSRC-2 and A498 cells. (b) CCK-8 assays of the viability of RCC cells after transfection with miR-101-3p mimics or NC. (c) Wound healing analysis of RCC cells after transfection with miR-101-3p mimics or NC. (d) Transwell assays of RCC cells after transfection with miR-101-3p mimics or NC (* $P < 0.05$, ** $P < 0.01$, *** $P < 0.001$, and **** $P < 0.0001$).

secondary antibody (1:1000). After three times of washing and film scanning, we analyzed the molecular weight and net optical density value of the target band with the gel image processing system.

2.6. Cell Proliferation Assays. Cell Counting Kit-8 is used to measure cell proliferation. Briefly, 1×10^3 transfected RCC cells per well were seeded into 96-well plates and cultured for 24-120 h. Every 24 h, we measured optical density values using an automatic microplate reader (BioTek Solutions, Thousand Oaks, CA, USA) and incubated with CCK-8 (10 μ l) in 5% CO₂ for 2 h [15].

2.7. Wound Healing Assays. First, draw horizontal lines evenly behind the 6-hole plate with a marker, cross the hole every 1 cm, and then lay the plate. On the next day, lines perpendicular to the horizontal lines were scratched with a spearhead. Then, wash the cells with PBS 3 times, and the cells were removed. After adding a serum-free medium, the cells were cultured in an incubator at 37°C and 5% CO₂. Samples were taken at 0, 6, 12, and 24 h, and photos were taken.

2.8. Transwell Assays. Dilute Matrigel gel with a serum-free cell culture medium or PBS buffer at the ratio of 1:8 at 4°C, take 100 μ l and evenly smear on the surface of the polycarbonate membrane in the upper chamber, place at 37°C for 0.5-1 h, and polymerize it into a gel. Add a medium containing 10% FBS or chemokines to the lower chamber of the 6-well plate, take cell suspension to the upper chamber, and finally put it into the incubator for 12-48 h culture, cell fixation, cell staining, and counting.

2.9. Cell Transfection. The miRNA negative control (miR-NC), miR-101-3p mimics, and inhibitors were transfected instantaneously using Lipofectamine 2000 according to the manufacturer's protocol. In the overexpressed EZH2, the EZH2 vector and the overexpressed plasmid (oeEZH2) were synthesized by

IBSBIO Biotechnology. We transfected the plasmid into HEK293T cells and packaged lentivirus. After 24 h, the lentivirus supernatant was collected and used to infect cells.

2.10. Luciferase Reporter Assays. The binding sites of miR-101-3p and EZH2 were obtained from TargetScan, and vectors containing the mutant-type (Mut) or wild-type (WT) sequence were synthesized by Genomeditech (China). Cultivate HEK293T cells, inoculate them in 24-well plates, and grow them for 10-24 hours. The reporter gene plasmid and transcription factor expression plasmid are cotransfected into cells. The protein is extracted and used for luciferase detection. Add the substrate and measure the luciferase activity. Calculate relative fluorescence intensity and compare with the no-load control.

2.11. Immunohistochemistry (IHC). IHC was performed to assess the expression level of EZH2 in the tissues, as described earlier [16]. Frozen sections 4-8 μ m were placed at room temperature for 30 minutes, fixed in acetone at 4°C for 10 minutes, washed with PBS for 5 minutes 3x, and incubated with hydrogen peroxide for 5-10 minutes to eliminate endogenous peroxidase activity.

2.12. Statistical Analysis. Statistical analysis was performed using GraphPad Prism 7 (GraphPad Software, CA). All data were mean \pm standard deviation (SD) of three independent experiments. Statistical significance between groups was analyzed using Student's *t*-test [17, 18]. Correlations between miR-101-3p and EZH2 were tested using Pearson's correlation coefficient analysis. All data were examined and statistically significant at $P < 0.05$ [19].

3. Results

3.1. miR-101-3p Was Upregulated in RCC Tissues and Cell Lines. To detect its expression in RCC tissues, we searched

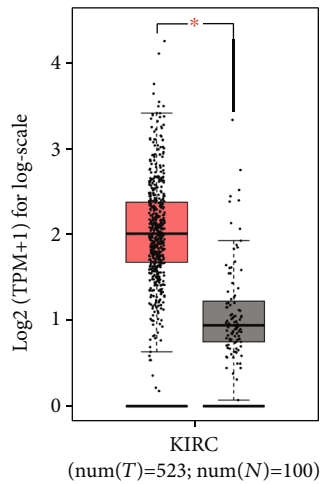
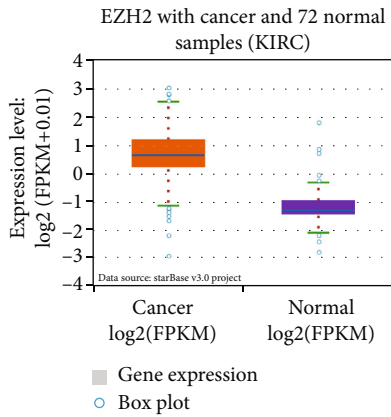
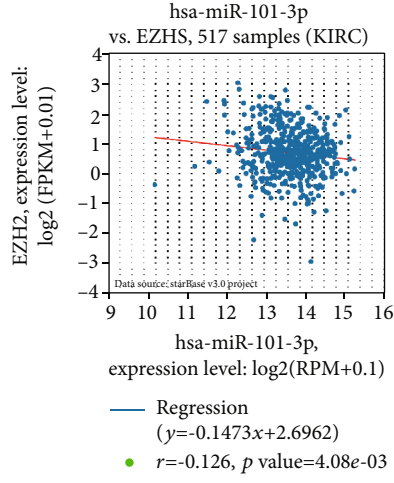
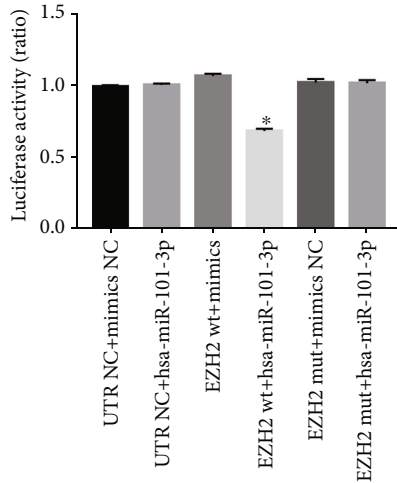
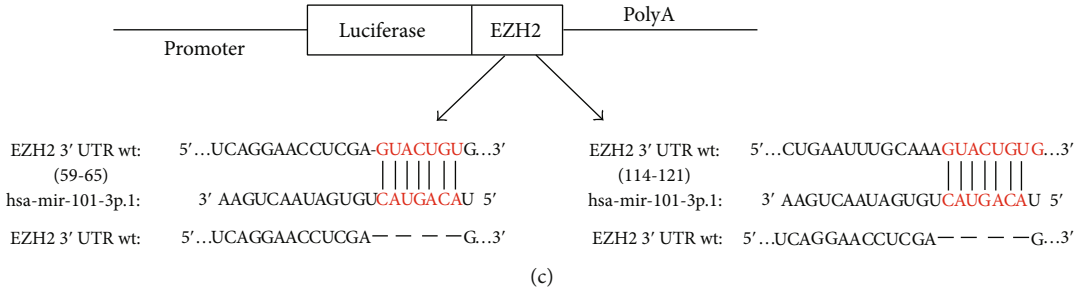
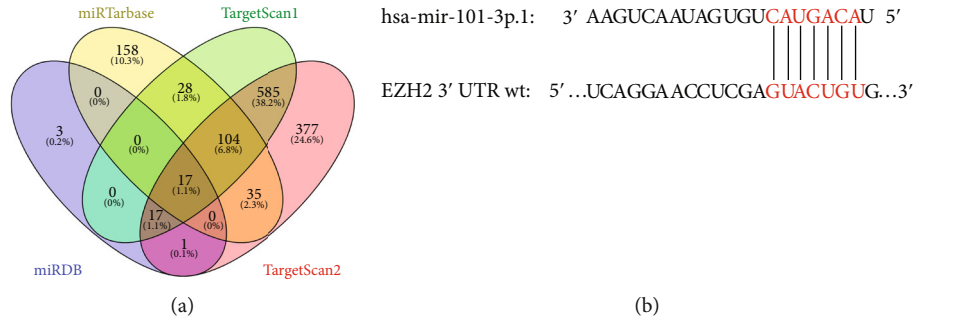


FIGURE 3: Continued.

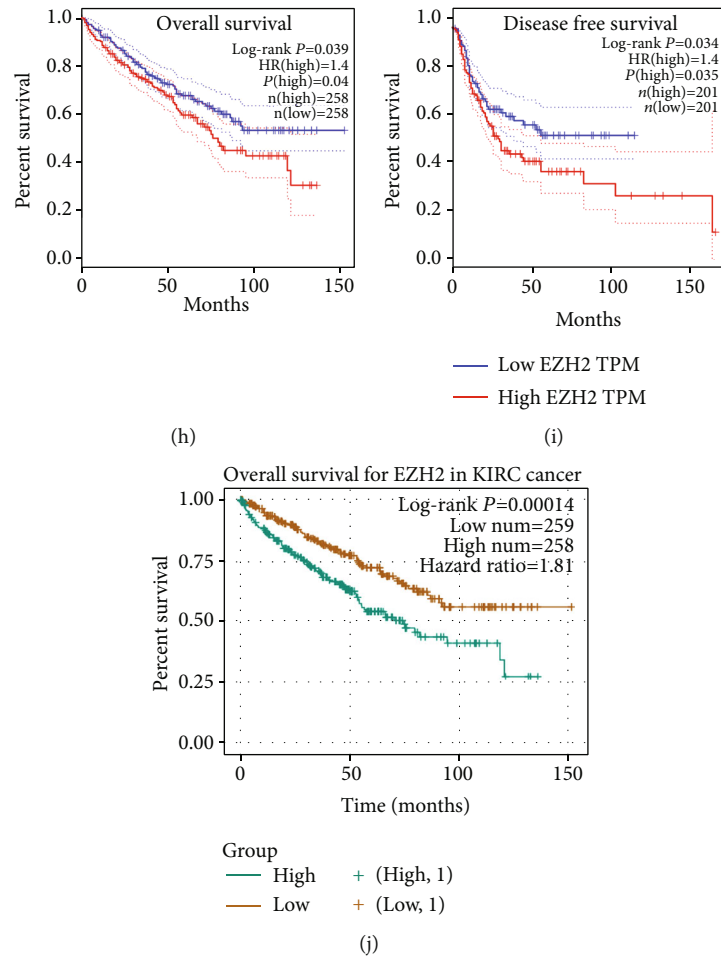


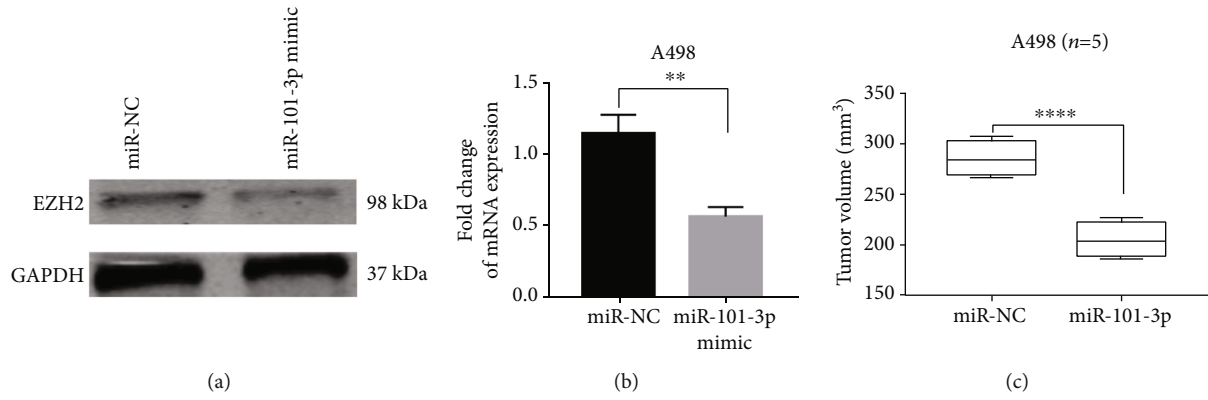
FIGURE 3: EZH2 was the downstream target of miR-101-3p. (a) The diagram of miR-101-3p potential target genes predicted by TargetScan, miRTarBase, and miRDB. (b, c) Schematic of EZH2 wild-type (WT) and mutant (Mut) luciferase reporter vectors. (d) Relative luciferase activity measured by luciferase assays in HEK293T cells cotransfected with miR-101-3p mimics or NC. (e) Pearson’s correlation coefficient analysis of miR-101-3p expression levels with EZH2 in starBase. (f, g) Relative expression of EZH2 in unpaired or paired RCC tissues based on starBase and GEPIA databases. (h–j) Kaplan-Meier survival analyses of EZH2 expression with poor survival. Data indicate mean \pm SD of three experiments (* $P < 0.05$).

the GEO dataset and identified GSE95384, which conducted miRNA expression profiling array analyses in 8 RCC tumor samples compared with matched nontumor samples. It was considerably upregulated in RCC samples (fold changes > 2 , P value < 0.05) (Figures 1(a) and 1(b)). Based on the starBase database, we also found overexpression of miR-101-3p in RCC tissues compared with normal samples ($P < 0.01$), and Kaplan-Meier survival analysis revealed that high expression of miR-101-3p was closely associated with poor survival ($P < 0.005$) (Figure 1(c)). And it was highly expressed compared with normal tissues and HK-2 (Figure 1(d)). Additionally, we also validated its expression in RCC cell lines and clinical specimens (Figures 1(e) and 1(f)). Because OSRC-2 and A498 showed higher expressions of miR-101-3p, we chose these two cell lines for further studies.

3.2. Overexpressing miR-101-3p Attenuated Proliferation, Migration, and Invasion of RCC Cells. miR-101-3p mimics were transfected into OSRC-2 and A498 cells, and the expression efficiency was detected by qRT-PCR (Figure 2(a)). CCK-

8 assays showed that the viability of RCC cells was attenuated after transfection with the mimics (Figures 2(b) and 2(c)). In addition, cell migration of OSRC-2 and A498 cells was significantly suppressed after transfection of the mimics (Figures 2(d) and 2(e)). Transwell assay also showed that overexpression of miR-101-3p mimics inhibited the migration and invasion of RCC cells (Figures 2(g) and 2(h)).

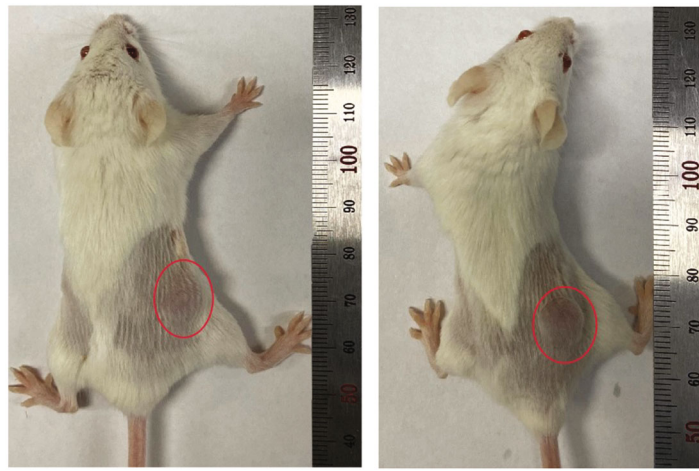
3.3. EZH2 Was the Downstream Target of miR-101-3p. We queried the TargetScan, miRTarBase, and miRDB databases to explore downstream target genes of miR-101-3p. Seventeen candidates emerged after overlapping the results from three databases (Figure 3(a)). Since the above results show that miR-101-3p acts as an anticancer gene in RCC, we focused on tumor agonists in the predicted targets. Based on starBase and GEPIA databases, we measured the expression of RCC samples (data not shown) and found that EZH2 was apparently upregulated in RCC tissues compared with normal samples (Figures 3(f) and 3(g)). Pearson’s correlation coefficient analysis also displayed that the miR-101-3p



(a)

(b)

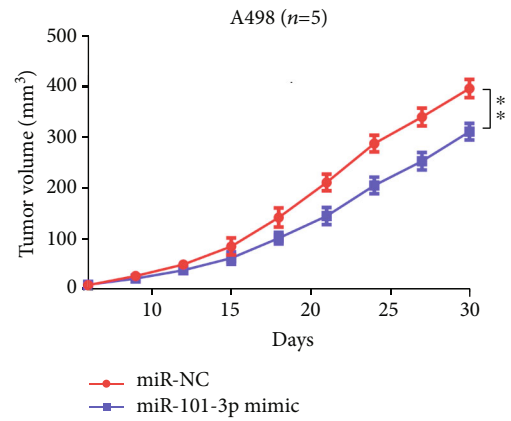
(c)



(d)



(e)



(f)

FIGURE 4: Continued.

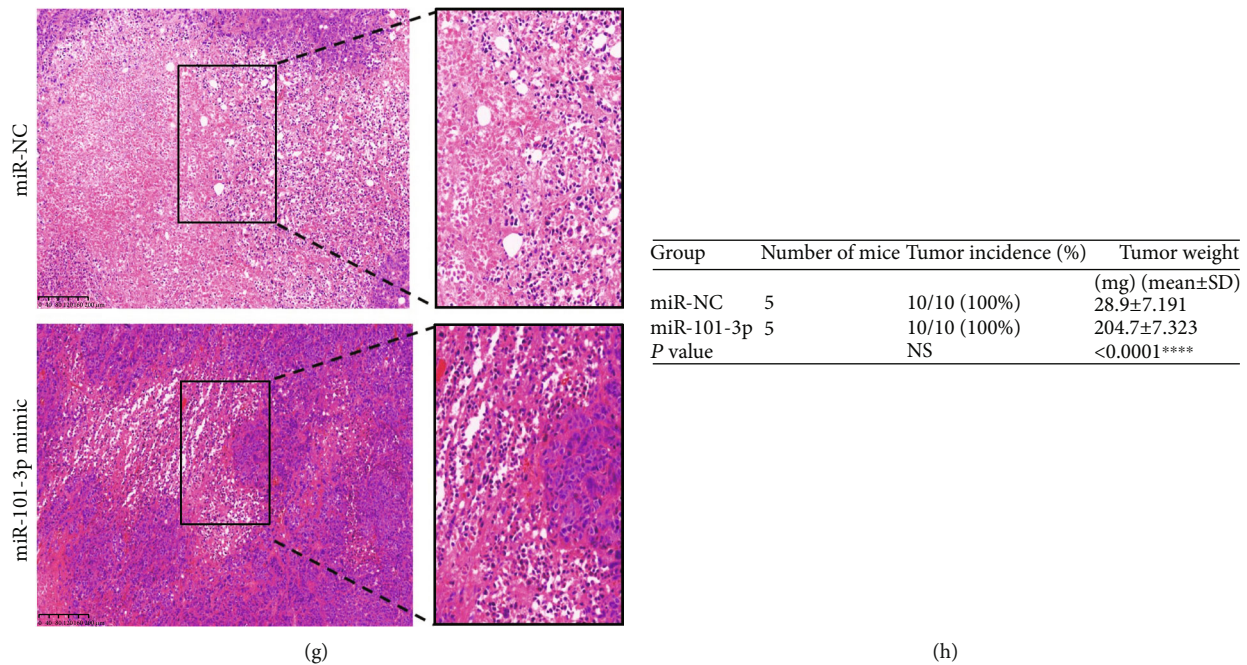


FIGURE 4: Overexpressing miR-101-3p prevented RCC proliferation in vivo. (a, b) The expression of EZH2 in A498 cell lines was measured by Western blotting and qRT-PCR. (c, d) Weights of the xenografts were shown in the box plot ($n = 10$). Macroscopic appearance of the tumors in nude mice from the 8-week-old groups. (f) Tumor volumes were periodically measured for each mouse, and tumor growth curves were plotted. Data represent mean \pm SD. (g) Representative IHC staining of EZH2 from the indicated tumors (200x, 400x). (h) Tumor incidence and weights of the xenografts were shown in the table (mean \pm SD) ($n = 10$) (** $P < 0.01$, **** $P < 0.0001$).

expression level was negatively correlated with EZH2 for both our clinical samples and starBase (Figure 3(e)). And Kaplan-Meier survival analyses indicated that high EZH2 expression was closely related to poor survival ($P < 0.05$) (Figures 3(h)–3(j)) to further verify that miR-101-3p targeted EZH2. We obtained the binding sites of miR-101-3p in the 3' -UTR of EZH2 and inserted the luciferase reporter into the wild-type or mutant sequence (Figures 3(b) and 3(c)). It revealed that the mimics significantly reduced relative luciferase activity in the transfected wild-type HEK293T cells compared with the mutant group (Figure 3(d)). According to interpretation, the above results imply that EZH2 is the target gene of miR-101-3p.

3.4. Overexpressing miR-101-3p Prevented RCC Proliferation In Vivo. Western blotting and qRT-PCR verified that overexpression of miR-101-3p could reduce the protein level of EZH2 (Figures 4(a) and 4(b)). A498 cells were infected with lentivirus overexpressing miR-101-3p, and the efficacy was verified by qRT-PCR and Western blotting. We concluded that its upregulation in RCC cells obviously prevented cell proliferation (Figures 4(c) and 4(d)). Additionally, the tumor volume, weight, and growth rate of A498 cells overexpressed with it were obviously decreased, compared with those in the control group (Figures 4(e)–4(h)). Specifically, IHC analysis showed that EZH2 levels were decreased in the miR-101-3p stimulation group compared to the control group. In RCC cells, these results reported that EZH2 exerted tumor effects conversely with miR-101-3p.

3.5. EZH2 Restoration Reversed the Effects of miR-101-3p in RCC Cells. We further validated that miR-101-3p attenuated RCC tumor characteristics via targeting EZH2 through rescue experiments. miR-101-3p mimics were cotransfected with EZH2 overexpressed plasmids or NC into RCC cells. Western blotting and qRT-PCR were implemented to assess the expression of EZH2 in RCC cells (Figures 5(a) and 5(b)). We concluded that miR-101-3p mimics inhibited the tumor characteristics of RCC cells, and EZH2 recovery partially attenuated these effects (Figures 5(c)–5(j)). And miR-101-3p mimics decreased the protein level of EZH2 while the effect was likewise reversed after transfection with EZH2 overexpressed plasmids. It suggested that miR-101-3p prevented the malignant progression of RCC by preventing the expression of EZH2.

4. Discussion

Currently, studies have demonstrated that miRNAs are closely related to RCC occurrence [20–23]. However, as far as we know, its expression level and function in RCC nonetheless remain to have a lot of questions. We found it was highly reflected in tumor tissues, which was consistent with data from the starBase database. Moreover, the results from miRNA expression profiling arrays (GSE16441) also revealed that it was significantly upregulated in RCC tumor specimens.

To date, miR-101-3p has been widely mentioned in other tumors; however, its role in renal carcinogenesis has not been determined. It prevents growth and metastasis of NSCLC by

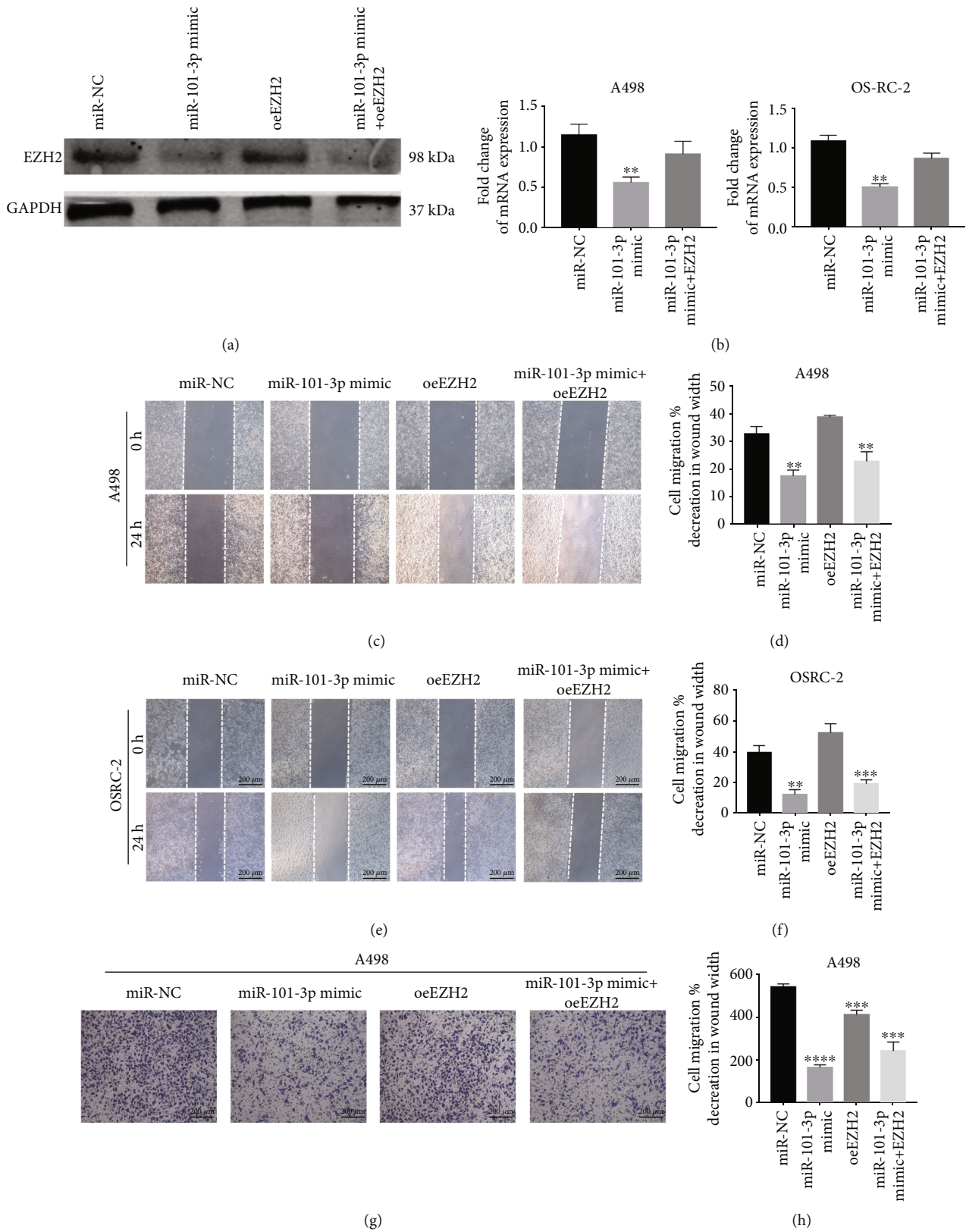


FIGURE 5: Continued.

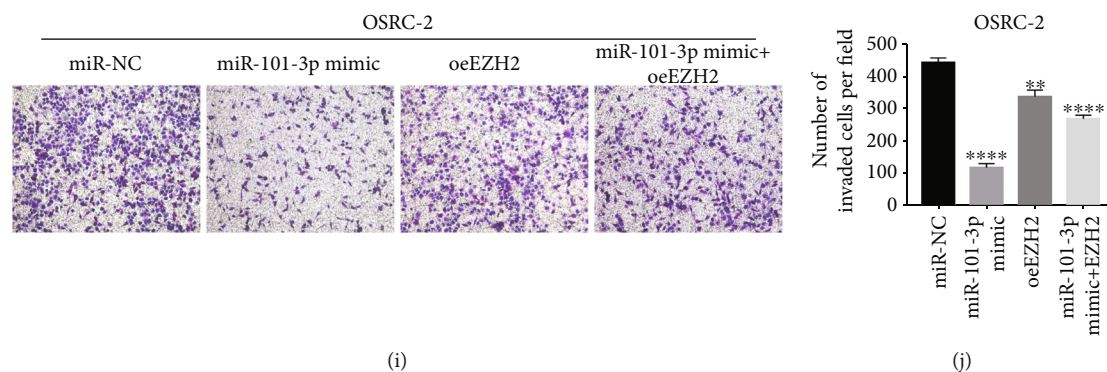


FIGURE 5: EZH2 restoration reversed the effects of miR-101-3p in RCC cells. (a, b) The protein level of EZH2 in RCC cells cotransfected with miR-101-3p mimics and EZH2 overexpressed plasmids or NC. (c–j) Wound healing and transwell assays of RCC cells cotransfected with miR-101-3p mimics and EZH2 overexpressed plasmids or NC. Data represent mean \pm SD (** $P < 0.01$, *** $P < 0.001$, and **** $P < 0.0001$).

blocking PI3K/Akt signaling by targeting MALAT-1 [11]. Likewise, miR-101-3p prevents EMT by targeting TRIM44 to reduce glioblastoma metastasis [24]. miR-101-3p can advance the apoptosis of oral cancer cells by targeting BICC1 [8]. A recent study reported that miR-101-3p prevented retinoblastoma cell proliferation by targeting EZH2 and HDAC9 [25]. Wang and Liu concluded that autophagy in endometrial cancer cells can be prevented by miR-101-3p targeting EZH2 [26].

In this research, we observed that tumor characteristics of RCC cells were suppressed after overexpression of miR-101-3p. Additionally, Kaplan-Meier survival analyses showed that higher miR-101-3p expression indicated a better survival, which also revealed that it exerted a tumor-preventing effect on RCC. A previous study has reported that the von Hippel-Lindau (VHL) tumor suppressor could change the expression of miRNA [27]. Interestingly, we observed that miR-101-3p was relatively lowly expressed in OSRC-2 and A498 cells compared with HK-2 cells.

Luciferase reporter analysis showed that it directly targeted EZH2 by binding to 3'-UTR and inhibiting the translation of EZH2 mRNA, which was consistent with Western blotting results. Pearson's correlation coefficient analysis also disclosed that the miR-101-3p expression level was negatively correlated with EZH2 in RCC tissues. EZH2 can alter downstream target gene expression by H3K27me3 [28]. EZH2 has been well studied in prostate cancer, and its mutations are the leading cause of the progression of prostate cancer [29]. Recently, EZH2 was said to play an important role in malignancy [28, 30]. For instance, Xia et al. showed that EZH2 promotes the aggregation of macrophages and the invasion of lung cancer by enhancing the expression of CCL5 [31]. EZH2-mediated miR-139-5p regulated pancreatic cancer's epithelial-mesenchymal transition and lymph node metastasis [32]. As far as we know, the role of EZH2 in RCC has not been previously studied.

In summary, we revealed that miR-101-3p acted as an antioncogene to prevent the progression of RCC through targeting EZH2, which perhaps may provide a new therapeutic target for RCC.

Data Availability

The related data would be provided if required.

Conflicts of Interest

The authors declare that they have no conflicts of interest.

Authors' Contributions

The contributions of the authors involved in this study are as follows: (i) conception and design: Yunfei Xu and Yunze Dong; (ii) administrative support: Yunfei Xu; (iii) provision of study materials or patients: Tiancheng Xie and Huan Liu; (iv) collection and assembly of data: Yuchen Gao; (v) data analysis and interpretation: Yunze Dong; (vi) manuscript writing: all authors; and (vii) final approval of manuscript: all authors. Yunze Dong and Yuchen Gao contributed equally to this work.

Acknowledgments

This study was funded by the National Natural Science Foundation of China (Nos. 81971371 and 81902567).

References

- [1] C. Gu, X. Shi, C. Dai et al., "RNA m6A modification in cancers: molecular mechanisms and potential clinical applications," *The Innovation*, vol. 1, no. 3, p. 100066, 2020.
- [2] U. Capitano, K. Bensalah, A. Bex et al., "Epidemiology of renal cell carcinoma," *European Urology*, vol. 75, no. 1, pp. 74–84, 2019.
- [3] J. J. Patard, G. Pignot, B. Escudier et al., "ICUD-EAU international consultation on kidney cancer 2010: treatment of metastatic disease," *European Urology*, vol. 60, no. 4, pp. 684–690, 2011.
- [4] W. Zhai, J. Ma, R. Zhu et al., "MiR-532-5p suppresses renal cancer cell proliferation by disrupting the ETS1-mediated positive feedback loop with the KRAS-NAP1L1/P-ERK axis," *British Journal of Cancer*, vol. 119, no. 5, pp. 591–604, 2018.
- [5] J. C. van der Mijn, J. W. Mier, H. J. Broxterman, and H. M. Verheul, "Predictive biomarkers in renal cell cancer: insights in drug resistance mechanisms," *Drug Resistance Updates*, vol. 17, no. 4-6, pp. 77–88, 2014.
- [6] B. Chai, Y. Guo, X. Cui et al., "MiR-223-3p promotes the proliferation, invasion and migration of colon cancer cells by

- negative regulating PRDM1," *American Journal of Translational Research*, vol. 11, no. 7, pp. 4516–4523, 2019.
- [7] L. Yu, X. Gong, L. Sun, H. Yao, B. Lu, and L. Zhu, "miR-454 functions as an oncogene by inhibiting CHD5 in hepatocellular carcinoma," *Oncotarget*, vol. 6, no. 36, pp. 39225–39234, 2015.
- [8] H. Wang, Y. Guo, N. Mi, and L. Zhou, "miR-101-3p and miR-199b-5p promote cell apoptosis in oral cancer by targeting BICC1," *Molecular and Cellular Probes*, vol. 52, p. 101567, 2020.
- [9] X. Y. Wu et al., "miR-101-3p suppresses HOX transcript antisense RNA (HOTAIR)-induced proliferation and invasion through directly targeting SRF in gastric carcinoma cells," *Oncology Research*, vol. 25, no. 8, pp. 1383–1390, 2017.
- [10] S. Yan, X. Shan, K. Chen et al., "LINC00052/miR-101-3p axis inhibits cell proliferation and metastasis by targeting SOX9 in hepatocellular carcinoma," *Gene*, vol. 679, pp. 138–149, 2018.
- [11] X. Q. Zhang, X. He, Y. Liu et al., "MiR-101-3p inhibits the growth and metastasis of non-small cell lung cancer through blocking PI3K/AKT signal pathway by targeting MALAT-1," *Biomedicine & Pharmacotherapy*, vol. 93, pp. 1065–1073, 2017.
- [12] C. Gu, J. Chen, X. Dang et al., "Hippo pathway core genes based prognostic signature and immune infiltration patterns in lung squamous cell carcinoma," *Frontiers in Oncology*, vol. 11, 2021.
- [13] C. Gu, X. Shi, W. Qiu et al., "Comprehensive analysis of the prognostic role and mutational characteristics of m6A-related genes in lung squamous cell carcinoma," *Frontiers in Cell and Development Biology*, vol. 9, p. 661792, 2021.
- [14] C. Gu, X. Shi, Z. Huang et al., "A comprehensive study of construction and analysis of competitive endogenous RNA networks in lung adenocarcinoma," *Biochimica et Biophysica Acta (BBA) - Proteins and Proteomics*, vol. 1868, no. 8, p. 140444, 2020.
- [15] C. Gu, Z. Huang, X. Chen et al., "TEAD4 promotes tumor development in patients with lung adenocarcinoma via ERK signaling pathway," *Biochimica et Biophysica Acta (BBA) - Molecular Basis of Disease*, vol. 1866, no. 12, p. 165921, 2020.
- [16] W. Zhai, R. Zhu, J. Ma et al., "A positive feed-forward loop between LncRNA-URRCC and EGFL7/P-AKT/FOXO3 signaling promotes proliferation and metastasis of clear cell renal cell carcinoma," *Molecular Cancer*, vol. 18, no. 1, p. 81, 2019.
- [17] J. Chen, C. Gu, X. Chen et al., "Clinicopathological and prognostic analyses of 86 resected pulmonary lymphoepithelioma-like carcinomas," *Journal of Surgical Oncology*, vol. 123, no. 2, pp. 544–552, 2021.
- [18] C. Chen, X. Zhang, C. Gu et al., "Surgery performed at night by continuously working surgeons contributes to a higher incidence of intraoperative complications in video-assisted thoracoscopic pulmonary resection: a large monocentric retrospective study," *European Journal of Cardio-Thoracic Surgery*, vol. 57, no. 3, pp. 447–454, 2020.
- [19] X. Pan, C. Gu, R. Wang, H. Zhao, J. Yang, and J. Shi, "Transmanubrial osteomuscular sparing approach for resection of cervico-thoracic lesions," *Journal of Thoracic Disease*, vol. 9, no. 9, pp. 3062–3068, 2017.
- [20] A. Batool, "Role of EZH2 in cell lineage determination and relative signaling pathways," *Frontiers in Bioscience-Landmark*, vol. 24, no. 5, pp. 947–960, 2019.
- [21] C. Cardoso, C. Mignon, G. Hetet, B. Grandchamps, M. Fontes, and L. Colleaux, "The human EZH2 gene: genomic organisation and revised mapping in 7q35 within the critical region for malignant myeloid disorders," *European Journal of Human Genetics*, vol. 8, no. 3, pp. 174–180, 2000.
- [22] G. Laible, A. Wolf, R. Dorn et al., "Mammalian homologues of the polycomb-group gene enhancer of zeste mediate gene silencing in Drosophila heterochromatin and at S-cerevisiae telomeres," *EMBO Journal*, vol. 16, no. 11, pp. 3219–3232, 1997.
- [23] R. L. Wang, M. Xin, Y. Li, P. Zhang, and M. Zhang, "The functions of histone modification enzymes in cancer," *Current Protein & Peptide Science*, vol. 17, no. 5, pp. 438–445, 2016.
- [24] L. Li, M. Y. Shao, S. C. Zou, Z. F. Xiao, and Z. C. Chen, "MiR-101-3p inhibits EMT to attenuate proliferation and metastasis in glioblastoma by targeting TRIM44," *Journal of Neuro-Oncology*, vol. 141, no. 1, pp. 19–30, 2019.
- [25] Q. F. Jin, W. He, L. Chen, Y. Yang, K. Shi, and Z. You, "MicroRNA-101-3p inhibits proliferation in retinoblastoma cells by targeting EZH2 and HDAC9," *Experimental and Therapeutic Medicine*, vol. 16, no. 3, pp. 1663–1670, 2018.
- [26] C. L. Wang and B. Liu, "miR-101-3p induces autophagy in endometrial carcinoma cells by targeting EZH2," *Archives of Gynecology and Obstetrics*, vol. 297, no. 6, pp. 1539–1548, 2018.
- [27] Z. Y. Lei, T. D. Klasson, M. M. Brandt et al., "Control of angiogenesis via a VHL/miR-212/132 axis," *Cell*, vol. 9, no. 4, p. 1017, 2020.
- [28] R. Duan, W. du, and W. J. Guo, "EZH2: a novel target for cancer treatment," *Journal of Hematology & Oncology*, vol. 13, no. 1, p. 104, 2020.
- [29] S. Varambally, S. M. Dhanasekaran, M. Zhou et al., "The polycomb group protein EZH2 is involved in progression of prostate cancer," *Nature*, vol. 419, no. 6907, pp. 624–629, 2002.
- [30] I. M. Bachmann, O. J. Halvorsen, K. Collett et al., "EZH2 expression is associated with high proliferation rate and aggressive tumor subgroups in cutaneous melanoma and cancers of the endometrium, prostate, and breast," *Journal of Clinical Oncology*, vol. 24, no. 2, pp. 268–273, 2006.
- [31] L. L. Xia, X. Zhu, L. Zhang, Y. Xu, G. Chen, and J. Luo, "EZH2 enhances expression of CCL5 to promote recruitment of macrophages and invasion in lung cancer," *Biotechnology and Applied Biochemistry*, vol. 67, no. 6, pp. 1011–1019, 2020.
- [32] J. Ma, J. Zhang, Y. C. Weng, and J. C. Wang, "EZH2-mediated microRNA-139-5p regulates epithelial-mesenchymal transition and lymph node metastasis of pancreatic cancer," *Molecules and Cells*, vol. 41, no. 9, pp. 868–880, 2018.

Retraction

Retracted: N-Acetylcysteine Improves Inflammatory Response in COPD Patients by Regulating Th17/Treg Balance through Hypoxia Inducible Factor-1 α Pathway

BioMed Research International

Received 12 March 2024; Accepted 12 March 2024; Published 20 March 2024

Copyright © 2024 BioMed Research International. This is an open access article distributed under the Creative Commons Attribution License, which permits unrestricted use, distribution, and reproduction in any medium, provided the original work is properly cited.

This article has been retracted by Hindawi following an investigation undertaken by the publisher [1]. This investigation has uncovered evidence of one or more of the following indicators of systematic manipulation of the publication process:

- (1) Discrepancies in scope
- (2) Discrepancies in the description of the research reported
- (3) Discrepancies between the availability of data and the research described
- (4) Inappropriate citations
- (5) Incoherent, meaningless and/or irrelevant content included in the article
- (6) Manipulated or compromised peer review

The presence of these indicators undermines our confidence in the integrity of the article's content and we cannot, therefore, vouch for its reliability. Please note that this notice is intended solely to alert readers that the content of this article is unreliable. We have not investigated whether authors were aware of or involved in the systematic manipulation of the publication process.

Wiley and Hindawi regrets that the usual quality checks did not identify these issues before publication and have since put additional measures in place to safeguard research integrity.

We wish to credit our own Research Integrity and Research Publishing teams and anonymous and named external researchers and research integrity experts for contributing to this investigation.

The corresponding author, as the representative of all authors, has been given the opportunity to register their agreement or disagreement to this retraction. We have kept a record of any response received.

References

- [1] X. Liu, Z. Hu, and H. Zhou, "N-Acetylcysteine Improves Inflammatory Response in COPD Patients by Regulating Th17/Treg Balance through Hypoxia Inducible Factor-1 α Pathway," *BioMed Research International*, vol. 2021, Article ID 6372128, 7 pages, 2021.

Research Article

N-Acetylcysteine Improves Inflammatory Response in COPD Patients by Regulating Th17/Treg Balance through Hypoxia Inducible Factor-1 α Pathway

Xiaopeng Liu, Zhixiong Hu, and Haiying Zhou 

Department of Respiratory Medicine, Jinshan Hospital, Fudan University, Shanghai 201508, China

Correspondence should be addressed to Haiying Zhou; mipanba234265682@163.com

Received 24 April 2021; Accepted 17 June 2021; Published 29 June 2021

Academic Editor: Tao Huang

Copyright © 2021 Xiaopeng Liu et al. This is an open access article distributed under the Creative Commons Attribution License, which permits unrestricted use, distribution, and reproduction in any medium, provided the original work is properly cited.

Introduction. This study was aimed to investigate the effects of N-acetylcysteine (NAC) on chronic obstructive pulmonary disease (COPD) and the change of Th17/Treg cytokine imbalance. **Material and Methods.** A total of 121 patients with stable COPD at the stage of C or D were consecutively enrolled and randomly divided into 2 groups. Patients in the treatment group received NAC granules (0.2 g \times 10 bags, 0.4 g each time, 3 times/d) for half a year. The control group was treated with the same amount of placebo therapy. The peripheral blood of the patient was collected and the cytokine, T lymphocyte subsets were detected. **Results.** We found the oral administration of NAC could regulate Th17/Treg balance to resist inflammation in COPD patients. Serum testing showed that the proportion of Treg in CD4+ T cells has increased and the Th17/Treg ratio has decreased during the NAC treatment. In vitro studies, we found that NAC regulated Th17/Treg balance through Hypoxia Inducible Factor-1 α pathway. **Conclusions.** Our result could provide new diagnosis and treatment for elderly patients with COPD from the perspective of immunity ideas.

1. Introduction

Chronic obstructive pulmonary disease (COPD) belongs to a class of common chronic respiratory diseases characterized by irreversible continuous airflow limitation and high fatality rate, which currently places a huge burden on the world's disease economy [1]. It is associated with both airway and extrapulmonary inflammation, as indicated by increased reactive oxygen species (ROS) levels and proinflammatory markers in peripheral blood. COPD manifests as a series of overlapping phenotypes, including chronic bronchitis, emphysema, small airway disease, and frequent exacerbations. Despite differences in pathology, they share many common but complex pathogenetic processes, including inflammation, excessive oxidative stress, apoptosis, and autoimmunity [2–6].

N-acetylcysteine (NAC) belongs to a class of antioxidants, which has both antioxidant and anti-inflammatory properties. NAC exerts its antioxidant effect by acting directly as a ROS scavenger and a precursor of reduced glutathione [7].

Oral NAC has been shown to affect the body's redox balance through increasing both plasma glutathione levels and lung lavage glutathione levels in patients with stable COPD. However, the clinical effectiveness of NAC in COPD treatment is still controversial. Although it was found in some early studies that NAC had no effect, more recent studies have shown that increasing the dose (1200 mg daily or above) of NAC can reduce the exacerbation of COPD patients and extend the time to the first exacerbation [8–11]. And the most principle of related mechanism is for its antioxidative effect, such as reducing ROS production by alveolar macrophages as well as reducing exhaled H₂O₂. There are limited data on the anti-inflammatory activity of NAC in COPD patients.

In recent years, lymphocytes, especially CD4+ T cells involved in the pathogenesis of COPD, have become an active topic of research [3, 5, 6, 12]. Studies have revealed that the imbalance between T helper (Th)17 cells and regulatory T (Treg) cells played a vital role in the development and outcome of COPD [5, 12]. Interestingly, though Th17 and Treg

cells shared a common requirement for TGF- β in their differentiation, they express distinct transcriptional regulators (ROR γ t versus Foxp3, respectively) and present opposing functions (inflammatory versus anti-inflammatory). Recent studies have shown that NAC could play as a regulatory role on T lymphocyte subsets differentiation and improve the patient's immune function [13–16]. However, the effect of NAC for T lymphocyte subtype transformation on patients with stable COPD is still unknown.

In this study, we explored the treatment effect of oral NAC on elderly patients with COPD in clinic. And we also determined the change of Th17/Treg balance in peripheral blood of patients who accepted NAC, in order to provide new diagnosis and treatment for elderly patients with COPD from the perspective of immunity ideas.

2. Materials and Methods

2.1. Ethics Statement. This research was approved by the research ethics committees of Jinshan Hospital Affiliated to Fudan University, China (approval number: Jinshan Medical Ethics Research 2019-13-02). All patients were approached in accordance with the approved ethical guidelines. They had agreed before participating in this study and signed informed consent. All methods used in the study were performed in accordance with the relevant guidelines and regulations developed by the aforementioned ethics committees.

2.2. Participants and Trial Design. A total of 121 patients with stable COPD at the stage of C or D based on the Global Initiative for Chronic Obstructive Lung Disease randomly selected from September 2018 to June 2019 were recruited in this research (Jinshan Hospital Affiliated to Fudan University, China). They were randomly divided into two groups. Patients in the treatment group were treated with conventional inhalation of bronchodilators (long-acting anticholinergic drugs (LAMA, tiotropium, 18 μ g daily) and oral NAC granules (0.2 g \times 10 bags, 0.4 g each time, 3 times/d, Guangdong Baiao Pharmaceutical) for half a year. The control group was treated with conventional airway expansion therapy and the same amount of placebo therapy. No other phlegm-resolving drugs, glucocorticoids, bronchodilators were used during the study. Lung function of each patient was evaluated at the beginning of the study. No significant differences were observed in terms of age, gender, and smoking status of patients between the treatment and control individuals ($P > 0.05$). Clinical data of all individuals are given in detail in Table 1.

2.3. Diagnosis of COPD. Diagnosis of COPD was confirmed in accordance with the diagnostic criteria of the Global initiative for chronic Obstructive Lung Disease. The diagnostic criteria for group C were as follows: CAT (COPD assessment test) score < 10 or mMRC (modified British Medical Research Council) score was between 0 and 1, the FEV1/pred% is less than 50%, and/or acute exacerbations occur more than 2 times in one year or at least one acute exacerbation occurs which is required in hospital treatment. The diagnostic criteria for group D were as follows: CAT score of 10 or more

TABLE 1: Comparison of baseline data between the two groups.

Term	Control group (N = 61)	Treatment group (N = 60)	P value
Gender (male)	28	30	0.269
Age (mean \pm SD)	72.65 \pm 7.96	70.89 \pm 8.62	0.116
Smoking index	569.07 \pm 264.32	592.76 \pm 228.54	0.305
mMRC score	2.62 \pm 0.85	2.69 \pm 0.91	0.277

or mMRC score of 2 or more, FEV1/pred% $< 50\%$ and/or acute exacerbations ≥ 2 times per year, or the number of hospitalizations for acute exacerbations is once or more.

2.4. Inclusion and Exclusion Criteria for the Study. The inclusion criteria were as follows: (1) patients confirmed as having COPD at stage of C and D; (2) patients who received no antibiotics, glucocorticoids, and theophylline medications within 2 weeks before entering the study; and (3) patients who signed informed consent forms for voluntary participation in the study. The exclusion criteria were as follows: (1) patients with acute exacerbations which may affect the natural process of IL-17 and IL-10 in COPD; (2) patients accompanied by pulmonary interstitial fibrosis, tuberculosis, bronchial pneumonia, and lung cancer; (3) patients with major diseases of nonrespiratory system, such as diabetes, severe cardiovascular and cerebrovascular diseases, and neurological diseases or liver and kidney dysfunction; and (4) patients with mental illness and cognitive impairment.

2.5. Blood Samples and Measurements. The peripheral venous blood of the patient was collected in tubes containing ethylene diamine tetraacetate acid (EDTA) in the early morning. The blood samples were immediately centrifuged at 3,000 rpm for 15 minutes after collected, and serum was obtained and stored at -80°C until used. The serum levels of IL-17, IL-10, IL-9, TGF- β , TNF- α , and IL-1 β were determined by using ELISA test kits (R&D Systems, Minneapolis, MN), following the manufacturer's instructions. Briefly, the antibody was diluted to a content of 5 μ g/mL, and then, 0.1 mL of that was added into the plate hole and placed at 4°C overnight. The next day, the solution in the plate was discarded, and a 0.1 mL aliquot of the sample was added into the reaction well. Then, place the reaction well into a humid chamber at 37°C for 1 hour. Then, discarding the solution and 0.1 mL of freshly diluted enzyme-labeled antibody was added at 37°C for 1 hour. Then, a 0.1 mL aliquot of substrate solution was added to each well at 37°C for 30 minutes, and 0.05 mL of stop solution was added to each reaction well. The color intensity was measured at a wavelength of 450 nm by using a photometer. The standard curve was plotted based on the concentration of the standard sample and the OD of each well.

2.6. Inflammation-Pathway Microarray. Expression microarray analysis was conducted with HWayen inflammation-

pathway microarray CSP100. All the procedures and data analysis were performed by HWayan, China.

2.7. Flow Cytometry Analysis. Peripheral blood mononuclear cells (PBMCs) were freshly isolated by Ficoll density gradient centrifugation (Pharmacia, Uppsala, Sweden). The isolated PBMCs were washed twice with PBS and resuspended at 106 cells/mL in complete culture medium (RPMI 1640 supplemented with 1% penicillin/streptomycin, 2 mM L-glutamine, and 10% heat-inactivated fetal bovine serum; Gibco BRL, Gaithersburg, MD, USA). For Th17 cells analysis, cells were detected as described previously. For the analysis of Treg cells, a human regulatory T-cell staining kit (BD Pharmingen™, USA) was used to measure CD4+ CD25+ Foxp3+ cells as Treg cells according to the manufacturer's protocol. Briefly, PBMCs were incubated with a cocktail of fluorescein isothiocyanate-conjugated anti-CD4 and APC-conjugated anti-CD25 for 30 minutes at 4°C. After fixation and permeabilization, the cells were blocked by normal rat serum and stained using PE-conjugated anti-Foxp3 for 45 minutes at 4°C. The flow cytometry analyses were performed on a FACS Calibur flow cytometer (BD biosciences, San Jose, CA, USA) equipped with the CellQuest software (BD biosciences). Isotype controls were conducted to ensure antibody specificity.

2.8. Western Blot Analysis. The cells were lysed in lysis buffer containing 4% sodium dodecyl sulfate (SDS), 20% glycerol, 100 mM dithiothreitol (DTT), and Tris-HCl, pH 6.8. A total of 30 µg of the supernatant proteins was loaded and separated by 8-15% sodium dodecyl sulfate-polyacrylamide gel electrophoresis. The samples were incubated with primary antibodies overnight at 4°C after the proteins were transferred to a polyvinylidene fluoride (PVDF) membrane (Millipore, 0.2 µm or 0.45 µm, as appropriate), following the electrophoresis [17]. The primary antibodies were used at dilutions of 1:1000 for GAPDH (Cell Signaling), 1:1000 for HIF1-α (Cell Signaling). Then, the membranes were incubated with HRP-conjugated secondary antibodies and visualized with an ECL Chemiluminescent kit (Novex™).

2.9. Statistical Analysis. All analyses were done by using the SPSS software, version 20.0 (IBM Corp., Armonk, NY, USA). Continuous variables were reported as mean ± SD [18]. For two-group comparisons, the independent sample *t*-test was used for normally distributed data [19]. All tests were two-tailed, and a value of *P* < 0.05 was considered statistically significant.

3. Results

3.1. Oral NAC downregulated the level of IL-17 while upregulated the level of IL-10 in the serum of patients with COPD. Previous studies demonstrated that increased IL-17 level and decreased IL-10 level in serum were positively correlated with the progression of COPD [20, 21]. To determine whether oral NAC regulated the level of IL-17, IL-10, and other related inflammation cytokine in the serum, we obtained peripheral blood from the patient with COPD for further evaluation. As shown in Figure 1, the level of IL-17 was downregulated in the serum of COPD patients treated

with oral NAC, compared to the control counterparts. Conversely, the serum level of IL-10 was upregulated by oral NAC treatment in the COPD patients, compared to the control counterparts (Figure 1). Meanwhile, other proinflammation cytokines, including IL-9, TGF-β, TNF-α, and IL-1β, were all downregulated. These data demonstrated that oral NAC treatment at a dose of 1200 mg/day was helpful for improving the inflammatory status of COPD patients.

3.2. Oral NAC suppressed circulating Th17 cells while promoted Treg cells in the serum of COPD patients. To further explore the effect of oral NAC, we used IL-17 and Foxp3 as the biomarker of Th17 and Treg cells in the flow cytometry analysis, respectively. As shown in Figures 2(a) and 2(b), the frequencies of Th17 cells were significantly decreased in the peripheral blood of COPD patients in the NAC treatment group than those in the control group (*P* < 0.05). On the contrary, the frequencies of Treg cells were increased accordingly (Figures 2(c) and 2(d)).

3.3. Oral NAC rebalances the Th17/Treg ratio. Constantly, we found that the Th17/Treg ratio was evidently decreased after taking oral NAC in the treatment group from 5.7 to 0.28. This result further proved that NAC could protect patients with COPD by suppressing Th17 immune responses and modulating the Th17/Treg balance in favor of Treg cells. Interestingly, we found that Th17 cells had a negative correlation with Treg cells whether COPD patients took NAC or not (Figure 3).

3.4. NAC decreased HIF1-α expression of T cells isolated from peripheral blood of COPD patients. Studies have shown that NAC can downregulate the protein of HIF-α by posttranscription mechanism [22, 23]. And specifically, HIF1-α is considered as a key regulatory molecule that could directly promote Th17 differentiation by inducing RORγt transcription and inhibit Treg differentiation through facilitating Foxp3 protein degradation [24]. So, we conducted an inflammation-pathway array to further analyze the pathway related to the change (*n* = 10), and we found that HIF1-α and MAPKp38 exhibited the greatest fold changes in Th17 and Treg cells. Next, we detected the protein and RNA change of HIF1-α and p38 expression in Th17 and Treg cells after NAC treatment in COPD patients (*n* = 121). As shown in Figure 4, in the treatment group, western blot revealed that HIF1-α significantly decreased in both cells, while p38 had no significant change. The result might reveal that NAC improves inflammatory response in COPD patients by regulating Th17/Treg balance through the HIF1-α pathway.

4. Discussion

COPD is a type of high-incidence chronic disease in the respiratory system. The occurrence and development of the disease have not been completely studied [1]. In recent years, immune system disorders have been closely related to the cause of the disease. Many researchers have conducted in-depth research in this area. Relevant data showed that, in addition to Th1 and Th2 cells that participated in immunopathological inflammation, Th17 cells and Treg cells, as

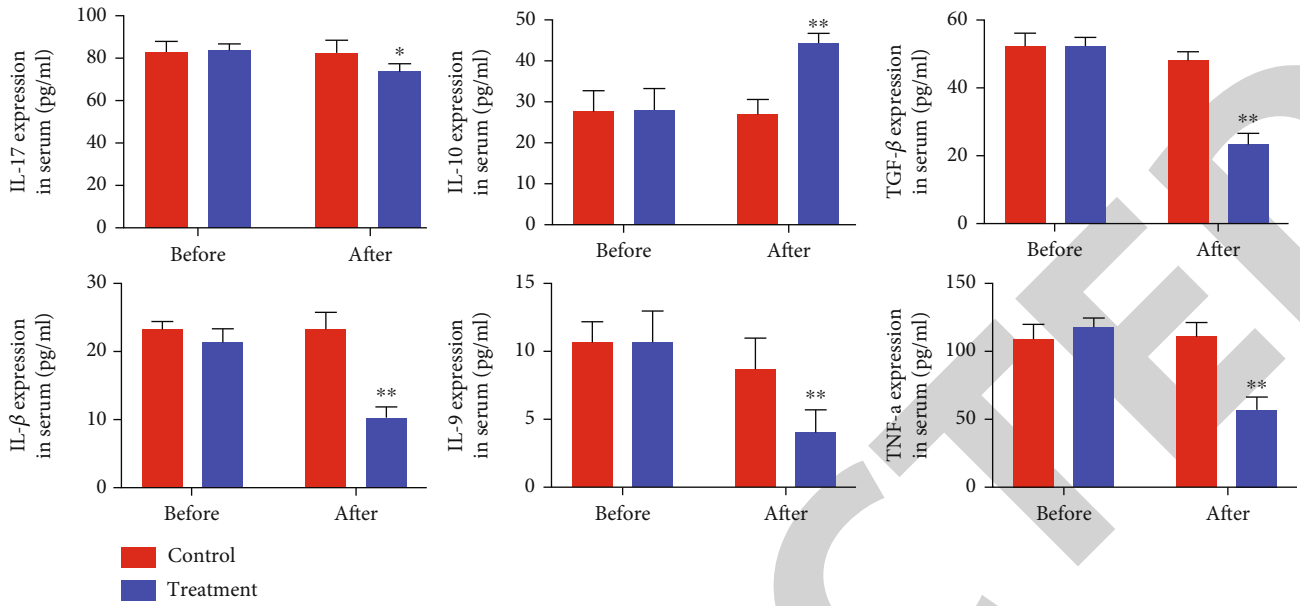


FIGURE 1: Oral NAC decreases the level of IL-17 and increases IL-10 in the serum of COPD patients. The level of serum IL-17 in the treatment group increased after oral administration of NAC. The level of serum IL-10 increased in the treatment group after oral administration of NAC. (* $P < 0.05$; ** $P < 0.01$; *** $P < 0.001$).

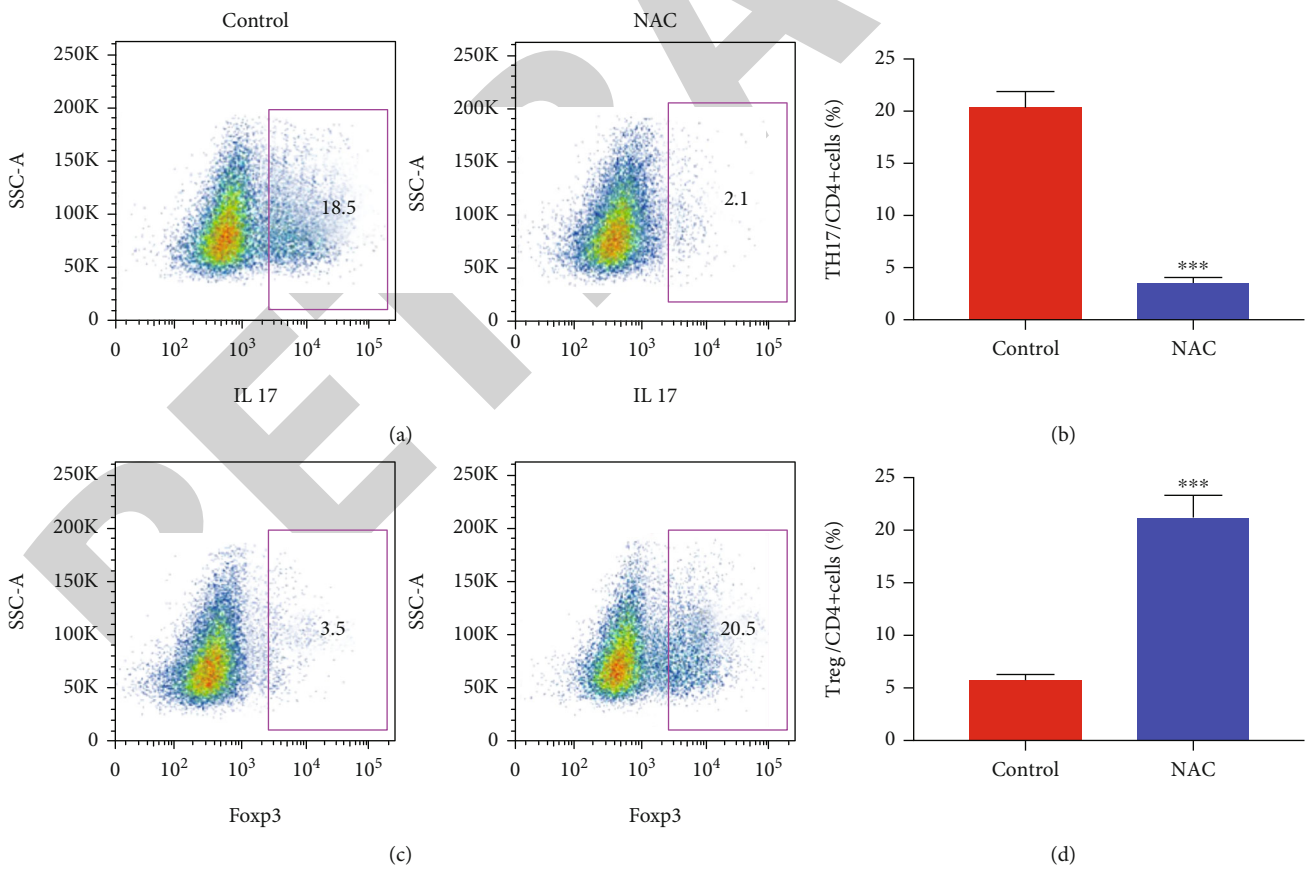


FIGURE 2: TH17 cell decreased while Treg increased after NAC treatment in the COPD patients. PBMC isolated from peripheral blood and were stained for IL-17 and Foxp3 in order to measure the percentage of Th17 and Treg. (a, b) The percentage of Th17 cells significantly decreased after oral administration of NAC. (c, d) The percentage of Treg cells significantly increased after oral administration of NAC (***) ($P < 0.01$).

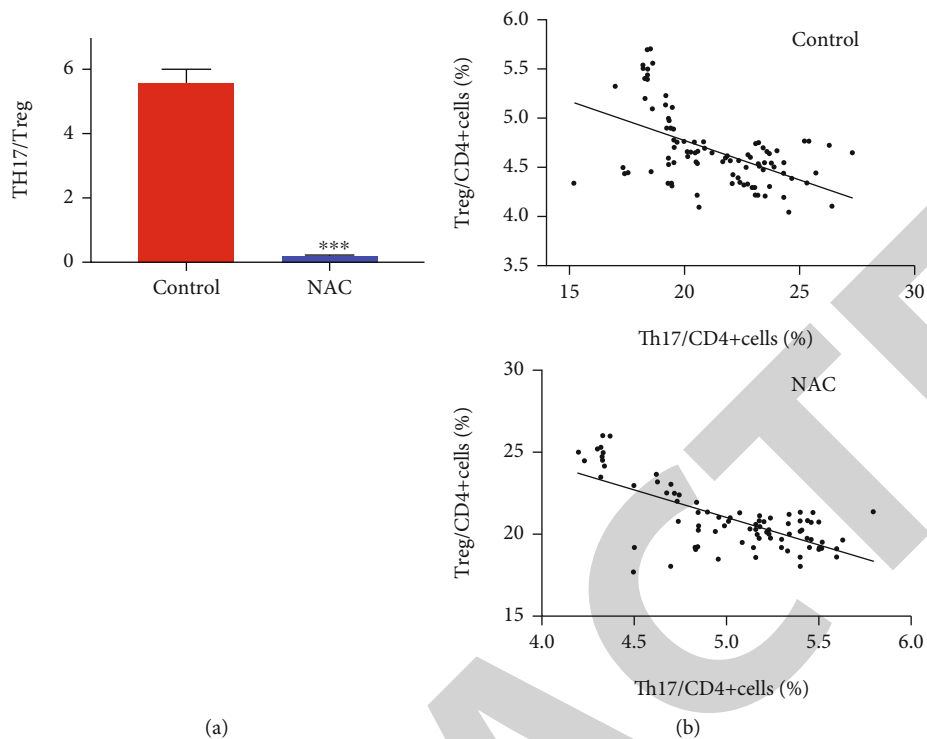


FIGURE 3: Oral NAC rebalance Th17/Treg ratio in the COPD patients. (a) The Th17/Treg ratio decreased significantly after oral administration of NAC compared with the control group. (b) Th17 cells had the negative correlation with Treg cells. (* $P < 0.05$; ** $P < 0.01$; *** $P < 0.001$).

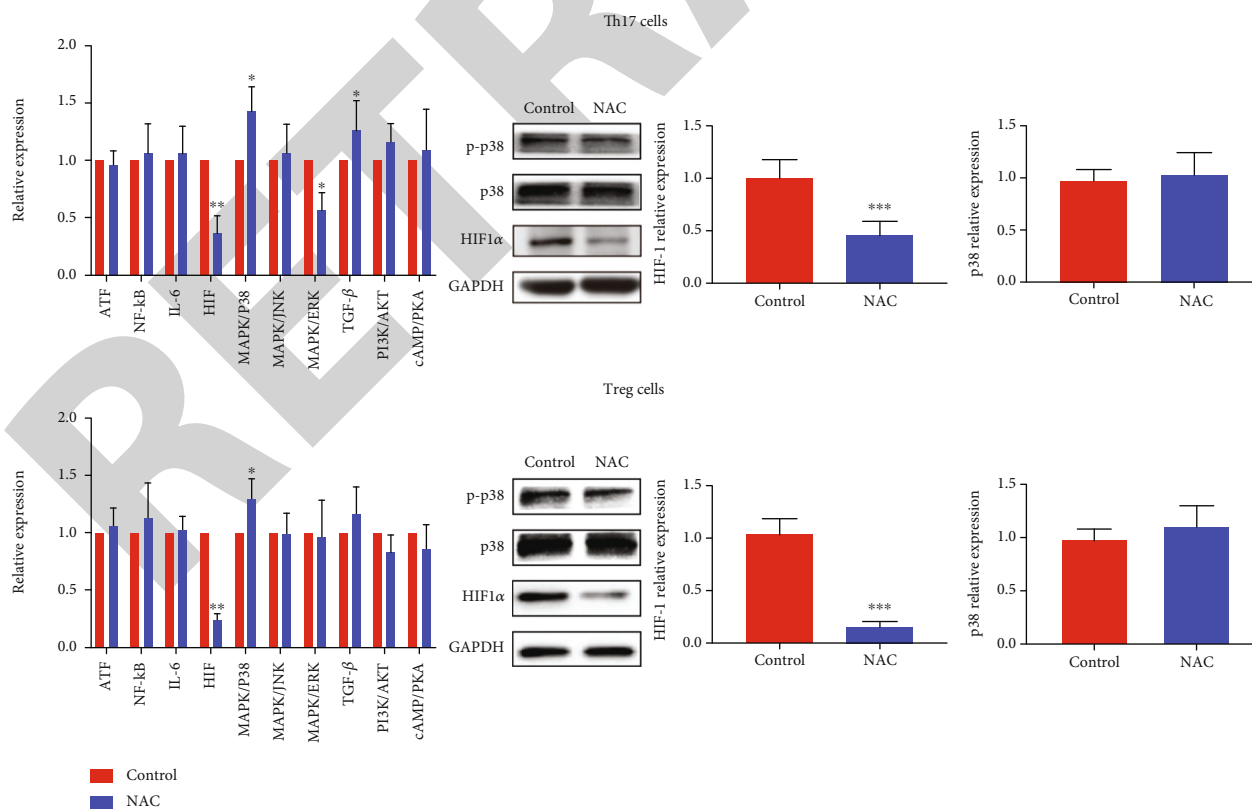


FIGURE 4: NAC significantly decreased HIF1- α expression of Th17 and Treg cells isolated from peripheral blood of COPD patients. Inflammation-pathway array, western-blot, and qRT-PCR revealed the decreased expression of HIF1- α in Th17 and Treg cells in the NAC control group. (* $P < 0.05$; ** $P < 0.01$; *** $P < 0.001$).

subgroups of CD4+ T cells, also played an important role in balancing COPD patients' immune status [5, 20]. Previous researches showed that during the development and acute exacerbation period in patients with COPD, the ratio of Treg and Th17 cells in the peripheral blood has changed significantly, as well as in bronchoalveolar lavage (BAL). The Th17 cells in the serum and Th17/Treg ratio showed a rising trend, but Treg cells were constantly falling. The normal Th17/Treg balance was broken, which led to the appearance of an inflammatory response. At the same time, the increase in Th17 cell level was negatively correlated with the decrease in Treg level, suggesting that the imbalance between these two subgroups might be one of the causes of COPD [21, 25]. Therefore, proper intervention in the Th17/Treg balance of COPD patients was important for the treatment of COPD.

Previous researches have confirmed that NAC had the capability to inhibit the accumulation of neutrophils in the lungs of COPD patients, reducing inflammation, and had a strong expectorant effect [7, 9, 10]. At the same time, NAC had a regulatory effect on immune function and could weaken cytokine activity. Some recent studies had shown that oral NAC could regulate the Th1/Th2 ratio balance, improving the quality of life of COPD patients in groups C and D, increasing lung function to a large extent [26]. Our study showed that the drug could increase the serum interleukin-10 level after oral NAC at a dosage of 1200 mg daily in the treatment group, while the proinflammation cytokine IL-9, TGF- β , TNF- α , IL-1 β , and IL-17 were all downregulated dramatically. Moreover, the proportion of Th17 in CD4+ T cells was decreased, and the proportion of Treg in CD4+ T cells was increased. Therefore, the Th17/Treg ratio was reduced compared with that before diagnosis and treatment. The results suggested that after NAC treatment, the Th17 immune response decreased, the Treg immune response increased, and Th17/Treg tended to back to a new balance, the immune status of COPD patients return to normal. To figure out the mechanism of this effect of NAC, we used inflammation-pathway microarray, western blot, and qRT-PCR to verified that HIF1- α might be a key metabolic sensor. In this study, we found HIF-1 α was truly significantly downregulated after treatment. Previous studies reported that HIF-1 α could upregulate IL-17 expression through ROR γ t; meanwhile, it also cooperated with ROR γ t protein to regulate IL-17A-related genes during Th17 development, thus enhanced the development of Th17 [13, 22]. On the other hand, reports showed that HIF-1 targeted Foxp3 for ubiquitination and proteasomal degradation, using the same ubiquitin ligase system that was responsible for the degradation of HIF-1 α itself [24]. So, based on the experimental data and result, we proposed a hypothesis that NAC could rebalance the Th17/Treg ratio and improve the immune status of COPD patients through downregulating HIF1- α .

In summary, this study reveals that NAC could affect the Th17/Treg balance in the COPD patients and had a good therapeutic effect for the immune status of COPD patients which might be through regulating the HIF1- α expression. By studying the Th17/Treg balance, possible intervention targets may be further found and developed.

Data Availability

All data in this article are available from the corresponding author upon reasonable request.

Conflicts of Interest

The authors declare no conflict of interest.

Authors' Contributions

Xiaopeng Liu and Haiying Zhou conceived and designed the experiments. Xiaopeng Liu performed the research, conducted the data analyses, and wrote the manuscript. Xiaopeng Liu and Zhixiong Hu contributed to the clinical data collection. Haiying Zhou revised the manuscript and coordinated the research team. All authors have read and approved the final manuscript.

Acknowledgments

This work was supported by Scientific Research Youth Project of Jinshan District Health Commission of Shanghai city (JSKJ-KTQN-2018-04)-LiuXiaoPeng, Hospital-level project of Jinshan Hospital Affiliated to Fudan University (2018-JSYKT-01)-LiuXiaoPeng, and Scientific Research Youth Project of Shanghai Municipal Health Commission (20204Y0172)-LiuXiaoPeng. The authors thank the patients who participated in this research and Mitchell Arico from Liwen Bianji, Edanz Group China (<http://www.liwenbianji.cn/ac>), for editing the English text of a draft of this manuscript.

References

- [1] A. I. Ritchie and J. A. Wedzicha, "Definition, causes, pathogenesis, and consequences of chronic obstructive pulmonary disease exacerbations," *Clinics in Chest Medicine*, vol. 41, no. 3, pp. 421–438, 2020.
- [2] F. Decrue, O. Gorlanova, J. Usemann, and U. Frey, "Lung functional development and asthma trajectories," *Seminars in Immunopathology*, vol. 42, no. 1, pp. 17–27, 2020.
- [3] W. W. Labaki, L. M. Kimmig, G. M. Mutlu, M. L. K. Han, and S. P. Bhatt, "Update in chronic obstructive pulmonary disease 2018," *American Journal of Respiratory & Critical Care Medicine*, vol. 199, no. 12, pp. 1462–1470, 2019.
- [4] S. M. Chan, S. Selemidis, S. Bozinovski, and R. Vlahos, "Pathobiological mechanisms underlying metabolic syndrome (MetS) in chronic obstructive pulmonary disease (COPD): clinical significance and therapeutic strategies," *Pharmacology & Therapeutics*, vol. 198, pp. 160–188, 2019.
- [5] Y. C. Su, F. Jalalvand, J. Thegerström, and K. Riesbeck, "The interplay between immune response and bacterial infection in COPD: focus upon non-typeable *Haemophilus influenzae*," *Frontiers in Immunology*, vol. 9, p. 2530, 2018.
- [6] L. Wen, S. Krauss-Etschmann, F. Petersen, and X. Yu, "Auto-antibodies in chronic obstructive pulmonary disease," *Frontiers in Immunology*, vol. 9, p. 66, 2018.
- [7] M. G. Matera, L. Calzetta, and M. Cazzola, "Oxidation pathway and exacerbations in COPD: the role of NAC," *Expert Review of Respiratory Medicine*, vol. 10, no. 1, pp. 89–97, 2016.

Research Article

The Silence of PSMC6 Inhibits Cell Growth and Metastasis in Lung Adenocarcinoma

Jian-Yu Zhang, Ke-Zhi Shi, Xiang-Yu Liao, Shi-Jun Li, Dan Bao, Ying Qian, and Dao-Jun Li 

The First College of Clinical Medical Science, Three Gorges University & Yichang Central People's Hospital, Yichang, China

Correspondence should be addressed to Dao-Jun Li; doyleli@sina.com

Received 8 March 2021; Revised 24 April 2021; Accepted 28 May 2021; Published 19 June 2021

Academic Editor: Tao Huang

Copyright © 2021 Jian-Yu Zhang et al. This is an open access article distributed under the Creative Commons Attribution License, which permits unrestricted use, distribution, and reproduction in any medium, provided the original work is properly cited.

The proteasome has been validated as an anticancer drug target, while the role of a subunit of proteasome, PSMC6, in lung adenocarcinoma (LUAD) has not been fully unveiled. In this study, we observed that both the RNA and protein of PSMC6 were highly upregulated in LUAD compared with the adjacent normal tissues. Moreover, a high PSMC6 expression was associated with poor prognosis. In accordance with this finding, PSMC6 was associated with poor tumor differentiation. Furthermore, the silence of PSMC6 by small interference RNAs (siRNAs) could significantly inhibit cell growth, migration, and invasion in lung cancer cell lines, suggesting that PSMC6 might serve as a promising therapeutic target in LUAD. To further explore the molecular mechanism of PSMC6 in LUAD, we observed that the proteasome subunits, such as PSMD10, PSMD6, PSMD9, PSMD13, PSMB3, PSMB1, PSMA4, PSMC1, PSMC2, PSMD7, and PSMD14, were highly correlated with PSMC6 expression. Based on the gene set enrichment analysis, we observed that these proteasome subunits were involved in the degradation of AXIN protein. The correlation analysis revealed that the positively correlated genes with PSMC6 were highly enriched in WNT signaling-related pathways, demonstrating that the PSMC6 overexpression may activate WNT signaling via degrading the AXIN protein, thereby promoting tumor progression. In summary, we systematically evaluated the differential expression levels and prognostic values of PSMC6 and predicted its biological function in LUAD, which suggested that PSMC6 might act as a promising therapeutic target in LUAD.

1. Introduction

Lung cancer is among the most frequent malignancies worldwide, accounting for nearly 20% of cancer-related deaths in 2018 [1]. The major risk factors for lung cancer are smoking, radon exposure, and exposure to other carcinogens [2, 3]. Patients with lung cancer often had unfavorable outcomes, and the 5-year survival rate for lung cancer remains less than 20% [4]. Novel treatments and drug designs are direly sought to improve patients' prognoses and relieve their financial burden [5].

Proteasome inhibition is considered a promising treatment strategy for various malignancies, including lung cancer. The 26S proteasome is an important protease in eukaryotic cells, which is composed of a 20S core particle (CP) and one or two 19S regulatory particles (RP) capping one or both ends of the 20S CP [6]. The 26S proteasome mediates degradation of numerous cellular proteins and

participates in multiple cellular processes, especially the cell cycle [7], which makes it a potential target in cancer therapy.

26S proteasome assembly induced by PSMD5 inactivation is observed during colorectal tumor progression, and it has been further validated that reduced 26S proteasome levels could impair cancer cell viability and that partial depletion of the 19S RP subunits could effectively result in inhibition of the 26S proteasome [8, 9]. Those subunits are essential for the 19S RP to carry out functions such as identification, binding, deubiquitination, unfolding, and translocation of substrates before proteolysis [10, 11]. Receptor RPN13 in the 19S regulatory particle is found overexpressed in ovarian and colon cancer, and it could interact with RA190, a bis-benzylidene piperidone active against cervical and ovarian cancer [12–14]. Of note, PSMC6 codes for one of the six AAA-type ATPase subunits of the 19S RP and has been identified as a protective gene in lower grade glioma [15, 16]. Its high bortezomib sensitivity makes it the most prominent

target in multiple myeloma [17]. A recent study has demonstrated that PSMC6 overexpression could impair cell cycle progression and cell proliferation via inhibiting the PI3K/AKT signaling pathway [18]. Meanwhile, S5aC, a multiubiquitin binding component of the 19S RP, is found capable of inducing A549 lung cancer cell death [19]. Therefore, a closer investigation of genes related to the 26S proteasome in lung cancer shall provide detailed information on the cellular functions of those subunits in lung cancer carcinogenesis and reveal potential therapeutic targets. In the present study, we investigated the clinical and functional relevance of PSMC6 in lung adenocarcinoma (LUAD) and explored its underlying mechanism in the initiation and progression of LUAD.

2. Materials and Methods

2.1. Data Acquisition. The gene expression data of The Cancer Genome Atlas (TCGA) and the protein expression data were downloaded from the UCSC Xena database [20] and an earlier study [21]. The Fragment Per Kilo-Million (FPKM) and read count-based data were collected from the TCGA cohort. Briefly, the raw fastq data were aligned to reference genome by STAR v2 [22] and gene expression levels were quantified by HTSeq [23]. The gene-level protein intensities were collected, imputed by the minimal protein intensity, and logarithm transformed.

2.2. Differential Expression. The differential expression between two groups was conducted by Wilcoxon rank sum test, while the multisample comparison was tested by the Kruskal-Wallis test. Moreover, the fold change was also employed to test the difference.

2.3. Survival Analysis. The Cox proportional hazard regression model was used to evaluate the association between PSMC6 expression and survival time. Particularly, the PSMC6 expression was discretized as high and low expression levels using the median as cut-off. The survival analysis was implemented in R survival package (<https://cran.r-project.org/web/packages/survival/index.html>).

2.4. Functional Inference of PSMC6. The prediction of the biological function for PSMC6 was conducted by integrating the correlation analysis, protein-protein interaction (PPI) analysis, and gene set enrichment analysis (GSEA). The PPI data was obtained from the BioGRID database [24]. Specifically, we first extracted the proteins (genes) directly interacting with PSMC6 from the PPI network. Secondly, those interacting proteins that showed a significantly positive correlation with PSMC6 were retained for the next step analysis (p value < 0.05, Spearman correlation > 0.3). Thirdly, those genes were subjected to the gene set enrichment analysis (GSEA) against the pathways curated from the Reactome database, and hypergeometric test was employed to test the statistical significance of the GSEA. The GSEA was implemented in the R clusterProfiler package [25].

2.5. Cell Culture, RNA Isolation, and Quantitative Real-Time PCR (qRT-PCR). The cells were cultured following a previous study [26]. Total RNA was isolated from the A549 and

H1299 cell lines using TRIzol reagent (Sangon, China). The reverse transcription of the RNAs was performed to synthesize the cDNAs following the instructions of PrimeScript™ RT reagent Kit (Takara Bio Inc.). The mRNA expression was quantified by qRT-PCR using SYBR premix Ex Taq II with LightCycler 480II (Roche) instrument. The sequences of the primers are as follows: PSMC6 forward, 5-CGGGTGAAAGTGCTCGTTTG-3 and reverse, 5-AGCAAAGCAGGATCCAGTGT-3 and GAPDH forward, 5-GTCGTGGAGTCTACTGGGTGTC-3 and reverse, 5-GAGCCCTTCCA CAATGCCAAA-3. All these experiments were conducted in triplicates.

2.6. RNA Interference and Transfection. We purchased the synthetic PSMC6 siRNAs and its negative control (NC) at the concentration of 100 nM from GenePharma (Shanghai, China). Specific siRNAs targeting PSMC6 are as follows: si-PSMC6 #1: 5'-ACAAGGAGATCGACGGCCGTCTTAA-3' and si-PSMC6 #2: 5'-CGGCCGTCTTAAGGAGTTAAGGGAA-3'. Following the manufacturer's procedure, the transfection was conducted with Lipofectamine 2000 Transfection Reagent (Life, USA), which was purchased from Life Technologies. All these experiments were conducted in triplicates.

2.7. Cell Counting Kit-8 (CCK-8) Analysis. The CCK-8 assay was used to determine the cell proliferation level following the method from a previous study [26]. All these experiments were conducted in triplicates.

2.8. Cell Invasion and Migration Assays. The cell invasion and migration assays were performed following the method of a previous study [27]. Specifically, Transwell plates (8 μm pore size, 6.5 mm diameter; Corning, USA) precoated with Matrigel Basement Membrane Matrix (coating concentration: 1 mg/ml; BD Biosciences, Franklin Lakes, NJ) were used for the migration assay according to the manufacturer's protocol. Subsequently, the media containing 1% FBS into the upper chamber of the Transwell filter on a 24-well plate were used for cell seeding after transfection, and those containing 10% FBS into the lower well of the plate were used as an attractant. After 72 h of incubation, cells on the upper side of the filters or migrated to the lower side were removed or fixed with methanol, stained with Giemsa, and counted under a microscope. Migration assays were performed with the same procedure, except that the Transwell chamber inserts were not coated with Matrigel, and the medium containing 10% FBS was used for cell suspensions. All these experiments were conducted in triplicates.

3. Results

3.1. PSMC6 Is a Poor Prognosis in Lung Adenocarcinoma. To reveal the expression pattern of PSMC6 in lung adenocarcinoma (LUAD), we collected two cohorts from the Cancer Genome Atlas (TCGA) and Xu et al. and evaluated its differential expression levels between the tumor and normal tissues. Specifically, the mRNA and protein expressions of PSMC6 were highly upregulated in LUAD as compared with

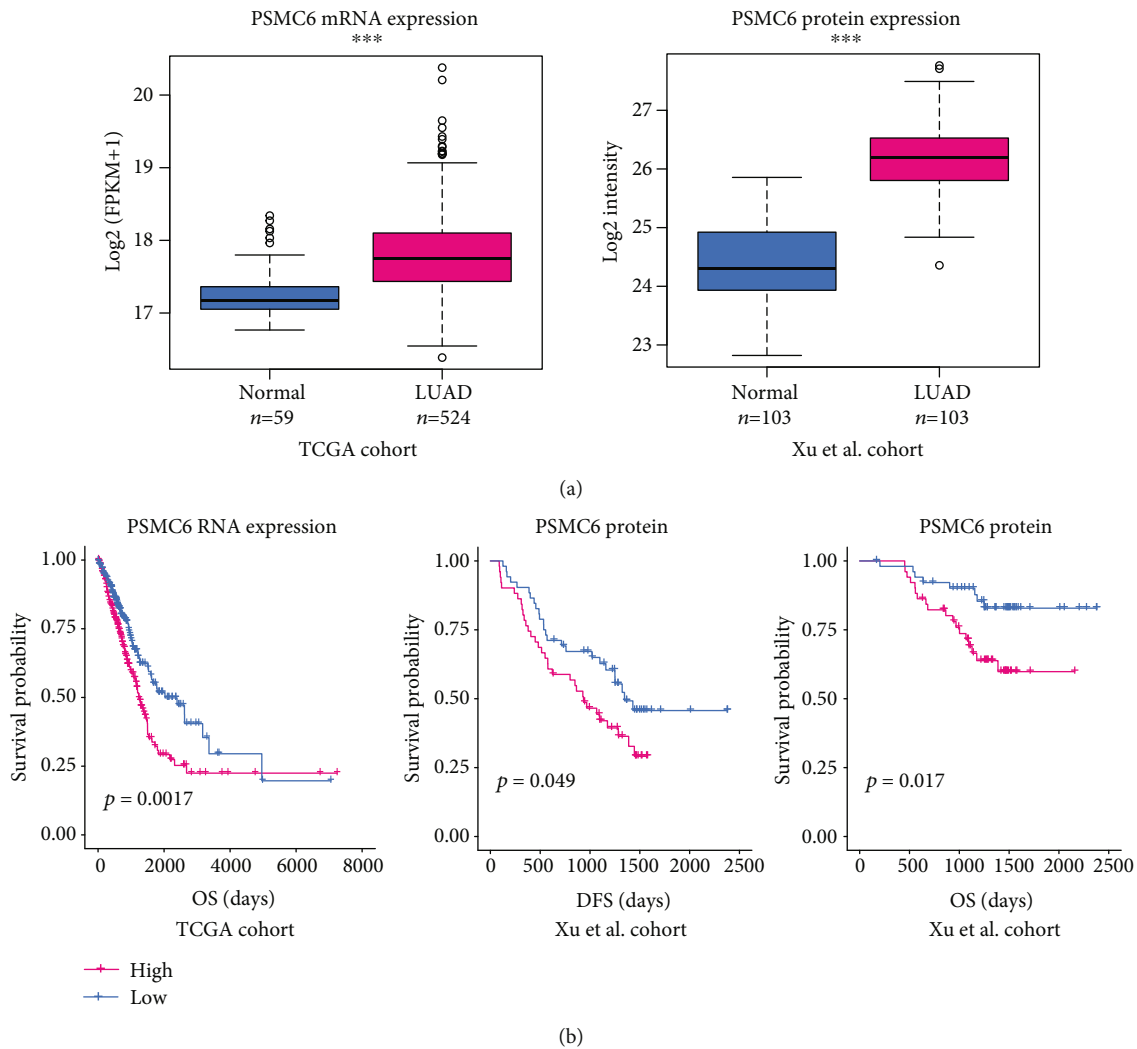


FIGURE 1: The upregulation of PSMC6 in lung adenocarcinoma (LUAD). (a) The RNA and protein expression levels of PSMC6 in LUAD and adjacent normal tissues. (b) The correlation between survival time and PSMC6 RNA or protein expression levels. The red and blue lines indicate the samples with high and low PSMC6 expression. DFS: disease-free survival; OS: overall survival.

the adjacent normal tissues (Figure 1(a), Wilcoxon rank sum test, p value < 0.001). Notably, the PSMC6 protein was expressed over fourfold in LUAD than that in the normal tissues (Figure 1(a)).

Moreover, the tumor samples were stratified into the high- and low-expression groups. The survival analysis of PSMC6 RNA and protein expressions revealed that patients with high PSMC6 RNA expression had shorter overall survival (OS) than those with a low expression (Figure 1(b), log-rank test, p value < 0.05). Consistently, the LUAD samples with high PSMC6 protein expression had both shorter disease-free survival (DFS) and OS than those with low PSMC6 protein expression (Figure 1(b), log-rank test, p value < 0.05). These results indicated that PSMC6 overexpression might result in a worse prognosis and act as a prognostic biomarker in LUAD.

3.2. The Association of PSMC6 with the Clinical Characteristics. To evaluate the clinical significance of PSMC6 in LUAD, we compared the RNA or protein expres-

sion of PSMC6 of tumor samples with different clinical characteristics. Notably, PSMC6 was expressed higher in LUAD with residual tumor than those without (Figure 2(a), p value < 0.01), suggesting that PSMC6 was associated with residual tumor, which was considered a risk factor of tumor recurrence [28, 29]. Among the three disease types, LUAD with adenomas and adenocarcinomas had a higher RNA expression of PSMC6 than the other two disease types (Figure 2(b), Kruskal-Wallis test, p value < 0.001), indicating that LUAD with the disease type of adenomas and adenocarcinomas might have a higher degree of malignancy. Consistently, PSMC6 RNA expression was higher in the LUAD patients with poorly differentiated tumor than those with well and moderately differentiated tumors (Figure 2(c)), suggesting that PSMC6 was associated with the tumor differentiation. Furthermore, among the 7 major subtypes of LUAD, solid adenocarcinoma of the lung had the highest protein expression of PSMC6 (Figure 2(d)), suggesting that solid adenocarcinoma of the lung might have a relatively worse prognosis than other subtypes. These results disclosed

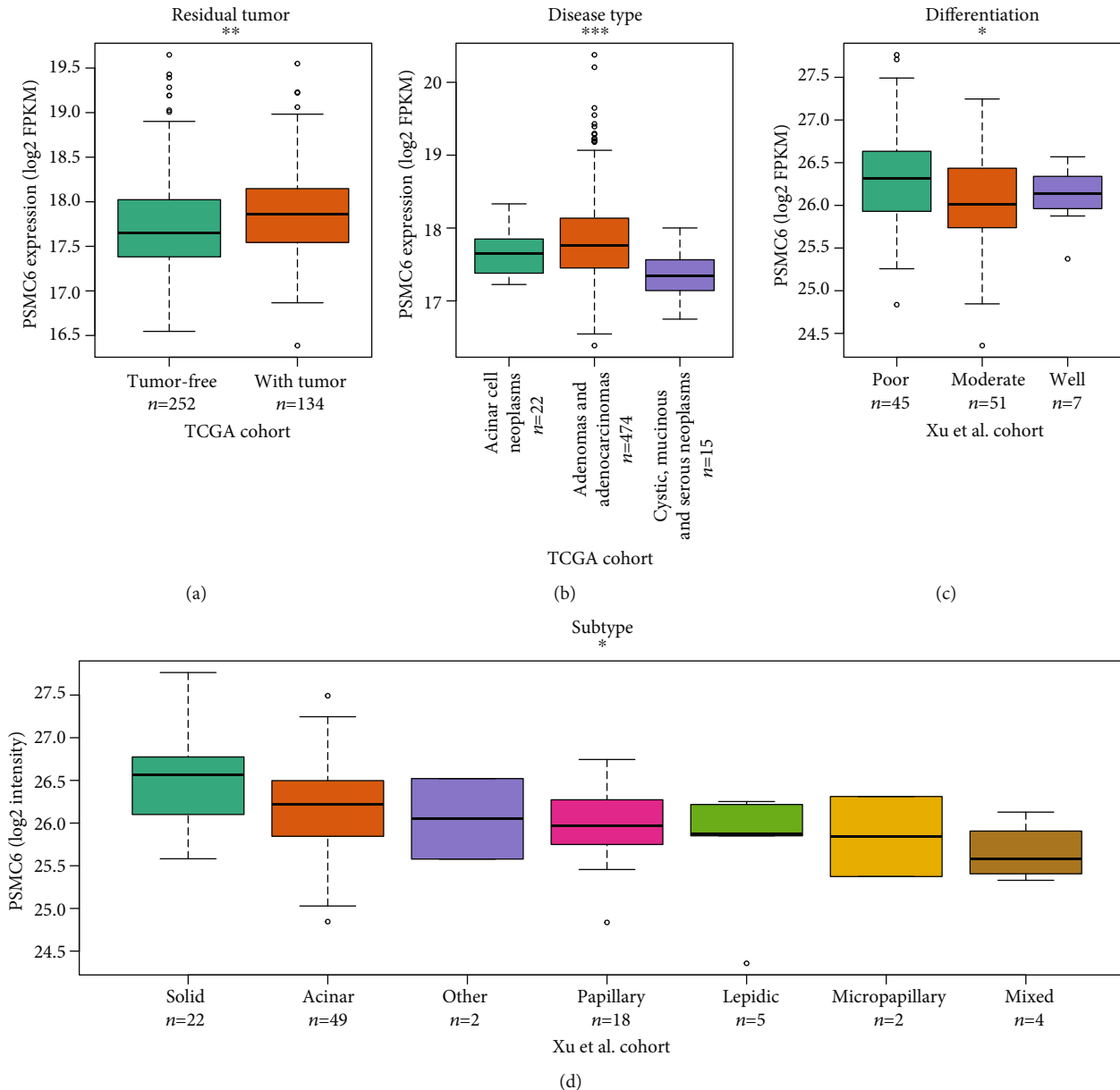


FIGURE 2: The association of PSMC6 expression with clinical factors. The association of PSMC6 expression with residual tumor, disease type, differentiation, and subtype are displayed in (a), (b), (c), and (d), respectively. *, **, and *** represent the p values below 0.05, 0.01, and 0.001.

that PSMC6 was clinically relevant to factors including residual tumor, disease type, tumor differentiation, and LUAD subtype.

3.3. Silence of PSMC6 Inhibits Cell Proliferation of Non-Small-Cell Lung Cancers. To uncover the functional role of PSMC6 in non-small-cell lung cancer (NSCLC), we performed CCK-8 assay to test the impact of PSMC6 on the cell proliferation (Materials and Methods). Specifically, we designed two small interface RNAs (siRNA) for PSMC6 mRNA, termed as si-PSMC6 #1 and si-PSMC6 #2, and transfected into two NSCLC cell lines, A549 and H1299. As shown in Figures 3(a) and 3(b), the siRNA transfection could efficiently suppress the RNA expression levels of PSMC6 in the two cell lines (p value < 0.01) using quantitative real-

time polymerase chain reaction (qPCR). With the siRNA transfection, the cell proliferation levels were found to be significantly inhibited at the fifth day (Figures 3(c) and 3(d), p value < 0.05). These results demonstrated that silence of PSMC6 could efficiently inhibit the cell proliferation of NSCLC.

3.4. Silence of PSMC6 Inhibits Migratory and Invasive Abilities of Non-Small-Cell Lung Cancer Cells. As PSMC6 was negatively associated with survival time of LUAD patients, we then investigated whether silence of PSMC6 could restrict the migratory and invasive abilities of NSCLC cells. Expectedly, the number of migratory cancer cells was obviously decreased in the cells with si-PSMC6 transfection than the negative controls (Figure 4(a)). The quantitative

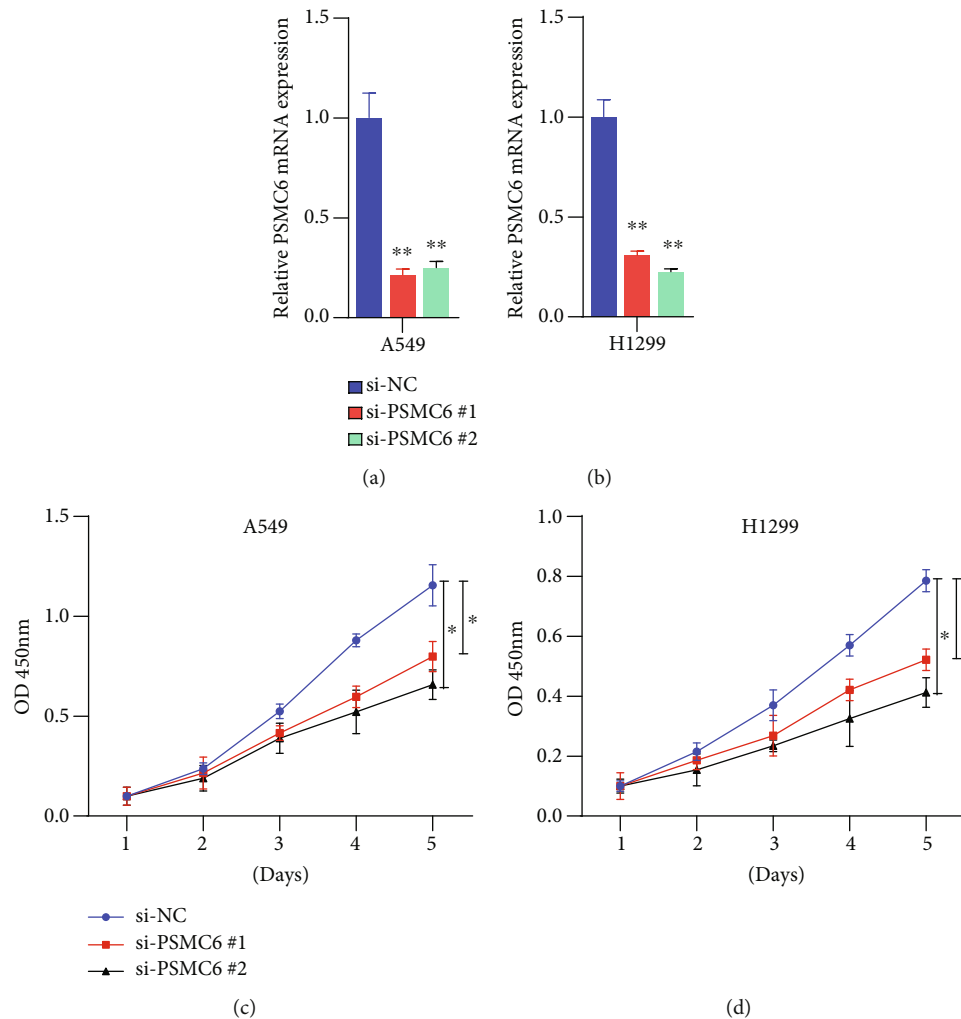


FIGURE 3: The impact of PSMC6 silencing on the tumor cell proliferation. The relative mRNA expression of PSMC6 in negative controls and cell lines with siRNA treatments (si-PSMC6 #1 or #2). The experiments for A549 and H1299 cell lines are shown in (a) and (b), respectively. The cell proliferation levels of A549 and H1299 with and without siRNA treatments (si-PSMC6 #1 and si-PSMC6 #2) are displayed in (c) and (d). *, **, and *** represent the *p* values below 0.05, 0.01, and 0.001.

analysis revealed that the number of migratory cells with si-PSMC6 transfection was greater in the cells with si-PSMC6 treatment (Figure 4(b)). Consistently, the tumor cell invasion was also inhibited by the PSMC6 silencing (Figures 4(c) and 4(d)). These results indicated that silencing of PSMC6 could inhibit migratory and invasive abilities of cancer cells.

3.5. The Proteasome Might Activate WNT Signaling via Degrading AXIN Protein. To gain insights into the molecular mechanism of PSMC6 in LUAD, we conducted a correlation analysis between PSMC6 and other genes using both RNA-seq and proteome data. Totally, we identified 1222 genes coexpressed with PSMC6 (Spearman correlation > 0.3), of which, 26 genes encoded proteins interacting with PSMC6 protein. The gene set enrichment analysis revealed that degradation of beta-catenin by the destruction complex and degradation of AXIN was significantly enriched by these 26 genes (Figure 5(a)). Specifically, the proteasome subunits such as PSMD10, PSMD6, PSMD9, PSMD13, PSMB3, PSMB1, PSMA4, PSMC1, PSMC2, PSMD7, and PSMD14

were involved in those two pathways (Figure 5(b)). As the AXIN protein acted as a tumor suppressor to inhibit WNT signaling pathway, its degradation might result in WNT signaling activation. Consistently, the positively correlated genes with PSMC6 were highly enriched in WNT signaling-related pathways such as beta-catenin-independent WNT signaling, signaling by WNT, and TCF-dependent signaling in response to WNT at both RNA (Figure 5(c), FDR < 0.05) and protein (Figure 5(d), FDR < 0.05) levels. These results indicated that PSMC6 might activate WNT signaling via degrading AXIN protein.

4. Discussion

The proteasome has been validated as an anticancer drug target [30], while the role of a subunit of proteasome, PSMC6, in lung adenocarcinoma (LUAD) has not been fully unveiled. In this study, we observed that both the RNA and protein of PSMC6 were highly upregulated in LUAD compared with the adjacent normal tissues. Moreover, high

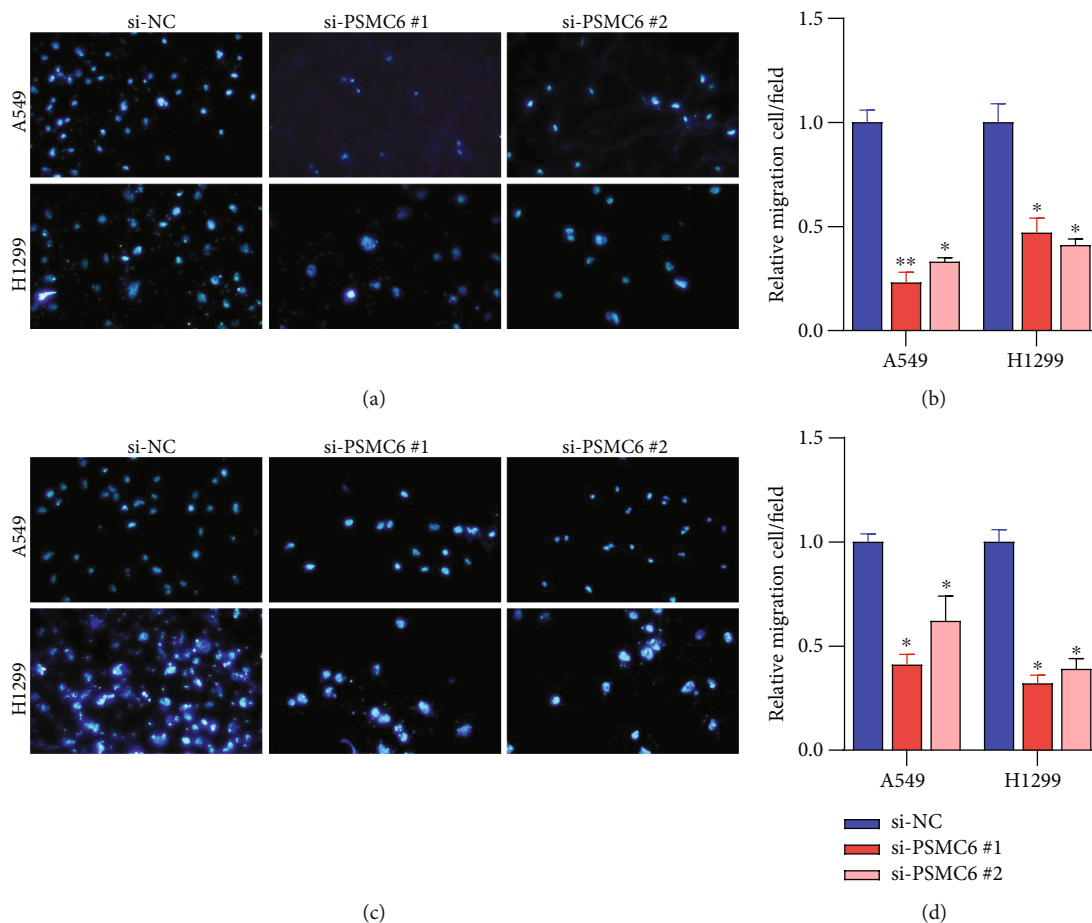


FIGURE 4: The impact of PSMC6 silencing on cell invasion and migration. The cell invasion (a, b) and migration (c, d) of A549 and H1299 after negative controls and siRNA transfections are counted by Transwell assay. *, **, and *** represent the p values below 0.05, 0.01, and 0.001.

PSMC6 expression was associated with poor prognosis. To our knowledge, previous studies rarely reported this finding. However, the other subunits of proteasome, such as PSMD3, PSMC2, and PSMD4, were upregulated in several cancers and associated with prognosis [31–33]. After systematic treatments, some LUAD patients might still have residual tumors, which had been considered a risk factor of recurrence [28, 29]. In accordance with this finding, PSMC6 was associated with poor tumor differentiation, suggesting that high expression of PSMC6 in patients with residual tumors or poor tumor differentiation indicates that PSMC6 may be associated with tumor recurrence. Moreover, the PSMC6 was also observed to have higher expression levels in some histology subtypes such as adenomas/adenocarcinomas and solid tumor subtypes. The solid predominant subtype of LUAD has been observed to have much worse prognosis than other subtypes [34].

Moreover, the silence of PSMC6 by siRNA could significantly inhibit cell growth, migration, and invasion in lung cancer cell lines. Consistently, PSMC6 was also identified as a target for bortezomib sensitivity in multiple myeloma by CRISPR genome-wide screening [16]. We thus speculated that PSMC6 might serve as a promising therapeutic target in LUAD.

To further explore the molecular mechanism of PSMC6 in LUAD, we observed that the proteasome subunits, such as PSMD10, PSMD6, PSMD9, PSMD13, PSMB3, PSMB1, PSMA4, PSMC1, PSMC2, PSMD7, and PSMD14, were highly correlated with PSMC6 expression. It should be noted that these proteins could directly interact with PSMC6 and act as components of proteasome. Among these proteasome subunits, PSMB3 [35] and PSMD14 [36] have been found to promote lung adenocarcinoma progression, while PSMA4 polymorphisms are associated with lung cancer susceptibility and response to cisplatin-based chemotherapy [37], suggesting that the proteasome may be associated with the LUAD progression and drug response due to numerous subunits. Based on the gene set enrichment analysis, we observed that these proteasome subunits were involved in the degradation of the AXIN protein. The correlation analysis revealed that the positively correlated genes with PSMC6 were highly enriched in WNT signaling-related pathways. The activity of WNT signaling was enhanced by the degradation of the AXIN complex via the proteasome [38], further demonstrating that the PSMC6 overexpression may activate WNT signaling via degrading AXIN protein, thereby promoting tumor progression. However, this mechanism needs to be validated by more experimental data.

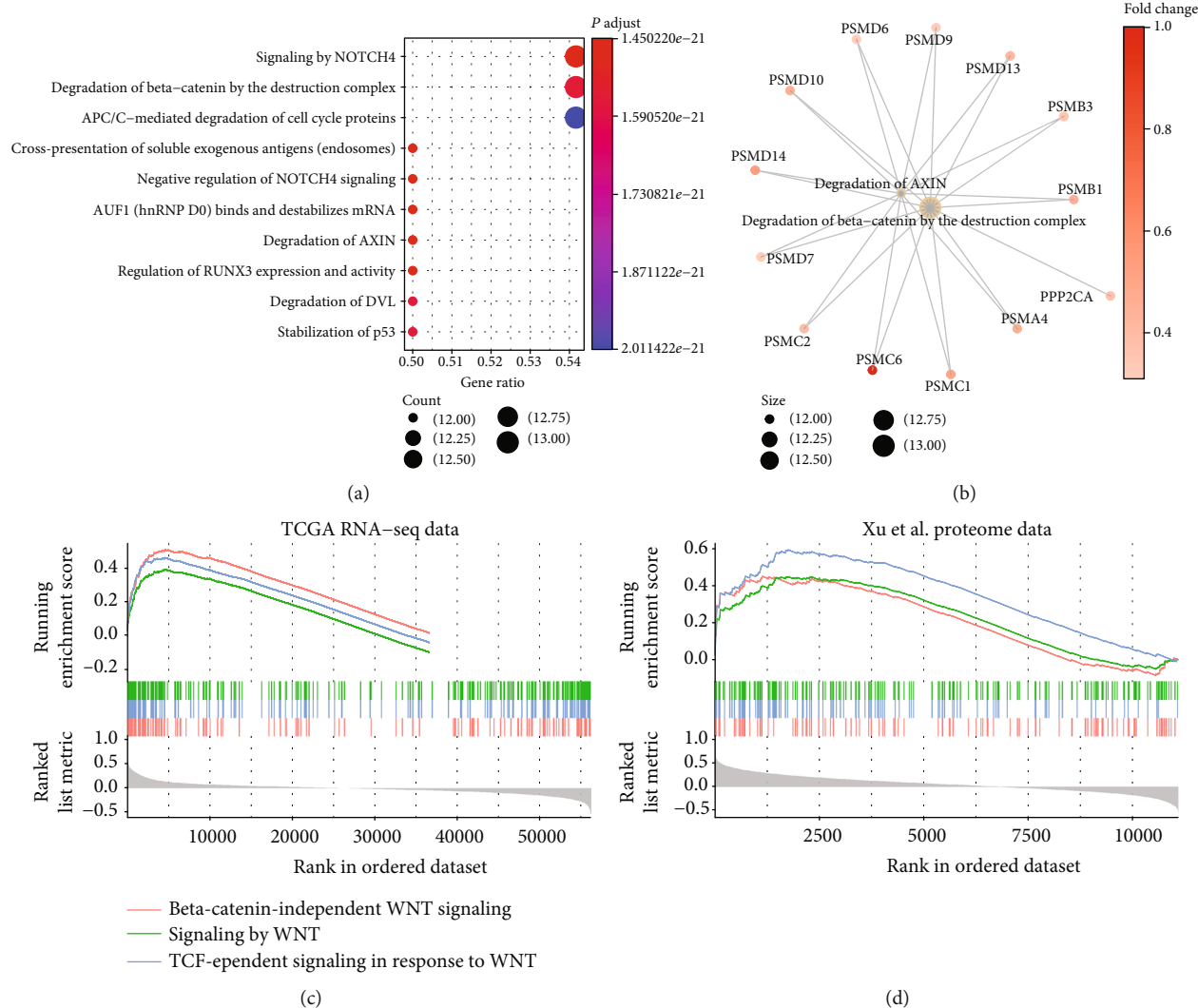


FIGURE 5: The proteins interacting with PSMC6 and the downstream pathways. (a) The pathway enriched by the proteins interacting with PSMC6. The node color and size represent the p value and number of genes within the pathways. (b) The WNT signaling-related pathways enriched by the proteasome subunits interacting with PSMC6. (c, d) The correlation between the PSMC6 and the genes involved in WNT signaling pathways. The lines under the curves represent the genes involved in the WNT signaling pathways, which were ranked by their correlation coefficients with PSMC6. The coefficients are represented by the grey bars.

In summary, we systematically evaluated the differential expression levels and prognostic values of PSMC6 and predicted its biological function in LUAD, which suggested that PSMC6 might act as a promising therapeutic target in LUAD.

Data Availability

All data supporting this study are collected from a public database such as TCGA and Gene Expression Omnibus (GEO), which have been cited as references in Materials and Methods.

Conflicts of Interest

The authors have declared that no competing interests exist.

References

- [1] F. Bray, J. Ferlay, I. Soerjomataram, R. L. Siegel, L. A. Torre, and A. Jemal, "Global cancer statistics 2018: GLOBOCAN estimates of incidence and mortality worldwide for 36 cancers in 185 countries," *CA: a Cancer Journal for Clinicians*, vol. 68, no. 6, pp. 394–424, 2018.
- [2] J. C. Martin-Sanchez, U. Bilal, R. Cleries et al., "Modelling lung cancer mortality rates from smoking prevalence: fill in the gap," *Cancer Epidemiology*, vol. 49, pp. 19–23, 2017.
- [3] A. G. Pallis and K. N. Syrigos, "Lung cancer in never smokers: disease characteristics and risk factors," *Critical Reviews in Oncology/Hematology*, vol. 88, no. 3, pp. 494–503, 2013.
- [4] F. R. Hirsch, G. V. Scagliotti, J. L. Mulshine et al., "Lung cancer: current therapies and new targeted treatments," *Lancet*, vol. 389, no. 10066, pp. 299–311, 2017.

- [5] F. Oberndorfer and L. Mullauer, "Molecular pathology of lung cancer: current status and perspectives," *Current Opinion in Oncology*, vol. 30, no. 2, pp. 69–76, 2018.
- [6] J. A. M. Bard, E. A. Goodall, E. R. Greene, E. Jonsson, K. C. Dong, and A. Martin, "Structure and function of the 26S proteasome," *Annual Review of Biochemistry*, vol. 87, no. 1, pp. 697–724, 2018.
- [7] X. Guo and J. E. Dixon, "The 26S proteasome: a cell cycle regulator regulated by cell cycle," *Cell Cycle*, vol. 15, no. 7, pp. 875–876, 2016.
- [8] A. Levin, A. Minis, G. Lalazar, J. Rodriguez, and H. Steller, "PSMD5 inactivation promotes 26S proteasome assembly during colorectal tumor progression," *Cancer Research*, vol. 78, no. 13, pp. 3458–3468, 2018.
- [9] P. Tsvetkov, J. Adler, N. Myers, A. Biran, N. Reuven, and Y. Shaul, "Oncogenic addiction to high 26S proteasome level," *Cell Death & Disease*, vol. 9, no. 7, p. 773, 2018.
- [10] I. Livneh, V. Cohen-Kaplan, C. Cohen-Rosenzweig, N. Avni, and A. Ciechanover, "The life cycle of the 26S proteasome: from birth, through regulation and function, and onto its death," *Cell Research*, vol. 26, no. 8, pp. 869–885, 2016.
- [11] X. Huang, B. Luan, J. Wu, and Y. Shi, "An atomic structure of the human 26S proteasome," *Nature Structural & Molecular Biology*, vol. 23, no. 9, pp. 778–785, 2016.
- [12] M. S. Fejzo, L. Anderson, E. M. von Euw et al., "Amplification target ADRM1: role as an oncogene and therapeutic target for ovarian cancer," *International Journal of Molecular Sciences*, vol. 14, no. 2, pp. 3094–3109, 2013.
- [13] R. K. Anchoori, B. Karanam, S. Peng et al., "A bis-benzylidene piperidone targeting proteasome ubiquitin receptor RPN13/ADRM1 as a therapy for cancer," *Cancer Cell*, vol. 24, no. 6, pp. 791–805, 2013.
- [14] W. Chen, X. T. Hu, Q. L. Shi, F. B. Zhang, and C. He, "Knockdown of the novel proteasome subunit Adrm1 located on the 20q13 amplicon inhibits colorectal cancer cell migration, survival and tumorigenicity," *Oncology Reports*, vol. 21, no. 2, pp. 531–537, 2009.
- [15] M. Zhang, X. Wang, X. Chen, Q. Zhang, and J. Hong, "Novel immune-related gene signature for risk stratification and prognosis of survival in lower-grade glioma," *Frontiers in Genetics*, vol. 11, p. 363, 2020.
- [16] C. X. Shi, K. M. Kortüm, Y. X. Zhu et al., "CRISPR genome-wide screening identifies dependence on the proteasome subunit PSMC6 for bortezomib sensitivity in multiple myeloma," *Molecular Cancer Therapeutics*, vol. 16, no. 12, pp. 2862–2870, 2017.
- [17] A. Schweitzer, A. Aufderheide, T. Rudack et al., "Structure of the human 26S proteasome at a resolution of 3.9 Å," *Proceedings of the National Academy of Sciences of the United States of America*, vol. 113, no. 28, pp. 7816–7821, 2016.
- [18] Y. Zhang, X. Cao, P. Li et al., "PSMC6 promotes osteoblast apoptosis through inhibiting PI3K/AKT signaling pathway activation in ovariectomy-induced osteoporosis mouse model," *Journal of Cellular Physiology*, vol. 235, no. 7-8, pp. 5511–5524, 2020.
- [19] M. Elangovan, E. S. Choi, B. G. Jang, M. S. Kim, and Y. J. Yoo, "The ubiquitin-interacting motif of 26S proteasome subunit S5a induces A549 lung cancer cell death," *Biochemical and Biophysical Research Communications*, vol. 364, no. 2, pp. 226–230, 2007.
- [20] M. J. Goldman, B. Craft, M. Hastie et al., "Visualizing and interpreting cancer genomics data via the Xena platform," *Nature Biotechnology*, vol. 38, no. 6, pp. 675–678, 2020.
- [21] J. Y. Xu, C. Zhang, X. Wang et al., "Integrative proteomic characterization of human lung adenocarcinoma," *Cell*, vol. 182, no. 1, pp. 245–261.e17, 2020, e217.
- [22] A. Dobin, C. A. Davis, F. Schlesinger et al., "STAR: ultrafast universal RNA-seq aligner," *Bioinformatics*, vol. 29, no. 1, pp. 15–21, 2013.
- [23] S. Anders, P. T. Pyl, and W. Huber, "HTSeq—a Python framework to work with high-throughput sequencing data," *Bioinformatics*, vol. 31, no. 2, pp. 166–169, 2015.
- [24] R. Oughtred, C. Stark, B. J. Breitkreutz et al., "The BioGRID interaction database: 2019 update," *Nucleic Acids Research*, vol. 47, no. D1, pp. D529–D541, 2019.
- [25] G. Yu, L. G. Wang, Y. Han, and Q. Y. He, "clusterProfiler: an R package for comparing biological themes among gene clusters," *OMICS*, vol. 16, no. 5, pp. 284–287, 2012.
- [26] X. Wan, S. Yang, W. Huang et al., "UHRF1 overexpression is involved in cell proliferation and biochemical recurrence in prostate cancer after radical prostatectomy," *Journal of Experimental & Clinical Cancer Research*, vol. 35, no. 1, p. 34, 2016.
- [27] C. Yi, X. Wan, Y. Zhang et al., "SNORA42 enhances prostate cancer cell viability, migration and EMT and is correlated with prostate cancer poor prognosis," *The International Journal of Biochemistry & Cell Biology*, vol. 102, pp. 138–150, 2018.
- [28] K. Pantel and C. Alix-Panabieres, "Liquid biopsy and minimal residual disease – latest advances and implications for cure," *Nature Reviews Clinical Oncology*, vol. 16, no. 7, pp. 409–424, 2019.
- [29] J. H. Zhou, D. Rosen, A. Andreou et al., "Residual tumor thickness at the tumor-normal tissue interface predicts the recurrence-free survival in patients with liver metastasis of breast cancer," *Annals of Diagnostic Pathology*, vol. 18, no. 5, pp. 266–270, 2014.
- [30] E. E. Manasanch and R. Z. Orlowski, "Proteasome inhibitors in cancer therapy," *Nature Reviews. Clinical Oncology*, vol. 14, no. 7, pp. 417–433, 2017.
- [31] S. Aydoğan Türkoğlu, G. Dayi, and F. Köçkar, "Upregulation of PSMD4 gene by hypoxia in prostate cancer cells," *Turkish Journal of Biology*, vol. 44, no. 5, pp. 275–283, 2020.
- [32] J. He, J. Xing, X. Yang et al., "Silencing of proteasome 26S subunit ATPase 2 regulates colorectal cancer cell proliferation, apoptosis, and migration," *Chemotherapy*, vol. 64, no. 3, pp. 146–154, 2019.
- [33] A. S. Fararjeh, L. C. Chen, Y. S. Ho et al., "Proteasome 26S subunit, non-ATPase 3 (PSMD3) regulates breast cancer by stabilizing HER2 from degradation," *Cancers*, vol. 11, no. 4, p. 527, 2019.
- [34] N. Miyahara, K. Nii, A. Benazzo et al., "Solid predominant subtype in lung adenocarcinoma is related to poor prognosis after surgical resection: a systematic review and meta-analysis," *European Journal of Surgical Oncology*, vol. 45, no. 7, pp. 1156–1162, 2019.
- [35] M. Blijlevens, M. A. Komor, R. Sciarillo, E. F. Smit, R. J. A. Fijneman, and V. W. van Beusechem, "Silencing core spliceosome Sm gene expression induces a cytotoxic splicing switch in the proteasome subunit beta 3 mRNA in non-small cell lung cancer cells," *International Journal of Molecular Sciences*, vol. 21, no. 12, p. 4192, 2020.

- [36] L. Zhang, H. Xu, C. Ma et al., "Upregulation of deubiquitinase PSMD14 in lung adenocarcinoma (LUAD) and its prognostic significance," *Journal of Cancer*, vol. 11, no. 10, pp. 2962–2971, 2020.
- [37] T. Wang, T. Chen, A. Thakur et al., "Association of PSMA4 polymorphisms with lung cancer susceptibility and response to cisplatin-based chemotherapy in a Chinese Han population," *Clinical & Translational Oncology*, vol. 17, no. 7, pp. 564–569, 2015.
- [38] V. S. Li, S. S. Ng, P. J. Boersema et al., "Wnt Signaling through inhibition of β -catenin degradation in an intact Axin1 complex," *Cell*, vol. 149, no. 6, pp. 1245–1256, 2012.

Research Article

PLOD3 Is Associated with Immune Cell Infiltration and Genomic Instability in Colon Adenocarcinoma

Xianyu Deng ¹, Yun Pan,¹ Muqing Yang,² Ying Liu,³ and Jiyu Li ¹

¹Colorectal Cancer Center, Tenth People's Hospital of Tongji University, Tongji University School of Medicine, China

²Center for Difficult and Complicated Abdominal Surgery, Tenth People's Hospital of Tongji University, Tongji University School of Medicine, China

³Department of General Surgery, Tenth People's Hospital of Tongji University, Tongji University School of Medicine, China

Correspondence should be addressed to Jiyu Li; leejiyu@sina.com

Received 6 April 2021; Revised 21 May 2021; Accepted 28 May 2021; Published 19 June 2021

Academic Editor: Tao Huang

Copyright © 2021 Xianyu Deng et al. This is an open access article distributed under the Creative Commons Attribution License, which permits unrestricted use, distribution, and reproduction in any medium, provided the original work is properly cited.

Procollagen-lysine, 2-oxoglutarate 5-dioxygenases (PLODs) are a family of enzymes. However, the clinical and functional roles of PLOD3 in colon adenocarcinoma (COAD) have not been investigated. The present study found that PLOD3 was highly upregulated in COAD, which may be resulted from its aberrant DNA methylation. The upregulation of both PLOD3 mRNA and protein was confirmed in our tissue samples. Moreover, high PLOD3 was identified to be associated with unfavorable prognosis in COAD. As genome instability is a hallmark of cancer, PLOD3 was expressed higher in COAD samples with high chromosomal instability (CIN-high) than those with low CIN (CIN-low) and higher in those with low MSI than high MSI, indicating that PLOD3 expression was associated with tumor genomic instability. Furthermore, immune cells showed significantly different infiltrating levels between the high and low PLOD3 expression groups, and the immune score was negatively correlated with PLOD3 expression and higher in samples with low PLOD3 expression, suggesting that high PLOD3 expression was associated with reduced immune cell infiltrating levels in COAD. To further uncover the underlying mechanism of PLOD3 in PLOD3, we compared the COAD samples of high PLOD3 expression with those of low PLOD3 expression and found that high expression of PLOD3 was associated with reduced expression of immune regulators and enhanced activities of two tumor-promoting pathways, including gluconeogenesis and TGF-beta signaling in epithelial-mesenchymal transition (EMT), suggesting that high expression of PLOD3 causes poor prognosis in COAD by weakening the immune cell infiltration and enhancing activities of tumor-promoting pathways. In summary, the present study highlights the importance of PLOD3 and provides the evidence about the functional role of PLOD3 in COAD.

1. Introduction

Colon cancer is one of the most prevalent malignancies worldwide. It is estimated globally that colorectal cancer would account for 6.1% of new cancer cases and for 9.2% of cancer-related deaths [1]. Heritable factors are not responsible for most colorectal cancer cases, and chronic intestinal inflammation has been widely detected in colon cancer patients, while environmental mutagens and modifiable factors like unhealthy diet and lifestyle are related to the occurrence of colorectal cancer [2, 3].

A previous study has demonstrated a systemic immune-inflammation index for colorectal cancer using the total number of neutrophils, platelets, and lymphocytes, which could serve as a prognostic indicator for predicting overall survival and help identify patients of higher risk [4]. Of note, glycoproteins are critical players in the cellular and humoral immune system, participating in the assembly of major histocompatibility complex (MHC) antigens, T cell recognition of antigen-presenting cells, and the classical antibody-antigen recognition by immunoglobulins [5]. Meanwhile, glycosylation, as an important posttranslational modification, is

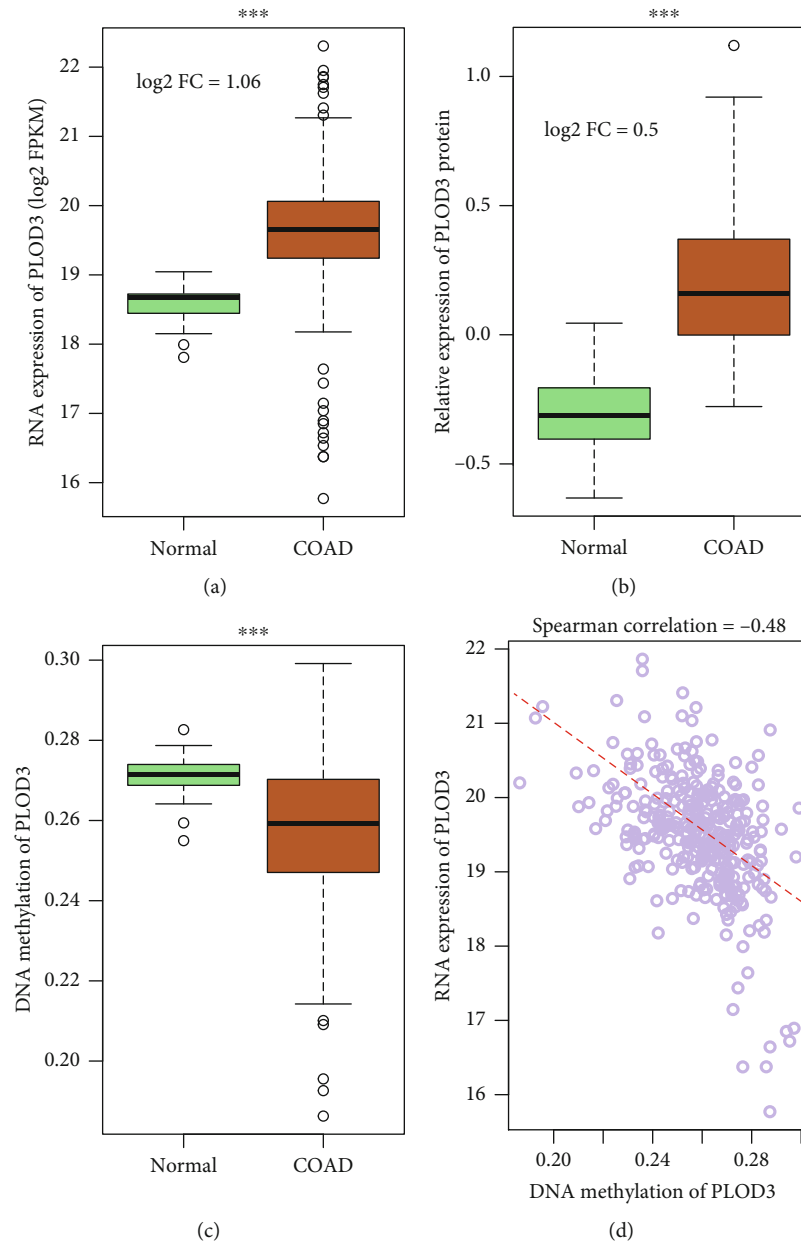


FIGURE 1: PLOD3 is upregulated in COAD. The RNA and protein expression of PLOD3 are upregulated in the COAD samples of (a) TCGA and (b) CPTAC cohorts, respectively. ($TCGA_{(tumor)} = 469$, $TCGA_{(normal)} = 41$, $CPTAC_{(tumor)} = 97$, and $CPTAC_{(normal)} = 100$). (c) The PLOD3 promoter is hypomethylated in COAD samples of TCGA cohort. (d) The promoter DNA methylation and RNA expression of PLOD3 are negatively correlated in TCGA cohort. The line was fitted by using RNA expression and DNA methylation of PLOD3 as response and predictor variables, respectively. The symbol *** indicates the P value < 0.001 (log₂ FC: log₂ fold change).

associated with multiple fundamental mechanisms in cancer development and progression other than immune modulation, further suggesting that glycoproteins and related genes could be potential biomarkers and drug targets in cancer diagnosis and management [6].

One of those glycoproteins is procollagen-lysine, 2-oxoglutarate 5-dioxygenase 3, which is encoded by PLOD3, and it is an enzyme essentially involved in the biosynthesis of several collagens and glycosylation activity [7]. Emerging evidence suggests that PLOD3 is associated with tumorigen-

esis in various cancer types. PLOD3 knockdown could inhibit tumor growth in lung cancer through regulating the PKC-delta signaling pathway [8], and also in lung cancer, PLOD3 is found to interact with STAT3 immunosuppressive signals, which promotes lung cancer metastasis via dysregulated RAS-MAP kinase pathway [9]. Moreover, it is reported that PLOD3 downregulation would lead to decreased expression levels of TWIST1, further resulting in the inhibition of β -catenin and AKT signaling and suppressing the progression of renal cell carcinoma [7]. In addition, a recent study

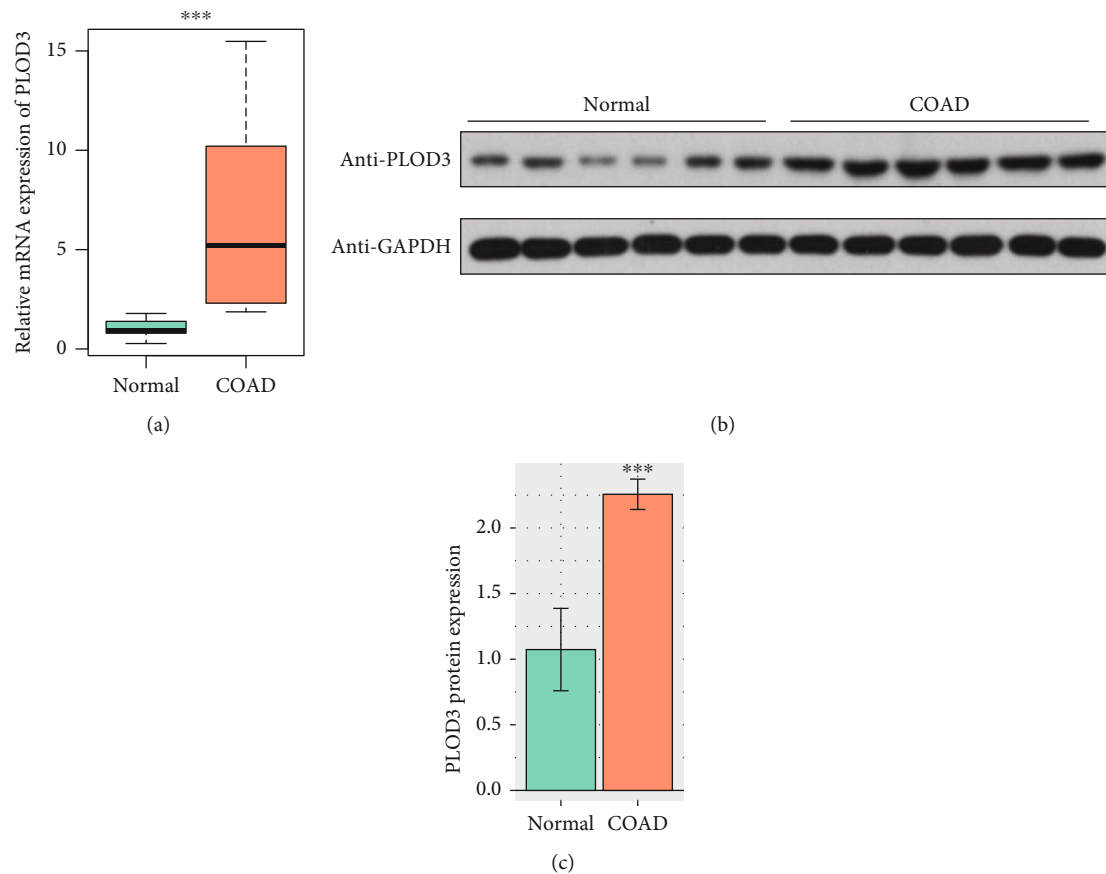


FIGURE 2: Validation of PLOD3 upregulation in COAD and adjacent normal tissue samples. (a) The mRNA expression of PLOD3 is upregulated in the COAD tissue of our cohort using the qPCR method ($n = 6$). (b, c) The protein expression of PLOD3 is upregulated in COAD samples of our cohort using Western blot. The symbol *** indicates the P value < 0.001 .

has implied that MYC and TWIST1 are essential for the activation of innate immunity and cellular invasion, as the recruitment and polarization of tumor-associated macrophages (TAMs) require a certain cytokinome elicited by them, and overexpression of TWIST1 could promote metastasis in hepatocellular carcinoma [10]; meanwhile in another study, inactivation of PLOD3 is found to inhibit in vitro and in vivo liver tumorigenesis in hepatocellular carcinoma [11]. Such findings hint an underlying association between PLOD3 and antitumor immunity, and such association may as well exist in the context of colon cancer, which we hope to elucidate in this study.

2. Materials and Methods

2.1. Public Datasets. The count-based mRNA expression data and protein expression data were obtained from UCSC Xena (<http://xena.ucsc.edu/>) and LinkedOmics (<http://www.linkedomics.org/>), respectively. The mRNA expression data was prenormalized by fragment per kilo-million reads (FPKM), and the protein expression was quantile-normalized for further analysis.

2.2. Clinical Sample Preparation. Six pairs of fresh colon adenocarcinoma and adjacent normal tissues were collected from

Tenth People's Hospital of Tongji University, Tongji University School of Medicine, which was approved by the Human Research Ethics Committee of this hospital. The written informed consent was collected from each patient. All samples were stored in -80°C for the following experiments.

2.3. Quantitative Real-Time Polymerase Chain Reaction (qPCR). The tissue samples were lysed using a Trizol reagent (Invitrogen, USA). Following the manufacturer's protocol, we performed the reverse transcription using RevertAid First Strand cDNA Synthesis Kit (Thermo, Fermentas, USA). The mRNA expression was quantitatively analyzed using an ABI Stepone plus (StepOnePlus™). GAPDH is an internal reference. The primers for PLOD3 are as follows: forward: 5'-CTGAAGAAGTTCGTCCAGAGTG-3' and reverse: 5'-ACCGATGAATCCACCAGAATTG-3'; the primers for GAPDH are as follows: forward: 5'-GGAGCGAGATCCTCCAAAAT-3' and reverse: 5'-GGCTGTTGTCATAC TTCTCATGG-3'. All these experiments were conducted in triplicates. The average values were used as the RNA expression levels of the samples.

2.4. Western Blot. Total protein was isolated from tissue samples using RIPA lysis buffer (Beyotime Biotechnology,

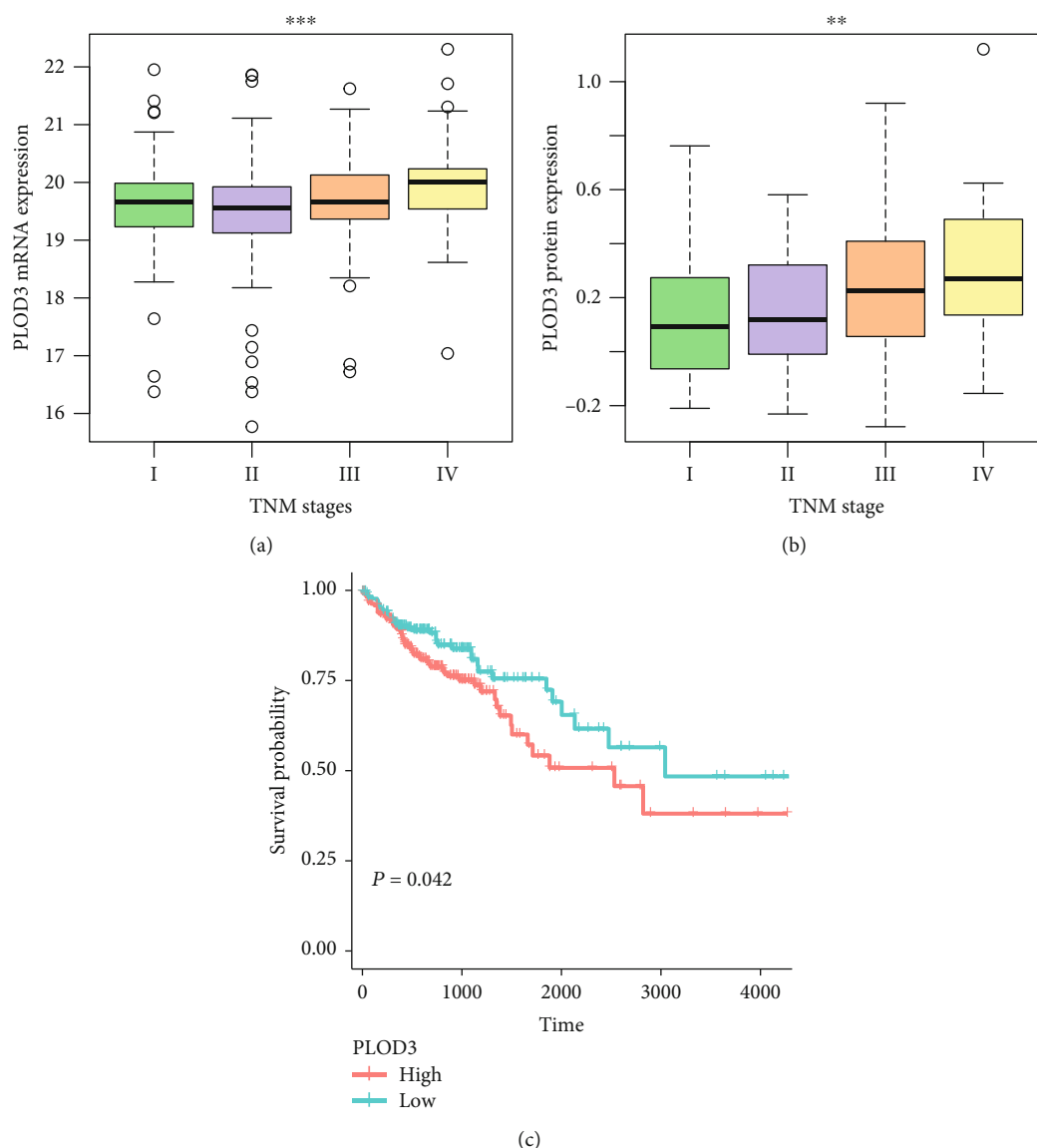


FIGURE 3: PLOD3 expression is increased with the progression of COAD. The (a) RNA and (b) protein expression are increased in advanced stages of COAD (TCGA_(stage I) = 78, TCGA_(stage II) = 182, TCGA_(stage III) = 131, TCGA_(stage IV) = 65, CPTAC_(stage I) = 10, CPTAC_(stage II) = 39, CPTAC_(stage III) = 40, and CPTAC_(stage IV) = 8). (c) COAD patients with high expression of PLOD3 have shorter overall survival than those with low expression of PLOD3. The symbols of *, **, and *** indicate the *P* values <0.05, 0.01, and 0.001, respectively.

China) and then quantified by the BCA assay kit (Beyotime Biotechnology, China). Each 20 μ g total protein was electrophoresed on 10% SDS-polyacrylamide gel and then transferred to polyvinylidene fluoride (PVDF) membranes (Millipore, USA). The primary antibodies used were anti-PLOD3 (Proteintech, China) and anti-GAPDH (Cell Signaling Technology, USA). Membranes were then washed three times in TBST solution for 15 min each and then incubated with secondary antibodies for 1 h.

2.5. Two-Sample and Multisample Comparisons and Survival Analysis. The two-sample and multisample comparisons were conducted using the Wilcoxon rank sum test and Kruskal-Wallis test, respectively. The tumor samples were stratified into high and low groups using the median expres-

sion of PLOD3 as the threshold. The Cox proportional hazard regression model was built to fit the survival time/status with the PLOD3 expression, and the log-rank test was used to evaluate the statistical significance.

2.6. Estimation of Immune Cell Proportion. The immune cell proportions were estimated using TIP (tracking tumor immunophenotype) [12], which used CIBERSORT [13] and marker genes of 14 immune cell types. The mRNA expression was normalized to transcript per million reads (TPM) using R scater package and coding length of gene. The TPM-based mRNA expression was used as the input in TIP. The immune scores were estimated by ESTIMATE (Estimation of STromal and Immune cells in Malignant Tumours using Expression data) [14].

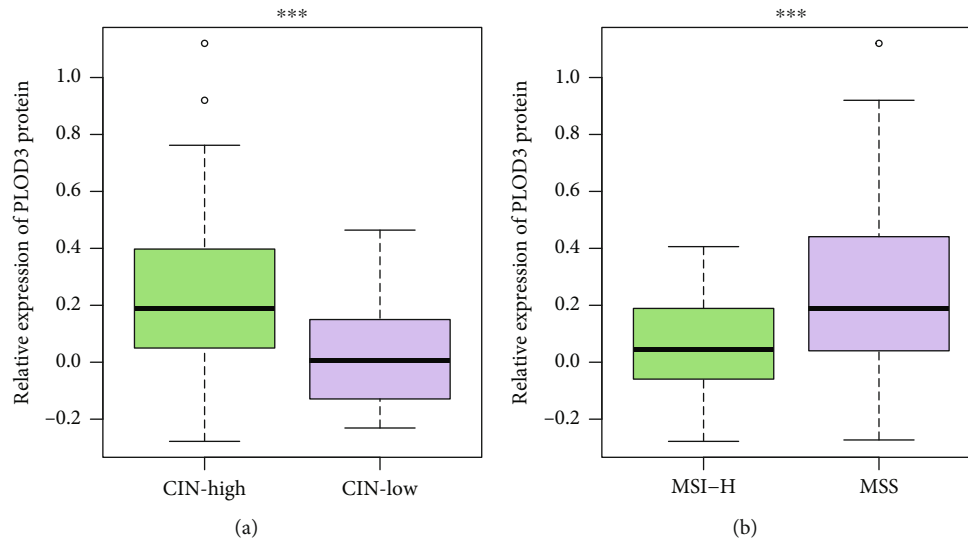


FIGURE 4: PLOD3 is associated with genomic instability. PLOD3 is expressed higher in COAD samples with (a) high chromosomal instability (CIN-high) or (b) low microsatellite instability (MSI-low) (CIN-high vs. CIN-low: 75 vs. 20 and MSI-high vs. MSI-low: 22 vs. 73). The symbol *** indicates the P value <0.001 .

2.7. Gene Set Enrichment Analysis. The genes were ranked by the correlation coefficients between PLOD3 and the remaining genes using TCGA mRNA expression data. The enrichment scores for genes of immune regulators and those involved in signaling pathways were calculated based on the ranks and correlation coefficients of these genes. A total of 1000 times permutation was used to evaluate the statistical significance of the enrichment score and the immune regulators and pathways. This analysis was implemented in R clusterProfiler package [15].

3. Results

3.1. The RNA and Protein Expression of PLOD3 Are Upregulated in COAD. To investigate the expression pattern of PLOD3 in colon adenocarcinoma (COAD), we collected mRNA expression data from The Cancer Genome Atlas (TCGA) [16] and protein expression data from Clinical Proteomic Tumor Analysis Consortium (CPTAC) [17]. Specifically, PLOD3 mRNA was found to be highly upregulated in COAD of TCGA cohort as compared with the adjacent normal tissues (Figure 1(a), P value <0.001). Consistently, the PLOD3 protein expression was also upregulated in COAD tissues of CPTAC cohort (Figure 1(b), P value <0.001). Moreover, we also collected the DNA methylation data of TCGA cohort and observed that the promoter DNA methylation levels of PLOD3 were decreased in COAD samples (Figure 1(c), P value <0.001). The correlation analysis revealed that the promoter DNA methylation of PLOD3 was negatively correlated with its mRNA expression (Figure 1(d), Spearman correlation = -0.48), suggesting that the dysregulation of PLOD3 was associated with its promoter hypomethylation.

3.2. Validating the Upregulation of PLOD3 in COAD and Adjacent Normal Tissues. To validate the upregulation of

PLOD3 in COAD and adjacent normal tissues, we collected six pairs of COAD and normal tissues and detected the mRNA and protein expression levels in these samples. The mRNA expression was also upregulated in the COAD samples compared with the adjacent normal tissues using the qPCR method (Figure 2(a), P value <0.001). Consistently, the Western blot assay confirmed the upregulation of PLOD3 protein in COAD (Figures 2(b) and 2(c), P value <0.001). These results further demonstrated high expression of PLOD3 in COAD.

3.3. High Expression of PLOD3 Indicates Poor Prognosis in COAD. As PLOD3 was highly upregulated in COAD samples, we then investigated whether its expression was associated with COAD prognosis. The comparison of the tumor samples with distinct TNM stages revealed that PLOD3 was increased in the advanced TNM stages in both TCGA and CPTAC cohorts (Figures 3(a) and 3(b), P value <0.01). Furthermore, we stratified the tumor samples into two groups by the PLOD3 expression (high vs. low). The comparison of the two tumor groups indicated that the high group had significantly shorter overall survival time than those of low group (Figure 3(c), P value <0.05). These results indicated that PLOD3 expression was associated with poor prognosis in COAD.

3.4. PLOD3 Expression Is Associated with Tumor Genomic Instability. The genomic instability in cancer includes abnormal chromosomal instability and microsatellite instability (MSI), which are characterized by widespread imbalances in chromosome number (aneuploidy) or loss of heterozygosity [18] and hypermutable phenotype caused by the loss of DNA mismatch repair activity [19]. To further investigate the association between PLOD3 and some genomic features, we found that PLOD3 was expressed higher in COAD samples with high chromosomal instability (CIN-high) than

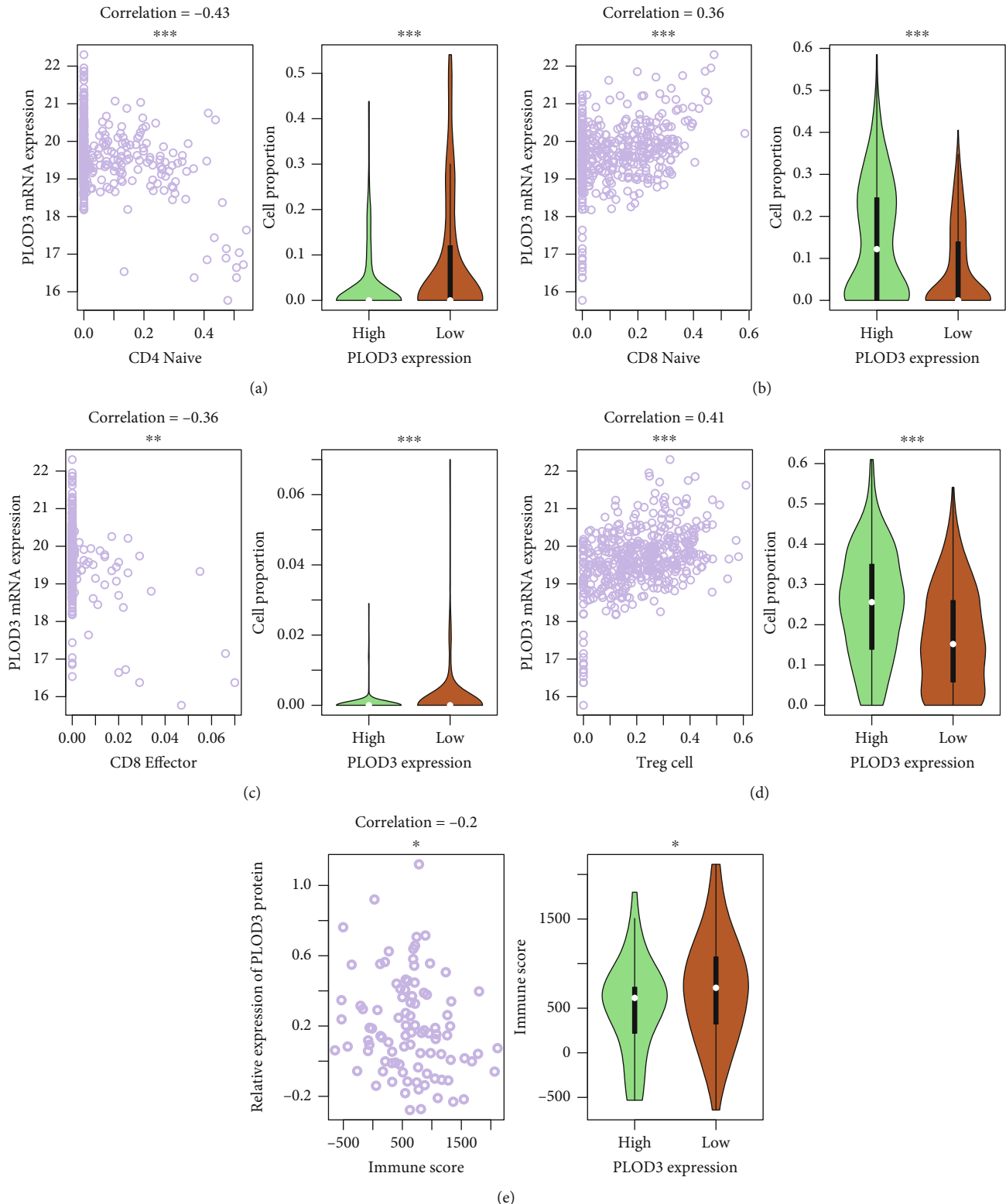


FIGURE 5: Correlation between immune cell infiltration and PLOD3 expression. The correlation between PLOD3 expression and the proportions of tumor-infiltrating immune cells, including CD4 naïve, CD8 naïve, CD8 effector, and Tregs, and immune scores are displayed in (a–d) and (e), respectively. The symbols of *, **, and *** indicate the P values <0.05 , 0.01 , and 0.001 , respectively.

those with low CIN (CIN-low) (Figure 4(a), P value <0.001). In contrast, PLOD3 was expressed lower in COAD samples with high microsatellite instability (MSI-high) than those

with low MSI (MSI-low) (Figure 4(b), P value <0.001). These results indicated that PLOD3 expression was associated with tumor genome instability.

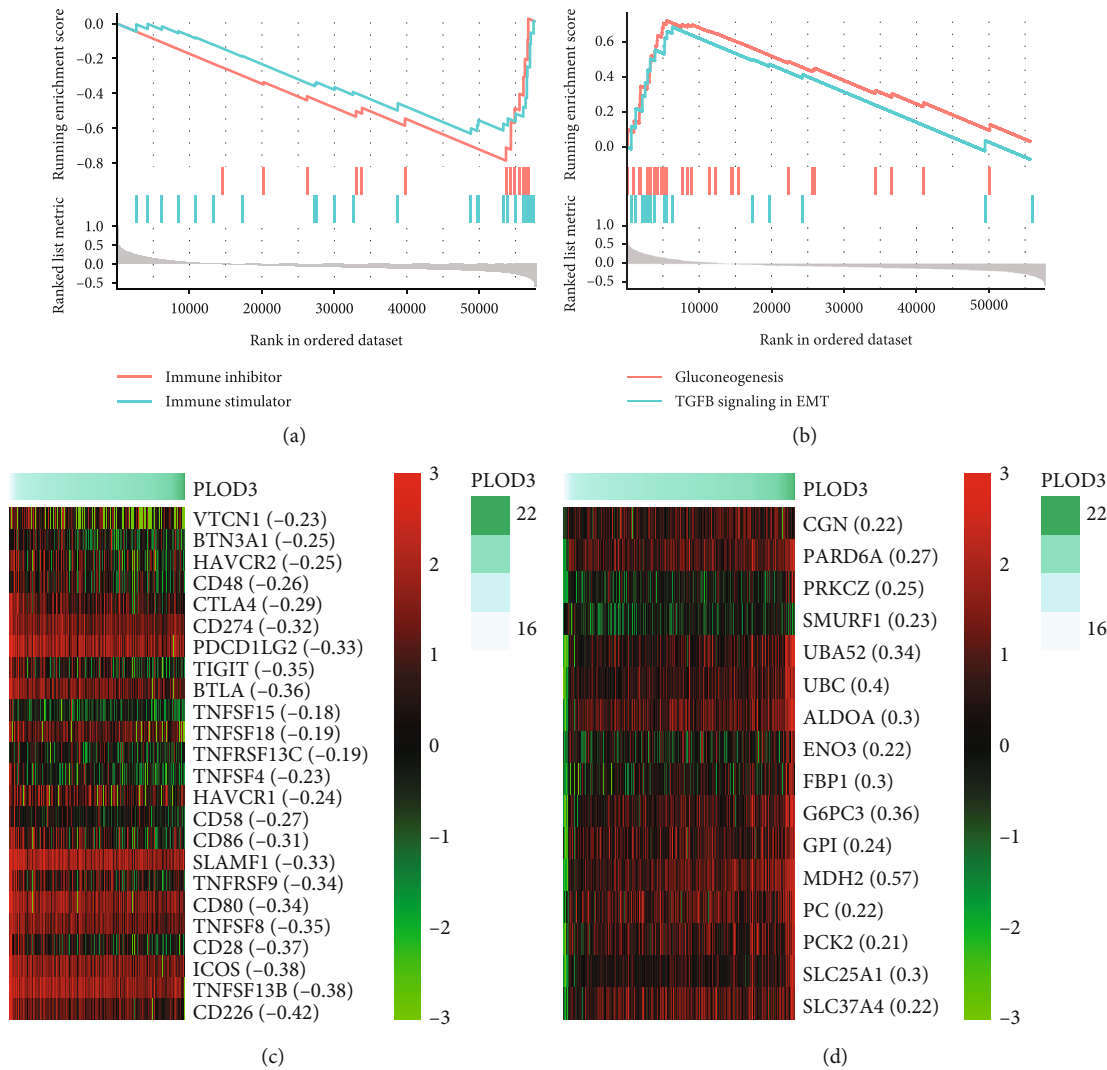


FIGURE 6: The association of PLOD3 expression with immune regulators and tumor-promoting pathways. The positively and negatively correlated genes with PLOD3 are enriched in immune inhibitors/stimulators and genes involved in tumor-promoting pathways including gluconeogenesis and TGF-beta signaling in epithelial-mesenchymal transition (EMT).

3.5. PLOD3 Expression Is Associated with the Immune Cell Infiltration. As high immune cell infiltration was associated with high tumor burden and PLOD3 was associated with tumor genome instability, we then investigated the association of PLOD3 expression with immune cell infiltration. We first estimated the immune cell proportions in TCGA tumor samples using CIBERSORT (Materials and Methods). We found that the proportions of CD4 naïve and CD8 effector were negatively correlated with PLOD3 expression (Figures 5(a) and 5(c)), while the proportions of CD8 naïve and regulatory T cells (Tregs) were positively correlated with PLOD3 expression (Figures 5(b) and 5(d)). Consistently, these immune cells showed significantly different infiltrating levels between the high and low PLOD3 groups (Figures 5(a)–5(d)). Furthermore, we also estimated the immune scores for TCGA samples using the ESTIMATE method (Materials and Methods) and found that the immune score was negatively correlated with PLOD3 expression and higher in samples with low PLOD3 expression

(Figure 5(e)). These results indicated that high PLOD3 expression was associated with reduced immune cell infiltrating levels in COAD.

3.6. PLOD3 Is Correlated with Immune Regulators and Tumor-Promoting Genes. As PLOD3 was associated with immune cell infiltration, we then tested association of PLOD3 expression with immune regulators and investigated the downstream pathways regulated by PLOD3 using TCGA mRNA expression data. The correlation analysis was conducted between PLOD3 and the remaining genes, and the genes were preranked by Spearman’s correlation with a decreasing order. The genes encoding immune stimulators and inhibitors and those involved in signaling pathways were collected from previous studies [20]. To test whether the genes involved in the pathways were significantly clustered within the positively or negatively correlated genes, we conducted gene set enrichment analysis on the preranked genes. Specifically, we found that both immune stimulators and

TABLE 1: The statistical significance of core genes involved in EMT and gluconeogenesis.

ID	NES	P value	P.adjust	q values	Core_enrichment
Gluconeogenesis	3.00	2.32E-10	2.40E-08	1.03E-08	MDH2, G6PC3, ALDOA, FBP1, SLC25A1, SLC25A10, GPI, PC, ENO3, SLC37A4, PCK2, TPI1, SLC25A11, GAPDH, ALDOB, GOT2, ALDOC, PCK1, SLC25A13
TGFB signaling in EMT	2.27	1.40E-04	1.03E-03	4.39E-04	UBC, UBA52, PARD6A, PRKCZ, SMURF1, CGN, ARHGEF18, UBB, F11R, RPS27A, TGFB1

inhibitors were enriched in genes negatively correlated with PLOD3 (Figure 6(a), FDR < 0.05). Moreover, the genes involved in two tumor-promoting pathways, including gluconeogenesis and TGF-beta signaling in epithelial-mesenchymal transition (EMT), were significantly enriched in those positively correlated with PLOD3 (Table 1 and Figure 6(b), FDR < 0.05). Consistently, the key genes involved in immune stimulation and inhibition showed reverse expression patterns with PLOD3 (Figure 6(c)), while those involved in gluconeogenesis and TGF-beta signaling in EMT, such as MDH2, G6PC3, ALDOA, TGFB1, and SMURF1, had similar expression patterns with PLOD3 (Figure 6(d) and Table 1). These results indicated that PLOD3 is correlated with immune regulators and tumor-promoting genes.

4. Discussion

Procollagen-lysine, 2-oxoglutarate 5-dioxygenases (PLODs) are a family of enzymes that regulate the hydroxylation of lysine and stabilization of collagen [21]. However, the clinical and functional roles of PLOD3 in COAD have not been investigated. The analysis of mRNA and protein expression data revealed that both mRNA and protein of PLOD3 were highly upregulated in COAD. The correlation analysis revealed that the promoter DNA methylation of PLOD3 was negatively correlated with its mRNA expression (Figure 1(d), Spearman correlation = -0.48). Consistently, the dysregulation of PLOD3 by aberrant DNA methylation has been found in melanoma [22]. Moreover, we also confirmed the upregulation of PLOD3 in COAD tissues using qPCR and Western blot (Figure 2). Furthermore, we also investigated the prognostic value of PLOD3 in COAD. PLOD3 was increased in the advanced TNM stages in both TCGA and CPTAC cohorts (Figures 3(a) and 3(b), P value < 0.01), and high expression of PLOD3 indicated relatively worse prognosis in COAD. The association of PLOD3 with poor prognosis has been found in ovarian cancer [23], gastric cancer [24], and glioma [25].

As genome instability is a hallmark of cancer [26], we then investigated the association between PLOD3 and genomic instability such as chromosomal instability (CIN) and microsatellite instability (MSI) in COAD. PLOD3 was expressed higher in COAD samples with high chromosomal instability (CIN-high) than those with low CIN (CIN-low) and higher in those with low MSI than high MSI (Figure 4), indicating that PLOD3 expression was associated with tumor genomic instability. The acquisition of genomic instability is a crucial feature in colon cancer development [18] and can

promote inflammatory signaling [27]. We found that immune cells showed significantly different infiltrating levels between the high and low PLOD3 groups, and the immune score was negatively correlated with PLOD3 expression and higher in samples with low PLOD3 expression (Figure 5), suggesting that high PLOD3 expression was associated with reduced immune cell infiltrating levels in COAD [28, 29]. To further uncover the underlying mechanism of PLOD3 in PLOD3, we compared the COAD samples of high PLOD3 expression with those of low PLOD3 expression and found that high expression of PLOD3 was associated with reduced expression of immune regulators and enhanced activities of two tumor-promoting pathways, including gluconeogenesis and TGF-beta signaling in epithelial-mesenchymal transition (EMT). The gluconeogenesis plays a role in signaling, proliferation, and the cancer stem cell (CSC) tumor phenotype [24]. Notably, TGF-beta signaling in EMT is a key player in angiogenesis, tumor growth, and metastasis in colon cancer [30], suggesting that PLOD3 might regulate immune microenvironment of COAD via TGF-beta signaling. In accordance with that, knockdown of PLOD3 inhibited HIF-1 α accumulation via the ERK signaling pathway under hypoxia, suggesting that PLOD3 had the potential to regulate the tumor microenvironment [25].

Although the present study uncovered the expression pattern and potential clinical and scientific significances of PLOD3 in COAD, it still has some limitations. For example, the upstream and downstream relationship between the PLOD3 expression and genomic instability or immune cell infiltration needs further investigation. Moreover, the downstream pathways of PLOD3 in COAD should be validated by *in vivo/vitro* experiments. However, the present study still highlights the importance of PLOD3 and provides the evidence about the functional role of PLOD3 in COAD.

Data Availability

The data that support the findings of this study are available from the corresponding author upon reasonable request.

Ethical Approval

The fresh colon adenocarcinoma and adjacent normal tissues were collected from Tenth People's Hospital of Tongji University, Tongji University School of Medicine, which was approved by the Human Research Ethics Committee of this hospital. The written informed consent was collected from each patient.

Consent

Participants gave their written informed consent for the materials to appear in publications without limit on the duration of publication.

Conflicts of Interest

The authors declare that they have no conflicts of interest.

Authors' Contributions

Jiyu Li conceived and designed the experiments. Xianyu Deng acquired the data, related materials, and analysis tools. Xianyu Deng, Yun Pan, and Muqing Yang analyzed the data. Xianyu Deng and Jiyu Li wrote the paper. Xianyu Deng, Ying Liu, and Jiyu Li revised the paper. All authors read and approved the final manuscript.

Acknowledgments

This study was supported by grants from the National Natural Science Foundation of China (No. 82072647).

References

- [1] F. Bray, J. Ferlay, I. Soerjomataram, R. L. Siegel, L. A. Torre, and A. Jemal, "Erratum: Global cancer statistics 2018: GLOBOCAN estimates of incidence and mortality worldwide for 36 cancers in 185 countries," *CA: a cancer journal for clinicians*, vol. 70, p. 313, 2020.
- [2] E. Giovannucci, "Modifiable risk factors for colon cancer," *Gastroenterology clinics of North America*, vol. 31, no. 4, pp. 925–943, 2002.
- [3] J. Terzic, S. Grivennikov, E. Karin, and M. Karin, "Inflammation and colon cancer," *Gastroenterology*, vol. 138, no. 2101–2114, article e5, 2010.
- [4] J. H. Chen, E. T. Zhai, Y. J. Yuan et al., "Systemic immune-inflammation index for predicting prognosis of colorectal cancer," *World journal of gastroenterology*, vol. 23, no. 34, pp. 6261–6272, 2017.
- [5] P. M. Rudd, T. Elliott, P. Cresswell, I. A. Wilson, and R. A. Dwek, "Glycosylation and the immune system," *Science*, vol. 291, no. 5512, pp. 2370–2376, 2001.
- [6] S. S. Pinho and C. A. Reis, "Glycosylation in cancer: mechanisms and clinical implications," *Nature reviews Cancer*, vol. 15, no. 9, pp. 540–555, 2015.
- [7] D. Xie, J. Li, S. Wei et al., "Knockdown of PLOD3 suppresses the malignant progression of renal cell carcinoma via reducing TWIST1 expression," *Molecular and cellular probes*, vol. 53, article 101608, 2020.
- [8] J. H. Baek, H. S. Yun, G. T. Kwon et al., "PLOD3 suppression exerts an anti-tumor effect on human lung cancer cells by modulating the PKC-delta signaling pathway," *Cell death & disease*, vol. 10, p. 156, 2019.
- [9] J. H. Baek, H. S. Yun, G. T. Kwon et al., "PLOD3 promotes lung metastasis via regulation of STAT3," *Cell death & disease*, vol. 9, p. 1138, 2018.
- [10] R. Dhanasekaran, V. Baylot, M. Kim et al., "MYC and Twist1 cooperate to drive metastasis by eliciting crosstalk between cancer and innate immunity," *eLife*, vol. 9, 2020.
- [11] Q. Shen, J. W. Eun, K. Lee et al., "Barrier to autointegration factor 1, procollagen-lysine, 2-oxoglutarate 5-dioxygenase 3, and splicing factor 3b subunit 4 as early-stage cancer decision markers and drivers of hepatocellular carcinoma," *Hepatology*, vol. 67, no. 4, pp. 1360–1377, 2018.
- [12] L. Xu, C. Deng, B. Pang et al., "TIP: a web server for resolving tumor immunophenotype profiling," *Cancer research*, vol. 78, no. 23, pp. 6575–6580, 2018.
- [13] A. M. Newman, C. L. Liu, M. R. Green et al., "Robust enumeration of cell subsets from tissue expression profiles," *Nature Methods*, vol. 12, no. 5, pp. 453–457, 2015.
- [14] K. Yoshihara, M. Shahmoradgoli, E. Martinez et al., "Inferring tumour purity and stromal and immune cell admixture from expression data," *Nature Communications*, vol. 4, no. 1, p. 2612, 2013.
- [15] G. Yu, L. G. Wang, Y. Han, and Q. Y. He, "clusterProfiler: an R package for comparing biological themes among gene clusters," *Omics : a journal of integrative biology*, vol. 16, no. 5, pp. 284–287, 2012.
- [16] N. Cancer Genome Atlas, "Comprehensive molecular characterization of human colon and rectal cancer," *Nature*, vol. 487, no. 7407, pp. 330–337, 2012.
- [17] S. Vasaikar, C. Huang, X. Wang et al., "Proteogenomic analysis of human colon cancer reveals new therapeutic opportunities," *Cell*, vol. 177, no. 1035–1049, article e19, 2019.
- [18] M. S. Pino and D. C. Chung, "The chromosomal instability pathway in colon cancer," *Gastroenterology*, vol. 138, no. 6, pp. 2059–2072, 2010.
- [19] C. R. Boland and A. Goel, "Microsatellite instability in colorectal cancer," *Gastroenterology*, vol. 138, no. 2073–2087, article e3, 2010.
- [20] Y. Xiao, D. Ma, S. Zhao et al., "Multi-omics profiling reveals distinct microenvironment characterization and suggests immune escape mechanisms of triple-negative breast cancer," *Clinical cancer research*, vol. 25, pp. 5002–5014, 2019.
- [21] S. S. Li, Y. F. Lian, Y. L. Huang, Y. H. Huang, and J. Xiao, "Overexpressing PLOD family genes predict poor prognosis in gastric cancer," *Journal of Cancer*, vol. 11, no. 1, pp. 121–131, 2020.
- [22] C. He, Y. Zhang, H. Jiang, X. Niu, R. Qi, and X. Gao, "Identification of differentially expressed methylated genes in melanoma versus nevi using bioinformatics methods," *PeerJ*, vol. 8, article e9273, 2020.
- [23] T. Guo, C. Gu, B. Li, and C. Xu, "PLODs are overexpressed in ovarian cancer and are associated with gap junctions via connexin 43," *Laboratory investigation*, vol. 101, no. 5, pp. 564–569, 2021.
- [24] B. Wang, L. Xu, Y. Ge et al., "PLOD3 is upregulated in gastric cancer and correlated with clinicopathologic characteristics," *Clinical laboratory*, vol. 65, 2019.
- [25] C. K. Tsai, L. C. Huang, W. C. Tsai, S. M. Huang, J. T. Lee, and D. Y. Hueng, "Overexpression of PLOD3 promotes tumor progression and poor prognosis in gliomas," *Oncotarget*, vol. 9, no. 21, pp. 15705–15720, 2018.
- [26] S. Negrini, V. G. Gorgoulis, and T. D. Halazonetis, "Genomic instability—an evolving hallmark of cancer," *Nature reviews Molecular cell biology*, vol. 11, no. 3, pp. 220–228, 2010.
- [27] S. F. Bakhom and L. C. Cantley, "The multifaceted role of chromosomal instability in cancer and its microenvironment," *Cell*, vol. 174, no. 6, pp. 1347–1360, 2018.

- [28] R. Zhou, J. Zhang, D. Zeng et al., "Immune cell infiltration as a biomarker for the diagnosis and prognosis of stage I-III colon cancer," *Cancer immunology, immunotherapy*, vol. 68, no. 3, pp. 433–442, 2019.
- [29] N. J. Llosa, M. Cruise, A. Tam et al., "The vigorous immune microenvironment of microsatellite instable colon cancer is balanced by multiple counter-inhibitory checkpoints," *Cancer discovery*, vol. 5, no. 1, pp. 43–51, 2015.
- [30] A. Chruscik, V. Gopalan, and A. K. Lam, "The clinical and biological roles of transforming growth factor beta in colon cancer stem cells: a systematic review," *European journal of cell biology.*, vol. 97, no. 1, pp. 15–22, 2018.

Research Article

FRL: An Integrative Feature Selection Algorithm Based on the Fisher Score, Recursive Feature Elimination, and Logistic Regression to Identify Potential Genomic Biomarkers

Chenyu Ge ¹, Liqun Luo ², Jialin Zhang ³, Xiangbing Meng ⁴, and Yun Chen ⁵

¹School of Mechanical, Electrical, & Information Engineering, Shandong University, Jinan 250000, China

²Department of Information Management, Peking University, Beijing 100000, China

³Laboratoire de Recherche en Informatique, Paris-Saclay University, Paris 91405, France

⁴Qufu Institute of Traditional Chinese Medical Health and Rehabilitation, Qufu 273100, China

⁵The Second Hospital Affiliated to Shandong University of TCM, Jinan 250000, China

Correspondence should be addressed to Chenyu Ge; 201800800274@mail.sdu.edu.cn

Received 22 April 2021; Accepted 21 May 2021; Published 14 June 2021

Academic Editor: Tao Huang

Copyright © 2021 Chenyu Ge et al. This is an open access article distributed under the Creative Commons Attribution License, which permits unrestricted use, distribution, and reproduction in any medium, provided the original work is properly cited.

Accurate screening on cancer biomarkers contributes to health assessment, drug screening, and targeted therapy for precision medicine. The rapid development of high-throughput sequencing technology has identified abundant genomic biomarkers, but most of them are limited to single-cancer analysis. Based on the combination of Fisher score, Recursive feature elimination, and Logistic regression (FRL), this paper proposes an integrative feature selection algorithm named FRL to explore potential cancer genomic biomarkers on cancer subsets. Fisher score is initially used to calculate the weights of genes to rapidly reduce the dimension. Recursive feature elimination and Logistic regression are then jointly employed to extract the optimal subset. Compared to the current differential expression analysis tool GEO2R based on the Limma algorithm, FRL has greater classification precision than Limma. Compared with five traditional feature selection algorithms, FRL exhibits excellent performance on accuracy (ACC) and F1-score and greatly improves computational efficiency. On high-noise datasets such as esophageal cancer, the ACC of FRL is 30% superior to the average ACC achieved with other traditional algorithms. As biomarkers found in multiple studies are more reliable and reproducible, and reveal stronger association on potential clinical value than single analysis, through literature review and spatial analyses of gene functional enrichment and functional pathways, we conduct cluster analysis on 10 diverse cancers with high mortality and form a potential biomarker module comprising 19 genes. All genes in this module can serve as potential biomarkers to provide more information on the overall oncogenesis mechanism for the detection of diverse early cancers and assist in targeted anticancer therapies for further developments in precision medicine.

1. Introduction

Cancers are genomic diseases that cause uncontrolled abnormal cell growth through the constant accumulation of certain genetic mutations [1]. Genes that present specific regulation signals to activate corresponding signaling pathways in cancers are called genomic biomarkers and can be tested by DNA chips [2]. Traditional methods for cancer diagnosis concentrate on abnormalities in human organs and cells, which are intended to be error prone and time consuming as they depend on individual arbitration by an ultrasonic

image diagnosis [3, 4]. Precision medicine is defined as the patient-targeted treatment based on the characteristics of genetic abnormalities and biomarkers. Currently, driven by the popularity of precision medicine [5], the goal of targeted therapies for cancers is to track and address biomarkers from multidimensional gene expression data [6].

The DNA chip is one of the applications of microarray technology. Chips can obtain gene expression data by synchronously tracking the expressions of a large number of genes. A gene expression profile has the characteristics of small sample sizes, high dimensionality, and large amounts

of noise and redundancy. Feature selection algorithms can identify genomic biomarkers by selecting prominent subsets and classifying the chosen features [7]. The diagnosis and treatment of diverse cancers in biomedicine can be improved and the time required can be reduced by using feature selection algorithms [8].

Feature selection is a classic and effective method to filter out redundant features and form comprehensible models between the eigenvalues and vectors from a given dataset, and it can be categorized into three categories: filter, wrapper, and embedded algorithms [9]. Liang and Vucetic present a filter algorithm for feature selection that uses auxiliary microarray data [7]. Based on divergence or correlation indicators, filter methods function at the intrinsic properties of the dataset to reduce feature redundancy and increase the new classification information [10]. Typically, features with scores above a set threshold are selected. If there is no set of the threshold, the highest-scoring groups are extracted. As open-loop methods, filter methods have good universality and are faster than wrapper and embedded methods [11]. Piao et al. presents a wrapper method of the support vector machine to generate and evaluate subsets of genes [12]. Wrapper methods search feature subsets and perform iterative computation until optimal characteristic features are obtained. In terms of performances on the final model, wrapper methods are better than filter methods, but their calculation costs are high [13]. Embedded feature selection methods integrate the processes of feature selection and model training, which are automatically completed in the same optimization procedure. However, these algorithms are prone to overfitting, as the parameters need to be set to stop the training process at an appropriate time. Sun presents an ensemble scheme for simultaneously reducing dimensionality and extracting features, which greatly improves computational efficiency and accuracy [14]. Normally, an ideal feature selection scheme works as follows: filter algorithms are applied for reducing data dimensionality, and wrapper or embedded methods are further conducted for feature selection [15, 16].

In biomedical fields, diverse kinds of feature selection algorithms have been applied in extracting specific genomic biomarkers for targeted anticancer therapies [17, 18]. Ensemble classifiers can generally achieve greater precision and generalization ability than individual classifiers [19]. Biomarkers that are more reliable and reproducible, and reveal great potential on clinical application, can be more easily discovered through multiple analyses than through a single study [20]. In order to promote the classification capability of current feature selection methods, this paper creatively proposes a new feature selection algorithm named FRL by combining the advantages of filter methods and embedded methods (Figure 1). This method is implemented as follows: The original data are downloaded, and RMA is utilized to perform based on the R platform. Then, extensive gene extraction is performed on the feature space via a filtering method called Fisher score. Next, Recursive feature elimination and Logistic regression are conjointly utilized to select the relevant features and remove redundant features from the previous dataset in the embedded layer. Furthermore, the selected genes from a total of 10 datasets are grouped

together, and ten datasets are compared in pairs and repeated genes on intersections are extracted. Lastly, validation of obtained gene groups is performed, and a genomic biomarker module is constructed through literature review and spatial analyses of functional enrichment and functional pathways.

The full thesis is structured as follows: Section 2 introduces the entire process of our novel FRL algorithm and the relevant validation method. In Section 3, the performance of our FRL is evaluated via four different methods, and esophageal cancer is the representative simulation scenario for comparison with Limma. The selected potential biomarkers in the biomarker module have been validated by diverse analyses in Section 3 as well. Section 4 and Section 5 present the discussion and conclusion.

2. Materials and Methods

2.1. Datasets. To validate the classification performance of the FRL and explore more reliable and reproducible potential biomarkers, we apply it to ten microarray gene expression datasets for cancers (GSE1420, GSE3325, GSE7696, GSE9750, GSE16088, GSE18520, GSE18842, GSE54129, GSE56315, and GSE65194). From among all cancer types, we selected the most common types of cancers that have high mortality, namely, lung cancer (21.5%), which is the leading cause of death among men, and breast cancer (15.5%), which is the leading cause for women death [21]. The qualities of these public gene expression datasets regarding diverse cancers are summarized in Table 1. All of the datasets are retrieved from a public repository called the Gene Expression Omnibus (GEO), which can be downloaded from the National Center for Biotechnology Information website (<https://www.ncbi.nlm.nih.gov/>).

2.2. Modulated Characteristics of the Gene Expression Data before Applying FRL. In the pretreatment step illustrated in the first column of Figure 1, we initially downloaded the original files of the gene expression data from the aforementioned database. A background correction method called the robust multiarray average (RMA), which eliminates more noise than other frequently used measures, such as the model-based expression index (MBEI) [35], is applied to the datasets through the bioconductor package on the R platform. The aim of background correction is to remove the effect of the labeled probe on gene expression by binding it to a non-specifically labeled DNA molecule. During this process, because of the diverse regions included in genes, which will directly lead to different probe signals corresponding to certain genes, the number of genes is often slightly less than the number of probes. In allusion to this, we first averaged the probe groups corresponding to a given gene and then choose the largest probe group as the representative to match with the corresponding gene. Then, according to the reference sequences in the public nucleic acid database, a matrix with samples and gene expression data is constructed. Normalization and summarization are performed on matrices for subsequent feature selection. In addition, the gene expression data are transformed into the form of \log_2 to reduce calculation complexity.

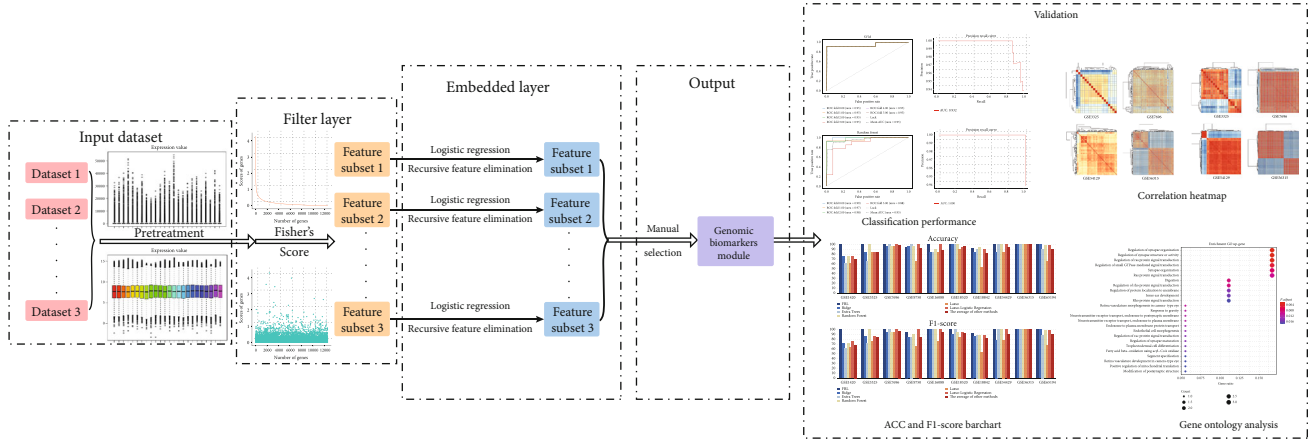


FIGURE 1: Each rectangle represents a dataset. In the first step, pretreatment on original data is performed. The filter layer performs gene extraction and removes redundancy. The embedded layer is utilized to accurately extract the relevant features from the last step. The selected genes are then grouped to form a genomic biomarker module and are validated through diverse methods.

TABLE 1: Introduction of the gene expression data on 10 cancers.

ID	Dataset	Cancer	Normal	References
GSE1420	Esophageal	8	16	[22]
GSE3325	Prostate	6	13	[23]
GSE7696	Glioblastoma	80	4	[24, 25]
GSE9750	Cervical	33	24	[26]
GSE16088	Osteosarcoma	14	6	[27]
GSE18520	Ovarian	53	10	[28]
GSE18842	Lung	46	45	[29]
GSE54129	Gastric	111	21	[30]
GSE56315	Diffuse large B-cell lymphoma	55	33	[31, 32]
GSE65194	Breast	153	11	[33, 34]

2.3. Integrative Feature Selection Scheme (FRL) for Identifying Multiple Genomic Biomarkers. Because of the curse of dimensionality, the high-dimensional data from gene expression profiles present challenges for the use of traditional feature selection methods, including overfitting, weak generalization ability, and high variance [36]. The relationship between the samples and features of the cancer datasets is formulated by the following matrix:

$$\begin{bmatrix} [\mathbf{x}_1 = (x_{11}, x_{12}, x_{13}, \dots, x_{1n}) ; \mathbf{y}_1] \\ [\mathbf{x}_2 = (x_{21}, x_{22}, x_{23}, \dots, x_{2n}) ; \mathbf{y}_2] \\ [\mathbf{x}_3 = (x_{31}, x_{32}, x_{33}, \dots, x_{3n}) ; \mathbf{y}_3] \\ \vdots \\ [\mathbf{x}_m = (x_{m1}, x_{m2}, x_{m3}, \dots, x_{mn}) ; \mathbf{y}_m] \end{bmatrix}, \quad (1)$$

where x_m is defined as the m link of the characteristic vector, and y_m describes the column vector representing the sample categories. Typically, in the machine learning field of a supervised pattern, every x_m is matched with a compatible labeled y_m ; the feature selection methods in a supervised pattern are

aimed at deducing the proper function that can describe the relationship between x_m and y_m . Furthermore, the function can suggest the main influencing factor in the original data. Thus, it is vital to propose an effective and robust feature selection method.

To precisely extract genomic biomarkers, we designed an integrative algorithm called FRL. This method is applied on the ten abovementioned cancer datasets. The aim of the FRL algorithm is to focus on dimensionality reduction and sift the optimal subset for further selection of genomic biomarkers. In this method, the scores of each feature are initially computed and ranked based on Fisher score evaluation system; after ranking the scores of genes in descending order, new subsets with high-score genes are formed for each type of cancer. Recursive feature elimination and Logistic regression are cooperatively used to improve the precision of subsets in the next feature selection round. Then, the most ideal subset among the obtained subsets is selected based on relevant measures. Finally, genes are classified into biomarker modules by literature review and spatial analysis of functional enrichment. These processes will be elaborated below in detail. Procedure 1 presents the entire process of the FRL feature selection method.

```

Method: FRL
Input: Gene expression original matrix  $M = \{(X_i, y_i)\}_{i=1}^m$ 
Output: Gene subset S
For  $n$  in 1 : 10
  Pretreat and Apply Robust Multi-Array average to remove the effect of labeled probes on real gene expression and form matrix  $A, B, C, D, E, F, G, H, I, J$ 
End
For  $i$  in 1 :  $N$ 
  Calculate the fisher score  $x_i$  of  $A$  based on formula (Equation (2))
End
Divide the same maximum number features as one cluster. Spot the inflection point and extract the abundant data. Name new matrix as  $A_1$ 
Set up the iteration step  $P$  and  $K$  according to diverse dimension  $D_1$ 
For  $x$  in 1 :  $P : D_1$ 
  For  $x$  in 1 :  $K$ -fold
    Train recursive feature elimination model with logistic regression classifier in  $A_1'_{\text{train}}$ 
    Calculate accuracy (ACC) in  $A_1'_{\text{test}}$ 
    Use  $K$ -fold cross validation to calculate average ACC
  End
End
Obtain the current dimension  $D_2$  with the optimal performance ACC
Select the feature subset according to  $D_2$  to make  $A_2$  matrix
Extract the repeated genes from  $A_2, B_2, C_2, D_2, E_2, F_2, G_2, H_2, I_2, J_2$  and make a new matrix
Obtain final feature subset S.

```

PROCEDURE 1: Procedures of FRL (mainly illustrated by Amatrix).

2.3.1. Filter Layer: Use Fisher Score to Identify and Delete Redundant Features and Enhance the Quality of Training Datasets. The filter method is implemented as follows: A threshold or correlation coefficient is set as an evaluation criterion by the tester(s), and then the genes of identical quality are extracted based on specific penalty functions and used to form brand-new subsets. This filter mechanism accelerates the speed and performance of classification by converting data with high dimensionality to binary classification problems. In the supervised feature selection field, the formula of Fisher score is defined as follows:

$$F(x_i) = \frac{\sum_{k=1}^c n_k (\mu_k^j - \mu^j)^2}{(\sigma^j)^2} \quad (2)$$

The equation uses c to represent the total number of categories. n_k refers to the sample amount of the j class. μ_k^j and μ^j indicate the mean values of the j class and the mean values of the current gene expression level, respectively. σ^j denotes the variance value of the j class across the whole dataset. Fisher score is employed as the evaluation standard in a filter layer. The scores of each sort can be calculated by equation (2). All genes within the same dataset are scored and arranged in descending order. We identify the inflection point of each cancer category, extract the data before this point to form a subset, and construct matrix A_1 . The dimension D_1 of the present matrix is reduced to 1593 averagely from the initial dimension of 21654. This procedure can produce a high-quality output, even with poor computing power.

2.3.2. Embedded Layer: Employ Recursive Feature Elimination and Logistic Regression to Narrow Down the Feature Space. High generalization ability is the core criterion used to identify whether a supervised learning algorithm is effective. Ensemble algorithms can be more effective than a single algorithm to achieve this standard. Thus, here, Recursive feature elimination and Logistic regression are jointly utilized to traverse the whole feature space. In this step, the iteration pace P varies from 2 to 5 and is established based on the dimensionality D_1 of each cancer. We set 5 for a dataset that has a dimension of over 2000, 3 for a dataset that has a dimension of over 1000 but less than 2000, and 2 for a dataset that has a dimension of less than 1000. Simultaneously, we divide matrix A_1 into K pieces to perform cross validation. The index K is set based on the dimensionality D_1 of either data set. If K is set as 4, the whole dataset will be divided into 4 pieces. The K -fold cross validation will orderly extract one as a test set among 4 sets, leaving the other 3 pieces as a training set for the training model and classifier.

Recursive feature elimination is a typical backward reduction algorithm. However, it cannot be used alone and must be implemented with appropriate classifiers. Recursive feature elimination processes as follows: Firstly, certain classifiers are combined with Recursive feature elimination to train the $A_1'_{\text{train}}$. Next, the value of each feature is calculated and irrelevant features are eliminated. Then, the dataset is automatically reconstructed and values for features are calculated again until the optimal feature subsets are obtained.

Logistic regression is applied as the classifier for Recursive feature elimination to determine the probability in each category. Logistic regression is a generalized linear algorithm on binary classification. It is based on the linear regression

model and sigmoid function. Hypothesize the linear function as follows:

$$g(x) = \omega^T x + b. \quad (3)$$

The sigmoid function can be defined by formula (4), and the logistic regression can be defined by formula (5):

$$\varphi(j) = \frac{1}{1 + e^{-j}}, \quad (4)$$

$$\varphi(x) = \frac{1}{1 + e^{-\omega^T x + b}}. \quad (5)$$

The cost function, which can be used to measure the quality of the Logistic regression model is listed as follows:

$$J(\omega, b) = \frac{1}{m} \sum_{i=1}^m (-y \ln a + (1 - y) \ln (1 - a)). \quad (6)$$

In equation (6), a denotes the probability that is calculated by Logistic regression. y represents the label of this sample, and there is a total of m samples. The aim for Logistic regression is to reduce the outcome of function (6) as much as possible via iteration. Through the use of multiple samples to fit the Logistic regression model for several times, the important features can be filtered out. After the above processes are completed, we obtain the matrix A_2 and sort all of the matrices obtained in this step on 10 cancers into corresponding S subsets. Finally, we validate the existing genes and form a biomarker module through meta-analysis in a biomedical field.

2.4. Performance Evaluation. Four evaluation indexes are applied to evaluate method performance. A confusion matrix is used to compute and output four types of records. False Negative (FN) represents the number of positive samples predicted as negative samples; False Positive (FP) represents the number of negative samples predicted as positive samples; True Negative (TN) represents the number of negative samples predicted as negative samples; True Positive (TP) represents the number of positive samples predicted as positive samples. The following equations demonstrate the calculation of common indicators based on TP, TN, FP, and FN:

$$\begin{aligned} \text{Accuracy : ACC} &= \frac{TP + TN}{TP + FN + FP + FN}, \\ \text{F1-score : } F_1 &= \frac{2TP}{2TP + FP + FN}, \\ \text{Precision : PRE} &= \frac{TP}{TP + FP}. \end{aligned} \quad (7)$$

Heat maps are presented to test the validation of selected genomic biomarkers of the FRL model. The efficiency level of features is reflected in the sharp edges of the heat map. The heat maps are constructed based on the rationale of the Euclidean distance with the ggplot2 package on the R platform. By clustering measurements of samples in Euclidean distance, the clustering results of samples are obtained.

X_{MN} and Y_{MN} denote two matrices, in which the rows and columns are indexed by i and j . The calculation of Euclidean distance is presented as follows:

$$X_{MN} = \begin{bmatrix} x_{11} & x_{12} & \cdots & x_{1n} \\ x_{21} & x_{22} & \cdots & x_{2n} \\ \vdots & \vdots & \cdots & \vdots \\ x_{i1} & x_{i2} & \cdots & x_{in} \\ \vdots & \vdots & \cdots & \vdots \\ x_{m1} & x_{m2} & \cdots & x_{mn} \end{bmatrix}, \quad (8)$$

$$Y_{MN} = \begin{bmatrix} y_{11} & y_{12} & \cdots & y_{1j} & \cdots & y_{1n} \\ \vdots & \vdots & \cdots & y_{2j} & \cdots & \vdots \\ y_{m1} & y_{m2} & \cdots & y_{mj} & \cdots & y_{mn} \end{bmatrix},$$

$$d(x_i, y_j) = \sqrt{\|x_i\|^2 + \|y_j\|^2 + 2x_i y_j^T}.$$

3. Results

3.1. Validation for Oncology Datasets via Diverse Indicators. The first column in Figure 1 displays the initial dataset and the same dataset that has been processed by the RMA method. Compared with the initial dataset, the pretreated datasets obviously exhibit high concentrations and are prone to discover an intrinsic relationship among genes.

Figure 2(a) exhibits the Fisher score values in a descending order, from which we can observe an obvious inflection point in each subimage. Figure 2(b) presents the distribution of genes with diverse scores in a more visible way. It is obvious that the genes with high scores only account for a tiny fraction among the whole dataset. As listed in Table 2, only a tiny quantity of genes remain, which demonstrates that Fisher score can rapidly and effectively reduce the dimensionality.

The 2-NUM column in Table 2 displays the results for the step of feature selection in the embedded layer. This outcome has higher accuracy and precision parameters than those in the previous filter step. A series of genes are consequently selected from the recurring data, and the ultimate output is shown below in Table 3. The relevant performance of each subset is examined. Through literature review and spatial analysis of functional enrichment and functional parameters, a biomarker module is formed.

To validate the capability of the biomarker module, Euclidean distance matrices are adopted for clustering based on GSE3325, GSE7696, GSE54129, and GSE56315. We can directly observe that the subset obtained after feature selection clearly delimits the area (Figure 3). Thus, the final subset can be key features to represent each cancer dataset.

To prove the validity of the FRL feature selection method on a single cancer, the diverse datasets of esophageal cancer (GSE1420, GSE23400) are chosen as representative datasets. GSE1420 is treated as the training set, and GSE23400 [37]

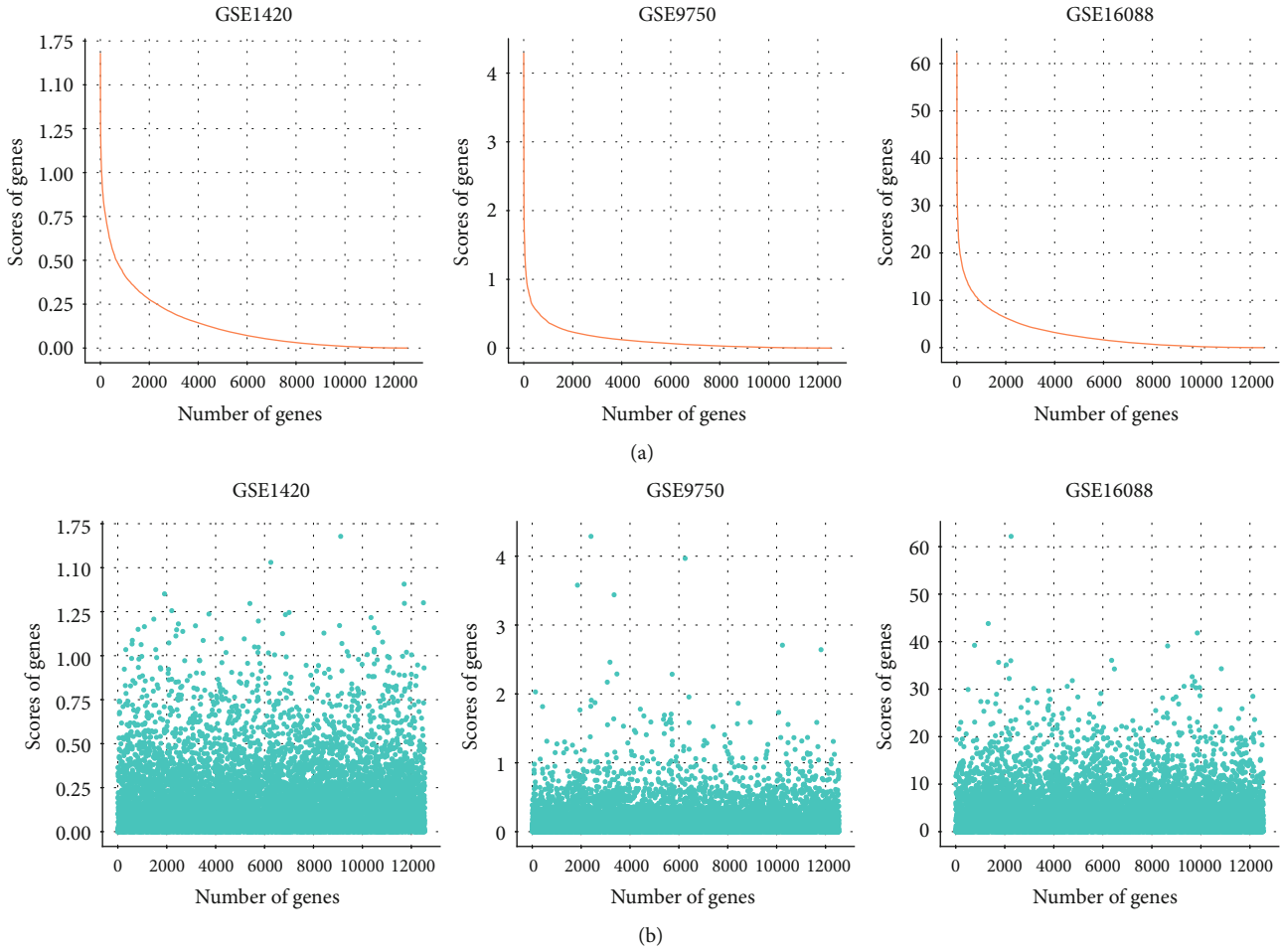


FIGURE 2: This figure directly displays the scores of genes in GSE1420, GSE9750, and GSE16088. (a) Image using a descending order to show the scores. (b) Original scores are shown in a scatter plot. The x axis represents the number of genes, while the y axis expresses the scores of genes.

TABLE 2: Performance measures of the original dataset, the first round, and the second round.

ID	0-ACC	0-NUM	1-ACC	1-F1-score	1-NUM	2-ACC	2-F1-score	2-NUM
GSE1420	62.50%	12549	100%	100%	1803	100%	100%	78
GSE3325	83.33%	21654	83.33%	75.76%	1302	100%	100%	69
GSE7696	96.15%	21654	100%	100%	1803	100%	100%	65
GSE9750	65.00%	21654	90.00%	89.52%	1403	100%	100%	78
GSE16088	66.67%	12549	83.33%	85.19%	2003	100%	100%	78
GSE18520	89.47%	21653	100%	100%	753	100%	100%	50
GSE18842	57.14%	21654	71.43%	69.60%	3453	96.43%	96.42%	77
GSE54129	85.00%	21654	85.00%	78.11%	1011	100%	100%	77
GSE56315	96.30%	21654	100%	100%	1603	100%	100%	78
GSE65194	94.00%	21654	100%	100%	801	100%	100%	79

is treated as the test set. We use genes selected by FRL on the esophageal dataset to examine the indicators of generalization ability through four main classifiers. Figure 4 shows the receiver operating characteristic (ROC) curve and the area under the ROC curve (AUC), which is an effective and intuitive measure for evaluating feature selection classifica-

tion performance. The AUC is more than 93% on three classifiers and the average AUC reaches 92%, obviously indicating that the generalization ability of the biomarker module is satisfied.

In addition, we build an isolated environment by dividing another dataset of esophageal cancer (GSE26886) into a test

TABLE 3: Performance indicators on the final subsets for diverse cancers.

ID	Dataset	Gene-num	PRE	ACC	F1-score
GSE1420	Esophageal	5	89.58%	87.50%	86.82%
GSE3325	Prostate	2	100%	100%	100%
GSE7696	Glioblastoma	3	92.46%	96.15%	94.27%
GSE9750	Cervical	5	92.22%	90%	90.21%
GSE16088	Osteosarcoma	4	100%	100%	100%
GSE18520	Ovarian	2	96.49%	94.74%	95.18%
GSE18842	Lung	3	91.29%	89.29%	89.24%
GSE54129	Gastric	3	100%	100%	100%
GSE56315	Diffuse large B-cell lymphoma	4	100%	100%	100%
GSE65194	Breast	3	100%	100%	100%

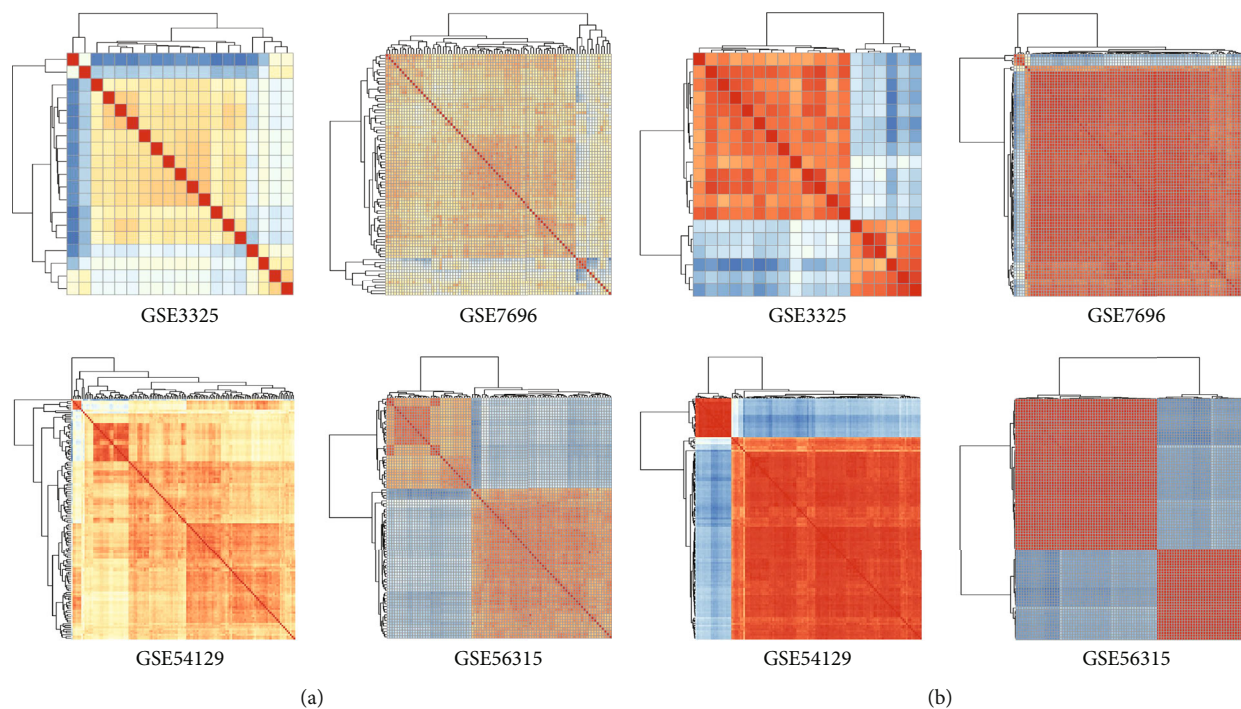


FIGURE 3: (a) Heat map of original matrix. (b) Heat map of the matrix that uses the Euclidean distance to cluster.

set and a training set. 35% of the samples in GSE26886 [38] are randomly chosen to construct the training set. The remaining samples are utilized as the test set. Figure 5 presents the ROC curve of each fold. Three of the classifiers reach a value of 0.99 on areas under the ROC curve (AUC), and the average Gini index on four classifiers is 0.97, which effectively implies that the potential genomic biomarkers selected by FRL may have strong associations with cancers.

Breast cancer (GSE65194) is chosen as another representative to examine the validation of FRL classification performance. *CREBBP*, *EP300*, *ESR1*, *GATA3*, and *MYC* are well-known genetic biomarkers and mutate frequently in breast tumors [39]. These five approved genetic biomarkers on breast cancer are compared with the same amount of potential biomarkers selected by FRL on GSE65194. Figure 6 displays the Precision-Recall (P-R) curve. The AUC

of the five known biomarkers is 93.2%. The AUC of FRL can be 6.8% higher than those on the five mentioned biomarkers. It is meaningful and feasible to develop further clinical experimental verification on potential genomic biomarkers selected by FRL.

3.2. Comparisons between FRL and Other Feature Selection Methods. To compare with the differential expression analysis tool GEO2R based on Limma, esophageal cancer (GSE26886) is chosen as the representative. Figure 7 displays the classification results on Limma by ROC curve in each fold, and the average AUC is 96.25%. It is 2.25% lower than the genes selected by FRL. On classification precision, the FRL algorithm can reach 95.56%, while Limma can only reach 91.11%. In order to obtain persuasive data, 10-fold cross validation is looped 20 times. The average ACC and

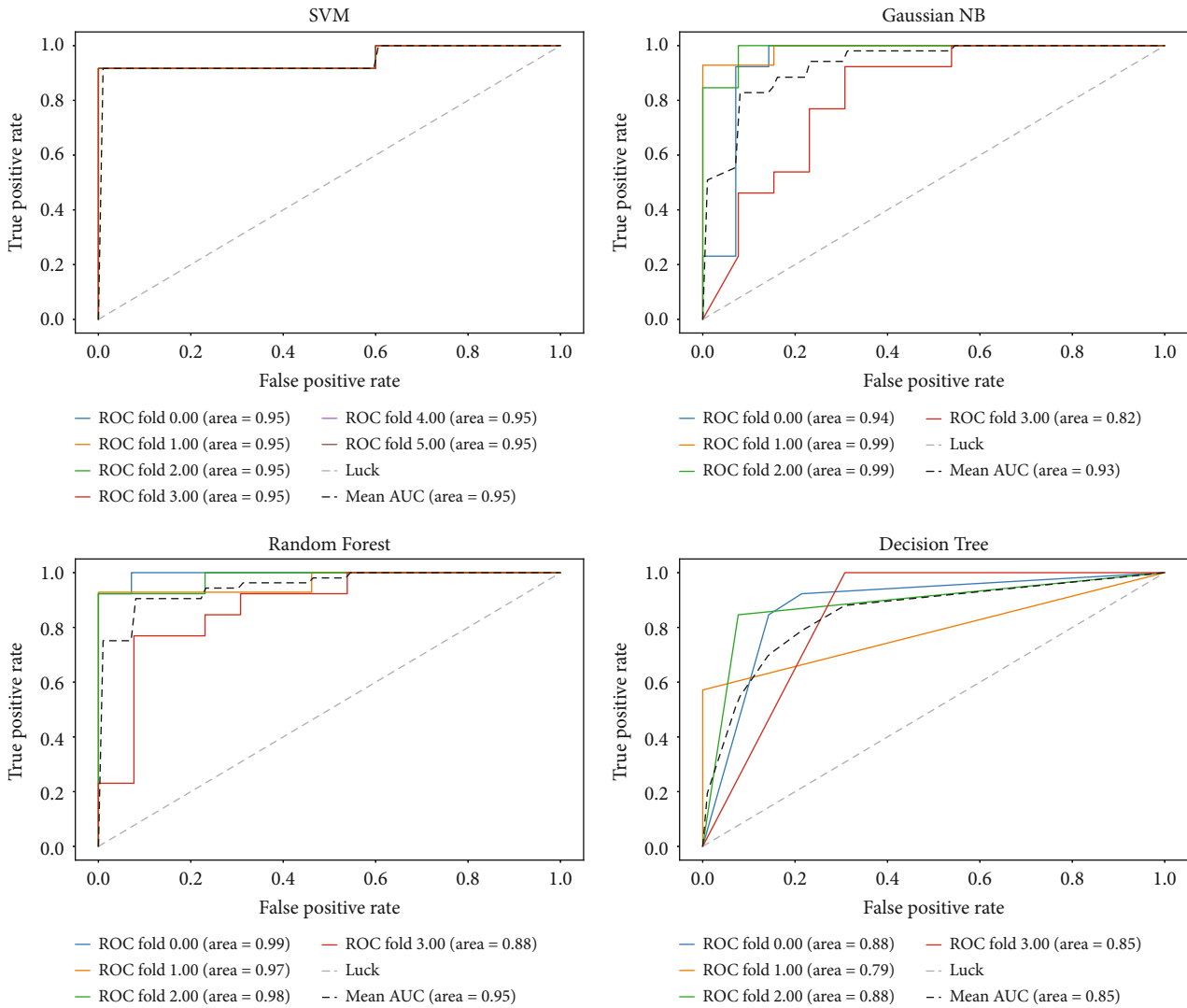


FIGURE 4: Esophageal cancer datasets (GSE1420, GSE23400) are used for experiments. GSE1420 is used as a training set, whereas GSE23400 is used as the test set. The ROC curve displays the generalization results.

F1-score of FRL are 96.24% and 96.37%, respectively. And the average ACC and F1-score of Limma are 96.04% and 95.91%, respectively. FRL is 0.2% and 0.46% superior to Limma. When looped 100 times, the metrics of FRL on ACC reaches 96.32% and can still reach 0.1759% higher than Limma. It is obvious that FRL has greater classification precision than the current differential expression analysis tool GEO2R based on the Limma algorithm on the GEO platform.

The following five methods are used for making comparisons with the FRL feature selection algorithm in terms of their ACCs and F1-scores (Figure 8): Ridge regression (Ridge), Extremely randomized trees (Extra Trees), Random Forest, Lasso, and Lasso-Logistic regression. Since there are only a few genes that have significance to carcinogenesis and can be regarded as biomarkers, by repeated experiments, we found that when the context confines the size of subset to approximately 80, it can achieve perfect classification capability. To follow variable-controlling approaches, 78 is chosen as the standard dimensionality for genes in all the subsets for all the participating methods being used as a comparison.

Table 4 lists the final prediction results of the aforementioned methods. Focusing on certain particularly low-quality datasets, such as GSE1420 (esophageal) and GSE18842 (ovarian), we summarize that the ACCs of FRL are 30% and 17.622%, respectively. These values are much higher than those of the other traditional algorithms. Regarding the average statistics (Table 4), it is clear that FRL is 10.01% and 10.428% superior to other traditional methods in terms of their average ACC and F1-score, respectively. Compared to the Lasso-Logistic regression, which is a current principal feature selection method for effective dimensionality reduction, FRL can be 5.464% and 4.534% higher than it on ACC and F1-score, respectively.

As GSE18842 (ovarian) has the highest dimensionality after the selection in a filter layer and may consume the longest time in the embedded layer, FRL and the abovementioned five methods are applied on GSE18842 (ovarian) to test the time consumed in the whole feature selection process. In order to follow variable-controlling approaches, the final subset dimensionality is restricted to 78 for all methods. As

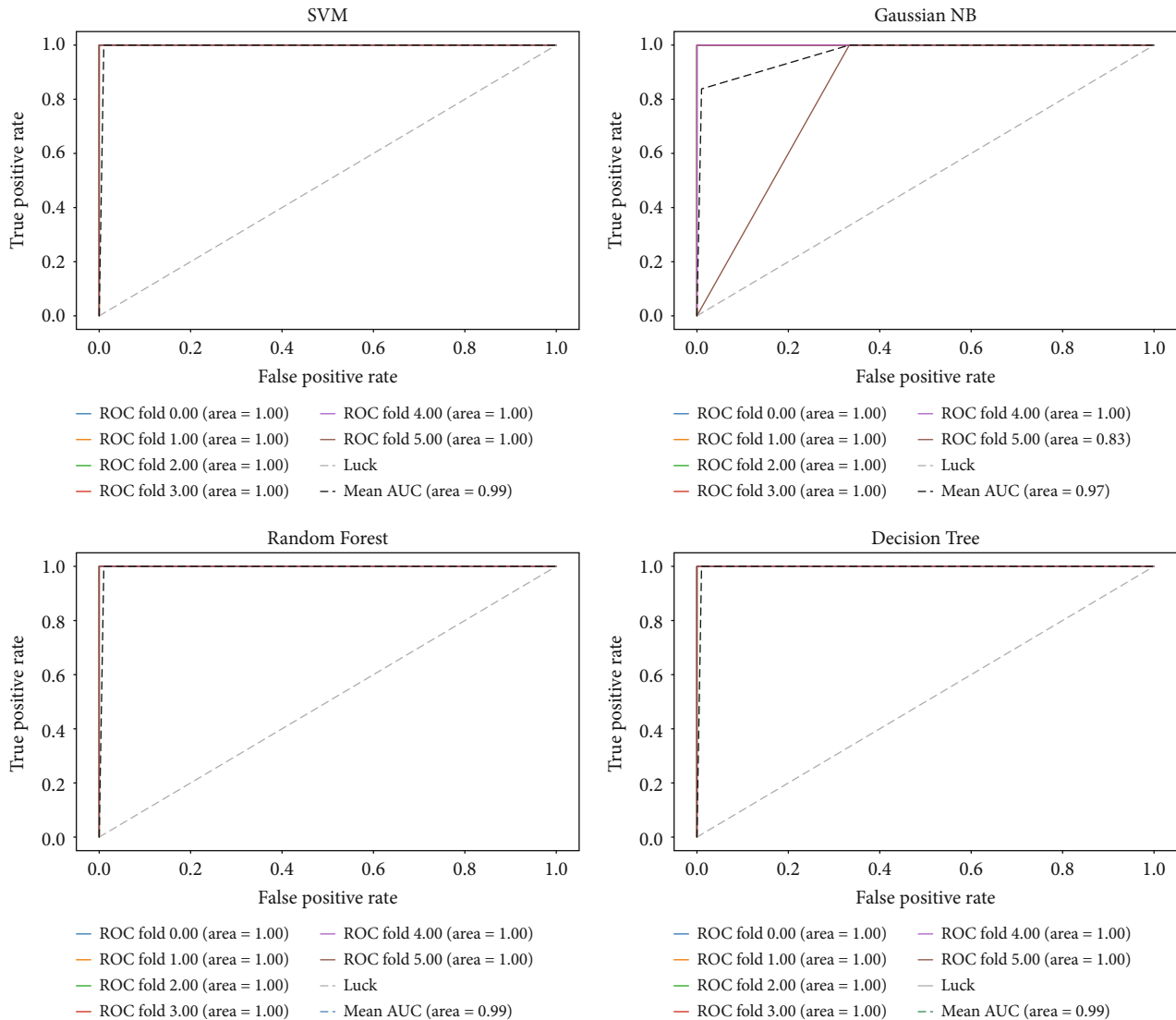


FIGURE 5: The results of another esophageal dataset (GSE26886) in the form of the ROC curve by FRL are visualized.

data shown in Table 5, FRL consumes only 79.619 s and can be at least three times faster than the second fastest method Lasso. However, Lasso displays low performance on ACC and F1-score. Compared to the method with approximate ACC, FRL calculates 52 times faster than Random Forest. Obviously, FRL can greatly decrease computation time, accelerate computation speed, and improve computation efficiency.

In general, an obvious and intuitive conclusion is that FRL exhibits better performance relative to current website analysis tools and other traditional feature selection methods. Compared with FRL, the conventional feature selection algorithms extract and establish unreliable and frail subsets, which may result from inappropriate performance of metrics, unbalanced labels for the dataset, and low noise immunity in the models themselves. For the remaining tested datasets, FRL also shows unique robustness, high precision, and stable classification capability.

3.3. A Functional Analysis of the Biomarker Module. The 19 genes in the biomarker module are as follows: *ALPI*,

AMACR, *ANKHD1*, *ARHGAP44*, *ARHGEF15*, *ARHGEF26*, *ATXN8OS*, *CRISP3*, *HOPX*, *HSPB8*, *LSM7*, *MAFB*, *NGRN*, *PPP3R1*, *RDH5*, *SLC5A1*, *SPARC*, *SPRR3*, and *TCTN2*. Initially, we corroborate genes in the biomarker module through the following four approaches: CCLE (the Cancer Cell Line Encyclopedia, <https://portals.broadinstitute.org/ccle>), COSMIC (the Catalogue Of Somatic Mutations In Cancer, <https://cancer.sanger.ac.uk/cosmic>), NCG (the Network of Cancer Genes, <https://ncg.kcl.ac.uk/index.php>), and literature reviews. To depict the hereditary characteristics of cancer cells, the CCLE project has cooperated with the Broad Institute, Dana Farber Cancer Institute, and Novartis Institute. CCLE exhibits expression of genes in diverse tumor cell lines, and all the genes in our biomarker module can be found in it. COSMIC has been a neutral worldwide reference standard as it provides a comprehensive and detailed introduction for over 700 mutated genes. [40, 41]. The NCG is a database of tumor-driven genes and includes cancer information, orthology, and gene expressions in normal tissues. Furthermore, the literature is also searched to

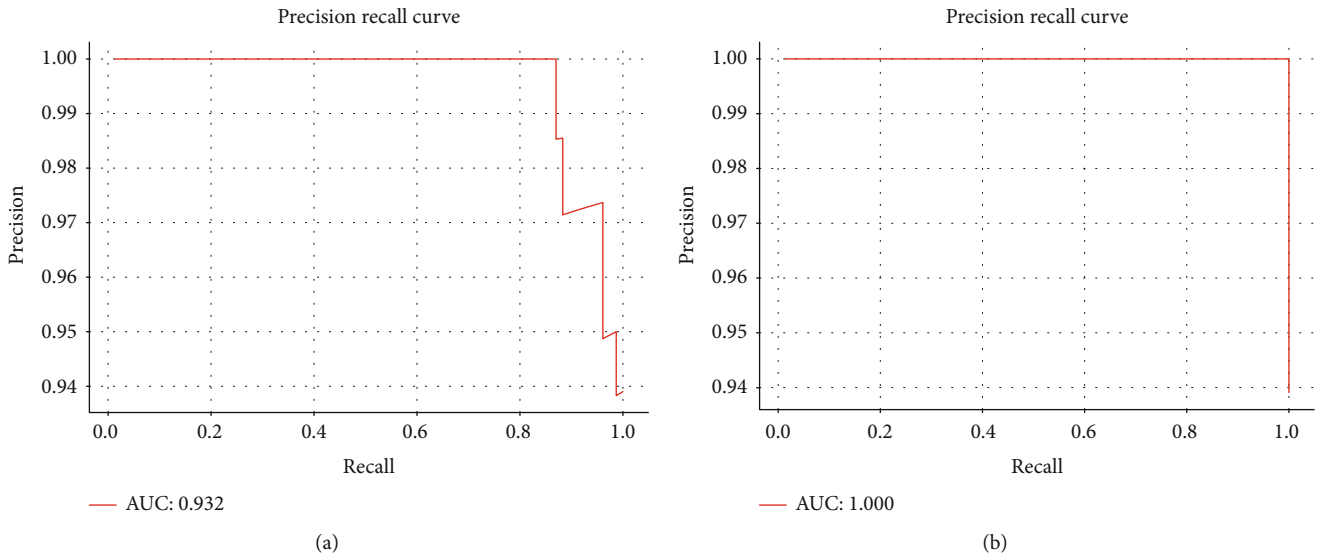


FIGURE 6: (a) The P-R curve of classification results by the five approved genetic biomarkers on GSE65194. (b) The P-R curve of classification results by potential genetic biomarkers selected by FRL on GSE65194.

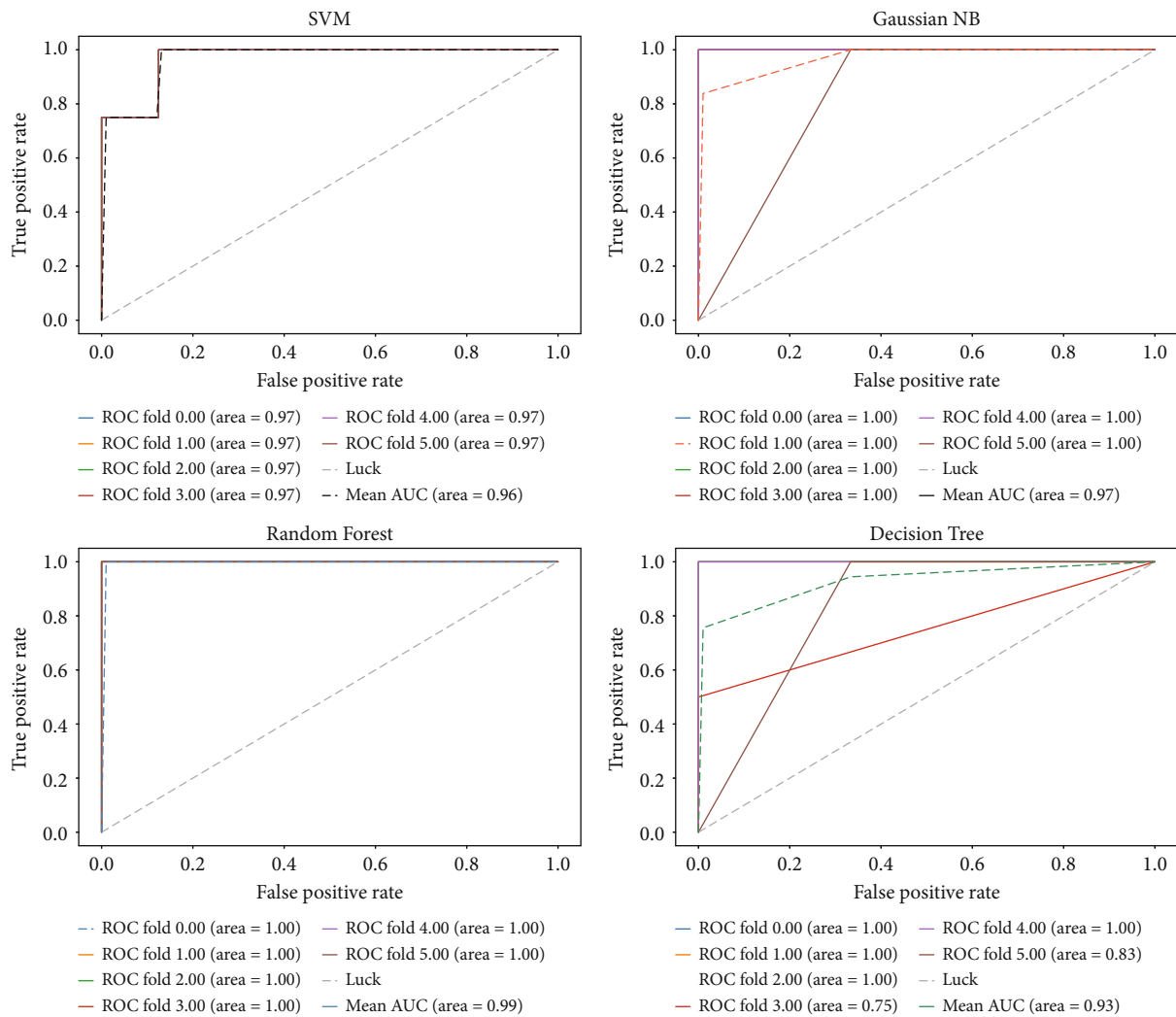


FIGURE 7: The results of another esophageal dataset (GSE26886) in the form of an ROC curve by Limma are visualized.

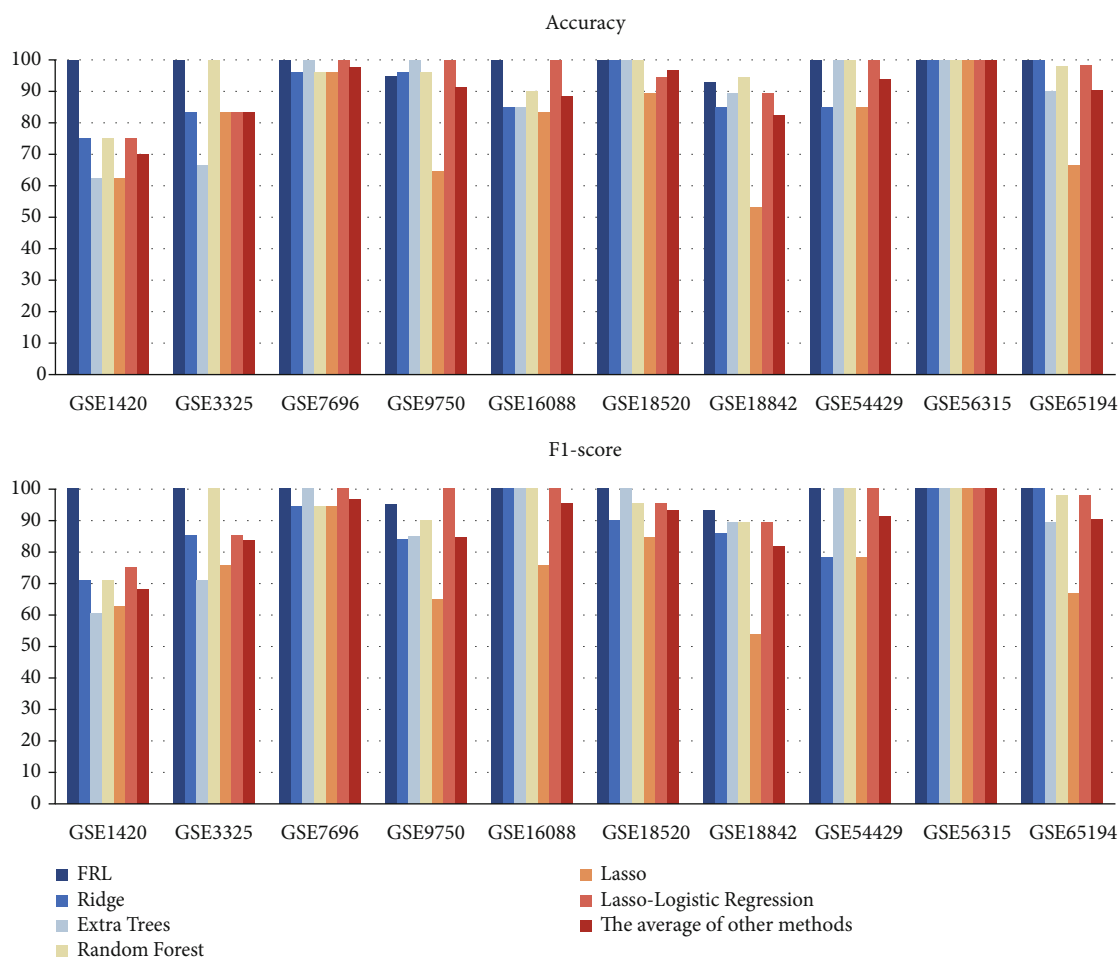


FIGURE 8: Comparisons on ACC and F1-score between FRL, Ridge regression (Ridge), Extremely randomized trees (Extra Trees), Random forest, Lasso, and Lasso-Logistic regression.

confirm the validation of the 19 genes in total, which introduces the detailed function and potential carcinogenic pathways of the above 19 genes. Table 6 apparently shows associations between the biomarker module and various cancers.

To further explore the basic biological functions of the biomarker module, cluster-Profiler from the R platform is used to perform a Gene Ontology (GO) analysis. The results concentrate in the range of $P < 0.05$, as shown in Figure 9. $P < 0.05$ is a statistics standard to denote that selected objects own significant difference. These 19 genes are mainly enriched with these three functional pathways: regulation of synapse organization, regulation of synapse structure or activity, and regulation of Ras protein signal transduction ($P < 0.0015$). These pathways are relative to the regulation of cellular component organizations and related protein expressions, which are consistent with the characteristics that cancer cells perform invasive and expansionary growth to the surrounding tissue. More detailed statistics are provided in the supplementary materials.

Through analysis of the biomarker module, we classify the genes into two main categories. The initial category, containing *ANKHD1*, *ATXN8OS*, *HSPB8*, *LSM7*, *MAFB*, and *TCTN2*, is involved in the direct regulation of cancer cell proliferation, apoptosis, and cancerization. We discovered that a

single biomarker in this category can activate various signaling pathways in different cancers. For instance, *ANKHD1* is an ankyrin-repeat-containing gene involved in the regulation of a variety of cellular functions, including transcription, cell cycling, ion channels, cell survival, and cell signaling pathways. *ANKHD1* is expressed in the cytoplasm or nuclei of different tissues. In prostate cancer cell lines, *ANKHD1* is a positive regulator of *YAP1* and promotes cell growth and cell cycle progression by promoting cyclin A [42]. In the K562 line of leukemia cells, *ANKHD1* acts as a skeleton protein and affects its malignant phenotype by interacting with *SHP2* [43]. In human multiple myeloma cell lines, *ANKHD1* can act on the promoter region of the cyclin-dependent kinase inhibitor p21 to upregulate the proliferation of multiple myeloma cells and affect the cell cycle progression [44]. Another example is *HSPB8*. As a gene involved in the heat shock protein family, *HSPB8* is ubiquitously expressed in a variety of human tissues. In triple-positive hormone-sensitive breast cancer cell lines (MCF-7), *HSPB8* regulates the proliferation and reduction of the migratory ability for MCF-7 cells [45]. In ovarian cancer cell lines, the downregulation of *HSPB8* positively directs the migration progress of the transforming growth factor alpha (TGF- α) for ovarian cancer cells [46]. *HSPB8* is detected to be overexpressed in

TABLE 4: Comparisons between FRL and other five feature selection algorithms.

Indicators	FRL		Ridge		Extra Trees		Random Forest		Lasso		Lasso-Logistic regression		Average of the other methods	
	ACC	F1-score	ACC	F1-score	ACC	F1-score	ACC	F1-score	ACC	F1-score	ACC	F1-score	ACC	F1-score
GSE1420	100	100	75	70.83	62.5	60.45	75	70.83	62.5	62.5	75	75	70	67.92
GSE3325	100	100	83.33	85.19	66.67	70.83	100	100	83.33	75.76	83.33	85.19	83.33	83.39
GSE7696	100	100	96.15	94.27	100	100	96.15	94.27	96.15	94.27	100	100	97.69	96.56
GSE9750	100	94.9	96.15	83.73	100	84.7	96.15	89.52	65	65	100	100	91.46	84.59
GSE16088	95	100	85	100	85	100	90	100	83.33	75.76	100	100	88.67	95.15
GSE18520	100	100	100	90	100	100	100	95.18	89.47	84.5	94.74	95.18	96.84	92.97
GSE18842	100	92.86	85	85.57	95	78.57	94.74	89.24	53.57	53.57	89.29	89.24	82.38	81.37
GSE54129	100	100	85	78.11	100	100	100	100	85	78.11	100	100	94	91.24
GSE56315	100	100	100	100	100	100	100	100	100	100	100	100	100	100
GSE65194	100	100	100	100	90	89.05	98	97.81	66.67	66.67	98	97.81	90.53	90.27
Average	99.5	98.776	90.563	88.77	89.917	88.36	95.004	93.685	78.502	75.614	94.036	94.242	89.49	88.348

TABLE 5: Comparisons between FRL and five other feature selection algorithms on time consumption.

Algorithm	Time consumption
FRL	79.619 s
Ridge	3328.9418 s
Extra Trees	2690.1589s
Random Forest	4148.396 s
Lasso	263.944 s
Lasso-Logistic regression	264.042 s

TABLE 6: Metavalidation results of selected genes.

	CCLC	Literature	COSMIC	NCG
ALPI	✓	✓	✓	
AMACR	✓	✓	✓	
ANKHD1	✓	✓	✓	
ARHGAP44	✓	✓	✓	
ARHGEF15	✓	✓	✓	
ARHGEF26	✓	✓	✓	
ATXN8OS	✓	✓		
CRISP3	✓	✓	✓	
HOPX	✓	✓	✓	
HSPB8	✓	✓	✓	✓
LSM7	✓	✓	✓	
MAFB	✓	✓	✓	✓
NGRN	✓	✓	✓	
PPP3R1	✓	✓	✓	
RDH5	✓	✓	✓	
SLC5A1	✓	✓	✓	
SPARC	✓	✓	✓	
SPRR3	✓	✓	✓	
TCTN2	✓	✓	✓	

gastric cancer, and it regulates the proliferation and apoptosis progress of gastric cells by activating the ERK-CREB signaling [47].

The second category contains protein-coding genes, namely, *ALPI*, *ARHGEF15*, *ARHGEF26*, *SLC5A1*, *AMACR*, *ARHGAP44*, *CRISP3*, *HOPX*, *NGRN*, *RDH5*, *SPRR3*, and *PPP3R1*, which indirectly play significant roles in the regulation progress of proteins. Mutations in these genes impact protein expression levels and further lead to the development of prostate, breast, and colorectal cancers, as well as other cancer types. For example, *ARHGEF15* regulates the activation of Rho family proteins. As essential signaling molecules, Rho family proteins modulate gene expression progress, cell motility progress, cell cycles, and other processes by regulating downstream molecules such as p21-activated kinase (PAK) and the myosin-binding subunit of myosin phosphatase (MYPT1) [48]. The transcripts of *CRISP3* are widespread in human glands such as the prostate. *CRISP3* induces the abundant changes in the cell adhesion protein subsets *Lasp1* and *TJP1*, which are included both in in vitro and in vivo environments, and *CRISP3* can therefore pro-

mote the development of tumors in the prostate [49]. The overexpression of *HOPX*, upregulation of p21, and downregulation of cyclin D1 and *CDK4* regulate the progress of migration and invasion of MDA-MB-468 cells to modulate tumor growth of the breast [50]. Colorectal cancer (CRC) is an example where the expression of *SPRR3* promotes the binding between PCAT18 and miR-759 and therefore restores a portion of the proliferation and invasion capabilities of CRC cells [51]. The combination of GO analysis and the literature review directly displays the connection between the proposed biomarker module and diverse cancers.

4. Discussion

The high cost and low reproducibility of microarray experiments make it arduous for experimental researchers to identify common genomic biomarkers of the same type of cancer [52]. Research reflects that tumors with similar phenotypes or representing the same type of cancer can have diverse responses to the same treatment, which may result from differences in gene expression [53]. By combining all the separate cancer datasets described above, highly universal clues can be summarized and missing important clustering details can be avoided, thereby enhancing the accuracy of the algorithm as well as revealing the gene expression mechanism [54].

The first contribution of this paper is the introduction of the FRL feature selection method. The FRL framework can effectively screen out robust genes with high accuracy. The traditional filter method, which aims at acquiring and removing redundant features, is not useful for extracting robust subsets of cancers. This paper uses Fisher score to screen subsets in the filter layer, and it mainly depends on human judgment to choose the optimal subset. A deficiency in the filter layer is the threshold setting requirement. In practice, the subset selected by human judgment will differ from the optimal subset. Therefore, in the future, we could explore more algorithms to obtain accurate calculations of the threshold, thereby enhancing flexibility and adaptability. In addition, Fisher score is effective for selecting high-score features. Thus, it is possible that some biomarkers with low scores are ignored in the selection process. In the future, we can pay more attention to low-score genes, which would be beneficial for the thorough exploration of certain cancers.

The second contribution of this paper is the effective extraction of genes to form a biomarker module based on 10 cancers associated with high mortality. Cluster studies can be beneficial in revealing the core mechanisms of high-mortality cancers [53]. Through GO analysis and multiple literature review, all the genes in this module have been verified to be related to diverse cancers. Furthermore, details of some of the pathways involving these genes have been obtained. The biomarker module tends to provide a range of genes that have great performances. It could overcome the difficulty of single genes, i.e., it is hard for a single gene to recur on gene chips; therefore, this narrows down the selection scope for clinical researchers. However, there is still a limitation for directly applying potential biomarkers in our module on a single type of cancer. With comprehensive

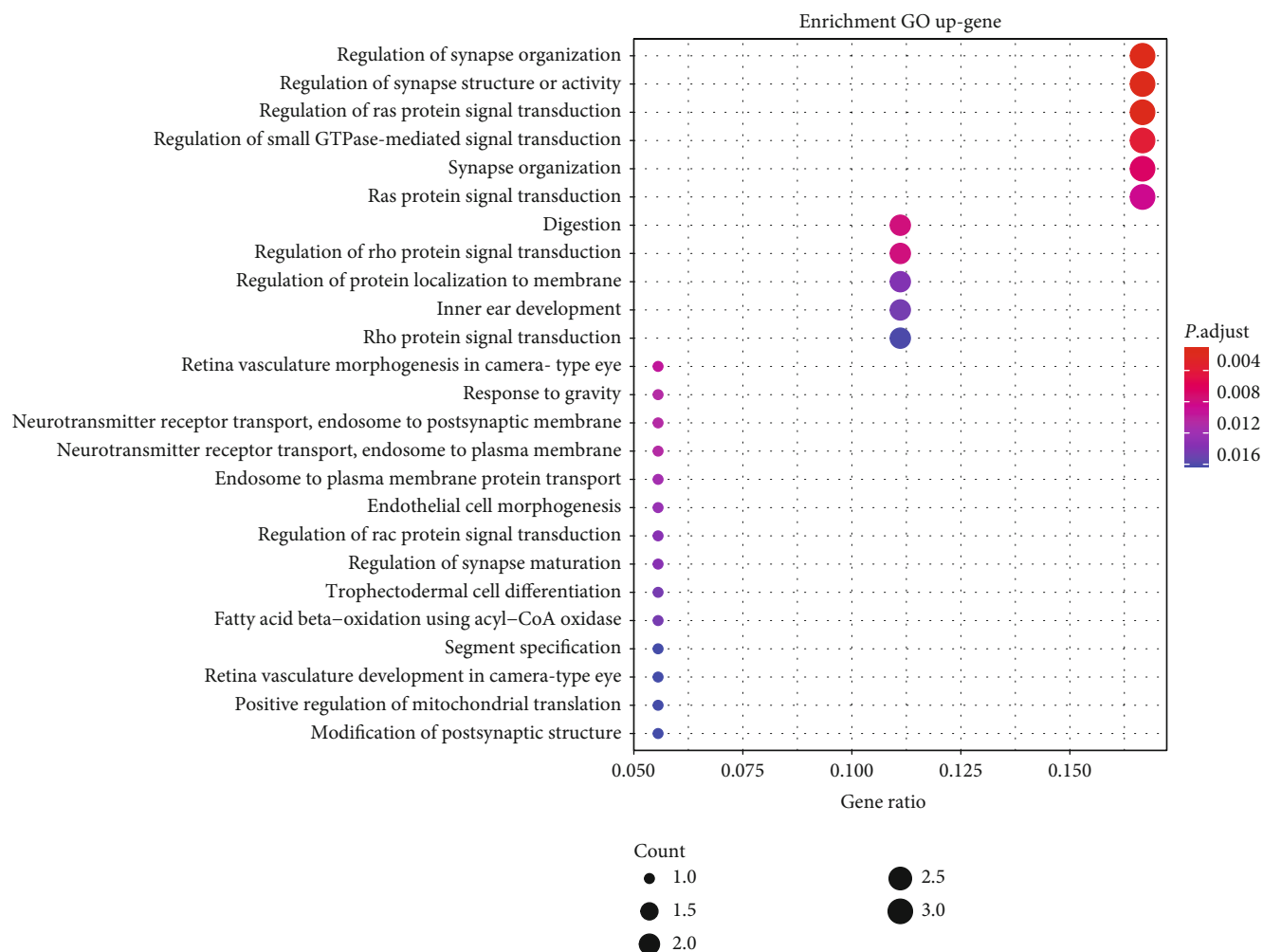


FIGURE 9: 25 pathways of GO analysis on 19 selected genes. The selected genes are mainly enriched in the following functional pathways: regulation of synapse organization, regulation of synapse structure or activity, and regulation of Ras protein signal transduction ($P < 0.0015$).

information obtained from cluster studies on multiple datasets, we can combine calculated data with clinical data, whole-genome sequencing, and the use of gene expression atlases to further explore the types and sites of gene mutations for single types of cancer in the future, which can attach great significance to the development of the health evaluation of ultra-early cancers associated with high mortality, the evaluation of radiotherapy efficacy, the prediction of the efficacy of target drugs, and monitoring for early postoperative recurrence of single types of cancers in precision medicine. Furthermore, we can upload our biomarker module data to a public database for other researchers to download, which can overcome drawbacks such as data deficiency and accelerate the identification process of all cancer biomarkers in *Homo sapiens*.

5. Conclusions

We present an integrative feature selection algorithm called FRL, which employs Fisher score, Recursive feature elimination, and Logistic regression (FRL). It has greater precision performance than differential expression analysis tools based

on Limma and five traditional feature selection methods. Time consumption has also been reduced through comparison with the abovementioned five methods. With the help of this method, we screened 19 genes from a total of 189224 genes in 10 high-mortality-cancer datasets to form a biomarker module. Via GO analysis and multiple meta-analysis in the biological field, all genes in this module are proven capable of serving as potential biomarkers of the regulation of cancer cellular component organization or related protein expressions, which corresponds to the characteristics that cancer cells perform invasive and expansionary growth to the surrounding tissue. This module is beneficial to health assessment, drug screening, and targeted therapy. In addition, the selected potential biomarker module can supply information on the development of cancers with high mortality, which assists in precision medicine.

Data Availability

The datasets for this study (GSE1420, GSE3325, GSE7696, GSE9750, GSE16088, GSE18520, GSE18842, GSE54129, GSE56315, GSE65194, GSE26886 and GSE23400) can be

found in <https://www.ncbi.nlm.nih.gov/>. The code of FRL can be found in <https://github.com/jianan-kristine/code.git>.

Conflicts of Interest

We declare that the research was conducted in the absence of any commercial or financial relationships that could be construed as a potential conflict of interest.

Supplementary Materials

Supplementary 1. Additional 1 presents the values of performance indicators of the selected model for esophageal cancer (GSE26886).

Supplementary 2. Additional 2 shows more detailed statistics for the *P* value which is less than 0.01 of GO analysis on the functional path in Figure 9.

References

- [1] O. Podlaha, M. Riester, S. De, and F. Michor, "Evolution of the cancer genome," *Trends in Genetics*, vol. 28, no. 4, pp. 155–163, 2012.
- [2] I. J. Majewski and R. Bernards, "Taming the dragon: genomic biomarkers to individualize the treatment of cancer," *Nature Medicine*, vol. 17, no. 3, pp. 304–312, 2011.
- [3] K. R. Kavitha, A. Prakasan, and P. J. Dhrishya, "Score-based feature selection of gene expression data for cancer classification," in *2020 Fourth International Conference on Computing Methodologies and Communication (ICCMC)*, Erode, India, 2020.
- [4] R. Nussinov, H. Jang, G. Nir, C. J. Tsai, and F. Cheng, "A new precision medicine initiative at the dawn of exascale computing," *Signal Transduction and Targeted Therapy*, vol. 6, no. 1, p. 3, 2021.
- [5] J. Larry Jameson and D. L. Longo, "Precision medicine—personalized, problematic, and promising," *Obstetrical & Gynecological Survey*, vol. 70, no. 10, pp. 612–614, 2015.
- [6] M. Francisco, F. Muios, D. P. J. Inés Sentis, and N. Lopez-Bigas, "A compendium of mutational cancer driver genes," *Nature reviews Cancer*, vol. 20, pp. 555–572, 2020.
- [7] L. Liang and S. Vucetic, "Improving accuracy of microarray classification by a simple multi-task feature selection filter," *International Journal of Data Mining and Bioinformatics*, vol. 5, pp. 189–208, 2011.
- [8] S. F. Farahbakhshian and M. T. Ahvanooey, "A new gene selection algorithm using fuzzy-rough set theory for tumor classification," *Control Engineering and Applied Informatics*, vol. 22, no. 1, pp. 14–23, 2020.
- [9] I. Guyon and E. André, "An introduction of variable and feature selection," *Journal of Machine Learning Research*, vol. 3, pp. 1157–1182, 2003.
- [10] C. Lazar, "A survey on filter techniques for feature selection in gene expression microarray analysis," *IEEE/ACM Transactions on Computational Biology & Bioinformatics*, vol. 9, no. 4, pp. 1106–1119, 2012.
- [11] J. Wang, L. Wu, J. Kong, Y. Li, and B. Zhang, "Maximum weight and minimum redundancy: a novel framework for feature subset selection," *Pattern Recognition*, vol. 46, no. 6, pp. 1616–1627, 2013.
- [12] Y. Piao, M. Piao, K. Park, and K. H. Ryu, "An ensemble correlation-based gene selection algorithm for cancer classification with gene expression data," *Bioinformatics*, vol. 28, no. 24, pp. 3306–3315, 2012.
- [13] D. Zhang, S. Chen, and Z. Zhou, "Constraint score: a new filter method for feature selection with pairwise constraints," *Pattern Recognition*, vol. 41, no. 5, pp. 1440–1451, 2008.
- [14] X. Sun, Y. Liu, and L. An, "Ensemble dimensionality reduction and feature gene extraction for single-cell RNA-seq data," *Nature Communications*, vol. 11, no. 1, p. 5853, 2020.
- [15] R. Kohavi and G. John, "Artificial intelligence wrappers for feature subset selection," *Cleve*, vol. 97, pp. 273–324, 1997.
- [16] R. Diao, F. Chao, T. Peng, N. Snooke, and Q. Shen, "Feature selection inspired classifier ensemble reduction," *IEEE Transactions on Cybernetics*, vol. 44, no. 8, pp. 1259–1268, 2014.
- [17] A. A. Friedman, A. Letai, D. E. Fisher, and K. T. Flaherty, "Precision medicine for cancer with next-generation functional diagnostics," *Nature Reviews Cancer*, vol. 15, no. 12, pp. 747–756, 2015.
- [18] F. Cheng, H. Liang, A. J. Butte, C. Eng, and R. Nussinov, "Personal mutanomes meet modern oncology drug discovery and precision health," *Pharmacological Reviews*, vol. 71, no. 1, pp. 1–19, 2019.
- [19] R. E. Banfield, L. O. Hall, K. W. Bowyer, and W. P. Kegelmeyer, "Ensemble diversity measures and their application to thinning," *Information Fusion*, vol. 6, no. 1, pp. 49–62, 2005.
- [20] T. Saegusa, Z. Zhao, H. Ke, Z. Ye, and T. Ma, "Detecting survival-associated biomarkers from heterogeneous populations," *Scientific Reports*, vol. 11, no. 1, p. 3203, 2021.
- [21] H. Sung, J. Ferlay, R. L. Siegel et al., "Global Cancer Statistics 2020: GLOBOCAN estimates of incidence and mortality worldwide for 36 cancers in 185 countries," *CA: a Cancer Journal for Clinicians*, vol. 71, no. 3, pp. 209–249, 2021.
- [22] E. T. Kimchi, M. C. Posner, J. O. Park et al., "Progression of Barrett metaplasia to adenocarcinoma is associated with the suppression of the transcriptional programs of epidermal differentiation," *Cancer Research*, vol. 65, no. 8, pp. 3146–3154, 2005.
- [23] S. Varambally, J. Yu, B. Laxman et al., "Integrative genomic and proteomic analysis of prostate cancer reveals signatures of metastatic progression," *Cancer Cell*, vol. 8, no. 5, pp. 393–406, 2005.
- [24] A. Murat, E. Migliavacca, T. Gorlia, W. L. Lambiv, and M. E. Hegi, "Stem cell-related "self-renewal" signature and high epidermal growth factor receptor expression associated with resistance to concomitant chemoradiotherapy in glioblastoma," *Journal of Clinical Oncology*, vol. 26, no. 18, pp. 3015–3024, 2008.
- [25] W. L. Lambiv, I. Vassallo, M. Delorenzi et al., "The Wnt inhibitory factor 1 (WIF1) is targeted in glioblastoma and has a tumor suppressing function potentially by induction of senescence," *Neuro-Oncology*, vol. 13, no. 7, pp. 736–747, 2011.
- [26] L. Scotto, G. Narayan, S. V. Nandula et al., "Identification of copy number gain and over-expressed genes on chromosome arm 20q by an integrative genomic approach in cervical cancer: potential role in progression," *Genes, Chromosomes & Cancer*, vol. 47, no. 9, pp. 755–765, 2008.
- [27] M. Paoloni, S. Davis, S. Lana et al., "Canine tumor cross-species genomics uncovers targets linked to osteosarcoma progression," *BMC Genomics*, vol. 10, no. 1, p. 625, 2009.

- [28] S. C. Mok, T. Bonome, V. Vathipadikeal et al., "A gene signature predictive for outcome in advanced ovarian cancer identifies a survival factor: microfibril-associated glycoprotein 2," *Cancer Cell*, vol. 16, no. 6, pp. 521–532, 2009.
- [29] A. Sanchez-Palencia, M. Gomez-Morales, J. A. Gomez-Capilla et al., "Gene expression profiling reveals novel biomarkers in nonsmall cell lung cancer," *International Journal of Cancer Journal International Du Cancer*, vol. 129, no. 2, pp. 355–364, 2011.
- [30] X. Chong, R. Peng, Y. Sun, L. Zhang, and Z. Zhang, "Identification of key genes in gastric cancer by bioinformatics analysis," *BioMed Research International*, vol. 2020, no. 5, 2020.
- [31] K. Dybkær, M. Bøgsted, S. Falgreen et al., "Diffuse large B-cell lymphoma classification system that associates normal B-cell subset phenotypes with prognosis," *Journal of Clinical Oncology*, vol. 33, no. 12, pp. 1379–1388, 2015.
- [32] C. H. Nørgaard, L. H. Jakobsen, A. J. Gentles, K. Dybkær, and M. Bøgsted, "Subtype assignment of CLL based on B-cell subset associated gene signatures from normal bone marrow—a proof of concept study," *Plos One*, vol. 13, no. 3, p. e0193249, 2018.
- [33] S. Maubant, B. Tesson, V. Maire et al., "Transcriptome analysis of Wnt3a-treated triple-negative breast cancer cells," *Plos One*, vol. 10, no. 4, p. e0122333, 2015.
- [34] V. Maire, F. Némati, M. Richardson et al., "Polo-like kinase 1: a potential therapeutic option in combination with conventional chemotherapy for the management of patients with triple-negative breast cancer," *Cancer Research*, vol. 73, no. 2, pp. 813–823, 2013.
- [35] R. A. Irizarry, B. Hobbs, F. Collin et al., "Exploration, normalization, and summaries of high density oligonucleotide array probe level data," *Biostatistics*, vol. 4, no. 2, pp. 249–264, 2003.
- [36] A. Spooner, E. Chen, A. Sowmya et al., "A comparison of machine learning methods for survival analysis of high-dimensional clinical data for dementia prediction," *Scientific Reports*, vol. 10, no. 1, p. 20410, 2020.
- [37] H. Su, N. Hu, H. H. Yang, C. Wang, and P. R. Taylor, "Global gene expression profiling and validation in esophageal squamous cell carcinoma and its association with clinical phenotypes," *Clinical Cancer Research an Official Journal of the American Association for Cancer Research*, vol. 17, no. 9, pp. 2955–2966, 2011.
- [38] Q. Wang, C. Ma, and W. Kemmner, "Wdr66 is a novel marker for risk stratification and involved in epithelial-mesenchymal transition of esophageal squamous cell carcinoma," *BMC Cancer*, vol. 13, no. 1, 2013.
- [39] GEMO Study Collaborators, EMBRACE Collaborators, KConFab Investigators et al., "Fine-mapping of 150 breast cancer risk regions identifies 191 likely target genes," *Nature Genetics*, vol. 52, no. 1, pp. 56–73, 2020.
- [40] P. A. Futreal, L. Coin, M. Marshall et al., "A census of human cancer genes," *Nature Reviews Cancer*, vol. 4, no. 3, pp. 177–183, 2004.
- [41] C. Turnbull, R. H. Scott, E. Thomas et al., "The 100 000 genomes project: bringing whole genome sequencing to the NHS," *BMJ (Clinical research ed.)*, vol. 361, p. k1687, 2018.
- [42] S. Wu, Y. Liu-Chittenden, Y. Zheng, J. Dong, and D. J. Pan, "The TEAD/TEF family protein Scalloped mediates transcriptional output of the Hippo growth-regulatory pathway," *Developmental Cell*, vol. 14, no. 3, pp. 388–398, 2008.
- [43] S. K. Zaidi, A. J. Sullivan, R. Medina et al., "Tyrosine phosphorylation controls Runx2-mediated subnuclear targeting of YAP to repress transcription," *The EMBO Journal*, vol. 23, no. 4, pp. 790–799, 2004.
- [44] A. Dhyan, A. S. S. Duarte, J. A. Machado-Neto, P. Favaro, M. M. Ortega, and S. T. O. Saad, "ANKHD1 regulates cell cycle progression and proliferation in multiple myeloma cells," *FEBS Letters*, vol. 586, no. 24, pp. 4311–4318, 2012.
- [45] M. Piccolella, V. Crippa, R. Cristofani, P. Rusmini, and A. Poletti, "The small heat shock protein b8 (hspb8) modulates proliferation and migration of breast cancer cells," *Oncotarget*, vol. 8, no. 6, pp. 10400–10415, 2017.
- [46] M. Suzuki, R. Matsushima-Nishiwaki, G. Kuroyanagi et al., "Regulation by heat shock protein 22 (hspb8) of transforming growth factor- α -induced ovary cancer cell migration," *Archives of Biochemistry and Biophysics*, vol. 571, pp. 40–49, 2015.
- [47] J. Shen, M. Li, and L. Min, "Hspb8 promotes cancer cell growth by activating the ERKCREB pathway and is indicative of a poor prognosis in gastric cancer patients," *Oncology Reports*, vol. 39, no. 6, pp. 2978–2986, 2018.
- [48] H. Fukushima, M. Yasumoto, S. Ogasawara et al., "ARH-GEF15 overexpression worsens the prognosis in patients with pancreatic ductal adenocarcinoma through enhancing the motility and proliferative activity of the cancer cells," *Molecular Cancer*, vol. 15, no. 1, pp. 1–13, 2016.
- [49] M. Volpert, L. Furic, J. Hu et al., "CRISP3 expression drives prostate cancer invasion and progression," *Endocrine Related Cancer*, vol. 27, no. 7, pp. 415–430, 2020.
- [50] Q. You, Y. Geng, H. Ye, G. Zhu, and H. Zhu, "HOPX is an epigenetically inactivated tumor suppressor and overexpression of HOPX induce apoptosis and cell cycle arrest in breast cancer," *Oncotargets and Therapy*, vol. Volume 13, pp. 5955–5965, 2020.
- [51] D. Yang, R. Li, J. Xia, W. Li, and H. Xue, "Long noncoding RNA PCAT18 upregulates SPRR3 to promote colorectal cancer progression by binding to mir-759," *Cancer Management and Research*, vol. Volume 12, pp. 11445–11452, 2020.
- [52] A. Nimgaonkar, D. Sanoudou, A. J. Butte et al., "Reproducibility of gene expression across generations of Affymetrix microarrays," *Bmc Bioinformatics*, vol. 4, no. 1, p. 27, 2003.
- [53] J. Zhang, D. Xu, K. Hao, Y. Zhang, and Y. D. Marinis, "FS-GBDT: identification multicancer-risk module via a feature selection algorithm by integrating Fisher score and gbdt," *Briefings in Bioinformatics*, pp. 1–13, 2021.
- [54] J. C. Mills and J. I. Gordon, "A new approach for filtering noise from high-density oligonucleotide microarray datasets," *Nucleic Acids Research*, vol. 29, no. 15, p. 772, 2001.

Research Article

Integrated MicroRNA Expression Profile Reveals Dysregulated miR-20a-5p and miR-200a-3p in Liver Fibrosis

Mu Ye ¹, Sheng Wang ², Peilong Sun ¹, and Jingbo Qie ²

¹Department of General Surgery, Jinshan Hospital, Fudan University, Shanghai 201508, China

²Institutes of Biomedical Sciences, Fudan University, Shanghai 200032, China

Correspondence should be addressed to Peilong Sun; sunpeilong@fudan.edu.cn and Jingbo Qie; jingboqie@fudan.edu.cn

Received 18 April 2021; Accepted 27 May 2021; Published 8 June 2021

Academic Editor: Tao Huang

Copyright © 2021 Mu Ye et al. This is an open access article distributed under the Creative Commons Attribution License, which permits unrestricted use, distribution, and reproduction in any medium, provided the original work is properly cited.

MicroRNAs (miRNAs) have been demonstrated to involve in liver fibrogenesis. However, the miRNA-gene regulation in liver fibrosis is still unclear. Herein, the miRNA expression profile GSE40744 was obtained to analyze the dysregulated miRNAs between liver fibrosis and normal samples. Then, we predicted the target genes of screened miRNAs by miRTarBase, followed by gene ontology (GO) and Kyoto Encyclopedia of Genes and Genomes (KEGG) analysis. Then, the protein-protein interaction (PPI) network was constructed to identify the functional miRNA-gene regulatory modules. Furthermore, we verified the hub gene expression using the gene expression profile GSE14323. Finally, 89 DEMs were identified in fibrotic liver samples compared to normal liver samples. The top 3 upregulated DEMs (miR-200b-3p, miR-200a-3p, and miR-182-5p) and downregulated DEMs (miR-20a-5p, miR-194-3p, and miR-148a-3p) were further studied. 516 and 1416 target genes were predicted, respectively. KEGG analysis demonstrated that the predicted genes were enriched in the p53 signaling pathway and hepatitis B, etc. Through constructing a PPI network, the genes with the highest connectivity were identified as hub genes. Of note, most of the hub genes were potentially targeted by miR-20a-5p and miR-200a-3p. Based on the data from GSE14323, the expression of EGFR, STAT3, CTNNA1, and TP53 targeted by miR-200a-3p was significantly downregulated in fibrotic liver samples. Oppositely, the expression of PTEN, MYC, MAPK1, UBC, and CCND1 potentially targeted by miR-20a-5p was significantly upregulated. In conclusion, it is demonstrated that miR-20a-5p and miR-200a-3p were identified as the novel liver fibrosis-associated miRNAs, which may play critical roles in liver fibrogenesis.

1. Introduction

Liver fibrosis results from chronic liver disease, which has the potential to progress into cirrhosis, complicating with the loss of architecture and attendant functional failure [1]. If advanced chronic fibrosis is not prevented, liver fibrosis may lead to liver cancer and liver failure, which are major causes of morbidity and mortality worldwide [2–5]. Increasing studies report that hepatocytes activated hepatic stellate cells and macrophages and cooperate in liver fibrosis. However, the underlying mechanism remains incompletely uncovered.

MicroRNA (miRNA) is a type of highly conserved tissue-specific nonsmall protein noncoding RNA. The dysregulation of miRNA expression is related to various cancers by acting as tumor suppressor and oncogene. miRNA actu-

ally participates at the posttranscriptional level and binds to the 3'UTR of its target messenger RNA (mRNA) to inhibit expression. The dysfunction of miRNA interferes with the expression of carcinogenic or tumor suppressor target genes, which is related to the pathogenesis of cancer [6]. Compelling evidence indicates that dysregulated expression of miRNAs is found in many types of diseases, including liver fibrosis [7–11]. It is well-studied that many miRNAs are aberrantly expressed in liver tissues from the patients with liver fibrosis. As we know, it is a complicated pathological process of liver fibrogenesis, involving large numbers of miRNAs and genes. To dig the miRNAs-to-gene regulatory network in complex cellular systems, increasing studies focus on the identification of novel liver fibrosis-associated miRNAs and their regulatory networks [12–16]. For example, miRNA-221 and miRNA-222 are screened out as the

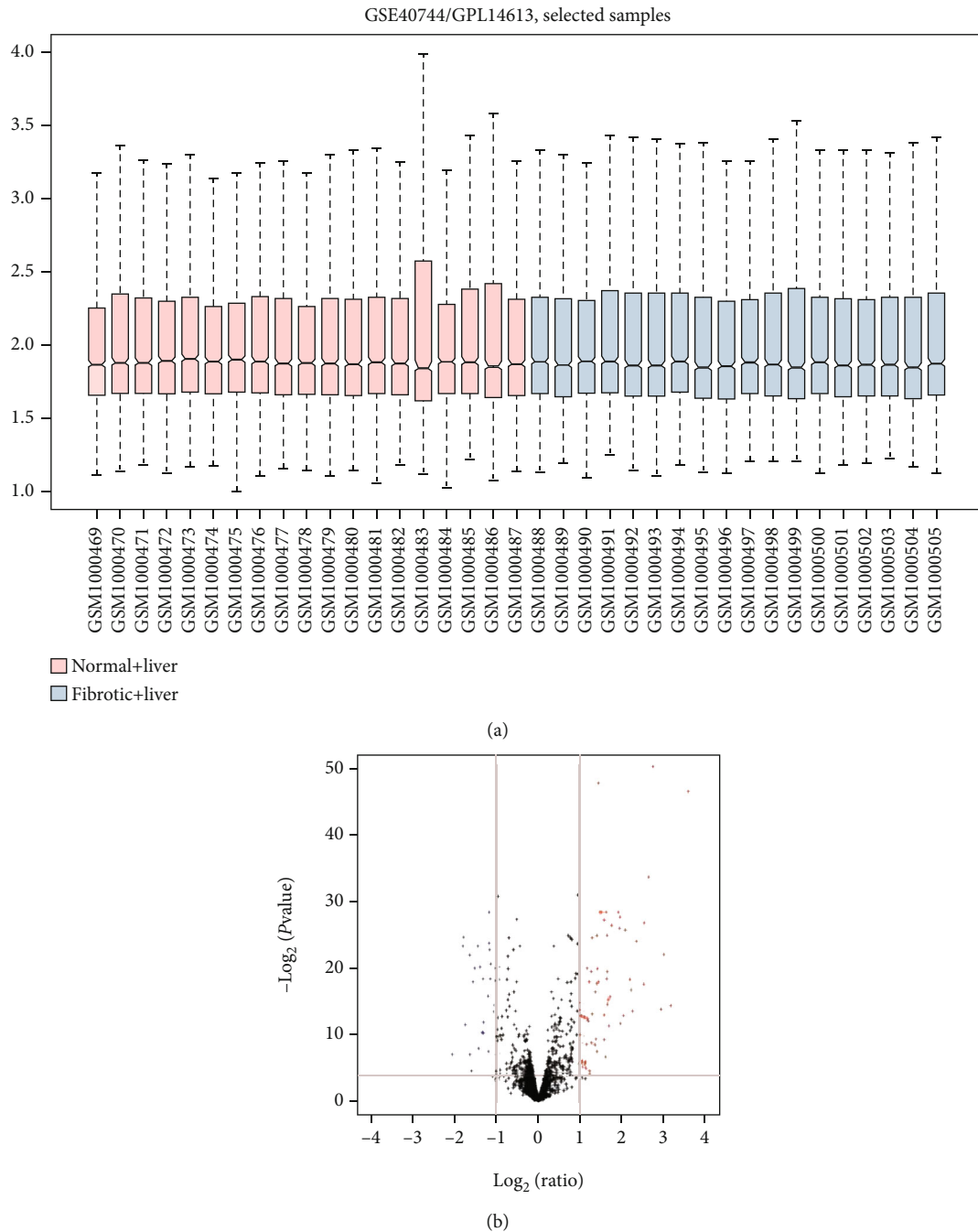


FIGURE 1: Identification of different expression miRNAs. (a) GSE40744 data after normalization. (b) Volcano plot of the DEMs. The black dots represent miRNAs that are not differentially expressed between liver fibrosis samples and normal liver samples, and the red dots and blue dots represent the upregulated and downregulated miRNAs in liver fibrosis samples, respectively.

biomarkers in liver fibrosis [17], and miR-19b-3p [18], miRNA-181a [19, 20], miR-873-5p [21], and miR-34a-5p [22] are reported to regulate the progression of liver fibrosis.

This study analyzed the GSE40744 data set and identified DEMs between fibrotic liver samples and normal liver samples. Using bioinformatics tools to predict various key miRNA target genes. On this basis, in corresponding databases, such as Kyoto Encyclopedia of Genes and Genomes (KEGG) and Gene Ontology (GO) databases, the consensus targets are combined for further analysis. Then, the

expression levels of hub target genes were explored in the GSE14323 database. This is of great value for improving the diagnosis and treatment of liver fibrosis.

2. Materials and Methods

2.1. Identification of DEMs Associated with Liver Fibrosis. GEO2R [23] was used to identify DEMs from the data of GSE40744 [24], containing the miRNA expression data from 18 fibrotic and 19 normal liver samples. The miRNAs with

TABLE 1: Top ten upregulated differentially expressed miRNAs between liver fibrosis samples and normal liver samples.

miRNA name	logFC	<i>t</i>	<i>B</i>	<i>P</i> value	Adj. <i>P</i> value
hsa-mir-182-5p	3.58038	14.95512	29.6132	1.66E-17	1.23E-14
hsa-mir-200a-3p	3.166491	5.59633	4.6646	2.04E-06	5.46E-05
hsa-mir-200b-3p	2.934094	5.47836	4.3002	2.96E-06	7.56E-05
hsa-mir-155-5p	2.736842	16.72755	33.1346	4.06E-19	9.05E-16
hsa-mir-452-5p	2.634678	11.13642	20.7549	1.58E-13	8.77E-11
hsa-miR-29b-3p	2.524444	8.92977	14.7507	7.19E-11	1.00E-08
hsa-mir-31-5p	2.517047	6.38599	7.1117	1.68E-07	5.68E-06
hsa-mir-150-5p	2.345526	8.08317	12.2786	8.86E-10	7.04E-08
hsa-mir-708-5p	2.249942	5.40739	4.0813	3.70E-06	9.08E-05
hsa-mir-224-3p	2.218392	6.17261	6.4504	3.30E-07	1.10E-05

TABLE 2: Top ten downregulated differentially expressed miRNAs between liver fibrosis samples and normal liver samples.

miRNA name	logFC	<i>t</i>	<i>B</i>	<i>P</i> value	Adj. <i>P</i> value
hsa-mir-20a-5p	-2.064474	-3.68137	-1.0193	7.18E-04	8.15E-03
hsa-miR-194-3p	-1.806374	-7.87003	11.6433	1.69E-09	1.11E-07
hsa-mir-148a-3p	-1.792602	-8.298	12.9139	4.65E-10	4.50E-08
hsa-mir-1281	-1.75383	-4.87317	2.4477	1.97E-05	3.77E-04
hsa-mir-574-3p	-1.648655	-7.51855	10.5856	4.94E-09	2.89E-07
hsa-mir-1308	-1.64269	-3.68312	-1.0145	7.14E-04	8.15E-03
hsa-mir-572	-1.603509	-2.86486	-3.1265	6.76E-03	4.56E-02
hsa-mir-378-3p	-1.570848	-6.46778	7.3648	1.30E-07	4.60E-06
hsa-mir-130b-3p	-1.530614	-7.04856	9.1541	2.11E-08	1.07E-06
hsa-mir-193b-3p	-1.450292	-7.89223	11.7097	1.58E-09	1.10E-07

adjusted *P* value (adj. *P*) < 0.05 and $|\log_2(\text{fold change})| > 1$ were identified as DEMs. GSE14323 is a gene expression microarray, including 41 fibrosis and 19 normal liver samples, used to evaluate miRNA-regulated hub gene expression.

2.2. Prediction of Target Genes. We used miRTarBase (<http://mirtarbase.mbc.nctu.edu.tw/php/index.php>) to predict the target genes [25].

2.3. GO and KEGG Pathway Analysis. DAVID (<https://david.ncifcrf.gov/>) was introduced to perform GO and KEGG pathway enrichment analysis [26, 27]. FDR < 0.05 was statistically significant.

2.4. Construction of PPI and miRNA-Gene Network. STRING (<http://string-db.org>) was used to construct the PPI network and to identify the hub genes with the highest connectivity [28].

2.5. Statistical Analysis. The gene expression was shown as mean \pm SD. Unpaired Student's *t*-test in Graphpad software was performed to estimate the differences. *P* < 0.05 was considered statistically significant.

3. Results

3.1. DEM Identification and Target Gene Prediction. In our study, we obtained the miRNA expression profile GSE40744 from GEO and checked the data consistency. The normalized data was visualized (Figure 1(a)) and then conducted a differential expression analysis using the GEO2R tool. Totally, 89 miRNAs were identified as DEMs between liver fibrosis samples and normal liver samples, including 62 upregulated miRNAs and 27 downregulated miRNAs (Figure 1(b)). As listed in Tables 1 and 2, miR-182-5p, miR-200a-3p, miR-200b-3p, miR-20a-5p, miR-194-3p, and miR-148a-3p were screened out as the top changed miRNAs, which was selected for further study. Furthermore, 516 and 1416 genes were predicted to be regulated by the top 3 upregulated and downregulated miRNAs through miRTarBase, respectively. (Table S1).

3.2. GO Functional Enrichment Analysis. DAVID and STRING databases were used to obtain the GO functional annotation of the target genes. For the genes targeted by the 3 upregulated miRNAs (Table S2), positive regulation of transcription from RNAP II promoter, negative regulation of apoptotic process, negative regulation of transcription from RNA RNAP II promoter, positive regulation of transcription, and DNA-templated and positive regulation of cell proliferation were enriched in the biological process

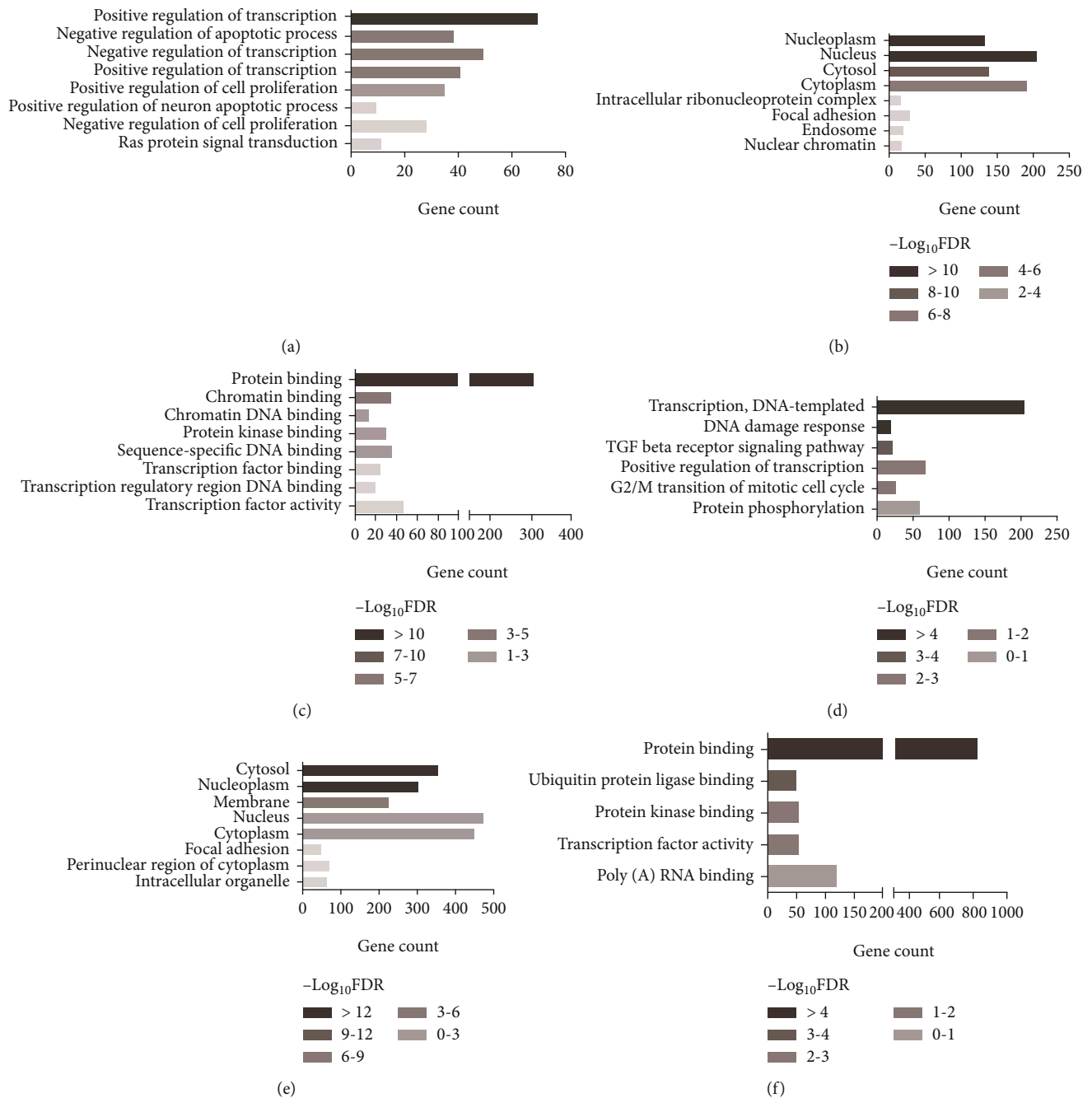


FIGURE 2: GO functions for the target genes of top three upregulated miRNAs and top three downregulated miRNAs. (a) Enriched biological process of the upregulated miRNAs. (b) Enriched cellular component of the upregulated miRNAs. (c) Enriched molecular function of the upregulated miRNAs. (d) Enriched biological process of the downregulated miRNAs. (e) Enriched cellular component of the downregulated miRNAs. (f) Enriched molecular function of the downregulated miRNAs.

(BP) category (Figure 2(a)); nucleoplasm, nucleus, cytosol, cytoplasm, intracellular ribonucleoprotein complex, and focal adhesion were enriched in the cellular component (CC) category (Figure 2(b)); protein binding, chromatin binding, chromatin DNA binding, protein kinase binding, and sequence-specific DNA binding were enriched in the molecular function (MF) category (Figure 2(c)). For the genes targeted by the 3 downregulated miRNAs (Table S3),

regulation of transcription, DNA damage response, TGFBR signaling pathway, positive regulation of transcription, and cell cycle were enriched in the BP category; cytosol, nucleoplasm, membrane, nucleus, and cytoplasm were enriched in the CC category; protein binding, ubiquitin-protein ligase binding, protein kinase binding, protein kinase activity, and poly(A) RNA binding were enriched in the MF category.

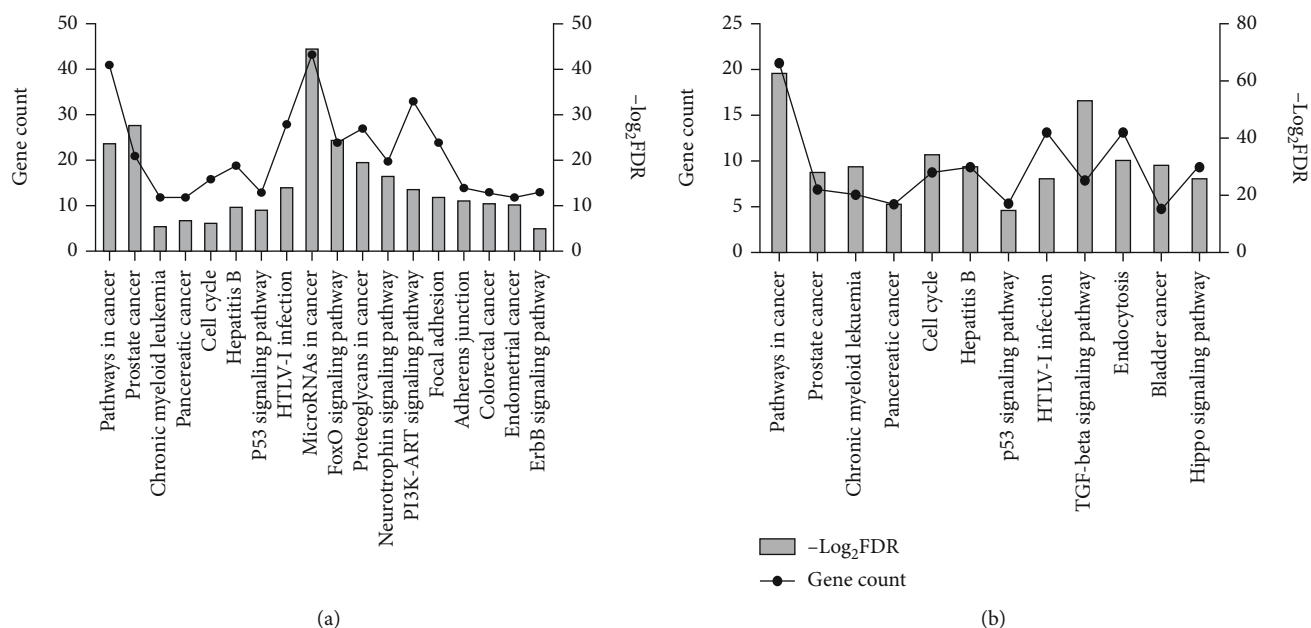


FIGURE 3: KEGG pathway enrichment analysis of target genes of six selected DEMs. (a) For upregulated miRNAs. (b) For downregulated miRNAs. The lines represent gene count and the columns represent $-\log_2 FDR$.

TABLE 3: Hub genes identified in the PPI interaction.

Gene symbol	Description	Degree	P1	P2	P3
Upregulated miRNA					
TP53	Tumor protein P53	136	+	+	+
EGFR	Epidermal growth factor receptor	106	-	-	-
PTEN	Phosphatase and tensin homolog	105	+	+	-
JUN	Jun proto-oncogene	93	+	-	-
VEGFA	Vascular endothelial growth factor A	89	-	-	-
KRAS	KRAS proto-oncogene, GTPase	87	+	-	-
STAT3	Signal transducer and activator of transcription 3	86	+	-	-
CTNNB1	Catenin beta 1	85	-	-	-
NOTCH1	Notch receptor 1	85	-	-	-
EP300	E1A binding protein p300	82	+	-	+
Downregulated miRNA					
TP53	Tumor protein P53	235	+	+	+
UBC	Ubiquitin C	191	-	-	-
RPS27A	Ribosomal protein S27a	184	-	-	-
MYC	MYC proto-oncogene, bHLH transcription factor	175	+	-	+
HSP90AA1	Heat shock protein 90 alpha family class A member 1	153	-	-	-
MAPK1	Mitogen-activated protein kinase 1	144	+	-	-
PTEN	Phosphatase and tensin homolog	134	+	+	-
CCND1	Cyclin D1	125	+	+	+
HSPA8	Heat shock protein family A (Hsp70) member 8	124	-	-	-
VEGFA	Vascular endothelial growth factor A	119	-	-	-

P1: hepatitis B; P2: p53 signaling pathway; P3: cell cycle. “+” and “-,” respectively, indicate genes can and cannot be found in corresponding KEGG pathways.

3.3. KEGG Pathway Analysis. To demonstrate the biological function of the 6 selected DEMs, the target genes were subsequently used in KEGG pathway analysis. For 3 upregulated miRNAs (Figure 3(a), Table S4), 18 significantly enriched

KEGG pathways were identified, containing microRNAs in cancer, prostate cancer, FoxO signaling pathway, pathways in cancer, and proteoglycans in cancer. And 12 significantly enriched KEGG pathways for downregulated miRNAs were



FIGURE 4: The regulatory network between dysregulated miRNAs and hub genes.

identified (Figure 3(b), Table S4), including pathways in cancer, TGF-beta signaling pathway, cell cycle, endocytosis, and bladder cancer. Interestingly, both of the 2 groups of genes targeted by upregulated miRNAs or downregulated miRNAs were enriched in the process, prostate cancer, pathways in cancer, HTLV-I infection, hepatitis B, p53 signaling pathway, pancreatic cancer, cell cycle, and chronic myeloid leukemia. Excluding the process of cancer, it is evident that hepatitis B, p53 signaling pathway, and cell cycle play central roles in liver fibrosis. Therefore, the genes targeted by upregulated miRNAs or downregulated miRNA, which are included in these three pathways, may modulate liver fibrosis progress.

3.4. PPI and miRNA-Hub Gene Network. The results revealed that most of the target genes displayed broad external relationships. According to the node degree, the genes with the highest connectivity were identified as the hub genes (Table 3), including TP53, EGFR, PTEN, JUN, VEGFA,

KRAS, STAT3, CTNNB1, NOTCH1, and EP300 for the 3 upregulated miRNAs, and TP53, UBC, RPS27A, MYC, HSP90AA1, MAPK1, PTEN, CCND1, HSPA8, and VEGFA for the downregulated miRNAs. Collectively, TP53 gained the highest connectivity in both groups (136 and 235). Meanwhile, TP53 and PTEN were the only two hub genes enriched in all three pathways.

Subsequently, the miRNA-hub gene network was constructed (Figure 4). We found that nine in ten hub genes (TP53, PTEN, RPS27A, MYC, MAPK1, UBC, CCND1, HSPA8, and VEGFA) were potentially regulated by miR-20a-5p. miR-200a-3p could potentially target five (TP53, PTEN, EGFR, STAT3, and CTNNB1) in ten hub genes. In another way, we also found that TP53, as the highest-degree node, was potentially targeted by miR-20a-5p, miR-200a-3p, and miR-194-3p; PTEN was potentially regulated by miR-20a-5p, miR-200a-3p, and miR-182-5p. The results above prompted that miR-20a-5p and miR-200a-3p are two potential regulators in liver fibrogenesis.

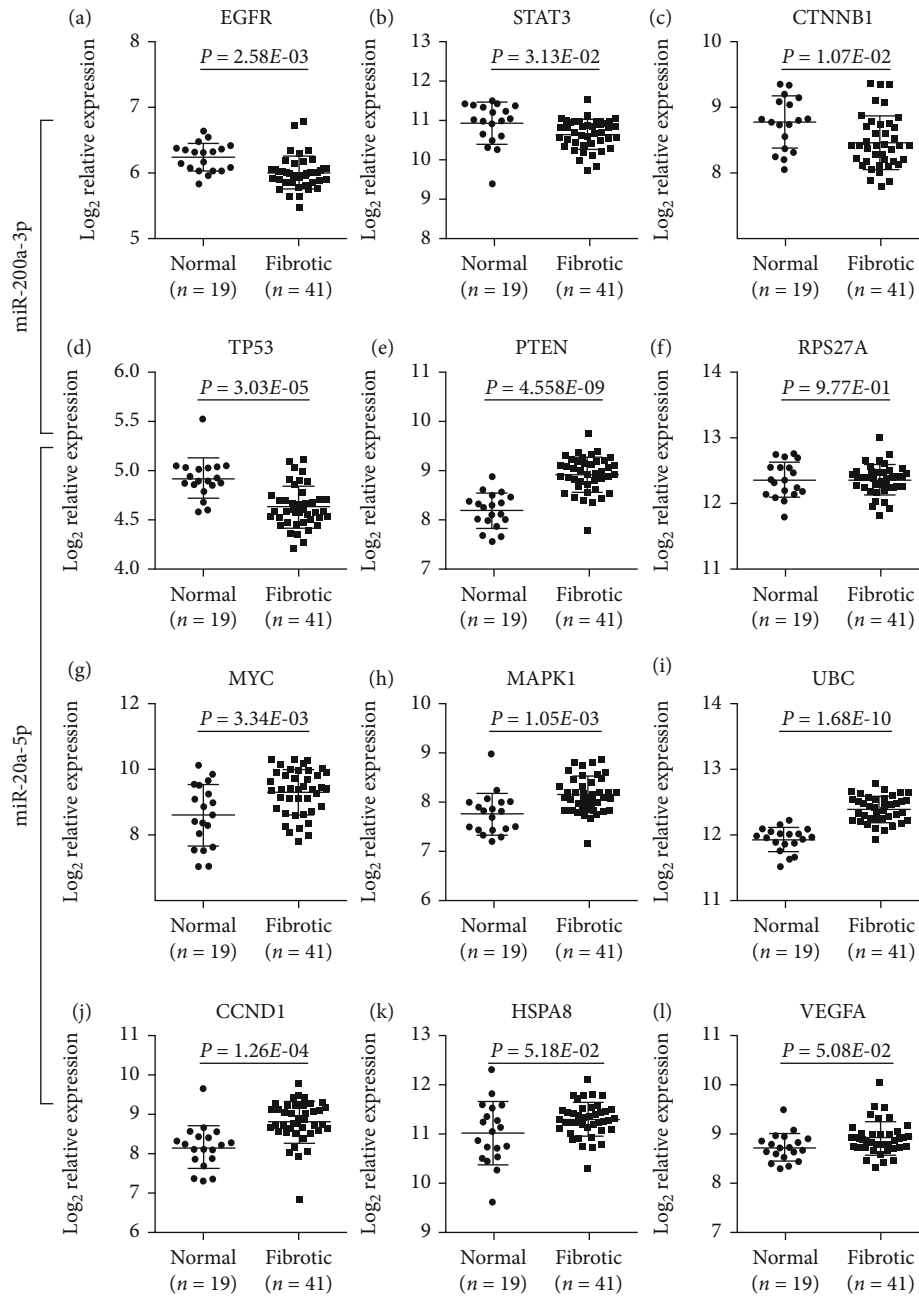


FIGURE 5: The mRNA expression of predicted targets of miR-200a-3p and miR-20a-5p from the GSE14323 dataset.

3.5. *Evaluation of the Hub Gene Expression.* Because there was no survival outcome data of miRNA in fibrosis, we just evaluated the hub gene expression regulated by the two selected miRNAs using GSE14323. We found that the expression of four (EGFR, STAT3, CTNNB1, and TP53) in five targets of miR-200a-3p (upregulated) was significantly downregulated in fibrotic liver samples compared with normal liver samples (Figures 5(a)–5(d)). Similarly, the upregulated genes, PTEN, MYC, MAPK1, UBC, and CCND1, may be regulated by miR-20a-5p (Figures 5(e) and 5(g)–5(j)). Although HSPA8 and VEGFA in fibrotic liver samples were not significantly higher than that in nor-

mal liver samples, the *P* values were near 0.05 (Figures 5(k) and 5(l)). And the expression level of RPS27A in normal liver tissue and fibrotic liver tissue has no significant difference (Figure 5(f)). To verify the relationship between miRNAs and genes, we rechecked the data from miRTarBase [29]. The regulation of PTEN, MYC, CCND1, and VEGFA by hsa-miR-20a-5p was identified in at least one luciferase reporter assay, qRT-PCR, ELISA, and western blot, previously. The result was similar for hsa-miR-200a-3p. So, it was reasonable that the miRNAs identified in our study participated in the liver fibrosis progress via regulating their target genes.

4. Discussion

Although it is extensively reported that miRNAs participate in the whole process of liver fibrogenesis, including cell death, the proinflammatory factor secretion by macrophage, and hepatic stellate cell (HSC) activation [11, 30], the profiles of liver fibrosis available are limited. In our study, we reanalyzed the miRNA expression profile GSE40744 for the identification of DEMs and the gene expression profile GSE14323 for validation of target gene expression. Finally, 89 DEMs were identified, including 27 downregulated DEMs and 62 upregulated DEMs.

Pathway enrichment analysis found that the top 3 upregulated miRNAs and top 3 downregulated miRNAs are involved in the regulation of signal pathways. For example, the hallmark feature of cancer is abnormal cell proliferation. Cell cycle dysregulation is the main body of abnormal cell proliferation, which leads to tumor progression. The abnormal function of cell cycle regulators leads to uncontrolled cell proliferation, making it an attractive therapeutic target in cancer treatment. According to reports, in the rat liver fibrosis model, miR-34a regulates cell proliferation and apoptosis by inhibiting SIRT1 to activate p53. The miR-34a/SIRT1/p53 signaling pathway is activated in liver cells and is a therapeutic target for liver fibrosis. By a series of integrated analyses, miR-20a-5p and miR-200a-3p were screened out as the most potential modulator in liver fibrosis. miR-20a-5p was reported to inhibit proliferation and metastasis of HCC by targeting Runt-Related Transcription Factor 3 (RUNX3) and Hepatocyte Growth Factor (HGF). miR-200a-3p was reported to promote HCC proliferation and metastasis by targeting Zinc Finger E-Box Binding Homeobox 1 (ZEB1) and Cyclin Dependent Kinase 6 (CDK6) [31, 32]. Until now, there is no study showing the role of miR-200a-3 and miR-20a-5p in liver fibrosis, besides our previous study on miR-20a-5p/TGFBR2 axis [30]. In this study, we also identified many other potential target genes of miR-200a-3 and miR-20a-5p involved in liver fibrosis. For example, a case-control analysis showed that TP53 mutation reflects a moderate dietary exposure to aflatoxins leading to liver fibrosis [33], and p53 signal pathway is involved in liver fibrosis by inducing hepatocyte apoptosis [34]. It was reported EGFR played the key role in CCl₄-induced liver fibrosis [35], if the expression of EGFR was inhibited, fibrosis and stellate cell activation were attenuated [36]. Another well-studied gene in liver fibrosis is PTEN, which was reported in the regulation of Kupffer cell activation [37]. The activation of the PTEN/p65 signaling pathway promoted liver fibrosis in nonalcoholic fatty liver disease [38].

This study has limitations. First, it is necessary to collect clinical samples to further study the expression levels of miR-20a-5p and miR-200a-3p. We plan to collect more samples in future studies to explore the correlation between the expression of miR-20a-5p, miR-200a-3p, and their target genes and the clinical parameters of patients with liver fibrosis. Second, it is necessary to further explore the regulation of miR-20a-5p and miR-200a-3p on the proliferation and cell cycle of liver fibrotic cells. Finally, we will further verify the regulation of miR-20a-5p and miR-200a-3p and their target genes on the progression of liver fibrosis.

In conclusion, this study identified 89 DEMs between fibrotic liver samples and normal liver samples by reanalyzing the GSE40744 data set. By constructing miRNA gene regulatory network and PPI network, further study miR-20a-5p and miR-200a-3p. Based on the GSE14323 database, our results showed that EGFR, STAT3, CTNNB1, and TP53 targeting by miR-200a-3p (upregulated) were significantly downregulated in fibrotic liver samples. The expression of PTEN, MYC, MAPK1, UBC, and CCND1 potentially regulated by miR-20a-5p (downregulated) was significantly overexpressed in fibrotic liver samples. In short, miR-200a-3 and miR-20a-5p were identified as the novel liver fibrosis-associated miRNAs, which may play key roles in liver fibrogenesis, suggesting the value of the further study.

Data Availability

The miRNA and mRNA expression data supporting this study are from previously reported studies and datasets, which have been cited. The processed data are available in the supplementary files or from the corresponding author upon request.

Consent

Not applicable. This manuscript does not contain data from any individual person.

Conflicts of Interest

The authors have declared that no conflict of interest exists.

Authors' Contributions

PS and JQ conceived and designed the research; SW collected the data used in our study; MY analyzed the data; MY and SW draw the figures; PS wrote the manuscript; JQ approved the final version of the manuscript.

Supplementary Materials

Supplementary 1. Table S1: list of predicted target genes.

Supplementary 2. Table S2: GO functions for target genes of the three upregulated miRNAs.

Supplementary 3. Table S3: GO functions for target genes of the three downregulated miRNAs.

Supplementary 4. Table S4: KEGG pathway enrichment analysis for selected DEMs.

References

- [1] R. Bataller and D. A. Brenner, "Liver fibrosis," *Journal of Clinical Investigation*, vol. 115, no. 4, pp. 1100–1100, 2005.
- [2] J. Li, M. Ghazwani, Y. Zhang et al., "miR-122 regulates collagen production via targeting hepatic stellate cells and suppressing P4HA1 expression," *Journal of Hepatology*, vol. 58, no. 3, pp. 522–528, 2013.

- [3] E. L. Ellis and D. A. Mann, "Clinical evidence for the regression of liver fibrosis," *Journal of Hepatology*, vol. 56, no. 5, pp. 1171–1180, 2012.
- [4] K. Zhao, A. Liu, and Y. Xia, "Insights into hepatitis B virus DNA integration-55 years after virus discovery," *The Innovation*, vol. 1, no. 2, article 100034, 2020.
- [5] X. Cheng and M. G. Ghany, "Key milestones in HCV discovery and therapeutics," *The Innovation*, vol. 1, no. 3, article 100067, 2020.
- [6] K. B. Reddy, "MicroRNA (miRNA) in cancer," *Cancer Cell International*, vol. 15, no. 1, p. 38, 2015.
- [7] W. Chen and C. Qin, "General hallmarks of microRNAs in brain evolution and development," *RNA Biology*, vol. 12, no. 7, pp. 701–708, 2015.
- [8] A. Shenoy and R. H. Blelloch, "Regulation of microRNA function in somatic stem cell proliferation and differentiation," *Nature Reviews Molecular Cell Biology*, vol. 15, no. 9, pp. 565–576, 2014.
- [9] C. C. Xiao, L. Srinivasan, D. P. Calado et al., "Lymphoproliferative disease and autoimmunity in mice with increased miR-17-92 expression in lymphocytes," *Nature Immunology*, vol. 9, no. 4, pp. 405–414, 2008.
- [10] J. Hyun, J. Park, S. Wang et al., "MicroRNA expression profiling in CCl4-induced liver fibrosis of *Mus musculus*," *International Journal of Molecular Sciences*, vol. 17, no. 6, p. 961, 2016.
- [11] M. Kitano and P. M. Bloomston, "Hepatic stellate cells and microRNAs in pathogenesis of liver fibrosis," *Journal of Clinical Medicine*, vol. 5, no. 3, p. 38, 2016.
- [12] J. Dymacek, B. N. Snyder-Talkington, D. W. Porter et al., "mRNA and miRNA regulatory networks reflective of multi-walled carbon nanotube-induced lung inflammatory and fibrotic pathologies in mice," *Toxicological Sciences*, vol. 144, no. 1, pp. 51–64, 2015.
- [13] J. G. Wang, S. Song, C. Xie et al., "MicroRNA profiling in the left atrium in patients with non-valvular paroxysmal atrial fibrillation," *BMC Cardiovascular Disorders*, vol. 15, no. 1, 2015.
- [14] V. Ramesh and K. Ganesan, "Integrative analysis of transcriptome and miRNome unveils the key regulatory connections involved in different stages of hepatocellular carcinoma," *Genes to Cells*, vol. 21, no. 9, pp. 949–965, 2016.
- [15] S. R. Yoon and G. de Micheli, "Prediction of regulatory modules comprising microRNAs and target genes," *Bioinformatics*, vol. 21, Supplement 2, pp. ii93–i100, 2005.
- [16] J. Ihmels, G. Friedlander, S. Bergmann, O. Sarig, Y. Ziv, and N. Barkai, "Revealing modular organization in the yeast transcriptional network," *Nature Genetics*, vol. 31, no. 4, pp. 370–377, 2002.
- [17] A. Abdel-al, E. el-Ahwany, M. Zoheiry et al., "miRNA-221 and miRNA-222 are promising biomarkers for progression of liver fibrosis in HCV Egyptian patients," *Virus Research*, vol. 253, pp. 135–139, 2018.
- [18] T. Lan, C. Li, G. Yang et al., "Sphingosine kinase 1 promotes liver fibrosis by preventing miR-19b-3p-mediated inhibition of CCR2," *Hepatology*, vol. 68, no. 3, pp. 1070–1086, 2018.
- [19] Y. Qu, Q. Zhang, X. Cai et al., "Exosomes derived from miR-181-5p-modified adipose-derived mesenchymal stem cells prevent liver fibrosis via autophagy activation," *Journal of Cellular and Molecular Medicine*, vol. 21, no. 10, pp. 2491–2502, 2017.
- [20] P. Gupta, T. N. Sata, A. K. Yadav et al., "TGF- β induces liver fibrosis via miRNA-181a-mediated down regulation of augmentor of liver regeneration in hepatic stellate cells," *PLoS One*, vol. 14, no. 6, article e0214534, 2019.
- [21] D. Fernández-Ramos, P. Fernández-Tussy, F. Lopitz-Otsoa et al., "miR-873-5p acts as an epigenetic regulator in early stages of liver fibrosis and cirrhosis," *Cell Death & Disease*, vol. 9, no. 10, p. 958, 2018.
- [22] X. Feili, S. Wu, W. Ye, J. Tu, and L. Lou, "MicroRNA-34a-5p inhibits liver fibrosis by regulating TGF- β 1/Smad3 pathway in hepatic stellate cells," *Cell Biology International*, vol. 42, no. 10, pp. 1370–1376, 2018.
- [23] S. Davis and P. S. Meltzer, "GEOquery: a bridge between the gene expression omnibus (GEO) and BioConductor," *Bioinformatics*, vol. 23, no. 14, pp. 1846–1847, 2007.
- [24] G. Diaz, M. Melis, A. Tice et al., "Identification of microRNAs specifically expressed in hepatitis C virus-associated hepatocellular carcinoma," *International Journal of Cancer*, vol. 133, no. 4, pp. 816–824, 2013.
- [25] C. H. Chou, C. D. Yang, N. W. Chang et al., "miRTarBase update 2018: a resource for experimentally validated microRNA-target interactions," *Nucleic Acids Research*, vol. 46, no. D1, pp. D296–D302, 2018.
- [26] D. W. Huang, B. T. Sherman, and R. A. Lempicki, "Bioinformatics enrichment tools: paths toward the comprehensive functional analysis of large gene lists," *Nucleic Acids Research*, vol. 37, no. 1, pp. 1–13, 2009.
- [27] D. W. Huang, B. T. Sherman, and R. A. Lempicki, "Systematic and integrative analysis of large gene lists using DAVID bioinformatics resources," *Nature Protocols*, vol. 4, no. 1, pp. 44–57, 2009.
- [28] D. Szklarczyk, A. Franceschini, M. Kuhn et al., "The STRING database in 2011: functional interaction networks of proteins, globally integrated and scored," *Nucleic Acids Research*, vol. 39, pp. D561–D568, 2011.
- [29] H. Y. Huang, J. Li, Y. C. Lin et al., "miRTarBase 2020: Updates to the experimentally validated microRNA-target interaction database," *Nucleic acids research*, vol. 48, no. D1, pp. D148–D154, 2020.
- [30] X. Fu, J. Qie, Q. Fu, J. Chen, Y. Jin, and Z. Ding, "miR-20a-5p/TGFBR2 axis affects pro-inflammatory macrophages and aggravates liver fibrosis," *Frontiers in Oncology*, vol. 10, 2020.
- [31] S. P. Li, H. X. Xu, Y. Yu et al., "LncRNA HULC enhances epithelial-mesenchymal transition to promote tumorigenesis and metastasis of hepatocellular carcinoma via the miR-200a-3p/ZEB1 signaling pathway," *Oncotarget*, vol. 7, no. 27, pp. 42431–42446, 2016.
- [32] Y. H. Gong, J. Mao, D. Wu et al., "Circ-ZEB1.33 promotes the proliferation of human HCC by sponging miR-200a-3p and upregulating CDK6," *Cancer Cell International*, vol. 18, no. 1, p. 18, 2018.
- [33] F. M. de Carvalho, P. L. Gonçalves, R. D. Jarske, F. E. L. Pereira, I. D. Louro, and T. de Almeida Pereira, "Hepatocellular carcinoma and liver cirrhosis TP53 mutation analysis reflects a moderate dietary exposure to aflatoxins in Espírito Santo State, Brazil," *Molecular Biology Reports*, vol. 40, no. 8, pp. 4883–4887, 2013.
- [34] X. F. Tian, F. J. Ji, H. L. Zang, and H. Cao, "Activation of the miR-34a/SIRT1/p53 signaling pathway contributes to the progress of liver fibrosis via inducing apoptosis in hepatocytes but not in HSCs," *PLoS One*, vol. 11, no. 7, article e0158657, 2016.

- [35] L. A. Scheving, X. Zhang, D. W. Threadgill, and W. E. Russell, "Hepatocyte ERBB3 and EGFR are required for maximal CCl₄-induced liver fibrosis," *American Journal of Physiology-Gastrointestinal and Liver Physiology*, vol. 311, no. 5, pp. G807–G816, 2016.
- [36] D. D. Liang, H. Chen, L. Zhao et al., "Inhibition of EGFR attenuates fibrosis and stellate cell activation in diet- induced model of nonalcoholic fatty liver disease," *Biochimica et Biophysica Acta-Molecular Basis of Disease*, vol. 1864, no. 1, pp. 133–142, 2018.
- [37] Y. Cheng, Y. Tian, J. Xia et al., "The role of PTEN in regulation of hepatic macrophages activation and function in progression and reversal of liver fibrosis," *Toxicology and Applied Pharmacology*, vol. 317, pp. 51–62, 2017.
- [38] J. Han, Y. He, H. Zhao, and X. Xu, "Hypoxia inducible factor-1 promotes liver fibrosis in nonalcoholic fatty liver disease by activating PTEN/p65 signaling pathway," *Journal of Cellular Biochemistry*, vol. 120, no. 9, pp. 14735–14744, 2019.

Research Article

Upregulation Mitochondrial Carrier 1 (MTCH1) Is Associated with Cell Proliferation, Invasion, and Migration of Liver Hepatocellular Carcinoma

Guolin Chen ¹, Shanshan Mo,² and Di Yuan³

¹Department of Infectious Diseases, The First Affiliated Hospital of Harbin Medical University, Harbin, China

²Pharmacy Department of Heilongjiang Sailors General Hospital, Harbin, China

³Clinical Laboratory, The First Affiliated Hospital of Harbin Medical University, Harbin, China

Correspondence should be addressed to Guolin Chen; chengzi548723914@163.com

Received 27 March 2021; Accepted 25 May 2021; Published 7 June 2021

Academic Editor: Tao Huang

Copyright © 2021 Guolin Chen et al. This is an open access article distributed under the Creative Commons Attribution License, which permits unrestricted use, distribution, and reproduction in any medium, provided the original work is properly cited.

Among the primary causes of cancer-associated death in the world, liver hepatocellular carcinoma (LIHC) ranks the third. LIHC is defined as the sixth most frequently diagnosed carcinoma. The gene mitochondrial carrier 1 (MTCH1) is a protein-coding gene. Recent research suggests that MTCH1 may be associated with some diseases. Here, our study attempts to explore the role and implication of MTCH1 in LIHC. Kaplan Meier Plotter and GEPIA (Gene Expression Profiling Interactive Analysis) databases were employed to determine the expression of MTCH1 and its correlation with prognostic status in LIHC patients. For the first time, our results suggested that MTCH1 was aberrantly expressed in human pan-cancer and highly expressed in LIHC. Its high expression was closely associated with metastasis of tumor, stage of cancer, and poor survival of patients. Then, through enrichment analysis, MTCH1 was found to be closely related to RNA splicing in LIHC. Subsequently, we conducted a series of functional experiments. PCR data showed that LIHC cell lines and samples are highly expressed MTCH1. CCK-8 (Cell Counting Kit-8) assays and Transwell assays indicated that silencing MTCH1 certainly suppressed cell proliferation, migration, and invasion. These findings shed the clue that MTCH1 could be regarded as the potential prognosis biomarker of LIHC and a promising therapeutic target for LIHC.

1. Background

As the International Agency for Research on Cancer reported, liver hepatocellular carcinoma (LIHC) is the third primary inducer amid cancer-associated death worldwide [1]. Meanwhile, LIHC is considered the sixth most diagnosed carcinoma [2, 3]. In the last few years, over 700,000 people are dying of LIHC annually, and the number is still growing every year. In the present, chemotherapy, surgical resection, and liver transplantation are effective methods for the early stage of LIHC [4]. Nevertheless, treatment strategies are limited to advanced-stage cases [5]. Compared to early primary LIHC, distant metastasis in the advanced stage is the pivotal inducer of tumor death, because LIHC is a highly aggressive and complex neoplasm disease [6–8]. No specific treatment

strategy that focuses on LIHC has been developed. Thus, uncovering the hidden mechanisms in the pathogenesis of LIHC would be conducive to offering a new strategy or predictive prognostic indicator for LIHC.

The mitochondrial carrier 1 (MTCH1) is a protein-coding gene and originally described as the interactor of presenilin 1 [9]. It is also named as presenilin 1-associated protein (PSAP). MTCH1 has two widely expressed transcripts from alternative splicing. Both of them are complete mitochondrial outer membrane proteins and contain two proapoptotic domains [10]. In the absence of proapoptotic proteins, the two transcripts can induce apoptosis when overexpressed in cells [11]. Recent research suggests that MTCH1 may be associated with some diseases. For instance, Vural et al. reported that the MTCH1 expression level was

associated with clinical and apoptotic parameters of neuro-Behcet's disease (NBD) [12]. Therefore, further characterization of the functional role of MTCH1 is needed.

Here, we studied the MTCH1 expression level in LIHC and its clinical implication. Also, to explore the role of MTCH1 in LIHC, we measured LIHC cell proliferation, invasion, and migration after ablating MTCH1. We first revealed the role of MTCH1 in LIHC and supplied new ideas for the treatment of LIHC.

2. Material and Methods

2.1. TNMplot Database. The database is available at <http://www.tnmplot.com>, including 56,938 samples from The Cancer Genome Atlas (TCGA, 394 metastatic, 9,886 tumorous, and 730 normal), gene chip-based studies (453 metastatic, 29,376 tumorous, and 3,691 normal samples), TARGET (1 metastatic, 1,180 tumorous, and 12 normal), and the Genotype-Tissue Expression (GTEx, 11,215 normal samples). In our research, we applied this database to determine the expression of MTCH1 in pan-cancer and make a comparison with MTCH1 expression profiles in normal and neoplasm tissues.

2.2. GEPIA Database. Gene Expression Profiling Interactive Analysis (GEPIA, <http://gepia.cancer-pku.cn/index.html>), functioning as an interactive web server, was applied for the analysis of RNA sequencing data from the TCGA and the GTEx projects utilizing standard processing pipeline. GEPIA offered several function analyses, containing the differential expression of neoplasm/normal samples, survival analysis of patients, profiling classified by carcinoma types or pathological stages, similar gene detection, correlation analysis, and others [13, 14]. Here, we conducted GEPIA to determine the relationship between MTCH1 expression and pathological stages and survival. Besides, we wanted to dig out MTCH1 coexpression genes.

2.3. The Kaplan Meier Plotter Database. The database is available at employed to evaluate 54k gene-exerted impacts on survival in 21 types of carcinomas, comprising lung (n = 3,452), breast (n = 6,234), gastric (n = 1,440), and ovarian (n = 2,190) carcinomas [15]. The main purpose of this database is to discover and verify survival biomarkers based on a meta-analysis. The sources of the database consisted of TCGA, European Genome-phenome Archive (EGA), and Gene Expression Omnibus (GEO).

2.4. Enrichment Analysis. Gene Ontology (GO) enrichment analysis was used for gene annotation and biological processes (BP) analysis. Gene information in the network was analyzed by the Kyoto Encyclopedia of Genes and Genomes (KEGG) database [16–18]. For DEGs' functions and signal pathway analysis, we employed the databases for Annotation, Visualization, and Integrated Discovery (DAVID; <http://david.ncifcrf.gov>). $P < 0.05$ with gene counts of >5 indicated a significant statistical difference.

2.5. Clinical Samples. 6 LIHC patients diagnosed by pathological and histological detection from our hospital were sub-

jected to our study. All patients did not receive chemotherapy or radiotherapy before surgery. Our experiments were officially approved by the Ethics Committee of our hospital. All patients acknowledged and signed informed consents.

Additionally, the expression detail of LIHC patients was from the TCGA database (<http://cancergenome.nih.gov>). 419 samples were chosen in total, containing 369 LIHC samples and 50 normal samples.

2.6. Cell Culture. Human LIHC cell lines (Hep3B, Huh-7, BEL-7402, and MHCC-97H) and normal liver cell HL7702 were acquired from the cell bank of the Chinese Academy of Sciences (Shanghai, China) and maintained in RPMI 1640 (Gibco, USA) medium supplied by 10% fetal bovine serum (FBS, Gibco, USA) and 1% streptomycin/penicillin (Sigma-Aldrich) under 37°C humidified chamber containing 5% CO₂ [19].

2.7. Cell Transfection. For transfection, siRNA of MTCH1 (si-MTCH1) was synthesized by Genepharma (Shanghai, China). Before transfection, cells were plated in 24-well plates. The next day, cells were transfected with siRNAs utilizing Lipofectamine 2000 (Invitrogen, USA) as manually instructed. Cells were reseeded and used for other studies after 48 hours of transfection. The siRNA sequences were as follows: si-MTCH1, 5'-CATCGTGCAAGTGGATGGTAAGATA-3'; si-NC, 5'-UUCUCCGAA CGUGUCACGUTT-3'.

2.8. RNA Extraction and Quantification. The whole RNA from LIHC cells and tissues was harvested with TRIzol reagent (Invitrogen, USA) and then reversely transcribed into cDNA using RevertAid First Strand complementary DNA Synthesis Kit (Fermentas, China). qRT-PCR reaction aiming at analyzing the relative RNA expression was performed on the Rotor-Gene 3000 system (Corbett Research, Australia) with IQ SYBR Green Supermix PCR kit (Bio-Rad, USA). All experiments were carried out in triplicate. The RNA primers were as follows: MTCH1, 5'-ATCCCC TGCTCTACGTGAAG-3' (forward), 5'-GTGAAGAAGCT CGGCAGATAG-3' (reverse); GAPDH, 5'-CTGGGCTAC ACTGAGCACC-3' (forward), 5'-AAGTGGTCGTTGAG GGCAATG-3' (reverse).

2.9. Cell Proliferation. The cell proliferation ability of BEL-7402 and MHCC-97H was measured by the CCK-8 kit (Beyotime Inst. Biotech, China). Taken briefly, 1×10^3 of si-MTCH1 or control-transfected cells in each well were plated in a 96-well plate. At different time incubations (0, 24, 48, 72, and 96 h), cell proliferation viability was measured by CCK8-kit. The wavelength at 450 nm was measured by a microplate reader (Bio-Rad).

2.10. Transwell Assay. 24-well plate of Transwell chamber (Costar, USA) was taken for Transwell assay. Taken briefly, 1×10^5 cells/well maintained in medium without serum were plated in the upper chambers precoated with fresh Matrigel (Corning, USA). 600 μ l of medium with 20% FBS was added into the lower chambers. A cotton swab was used to remove

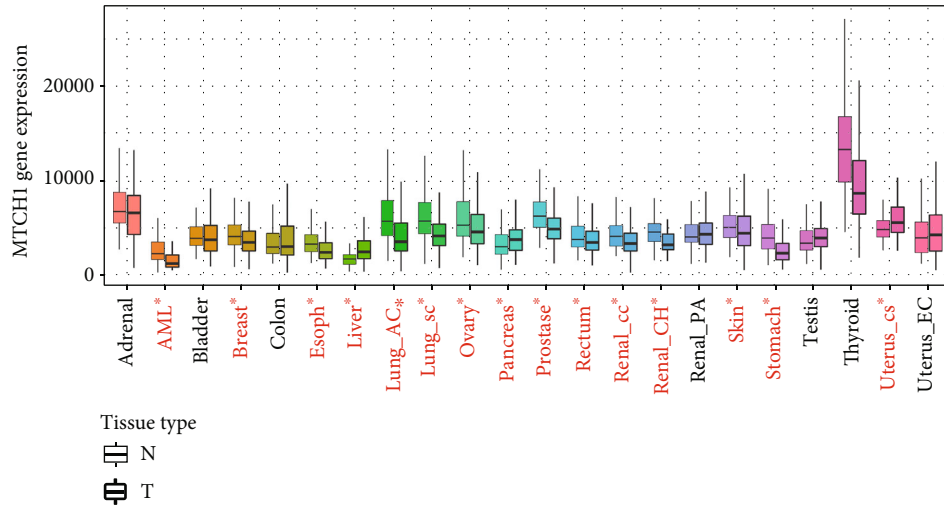


FIGURE 1: To analyze MTCH1 mRNA level in human pan-cancer by online tool TNMplot. N indicates normal tissues, and T represents tumor tissues. Significant differences by the Mann–Whitney U test between normal and tumor tissues were marked with red. * $P < 0.05$.

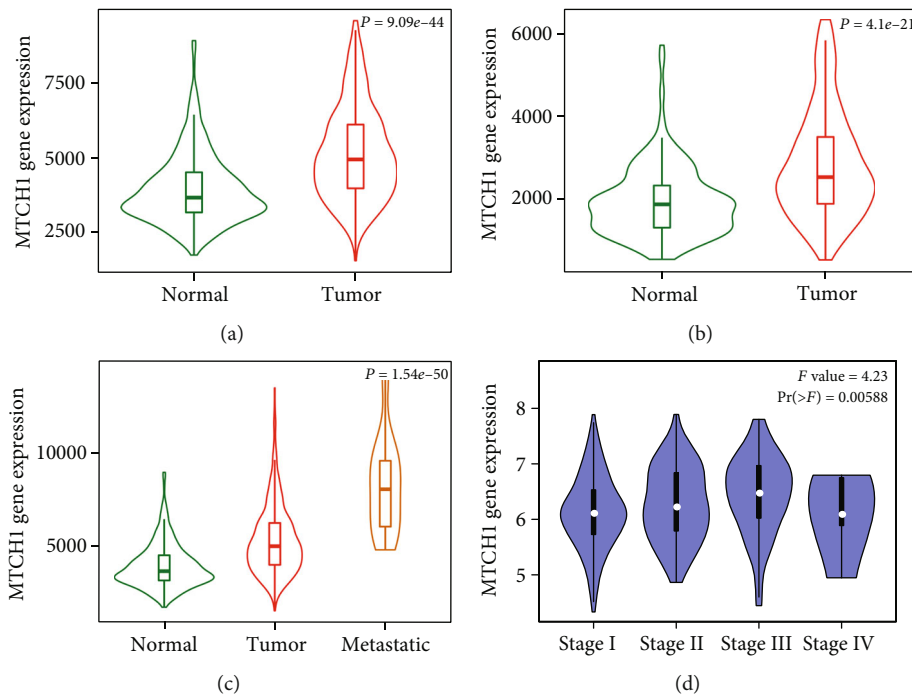


FIGURE 2: Diagnostic value of MTCH1 in liver cancer. (a) Violin plots of the expression of MTCH1 in liver normal and tumor tissues based on gene chip data of TNMplot. (b) Violin plots of the expression of MTCH1 in liver normal and tumor tissues based on RNA microarray data of TNMplot. (c) Violin plots of the expression of MTCH1 in liver normal, tumor, and metastatic tissues based on gene chip data of TNMplot. (d) Box plots of MTCH1 gene expression in different liver cancer stages based on the GEPIA database.

noninvaded cells. The invaded cells were washed twice by PBS and then fixed by methanol for 10 min. And then they are stained with DAPI for 10 minutes. The cells at random 5 fields were photographed under a microscope. Similar experimental procedures were performed in migration assays. The only difference was that for the migration assay, chambers needed not to precoat with Matrigel.

2.11. *Statistical Analysis.* SPSS 22.0 (Chicago, USA) and GraphPad Prism 5.0 (San Diego, USA) software were employed to analyze the data. All derived data were shown as the mean \pm SD of three separate experiments in triplicate. The difference between two compared groups or among more groups was separately analyzed by Student's t -test and ANOVA [20, 21]. The differences existing in survival-

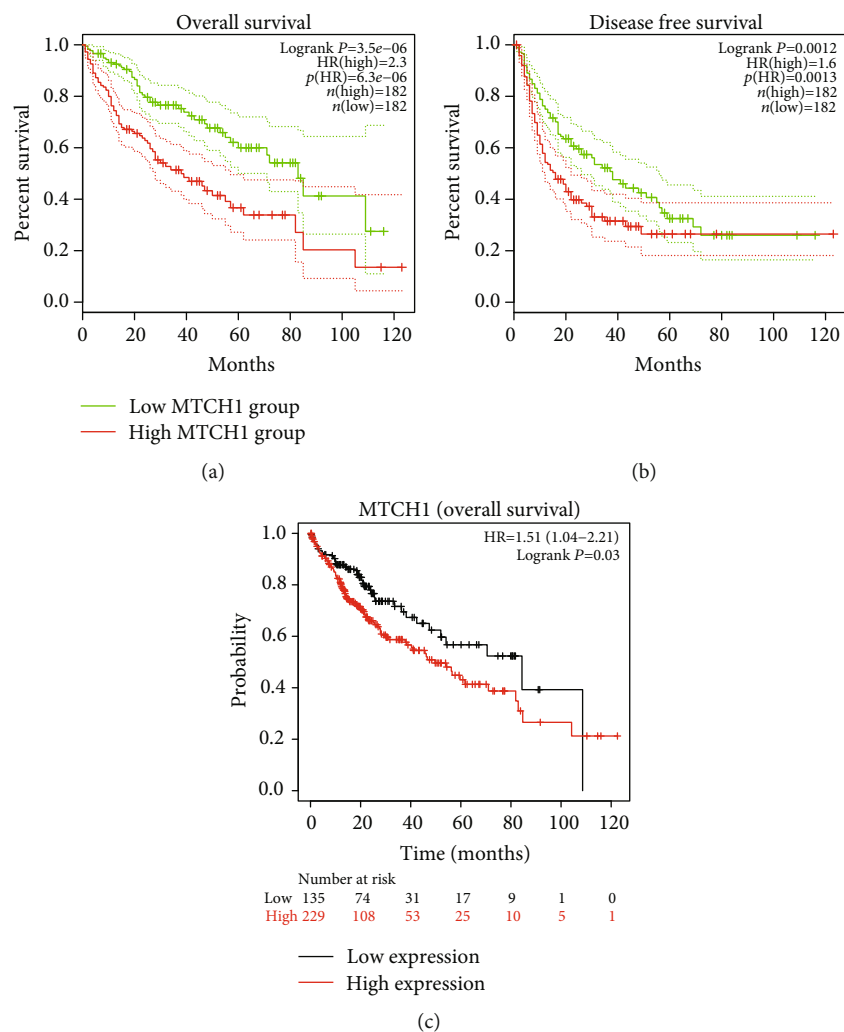


FIGURE 3: Analysis of the association between the prognostic value and MTCH1 expression in liver carcinoma. (a) GEPIA database analysis of OS curve of LIHC patients with highly expressed or lowly expressed MTCH1. (b) GEPIA database analysis of DFS curves of LIHC patients with highly expressed or lowly expressed MTCH1. (c) Kaplan Meier Plotter database analysis of OS curves of LIHC patients with highly expressed or lowly expressed MTCH1.

associated curves were assessed by the log-rank test. $P < 0.05$ represented a significant statistical difference [22–24].

3. Results

3.1. Abnormal Expression of MTCH1 Was Shown in Human Pan-Cancer. There were few types of carcinomas used for the study of MTCH1 expression. Here, we employed the Kaplan Meier Plotter online tool to investigate the MTCH1 expression profile in human pan-cancer. The data revealed that MTCH1 expression was largely heightened in three types of carcinomas, containing liver carcinoma, pancreas carcinoma, and uterine carcinoma, but decreased in 13 types of carcinomas tissues, such as Acute Myeloid Leukemia (AML) and breast carcinoma (Figure 1). Our results suggested that MTCH1 expression was abnormal in human pan-cancer.

3.2. Diagnostic Value of MTCH1 in Liver Cancer. To analyze MTCH1 expression profiles in normal and tumor tissues, we

conducted the TNMplot online tool. Gene chip and RNA-seq data displayed that, compared to normal tissues, MTCH1 expression was increased in liver carcinoma tissues (Figures 2(a) and 2(b)) ($P < 0.001$). Next, we in-depth validated MTCH1 expression in metastatic tissues, and our data indicated MTCH1 expression was greatly higher in metastatic tumor tissues and normal tissues (Figure 2(c)). Tumor metastasis often means advanced tumor stage and tumor deterioration, so we analyzed the association between the expression of MTCH1 and tumor stage by the GEPIA database. As presented in Figure 2(d), the MTCH1 expression was significantly different among different cancer stages with the highest expression in stage III. Our result implied that MTCH1 was a probably useful biomarker for the diagnosis of liver carcinoma.

3.3. Highly Expressed MTCH1 in LIHC Exhibited an Association with Poorly Prognostic Status. To explore

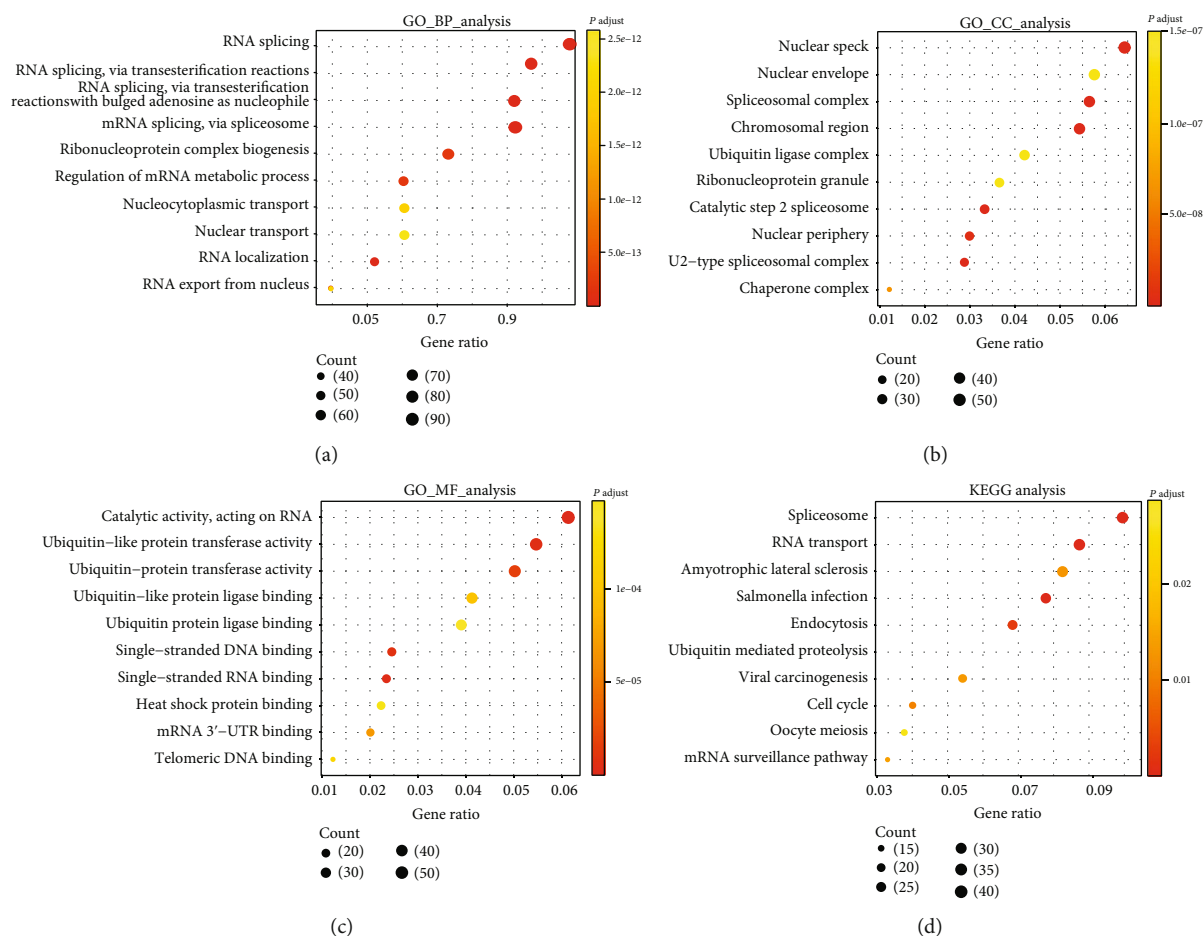


FIGURE 4: Enrichment analysis of MTCH1 coexpression genes, with the GO biological process (a), cell component (b), molecular function (c), and KEGG pathway (d). GO: Gene Ontology; BP: biological process; CC: cellular component; MF: molecular function; KEGG: Kyoto Encyclopedia of Genes and Genomes.

MTCH1 expression-exerted influence on the prognosis of LIHC patients, we conducted survival analysis for LIHC patients using the GEPIA database. It could be seen clearly from Figures 3(a) and 3(b) that, compared to LIHC patients with low expression of MTCH1, LIHC patients with high expression of MTCH1 exhibited lower overall survival (OS) rate and disease-free survival (DFS) rate. Besides, Kaplan Meier Plotter analysis showed that patients with highly expressed MTCH1 demonstrated short survival time (Figure 3(c)). These data indicated that high expression of MTCH1 presented an association with poor survival in patients with LIHC.

3.4. Enrichment Analysis of MTCH1 Coexpression Genes. For identifying the most likely involved biological pathways of MTCH1, we submitted coexpressed genes with MTCH1 into DAVID for GO and KEGG pathway enrichment analysis. Figure 4(a) presents biological process terms by GO analysis. MTCH1 coexpression genes were mainly enriched in RNA splicing (via transesterification reactions), RNA splicing (via transesterification reactions with bulged adenosine as a nucleophile), mRNA splicing (via spliceosome), RNA splicing, RNA localization, and so on. In cell component terms

(Figure 4(b)), those genes were mainly enriched in spliceosomal complex, catalytic step 2 spliceosome, nuclear speck, U2-type spliceosomal complex, chromosomal region, nuclear periphery, chaperone complex, nuclear envelope, ubiquitin ligase complex, and ribonucleoprotein granule. Figure 4(c) suggests that molecular function terms primarily participated in catalytic activity (acting on RNA), single-stranded RNA/DNA binding, ubiquitin-like protein transferase activity, mRNA 3'-UTR binding, and so on. Additionally, KEGG pathway analysis (Figure 4(d)) revealed that MTCH1 coexpression genes were significantly enriched in spliceosome, RNA transport, amyotrophic lateral sclerosis, Salmonella infection, endocytosis, ubiquitin-mediated proteolysis, viral carcinogenesis, cell cycle, oocyte meiosis, and mRNA surveillance pathway. MTCH1 coexpression genes in LIHC were mostly involved in the processes and pathways related to RNA.

3.5. Increased Expression of MTCH1 Was Shown in the Tissues and Cell Lines of LIHC. We employed TCGA database to analyze MTCH1 expression. Among 369 LIHC tumor samples and 50 normal samples, it was found that compared to normal samples, tumor samples were highly expressed

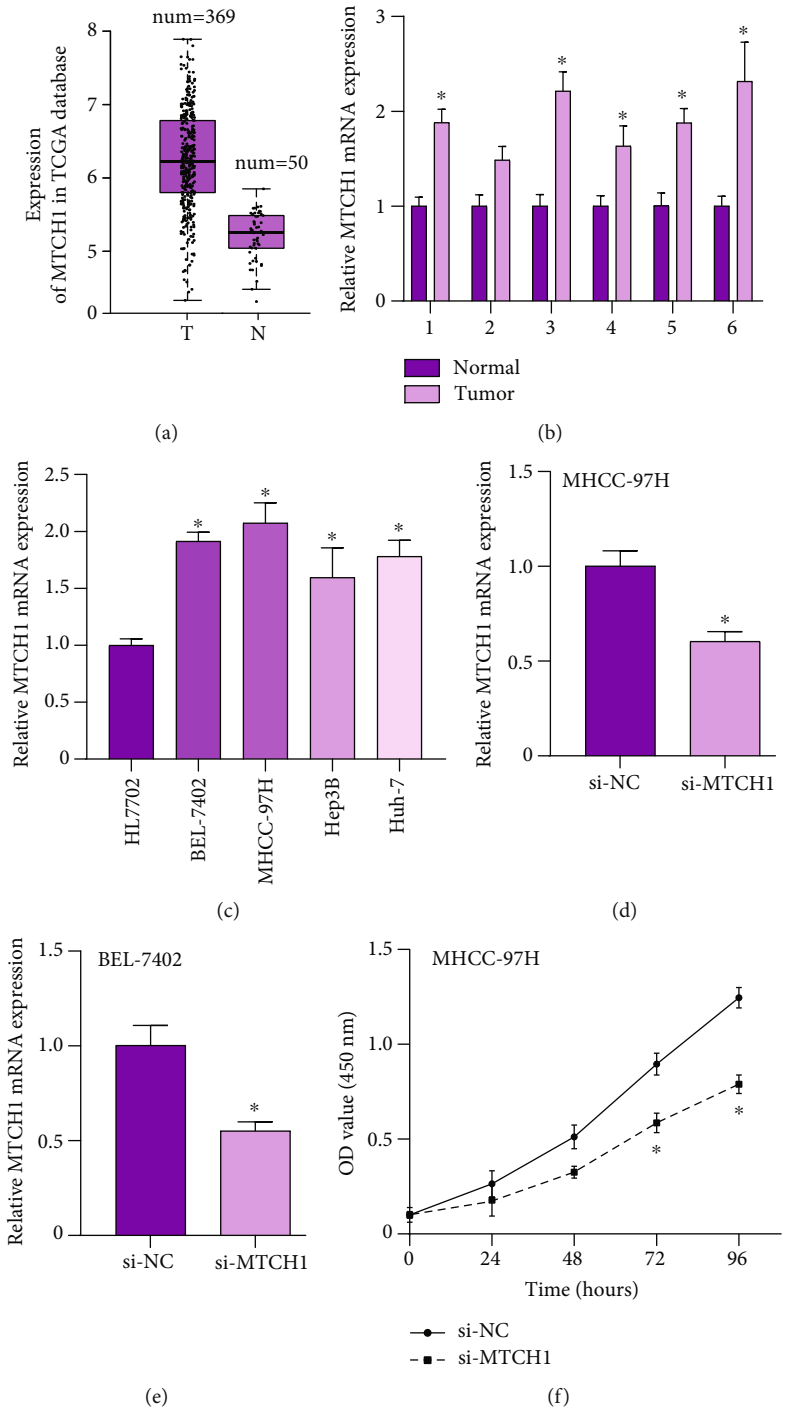


FIGURE 5: Continued.

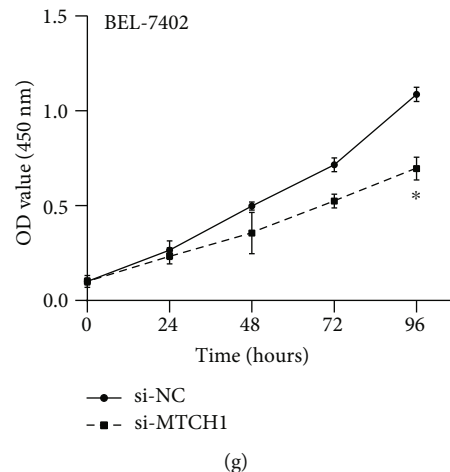


FIGURE 5: MTCH1 expression was raised in the tissues and cell lines of LIHC. (a) Analysis of MTCH1 expressions in LIHC tumor and normal samples in TCGA database. (b) To analyze MTCH1 expressions in 6 pairs LIHC tumor and normal liver samples. (c) Assessment of MTCH1 expressions in LIHC cell lines and normal liver cell lines. (d, e) Detection of MTCH1 mRNA expression in BEL-7402 and MHCC-97H cell lines transfected with si-MTCH1. (f, g) Si-MTCH1 suppressed cell proliferation in BEL-7402 and MHCC-97H. * $P < 0.05$.

MTCH1 (Figure 5(a)). To further validate that result, we additionally screened 6 pairs of LIHC samples and normal samples by PCR (quantitative reverse transcription) assays. The experimental data were the same as the findings in TCGA (Figure 5(b)). Besides, we also detected MTCH1 expression in LIHC cell lines. According to Figure 5(c), MTCH1 was upregulated in carcinoma cell lines, particularly in BEL-7402 and MHCC-97H. Our findings showed that MTCH1 probably played an important part in the progression of LIHC.

3.6. Knockdown of MTCH1 Suppressed the Capability of Cell Proliferation In Vitro. siRNAs were transfected into BEL-7402 and MHCC-97H cells to explore the impacts of reduction of MTCH1 on cell proliferation. The expression of MTCH1 mRNA was greatly reduced (Figures 5(d) and 5(e)). Subsequently, the data of CCK-8 assay detection showed that ablating MTCH1 could significantly reduce cell proliferation capability (Figures 5(f) and 5(g)).

3.7. Knockdown of MTCH1 Inhibited LIHC Cell Invasive and Migration Abilities. We evaluated the influence of reduced MTCH1 on cell invasion and migration by Transwell assay. Based on the results in cell lines, MHCC-97H was chosen for Transwell assays. As Figures 6(a) and 6(b) demonstrate, si-MTCH1 could significantly weaken cell migration and invasion rates. Taken together, MTCH1 might be involved in the development of LIHC and displayed as an oncogene.

4. Discussion

Many biomarkers have been studied in cancers [25]. Apoptosis is a way of programmed cell death [26], which is required for multicellular organism's development and internal environment stability. Apoptosis exhibits importance in the pathogenesis of several diseases [27]. However, the extent of apoptosis varies from one to another. For instance, excessive

apoptosis is shown in degenerative diseases [28], while a small amount of apoptosis is in carcinoma. Actually, apoptosis is intricate and participated in various pathways. Exogenous and endogenous connections are well-studied amid apoptotic pathways [29]. The first is the response of death receptors on the plasma membrane-mediated response to external signals. The second is the transition of cells to the final executor of mitochondria. MTCH1 and MTCH2 displayed importance in the process of mitochondrial apoptosis [30]. They are named mitochondrial carrier homologs because their sequence is similar to inner membrane carriers. MTCH1 possesses two isoforms produced by alternative splicing, both of which contain two proapoptotic domains and are complete mitochondrial outer membrane proteins. Previous reports have shown that MTCH1 is vital in apoptosis, suggesting that it displays importance in carcinoma [12]. Nevertheless, it is still elusive towards the part of MTCH1 in human carcinomas. Our study for the first time explores the MTCH1 expression profile in twenty-two types of carcinomas by TNMplot databases. Bioinformatics analysis and functional verification imply that MTCH1 acts as an oncogene in LIHC.

Till now, there are few studies to validate MTCH1 expression and implication in some types of carcinomas. However, in our literature, we analyzed MTCH1 expression and explored the corresponding implication in LIHC. After the analysis of MTCH1 expression in the TNMplot database and clinical samples, we found LIHC tissues and cells are highly expressed MTCH1. Additionally, our data indicated that higher expression of MTCH1 exhibited an association with metastasis of neoplasm, stage of carcinoma, and poor survival of LIHC patients. Our data implied that MTCH1 expression was a probable indicator of LIHC patients' prognosis. Subsequently, we carried out GO and KEGG enrichment analysis to explore the function and the mechanism of MTCH1 involved in LIHC. The results suggested that MTCH1 possibly participates in the regulated process of RNA splicing in LIHC.

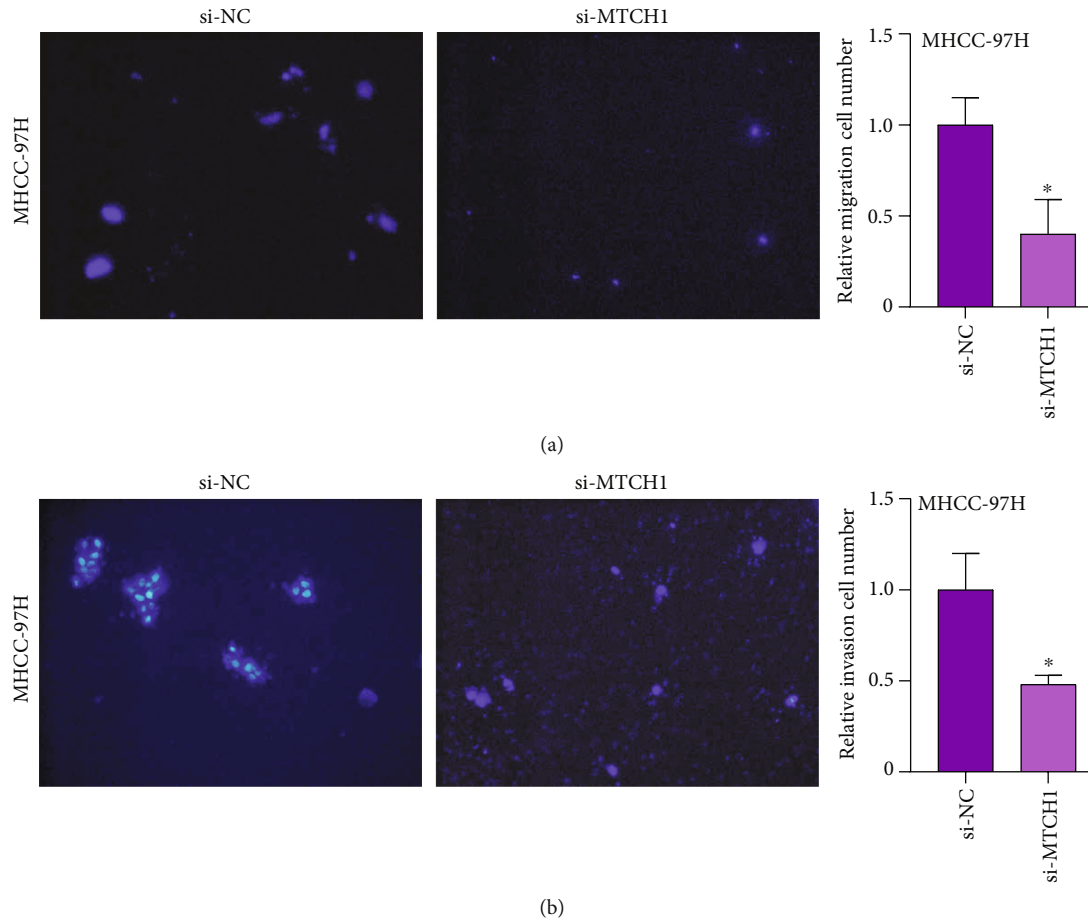


FIGURE 6: Knockdown of MTCH1 inhibited the invasive and migration abilities of LIHC cells. (a, b) Analysis of cell migration and invasion in siRNA-transfected MHCC-97H. * $P < 0.05$.

As we all know, RNA splicing is an extensive process that causes a transcriptional variation of structural and the diversity of proteomic [31]. Deregulated splicing occurs in carcinomas, resulting in various products with function and nonfunction. The events from cancer-specific splicing easily promote the development of disease [32]. Abnormal splicing exerts an effect on many carcinomas and brought about multiple features. Apoptosis and metastasis could be influenced by alternative splicing of numerous genes [33]. For instance, BCL2L1 (BCLXL), as a transcript variant of anti-apoptotic protein, is highly expressed in carcinoma and resistant to apoptosis [34]. Transcripts from abnormal TP53 splicing showed a relationship with apoptosis and proliferation. The above-mentioned studies suggest that abnormal splicing widely occurred in carcinomas, and MTCH1 might affect LIHC progression via RNA splicing.

Finally, we assessed the impacts of reduced MTCH1 on LIHC cell metabolism. The results demonstrated that reducing MTCH1 powerfully suppressed MHCC-97H and BEL-7402 cell proliferation, invasion, and migration. Our data collectively revealed that MTCH1 was displayed as an oncogene and functioned crucially in the oncogenesis and development of LIHC.

This study has some limitations. First, the number of clinical samples is not large enough. In future research, we

will collect more LIHC clinical samples to detect MTCH1 gene expression and MTCH1 protein expression. Second, we plan to analyze the function of MTCH1 in animal models in subsequent studies.

5. Conclusions

Based on multiple public databases, we analyzed the high expression of MTCH1 in LIHC, and its high expression is closely related to tumor metastasis, tumor staging, and poor patient quality of life. Highly expressed MTCH1 was found in LIHC samples and cell lines. The unsatisfying prognosis of LIHC patients was also found to be related to high MTCH1 expression. Besides, our findings suggested that MTCH1 facilitated LIHC cell proliferation, invasion, and migration. We have revealed for the first time that MTCH1 may play a role in the occurrence and development of LIHC. Collectively, our findings suggested that MTCH1 was a promising prognosis factor and therapeutic target for LIHC, providing new and useful information for the study of the mechanism of LIHC.

Data Availability

The expression detail of LIHC patients was from the TCGA database (<http://cancergenome.nih.gov>).

Conflicts of Interest

There is no conflict of interest.

Acknowledgments

This work is supported by the Foundation of the First Affiliated Hospital of Harbin Medical University (No. 2020M28).


References

- [1] C. Gu, X. Shi, C. Dai et al., "RNA m⁶A modification in cancers: molecular mechanisms and potential clinical applications," *The Innovation*, vol. 1, no. 3, p. 100066, 2020.
- [2] S. G. Zheng, H. X. Xu, and L. N. Liu, "Management of hepatocellular carcinoma: the role of contrast-enhanced ultrasound," *World Journal of Radiology*, vol. 6, no. 1, pp. 7–14, 2014.
- [3] Y. Li, J. Wang, F. Jiang, W. Lin, and W. Meng, "Association of polymorphisms in survivin gene with the risk of hepatocellular carcinoma in Chinese Han population: a case control study," *BMC Medical Genetics*, vol. 13, no. 1, p. 1, 2012.
- [4] J. P. Bronowicki, K. Boudjema, L. Chone et al., "Comparison of resection, liver transplantation and transcatheter oily chemoembolization in treatment of hepatocellular carcinoma," *Journal of Hepatology*, vol. 24, no. 3, pp. 293–300, 1996.
- [5] M. Kudo, R. Tateishi, T. Yamashita et al., "Current status of hepatocellular carcinoma treatment in Japan," *Clinical Drug Investigation*, vol. 32, Suppl 2, pp. 37–51, 2012.
- [6] S. Colagrande, A. L. Inghilesi, S. Aburas, G. G. Taliani, C. Nardi, and F. Marra, "Challenges of advanced hepatocellular carcinoma," *World Journal of Gastroenterology*, vol. 22, no. 34, pp. 7645–7659, 2016.
- [7] L. Yang, J. Xu, D. Ou, W. Wu, and Z. Zeng, "Hepatectomy for huge hepatocellular carcinoma: single institute's experience," *World Journal of Surgery*, vol. 37, no. 9, pp. 2189–2196, 2013.
- [8] R. S. Finn, "Development of molecularly targeted therapies in hepatocellular carcinoma: where do we go now?," *Clinical Cancer Research*, vol. 16, no. 2, pp. 390–397, 2010.
- [9] M. A. Nelo-Bazán, P. Latorre, A. Bolado-Carrancio et al., "Early growth response 1 (EGR-1) is a transcriptional regulator of mitochondrial carrier homolog 1 (MTCH 1)/presenilin 1-associated protein (PSAP)," *Gene*, vol. 578, no. 1, pp. 52–62, 2016.
- [10] A. Ferramosca and V. Zara, "Biogenesis of mitochondrial carrier proteins: molecular mechanisms of import into mitochondria," *Biochimica et Biophysica Acta*, vol. 1833, no. 3, pp. 494–502, 2013.
- [11] W. L. Liang, L. Xiao, H. W. Gu et al., "Solid lipid nanoparticle induced apoptosis of macrophages via a mitochondrial-dependent pathway in vitro and in vivo," *International Journal of Nanomedicine*, vol. Volume 14, pp. 3283–3295, 2019.
- [12] B. Vural, E. Şehitoğlu, F. Çavuş et al., "Mitochondrial carrier homolog 1 (Mtch1) antibodies in neuro-Behçet's disease," *Journal of Neuroimmunology*, vol. 263, no. 1–2, pp. 139–144, 2013.
- [13] C. Gu, J. Chen, X. Dang et al., "Hippo pathway core genes based prognostic signature and immune infiltration patterns in lung squamous cell carcinoma," *Frontiers in Oncology*, vol. 11, no. 1486, 2021.
- [14] C. Gu, X. Shi, W. Qiu et al., "Comprehensive analysis of the prognostic role and mutational characteristics of m6A-related genes in lung squamous cell carcinoma," *Frontiers in Cell and Development Biology*, vol. 9, p. 661792, 2021.
- [15] C. Gu, X. Shi, Z. Huang et al., "A comprehensive study of construction and analysis of competitive endogenous RNA networks in lung adenocarcinoma," *Biochimica et Biophysica Acta (BBA) - Proteins and Proteomics*, vol. 1868, no. 8, 2020.
- [16] L. Zhang, X. Shi, C. Gu et al., "Identification of cell-to-cell interactions by ligand-receptor pairs in human fetal heart," *Biochimica et Biophysica Acta - Molecular Basis of Disease*, vol. 1866, no. 12, 2020.
- [17] X. Shi, T. Huang, J. Wang et al., "Next-generation sequencing identifies novel genes with rare variants in total anomalous pulmonary venous connection," *eBioMedicine*, vol. 38, pp. 217–227, 2018.
- [18] C. Gu, X. Shi, X. Dang et al., "Identification of common genes and pathways in eight fibrosis diseases," *Frontiers in Genetics*, vol. 11, 2020.
- [19] C. Gu, Z. Huang, X. Chen et al., "TEAD4 promotes tumor development in patients with lung adenocarcinoma via ERK signaling pathway," *Biochimica et Biophysica Acta (BBA) - Molecular Basis of Disease*, vol. 1866, no. 12, 2020.
- [20] Y. Sun, C. Gu, J. Shi et al., "Reconstruction of mediastinal vessels for invasive thymoma: a retrospective analysis of 25 cases," *Journal of Thoracic Disease*, vol. 9, no. 3, pp. 725–733, 2017.
- [21] J. Chen, C. Gu, X. Chen et al., "Clinicopathological and prognostic analyses of 86 resected pulmonary lymphoepithelioma-like carcinomas," *Journal of Surgical Oncology*, vol. 123, no. 2, pp. 544–552, 2021.
- [22] C. Gu, R. Wang, X. Pan et al., "Comprehensive study of prognostic risk factors of patients underwent pneumonectomy," *Journal of Cancer*, vol. 8, no. 11, pp. 2097–2103, 2017.
- [23] C. Gu, X. Pan, R. Wang et al., "Analysis of mutational and clinicopathologic characteristics of lung adenocarcinoma with clear cell component," *Oncotarget*, vol. 7, no. 17, pp. 24596–24603, 2016.
- [24] C. Chen, X. Zhang, C. Gu et al., "Surgery performed at night by continuously working surgeons contributes to a higher incidence of intraoperative complications in video-assisted thoracoscopic pulmonary resection: a large monocentric retrospective study," *European Journal of Cardio-Thoracic Surgery*, vol. 57, no. 3, pp. 447–454, 2020.
- [25] C. Gu and C. Chen, "Methylation in lung cancer: a brief review," *Methods in Molecular Biology*, vol. 2204, pp. 91–97, 2020.
- [26] H. AnvariFar, A. K. Amirkolaie, H. K. Miandare, H. Ouraji, M. A. Jalali, and S. İ. Üçüncü, "Apoptosis in fish: environmental factors and programmed cell death," *Cell and Tissue Research*, vol. 368, no. 3, pp. 425–439, 2017.
- [27] E. Olszewska, S. Chodynicki, and L. Chyczewski, "Apoptosis in the pathogenesis of cholesteatoma in adults," *European Archives of Oto-Rhino-Laryngology*, vol. 263, no. 5, pp. 409–413, 2006.
- [28] J. Pannek, C. Kurmann, E. Imbach, F. Amsler, and S. Pannek-Rademacher, "In vitro effects of homeopathic drugs on cultured *Escherichia coli*," *Homeopathy*, vol. 107, no. 2, pp. 150–154, 2018.
- [29] T. S. Weiss, M. Lupke, S. Ibrahim et al., "Attenuated lipotoxicity and apoptosis is linked to exogenous and endogenous augmenters of liver regeneration by different pathways," *PLoS One*, vol. 12, no. 9, article e0184282, 2017.

- [30] A. J. Robinson, E. R. Kunji, and A. Gross, "Mitochondrial carrier homolog 2 (MTCH2): the recruitment and evolution of a mitochondrial carrier protein to a critical player in apoptosis," *Experimental Cell Research*, vol. 318, no. 11, pp. 1316–1323, 2012.
- [31] D. L. Black, "Mechanisms of alternative pre-messenger RNA splicing," *Annual Review of Biochemistry*, vol. 72, no. 1, pp. 291–336, 2003.
- [32] K.-V. Lehmann, A. Kahles, C. Kandoth et al., "Integrative genome-wide analysis of the determinants of RNA splicing in kidney renal clear cell carcinoma," in *Pacific Symposium on Biocomputing*, pp. 44–55, Fairmont Orchid, Hawaii, 2015.
- [33] D. Roy Burman, S. Das, C. Das, and R. Bhattacharya, "Alternative splicing modulates cancer aggressiveness: role in EMT/-metastasis and chemoresistance," *Molecular Biology Reports*, vol. 48, no. 1, pp. 897–914, 2021.
- [34] L. Sevilla, A. Zaldumbide, P. Pognonec, and K. E. Boulukos, "Transcriptional regulation of the bcl-x gene encoding the anti-apoptotic Bcl-xL protein by Ets, Rel/NFkappaB, STAT and API transcription factor families," *Histology and Histopathology*, vol. 16, no. 2, pp. 595–601, 2001.

Research Article

Marker Genes Change of Synovial Fibroblasts in Rheumatoid Arthritis Patients

Lifen Liao,¹ Ke Liang,² Lan Lan,¹ Jinheng Wang,¹ and Jun Guo³ 

¹Department of Laboratory, Affiliated Hospital of Guilin Medical University, Xiufeng District, Guilin, 541001 Guangxi, China

²Department of Laboratory, Nanxishan Hospital of Guangxi Zhuang Autonomous Region, Xiangshan District, Guilin, 541002 Guangxi, China

³Department of Hematology, Rizhao People's Hospital, Donggang District, Rizhao, 276800 Shandong, China

Correspondence should be addressed to Jun Guo; konganzhi810@163.com

Received 27 February 2021; Revised 14 May 2021; Accepted 24 May 2021; Published 7 June 2021

Academic Editor: Tao Huang

Copyright © 2021 Lifen Liao et al. This is an open access article distributed under the Creative Commons Attribution License, which permits unrestricted use, distribution, and reproduction in any medium, provided the original work is properly cited.

Background. Rheumatoid arthritis (RA) is a chronic condition that manifests as inflammation of synovial joints, leading to joint destruction and deformity. **Methods.** We identified single-cell RNA-seq data of synovial fibroblasts from RA and osteoarthritis (OA) patients in GSE109449 dataset. RA- and OA-specific cellular subpopulations were identified, and enrichment analysis was performed. Further, key genes for RA and OA were obtained by combined analysis with differentially expressed genes (DEGs) between RA and OA in GSE56409 dataset. The diagnostic role of key genes for RA was predicted using receiver operating characteristic (ROC) curve. Finally, we identified differences in immune cell infiltration between RA and OA patients, and utilized flow cytometry, qRT-PCR, and Western blot were used to examine the immune cell and key genes in RA patients. **Results.** The cluster 0 matched OA and cluster 3 matched RA and significantly enriched for neutrophil-mediated immunity and ECM receptor interaction, respectively. We identified 478 DEGs. In the top 20 degrees of connection in the PPI network, the key genes for RA were obtained by comparing with the gene markers of cluster 0 and cluster 3, respectively. ROC curve showed that CCL2 and MMP13 might be diagnostic markers for RA. We found aberrant levels of CD8+T, neutrophil, and B cells in RA fibroblasts, which were validated in clinical samples. Importantly, we also validated the differential expression of key genes between RA and OA. **Conclusion.** High expression of CCL2 and MMP13 in RA may be a diagnostic and therapeutic target.

1. Introduction

Rheumatoid arthritis (RA) is a chronic inflammatory disease that affects joint synovial tissue, causing joint pain and disability [1]. RA is characterized by infiltration of synovium with inflammatory cells, hyperplasia of synovial fibroblasts, and progressive inflammation of the joint, leading to cartilage destruction, bone erosion, and disability [2, 3]. A large population studies found that in RA patients, the mortality was increased with years compared to the general population [4]. Within 10 years of RA onset, at least 50% of patients in developed countries are unable to take full-time jobs, probably due to the resulting disability [5]. Patients with RA represent approximately 0.5%-1% of the world's population and have regional variations [6]. The prevalence is higher in women aged between 35 and 50 years than in age-matched men [7].

The etiology of RA is complex and includes not only genetic and epigenetic factors but also smoking, infection, microbiota, and others [8]. Although the etiology of RA is not fully understood, its autoimmune properties have been widely recognized. Autoreactive CD4+T cells will stimulate macrophages and synovial fibroblasts to secrete cytokines, including TNF, IL-1, and IL-17, which contribute to invasive vasculitis through recruitment of immune cells and expansion of synovial fibroblasts [9, 10]. In addition, RA has a specific tissue response characterized by an aggressive proinflammatory phenotype of local fibroblasts with stromal regulatory, osteoclastogenic, and invasive properties [11]. In RA, stable reprogramming of synovial fibroblasts disrupts their protective regulatory processes, promotes their survival, and increases their production of proinflammatory agents and proteases [12]. Rheumatoid synovial fibroblasts are able

to generate and support a sustained leukocyte infiltration [13]. Therefore, a deep and extensive understanding of synovial fibroblasts and their potential roles in the pathogenesis of RA is of great importance for the prevention and treatment of RA.

With the continuous development of medical standards, conventional treatments can alleviate the condition of RA patients, but cannot completely cure them [14]. Notably, patient awareness of RA, the willingness to seek medical treatment, the time to receive appropriate treatment, and the diagnostic capability of physicians all influence the treatment and prognosis of RA [15]. Early diagnosis and treatment often delay and prevent joint deformities, improve the quality and life span of patients, and are a prerequisite for early detection of patients.

Therefore, it is very important to explore the pathogenesis of RA to develop accurate treatments and new drug targets. This study broadens the candidate list of therapeutic targets for RA, as well as the underlying mechanisms of inflammatory infiltration, by exploring the differences in gene expression and the different biological functions between RA and OA patients. It was further clarified that chemokines and matrix metalloproteinases (MMPs) signaling were involved in the pathological process of RA associated with immune cell infiltration.

2. Materials and Methods

2.1. Rheumatoid Arthritis Data Collection. Data used in this study were obtained from the gene expression omnibus (GEO) public database (<https://www.ncbi.nlm.nih.gov/geo>). GSE109449 included gene expression profile of 192 single synovial fibroblasts from 2 rheumatoid arthritis (RA) patients and 192 single synovial fibroblasts from 2 osteoarthritis (OA) patients through single-cell RNA-seq (scRNA-seq) based on GPL18573 [16].

GSE56409 included gene expression profile of fibroblasts which were isolated from synovium, bone marrow, or skin tissue samples of 12 rheumatoid arthritis patients and 6 osteoarthritis patients at the time of knee or hip replacement surgery based on GPL570 of array [17]. The raw data was processed and normalized using the Robust Multiarray Averaging (RMA) methodology.

2.2. Processing of the scRNA-Seq Data. The quality control, statistical analysis, and exploration of the scRNA-seq data for GSE109449 were performed using the Seurat R package [18, 19]. Principal component analysis (PCA) was used to identify significantly available dimensions with a P value < 0.05 . The uniform manifold approximation and projection (UMAP) algorithm [20] was used for the visualization of unsupervised clustering. The differential expression analysis was used the limma R package [21, 22]. Set the filtering threshold P value < 0.05 . Different cell clusters were annotated by the singleR package [23].

2.3. Enrichment Analysis. Biological process (BP) in Gene Ontology (GO) and Kyoto Encyclopedia of Genes and Genomes (KEGG) enrichment analysis [24–27] of gene

TABLE 1: The primers of this study.

Genes	Primers
GAPDH	F: 5'-TGACCGTCGAGTCAGGGATTT-3'
	R: 5'-GCCAACGAATTTGCCATGGGTGG-3'
ICAM1	F: 5'-TGCAAGAAGATAGCCAACCAAT-3'
	R: 5'-GTACACGGTGAGGAAGGTTT-3'
CXCL1	F: 5'-AAGAACATCCAAAGTGTGAACG-3'
	R: 5'-CACTGTTTCAGCATCTTTTCGAT-3'
MMP1	F: 5'-AGATTCTACATGCGCACAAATC-3'
	R: 5'-CCTTTGAAAAACCGGACTTCAT-3'
ITGA6	F: 5'-GTGCTTGCTCTACCTGTCGG-3'
	R: 5'-GCTCCCGGGTCTCCATATT-3'
MMP3	F: 5'-GGGTCTCTTCACTCAGCCAACAC-3'
	R: 5'-ACAGGCGGAACCGAGTCAGG-3'
CCL2	F: 5'-ACCAGCAGCAAGTGTCCCAAAG-3'
	R: 5'-TTTGCTTGCCAGGTGGTCCATG-3'
THBS1	F: 5'-TTTGACATCTTTGAACTCACCG-3'
	R: 5'-AGAAGGAGGAAACCCCTTTCTG-3'
MMP13	F: 5'-CACTTTATGCTTCTCTGATGACG-3'
	R: 5'-TCTGGCGTTTTTGGATGTTTAG-3'

markers of clusters was performed using Enrichr online tool [28]. The P value < 0.05 was considered significantly enriched.

2.4. Difference Analysis. Differential expression analysis between RA and OA in GSE56409 was performed using the limma R package [21, 29]. Genes with an $|\log_2(\text{FoldChange})| > 1$ and P value < 0.05 were identified as differentially expressed genes (DEGs).

2.5. Generation of Protein-Protein Interaction (PPI) Network. The PPI network of common genes was identified through the Search Tool for the Retrieval of Interacting Genes (STRING) (<http://string-db.org/>) database. The combined score > 0.7 was considered significant. The PPI network was visualized by the Gephi software [30]. The PPI network genes were ranked based on their degree of connectivity with other genes.

2.6. Identification of Immune Cell Infiltration. The marker gene sets of different immune cell types were obtained from Bindea et al [31]. We used the single-sample gene set enrichment analysis (ssGSEA) in R package GSVA [32] to derive the enrichment scores of each immune cell. The ssGSEA applies gene signatures expressed by immune cell populations to individual samples. A threshold value of 0.05 was established for P values < 0.05 .

2.7. Sample Collection. Synovial tissue and peripheral blood samples from 5 patients of RA and 5 patients of OA were collected from the Nanxishan hospital of Guangxi Zhuang

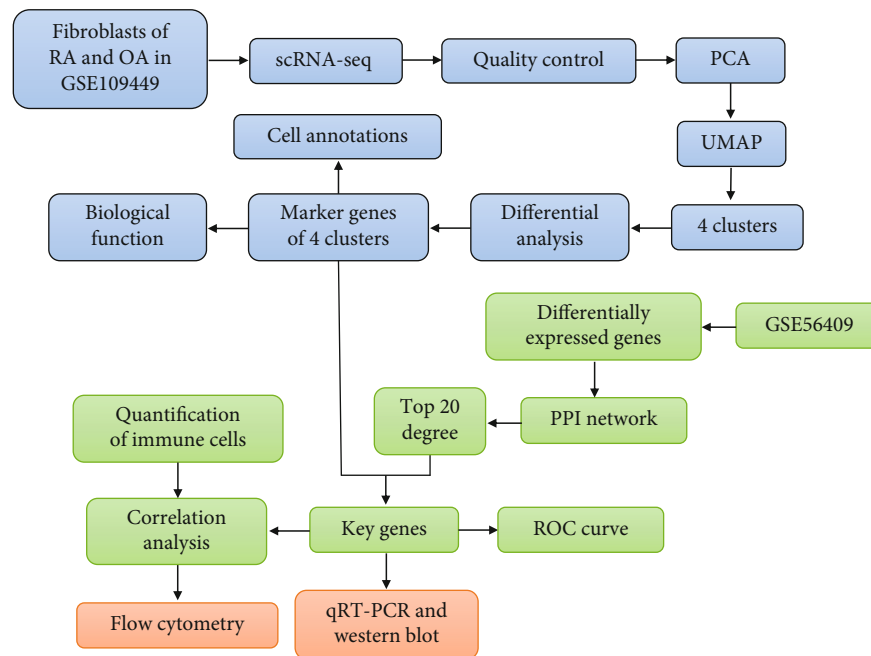


FIGURE 1: The flowchart of this study. Using single-cell sequencing data and transcriptome data to identify gene signatures and potential diagnostic markers of RA patient. OA: osteoarthritis; PCA: principal component analysis; PPI: protein-protein interaction; RA: rheumatoid arthritis; ROC: receiver operating characteristic curve; UMAP: uniform manifold approximation and projection.

Autonomous Region. All subjects read and signed the informed consent form. The study was in conformance with the guidelines of the 1975 Declaration of Helsinki and was approved by the ethics committee of the Nan-xishan hospital of Guangxi Zhuang Autonomous Region (2021NXSYEC-001).

2.8. Quantitative Real-Time Polymerase Chain Reaction (qRT-PCR). The total RNA was isolated from synovial tissue samples by using Trizol (Thermo, California, USA). After uniform quality between groups, total RNA was reverse transcribed to complementary DNA (cDNA) using PrimeScript™ RT Master Mix (TaKaRa, Tokyo, Japan). The qRT-PCR was performed using the SYBR Green Master Mix (Thermo, California, USA) using cDNA according to the manufacturer. The primer sequence of genes was shown in Table 1. Genes were normalized to GAPDH. Relative expression of mRNA was calculated through the $2^{-\Delta\Delta CT}$ method [33].

2.9. Western Blot. The synovial tissue samples of RA and OA were lysed on ice for 40 min in radio immunoprecipitation assay (RIPA) buffer (Beyotime, Shanghai, China). Proteins were loaded and separated by 10% SDS-polyacrylamide gel electrophoresis (SDS-PAGE) and then transferred onto polyvinylidene fluoride (PVDF) membranes. The membranes were incubated with the primary antibodies (all antibodies were purchased from Abcam) after blocking with skim milk. Protein bands were then incubated with corresponding secondary antibodies and detected by enhanced chemiluminescence (ECL) reagents. GAPDH protein was used as an internal reference protein.

2.10. Flow Cytometry. Peripheral blood samples were surface-labeled with anti-CD19 FITC (BD, California, USA), anti-CD3 PC5.5 (BD, California, USA), anti-CD8-PE antibody (BD, California, USA), or anti-CD45 PC7 (BD, California, USA) for 10 min at room temperature. The red blood cells in the blood were lysed with red blood cell lysate (BD, California, USA), then washed with PBS twice, and detected on the Dxflex Flow cytometry (Beckman, California USA). The results were analyzed using the Kaluza v2.1.1 software.

2.11. Statistical Analysis. Data analysis was used SPSS 20.0 software. Data were presented as mean \pm standard deviations (SD) [34, 35]. Student's *t*-test was used to compare the differences between two groups [36]. The *P* value < 0.05 was considered statistically significant. Test level $\alpha = 0.05$ (two-sided).

3. Results

3.1. The mRNA Signatures in Fibroblast of Synovial Tissue. The article flow chart is shown in Figure 1. First, we analyzed scRNA-seq data from fibroblasts of 2 RA and 2 OA patients (GSE109449). Based on quality control and normalization of the data, 31654 genes were found in the 384 cells (Figure 2(a)). The number of detected genes was significantly correlated with sequencing depth (Figure 2(b)). Among 31654 corresponding genes, the variant analysis revealed 2000 highly variable genes (Figure 2(c)). In addition, principal component analysis (PCA) results showed significant separation between fibroblasts from RA and OA patients (Figure 2(d)). To identify the available dimensions and screen the related genes by PCA, we finally selected 13

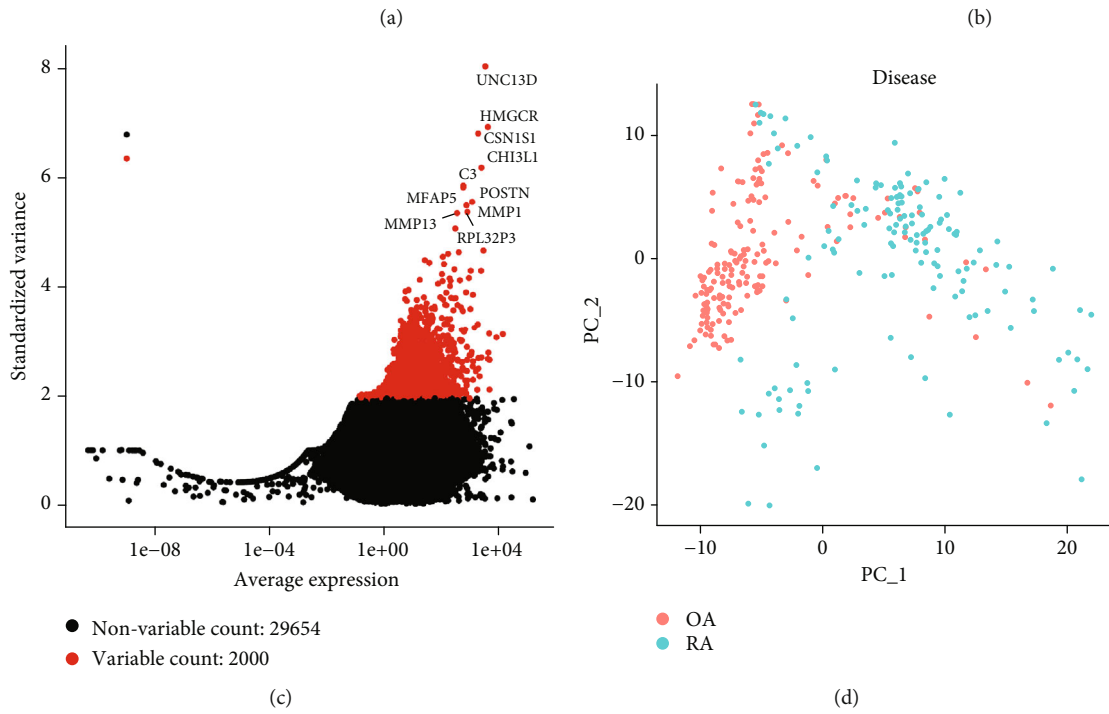
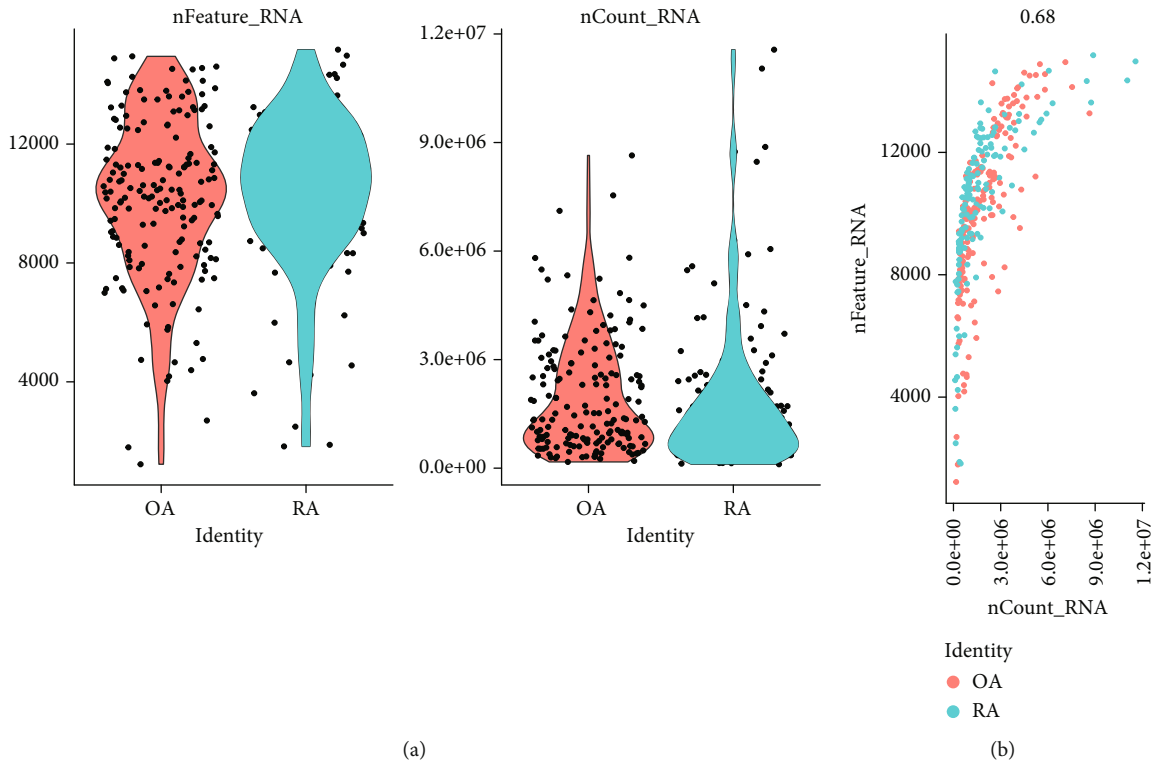


FIGURE 2: Continued.

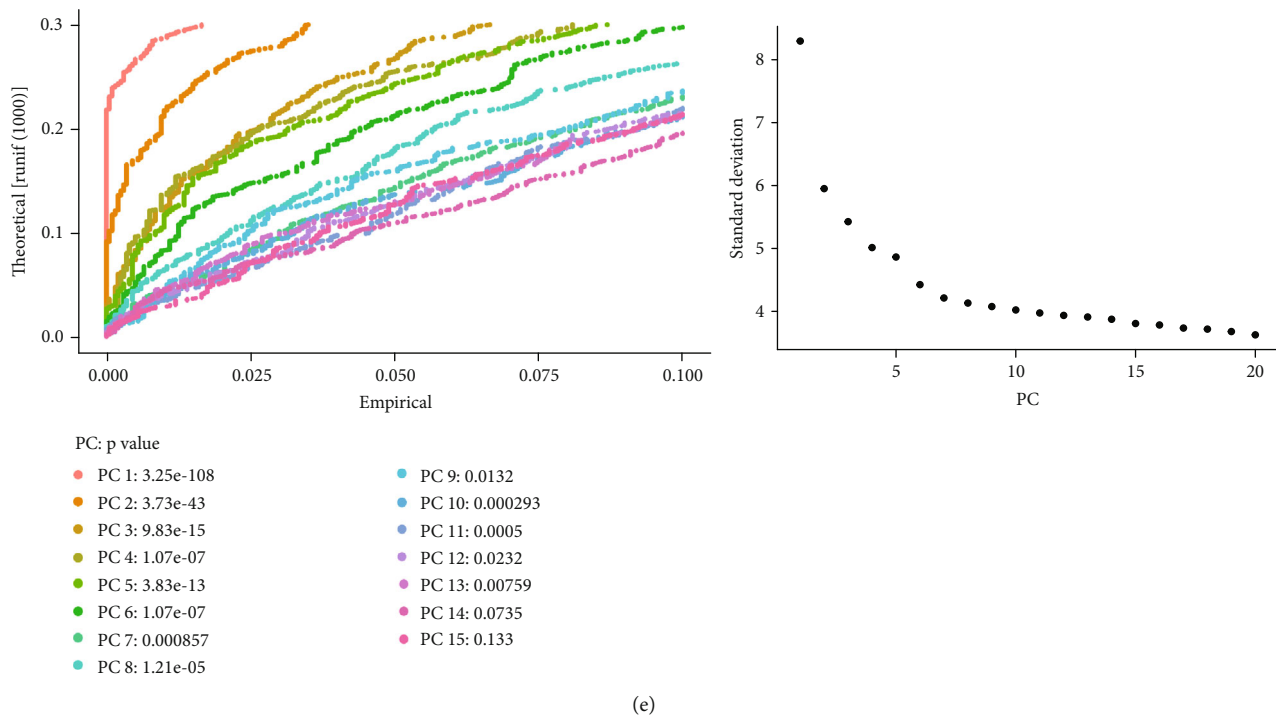


FIGURE 2: RA-related principal component genes were screened based on single-cell sequencing. (a) Quality control of synovial fibroblasts in RA. There were 31654 genes in 384 cells. RA: rheumatoid arthritis; OA: osteoarthritis. (b) The depth of sequencing was significantly correlated with the number of genes detected. Pearson's correlation coefficient was 0.68. (c) The variance diagram of gene expression for all fibroblast. The red dots represent 2000 highly variable genes, and the black dots represent nonvariable genes. (d) PCA demonstrates significant separations of cells between RA and OA. PC: principal components; RA: rheumatoid arthritis; OA: osteoarthritis. (e) PCA identified the 13 significant PCs. PC: principal components.

principal components (PCs) to travel further analysis (P value < 0.05) (Figure 2(e)).

3.2. Cell Subpopulations in Fibroblast of RA and OA. To determine whether fibroblast subpopulations differ between RA and OA, we performed clustering analysis for the cells. Through the uniform manifold approximation and projection (UMAP) algorithm, we clustered fibroblasts into 4 separate clusters (Figure 3(a)). When these cell subpopulations were compared with the clinical phenotypes, we found that cluster 0 matched the OA group, and cluster 3 matched the RA group (Figure 3(b)). Next, we performed differential expression analysis, identifying 1561 marker genes in the four clusters (Figure 3(c)). Gene markers of cluster 0 were more highly expressed in OA than in RA, whereas gene markers of cluster 3 were more highly expressed in RA than in OA (Figure 3(d)). These clusters were annotated as cell types based on the score by singleR. However, different clusters were not annotated as different cell fibroblast subpopulations for RA and OA (Figure 3(e)).

3.3. Different Biological Function of Cell Subpopulations. To identify distinct biological roles for subpopulations of RA and OA patient fibroblasts, we performed enrichment analysis of gene markers of cluster 0 and cluster 3. It was found that gene markers of cluster 0 were significantly enriched in biological process (BP) of neutrophil activation involved in immune response, neutrophil-mediated immunity, and neu-

trophil degranulation (Figure 4(a)). Gene markers of cluster 3 were significantly enriched in BP of extracellular matrix organization, collagen fibril organization, and skeletal system development (Figure 4(b)). KEGG enrichment results showed that gene markers of cluster 0 were significantly enriched in protein processing in protein processing in the endoplasmic reticulum, glycolysis/gluconeogenesis, and proteoglycans in cancer (Figure 4(c)). While gene markers of cluster 3 were significantly enriched in focal adhesion, ECM receptor interaction, and phagosome (Figure 4(d)).

3.4. Gene Expression in Fibroblasts of RA. Afterwards, we obtained 478 differentially expressed genes (DEGs) using gene expression data in fibroblasts from RA patients and OA patients (Figure 5(a), Table S1). The 294 upregulated DEGs and 184 downregulated DEGs were included (Figure 5(b)). The PPI network of DEGs with interactions was acquired through a string database (Figure 5(c)). We screened the top 20 greatest degree genes of connection in the PPI network as candidates (Table 2). Comparing with the gene markers of clusters, we found that MMP3, ITGA6, MMP1, and CXCL1 were the intersection genes for cluster 0, and THBS1, CCL2, MMP13, and ICAM1 were the intersection genes for cluster 3 (Figure 5(d)). Therefore, we considered that these 8 genes might be associated with arthritis and were defined as key genes. THBS1, CCL2, MMP13, and ICAM1 may be potential markers for RA. Among the differential results, THBS1, CCL2, MMP13,

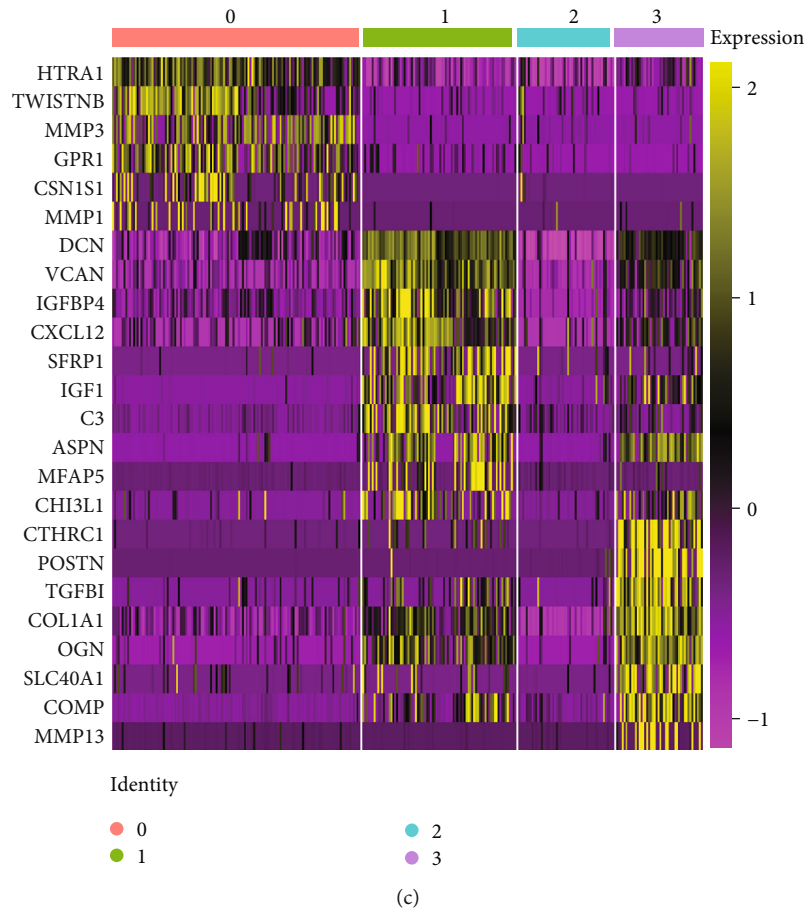
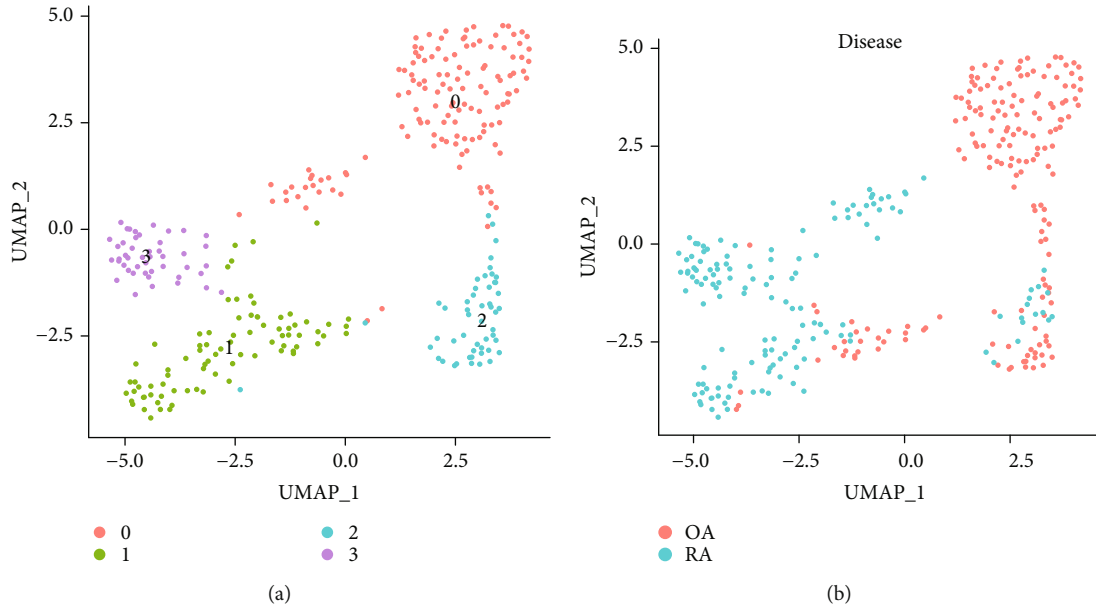


FIGURE 3: Continued.

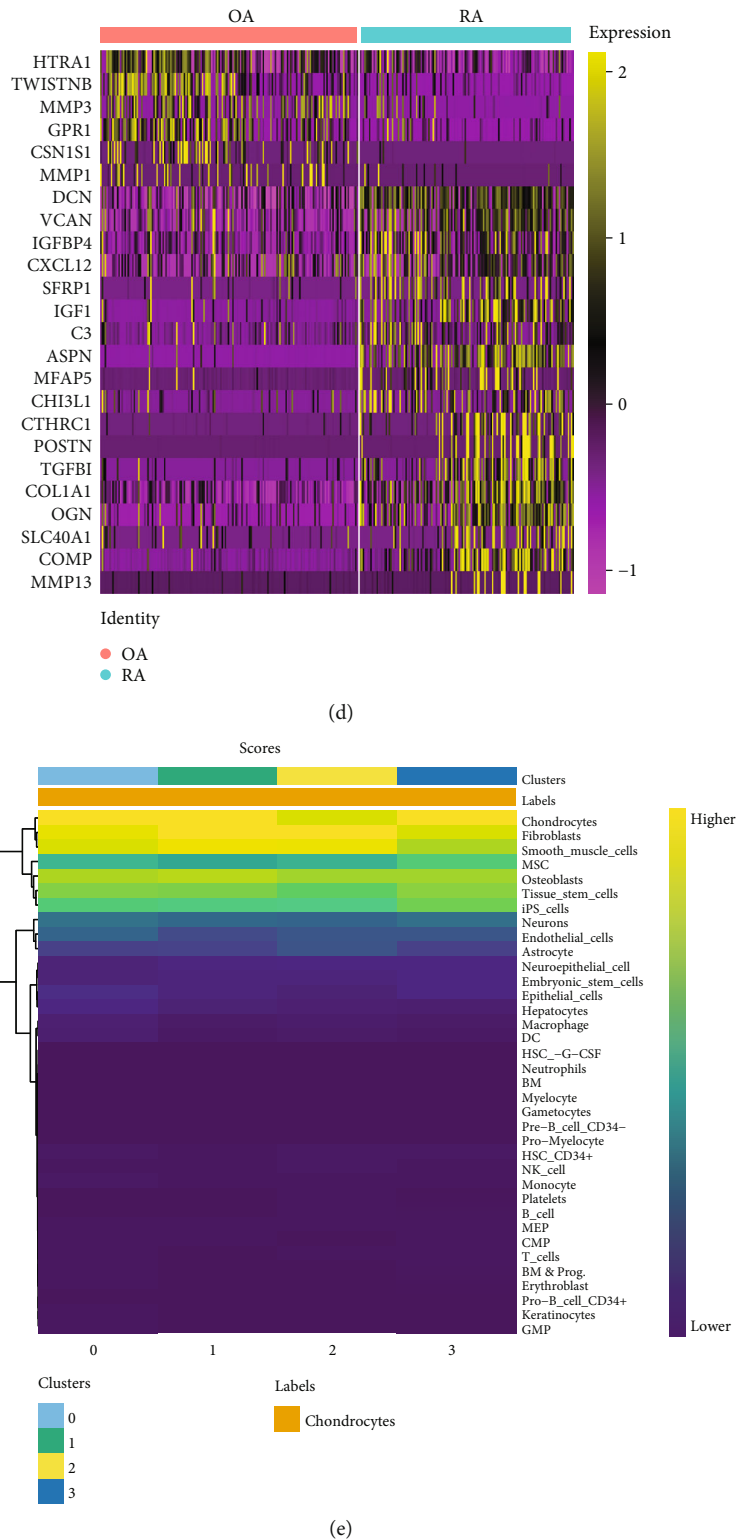
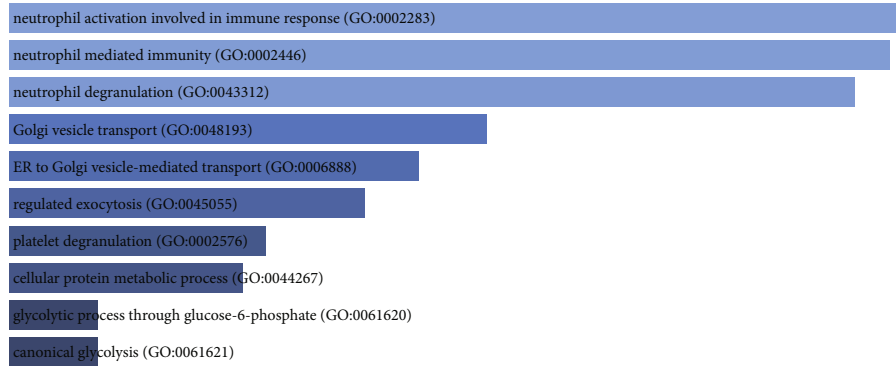
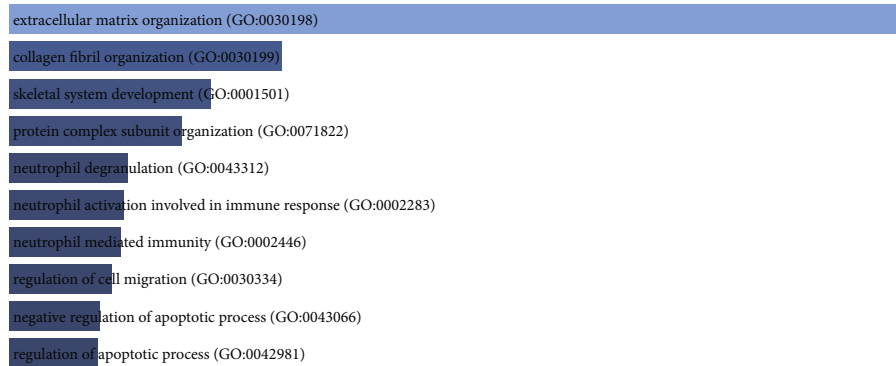


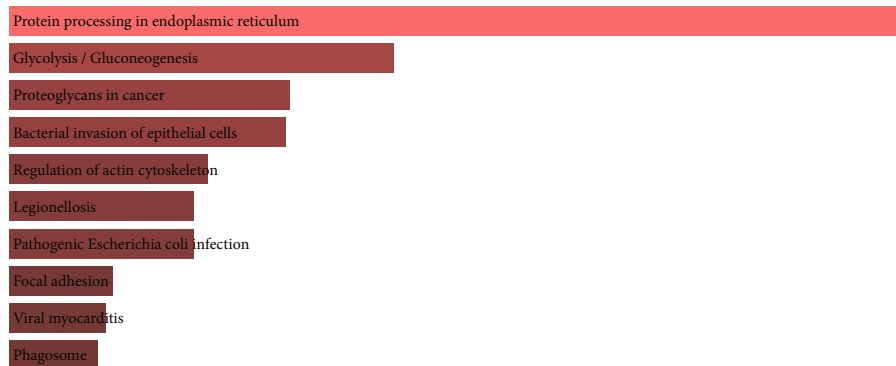
FIGURE 3: Identification of four cell subpopulations for fibroblast. (a) The UMAP algorithm reduced the dimensionality of 13 PCs and clustered into four cell clusters. UMAP: uniform manifold approximation and projection. (b) The cell clusters were matched to the sample types for RA or OA. RA: rheumatoid arthritis; OA: osteoarthritis; UMAP: uniform manifold approximation and projection. (c) Differential analysis identified 1561 gene markers. The top six gene markers for each cell cluster were listed on the left of heatmap. The colors from purple to yellow indicate the gene expression levels in each cell sample from low to high. (d) The expression of genes was matched to the sample types for RA or OA. RA: rheumatoid arthritis; OA: osteoarthritis. The colors from purple to yellow indicate the gene expression levels in each cell sample from low to high. (e) All clusters of cells were annotated according to the scores of singleR. The colors from blue to yellow indicate the gene expression levels from low to high.



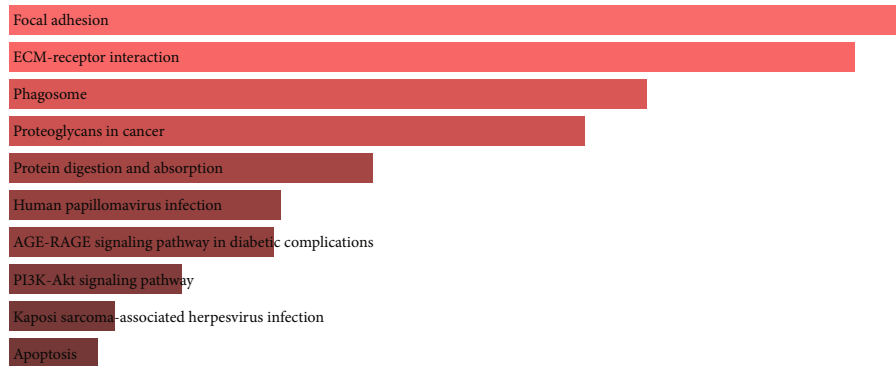
(a)



(b)

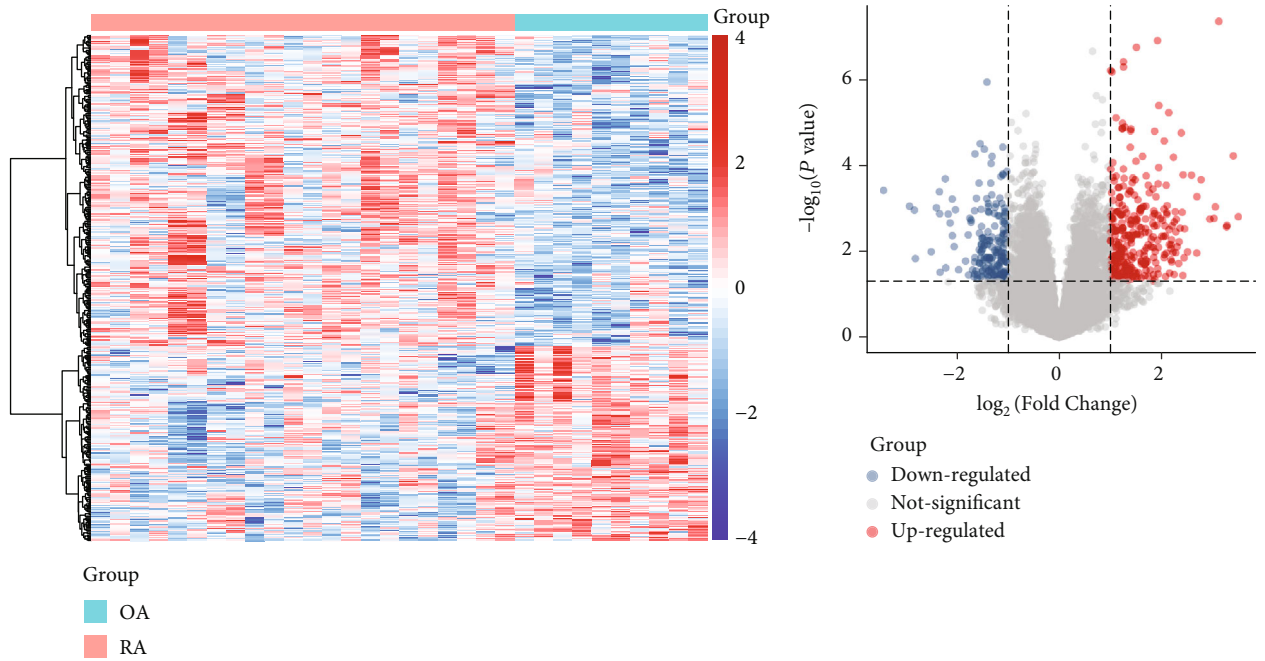


(c)



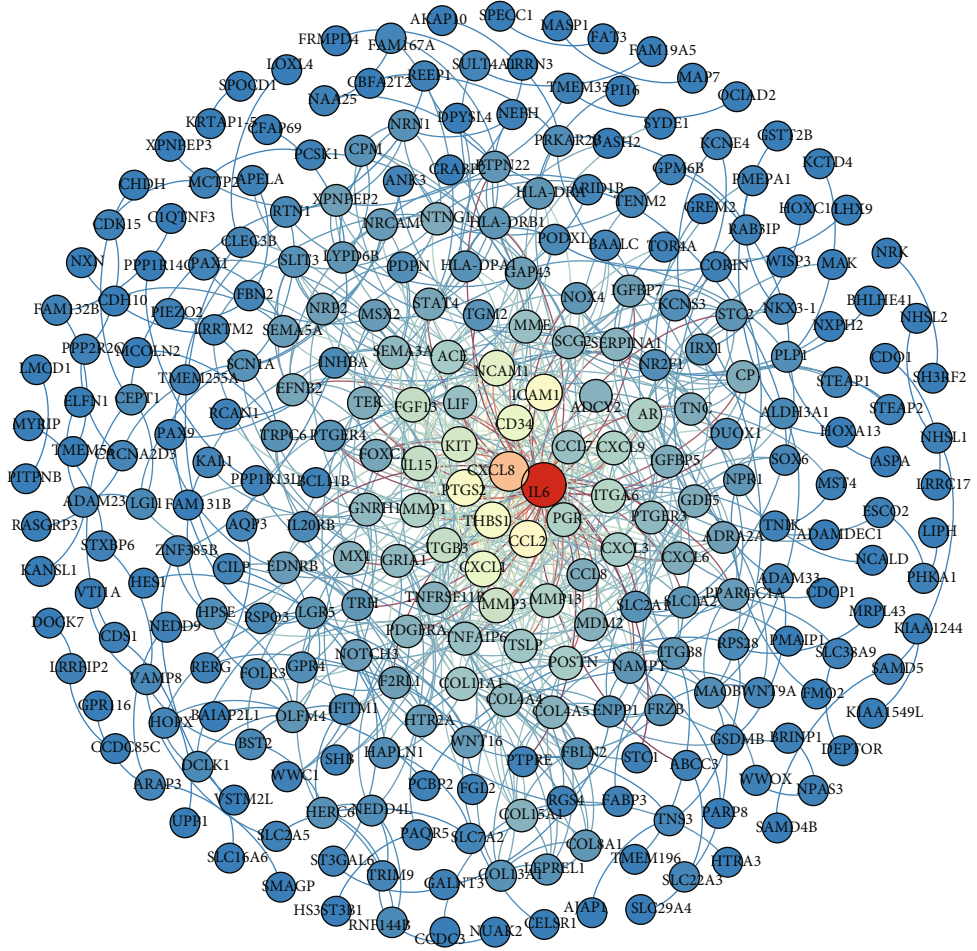
(d)

FIGURE 4: Enrichment analysis of gene markers of cell subpopulations matched to RA or OA. (a) Significantly enriched biological processes of cell subpopulations for cluster 0 who matched the OA patients. (b) Significantly enriched KEGG pathway of cell subpopulations for cluster 0. (c) Significantly enriched biological processes of cell subpopulations for cluster 3 who matched the RA patients. (d) Significantly enriched KEGG pathway of cell subpopulations for cluster 3.



(a)

(b)



(c)

FIGURE 5: Continued.

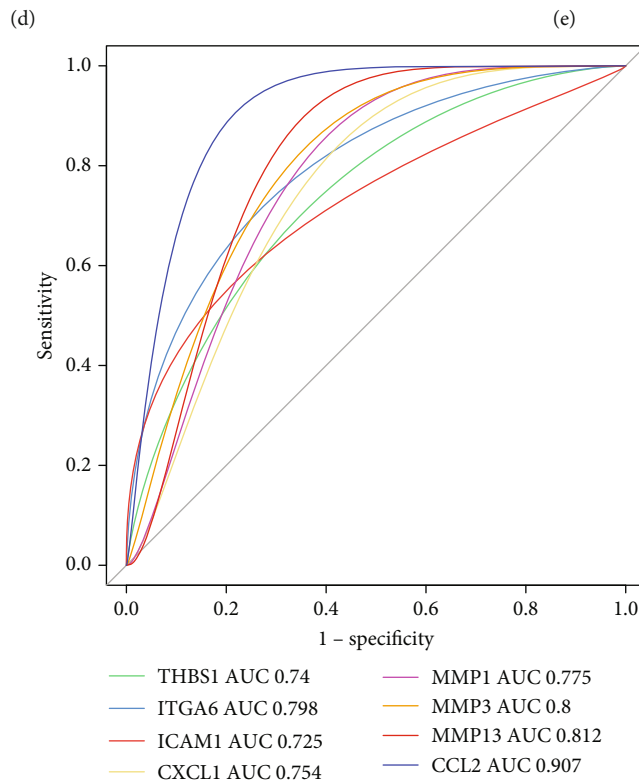
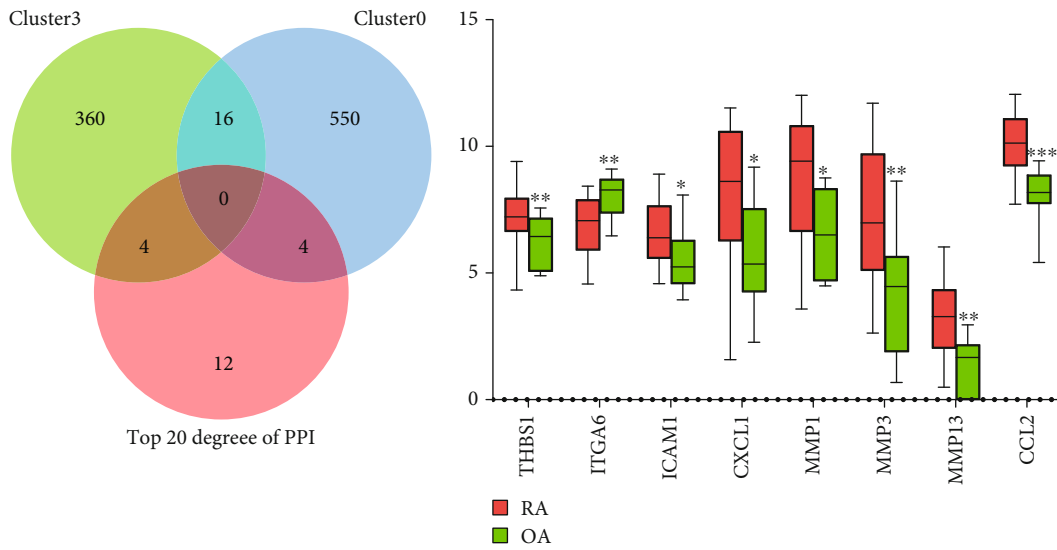


FIGURE 5: Identification of differentially expressed genes between RA and OA in GSE56409. (a) Heatmap of differential gene expression in RA and OA. RA: rheumatoid arthritis; OA: osteoarthritis. Red are upregulation and blue are downregulation. (b) Volcano plot of differentially expressed genes between RA and OA. Red are upregulation and blue are downregulation. (c) PPI network of differentially expressed genes. The colors from blue to red, representing the greater degree to which genes are connected in the network. (d) Venn diagram of the intersection among cluster 0, cluster 3, and the top 20 degrees in the PPI network. Then obtained eight key genes. (e) Differential expression of key genes between RA and OA in GSE56409. RA: rheumatoid arthritis; OA: osteoarthritis. (f) ROC curve of key genes for predicting diagnosis of RA. AUC: area under ROC curve.

ICAM1, MMP3, MMP1, and CXCL1 showed higher expression in RA compared with OA, while ITGA6 showed lower expression in RA (Figure 5(e)). Receiver operating characteristic (ROC) curve results showed that CCL2 and

MMP13 had a good predictive diagnostic role for RA (Figure 5(f)). CCL2 and MMP13 with the highest area under the receiver operating characteristic curve (AUC) values (AUC > 0.8).

TABLE 2: Top 20 genes with the largest degree in the PPI network.

Genes	Degree
IL6	60
CXCL8	40
CCL2	30
PTGS2	28
ICAM1	28
THBS1	27
CXCL1	25
CD34	25
NCAM1	24
KIT	22
MMP3	21
ITGB3	20
IL15	20
FGF13	20
ITGA6	18
MMP13	17
PGR	17
AR	17
CXCL9	17
MMP1	17

3.5. Immune Cell Changes in RA Patients. Immunoinflammation appeared in our enrichment results, especially cluster 0 which matched OA. To compare the differences in immune responses between RA and OA patients, we quantified the infiltration of immune cells according to the immune score (Figure 6(a)). We found that B cells were significantly decreased, and CD8+T cells and neutrophil were significantly increased in RA compared to OA (Figure 6(b)). The results of the correlation analysis with the key genes showed that neutrophil was significantly associated with all of the key genes (Figure 6(c)).

Importantly, we validated significant results of our analysis in blood or synovial tissue samples from RA and OA patients. Using flow cytometry, we found that the levels of CD8+T cells and neutrophil were significantly higher in RA patients than in OA patients, while the levels of B cells were significantly decreased (Figure 6(d)). QRT-PCR results found that the mRNA levels of THBS1, CCL2, MMP13, ICAM1, MMP3, MMP1, and CXCL1 were higher in RA compared with OA, and ITGA6 was lower expressed in RA (Figure 6(e)). The differential expression results of the genes were also validated by Western blot experiments, except ITGA6 (Figure 6(f)).

4. Discussion

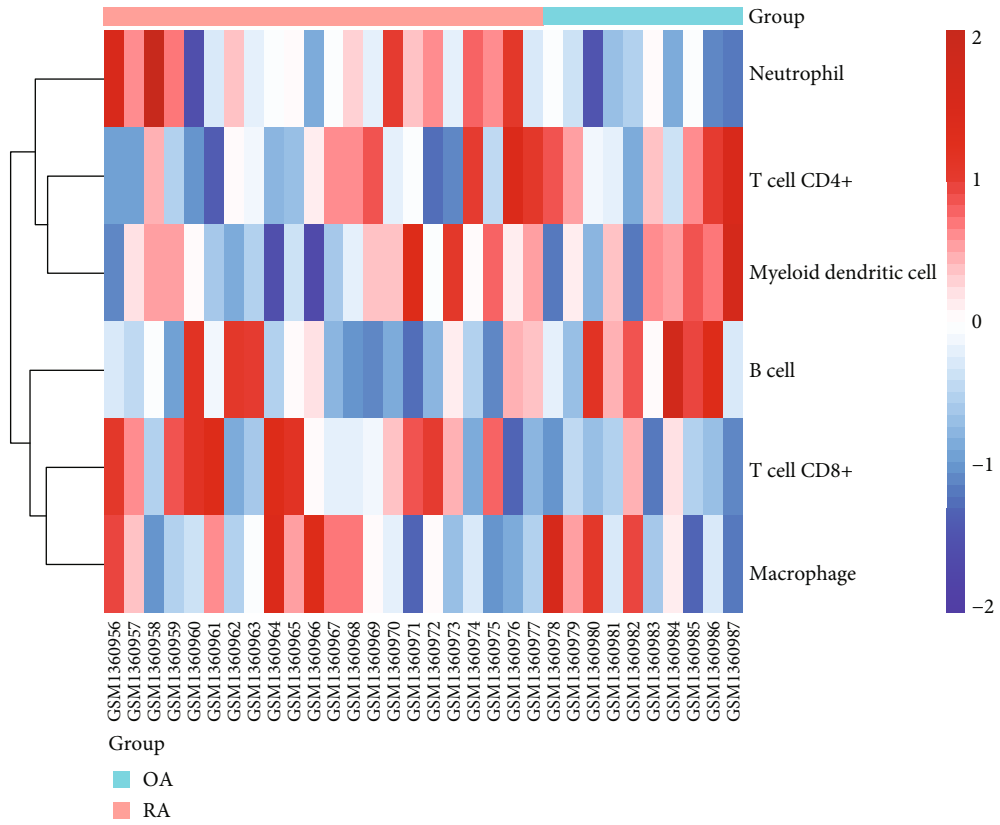
Previous studies have highlighted fibroblasts as potential therapeutic targets for RA [37]. In the present study, we sought to identify cell subpopulations of RA patient fibroblasts by comparing the results of single-cell sequencing of synovial tissue fibroblasts from RA and OA patients. And describe the contribution of different cell subpopulations to

the molecular mechanisms of RA. Transcriptome data were further combined to screen for potential fibroblast-specific markers. Importantly, we utilized molecular experiments to validate key results. These are particularly important, as such biomarkers may contribute to the early diagnosis and early treatment of the disease.

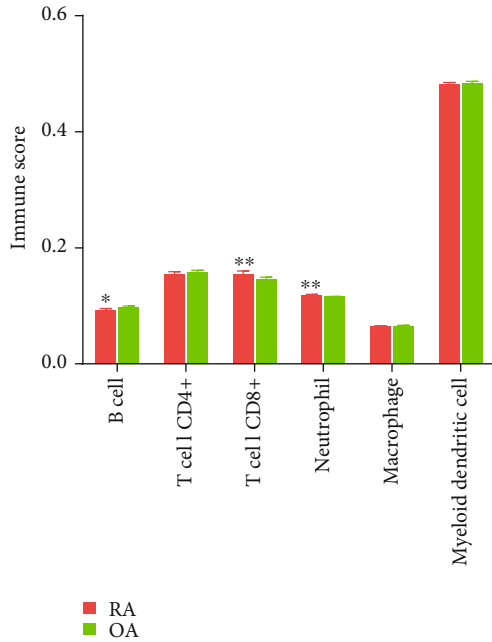
Unfortunately, we did not get different annotations for the different cell subpopulations. Of the four subpopulations identified, cluster 0 may be more representative for OA, whereas cluster 3 may be representative for RA. Gene markers for cluster 3 (MMP13, COMP, SLC40A1, OGN, COL1A1, and TGFBI) play a significant role in collagen, fibronectin, and laminin interactions that increase fibroblast migration, invasion, and cell adhesion [38–40]. In healthy joints, synovial fibroblasts form a layer in synovial tissue with a thickness of one to two cells [41]. In synovial tissue of RA patients, synovial fibroblasts form thicker layers (15–20 cells thick), mainly due to a higher proliferation rate, and the formation of antiapoptotic properties [42]. In addition, these gene markers are also major drivers of the inflammatory response in RA patients and are identified as potential markers for RA [5, 43]. The synovium is a major target of inflammation in RA.

Here, we first recognize that distinct fibroblast subpopulations differ in their molecular functions. Gene markers for cluster 0 are mainly enriched in neutrophil-mediated immunity, glycolysis/gluconeogenesis. Aberrant neutrophil responses contribute to tissue damage and are associated with arthritic pathological conditions [44, 45]. Aerobic glycolysis is manifested by inflammatory signals or rapid cell division, reflecting systemic inflammation [46]. Marker genes of cluster 3 were mainly associated with ECM receptor interaction, collagen fibril organization. Activated synovial fibroblasts produce multiple ECM remodelling components, such as matrix metalloproteinases, cytokines, and chemokines, which actively promote cellular resorption and infiltration of the joint, perpetuating and perpetuating joint inflammation [47]. Previous studies have found that collagen fibril organization is associated with the pathology of RA [48]. The presence of thinner fibers and high concentrations of collagen cleavage products have been associated with RA events [49].

Among the key genes we identified, chemokine ligand 2 (CCL2) and matrix metalloproteinases 13 (MMP13) were predicted as potential diagnostic markers for RA. Essential cytokines in the development of RA are IL-6, and IL-6 activation of endothelial cells increases adhesion molecule expression and CCL2 production [50]. CCL2 levels are increased in the plasma and synovial fluid of RA patients, closely correlating with increased joint infiltration of immune cells, particularly macrophages [51]. Studies have shown that CCL 2 is an effective therapeutic target for RA patients [52, 53]. MMP13 expression is increased in synovial fibroblasts of RA patients [54]. Elevated expression of MMP13 in RA patients may promote fibroblast migration and invasion [55]. MMP13 is also an effective therapeutic target for multiple drugs in RA patients [56]. In contrast to OA patients, we observed

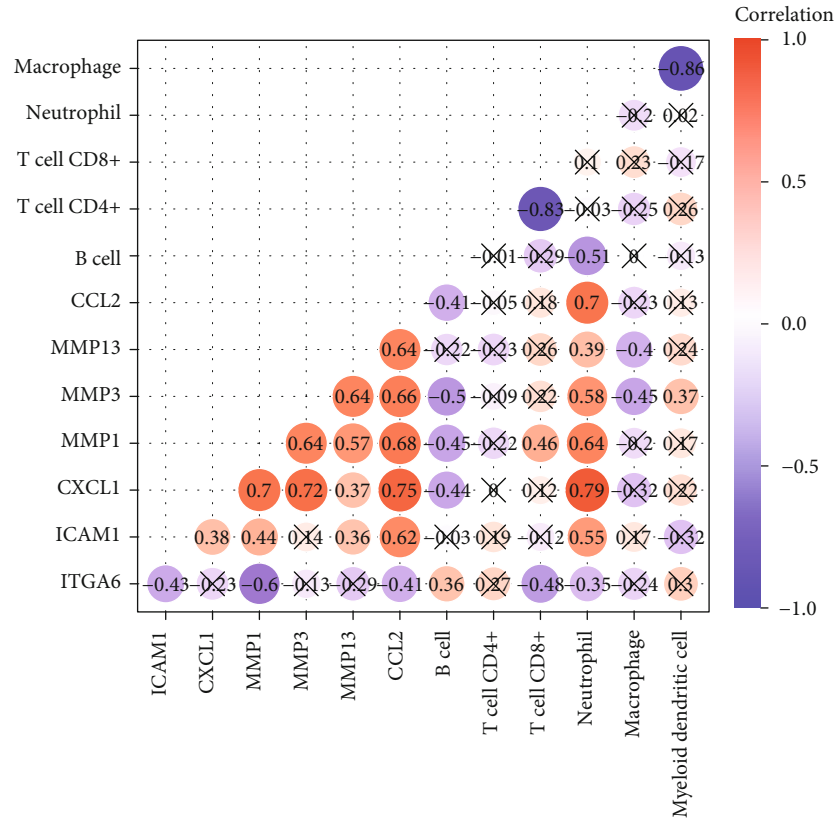


(a)

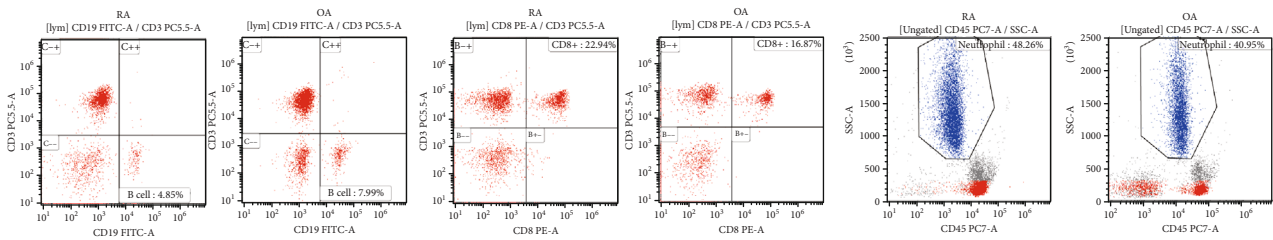


(b)

FIGURE 6: Continued.

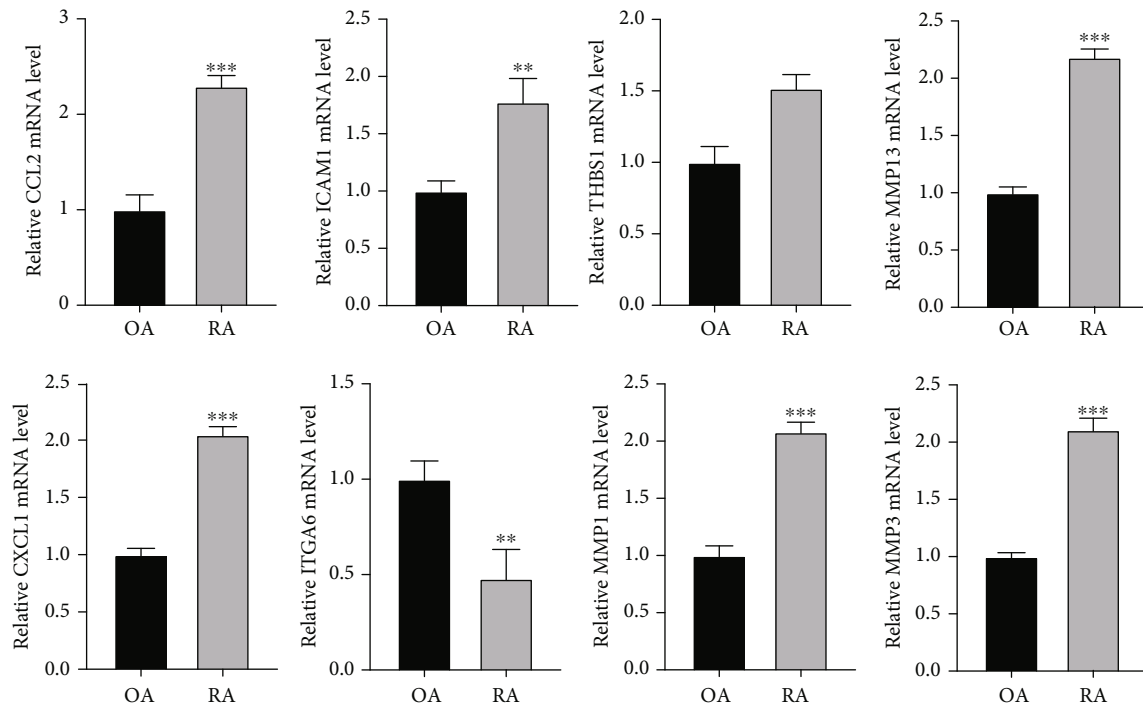


(c)

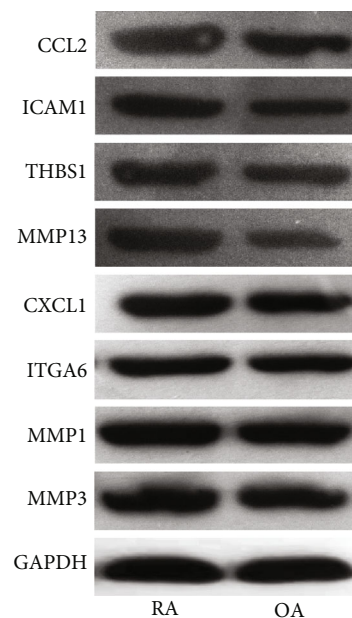


(d)

FIGURE 6: Continued.



(e)



(f)

FIGURE 6: Changes of immune cell and key genes in RA patients. (a) Infiltration levels of immune cells in RA and OA. RA: rheumatoid arthritis; OA: osteoarthritis. Red represents high infiltration and blue represents low infiltration. (b) The difference of infiltration for immune cells in RA compared to OA. RA: rheumatoid arthritis; OA: osteoarthritis. (c) Correlations between immune cells and key genes were analyzed through Pearson correlation. Node color from blue to red represents negative to positive correlation. $\times P > 0.05$. (d) The levels of CD8+T cell, neutrophils, and B cell in blood samples of RA and OA patients were detected by flow cytometry. (e) QRT-PCR was used to detect the mRNA levels of key genes in synovial tissue of RA and OA patients. $**P < 0.01$, $***P < 0.001$. (f) Western blot was used to detect the expression of key genes in synovial tissue of RA and OA patients.

upregulation of CCL2, MMP13 in RA patients, suggesting potential novel targets.

Specifically, in the differential immune cell infiltration results, we found that the levels of CD8+T cells and neutro-

phils were higher in RA fibroblasts than in OA patients, whereas the levels of B cells were decreased. CD8+T cells are activated in RA and produce a large number of chemokines and proinflammatory cytokines [57, 58]. Neutrophil

entry into the synovium is an important feature of the RA inflammatory response, which is again fueled by an intricate network of cytokines [59]. Neutrophils damage cartilage in synovial fluid and damage surrounding tissues, leading to a state of oxidative stress resulting from the release of reactive oxygen species (ROS) and increasing inflammatory conditions [60]. The number of total B cells in the blood of rheumatoid arthritis patients has been shown to be reduced compared to healthy controls [61]. However, it has also been shown that B cell depletion in RA patients is a potential therapeutic intervention [62].

Some limitations are included in this study. The low number of samples we analyzed may have biased the interpretation of the results. Whether the identified potential targets have clinically significant will requires subsequent in-depth exploration. Although we validated the differences in key genes and immune cells between RA and OA, this has some limitations for interpretation of validation results as we failed to isolate fibroblast samples for experimentation.

5. Conclusion

Chemokine and matrix metalloproteinases (MMPs) signaling plays an important role in RA pathogenesis, as several chemokines and their receptors have been implicated in the inflammatory response and immune infiltration in fibroblasts. Therefore, targeting chemokines and MMPs is a suitable approach for the diagnosis and treatment of RA, especially CCL2, and MMP13. The significance of potential target genes in RA disease is evaluated herein. This information provides a solid background for the development of new drugs or other treatments.

Data Availability

The raw data can be found in GSE109449 and GSE56409.

Ethical Approval

The study was approved by the ethics committee of the Nanxishan hospital of Guangxi Zhuang Autonomous Region (2021NXSYEC-001).

Consent

Written informed consent was obtained from each participant before authors commenced any samples collection.

Conflicts of Interest

All authors declare no competing interests.

Authors' Contributions

Lifen Liao and Ke Liang contributed equally to the manuscript preparation and supervised the experimental work, data analysis, and interpretation. Lan Lan coordinated the experimental work and contributed to data and manuscript preparation. Jinheng Wang contributed to the experimental work and manuscript preparation. Jun Guo conceived and

designed the study and supervised the experimental work, data analysis and interpretation, and manuscript critical review. Lifen Liao and Ke Liang contributed equally to this work.

Acknowledgments

The work was supported by the self-funded scientific research topic by the Health Selected Committee of Guangxi Zhuang Autonomous Region (No. Z20201192).

Supplementary Materials

Table S1: the differentially expressed genes between RA patients and OA patients in GSE56409. (*Supplementary Materials*)

References

- [1] G. R. Burmester and J. E. Pope, "Novel treatment strategies in rheumatoid arthritis," *Lancet*, vol. 389, no. 10086, pp. 2338–2348, 2017.
- [2] E. Karouzakis, M. Neidhart, R. E. Gay, and S. Gay, "Molecular and cellular basis of rheumatoid joint destruction," *Immunology Letters*, vol. 106, no. 1, pp. 8–13, 2006.
- [3] J. S. Smolen, D. Aletaha, and I. B. McInnes, "Rheumatoid arthritis," *Lancet*, vol. 388, no. 10055, pp. 2023–2038, 2016.
- [4] J. Widdifield, J. M. Paterson, A. Huang, and S. Bernatsky, "Causes of death in rheumatoid arthritis: how do they compare to the general population?," *Arthritis Care Res (Hoboken)*, vol. 70, no. 12, pp. 1748–1755, 2018.
- [5] H. Y. Yap, S. Tee, M. Wong, S. K. Chow, S. C. Peh, and S. Y. Teow, "Pathogenic role of immune cells in rheumatoid arthritis: implications in clinical treatment and biomarker development," *Cell*, vol. 7, no. 10, p. 161, 2018.
- [6] A. J. Silman and J. E. Pearson, "Epidemiology and genetics of rheumatoid arthritis," *Arthritis Research*, vol. 4, Supplement 3, pp. S265–S272, 2002.
- [7] K. Areskoug-Josefsson and U. Åberg, "A literature review of the sexual health of women with rheumatoid arthritis," *Musculoskeletal Care*, vol. 7, no. 4, pp. 219–226, 2009.
- [8] C. Croia, R. Bursi, D. Sutera, F. Petrelli, A. Alunno, and I. Puxeddu, "One year in review 2019: pathogenesis of rheumatoid arthritis," *Clinical and Experimental Rheumatology*, vol. 37, no. 3, pp. 347–357, 2019.
- [9] K. Schinnerling, C. Rosas, L. Soto, R. Thomas, and J. C. Aguilón, "Humanized mouse models of rheumatoid arthritis for studies on immunopathogenesis and preclinical testing of cell-based therapies," *Frontiers in Immunology*, vol. 10, p. 203, 2019.
- [10] M. Robert and P. Miossec, "IL-17 in rheumatoid arthritis and precision medicine: from synovitis expression to circulating bioactive levels," *Frontiers in medicine*, vol. 5, p. 364, 2019.
- [11] Y. J. Lin, M. Anzaghe, and S. Schulke, "Update on the pathomechanism, diagnosis, and treatment options for rheumatoid arthritis," *Cell*, vol. 9, no. 4, p. 880, 2020.
- [12] J. D. Turner and A. Filer, "The role of the synovial fibroblast in rheumatoid arthritis pathogenesis," *Current Opinion in Rheumatology*, vol. 27, no. 2, pp. 175–182, 2015.
- [13] A. Filer, L. S. C. Ward, S. Kemble et al., "Identification of a transitional fibroblast function in very early rheumatoid

- arthritis," *Annals of the Rheumatic Diseases*, vol. 76, no. 12, pp. 2105–2112, 2017.
- [14] Q. Fang, J. Ou, and K. S. Nandakumar, "Autoantibodies as diagnostic markers and mediator of joint inflammation in arthritis," *Mediators of Inflammation*, vol. 2019, Article ID 6363086, 22 pages, 2019.
- [15] Q. Guo, D. Xu, J. Nossent, N. J. Pavlos, J. Xu, and Y. Wang, "Rheumatoid arthritis: pathological mechanisms and modern pharmacologic therapies," *Bone research*, vol. 6, no. 1, p. 15, 2018.
- [16] F. Mizoguchi, K. Slowikowski, K. Wei et al., "Functionally distinct disease-associated fibroblast subsets in rheumatoid arthritis," *Nature Communications*, vol. 9, no. 1, p. 789, 2018.
- [17] A. Filer, P. Antczak, G. N. Parsonage et al., "Stromal transcriptional profiles reveal hierarchies of anatomical site, serum response and disease and identify disease specific pathways," *PLoS One*, vol. 10, no. 3, article e0120917, 2015.
- [18] R. Satija, J. A. Farrell, D. Gennert, A. F. Schier, and A. Regev, "Spatial reconstruction of single-cell gene expression data," *Nature Biotechnology*, vol. 33, no. 5, pp. 495–502, 2015.
- [19] L. Zhang, X. Shi, C. Gu et al., "Identification of cell-to-cell interactions by ligand-receptor pairs in human fetal heart," *Biochimica et Biophysica Acta - Molecular Basis of Disease*, vol. 1866, no. 12, article 165917, 2020.
- [20] E. Becht, L. McInnes, J. Healy et al., "Dimensionality reduction for visualizing single-cell data using UMAP," *Nature Biotechnology*, vol. 37, no. 1, pp. 38–44, 2019.
- [21] M. E. Ritchie, B. Phipson, D. Wu et al., "limma powers differential expression analyses for RNA-sequencing and microarray studies," *Nucleic acids research*, vol. 43, no. 7, p. e47, 2015.
- [22] C. Gu, X. Shi, W. Qiu et al., "Comprehensive analysis of the prognostic role and mutational characteristics of m6A-related genes in lung squamous cell carcinoma," *Frontiers in cell and developmental biology*, vol. 9, no. 559, 2021.
- [23] D. Aran, A. P. Looney, L. Liu et al., "Reference-based analysis of lung single-cell sequencing reveals a transitional profibrotic macrophage," *Nature Immunology*, vol. 20, no. 2, pp. 163–172, 2019.
- [24] C. Gu, J. Chen, X. Dang et al., "Hippo pathway core genes based prognostic signature and immune infiltration patterns in lung squamous cell carcinoma," *Frontiers in oncology*, vol. 11, no. 1486, 2021.
- [25] C. Gu, X. Shi, X. Dang et al., "Identification of common genes and pathways in eight fibrosis diseases," *Frontiers in Genetics*, vol. 11, article 627396, 2021.
- [26] X. Shi, X. Shao, B. Liu et al., "Genome-wide screening of functional long noncoding RNAs in the epicardial adipose tissues of atrial fibrillation," *Biochimica et Biophysica Acta - Molecular Basis of Disease*, vol. 1866, no. 7, article 165757, 2020.
- [27] X. Shi, T. Huang, J. Wang et al., "Next-generation sequencing identifies novel genes with rare variants in total anomalous pulmonary venous connection," *eBioMedicine*, vol. 38, pp. 217–227, 2018.
- [28] M. V. Kuleshov, M. R. Jones, A. D. Rouillard et al., "Enrichr: a comprehensive gene set enrichment analysis web server 2016 update," *Nucleic Acids Research*, vol. 44, no. W1, pp. W90–W97, 2016.
- [29] C. Gu, X. Shi, Z. Huang et al., "A comprehensive study of construction and analysis of competitive endogenous RNA networks in lung adenocarcinoma," *Biochimica et Biophysica Acta (BBA)-Proteins and Proteomics*, vol. 1868, no. 8, article 140444, 2020.
- [30] J. Groshek, V. de Mees, and R. Eschmann, "Modeling influence and community in social media data using the digital methods initiative-twitter capture and analysis toolkit (DMI-TCAT) and Gephi," *MethodsX*, vol. 7, article 101164, 2020.
- [31] G. Bindea, B. Mlecnik, M. Tosolini et al., "Spatiotemporal dynamics of intratumoral immune cells reveal the immune landscape in human cancer," *Immunity*, vol. 39, no. 4, pp. 782–795, 2013.
- [32] S. Hanzelmann, R. Castelo, and J. Guinney, "GSVA: gene set variation analysis for microarray and RNA-seq data," *BMC Bioinformatics*, vol. 14, no. 1, p. 7, 2013.
- [33] C. Gu, Z. Huang, X. Chen et al., "TEAD4 promotes tumor development in patients with lung adenocarcinoma via ERK signaling pathway," *Biochimica et Biophysica Acta - Molecular Basis of Disease*, vol. 1866, no. 12, article 165921, 2020.
- [34] Y. Sun, C. Gu, J. Shi et al., "Reconstruction of mediastinal vessels for invasive thymoma: a retrospective analysis of 25 cases," *Journal of Thoracic Disease*, vol. 9, no. 3, pp. 725–733, 2017.
- [35] J. Chen, C. Gu, X. Chen et al., "Clinicopathological and prognostic analyses of 86 resected pulmonary lymphoepithelioma-like carcinomas," *Journal of Surgical Oncology*, vol. 123, no. 2, pp. 544–552, 2021.
- [36] C. Chen, X. Zhang, C. Gu et al., "Surgery performed at night by continuously working surgeons contributes to a higher incidence of intraoperative complications in video-assisted thoracoscopic pulmonary resection: a large monocentric retrospective study," *European Journal of Cardio-Thoracic Surgery*, vol. 57, no. 3, pp. 447–454, 2020.
- [37] A. Filer, "The fibroblast as a therapeutic target in rheumatoid arthritis," *Current Opinion in Pharmacology*, vol. 13, no. 3, pp. 413–419, 2013.
- [38] C. C. Tseng, L. Y. Wu, W. C. Tsai et al., "Differential expression profiles of the transcriptome and miRNA interactome in synovial fibroblasts of rheumatoid arthritis revealed by next generation sequencing," *Diagnostics (Basel)*, vol. 9, no. 3, p. 98, 2019.
- [39] A. Gratchev, P. Guillot, N. Hakiy et al., "Alternatively activated macrophages differentially express fibronectin and its splice variants and the extracellular matrix protein β IG-H3," *Scandinavian Journal of Immunology*, vol. 53, no. 4, pp. 386–392, 2001.
- [40] K. C. Denninger, T. Marstrand, K. Moller et al., "Kinetics of gene expression and bone remodelling in the clinical phase of collagen-induced arthritis," *Arthritis Research & Therapy*, vol. 17, no. 1, p. 43, 2015.
- [41] C. Ospelt, "Synovial fibroblasts in 2017," *RMD Open*, vol. 3, no. 2, article e000471, 2017.
- [42] L. Ouboussad, A. Melville, M. H. Buch, and A. N. Burska, "Synovial tissue heterogeneity in rheumatoid arthritis and changes with biologic and targeted synthetic therapies to inform stratified therapy," *Frontiers in medicine*, vol. 6, p. 45, 2019.
- [43] Y. H. Huh, G. Lee, W. H. Song, J. T. Koh, and J. H. Ryu, "Crosstalk between FLS and chondrocytes is regulated by HIF-2 α -mediated cytokines in arthritis," *Experimental & Molecular Medicine*, vol. 47, no. 12, article e197, 2015.
- [44] Y. Miyabe, C. Miyabe, T. T. Murooka et al., "Complement C5a receptor is the key initiator of neutrophil adhesion igniting

- immune complex-induced arthritis,” *Science immunology*, vol. 2, no. 7, 2017.
- [45] F. C. Liu, H. P. Yu, P. J. Chen et al., “A novel NOX2 inhibitor attenuates human neutrophil oxidative stress and ameliorates inflammatory arthritis in mice,” *Redox Biology*, vol. 26, article 101273, 2019.
- [46] S. You, J. H. Koh, L. Leng, W. U. Kim, and R. Bucala, “The tumor-like phenotype of rheumatoid synovium: molecular profiling and prospects for precision medicine,” *Arthritis & Rheumatology*, vol. 70, no. 5, pp. 637–652, 2018.
- [47] N. Zerrouk, Q. Miagoux, A. Dispot, M. Elati, and A. Niarakis, “Identification of putative master regulators in rheumatoid arthritis synovial fibroblasts using gene expression data and network inference,” *Scientific Reports*, vol. 10, no. 1, article 16236, 2020.
- [48] S. Ham, J. B. Bae, S. Lee et al., “Epigenetic analysis in rheumatoid arthritis synoviocytes,” *Experimental & Molecular Medicine*, vol. 51, no. 2, pp. 1–13, 2019.
- [49] O. Antipova and J. P. Orgel, “Non-enzymatic decomposition of collagen fibers by a biglycan antibody and a plausible mechanism for rheumatoid arthritis,” *PLoS One*, vol. 7, no. 3, article e32241, 2012.
- [50] S. Alivernini, B. Tolusso, G. Ferraccioli, E. Gremese, M. Kurowska-Stolarska, and I. B. McInnes, “Driving chronicity in rheumatoid arthritis: perpetuating role of myeloid cells,” *Clinical and Experimental Immunology*, vol. 193, no. 1, pp. 13–23, 2018.
- [51] N. M. Elemam, S. Hannawi, and A. A. Maghazachi, “Role of chemokines and chemokine receptors in rheumatoid arthritis,” *ImmunoTargets and therapy*, vol. 9, pp. 43–56, 2020.
- [52] J. Bao, W. Liu, and Y. X. Bao, “Recombinant human interleukin receptor antagonist influences serum chemokines in patients with rheumatoid arthritis,” *Central-European journal of immunology*, vol. 39, no. 2, pp. 170–173, 2014.
- [53] D. L. Boyle, K. Soma, J. Hodge et al., “The JAK inhibitor tofacitinib suppresses synovial JAK1-STAT signalling in rheumatoid arthritis,” *Annals of the Rheumatic Diseases*, vol. 74, no. 6, pp. 1311–1316, 2015.
- [54] B. A. Moore, S. Aznavoorian, J. A. Engler, and L. J. Windsor, “Induction of collagenase-3 (MMP-13) in rheumatoid arthritis synovial fibroblasts,” *Biochimica et Biophysica Acta*, vol. 1502, no. 2, pp. 307–318, 2000.
- [55] D. Hammaker and G. S. Firestein, “Epigenetics of inflammatory arthritis,” *Current Opinion in Rheumatology*, vol. 30, no. 2, pp. 188–196, 2018.
- [56] S. Dudics, D. Langan, R. Meka et al., “Natural products for the treatment of autoimmune arthritis: their mechanisms of action, targeted delivery, and interplay with the host microbiome,” *International Journal of Molecular Sciences*, vol. 19, no. 9, p. 2508, 2018.
- [57] L. Wang, Y. Zhang, and S. Y. Zhang, “Immunotherapy for the rheumatoid arthritis-associated coronary artery disease: promise and future,” *Chinese Medical Journal*, vol. 132, no. 24, pp. 2972–2983, 2019.
- [58] M. Mellado, L. Martínez-Muñoz, G. Cascio, P. Lucas, J. L. Pablos, and J. M. Rodríguez-Frade, “T cell migration in rheumatoid arthritis,” *Frontiers in Immunology*, vol. 6, p. 384, 2015.
- [59] N. Jung, J. L. Bueb, F. Tolle, and S. Bréchar, “Regulation of neutrophil pro-inflammatory functions sheds new light on the pathogenesis of rheumatoid arthritis,” *Biochemical Pharmacology*, vol. 165, pp. 170–180, 2019.
- [60] H. B. Ferreira, T. Melo, A. Paiva, and M. . R. Domingues, “Insights in the role of lipids, oxidative stress and inflammation in rheumatoid arthritis unveiled by new trends in lipidomic investigations,” *Antioxidants (Basel)*, vol. 10, no. 1, p. 45, 2021.
- [61] O. Pala, A. Diaz, B. B. Blomberg, and D. Frasca, “B lymphocytes in rheumatoid arthritis and the effects of anti-TNF- α agents on B lymphocytes: a review of the literature,” *Clinical Therapeutics*, vol. 40, no. 6, pp. 1034–1045, 2018.
- [62] S. Bugatti, B. Vitolo, R. Caporali, C. Montecucco, and A. Manzo, “B cells in rheumatoid arthritis: from pathogenic players to disease biomarkers,” *BioMed Research International*, vol. 2014, Article ID 681678, 14 pages, 2014.

Research Article

PD-1 Coexpression Gene Analysis and the Regulatory Network in Endometrial Cancer Based on Bioinformatics Analysis

Lina Wang,^{1,2,3,4} Zhen Liu,⁵ Wenwen Zhang,⁶ Aihua Zhang,² and Pengpeng Qu⁶ 

¹Third Central Hospital of Tianjin, Tianjin, China

²Tianjin Key Laboratory of Artificial Cell, China

³Artificial Cell Engineering Technology Research Center of Public Health Ministry, Tianjin, China

⁴Tianjin Institute of Hepatobiliary Disease, Tianjin, China

⁵Department of Gynecology, Chifeng Municipal Hospital, Chifeng Clinical Medical School of Inner Mongolia Medical University, Chifeng, China

⁶Tianjin Central Hospital of Gynecology and Obstetrics, Tianjin, China

Correspondence should be addressed to Pengpeng Qu; qu.pengpeng@hotmail.com

Lina Wang and Zhen Liu contributed equally to this work.

Received 2 April 2021; Revised 30 April 2021; Accepted 15 May 2021; Published 26 May 2021

Academic Editor: Tao Huang

Copyright © 2021 Lina Wang et al. This is an open access article distributed under the Creative Commons Attribution License, which permits unrestricted use, distribution, and reproduction in any medium, provided the original work is properly cited.

Gynecological malignancies are tumors of the female reproductive system, mainly cervical cancer, endometrial cancer, and ovarian cancer. Endometrial cancer (EC) is the most common gynecological malignant tumor in developed countries. The aim of this study was to construct a network of programmed cell death protein 1 (PD-1) coexpressed genes through bioinformatics analysis and screen the potential biomarkers of PD-1 in endometrial cancer. In addition, genes and pathways involved in PD-1 and modulating tumor immune status were identified. We select the EC transcriptomic dataset in TCGA to retrieve gene sets on the cBioPortal platform, and the PD-1 coexpressed genes were obtained on the platform. GO and KEGG enrichment analysis of coexpressed genes was performed using the DAVID database. The target protein-protein interaction (PPI) network was constructed using Cytoscape 3.7.1 software, and the hub genes were then screened. A total of 976 coexpression genes were obtained. The enrichment analysis showed that PD-1 coexpressed genes were significantly enriched in overall components of the cell structure, the interaction of cytokines with cytokine receptors, chemokine signaling pathways, and cell adhesion molecules (CAMs). Ten hub genes were obtained by node degree analysis. CD3E gene is involved in the prognosis and immune process of EC, and the expression level is related to PD-1 (Pearson correlation coefficient is 0.82, $P < 0.01$). Patients with low CD3E gene expression in EC have a poor prognosis. The coexpression hub genes of PD-1 are related to immunity, in which CD3E is a prognostic marker that is involved in the PD-1/PD-L1-induced tumor immune escape. This study provides a new area to study the mechanism of PD-1/PD-L1 in EC and the precise treatment with targeted drugs.

1. Introduction

Gynecological malignancies are tumors of the female reproductive system, mainly cervical cancer, endometrial cancer, and ovarian cancer. Endometrial cancer is the most common gynecological malignant tumor in developed countries [1]. Although people continue to improve the existing treatment methods to improve the effect of surgical treatment, combined with chemotherapy and radiotherapy-based auxiliary

treatment methods, the treatment effect and disease prognosis are still not satisfactory. In recent years, with the importance of the concept of the tumor microenvironment and the continuous deepening of research on the tumor immune mechanism, the role of tumor immunotherapy in the treatment of malignant tumors has been increasing.

The goal of immunotherapy is usually to reverse the immune escape mechanism of tumors and restore the local immune response against cancer cells [2, 3]. Recent

immunotherapy research focuses on antibodies that block programmed cell death protein 1 (PD-1) or its ligands (such as PD-L1). The combination of PD-L1 and PD-1 can cause T cell dysfunction and failure and promote the production of IL-10 in tumors and thus promote T cell apoptosis [4]. Some scholars have found that PD-1 is significantly expressed in peripheral blood of patients with liver cancer, kidney cancer, and gastric cancer [5], and the expression level of PD-1 on T cells may be positively correlated with the progression of gastric cancer and chronic lymphocytic leukemia [6, 7]. Since the first PD-1/PD-L1 inhibitor (pembrolizumab) was approved by the Food and Drug Administration in 2014, many immune checkpoint inhibitors have been used in clinical practice [8]. PD-1/PD-L1 has shown effective and long-lasting antitumor effects on inhibitors, especially in some refractory tumors [9, 10]. Although PD-1/PD-L1 inhibitors have still attracted widespread attention, their relatively low response rate has limited their use in patients [11, 12]. In addition, some patients still show resistance and related adverse reactions. There is a need for high-sensitivity assays or comarkers for identifying biomarker expression in patient populations to identify more precise targets for PD-1/PD-L1 and improve the feasibility of treatment. The urgent problem is to improve the accuracy and effectiveness of PD-1/PD-L1 inhibitors in EC treatment. At the same time, it also helps to understand the PD-1/PD-L1 pathway regulation mechanism in EC more clearly and deeply. In addition, PD-1/PD-L1 therapy can also be combined with other therapies (such as chemotherapy and targeted therapy), which is expected to achieve the purpose of improving efficacy, reducing side effects, and improving patient survival and quality of life.

The purpose of this study was to analyze the EC dataset in The Cancer Genome Atlas (TCGA) database (<https://cancergenome.nih.gov/>) using bioinformatics methods, which will help to screen and analyze PD-1 coexpressed genes, describe the PD-1 molecular regulatory network, explore the possible involvement of PD-1 in EC biological processes and core genes related to prognosis, and provide new clues for EC anti-PD-1 research.

2. Materials and Methods

2.1. Materials. The dataset downloaded from this study is from the TCGA database, a research project of the National Cancer Institute, which uses a consistent genomic platform to analyze at least 20 different tumor types and provide researchers with original and processed data [13]. cBioPortal is one of the TCGA online data analysis platforms, which contains genetic mutations and transcriptome and proteomics data. In this study, the EC dataset in the TCGA database was selected on the cBioPortal platform. There were 549 clinical samples, including 177 RNA-seq samples.

2.2. PD-1 Expression in EC. Dynamic analysis of PD-1 gene expression profile data was performed through the GEPIA (<http://gepia.cancer-pku.cn/>) website to obtain the PD-1 expression level and survival analysis results in EC tissues.

2.3. Data Processing and PD-1 Coexpression Gene Screening. The data of 177 RNA-seq samples were statistically analyzed

through the cBioPortal platform, and information on PD-1 coexpressed genes was obtained. The screening criteria for genes with coexpression relationship were Spearman coefficient > 0.3 .

2.4. Function and Enrichment Analysis. The DAVID database (<https://david.ncifcrf.gov/summary.jsp>) was used to perform GO function enrichment and KEGG pathway enrichment analysis of PD-1 coexpressed genes. DAVID is an online bioinformatics resource designed to provide researchers with a comprehensive set of functional annotation tools to understand the biological mechanisms involved in the function of a large number of genes or proteins [14]. A P value of < 0.05 and the number of genes greater than 10 represent statistically significant results.

2.5. Construction of PPI Network and Hub Gene Screening. The STRING database [15] (<https://string-db.org>) and Cytoscape 3.7.1 software [16] were used to jointly construct a protein-protein interaction (PPI) network for PD-1 coexpressed genes. The STRING database integrates a text library, experimental/biochemical evidence, coexpression data in PubMed, and database correlations, thereby providing an interactive analysis platform where proteins can be evaluated for connections, associations, and interactions. The Cytohubba plug-in is based on the top 10 genes with the highest degree as core genes. 10 hub genes and PD-1 genes were introduced for interaction analysis in the STRING database online analysis platform, an interaction analysis network was established between hub genes and PD-1, and the interaction between hub genes and PD-1 was described.

2.6. Survival Analysis. Combined with the clinical information of EC, the gene expression of hub (transcripts per million (TPM)) was grouped on the GEPIA website, and the quartile method was used to separate the high expression group ($\geq 75\%$) and the low expression group ($\leq 25\%$). These hub genes were analyzed for survival using the logrank test and Kaplan-Meier test. The logrank test results $P < 0.05$ considered the differences to be statistically significant, and then, coexpressed genes related to the prognosis of EC were screened.

2.7. Correlation Analysis between Prognosis-Related Hub Genes and PD-1. The 10 hub genes were analyzed on the GEPIA website, and the hub genes related to the prognosis of EC were screened, and their correlation with PD-1 expression was analyzed and plotted.

3. Results

3.1. PD-1 Expression in Endometrial Cancer and Its Impact on Prognosis. The difference in PD-1 expression between endometrial cancer and normal tissues in the TCGA database was analyzed on the GEPIA website. The results showed that compared with normal tissues, PD-1 expression was significantly increased in EC. In addition, the overall survival time of patients with high expression of PD-1 EC was significantly higher than that of patients with low expression.

3.2. PD-1 Coexpression Gene Screening and Enrichment Analysis. Coexpressed genes of PD-1 gene were screened on

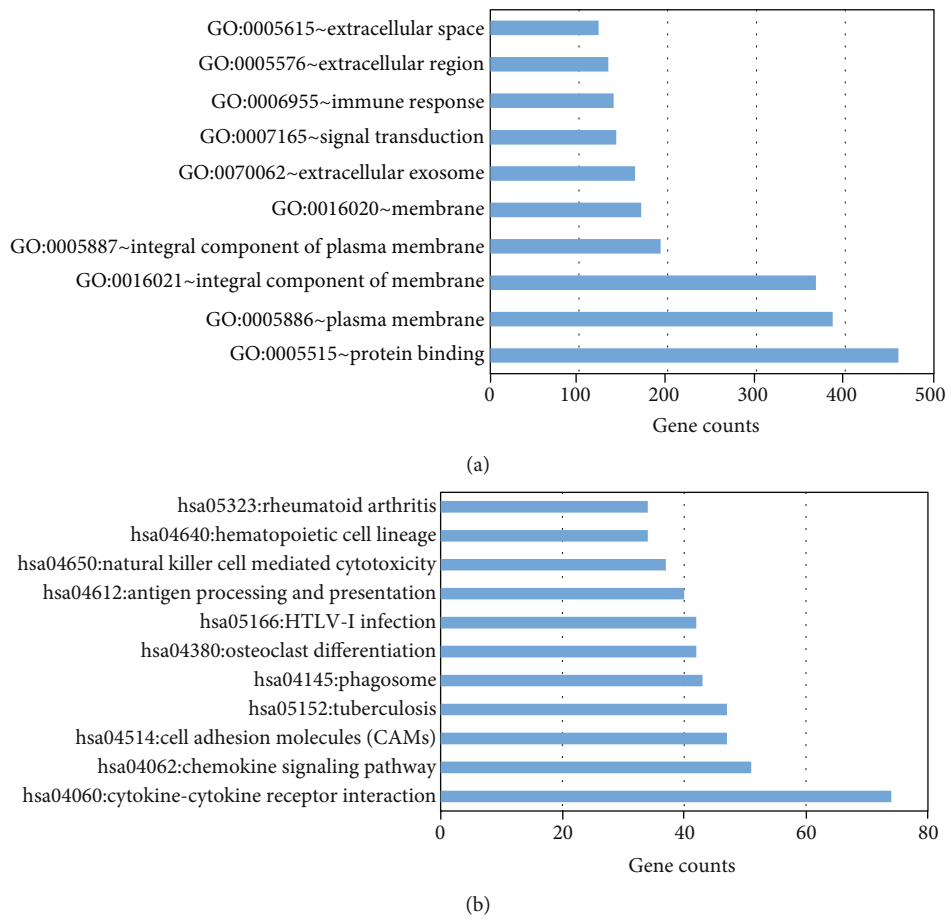


FIGURE 1: (a) The significantly enriched KEGG pathways of coexpression genes. (b) The significantly enriched GO biological processes of coexpression genes.

the cBioPortal platform, and there were 976 coexpressed genes. The GO enrichment analysis of the coexpressed genes showed that the coexpressed genes were mainly concentrated in biological processes such as protein binding, cytoplasmic membrane, cell membrane and plasma membrane components, and cell structure (Figure 1(a)). KEGG enrichment analysis showed that PD-1 coexpressed genes were significantly enriched in the interaction of cytokines with cytokine receptors, chemokine signaling pathways, and cell adhesion molecules (CAMs) as seen in Figure 1(b).

3.3. PPI Network Construction and Interaction Analysis of Coexpressed Genes. The STRING database shows that there are 5384 pairs of interactions between these coexpressed genes, which are much higher than the expected value of 532, and the average node degree is 33.9. The top 10 genes with the highest degree are CD2, PRF1, CTLA4, TBX21, CD3E, CCR5, CXCR3, LCK, IL2RG, and CD247. These genes occupy an important position in the entire network structure. 10 hub genes and PD-1 genes are introduced to the STRING database online analysis platform, and an interaction analysis network was established between hub genes and PD-1 (Figure 2). The results show that the hub genes that interact with PD-1 are CD2, PRF1, CTLA4, TBX21, CD3E, CCR5, CXCR3, LCKH, and CD247. CD3E is an important

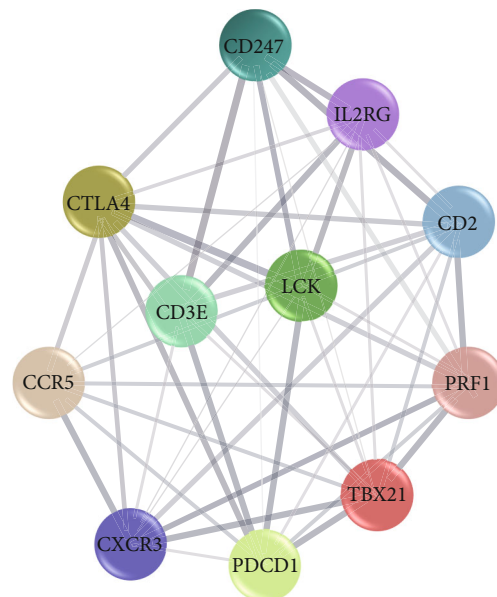


FIGURE 2: The protein-protein interaction analysis of PD-1 and hub genes.

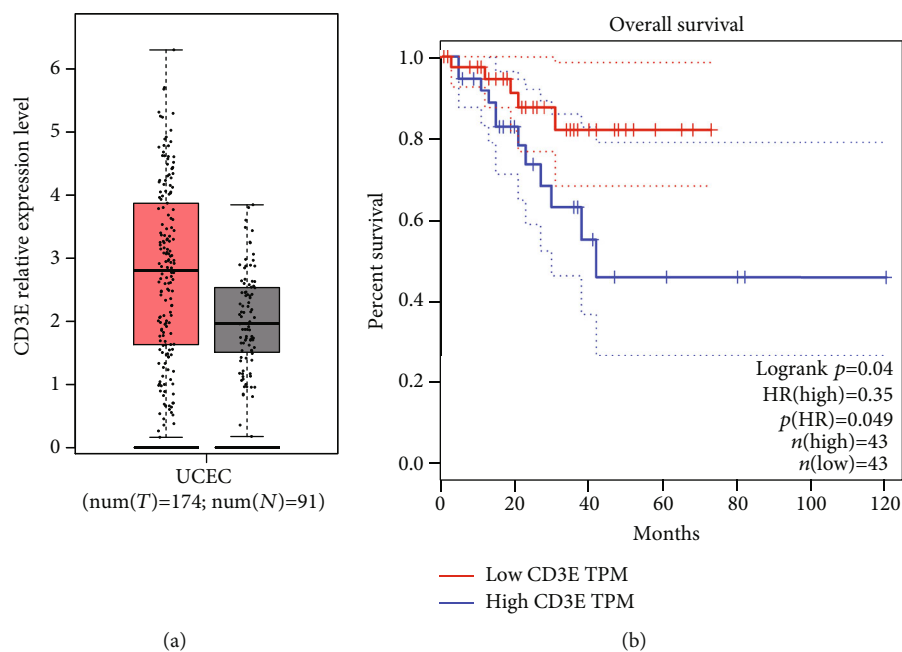


FIGURE 3: (a) Expression differences between endometrial cancer and normal tissues. Note: * P value < 0.01. (b) Survival analysis of CD3E in EC patients.

gene related to the prognosis of EC. CD3E gene is involved in the immune process, and its expression is related to PD-1 (Pearson correlation coefficient is 0.82; P value is less than 0.01). Those with low CD3E gene expression in EC have a poor prognosis.

3.4. Hub Gene Survival Analysis. On the GEPIA website, using the EC data available on the platform, the hub genes of the top 10 degrees were analyzed for survival. The results showed that among EC patients, only the expression level of CD3E gene was different from the overall survival time of EC patients. Compared with normal tissues, CD3E expression was significantly increased in EC (Figure 3(a)), and EC patients with high CD3E gene expression had a better prognosis than the CD3E gene low expression group (Figure 3(b)). CD3E gene is involved in the immune regulation of cells. Defects in this gene lead to immune deficiency and may be important genes related to the prognosis of EC.

3.5. Correlation Analysis of CD3E Gene and PD-1. The correlation between the expression of CD3E gene and PD-1 in EC was analyzed on the GEPIA platform (Figure 4). The Pearson correlation coefficient of CD3E gene and PD-1 was 0.82, and the P value was less than 0.01, indicating that this gene not only was related to the prognosis of EC but also has a co-expression relationship with PD-1. In EC, CD3E gene may be involved in the PD-1/PD-L1-mediated tumor immune escape process.

4. Discussion

In recent years, immunotherapy has become a promising cancer treatment, which has shown a lasting response in some patients. PD-1/PD-L1 as a target for cancer immuno-

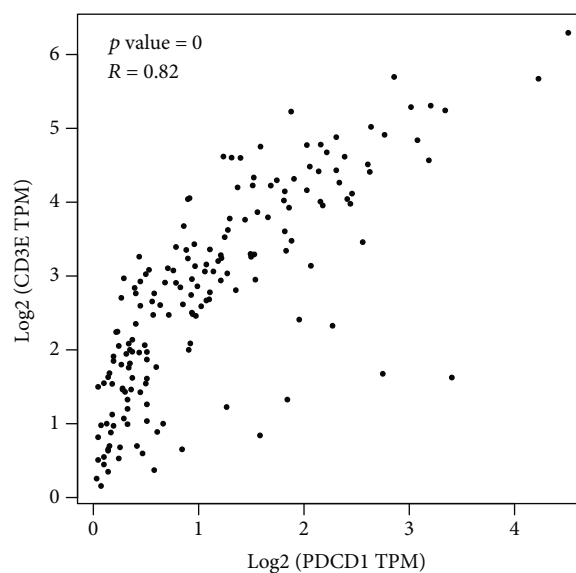


FIGURE 4: Analysis of the relationship between the expression of CD3E protein and PD-1 protein.

therapy has shown clinical therapeutic value in a variety of tumors. PD-1/PD-L1 inhibitors are currently in phase II clinical trials for advanced endometrial cancer. One patient had disease progression after the previous three chemotherapy treatments and had a complete remission (CR) of up to 17 months after receiving pembrolizumab [17]. Twenty-four patients with endometrial tumor tissue or mesenchymal cells with PD-L1 expression $\geq 1\%$ in immunohistochemical staining participated in a phase Ib clinical trial (NCT 02054806), indicating that pembrolizumab has tolerable drug toxicity and is resistant to treatment. The follow-up of the effect found that the objective response rate (ORR) was 13%

(3/24) and stable disease (SD) was 13% (3/24) of the treatment [18]. The response rate of patients in the Mumizumab-treated group was 13%, and most of the tumor patients were ineffective in anti-PD-1/PD-L1 treatment. All these suggest that the role of the PD-1/PD-L1 pathway in EC and the network regulation mechanism need to be further studied in order to obtain more accurate and effective antitumor effects.

In this study, TCGA's EC dataset was analyzed, and 976 genes coexpressed with PD-1 were screened from the transcriptome data. These genes are mainly enriched in integral components of the plasma membrane such as the cytoplasmic membrane and cell membrane and participate in the interaction of cytokines and cytokine receptors and cell adhesion molecules (CAMs). The chemokine signaling pathway may play a role in cellular immune regulation and signal transfer and may be involved in the immune escape mediated by the PD-1/PD-L1 pathway. Network interaction analysis of PD-1 coexpressed genes revealed that 10 genes had the most extensive effects with other genes. Gene annotation of these genes found that they are involved in the immune response and play an important role in the immune response. Among them, CD2, CTLA4, LCK, TBX21, CD247, and CD3 are related to T cell development and maturation, functional regulation, and signaling functions and play a vital role in adaptive immune response. CTLA4 is a negative regulator of T cells and can control T cell activation by competing with the costimulatory molecule CD28 for binding to the shared ligands CD80 and CD86. Some scholars have found that patients with stage IV endometrial cancer with mismatch repair defects and PD-L1 negative stage show a strong clinical response to the combined inhibition of PD-1 and CTLA-4 [19]. Lymphocyte-specific protein tyrosine kinase (LCK) signaling regulates cisplatin resistance and induces DNA repair genes. Targeting LCK signaling through the immunosuppressive drug saracatinib, which is currently undergoing clinical evaluation, can make chemoresistant tumor cells sensitive to cisplatin and provide opportunities for targeting signaling pathways in endometrioid tumors [20]. The function of CD247 enhances the T cell antigen receptor (TCR) signaling cascade. Defects in CD247 function can cause TCR to participate in impaired T cell activation. Some scholars have shown that compared with patients with ovarian cysts, the expression of CD247 in peripheral blood lymphocytes of patients with ovarian cancer is reduced, while the expression of CD247 in tumor-infiltrating lymphocytes of cancer tissues is reduced compared to adjacent tissues, and the abnormal expression of CD247 is related to differentiation and classification of ovary cancer. This finding suggests that CD247 targeted therapy could be a potential treatment strategy for ovarian cancer. CXCR3 is a receptor for C-X-C chemokines CXCL9, CXCL10, and CXCL11. It mediates the proliferation, survival, and angiogenic activity of human mesangial cells (HMCs) through the heterotrimeric G protein signaling pathway and may promote cell chemotaxis. Studies have found that changes in the expression level of CXCR3 are closely related to endometriosis and endometrial cancer and provide help for the differential diagnosis of endometrial cancer [21]. The IL2RG gene is

located on the X chromosome and is mutated in humans with X-linked severe combined immunodeficiency (XSCID). IL2RG controls lymphocyte development, growth, differentiation, and survival and is associated with allergic and autoimmune diseases, cancer, and immune deficiency [22]. PRF1 (perforin-1) plays an important role in killing other cells recognized by the immune system as nonself. Some scholars have reported that the expression of perforin in CD8⁺ tumor-infiltrating lymphocytes and peripheral blood T lymphocytes in patients with endometrial cancer increases the cytolytic capacity of CD8⁺ T cells [23]. CCR5 is a cell membrane protein that is a member of the G protein-coupled receptor (GPCR) superfamily. Both CCL5/CCR5 axis and CCL3/CCR5 axis may be involved in the migration and proliferation of oral cancer cells [24]. The STRING network interaction analysis of the hub gene and PD-1 showed that except for the IL2RG gene, the remaining nine hub genes interacted with PD-L1. It is speculated that these nine hub genes in the PD-1/PD-L1 pathway play an important role. Further analysis of the survival of 10 hub genes revealed that among EC patients, only the CD3E gene was associated with the prognosis of EC, and the prognosis in the high expression group was better than that in the low expression group.

CD3 is a T cell coreceptor complex and is essential for TCR signaling and T cell differentiation. The CD3 complex consists of four transmembrane proteins, δ , γ , ϵ , and ζ . Abnormal expression of any of these proteins has been found to be associated with immunodeficiency diseases [25]. CD3E is a member of the CD3 complex, which exists on the surface of T lymphocytes and plays a vital role in the adaptive immune response. Studies have shown that although the expression of PD-L1 in tumor biopsy tissue can indeed predict the response to anti-PD-1 treatment, many tumors predicted to be PD-L1 positive do not respond, and there are also in PD-L1 negative tumors some reactions [26, 27]. Therefore, some scholars examined the correlation between CD3E expression and putative targets in 9,601 human tumors spanning 31 cancer types. In a dataset of 26 patients receiving anti-PD-1 treatment, CD3E and the coexpression of PD-1 were higher than that of nonresponders. Some patients with a high correlation of CD3E-PD-1 did not respond, while other patients with low correlation did respond to anti-PD-1 treatment. When examining anti-PD-1 responders and nonresponders in metastatic melanoma, scholars found a significantly higher correlation between CD3E and PD-1 between responders and nonresponders, which supports the tumor hypothesis related to CD3E expression in the microenvironment [28]. That can be used as a useful criterion for identifying new therapeutic targets with potential for therapeutic response. Similarly, in a similar analysis of clear cell renal cancer patients' response to immune checkpoint therapy, no significant difference in CD3E-PD-1 correlation was found between responders and nonresponders [29]. More detailed expression analysis of responders and nonresponders in other cancer types will help elucidate other genetic and tumor microenvironmental factors that influence the response to new and existing therapies [29, 30]. We believe that CD3E may be expressed in T cells in the tumor microenvironment and is a promising

therapeutic target. The high expression of CD3E in this study is a favorable prognostic factor in EC, and it is related to the occurrence and invasion of EC. CD3E may become a biomarker to evaluate the prognosis of EC anti-PD-1 therapy. The prediction of disease and the prognosis are of certain clinical significance.

The limitation of this study is that further research is still needed to verify our findings. In addition, functional research on the screened genes needs to be explored.

5. Conclusions

PD-1 as an important molecular target for tumor immunotherapy plays an important role in the antitumor treatment of EC. In this study, by analyzing the EC dataset in TCGA, the coexpressed CD3E gene of PD-1 related to the prognosis of EC was screened, and their regulatory network was analyzed, which provided a new reference for the anti-PD-1 research of EC.

Abbreviations

TCGA: The Cancer Genome Atlas
 DAVID: Database for Annotation, Visualization, and Integrated Discovery
 KEGG: Kyoto Encyclopedia of Genes and Genomes
 GO: Gene Ontology
 PD-1: Programmed cell death protein 1
 EC: Endometrial cancer
 PPI: Protein-protein interaction
 CAMs: Cell adhesion molecules.

Data Availability

The data generated during the present study are available from the corresponding author on reasonable request.

Conflicts of Interest

The authors declare that they have no competing interests.

Authors' Contributions

LN Wang and Z Liu handled data collection, data analysis, and manuscript writing; AH Zhang and Wenwen Zhang worked on data collection; PP Qu took care of supervision and acquired resources. Lina Wang and Zhen Liu contributed equally to this work.

Acknowledgments

The project is supported by the National Science Foundation for Young Scientists of China (Grant No. 81802605).

References

- [1] A. Bregar, A. Deshpande, C. Grange et al., "Characterization of immune regulatory molecules B7-H4 and PD-L1 in low and high grade endometrial tumors," *Gynecologic Oncology*, vol. 145, no. 3, pp. 446–452, 2017.
- [2] K. M. Mahoney, G. J. Freeman, and D. F. McDermott, "The next immune-checkpoint inhibitors: PD-1/PD-L1 blockade in melanoma," *Clinical Therapeutics*, vol. 37, no. 4, pp. 764–782, 2015.
- [3] A. Kythreotou, A. Siddique, F. A. Mauri, M. Bower, and D. J. Pinato, "PD-L1," *Journal of clinical pathology*, vol. 71, no. 3, pp. 189–194, 2018.
- [4] M. Wang, C. Zhang, Y. Song et al., "Mechanism of immune evasion in breast cancer," *Oncotargets and Therapy*, vol. - Volume 10, pp. 1561–1573, 2017.
- [5] R. J. Motzer, B. Escudier, D. F. McDermott et al., "Nivolumab versus everolimus in advanced renal-cell carcinoma," *New England Journal of Medicine*, vol. 373, no. 19, pp. 1803–1813, 2015.
- [6] J. M. Taube, "Unleashing the immune system: PD-1 and PD-Ls in the pre-treatment tumor microenvironment and correlation with response to PD-1/PD-L1 blockade," *Oncoimmunology*, vol. 3, no. 11, article e963413, 2014.
- [7] A. V. Maker, "Precise identification of immunotherapeutic targets for solid malignancies using clues within the tumor microenvironment—evidence to turn on the LIGHT," *Oncoimmunology*, vol. 5, no. 1, article e1069937, 2016.
- [8] A. K. Karlsson and S. N. Saleh, "Checkpoint inhibitors for malignant melanoma: a systematic review and meta-analysis," *Clinical, cosmetic and investigational dermatology*, vol. 10, p. 325, 2017.
- [9] H. O. Alsaab, S. Sau, R. Alzhrani et al., "PD-1 and PD-L1 checkpoint signaling inhibition for cancer immunotherapy: mechanism, combinations, and clinical outcome," *Frontiers in Pharmacology*, vol. 8, p. 561, 2017.
- [10] V. Jindal and S. Gupta, "Expected paradigm shift in brain metastases therapy—immune checkpoint inhibitors," *Molecular Neurobiology*, vol. 55, no. 8, pp. 7072–7078, 2018.
- [11] A. Polk, I.-M. Svane, M. Andersson, and D. Nielsen, "Checkpoint inhibitors in breast cancer - current status," *Cancer Treatment Reviews*, vol. 63, pp. 122–134, 2018.
- [12] Z. Sheng, X. Zhu, Y. Sun, and Y. Zhang, "The efficacy of anti-PD-1/PD-L1 therapy and its comparison with EGFR-TKIs for advanced non-small-cell lung cancer," *Oncotarget*, vol. 8, no. 34, pp. 57826–57835, 2017.
- [13] U. R. Chandran, O. P. Medvedeva, M. M. Barmada et al., "TCGA expedition: a data acquisition and management system for TCGA data," *PLoS One*, vol. 11, no. 10, article e0165395, 2016.
- [14] X. Jiao, B. T. Sherman, D. W. Huang et al., "DAVID-WS: a stateful web service to facilitate gene/protein list analysis," *Bioinformatics*, vol. 28, pp. 1805–1806, 2012.
- [15] D. Szklarczyk, J. H. Morris, H. Cook et al., "The STRING database in 2017: quality-controlled protein-protein association networks, made broadly accessible," *Nucleic acids research*, vol. 45, no. D1, pp. D362–D368, 2017.
- [16] P. Shannon, A. Markiel, O. Ozier et al., "Cytoscape: a software environment for integrated models of biomolecular interaction networks," *Genome Research*, vol. 13, no. 11, pp. 2498–2504, 2003.
- [17] E. Sharon, H. Streicher, P. Goncalves, and H. X. Chen, "Immune checkpoint inhibitors in clinical trials," *Chinese Journal of Cancer*, vol. 33, no. 9, pp. 434–444, 2014.
- [18] P. A. Ott, Y.-J. Bang, D. Berton-Rigaud et al., "Safety and anti-tumor activity of pembrolizumab in advanced programmed death ligand 1-positive endometrial cancer: results from the

- KEYNOTE-028 study,” *Obstetrical & Gynecological Survey*, vol. 73, no. 1, pp. 26-27, 2018.
- [19] M. S. Oh and Y. K. Chae, “Deep and durable response with combination CTLA-4 and PD-1 blockade in mismatch repair (MMR)-proficient endometrial cancer,” *Journal of Immunotherapy*, vol. 42, no. 2, pp. 51–54, 2019.
- [20] C. Saygin, A. Wiechert, V. S. Rao et al., “CD55 regulates self-renewal and cisplatin resistance in endometrioid tumors,” *Journal of Experimental Medicine*, vol. 214, no. 9, pp. 2715–2732, 2017.
- [21] I. Y. Grigorian, N. Linkova, V. Polyakova, E. Paltseva, and K. Kozlov, “Signal molecules of endometrium: gerontological and general pathological aspects,” *Advances in gerontology*, vol. 28, pp. 453–461, 2015.
- [22] J.-X. Lin and W. J. Leonard, “The common cytokine receptor γ chain family of cytokines,” *Cold Spring Harbor Perspectives in Biology*, vol. 10, no. 9, p. a028449, 2018.
- [23] H.-B. Jie, R. M. Srivastava, A. Argiris, J. E. Bauman, L. P. Kane, and R. L. Ferris, “Increased PD-1+ and TIM-3+ TILs during cetuximab therapy inversely correlate with response in head and neck cancer patients,” *Cancer Immunology Research*, vol. 5, no. 5, pp. 408–416, 2017.
- [24] J. M. da Silva, T. P. M. Dos Santos, L. M. Sobral et al., “Relevance of CCL3/CCR5 axis in oral carcinogenesis,” *Oncotarget*, vol. 8, no. 31, pp. 51024–51036, 2017.
- [25] G. de Saint Basile, F. Geissmann, E. Flori et al., “Severe combined immunodeficiency caused by deficiency in either the δ or the ϵ subunit of CD3,” *The Journal of Clinical Investigation*, vol. 114, no. 10, pp. 1512–1517, 2004.
- [26] Q. Sodji, K. Klein, K. Sravan, and J. Parikh, “Predictive role of PD-L1 expression in the response of renal medullary carcinoma to PD-1 inhibition,” *Journal for Immunotherapy of Cancer*, vol. 5, pp. 1–6, 2017.
- [27] S.-P. Wu, R.-Q. Liao, H.-Y. Tu et al., “Stromal PD-L1-positive regulatory T cells and PD-1-positive CD8-positive T cells define the response of different subsets of non-small cell lung cancer to PD-1/PD-L1 blockade immunotherapy,” *Journal of Thoracic Oncology*, vol. 13, no. 4, pp. 521–532, 2018.
- [28] S. G. Gaffney, E. B. Perry, P.-M. Chen, A. Greenstein, S. M. Kaech, and J. P. Townsend, “The landscape of novel and complementary targets for immunotherapy: an analysis of gene expression in the tumor microenvironment,” *Oncotarget*, vol. 10, no. 44, pp. 4532–4545, 2019.
- [29] D. Miao, C. A. Margolis, W. Gao et al., “Genomic correlates of response to immune checkpoint therapies in clear cell renal cell carcinoma,” *Science*, vol. 359, pp. 801–806, 2018.
- [30] S. Gettinger, J. Choi, N. Mani et al., “A dormant TIL phenotype defines non-small cell lung carcinomas sensitive to immune checkpoint blockers,” *Nature Communications*, vol. 9, pp. 1–15, 2018.

Research Article

Cell Heterogeneity Analysis in Single-Cell RNA-seq Data Using Mixture Exponential Graph and Markov Random Field Model

Yishu Wang ¹, Xuehan Tian,² and Dongmei Ai ^{1,3}

¹*School of Mathematics and Physics, University of Science & Technology Beijing, China*

²*School of Mathematics and Statistics, Qingdao University, China*

³*Basic Experimental Center of Natural Science, University of Science and Technology Beijing, China*

Correspondence should be addressed to Yishu Wang; yishu6661@126.com and Dongmei Ai; aidongmei@ustb.edu.cn

Received 15 March 2021; Accepted 30 April 2021; Published 22 May 2021

Academic Editor: Tao Huang

Copyright © 2021 Yishu Wang et al. This is an open access article distributed under the Creative Commons Attribution License, which permits unrestricted use, distribution, and reproduction in any medium, provided the original work is properly cited.

Advanced single-cell profiling technologies promote exploration of cell heterogeneity, and clustering of single-cell RNA (scRNA-seq) data enables discovery of coexpression genes and network relationships between genes. In particular, single-cell profiling of circulating tumor cells (CTCs) can provide unique insights into tumor heterogeneity (including in triple-negative breast cancer (TNBC)), while scRNA-seq leads to better understanding of subclonal architecture and biological function. Despite numerous reports suggesting a direct correlation between circulating tumor cells (CTCs) and poor clinical outcomes, few studies have provided a thorough heterogeneity characterization of CTCs. In addition, TNBC is a disease with not only intertumor but also intratumor heterogeneity and represents various biological distinct subgroups that may have relationships with immune functions that are not clearly established yet. In this article, we introduce a new scheme for detecting genotypic characterization of single-cell heterogeneities and apply it to CTC and TNBC single-cell RNA-seq data. First, we use an existing mixture exponential family graph model to partition the cell-cell network; then, with the Markov random field model, we obtain more flexible network rewiring. Finally, we find the cell heterogeneity and network relationships according to different high coexpression gene modules in different cell subsets. Our results demonstrate that this scheme provides a reasonable and effective way to model different cell clusters and different biological enrichment gene clusters. Thus, using different internal coexpression genes of different cell clusters, we can infer the differences in tumor composition and diversity.

1. Introduction

Cells in the same tissue are commonly viewed as identical functional units. The analysis of traditional detection methods is always based on the overall average reaction of cells [1]. However, it has been suggested that the system-level function of a tissue is produced by heterogeneous cells between which there is a slight difference. Particularly in cancer cells, there is phenotypic and functional heterogeneity even in the same tumor [2]. The functional heterogeneity of cancer cells within tumors merits careful consideration in the conceptual history of metastasis, which involves weak and varying genetic expression between cells, or different functional cell subpopulations [3]. Traditional sequencing is always based on the average

reaction of cells, so it is difficult to detect the difference. Sequencing studies on bulk tumor tissue can only identify the average gene expression. One basic aspect of cancer cell heterogeneity in the same tumor is the different levels of gene expression. By sequencing the transcriptomes of single cells in depth, low-abundance mutations can be detected that facilitate cancer classification and identification of cell heterogeneity. Recent advances have enabled the analysis of DNA and RNA within a single cell. Single-cell RNA-Seq technology is feasible and reproducible for gene expression-based classification of cell subpopulations [4–7]. Zhang et al. have demonstrated that scRNA-seq allows researchers to study the heterogeneity of gene expression in individual cells [8]. Here, we leverage the power of single-cell RNA-seq to identify individual cells with

specific genetic alterations or genomic expression profiles that could be responsible for treatment resistance.

In metastatic pancreatic cancer research, the significance of CTCs in selecting appropriate therapies, monitoring therapeutic response, and innovating new treatments has been widely recognized. The heterogeneity and rarity of CTCs warrant the use of single-cell technologies to provide us with a more comprehensive understanding of these cells. Moreover, triple-negative breast cancer (TNBC) is a special type of breast cancer which represents various clinical and biological subgroups that have not yet been clearly defined [9]. Intertumor heterogeneity denotes patients who suffer from the same type of cancer but have greatly different gene expression patterns, which may be related to the tumor immune system. Single-cell RNA sequencing technology has been used to explain tumor microenvironment heterogeneity by identifying distinct cell subsets that may be associated with immunosurveillance and are potential immunotherapy targets.

However, large-scale data is a significant obstacle to obtaining the highest-resolution analysis of intracellular genetic heterogeneity, due to the data complexity of scRNA-seq datasets. Recent research on heterogeneity analysis has focused almost completely on using clustering algorithms (such as PCA, SVM, and hierarchical clustering) to find modularity in gene expression [10, 11]. Wang et al. [12] have reviewed the methods and tools that dedicate to the different task and usages. They also provided a guide to utilize scRNA-seq technology [8]. Although these methods have achieved impressive results, as gene expression data and module complexity increase, traditional clustering algorithms have difficulty discovering the different expression modules. The corresponding computational problem has fewer objects (cells) than the number of variables (genes). Usually only a few out of 1000 genes are significantly differentially expressed in distinct cell types, which reduces the effectiveness of traditional models. Because when clustering on the whole transcriptome, many genes would be regarded as irrelevant attributes and may even impede the identification of cell types. It has been claimed that for a broad range of data distributions, the conventional similarities (such as Euclidean norm or Cosine measure) become less reliable as the dimensionality increases [13]. The reason is that all data become sparse in high dimensional space, and therefore, the similarities between objects measured by these metrics are generally low. This inspired us to propose a more favorable network clustering algorithm to uncover additional unknown genetic changes and cellular states, which would normally be regarded as irrelevant attributes.

Graphical models bring together graph theory and probability theory in a powerful formalism for multivariate statistical modeling. The key idea is factorization: the collection of probability distributions that factorize according to the structure of an underlying graph. Inspired by this ideology, if single cells construct a network, one can use a graphical model to divide this graph. One of the most deliberate graphical models is the exponential random graph model (ERGM) [14], which takes into consideration the probability distribution of the existing network ensuing from the exponential family to model the edge distribution of the existing graph. But, the ERGM model on its own cannot represent the clus-

tering feature of the network. In this study, we adopted a mixture ERGM model proposed by Wang et al. [1], which extends the latent space model to take account of the clustering feature and identify single-cell RNA-seq data for different cell subtypes.

By representing data as a relationship graph in which nodes correspond to data points and edges (valued as 0 or 1) represent the relationships between data points, the graph can be partitioned into homogeneous and well-separated subgraphs to achieve the clustering task. Regarding the single-cell RNA-seq data, we first calculated the Pearson correlation coefficients (PCCs) among all the cells pairwise, based on their mRNA expressing profile. More specifically, we used Fisher's method to test the significance of the difference between PCCs (see Materials and Methods). We thus obtained a cell-cell network with valued edges (0 or 1).

However, in the original MixtureERGM model, subnetworks were based on the hypothesis that edges between nodes from different two subnetworks arise randomly. We found that this assumption was not accurate enough for the gene co-expression network. Because gene subnetworks denote different functional assemblies or gene pathways, there are usually latent relationships between different subnetworks, such as hub nodes or functional genes. Based on this, we improved the original MixtureERGM model by introducing forms of dependence between subnetworks with a Markov structure. That is, using the MixtureERGM model, when given the network structure and node classifications grouped by MixtureERGM, the posterior probability of the intercluster network configured by the Markov random field model can be inferred through a Bayesian framework. Meanwhile, there are two advantages to the Markov random field model. First, the model can incorporate network structures, which account for long-distance dependencies in associate states. Second, the computational framework with the Monte Carlo Markov chain is well established. In addition, we proposed an online EM algorithm for our MixtureERGM model which can solve the computation challenge for large networks. Actually, online parameter estimation using mixture models has already been studied by [15, 16].

We downloaded the single-cell RNA-seq data from Ting et al. [17] and Wang et al. [18]. These two scRNA-seq datasets are for pancreatic CTCs and triple-negative breast cancer (TNBC), respectively, and both focus on defining subsets of tumors with different molecular characterizations and finding the highly differentially expressed genes. Studies of bulk sequencing populations cannot resolve the degree of heterogeneity across these poorly understood cell populations. In the original studies connected with these datasets, cell types corresponding to each cell cluster were inferred based on prior knowledge about type-specific marker genes and the clustering results of gene expressions. In the present study, our scheme based on MixtureERGM and the MRF model provided powerful technical support for mining biological information in gene expression data and revealing the heterogeneity of gene expression between different tumor cells. Furthermore, we found various expressing genes and enriched GO functional patterns which helped us to determine the functions of cell subgroups.

Because our research was focused on the network clustering for scRNA-seq analysis, in order to demonstrate the

effectiveness of our methodology for identifying cell types, we compared it with another network clustering algorithm proposed by Salter et al. [13], on one synthetic dataset and two real scRNA-seq datasets. To avoid the simulation setup favoring our own model, we generated synthetic dataset from [13].

2. Materials and Methods

2.1. Cell-Cell Network. To obtain cell clustering information and determine different gene coexpression patterns in different cell subgroups, we first transformed the single-cell gene expression data into a cell-cell network. We excluded the edges between cells if the Pearson correlation coefficient between two cell data arrays in the gene expression matrix was $\text{cor}_{\text{Pearson correlation}} < 0.27$, which corresponds to the 0.95 quantile of the Student t -distribution. In Eq. (1), n_m is the number of gene samples and r is the Pearson correlation coefficient (PCC). Otherwise, one edge was selected to represent a relationship between the two cells.

$$T = r \sqrt{\frac{n_m - 2}{1 - r^2}} \sim t_{n_m - 2}. \quad (1)$$

2.2. MixtureERGM Model. In the network, each node is a cell, with an adjacent matrix Y , where $y_{i,j}$ denotes the value of the relationship between nodes i and j . $y_{i,j} = 1$ denotes an edge between nodes i and j . In the ERGM model, the probability of one observed network Y is proportional to the exponent of the sum of the network statistics multiplied by some parameters:

$$P(Y|\theta) = \exp \left(\theta^T (S(Y)) - \gamma(\theta) \right), \quad (2)$$

where θ is the parameters of the model, $S(Y)$ are network summary statistics chosen by the analyst, and $\gamma(\theta)$ is a normalization constant (also called a partition function in statistical physics).

We introduce unobserved indicator variables Z_i as the class vector for every node classification, following a multinomial distribution:

$$Z_i = (Z_{i1}, Z_{i2}, \dots, Z_{iG}) \sim M(1, \alpha_1, \dots, \alpha_g), \quad (3)$$

where the latent variable $Z_{ig}=1$ if node i belongs to class g and zero otherwise.

Then, we assume that the network of each subgroup of cells with the attached edges fits a finite ERGM model and has a specific parameter vector θ_g . The probability of network Y_g given the classification of nodes is as follows:

$$P_{\emptyset}(Y | Z) = \prod_{q,l,i,j} \left[\exp \left\{ \theta_{l,q}^T (S(Y))_{ij} - \gamma(\theta_{l,q}) \right\} \right]^{Z_{iq} Z_{jl}}, \quad (4)$$

where $\theta_{l,q}$ is the parameter of ERGM and $(S(Y))_{ij}$ is the sum of network statistics calculated by the analyst, such as edges, geometrically weighted in-degree distribution, geometrically

weighted out-degree distribution, mixed 2-stars, and triangles. According to Cho et al. [9], the latent variable $Z_{iq} = 1$ if node i belongs to class g and zero otherwise. Since we focused on finding the clustering results of mixture ERGMs, we tried to select network statistics, such as the differences of network attributes of nodes, with the attached edges inside or outside one cluster. In order to infer the properties of subnetworks, we selected the terms of ERGM in one cluster, including the following: edges, geometrically weighted in-degree distribution, geometrically weighted out-degree distribution, and mixed 2-stars. So, the joint probability of network Y under given conditions Z is as follows:

$$\begin{aligned} P_{\emptyset}(Y, Z) &= P_{\emptyset}(Z) P_{\emptyset}(Y | Z) \\ &= \prod_{i,q} \alpha_i^{Z_{iq}} \prod_{q,l,i,j} \left[\exp \left\{ \theta_{l,q}^T (S(Y))_{ij} - \gamma(\theta_{l,q}) \right\} \right]^{Z_{iq} Z_{jl}}. \end{aligned} \quad (5)$$

The classifications of nodes and parameter estimation can be inferred with an iterated online EM algorithm [1].

2.3. Markov Random Field Modeling Approach. After exploiting the network features with the MixtureERGM model, we obtained the node classifications and network joint optimal probability distribution simultaneously. Nevertheless, in order to take the intercluster relationships into consideration by prioritizing hub nodes, we introduced a new indicator value *hub value*: $hv_i = n_i / \text{degree}_i$ for each node i , where n_i is the number of subgroups attached with node i , and degree_i is the degree of node i in the network. Then, we normalized the hub value to a range between 0 and 1. We utilized a Gaussian Markov random field model to formulate the intercluster network probability. Under the null hypothesis of no hub node, each hub value has a uniform (0,1) distribution. In this paper, we consider $\omega = (\omega_1, \omega_2, \dots, \omega_n)$, where $\omega_i = \Phi^{-1}(1 - hv_i/2)$ and $\Phi(\cdot)$ are the CDF (Cumulative Distribution Function) of $N(0, 1)$. Define the state of node i by $T_i = 1$ (H_{i0} is false) if node i is the hub node; that is, $T_i = 1$ or $T_i = 0$ corresponds to whether H_{i1} or H_{i0} holds. Then, the null distribution of ω_i will be exactly the standard normal (Eq. (6)). Under the alternative hypothesis, i.e., the node state is not a hub node, $T_i = 0$, we follow Chen et al. [19] by assuming the distribution (Eq. (7)).

$$P(\omega_i | T_i = 0) \sim N(0, 1), \quad (6)$$

$$P(\omega_i | T_i = 1) \sim N(\mu_i, \sigma_i^2), \quad (7)$$

and $\mu_i | \sigma_i^2 \sim N(\bar{\mu}, \sigma_i^2/a), \sigma_i^2 \sim \text{InverseGamma}(v/2, vd/2)$.

The distribution of network configuration is defined as follows:

$$\begin{aligned} P(T_1, \dots, T_n | \theta_0) &= \frac{1}{Z(\theta_0)} \exp \left(h \sum_i I_1(T_i) + \tau_0 \sum_{\langle i,j \rangle \in E} (d_i + d_j) I_0(T_i) I_0(T_j) \right. \\ &\quad \left. + \tau_1 \sum_{\langle i,j \rangle \in E} (d_i + d_j) I_1(T_i) I_1(T_j) \right), \end{aligned} \quad (8)$$

where $\theta_0 = (h\tau_0, \tau_1)$ are the prior parameters or hyper-parameters, $I_0(\cdot)$ and $I_1(\cdot)$ are the indicator functions, $d_i = \text{degree}_i^{1/2}$, and $Z(\theta_0)$ is a normalizing function that is summed over all 2^n possible configurations.

Given the network structure and the node classification grouped by the MixtureERGM algorithm, the posterior probability of the intercluster network configuration can be inferred with a Bayesian framework:

$$P(T | \omega, \theta_0) \propto P(\omega | T)P(T | \theta_0). \quad (9)$$

The inference of labels and parameters are according to the posterior distribution of T :

$$\hat{T} = \underset{T}{\operatorname{argmax}} P(\omega | T)P(T | \theta_0). \quad (10)$$

A Gibbs sampler as outlined above can be applied to stochastically search for the solution to the above optimization problem [20].

2.4. Gene Set Enrichment Analysis. Suppose that there are M genes in the background set, and m of those genes is prioritized. The number of overlap genes between the background set and the prioritized set with a functional gene set is M_p and m_p , respectively. In the hypergeometric test, the enrichment P value was calculated as follows:

$$P = \frac{C_{M_p}^{m_p} C_{M-M_p}^{m-m_p}}{C_M^m}. \quad (11)$$

2.5. Choosing the Number of Clusters. The integrated classification likelihood (ICL) is used to choose the optimal number of classes, as explained in [21]. This strategy was carried out by running the MixtureERGM algorithm from 2 to Q classes and selecting the solution which maximized the ICL criterion (Q can be decided by the researchers). The ICL criterion can be defined as follows:

$$\text{ICL}(G) = -2L_C(X, Z, \emptyset) + (GM + G - 1) \log(n), \quad (12)$$

where L_C is the value of the classification log-likelihood, G is the number of groups, and M is the number of summary statistics in the model.

3. Results

3.1. Simulation Results. We simulated one undirected network from three ERGM types using sufficient network statistics: the number of edges and m2stars, the geometrically weighted edgewise shared partner distribution, and the geometrically weighted degree distribution. These three ERGMs formed three separate clusters, the parameters of which were generated:

We then applied our algorithm and the role analysis algorithm [13] to fit a mixture of ERGMs. When we ran this experiment 50 times, the averaged parameters estimated by these two algorithms were as follows:

$$\begin{aligned} \bar{\alpha}_{\text{role}} &= \begin{bmatrix} 0.8 \\ 0.15 \\ 0.05 \end{bmatrix} & \bar{\theta}_{\text{role}} &= \begin{bmatrix} 1.55 & 0.9 & 0.08 & 0 \\ -18.1 & 1 & 5.8 & 10 \\ -35.2 & -7.6 & 4.5 & 4.8 \end{bmatrix}, \\ \bar{\alpha}_{\text{MixtureERGM}} &= \begin{bmatrix} 3 \\ \frac{11}{11} \\ \frac{4}{11} \\ \frac{4}{11} \end{bmatrix} & \bar{\theta}_{\text{MixtureERGM}} &= \begin{bmatrix} 1.2 & 0.5 & -1.3 & -1 \\ -1.2 & -1 & -2.3 & 10 \\ 18 & -7.6 & 5 & 7 \end{bmatrix}. \end{aligned} \quad (13)$$

This showed that our method estimated much more accurately than role analysis. The method was also better at clustering the ERGM networks and estimating ERGM parameters in the synthetic dataset. On the other hand, Figure 1 shows the clustering of the synthetic dataset by the two models. It is evident that the clustering results of MixtureERGM almost agreed with the ground truth, while the role analysis nearly clustered into one group.

3.2. CTC scRNA-seq Datasets. We applied the MixtureERGM model and MRF approach to the two single-cell RNA-seq datasets. The first one was from mouse pancreatic circulating tumor cells, from Ting et al. [17], containing 149 cells and 19,681 genes; the second was from triple-negative breast cancer, from Wang et al. [18], containing 1534 cells and 21785 genes.

3.2.1. Pancreatic CTCs. Circulating tumor cells (CTCs) are shed from primary tumors into the bloodstream, mediating the hematogenous spread of cancer to distant organs. Analyzing the CTC RNA-seq enabled us to define and classify the subsets of CTCs with different highly expressed marker genes.

To construct a more meticulous interrelationship network of pancreatic circulating tumor single cells and cell heterogeneity from the network angle, we first constructed a cell-cell network according to this single-cell RNA expressing profile and applied the MixtureERGM model to it, resulting in five cell clusters. ICL of the MixtureERGM algorithm led to selection of 3 groups (Figure 2). Meanwhile, we compared the results from our methodology and from role analysis in detecting the number of significant enrichment functional GO items (P value < 0.05) (see Table 1(a)).

Figure 3(a) gives the clustering results of MixtureERGM, in which there were five cell clusters, three of which had significant GO functional enrichment. These were cell clusters 1, 3, and 5 in our clustering results, where cluster 1 was consistent with pancreatic dual adenocarcinoma (PDAC) cell lines (P value of GO enrichment was 3.12×10^{-15}), cluster 3 was consistent with the classical CTCs (P value of GO enrichment was 5.36×10^{-16}), and cluster 5 was consistent with the primary tumor cells with Ting et al. (P value of GO enrichment was 7.42×10^{-17}). Figure 1(b) gives the high coexpression gene GO enrichment items.

In order to explore the detailed coexpression gene module in different cell types, we adopted the WGCNA approach

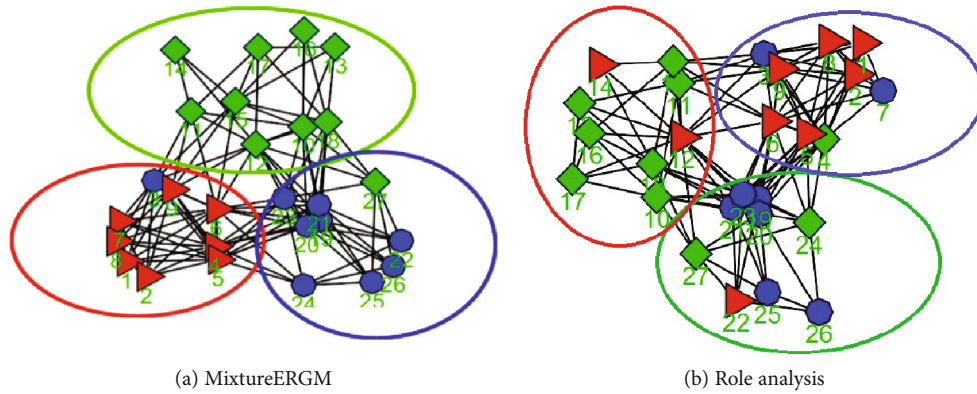


FIGURE 1: Clustering results with three groups of synthetic dataset by (a) MixtureERGM and (b) role analysis, where the original groups are denoted by the different color circles and grouping results by algorithm are denoted by the different color nodes.

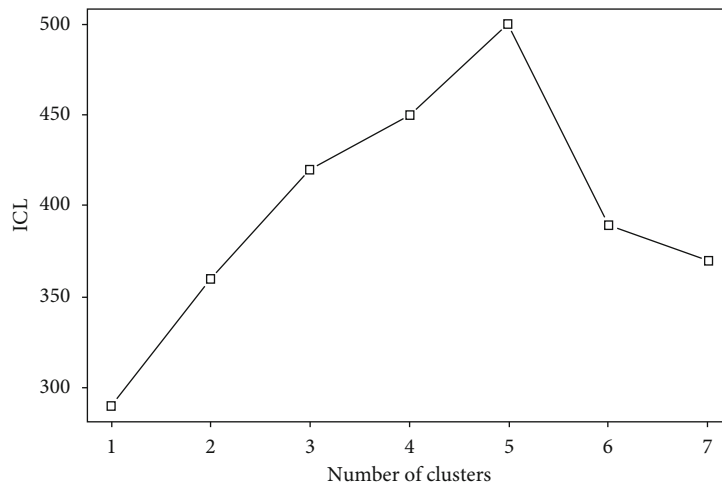


FIGURE 2: The plot of ICL of MixtureERGM algorithm against number of clusters for CTC dataset.

TABLE 1

(a) Comparison results of MixtureERGM model and role analysis model in pancreatic CTC database

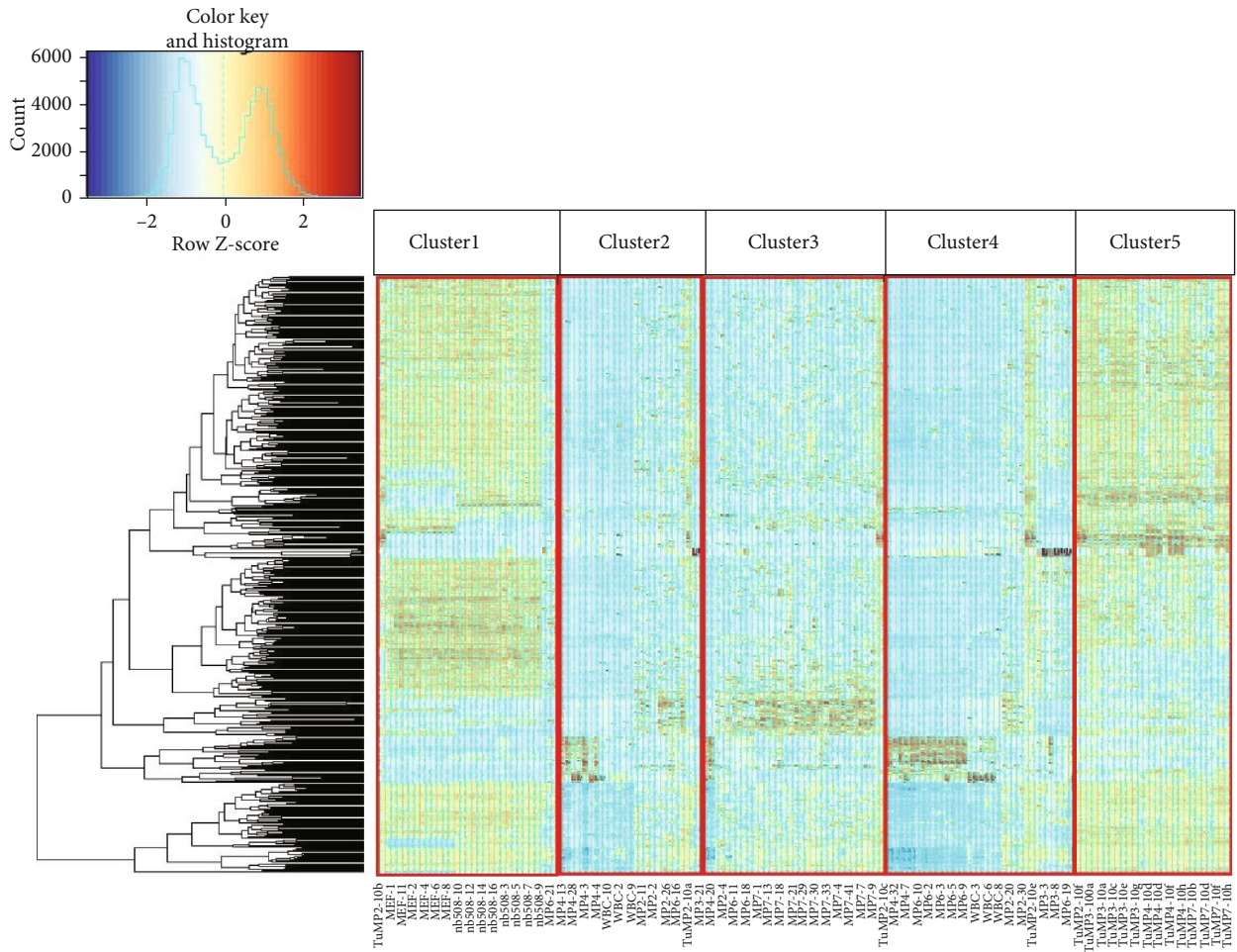
Method Num	MixtureERGM model	Role analysis model
Number of different expressing genes across different cell groups	236	185
Number of GO enrichment gene modules, in which numbers of genes > 20 (P value < 0.05)	15	10

(b) Comparison results of MixtureERGM model and role analysis model in triple-negative breast cancer (TNBC) database

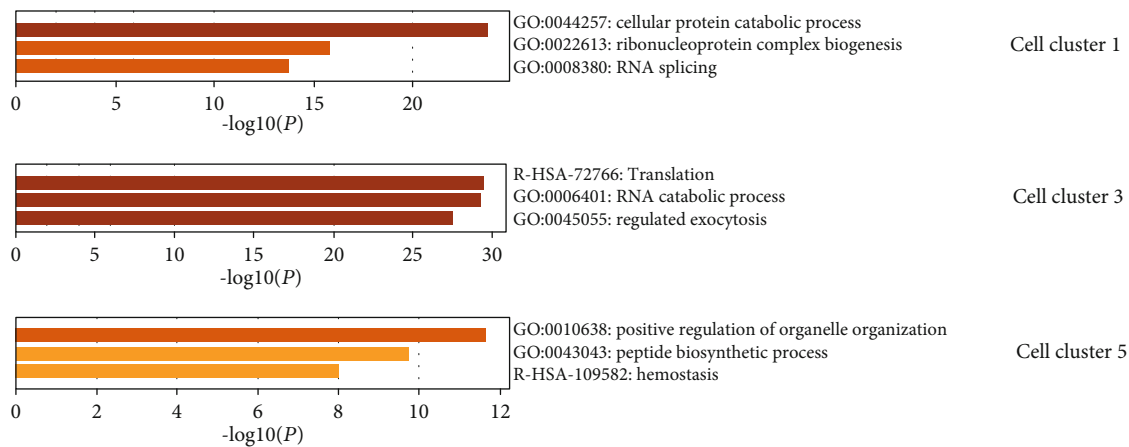
Method Num	MixtureERGM model	Role analysis model
Number of different expressing genes across different cell groups	556	323
Number of GO enrichment gene modules, in which numbers of genes > 20 (P value < 0.05)	28	21

for these three clusters. Figure 4 gives the heat map results of the coexpression gene patterns and the biologically significant results in these three cell populations, where yellow bars indicate the negative log of P values in formula (11). In this figure,

we can see that the high-expression genes in cell cluster 1 mainly participated in functions that regulated exocytosis, cellular responses to external stimuli, extracellular structure organization, and transport to the Golgi, in addition to subsequent



(a)



(b)

FIGURE 3: (a) Gene expression profiles of circulating tumor cells were clustered using MixtureERGM algorithm with 5 underlying clusters. Each column represents one cell. (b) GO enrichment results of high coexpression genes in these three cell clusters generated by MixtureERGM algorithm. *P* values are denoted by the color bars.

modification. Meanwhile, the high-expression genes in cell cluster 3 mainly participated in positive regulation of the cellular catabolic process and protein folding, ribosome leukocyte- and myeloid leukocyte-mediated immunity, and the adaptive immune system, which is consistent with its cell category.

Furthermore, the high-expression genes in cell cluster 5 mainly participated in positive regulation of organelle organization, histone deacetylation, and selenoamino acid metabolism, which are all important functions in primary tumor development.

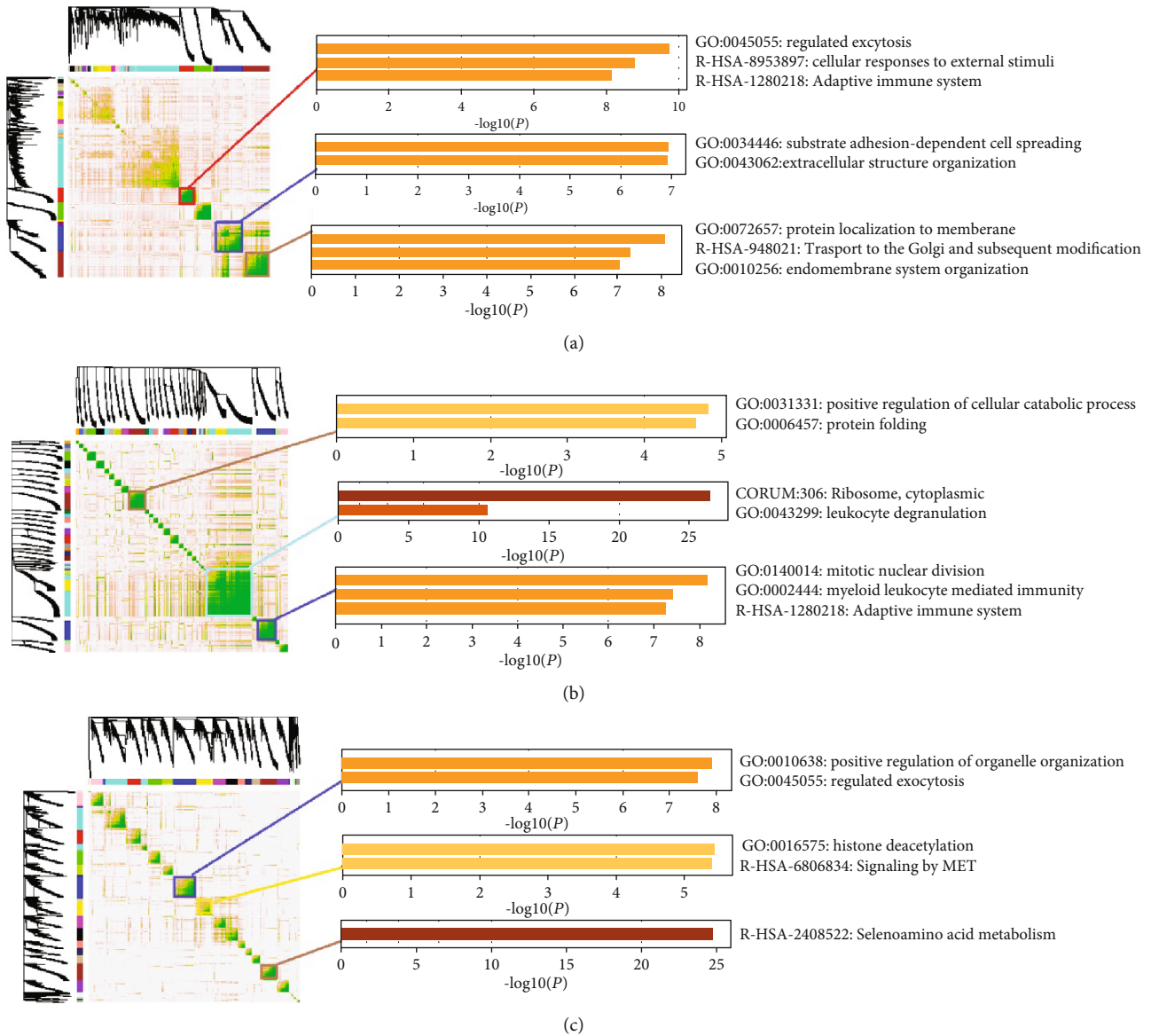
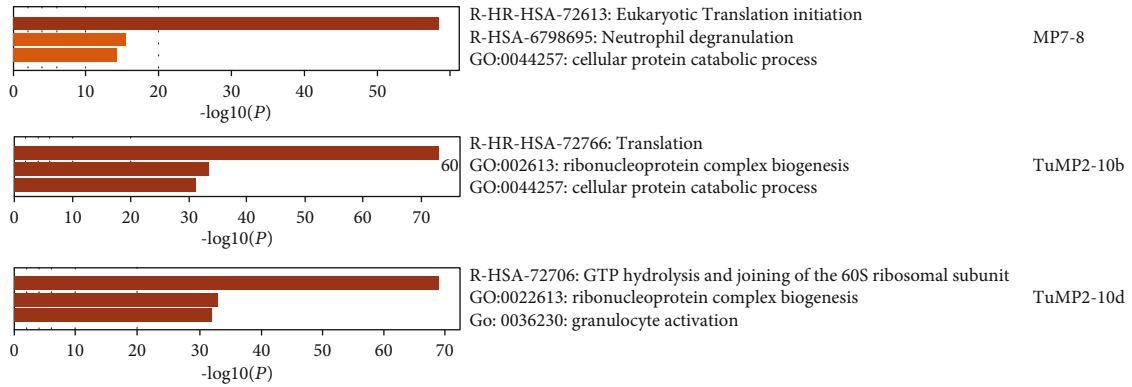


FIGURE 4: Coexpression gene modules in cell cluster 1 (A), cell cluster 3 (B), and cell cluster 5 (C). Yellow bars indicate the negative log of P values.

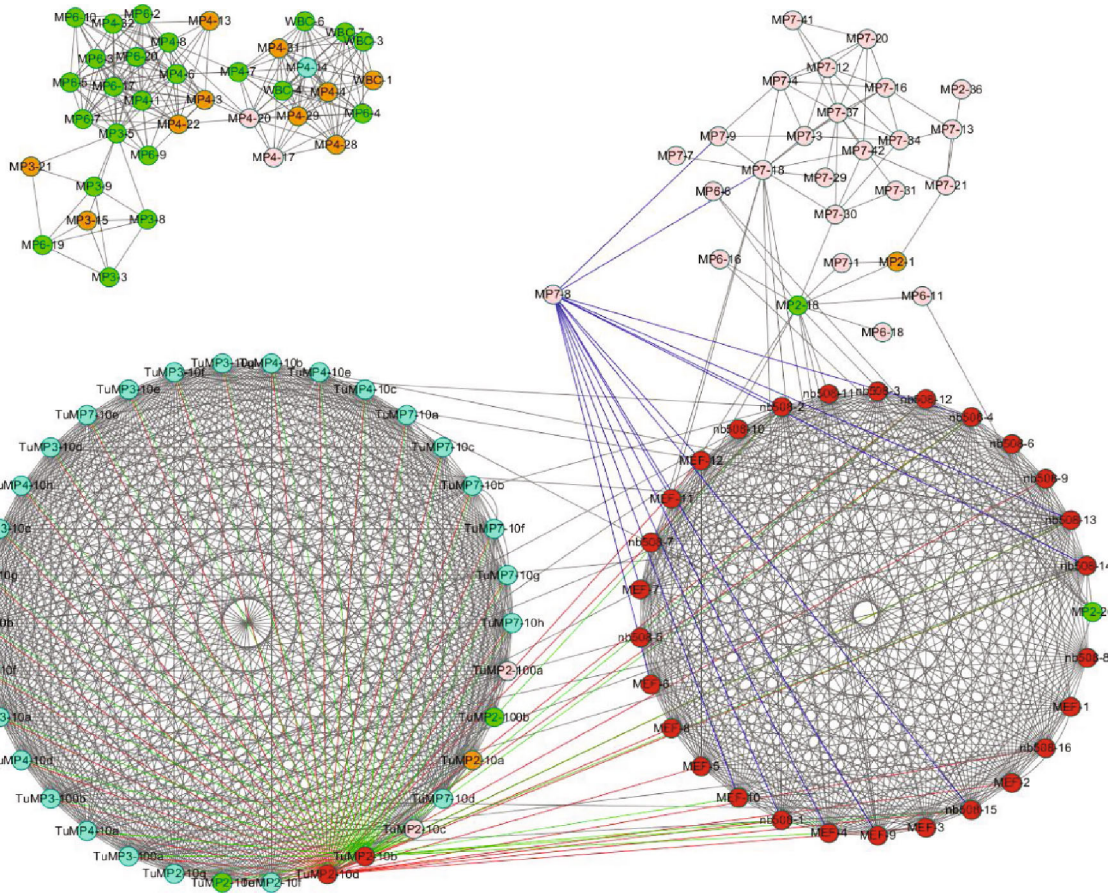
Next, to find the hub node cells, which are important connectors among different function patterns and for inter-network rewiring information, we applied the MRF model to the classified cell-cell mixture network. Figure 5 gives the results for hub nodes in the cell network, in which we found three important hub nodes. The hub nodes specifically expressed in immune cells were MP7-8, TuMP2-10b, and TuMP2-10d. These hub cell nodes indicated a link with translation or GTP hydrolysis, which are both important in the metabolism and evolution of tumors. The coexpression of these genes identified in some regulatory T-cell clusters may be potential immunotherapy targets. From gene expression profile, we can find that TuMP2 cell has high expressed gene KRT7, KRT8, which is functional in epithelial, and low expressed gene Cd61, which is functional in hematopoietic. Specially, gene KRT8 is also found in the triple-negative breast cancer dataset, which may be a generic cancer gene.

On the other hand, although MixtureERGM and the MRF model gave the CTC clusters and the molecular features of tumor cells, defining cell heterogeneity required additional analysis. For this, we used nonparametric differential gene expression analysis, including a rank product (RP) methodology [22] to identify relevant differentially expressed genes between two different cell clusters. CD45 is found to express differently in CTC cells and primary tumor cells.

The first step was to analyze the differentially expressed genes between cell clusters 3 and 5. There were 63 differentially expressed genes and 476 edges in this gene-gene network. Through MFR algorithm analysis, we found three important hub node genes. Pathway and process enrichment analysis gave the significant biology functions, expressed in (Figure 6(a)). These hub genes play an important role in protein coding. Other similar results are shown in Figures 6(b) and 6(c).



(a)

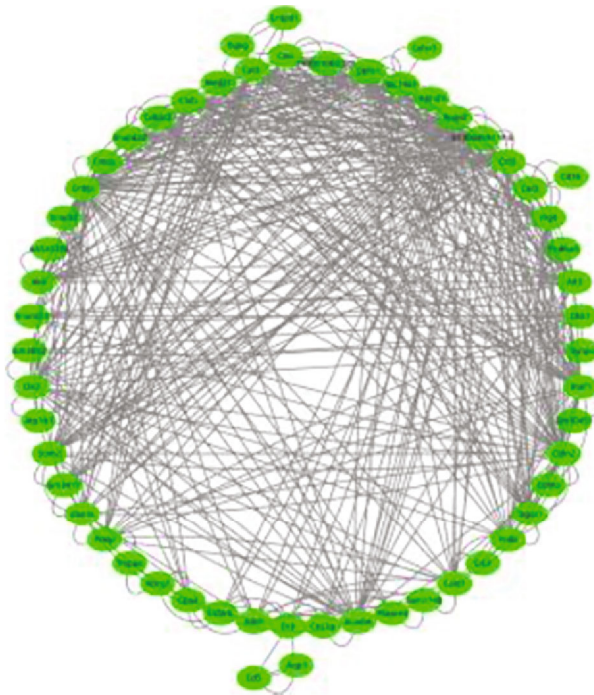


(b)

FIGURE 5: Hub nodes were generated by MRF algorithm, green nodes denote cell cluster1, red nodes denote cell cluster 3, and light blue nodes denote cell cluster 5. (a) Negative log of *P* values when calculating the significance of GO enrichment functions of high-expression genes in these hub cells are indicated by yellow bars.

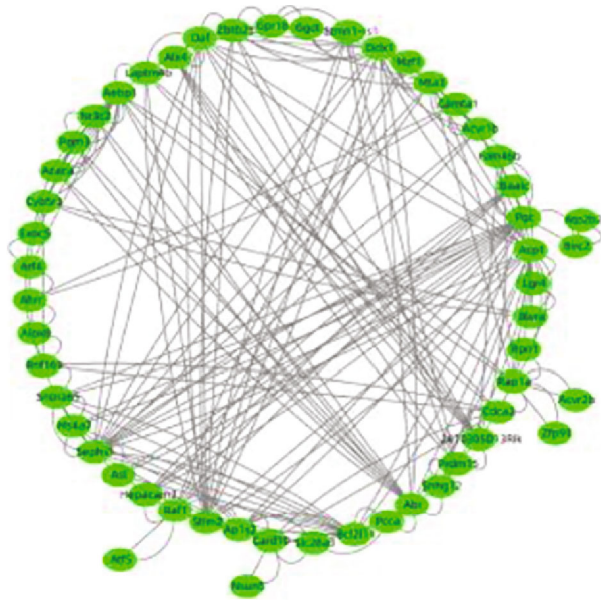
Next, we analyzed the protein-protein interaction enrichment translated by these differentially expressed genes from CTC cell clusters and tumor cell clusters. We obtained the protein-protein network by protein-protein interaction enrichment analysis (*P* value <0.05). Then, we used a molecular complex detection (MCODE) algorithm, obtaining the function enriched protein modules shown in Figure 7. Function enrichment analysis demonstrated that these proteins

were mostly involved in cancer pathways, cytokine-mediated signaling pathways, and interleukin signaling, which are all important pathways in tumor evolution. We found that the difference between CTC cell clusters and tumor cell clusters was mainly caused by these different gene functions. As indicated in that study, our method based on scRNA-seq data enabled the discovery of minor subgroups of CTC cells that were related to immunosuppression or cancer metastasis.



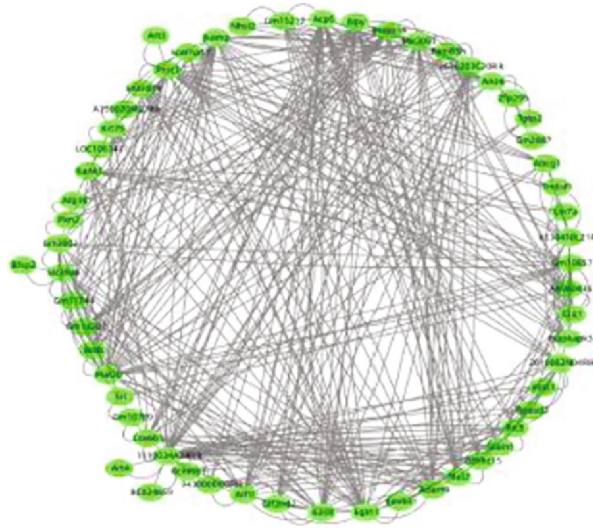
Gene name	Gene function
Cldn2	claudin 2
Rplp0	ribosomal protein, large, P0
Cnbp	cellular nucleic acid binding protein

(a)



Gene name	Gene function
Ddx1	DEAD box helicase 1
Cdca2	cell division cycle associated 2
Sephs1	selenophosphate synthetase 1

(b)



Gene name	Gene function
vnaaf2	dynein, axonemal assembly factor 2
Egl1	egl-9 family hypoxia-inducible factor 1
Ma:2b	methionine adenosyltransferase II, beca

(c)

FIGURE 6: (a) Gene network of differentially expressed genes between cell clusters 3 and 5 and hub node genes. (b) Gene network of differentially expressed genes between cell clusters 1 and 3 and hub node genes. (c) Gene network of differentially expressed genes between cluster 1 and cluster 5.

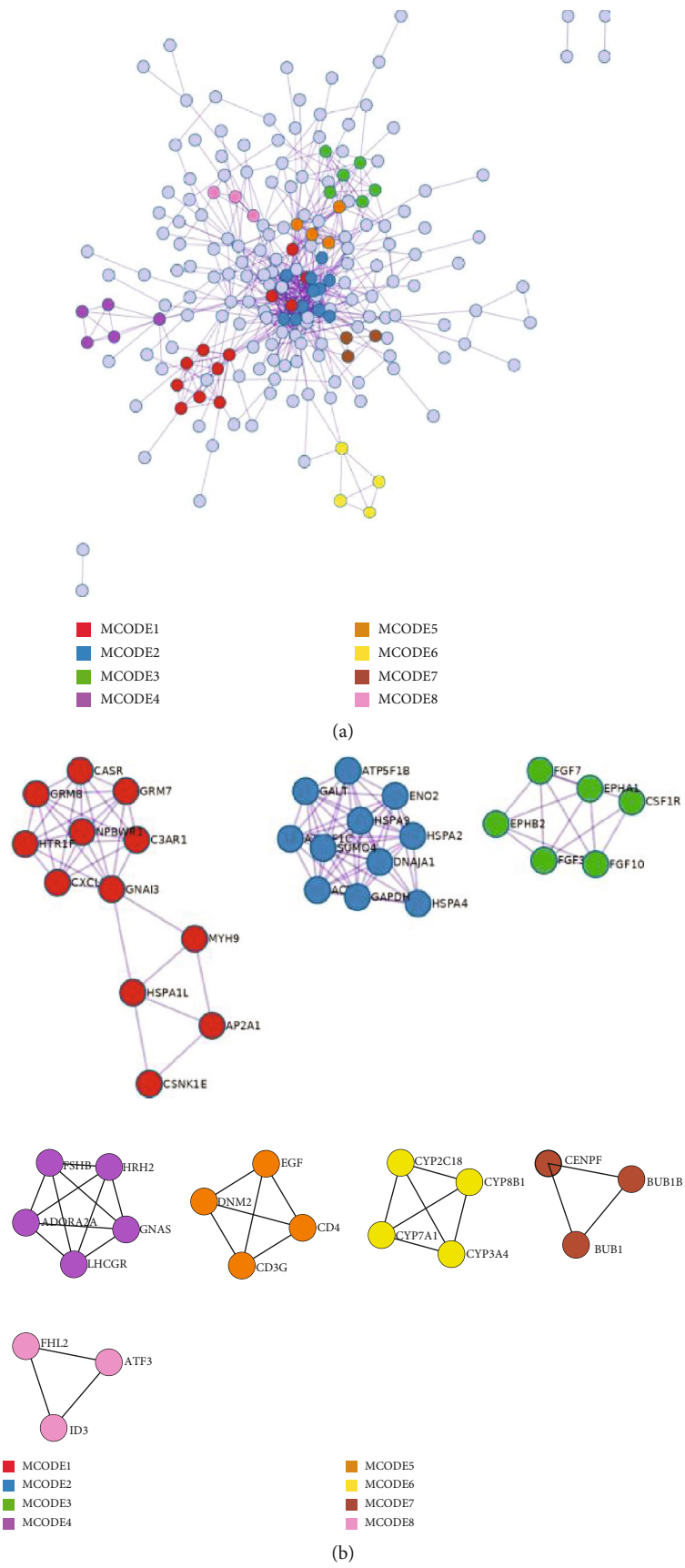


FIGURE 7: (a) Protein fully connected interaction network. Different colors denote different protein modules. (b) Enriched protein clusters in the protein-protein network translated by these differentially expressed genes.

TABLE 2: Results of cell type functional annotations found by MixtureERGM model.

Cluster ID	GO annotations
1	Epithelial cells
2	Chondrocytes
3	CD8+ T-cells
4	Macrophages
5	Fibroblasts
6	B-cells
7	Endothelial cells

3.2.2. *Triple-negative breast cancer (TNBC)*. TNBC is the most vicious subtype of breast cancer usually with bad prognosis. The identification of cell types using scRNA-seq technology promoted to identify the constitution of cell types, followed by differentially expressed genes or “marker gene” which maybe related with prognosis [12]. We downloaded the TNBC single-cell RNA-seq data, which included 1534 cells, from the GEO database (<https://www.ncbi.nlm.nih.gov/geo/>). Similar to the scheme for CTC data, we introduced the MixtureERGM and MRF model into this single-cell gene expression profile and obtained cell type classifications and hub nodes in the cell-cell network. We divided these 1534 cells into 15 clusters, where there were 7 GO-enriched cell types. Table 2 gave the results of cell type functional annotations, where P value < 0.001 (here, we adopted a more strictly hypergeometric test level than that in Table 1). We also give the comparison results with the role analysis clustering algorithm in Table 1(b).

In order to introduce how cell moved through biological progress in pseudo time, we employed the Monocle algorithm proposed by Trapnell et al., for which we chose the different expressing genes among our cell clusters. Figure 8 shows these single-cell trajectories, where CD8+ T-cell (cluster 3 in our clustering results) and macrophages (cluster 4 in our clustering results) have similar branching trajectories. This is consistent with the high coexpression gene patterns. Genes “JUNB,” “DUSP1,” “FOS,” “EGR1,” “KRT19,” “KRT8,” and “SPARC” were all marker genes in both of these clusters. Figure 9 shows a two-dimensional projection of expressing pattern for the “KRT19” and “KRT8” genes in different cells, which illustrates the consistently high expression in the typical cell subgroups.

The final stage was to deeply exploit these specific expressed genes. First, we performed enrichment analysis in the PaGenBase (a pattern gene database for the global and dynamic understanding of gene function) [23]. The FOS, KRT8, and KRT19 genes belong to specific breast cells (P value = 0.00136). Next, we adopted a comprehensive platform integrating information on human disease-associated genes—DisGeNET [24]—and found several of these genes to be closely related with other malignant tumors. For example, DUSP1, JUNB, and SPARC genes were significantly related with Endometrioid (P value = 0.0082); DUSP1, EGR1, FOS, and JUNB genes were significantly related with lung tumor (P value = 0.0074); more results are given in Figures 10(a) and 10(b).

It is worth mentioning that we also found several genes to be significantly related with COVID [25]. For example: genes DUSP1, EGR1, FOS, and JUNB are enriched in GO COVID245. These genes are functioned as RNA-Wilk-CD14+monocytes, which is related with patient-C1A-mild-down. More results could be found in Table 3. From the functional category results, we can see that most of these genes are involved in the CD14+monocyte function, which is an important role in the immune system (see Figure 10(c)).

4. Discussion

In this study, we introduced the MixtureERGM MRF model into single-cell RNA-seq data, demonstrating that the algorithm can perform effective clustering and simultaneously find the hub nodes in cell networks. We also compare our approach with another method of network clustering algorithm: role analysis which is focused on finding roles of nodes in networks. It extracts a network into several ego-networks, in which every node is interlinked with the others. However, this assumption would destroy the inherent correlation of one network and may amplify the conditional correlation, which is not real connections among nodes. In contrast, the MixtureERGM model considers the joint probability of the observed network proportional to the exponent of the sum of the subnetwork statistics, where $S(Y)_{ij}$ are different network statistics according to the belongings of nodes i and j . For the relationships between two different subnetworks, we adopted the Hidden Markov random field model to prioritize hub nodes with network rewiring. The MixtureERGM and MRF models fit the cell-cell network with graph angle, which overcomes the high-dimension problems in single-cell RNA-seq data. RNA-seq data is generally on the scale of tens of thousands, which can greatly complicate the clustering problem.

We applied the MixtureERGM network clustering model and MRF algorithm to find the heterogeneity and hub nodes of two datasets. In the first dataset, cluster 1 is consistent with pancreatic dual adenocarcinoma (PDAC) cell lines, cluster 3 is consistent with classical CTCs, and cluster 5 is consistent with the primary tumor cells clustered by Ting et al. From the heat map (Figure 3), it is clear that genes within the same cluster have a strong correlation, while there are marked differences between genes in different clusters. Meanwhile, we used a non-parametric differential gene expression analysis including rank product (RP) methodology to identify relevant differentially expressed genes between two different cell clusters. Finally, we analyzed the protein-protein interaction enrichment translated by these differentially expressed genes from CTC cell clusters and tumor cell clusters. We found that the difference between CTC cell clusters and tumor cell clusters is mainly caused by these different gene functions. Identifying immune cell subtypes and their distribution is important to reveal immune cell infiltration patterns among different patients, which may provide an opportunity for the design of personalized treatments. With the second dataset, we obtained the trajectories for different cell types using our methodology, as well as the different expression genes across different cell clusters. Specifically, we found seven important marker genes

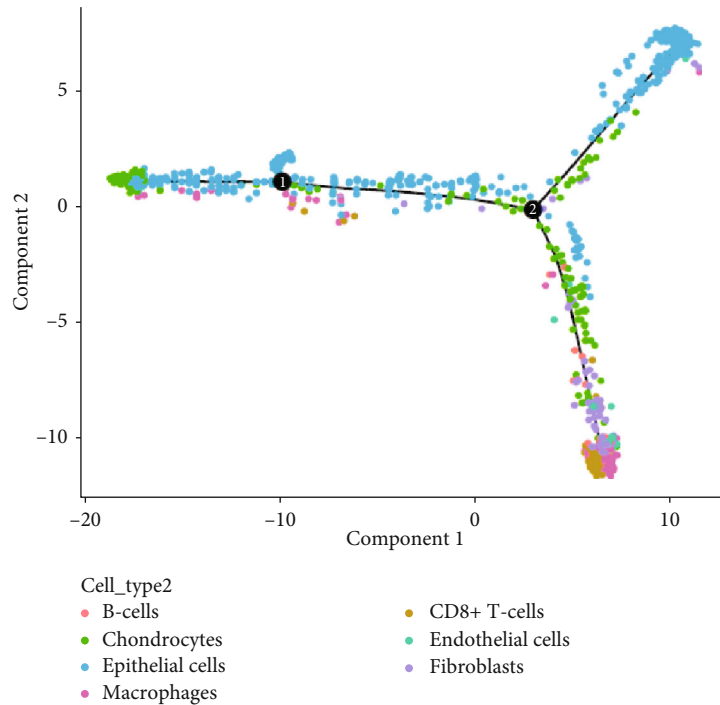


FIGURE 8: Single-cell trajectory results. Different color nodes represent different cells.

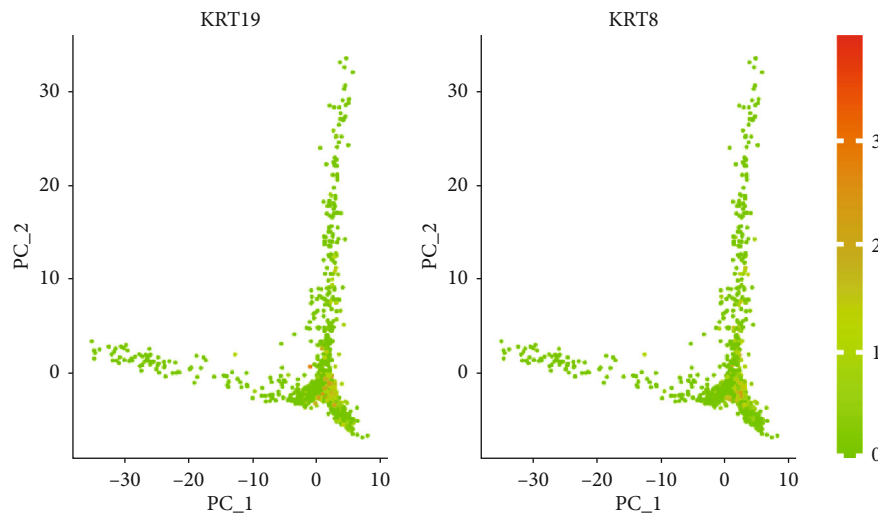


FIGURE 9: Genes “KRT19” and “KRT8” expressing pattern in different cells.

playing important roles in the immune system, all of which were closely linked to generic cancer genes.

As the statement of Zhang et al. [8], there have been many scRNA data analysis tools, with different advantages and disadvantages. For avoiding the model-based methods heavily depending on whether the data fit the model, they present one multiple kernel combination methods, which could automatically learn similarity information from scRNA-seq data and transform the candidate solution into a new one. Different with the kernel learning method, our method was focused on clustering cells according to their

network property, determined by the correlation of gene expression profiles. So we did not compare these two methods in different directions. However, some limitations of our method can be found. (i) The computation time would rapidly increase when the cell numbers are more than ten thousands. (ii) The number of clusters needs to be determined in advance, which may lead to subjective assumptions by researchers. In the future, we will continue improving efficiency and effectiveness of the network clustering algorithm based on characteristics of scRNA-seq data.

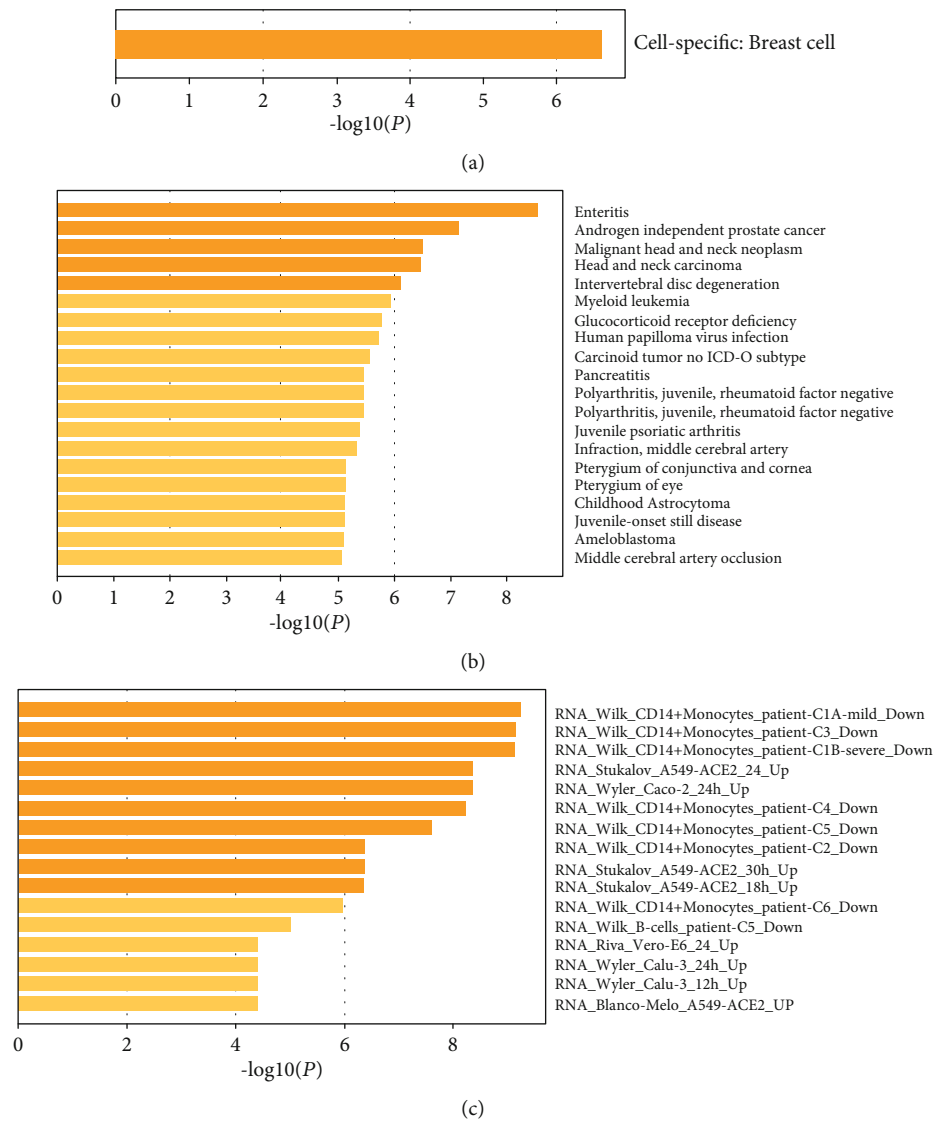


FIGURE 10: Enrichment function items of genes “JUNB,” “DUSP1,” “FOS,” “EGR1,” “KRT19,” “KRT8,” and “SPARC.” (a) Cell category in which genes high expressed, (b) comparison with the information on human disease-associated genes, and (c) comparison with COVID gene functional dataset.

TABLE 3: Genes found to be significantly related with COVID.

GO items	GO functions	<i>P</i> value	Gene names
COVID245	RNA_Wilk_CD14+monocytes_patient-C1A-mild_down	0.0001	DUSP1 EGR1 FOS JUNB
COVID191	RNA_Stukalov_A549-ACE2_24h_up	0.00025	DUSP1 EGR1 FOS JUNB
COVID046	RNA_Wyler_Caco-2_24h_up	0.00025	DUSP1 EGR1 FOS JUNB
COVID253	RNA_Wilk_CD14+monocytes_patient-C4_down	0.00027	DUSP1 EGR1 FOS JUNB
COVID189	RNA_Stukalov_A549-ACE2_18h_up	0.0017	DUSP1 EGR1 JUNB
COVID257	RNA_Wilk_CD14+monocytes_patient-C6_down	0.0025	DUSP1 FOS JUNB
COVID346	RNA_Wilk_B-cells_patient-C5_down	0.0067	DUSP1 FOS JUNB

Data Availability

Datasets in this article were held in the NCBI Gene Expression Omnibus with the accession numbers GSE51372 and GSE118389.

Conflicts of Interest

The authors confirm that there are no conflicts of interest.

Authors' Contributions

Yishu Wang and Dongmei Ai conceived and designed the im-ERGM and MRF models. Xuehan Tian implemented the simulation study and real dataset analysis, Y.W. wrote the experiment codes. Y.W. and D.A. wrote the whole manuscript. All authors have participated sufficiently in the work to take responsibility for it. All authors have reviewed the final manuscript and approve it for publication.

Acknowledgments

This work is supported by the National Natural Science Foundation of China (no. 3161194) and the National Science Foundation of China (no. 61873027).

References

- [1] Y. Wang, H. Fang, D. Yang, H. Zhao, and M. Deng, "Network clustering analysis using mixture exponential-family random graph models and its application in genetic interaction data," *IEEE/ACM Transactions on Computational Biology and Bioinformatics*, vol. 16, no. 5, pp. 1743–1752, 2019.
- [2] T. R. Golub, D. K. Slonim, P. Tamayo et al., "Molecular classification of cancer: class discovery and class prediction by gene expression monitoring," *Science*, vol. 286, no. 5439, pp. 531–537, 1999.
- [3] S. Y. Park, M. G'onen, H. J. Kim, F. Michor, and K. Polyak, "Cellular and genetic diversity in the progression of in situ human breast carcinomas to an invasive phenotype," *The Journal of clinical investigation*, vol. 120, no. 2, pp. 636–644, 2010.
- [4] D. Ramsköld, S. Luo, Y.-C. Wang et al., "Full-length mRNA-Seq from single-cell levels of RNA and individual circulating tumor cells," *Nature Biotechnology*, vol. 30, no. 8, pp. 777–782, 2012.
- [5] G. M. Cann, Z. G. Gulzar, S. Cooper et al., "mRNA-Seq of single prostate cancer circulating tumor cells reveals recapitulation of gene expression and pathways found in prostate cancer," *PLoS ONE*, vol. 7, no. 11, p. e49144, 2012.
- [6] S. Islam, U. Kjallquist, A. Moliner et al., "Characterization of the single-cell transcriptional landscape by highly multiplex RNA-seq," *Genome Research*, vol. 21, no. 7, pp. 1160–1167, 2011.
- [7] G. K. Marinov, B. A. Williams, K. McCue et al., "From single-cell to cell-pool transcriptomes: stochasticity in gene expression and RNA splicing," *Genome Research*, vol. 24, no. 3, pp. 496–510, 2014.
- [8] Z. Zhang, F. Cui, C. Wang, L. Zhao, and Q. Zou, "Goals and approaches for each processing step for single-cell RNA sequencing data," *Briefings in Bioinformatics*, vol. 1, 2020.
- [9] E. Y. Cho, M. H. Chang, Y. L. Choi et al., "Potential candidate biomarkers for heterogeneity in triple-negative breast cancer (TNBC)," *Cancer chemotherapy and pharmacology*, vol. 68, no. 3, pp. 753–761, 2011.
- [10] A. A. Kolodziejczyk, J. K. Kim, J. C. H. Tsang et al., "Single cell RNA-sequencing of pluripotent states unlocks modular transcriptional variation," *Cell stem cell*, vol. 17, no. 4, pp. 471–485, 2015.
- [11] Y. Huang, X. Yu, N. Sun, N. Qiao, and Y. Cao, "Single-cell-level spatial gene expression in the embryonic neural differentiation niche," *Genome research*, vol. 25, no. 4, pp. 570–581, 2015.
- [12] Z. Wang, H. Ding, and Q. Zou, "Identifying cell types to interpret scRNA-seq data: how, why and more possibilities," *Briefings in functional genomics*, vol. 19, no. 4, pp. 286–291, 2020.
- [13] M. Salter-Townshend and T. B. Murphy, "Role analysis in networks using mixtures of exponential random graph models," *Journal of Computational and Graphical Statistics*, vol. 24, no. 2, pp. 520–538, 2015.
- [14] J. Besag, "Statistical analysis of non-lattice data," *The statistician*, vol. 24, no. 3, p. 179, 1975.
- [15] D. M. Titterton, "Recursive parameter estimation using incomplete data," *Journal of the Royal Statistical Society Series B (Methodological)*, vol. 46, no. 2, pp. 257–267, 1984.
- [16] S. Wang and Y. Zhao, "Almost sure convergence of Titterton's recursive estimator for mixture models," *Statistics & probability letters*, vol. 76, no. 18, pp. 2001–2006, 2006.
- [17] D. T. Ting, B. S. Wittner, M. Ligorio et al., "Single-cell RNA sequencing identifies extracellular matrix gene expression by pancreatic circulating tumor cells," *Cell Reports*, vol. 8, no. 6, pp. 1905–1918, 2014.
- [18] W. Wang, J. Xu, S. Wang et al., "Single-cell RNA-seq data reveals TNBC tumor heterogeneity through characterizing subclone compositions and proportions," *bioRxiv 858290*, 2019.
- [19] M. Chen, J. Cho, and H. Zhao, "Incorporating biological pathways via a Markov random field model in genome-wide association studies," *PLoS Genetics*, vol. 7, no. 4, p. e1001353, 2011.
- [20] J. Besag, "On the statistical analysis of dirty pictures," *Journal of the Royal Statistical Society: Series B (Methodological)*, vol. 48, pp. 259–302, 1986.
- [21] C. Biernacki, G. Celeux, and G. Govaert, "Assessing a mixture model for clustering with the integrated completed likelihood," *IEEE Transactions on Pattern Analysis and Machine Intelligence*, vol. 22, no. 7, pp. 719–725, 2000.
- [22] R. Breitling, P. Armengaud, A. Amtmann, and P. Herzyk, "Rank products: a simple, yet powerful, new method to detect differentially regulated genes in replicated microarray experiments," *FEBS Letters*, vol. 573, no. 1-3, pp. 83–92, 2004.
- [23] J.-B. Pan, S.-C. Hu, D. Shi et al., "PaGenBase: a pattern gene database for the global and dynamic understanding of gene function," *PLoS One*, vol. 8, no. 12, p. e80747, 2013.
- [24] J. Piñero, À. Bravo, N. Queralt-Rosinach et al., "DisGeNET: a comprehensive platform integrating information on human disease-associated genes and variants," *Nucleic acids research*, vol. 45, no. D1, pp. D833–D839, 2017.
- [25] <https://metascape.org/COVID>.

Research Article

Identification of Molecular Characteristics and New Prognostic Targets for Thymoma by Multiomics Analysis

Dazhong Liu, Pengfei Zhang, Jiaying Zhao, Lei Yang, and Wei Wang 

Department of Thoracic Surgery, Second Affiliated Hospital of Harbin Medical University, Harbin 150086, China

Correspondence should be addressed to Wei Wang; h05732@hrbmu.edu.cn

Received 16 January 2021; Revised 16 March 2021; Accepted 1 April 2021; Published 20 May 2021

Academic Editor: Tao Huang

Copyright © 2021 Dazhong Liu et al. This is an open access article distributed under the Creative Commons Attribution License, which permits unrestricted use, distribution, and reproduction in any medium, provided the original work is properly cited.

Background. Thymoma is a heterogeneous tumor originated from thymic epithelial cells. The molecular mechanism of thymoma remains unclear. **Methods.** The expression profile, methylation, and mutation data of thymoma were obtained from TCGA database. The coexpression network was constructed using the variance of gene expression through WGCNA. Enrichment analysis using clusterProfiler R package and overall survival (OS) analysis by Kaplan-Meier method were carried out for the intersection of differential expression genes (DEGs) screened by limma R package and important module genes. PPI network was constructed based on STRING database for genes with significant impact on survival. The impact of key genes on the prognosis of thymoma was evaluated by ROC curve and Cox regression model. Finally, the immune cell infiltration, methylation modification, and gene mutation were calculated. **Results.** We obtained eleven coexpression modules, and three of them were higher positively correlated with thymoma. DEGs in these three modules mainly involved in MAPK cascade and PPAR pathway. LIPE, MYH6, ACTG2, KLF4, SULT4A1, and TF were identified as key genes through the PPI network. AUC values of LIPE were the highest. Cox regression analysis showed that low expression of LIPE was a prognostic risk factor for thymoma. In addition, there was a high correlation between LIPE and T cells. Importantly, the expression of LIPE was modified by methylation. Among all the mutated genes, GTF2I had the highest mutation frequency. **Conclusion.** These results suggested that the molecular mechanism of thymoma may be related to immune inflammation. LIPE may be the key genes affecting prognosis of thymoma. Our findings will help to elucidate the pathogenesis and therapeutic targets of thymoma.

1. Introduction

Thymoma is the most common anterior mediastinal compartment tumor, originating from the thymic epithelial cell population [1]. The incidence of thymomas is approximately 2.5 cases per million people per year, with an age distribution ranging from 10 to 80 years [2]. In addition, thymoma is often associated with autoimmune diseases, especially myasthenia gravis (MG) [3, 4]. However, the potential molecular oncogenesis of thymoma remains unknown. Generally, when a thymoma is diagnosed, the patient will receive surgical treatment. For stages III and IV patients, the 5-year survival rates were 74% and <25%, respectively [5]. At present, neither surgeon nor physician can predict the prognosis and metastasis status of thymoma patients through X-ray examination, nor can detailed treatment plan be formulated before

operation [6]. Obviously, the establishment of additional predictors is very beneficial for the identification and treatment of thymoma.

The pathogenesis of thymoma is various, and the rapid development of “genome” technology, including whole-genome expression analysis and next-generation sequencing (NGS), provides new means to explore the complexity and map of genomic alterations in thymoma [7–9]. Epigenetic modifications, including epigenetic alterations, are a feature of cancer because they play an important role in the process of carcinogenesis [10, 11]. In addition, the thymus provides a special microenvironment for the development and selection of mature T cells. Recent evidence suggests that immune responses such as T cells are involved in the development of thymoma [12, 13]. However, the understanding of the pathogenesis of thymoma is still limited.

In recent years, with the development of molecular biology, more and more research projects have begun to explore methods to accurately predict the prognosis of thymoma. In this study, we used multiomics datasets from the tumor genome map (TCGA). The results may be helpful to understand the pathogenesis of thymoma and identify LIPE as a potential new therapeutic target through bioinformatics analysis. The novelty of this work is that we combined the variance and difference of gene expression to screen the genes related to the prognosis of thymoma through coexpression network and PPI network. Then, the key genes were further screened by methylation modification.

2. Materials and Methods

2.1. TCGA Dataset Processing and Coexpression Analysis. Thymoma mRNA-seq expression data, methylation data, mutation data, and clinical materials were obtained from TCGA website (<https://portal.gdc.cancer.gov/>). The variance of gene expression was calculated, and the top 1/4 genes were intercepted for coexpression analysis through weighted gene coexpression network analysis (WGCNA).

2.2. Screening of Differentially Expressed Genes. The differentially expressed genes (DEGs) between thymoma and control were identified by limma R package. Set the filtering threshold $P < 0.05$.

2.3. Construction of PPI Network. The gene was mapped into the STRING database (<https://string-db.org>) to obtain the protein-protein interaction (PPI) network. A significant PPI network was obtained by comprehensive score ≥ 0.7 , which was demonstrated by the Cytoscape software. The selection of key genes was based on their association with other proteins: genes with higher connectivity were considered to play an important role in the PPI network [14, 15].

2.4. Enrichment Analysis. In order to analyze the biological functions and signaling pathways of differentially expressed genes in thymoma-related modules, we performed enrichment analysis. Gene Ontology (GO) and the Kyoto Encyclopedia of Genes and Genomes (KEGG) were enriched by clusterProfiler R package. $P < 0.05$ was the threshold used for the significant terms. Gene set enrichment analysis (GSEA) was performed with the GSEA software for genes [16, 17].

2.5. Differential Methylation and Mutation Analysis. The quality of the original probe data obtained from the methylated microarray was checked, including background correction, probe type difference adjustment, and probe exclusion. According to these in sample standardized procedures, DNA methylation was scored as a β value. We used samr R package for differential methylation analysis. For a CpG site to be considered differentially methylated, the difference in the median β value in thymoma and normal samples should be at least 0.1 and the P value < 0.05 . The nonsilent mutation (gene-level) data were analyzed using Maftools R-package.

2.6. Statistical Analysis. Statistical analysis was performed using the SPSS software, version 23.0 (SPSS Inc., Chicago,

USA). Kaplan-Meier method was used to estimate the overall survival (OS). Cox regression model and Cox proportional hazards regression method were used to identify predictors of OS [18]. P value < 0.05 was considered statistically significant [19].

3. Results

3.1. Coexpression of Genes in Thymoma. According to the variance results of thymoma gene expression, the top 1/4 genes with larger variance were selected for coexpression analysis. A coexpression network consisting of 5758 genes was obtained. Taken 0.9 as the threshold of correlation coefficient, select the soft threshold as 7 (Figure 1(a)). A total of 11 coexpression modules were identified through WGCNA analysis (Figure 1(b)). In addition, we calculated the correlation between module genes and thymoma. We found that MEgreen, MEblue, and MEturquoise had the highest correlation with tumor samples (Figure 1(c)). Furthermore, 2559 differentially expressed genes (DEGs) were screened between thymoma and control group ($P < 0.05$) (Figure 1(d)).

3.2. Enrichment of Differentially Expressed Genes in Modules. Further, 913 intersection genes between DEGs and the three modules with the highest correlation were selected as the important genes for subsequent study and enrichment analysis. The results of GO enrichment showed that these genes were involved in 1234 biological processes (BP), 151 cell components (CC), and 214 molecular functions (MF). It mainly included cell growth, positive regulation of MAPK cascade, ERK1 and ERK2 cascade, response to transforming growth factor beta, and Wnt signaling pathway (Figure 2(a)). KEGG enrichment results showed a total of 40 terms, mainly involving cell adhesion molecules, ECM-receptor interaction, focal adhesion, and PPAR signaling pathway (Figure 2(b)). In addition, the GSEA results showed some of the same results as KEGG, mainly including cGMP-PKG signaling pathway, cholesterol metadata, and PPAR signaling pathway (Figure 2(c)). These same signaling pathways cover a large number of differentially expressed genes (Figure 2(d)).

3.3. Identification of Key Prognostic Genes. The overall survival (OS) analysis of selected important genes identified 88 genes with significant impact on prognosis ($P < 0.05$). Mapping these genes into the STRING database yielded a PPI network of 45 genes, which was displayed by Cytoscape (Figure 3(a)). The top six genes with the highest connectivity were analyzed in depth as key genes. Among them, the expression of MYH6 and SULT4A1 in osteosarcoma was higher than that in control group, while the expression of LIPE, ACTG2, KLF4, and TF was decreased (Figure 3(b)). In addition, high expression of LIPE and MYH6 could improve the OS of patients, and ACTG2, KLF4, SULT4A1, and TF decreased the OS of patients (Figure 3(c)). ROC curves showed that the AUC values of these six genes were all greater than 0.6, especially those of LIPE, and KLF4 and TF were greater than 0.9 (Figure 3(d)).

3.4. The Effect of Key Genes on Prognosis. Multivariate survival analysis was performed by Cox regression model, and nomogram was generated by Cox regression coefficients.

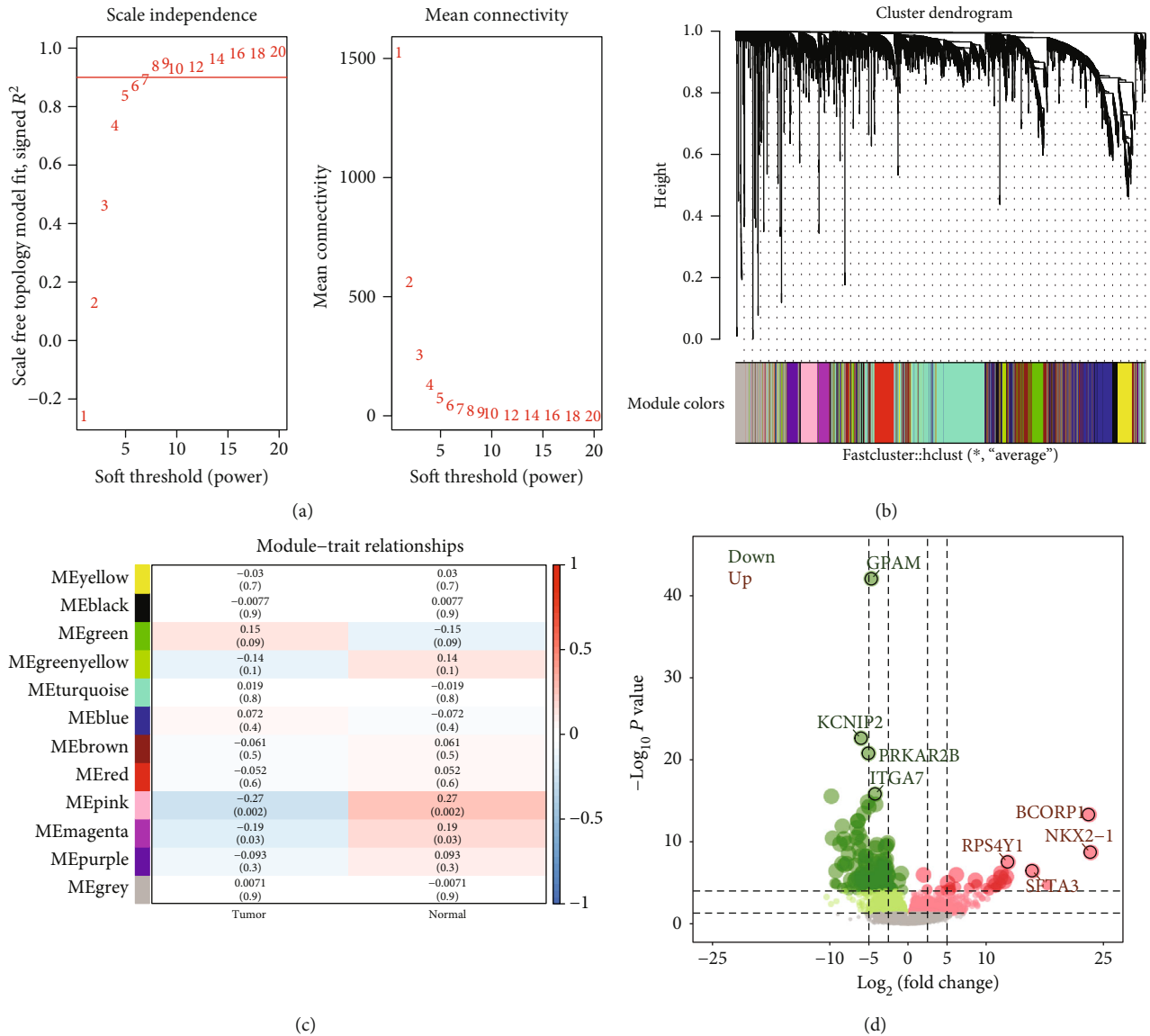
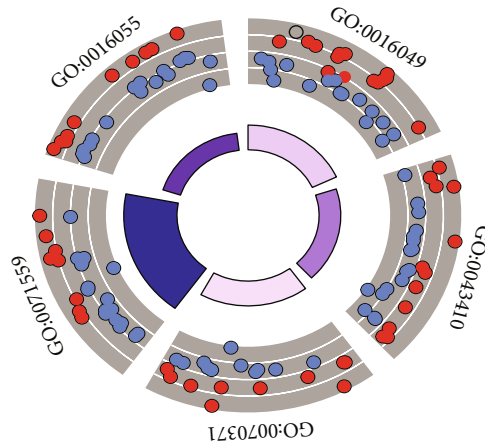


FIGURE 1: Coexpression analysis of gene expression in thymoma. (a) Determination of soft threshold power in coexpression analysis. The left image shows the scale-free fit index (y -axis) as a function of the soft-thresholding power (x -axis). The right image shows the average connectivity (degree, y -axis) as a function of the soft-thresholding power (x -axis). (b) Module cluster tree of thymoma genes with large variance. Branches with different colors correspond to different modules. (c) The correlation between module and clinical trait. Each row corresponds to a module, and each column corresponds to a feature. Each cell contains the corresponding correlation and P value. (d) The differentially expressed genes between thymoma and control. Red nodes were significantly upregulated genes, and green nodes were significantly downregulated genes.

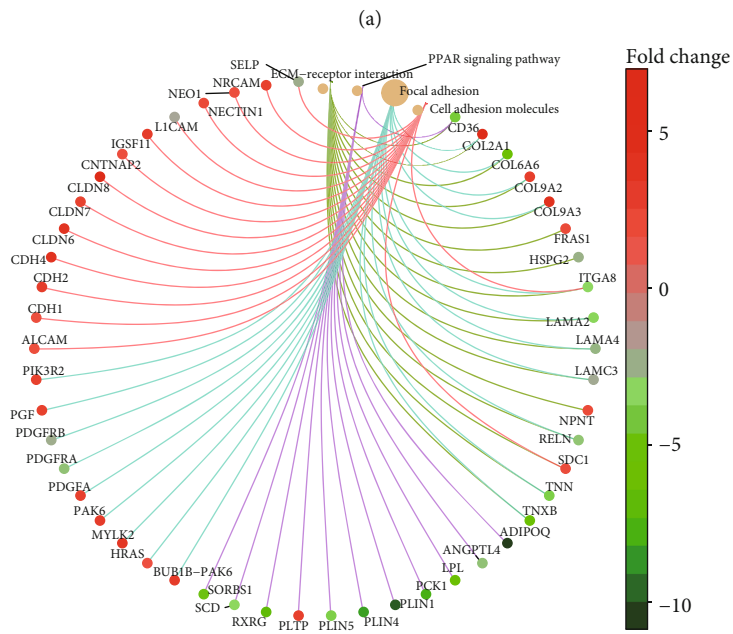
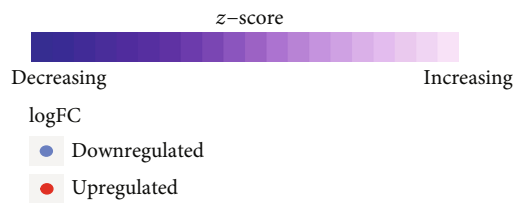
The nomogram showed that low expression of LIPE was a risk factor for predicting the overall survival time of thymoma at 5 and 8 years (Figure 4(a)). Calibration plots showed that the nomograms performed well compared with an ideal model (Figure 4(b)). In addition, Cox risk ratio model suggested that the survival rate of the high-risk population for thymoma was poor (Figure 4(c)). Among them, low expression of LIPE and MYH6 and high expression of ACTG2, KLF4, SULT4A1, and TF were important risk factors.

3.5. Changes of Immune Microenvironment in Thymoma. By comparing the immune cell infiltration between thymoma

and control, we found that dendritic cells (DC) decreased most significantly in thymoma (Figure 5(a)). These differentially infiltrated immune cells were clustered into four groups (Figure 5(b)). The strongest correlation was found between T cells and CD8 T cells or Th17 cells in thymoma tissues (Figure 5(c)). In addition, we analyzed the correlation between key genes and immune cells (Figure 5(d)). LIPE had the strongest positive correlation with T cells and Th2 cells, MYH6 had the strongest positive correlation with NK cells, TF, KLF4, and aDC had the strongest positive correlation, SULT4A1 and pDC had the strongest positive correlation, and ACTG2 and neutrophils had the strongest positive correlation.



ID	Description
GO:0016049	Cell growth
GO:0043410	Positive regulation of MAPK cascade
GO:0070371	ERK1 and ERK2 cascade
GO:0071559	Response to transforming growth factor beta
GO:0016055	Wnt signaling pathway



Category

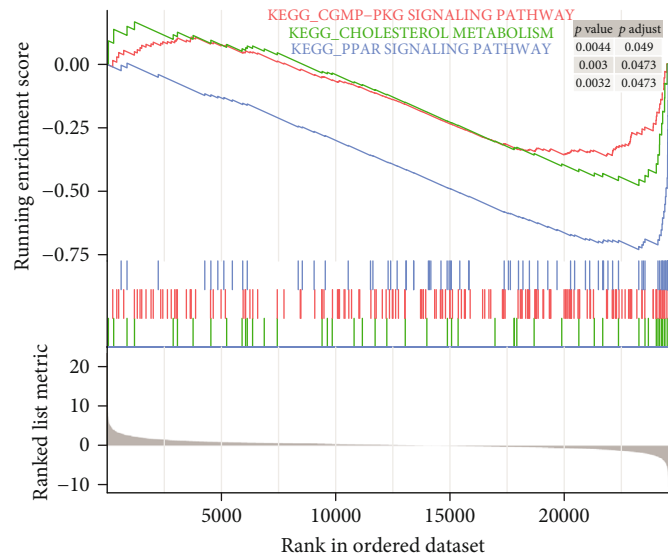
- Cell adhesion molecules
- ECM-receptor interaction
- Focal adhesion
- PPAR signaling pathway

Size

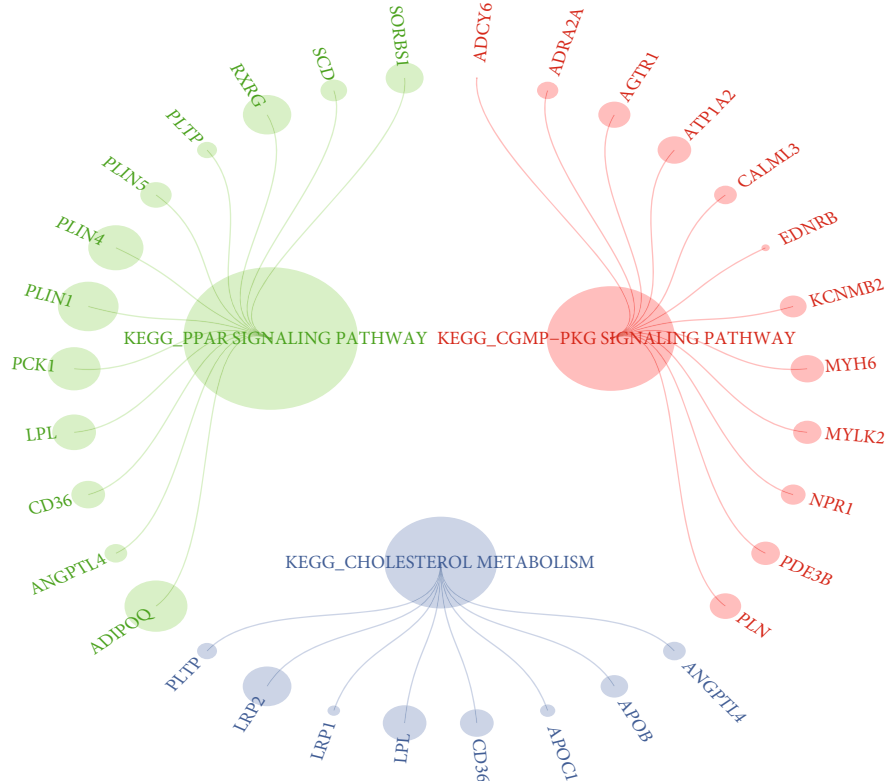
- 12
- 15
- 17
- 20

(b)

FIGURE 2: Continued.



(c)

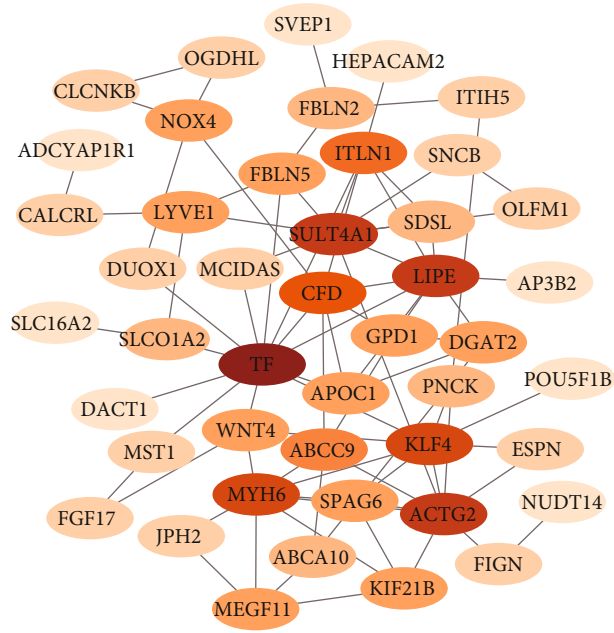


(d)

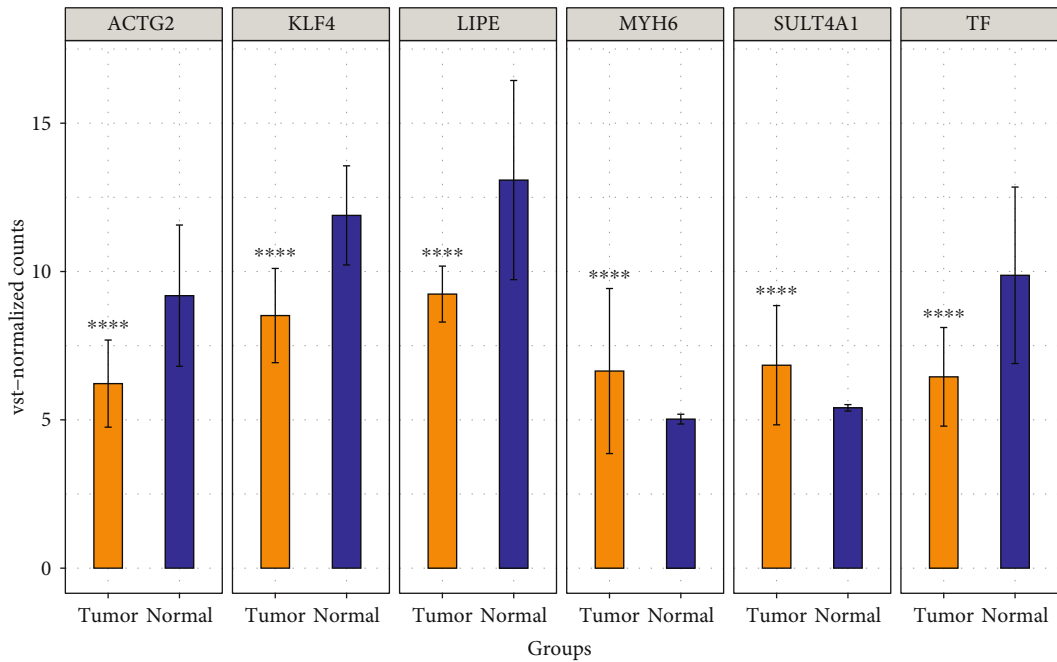
FIGURE 2: Enrichment analysis of thymoma-related module genes. (a) Important genes were involved in biological processes. Red nodes are upregulated genes, and blue nodes are downregulated genes. (b) Important genes were involved in KEGG pathway. Different line colors represent different signaling pathways which genes involved in. (c) KEGG pathway in GSEA for important genes. These pathways were significantly upregulated in thymoma. (d) The DEGs involved in the same KEGG pathway in the results of enrichment and GSEA. Different colors represent genes involved in different signaling pathways.

3.6. *Regulatory Factors Associated with Thymoma.* By comparing gene methylation modifications between thymoma and control, we obtained 943 differential methylation sites (Figure 6(a)). Among them, the methylation sites of chr1

accounted for the most, accounting for 13% (Figure 6(b)). Fourteen genes were identified as methylation factors because they had opposite levels of methylation and expression (Figure 6(c)). Among them, LIPE was significantly

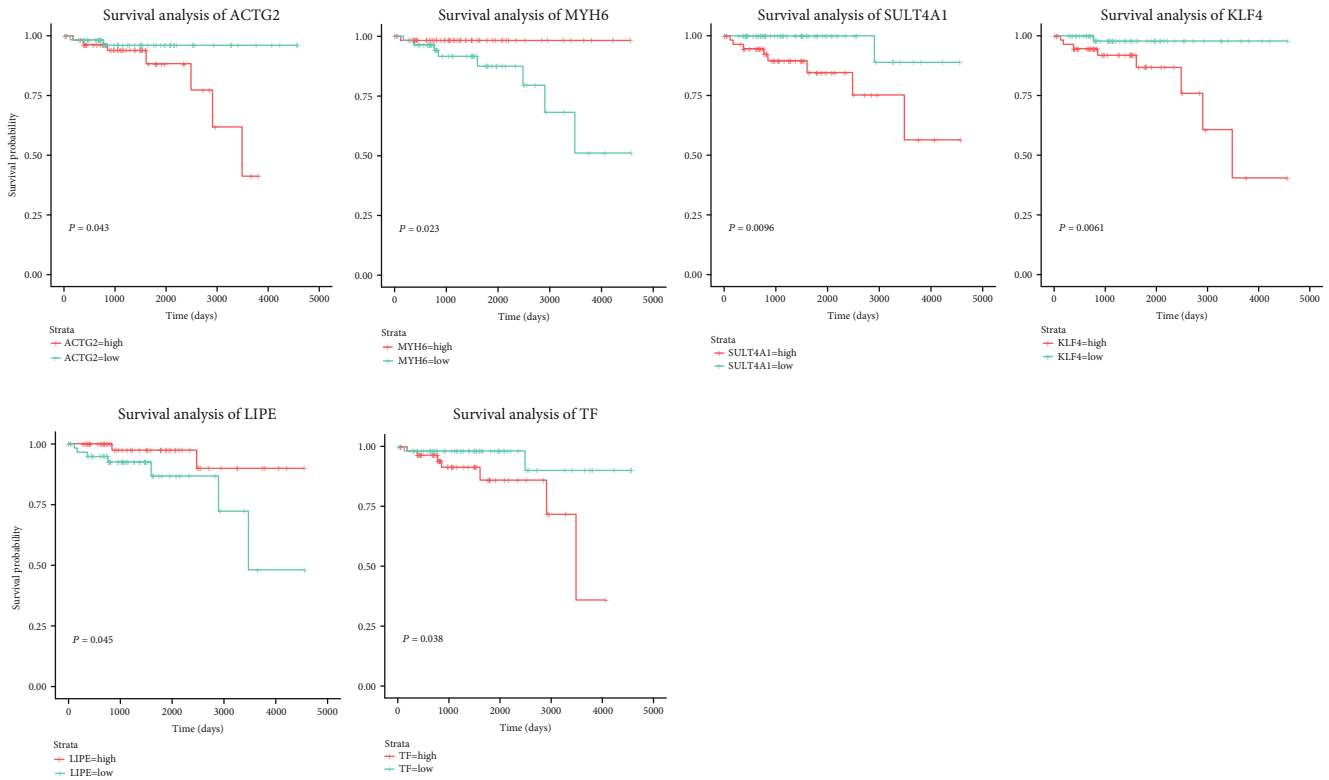


(a)

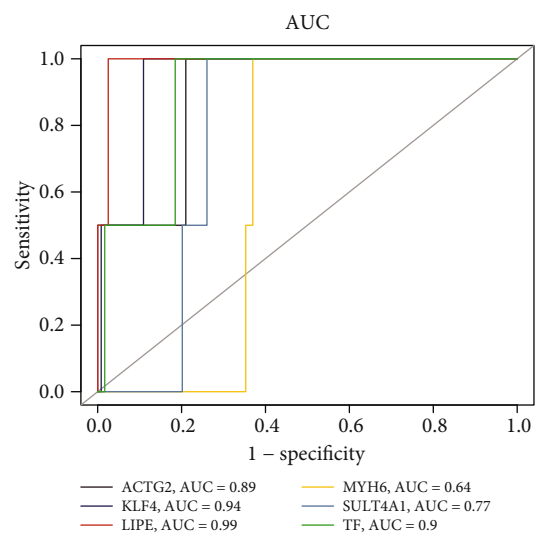


(b)

FIGURE 3: Continued.



(c)



(d)

FIGURE 3: Identification of key genes affecting overall survival of thymoma. (a) Cytoscape software shows the PPI network of important genes based on the STRING database. (b) The expression of six genes with the highest connectivity in the PPI network. *** $P < 0.001$. (c) The effect of six genes with the highest connectivity in the PPI network on the overall survival of thymoma (Kaplan-Meier plot). Red and green curves are for high expression and low expression, respectively. (d) ROC curve of key genes. Different color curves represent different genes.

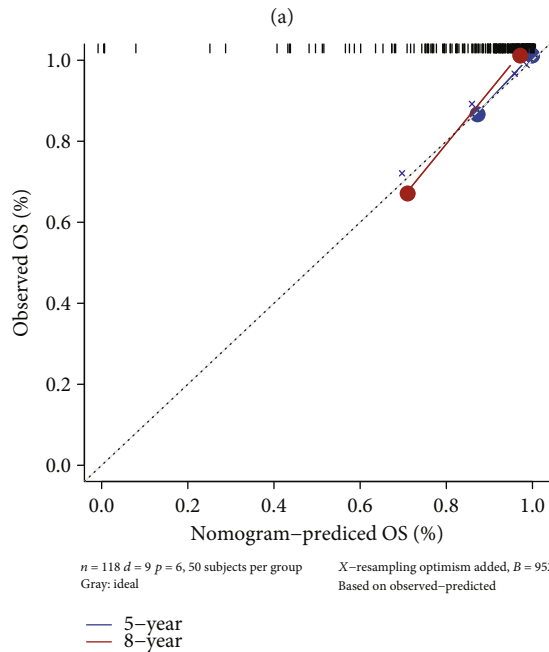
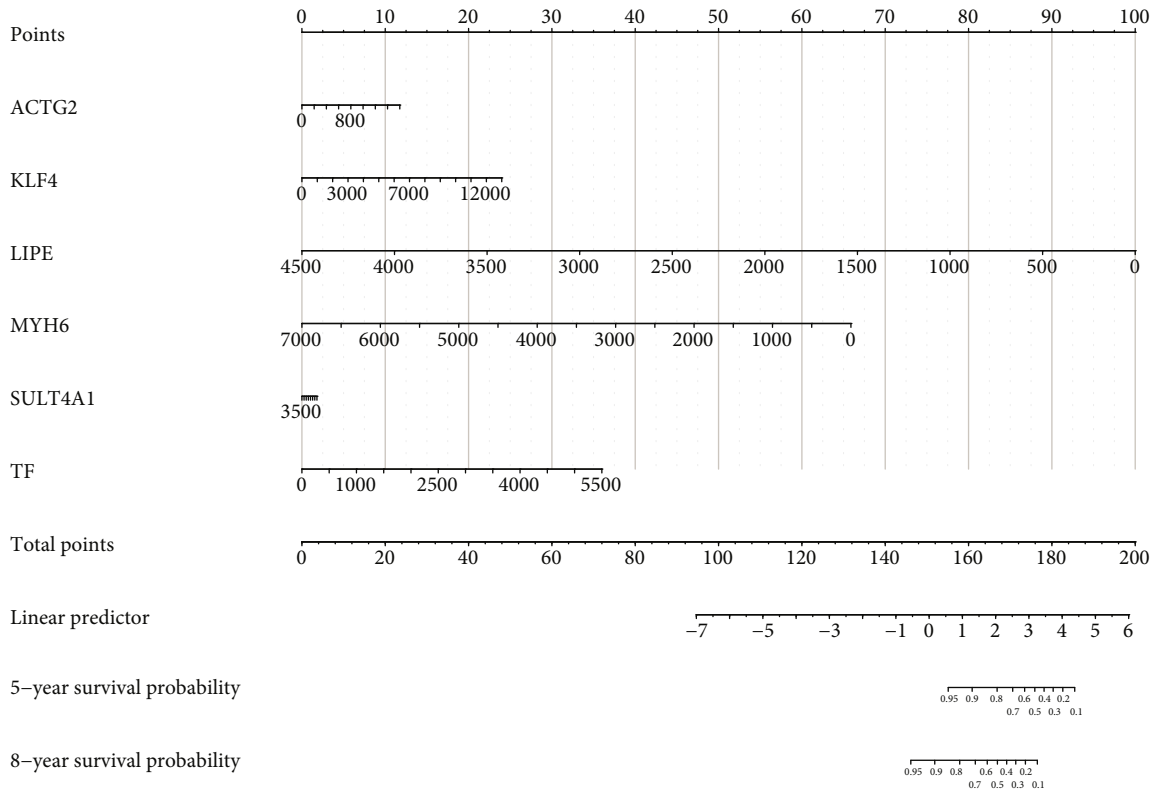
associated with OS in thymoma. In addition, GTF2I, the gene with the highest frequency of mutations in thymoma, was missense mutation in all samples (Figure 6(d)).

4. Discussion

Like other malignant tumors, the growth and proliferation of thymoma have many biological factors. However, the exact

molecular basis of thymoma occurrence remains unclear. In this study, the possible molecular mechanism and regulatory factors of thymoma were explored through multiomics.

Early studies have shown that changes in certain genes seem to be associated with the development of thymic tumors [20, 21]. Our data suggest that there is a large difference in gene expression between thymoma and control. By identifying inter-coexpression network constructed by genes with larger



(b)

FIGURE 4: Continued.

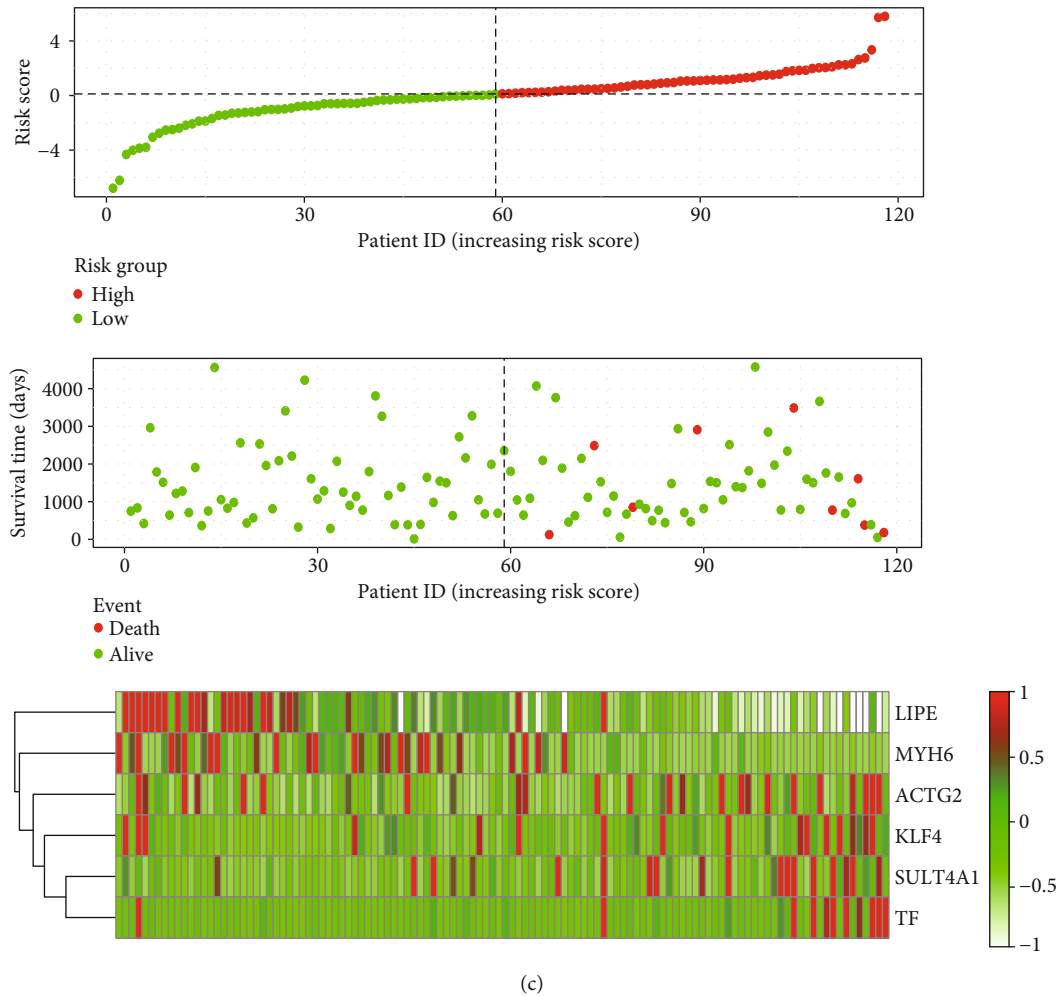


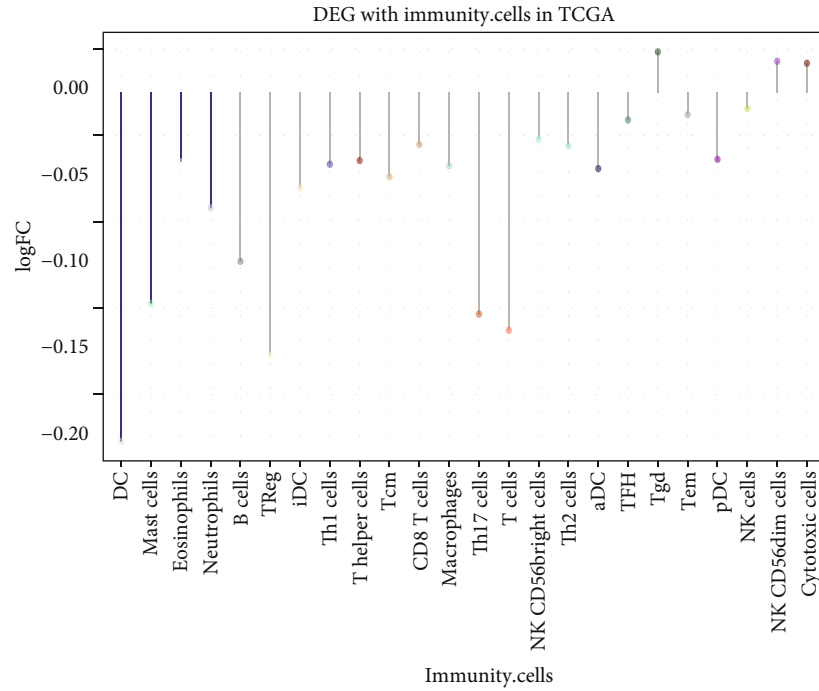
FIGURE 4: The expression of key genes affects the prognosis of patients with thymoma. (a) Nomogram for predicting overall survival in patients with thymoma. (b) Plots depict the calibration of each model in terms of agreement between predicted and observed 5-year and 8-year outcomes. (c) Risk factor correlation diagram. The green dot was the survival thymoma patient, and the red dot was the dead thymoma patient. The dotted line was the median risk score, the left side was the low-risk group, and the right side was the high-risk group.

variance, module genes with high correlation with thymoma were obtained. Intersection with differentially expressed genes yielded 913 genes possibly associated with thymoma development.

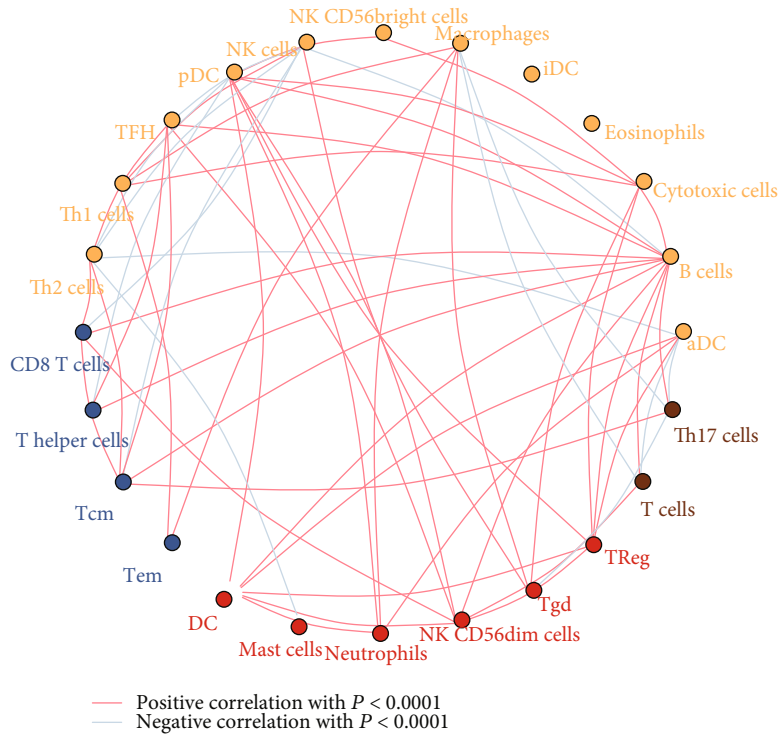
GO functional enrichment analysis is very powerful and widely used to identify biological functions of gene expression data [22]. In the GO functional enrichment results, MAPK cascade, ERK1 and ERK2 cascade, response to transforming growth factor beta (TGF- β), and Wnt signaling pathway were mainly involved. Mitogen-activated protein kinase (MAPK) is a complex and interrelated signal cascade, which is closely related to the occurrence and progress of tumor, and plays an important regulatory role in cell proliferation, differentiation, migration, and survival [23, 24]. ERK 1/2 is also an effective target for anticancer [25]. Studies have shown that MAPK signal and ERK 1/2 were significantly activated in thymoma [26]. TGF- β inhibited apoptosis and had reduced expression of IFN- γ in effector cell, a key mediator of antitumor immunity [27]. Recently, it had been

proved that Wnt pathway was activated in human thymoma, which may be involved in the tumorigenesis [28]. These findings further confirmed that a variety of inflammatory processes and cytokines were involved in the pathogenesis of thymoma.

In addition, in KEGG enrichment results, ECM also regulated intercellular communication, cell connectivity plasticity, and cell adhesion molecules interacting with various cytokines/chemokines or growth factors [29, 30]. There were 34% of the genes in the ECM-receptor interaction pathway mutated repeatedly in cancer [31]. Focal adhesion kinase (FAK) is highly expressed in thymic epithelial tumors and can be used as an independent prognostic biomarker [32]. PPAR γ overexpression more than doubled insulin-stimulated thymoma viral protooncogene phosphorylation during low lipid availability [33]. GSEA results had the same terms as KEGG enrichment results, in which cholesterol accumulation was a common feature of cancer tissues. Recent evidence showed that cholesterol played a crucial role in the progress of cancer including breast,



(a)



(b)

FIGURE 5: Continued.

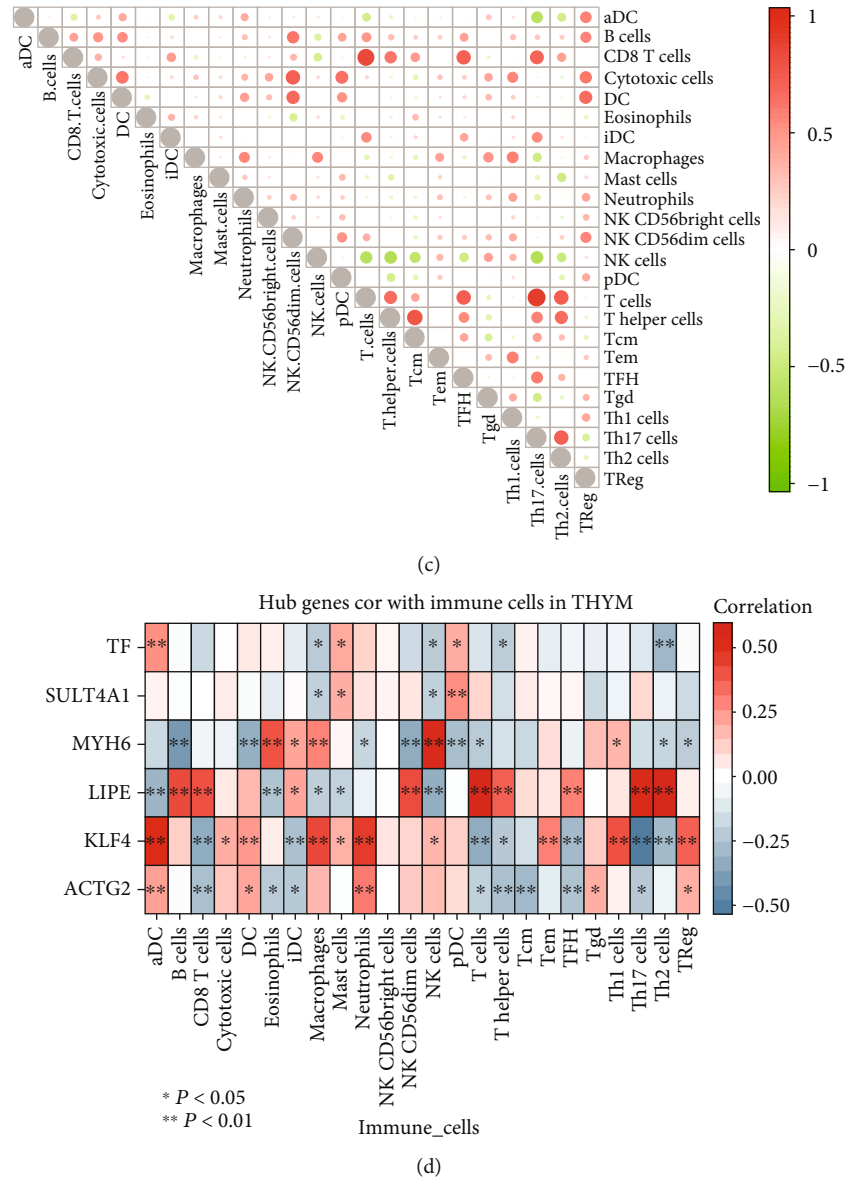
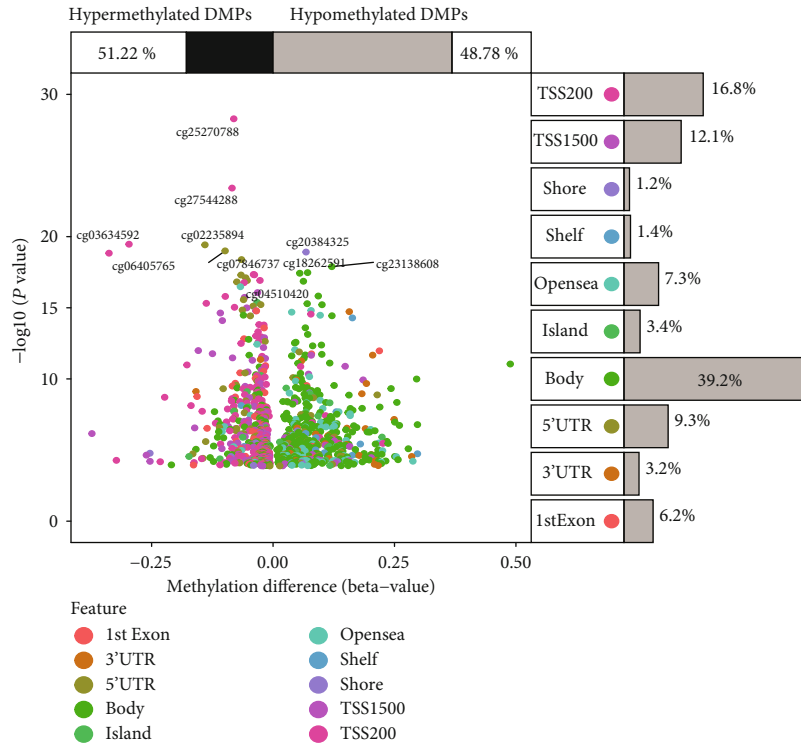


FIGURE 5: Immune cell infiltration in thymoma. (a) The difference of immune cell infiltration between thymoma and control. The blue line represents a significant difference. (b) Clustering of immunocytes with differential infiltration. The red line represents the positive correlation between immune cells, and the blue line represents the negative correlation. (c) Correlation between immune cells in thymoma. Red represents positive correlation between immune cells, and blue line represents negative correlation. The size of the node represents the size of the correlation coefficient. (d) Correlation between key genes and immune cells. Red represents positive correlation between immune cells, and blue line represents negative correlation. * $P < 0.05$ and ** $P < 0.01$.

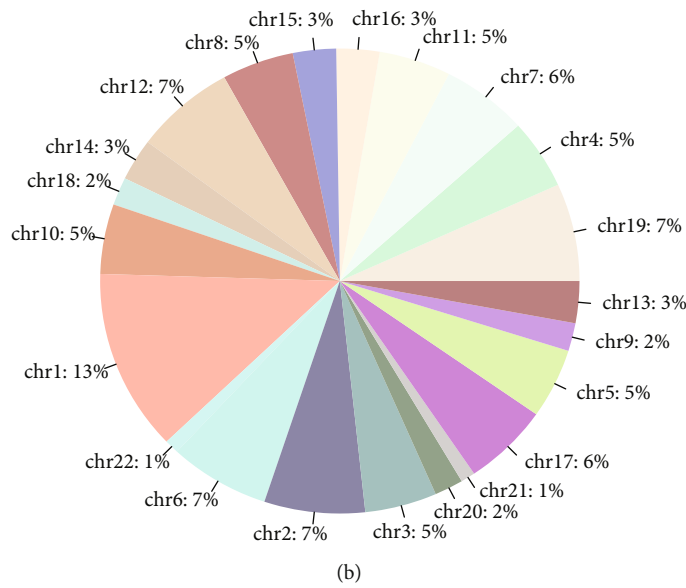
prostate, and colorectal cancer [34]. Activation of cGMP PKG signal may promote the growth of cervical cancer cells [35].

By screening the DEGs that had a significant impact on the prognosis of thymoma, we identified LIPE, MYH6, ACTG2, KLF4, SULT4A1, and TF as key genes. LIPE was also predicted as a new prognostic marker of thymoma in other studies [36]. Consistent with our analysis, MYH6 was differentially expressed in thymoma [37]. We found that MYH6 may be a potential target for thymoma. ACTG2, KLF4, SULT4A1, and TF were all involved in the occurrence or development of cancer, but their biological significance in thymoma was not clear [38–41]. This needs further study and discussion of the follow-up experiments.

From the perspective of immune microenvironment, innate immune cells such as DC and adaptive immune cells such as T cells played an important role in thymoma [13, 42, 43]. There was a strong correlation between LIPE and immune cells, suggesting that LIPE may participate in the prognosis of thymoma by regulating the immunity system. Interestingly, we found that LIPE was also a gene regulated by methylation. DNA and RNA methylation genes are commonly studied as biomarkers [44, 45], which also seems to be a way for LIPE to participate in the development of thymoma [46]. On the other hand, genetic difference in thymoma was also an effective way to screen potential therapeutic targets [9]. GTF2I mutation occurs at high frequency in thymoma and is a marker of good prognosis [47].



(a)



(b)

FIGURE 6: Continued.

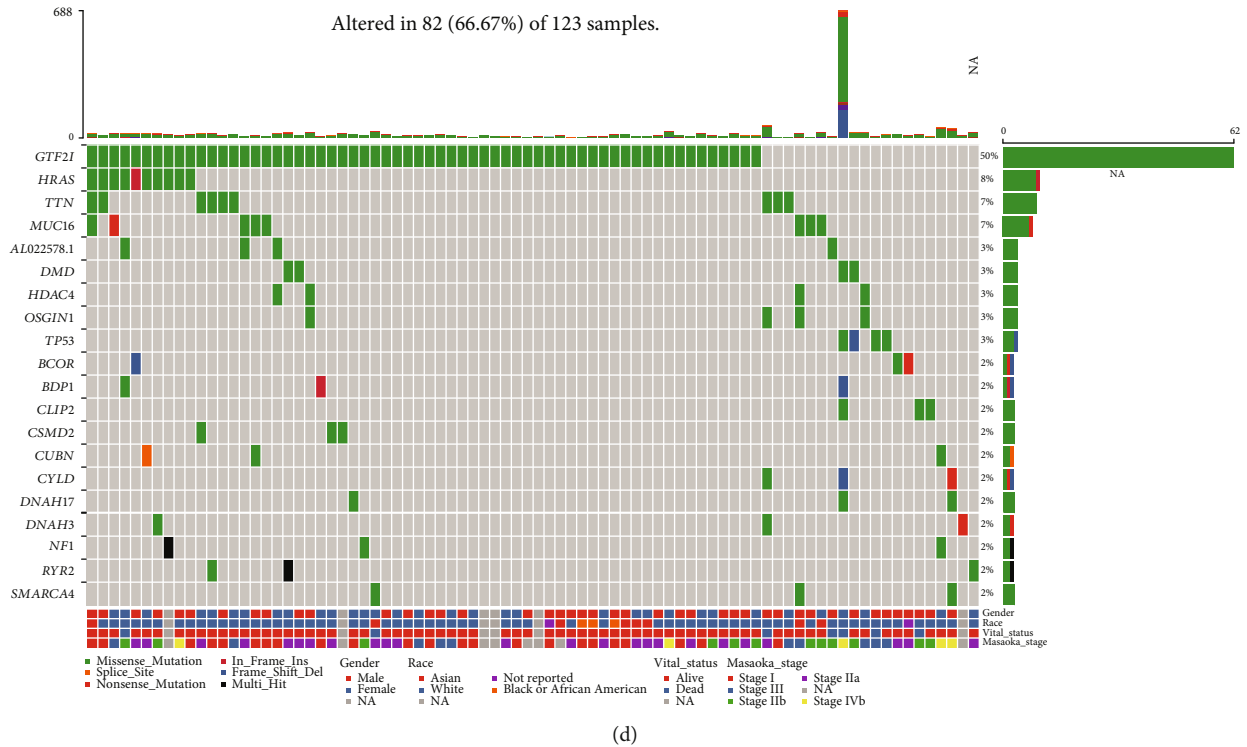
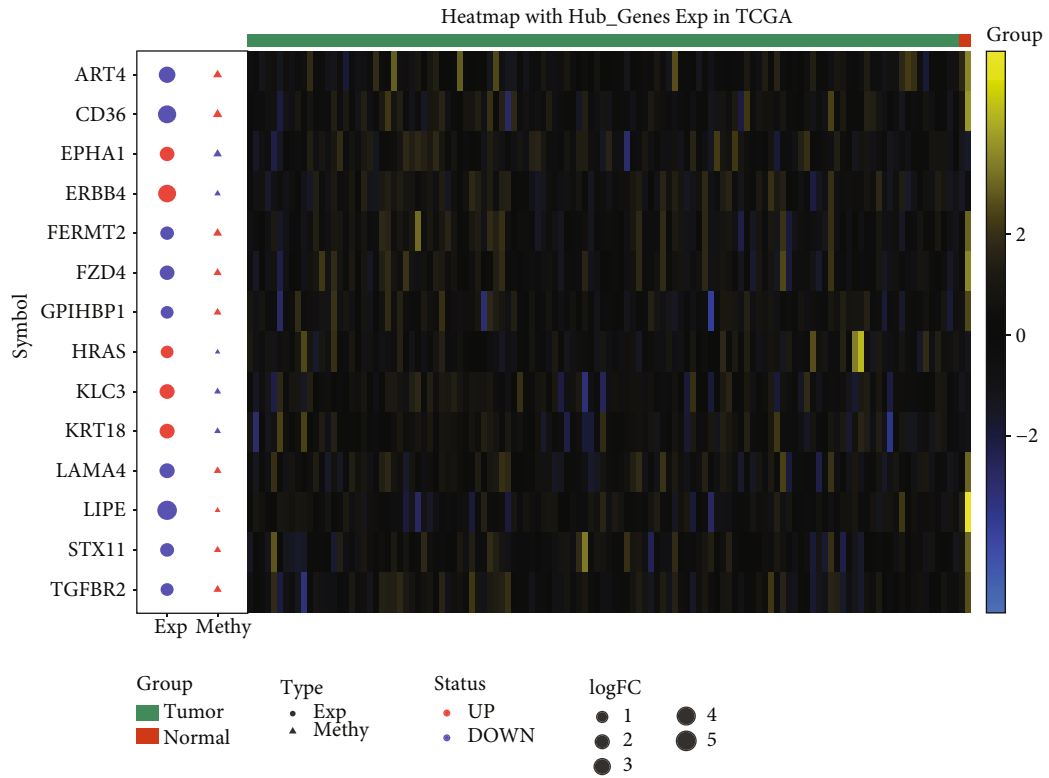


FIGURE 6: Methylation and mutation in thymoma. (a) Differential methylation sites between thymoma and control. (b) The proportion of methylation sites in different chromosomes. (c) The expression and methylation of methylation factors. Red node represents upregulation, and blue node represents downregulation. Yellow represents positive gene expression, while blue represents negative gene expression. (d) The top 20 genes with the highest mutation frequency in thymoma. Each cell represents a sample.

However, this study also had some limitations. Firstly, conclusions may be limited by small samples, especially control samples. Secondly, the results of this study had not been verified by molecular experiments, so the interpretation of the results may be cautious. In this study, the possible molecular changes and pathogenesis of thymoma were investigated using the multiomics data from TCGA database. This study identified key genes related to the prognosis of thymoma, including LIPE, MYH6, ACTG2, KLF4, SULT4A1, and TF. The expression of these genes in thymoma may be a promising biomarker, which needs further study.

5. Conclusion

In this study, potential targets associated with thymoma were identified by combining thymoma-related gene expression, methylation, and mutation data. Using a variety of bioinformatics analysis methods, we found that important genes related to thymoma were associated with immune inflammatory response. LIPE, MYH6, ACTG2, KLF4, SULT4A1, and TF were the key genes affecting the prognosis of thymoma. Among them, LIPE was also modified by methylation.

Data Availability

Thymoma mRNA-seq expression data, methylation data, mutation data, and clinical materials were obtained from TCGA website (<https://portal.gdc.cancer.gov/>).

Conflicts of Interest

The authors declare that the research was conducted in the absence of any commercial or financial relationships that could be construed as a potential conflict of interest.

Authors' Contributions

Dazhong Liu and Pengfei Zhang contributed equally to this article as co-first authors.

Acknowledgments

This study was supported by the Project of Heilongjiang Health and Family Planning Commission (2016-066) and Science and Technology Innovation Talent Project of Harbin Science and Technology Bureau (2016RAQXJ149).

References

- [1] L. Yu, J. Ke, X. du, Z. Yu, and D. Gao, "Genetic characterization of thymoma," *Scientific Reports*, vol. 9, no. 1, p. 2369, 2019.
- [2] M. A. den Bakker, A. C. Roden, A. Marx, and M. Marino, "Histologic classification of thymoma: a practical guide for routine cases," *Journal of Thoracic Oncology*, vol. 9, no. 9, pp. S125–S130, 2014.
- [3] B. Aydemir, "The effect of myasthenia gravis as a prognostic factor in thymoma treatment," *Northern Clinics of Istanbul*, vol. 3, no. 3, pp. 194–200, 2016.
- [4] Y. Sun, C. Gu, J. Shi et al., "Reconstruction of mediastinal vessels for invasive thymoma: a retrospective analysis of 25 cases," *Journal of Thoracic Disease*, vol. 9, no. 3, pp. 725–733, 2017.
- [5] D. J. Kim, W. I. Yang, S. S. Choi, K. D. Kim, and K. Y. Chung, "Prognostic and clinical relevance of the World Health Organization schema for the classification of thymic epithelial tumors: a clinicopathologic study of 108 patients and literature review," *Chest*, vol. 127, no. 3, pp. 755–761, 2005.
- [6] D. Bian, F. Zhou, W. Yang et al., "Thymoma size significantly affects the survival, metastasis and effectiveness of adjuvant therapies: a population based study," *Oncotarget*, vol. 9, no. 15, pp. 12273–12283, 2018.
- [7] M. Radovich, C. R. Pickering, I. Felau et al., "The integrated genomic landscape of thymic epithelial tumors," *Cancer Cell*, vol. 33, no. 2, pp. 244–258.e10, 2018, e10.
- [8] T. Sakane, T. Murase, K. Okuda et al., "A mutation analysis of the EGFR pathway genes, RAS, EGFR, PIK3CA, AKT1 and BRAF, and TP53 gene in thymic carcinoma and thymoma type A/B3," *Histopathology*, vol. 75, no. 5, pp. 755–766, 2019.
- [9] F. Enkner, B. Pichlhöfer, A. T. Zaharie et al., "Molecular profiling of thymoma and thymic carcinoma: genetic differences and potential novel therapeutic targets," *Pathology Oncology Research*, vol. 23, no. 3, pp. 551–564, 2017.
- [10] S. Li, Y. Yuan, H. Xiao et al., "Discovery and validation of DNA methylation markers for overall survival prognosis in patients with thymic epithelial tumors," *Clinical Epigenetics*, vol. 11, no. 1, p. 38, 2019.
- [11] M. Venza, M. Visalli, C. Beninati, C. Biondo, D. Teti, and I. Venza, "Role of genetics and epigenetics in mucosal, uveal, and cutaneous melanomagenesis," *Anti-Cancer Agents in Medicinal Chemistry*, vol. 16, no. 5, pp. 528–538, 2016.
- [12] P. Christopoulos and P. Fisch, "Acquired T-cell immunodeficiency in thymoma patients," *Critical Reviews in Immunology*, vol. 36, no. 4, pp. 315–327, 2016.
- [13] M. Omatsu, T. Kunimura, T. Mikogami et al., "Difference in distribution profiles between CD163+ tumor-associated macrophages and S100+ dendritic cells in thymic epithelial tumors," *Diagnostic Pathology*, vol. 9, no. 1, p. 215, 2014.
- [14] C. Gu, X. Shi, Z. Huang et al., "A comprehensive study of construction and analysis of competitive endogenous RNA networks in lung adenocarcinoma," *Biochimica et Biophysica Acta (BBA) - Proteins and Proteomics*, vol. 1868, no. 8, p. 140444, 2020.
- [15] X. Shi, T. Huang, J. Wang et al., "Next-generation sequencing identifies novel genes with rare variants in total anomalous pulmonary venous connection," *eBioMedicine*, vol. 38, pp. 217–227, 2018.
- [16] C. Gu, Z. Huang, X. Chen et al., "TEAD4 promotes tumor development in patients with lung adenocarcinoma via ERK signaling pathway," *Biochimica et Biophysica Acta - Molecular Basis of Disease*, vol. 1866, no. 12, article 165921, 2020.
- [17] C. Gu, X. Shi, X. Dang et al., "Identification of common genes and pathways in eight fibrosis diseases," *Frontiers in Genetics*, vol. 11, p. 627396, 2020.
- [18] C. Gu, R. Wang, X. Pan et al., "Comprehensive study of prognostic risk factors of patients underwent pneumonectomy," *Journal of Cancer*, vol. 8, no. 11, pp. 2097–2103, 2017.
- [19] C. Gu, X. Pan, R. Wang et al., "Analysis of mutational and clinicopathologic characteristics of lung adenocarcinoma with clear cell component," *Oncotarget*, vol. 7, no. 17, pp. 24596–24603, 2016.

- [20] X. D. Wang, P. Lin, Y. X. Li et al., "Identification of potential agents for thymoma by integrated analyses of differentially expressed tumour-associated genes and molecular docking experiments," *Experimental and Therapeutic Medicine*, vol. 18, no. 3, pp. 2001–2014, 2019.
- [21] F. J. Meng, S. Wang, J. Zhang et al., "Alteration in gene expression profiles of thymoma: genetic differences and potential novel targets," *Thoracic Cancer*, vol. 10, no. 5, pp. 1129–1135, 2019.
- [22] K. Rue-Albrecht, P. A. McGettigan, B. Hernández et al., "GOexpress: an R/bioconductor package for the identification and visualisation of robust gene ontology signatures through supervised learning of gene expression data," *BMC Bioinformatics*, vol. 17, no. 1, p. 126, 2016.
- [23] C. Braicu, M. Buse, C. Busuioc et al., "A comprehensive review on MAPK: a promising therapeutic target in cancer," *Cancers*, vol. 11, no. 10, p. 1618, 2019.
- [24] M. Cargnello and P. P. Roux, "Activation and function of the MAPKs and their substrates, the MAPK-activated protein kinases," *Microbiology and Molecular Biology Reviews*, vol. 75, no. 1, pp. 50–83, 2011.
- [25] A. Plotnikov, K. Flores, G. Maik-Rachline et al., "The nuclear translocation of ERK1/2 as an anticancer target," *Nature Communications*, vol. 6, no. 1, p. 6685, 2015.
- [26] Z. Yang, S. Liu, Y. Wang et al., "High expression of KITLG is a new hallmark activating the MAPK pathway in type A and AB thymoma," *Thoracic Cancer*, vol. 11, no. 7, pp. 1944–1954, 2020.
- [27] M. Ibrahim, D. Scozzi, K. A. Toth et al., "Naive CD4+T cells carrying a TLR2 agonist overcome TGF- β -mediated tumor immune evasion," *Journal of Immunology*, vol. 200, no. 2, pp. 847–856, 2018.
- [28] P. Vodicka, L. Krskova, I. Odintsov et al., "Expression of molecules of the Wnt pathway and of E-cadherin in the etiopathogenesis of human thymomas," *Oncology Letters*, vol. 19, no. 3, pp. 2413–2421, 2020.
- [29] H. E. Barker, J. T. E. Paget, A. A. Khan, and K. J. Harrington, "The tumour microenvironment after radiotherapy: mechanisms of resistance and recurrence," *Nature Reviews. Cancer*, vol. 15, no. 7, pp. 409–425, 2015.
- [30] C. Ionescu, C. Braicu, R. Chiorean et al., "TIMP-1 expression in human colorectal cancer is associated with SMAD3 gene expression levels: a pilot study," *Journal of Gastrointestinal and Liver Diseases*, vol. 23, no. 4, pp. 413–418, 2020.
- [31] B. Liu, F. F. Hu, Q. Zhang et al., "Genomic landscape and mutational impacts of recurrently mutated genes in cancers," *Molecular Genetics & Genomic Medicine*, vol. 6, no. 6, pp. 910–923, 2018.
- [32] M. Li, F. Hou, J. Zhao et al., "Focal adhesion kinase is overexpressed in thymic epithelial tumors and may serve as an independent prognostic biomarker," *Oncology Letters*, vol. 15, no. 3, pp. 3001–3007, 2018.
- [33] S. Hu, J. Yao, A. A. Howe et al., "Peroxisome proliferator-activated receptor γ decouples fatty acid uptake from lipid inhibition of insulin signaling in skeletal muscle," *Molecular Endocrinology*, vol. 26, no. 6, pp. 977–988, 2012.
- [34] T. Murai, "Cholesterol lowering: role in cancer prevention and treatment," *Biological Chemistry*, vol. 396, no. 1, pp. 1–11, 2015.
- [35] L. Gong, Y. Lei, X. Tan et al., "Propranolol selectively inhibits cervical cancer cell growth by suppressing the cGMP/PKG pathway," *Biomedicine & Pharmacotherapy*, vol. 111, pp. 1243–1248, 2019.
- [36] Q. Li, Y. L. Su, and W. X. Shen, "A novel prognostic signature of seven genes for the prediction in patients with thymoma," *Journal of Cancer Research and Clinical Oncology*, vol. 145, no. 1, pp. 109–116, 2019.
- [37] J. Xi, L. Wang, C. Yan et al., "The Cancer Genome Atlas dataset-based analysis of aberrantly expressed genes by GeneAnalytics in thymoma associated myasthenia gravis: focusing on T cells," *Journal of Thoracic Disease*, vol. 11, no. 6, pp. 2315–2323, 2019.
- [38] A. Simiczjew, A. J. Mazur, E. Dratkiewicz, and D. Nowak, "Involvement of β - and γ -actin isoforms in actin cytoskeleton organization and migration abilities of bleb-forming human colon cancer cells," *PLoS One*, vol. 12, no. 3, article e0173709, 2017.
- [39] M. Moral, C. Segrelles, A. B. Martínez-Cruz et al., "Transgenic mice expressing constitutively active Akt in oral epithelium validate KLFA as a potential biomarker of head and neck squamous cell carcinoma," *In Vivo*, vol. 23, no. 5, pp. 653–660, 2009.
- [40] J. Dai, Z. Bing, Y. Zhang et al., "Integrated mRNAseq and microRNAseq data analysis for grade III gliomas," *Molecular Medicine Reports*, vol. 16, no. 5, pp. 7468–7478, 2017.
- [41] D. Ferreira, R. Ponraj, A. Yeung, and J. de Malmanche, "Pure red cell aplasia associated with thymolipoma: complete anaemia resolution following thymectomy," *Case Reports in Hematology*, vol. 2018, Article ID 8627145, 4 pages, 2018.
- [42] L. Wang, O. E. Branson, K. Shilo, C. L. Hitchcock, and M. A. Freitas, "Proteomic signatures of thymomas," *PLoS One*, vol. 11, no. 11, article e0166494, 2016.
- [43] S. Shelly, N. Agmon-Levin, A. Altman, and Y. Shoenfeld, "Thymoma and autoimmunity," *Cellular & Molecular Immunology*, vol. 8, no. 3, pp. 199–202, 2011.
- [44] C. Gu, X. Shi, C. Dai et al., "RNA m6A modification in cancers: molecular mechanisms and potential clinical applications," *The Innovation*, vol. 1, no. 3, p. 100066, 2020.
- [45] C. Gu and C. Chen, "Methylation in lung cancer: a brief review," *Methods in Molecular Biology*, vol. 2204, pp. 91–97, 2020.
- [46] Y. Bi, Y. Meng, Y. Niu et al., "Genome-wide DNA methylation profile of thymomas and potential epigenetic regulation of thymoma subtypes," *Oncology Reports*, vol. 41, no. 5, pp. 2762–2774, 2019.
- [47] I. Petrini, P. S. Meltzer, I. K. Kim et al., "A specific missense mutation in GTF2I occurs at high frequency in thymic epithelial tumors," *Nature Genetics*, vol. 46, no. 8, pp. 844–849, 2014.

Research Article

PD-L1 and Immune Infiltration of m⁶A RNA Methylation Regulators and Its miRNA Regulators in Hepatocellular Carcinoma

Yingxue Lin,¹ Yinhui Yao ,¹ Ying Wang ,¹ Lingdi Wang,¹ and Haipeng Cui ²

¹Department of Medicine, Affiliated Hospital of Chengde Medical University, Nanyingzi Road, Shuangqiao District, Chengde, Hebei, China

²Department of Pathophysiology, Chengde Medical University, Anyuan Road, Shuangqiao District, Chengde, Hebei, China

Correspondence should be addressed to Haipeng Cui; han984746810@163.com

Received 23 January 2021; Accepted 1 May 2021; Published 17 May 2021

Academic Editor: Tao Huang

Copyright © 2021 Yingxue Lin et al. This is an open access article distributed under the Creative Commons Attribution License, which permits unrestricted use, distribution, and reproduction in any medium, provided the original work is properly cited.

Background. The aim of this study was to systematically evaluate the relationship between the expression of m⁶A RNA methylation regulators and prognosis in HCC. **Methods.** We compared the expression of m⁶A methylation modulators and PD-L1 between HCC and normal in TCGA database. HCC samples were divided into two subtypes by consensus clustering of data from m⁶A RNA methylation regulators. The differences in PD-L1, immune infiltration, and prognosis between the two subtypes were further compared. The LASSO regression was used to build a risk score for m⁶A modulators. In addition, we identified miRNAs that regulate m⁶A regulators. **Results.** We found that fourteen m⁶A regulatory genes were significantly differentially expressed between HCC and normal. HCC samples were divided into two clusters. Of these, there are higher PD-L1 expression and poorer overall survival (OS) in cluster 1. There was a significant difference in immune cell infiltration between cluster 1 and cluster 2. Through the LASSO model, we obtained 12 m⁶A methylation regulators to construct a prognostic risk score. Compared with patients with a high-risk score, patients with a low-risk score had upregulated PD-L1 expression and worse prognosis. There was a significant correlation between risk score and tumor-infiltrating immune cells. Finally, we found that miR-142 may be the important regulator for m⁶A RNA methylation in HCC. **Conclusion.** Our results suggest that m⁶A RNA methylation modulators may affect the prognosis through PD-L1 and immune cell infiltration in HCC patients. In addition, the two clusters may be beneficial for prognostic stratification and improving immunotherapeutic efficacy.

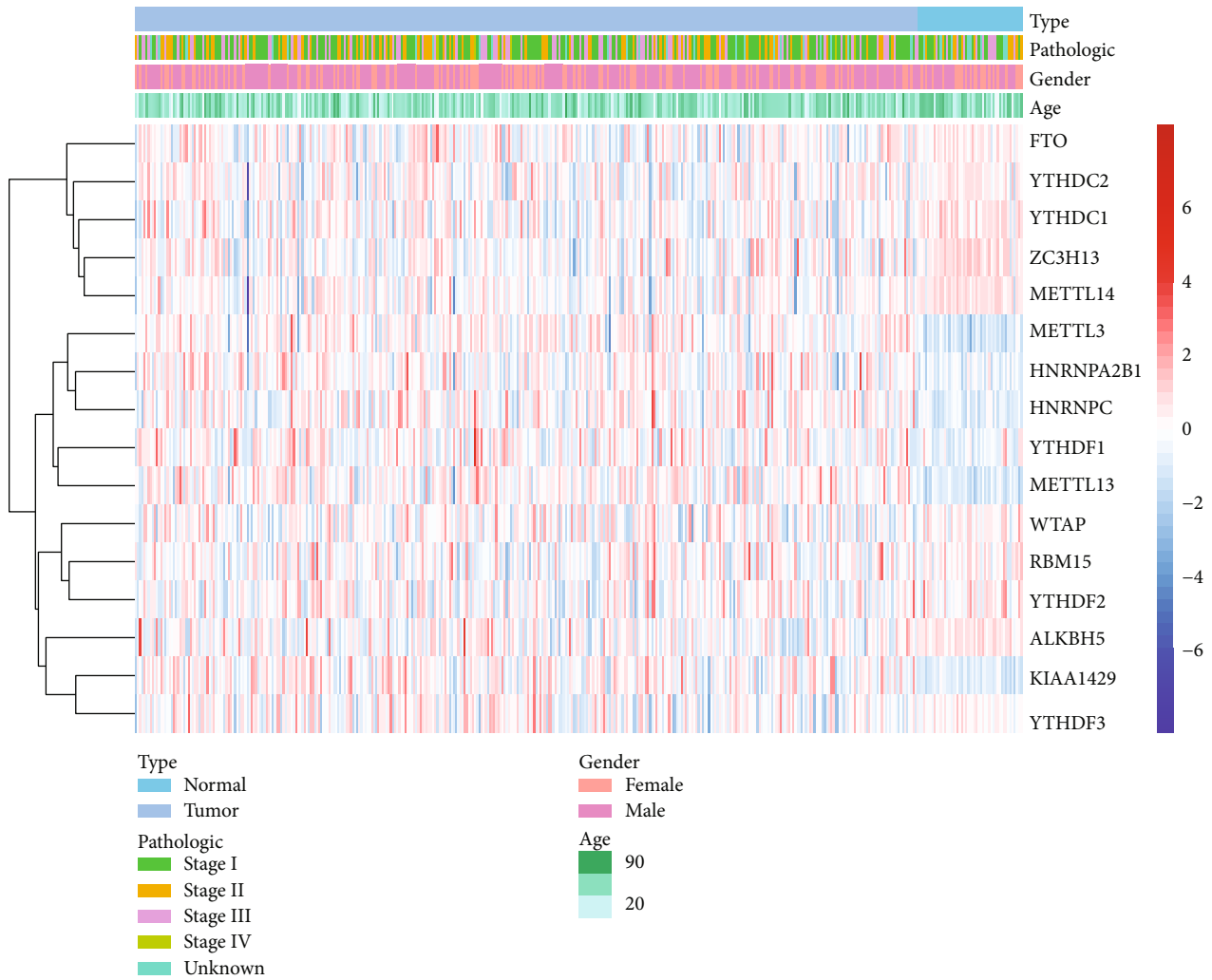
1. Introduction

Hepatocellular carcinoma (HCC) is an increasingly serious health problem with nearly 600,000 newly diagnosed patients with liver cancer [1]. The most prominent features of HCC are invasiveness and frequent recurrence [2]. Although great progress has been made in the treatment methods in recent decades, the prognosis of HCC patients is not optimistic, and the 5-year survival rate is less than 20% [3]. Most patients with advanced HCC have a high rate of recurrence and metastasis after treatment, which may be one of the reasons for poor prognosis [4].

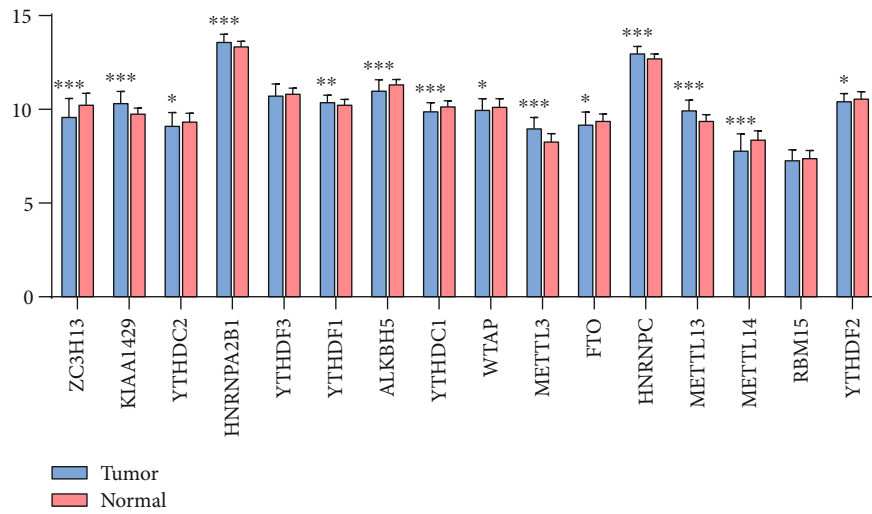
The occurrence of liver cancer is a complex process involving multiple risk factors. It mainly includes cirrhosis,

alcoholism, diabetes, and metabolic syndrome [5]. Surgical resection and liver transplantation are common effective treatments [6]. However, as most patients with advanced disease are diagnosed, only 15% of HCC patients are likely to receive effective treatment [7]. Patients with early HCC are always asymptomatic or present with nonspecific symptoms, such as abdominal pain, jaundice, and weight loss, leading to HCC being initially undetected. Therefore, exploring the pathogenesis of hepatocellular carcinoma and searching for promising biomarkers for diagnosis and prognosis of hepatocellular carcinoma are helpful to provide effective therapeutic targets and improve the prognosis of patients.

N⁶-methyladenosine (m⁶A) is a ubiquitous internal modification of RNA at the posttranscriptional level [8]. It plays a

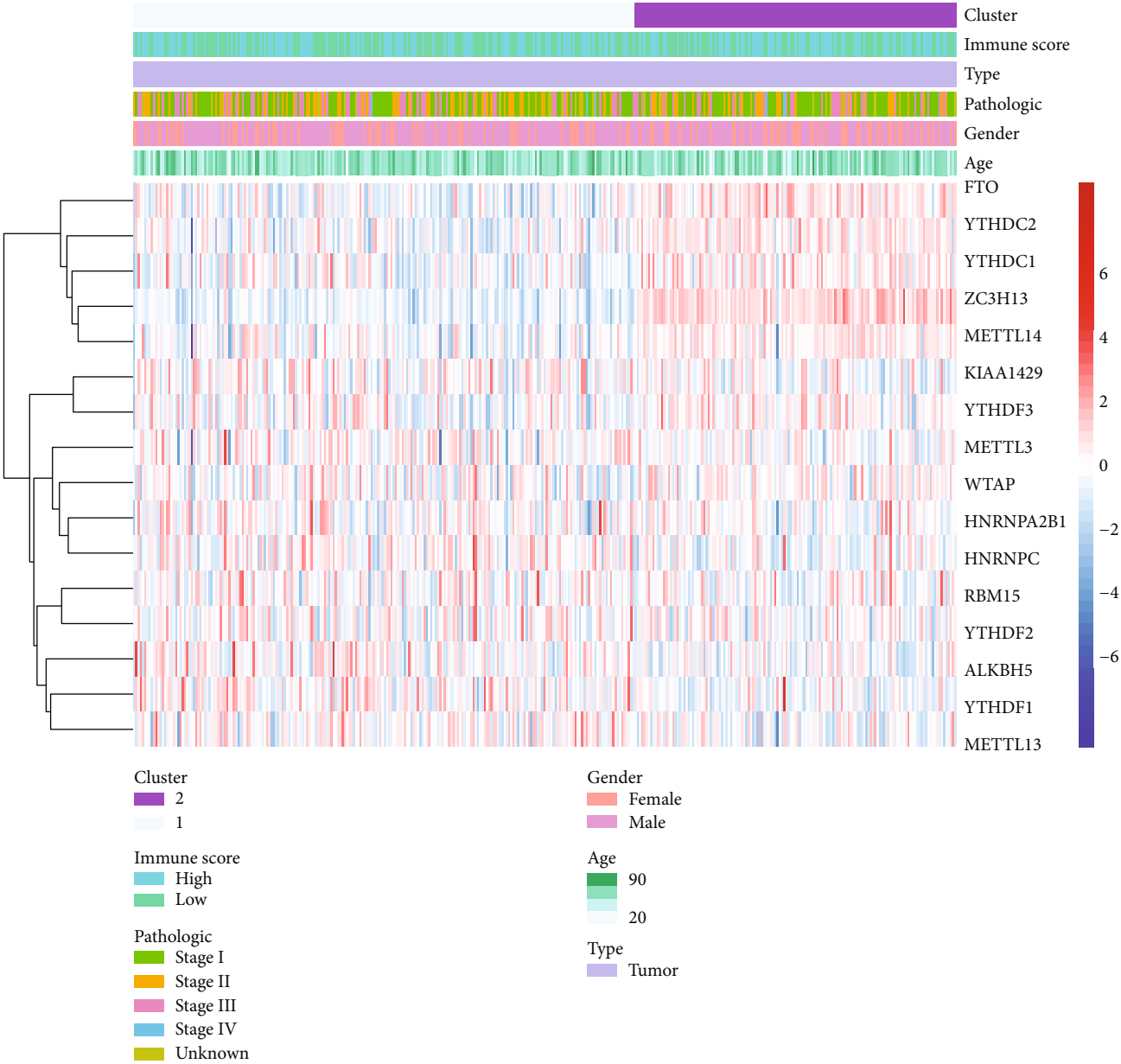


(a)



(b)

FIGURE 1: Continued.



(c)

FIGURE 1: Continued.

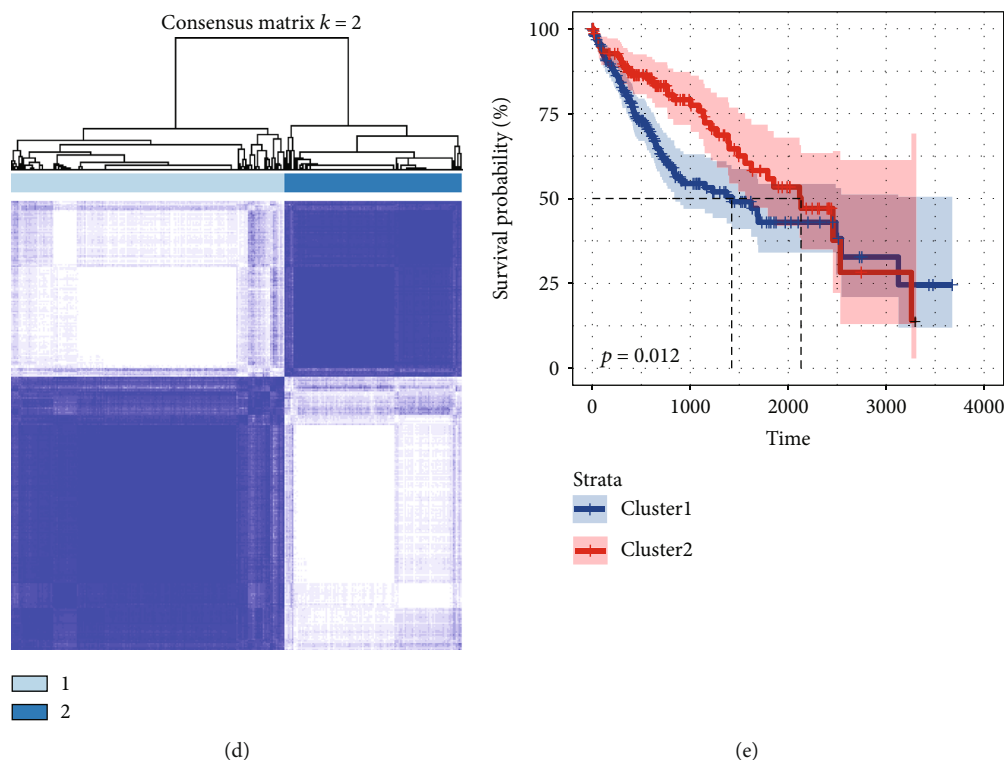


FIGURE 1: Differential features of m⁶A methylation regulators of HCC patients. (a) Expression of m⁶A RNA methylation regulators in HCC and normal. (b) Differential expression of m⁶A RNA methylation regulators in HCC and normal. (c) The $k = 2$ in consensus clustering matrix. (d) Heatmap for cluster 1 and cluster 2 samples of HCC patients. (e) Kaplan-Meier curves of overall survival in two clusters for HCC patients.

key role in pre-RNA splicing, translation regulation, and RNA decay [9, 10]. Studies showed that abnormal m⁶A modification is closely related to the progression of hepatocellular carcinoma [11, 12].

The liver tissue can stimulate immune response and prevent undesirable pathogen attack and tumorigenesis [13]. Sinusoidal endothelial cells in the liver can express programmed cell death ligand-1 (PD-L1) of immunosuppressive molecules, thereby regulating the immunogenicity of the liver microenvironment [14]. Immunotherapy has been shown effective and safe in the treatment of large numbers of solid tumors, prolonging overall survival (OS) [15, 16]. Han et al. found that YTHDF1-deficient (YTHDF1^{-/-}) mice exhibited an antigen-specific elevation of antitumor response [17]. Therefore, m⁶A regulators involved in immune pathways may be considered a target to enhance the response of tumor immunotherapy [18].

It is well known that carcinogenesis is a multistep process that triggers the accumulation of genetic alteration [19]. Like other solid cancers, this also occurs in the development of HCC. With the advancement of HCC biology and molecular classification, it led to the discovery of different phenotypes of HCC and the discovery of significant molecular markers for treatment [20]. Therefore, molecular subtype-related features provide valuable information for treatment and prognosis. The aim of this study was to systematically evaluate the relationship between the expression of m⁶A RNA methylation regulators and prognosis in HCC.

2. Materials and Methods

2.1. Dataset. We obtained RNA-Seq transcriptome data and relevant clinical data from The Cancer Genome Atlas (TCGA) database for patients with primary hepatocellular carcinoma. This included 374 tumor specimens of hepatocellular carcinoma and 50 normal tissues. We downloaded transcript per million mapped read (FPKM) data which had been normalized by using Perl. All data are open; therefore, approval from the Ethics Committee is not required. GSE147889 included microRNA (miRNA) profiling of liver tissue specimens from ninety-seven samples of HCC tumor tissue, with corresponding samples of surrounding tissue.

2.2. Difference Analysis. The FTO, YTHDC2, YTHDC1, ZC3H13, METTL14, METTL3, HNRNPA2B1, HNRNPC, YTHDF1, METTL13, WTAP, RBM15, YTHDF2, ALKBH5, KIAA1429, and YTHDF3 are m⁶A methylation regulators. Differential expression analysis of m⁶A regulators and PD-L1 between HCC samples and normal was analyzed through the EdgeR R package [21]. A $P < 0.05$ was significant [22–24]. The immunoscore for each HCC patient was calculated through the estimate R package.

2.3. Consensus Clustering Analysis. The consensus clustering analysis of m⁶A RNA methylation regulators based on the expression in HCC samples was performed through the ConsensusClusterPlus package [25]. The Kaplan-Meier survival

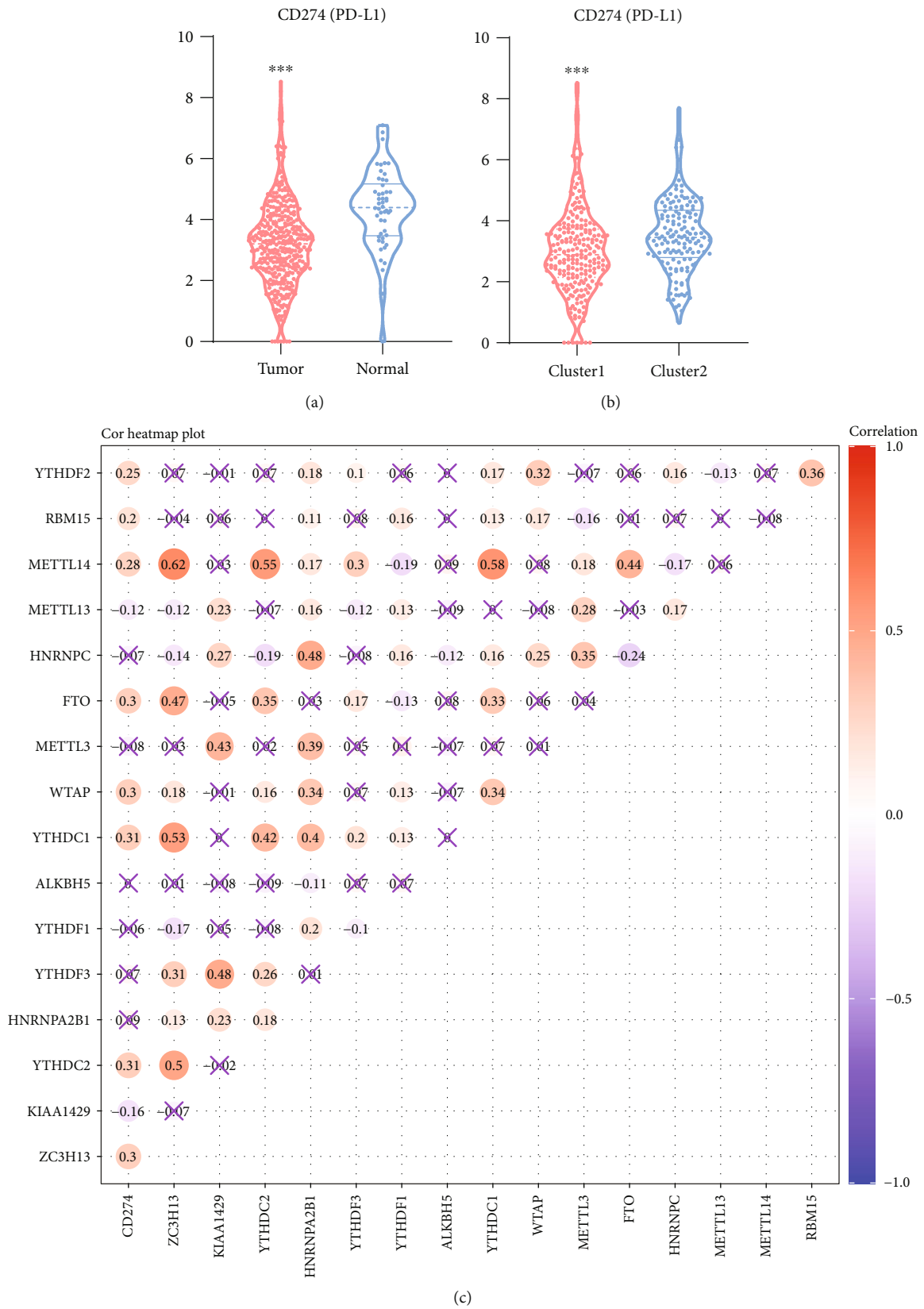


FIGURE 2: Expression level of PD-L1 was associated with m⁶A methylation. (a) Differential expression of PD-L1 between HCC and normal. (b) Differential expression of PD-L1 between cluster 1 and cluster 2. (c) Correlation between PD-L1 and m⁶A RNA methylation regulators. × represents $P > 0.05$.



(a)

FIGURE 3: Continued.

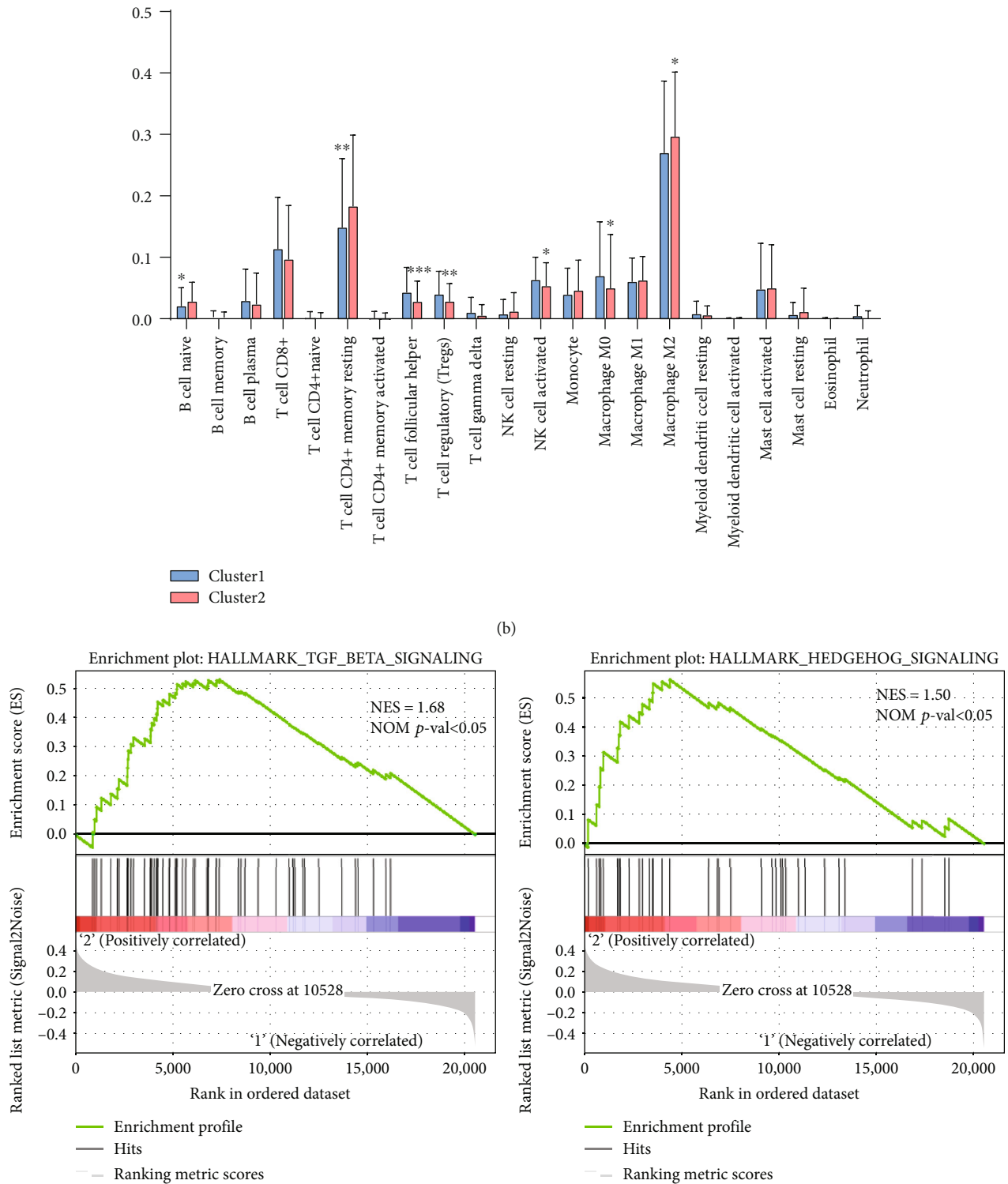
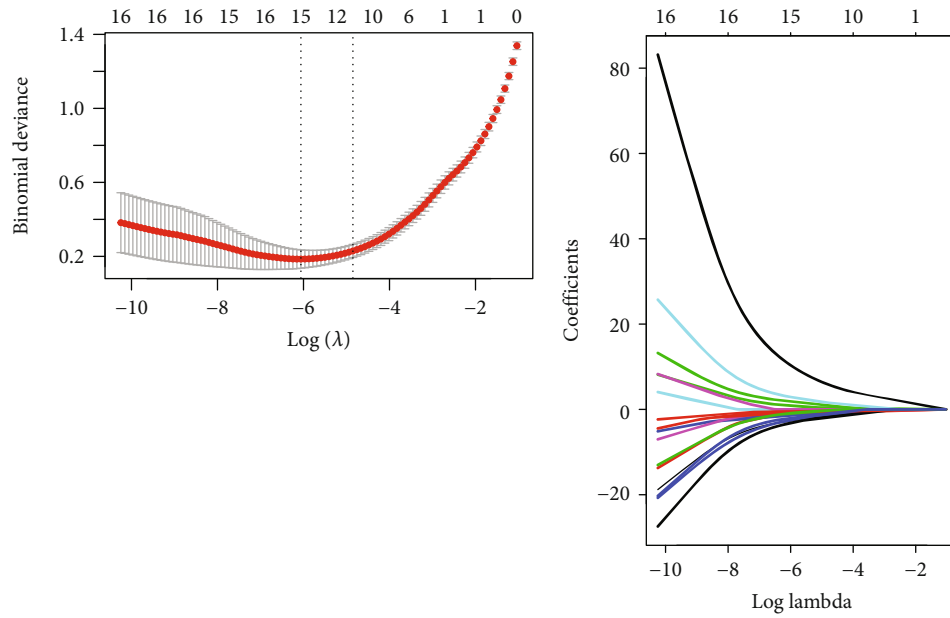


FIGURE 3: Immune cell infiltration in two clusters. (a) Infiltration level of immune cells in two clusters. (b) Differences of immune cell infiltration between cluster 1 and cluster 2. (c) GSEA showed that biological functions were differentially enriched in cluster 1 and cluster 2.

curves were plotted using survival R package. $P < 0.05$ was considered statistically significant. The Hallmark gene set for different HCC subtypes was analyzed through GSEA software. The enrichment pathway was determined by P value < 0.05 and NES.

2.4. Risk Score and Prognosis. Cox regression analysis and least absolute shrinkage and selection operator (LASSO) were performed to evaluate the impact of m⁶A methylation regulators on the prognosis of HCC, which is a regression analysis method that performs both variable selection and



(a)

(b)

Variable	<i>N</i>	Hazard ratio	<i>p</i>
ZC3H13	371	0.82 (0.69, 0.97)	0.020
KIAA1429	371	1.36 (1.00, 1.86)	0.051
YTHDC2	371	0.98 (0.77, 1.23)	0.830
HNRNPA2B1	371	1.59 (0.99, 2.56)	0.058
ALKBH5	371	0.74 (0.53, 1.05)	0.090
YTHDC1	371	1.10 (0.72, 1.69)	0.649
WTAP	371	1.20 (0.87, 1.66)	0.259
METTL3	371	1.40 (0.97, 2.01)	0.073
FTO	371	0.86 (0.65, 1.13)	0.281
METTL13	371	1.45 (1.03, 2.05)	0.033
RBM15	371	1.09 (0.78, 1.52)	0.617
YTHDF2	371	2.19 (1.33, 3.61)	0.002

1 1.5 2 2.5 3 3.5

(c)

FIGURE 4: Continued.

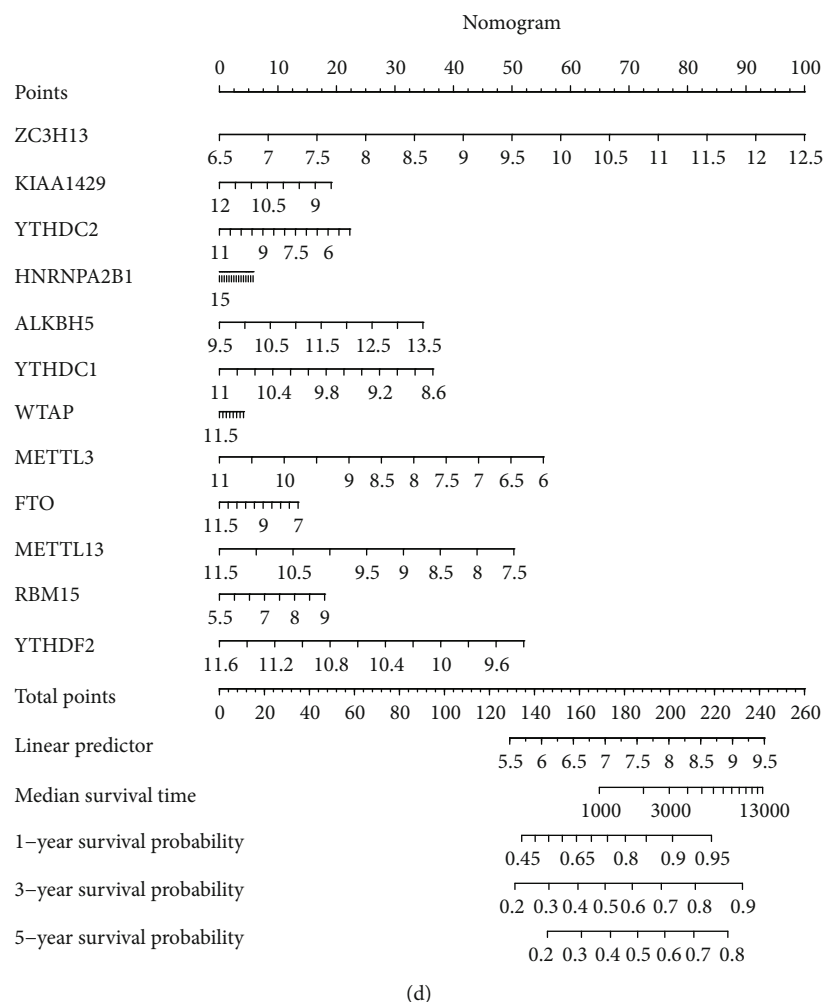


FIGURE 4: m⁶A methylation regulators influenced the prognosis of HCC. (a, b) LASSO regression analysis of m⁶A methylation regulators. (c) Forest map of twelve m⁶A methylation regulators predicting the impact on prognosis of HCC. (d) The nomogram to predict overall survival in HCC patients.

regularization in order to enhance the prediction accuracy and interpretability of the resulting statistical model. HCC samples were divided into different groups through the median risk score based on the coefficients of LASSO and the expression of m⁶A regulators.

3. Results

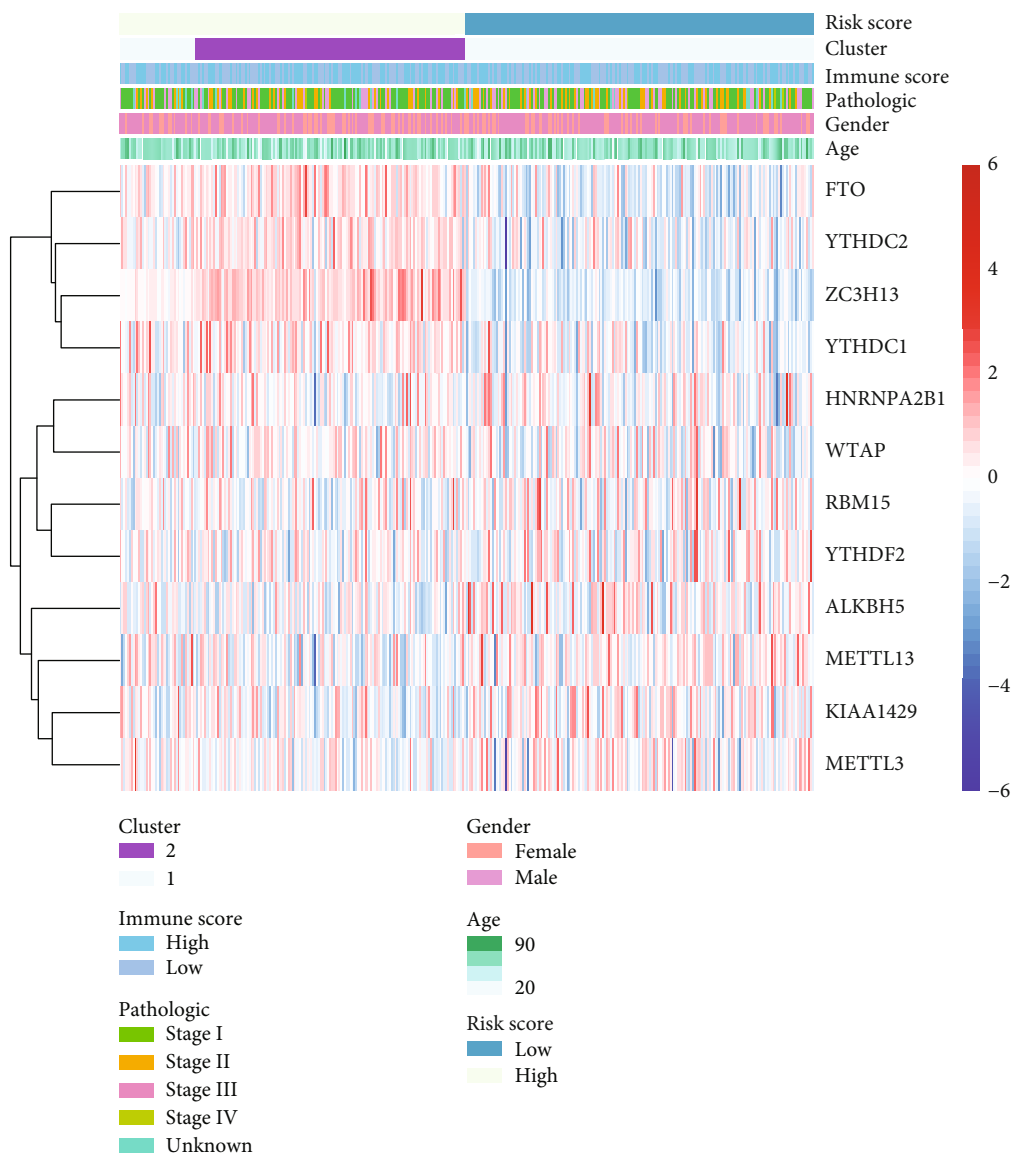
3.1. m⁶A RNA Methylation Regulator Levels in HCC. We compared the expression of sixteen m⁶A regulators between HCC and normal (Figure 1(a)). In addition to YTHDF3 and RBM15, the expression of these genes was significantly different in HCC compared with normal tissues (Figure 1(b)). This suggested that m⁶A RNA methylation regulators played an important role in the development of HCC.

$k = 2$ was determined based on consensus clustering analysis, and HCC samples were divided into two subtypes according to the expression of m⁶A methylation regulators, namely, cluster 1 and cluster 2 (Figure 1(c)). The expression of FTO, YTHDC2, YTHDC1, ZC3H13, and METTL14 in

cluster 1 was significantly lower than that in cluster 2 (Figure 1(d)). The overall survival (OS) of cluster 2 was longer than that of cluster 1 (Figure 1(e)). The results showed that the subtypes of expression clustering in the m⁶A regulator were associated with the prognosis of HCC.

3.2. m⁶A RNA Methylation Affected PD-L1. We then evaluated the correlation between m⁶A methylation regulators and PD-L1. Compared with normal, the expression level of PD-L1 in HCC tissues was significantly higher (Figure 2(a)). As well as compared with cluster 2, PD-L1 was significantly higher in cluster 1 (Figure 2(b)). The results of correlation analysis showed that the expression of PD-L1 was positively correlated with the expression of METTL14, RBM15, YTHDF2, FTO, YTHDC1, WTAP, YTHDC2, and ZC3H13 and negatively correlated with the expression of METTL13 and KIAA1429 (Figure 2(c)).

3.3. Association of Immune Cell Infiltration with m⁶A RNA Methylation. Next, we calculated the infiltration levels of 22 immune cell types between the two subgroups



(a)

FIGURE 5: Continued.

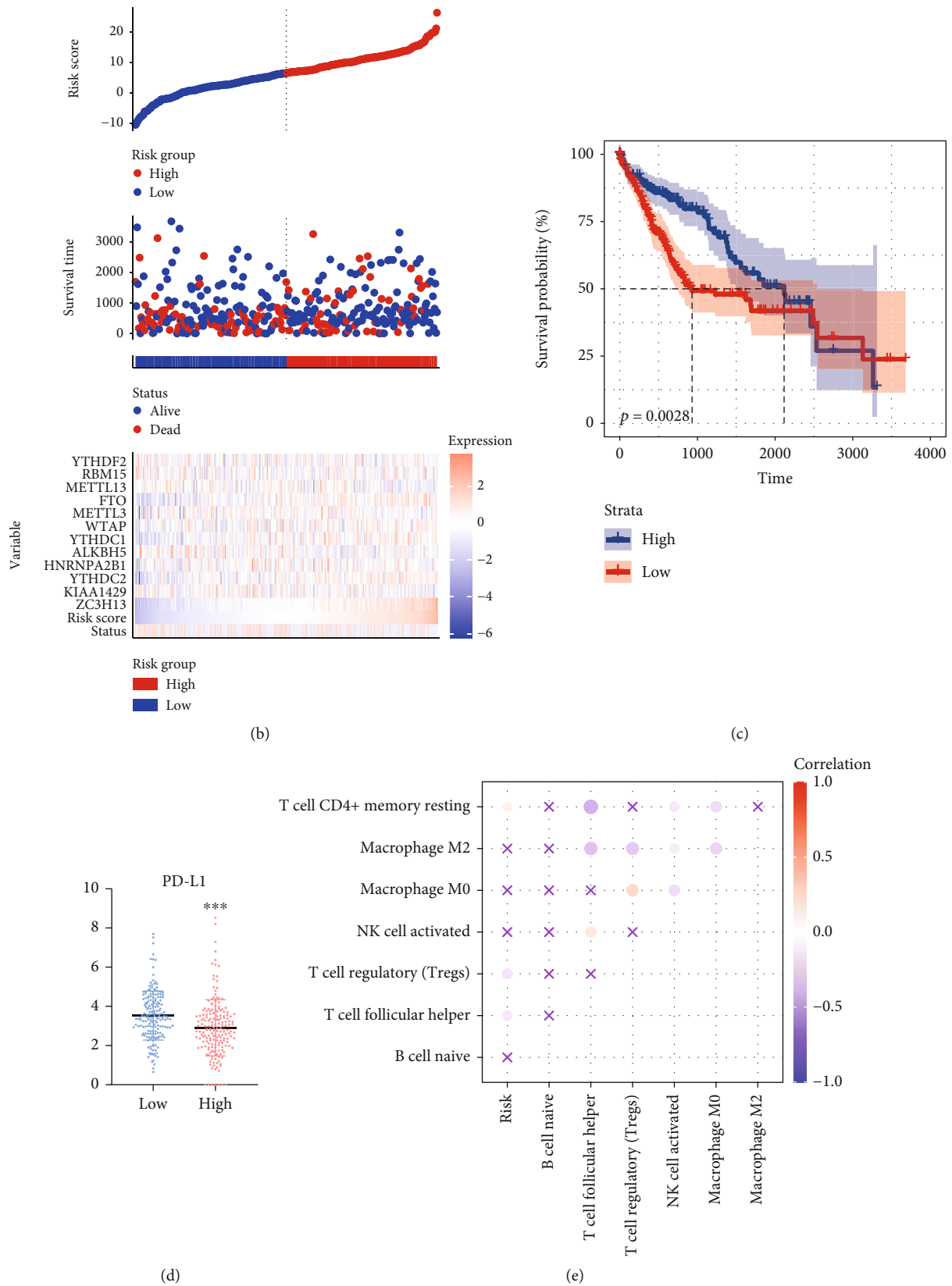
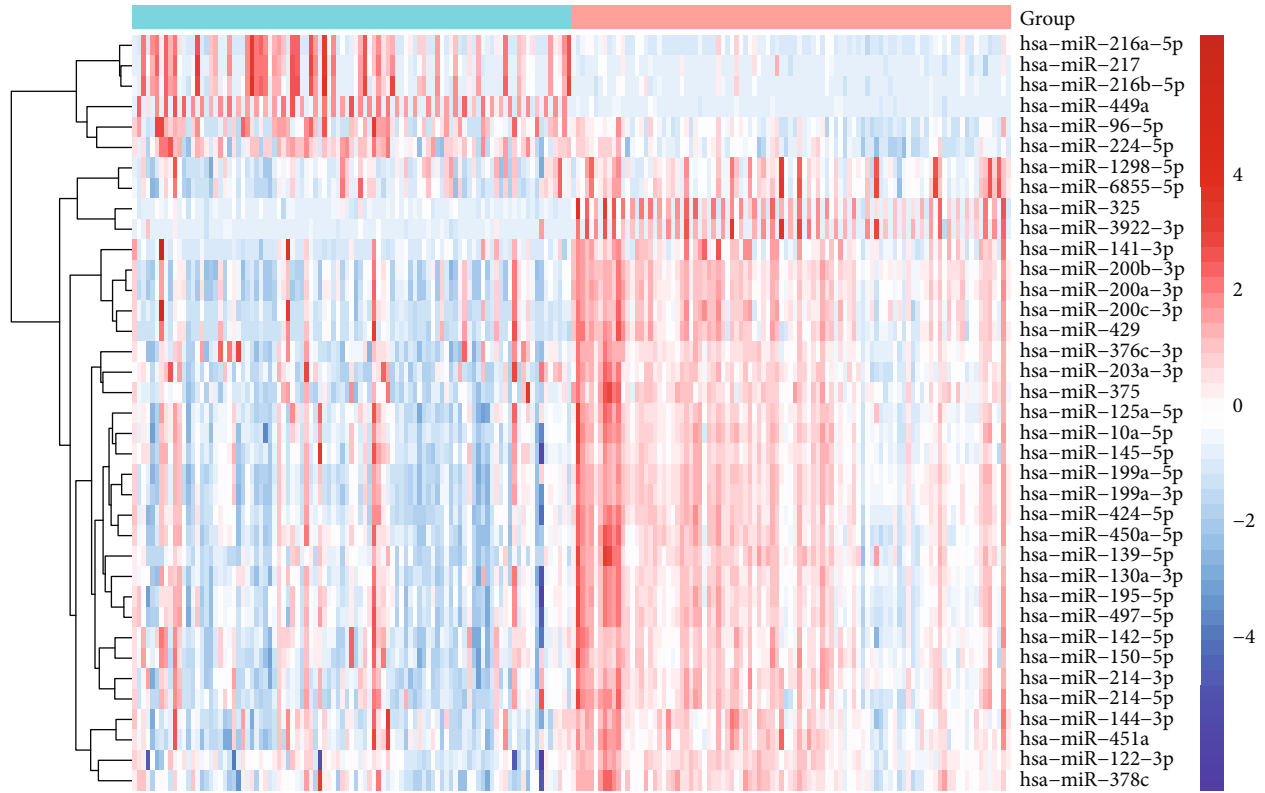
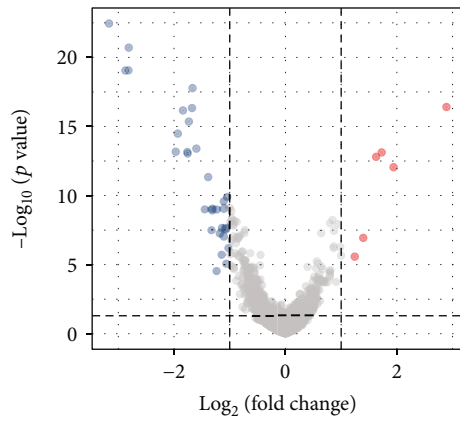


FIGURE 5: The role of risk score in the prognosis of HCC. (a) Heatmap of the high- and low-risk groups. (b) The risk score, OS, and heatmap of the twelve m⁶A regulator signatures. (c) Kaplan-Meier curves of OS based on the risk score for patients with HCC. (d) PD-L1 expression between the high- and low-risk groups. (e) Correlation between risk score and significant immune infiltrating cells.

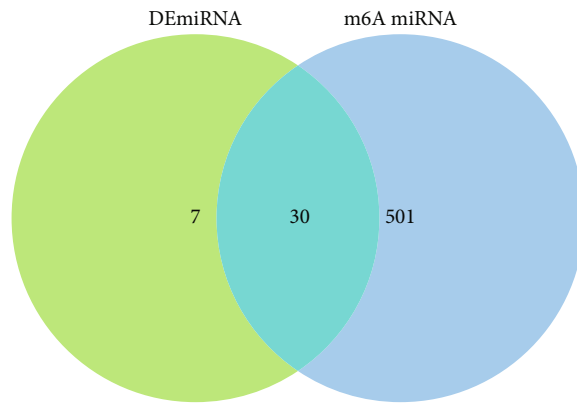


Group
HCC
Normal



Group
Down-regulated
Not-significant
Up-regulated

(a)



(c)

FIGURE 6: Continued.

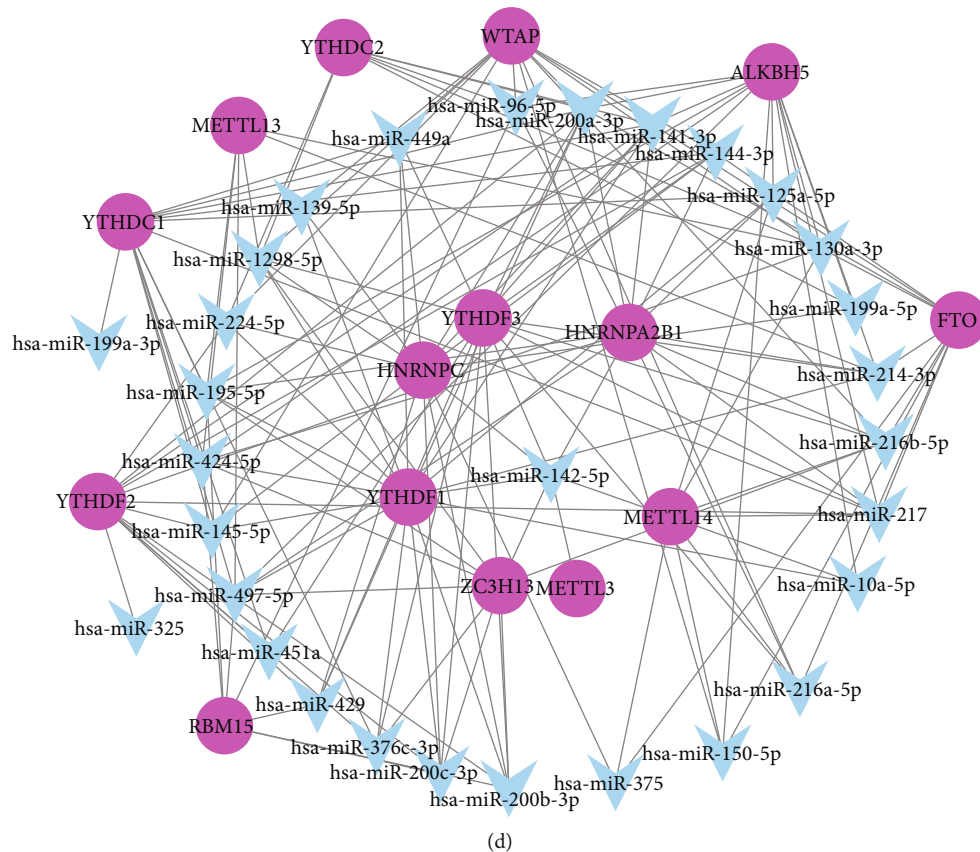


FIGURE 6: Regulatory network of miRNAs. (a) Heatmap of differential miRNA expression in GSE147889. (b) Volcano map of differential miRNA expression in GSE147889. (c) Intersection of differential miRNAs with predictive regulators of m⁶A regulator. (d) Regulation network of m⁶A regulators by HCC-related miRNAs.

(Figure 3(a)). Cluster 1 showed higher levels of T cell follicular helper, NK cell activated, T cell regulatory (Tregs), and macrophage M0 (Figure 3(b)). Cluster 2 showed higher levels of B cell nave, T cell CD4+ memory resting, and macrophage M2. GSEA was used to elucidate the biological functional differences between the two subtypes. The results showed that TGF-beta signaling and Hedgehog signaling were dynamically correlated with cluster 2 (Figure 3(C)). Therefore, TGF-beta and Hedgehog signaling may be related to the tumor microenvironment of cluster 1/2.

3.4. Prognosis of HCC Affected by m⁶A RNA Methylation Regulators. We performed LASSO regression analysis to identify the clinical significance of m⁶A regulators in HCC (Figures 4(a) and 4(b)). Twelve m⁶A regulators, namely, ZC3H13, KIAA1429, YTHDC2, HNRNPA2B1, ALKBH5, YTHDC1, WTAP, METTL3, FTO, METTL13, RBM15, and YTHDF2, were identified. Univariate Cox regression analysis showed that ZC3H13 may be a protective factor for HCC, while METTL13 and YTHDF2 are risk factors for HCC (Figure 4(c)). Nomogram results showed that increased expression of ZC3H13 was associated with longer OS of HCC (Figure 4(d)). Decreased expression of YTHDF2, METTL13, and METTL3 is beneficial to OS of HCC.

3.5. Risk Scores of m⁶A Methylation Regulators. The risk scores were calculated through the coefficients from the results of LASSO. Risk score = coefficients × expression of genes (5.9813 × ZC3H13 – 0.6146 × KIAA1429 + 0.3476 × YTHDC2 – 0.7669 × HNRNPA2B1 – 1.6292 × ALKBH5 – 0.1771 × YTHDC1 + 0.8649 × WTAP – 1.2779 × METTL3 + 1.6007 × FTO – 1.7691 × METTL13 – 0.2269 × RBM15 – 1.0176 × YTHDF2). The median risk score was used to divide HCC patients into the high-risk and low-risk groups (Figure 5(a)). Compared to the high-risk group, the levels of FTO, ZC3H13, YTHDC2, and YTHDC1 were lower in low risk. The mortality rate gradually decreased with the increase of the risk score (Figure 5(b)). The OS was longer, and the PD-L1 expression was lower in the high-risk group than in the low-risk group (Figures 5(c) and 5(d)). In addition, the risk score was significantly positively correlated with the level of T cell CD4+ memory resting and negatively correlated with infiltration level of Tregs and T cell follicular helper (Figure 5(e)). This result confirmed that the risk scores of m⁶A methylation regulator were associated with the immune microenvironment of HCC.

3.6. miRNAs Regulating m⁶A Regulators. By comparing differentially expressed miRNAs between HCC and control in

GSE147889, we identified 37 miRNAs that may be involved in the regulation of HCC (Figures 6(a) and 6(b)). To identify the miRNAs that regulate m⁶A regulators, we predicted 531 miRNAs with targeted regulatory relationships through miR-target. Among them, 30 miRNAs and differentially expressed miRNAs intersect and were considered regulators of m⁶A regulators related to HCC (Figure 6(c)), because hsa-miR-142-5p may be an important regulator as it regulated more m⁶A regulators (Figure 6(d)).

4. Discussion

The m⁶A methylation has many important biological functions and participates in the process of cancer [26, 27]. Herein, we found that the expression of m⁶A regulator is related to the prognosis of HCC and to the immune microenvironment. We have also attempted to elucidate some potential molecular mechanisms that may help make early diagnosis and develop molecular targeted therapies for hepatocellular carcinoma. In addition, we used the selected twelve m⁶A regulator to obtain a prognostic risk score.

At present, many evidences showed that m⁶A regulator is related to the progression of HCC [28]. In this study, compared with normal, YTHDF1 expression in HCC tissues was significantly increased, while YTHDF2 expression was significantly decreased. Elevated YTHDF1 promotes poor prognosis in HCC patients and is involved in regulating the metabolism and cell cycle progression of HCC cells [29]. A study reported that overexpression of YTHDF2 inhibits the proliferation and growth of HCC cells and promotes the apoptosis of HCC cells [30]. Studies have shown that YTHDC2 and METTL3 can promote the development of hepatocellular carcinoma [31, 32]. METTL3 promotes the growth and metastasis of HCC and is related to the survival status [33]. Consistent with our analysis results, the expression of METTL4 in HCC tissues was lower than that in normal tissues [34]. Contrary to our analysis, WTAP was significantly elevated in HCC, which was associated with poor survival outcomes [35]. ZC3H13 was downregulated in HCC and was a protective gene, which was also confirmed by other studies [36, 37]. The Cox risk score and clinical characteristic analysis confirmed that ZC3H13, METTL3, and YTHDF2 could be used as prognostic indicators and even as targets for new treatment of liver cancer.

Our results suggested that m⁶A methylation was associated with the development of hepatocellular carcinoma. OS and PD-L1 expression in cluster 2 was significantly different from that in cluster 1. The better prognosis of cluster 2 patients may be related to the lower expression level of PD-L1 [38]. GSEA results showed that TGF- β signaling and Hedgehog signaling were significantly enriched in cluster 2. Transforming growth factor beta (TGF- β) inhibits the occurrence of early HCC by inducing cell arrest and apoptosis but promotes the malignant progression of advanced HCC by promoting the survival, metastasis, migration, and invasion of tumor cells [39]. In HCC, aberrantly activated Hedgehog signaling promotes the development and invasion of HCC [40, 41]. This seems controversial with the good prognosis

of patients with cluster 2. m⁶A methylation is complex in tumors, and its prognostic value in HCC needs further study.

In addition, the risk score was correlated with the expression of PD-L1. In the high-risk group, the PD-L1 expression was lower and had a good prognosis. Cluster 2 is in the high-risk score subtype of HCC. These findings suggested that m⁶A methylation regulation participated in the regulation of the immune microenvironment of HCC to some extent. Overexpression of miR-142 inhibits the invasion and angiogenesis of HCC cells and may be a potential therapeutic target for HCC [42]. Our results suggest that miR-142 may have a regulatory effect on m⁶A regulator. Interestingly, it was found that miR-142 was modified by methylation in tumor patients and cell lines and participated in the growth of HCC [43].

However, this study has some limitations. Firstly, our analytical data were from public databases; there may be some deviations. Secondly, more data, as well as large numbers of clinical and experimental data, are needed to verify the accuracy and reliability of our analysis results. In addition, whether the classification based on consistent clustering has clinical significance for HCC needs further confirmation.

5. Conclusions

In conclusion, the results suggested that the levels of m⁶A methylation regulator were related to the OS and immunity in HCC. This study has important proof value for demonstrating the impact of m⁶A methylation in HCC. Furthermore, ZC3H13, METTL3, and YTHDF2 may be potential predictors and therapeutic targets for HCC. miR-142 may regulate m⁶A methylation and participate in HCC.

Data Availability

We obtained RNA-Seq transcriptome data and relevant clinical data from The Cancer Genome Atlas (TCGA) database for patients with primary hepatocellular carcinoma. GSE147889 included microRNA (miRNA) profiling of liver tissue specimens from ninety-seven samples of HCC tumor tissue, with corresponding samples of surrounding tissue.

Conflicts of Interest

The authors declare that they have no conflicts of interest.

Acknowledgments

This work was funded by the Youth Science and Technology Research Project of Health and Family Planning Commission in Hebei Province (20200183).

References

- [1] J. Zhang and W. Lou, "A key mRNA-miRNA-lncRNA competing endogenous RNA triple sub-network linked to diagnosis and prognosis of hepatocellular carcinoma," *Frontiers in Oncology*, vol. 10, p. 340, 2020.

- [2] R. M. Critelli, N. De Maria, and E. Villa, "Biology of hepatocellular carcinoma," *Digestive Diseases*, vol. 33, no. 5, pp. 635–641, 2015.
- [3] W. Lou, J. Liu, Y. Gao et al., "MicroRNA regulation of liver cancer stem cells," *American Journal of Cancer Research*, vol. 8, no. 7, pp. 1126–1141, 2018.
- [4] J. H. Zhong, X. Xiang, Y. Y. Wang et al., "The lncRNA SNHG16 affects prognosis in hepatocellular carcinoma by regulating p62 expression," *Journal of Cellular Physiology*, vol. 235, no. 2, pp. 1090–1102, 2020.
- [5] X. Zhao, J. Dou, J. Cao et al., "Uncovering the potential differentially expressed miRNAs as diagnostic biomarkers for hepatocellular carcinoma based on machine learning in The Cancer Genome Atlas database," *Oncology Reports*, vol. 43, no. 6, pp. 1771–1784, 2020.
- [6] H. Liu, X. Wang, B. Feng et al., "Golgi phosphoprotein 3 (GOLPH3) promotes hepatocellular carcinoma progression by activating mTOR signaling pathway," *BMC Cancer*, vol. 18, no. 1, p. 661, 2018.
- [7] P. Roxburgh and T. R. Evans, "Systemic therapy of hepatocellular carcinoma: are we making progress?," *Advances in Therapy*, vol. 25, no. 11, pp. 1089–1104, 2008.
- [8] Y. Fu, D. Dominissini, G. Rechavi, and C. He, "Gene expression regulation mediated through reversible m⁶A RNA methylation," *Nature Reviews. Genetics*, vol. 15, no. 5, pp. 293–306, 2014.
- [9] J. Y. Roignant and M. Soller, "m⁶A in mRNA: an ancient mechanism for fine-tuning gene expression," *Trends in Genetics*, vol. 33, no. 6, pp. 380–390, 2017.
- [10] C. Gu, X. Shi, C. Dai et al., "RNA m⁶A modification in cancers: molecular mechanisms and potential clinical applications," *The Innovation.*, vol. 1, no. 3, p. 100066, 2020.
- [11] N. Qu, S. Qin, X. Zhang et al., "Multiple m6A RNA methylation modulators promote the malignant progression of hepatocellular carcinoma and affect its clinical prognosis," *BMC Cancer*, vol. 20, no. 1, p. 165, 2020.
- [12] W. Liu, C. Zhong, D. Lv, M. Tang, and F. Xie, "N6-methyladenosine RNA methylation regulators have clinical prognostic values in hepatocellular carcinoma," *Frontiers in Genetics*, vol. 11, p. 863, 2020.
- [13] Y. Fu, S. Liu, S. Zeng, and H. Shen, "From bench to bed: the tumor immune microenvironment and current immunotherapeutic strategies for hepatocellular carcinoma," *Journal of Experimental & Clinical Cancer Research*, vol. 38, no. 1, p. 396, 2019.
- [14] C. Kole, N. Charalampakis, S. Tsakatikas et al., "Immunotherapy for hepatocellular carcinoma: a 2021 update," *Cancers (Basel)*, vol. 12, no. 10, p. 2859, 2020.
- [15] D. Schizas, N. Charalampakis, C. Kole et al., "Immunotherapy for pancreatic cancer: a 2020 update," *Cancer Treatment Reviews*, vol. 86, p. 102016, 2020.
- [16] D. Schizas, N. Charalampakis, C. Kole et al., "Immunotherapy for esophageal cancer: a 2019 update," *Immunotherapy*, vol. 12, no. 3, pp. 203–218, 2020.
- [17] D. Han, J. Liu, C. Chen et al., "Anti-tumour immunity controlled through mRNA m⁶A methylation and YTHDF1 in dendritic cells," *Nature*, vol. 566, no. 7743, pp. 270–274, 2019.
- [18] L. Yi, G. Wu, L. Guo, X. Zou, and P. Huang, "Comprehensive analysis of the PD-L1 and immune infiltrates of m⁶A RNA methylation regulators in head and neck squamous cell carcinoma," *Molecular Therapy–Nucleic Acids*, vol. 21, pp. 299–314, 2020.
- [19] Z. S. Niu, X. J. Niu, and W. H. Wang, "Genetic alterations in hepatocellular carcinoma: an update," *World Journal of Gastroenterology*, vol. 22, no. 41, pp. 9069–9095, 2016.
- [20] A. Rastogi, "Changing role of histopathology in the diagnosis and management of hepatocellular carcinoma," *World Journal of Gastroenterology*, vol. 24, no. 35, pp. 4000–4013, 2018.
- [21] C. Gu, X. Shi, X. Dang et al., "Identification of common genes and pathways in eight fibrosis diseases," *Frontiers in Genetics*, vol. 11, article 627396, 2020.
- [22] C. Gu, Z. Huang, X. Chen et al., "TEAD4 promotes tumor development in patients with lung adenocarcinoma via ERK signaling pathway," *Biochimica et Biophysica Acta - Molecular Basis of Disease*, vol. 1866, no. 12, article 165921, 2020.
- [23] L. Zhang, X. Shi, C. Gu et al., "Identification of cell-to-cell interactions by ligand-receptor pairs in human fetal heart," *Biochimica et Biophysica Acta - Molecular Basis of Disease*, vol. 1866, no. 12, p. 165917, 2020.
- [24] X. Shi, X. Shao, B. Liu et al., "Genome-wide screening of functional long noncoding RNAs in the epicardial adipose tissues of atrial fibrillation," *Biochimica et Biophysica Acta - Molecular Basis of Disease*, vol. 1866, no. 7, p. 165757, 2020.
- [25] C. Gu, X. Shi, Z. Huang et al., "A comprehensive study of construction and analysis of competitive endogenous RNA networks in lung adenocarcinoma," *Biochimica et Biophysica Acta, Proteins and Proteomics*, vol. 1868, no. 8, article 140444, 2020.
- [26] X. Deng, R. Su, X. Feng, M. Wei, and J. Chen, "Role of N⁶-methyladenosine modification in cancer," *Current Opinion in Genetics & Development*, vol. 48, pp. 1–7, 2018.
- [27] C. Gu, X. Shi, W. Qiu et al., "Comprehensive analysis of the prognostic role and mutational characteristics of m6A-related genes in lung squamous cell carcinoma," vol. 9, no. 559, p. 140444, 2021.
- [28] J. Lu, J. Qian, S. Yin, L. Zhou, S. Zheng, and W. Zhang, "Mechanisms of RNA N6-methyladenosine in hepatocellular carcinoma: from the perspectives of etiology," *Frontiers in Oncology*, vol. 10, p. 1105, 2020.
- [29] X. Zhao, Y. Chen, Q. Mao et al., "Overexpression of YTHDF1 is associated with poor prognosis in patients with hepatocellular carcinoma," *Cancer Biomarkers*, vol. 21, no. 4, pp. 859–868, 2018.
- [30] L. Zhong, D. Liao, M. Zhang et al., "YTHDF2 suppresses cell proliferation and growth via destabilizing the EGFR mRNA in hepatocellular carcinoma," *Cancer Letters*, vol. 442, pp. 252–261, 2019.
- [31] A. Tanabe, J. Konno, K. Tanikawa, and H. Sahara, "Transcriptional machinery of TNF- α -inducible YTH domain containing 2 (YTHDC2) gene," *Gene*, vol. 535, no. 1, pp. 24–32, 2014.
- [32] M. Chen, L. Wei, C. T. Law et al., "RNA N6-methyladenosine methyltransferase-like 3 promotes liver cancer progression through YTHDF2-dependent posttranscriptional silencing of SOCS2," *Hepatology*, vol. 67, no. 6, pp. 2254–2270, 2018.
- [33] L. Li, Y. L. Zheng, C. Jiang et al., "HN1L-mediated transcriptional axis AP-2 γ /METTL13/TCF3-ZEB1 drives tumor growth and metastasis in hepatocellular carcinoma," *Cell Death and Differentiation*, vol. 26, no. 11, pp. 2268–2283, 2019.
- [34] J. Z. Ma, F. Yang, C. C. Zhou et al., "METTL14 suppresses the metastatic potential of hepatocellular carcinoma by

- modulating N⁶-methyladenosine-dependent primary micro-RNA processing,” *Hepatology*, vol. 65, no. 2, pp. 529–543, 2017.
- [35] Y. Chen, C. Peng, J. Chen et al., “WTAP facilitates progression of hepatocellular carcinoma via m⁶A-HuR-dependent epigenetic silencing of ETS1,” *Molecular Cancer*, vol. 18, no. 1, p. 127, 2019.
- [36] Z. Li, F. Li, Y. Peng, J. Fang, and J. Zhou, “Identification of three m⁶A-related mRNAs signature and risk score for the prognostication of hepatocellular carcinoma,” *Cancer Medicine*, vol. 9, no. 5, pp. 1877–1889, 2020.
- [37] W. Li, Q. F. Chen, T. Huang, L. Shen, Z. L. Huang, and P. Wu, “Profiles of m⁶A RNA methylation regulators for the prognosis of hepatocellular carcinoma,” *Oncology Letters*, vol. 19, no. 4, pp. 3296–3306, 2020.
- [38] L. Chen, X. Huang, W. Zhang et al., “Correlation of PD-L1 and SOCS3 co-expression with the prognosis of hepatocellular carcinoma patients,” *Journal of Cancer*, vol. 11, no. 18, pp. 5440–5448, 2020.
- [39] S. Tu, W. Huang, C. Huang, Z. Luo, and X. Yan, “Contextual regulation of TGF- β signaling in liver cancer,” *Cell*, vol. 8, no. 10, p. 1235, 2019.
- [40] M. Dimri and A. Satyanarayana, “Molecular signaling pathways and therapeutic targets in hepatocellular carcinoma,” *Cancers (Basel)*, vol. 12, no. 2, p. 491, 2020.
- [41] K. S. Jeng, C. J. Jeng, W. J. Jeng et al., “Sonic Hedgehog signaling pathway as a potential target to inhibit the progression of hepatocellular carcinoma (Review),” *Oncology Letters*, vol. 18, no. 5, pp. 4377–4384, 2019.
- [42] F. Su, J. Zhao, S. Qin et al., “Over-expression of thrombospondin 4 correlates with loss of miR-142 and contributes to migration and vascular invasion of advanced hepatocellular carcinoma,” *Oncotarget*, vol. 8, no. 14, pp. 23277–23288, 2017.
- [43] Q. Yu, L. Xiang, L. Yin, X. Liu, D. Yang, and J. Zhou, “Loss-of-function of miR-142 by hypermethylation promotes TGF-beta-mediated tumour growth and metastasis in hepatocellular carcinoma,” *Cell Proliferation*, vol. 50, no. 6, article e12384, 2017.

Retraction

Retracted: A Systematic Analysis on COVID-19 Patients in Inner Mongolia Based on Dynamic Monitoring

BioMed Research International

Received 12 March 2024; Accepted 12 March 2024; Published 20 March 2024

Copyright © 2024 BioMed Research International. This is an open access article distributed under the Creative Commons Attribution License, which permits unrestricted use, distribution, and reproduction in any medium, provided the original work is properly cited.

This article has been retracted by Hindawi following an investigation undertaken by the publisher [1]. This investigation has uncovered evidence of one or more of the following indicators of systematic manipulation of the publication process:

- (1) Discrepancies in scope
- (2) Discrepancies in the description of the research reported
- (3) Discrepancies between the availability of data and the research described
- (4) Inappropriate citations
- (5) Incoherent, meaningless and/or irrelevant content included in the article
- (6) Manipulated or compromised peer review

The presence of these indicators undermines our confidence in the integrity of the article's content and we cannot, therefore, vouch for its reliability. Please note that this notice is intended solely to alert readers that the content of this article is unreliable. We have not investigated whether authors were aware of or involved in the systematic manipulation of the publication process.

Wiley and Hindawi regrets that the usual quality checks did not identify these issues before publication and have since put additional measures in place to safeguard research integrity.

We wish to credit our own Research Integrity and Research Publishing teams and anonymous and named external researchers and research integrity experts for contributing to this investigation.

The corresponding author, as the representative of all authors, has been given the opportunity to register their agreement or disagreement to this retraction. We have kept a record of any response received.

References

- [1] L. Yu, T. Li, L. Gao et al., "A Systematic Analysis on COVID-19 Patients in Inner Mongolia Based on Dynamic Monitoring," *BioMed Research International*, vol. 2021, Article ID 5559187, 8 pages, 2021.

Research Article

A Systematic Analysis on COVID-19 Patients in Inner Mongolia Based on Dynamic Monitoring

Lan Yu,¹ Tianbao Li ,^{2,3} Li Gao,⁴ Bo Wang,^{2,3} Jun Chai,⁵ Xiaoli Shi,^{2,3} Rina Su,⁶ Geng Tian,^{2,3} Jialiang Yang ,^{2,3} and Dejun Sun ⁴

¹Clinical Medical Research Center/Inner Mongolia Key Laboratory of Gene Regulation of the Metabolic Diseases, Inner Mongolia People's Hospital, Hohhot, Inner Mongolia, China

²Geneis (Beijing) Co., Ltd., Beijing, China

³Qingdao Geneis Institute of Big Data Mining and Precision Medicine, Qingdao, China

⁴Department of Pulmonary and Critical Care Medicine/Key Laboratory of National Health Commission for the Diagnosis & Treatment of COPD, Inner Mongolia People's Hospital, Hohhot, Inner Mongolia, China

⁵Medical Imaging Department, Inner Mongolia People's Hospital, Hohhot, Inner Mongolia, China

⁶Telemedicine Center, Inner Mongolia People's Hospital, Hohhot, Inner Mongolia, China

Correspondence should be addressed to Dejun Sun; nmresearch@foxmail.com

Lan Yu and Tianbao Li contributed equally to this work.

Received 15 January 2021; Revised 27 January 2021; Accepted 7 April 2021; Published 21 April 2021

Academic Editor: Andrea Scribante

Copyright © 2021 Lan Yu et al. This is an open access article distributed under the Creative Commons Attribution License, which permits unrestricted use, distribution, and reproduction in any medium, provided the original work is properly cited.

COVID-19 has spread globally with over 90,000,000 incidences and 1,930,000 deaths by Jan 11, 2021, which poses a big threat to public health. It is urgent to distinguish COVID-19 from common pneumonia. In this study, we reported multiple clinical feature analyses on COVID-19 in Inner Mongolia for the first time. We dynamically monitored multiple clinical features of all 75 confirmed COVID-19 patients, 219 pneumonia patients, and 68 matched healthy people in Inner Mongolia. Then, we studied the association between COVID-19 and clinical characteristics, based on which to construct a novel logistic regression model for predicting COVID-19. As a result, among the tested clinical characteristics, WBC, hemoglobin, C-reactive protein (CRP), ALT, and Cr were significantly different between COVID-19 patients and patients in other groups. The area under the curve (AUC) of the receiver operating characteristic (ROC) curve was 0.869 for the logistic regression model using multiple factors associated with COVID-19. Furthermore, the CRP reaction showed five different time-series patterns with one-peak and double-peak modes. In conclusion, our study identified a few clinical characteristics significantly different between COVID-19 patients and others in Inner Mongolia. The features can be used to establish a reliable logistic regression model for predicting COVID-19.

1. Introduction

Since early 2020, there has been an outbreak of a novel highly infectious disease called coronavirus disease 2019 (COVID-19), which quickly spread globally. As reported by the World Health Organization (WHO), there are more than 90 million confirmed COVID-19 cases and 1.9 million deaths across 212 countries by Jan 11, 2021, and these two numbers are still increasing. COVID-19 is a new type of pneumonia with several kinds of clinical manifestations caused by severe acute

respiratory syndrome coronavirus (SARS-CoV-2) [1]. SARS-CoV-2 belongs to the coronavirus family, whose members also cause infectious diseases like severe respiratory to viral cold, severe acute respiratory syndrome (SARS), and Middle East respiratory syndrome (MERS) [2]. By binding to angiotensin-converting enzyme-2 (ACE-2), SARS-CoV-2 primarily targets respiratory epithelium cells, which results in inflammatory response and thereby induces epithelium cell apoptosis. The transmission modes of COVID-19 are similar to those of SARS, including contact, droplet, airborne, vomit,

fecal-oral, bloodborne, mother-to-child, and animal-to-human transmission [3, 4]. Based on the Diagnosis and Treatment for COVID-19 (Trial version 7) published on Aug 19, 2020, a suspected case is classified as a confirmed case if it has one of the following etiological or serological evidence: RT-PCR detection of SARS-CoV-2 nucleic acid is positive; viral gene sequence is highly homologous with known SARS-CoV-2; the SARS-CoV-2-specific IgM antibody and IgG antibody are positive; the SARS-CoV-2-specific IgG antibody turns from negative to positive, or the IgG antibody titer in the recovery phase is at least 4 times higher than that in the acute phase [5].

Similar to SARS, pulmonary dysfunction and fibrosis are the primary cause for the death of COVID-19 patients [6]. Cardiac arrest and total organ failure are the secondary cause, indicating that the immune system also participates in the course of disease progression [7–9]. The illness severity can range from mild to critical in the cohort, including mild (mild symptoms and no manifestations of pneumonia on imaging), moderate (fever, respiratory symptoms, and manifestations of pneumonia on imaging), severe (dyspnea, hypoxia, ≥ 30 breaths per minutes, and oxygen saturation $\leq 93\%$ at rest, or more than 50% lung involvement on imaging), and critical (respiratory failure, mechanical ventilation required, shock, or multiorgan system dysfunction) [5, 10, 11]. Furthermore, some patients died from “consequent cytokine storm” due to total organ failure by viral inflammatory response [12, 13]. When plenty of cytokines release to blood circulation, they lead to electrolyte imbalance, metabolic acidosis, multiple organ dysfunction, and total organ failure. Therefore, it is critical to have early diagnosis and frequent monitor especially for patients with underlying diseases, whose immune systems could be suppressed and are sensitive to cytokine release.

Though the RT-PCR test is served as the gold standard technique to confirm the infection of SARS-CoV-2, the technique is time consuming and subject to false negative [11]. Therefore, other auxiliary tests combining clinical, molecular, and radiological features would be beneficial for diagnosis. In clinical, COVID-19 is mostly characterized by inflammatory exudative pulmonary lesions with symptoms including fever, dry cough, headache, myalgia, breathlessness, and asthenia [14, 15]. Although clinical tests are essential for diagnosis, the symptoms of patients at the early stage of COVID-19 could not be differentiated from common viral pneumonia. Thus, it is critical to study the association between cellular or molecular markers and the severity and prognosis of COVID-19. Recently, several strongly associated biomarkers, such as the lymphopenia (defined as lymphocyte count < 1000), elevated C-reactive protein (CRP), and lactate dehydrogenase (LDH), were identified [16, 17]. In addition, non- or less-specific myocardial biomarkers, such as creatine kinase (CK), elevated level of hepatic enzyme, d-dimers, interleukin-6, C-reactive protein, and procalcitonin, were also suggested to associate with the poor prognosis of COVID-19 [18–20].

It has been reported that clinical, molecular, and radiological features of COVID-19 patients are all varied with time. However, the dynamic patterns of COVID-19 patients have not been fully studied. For example, a series of clinical factors such as white blood cell (WBC), C-reactive protein (CRP), and lymphocyte (LYM) have been reported to be associated with

COVID-19 progression in previous studies [21]. Dynamic monitoring of these inflammatory factors would be a benefit for developing a suitable plan as well as predicting disease outcome. COVID-19 is an acute infectious disease, and the early symptom is similar to common cold; however, some patients will develop rapid disease progression and multiple organ failures within only a few days from diagnosis.

Finally, previous studies have suggested that patients of different races or in different regions may have differences in COVID-19 progression, symptoms, and prognosis. Several studies have reported people living at multiple regions, such as Asia, Europe, and North America, presented different clinical symptoms of the disease. To date, about eighty thousand COVID-19 confirmed cases have been reported in China, worse more, there are nearly 31,021,218 confirmed cases with approximately 960 thousand deaths globally, and the number is more likely to increase [22]. Currently, most cases were from the United States, which accounts for nearly 80% of total cases globally. However, since the Inner Mongolia population has unique characteristics in terms of ethnicity, climate, and dietary culture, we conducted this study from multicenter hospitals across Inner Mongolia, aiming to investigate the difference among people living in Inner Mongolia, China, during the time of COVID-19 occurrence. We found several familial cluster cases which confirmed with the previous study indicting the possibility of human-to-human transmission of SARS-CoV-2 [23].

We conducted a retrospective cohort study from multiple medical centers in the Inner Mongolia autonomous region, China. This study is aiming to investigate the association between the clinical parameters and prognosis in Inner Mongolia, especially the time-series patterns. Moreover, we try to preliminarily study whether COVID-19 has the homogeneity across different ethnic groups, viral load, clinical features as well as transmission mode, and possible other influencing factors as well.

2. Materials and Methods

2.1. Cohort Population of the Study. This retrospective population-based cohort study was performed in eleven cities across the Inner Mongolia region of China. Seventy-five patients with COVID-19, 219 viral or bacterial acquired pneumonia patients, and 68 health individuals of Han or Mongolian ethnicity were enrolled in the present study. All COVID-19 patients were laboratory-confirmed clinically diagnosed, and the admission date was ranged between January 21, 2020, and February 23, 2020. The criteria used for the diagnosis of COVID-19 was confirmed by RT-PCR as the following: RT-PCR detection of SARS-CoV-2 nucleic acid is positive, and viral gene sequence is highly homologous with known SARS-CoV-2. Pneumonia was classified combining with clinical features of fever and cough or cough phlegm and chest X-ray scanning, which show marked thickening of the lung texture and could hear moist rales or pronounced sputum purr in the lungs with stethoscope auscultation. Pneumonia patients and healthy people were randomly selected from hospitals within the last 6 months before the COVID-19 pandemic. The clinical information including age, gender, severity of disease, incubation time,

and hospitalization with clinical lab exams at different points was collected. For COVID-19 and pneumonia patients, the clinical laboratory test results were collected from medical facilities for each patient on both the admission day to the hospital and monitoring during the entire hospital stay every two days. For healthy people, the clinical laboratory test results were collected on the date of regular health exam. Generally, lab exams were performed approximately every two days which included WBC, lymphocyte, neutrophils, hemoglobin, platelet, C-reactive protein (CRP), procalcitonin (PCT), alanine aminotransferase (ALT), aspartate aminotransferase (AST), lactate dehydrogenase (LDH), and serum concentration of creatinine (Cr). On admission day, patients were clinically diagnosed as mild-moderate, severe, or critical facilitating physicians to design the treatment plan according to the WHO classification for COVID-19 [5, 10]. Informed consent was waived since this retrospective study represents no more than minimal risk to subjects and will not adversely affect their rights.

2.2. Logistic Regression Model to Distinguish Patients with COVID-19 from Viral or Bacterial Acquired Pneumonia. Continuous variables were expressed as mean \pm standard deviation, and categorical variables were presented as number of subjects (frequencies). The Wilcoxon rank-sum test was used for testing the difference of variables between COVID-19 groups and pneumonia or healthy people, respectively, with multiple correction tests, and the significance threshold was 0.05. A logistic regression model was built to distinguish COVID-19 from seasonal pneumonia identified by single or multiple laboratory features. Logistic regression was applied for the probability model for predicting the probability of an event by fitting a logic function/hypothesis function. The output of the logistic regression formula means the probability of $y = 1$ given X and b . $g(x)$ is sigmoid function as the following:

$$P(y = 1 | X; b) = g(b^T X) = \frac{1}{1 + e^{-b^T X}}, \quad (1)$$

where b stands for a linear coefficient of logistic regression, X stands for the features extracted from data, and $g()$ stands for the function of sigmoid. In addition, this equation shown above predicts P as a function of X . Using this equation, note that as $b^T X$ approaches negative infinity, the result in the formula for P approaches zero, so P approaches zero. When $b^T X$ approaches positive infinity, P approaches one. Thus, the function is bounded by 0 and 1 which are the limits for P . Furthermore, the logistic regression model was used to predict the type of disease and receiver operating characteristic (ROC) curve was created for prediction model assessment and 95% confidence interval was calculated by Python package of statsmodels (v0.12.1).

3. Results

3.1. A Few Clinical Laboratory Features of COVID-19 Patients in Inner Mongolia Were Significantly Different with Those of Common Pneumonia and Healthy People. We

reported a retrospective cohort study with 75 COVID-19 patients from multiple medical centers. All COVID-19 patients were confirmed by laboratory RT-PCR, along with randomly selected 39 patients with seasonal pneumonia, and 68 nonpneumonia healthy people (Table 1). The mean age of the four cohorts was 43.67, 36.12, 55.46, and 45.39, respectively, and the age of most COVID-19 patients was over 60. According to the WHO definition, there were 13 mild symptom cases, 48 moderate symptom cases, two severe cases, and one death which are due to COVID-19-related complication. The youngest COVID-19 patient was 17 months old with the diagnosis of mild, and a severe case of most aged patient was 86. The imported COVID-19 patient cohort includes 25 mild symptom cases and 25 moderate cases with 2 severity cases. Epidemiology investigation illustrated the average incubation period of COVID-19 was approximately 9 days and the longest incubation day was 26 days, which was consistent with previous studies [24]. The average hospitalization stay was 22 days. For epidemiology tracking, several patients had visited the city with COVID-19 patients and almost all confirmed cases were directly or indirectly related to other patients. In addition, the people participated in our study presented significant as family cluster and community-acquired transmission pattern (data not shown).

Almost all patients on admission day presented fever symptom, 16% with dyspnea, 28% with cough, 31% with fatigue, 64% with myalgia, 11% with diarrhea, and 21% with other atypical symptoms including abdominal discomfort, nausea/vomiting, and headache. The elderly and men have relatively high susceptibility to SARS-CoV-2, and previous studies also reported that MERS-CoV and SARS-CoV infected more men than female [21, 24]. One hypothesis is that women have relatively strong immune response ability including both innate and adaptive immune response, which might be due to additional X chromosome and sexual hormone [25, 26]. At admission, multiple lab exams were performed including white blood cell counts, lymphocyte, neutrophil granulocyte, hemoglobin, platelet count (PCT), C-reactive protein (CRP), and several hepatic enzymes. The comparison of serum creatinine (Cr), white blood cell count (WBC), CRP, neutrophil granulocyte, hemoglobin, and aspartate aminotransferase (AST) showed statistically significant difference between COVID-19 and seasonal pneumonia patients as well as nonpneumonia (Figure 1). The COVID-19 patients could be distinguished by the combination of clinical laboratory features, while no significant showed between seasonal pneumonia and nonpneumonia patients.

3.2. Logistic Regression Model on Clinical Laboratory Features Can Diagnose COVID-19 with Relative Good Performance. On the diagnosis of COVID-19, most patients presented with increasing lymphocytopenia and neutropenia; furthermore, most patients also had elevated ALT, lymphocyte, and creatinine. In order to evaluate the performance of the statistical model, we selected two cohorts (COVID patients and pneumonia patients) to find out whether the logistic regression model could separate those variables accurately. The results showed our logistic regression model could differentiate

TABLE 1: Patient cohort information.

Clinical variable	Category	COVID-19	Imported COVID-19	Pneumonia	Control
Age	Mean (range)	43.67 (1-86)	36.12 (25-27)	55.46 (1-95)	45.36 (1-89)
Gender	Male	38	25	126	40
	Female	37	27	93	28
Severity degree	Mild	13	25	95	—
	Moderate	48	25	128	—
	Serious and death	3	2	0	—
Incubation time	Average (days)	9.22 ± 5.83	—	—	—
Hospitalization	Average (days)	22.28 ± 7.55	17.42 ± 8.23	—	—

COVID patients from healthy people within three clinical laboratory features, which indicated our model has good performance (Figure 2(a)). Lymphocytes, white blood cells, and CRP associated with disease severity and prognosis were chosen to further evaluate the model performance. The cutoff value of 0.5 was applied in the model to evaluate the effect on the model, and the cutoff values of lymphocytes were 8.34, CRP was 98.60, and WBC was 9.17. The AUC of lymphocytes, CRP, and white blood cell were 0.68, 0.56, and 0.76, respectively, indicating lymphocytes and white blood cell were closely associated with the progression and prognosis of COVID-19 and were a good indicator for COVID-19 diagnosis. The AUC of all three features reached 0.82 with a 95% confidence interval of 0.856 to 0.909 and was relatively better than a single marker, which is approved that COVID-19 had multiple influencing factors and the result would assist health professionals to develop better diagnosis estimation for patients (Figure 2(b)).

3.3. There Are Several Dynamic Patterns of C-Reactive Protein in COVID-19 Patients in Inner Mongolia. In order to monitor the CRP which would reflect the disease severity, progress, and effectiveness of treatment, we plotted the dynamic monitoring figure. According to CRP result on the admission day, CRP values were collected as initial monitor point and continue to monitor every other day for several time points. As shown in Figure 3(a), there were five patterns during hospital stay, indicating the treatment efficacy. The CRP level of most patients had been decreased after 4 days and responds to treatment within a week (Figure 3(b)). Another specific pattern is shown in Figure 3(c).

Figure 3(b) shows the dynamic monitoring of CRP pattern from patients; the first peak was showing at the first week of hospital stay, which means patients' condition deteriorated for a period of time; they started to respond to treatment after hospital stay, showing that the treatment was effective and CRP level remained stable, still not fully recovered to normal though.

4. Discussion

Coronavirus is a family of enveloped single-stranded positive-sense RNA viruses and has a worldwide distribution. Six types of coronaviruses in the world can infect humans,

and most infections are mild. However, severe acute respiratory syndrome (SARS-CoV) and Middle East respiratory syndrome (MERS-CoV) caused a large pandemic outbreak, and the mortality rate was approximately 10% and 30%, respectively [27]. Comparing with the SARS-CoV outbreak in 2003 which was a high-pathogenicity virus with high mortality, SARS-CoV-2 seems to be relatively more contagious with approximately 2% [28]. However, people infected with SARS-CoV-2 could develop neutralizing antibody and have prolonged disease progress. The fact might illustrate the following two phenomena: firstly, in addition to the respiratory system, SARS-CoV-2 might cause multiple organ damages, including gastroenterological, and neurological, kidney damages, and even total organ failure.

Similar to other coronaviruses, SARS-CoV-2 also utilizes an angiotensin-converting enzyme-2 (ACE-2) functional receptor which is widely expressed in vascular endothelial cells and renal tubular epithelium, hepatic cells, neuron, and pulmonary and gastrointestinal systems. There are several hypotheses trying to explore the underline mechanism of SARS-CoV-2 infection, development, and efforts to deliver effective treatment and vaccination. To date, the mechanisms of immunopathology of SARS-CoV-2 infection include both innate and adaptive immunity. The epithelium of the lungs serves as the physical barrier, and epithelial cells, dendritic cells, and macrophages can trigger proinflammatory response of macrophages in bronchoalveolar cells. Those cells serve as an initial immune defense against viruses. Previous studies indicated that the macrophage accumulation or depletion was associated with severity of disease [29]. Moreover, neutrophils play a critical role in acute inflammatory response of bronchoalveolar. Therefore, elevated neutrophils are believed to produce reactive oxygen species, which is considered as the potent antibacterial mechanism. In one situation, virus infection could directly infect lymphocytes resulting in cell apoptosis. Another situation is that it could also destroy the lymphocyte-produced organs, such as bone marrow or thymus, interfering lymphocyte production or dysfunction.

The early stage symptoms of COVID-19 include dry cough, fever, chill, tiredness, and upper respiratory symptom shortness or difficulty breathing, and some atypical symptoms, such as gastrointestinal discomfort, diarrhea, etc. [30, 31], which is consistent with the previous report of early stage

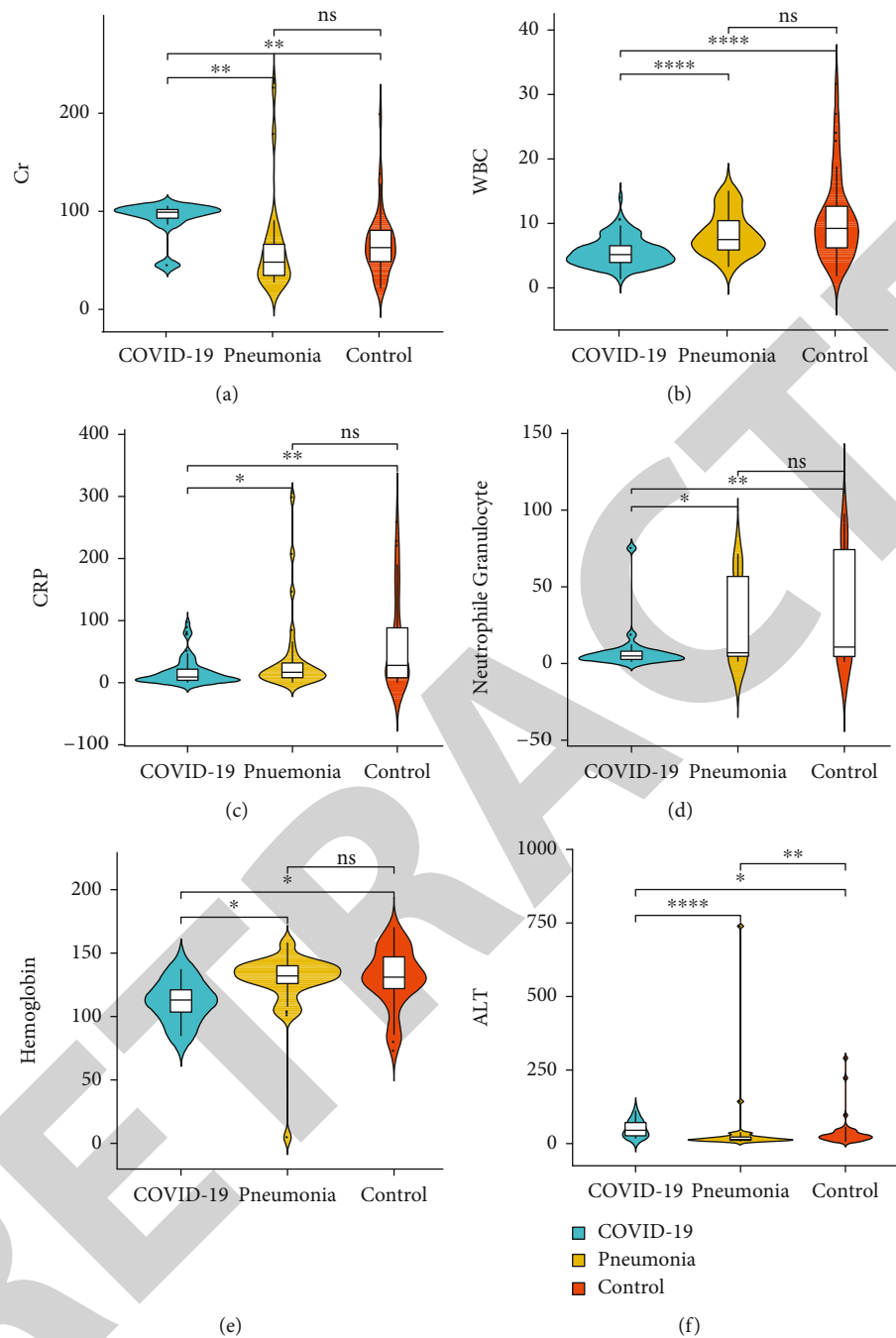


FIGURE 1: Clinical characteristic comparison between COVID-19 among pneumonia and healthy people. ns presents no significant, “**” presents p value < 0.01 , “***” presents p value < 0.001 , and “****” presents p value $< 10^{-8}$ which has been added into the figure legend.

of SARS and seasonal influenza [32, 33]. COVID-19 patients usually have decreased white blood cell count and lymphocyte cell count caused by suppressed immune response resulting in sequential infection. Though decreased lymphocyte count is not a specific factor for COVID patients, it can distinguish other common bacterial and viral infection, and it could only present in the late stage of the disease. CT imaging features of SARS-CoV-2 are highly sensitive for patients who have false-negative RT-PCR results. Moreover, CT image could be a good indicator for monitoring patient disease prognosis as well as therapy effectiveness. The typical fea-

tures from the CT exam for SARS-CoV-2-infected patients are bilateral lung lobe involvements and ground-glass opacities (GGO) shown in the early stage of the disease, followed by pulmonary consolidation, increasing the area of GGO and fibrosis shown in late stage [34, 35]. Finally, the pulmonary tissue turned into “white lung” which leads to severe dyspnea requiring mechanical ventilation and results in septic shock, total multiple organ failure, and cardiac arrest due to increased viral titers.

In our study, the clinical laboratory test of CRP showed significant difference between COVID-19 patients and

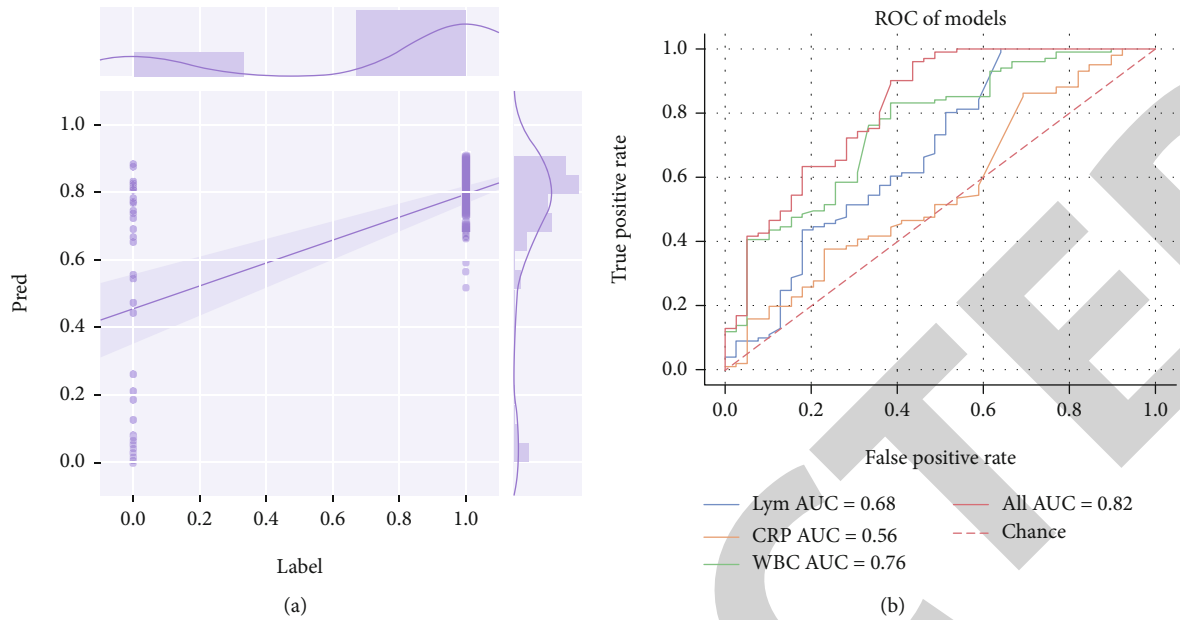


FIGURE 2: (a) Logistic regression model for COVID-19 prediction with single or multiple laboratory features and applied for probability model for predicting the probability of hypothesis function. (b) The area under the curve of receiver operating characteristic of different clinical markers associated with COVID-19 for leukomonocyte, CRP, and white blood cell, respectively.

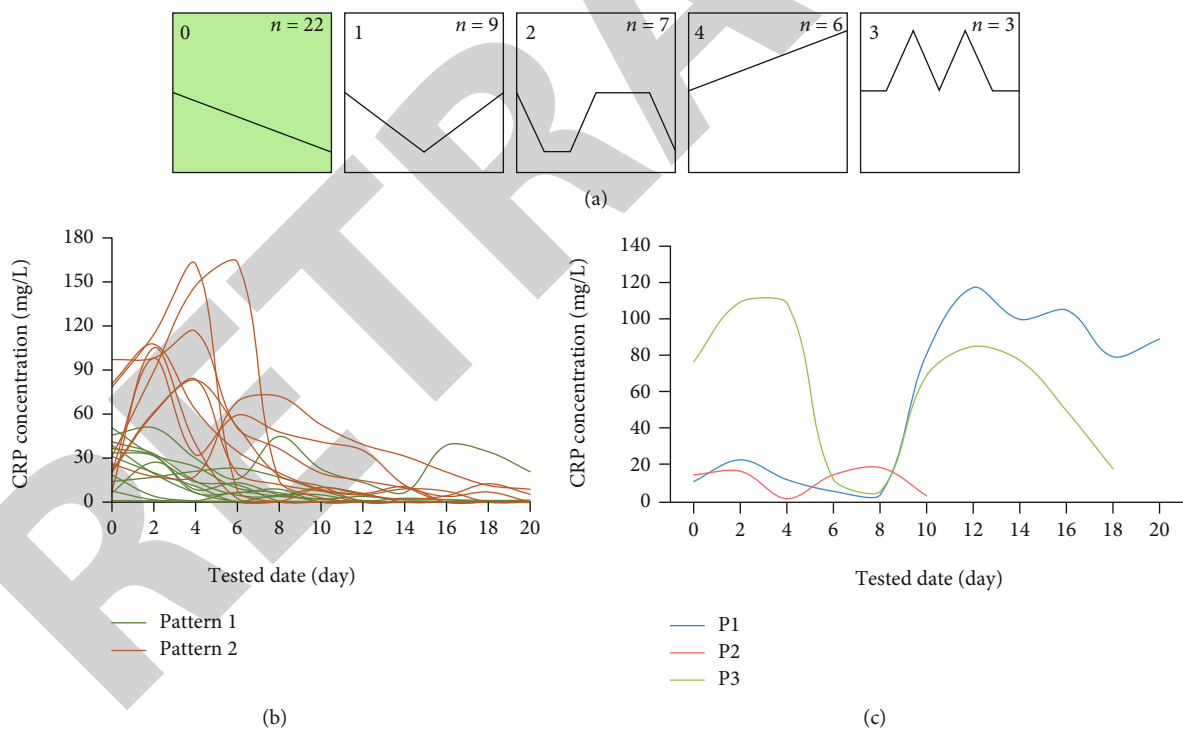


FIGURE 3: Dynamic monitoring of C-reactive protein in COVID-19 patients. (a) Detected CRP pattern with dynamic monitoring. (b) CRP response in a specific pattern of individual patient.

control. CRP, secreted by the hepatocytes, is a well-known indication of inflammation in the inertial thinking way [36, 37]. The elevated CRP is founded not only in the acute phase of inflammatory disease but also in most chronic coronary and metabolic diseases, such as cardiovascular disease, diabetes, and obesity [38]. However, another important role of

CRP is to regulate the human innate immune process and adjust the interaction between the inflammatory intruder and the immune system. It is logical that among the COVID-19 cases, the level of CRP was increased as the disease was diagnosed. Furthermore, three types of dynamic elevation patterns were revealed in our study; the value of CRP

was gradually risen at the beginning of the hospitalization in pattern 1, signifying that the immune response was activated. As the treatment progresses, the SARS-CoV-2 was eliminated, and the level of CRP decreased. The CRP in the patients of pattern 2 had not shown an obvious peak but a flattened one, probably because of the testing time. That is, the sample or hospitalization time point was later than the CRP increasing time; there is another probability: the SARS-CoV-2 load was not enough to induce a strong reaction of the host defense, and the virus was wiped out soon. As far as pattern 3 is concerned, 2 peaks were shown in sequential order. This phenomenon might be indicated that CRP played a pleiotropic role in the process. Either anti-inflammation or proinflammation could be the major role in the different phases of the disease. The first peak of CRP might be the anti-inflammation activation when SARS-CoV-2 infected the host at the beginning, while the function of the second peak of CRP might largely rely on the context, either the relapse of the SARS-CoV-2 eliciting the reactivation of the complement pathway or the change of complement components induced by CRP, leading to the proinflammation course. In summary, the CRP-activated complement pathway is different from the activation mediated by antigen-antibody complexes, with rarely activated late phase component proteins.

5. Conclusion

In this study, we collected clinical data from multicenter hospitals in Inner Mongolia, China. We performed statistical analysis of clinical laboratory features associated with SARS-CoV-2 infection between COVID-19 and common pneumonia patients. Second, we further explore the dynamic changes of clinical parameters during the incubation period as well as hospital stays. This study provides primary results to benefit health care physicians in diagnosis evaluation.

Data Availability

The data used to support the findings of this study are available from the corresponding author upon request.

Ethical Approval

This study was approved by the Ethics Committee of Inner Mongolia People's Hospital.

Consent

Human samples were obtained with informed consent.

Conflicts of Interest

Author TL, XM, BW, XS, and JY were employed by the company Geneis Beijing Co., Ltd. The remaining authors declare that the research was conducted in the absence of any commercial or financial relationships that could be construed as a potential conflict of interest.

Authors' Contributions

DS and JY conceived the project; LY and TL implemented the experiments and analyzed the data; LG, XM, JC, BW, and XS prepared the data and performed literature search; LY, TL, RS, and JY wrote the manuscript. All authors approved the final manuscript. Lan Yu and Tianbao Li contributed equally to this work.

Acknowledgments

This study was partially supported by the Science and Technology Planning Project of Inner Mongolia (No. 2020GG0004), the Natural Science Foundation of Hunan Province (No. 2018JJ2461), the talent training plan for the key laboratory of Inner Mongolia Science and Technology Department, and the Project to Introduce Intelligence from Oversea Experts to the Changsha City (No. 2089901).

References

- [1] Gemelli Against COVID-19 Post-Acute Care Study Group, "Post-COVID-19 global health strategies: the need for an interdisciplinary approach," *Aging Clinical and Experimental Research*, vol. 32, no. 8, pp. 1613–1620, 2020.
- [2] M. Mehdi Abdol, A. Mohabati Mobarez, N. khoramabadi, S. Papian, and A. Talebi Bezmin Abadi, "Potent T-cell mediated immune response against *Legionella pneumophila* in mice following vaccination with detoxified lipopolysaccharide non-covalently combined with recombinant flagellin A and peptidoglycan-associated lipoprotein," *Microbial Pathogenesis*, vol. 149, article 104364, 2020.
- [3] J. F. Chan, S. Yuan, K. H. Kok et al., "A familial cluster of pneumonia associated with the 2019 novel coronavirus indicating person-to-person transmission: a study of a family cluster," *Lancet*, vol. 395, no. 10223, pp. 514–523, 2020.
- [4] World Health Organization, *Transmission of SARS-CoV-2: implications for infection prevention precautions: scientific brief, 09 July 2020*, World Health Organization, 2020.
- [5] Chinese Health Commission, "Diagnosis and treatment for COVID-19 (trial version, 7)," *Chinese Medicine*, vol. 15, pp. 801–805, 2020.
- [6] T. Menter, J. D. Haslbauer, R. Nienhold et al., "Postmortem examination of COVID-19 patients reveals diffuse alveolar damage with severe capillary congestion and variegated findings in lungs and other organs suggesting vascular dysfunction," *Histopathology*, vol. 77, no. 2, pp. 198–209, 2020.
- [7] P. F. Stahel and S. R. Barnum, "Complement inhibition in coronavirus disease (COVID)-19: a neglected therapeutic option," *Frontiers in Immunology*, vol. 11, 2020.
- [8] A. Alshukry, H. Ali, Y. Ali et al., "Clinical characteristics of coronavirus disease 2019 (COVID-19) patients in Kuwait," *PloS One*, vol. 15, no. 11, article e0242768, 2020.
- [9] W. Tian, W. Jiang, J. Yao et al., "Predictors of mortality in hospitalized COVID-19 patients: a systematic review and meta-analysis," *Journal of Medical Virology*, vol. 92, no. 10, pp. 1875–1883, 2020.
- [10] World Health Organization, *Clinical management of severe acute respiratory infection (SARI) when COVID-19 disease is suspected: interim guidance, 13 March 2020*, World Health Organization, 2020.

Research Article

Identification of Inflammatory Genes, Pathways, and Immune Cells in Necrotizing Enterocolitis of Preterm Infant by Bioinformatics Approaches

Lili Zhang,¹ Lizhen Sun,² Mingli Wu,¹ and Jie Huang¹ 

¹Neonatal Intensive Care Unit, Liaocheng Dongchangfu People's Hospital, Liaocheng 252000, China

²Neonatal Intensive Care Unit, Liaocheng Dongchangfu Maternal and Child Health Care Hospital, Liaocheng 252000, China

Correspondence should be addressed to Jie Huang; ejie09181817492@163.com

Received 6 January 2021; Revised 12 March 2021; Accepted 23 March 2021; Published 7 April 2021

Academic Editor: Tao Huang

Copyright © 2021 Lili Zhang et al. This is an open access article distributed under the Creative Commons Attribution License, which permits unrestricted use, distribution, and reproduction in any medium, provided the original work is properly cited.

Background. Necrotizing enterocolitis (NEC) is one of the most serious gastrointestinal disease-causing high morbidity and mortality in premature infants. However, the underlying mechanism of the pathogenesis of NEC is still not fully understood. **Methods.** RNA sequencing of intestinal specimens from 9 NEC and 5 controls was employed to quantify the gene expression levels. RNA sequencing was employed to quantify the gene expression levels. DESeq2 tool was used to identify the differentially expressed genes. The biological function, pathways, transcription factors, and immune cells dysregulated in NEC were characterized by gene set enrichment analysis. **Results.** In the present study, we analyzed RNA sequencing data of NECs and controls and revealed that immune-related pathways were highly activated, while some cellular responses to external stimuli-related pathways were inactivated in NEC. Moreover, B cells, macrophages M1, and plasma cells were identified as the major cell types involved in NEC. Furthermore, we also found that inflammation-related transcription factor genes, such as STAT1, STAT2, and IRF2, were significantly activated in NEC, further suggesting that these TFs might play critical roles in NEC pathogenesis. In addition, NEC samples exhibited heterogeneity to some extent. Interestingly, two subgroups in the NEC samples were identified by hierarchical clustering analysis. Notably, B cells, T cells, Th1, and Tregs involved in adaptive immune were predicted to highly infiltrate into subgroup I, while subgroup II was significantly infiltrated by neutrophils. The heterogeneity of immune cells in NEC indicated that both innate and adaptive immunes might induce NEC-related inflammatory response. **Conclusions.** In summary, we systematically analyzed inflammation-related genes, signaling pathways, and immune cells to characterize the NEC pathogenesis and samples, which greatly improved our understanding of the roles of inflammatory responses in NEC.

1. Introduction

Necrotizing enterocolitis (NEC), one of the most serious gastrointestinal diseases in premature infants, is a significant cause of morbidity and mortality [1]. In North America, it affects about 1-3 per 1000 births annually [2]. Typical yet subtle signs of NEC in an infant include feeding intolerance, abdominal distention, and bloody stools, which could progress rapidly within hours [3]. Excessive inflammatory process in intestine, which could damage distant organs, is often observed in NEC patients, and NEC-affected infants are facing risks for developing microcephaly or suffering from neu-

rodevelopmental delays [4]. However, the diagnosis of NEC largely depends on an abdominal X-ray and few breakthroughs are made in preventive strategies for NEC, regardless of considerable researches done in this field [5]. As nonspecific biomarkers in blood such as platelets and white blood cells could merely guide medical care for NEC patients, researchers have been exploring other markers to aid the early diagnosis of NEC and to measure the severity of it. Besides a spectrum of pro-/anti-/inflammatory mediators, such as serum amyloid A (SAA) and calprotectin, gut-associated specific biomarkers like trefoil factor-3 (TFF-3), claudin-3, and intestinal fatty acid-binding protein (I-FABP)

have been widely introduced [6]. Notably, utilizing I-FABP in neonates studied between July 2005 and August 2010 could ensure a sensitivity of 93% and a specificity of 90% in assessing enterocyte damage [7]. Meanwhile, the investigation of the molecular mechanisms behind NEC has also promoted the understanding of this disease. Analyses of genome-wide expression profiles of bowel tissues from NEC patients have revealed several pathophysiological pathways that are related to inflammation, cell adhesion, extracellular matrix remodeling, and muscle contraction, triggered by a series of dysregulated genes [6], and the involvement of major transcriptional factors and growth factors are confirmed in NEC [8]. Moreover, several studies have indicated that gene polymorphism could also contribute to the development of NEC, but further investigation is still needed [9].

In the present study, we collected RNA sequencing data of human bowel tissues from nine NEC and five controls and conducted differential expression analysis, functional enrichment analysis, transcription factor activity prediction, and estimation of immune cell abundance, which revealed some key regulators, pathways, and immune cells involved in the pathogenesis of NEC.

2. Materials and Methods

2.1. The RNA Sequencing Data Analysis. The RNA-seq data with accession number SRP051825 was deposited in Sequence Read Archive (SRA, <https://www.ncbi.nlm.nih.gov/sra>) database [10]. The fastq files were downloaded from this database and, then, mapped to UCSC hg19 human genome by hisat [11]. The resulting bam files were used for quantifying the gene expression levels by Stringtie [12].

2.2. Differential Expression Analysis. The raw count data at gene level was used to identify the differentially expressed genes (DEGs), which was implemented in R package DESeq2 [13]. The thresholds of adjusted P value and fold change at 0.05 and 2 determined the DEGs [14].

2.3. The Dysregulated Pathways, Transcription Factors, and Immune Cells. The Reactome pathways were collected from MSigDB database [15], which curated a series of gene sets characterizing the pathways and target genes of transcription factors. Moreover, the immune cells were collected from previous studies [16, 17], which were used to quantify the tumor-infiltrating immune cells. The overrepresentation gene set enrichment analysis (ORA) was used to associate the dysregulated pathways, TFs, and immune cells with NEC. Which were implemented in R package clusterProfiler [18–20]. The threshold of adjusted P value was determined at 0.05.

2.4. The Hierarchical Clustering Analysis. The NEC cases and controls were clustered by the hierarchical clustering analysis based on the expression levels of dysregulated genes in NEC. Similarly, the two subgroups were also identified by the hierarchical clustering analysis and determined by the tree height with the largest difference.

2.5. Statistical Analysis. The statistical analysis was implemented in R programming tool. The two-sample compar-

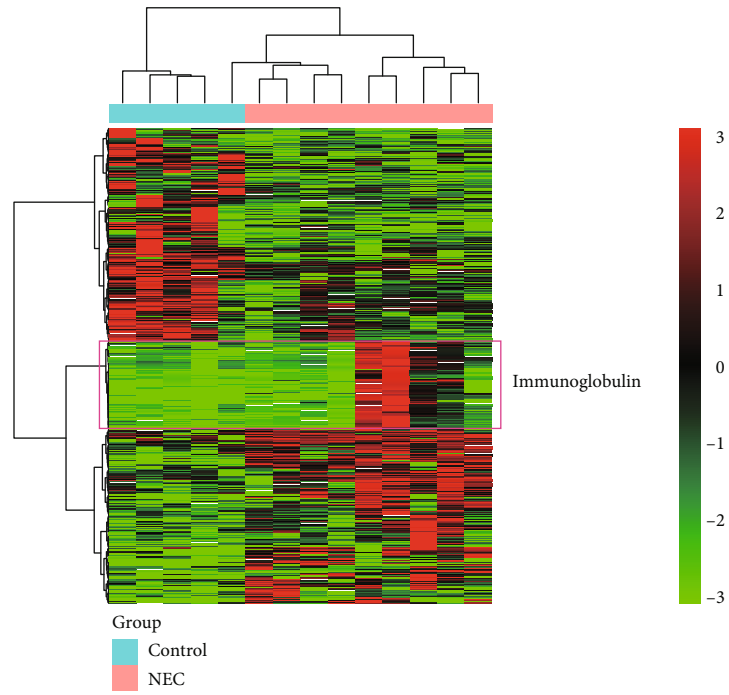
isons were performed by Wilcoxon rank-sum test or student t -test. Multiple-sample comparisons were performed by analysis of variance (ANOVA) or Kruskal-Wallis test. P value of 0.05 was indicated as statistical significance.

3. Results

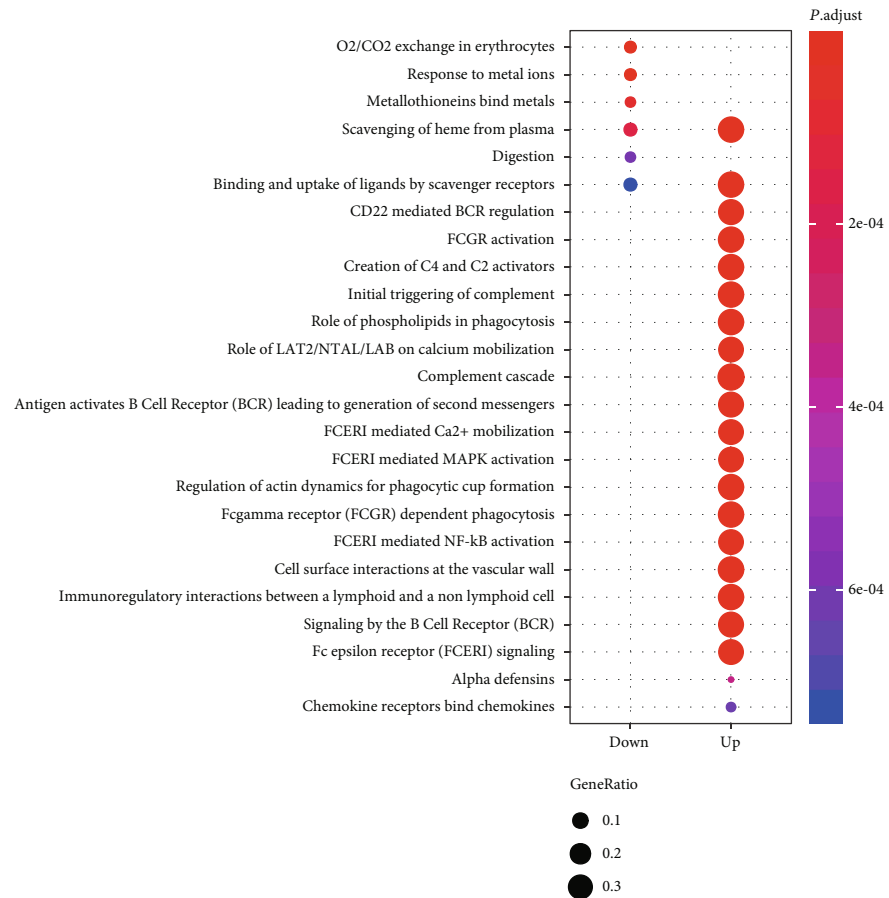
3.1. Samples from NEC and Controls. The RNA sequencing data of resected intestinal specimens of nine NEC and five controls who underwent bowel resection were downloaded from Sequence Read Archive (SRA) database, which was submitted by the researchers of the previous study [21], which took resected intestinal specimens of nine NEC and five controls who underwent bowel resection. The preterm patients who were diagnosed with stage III acute NEC and diseases other than NEC made up the case and control groups, respectively. The age (case vs. control: 27.42 vs. 32.02, P value = 0.07) and gender (female ratio case vs. control: 5/9 vs. 3/5, P value = 0.99) were not observed to have a difference between the two groups.

3.2. Identification of Dysregulated Genes in NEC. The differential expression analysis was conducted to identify the dysregulated genes in NEC. Totally, we identified 395 upregulated and 326 downregulated genes by comparing the gene expression profiles of NEC with those of controls (P value < 0.05 and fold change >2 or <1/2). As shown in Figure 1(a), the samples of NEC could be clearly differentiated from the controls by unsupervised clustering analysis. To characterize the biological function of these dysregulated genes, we conducted gene set enrichment analysis of the upregulated and downregulated genes, respectively. The Reactome pathways, such as signaling by the B Cell Receptor (BCR), immunoregulatory interactions between a lymphoid and a nonlymphoid cell, FCERI-mediated NF- κ B activation, antigen activates B Cell Receptor (BCR) leading to generation of second messengers, and CD22 mediated BCR regulation, were significantly enriched by the upregulated genes (Figure 1(b), adjusted P value < 0.05), suggesting that the dysregulation of immune system was a major hallmark of NEC. In accordance with these pathways, many genes encoding immunoglobulin were also found to be upregulated in NEC (Figure 1(a)). Moreover, we also observed some cellular responses to external stimuli-related pathways, such as metallothioneins bind metals, response to metal ions, and vesicle-mediated transport-related pathways, such as binding and uptake of ligands by scavenger receptors and scavenging of heme from plasma, were enriched by the downregulated genes (Figure 1(b)). In addition, the digestion was also observed to be downregulated in NEC, suggesting that the disease might cause the loss of digestion.

3.3. Identification of Immune Cells Involved in NEC. As described above, the upregulation of immune-related pathways and inflammation might be the hallmark of NEC. We then investigated the immune cells that participate in the pathogenesis of NEC. Two sets of marker genes for the immune cell were collected from previous studies [16, 17]. Based on the GSEA, B cells, macrophages M1, and plasma



(a)



(b)

FIGURE 1: The expression patterns and biological function of differentially expressed genes (DEGs) in NEC. (a) The heat map displayed the expression patterns of the DEGs. A set of genes encoding immunoglobulin was highly upregulated in some of the NEC samples. (b) The Reactome pathways dysregulated in NEC. The pathways were enriched by the DEGs based on overrepresentation gene set enrichment analysis.

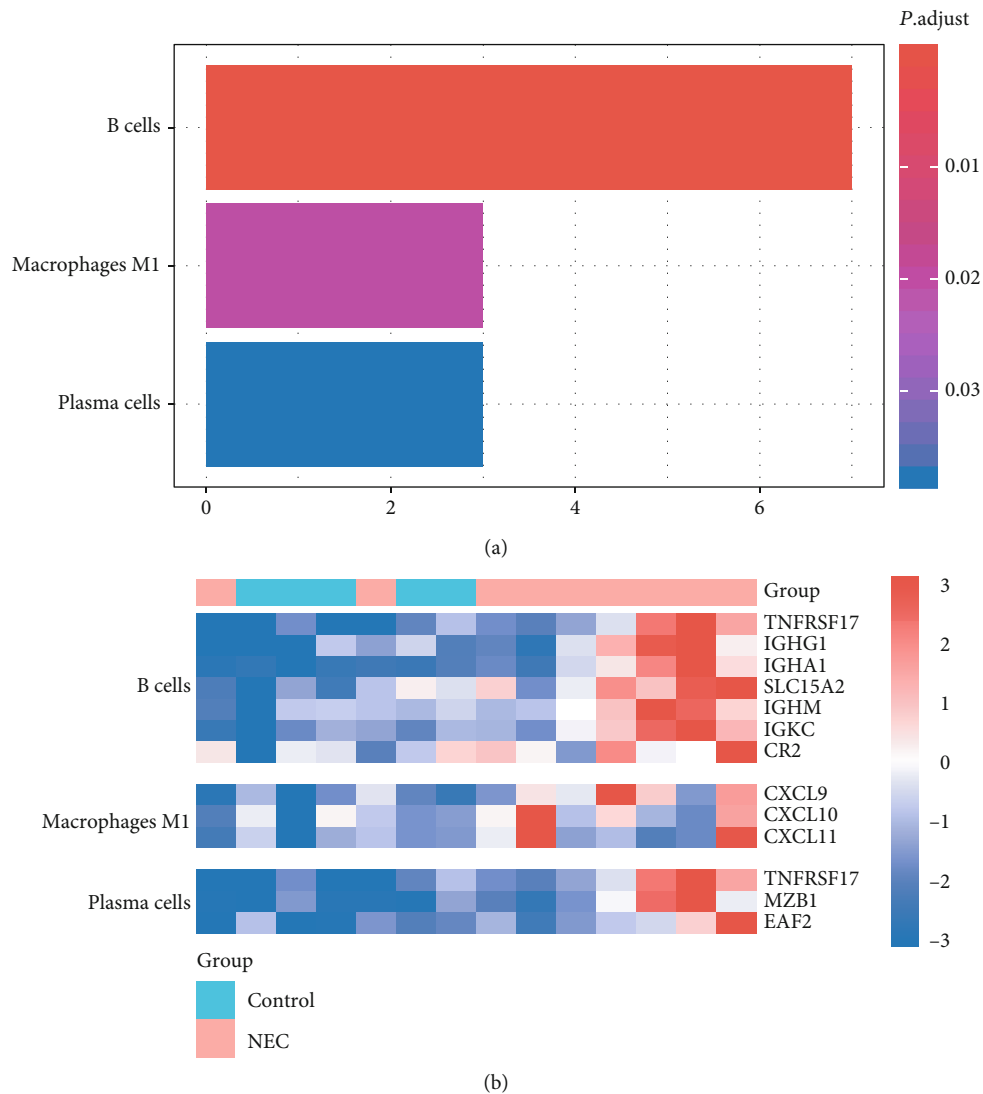


FIGURE 2: The immune cells infiltrating into the NEC samples. (a) The B cells, macrophage M1, and plasma cells were predicted to be activated in NEC samples. (b) The expression patterns of B cell, macrophage M1, and plasma cell-specific gene signatures in NEC and controls.

cells were identified as the major cell types involved in NEC (Figure 2(a)). Further analysis revealed that B cell-specific genes, such as TNFRSF17, IGHG1, IGHA1, SLC15A2, IGHM, IGKC, and CR2, macrophage M1-specific genes, such as CXCL9, CXCL10, and CXCL11, and plasma cell-specific genes, such as TNFRSF17, MZB1, and EAF2, were highly upregulated in NEC (Figure 2(b)). Notably, the macrophage M1-specific genes were chemokine ligands, suggesting that chemokine ligands were critical regulators in NEC pathogenesis.

3.4. Key Transcription Factors Involved in NEC. To identify key transcription factors (TF) regulating the transcription of these dysregulated genes in NEC, we tested the degree of enrichment for the dysregulated genes in the TF targets. We found target genes of three TF or TF families, including *ISRE*, *IRF1*, and *IRF2*, were significantly enriched by the upregulated genes (Figure 3(a)). Notably, as *IRF1* and *IRF2* belonged to interferon regulatory factors, they jointly regu-

lated the target genes encoding chemokine ligands, *CXCL10*, and *CXCL11* (Figure 3(a)). Moreover, most of these target genes, such as *CXCL10*, *CXorf21*, *TNFSF13B*, and *PIGR*, were regulated by all the three TFs.

Furthermore, we also investigated the expression patterns of the genes encoding the TFs. It should be noted that the ISRE TF family consisted of STAT1 and STAT2. We only observed STAT1 was significantly upregulated in NEC (Figure 3(b)), but the other genes encoding the TFs did not exhibit significant upregulation. However, *IRF2* was slightly upregulated in NEC with a lower statistical significance ($P = 0.07$). To further investigate the expression patterns of *IRF2* in NEC, we analyzed the expression levels of *IRF2* isoforms. Remarkably, two of *IRF2* isoforms were highly dysregulated in NEC, but only NM_002199.4, a major isoform of *IRF2*, was significantly upregulated in NEC (Figure 3(c)), suggesting that the protein encoded by NM_002199.4 was involved in the transcriptional regulation of the target genes.

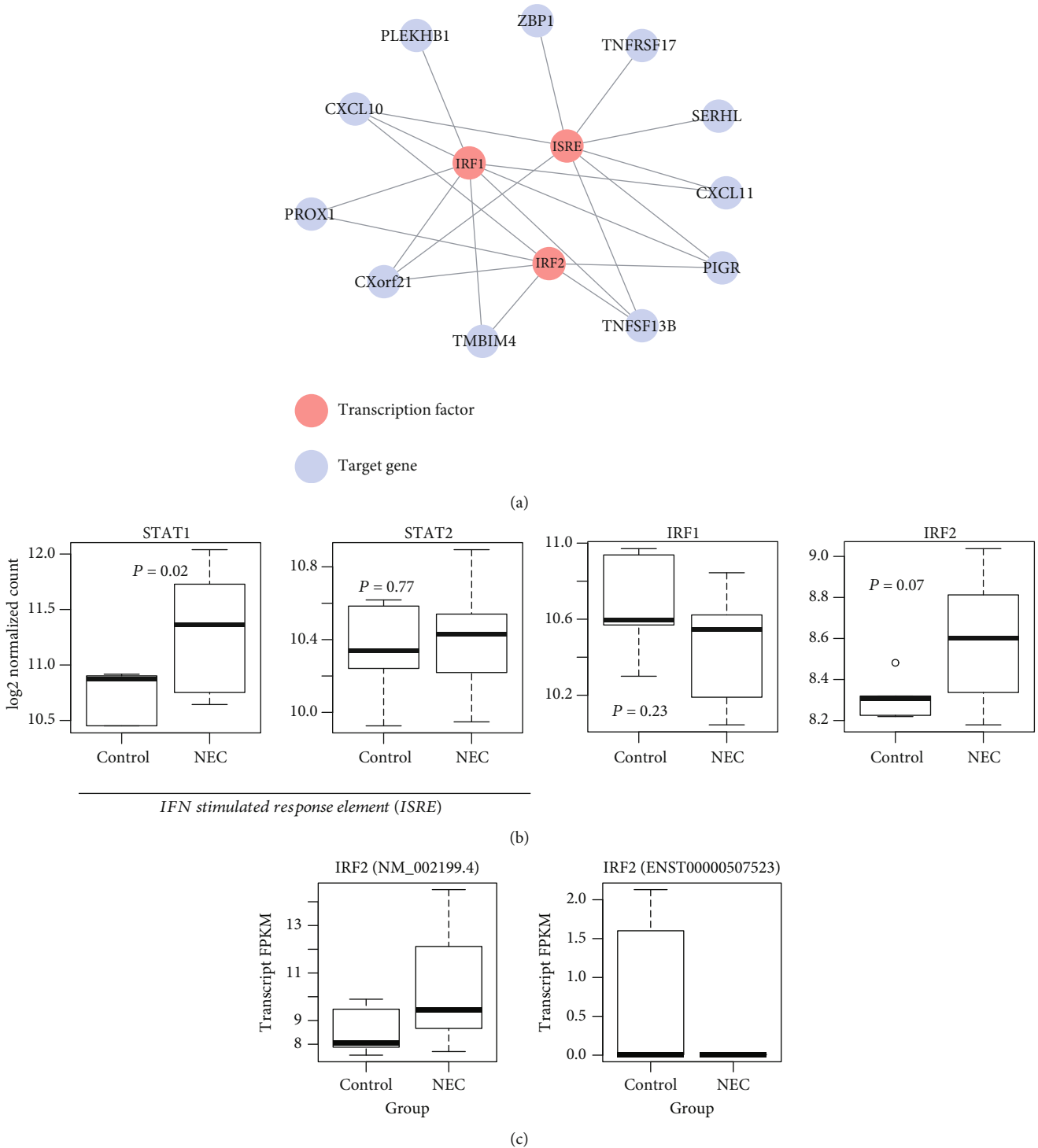
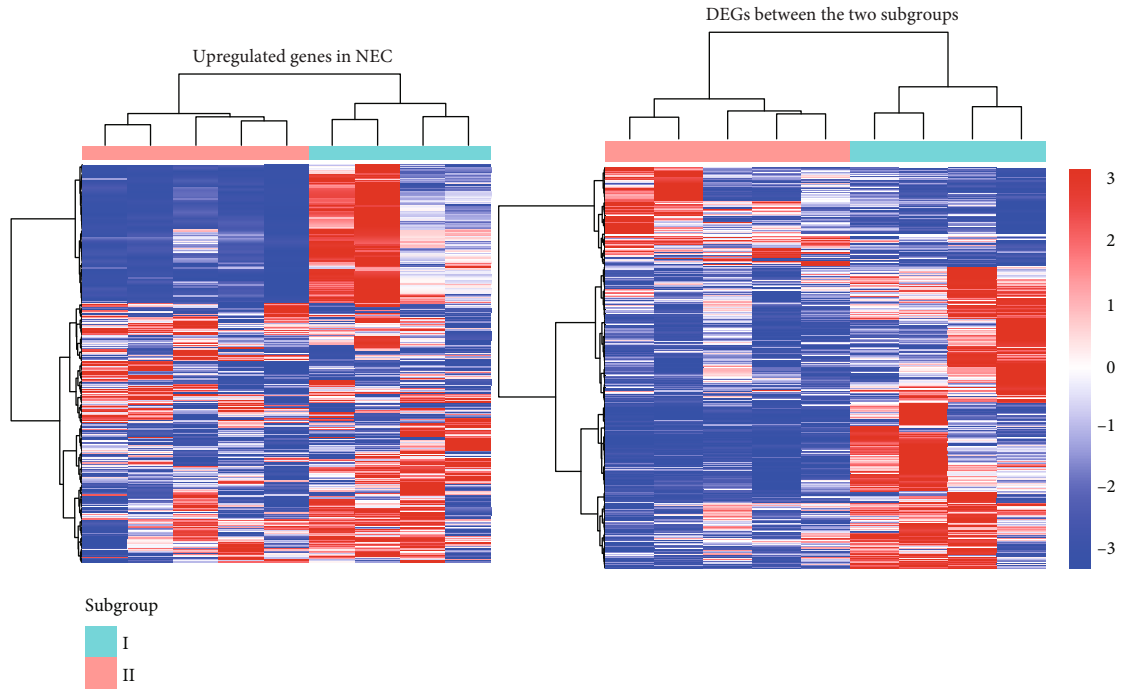


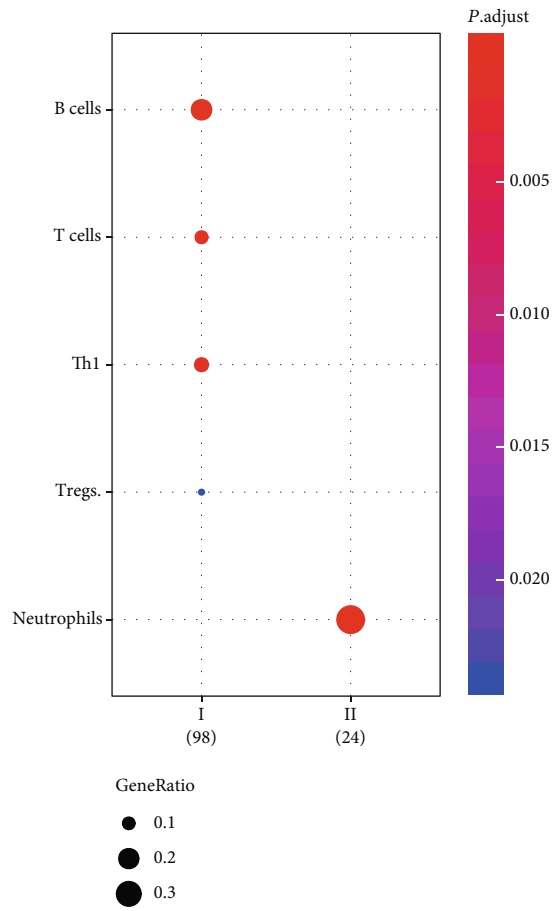
FIGURE 3: The dysregulated transcription factor (TF) regulatory network in NEC. (a) The TFs and target genes network in NEC. (b) The differential expression levels of TFs between NEC and controls. (c) Isoform switch event in two isoforms of IRF2.

3.5. Two Subgroups of NEC Identified by the Gene Expression Profiles. As shown in Figure 1(a), the genes encoding immunoglobulin exhibited upregulated in only a subset of NEC patients, which gave us a hint that the NEC samples might exhibit heterogeneity to some extent. We then conducted unsupervised clustering analysis of the NEC samples based on the upregulated genes and identified two subgroups in

NEC (Figure 4(a)). Similarly, the differential expression analysis was also conducted to identify the genes specifically dysregulated in either of the two subgroups (Figure 4(a)). As NEC was characterized by dysregulation of inflammatory response, we investigated the immune cells infiltrating into the two subgroups. Notably, B cells, T cells, Th1, and Tregs were predicted to highly infiltrate into the tissues of subgroup

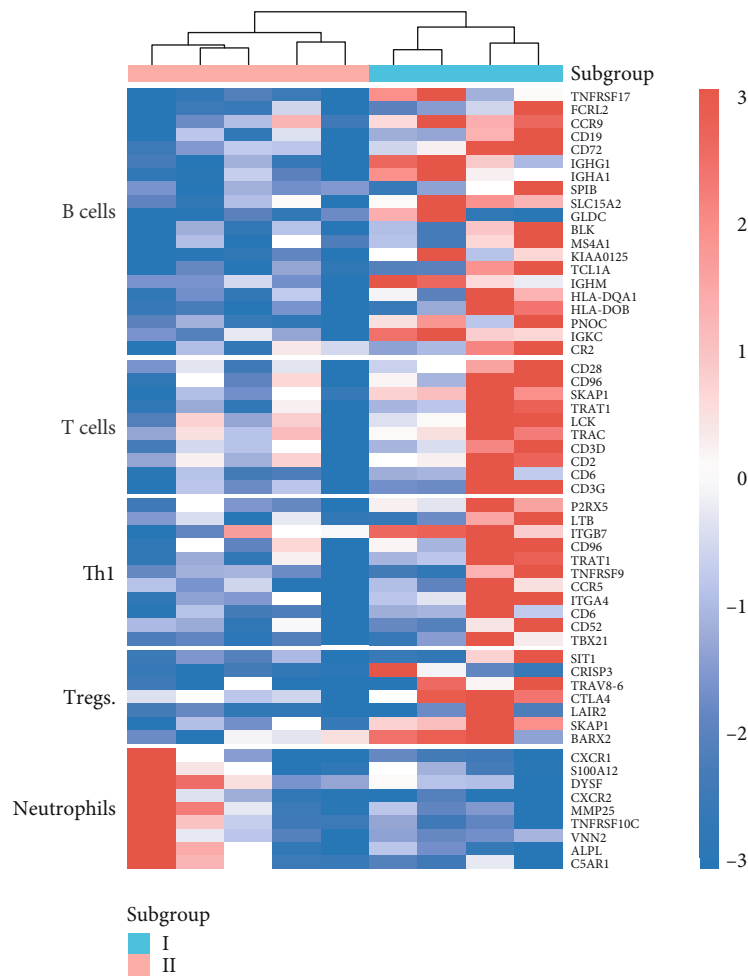


(a)



(b)

FIGURE 4: Continued.



(c)

FIGURE 4: The two NEC subgroups based on gene expression profiles. (a) The expression patterns of DEGs in NEC (left) and between the two subgroups. (b) The immune cells infiltrating into two NEC subgroups. (c) The expression patterns of the genes specifically expressed in the immune cells.

I, while subgroup II was significantly infiltrated by neutrophils (Figure 4(b), BH-adjusted P value < 0.05). Specifically, the signature genes of these immune cells were also observed to be dysregulated between the two subgroups. These results indicated that the heterogeneity in NEC-related inflammatory response is associated with both innate and adaptive immunes.

4. Discussion

Necrotizing enterocolitis is one of the most serious gastrointestinal diseases in premature infants, which causes high morbidity and mortality [1]. However, the underlying mechanism of the pathogenesis of NEC is still not fully understood. In the present study, we identified 395 upregulated and 326 down-regulated genes in NEC samples, which could clearly distinguish the NEC from controls. Functional analysis of these dysregulated genes revealed that immune-related pathways were highly activated, while some cellular responses to external stimuli-related pathways were inactivated in NEC. The importance of immune response in NEC has been widely

reported by previous studies [22, 23]. The attenuated cellular responses to external stimuli might result from the necrotic intestinal cells [24]. In addition, the digestion was also observed to be downregulated in NEC, suggesting that the disease might cause the loss of digestion.

Moreover, the comparison between NECs and controls identified immune cells and key transcription factors involved in NEC pathogenesis. Specifically, B cells, macrophages M1, and plasma cells were identified as the major cell types involved in NEC. Particularly, M1 macrophage had the potential to promote the progression of NEC [25], and necrotizing enterocolitis could be prevented by inhibiting M1 macrophage polarization [26]. Furthermore, we also found that inflammation-related TF genes, such as STAT1, STAT2, and IRF2, were significantly activated in NEC, further suggesting that these TFs might play critical roles in NEC pathogenesis.

Furthermore, we also found NEC samples might exhibit heterogeneity to some extent. Interestingly, two subgroups in the NEC samples were identified by hierarchical clustering analysis (Figure 4(a)). Notably, B cells, T cells, Th1, and Tregs

involved in adaptive immune were predicted to highly infiltrate into the tissues of subgroup I, while subgroup II was significantly infiltrated by neutrophils (Figure 4(b), BH-adjusted P value < 0.05). The innate immune has been widely studied in NEC; however, the underlying mechanism of immune cells involved in adaptive immune has not been well established [27–29]. The heterogeneity of immune cells in NEC indicated that both innate and adaptive immunes might induce NEC-related inflammatory response, and this difference in NEC samples might also be associated with the course of the disease.

Overall, the present study still has some limitations, such as small sample size, lack of experimental validation, and specific molecular mechanism. However, we systematically analyzed inflammation-related genes, signaling pathways, and immune cells to characterize the NEC pathogenesis and samples, which greatly improved our understanding of the roles of inflammatory responses in NEC.

Data Availability

The data used in this manuscript can be found in SRP051825, which was deposited in Sequence Read Archive (SRA, <https://www.ncbi.nlm.nih.gov/sra>) database.

Conflicts of Interest

The authors declare no financial conflicts of interest.

Authors' Contributions

JH was the guarantor of integrity of the entire study and performed the study concepts and design; LZ did the literature research; LS did the experimental studies; LZ and LS performed the data acquisition; MW performed the data analysis and statistical analysis. All authors prepared and edited the manuscript.

References

- [1] B. L. Frost, B. P. Modi, T. Jaksic, and M. S. Caplan, "New medical and surgical insights into neonatal necrotizing enterocolitis: a review," *JAMA Pediatrics*, vol. 171, no. 1, pp. 83–88, 2017.
- [2] D. F. Nino, C. P. Sodhi, and D. J. Hackam, "Necrotizing enterocolitis: new insights into pathogenesis and mechanisms," *Nature Reviews. Gastroenterology & Hepatology*, vol. 13, no. 10, pp. 590–600, 2016.
- [3] J. Neu and W. A. Walker, "Necrotizing enterocolitis," *The New England Journal of Medicine*, vol. 364, no. 3, pp. 255–264, 2011.
- [4] A. D. Bedrick, "Necrotizing enterocolitis: neurodevelopmental "risky business"," *Journal of Perinatology*, vol. 24, no. 9, pp. 531–533, 2004.
- [5] S. Eaton, "Necrotizing enterocolitis symposium: epidemiology and early diagnosis," *Journal of Pediatric Surgery*, vol. 52, no. 2, pp. 223–225, 2017.
- [6] P. C. Ng, "An update on biomarkers of necrotizing enterocolitis," *Seminars in Fetal & Neonatal Medicine*, vol. 23, no. 6, pp. 380–386, 2018.
- [7] K. W. Reisinger, D. C. van der Zee, H. A. Brouwers et al., "Noninvasive measurement of fecal calprotectin and serum amyloid A combined with intestinal fatty acid-binding protein in necrotizing enterocolitis," *Journal of Pediatric Surgery*, vol. 47, no. 9, pp. 1640–1645, 2012.
- [8] B. D. Garg, D. Sharma, and A. Bansal, "Biomarkers of necrotizing enterocolitis: a review of literature," *The Journal of Maternal-Fetal & Neonatal Medicine*, vol. 31, no. 22, pp. 3051–3064, 2018.
- [9] A. Treszl, I. Kocsis, M. Szathmari, Á. Schuler, T. Tulassay, and B. Vászárhelyi, "Genetic variants of the tumour necrosis factor- α promoter gene do not influence the development of necrotizing enterocolitis," *Acta Paediatrica*, vol. 90, no. 10, pp. 1182–1185, 2001.
- [10] R. Leinonen, H. Sugawara, M. Shumway, and on behalf of the International Nucleotide Sequence Database Collaboration, "The sequence read archive," *Nucleic Acids Research*, vol. 39, no. Database, pp. D19–D21, 2011.
- [11] D. Kim, B. Langmead, and S. L. Salzberg, "HISAT: a fast spliced aligner with low memory requirements," *Nature Methods*, vol. 12, no. 4, pp. 357–360, 2015.
- [12] M. Pertea, G. M. Pertea, C. M. Antonescu, T. C. Chang, J. T. Mendell, and S. L. Salzberg, "StringTie enables improved reconstruction of a transcriptome from RNA-seq reads," *Nature Biotechnology*, vol. 33, no. 3, pp. 290–295, 2015.
- [13] M. I. Love, W. Huber, and S. Anders, "Moderated estimation of fold change and dispersion for RNA-seq data with DESeq2," *Genome Biology*, vol. 15, no. 12, p. 550, 2014.
- [14] X. Shi, T. Huang, J. Wang et al., "Next-generation sequencing identifies novel genes with rare variants in total anomalous pulmonary venous connection," *eBioMedicine*, vol. 38, pp. 217–227, 2018.
- [15] A. Liberzon, A. Subramanian, R. Pinchback, H. Thorvaldsdottir, P. Tamayo, and J. P. Mesirov, "Molecular signatures database (MSigDB) 3.0," *Bioinformatics*, vol. 27, no. 12, pp. 1739–1740, 2011.
- [16] Y. Şenbabaoglu, R. S. Gejman, A. G. Winer et al., "Tumor immune microenvironment characterization in clear cell renal cell carcinoma identifies prognostic and immunotherapeutically relevant messenger RNA signatures," *Genome Biology*, vol. 17, no. 1, p. 231, 2016.
- [17] Y. Xiao, D. Ma, S. Zhao et al., "Multi-omics profiling reveals distinct microenvironment characterization and suggests immune escape mechanisms of triple-negative breast cancer," *Clinical Cancer Research*, vol. 25, no. 16, pp. 5002–5014, 2019.
- [18] G. Yu, L. G. Wang, Y. Han, and Q. Y. He, "clusterProfiler: an R package for comparing biological themes among gene clusters," *OMICS*, vol. 16, no. 5, pp. 284–287, 2012.
- [19] C. Gu, X. Shi, Z. Huang et al., "A comprehensive study of construction and analysis of competitive endogenous RNA networks in lung adenocarcinoma," *Biochimica et Biophysica Acta - Proteins & Proteomics*, vol. 1868, no. 8, article 140444, 2020.
- [20] C. Gu, Z. Huang, X. Chen et al., "TEAD4 promotes tumor development in patients with lung adenocarcinoma via ERK signaling pathway," *Biochimica et Biophysica Acta - Molecular Basis of Disease*, vol. 1866, no. 12, article 165921, 2020.
- [21] E. Tremblay, M. P. Thibault, E. Ferretti et al., "Gene expression profiling in necrotizing enterocolitis reveals pathways common to those reported in Crohn's disease," *BMC Medical Genomics*, vol. 9, p. 6, 2016.

- [22] J. Shulhan, B. Dicken, L. Hartling, and B. M. K. Larsen, "Current knowledge of necrotizing enterocolitis in preterm infants and the impact of different types of enteral nutrition products," *Advances in Nutrition*, vol. 8, no. 1, pp. 80–91, 2017.
- [23] H. Renz, P. Brandtzaeg, and M. Hornef, "The impact of perinatal immune development on mucosal homeostasis and chronic inflammation," *Nature Reviews. Immunology*, vol. 12, no. 1, pp. 9–23, 2011.
- [24] S. Fulda, A. M. Gorman, O. Hori, and A. Samali, "Cellular stress responses: cell survival and cell death," *International Journal of Cell Biology*, vol. 2010, Article ID 214074, 23 pages, 2010.
- [25] J. Wei and G. E. Besner, "M1 to M2 macrophage polarization in heparin-binding epidermal growth factor-like growth factor therapy for necrotizing enterocolitis," *The Journal of Surgical Research*, vol. 197, no. 1, pp. 126–138, 2015.
- [26] J. Wei, D. Tang, C. Lu et al., "Irf5 deficiency in myeloid cells prevents necrotizing enterocolitis by inhibiting M1 macrophage polarization," *Mucosal Immunology*, vol. 12, no. 4, pp. 888–896, 2019.
- [27] M. A. Mara, M. Good, and J. H. Weitkamp, "Innate and adaptive immunity in necrotizing enterocolitis," *Seminars in Fetal & Neonatal Medicine*, vol. 23, no. 6, pp. 394–399, 2018.
- [28] Z. Hodzic, A. M. Bolock, and M. Good, "The role of mucosal immunity in the pathogenesis of necrotizing enterocolitis," *Frontiers in Pediatrics*, vol. 5, p. 40, 2017.
- [29] S. M. Tanner, T. F. Berryhill, J. L. Ellenburg et al., "Pathogenesis of necrotizing enterocolitis: modeling the innate immune response," *The American Journal of Pathology*, vol. 185, no. 1, pp. 4–16, 2015.

Research Article

circRNA circFAT1(e2) Elevates the Development of Non-Small-Cell Lung Cancer by Regulating miR-30e-5p and USP22

Wenmin Dong ^{1,2}, Huiqian Zhang ¹, YanCheng Dai ¹, Yi Zhou ¹, Yun Luo ¹,
Cheng Zhao ¹, Yiyuan Cao ^{1,2}, Yuping Du ¹, and Ying Chen ^{1,2}

¹Shanghai TCM-Integrated Hospital Affiliated to Shanghai University of Traditional Chinese Medicine, Shanghai 200082, China

²Shanghai University of Traditional Chinese Medicine, Shanghai 201203, China

Correspondence should be addressed to Yuping Du; sky_shanghai@163.com and Ying Chen; yingchen011@163.com

Received 29 December 2020; Revised 4 February 2021; Accepted 6 March 2021; Published 5 April 2021

Academic Editor: Tao Huang

Copyright © 2021 Wenmin Dong et al. This is an open access article distributed under the Creative Commons Attribution License, which permits unrestricted use, distribution, and reproduction in any medium, provided the original work is properly cited.

Background. As a newly discovered regulatory RNA, circular RNA (circRNA) has become a hot spot in many tumor pieces of research. In recent years, it has been discovered that circRNAs have multiple biological effects in different stages of cancer. However, the expression pattern and mechanism of circFAT1(e2) in non-small-cell lung cancer (NSCLC) are still unclear. **Methods.** The expressions of circFAT1(e2) in NSCLC tissues and cell lines were studied. Functionally, CCK-8 and transwell experiments were performed in A549 and H1299. In addition, we also performed a dual-luciferase report analysis to clarify the mechanism of action of circFAT1(e2). **Results.** circFAT1(e2) was significantly upregulated in NSCLC tissues and cell lines. circFAT1(e2) gene knockdown could significantly inhibit the proliferation, migration, and invasion of NSCLC cells. Loss of function testing found that circFAT1(e2) functioned as an oncogene in NSCLC cells. In addition, circFAT1(e2) acted as a ceRNA to spongy miR-30e-5p, which led to the increase in USP22 and promoted cell growth. **Conclusions.** The circFAT1(e2)-miR-30e-5p-USP22 axis is a crucial part of the progression of NSCLC. This study suggests that circFAT1(e2) may be an important potential of prognostic prediction and treatment targets for NSCLC patients.

1. Introduction

The tumorigenesis of cancer is due to the abnormal changes of regulatory mechanisms in cells, resulting in uncontrolled growth and division [1]. However, the mechanisms underlying tumorigenesis remain unclear. circRNA is a novel type of ncRNAs (noncoding RNAs) and exists in both the cytoplasm and nucleus of eukaryotes [2]. It is characterized by a ring-shaped structure without free ends [3]. circRNA is produced through special types of alternative splicing [4]. With the deepening of research, the understanding of circRNA has been gradually enriched. The reverse splicing pathway of exons is the key mechanism involved in producing circRNAs [5]. Of note, emerging studies demonstrate circRNAs play important roles in regulating the development of cancers [6]. For example, studies have found that the downregulated expression of circRNA circ-Ccnb1 in breast cancer can interact with Bclaf1 in cancer cells through H2AX, resulting in the

inhibition of uncontrolled division and growth of cancer cells [7]. Researchers also find that circITGA7 can inhibit the metastasis and proliferation of colorectal cancer cells by inhibiting the pathway of Ras signal and promoting the transcription of its downstream target gene ITGA7, thus playing its antitumor roles in colorectal cancer [8].

According to the latest reports, among all kinds of cancers, lung cancer leads to the highest morbidity and mortality [9]. More than 2 million new cases are diagnosed as NSCLC, and 1.8 million deaths are caused by NSCLC per year [10]. NSCLC can be divided into two subtypes, small-cell lung cancer (SCLC) and non-small-cell lung cancer (NSCLC). NSCLC includes large-cell NSCLC, lung squamous cell carcinoma, and lung adenocarcinoma [11]. Clinically, NSCLC is diagnosed mainly by small biopsies and cytological specimens [12]. According to recent reports, there are significant differences in circRNA expression levels between NSCLC tissues and normal tissues. It suggests that they may be involved

in different stages or pathways of cancer cell progression [13]. It is found that NSCLC lowly expressed circRNA-ITCH which could be used as a sponge of miR-7 and miR-214, reducing their expression levels, reducing the regulatory effect of miRNA on downstream target genes, resulting in downregulation of b-catenin, c-myc, and cyclinD1, and then inhibiting the activation of Wnt/b-catenin signal in NSCLC cells [14]. In addition, Luo et al. found that hsa_circ_0000064 expression increased in NSCLC tissues and cell lines, suggesting that this circRNA might be an oncogene. Gene knockout experiment showed that the proliferation, migration, and invasion of NSCLC cells were significantly inhibited, the cell cycle process was accelerated, and the number of apoptotic cells increased [15].

Previous studies have shown that circFAT1(e2) is a new circRNA derived from exon 2 of the FAT1 gene [16]. In PTC, circFAT1(e2) plays a carcinogenic effect by promoting cell invasion and metastasis and is a potential new target for PTC therapy [17]. It is found in gastric cancer (GC) that the overexpression of circFAT1(e2) inhibits the proliferation, migration, and invasion of GC cells and is related to the overall survival rate of GC patients [16]. Studies in osteosarcoma (OS) show that circFAT1(e2) plays a carcinogenic role in OS and suggest that the circFAT1(e2)/miR-181b/HK2 axis is a potential therapeutic target [18]. However, the function and mechanism of circFAT1(e2) related to NSCLC are still unclear.

In this study, we observed that circFAT1(e2) was highly expressed in NSCLC tissues compared with normal tissues. We found that the proliferation ability of NSCLC cells was significantly limited, and the ability to invade and metastasize was also significantly decreased after knockdown of circFAT1(e2) with siRNA. Using the luciferase reporter assay, it was found that circFAT1(e2) could reduce the activity of miR-30e-5p by acting as a sponge, which weakened the regulation of the downstream target gene USP22, and finally restricted the metastasis and growth of NSCLC cells. We could provide new targets and pathways to regulate the development of NSCLC, which had potential value as a target for screening and diagnosis of NSCLC.

2. Materials and Methods

2.1. Patients and Tissue Samples. We collected paired NSCLC tissue and adjacent normal tissue from 5 patients who underwent surgical resection without any chemoradiotherapy at the Shanghai TCM-Integrated Hospital affiliated to Shanghai University of Traditional Chinese Medicine. We stored the resected tissues immediately in liquid nitrogen at -80°C for further RNA isolation. All experiments were approved by the Institutional Review Board, and all patients provided informed consent in writing prior to participation.

2.2. Cell Lines and Cell Culture. We collected the NSCLC cells (A549, H1299, and NCI-H1975) and normal cells (BEAS-2B) from the American Type Culture Collection. We then maintained the cells in RPMI-1640 and supplemented them with 100 U/mL penicillin, 100 $\mu\text{g}/\text{ml}$ streptomycin, and 10% fetal bovine serum (FBS). A humidified incubator with 5% carbon

dioxide at 37°C was applied. The culture medium was changed every 3 days.

2.3. Cell Transfection. siRNA was purchased from GenePharma Co., Ltd. (Shanghai, China). The siRNA sequence was as follows: si-circFAT1(e2), GAGACAGATTCCCGACAGTTADTDT, and si-NC, UUCUCCGAACGUGUCA CGUTT. When the cells reached 80% confluence, the cells used for transfection were plated in a 6-well plate. According to the manufacturer's protocol, all transfections were performed using Lipofectamine 2000 (Invitrogen, Carlsbad, CA, USA). Cells were harvested 48 hours after transfection for subsequent experiments.

2.4. RNA Extraction and qRT-PCR. The TRIzol reagent was used to extract total RNA from NSCLC cells. The PrimeScript RT reagent kit was used to reverse-transcribe the isolated RNA (1 μg) into cDNA. qRT-PCR was performed using the StepOne™ Real-Time PCR System and the SYBR® Green Mixture. Relative data were normalized to GAPDH.

2.5. CCK-8 Assay. The Cell Counting Kit-8 (CCK-8) was used to examine the proliferation ability of NSCLC cells (A549, H1299). By the manufacturer's instructions, at a specific time, we added CCK-8 (10 μL per well) to the cells after transfection and incubated them for two hours before measuring the absorbance at 450 nm.

2.6. Transwell Migration and Invasion Assay. After 12 hours of transfection, we seeded the cells (1×10^5 cells/well) into the upper transwell chamber for the migration assay, or cells were preapplied with 70 μL diluted Matrigel for the invasion assay, with 100 μL of RPMI-1640 medium containing 1% FBS. After 48 hours, we wiped the cells on the upper surface with a cotton swab, fixed them with methanol, and then stained them with 10 $\mu\text{g}/\text{mL}$ DAPI (Solarbio, Beijing, China).

2.7. Public Database. The GSE9188 database [19] (<https://www.ncbi.nlm.nih.gov/geo/query/acc.cgi>) contains 5 subdatasets, and the GEO2R online network tool (<https://www.ncbi.nlm.nih.gov/geo/geo2r/?acc=GSE9188>) allows users to compare different gene expression data of two or more sets of samples. We use GEO2R to analyze gene expression levels. Through bioinformatics tools circBase (<http://www.circbase.org/>) and starBase 2.0 (<http://starbase.sysu.edu.cn/starbase2/index.php>), we determined the downstream of the circFAT1(e2) target gene.

2.8. Dual-Luciferase Reporter Assay. USP22 mRNA wild type (USP22-3UTR-wt) or circFAT1(e2) wild type (circFAT1(e2)-wt) with potential miR-30e-5p binding sites and mutant without miR-30e-5p binding sites (USP22-3UTR-mut, circFAT1(e2)-mut) were constructed for the dual-luciferase reporter assay. Then, we amplified and cloned them into the luciferase reporter vector psi-CHECK-2. We cotransfected HEK293T cells with luciferase plasmids and miR-30e-5p or control. The Dual-Luciferase Reporter Assay System was employed based on the Renilla luciferase activity.

2.9. Statistical Analysis. We performed Student's *t*-test or one-way ANOVA to test the differences between groups.

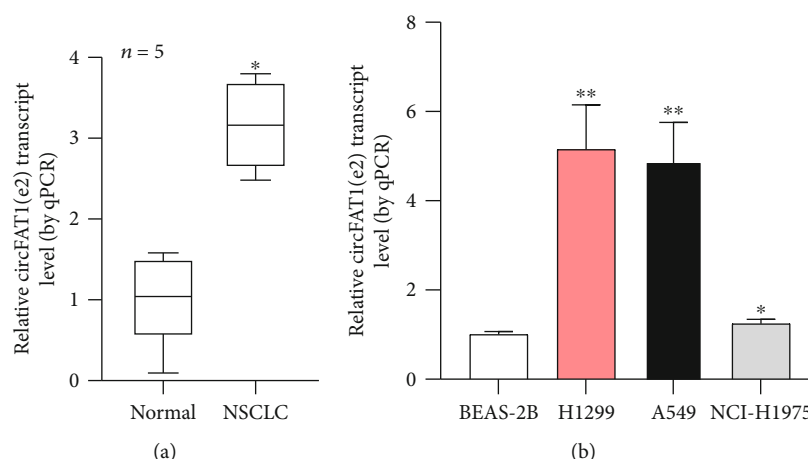


FIGURE 1: In the NSCLC tissue and cells, circFAT1(e2) was overexpressed. (a) As shown by qRT-PCR analysis, the relative expression levels of circFAT1(e2) ($n = 5$) in the matched noncancerous tissues and NSCLC tissues. (b) As shown by qRT-PCR, circFAT1(e2) expression in three CRC cell lines was also higher than that in the normal cell line BEAS-2B. * $P < 0.05$, ** $P < 0.01$.

Each experiment was repeated at least three times. Data were presented as mean \pm SD (standard deviation). The P value less than 0.05 was considered statistically significant. The SPSS software was used to perform all the statistical analyses, and the GraphPad Prism software was used to graph.

3. Results

3.1. circFAT1(e2) Was Probably Overexpressed in the NSCLC Tissue and Cells. In this study, we aimed to explore the potential functions of circFAT1(e2) in NSCLC. In the 5 clinical NSCLC tissues, circFAT1(e2) expression was significantly overexpressed (Figure 1(a)), and the results were similar in NSCLC cells (Figure 1(b)). It suggested that circFAT1(e2) was probably overexpressed in NSCLC tissues and cells.

3.2. circFAT1(e2) Knockdown Repressed the Proliferation and Metastasis of NSCLC Cells. Loss-of-function experiments were performed using siRNA targeting circFAT1(e2) in NSCLC cells (A549, H1299) (Figure 2(a)). The CCK-8 assay was carried out to investigate the inhibition of circFAT1(e2) knockdown on cell proliferation (Figure 2(b)). The transwell assay was carried out and found that circFAT1(e2) knockdown inhibited the invasion and migration of NSCLC cells compared to the control group (Figure 2(c)). These results indicated that circFAT1(e2) knockdown represses the metastasis and proliferation of NSCLC cells.

3.3. circFAT1(e2) Targeted miR-30e-5p as a miRNA Sponge. Research shows that circRNAs can target miRNAs by acting as miRNA sponges and binding with the RNA-binding protein (RBP) to exert their function. Results from this study found that miR-30e-5p had complementary binding sites with the circFAT1(e2). The luciferase activity demonstrated the interaction between the molecular binding of circFAT1(e2) and miR-30e-5p (Figure 3(a)). Results also found that miR-30e-5p was highly expressed in the circFAT1(e2) knockdown transfection in the NSCLC cells (Figure 3(b)). However, we found that overexpression of miR-30e-5p

remarkably suppresses the expression level of circFAT1(e2) in both A549 and H1299 cells (Figure 3(c)). The results suggest that circFAT1(e2) serves as a miRNA sponge for miR-30e-5p.

3.4. USP22 Served as the Functional Protein of circFAT1(e2)/miR-30e-5p. Further experiments were aimed at investigating the downstream target of circFAT1(e2) and miR-30e-5p. Previous reports indicated that USP22 was a potential target of miR-30e-5p [20, 21]. In this study, the dual-luciferase assay also validated the molecular binding between miR-30e-5p and USP22 mRNA (Figure 4(a)). The expression of USP22 in NSCLC tissues was higher than that in normal tissues using the GSE9188 database (Figure 4(b)). We also found that overexpression of miR-30e-5p and knockdown of circFAT1(e2) significantly reduced the mRNA levels of USP22 (Figures 4(c) and 4(d)). RT-PCR illustrated that USP22 mRNA expression was increased in the miR-30e-5p silencing group, which was recovered by circFAT1(e2) siRNA (Figure 4(e)). These results demonstrate that USP22 acts as the functional protein of circFAT1(e2)/miR-30e-5p.

4. Discussion

NSCLC, as the deadliest cancer in the world, has received extensive attention [22]. Although many countries have begun to pay attention to and take measures to restrict smoking to prevent NSCLC, the incidence and mortality of NSCLC are still increasing [23]. Understanding the molecular pathogenesis of NSCLC is helpful to improve the life quality and prolong the survival time of patients [24]. As a large number of important substances are involved in cell regulation, circRNA is playing more and more important roles in the diagnosis and treatment of cancer [25]. Our study found that the expression level of circFAT1(e2) in normal tissues is lower than that in NSCLC tissues. Using a series of experiments, it was found that circFAT1(e2) could decrease the expression level of miR-30e-5p, which in turn inhibited

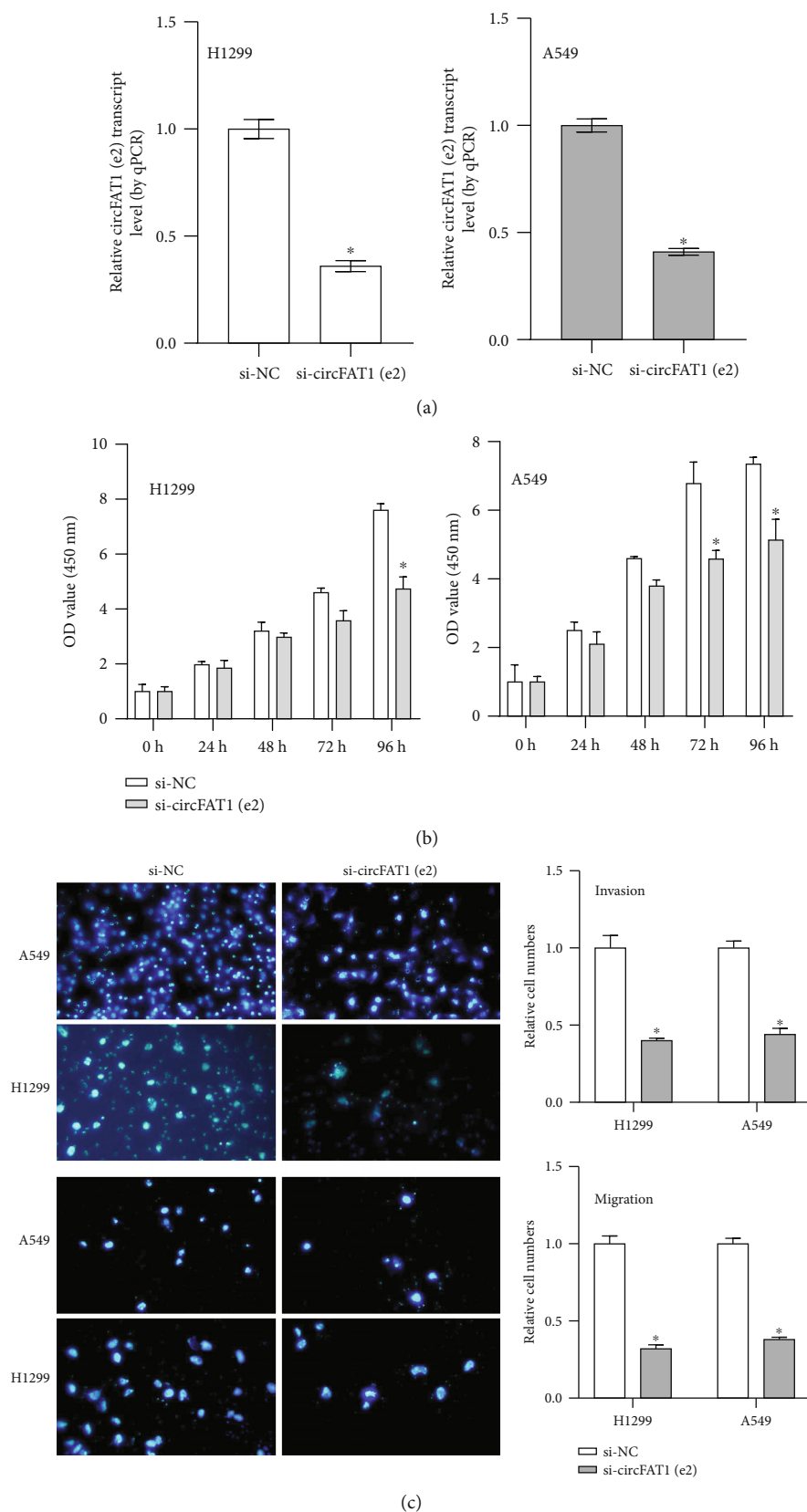


FIGURE 2: circFAT1(e2) knockdown repressed NSCLC cells' metastasis and proliferation. (a) To knock down circFAT1(e2) level, siRNA which specifically targeted the circFAT1(e2) (si-circFAT1(e2)) were transfected into NSCLC cells. (b) That circFAT1(e2) downexpression inhibited NSCLC cell proliferation was demonstrated by the CCK-8 assay. (c) That knockdown of circFAT1(e2) decreased cell invasion and migration was indicated by transwell assays. * $P < 0.05$.

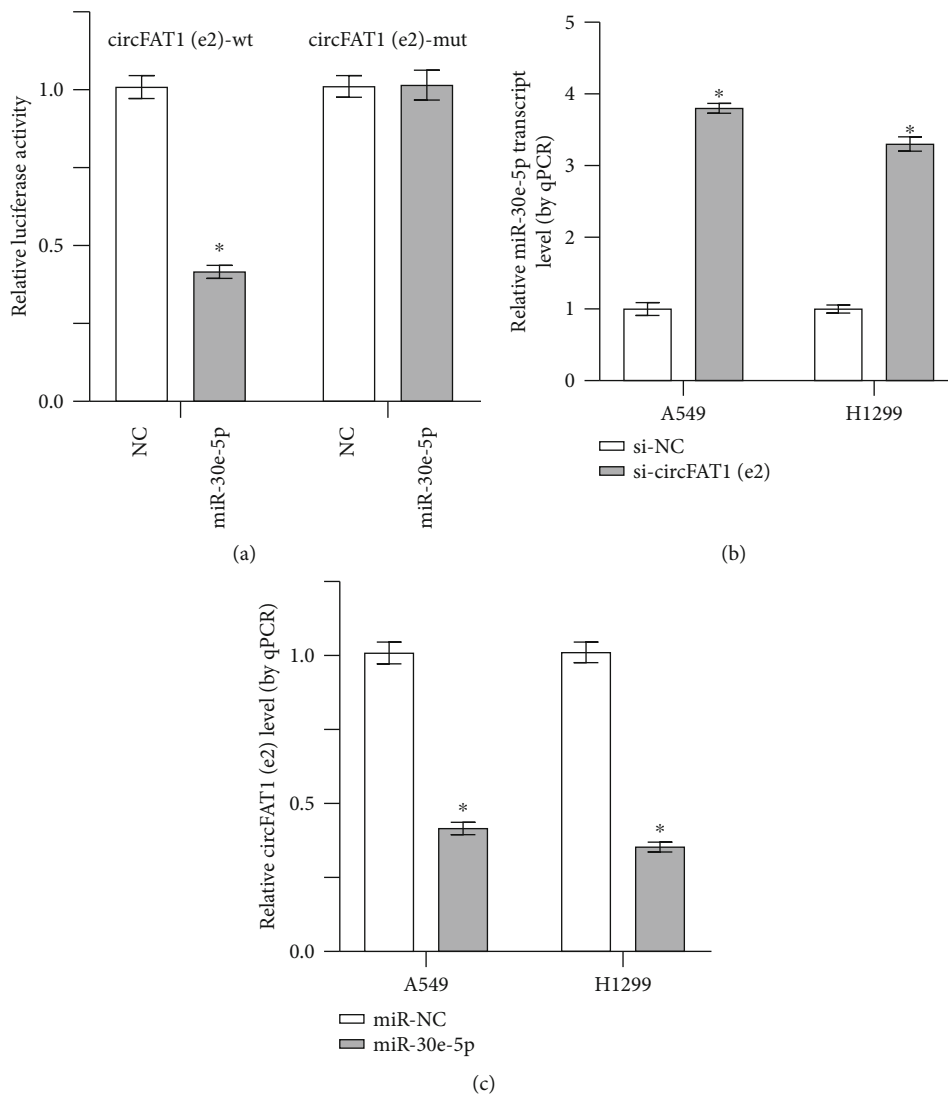


FIGURE 3: circFAT1(e2) targeted miR-30e-5p as a miRNA sponge. (a) The dual-luciferase reporter assays indicated that luciferase activity was decreased in HEK 293T cells after cotransfecting with circFAT1(e2)-wt and miR-30e-5p. (b) In NSCLC cells that knocked down circFAT1(e2), the expression of miR-30e-5p was higher. (c) In miR-30e-5p overexpression cells, circFAT1(e2) expression decreased. * $P < 0.05$.

miR-30e-5p on the regulation of the downstream target gene USP22. This study demonstrated that knockdown of circFAT1(e2) decreased the ability of NSCLC cells to proliferate, invade, and metastasize.

A large number of noncoding RNAs such as miRNAs, lncRNAs, and circRNAs existed in cells, [26]. Current studies have found that circRNAs may be used as a ceRNA to competitively bind to miRNA binding sites, thus interfering with the activity of miRNAs to regulate downstream target genes [27]. For example, ciRS-7 can affect the binding activity of miR-7 [28]. In addition, studies have found that CIRC_0067934 directly inhibits the interaction between mRNA 3'-UTR of FZD5 and miR-1324 and activates the FZD5/Wnt/ β -catenin signal pathway to promote the proliferation, invasion, and migration of hepatocellular carcinoma cells [29]. The circFAT1(e2) is derived from exon 2 of the FAT1 gene. Studies in gastric cancer cells have shown that

overexpressed circFAT1(e2) inhibits the proliferation, migration, and invasion of gastric cancer cells by targeting binding to miR-548g and releasing RUNX1 [16]. In contrast, our results in NSCLC show that circFAT1(e2) knockdown can inhibit the growth of NSCLC cells. The highly expressed circFAT1(e2) decreases the activity of miR-30e-5p through competitively binding with miR-30e-5p, thus promoting the invasive ability and growth of NSCLC cells.

Ubiquitin-specific protease 22 (USP22), as a part of the mammalian SAGA complex, can affect histone modifications by deubiquitination of H2A and H2B, which is one of the key regulators of the cell cycle. Studies have shown that overexpression of USP22 can enhance the inhibitory effect of cell cycle inhibitors such as p21 and enhance the proliferation of tumor cells, thus promoting the occurrence and development of tumors [30]. By knocking out circFAT1(e2), we found that the ability of cells to proliferate, invade, and

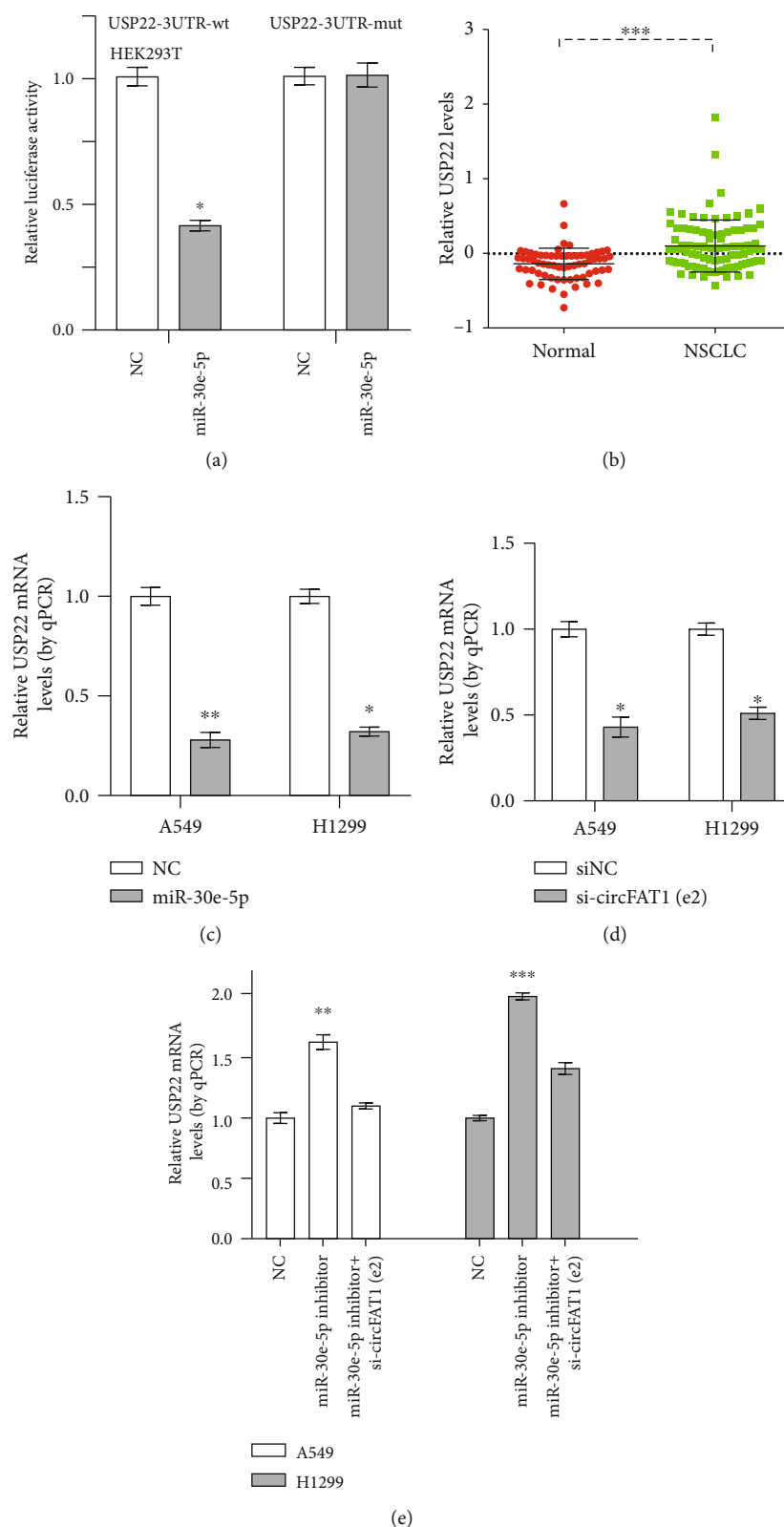


FIGURE 4: USP22 served as the functional protein of circFAT1(e2)/miR-30e-5p. (a) The relative fluorescence intensity was confirmed by the luciferase reporter assay when the cotransfection between USP22 3'-UTR wild-type or mutant and miR-30e-5p or control happened. (b) There was difference between the expression of USP22 in normal tissues and that in NSCLC tissues. (c) After overexpression of miR-30e-5p, USP22 mRNA levels decreased. (d) USP22 mRNA level decreased after knockdown of circFAT1(e2) in A549 and H1299 cells. (e) USP22 mRNA expression can be increased by the miR-30e-5p inhibitor which can also resist the reduction of USP22 mRNA caused by circFAT1(e2) knockdown. * $P < 0.05$, ** $P < 0.01$, and *** $P < 0.001$.

metastasize was significantly inhibited. Luciferase report experiment showed that overexpressed circFAT1(e2) could sponge miR-30e-5p and reduce the expression level of this miRNA, thus weakening the regulation of miR-30e-5p on the downstream target gene USP22 and increasing the expression of USP22.

In addition, this study has some limitations. First of all, although the expression level of circFAT1(e2) was detected in a small sample size of NSCLC samples, a larger sample size should be used to further verify the correlation between the expression of circFAT1(e2), miR-30e-5p, and USP22 and clinical parameters. Second, the findings of this study were derived from *in vitro* analysis. Therefore, *in vivo* analysis should be performed to further verify our findings.

In conclusion, the present study for the first time demonstrated that circFAT1(e2) acted as an oncogene in NSCLC, and circFAT1(e2) promoted NSCLC cell proliferation, migration, and invasion. Using a series of experiments, we found that circFAT1(e2) knockdown decreased the expression level of USP22 through sponging miR-30e-5p. Our study indicated that circFAT1(e2) might be a potential biomarker of NSCLC and provided a variety of options for screening, diagnosis, and treatment of NSCLC.

Abbreviations

ncRNA: Noncoding RNA
 circRNA: Circular RNA
 NSCLC: Non-small-cell lung cancer
 ncRNAs: Noncoding RNAs
 SCLC: Small-cell lung cancer
 FBS: Fetal bovine serum
 CCK-8: Cell Counting Kit-8
 RBP: RNA-binding protein
 USP22: Ubiquitin-specific protease 22.

Data Availability

The datasets used and/or analyzed during the current study are available from the corresponding author on reasonable request.

Conflicts of Interest

The authors declare that they have no conflict of interest.

Authors' Contributions

Ying Chen and Yuping Du contributed to the conception and design. Yuping Du and Huiqian Zhang contributed to the development of methodology. Cheng Zhao was responsible for the sample collection. Yiyuan Cao and YanCheng Dai were responsible for the analysis and interpretation of data. Wenmin Dong, Huiqian Zhang, YanCheng Dai, Yi Zhou, and Yun Luo were responsible for the writing, review, and/or revision of the manuscript. Wenmin Dong and Huiqian Zhang contributed equally to this work.

Acknowledgments

This work was supported by the project within the budget of Shanghai University of Traditional Chinese Medicine (Grant Number 18LK073, applicant: Yuping Du), Development of Traditional Medicine Project of Hongkou District Health Committee (Grant Number HGY-MGB-2018-01-08, applicant: Ying Chen), Shanghai Three-Year Action Plan of Traditional Chinese Medicine (Grant Number ZY (2018-2020)-cccX-4005, applicant: Cheng Zhao), Shanghai New Interdisciplinary Program of Traditional Chinese Medicine (Grant Number SHZYYJCXK201715, applicant: Yongbin Cao), and Scientific Research Project of Shanghai Health Committee (Grant Number 201740166, applicant: Ying Chen).

References

- [1] H. Doucas and D. P. Berry, "Basic principles of the molecular biology of cancer I," *Surgery (Oxford)*, vol. 24, no. 2, pp. 43–47, 2006.
- [2] L. M. Holdt, A. Kohlmaier, and D. Teupser, "Molecular roles and function of circular RNAs in eukaryotic cells," *Cellular and Molecular Life Sciences*, vol. 75, no. 6, pp. 1071–1098, 2018.
- [3] L.-L. Chen and L. Yang, "Regulation of circRNA biogenesis," *RNA Biology*, vol. 12, no. 4, pp. 381–388, 2015.
- [4] N. Eger, L. Schoppe, S. Schuster, U. Laufs, and J.-N. Boeckel, "Circular RNA splicing," *Advances in Experimental Medicine and Biology*, vol. 1087, pp. 41–52, 2018.
- [5] J. Salzman, "Circular RNA expression: its potential regulation and function," *Trends in Genetics*, vol. 32, no. 5, pp. 309–316, 2016.
- [6] R. Zhou, Y. Wu, W. Wang et al., "Circular RNAs (circRNAs) in cancer," *Cancer Letters*, vol. 425, pp. 134–142, 2018.
- [7] L. Fang, W. W. Du, J. Lyu et al., "Enhanced breast cancer progression by mutant p53 is inhibited by the circular RNA circ-Ccnb1," *Cell Death & Differentiation*, vol. 25, no. 12, pp. 2195–2208, 2018.
- [8] X. Li, J. Wang, C. Zhang et al., "Circular RNA circITGA7 inhibits colorectal cancer growth and metastasis by modulating the Ras pathway and upregulating transcription of its host gene ITGA7," *The Journal of Pathology*, vol. 246, no. 2, pp. 166–179, 2018.
- [9] J. She, P. Yang, Q. Hong, and C. Bai, "Lung cancer in China: challenges and interventions," *Chest*, vol. 143, no. 4, pp. 1117–1126, 2013.
- [10] R. Lopez Castro, P. Lianes, E. Noguero Martinez et al., "Spanish registry of thoracic tumors (TTR): interim analyses of comorbidities, risk associations, personal and family history of cancer," *Annals of Oncology*, vol. 30, p. v750, 2019.
- [11] S. S. Ramalingam, T. K. Owonikoko, and F. R. Khuri, "Lung cancer: new biological insights and recent therapeutic advances," *CA: A Cancer Journal for Clinicians*, vol. 61, no. 2, pp. 91–112, 2011.
- [12] W. D. Travis, N. Rekhtman, G. J. Riley et al., "Pathologic diagnosis of advanced lung cancer based on small biopsies and cytology: a paradigm shift," *Journal of Thoracic Oncology*, vol. 5, no. 4, pp. 411–414, 2010.
- [13] J. Zhao, L. Li, Q. Wang, H. Han, Q. Zhan, and M. Xu, "circRNA expression profile in early-stage lung adenocarcinoma

- patients,” *Cellular Physiology and Biochemistry*, vol. 44, no. 6, pp. 2138–2146, 2018.
- [14] L. Wan, L. Zhang, K. Fan, Z.-X. Cheng, Q.-C. Sun, and J.-J. Wang, “Circular RNA-ITCH suppresses lung cancer proliferation via inhibiting the Wnt/ β -catenin pathway,” *BioMed research international*, vol. 2016, Article ID 1579490, 11 pages, 2016.
- [15] Y.-H. Luo, X.-Z. Zhu, K.-W. Huang et al., “Emerging roles of circular RNA hsa_circ_0000064 in the proliferation and metastasis of lung cancer,” *Biomedicine & Pharmacotherapy*, vol. 96, pp. 892–898, 2017.
- [16] J. Fang, H. Hong, X. Xue et al., “A novel circular RNA, circFAT1(e2), inhibits gastric cancer progression by targeting miR-548g in the cytoplasm and interacting with YBX1 in the nucleus,” *Cancer Letters*, vol. 442, pp. 222–232, 2019.
- [17] J. Liu, H. Li, C. Wei et al., “circFAT1(e2) promotes papillary thyroid cancer proliferation, migration, and invasion via the miRNA-873/ZEB1 axis,” *Computational and Mathematical Methods in Medicine*, vol. 2020, Article ID 1459368, 9 pages, 2020.
- [18] H. Gu, X. Cheng, J. Xu et al., “Circular RNA circFAT1(e2) promotes osteosarcoma progression and metastasis by sponging miR-181b and regulating HK2 expression,” *BioMed Research International*, vol. 2020, Article ID 3589871, 7 pages, 2020.
- [19] T. Danford, A. Rolfe, and D. Gifford, “GSE: a comprehensive database system for the representation, retrieval, and analysis of microarray data,” *Pacific Symposium on Biocomputing*, vol. 2008, pp. 539–550, 2008.
- [20] G. Xu, J. Cai, L. Wang et al., “MicroRNA-30e-5p suppresses non-small cell lung cancer tumorigenesis by regulating USP22-mediated Sirt1/JAK/STAT3 signaling,” *Experimental Cell Research*, vol. 362, no. 2, pp. 268–278, 2018.
- [21] Y.-X. Ma, H. Zhang, X.-H. Li, and Y.-H. Liu, “miR-30e-5p inhibits proliferation and metastasis of nasopharyngeal carcinoma cells by target-ing USP22,” *European review for medical and pharmacological sciences*, vol. 22, no. 19, pp. 6342–6349, 2018.
- [22] R. S. Herbst and S. M. Lippman, “Molecular signatures of lung cancer—toward personalized therapy,” *New England Journal of Medicine*, vol. 356, no. 1, pp. 76–78, 2007.
- [23] F. Islami, L. A. Torre, and A. Jemal, “Global trends of lung cancer mortality and smoking prevalence,” *Translational lung cancer research*, vol. 4, no. 4, pp. 327–338, 2015.
- [24] S. Zöchbauer-Müller, A. F. Gazdar, and J. D. Minna, “Molecular pathogenesis of lung cancer,” *Annual Review of Physiology*, vol. 64, no. 1, pp. 681–708, 2002.
- [25] S. Meng, H. Zhou, Z. Feng et al., “circRNA: functions and properties of a novel potential biomarker for cancer,” *Molecular Cancer*, vol. 16, no. 1, p. 94, 2017.
- [26] H. Großhans and W. Filipowicz, “The expanding world of small RNAs,” *Nature*, vol. 451, no. 7177, pp. 414–416, 2008.
- [27] J.-H. Li, S. Liu, H. Zhou, L.-H. Qu, and J.-H. Yang, “starBase v2.0: decoding miRNA-ceRNA, miRNA-ncRNA and protein-RNA interaction networks from large-scale CLIP-Seq data,” *Nucleic Acids Research*, vol. 42, no. D1, pp. D92–D97, 2013.
- [28] P. Li, Q. Y. Xiao, and C. L. Guan, “The emerging landscape of circular RNA ciRS-7 in cancer (review),” *Oncology Reports*, vol. 33, no. 6, pp. 2669–2674, 2015.
- [29] Q. Zhu, G. Lu, Z. Luo et al., “circRNA circ_0067934 promotes tumor growth and metastasis in hepatocellular carcinoma through regulation of miR-1324/FZD5/Wnt/ β -catenin axis,” *Biochemical and Biophysical Research Communications*, vol. 497, no. 2, pp. 626–632, 2018.
- [30] B. S. Atanassov and S. Y. R. Dent, “USP22 regulates cell proliferation by deubiquitinating the transcriptional regulator FBP1,” *EMBO reports*, vol. 12, no. 9, pp. 924–930, 2011.

Research Article

circSLC8A1 Acts as a Tumor Suppressor in Prostate Cancer via Sponging miR-21

Daoyuan Wang,^{1,2} Shuxian Yan,² Lihui Wang,¹ Yunlong Li,¹ and Baoping Qiao ¹

¹Department of Urology, The First Affiliated Hospital of Zhengzhou University, Zhengzhou, China

²Department of Urology, 989th Hospital of the Joint Logistic Support Force, Luoyang, China

Correspondence should be addressed to Baoping Qiao; baoba66946@163.com

Received 28 December 2020; Revised 12 March 2021; Accepted 17 March 2021; Published 2 April 2021

Academic Editor: Tao Huang

Copyright © 2021 Daoyuan Wang et al. This is an open access article distributed under the Creative Commons Attribution License, which permits unrestricted use, distribution, and reproduction in any medium, provided the original work is properly cited.

Background. There is more and more evidence showed that circRNAs played essentially role in the regulation of various biological processes. The role of circSLC8A1 in prostate cancer (PCa) is yet little known. **Methods.** The CircSLC8A1 expression in human prostate cancer was measured by qRT-PCR. The interplay between the specific circRNA, miRNA, and mRNA was investigated by RT-PCR and luciferase reporter assay. Through transient transfection of siRNA, the impacts of circSLC8A1 on PCa were discussed. Cell cycle evaluation, transwell assay, and CCK-8 assay were employed to determine its biological influences. **Results.** In this study, our data revealed that circSLC8A1 was downregulated in PCa tissues and cells. The reduction of circSLC8A1 resulted in the inhibition of cell proliferation and migration. In mechanism, circSLC8A1 exhibited a direct interaction with miR-21 and displayed as a miRNA sponge to inhibit PCa progression. The functional analysis revealed that the circSLC8A1/miR-21 axis may regulate the cell proliferation, angiogenesis, cell migration, epithelial to mesenchymal transition, MAPK signaling pathway, and chemokine signaling pathway. **Conclusions.** CircSLC8A1 functioned as an inhibitor of neoplasm via modulating the miR-21 and might serve as a prospective target for the treatment of PCa.

1. Background

The incidence rate of prostate cancer (PCa) ranked second amid all commonly occurred carcinomas, and the lethality of it was in fifth place among carcinoma-associated deaths in men worldwide [1]. As far as the treatment of PCa, radiotherapy is a commonly employed adjuvant treatment for surgery and chemotherapy, which could extend the dominant time for controlling carcinoma. Even though most of PCa stayed in the form of or inactivation for a long time, the metastasis progression perhaps contributed to poor prognostic status and more death. Herein, it is necessary to deeply elaborate the thorough molecular mechanisms related to PCa, which is conducive to uncovering new targets for diagnosis and treatment.

Circular RNAs (circRNAs) are a sort of ground substance that is not typically bound to the endogenously generated RNA [2, 3]. As a new class of endogenous noncoding RNA, circRNAs did not possess 5' cap and 3' poly covalently closed structure-like tail [4]. It is different from linear RNA,

and circRNA is usually derived from reverse splicing event of an exon or intron. The reverse complementary sequence, containing the inverted repeat Alu pair and exon skipping, is essential for the formation of circRNA [5, 6]. Genome and transcriptome data generated from the next generation sequencing (NGS) projects and bioinformatic algorithms have screened and defined numerous circRNAs in eukaryotes [7–10], revealing that they are not just casual byproducts or “splicing noise.” High-throughput technology has been applied to in-depth characterize the identification and potential functions of circRNA [11, 12]. circRNA is a class of abundant and conserved RNA, existing widely in intricate tissues, cell types, or specific stages. Various circRNAs displayed importantly in carcinoma development [4, 13]. The differential expressed circular RNA in PCa was probably related to the resistance to enzalutamide [14]. Circfoxo3 facilitates PCa progression via sponging miR-29a-3p [15]. CircRNA-UCK2-caused increase expression of Tet1 would hinder PCa cell proliferation and invasion by sponging mirna-767-5p [16]. Increased expression of HOXB13 induced by the

linkage of circular RNA *ITCH* and sponge-like miR-17-5p caused the suppression of PCa progression [17].

The circRNAs are emerging as a new class of noncoding RNAs implicated in multiple cancer types, and to explore the functional roles of circRNAs in PCa, we screened the circRNAs potentially involved in PCa by systematic literature review. In the present study, we found that the circSLC8A1 expression in the tissues and cells of PCa was dramatically reduced, and its expression displayed a positive correlation with the clinical DFS of PCa. Overall, our findings implied that CircSLC8A1 functioned as an inhibitor of neoplasm via modulating the miR-21, affording a prospective target for the treatment of PCa.

2. Methods

2.1. Public Gene Expression Dataset. The analysis of SLC8A1 expression levels in PCa was implemented in the GEPIA web server [18, 19], which curated all the cancer types of the Cancer Genome Atlas (TCGA) project.

2.2. Human Cell Lines and Tissues. Human PCa cell lines were obtained from SIBCB (Shanghai, China). PCa specimens and paired adjacent control specimens were collected from surgical patients in The First Affiliated Hospital of Zhengzhou University. All patients have autonomously signed written consent. Our experiments got approval of the ethics committee of our hospital. All tissues were stored in liquid nitrogen for long-term use.

2.3. Isolation and Quantation of RNA. Whole RNA was isolated by Trizol Reagent (TIANGEN, China) as manually described. RNA was reversely transcribed into the cDNA using Takara system (TIANGEN, China). AceQ qPCR SYBR Green Master Mix kit was employed to perform qRT-PCR on Roche 480. $2^{-\Delta\Delta CT}$ was carried to calculate the cycle threshold (CT) value of the normalized target gene expression [20].

2.4. Construction of siRNA. The sequences of siRNAs were acquired from GenePharma (Shanghai, China). Synthetic promiscuous siRNA was treated as scramble control. siRNAs were transfected into cells utilizing Lipofectamine 3000 (Invitrogen) referring to the instruction. Overall, RNA and protein were harvested at 48 hours posttransfection.

2.5. Transwell Assay. A density of 1×10^5 cells in 500 μ L medium without FBS was plated in the upper chamber. Medium containing 10% FBS was added into the lower chamber as a chemical attractant. Cotton-tipped swabs were used to remove the cells staying in the upper chamber after culturing for the indicated time. The number of invaded or migrated cells at stochastic six fields was calculated.

2.6. Cell Proliferation Assay. CCK-8 kit (Dojindo, Japan) was utilized to determine the ability of PCa cell viability. Totally, 6,000 cells were plated in 96-well and then subjected to different treatments at the indicated time. The OD value of 450 nm was detected after incubation with 10 μ L CCK-8 solution for another 2 hours.

2.7. Luciferase Reporter Assay. Wild type circSLC8A1 sequence comprising the assumed binding site of miR-21 was inserted into the reporter vector. All final positive clones were verified by sequencing. Mutant circSLC8A1 sequence was also inserted into *t* reporter construct so as to examine the specific binding activity with miR-21. The luciferase activity was detected by luciferase assay kit (Promega, USA) at 24 hours posttransfection.

2.8. Statistical Analysis. All derived data were shown as the mean \pm SD. Paired Student's *t*-test was introduced to assess the differences of the levels of circSLC8A1 and miR-21 in compared groups, and chi-square test was applied to determine the differences of more than two groups. The Pearson correlation coefficient analysis was also conducted [21]. A *p* value of <0.05 was thought to be statistically significant [22].

3. Results

3.1. CircSLC8A1 (*hsa_circ_0000994*) Is Obviously Reduced in PCa. As shown in Figure 1(a), the linear RNA of circSLC8A1 was significantly downregulated in PCa compared to normal samples using the Cancer Genome Atlas (TCGA) dataset. Accordingly, the low expression of SLC8A1 was associated with shorter disease-free survival time in patients in the TCGA cohort (Figure 1(b)). Further investigation of SLC8A1 RNA products revealed that circSLC8A1 and SLC8A1 were reduced in PCa cells, including DU145, PC-3, 22Rv1, and LNCaP, in comparison with normal urothelial cells WPMY-1 (Figures 1(c) and 1(d)). The analysis of circSLC8A1 in 15 paired PCa and normal prostate tissues revealed that circSLC8A1 was downregulated in PCa tissues (Figure 1(e)). Moreover, the incubation of RNase R led to a reduction in the level of SLC8A1 linear mRNA, not the levels of circSLC8A1 (Figure 1(f)), suggesting that circSLC8A1 was more stable than its linear RNA.

3.2. Knockdown of circSLC8A1 Enhanced the Proliferation and Migration. To further evaluate the functional impact of circSLC8A1 on PCa, we conducted functional assays to deeply investigate its functionalities. Firstly, we transfected the siRNA of circSLC8A1 into DU145 and PC-3 cells and observed that the circSLC8A1 expression was significantly reduced (Figures 2(a) and 2(b)). The CCK-8 assay showed that the proliferation capabilities of prostate cancer cells were dominantly enhanced by the knockdown of circSLC8A1 (Figures 2(c) and 2(d)). Transwell results showed that knockdown circSLC8A1 significantly increased migration of cells of DU145 and PC-3 (Figures 2(e) and 2(f)). These results indicated that circSLC8A1 exerted tumor-suppressing effect by inhibiting the proliferation and migration of PCa cells.

3.3. circSLC8A1 Functions as a Sponge for miR-21 in PCa Cells. Previous reports have shown that circRNA played as a miRNA sponge to modulate the miRNA expression [23, 24]. To further explore whether circSLC8A1 could function as a miRNAs sponge in PCa cells, we employed two widely used prediction websites including circBANK and RegRNA 2.0. We selected 5 candidate miRNAs, including miR-133b,

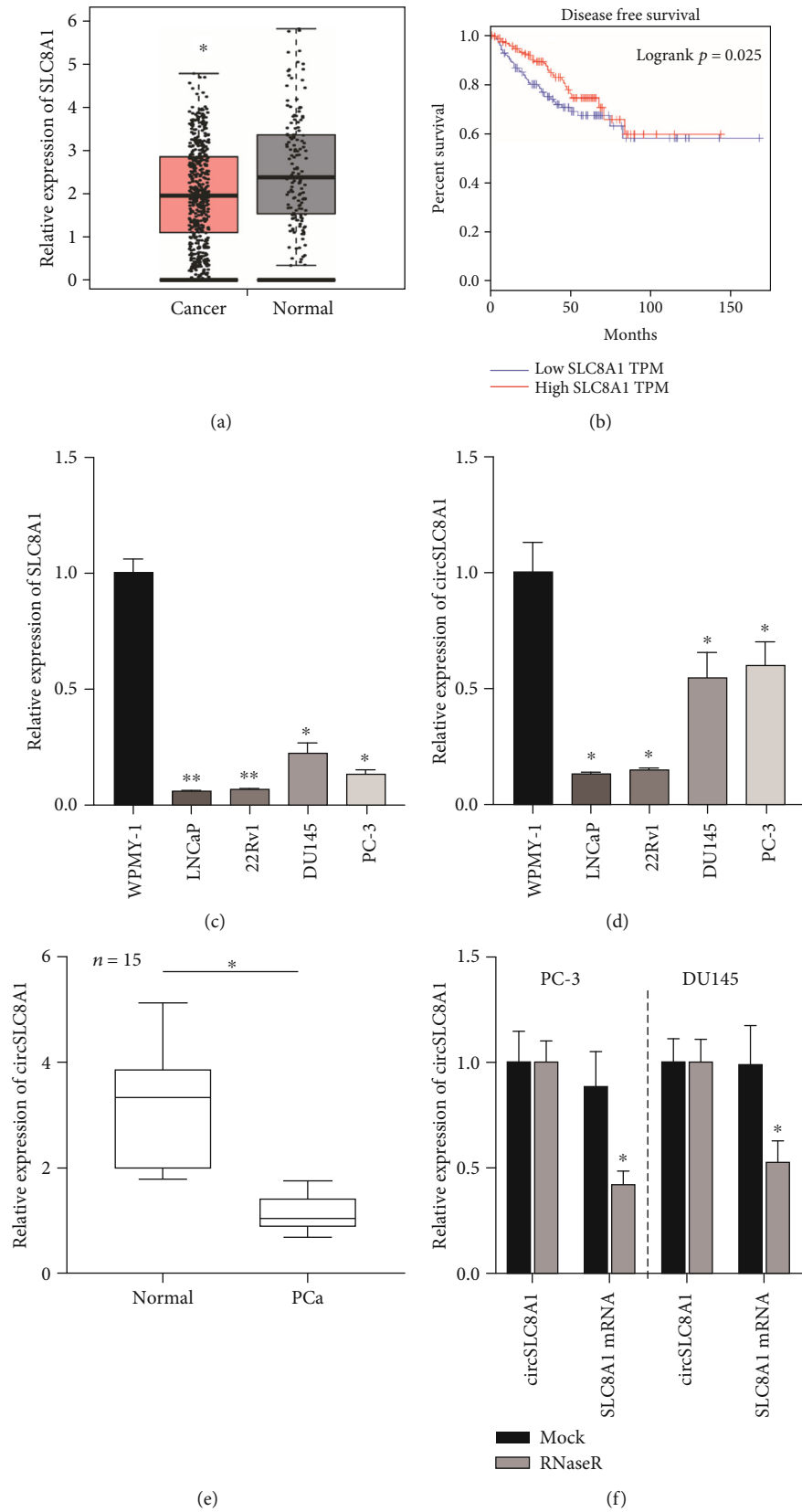


FIGURE 1: The circSLC8A1 expression is obviously reduced in PCa. (a) The TCGA dataset showed that SLC8A1 is significantly downregulated in PCa. (b) The circSLC8A1 expression exhibited an association with disease-free survival time in patients. (c) The SLC8A1 and (d) circSLC8A1 expression was found reduced in PCa cells. (e) The circSLC8A1 expression was found reduced in PCa tissues. (f) circSLC8A1 but not SLC8A1 was reduced by RNase R.

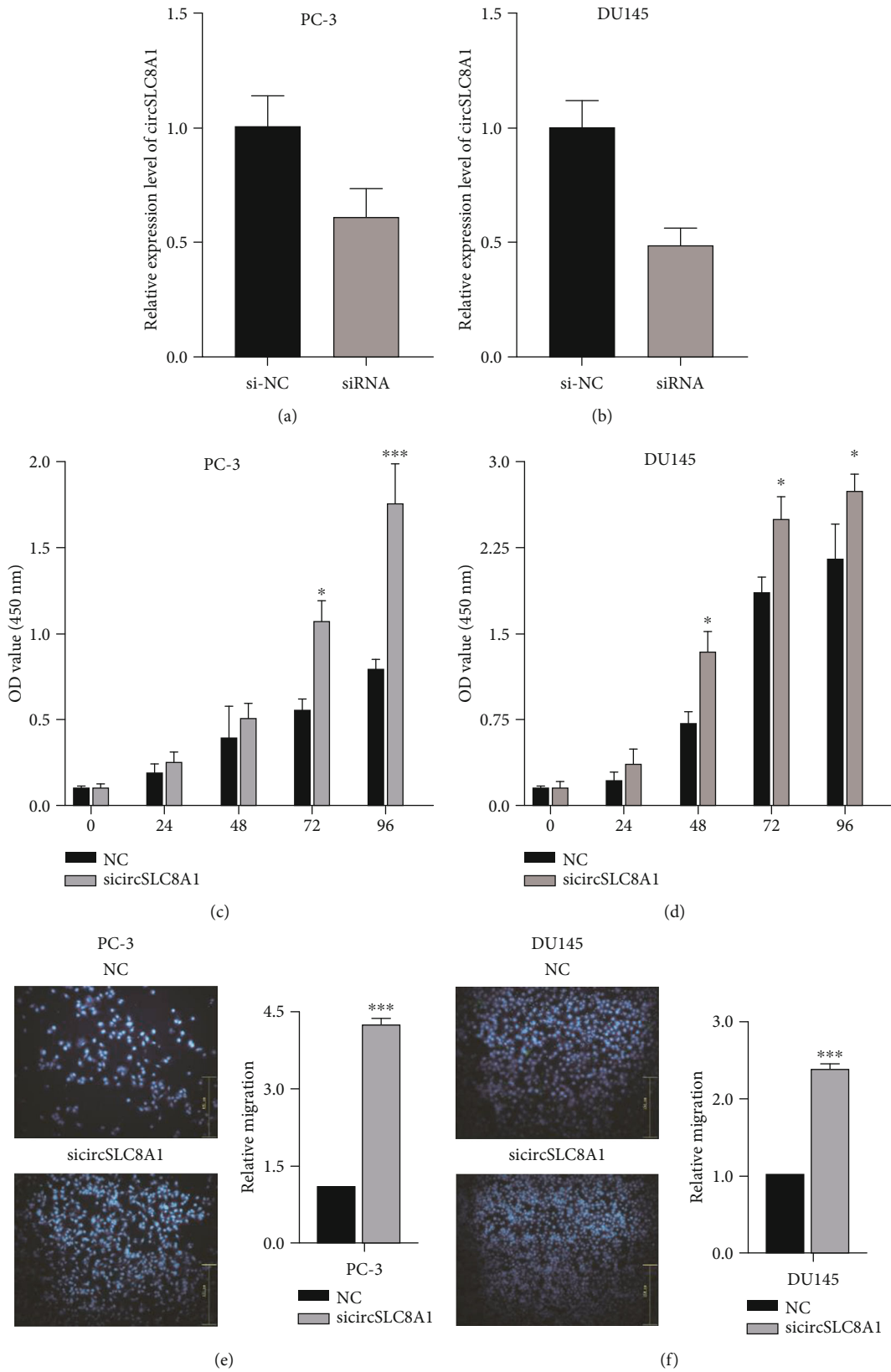


FIGURE 2: Knockdown of circSLC8A1 enhanced the migration and invasion. (a, b) circSLC8A1 was significantly decreased after transfected the si-circSLC8A1. (c, d) Knockdown of circSLC8A1 increases the proliferation capabilities. (e, f) Knockdown of circSLC8A1 increase the migration.

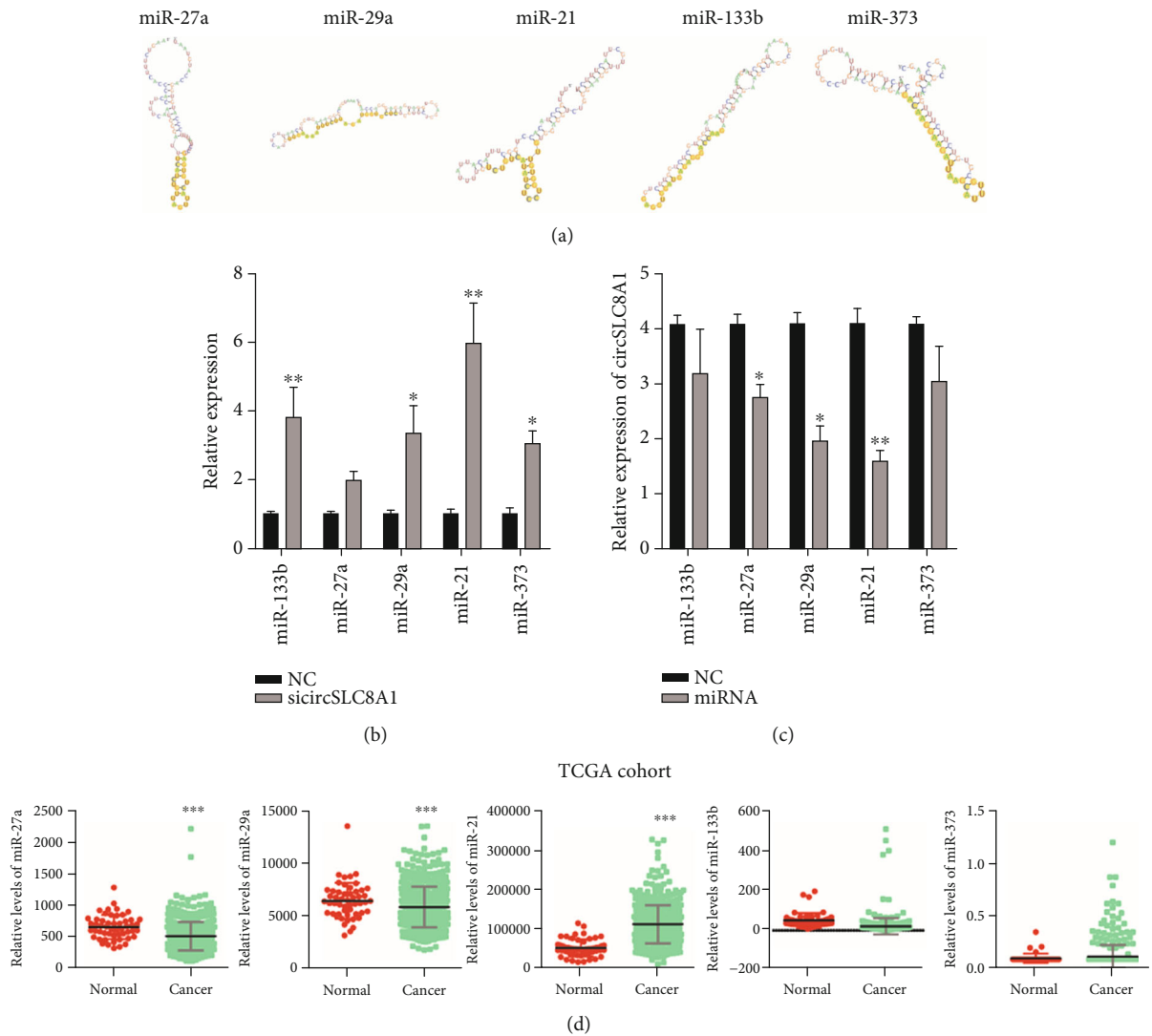


FIGURE 3: circSLC8A1 sponged miR-21 in PCa. (a)The interaction between miR-133b, miR-27a, miR-29a, miR-21 and miR-373, and circSLC8A1. (b) Knockdown of circSLC8A1 significantly induced the level of miR-133b, miR-29a, miR-21, and miR-373. (c) Overexpress miR-27a, miR-29a, and miR-21 reduced the expression of circSLC8A1. (d) The expression of miR-133b, miR-27a, miR-29a, miR-21, and miR-373 in PCa.

miR-27a, miR-29a, miR-21, and miR-373, which were predicted to bind to circSLC8A1 (Figure 3(a)). Subsequently, we knockdown circSLC8A1 and detected the effect of circSLC8A1 on these candidate miRNAs. It was confirmed that the knockdown of circSLC8A1 significantly increased the expression of miR-133b, miR-29a, miR-21, and miR-373 (Figure 3(b)). Moreover, we detected the circSLC8A1 levels after the overexpression of these miRNAs to confirm the circSLC8A1 sponge effect. As expected, the overexpression of miR-27a, miR-29a, and miR-21 reduced the circSLC8A1's expression (Figure 3(c)). Finally, we showed that miR-27a and miR-29a were downregulated in PCa (Figure 3(d)); however, miR-21 was upregulated in PCa, and miR-133b and miR-373 were not differently expressed between PCa and normal tissues. These results indicated that miR-21 might directly interact with circSLC8A1 in PCa and was selected for further validation.

3.4. CircSLC8A1 Suppressed PCa Progression through Targeting miR-21. To confirm to the interaction between miR-21 and circSLC8A1, we conducted luciferase reporter gene analysis. miR-21 mimics could significantly reduce the luciferase of wild type circSLC8A1 compared with mimic NC (Figure 4(a)). We next evaluated the miR-21 potential functional role in prostate cancer. The qRT-PCR results showed that miR-21 was upregulated in the PCa tissue as compared with the normal prostate tissue (Figure 4(b)). Notably, the enhanced expression of miR-21 promoted the proliferation of DU145 and PC-3 (Figures 4(c) and 4(d)), suggesting that miR-21 might be a tumor-promoting miRNA. In order to evaluate whether circSLC8A1 inhibits the progression of PCa through miR-21, we cotransfected sicircSLC8A1 and miR-21 inhibitor mimics into PCa cells. CCK-8 experiment showed that knockdown of circSLC8A1 could enhance the proliferation ability, while this enhance

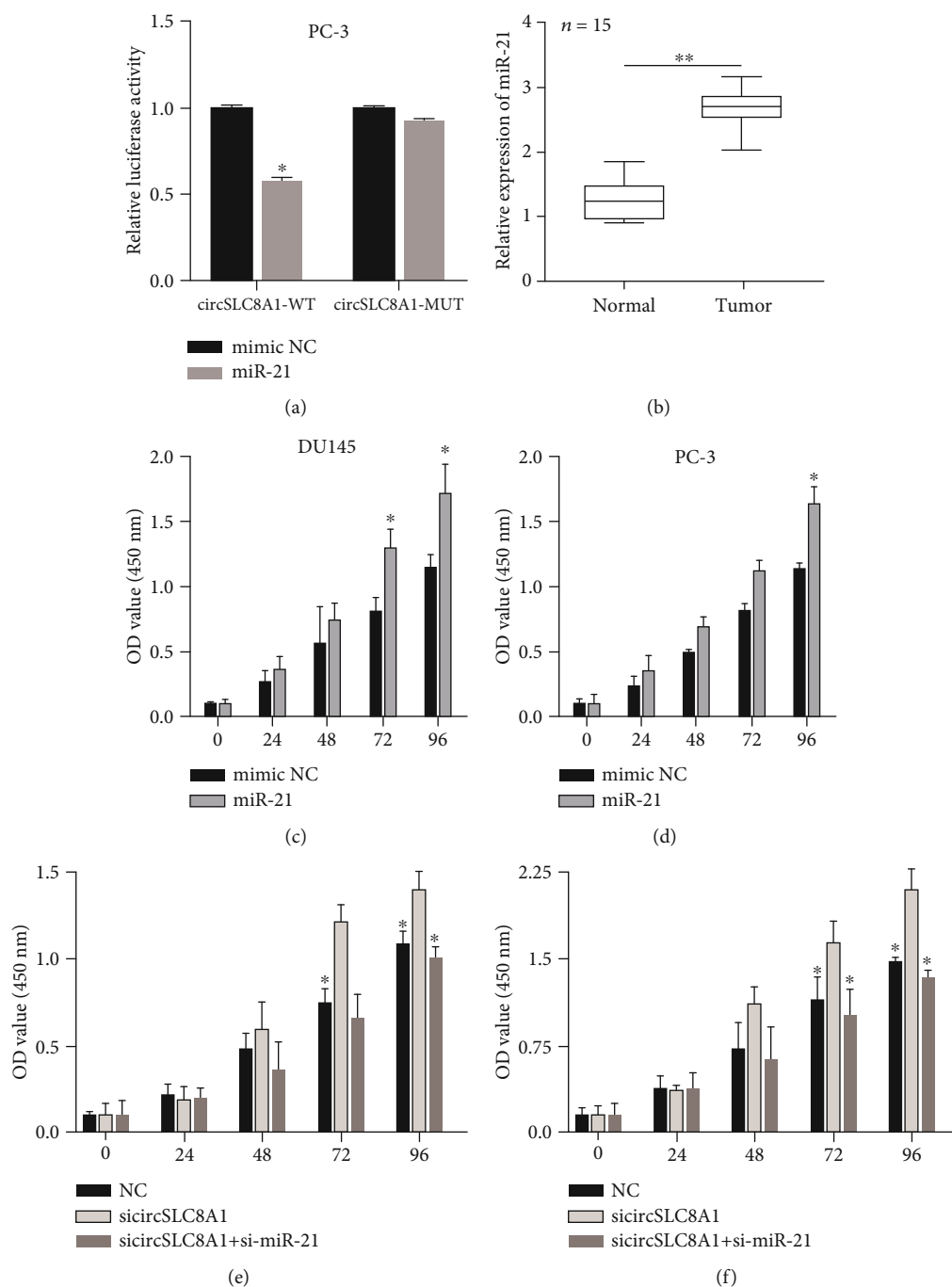


FIGURE 4: circSLC8A1 suppressed prostate cancer progression through targeting miR-21. (a) miR-21 mimics significantly reduced the luciferase of wild type circSLC8A1. (b) miR-21 was upregulated in the prostate cancer tissue. (c, d) miR-21 mimics significantly promoted the proliferation of DU145 and PC-3. (e, f) Knockdown of circSLC8A1 enhanced the proliferation ability, but this effect can be partially attenuated by the knockdown of miR-21.

can be partially attenuated by the knockdown of miR-21 (Figures 4(e) and 4(f)). These results indicated that circSLC8A1 could inhibit the progression of prostate cancer through sponging miR-21.

3.5. The Downstream Pathways of the circSLC8A1/miR-21 Axis. To further investigate the potential mechanism of the circSLC8A1/miR-21 axis, we searched for the target genes

of miR-21 using four miRNA-mRNA interaction databases, including TargetScan, miRDB, miRanda, and Starbase. Totally, we identified 91 genes which had the potential to interact with miR-21 in PCa (Figure 5(a)). The Gene Ontology (GO) enrichment analysis showed that circSLC8A1/miR-21 was related to the regulation of cell proliferation, angiogenesis, cell migration, and epithelial to mesenchymal transition (Figure 5(b)). KEGG pathway analysis showed that

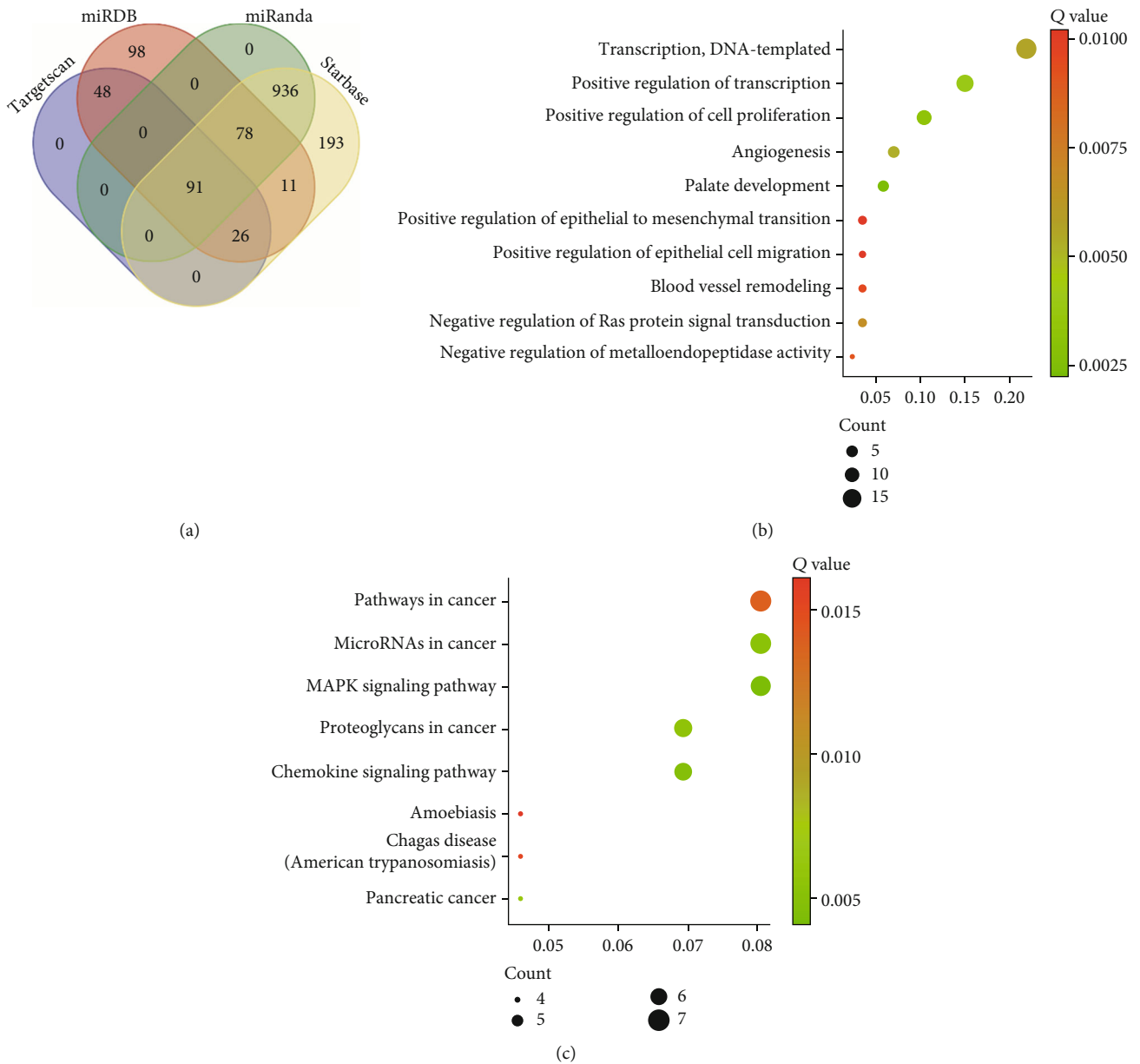


FIGURE 5: Bioinformatic analysis of the circSLC8A1/miR-21 axis. (a) Identification of targets of miR-21 by analyzing TargetScan, miRDB, miRanda, and Starbase. (c, d) GO analysis and KEGG pathway analysis of the 91 genes.

circSLC8A1/miR-21 was related to the MAPK signaling pathway and chemokine signaling pathway (Figure 5(c)). These results indicated that circSLC8A1 might act as a tumor suppressor by regulating cancer-promoting pathways via miR-21, thereby inhibiting cell growth and progression in PCa.

4. Discussion

Prostate cancer (PCa) is the second most commonly diagnosed cancer in men worldwide. Here, for the first time, we identified circSLC8A1 as a key circRNA, which is frequently decreased in PCa. The PCa patients with high circSLC8A1 expression had significantly longer overall survival than those with low expression. Our data demonstrated that circSLC8A1 could restrain PCa progression by sponging miR-21.

CircSLC8A1 is a new circRNA that has been found to be related to the progression of a variety of human benign diseases, such as osteoporosis [25], Parkinson’s disease (PD) [26], and dilated cardiomyopathy (DCM) [27]. For instance, circ-SLC8A1 modulates osteoporosis via occluding the inhibited impacts of miR-516b-5p on the expression of AKAP2 [25]. Large number of independent reports have suggested that circSLC8A1 plays essential role in cardiomyocytes. Cytoplasmically localized circSLC8A1 can interact with miRNA133a-3p. Blockade of circSLC8A1 reduces the release of active oxygen by ischemia/reperfusion during the deteriorous effects of reactive oxygen in vivo and in turn was decreased by CDIP1, an apoptosis promoter gene to inhibit cardiomyocyte apoptosis [28]. Very interestingly, a recent study showed that circSLC8A1 is implicated in tumorigenesis.

For example, Lu et al. reported that circSLC8A1 curbed PCa progression via modulating PTEN [29]. circSLC8A1 is reduced in the tissues and cell lines of PCa, and its expression is associated with the pathological and histological stages of PCa. The overexpression of circSLC8A1 resulted in the reduction of cell migration, invasion, and proliferation [29]. In mechanism, we found that circSLC8A1 directly interacted with miR-21 and consequently acted as a sponge of miRNA to modulate miR-21, and we found that miR-21 could be phagocytosed by circSLC8A1. Small RNA-21 (miR-21), as a solid body neoplasm, commonly upregulated miRNA. miR-21 has been found to participate in cell proliferation, migration, invasion, apoptosis, and drug resistance [30]. Several target genes of miR-21 have been determined, including PDCD4, SPRY2, PTEN, RECK, TPM1, and BCL2 [31]. The present study showed that miR-21 was upregulated in PCa tissue and exhibited a negative correlation with circSLC8A1. The high miR-21 expression was widely reported by previous studies [32, 33] and could significantly induce DU145 and PC-3 cell proliferation. Moreover, our data suggested that circSLC8A1 mediated that the tumor-suppressing effect could be weakened by overexpressing miR-21.

In mechanism, we predicted the downstream pathways regulated by the circSLC8A1/miR-21 axis. Specifically, circSLC8A1/miR-21 was associated with the GO terms such as regulation of cell proliferation, cell migration, and KEGG pathways such as MAPK signaling pathway and chemokine signaling pathway, indicating that circSLC8A1 might act as a tumor suppressor by regulating cancer-promoting pathways via miR-21, thereby inhibiting cell growth and progression in PCa.

5. Conclusions

In conclusion, our results showed that circSLC8A1 was downregulated in PCa and could function as a sponge of miR-21. In addition, we also demonstrated that circSLC8A1 inhibited PCa progression through targeting miR-21 and might serve as a novel biomarker for the treatment of PCa.

Data Availability

All the raw data can be provided if any qualified researchers required.

Conflicts of Interest

The authors declare that the research was conducted in the absence of any commercial or financial relationships that could be construed as a potential conflict of interest.

References

- [1] C. Gu, X. Shi, C. Dai et al., "RNA m6A Modification in Cancers: Molecular Mechanisms and Potential Clinical Applications," *The Innovation*, vol. 1, no. 3, article 100066, 2020.
- [2] G. Huang, S. Li, N. Yang, Y. Zou, D. Zheng, and T. Xiao, "Recent progress in circular RNAs in human cancers," *Cancer Letters*, vol. 404, pp. 8–18, 2017.
- [3] S. Meng, H. Zhou, Z. Feng et al., "CircRNA: functions and properties of a novel potential biomarker for cancer," *Molecular Cancer*, vol. 16, no. 1, p. 94, 2017.
- [4] R. Zhou, Y. Wu, W. Wang et al., "Circular RNAs (circRNAs) in cancer," *Cancer Letters*, vol. 425, pp. 134–142, 2018.
- [5] S. Qu, X. Yang, X. Li et al., "Circular RNA: a new star of non-coding RNAs," *Cancer Letters*, vol. 365, no. 2, pp. 141–148, 2015.
- [6] W. R. Jeck, J. A. Sorrentino, K. Wang et al., "Circular RNAs are abundant, conserved, and associated with ALU repeats," *RNA*, vol. 19, no. 2, pp. 141–157, 2013.
- [7] X. Mao, Y. Guo, J. Qiu et al., "Next-generation sequencing to investigate circular RNA profiles in the peripheral blood of preterm neonates with bronchopulmonary dysplasia," *Journal of Clinical Laboratory Analysis*, vol. 34, no. 7, article e23260, 2020.
- [8] A. Saleemhasha and S. Mishra, "Novel molecules lncRNAs, tRFs and circRNAs deciphered from next-generation sequencing/RNA sequencing: computational databases and tools," *Briefings in Functional Genomics*, vol. 17, no. 1, pp. 15–25, 2018.
- [9] Y. Gao, J. Wang, and F. Zhao, "CIRI: an efficient and unbiased algorithm for de novo circular RNA identification," *Genome Biology*, vol. 16, no. 1, p. 4, 2015.
- [10] J. N. Vo, M. Cieslik, Y. Zhang et al., "The landscape of circular RNA in cancer," *Cell*, vol. 176, no. 4, pp. 869–881.e13, 2019.
- [11] X. Qiu, X. Ke, H. Ma et al., "Profiling and bioinformatics analyses reveal differential expression of circular RNA in tongue cancer revealed by high-throughput sequencing," *Journal of Cellular Biochemistry*, vol. 120, no. 3, pp. 4102–4112, 2018.
- [12] D. D. Xiong, Z. B. Feng, Z. F. Lai et al., "High throughput circRNA sequencing analysis reveals novel insights into the mechanism of nitidine chloride against hepatocellular carcinoma," *Cell Death & Disease*, vol. 10, no. 9, p. 658, 2019.
- [13] H. D. Zhang, L. H. Jiang, D. W. Sun, J. C. Hou, and Z. L. Ji, "CircRNA: a novel type of biomarker for cancer," *Breast Cancer*, vol. 25, no. 1, pp. 1–7, 2018.
- [14] J. Greene, A. M. Baird, O. Casey et al., "Circular RNAs are differentially expressed in prostate cancer and are potentially associated with resistance to enzalutamide," *Scientific Reports*, vol. 9, no. 1, p. 10739, 2019.
- [15] Z. Kong, X. Wan, Y. Lu et al., "Circular RNACircFOXO3promotes prostate cancer progression through spongingmiR-29a-3p," *Journal of Cellular and Molecular Medicine*, vol. 24, no. 1, pp. 799–813, 2020.
- [16] Z. Xiang, C. Xu, G. Wu, B. Liu, and D. Wu, "CircRNA-UCK2 increased TET1 inhibits proliferation and invasion of prostate cancer cells via sponge MiRNA-767-5p," *Open Medicine*, vol. 14, no. 1, pp. 833–842, 2019.
- [17] X. Wang, R. Wang, Z. Wu, and P. Bai, "Circular RNA ITCH suppressed prostate cancer progression by increasing HOXB13 expression via spongy miR-17-5p," *Cancer Cell International*, vol. 19, no. 1, p. 328, 2019.
- [18] Z. Tang, C. Li, B. Kang, G. Gao, C. Li, and Z. Zhang, "GEPIA: a web server for cancer and normal gene expression profiling and interactive analyses," *Nucleic Acids Research*, vol. 45, no. W1, pp. W98–W102, 2017.
- [19] C. Gu, X. Shi, Z. Huang et al., "A comprehensive study of construction and analysis of competitive endogenous RNA networks in lung adenocarcinoma," *Biochimica et Biophysica*

- Acta (BBA) - Proteins and Proteomics*, vol. 1868, no. 8, article 140444, 2020.
- [20] C. Gu, Z. Huang, X. Chen et al., "TEAD4 promotes tumor development in patients with lung adenocarcinoma via ERK signaling pathway," *Biochimica et Biophysica Acta - Molecular Basis of Disease*, vol. 1866, no. 12, article 165921, 2020.
- [21] C. Gu, X. Pan, R. Wang et al., "Analysis of mutational and clinicopathologic characteristics of lung adenocarcinoma with clear cell component," *Oncotarget*, vol. 7, no. 17, pp. 24596–24603, 2016.
- [22] C. Gu, X. Pan, Y. Chen, J. Yang, H. Zhao, and J. Shi, "Short-term and mid-term survival in bronchial sleeve resection by robotic system versus thoracotomy for centrally located lung cancer," *European Journal of Cardio-Thoracic Surgery*, vol. 53, no. 3, pp. 648–655, 2018.
- [23] K. L. Harper, E. McDonnell, and A. Whitehouse, "CircRNAs: from anonymity to novel regulators of gene expression in cancer (review)," *International Journal of Oncology*, vol. 55, no. 6, pp. 1183–1193, 2019.
- [24] C. Jiang, X. Zeng, R. Shan et al., "The emerging picture of the roles of CircRNA-CDR1as in cancer," *Frontiers in Cell and Development Biology*, vol. 8, p. 590478, 2020.
- [25] C. Lin, W. Zhong, W. Yan, J. Yang, W. Zheng, and Q. Wu, "Circ-SLC8A1 regulates osteoporosis through blocking the inhibitory effect of miR-516b-5p on AKAP2 expression," *The Journal of Gene Medicine*, vol. 22, no. 11, article e3263, 2020.
- [26] M. Hanan, A. Simchovitz, N. Yayon et al., "A Parkinson's disease CircRNAs resource reveals a link between circSLC8A1 and oxidative stress," *EMBO Molecular Medicine*, vol. 12, no. 11, article e13551, 2020.
- [27] W. Lei, T. Feng, X. Fang et al., "Signature of circular RNAs in human induced pluripotent stem cells and derived cardiomyocytes," *Stem Cell Research & Therapy*, vol. 9, no. 1, p. 56, 2018.
- [28] C. Jahn, C. Bar, and T. Thum, "CircSlc8a1, breaking a vicious circle in cardiac hypertrophy," *Cardiovascular Research*, vol. 115, no. 14, pp. 1946-1947, 2019.
- [29] Q. Lu, T. Liu, H. Feng et al., "Circular RNA circSLC8A1 acts as a sponge of miR-130b/miR-494 in suppressing bladder cancer progression via regulating PTEN," *Molecular Cancer*, vol. 18, no. 1, p. 111, 2019.
- [30] Y. R. Wu, H. J. Qi, D. F. Deng, Y. Y. Luo, and S. L. Yang, "MicroRNA-21 promotes cell proliferation, migration, and resistance to apoptosis through PTEN/PI3K/AKT signaling pathway in esophageal cancer," *Tumour Biology*, vol. 37, no. 9, pp. 12061–12070, 2016.
- [31] G. Wang, J. J. Wang, H. M. Tang, and S. S. T. To, "Targeting strategies on miRNA-21 and PDCD4 for glioblastoma," *Archives of Biochemistry and Biophysics*, vol. 580, pp. 64–74, 2015.
- [32] M. Folini, P. Gandellini, N. Longoni et al., "miR-21: an oncomir on strike in prostate cancer," *Molecular Cancer*, vol. 9, no. 1, p. 12, 2010.
- [33] S. R. Pfeffer, C. H. Yang, and L. M. Pfeffer, "The role of miR-21 in cancer," *Drug Development Research*, vol. 76, no. 6, pp. 270–277, 2015.

Retraction

Retracted: Pentoxifylline Can Reduce the Inflammation Caused by LPS after Inhibiting Autophagy in RAW264.7 Macrophage Cells

BioMed Research International

Received 12 March 2024; Accepted 12 March 2024; Published 20 March 2024

Copyright © 2024 BioMed Research International. This is an open access article distributed under the Creative Commons Attribution License, which permits unrestricted use, distribution, and reproduction in any medium, provided the original work is properly cited.

This article has been retracted by Hindawi following an investigation undertaken by the publisher [1]. This investigation has uncovered evidence of one or more of the following indicators of systematic manipulation of the publication process:

- (1) Discrepancies in scope
- (2) Discrepancies in the description of the research reported
- (3) Discrepancies between the availability of data and the research described
- (4) Inappropriate citations
- (5) Incoherent, meaningless and/or irrelevant content included in the article
- (6) Manipulated or compromised peer review

The presence of these indicators undermines our confidence in the integrity of the article's content and we cannot, therefore, vouch for its reliability. Please note that this notice is intended solely to alert readers that the content of this article is unreliable. We have not investigated whether authors were aware of or involved in the systematic manipulation of the publication process.

Wiley and Hindawi regrets that the usual quality checks did not identify these issues before publication and have since put additional measures in place to safeguard research integrity.

We wish to credit our own Research Integrity and Research Publishing teams and anonymous and named external researchers and research integrity experts for contributing to this investigation.




The corresponding author, as the representative of all authors, has been given the opportunity to register their agreement or disagreement to this retraction. We have kept a record of any response received.

References

- [1] D. Ruan, S. Deng, Z. Liu, and J. He, "Pentoxifylline Can Reduce the Inflammation Caused by LPS after Inhibiting Autophagy in RAW264.7 Macrophage Cells," *BioMed Research International*, vol. 2021, Article ID 6698366, 12 pages, 2021.

Research Article

Pentoxifylline Can Reduce the Inflammation Caused by LPS after Inhibiting Autophagy in RAW264.7 Macrophage Cells

Danping Ruan ¹, Sinan Deng,¹ Zhonglong Liu ² and Jie He ²

¹Department of Stomatology, Minhang Branch, Zhongshan Hospital, Fudan University, Shanghai, China

²Department of Oral and Maxillofacial-Head and Neck Surgery, Ninth People's Hospital, Shanghai Jiao Tong University School of Medicine, Shanghai Key Laboratory of Stomatology & Shanghai Research Institute of Stomatology, National Clinical Research Center of Stomatology, Shanghai, China

Correspondence should be addressed to Zhonglong Liu; zhonglong021@126.com and Jie He; hejie2310@126.com

Received 21 December 2020; Revised 27 January 2021; Accepted 8 February 2021; Published 16 March 2021

Academic Editor: Tao Huang

Copyright © 2021 Danping Ruan et al. This is an open access article distributed under the Creative Commons Attribution License, which permits unrestricted use, distribution, and reproduction in any medium, provided the original work is properly cited.

Pentoxifylline (PTX), as a methylxanthine derivative and nonspecific phosphodiesterase inhibitor, has the characteristics of anti-inflammatory and partial inflammatory process inhibition. However, the regulatory effect of PTX on inflammatory cytokines is unclear. Autophagy can regulate the activation of inflammasomes and then inhibit inflammation as previously described. Our study attempts to explore the relationship between autophagy and PTX-mediated regulation of inflammasome suppression. Macrophage-like RAW264.7 cells were studied as the *in vitro* macrophage model. We investigated the anti-inflammatory effect caused by PTX with time and dose response against the LPS-induced inflammatory factors (TNF- α , IL-1 β). Western blot detected the levels of autophagy-related proteins Beclin-1 and LC3, as well as the signal pathways of AMPK and p-AMPK. Fluorescence microscope and transmission electron microscope were used to observe the autophagy bodies in cells influenced by PTX. The autophagy in cells inhibited by PTX exhibited dose- and time-dependent effects, and PTX alleviated LPS-induced inflammation caused by retarded autophagy. Furthermore, in RAW264.7 macrophage cells, our data indicated that AMPK signaling perhaps functioned importantly in repressed autophagy. In addition, in RAW264.7 macrophages, our data suggested that AMPK signaling might play an important role in inhibiting autophagy during the process of PTX ameliorating LPS-mediated inflammation.

1. Introduction

Inflammation is a complex pathological reaction, which resulted from multiple physical responses from the immune system when exposed to external injury or infection [1, 2]. Despite the fact that inflammation could compensate the wound, it was sometimes regarded as a protective process. In some cases, reduction of inflammation is of usefulness, but not usually essential. Macrophages originating from peripheral blood monocytes play fundamentally in cellular immunity and possess numerous complicated performances in specific and nonspecific inflammatory process, consisting of surveying objective organisms, chemotaxis, phagocytosis, and damage [3–6]. Multiple soluble factors, such as several secreted polypeptides (also known as macrophage-derived inflammatory cytokines), could lead to inflammation. Some

of them, such as proinflammatory cytokines, could aggravate disease [7–9], while others, such as anti-inflammatory cytokines, were conducive to wound healing and also reduced inflammation [9–11]. Proinflammatory cytokine stimulated systemic inflammation, such as interleukin-1 (IL-1) and tumor necrosis factor alpha (TNF- α) [12, 13].

Autophagy is a basic steady-state process through which cells decompose their assembly [14]. Recently, increasing evidences have suggested that autophagy displayed an important role in inflammation by affecting the development, homeostasis, and survival of inflammatory cells *in vivo* including macrophages, neutrophils, and lymphocytes, along with the transcription and secretion of many cytokines [15–17]. Monkkonen and Debnath found out that the pathways included in inflammation curbed or promoted autophagy in a context-dependent manner. Conversely, autophagy

retarded or pushed inflammation in numerous carcinomas [18]. As Haq et al. demonstrated, identifying newly produced autophagy regulators in gut inflammation probably promoted new therapeutic regimes for intestinal inflammatory diseases [19]. Autophagy can raise or reduce disparate sections of identical inflammatory signaling concatenation in a context-dependent manner [20]. Autophagy is an extremely conservative homeostasis and inducible process that affects several aspects of the immune system, and is necessary for macrophages production and activation (comprising migration of monocyte/macrophage and differentiation of monocyte into macrophages), making autophagy become an appealing therapeutic target to further modulate macrophage response and a promising strategy for anticancer treatment [21]. AMP-activated protein kinase (AMPK) is a central mediator of cellular energy homeostasis, playing pivotal roles in regulating proliferation, metabolism reprogramming, autophagy, apoptosis, and cell differentiation. The kinase is activated in response to stresses that deplete ATP supplies such as low glucose, hypoxia, ischemia, and heat shock.

Pentoxifylline (PTX, $C_{13}H_{18}N_4O_3$), a methylxanthine derivative originally introduced for its rheologic effects, is a competitive nonselective phosphodiesterase inhibitor that can increase the decomposition rate of cyclic adenosine monophosphate (cAMP) and cyclic guanosine monophosphate (cGMP) and inhibit the synthesis of TNF and leukotriene. It is also an inhibitor with favorable anti-inflammatory effects and immunoregulatory properties [22, 23]. The drug can inhibit proinflammatory cytokine synthesis (IL-1, IL-6, IL-12, TNF- α) via lymphocytes and keratinocytes and retard the adhesion between leukocytes and endothelial cells or epithelial cells [24–26]. In humans, PTX demonstrated anti-inflammatory activity in some diseases such as cardiac surgery, acute radiation damage, chronic kidney disease, and HIV-infected patients [27–30]. Effects of pentoxifylline on inflammatory cytokine expression and inflammation-related disease inhibition were also found in animal models [31, 32]. PTX not only promotes the increase in anti-inflammatory cytokines towards a more stable immune phenotype but also prevents the production of pro-inflammatory cytokines [33, 34]. Therefore, it is a promising anti-inflammatory regulator candidate for ameliorating inflammatory environment. Sharma et al. indicated that activated ER stress response and autophagy were resistant to PTX-mediated apoptosis and thereby influenced the activity of PTX against cancer in human melanoma cells [35]. Nevertheless, there is little known towards the mediation role of PTX on inflammatory via regulation of autophagy, inflammasome, and the corresponding signaling pathways in macrophages.

Given that autophagy participates in the process of inflammation and PTX displays anti-inflammatory activities though the inhibition of proinflammatory cytokines, the autophagy machinery that controls the influence of PTX against inflammatory needs to be further explored in a macrophage-like cell model. Our study tried to unearth PTX-induced regulation of the inflammatory responses and cytokine production by activating autophagy and inhibiting inflammasome as well as signaling pathway in RAW264.7

macrophage cells. We also hypothesized that the AMPK signaling played a crucial role in autophagy regulation and suppression of inflammation.

2. Materials and Methods

2.1. Reagents and Cell Culture. Pentoxifylline (PTX) was ordered from BD Biosciences (San Jose, CA, USA). α -MEM, FBS, penicillin, and streptomycin were ordered from Hyclone. 3-Methyadenine (3-MA) and LY294002 were ordered from Selleck Chemicals (Houston, TX, USA). Rabbit polyclonal anti-LC3, anti-IL-1-beta, anti-NLRP3, and anti-Beclin1 were obtained from Cell Signaling Technology Inc. (Danvers, MA, USA). Anti-TNF- α , anti-ERK1/2, and p-ERK1/2 were ordered from Abcam (Cambridge, MA, USA). Mouse polyclonal anti-GAPDH and rabbit polyclonal anti-P62 were ordered from Proteintech Group, Inc. Anti- α -tubulin rabbit polyclonal was ordered from Beyotime Biotechnology (Shanghai, China). Secondary antibodies were ordered from Thermo Scientific.

Murine macrophage cells RAW264.7 were derived from the Institute of Biochemistry and Cell Biochemistry and Cell Biology (Shanghai, China). RAW264.7 were kept in DMEM containing 10% FBS and 5% penicillin/streptomycin at 37°C in a humidified 5% CO₂ atmosphere.

2.2. Cell Viability Assay. 1.0×10^3 of cells in each well were inoculated in 96-well plates prior to PTX treatment. Cells were treated with 0, 0.2, 0.3, 0.5, and 0.8 mg/mL PTX at 24 h and 48 h. Then, the cell viability was determined with α -MEM containing Cell Counting Kit 8 (CCK-8) solution (Dojindo, Japan) in each well. The medium was then discarded and maintained for 2 h at 37°C in the dark. The absorbance value of 490 nm was detected by an ELISA reader.

2.3. PTX Time- and Dose-Response Detection. Whole-blood assays were conducted in many parts of this literature in order to reflect the aspect closest to physiological environment. Serum was not included. 0.5 mL of samples was maintained in 24-well plates with treatment of LPS (10 ng/mL) and PTX (20, 200, and 2,000 μ g/mL) for 4, 8, or 24 h at 37°C, 5% CO₂. To detect cytokine production, supernatants were harvested, centrifuged, and maintained at -80°C until use at different postincubation time.

2.4. Cytokine Quantification in Supernatants. In the experiments, indicated cells pretreated with lipopolysaccharide (LPS) were then stimulated with 20 ng/mL interferon- γ (IFN- γ). The cells were exposed to 0, 50, 100, 200, and 400 ng/mL LPS in a concentration-dependent manner for 24 h; in addition, we also treated cells with 100 ng/mL LPS at 0, 3, 6, 12, and 24 h in a time-dependent manner. Through this two groups' analysis, we can determine the best treated concentration and time point. All samples were centrifuged after a specified time point of stimulation. Supernatants without cells were harvested and fast-frozen at -80°C until the following use. The IL-1 β and TNF- α and other cytokine levels in supernatants were determined utilizing commercially available ELISA kits (Absin, Shanghai, China) as

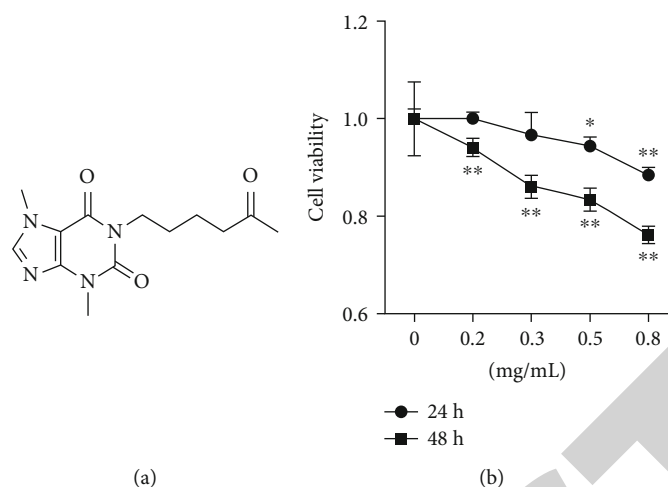


FIGURE 1: (a) Molecular structure of pentoxifylline (PTX). (b) CCK8 assay detected RAW264.7 cell viability with 0, 0.2, 0.3, 0.5, and 0.8 mg/mL PTX treatment after 24 h and 48 h (* $P < 0.05$ and ** $P < 0.01$, compared to control).

described in the manual. The threshold of detection sensitivity was 3.3 pg/mL for IL1- β and 3.7 pg/mL for TNF- α .

2.5. Western Blot Analysis. For per well, 1.0×10^6 cells/mL were inoculated in $\varnothing 60$ mm dishes as indicated. Whole cell lysate with 2% protease inhibitor and phosphatase inhibitors (Beyotime Biotechnology, China) was applied to harvest overall proteins. Bicinchoninic Acid (BCA) Protein Assay Reagent (Pierce, USA) was executed to determine protein concentrations. Approximately 20 μ g sample protein was loaded and ran on 10-15% SDS-PAGE gel, followed by transferring into polyvinylidene difluoride (PVDF) membrane (Millipore). 5% nonfat milk diluted in phosphate-buffered saline (PBS)/Tween 20 was used to block PVDF membrane for 1 h. PVDF membranes were rinsed three times with Tris-buffered saline Tween (TBST) and then incubated with primary antibody overnight at 4°C. At the following day, PVDF membrane was rinsed three times with TBST. Secondary antibodies were incubated with membrane for 1 h at ambient temperature.

2.6. Immunofluorescence Staining and Fluorescence Microscope. The adenoviral constructs carrying mRFP-GFP-LC3 were obtained from HanBio Technology Co. Ltd. (Shanghai, China). Raw 264.7 cells were infected with adenovirus carrying mRFP-GFP-LC3 at MOI 200 upon cell confluence at approximately 80%. Macrophages were incubated in a 12-well plate with adenovirus diluted in 1 mL complete medium for 4 h in a 37°C incubator as described by the manufacturers. The macrophages after transfection were incubated with DMEM containing 10% FBS overnight. Autophagosomes and autolysosomes in survival macrophages were counted by Cell Imaging Multi-Mode Reader (Cytation™5, BioTek Company, USA) with 40 \times image.

2.7. Transmission Electron Microscopy (TEM). RAW264.7 cells were fixed with 2% glutaraldehyde for 2 h after 12 h PTX (0, 0.2, 0.5 mg/mL) treatment. After fixation, RAW264.7 incubated with 1% osmium tetroxide were dehy-

drated with gradient ethanol and then embedded in Epon-Araldite resin. The autophagosomes were visualized under the TEM (Tecnai G2 Spirit Bio TWIN, FEI Company, USA).

2.8. Statistical Analysis. The representative data was shown as the mean \pm SEM of three separate experiments in triplicate one time. All data were processed and analyzed by *t*-test and ANOVA in SPSS 20 (Chicago, IL, USA). Obvious differences existing in different groups were shown as $P < 0.05$.

3. Results

3.1. Evaluation of Cell Viability after Pentoxifylline Treatment. The molecular structure of pentoxifylline (PTX) was shown in Figure 1(a). To get the safe concentrations (SCs) of PTX, we examined and evaluated the cytotoxicity of PTX with different concentrations (0, 0.2, 0.3, 0.5, and 0.8 mg/mL), as shown in Figure 1(b). After 24 h incubation, we found that cell survival had no significant difference among groups with PTX less than 0.5 mg/mL. Although with statistical significance between the 0.3 and 0.5 mg/mL groups, it holds no big difference with regard to the cell viability at a time point of 24 hours. Therefore, the concentration of PTX drug used in the following study was no more than 0.5 mg/mL.

3.2. LPS/IFN- γ Induced Inflammation in RAW264.7 Cells. LPS, a sort of endotoxin produced by outer membrane of bacteria, is famous as inducing inflammation [36], while interferon gamma (IFN- γ) is a pleiotropic molecule which can enhance proinflammatory signaling by activating macrophages for inflammatory cytokine level [37]. LPS stimulation of macrophages combined with IFN- γ can enhance macrophage activation and increase the expression of inflammatory factors [38, 39]. The lipopolysaccharide- (LPS-) primed inflammasome activation would induce some active proinflammatory cytokines and chemokine, such as interleukin-1 β (IL-1 β) and tumor necrosis factor α (TNF- α). Emerging data have shown that PTX can ameliorate inflammatory

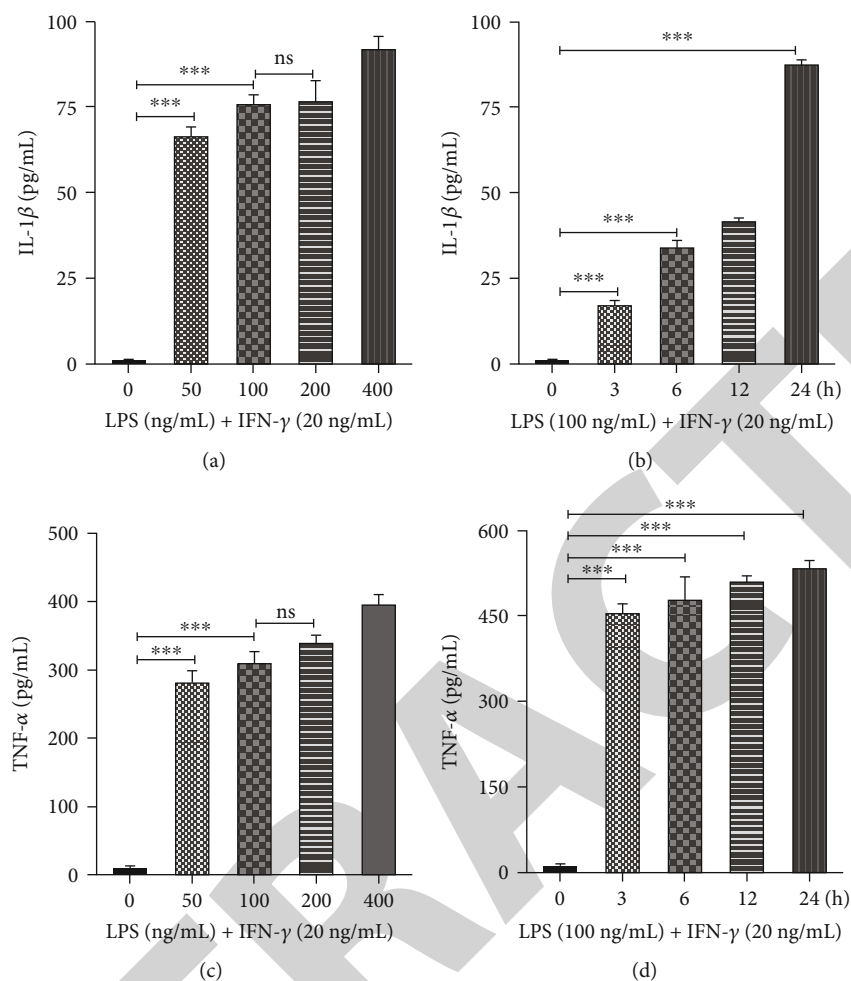


FIGURE 2: LPS-caused inflammasome activation in macrophage under different conditions detected with enzyme-linked immunosorbent assay (ELISA) among supernatants. The IL-1 β expression level was influenced by (a) a concentration-treatment manner (0, 50, 100, 200, and 400 ng/mL), and (b) a time-dependent manner (0, 3, 6, 12, and 24 h) treating with 100 ng/mL LPS and 20 ng/mL IFN- γ . The TNF- α expression level affected by (c) a concentration-treatment manner (0, 50, 100, 200, and 400 ng/mL) and (d) a time-dependent manner (0, 3, 6, 12, and 24 h) treating with 100 ng/mL LPS and 20 ng/mL IFN- γ (** P < 0.001 compared to control, ns means no significance when compared to 100 ng/mL LPS-treated group).

factor expression [40]. In order to set a model of IFN- γ /LPS-caused proinflammatory phenotype in RAW264.7 cells, IFN- γ (20 ng/mL) combined with 0, 50, 100, 200, and 400 ng/mL LPS were explored (Figures 2(a) and 2(c)). It was found that inflammatory factor (TNF- α , IL-1 β) expression could be evidently raised when the LPS concentration was 100 ng/mL. When the concentration was increased to 200 ng/mL, the increasing effects of the expression of inflammatory factors were not obvious. Furthermore, we examined the influence of 100 ng/mL LPS and 20 ng/mL IFN- γ at different stimulating times (0, 3, 6, 12, and 24 h). Figures 2(b) and 2(d) showed that with the time gradient changes, significant inflammatory factor expression (TNF- α , IL-1 β) was found at 24 h. Therefore, we chose the condition of IFN- γ /LPS-induced macrophage activation with LPS 100 ng/mL and IFN- γ 20 ng/mL, and the stimulation time was 24 h.

3.3. PTX Ameliorated LPS-Caused Inflammatory Factors in RAW264.7 Cells.

To verify that PTX has an inhibitory effect

on LPS-mediated inflammation, we first pretreated macrophages with 0.2 and 0.5 mg/mL of PTX for 12 hours and then used 100 ng/mL+20 ng/mL of LPS/IFN- γ to treat cells for 24 hours. Inflammatory factor (IL-1 β and TNF- α) level in the supernatant was measured by ELISA. Figures 3(a) and 3(b) illustrated that IL-1 β and TNF- α level was inhibited with treatment of 0.2 and 0.5 mg/mL PTX, and the inhibited impact was significant when cells were treated with 0.5 mg/mL PTX. Then, PTX with a concentration of 0.5 mg/mL was adopted to pretreat cells with different times (6, 12, 24 hours) and followed by cotreating with LPS/IFN- γ for 24 h. With respect to the time of PTX treatment, the maximum inhibitory effect on the expression of IL-1 β and TNF- α was found to be 12 h (Figure 3(c)). Furthermore, we maintained PTX treat time with 12 h, altered PTX with 0.2, 0.3, and 0.5 mg/mL, and then stimulated by LPS/IFN- γ for 24 h. It was found that as the PTX concentration increases, the inhibitory effect on IL-1 β and TNF- α increases accordingly, and the inhibitory effect is significant after treatment

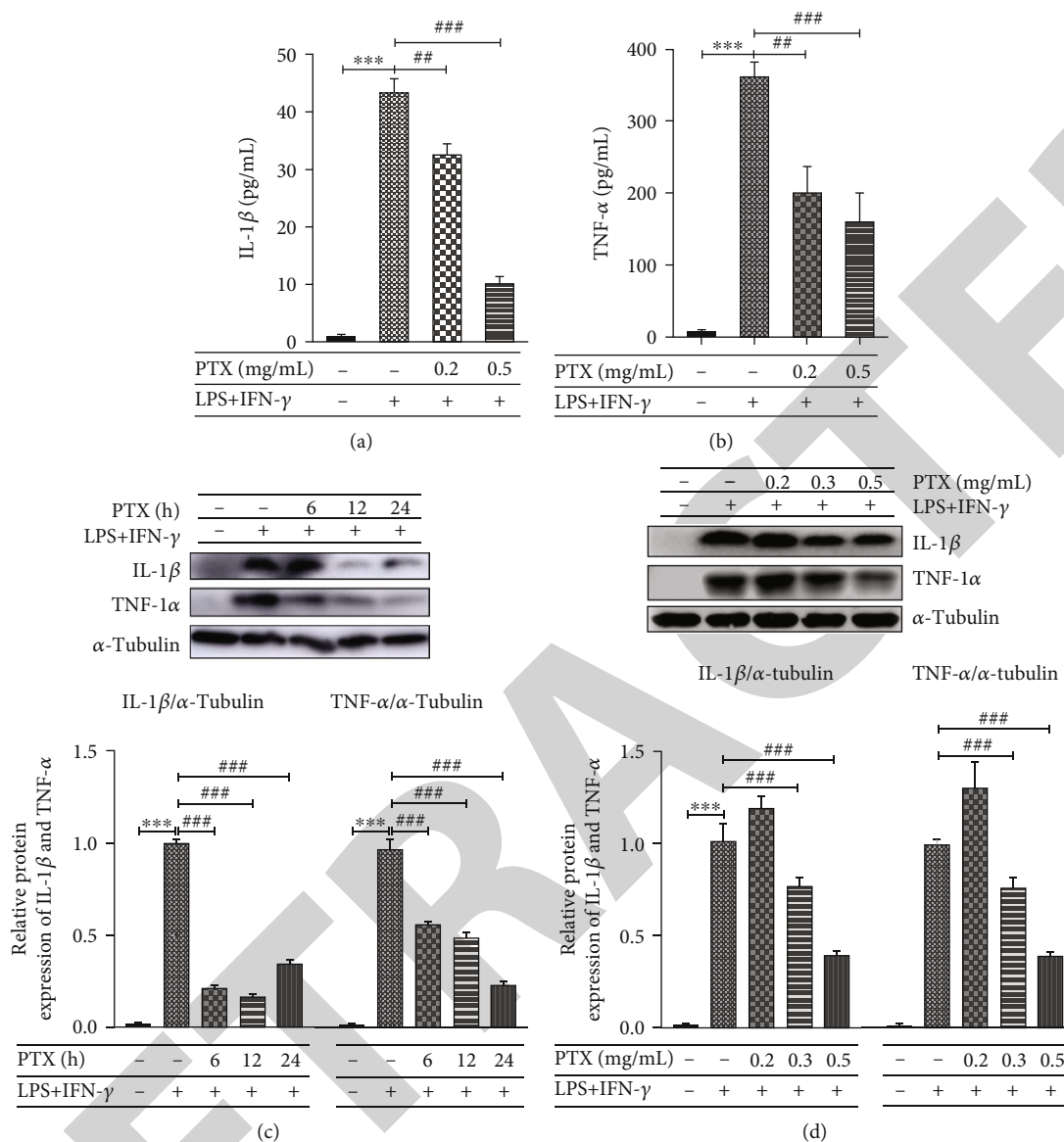


FIGURE 3: The content of IL-1 β and TNF- α in supernatants was examined with ELISA. RAW264.7 cells were firstly treated with 0.2 mg/mL PTX (a) and 0.5 mg/mL (b) for 12 h, respectively, and then treated with 100 ng/mL LPS and 20 ng/mL IFN- γ . After 24 h incubation, carefully remove the medium without disturbing the layer of cells and collect the supernatant for ELISA analysis (** $P < 0.001$; # $P < 0.01$; ### $P < 0.001$). (c) The influences of pretreatment of PTX on the expression of IL-1 β and TNF- α in RAW264.7 cells. The cells were firstly treated with 0.5 mg/mL of PTX for 6, 12, and 24 h, respectively. Then, cells were treated with 100 ng/mL LPS and 20 ng/mL IFN- γ for 24 h. After that, the cellular proteins were collected and examined by Western blotting. (d) The effects of PTX pretreatment concentration on protein expression of IL-1 β and TNF- α in RAW264.7 cells. The cells were pretreated with 0.2, 0.3, and 0.5 mg/mL PTX for 12 h, respectively, and then treated with 100 ng/mL LPS and 20 ng/mL IFN- γ for 24 h. After that, the cellular proteins were collected and detected by Western blotting. Both in (c) and (d) the α -tubulin was the internal control, and quantitative analyses of protein expressions are represented by a bar graph (** $P < 0.001$; ### $P < 0.001$).

of PTX of 0.5 mg/mL within the safe usage. The data indicated that 0.5 mg/mL PTX had significant inhibitory effect on LPS-mediated inflammation in RAW264.7 cells.

3.4. PTX Inhibited Autophagy in RAW264.7 Cells in a Dose- and Time-Dependent Manner. Autophagy, being a regulation process of the innate immune system, is thought to modulate inflammatory cytokine generation [14–16]. Whether PTX had influence on the regulation of macrophage autophagy or not was checked in our following experiments.

RAW264.7 cells were treated with 0.5 mg/mL PTX at 0, 6, 12, and 24 h. Autophagy-related protein (LC3, P62, and Beclin1) expressions were measured by Western blotting. Figure 3(a) showed that with the increase of the treatment time, the expression of LC3 increased. Similarly, the expression of SQSTM1/P62 also increased accordingly. However, the expression of the autophagy-related protein Beclin1 decreased (Figure 3(b)). With respect to the cells treated with PTX of 0, 0.2, 0.3, and 0.5 mg/mL for 12 hours, LC3 and SQSTM1/P62 expression increased with raised drug

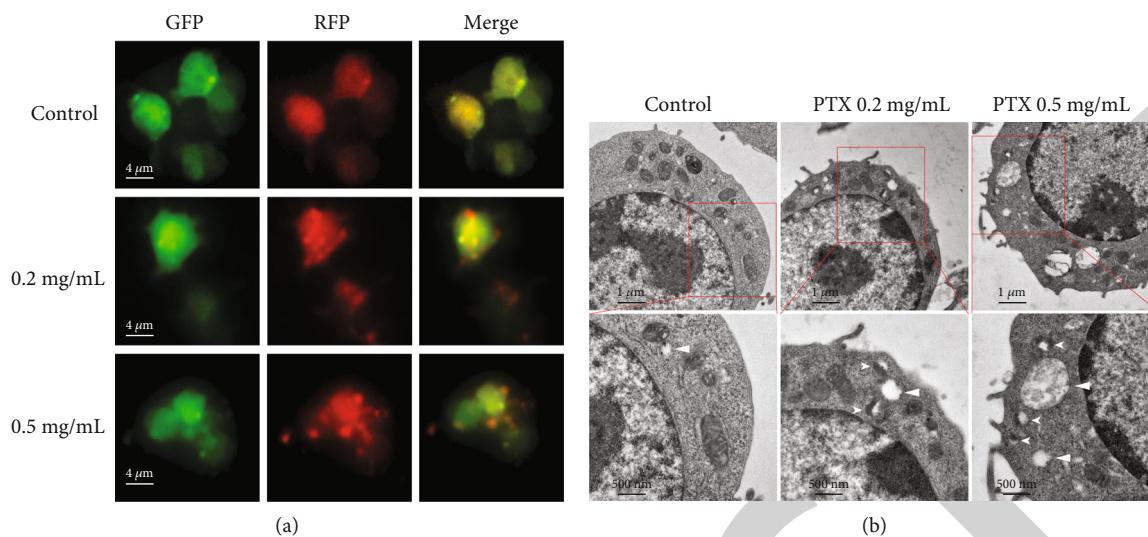


FIGURE 4: Morphological observation of autophagy after PTX stimulation. (a) Fluorescence microscope observation of autophagy bodies (yellow) and autophagy lysosomes (red) affected by PTX concentration in cells and the GFP-RFP-LC3-transfected RAW264.7 cells treated with different PTX (0, 0.2, and 0.5 mg/mL). (b) Electron microscopy of autophagic bodies. RAW264.7 cells treated with different PTX (0, 0.2, and 0.5 mg/mL) were visualized by transmission electron microscopy. In control roots, few vesicles are apparent within the vacuole as they are immediately degraded. The autophagic bodies (big arrows) and autophagic lysosomes (small arrows) could be clearly observed.

concentration (Figure 3(c)), while Beclin1 expression was significantly reduced (Figure 3(d)). Therefore, we make a hypothesis that it might be the effects of PTX on macrophages that blocked the autophagy flux of the cells and thus suppressed the autophagy of the cells.

The LC3 proteins functioned critically in autophagy, and the localization of these proteins to autophagosomes can be used as a general marker for the accumulation of autophagosomes during inhibition of autophagic flux. To facilitate the high-throughput screening of autophagy-related PTX on macrophage cells, the RFP-GFP-LC3 construct was transfected into RAW264.7 cells. Then, GFP-RFP-LC3-transfected macrophages were treated with PTX of different concentrations (0, 0.2, and 0.5 mg/mL), and the autophagy flux situation image verifying RFP-GFP-LC3 expression in living cells was obtained with a fluorescent microscope (Figure 4(a)). When the concentration of PTX drug increased, the number of intracellular autophagosomes (yellow) was increased, and accordingly, the number of corresponding autophagolysosomes (red) was increased. Furthermore, the size and number of autophagic bodies were observed by electron microscopy [41].

It was found that with the concentration of PTX increasing, the number of intracellular autophagosomes (large arrows) increased, and so did the number of autophagolysosomes (small arrows). The experimental results of autophagy-related protein expressions, immunofluorescence tracking, and electron microscopy examinations all confirmed that the autophagy of RAW264.7 cells was blocked by PTX, which supports the hypothesis that PTX might block the autophagy flux of macrophage cells and thus result in the autophagy of the cells suppressed.

3.5. PTX Ameliorated LPS-Induced Inflammation by Reducing Autophagy in RAW264.7 Cells. NLRP3 is a critical

component of the inflammasome process [42]. There has been an increasing research concern on the crosstalk between autophagy and inflammation [20]. NLRP3 is found in autophagosomes upon activating inflammasome. To explore the feature of autophagy in determining the anti-inflammatory sensitivity of RAW264.7 cell response to PTX agent, we first examined the activity of autophagy in RAW264.7 cells with treatment of autophagy inhibitors like 3-methyladenine (3-MA, 5 mM) or LY294002 (5 μM) with 0.5 mg/mL PTX and 100 ng/mL LPS. As shown in Figures 5(a) and 5(b), under the presence of 3-MA or LY294002, the stimulation with PTX obviously reduced IL-1β and TNF-α secretion to the supernatant of RAW264.7 cells in an intensity-dependent manner ($^{\#}P < 0.05$ or $^{\#\#}P < 0.001$ compared to LPS+IFN-γ-treated cells). These results indicate that PTX might play its anti-inflammation role through autophagy regulation to a certain extent. In addition, NLRP3 is a critical component of the inflammatory process. After the pretreatment of LPS-treated RAW264.7 cells with autophagy inhibitors (3-MA or LY294002) or null, we found that 0.5 mg/mL PTX could decrease the proinflammatory cytokine (TNF-α) level and reduce NLRP3 level through autophagy inhibition. In summary, the results above imply that PTX influence on autophagy inhibition of RAW264.7 cells would present crucially in suppressing IL-1β and TNF-α secretion. The effects on IL-1β and TNF-α secretion were due to differences in inflammasome activation. To confirm this finding, we next used autophagy inhibitors to block AMP-activated protein kinase (AMPK) signaling to investigate to correlation of autophagy regulation and suppression of inflammation by PTX in RAW264.7 cells.

3.6. AMPK Signaling Pathway Displays Crucially in Regulating Autophagy and PTX Anti-Inflammation. Adenosine 5'-monophosphate-activated protein kinase (AMPK),

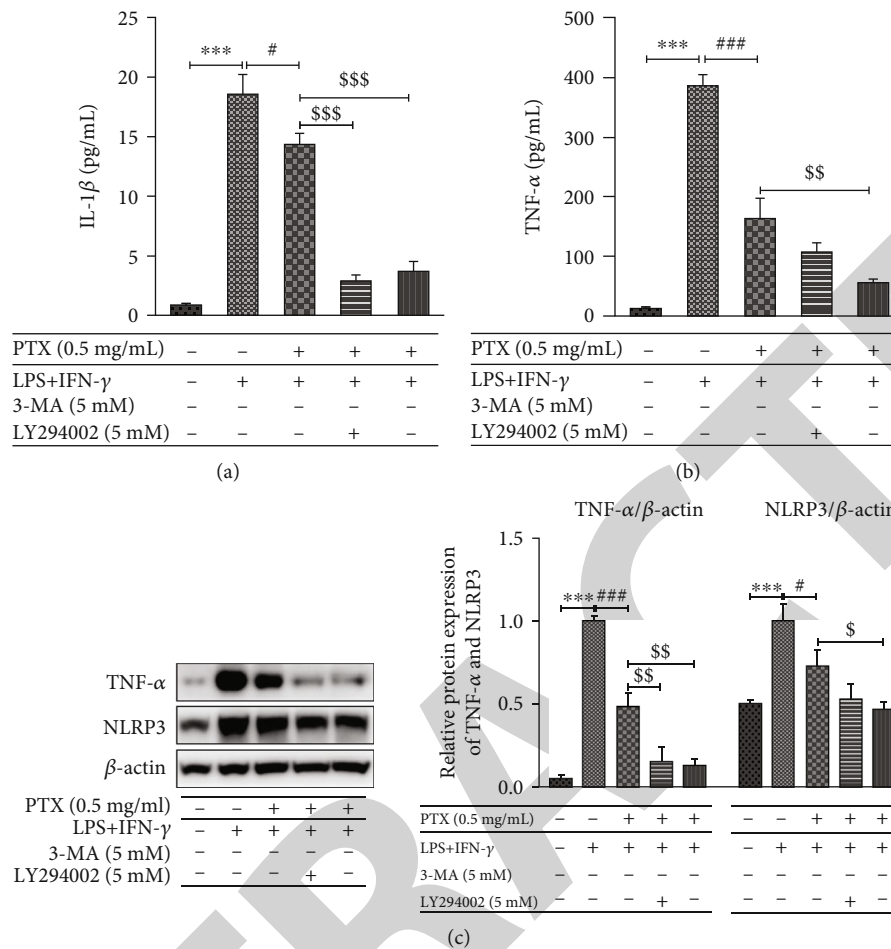


FIGURE 5: (a) IL-1 β and (b) TNF- α level in supernatants of RAW264.7 cells treated with PTX with or without autophagy inhibitor 3-MA/LY294002 was measured by ELISA. The cells were pretreated with 0.5 mg/mL PTX with or without autophagy inhibitor 3-MA and LY294002 for 12 h and then treated with 100 ng/mL LPS and 20 ng/mL IFN- γ for 12 h. Finally, the supernatants were collected for ELISA measurement (** $P < 0.001$; # $P < 0.05$, ### $P < 0.001$; \$\$ $P < 0.01$). (c) TNF- α and NLRP3 protein level in RAW264.7 cells cultured with or without the autophagy inhibitor 3-MA/LY294002 detected by Western blotting, and β -actin was the internal control. The cells were firstly treated with 0.5 mg/mL PTX for 12 h and then treated with 100 ng/mL LPS and 20 ng/mL IFN- γ for 12 h. The quantitative analysis of different protein expressions is shown by a bar graph (** $P < 0.01$, *** $P < 0.001$; # $P < 0.05$, ### $P < 0.001$; \$ $P < 0.05$, \$\$ $P < 0.01$).

a vital metabolic modulator of cellular and organismal process, impeded inflammation. Drug-induced activation of AMPK kinase could protect against inflammation [43, 44]. The cell autophagy can be coordinated by the AMPK signaling pathway [45]. To investigate the possible molecular mechanism of the relationship of PTX anti-inflammatory and autophagy, we explored the AMPK signaling pathway in autophagy and PTX anti-inflammatory in macrophages. The macrophage treated with PTX of 0.5 mg/mL was used as control. Figure 6(a) showed that p-AMPK expression in cells treated with LPS+IFN- γ was obviously increased. However, p-AMPK expression was dramatically inhibited in cells pretreated with PTX.

The results demonstrated that the AMPK signaling pathway of macrophages was suppressed by PTX. In accordance with the addition of the AMPK pathway activator A769662, the expression of autophagy-related proteins LC-3 and Beclin1 was also increased (Figures 6(b) and 6(c)), which demonstrated the effect of AMPK signaling pathway involved with autophagy induction. In addition, the expres-

sion of TNF- α and NLRP3 in PTX pretreatment cells was dramatically lower relative to that in the LPS+IFN- γ group (Figure 6(d)), while with the addition of the AMPK pathway promoter A769662, the expression of TNF- α and NLRP3 increased obviously, and the anti-inflammatory effect of PTX was suppressed. The data indicated that the inhibition of PTX anti-inflammatory effects was related with the activated AMPK signaling pathway. Therefore, the AMPK pathway perhaps displayed an important role in the mechanism of PTX inhibiting autophagy and anti-inflammatory effect.

4. Discussion

PTX, approved by FDA, was applied in anti-inflammatory therapy. PTX can suppress proinflammatory cytokine gene transcription, such as TNF- α , but increase anti-inflammatory expression, such as IL-10 [25, 37], and it also inhibits other cytokines' key roles in inflammation such as IL-1 β and IL-6 [31, 33]. However, it is still elusive whether

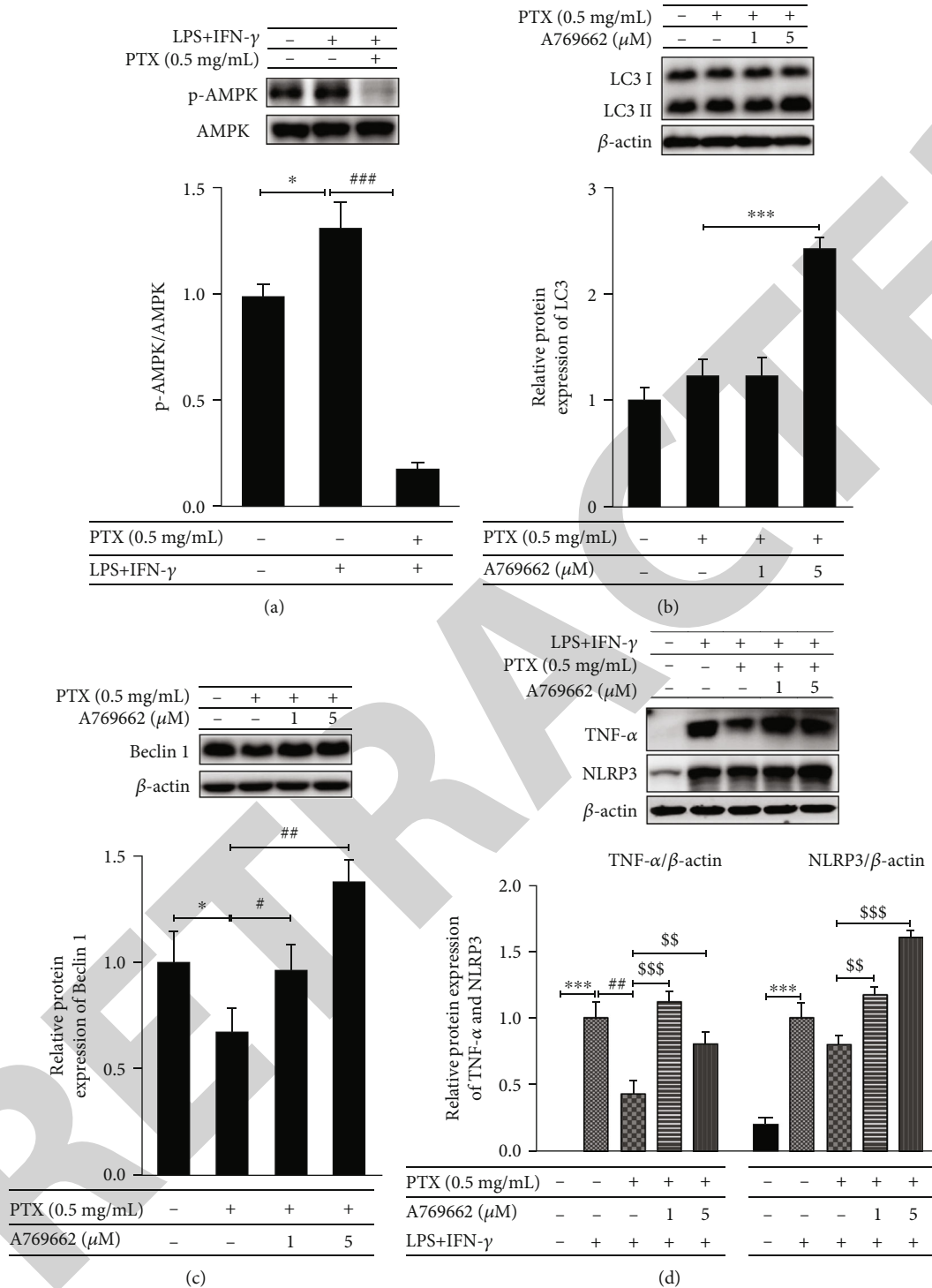


FIGURE 6: (a) AMPK and p-AMPK protein level in RAW264.7 cells detected by Western blotting. The cells were initially treated with 0.5 mg/mL PTX for 12 h and then treated with 100 ng/mL LPS and 20 ng/mL IFN- γ for 6 h (* P < 0.05; *** P < 0.001). (b, c) LC3 and Beclin 1 protein level in RAW264.7 cells cultured with or without the activator A-769662 of AMPK signaling pathways detected by Western blotting, and β -actin expression was the internal control. The cells were pretreated with PTX (0.5 mg/mL) for 12 h. The quantitative analysis of different protein expressions is shown by a bar graph (* P < 0.05, # P < 0.05, ## P < 0.01, *** P < 0.001). (d) TNF- α and NLRP3 protein level in RAW264.7 cells with or without activator A-769662 of AMPK signaling pathways was examined by Western blotting; and β -actin expression was the internal control. The cells were initially treated with 0.5 mg/mL PTX for 12 h and then treated with 100 ng/mL LPS and 20 ng/mL IFN- γ for 6 h. The quantitative analysis of different protein expressions is shown by a bar graph (*** P < 0.001; ## P < 0.01; # P < 0.05, *** P < 0.001).

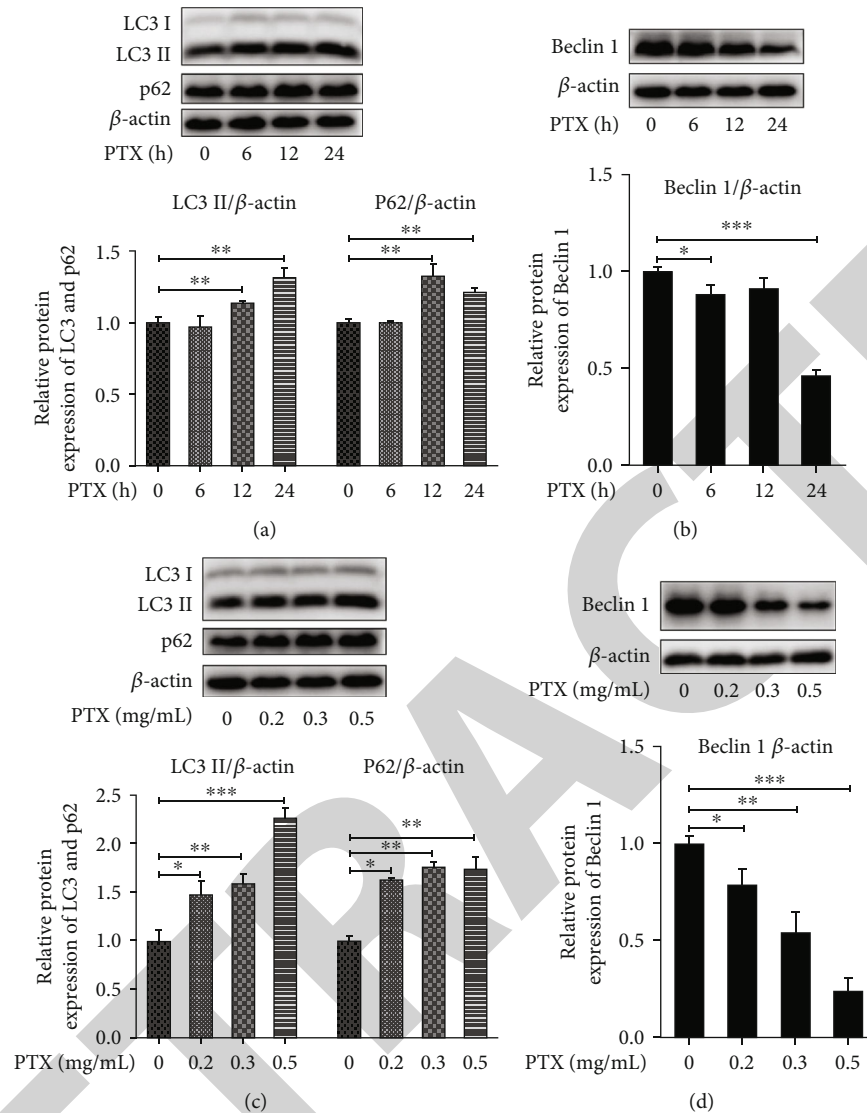


FIGURE 7: Western blotting analysis of the effects of PTX (0.5 mg/mL) treatment time (0, 6, 12, and 24 h) on protein expression of (a) LC3 and SQSTM1/p62 and (b) Beclin1 and the concentration (0.2, 0.3, and 0.5 mg/mL) influence of PTX treatment for 12 h on protein expression of (c) LC3 and SQSTM1/p62 and (d) Beclin1 in RAW264.7 cells. β -Actin was the internal control (* $P < 0.05$, ** $P < 0.01$, and *** $P < 0.001$ compared to control).

PTX modulated the inflammatory responses via activating autophagy, inhibiting inflammasome, and the signaling pathway in macrophages. Our study illustrates that PTX inhibited autophagy in a dose- and time-dependent manner, and PTX ameliorated LPS-caused inflammation by reducing autophagy in RAW264.7 macrophage cells, and the AMPK signaling played a crucial role in autophagy regulation and PTX suppressed inflammation.

Inflammation is produced in the body upon exposure to injury or pathological infection. The adaptive immune system, particularly DCs and T cells, functioned primarily and specifically to regulate the inflammatory response. Macrophages are major participants in innate immune responses. The proinflammatory factors, such as cytokines and chemokines, are generated during infections or stimulus of inflammation. IL-1 β and TNF- α are typical proinflammatory cytokines widely used in the study of inflammation-related

diseases. Therefore, IL-1 β and TNF- α were investigated to further confirm the success of LPS-primed inflammasomes activation in RAW264.7 macrophage cells (Figure 2). LPS-motivated IL-1 β maturation in RAW264.7 cells was dramatically upregulated by 50 and 100 ng/mL of PTX at 3, 6, and 24 h as shown in Figures 2(a) and 2(b). Meanwhile, TNF- α activated by LPS-primed inflammasome in macrophages was significantly upregulated which was consistent with both dose (50, 100 ng/mL) and time (3, 6, 12, and 24 h), shown in Figures 2(c) and 2(d).

As a nonspecific phosphodiesterase inhibitor, PTX would heighten intracellular cAMP and anti-inflammatory cytokine levels but reduce proinflammatory mediator production [22, 23]. In this study, our results indicated the maximum inhibited influences on IL-1 β and TNF- α expression when treated with 0.5 mg/mL of PTX for 12 h (Figure 3). Similarly, Kalaiselvan [46] reported triphala (0.1–0.3 mg/mL) largely curbed

inflammatory mediator production (e.g., $\text{TNF}\alpha$, $\text{IL-1}\beta$) in a dose-related manner [38].

Cells could decompose their assembly by autophagy, which is a fundamental eukaryotic homeostatic process. NLRP3 is a key sensor molecule in the inflammasome activity [42]. Recently, current advances suggested that the pathway and proteins of autophagy exhibited a pivotal role in immunity and inflammation [20]. Many studies have confirmed that the effects of autophagy on inflammation have a two-way effect. On the one hand, autophagy might confront the inflammatory response by removing inflammatory protein aggregates and downregulating proinflammatory cytokines of tissue damage; on the other hand, autophagy would activate the inflammasome to produce a lot of inflammatory factors, thus accelerating the inflammation process. After balancing positive and negative sides of immunity and inflammation, autophagy could be regarded as a protector for infection, autoimmunity, and inflammation [14–17]. Our findings indicated that autophagy regulation probably contributed to therapeutic interventions towards diseases with inflammation. However, PTX performs the anti-inflammatory responses through autophagy activation as well as signaling pathways of inflammasome inhibition are still not well-known. Considering autophagy-related protein (LC3, P62, and Beclin1) expression, immunofluorescence tracking, and electron microscopy examinations (Figures 7 and 4), we found out that the PTX inhibited autophagy of RAW264.7 cells in a manner of dose and time dependence. Furthermore, when autophagy inhibitors 3-MA and LY294002 were added to PTX-treated cell, the PTX alleviated LPS-induced inflammation by reducing the proinflammatory cytokine ($\text{TNF-}\alpha$, $\text{IL-1}\beta$) level. NLRP3 expression was greatly ablated (Figure 5). Therefore, PTX could block the autophagy flow of autophagic cells, and its inhibitory effect on LPS-mediated inflammation was significant in autophagy-inhibited cells.

The AMPK signaling pathway functioned importantly in energy homeostasis and metabolism [44]. Some previous studies have shown that AMPK signaling perhaps functioned importantly in activated inflammatory body modulation. For example, Kim et al. [40] showed that adiponectin hindered LPS-caused activated inflammasomes in macrophages via inducing autophagy and activating the AMPK signaling pathway. Similarly, our data suggested that AMPK signaling displayed an important role in the regulation of PTX-mediated autophagy and inflammation (Figure 6). It is interesting that our data indicated that PTX inhibited the AMPK signaling pathway in macrophages, and it would cause anti-inflammatory response by inhibiting this pathway to suppress autophagy flow. Since the AMPK pathway links energy sensing to the anti-inflammatory signaling pathway, when autophagy was being inhibited, the formation of autophagosomes should be reduced. Similarly, Xie et al. reported that MAPK/ERK signaling pathways participated in the regulation of BRF1-mediated inhibition of LPS-induced inflammatory factor level and the autophagy flux in macrophage [47].

In summary, pentoxifylline suppresses inflammation in LPS-caused RAW264.7 macrophage cells that are relying on proper treatment time and dose. The autophagy in cells

inhibited by PTX was found with dose and time dependence, and PTX alleviated LPS-induced inflammation which was caused by the downregulation of autophagy. Furthermore, AMPK signaling might display important function in autophagy inhibition during the process of PTX attenuating LPS-caused inflammation in RAW264.7 macrophage cells. New insight into the regulation basis of inflammation and autophagy will provide new perspective of anti-inflammatory drugs. Although the process of PTX inhibiting the AMPK signaling correlated with the number of autophagosomes followed by dose and time dependence in RAW264.7 cells, the phenomenon of AMPK inhibition and autophagosome increase might involve other pathways, which deserves further study in the future.

Data Availability

The data that support the findings of this study are available with approval from the author.

Conflicts of Interest

The authors have no conflicts of interest to declare.

Acknowledgments

This research was financially supported by the National Nature Science Foundation of China (Grant No. 31400859), Shanghai Natural Science Foundation (Grant No. 19ZR1429900), Shanghai Municipal Commission of Health and Family Planning Foundation (Grant No: 201840021), and Nature Science Foundation of Minhang District (Grant No. 2018MHZ030).

Supplementary Materials

PTX display an obvious inhibited influence on inflammatory factor expression caused by LPS-stimulated macrophages through autophagy suppression, in which the AMPK signaling pathway involved in the autophagy flux. (*Supplementary Materials*)

References

- [1] R. Medzhitov, "Origin and physiological roles of inflammation," *Nature*, vol. 454, no. 7203, pp. 428–435, 2008.
- [2] M. Karin, T. Lawrence, and V. Nizet, "Innate immunity gone awry: linking microbial infections to chronic inflammation and cancer," *Cell*, vol. 124, no. 4, pp. 823–835, 2006.
- [3] E. Dalmas, J. Tordjman, M. Guerre-Millo, and K. Clément, *Macrophages and inflammation. Adipose tissue biology: Second Edition*, Springer International Publishing, 2017.
- [4] D. G. DeNardo and B. Ruffell, "Macrophages as regulators of tumour immunity and immunotherapy," *Nature Reviews. Immunology*, vol. 19, no. 6, pp. 369–382, 2019.
- [5] J. Shalhoub, M. A. Falck-Hansen, A. H. Davies, and C. Monaco, "Innate immunity and monocyte-macrophage activation in atherosclerosis," *Journal of Inflammation*, vol. 8, no. 1, p. 9, 2011.

- [6] S. D. Merkley, C. J. Chock, X. O. Yang, J. Harris, and E. F. Castillo, "Modulating T cell responses via autophagy: the intrinsic influence controlling the function of both antigen-presenting cells and T cells," *Front Immunol NLM (Medline)*, vol. 9, p. 2914, 2018.
- [7] W. Strober, F. Zhang, A. Kitani, I. Fuss, and S. Fichtner-Feigl, "Pro-inflammatory cytokines underlying the inflammation of Crohn's disease," *Current Opinion in Gastroenterology*, vol. 26, no. 4, pp. 310–317, 2010.
- [8] J. M. Cavaillon, "Pro- versus anti-inflammatory cytokines: myth or reality," *Cellular and Molecular Biology*, vol. 47, no. 4, pp. 695–702, 2001.
- [9] N. Uceyler, R. Valenza, M. Stock, R. Schedel, G. Sprotte, and C. Sommer, "Reduced levels of anti-inflammatory cytokines in patients with chronic widespread pain," *Arthritis R*, vol. 54, no. 8, pp. 2656–2664, 2006.
- [10] S. M. Opal and V. A. DePalo, "Anti-inflammatory cytokines," *Chest*, vol. 117, no. 4, pp. 1162–1172, 2000.
- [11] A. Mantovani, R. Bonecchi, and M. Locati, "Tuning inflammation and immunity by chemokine sequestration: decoys and more," *Nature Reviews. Immunology*, vol. 6, no. 12, pp. 907–918, 2006.
- [12] C. Zhang, J. Feng, J. Du et al., "Macrophage-derived IL-1 α promotes sterile inflammation in a mouse model of acetaminophen hepatotoxicity," *Cellular & Molecular Immunology*, vol. 15, no. 11, pp. 973–982, 2018.
- [13] M. J. Chuang, K. H. Sun, S. J. Tang et al., "Tumor-derived tumor necrosis factor- α promotes progression and epithelial-mesenchymal transition in renal cell carcinoma cells," *Cancer Science*, vol. 99, no. 5, pp. 905–913, 2008.
- [14] B. Levine, N. Mizushima, and H. W. Virgin, "Autophagy in immunity and inflammation," *Nature*, vol. 469, no. 7330, pp. 323–335, 2011.
- [15] V. Deretic, T. Saitoh, and S. Akira, "Autophagy in infection, inflammation and immunity," *Nature Reviews. Immunology*, vol. 13, no. 10, pp. 722–737, 2013.
- [16] Y. Mo, Y. Y. Sun, and K. Y. Liu, "Autophagy and inflammation in ischemic stroke," *Neural Regeneration Research*, vol. 15, no. 8, pp. 1388–1396, 2020.
- [17] T. T. Wu, W. M. Li, and Y. M. Yao, "Interactions between autophagy and inhibitory cytokines," *International Journal of Biological Sciences*, vol. 12, no. 7, pp. 884–897, 2016.
- [18] T. Monkkonen and J. Debnath, "Inflammatory signaling cascades and autophagy in cancer," *Autophagy*, vol. 14, no. 2, pp. 190–198, 2018.
- [19] S. Haq, J. Grondin, S. Banskota, and W. I. Khan, "Autophagy: roles in intestinal mucosal homeostasis and inflammation," *Journal of Biomedical Science*, vol. 26, no. 1, p. 19, 2019.
- [20] K. Cadwell, "Crosstalk between autophagy and inflammatory signalling pathways: balancing defence and homeostasis," *Nature Reviews. Immunology*, vol. 16, no. 11, pp. 661–675, 2016.
- [21] P. Chen, M. Cescon, and P. Bonaldo, "Autophagy-mediated regulation of macrophages and its applications for cancer," *Autophagy*, vol. 10, no. 2, pp. 192–200, 2013.
- [22] J. L. Fernandes, R. T. de Oliveira, R. L. Mamoni et al., "Pentoxifylline reduces pro-inflammatory and increases anti-inflammatory activity in patients with coronary artery disease—a randomized placebo-controlled study," *Atherosclerosis*, vol. 196, no. 1, pp. 434–442, 2008.
- [23] K. Rieneck, M. Diamant, P. M. Haahr, M. Schönharting, and K. Bendtzen, "In vitro immunomodulatory effects of pentoxifylline," *Immunology Letters*, vol. 37, no. 2-3, pp. 131–138, 1993.
- [24] G. W. Sullivan, H. T. Carper, W. J. Jr Novick, and G. L. Mandell, "Inhibition of the inflammatory action of interleukin-1 and tumor necrosis factor (alpha) on neutrophil function by pentoxifylline," *Infection and Immunity*, vol. 56, no. 7, pp. 1722–1729, 1988.
- [25] A. M. van Furth, E. M. Verhard-Seijmonsbergen, R. van Furth, and J. A. M. Langermans, "Effect of lisofylline and pentoxifylline on the bacterial-stimulated production of TNF- α , IL-1 β and IL-10 by human leucocytes," *Immunology*, vol. 91, no. 2, pp. 193–196, 1997.
- [26] L. A. Green, C. Kim, S. K. Gupta, G. Rajashekhar, J. Rehman, and M. Clauss, "Pentoxifylline reduces tumor necrosis factor- α and HIV-induced vascular endothelial activation," *AIDS Research and Human Retroviruses*, vol. 28, no. 10, pp. 1207–1215, 2012.
- [27] H. V. Groesdonk, M. Heringlake, and H. Heinze, "Anti-inflammatory effects of pentoxifylline: importance in cardiac surgery," *Der Anaesthetist*, vol. 58, no. 11, pp. 1136–1143, 2009.
- [28] G. Hepgül, S. Tanrkulu, H. R. Ünalp et al., "Preventive effect of pentoxifylline on acute radiation damage via antioxidant and anti-inflammatory pathways," *Digestive Diseases and Sciences*, vol. 55, no. 3, pp. 617–625, 2010.
- [29] M. Goicoechea, S. G. de Vinuesa, B. Quiroga et al., "Effects of pentoxifylline on inflammatory parameters in chronic kidney disease patients: a randomized trial," *Journal of Nephrology*, vol. 25, no. 6, pp. 969–975, 2012.
- [30] S. K. Gupta, D. Mi, M. P. Dubé et al., "Pentoxifylline, inflammation, and endothelial function in HIV-infected persons: a randomized, placebo-controlled trial," *PLoS One*, vol. 8, no. 4, article e60852, 2013.
- [31] M. J. Myers, M. J. Baarsch, and M. P. Murtaugh, "Effects of pentoxifylline on inflammatory cytokine expression and acute pleuropneumonia in swine," *Immunobiology*, vol. 205, no. 1, pp. 17–34, 2002.
- [32] Y. Shirakami, T. Kochi, M. Kubota et al., "Inhibitory effects of pentoxifylline on inflammation-related tumorigenesis in rat colon," *Oncotarget*, vol. 9, no. 74, pp. 33972–33981, 2018.
- [33] E. Speer, D. Dowling, L. Ozog et al., "Pentoxifylline inhibits TLR- and inflammasome-mediated in vitro inflammatory cytokine production in human blood with greater efficacy and potency in newborns," *Pediatric Research*, vol. 81, no. 5, pp. 806–816, 2017.
- [34] S. K. Muchhala and K. E. Benzeroual, "Pentoxifylline suppressed LPS-induced inflammatory and apoptotic signaling in neuronal cells," *Advances in Bioscience and Biotechnology*, vol. 3, no. 6, pp. 731–739, 2012.
- [35] K. Sharma, M. Ishaq, G. Sharma, M. A. Khan, and S. Majumdar, "Pentoxifylline triggers autophagy via ER stress response that interferes with pentoxifylline induced apoptosis in human melanoma cells," *Biochemical Pharmacology*, vol. 103, pp. 17–28, 2016.
- [36] P. C. Lopes, "LPS and neuroinflammation: a matter of timing," *Inflammopharmacology*, vol. 24, no. 5, pp. 291–293, 2016.
- [37] N. Kopitar-Jerala, "The role of interferons in inflammation and inflammasome activation," *Frontiers in Immunology*, vol. 8, p. 873, 2017.

Research Article

Bcl-2 Is Involved in Cardiac Hypertrophy through PI3K-Akt Pathway

Xianwei Meng ¹, Jun Cui ², and Guibin He ¹

¹Department of Cardiovascular Medicine, Luodian Hospital of District, No. 88 Yongshun Road, Shanghai 201908, China

²Shanghai Luodian Town Community Health Service Center, No. 355 Dongtai Road, Shanghai 201908, China

Correspondence should be addressed to Guibin He; 15316758813@163.com

Received 17 December 2020; Revised 22 January 2021; Accepted 18 February 2021; Published 12 March 2021

Academic Editor: Tao Huang

Copyright © 2021 Xianwei Meng et al. This is an open access article distributed under the Creative Commons Attribution License, which permits unrestricted use, distribution, and reproduction in any medium, provided the original work is properly cited.

Cardiac hypertrophy (CH) is a common cause of sudden cardiac death and heart failure, resulting in a significant medical burden. The present study is aimed at exploring potential CH-related pathways and the key downstream effectors. The gene expression profile of GSE129090 was obtained from the Gene Expression Omnibus database (GEO), and 1325 differentially expressed genes (DEGs) were identified, including 785 upregulated genes and 540 downregulated genes. Kyoto Encyclopedia of Genes and Genomes (KEGG) and Reactome pathway enrichment analysis of DEGs were then performed. Although there were no pathways enriched by downregulated genes, many CH-related pathways were identified by upregulated genes, including PI3K-Akt signaling pathway, extracellular matrix- (ECM-) receptor interaction, regulation of actin cytoskeleton, and hypertrophic cardiomyopathy (HCM). In the deeper analysis of PI3K-Akt signaling pathway, we found all the signaling transduction pointed to B cell lymphoma-2- (Bcl-2-) mediated cell survival. We then demonstrated that PI3K-Akt signaling pathway was indeed activated in cardiac hypertrophy. Furthermore, no matter LY294002, an inhibitor of the PI3K/AKT signaling pathway, or Venetoclax, a selective Bcl-2 inhibitor, protected against cardiac hypertrophy. In conclusion, these data indicate that Bcl-2 is involved in cardiac hypertrophy as a key downstream effector of PI3K-Akt signaling pathway, suggesting a potential therapeutic target for the clinical management of cardiac hypertrophy.

1. Introduction

Cardiac hypertrophy (CH) is the heart's response to stressful situations that impose increased biomechanical stress by increasing muscle mass. This physiological process contributes to reducing the ventricular wall stress, when the heart undergoes a greater than normal workload. Although hypertrophy of the myocardium is a biological response of stress by augmenting cardiac output, prolonged hypertrophy can lead to ventricular arrhythmias, heart failure, and subsequent cardiovascular mortality [1–3]. As reported previously, many signaling transduction pathways were illustrated to contribute to the development of cardiac hypertrophy [4, 5]. Among the CH-related pathways, PI3K-Akt signaling pathway, which is activated by many types of cellular stimuli or toxic insults to regulate fundamental cellular processes including protein synthesis, proliferation, and survival, was well established [6]. It is demonstrated that sustained activated PI3K in

the heart aggravates cardiac hypertrophy and myocardial dysfunction; once PI3K is completely blocked, the hearts lose the hypertrophic response to physiological stimuli [7]. The PI3K-promoting hypertrophic response needs the involvement of PI3K downstream AKT [8], GSK3 β [9], mTOR [10], P70S6K, and eIF-4E [11], which are involved in the regulation of fundamental cellular processes, including metabolism, glucose uptake, proliferation, and protein synthesis. Furthermore, we found that all the fundamental cellular processes were assigned towards a single goal of cell survival. However, the central downstream effector of the PI3K-Akt signaling pathway, which regulates cell survival, remains incompletely defined.

Bcl-2 is a founding member of the BCL-2 apoptosis regulatory protein family, which can induce (proapoptotic) or inhibit (antiapoptotic) apoptosis [12]. Bcl-2 is overexpressed in more than half of human cancers [13]. As an important oncogene, Bcl-2 can inhibit cell apoptosis by inhibiting the

activation of apoptosis proteins (such as BAX and BAK), thereby promoting the survival of cancer cells [14]. The expression of Bcl-2 in human breast cancer is associated with a good prognosis, and ongoing studies have shown that destroying Bcl-2 can cause cell death [15]. Bcl-2 and related cytoplasmic proteins are key regulators of apoptosis, and the cell suicide program is essential for the development, tissue homeostasis, and protection of pathogens. Previous reports indicate that whether cells should survive or die depends largely on the Bcl-2 family of antiapoptotic and apoptosis regulators [16]. Bcl-2 has a cell cycle inhibitory function, which can be separated from improving cell survival [17].

In this study, we reanalyzed the gene expression profile of GSE129090 to explore the molecular mechanism of cardiac hypertrophy. KEGG enrichment analysis showed that the upregulated DEGs were enriched in PI3K-Akt signaling pathway and the central downstream effector was Bcl-2, which functioned in cell survival. To verify the results above, the validation experiments were performed. It was demonstrated that the cross-sectional area in the TAC group was significantly higher than that in the Sham group, accompanying the activation of PI3K-Akt signaling pathway, resulting from the level of phosphorylated PI3K, AKT, GSK3 β , mTOR, P70S6K, and eIF-4E. Once the phosphorylation of PI3K or Bcl-2 was blocking by their selective inhibitors, the development of CH was retarded. In conclusion, these data indicate that Bcl-2 is involved in cardiac hypertrophy as a central downstream effector of PI3K-Akt signaling pathway, suggesting a potential therapeutic target for the clinical management of cardiac hypertrophy.

2. Methods and Materials

2.1. Data Collection. The gene expression profile of GSE129090 was obtained from the Gene Expression Omnibus (GEO) database (<http://www.ncbi.nlm.nih.gov/geo/>) based on the platform of Illumina MouseRef-8 v2.0 expression beadchip. A total of 6 samples were available, including 3 hypertrophic cardiomyocytes (hypertrophy induced by trans-aortic constriction (TAC)) samples and 3 normal adult cardiomyocyte (ACM) samples.

2.2. Identification for DEGs. For the analysis of DEGs, the expression data were first normalized using the normalize-BetweenArray function from R package “Limma” [18]. Then, the normalized data were used to analyze DEGs using the Limma software package in the R software (<http://www.bioconductor.org/packages/release/bioc/html/limma.html>) [19]. The cut-off value was set as P value <0.05 and $\log_2(|\text{fold change (FC)}|) > 1$ for DEG analysis [20].

2.3. Pathway Analysis of DEGs. The Kyoto Encyclopedia of Genes and Genomes (KEGG: <http://www.genome.ad.jp/KEGG>) and Reactome (<https://reactome.org/>) pathway enrichment analysis were performed to investigate the signaling pathways that were related to the unique DEGs.

2.4. Animals and Transverse Aortic Constriction (TAC) Model. Male C57BL/6J mice aged 10 weeks were purchased from Shanghai SLAC Laboratory Animal CO, LTD (China).

The experimental procedures were approved by the Institutional Animal Ethical Committee of Luodian hospital of Baoshan District. The experiments were proceeded according to NIH guidelines for Care and Use of Laboratory Animals (NIH, 8th Edition, 2011). The mice were maintained in individually ventilated cages (at 22°C, 12 h light/dark cycle) with free access to standard laboratory chow. 40 rats were randomly divided into 4 groups (10 for each group), which were, namely, Sham group, TAC group, TAC+LY294002 group, and TAC+Venetoclax group.

TAC operation was performed as a previous report [21]. Briefly, for the TAC group, after carotid arteries explosion and 60%-75% diameter of ligation, mice were administrated with normal saline (NS, 1 ml/day) for 8 weeks; for the TAC+LY294002 group, mice were treated with LY294002 (20 mg/kg/day, Sigma, USA) for 8 weeks by intraperitoneal injections; for the TAC+ Venetoclax group, mice were treated with Venetoclax (100 mg/kg/day, Selleckchem) for 8 weeks by oral gavage.

After administration of TAC operation, mice were maintained for another 8 weeks. Subsequently, the hearts were collected and fixed with 10% neutral formalin and preserved in -80°C for further research.

2.5. Western Blotting Analysis. Standard western blot analysis was performed as described in the literature [22]. The primary antibodies used in this study were anti-AKT (ab32505, Abcam), anti-phospho-AKT (ab81283, Abcam), anti-GSK3 β (ab32391, Abcam), anti-phospho-GSK3 β (ab131097, Abcam), anti-mTOR (ab2732, Abcam), anti-phospho-mTOR (ab84400, Abcam), anti-eIF-4E (ab32024, Abcam), anti-phosphoeIF-4E (ab76256, Abcam), anti-PI3K (#4257, CST), anti-phospho-PI3K (#4228, CST), anti-P70S6K (#2708, CST), anti-phospho-P70S6K (#9208, CST), and anti-Actin (ab8227, Abcam).

2.6. Quantitative Real-Time PCR. Total RNA was isolated from heart tissues using TRIzol Reagent (Invitrogen), and the qRT-PCR experiments were performed according to the literature [22] using SYBR Green (Roche). The expression levels of atrial natriuretic peptide (ANP), brain natriuretic peptide (BNP), and β -myosin heavy chain (β -MHC) were used as markers of cardiac hypertrophy [23]. GAPDH was used as control, and the $2^{-\Delta\Delta C_t}$ method was used to measure the relative gene expressions. All the primers used in this study were obtained from Sangon (Shanghai, China). The real-time PCR primers were as follows:

ANP-forward: 5'-ACCTGCTAGACCACCTGGAG-3', ANP-reverse: 5'-CCTTGGCTGTTATCTTCGGTACCGG-3'; BNP-forward: 5'-GAGGTCACCTCTATCCTCTGG-3', BNP-reverse: 5'-GCCATTTCCCTCCGACTTTTCTC-3'; β -MHC-forward: 5'-CCGAGTCCCAGGTCAACAA-3', β -MHC-reverse: 5'-CTTACGGGCACCCTTGA-3'; GAPDH-forward: 5'-TTGCTTCAGGGTTTCATCCAG-3', GAPDH-reverse: 5'-GACACTCGCTCAGCTTCTTG-3'.

2.7. Histological Analysis. 8 weeks after TAC or sham surgery, the animals were sacrificed, and the hearts were arrested with

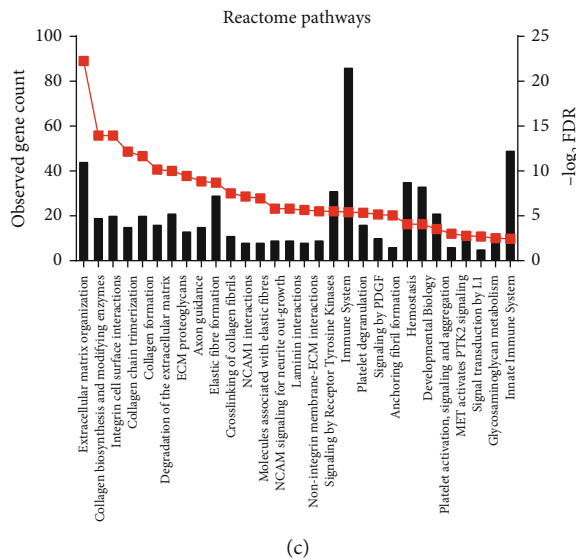
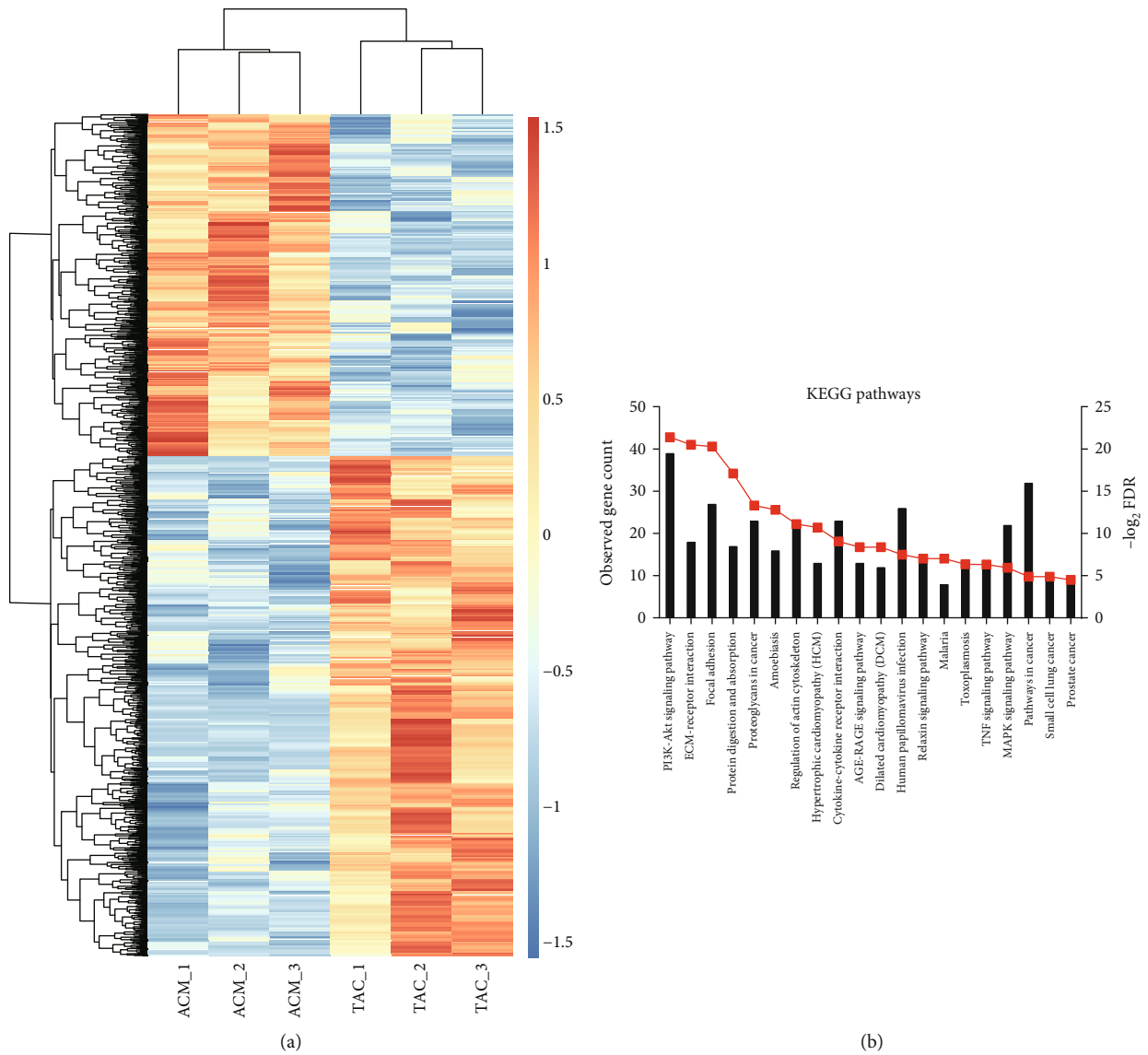


FIGURE 1: Selection of DEGs and function annotation: (a) heat map of DEGs (785 upregulated and 540 downregulated genes); (b) KEGG pathway analysis of upregulated DEGs; (c) Reactome pathway analysis of upregulated DEGs.

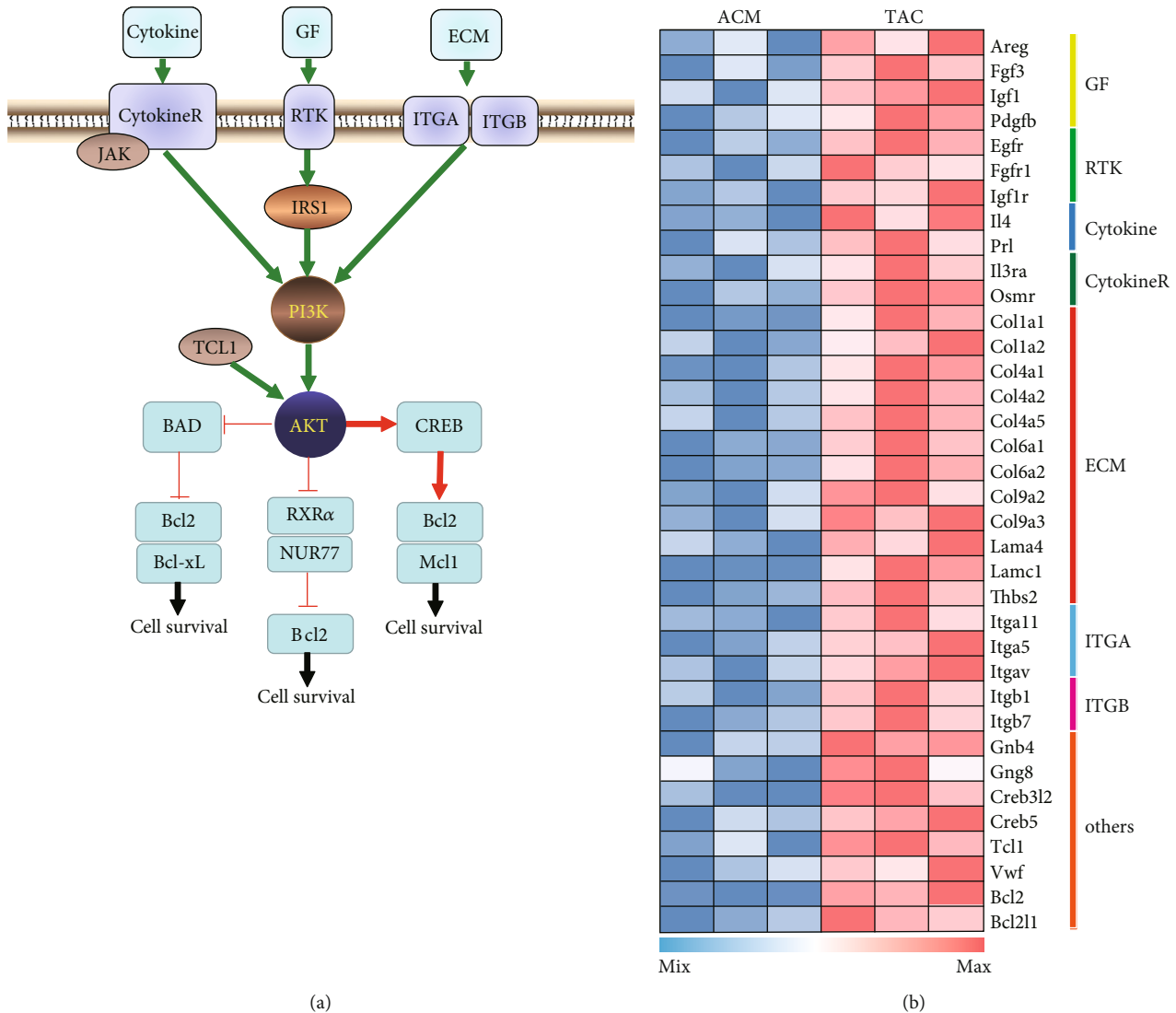


FIGURE 2: PI3K-Akt signaling pathway in CH: (a) PI3K-Akt signaling pathway in CH manually curated based on KEGG; (b) heat map of DEGs in PI3K-Akt signaling pathway. GF: growth factors; RTK: receptor tyrosine kinase; ECM: extracellular matrix; ITGA: integrin subunit alpha; ITGB: integrin subunit beta; CytokineR: cytokine receptor.

a 10% potassium chloride solution at end-diastole and then fixed in 10% formalin. The paraffin-embedded hearts were cut transversely into 4-5 μm sections. Heart sections were stained with HE, and the cell size was measured using a quantitative digital image analysis system (ImageJ, 1.52a).

2.8. Statistical Analysis. All experiments were performed in three independent parallel experiments, and the results were shown as mean \pm standard deviation (SD). Differences between groups were estimated using unpaired Student's *t*-test. A two-tailed value of *P* value <0.05 was considered statistically significant.

3. Results

3.1. Identification of DEGs and Enrichment Pathway Analyses. The study included 3 TAC samples and 3 ACM

samples. A total of 1325 DEGs were identified after the analysis of GSE129090 by Limma package in R language. Of these, 785 were upregulated, and 540 were downregulated in TAC samples compared with ACM samples. A heat map of DEGs was shown in Figure 1(a).

For a deeper insight into the DEGs, we performed KEGG and Reactome pathway enrichment analyses. Upregulated DEGs were mainly enriched in CH-related pathways (Figure 1(b) and 1(c)), such as PI3K-Akt signaling pathway, ECM-receptor interaction, regulation of actin cytoskeleton, hypertrophic cardiomyopathy (HCM), and cytokine-cytokine receptor interactions. However, the downregulated DEGs were not significantly enriched in any pathway.

3.2. PI3K-Akt Signaling Pathway in CH Development. Given that the upregulated DEGs were most significantly enriched in PI3K-Akt signaling pathway, we selected the 36-related

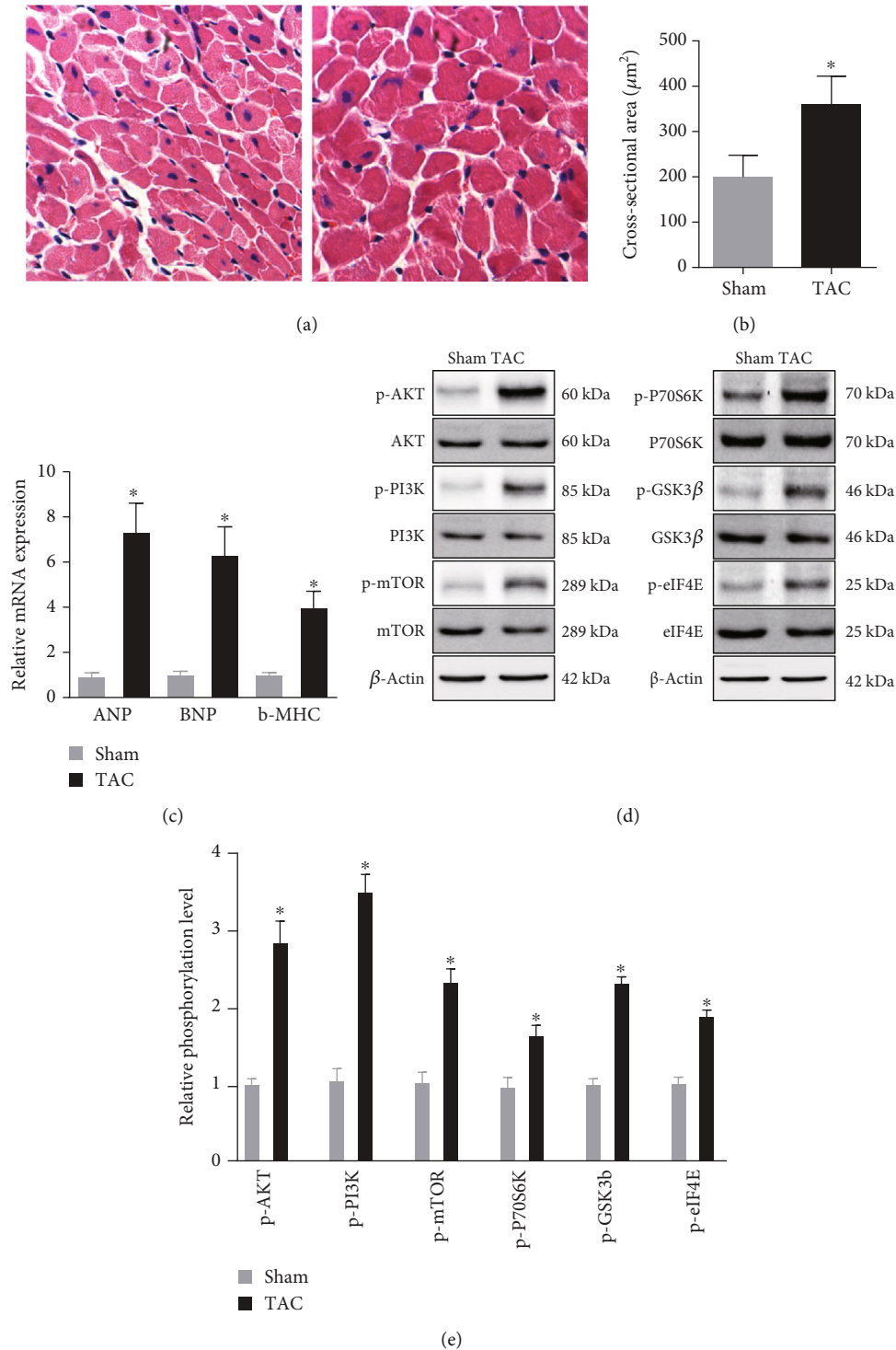


FIGURE 3: PI3K-Akt signaling pathway was involved in the response to hypertrophic stimuli: (a) histological analyses of the hematoxylin and eosin (H&E) staining of each group of mice at 8 weeks after TAC or sham surgery ($n = 10$); (b) statistical results for the cardiomyocyte cross-sectional area (CSA, $n = 50$ cells); (c) real-time PCR analysis of the hypertrophy markers atrial natriuretic peptide (ANP), brain natriuretic peptide (BNP), and β -myosin heavy chain (β -MHC); (d) the levels of total and phosphorylated AKT, GSK3 β , mTOR, PI3K, P70S6K, and eIF-4E expression in heart tissues of mice in the indicated groups; (e) quantitative results of (d) ($n = 10$). * $P < 0.05$ versus Sham group.

genes for further study (Figure 2(a)). Among the 36 selected genes, 28 genes were involved in ligand-receptor interaction, 18 of which were ECM-ITGA/B interaction (Figure 2(b)),

showing that the development of CH was mainly promoted by the microenvironment. More importantly, we found that all the signaling transduction pointed to Bcl-2-mediated cell

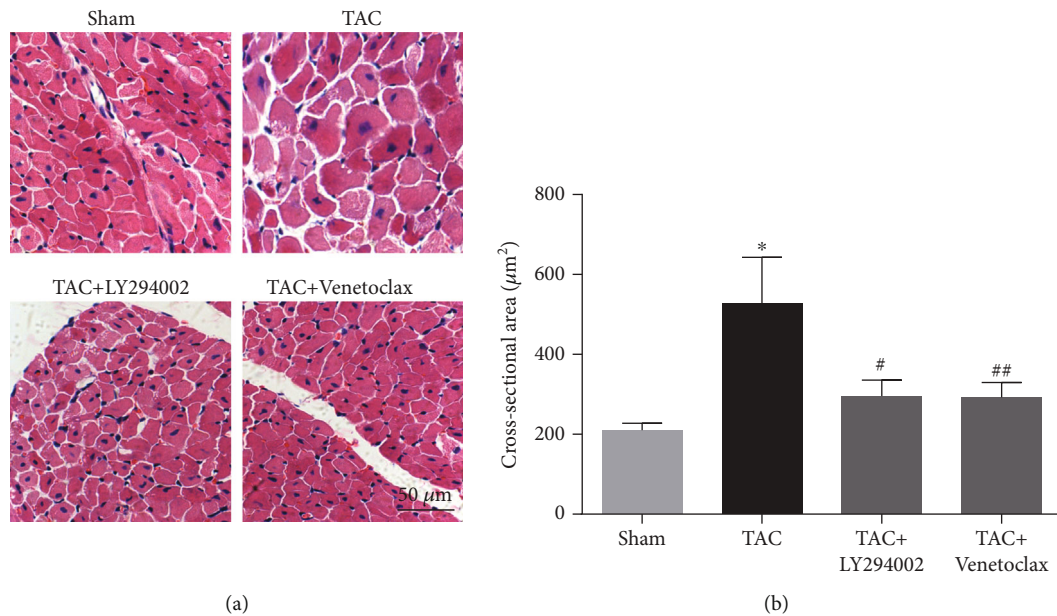


FIGURE 4: LY294002 and Venetoclax protected against cardiac hypertrophy: (a) histological analyses of the hematoxylin and eosin (H&E) staining; (b) statistical results for the cardiomyocyte cross-sectional area (CSA, $n = 50$ cells). * $P < 0.05$ versus Sham group. # $P < 0.05$ versus TAC group.

survival. These results prompted us to hypothesize that PI3K-Akt signaling pathway-induced Bcl-2-mediated cell survival was involved in the development of CH.

3.3. PI3K-Akt Signaling Pathway Was Involved in the Response to Hypertrophic Stimuli. Given that PI3K-Akt signaling pathway was involved in the development of cardiac hypertrophy, we first examined whether PI3K-Akt signaling pathway was activated in cardiac hypertrophy tissues. As shown in Figures 3(a)–3(c), we successfully constructed the TAC mice model. The cross-sectional area (CSA) was significantly higher in the TAC group than that in the Sham group, and the expression of ANP, BNP, and β -MHC was increased in the TAC group. As expected, it was observed that PI3K, AKT, GSK3 β , mTOR, P70S6K, and eIF-4E were significantly phosphorylated in the TAC group, suggesting that PI3K-Akt signaling pathway was indeed activated in cardiac hypertrophy (Figures 3(d) and 3(e)).

3.4. LY294002 And Venetoclax Protected against Cardiac Hypertrophy. To further examine whether PI3K-Akt signaling pathway had a causative role in the development of cardiac hypertrophy and Bcl-2 was the central downstream effector, additional *in vivo* experiments were performed. We treated the TAC mice with LY294002 (a PI3K inhibitor that prevents PI3K phosphorylation) or Venetoclax (a selective Bcl-2 inhibitor) as described in Methods and Materials. We found that no matter LY294002 or Venetoclax protected against TAC-induced cardiac hypertrophy (Figure 4(a)). The cross-sectional area was decreased in the treatment group. The results determined that PI3K-Akt signaling pathway played a critical role in TAC-induced CH, and Bcl-2-mediated cell survival was the key cause of the cardiovascular lesions.

4. Discussion

Cardiac hypertrophy is one of the most common causes of heart failure, which is increasing in prevalence and is a debilitating disease with high rates of mortality and morbidity worldwide [24]. Although many studies have reported that long-term cardiac hypertrophy increases the likelihood of heart failure, treatment of cardiac hypertrophy has not been well defined, due to the obscure molecular mechanism [25]. Recently, multiple CH-related signaling pathways have been identified in many individual studies, such as the PI3K-Akt, calcineurin/NFAT, and MAPK pathway [26]. Originally, it was thought that the pharmacological agents that selectively modulate the CH-related pathways could inhibit the development of pathological cardiac hypertrophy, but up to now, no effective drugs targeting cardiac hypertrophy have been found [27]. The reason is clear that it is impossible to inhibit all the pathways relating to cardiac hypertrophy. So, finding the central downstream effectors of the CH-related pathways has attracted our attention. In this study, we reanalyzed the gene expression profile of GEO129090, including 3 TAC mice samples and 3 ACM mice samples. 1325 DEGs were identified using R, including 785 upregulated genes and 540 downregulated genes. KEGG and Reactome pathway enrichment analysis of DEGs were then performed. Although there were no pathways identified by downregulated genes, many CH-related pathways were identified by upregulated genes, including PI3K-Akt signaling pathway, ECM-receptor interaction, regulation of actin cytoskeleton, and hypertrophic cardiomyopathy (HCM). The genes involved in the ECM-receptor interaction signaling pathway found in ductal breast carcinoma could be used as effective independent prognostic biomarkers for ductal breast carcinoma. The reorganization of the actin cytoskeleton was a key mechanical driving force

for cancer cells to acquire invasive properties. Related genes regulated cell shape by affecting the actin cytoskeleton and were important regulators of migration and proliferation. HCM is the most common genetic heart disease in humans and causes significant morbidity and mortality [28].

In the deeper analysis of PI3K-Akt signaling pathway, we found all the signaling transduction pointed to Bcl-2-mediated cell survival. These results showed that a microenvironment-promoted, PI3K-Akt signaling pathway-activated, and Bcl-2-mediated cell survival may be the key cause of cardiac hypertrophy. To verify the results from the bioinformatical analysis, we then examined the PI3K-Akt signaling pathway in TAC-induced cardiac hypertrophy samples. As reported previously, it was observed that PI3K, AKT, GSK3 β , mTOR, P70S6K, and eIF-4E were significantly phosphorylated in TAC mice, suggesting that PI3K-Akt signaling pathway was indeed activated in cardiac hypertrophy.

Cardiac hypertrophy is the adaptive response of the heart muscle to pressure or volume overload [29]. PI3K is a highly conserved lipid kinase involved in physiological cardiac hypertrophy (PHH) [30]. The AKT pathway is an important intracellular signaling pathway in eukaryotic cells, especially a regulator of cardiac hypertrophy [31]. There is increasing evidence proving that autophagy is involved in the regulation of cardiac hypertrophy [32]. Studies have shown that related genes can inhibit cardiac hypertrophy caused by pressure overload by inhibiting the AKT/mTOR pathway to promote autophagy [33]. The role of PI3K/Akt/mTOR pathway in cardiac hypertrophy has been fully demonstrated. Dioscin improves cardiac hypertrophy by inhibiting the Akt/GSK3 β /mTOR pathway [34]. Studies have shown that Apelin-13 promotes cardiomyocyte hypertrophy through PI3K-Akt-ERK1/2-p70S6K and PI3K-induced autophagy [35]. Phosphorylation of eIF-4E is a mechanism by which increased heart load is related to the accelerated rate of protein synthesis [36]. As we know, all the examined proteins, PI3K, AKT, GSK3 β , mTOR, p70S6K, and eIF-4E, are regulators but not effectors. So, we hypothesized that the downstream protein of PI3K-Akt signaling pathway, Bcl-2, was the effector. In our study of TAC mice treated with inhibitors in vivo, we found that no matter LY294002, an inhibitor of the PI3K/AKT signaling pathway, or Venetoclax, a selective Bcl-2 inhibitor, protected against cardiac hypertrophy. These results suggested that PI3K-AKT signaling pathway was involved in cardiac hypertrophy by regulating Bcl-2-mediated cell survival.

In conclusion, the present study evidences that Bcl-2 works as the central downstream effector of PI3K-Akt signaling pathway to keep cardiomyocyte survival, resulting in cardiac hypertrophy. It is indicated that Bcl-2 is of great possibility to be a therapeutic target for the clinical management of cardiac hypertrophy. This study provides novel and useful information for the potential functions of Bcl-2 and at the same time provides a new direction for the study of the mechanism of CH.

Data Availability

The gene expression profile data supporting this article is from previously reported studies and datasets, which have

been cited. The processed data are available from the corresponding author upon request.

Ethical Approval

Ethical approval is not applicable.

Consent

Consent is not applicable. This manuscript does not contain data from any person.

Conflicts of Interest

The authors have declared that no conflict of interest exists.

Authors' Contributions

GH conceived and designed the research. XM and JC performed experiments. XM and GH analyzed data. GH approved the final version of manuscript.

Acknowledgments

This work was supported by a grant from the Luodian hospital of Baoshan District (No. 18-A-2).

References

- [1] C. J. Oldfield, T. A. Duhamel, and N. S. Dhalla, "Mechanisms for the transition from physiological to pathological cardiac hypertrophy," *Canadian Journal of Physiology and Pharmacology*, vol. 98, no. 2, pp. 74–84, 2019.
- [2] J. Tamargo and J. Lopez-Sendon, "Novel therapeutic targets for the treatment of heart failure," *Nature Reviews. Drug Discovery*, vol. 10, no. 7, pp. 536–555, 2011.
- [3] N. Koitabashi and D. A. Kass, "Reverse remodeling in heart failure—mechanisms and therapeutic opportunities," *Nature Reviews. Cardiology*, vol. 9, no. 3, pp. 147–157, 2011.
- [4] J. Heineke and J. D. Molkentin, "Regulation of cardiac hypertrophy by intracellular signalling pathways," *Nature Reviews. Molecular Cell Biology*, vol. 7, no. 8, pp. 589–600, 2006.
- [5] B. H. Lorell and B. A. Carabello, "Left ventricular hypertrophy: pathogenesis, detection, and prognosis," *Circulation*, vol. 102, no. 4, pp. 470–479, 2000.
- [6] P. Guan, Z. M. Sun, N. Wang et al., "Resveratrol prevents chronic intermittent hypoxia-induced cardiac hypertrophy by targeting the PI3K/AKT/mTOR pathway," *Life Sciences*, vol. 233, p. 116748, 2019.
- [7] T. Aoyagi and T. Matsui, "Phosphoinositide-3 kinase signaling in cardiac hypertrophy and heart failure," *Current Pharmaceutical Design*, vol. 17, no. 18, pp. 1818–1824, 2011.
- [8] B. DeBosch, N. Sambandam, C. Weinheimer, M. Courtois, and A. J. Muslin, "Akt2 regulates cardiac metabolism and cardiomyocyte survival," *The Journal of Biological Chemistry*, vol. 281, no. 43, pp. 32841–32851, 2006.
- [9] P. H. Sugden, S. J. Fuller, S. C. Weiss, and A. Clerk, "Glycogen synthase kinase 3 (GSK3) in the heart: a point of integration in hypertrophic signalling and a therapeutic target? A critical analysis," *British Journal of Pharmacology*, vol. 153, no. S1, pp. S137–S153, 2008.

- [10] C. F. Clemente, J. Xavier-Neto, A. P. Dalla Costa et al., "Focal adhesion kinase governs cardiac concentric hypertrophic growth by activating the AKT and mTOR pathways," *Journal of Molecular and Cellular Cardiology*, vol. 52, no. 2, pp. 493–501, 2012.
- [11] Z. Yang and X. F. Ming, "mTOR signalling: the molecular interface connecting metabolic stress, aging and cardiovascular diseases," *Obesity Reviews*, vol. 13, pp. 58–68, 2012.
- [12] A. Gross, J. M. McDonnell, and S. J. Korsmeyer, "BCL-2 family members and the mitochondria in apoptosis," *Genes & Development*, vol. 13, no. 15, pp. 1899–1911, 1999.
- [13] R. Nahta and F. J. Esteva, "Bcl-2 antisense oligonucleotides: a potential novel strategy for the treatment of breast cancer," *Seminars in Oncology*, vol. 30, 5 Suppl 16, pp. 143–149, 2003.
- [14] R. J. Youle and A. Strasser, "The BCL-2 protein family: opposing activities that mediate cell death," *Nature Reviews. Molecular Cell Biology*, vol. 9, no. 1, pp. 47–59, 2008.
- [15] D. Del Bufalo, A. Biroccio, C. Leonetti, and G. Zupi, "Bcl-2 overexpression enhances the metastatic potential of a human breast cancer line," *The FASEB Journal*, vol. 11, no. 12, pp. 947–953, 1997.
- [16] P. E. Czabotar, G. Lessene, A. Strasser, and J. M. Adams, "Control of apoptosis by the BCL-2 protein family: implications for physiology and therapy," *Nature Reviews. Molecular Cell Biology*, vol. 15, no. 1, pp. 49–63, 2014.
- [17] G. Vairo, K. M. Innes, and J. M. Adams, "Bcl-2 has a cell cycle inhibitory function separable from its enhancement of cell survival," *Oncogene*, vol. 13, no. 7, pp. 1511–1519, 1996.
- [18] G. K. Smyth, J. Michaud, and H. S. Scott, "Use of within-array replicate spots for assessing differential expression in microarray experiments," *Bioinformatics*, vol. 21, no. 9, pp. 2067–2075, 2005.
- [19] M. K. Kerr, "Linear models for microarray data analysis: hidden similarities and differences," *Journal of Computational Biology*, vol. 10, no. 6, pp. 891–901, 2003.
- [20] J. Y. Li, L. L. Zheng, T. T. Wang, and M. Hu, "Functional annotation of metastasis-associated microRNAs of melanoma: a meta-analysis of expression profiles," *Chinese Medical Journal*, vol. 129, no. 20, pp. 2484–2490, 2016.
- [21] A. C. de Almeida, R. J. van Oort, and X. H. Wehrens, "Transverse aortic constriction in mice," *JoVE (Journal of Visualized Experiments)*, vol. 38, 2010.
- [22] H. Li, J. Hong, and W. Wijayakulathilaka, "Long non-coding RNA SNHG4 promotes cervical cancer progression through regulating c-Met via targeting miR-148a-3p," *Cell Cycle*, vol. 18, no. 23, pp. 3313–3324, 2019.
- [23] Q. Bao, L. Chen, J. Li et al., "Role of microRNA-124 in cardiomyocyte hypertrophy induced by angiotensin II," *Cellular and Molecular Biology (Noisy-le-Grand, France)*, vol. 63, no. 4, pp. 23–27, 2017.
- [24] M. G. Rosca, B. Tandler, and C. L. Hoppel, "Mitochondria in cardiac hypertrophy and heart failure," *Journal of Molecular and Cellular Cardiology*, vol. 55, pp. 31–41, 2013.
- [25] P. H. Sugden and A. Clerk, "Cellular mechanisms of cardiac hypertrophy," *Journal of Molecular Medicine (Berlin, Germany)*, vol. 76, no. 11, pp. 725–746, 1998.
- [26] M. Asokan Shibu, W. W. Kuo, C. H. Kuo et al., "Potential phytoestrogen alternatives exert cardio-protective mechanisms via estrogen receptors," *Biomedicine*, vol. 7, no. 2, p. 11, 2017.
- [27] V. Krystof, I. Chamrád, R. Jorda, and J. Kohoutek, "Pharmacological targeting of CDK9 in cardiac hypertrophy," *Medicinal Research Reviews*, vol. 30, no. 4, pp. 646–666, 2010.
- [28] A. J. Marian and R. Roberts, "The molecular genetic basis for hypertrophic cardiomyopathy," *Journal of Molecular and Cellular Cardiology*, vol. 33, no. 4, pp. 655–670, 2001.
- [29] N. Takeda, I. Manabe, Y. Uchino et al., "Cardiac fibroblasts are essential for the adaptive response of the murine heart to pressure overload," *The Journal of Clinical Investigation*, vol. 120, no. 1, pp. 254–265, 2010.
- [30] J. R. McMullen and S. Izumo, "Role of the insulin-like growth factor 1 (IGF1)/phosphoinositide-3-kinase (PI3K) pathway mediating physiological cardiac hypertrophy," in *Novartis Foundation symposium*, vol. 274, p. 90, John Wiley, Chichester; New York, 2006.
- [31] J. Li, Y. P. Yuan, S. C. Xu et al., "Arctiin protects against cardiac hypertrophy through inhibiting MAPKs and AKT signaling pathways," *Journal of Pharmacological Sciences*, vol. 135, no. 3, pp. 97–104, 2017.
- [32] R. Xue, J. Jiang, B. Dong et al., "DJ-1 activates autophagy in the repression of cardiac hypertrophy," *Archives of Biochemistry and Biophysics*, vol. 633, pp. 124–132, 2017.
- [33] D. Zhao, W. Wang, H. Wang et al., "PKD knockdown inhibits pressure overload-induced cardiac hypertrophy by promoting autophagy via AKT/mTOR pathway," *International Journal of Biological Sciences*, vol. 13, no. 3, pp. 276–285, 2017.
- [34] L. Chen, Q. Li, L. Lei, and T. Li, "Dioscin ameliorates cardiac hypertrophy through inhibition of the MAPK and Akt/GSK3 β /mTOR pathways," *Life Sciences*, vol. 209, pp. 420–429, 2018.
- [35] F. Xie, W. Liu, F. Feng et al., "Apelin-13 promotes cardiomyocyte hypertrophy via PI3K-Akt-ERK1/2-p70S6K and PI3K-induced autophagy," *Acta biochimica et biophysica Sinica*, vol. 47, no. 12, pp. 969–980, 2015.
- [36] H. Wada, C. T. Ivester, B. A. Carabello, G. Cooper IV, and P. J. McDermott, "Translational initiation factor eIF-4E," *The Journal of Biological Chemistry*, vol. 271, no. 14, pp. 8359–8364, 1996.

Research Article

Correlation between TNF- α -308 and +489 Gene Polymorphism and Acute Exacerbation of Chronic Obstructive Pulmonary Diseases

Suyun Yu ¹, Min Xue ¹, Zhijun Yan ¹, Bin Song ², Haiping Hong ³, and Xiwen Gao ¹

¹Department of Respiratory, Minhang Hospital, Fudan University, Shanghai 201199, China

²Department of Radiology, Minhang Hospital, Fudan University, Shanghai 201199, China

³Shanghai Songjiang District Fangta Hospital of Traditional Chinese Medicine, Shanghai 201699, China

Correspondence should be addressed to Haiping Hong; xinxinyu8120@sina.com and Xiwen Gao; xiwengao@sina.com

Received 24 December 2020; Revised 5 February 2021; Accepted 22 February 2021; Published 2 March 2021

Academic Editor: Tao Huang

Copyright © 2021 Suyun Yu et al. This is an open access article distributed under the Creative Commons Attribution License, which permits unrestricted use, distribution, and reproduction in any medium, provided the original work is properly cited.

Acute exacerbation of chronic obstructive pulmonary disease (AECOPD) is becoming a common respiratory disease, leading to increased morbidity and mortality worldwide. Tumor necrosis factor-alpha (TNF- α) is a powerful proinflammatory cytokine involved in the pathogenesis of AECOPD. Therefore, we proposed a close correlation between the TNF- α polymorphism [-308G/A (rs1800629), +489G/A (rs1800610)] and the disease progress of patients with AECOPD. Comparison of the TNF- α genotypes between the 198 AECOPD diagnosed patients groups and 195 healthy peoples suggested their significant differences of the three genotypes (AA, GA, GG) distribution for TNF- α -308 ($P < 0.05$), but no differences of that for TNF- α +489. We found that patients with TNF- α -308 GA/AA genotypes showed smaller adjacent arterial diameter, thicker bronchial wall, higher bronchial artery ratio, higher bronchial wall grading, and higher frequency of acute exacerbations than those with TNF- α -308 GG genotype. Patients with TNF- α +489 GA/AA genotypes showed the same AECOPD properties as patients with TNF- α -308 except for the high frequency of acute exacerbations. Further experiment showed that the TNF- α -308 and +489 gene polymorphisms could affect the expression level of TNF- α in macrophages, suggesting the involvement of the macrophage population in disease regulation of AECOPD patients with TNF- α -308G/A and +489G/A genotype heterogeneity. In conclusion, the TNF- α -308 G/A genotype was related to AECOPD susceptibility and progress, while the TNF- α +489G/A genotype was related to AECOPD progress, but not AECOPD susceptibility.

1. Introduction

Chronic obstructive pulmonary disease (COPD) refers to a group of chronic inflammatory diseases that cause airflow blockage and breathing-related problems [1, 2]. Although causing high morbidity and mortality, there is no specific treatment for COPD, and the pathogenesis remains unclear. COPD can develop into acute exacerbation of COPD (AECOPD). The patients with AECOPD suffer from rapid deterioration of the lung, accompanied by inflammation and fever. Frequent recurrence of AECOPD is an important factor in promoting the progression of COPD, leading to

increased morbidity and mortality worldwide [3–5]. Smoking is previously shown to be significant associated with AECOPD; however, it is reported that only 10–15% of smokers could develop AECOPD [6, 7]. Besides, there also appears to be a familial clustering of AECOPD [8]. These studies suggest that genetic factors may play an important role in AECOPD development. Therefore, exploring the association of heterogeneity of AECOPD phenotypes and gene polymorphism is necessary for individualized prevention and treatment programs.

Macrophages are the most abundant cells in the tumor stroma and exhibit obvious plasticity, which enables them

TABLE 1: Clinical baseline data comparison for the AECOPD and the control group.

Groups	Gender		Age (years)
	M	F	
AECOPD	159	39	79.76 ± 8.56
Control	157	38	81.26 ± 9.29
<i>P</i> value	0.958		0.06

to perform multiple functions in the tumor microenvironment [9]. Tumor-associated macrophages usually refer to another type of M2, which exhibits anti-inflammatory and tumor-promoting effects [10]. In large series of nonresponding community-acquired pneumonia (CAP) patients, COPD is observed to be a protective factor for nonresponse to initial antibiotics [11]. This result is related to changes in the phenotype of inflammatory cells, especially the induction of classic M1 or alternative M2 activation of macrophages is involved, which leads to different inflammatory conditions [12]. Previous studies indicate that the microenvironment in the lung regulates the activation of macrophages, resulting in different phenotypes in AECOPD, CAP, and COPD + CAP patients [11].

Tumor necrosis factor- (TNF-) α , working as a proinflammatory cytokine, plays an important role in an inflammatory response. Many studies show that TNF- α is upregulated in the sputum, broncho alveolar lavage fluid, and bronchial biopsies of patients with COPD [13, 14], suggesting the key role of TNF- α in the COPD progress. As a well-studied proinflammatory cytokine, many biallelic polymorphisms of TNF- α , including -308G/A (rs1800629), -376G/A (rs1800750), -238G/A (rs361525), and +489 (rs1800610) gene polymorphisms, are discovered. Among these polymorphic sites, -308G/A, -376G/A, and -238G/A polymorphisms are located in the promoter region of the gene, whereas +489 polymorphism is located in the first intron of the gene [15]. Many studies have assessed the relationship between COPD risk and TNF- α polymorphisms. As the best-studied TNF- α polymorphism [16, 17], -308 G/A variant has been reported to be closely related with COPD development in a Taiwanese [18] cohort and a Japanese cohort [19], but not in Caucasian populations [20–22]. Besides, TNF- α +489 G/A polymorphism, which is involved in prostate cancer, systemic lupus erythematosus, and rheumatoid arthritis development [23], is also recently identified to be related to COPD development [24, 25]. However, few studies are performed on the Asian population. Therefore, we perform a correlation analysis between TNF- α polymorphisms (-308 G/A and +489 G/A) and AECOPD susceptibility of the Shanghai Han Population.

2. Materials and Methods

2.1. Specimen Acquisition. The AECOPD (159 males and 39 females) patients and healthy populations (157 males and 38 females) studied in this work were obtained from the Department of Respiratory Medicine at Minhang Hospital, Fudan University. A total of 198 patients and 195 healthy

peoples of the Shanghai Han population were selected from January 2014 to June 2015. The Research Ethics Committees of Minhang Hospital approved the study, and all patients provided written informed consent.

Specifically, patients were diagnosed as AECOPD according to the criteria described in “Chronic obstructive pulmonary disease treatment guidelines (2013 Revision)” established by the Chinese Medical Association Respiratory Diseases Committee. To be specific, eliminate other disease possibilities, after inhaling bronchodilator, FEV₁/FVC < 70 %; patient respiratory symptoms deteriorated more than the daily variation range, and when there is a need to change the drug regimen, during the disease, patients often had a short-term cough, sputum, shortness of breath and/or exacerbated wheezing, increased sputum, purulent or mucopurulent sputum, fever, and inflammation to significantly exacerbate symptoms. Patients with the genetic predisposition of other diseases, including hypertension, diabetes, coronary heart disease, or rheumatism, were excluded from the sample cohort. As for the control cohort, 195 healthy Han individuals (157 males and 38 females) without disease history of other respiratory or systemic diseases, such as bronchiectasis, pulmonary fibrosis, sarcoidosis, asthma, lung cancer, diabetes, and heart disease, were selected. All of the individuals were confirmed as the normal lung and chest function through high-resolution computerized tomography (HRCT) examination.

Detailed pathological datum, including medical history, age, gender, smoking index, and specific symptoms (cough, sputum, or dyspnea) was collected from the patients with AECOPD or the control subjects. Besides, the following two types of COPE classification were considered: Pistolesi et al. [26] revealed that based on the clinical manifestations, spirometry results, chest imaging data, and pathologic features, COPD could be divided into bronchitis- and emphysematous: the criteria outlined by Hurst et al. [27], and AECOPD phenotypes can be divided into nonfrequent- (0-1 time/year-) and frequent- (≥ 2 times/year-) types. Spirometry was performed for all patients. The lung functions of all subjects were evaluated using the COSMED quark-PFT4 spirometer.

All patients underwent chest HRCT examination at the end of a calm breath, using a 64-slice helical CT scan, from the apex to the bottom of the lung. Scanning parameters were as follows: voltage 140 kV, thickness 1.25 mm, current 112 mas, pitch 1.375:1, and lap speed 12.25 s. Workstation syngo. via was used to read the sections.

2.2. Data Analysis. Two radiologists evaluated the clinical data under double-blinded conditions. The average values of all indicators were taken into analysis. Based on the principles using 960 HU to define the normal lung and low attenuation area (LAA) published by Kitagichi et al. [28, 29], the 3 anatomical levels at the edge of the aortic arch, lower spine, and pulmonary vein were evaluated, and the area of LAA on either side was calculated as a percentage of the whole lung. Subsequent comparison and classification were performed. The rating criteria were as follows: LAA < 5%, 1 point; 5% ≤ LAA < 25%, 2 points; 50% ≤ LAA < 75%, 3 points; and LAA ≥ 75%, 4 points. The 6 viewpoint scores were added to calculate the emphysema

TABLE 2: Distribution of TNF- α -308 and+489 genotypes in the AECOPD and control groups.

Group	No. of samples	Genotypes					Alleles	
		GG (%)	GA (%)	AA (%)	G (%)	A (%)		
<i>TNF-α-308</i>								
AECOPD	198	173 (87.37)	21 (10.61)	4 (2.02)	367 (92.68)	29 (7.32)		
Control	195	186 (95.38)	9 (4.62)	0 (0)	381 (97.69)	9 (2.31)		
<i>P</i> value			0.001			0.001		
<i>TNF-α+489</i>								
AECOPD	198	140 (70.71)	46 (23.23)	12 (6.06)	326 (82.32)	70 (17.68)		
Control	195	148 (75.90)	39 (20.00)	8 (4.10)	329 (84.36)	61 (15.64)		
<i>P</i> value			0.455			0.203		

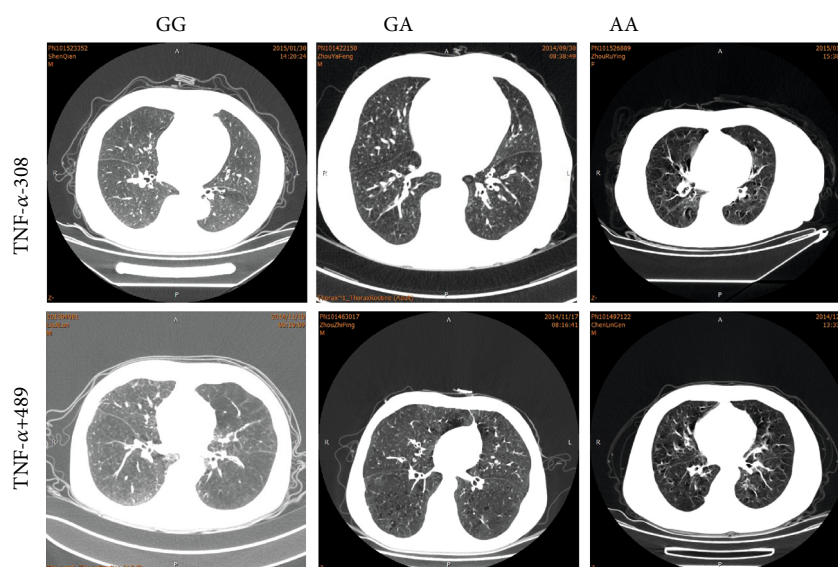


FIGURE 1: Differences among AECOPD patients with different genotypes on inspiratory-expiratory high-resolution computerized tomography (HRCT) imaging.

score: 0 points, stage 0; 1 to 6 points, stage I; 7 to 12 points, stage II; 13 to 18 points, stage III; 19 to 24 points, and stage IV. Bronchial wall thickness was graded as follows: 0, bronchial wall thickness < 30% of the adjacent pulmonary artery diameter; grade 1, 30% of the adjacent pulmonary artery diameter \leq bronchial wall thickness < 50% of the adjacent pulmonary artery diameter; and grade 2, bronchial wall thickness \geq 50% of the adjacent pulmonary artery diameter. COPD phenotypes were divided as follows: A-type: absent or minor emphysema, LAA \leq stage 1, regardless of whether the bronchial wall was thickening; E-type: the presence of LAA \geq stage II emphysema, regardless of whether the bronchial wall was thickening; and M-type: having LAA \geq stage II emphysema and bronchial wall thickening \geq grade 1.

2.3. DNA Isolation and TNF- α Gene Polymorphism Typing.

The TNF- α gene polymorphisms located on positions -308 G/A and +489 G/A, which are related to the transcriptional start site (TSS) of the TNF- α gene, were detected in genomic DNA derived from peripheral blood leukocytes. Briefly, 3 mL of blood was drawn from each subject after fast-

ing and stored at -80°C after separation. Gene amplification was conducted using PCR-ABI 2700. Whole blood genomic DNA extraction was performed by Shanghai Yixiang Biotechnology Ltd. DNA was detected after cell lysis, precipitation, protease digestion, DNA adsorption, elution, and agarose gel electrophoresis. The primers for TNF- α -308 were designed as follows: TNF- α -forward (-308): 5'-AGGCCTCAGGACTCAACACA-3'; TNF- α -reverse (-308): 5'-GTTGCTTCTCTCCCTCTT-3'. The primers for TNF- α +489 were designed as follows: TNF- α -forward (+489): 5'-GTGTATGGAGTGAA TGAATGAA-3'; TNF- α -reverse (+489): 5'-CCTGAGTGTCTTCTGTGT-3'. The desired gene product was isolated by agarose gel electrophoresis. PCR products were purified and sequenced by Suzhou Genewiz Biotechnology Company. If the result was bimodal at a given position, the position was interpreted as heterozygous; a single peak was interpreted as homozygous.

2.4. The Expression Level of TNF- α Based on Public Online Databases and Blood Samples. To gather the expression data

TABLE 3: Comparison of the different indicators for the GG genotype and non-GG genotypes.

Group	No. of samples	Adjacent arterial diameter	Bronchial wall thickness	Bronchial artery ratio	Bronchial wall grading
<i>TNF-α-308</i>					
GG	173	1.04 \pm 0.59	0.17 \pm 0.04	0.28 \pm 0.11	0.38 \pm 0.55
Non-GG	25	0.65 \pm 0.20	0.27 \pm 0.14	0.38 \pm 0.14	0.90 \pm 0.75
<i>P</i> value		0.037	0.014	0.017	0.022
<i>TNF-α+489</i>					
GG	116	0.96 \pm 0.56	0.26 \pm 0.13	0.28 \pm 0.12	0.49 \pm 0.59
Non-GG	82	0.74 \pm 0.39	0.21 \pm 0.09	0.32 \pm 0.13	0.69 \pm 0.72
<i>P</i> value		0.003	0.003	0.019	0.031

TABLE 4: Comparison of the different indicators for the GG genotype and non-GG genotypes.

Group	No. of samples	Frequency of acute exacerbations		Cough or dyspnea (frequency)	
		Once/year	>twice/year	Cough	Dyspnea
<i>TNF-α-308</i>					
GG	173	153	20	105	68
Non-GG	25	11	14	8	17
<i>P</i> value			0.001		0.007
<i>TNF-α+489</i>					
GG	116	93	23	14	102
Non-GG	82	60	22	27	55
<i>P</i> value			0.324		0.001

of TNF- α , we downloaded the microarray expression profiles, including GSE71220, GSE42057, and GSE54837, from the Gene Expression Omnibus (GEO) database (<https://www.ncbi.nlm.nih.gov/geo/query/acc.cgi>).

The blood samples from the AECOPD group and control group were obtained in the morning on or before breakfast from the median cubital vein, then immediately centrifuged at 3,000 rpm for 10 minutes. The serum was extracted for TNF- α concentration assessment using TNF- α (human) EIA Kit (589201-480, Cayman).

2.5. Peripheral Blood Mononuclear Cell (PBMC) Isolation, Culture, and Differentiation. Whole blood (20-25 mL) collected in tubes containing ethylenediaminetetraacetic acid (EDTA) as anticoagulant was processed between 9:00 am and 12:00 noon, within 3 h of collection. PBMCs were isolated by Ficoll-Paque (Histopaque 1077; Sigma-Aldrich, Gillingham, UK) density gradient centrifugation (at 400 g for 30 min at RT with the break turned off) and washed twice with PBS (at 300 g for 10 min at 4°C). PBMCs were resuspended at 2.5×10^6 cells/mL in RPMI 1640 medium containing 10% FCS and 1% penicillin-streptomycin. Then, the PBMCs were cultured in 24-well plates (500 μ l/well) and stimulated for 4 h with phorbol 12-myristate 13-acetate (PMA; 100 ng/ml; Sigma-Aldrich) and ionomycin (1 μ g/ml; Sigma-Aldrich) in the presence of $1 \times$ monensin (BioLegend, UK) to obtain macrophage. The culture supernatants of macrophage were collected, centrifuged for 5 min at 300 g at 4°C, and aliquoted and stored at -80°C until analysis.

2.6. Statistical Analysis. Data were analyzed and graphed using SPSS 19.0 statistical software (SPSS, Chicago, IL, USA). Data significance was measured using a *t*-test and χ^2 test. The Hardy-Weinberg equilibrium was used to calculate the genotypic equilibrium, and the Fisher exact test was used to compare differences between genotype and allele frequency; $P < 0.05$ was considered as statistically significant.

3. Results

3.1. Characteristics of the AECOPD Populations. The AECOPD cohort consisted of 198 Shanghai Han patients (79.76 \pm 8.56 years old). Around 81% of the AECOPD patients were male. A total of 121 (61%) patients were smokers or exsmokers, and 77 patients (39%) stated that they had never smoked.

The healthy population consisted of 195 Shanghai Han subjects derived from an anonymous panel of blood donors (81.26 \pm 9.29 years old), including 157 males (81%) and 38 females (19%). The statistical analysis revealed no significant difference between the AECOPD cohort and the control subjects in terms of age and gender (Table 1).

3.2. TNF- α Gene Polymorphism and Population Susceptibility to AECOPD. To assess the differences of AECOPD susceptibility between the patients and control group, the genotype frequencies of TNF- α -308G/A and the TNF- α +489G/A gene polymorphisms in the two cohorts were analyzed, respectively (Table 2). As a result, in both healthy subjects

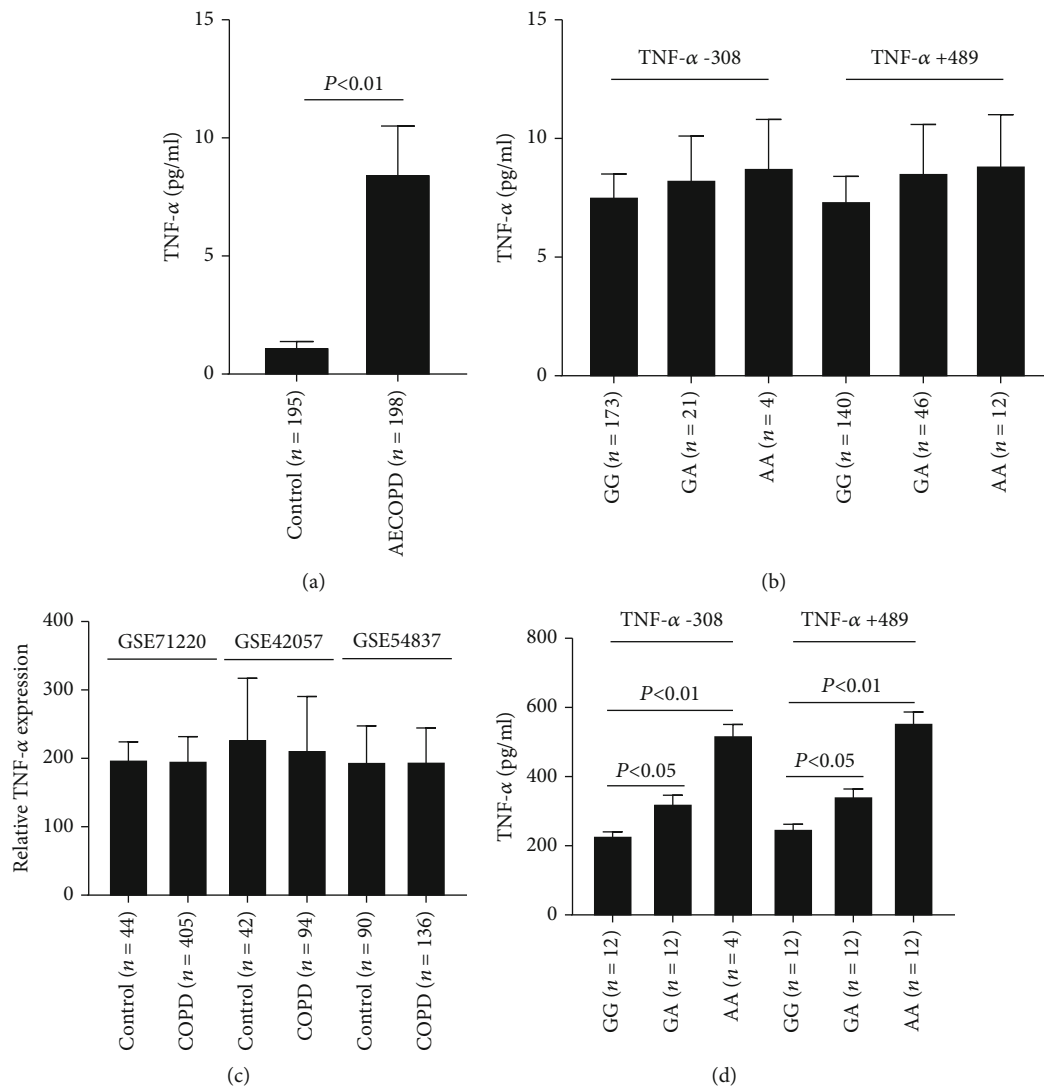


FIGURE 2: TNF- α gene genotypes affect the expression level of TNF- α in macrophage. (a) TNF- α concentration is increased in serum from AECOPD patients. (b) TNF- α concentration in serum from AECOPD patients with different TNF- α gene genotypes. (c) The expression of TNF- α in the data from public online databases. (d) TNF- α secreted by macrophages with different TNF- α gene genotypes.

and patients with AECOPD, the alleles at the individual loci of the TNF- α gene were in Hardy-Weinberg equilibrium, with nonsignificant χ^2 values.

For TNF- α -308G/A gene polymorphism, the frequencies of the 3 genotypes (GG, GA, and AA) in the AECOPD group were 87.37%, 10.61%, and 2.02%, respectively, while the occurrence rates of the 3 genotypes in the control group were 95.38%, 4.62%, and 0%, respectively. Besides, the frequencies of G and A in the AECOPD group were 92.68% and 7.32%, while the frequencies in the control group were 97.69% and 2.31%, respectively. The results showed a significant difference in genotype frequency of TNF- α between the AECOPD group and control group ($P = 0.001$), ascribing to the enhanced frequencies of GA and AA in the patient group.

For TNF- α +489G/A gene polymorphism, the frequencies of the 3 genotypes (GG, GA, and AA) in the AECOPD group were 70.71%, 23.23%, and 6.06%, respectively, while

the frequencies of the 3 genotypes in the control group were 75.90%, 20.00%, and 4.10%, respectively. The statistical analysis revealed that there was no significant difference in the occurrence distribution of the 3 TNF- α genotypes between the two groups ($P = 0.455$, R by C table Chi square test). Besides, the frequencies of G and A in the AECOPD group were 82.32% and 17.68%, while the frequencies of G and A in the control group were 85.90% and 14.10%, respectively. There was also no significant difference discovered in the occurrence distribution of the 3 TNF- α genotypes between the two groups ($P = 0.455$, R by C table Chi square test).

3.3. Correlation Analyses of TNF- α Gene Genotypes and AECOPD Phenotypes. To investigate the correlation of TNF- α -308 or+489 genotypes and AECOPD phenotypes, the adjacent arterial diameter and bronchial wall thickness of AECOPD patients were measured (Figure 1 and Table 3). As a result, we found that no matter for TNF- α

-308 or TNF- α +489, the patients with non-GG genotypes showed lower adjacent arterial diameter and higher bronchial wall thickness ($P < 0.05$). Two key indexes of the character of AECOPD, the ratio of bronchial wall thickness to adjacent artery diameter (bronchial artery ratio) and bronchial wall grading, were calculated. The results showed that the patients with non-GG genotypes (TNF- α -308 and TNF- α +489) had higher bronchial artery ratio and bronchial wall grading, suggesting more serious AECOPD phenotypes ($P < 0.05$).

Furthermore, for TNF- α -308, patients carrying non-GG genotypes showed significantly more frequent exacerbations ($P = 0.001$) and dyspnea ($P = 0.007$) than patients carrying GG genotype. Unlike TNF- α -308, there was no significant difference between the TNF- α +489AA/GA group and GG group in frequency of acute exacerbations ($P = 0.324$), while the patients with AA/GA genotype presented a higher ratio of cough to dyspnea than patients with GG genotype ($P = 0.001$). The detailed data were presented in Table 4.

3.4. TNF- α Gene Genotypes Affect the Expression Level of TNF- α in Macrophage. To investigate whether the TNF- α gene genotypes affect its expression level, we firstly detected the level of TNF- α in blood samples of the AECOPD group and control group. As a result, TNF- α was overexpressed in the AECOPD group (Figure 2(a)), and the expression level was closely correlated with the TNF- α gene genotypes (Figure 2(b)). However, there were no significant differences in TNF- α expression values in three different microarray expression profiles, including GSE71220, GSE42057, and GSE54837 (Figure 2(c)). These results indicated that TNF- α in blood was derived from other cell types rather than lung cells. Considering that macrophage exhibited a more extensive distribution along airways, lung parenchyma, and bronchoalveolar lavage (BAL) fluid in COPD patients [30], we hypothesized that the elevation of the expression value of TNF- α in blood was mainly due to the extensive distribution of the macrophage population in the lung, and TNF- α gene genotypes could affect the expression of TNF- α in the lung macrophages. To verify our hypothesis, the PBMCs were isolated from blood samples of AECOPD patients carrying different TNF- α gene genotypes. Then, the cells were cultured and differentiated into macrophage-like cells using PMA. The TNF- α concentration in the culture medium was detected. The result showed that the TNF- α concentration was the highest in the TNF- α -308AA group (Figure 2(d)). A similar result was obtained for the TNF- α +489AA group (Figure 2(d)). These results demonstrated that TNF- α gene genotypes affect the expression of TNF- α in macrophages.

4. Discussion

The clinical manifestations of COPD are heterogeneous. In recent years, identifying differences between COPD phenotypes, which could facilitate the exploration of different diagnosis and treatment methods, is becoming a popular topic. The conventional drug treatment for COPD yields suboptimal responses in many patients. However, they often suffer from increasing risks of exacerbations, rapid progression,

and poor prognosis. Researchers have identified and classified COPD into different categories and form different archetypes [31], which could predict the prognosis of the disease and guide the treatment for different patients.

It is now widely recognized that COPD is a chronic inflammatory disease, in which multiple inflammatory cells, inflammatory mediators, cytokines in the lung parenchyma, and pulmonary vasculature that ultimately extends to multiple systems in the body are involved. In recent years, TNF- α has drawn attention on account of its role in the pathogenesis of COPD. Previous studies showed that the TNF- α level is increased in the muscle biopsy, serum, bronchoalveolar lavage fluid (BALF), bronchial biopsy, and sputum samples of patients with COPD and associated with an elevated risk of acute exacerbation. These findings suggest that TNF- α is potentially involved with a local and systemic inflammatory response in the COPD process and may play an important role in determining the severity of the disease. Our previous study detecting TNF- α in the exhaled breath condensate of patients with AECOPD yielded similar results. Thus, TNF- α is one of the most active inflammatory cytokines in AECOPD. The genetic factor determines the changes in protein structures, which corresponds with pathophysiological changes. Therefore, exploring the relationship of heterogeneity of COPD phenotypes and genotype is necessary and is becoming the future trend for identifying the individualized prevention and treatment programs. The gene coding for TNF- α locates in the histocompatibility complex III region on chromosome 6.

Our study supported the previous reports about the role of TNF- α -308 gene polymorphism in AECOPD susceptibility. Meanwhile, our current study also showed that the TNF- α +489 GA and AA genotypes did not correlate with AECOPD susceptibility in Chinese patients of the Shanghai Han ethnicity, under the results of Hegab et al. [32], while contradictory to the opinion suggested by Kucukaycan et al. [33]. The main clinical manifestations, including dyspnea, frequent exacerbations, and significantly thickened bronchial wall, were shown by CT. Both our study and the study conducted by Kucukaycan et al. [33] yielded similar results. Among the North Caucasian population, the TNF- α +489G/A gene polymorphism was correlated to a higher risk of developing breathing problems. This was especially true for patients with COPD without radiographic manifestations of emphysema. Matheson et al. [34] also described that, in the Australian COPD population, patients carrying the TNF- α +489AA allele had a higher risk of developing breathing problems, which was associated with small airway diseases. Han et al. [35] found a 10% increase in bronchial wall thickness and a 1.42-fold increase in the number of exacerbations, suggesting that the thickening of the bronchial wall can affect clinical symptoms. Hurst et al. [27] described that acute exacerbation itself was the best predictor for disease exacerbations. Overall, COPD patients with more severe disease had a higher risk of acute exacerbation, lower quality of life, and worse disease prognosis. These findings suggested that the race, sample size, and polygenic variance of COPD could all contribute to the disease prognosis and should be validated in future clinical studies. However, the sample size

of this study is small, and animal model tests are needed to further verify the results of the study. In future research, we will further explore the regulation of TNF- α -308 and +489 on macrophages in AECOPD.

This study included subjects of the Shanghai Han ethnicity and excluded those with hypertension, diabetes, coronary heart disease, rheumatism, and other genetic diseases. Our hypothesis for the association of the gene polymorphisms and the clinical phenotypes is that the TNF- α -308 and +489 locus G > A mutation may result in a higher expression value of TNF- α in macrophage. As a proinflammatory factor, TNF- α can induce the onset of COPD. The inflammation in the airway leads to a quick infiltration of neutrophils and promotes neutrophil cell adhesion, elastic peripheral cell dissociation, and proteolytic enzyme activity, which are conducive to the formation of emphysema. TNF- α could also induce the secretion of endothelin-1 by airway smooth muscle cells, resulting in the contraction of airway smooth muscle and airway cell proliferation, causing airway remodeling. TNF- α also promotes the production of IL-6 and IL-8 by bronchial epithelial cells and alveolar macrophages, thereby increasing the damage to lung tissues. In sum, TNF- α -308 and +489 gene polymorphisms are associated with disease severity and poor prognosis of patients with AECOPD in the Chinese Shanghai Han ethnicity. The results laid a theoretical foundation for AECOPD prevention, assessment, and personalized treatment development, thus improving the prognosis of the disease.

Abbreviations

AECOPD:	Acute exacerbation of COPD
COPD:	Chronic obstructive pulmonary disease
HRCT:	High-resolution computerized tomography
LAA:	Low attenuation area
TNF- α :	Tumor necrosis factor-alpha
TSS:	Transcriptional start site
GEO:	Gene Expression Omnibus
EDTA:	Ethylenediaminetetraacetic acid.

Data Availability

The data that support the findings of this study are available with approval from the author.

Disclosure

The funders had no role in study design, data collection and analysis, decision to publish, or preparation of the manuscript.

Conflicts of Interest

The authors declare that they have no conflicts of interest.

Authors' Contributions

SY conceived the study, carried out the molecular genetic studies, and drafted the manuscript. XM and ZY participated in the design of the study and performed sequences analysis.

BS and YZ coordinated the study, participated in the experimental design, and helped to draft the manuscript. XG proposed the concept of the study, designed the study, formulated the major conclusion, and revised this manuscript. All authors read and approved the final manuscript.

Acknowledgments

This study was funded by the Shanghai Ministry of Health Youth Research Projects (20134y084) and Beijing Medical and Health Foundation (YWJKJHHKYJJ-HX16).

References

- [1] M. I. Restrepo, O. Sibila, and A. Anzueto, "Pneumonia in patients with chronic obstructive pulmonary disease," *Tuberculosis and Respiratory Diseases*, vol. 81, no. 3, pp. 187–197, 2018.
- [2] H. K. Yoon, Y. B. Park, C. K. Rhee, J. H. Lee, Y. M. Oh, and Committee of the Korean COPD Guideline 2014, "Summary of the chronic obstructive pulmonary disease clinical practice guideline revised in 2014 by the Korean academy of tuberculosis and respiratory disease," *Tuberculosis and Respiratory Diseases*, vol. 80, no. 3, pp. 230–240, 2017.
- [3] J. Vestbo, S. S. Hurd, and R. Rodriguez-Roisin, "The 2011 revision of the global strategy for the diagnosis, management and prevention of COPD (GOLD)—why and what?," *The Clinical Respiratory Journal*, vol. 6, no. 4, pp. 208–214, 2012.
- [4] H. Chen, Y. Wang, C. Bai, and X. Wang, "Alterations of plasma inflammatory biomarkers in the healthy and chronic obstructive pulmonary disease patients with or without acute exacerbation," *Journal of Proteomics*, vol. 75, no. 10, pp. 2835–2843, 2012.
- [5] B. Wei and C. Sheng Li, "Changes in Th1/Th2-producing cytokines during acute exacerbation chronic obstructive pulmonary disease," *The Journal of International Medical Research*, vol. 46, no. 9, pp. 3890–3902, 2018.
- [6] J. L. Corhay, N. Frusch, and R. Louis, "COPD: genetics and environmental interactions," *Revue Médicale de Liège*, vol. 67, no. 5-6, pp. 292–297, 2012.
- [7] D. M. Mannino, D. M. Homa, L. J. Akinbami, E. S. Ford, and S. C. Redd, "Chronic obstructive pulmonary disease surveillance—United States, 1971–2000," *MMWR Surveillance Summaries*, vol. 51, no. 6, pp. 1–16, 2002.
- [8] P. Zhan, J. Wang, S. Z. Wei et al., "TNF-308 gene polymorphism is associated with COPD risk among Asians: meta-analysis of data for 6,118 subjects," *Molecular Biology Reports*, vol. 38, no. 1, pp. 219–227, 2011.
- [9] M. Najafi, N. Hashemi Goradel, B. Farhood et al., "Macrophage polarity in cancer: a review," *Journal of Cellular Biochemistry*, vol. 120, no. 3, pp. 2756–2765, 2019.
- [10] A. Valeta-Magara, A. Gadi, V. Volta et al., "Inflammatory breast cancer promotes development of M2 tumor-associated macrophages and cancer mesenchymal cells through a complex chemokine network," *Cancer Research*, vol. 79, no. 13, pp. 3360–3371, 2019.
- [11] P. Gutierrez, D. Closa, R. Piner, O. Bulbena, R. Menendez, and A. Torres, "Macrophage activation in exacerbated COPD with and without community-acquired pneumonia," *The European Respiratory Journal*, vol. 36, no. 2, pp. 285–291, 2010.

- [12] N. Wang, H. Liang, and K. Zen, "Molecular mechanisms that influence the macrophage m1-m2 polarization balance," *Frontiers in Immunology*, vol. 5, p. 614, 2014.
- [13] Y.-j. Du, C.-j. Yang, B. Li et al., "Association of pro-inflammatory cytokines, cortisol and depression in patients with chronic obstructive pulmonary disease," *Psychoneuroendocrinology*, vol. 46, pp. 141–152, 2014.
- [14] D. G. Yanbaeva, M. A. Dentener, E. C. Creutzberg, and E. F. M. Wouters, "Systemic inflammation in COPD: is genetic susceptibility a key factor?," *COPD: Journal of Chronic Obstructive Pulmonary Disease*, vol. 3, no. 1, pp. 51–61, 2006.
- [15] S. Fargion, L. Valenti, P. Dongiovanni et al., "Tumor necrosis factor alpha promoter polymorphisms influence the phenotypic expression of hereditary hemochromatosis," *Blood*, vol. 97, no. 12, pp. 3707–3712, 2001.
- [16] N. Ezzeldin, A. Shalaby, A. Saad-Hussein et al., "Association of TNF- α -308G/a, SP-B 1580 C/T, IL-13 -1055 C/T gene polymorphisms and latent adenoviral infection with chronic obstructive pulmonary disease in an Egyptian population," *Archives of Medical Science*, vol. 8, no. 2, pp. 286–295, 2012.
- [17] S. Zhang, C. Wang, B. Xi, and X. Li, "Association between the tumor necrosis factor- α -308G/A polymorphism and chronic obstructive pulmonary disease: an update," *Respirology*, vol. 16, no. 1, pp. 107–115, 2011.
- [18] M. J. Hsieh, S. Y. Huang, T. M. Yang et al., "The impact of 2011 and 2017 global initiative for chronic obstructive pulmonary disease (GOLD) guidelines on allocation and pharmacological management of patients with COPD in Taiwan: Taiwan obstructive lung disease (TOLD) study," *International Journal of Chronic Obstructive Pulmonary Disease*, vol. 13, pp. 2949–2959, 2018.
- [19] S. Sakao, K. Tatsumi, H. Igari, Y. Shino, H. Shirasawa, and T. Kuriyama, "Association of tumor necrosis factor alpha gene promoter polymorphism with the presence of chronic obstructive pulmonary disease," *American Journal of Respiratory and Critical Care Medicine*, vol. 163, no. 2, pp. 420–422, 2001.
- [20] V. M. Keatings, S. J. Cave, M. J. Henry et al., "A polymorphism in the tumor necrosis factor-alpha gene promoter region may predispose to a poor prognosis in COPD," *Chest*, vol. 118, no. 4, pp. 971–975, 2000.
- [21] C. Patuzzo, L. S. Gilè, M. Zorzetto et al., "Tumor necrosis factor gene complex in COPD and disseminated bronchiectasis," *Chest*, vol. 117, no. 5, pp. 1353–1358, 2000.
- [22] M. A. Higham, N. B. Pride, A. Alikhan, and N. W. Morrell, "Tumour necrosis factor- α gene promoter polymorphism in chronic obstructive pulmonary disease," *The European Respiratory Journal*, vol. 15, no. 2, pp. 281–284, 2000.
- [23] Y. J. Lin, R. H. Chen, L. Wan et al., "Association of TNF- α gene polymorphisms with systemic lupus erythematosus in Taiwanese patients," *Lupus*, vol. 18, no. 11, pp. 974–979, 2009.
- [24] K. Cui, X. Y. Ge, and H. L. Ma, "Association of the TNF- α +489 G/a polymorphism with chronic obstructive pulmonary disease risk in Asians: meta-analysis," *Genetics and Molecular Research*, vol. 14, no. 2, pp. 5210–5220, 2015.
- [25] J. Smolonska, C. Wijmenga, D. S. Postma, and H. M. Boezen, "Meta-analyses on suspected chronic obstructive pulmonary disease genes: a summary of 20 years' research," *American Journal of Respiratory and Critical Care Medicine*, vol. 180, no. 7, pp. 618–631, 2009.
- [26] M. Pistolesi, G. Camiciottoli, M. Paoletti et al., "Identification of a predominant COPD phenotype in clinical practice," *Respiratory Medicine*, vol. 102, no. 3, pp. 367–376, 2008.
- [27] J. R. Hurst, J. Vestbo, A. Anzueto et al., "Susceptibility to exacerbation in chronic obstructive pulmonary disease," *The New England Journal of Medicine*, vol. 363, no. 12, pp. 1128–1138, 2010.
- [28] Y. Kitaguchi, K. Fujimoto, K. Kubo, and T. Honda, "Characteristics of COPD phenotypes classified according to the findings of HRCT," *Respiratory Medicine*, vol. 100, no. 10, pp. 1742–1752, 2006.
- [29] K. Fujimoto, Y. Kitaguchi, K. Kubo, and T. Honda, "Clinical analysis of chronic obstructive pulmonary disease phenotypes classified using high-resolution computed tomography," *Respirology*, vol. 11, no. 6, pp. 731–740, 2006.
- [30] N. Li, Y. Liu, and J. Cai, "LncRNA MIR155HG regulates M1/M2 macrophage polarization in chronic obstructive pulmonary disease," *Biomedicine & Pharmacotherapy*, vol. 117, article 109015, 2019.
- [31] M. K. Han, A. Agusti, P. M. Calverley et al., "Chronic obstructive pulmonary disease phenotypes: the future of COPD," *American Journal of Respiratory and Critical Care Medicine*, vol. 182, no. 5, pp. 598–604, 2010.
- [32] A. E. Hegab, T. Sakamoto, W. Saitoh et al., "Polymorphisms of TNF α , IL1 β , and IL1RN genes in chronic obstructive pulmonary disease," *Biochemical and Biophysical Research Communications*, vol. 329, no. 4, pp. 1246–1252, 2005.
- [33] M. Küçükaycan, M. Van Krugten, H.-J. Pennings et al., "Tumor necrosis factor-alpha +489G/a gene polymorphism is associated with chronic obstructive pulmonary disease," *Respiratory Research*, vol. 3, p. 29, 2002.
- [34] M. C. Matheson, J. A. Ellis, J. Raven, E. H. Walters, and M. J. Abramson, "Association of IL8, CXCR2 and TNF-alpha polymorphisms and airway disease," *Journal of Human Genetics*, vol. 51, no. 3, pp. 196–203, 2006.
- [35] M. K. Han, E. A. Kazerooni, D. A. Lynch et al., "Chronic obstructive pulmonary disease exacerbations in the COPD-Gene study: associated radiologic phenotypes," *Radiology*, vol. 261, no. 1, pp. 274–282, 2011.

Research Article

miR-145-5p Inhibits the Proliferation, Migration, and Invasion of Esophageal Carcinoma Cells by Targeting ABRACL

Shengming Fan , Pei Chen , and Shugang Li 

Department of Thoracic Surgery, People's Hospital of Anji, 313300 Huzhou, China

Correspondence should be addressed to Shugang Li; li890876@163.com

Received 23 December 2020; Revised 26 January 2021; Accepted 3 February 2021; Published 28 February 2021

Academic Editor: Tao Huang

Copyright © 2021 Shengming Fan et al. This is an open access article distributed under the Creative Commons Attribution License, which permits unrestricted use, distribution, and reproduction in any medium, provided the original work is properly cited.

Objective. The study is aimed at investigating the regulatory relationship between miR-145-5p and ABRACL, and has tried at clarifying the mechanisms underlying the proliferation, migration, and invasion of esophageal carcinoma (EC) cells. **Methods.** Gene expression data related to EC were accessed from TCGA database, and the “edgeR” package was used to screen differentially expressed genes. TargetScan, miRDB, and miRTarBase databases were used to predict potential targets for the target miRNA miR-145-5p. qRT-PCR and Western blot were performed to assess the expression of miR-145-5p and ABRACL in EC cells. Dual-luciferase reporter assay was performed to validate the targeting relationship between miR-145-5p and ABRACL. Functional experiments including CCK-8 assay, Transwell migration, and invasion assays were used to detect the proliferation, migration, and invasion of EC cells. **Results.** The expression of miR-145-5p was significantly decreased in EC, while ABRACL was remarkably increased. In addition, there was a negative correlation identified between miR-145-5p and ABRACL mRNA. Overexpressing miR-145-5p was able to suppress cell proliferation, migration, and invasion, whereas silencing miR-145-5p posed an opposite effect. In the meantime, ABRACL was identified as a direct target of miR-145-5p by dual-luciferase reporter assay. Furthermore, miR-145-5p could inhibit the expression of ABRACL, in turn inhibiting the proliferation, migration, and invasion of EC cells. **Conclusion.** miR-145-5p functions on the proliferation, migration, and invasion of EC cells via targeting ABRACL, and it may be a novel therapeutic target in EC treatment.

1. Introduction

Esophageal carcinoma (EC) is a common gastrointestinal tumor characterized by a high incidence around the world, and it is the sixth most common cause leading to cancer-related death [1]. Lung cancer, gastric cancer, hepatocellular carcinoma, and EC are the four most common cancers in China. Among them, EC is the most prevalent disease and its incidence gradually increases [2]. As there are no typical clinical symptoms manifested in early stages of EC, the illness of many patients may progress to an advanced stage when they are initially diagnosed, and that is the main reason for a high mortality. Special local vascular structure and abundant lymphatic capillaries are favorable factors for migration of EC cells, which contributes to the fact that most people are confirmed with EC accompanied by metastasis. Esophageal

squamous cell carcinoma (ESCC) is the most common type of EC with a relatively high incidence in China [3, 4]. At present, treatment of EC is mainly based on surgery combined with radiotherapy or chemotherapy. Such treatment can have a significant effect on the progress of the illness, yet the overall prognosis is still poor. Therefore, identifying effective therapeutic targets is of great significance for the treatment of EC.

MicroRNAs (miRNAs) are small noncoding RNA molecules that regulate translation or degradation of mRNA by binding to the 3'-UTR of their target mRNAs [5, 6]. miRNAs play pivotal roles in tumors including EC by acting as oncogenes or tumor suppressor genes. For example, miR-124-3p directly targets the 3'-UTR region of BCAT1 in ESCC, and downregulation of miR-124-3p is highly correlated with ESCC cell proliferation and migration [7]. In addition,

miR-125b was reported to be able to negatively regulate the expression of BCL-2-modifying factor (BMF) in ESCC by interacting with the 3'-UTR within BMF, and overexpressing miR-125b can significantly inhibit the growth of ESCC and induce apoptosis [8]. miR-145-5p, a crucial member of the miRNA family, was identified to be involved in malignant progression of a variety of cancers, such as colorectal cancer [9], breast cancer [10], and gastric cancer [11], and has fantastic potential applications in the field of cancer.

The human ABRACL (ABPA C-terminal like) gene locates on chromosome 6 and encodes a small protein of 81 amino acids, which can enhance actin activity and cell viability [12]. As an atypical winged-helix protein previously named as HSPC280, ABRACL belongs to a new family of low-molecular-weight proteins and is only present in eukaryotes but absent in fungi, with highly conserved sequences across different species [13]. A mouse study conducted by Stylianopoulou et al. found that ABRACL is a nucleoprotein that inhibits neuronal differentiation *in vitro* when it is overexpressed in Neuro2a cells, suggesting its involvement in the regulation of neural progenitor cell proliferation [14]. A report showed that ABRACL can be detected in uterine aspirate of endometrial cancer rather than in that of healthy uterus [15]. Besides, ABRACL was proven to have elevated expression in gastric cancer tissue relative to that in normal tissue, while increased ABRACL indicates unfavorable clinical outcomes of cancer sufferers [16]. However, the role of ABRACL in EC has not been reported.

The aim of this study was to investigate the expression of miR-145-5p in EC cells and its role in cell proliferation, migration, and invasion, and also tried to clarify the underlying mechanisms.

2. Materials and Methods

2.1. Bioinformatics Analysis. Gene and miRNA Expression Quantification Data related to EC were accessed from TCGA-ESCA (esophageal carcinoma) dataset in TCGA (<https://portal.gdc.cancer.gov/>). Package “edgeR” was used to identify differentially expressed genes (DEGs), with the threshold set as $|\log_{2}FC| > 1$ and $\text{padj} < 0.05$. TargetScan (http://www.targetscan.org/vert_72/), miRTarBase (<http://mirtarbase.mbc.ntu.edu.tw/php/index.php>), and miRDB (<http://www.mirdb.org/>) databases were used to predict downstream target mRNAs for the target miRNA, and a Venn diagram was plotted to find the target mRNA. Survival significance of the target mRNA was evaluated using the clinical information obtained from TCGA.

2.2. Cell Culture. Normal human esophageal epithelial cell line HET-1A was purchased from Riken BioResource Center (Tsukuba, Japan). Five EC cell lines Eca-109, EC9706, KYSE150, KYSE180, and BIC-1 were purchased from Cell Center of the Shanghai Institutes for Biological Sciences, Chinese Academy of Sciences (Shanghai, China). All cells were cultured in RPMI-1640 medium (Gibco, USA) containing 10% fetal bovine serum (FBS; Gibco), streptomycin (100 mg/ml; Gibco), and penicillin (100 units/ml; Gibco), and maintained in an incubator at 37°C with 5% CO₂.

2.3. Vector Construction and Cell Transfection. MiR-145-5p mimic, miR-145-5p inhibitor, corresponding negative control and si-abracl respectively purchased from GenePharma (Shanghai, China) were transiently transfected into EC cells by Lipofectamine 2000 (Thermo Fisher Scientific, Inc.), and then maintained in corresponding medium under the environment of 5% CO₂ at 37°C. The lentiviral expression vector pLVX-IRES-neo (Clontech) was used to establish ABRACL-overexpressed vector oe-ABRACL, which was then used to infect cancer cells, with the virus particle as the negative control. Sequences of the materials for transfection are as follows: miR-145-5p mimic sense: 5'-GUCCAGUUUCCCAGGAAUCCCU-3', antisense: 5'-GGAUCCUGGGAAAACUGGACUU-3'; mimic NC sense: 5'-UUCUCCGAACGUGUCA CGUUU-3', antisense: 5'-ACGUGACACGUUCGGAGAAUU-3'; miR-145-5p inhibitor: 5'-CUUAGCAUCUAAGGGAUUCUGGG-3'; inhibitor NC: 5'-CGAACUUCACCUCGCGCGGG-3'; si-ABRACL: 5'-GCGCUCACAGUAGGAGUUU-3'.

2.4. RNA Extraction and qRT-PCR. Total RNA was extracted from cells using TRIzol (Thermo Fisher Scientific, Waltham, MA, USA) and then reversely transcribed into complementary (cDNA) by cDNA synthesis kit (Thermo Fisher Scientific, Waltham, MA, USA).

Quantitative PCR was performed using miScript SYBR Green PCR Kit (Qiagen, Hilden, Germany) under following thermal cycling conditions: predenaturation at 95°C for 10 min, 40 cycles of 95°C for 15 s, and 60°C for 1 min [17]. Primers for miR-145-5p, U6, ABRACL, and GAPDH were purchased from GeneCopoeia (GeneCopoeia Inc., Guangzhou, China) and sequenced as below: miR-145-5p forward (stem-loop): 5'-TCGGCAGGGTCCAGTTTTCCCA-3', reverse: 5'-CTCAAC TGGTGTCTGTTGGA-3'; U6 forward: 5'-GGAGCGAGATCCCTCCAAAAT-3', reverse: 5'-GGCTGTTGTCATACTTCTCATGG-3'; ABRACL forward: 5'-ACCTCTTTGAAGCATTGGTAGG-3', reverse: 5'-GCAGCTCTCCTGGATATGTTAC-3'; and GAPDH forward: 5'-GGAGCGAGATCCCTCCAAAAT-3', reverse: 5'-GGCTGTTGTCATACTTCTCATGG-3'. The $2^{-\Delta\Delta Ct}$ value was used to compare the difference in relative expression of the target mRNA and miRNA between the control group and the experimental group. The experiment was repeated three times.

2.5. Western Blot. After transfection for 48 h, cells were washed 3 times with cold PBS. Whole cell lysate was added for cell lysate on ice for 10 min, and the BCA protein assay kit (Thermo, USA) was applied to determine protein concentration. A measure of 30 μg of protein samples was processed for separation by polyacrylamide gel electrophoresis (PAGE) at a constant voltage of 80 V for 35 min followed by 120 V for 45 min, and sequentially transferred to polyvinylidene fluoride (PVDF) membranes (Amersham, USA). After blocked with 5% skim milk for 1 h at room temperature, the membranes were incubated with rabbit polyclonal anti-ABRACL antibody (Abcam, Cambridge, UK) and rabbit polyclonal

anti-GAPDH antibody (Abcam, Cambridge, UK) overnight at 4°C. The membranes were washed 3 times with PBST (phosphate-buffered saline containing 0.1% Tween-20) for 10 min each time. Subsequently, the membranes were incubated with horseradish peroxidase- (HRP-) labeled secondary antibody goat anti-rabbit IgG H&L (Abcam, Cambridge, UK) for 1 h at room temperature. The membranes were washed 3 times with PBST buffer again. An optical luminometer (GE, USA) was employed to visualize protein bands, and the Image Pro Plus 6.0 (Media Cybernetics, USA) software was applied for further analysis.

2.6. CCK-8 Assay. Proliferative capability of EC cells was evaluated by CCK-8 assay. In short, Eca-109 cells (2×10^4 cells/ml) were firstly inoculated into a 96-well plate for culture under the regular culture environment (5% CO₂ and 37°C). Following 0, 24, 48, and 72 h, respectively, 10 μl of CCK-8 reagent was added into each well for 2 h. After incubation, the optical density (OD) value at 450 nm of each well was measured using a microplate reader (Model 550; Bio-Rad Laboratories, Inc., Hercules, CA, USA). CCK-8 reagent used here was provided by the Cell Counting Kit-8 produced by Dojindo Molecular Technologies, Inc. (Kumamoto, Japan). The experiment was repeated three times.

2.7. Transwell Assay

2.7.1. Transwell Migration Assay. Cancer cells in logarithmic growth phase were starved for 24 h at first. On the following day, cells were digested, centrifuged, and resuspended to a final concentration of 2×10^5 cells/ml. A measure of 0.2 ml of cell suspension was added into Transwell upper compartment, while 700 μl of precooled RPMI-1640 medium containing 10% FBS was added into the lower compartment. Cells were cultured in an incubator containing 5% CO₂ at a temperature of 37°C. After 24 h, the cells still in the upper compartment were wiped off with a wet cotton swab, and the cells in the lower compartment were fixed using methanol for 30 min and then stained by 0.1% crystal violet for 20 min. Finally, cells were observed under an inverted microscope and five fields of view were randomly selected for cell count.

2.7.2. Transwell Invasion Assay. A 24-well Transwell chamber (8 μm in aperture, BD Biosciences) was used for cell invasion assay. Approximately 2×10^4 cells were plated in the upper chamber which was precoated with Matrigel matrix (Corning, Corning, NY). RPMI-1640 medium containing 10% FBS was filled into the lower chamber. The following procedures were as similar as the above migration assay.

2.8. Dual-Luciferase Reporter Gene Assay. Eca-109 cells were seeded at 6×10^5 cells/well in a 24-well plate and incubated for 24 h. The mutant (MUT) or wild-type (WT) 3'-UTR of ABRACL mRNA was amplified and then cloned into pmir-GLO (Promega, WI, USA) to construct luciferase reporter vectors ABRACL-WT and ABRACL-MUT. Subsequently, ABRACL-WT and ABRACL-MUT were transfected into cells with miR-145-5p mimic or mimic NC by using Lipofectamine 2000, respectively. The Renilla luciferase vector pRL-

TK (TaKaRa, Dalian, China) was used as a control reporter for normalization. After transfection, cells were cultured in RPMI-1640 medium containing 10% FBS. After 48 h, luciferase activities were measured using Dual-Luciferase Reporter Assay System Kit (Promega Corp., Madison, WI, USA). The experiment was repeated three times.

2.9. Statistical Analysis. All data were processed using SPSS 22.0 statistical software, and the measurement data were expressed in the form of the mean ± standard deviation. One-way analysis of variance (ANOVA) was used for pairwise comparison in data of multiple groups, while the *t*-test was implemented for data comparison between two groups. Student's *t*-test and one-way analysis of variance (ANOVA) were applied for analyzing the comparisons between two groups and among multiple groups. $p < 0.05$ indicates statistically significant difference.

3. Results

3.1. miR-145-5p Is Poorly Expressed in EC Cells. A total of 158 differentially expressed miRNAs (DEmiRNAs) were screened via differential analysis using the "edgeR" package (Figure 1(a)). Among the DEmiRNAs, miR-145-5p was found to be significantly decreased in EC tumor tissues ($n = 153$) relative to that in normal tissues ($n = 11$) in TCGA database (Figure 1(b)). In addition, EC cell lines Eca-109, EC9706, KYSE150, KYSE180, and BIC-1 and normal esophageal cell line HET-1A were collected to examine miR-145-5p expression. qRT-PCR was performed and it was showed that compared with HET-1A, EC cells especially Eca-109 cells had significantly reduced expression of miR-145-5p (Figure 1(c)). Thus, Eca-109 cell line was chosen for subsequent experiments for further analysis.

3.2. miR-145-5p Inhibits the Proliferation, Migration, and Invasion of EC Cells. A series of functional experiments were conducted to identify the mechanism by which miR-145-5p regulates EC cell biological behaviors. Mimic NC, miR-145-5p mimic, inhibitor NC, and miR-145-5p inhibitor were transfected into Eca-109 cells. CCK-8 assay suggested that the proliferative ability of Eca-109 cells was greatly decreased in the miR-145-5p mimic group relative to that in the NC group, but significantly increased in the miR-145-5p inhibitor group (Figure 2(a)). Similarly, cell migratory and invasive abilities were both reduced in the miR-145-5p mimic group but enhanced in the miR-145-5p inhibitor group relative to those in the NC groups, as judged by Transwell migration and invasion assays (Figures 2(b) and 2(c)). Overall, all results indicated that high expression of miR-145-5p could inhibit the proliferation, migration, and invasion of EC cells.

3.3. ABRACL Is a Direct Target of miR-145-5p. Differential analysis showed that there were 3,224 differentially expressed mRNAs (DEmRNAs) identified in TCGA-ESCA dataset (Figure 3(a)). TargetScan, miRDB, and miRTarBase databases were applied to predict target mRNAs of miR-145-5p, and the results were then mapped into a Venn diagram with the upregulated DE mRNAs in TCGA-ESCA dataset. Eventually, 10 overlapping mRNAs were obtained (Figure 3(b)).

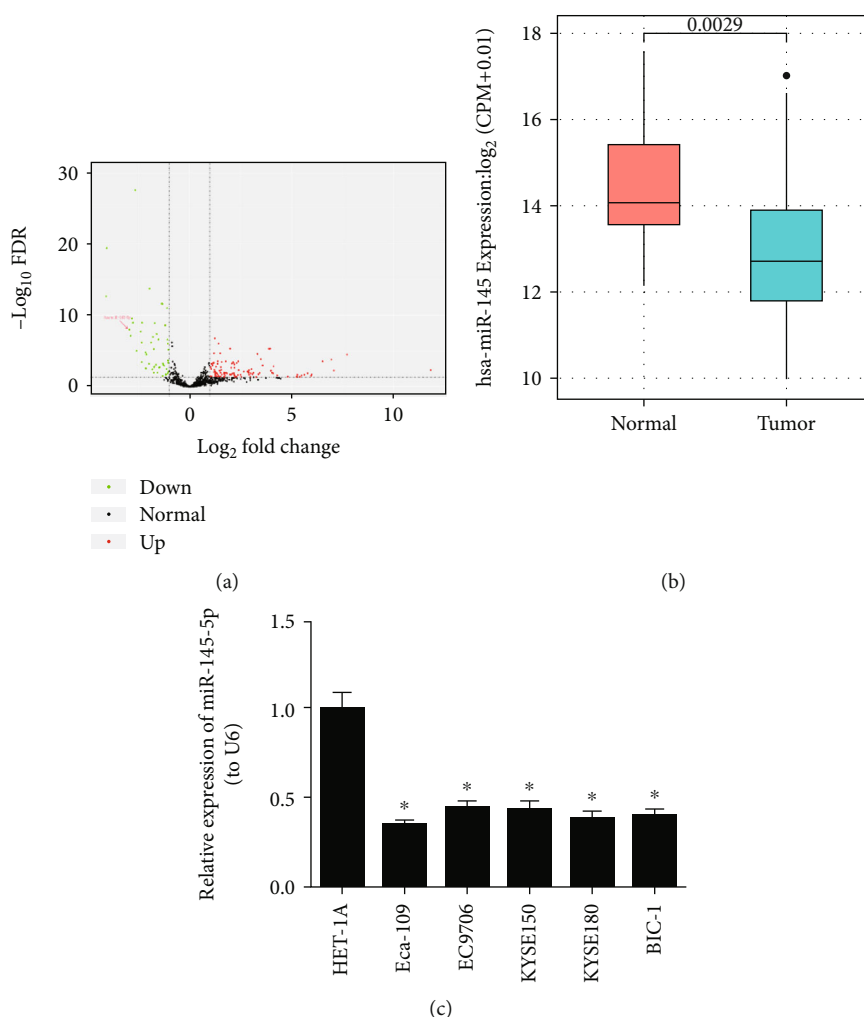
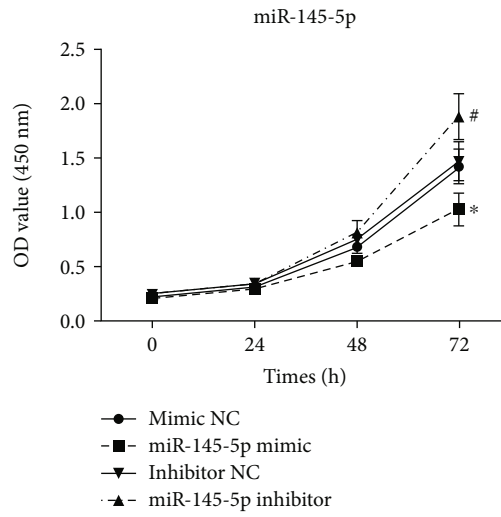


FIGURE 1: miR-145-5p is poorly expressed in EC tissue and cells. (a) Volcano plot shows the DE miRNAs in TCGA-ESCA dataset. (b) Relative expression of miR-145-5p in EC samples in TCGA-ESCA dataset. (c) qRT-PCR shows the relative expression of miR-145-5p in EC cell lines Eca-109, EC9706, KYSE150, KYSE180, and BIC-1 and in normal esophageal cell line HET-1A. * indicates $p < 0.05$.

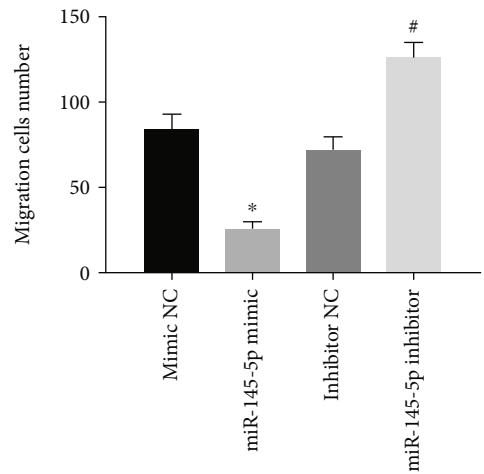
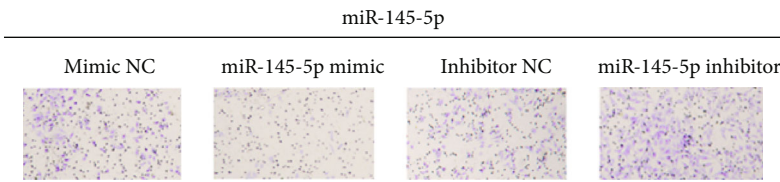
Among the 10 mRNAs, four genes including TGFBR2, ABRACL, ZBTB47, and MASTL were detected to be significantly associated with the prognosis of EC patients as revealed by survival analysis based on the clinical samples ($n = 204$) obtained from TCGA-ESCA dataset. Meanwhile, ABRACL was shown to be the most elevated in EC tissue samples ($n = 176$) relative to that in normal tissue samples ($n = 13$) (Figure 3(c)). Additionally, Pearson correlation analysis suggested that there was a negative correlation between the expression levels of miR-145-5p and ABRACL (Figure 3(d)). In order to validate whether ABRACL is associated with the survival of patients with EC, a total of 114 samples (including 57 samples with low ABRACL and 57 samples with high ABRACL) and corresponding complete clinical data were accessed from TCGA database and then used for survival analysis (Figure 3(e)). Results showed that high expression of ABRACL was able to predict poor prognosis. In the meantime, the expression of ABRACL was tested in EC cell lines. Compared with HET-1A cell line, EC cell lines had remarkably elevated expression of ABRACL (Figures 3(f) and 3(g)).

To further understand the regulatory effect of miR-145-5p on ABRACL, the expression of ABRACL was detected in cells with miR-145-5p overexpression. The results showed that overexpression of miR-145-5p significantly decreased the expression of ABRACL (Figures 3(h) and 3(i)). Additionally, TargetScan database was consulted and it was shown that there were potential binding sites of miR-145-5p on ABRACL 3'-UTR (Figure 3(j)). Dual-luciferase reporter assay was conducted for further verification and indicated that overexpression of miR-145-5p significantly decreased the luciferase activity of Eca-109 cells cotransfected with ABRACL-WT but had no effect in cells containing ABRACL-MUT. Collectively, these results supported the notion that ABRACL was a direct target of miR-145-5p.

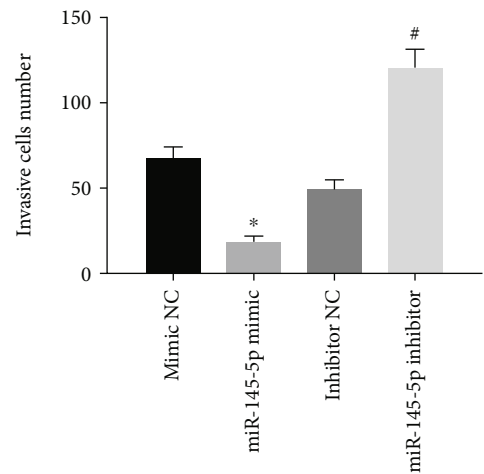
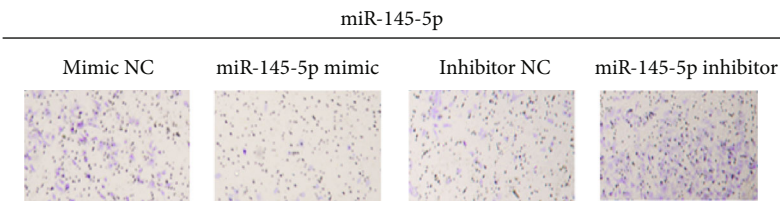
3.4. miR-145-5p Regulates ABRACL to Affect the Proliferation, Migration, and Invasion of EC Cells. To further explore the regulatory mechanism by which miR-145-5p targets ABRACL to mediate cell biological behaviors of EC, rescue experiments were performed on Eca-109 cells. Since we had verified that low expression of miR-145-5p could



(a)



(b)



(c)

FIGURE 2: miR-145-5p inhibits the proliferation, migration, and invasion of EC cells. miR-145-5p mimic, miR-145-5p inhibitor, mimic NC, and inhibitor NC were transfected into Eca-109 cells. (a) CCK-8 assay and (b) migration and (c) invasion assays (Transwell (100x)) show cell proliferative, migratory, and invasive abilities in each treatment group. * indicates $p < 0.05$ relative to mimic NC; # indicates $p < 0.05$ relative to inhibitor NC.

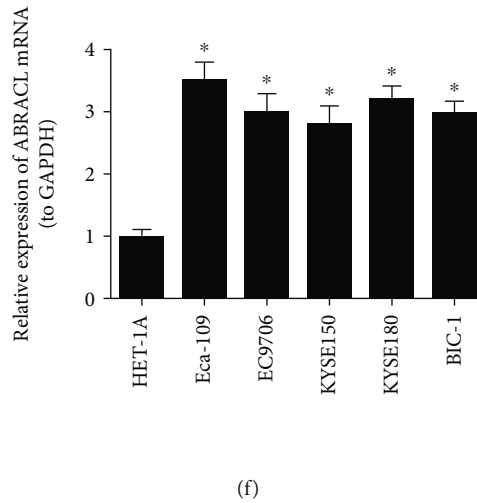
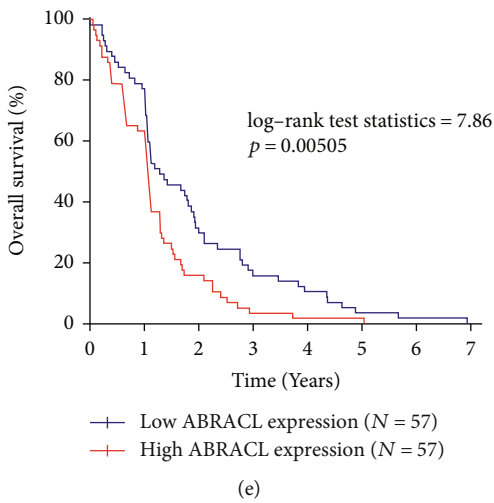
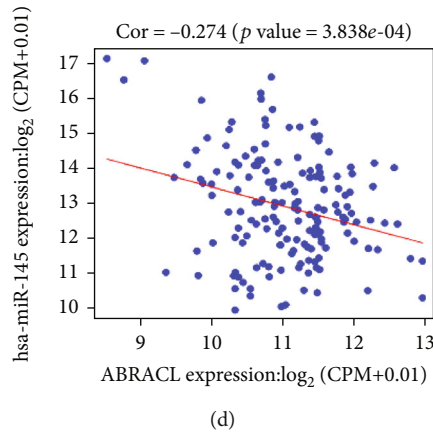
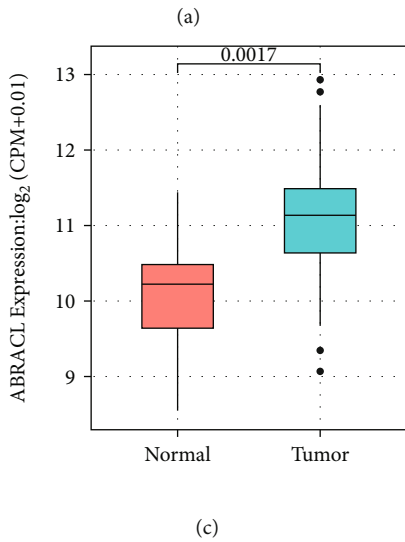
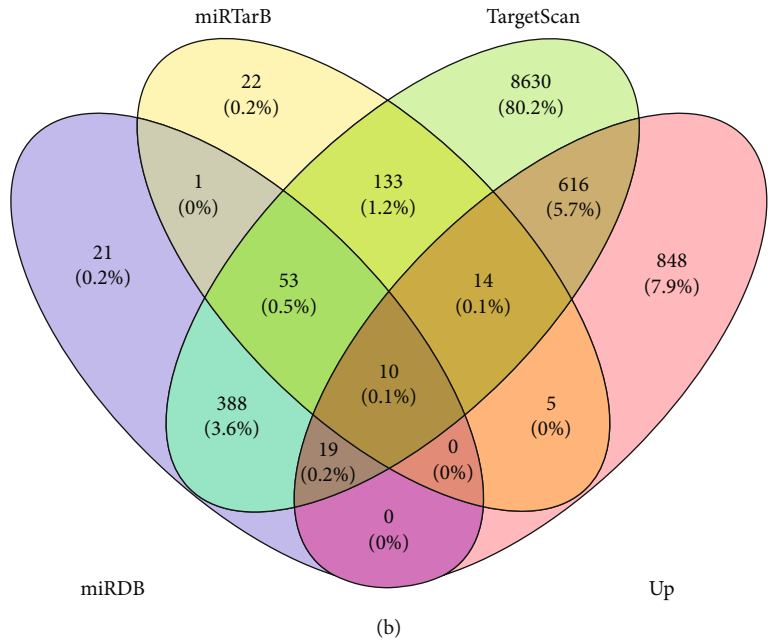
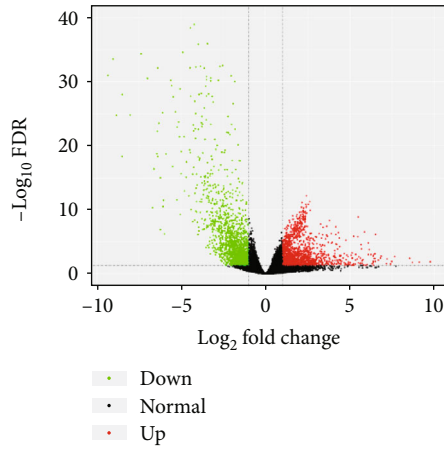


FIGURE 3: Continued.

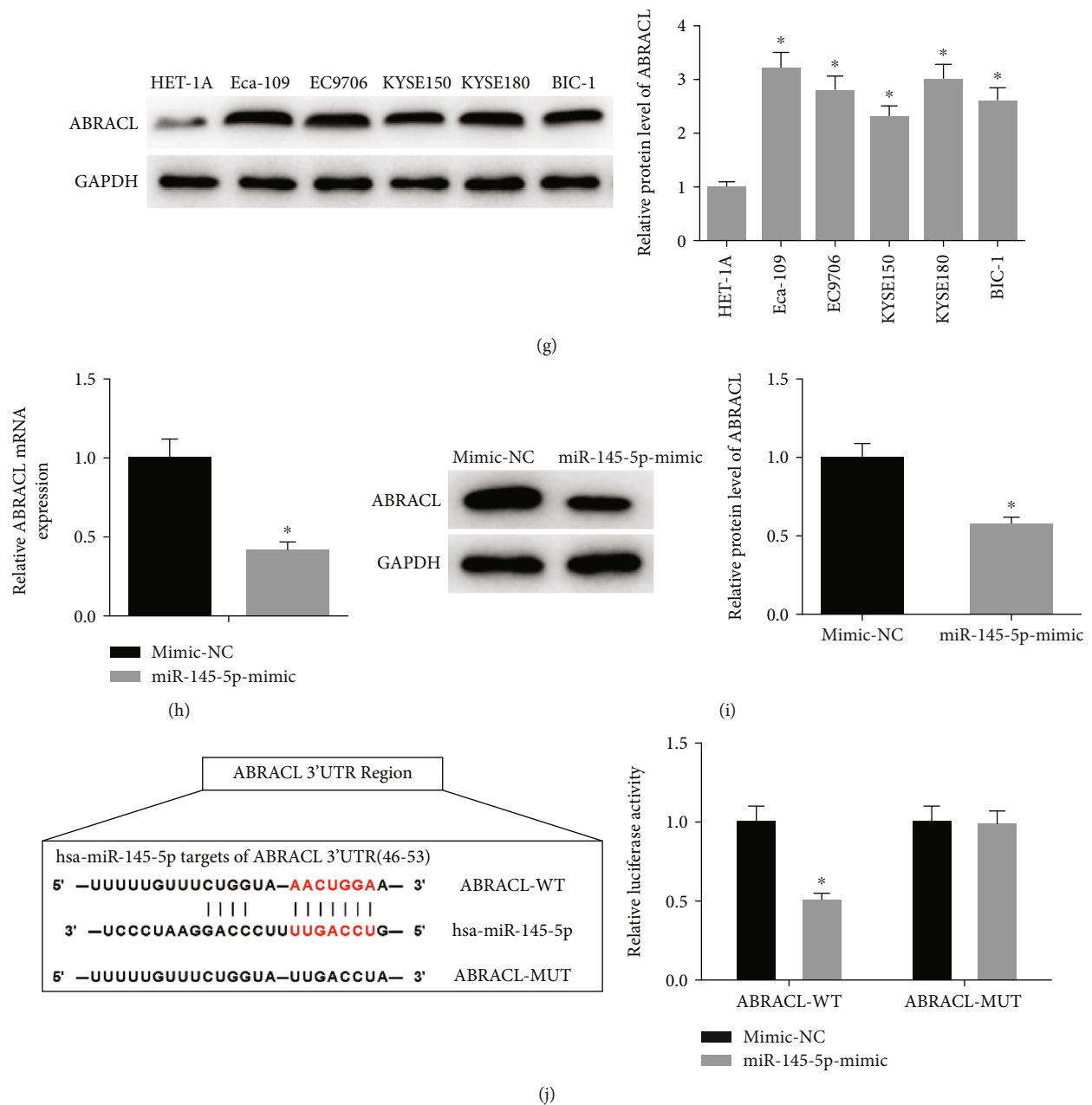


FIGURE 3: ABRACL is a direct target of miR-145-5p. (a) Volcano plot shows the DEMRNAs in TCGA-ESCA dataset. (b) Venn diagram shows the overlapping mRNAs between the predicted targets of miR-145-5p and the upregulated DEMRNAs in TCGA-ESCA dataset. (c) Relative expression of ABRACL in the samples obtained from TCGA-ESCA dataset. (d) The correlation between miR-145-5p and ABRACL. (e) The survival analysis for ABRACL in TCGA-ESCA dataset (each vertical node represents a death of a follow-up individual), (f, g) qRT-PCR and Western blot show the relative mRNA and protein levels of ABRACL in EC cell lines Eca-109, EC9706, KYSE150, KYSE180, and BIC-1 and in normal esophageal cell line HET-1A. (h, i) The relative mRNA and protein expression of ABRACL in mimic NC and miR-145-5p mimic groups. (j) Putative binding sites of miR-145-5p on ABRACL 3'-UTR along with corresponding mutation sites and relative luciferase activity in each treatment group. * indicates $p < 0.05$.

promote cell proliferation, we then simultaneously transfected si-ABRACL and miR-145-5p inhibitor into Eca-109 cells. The results revealed that the cell proliferative ability was significantly decreased after cotransfection compared to that of the miR-145-5p inhibitor group (Figure 4(a)). Similarly, cell migration and invasion were noted to show similar changes, as detected by Transwell migration and invasion assays (Figures 4(b) and 4(c)). It was suggested that miR-

145-5p affected the physiological activities of cancer cells by regulating the expression of ABRACL.

4. Discussion

miRNAs compose a large family widely present in eukaryotic cells and some of them harbor a targeting relationship with mRNAs. Genomic analysis showed that there are over 5,300

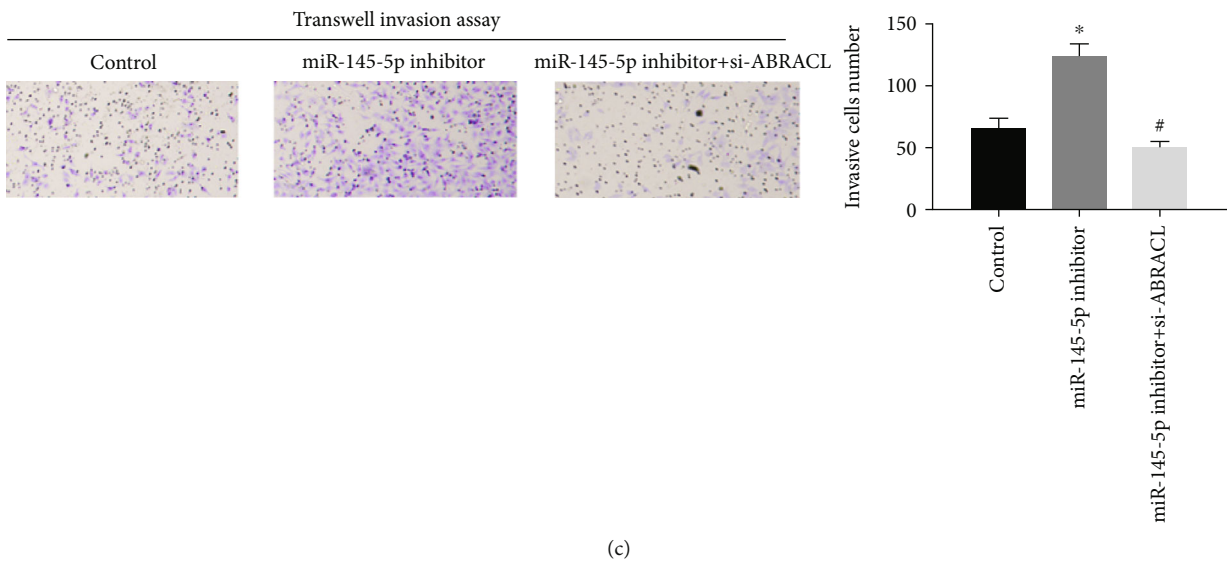
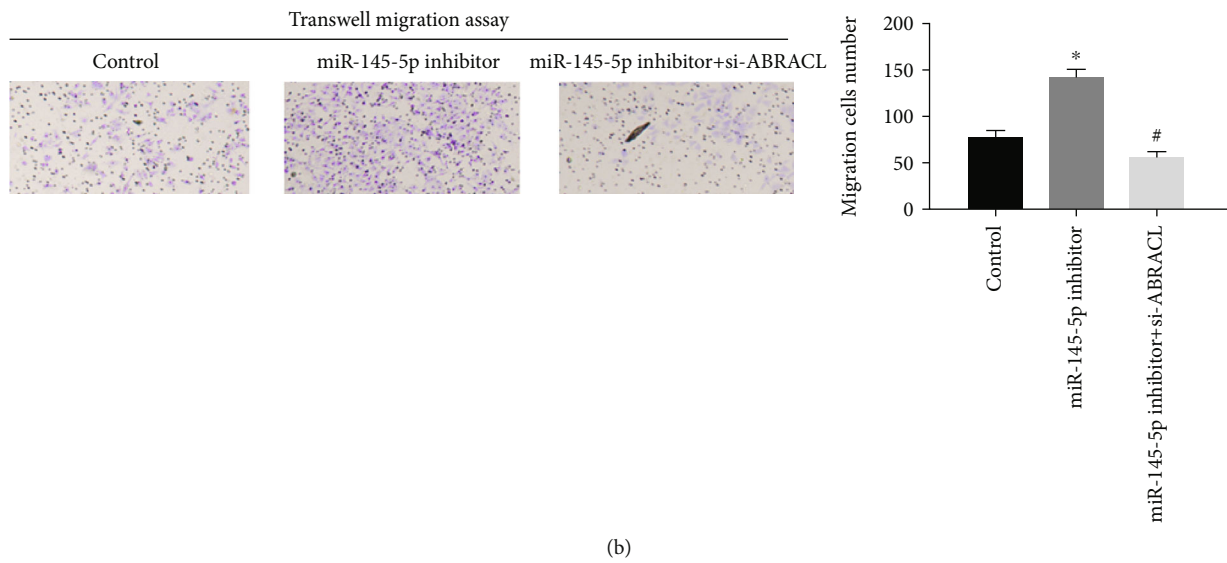
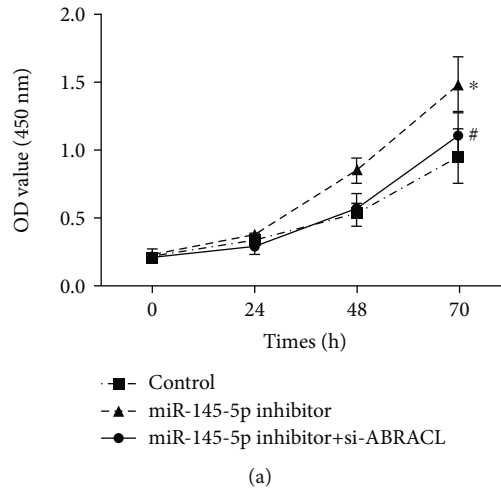


FIGURE 4: miR-145-5p functions on the proliferation, migration, and invasion of EC cells via targeting the expression of ABRACL. Control, miR-145-5p inhibitor, and miR-145-5p inhibitor+si-ABRACL were transfected into Eca-109 cells. (a) CCK-8 assay and (b) migration and (c) invasion assays (Transwell (100x)) show cell proliferative, migratory, and invasive abilities in each treatment group. * indicates $p < 0.05$ relative to the control group; # indicates $p < 0.05$ relative to the miR-145-5p inhibitor group.

human genes that targeted by miRNAs, accounting for 30% of all human genes, and their expression shows an intimate correlation with cancers [18, 19]. Studies revealed that there are many miRNAs altered between EC patients and healthy people. miR-145 was reported to be significantly downregulated in ESCC tissue and cell lines and play an important role in inhibiting cancer cell proliferation, migration, and metastasis. For example, miR-145 can directly target the 3'-UTR of PLCE1, and the downregulation of PLCE1 induces cell apoptosis as well as enhances the sensitivity of tumor cells to chemotherapeutic drugs [20]. Meanwhile, miR-145 is able to inhibit the growth of ESCC cells by targeting c-Myc [21]. In addition, there is a study showing that miR-145 can target and interact with connective tissue growth factor (CTGF) to affect EC cell proliferation, migration, invasion, and epithelial-mesenchymal transition (EMT) process [22]. In our study, we also observed that the proliferation, migration, and invasion of EC cells were affected significantly after miR-145-5p was overexpressed or inhibited, and high miR-145-5p negatively worked in EC progression. To further analyze the mechanism by which miR-145-5p regulates cell activities of EC, target prediction was performed and it was found that ABRACL was a potential target of miR-145-5p. Additionally, survival analysis revealed that there was a close relationship between ABRACL and the prognosis of EC patients, and dual-luciferase reporter gene assay further validated that miR-145-5p could target and bind with ABRACL to suppress its expression. Therefore, we speculated that miR-145-5p mediated EC progression probably via targeting the expression of ABRACL.

ABRACL, a winged-helix protein, plays an important role in a variety of developmental processes. A comparative expression analysis of ABRACL with Dlx2, cyclinD2, and Lhx6 revealed that ABRACL is restricted in the proliferating cell population in the subventricular zone within ganglionic eminences, with a pattern similar to that of cyclinD2 [14]. In addition, ABRACL was detected to be upregulated in gastric cancer tissue compared to that in normal gastric tissue, which is associated with poor prognosis. Meanwhile, an enrichment analysis revealed that ABRACL is mostly enriched in some signaling pathways, such as cell cycle, TNFR pathway, proteasome degradation, and mitochondrial pathway [16]. Besides, studies found that ABRACL bears a similar structure to ABD2 and may be a transcriptional synergistic activator [13, 23, 24] closely related to cell cycle [25]. In this study, dual-luciferase reporter assay demonstrated that ABRACL was a direct target of and negatively regulated by miR-145-5p. Rescue experiments suggested that the effect of silenced miR-145-5p on cell proliferation, migration, and invasion could be attenuated upon ABRACL knockdown. These results suggested that miR-145-5p regulated the cellular functions of EC cells by targeting ABRACL.

In conclusion, our study first proposes that miR-145-5p targets ABRACL to inhibit the proliferation, migration, and invasion of EC cells, which helps to provide a novel therapeutic target for future EC treatment.

Data Availability

The data and materials in the current study are available from the corresponding author on reasonable request.

Consent

Consent is not applicable.

Conflicts of Interest

The authors declare no conflicts of interest.

Acknowledgments

Thanks are due to the Cancer Cell International for publishing this article as a preprint and the Research Square for accepting this article as a preprint.

References

- [1] M. Maghsudlu and E. Farashahi Yazd, "Heat-induced inflammation and its role in esophageal cancer," *Journal of Digestive Diseases*, vol. 18, no. 8, pp. 431–444, 2017.
- [2] W. Chen, R. Zheng, P. D. Baade et al., "Cancer statistics in China, 2015," *CA: a Cancer Journal for Clinicians*, vol. 66, no. 2, pp. 115–132, 2016.
- [3] P. Bohanes, D. Yang, R. S. Chhibar et al., "Influence of sex on the survival of patients with esophageal cancer," *Journal of Clinical Oncology*, vol. 30, no. 18, pp. 2265–2272, 2012.
- [4] F. Kamangar, G. M. Dores, and W. F. Anderson, "Patterns of cancer incidence, mortality, and prevalence across five continents: defining priorities to reduce cancer disparities in different geographic regions of the world," *Journal of Clinical Oncology*, vol. 24, no. 14, pp. 2137–2150, 2006.
- [5] C. Baer, M. L. Squadrito, D. Laoui et al., "Suppression of microRNA activity amplifies IFN- γ -induced macrophage activation and promotes anti-tumour immunity," *Nature Cell Biology*, vol. 18, no. 7, pp. 790–802, 2016.
- [6] C. M. Croce, "Causes and consequences of microRNA dysregulation in cancer," *Nature Reviews. Genetics*, vol. 10, no. 10, pp. 704–714, 2009.
- [7] B. Zeng, X. Zhang, J. Zhao et al., "The role of DNMT1/hsa-miR-124-3p/BCAT1 pathway in regulating growth and invasion of esophageal squamous cell carcinoma," *BMC Cancer*, vol. 19, no. 1, p. 609, 2019.
- [8] Y. X. Fan, X. H. Bian, P. D. Qian et al., "MicroRNA-125b inhibits cell proliferation and induces cell apoptosis in esophageal squamous cell carcinoma by targeting BMF," *Oncology Reports*, vol. 40, no. 1, pp. 61–72, 2018.
- [9] Q. Chen, L. Zhou, X. Ye, M. Tao, and J. Wu, "miR-145-5p suppresses proliferation, metastasis and EMT of colorectal cancer by targeting CDCA3," *Pathology - Research and Practice*, vol. 216, no. 4, p. 152872, 2020.
- [10] W. Tang, X. Zhang, W. Tan et al., "miR-145-5p suppresses breast cancer progression by inhibiting SOX2," *The Journal of Surgical Research*, vol. 236, pp. 278–287, 2019.
- [11] T. Zhou, S. Chen, and X. Mao, "miR-145-5p affects the differentiation of gastric cancer by targeting KLF5 directly," *Journal of Cellular Physiology*, vol. 234, no. 5, pp. 7634–7644, 2019.

- [12] T. L. Pang, F. C. Chen, Y. L. Weng et al., “Costars, a Dictyostelium protein similar to the C-terminal domain of STARS, regulates the actin cytoskeleton and motility,” *Journal of Cell Science*, vol. 123, no. 21, pp. 3745–3755, 2010.
- [13] J. Lin, T. Zhou, and J. Wang, “Solution structure of the human HSPC280 protein,” *Protein Science*, vol. 20, no. 1, pp. 216–223, 2011.
- [14] E. Stylianopoulou, G. Kalamakis, M. Pitsiani et al., “HSPC280, a winged helix protein expressed in the subventricular zone of the developing ganglionic eminences, inhibits neuronal differentiation,” *Histochemistry and Cell Biology*, vol. 145, no. 2, pp. 175–184, 2016.
- [15] B. Ura, L. Monasta, G. Arrigoni et al., “A proteomic approach for the identification of biomarkers in endometrial cancer uterine aspirate,” *Oncotarget*, vol. 8, no. 65, pp. 109536–109545, 2017.
- [16] D. Wang, H. Q. Liu, C. Ren, and L. Wang, “High expression of ABRACL is associated with tumorigenesis and affects clinical outcome in gastric cancer,” *Genetic Testing and Molecular Biomarkers*, vol. 23, no. 2, pp. 91–97, 2019.
- [17] L. L. Mei, W. J. Wang, Y. T. Qiu, X. F. Xie, J. Bai, and Z. Z. Shi, “miR-145-5p suppresses tumor cell migration, invasion and epithelial to mesenchymal transition by regulating the Sp1/NF- κ B signaling pathway in esophageal squamous cell carcinoma,” *International Journal of Molecular Sciences*, vol. 18, no. 9, article 1833, 2017.
- [18] G. A. Calin, C. Sevignani, C. D. Dumitru et al., “Human microRNA genes are frequently located at fragile sites and genomic regions involved in cancers,” *Proceedings of the National Academy of Sciences of the United States of America*, vol. 101, no. 9, pp. 2999–3004, 2004.
- [19] B. P. Lewis, C. B. Burge, and D. P. Bartel, “Conserved seed pairing, often flanked by adenosines, indicates that thousands of human genes are microRNA targets,” *Cell*, vol. 120, no. 1, pp. 15–20, 2005.
- [20] X. B. Cui, S. Li, T. T. Li et al., “Targeting oncogenic PLCE1 by miR-145 impairs tumor proliferation and metastasis of esophageal squamous cell carcinoma,” *Oncotarget*, vol. 7, no. 2, pp. 1777–1795, 2016.
- [21] F. Wang, J. Xia, N. Wang, and H. Zong, “miR-145 inhibits proliferation and invasion of esophageal squamous cell carcinoma in part by targeting c-Myc,” *Onkologie*, vol. 36, no. 12, pp. 754–758, 2013.
- [22] Q. Han, H. Y. Zhang, B. L. Zhong, X. J. Wang, B. Zhang, and H. Chen, “MicroRNA-145 inhibits cell migration and invasion and regulates epithelial-mesenchymal transition (EMT) by targeting connective tissue growth factor (CTGF) in esophageal squamous cell carcinoma,” *Medical Science Monitor*, vol. 22, pp. 3925–3934, 2016.
- [23] C. Fogl, L. Puckey, U. Hinssen et al., “A structural and functional dissection of the cardiac stress response factor MS1,” *Proteins*, vol. 80, no. 2, pp. 398–409, 2012.
- [24] V. E. Galkin, A. Orlova, O. Cherepanova, M. C. Lebart, and E. H. Egelman, “High-resolution cryo-EM structure of the F-actin-fimbrin/plastin ABD2 complex,” *Proceedings of the National Academy of Sciences of the United States of America*, vol. 105, no. 5, pp. 1494–1498, 2008.
- [25] D. G. Baumann, M. S. Dai, H. Lu, and D. S. Gilmour, “GFZF, a GlutathioneS-Transferase protein implicated in cell cycle regulation and hybrid Inviability, is a transcriptional coactivator,” *Molecular and Cellular Biology*, vol. 38, no. 4, 2018.

Retraction

Retracted: 3D Printed Guides and Preoperative Planning for Uncemented Stem Anteversion Reconstruction during Hip Arthroplasty: A Pilot Study

BioMed Research International

Received 12 March 2024; Accepted 12 March 2024; Published 20 March 2024

Copyright © 2024 BioMed Research International. This is an open access article distributed under the Creative Commons Attribution License, which permits unrestricted use, distribution, and reproduction in any medium, provided the original work is properly cited.

This article has been retracted by Hindawi following an investigation undertaken by the publisher [1]. This investigation has uncovered evidence of one or more of the following indicators of systematic manipulation of the publication process:

- (1) Discrepancies in scope
- (2) Discrepancies in the description of the research reported
- (3) Discrepancies between the availability of data and the research described
- (4) Inappropriate citations
- (5) Incoherent, meaningless and/or irrelevant content included in the article
- (6) Manipulated or compromised peer review

The presence of these indicators undermines our confidence in the integrity of the article's content and we cannot, therefore, vouch for its reliability. Please note that this notice is intended solely to alert readers that the content of this article is unreliable. We have not investigated whether authors were aware of or involved in the systematic manipulation of the publication process.

Wiley and Hindawi regrets that the usual quality checks did not identify these issues before publication and have since put additional measures in place to safeguard research integrity.

We wish to credit our own Research Integrity and Research Publishing teams and anonymous and named external researchers and research integrity experts for contributing to this investigation.

The corresponding author, as the representative of all authors, has been given the opportunity to register their agreement or disagreement to this retraction. We have kept a record of any response received.

References

- [1] Y. Zhang, Z. Rao, J. Zhang, S. Li, S. Chang, and Y. Sun, "3D Printed Guides and Preoperative Planning for Uncemented Stem Anteversion Reconstruction during Hip Arthroplasty: A Pilot Study," *BioMed Research International*, vol. 2021, Article ID 6621882, 8 pages, 2021.

Research Article

3D Printed Guides and Preoperative Planning for Uncemented Stem Anteversion Reconstruction during Hip Arthroplasty: A Pilot Study

Yingqi Zhang,¹ Zhitao Rao,¹ Jincheng Zhang,¹ Shijie Li,² Shimin Chang^{ID},²
and Yeqing Sun^{ID}¹

¹Department of Orthopedic Surgery, Tongji Hospital, Tongji University School of Medicine, Shanghai 200065, China

²Department of Orthopedic Surgery, Yangpu Hospital, Tongji University School of Medicine, Shanghai 200090, China

Correspondence should be addressed to Shimin Chang; jiu222117464@163.com and Yeqing Sun; yeqingsun@tongji.edu.cn

Received 21 December 2020; Revised 16 January 2021; Accepted 30 January 2021; Published 19 February 2021

Academic Editor: Tao Huang

Copyright © 2021 Yingqi Zhang et al. This is an open access article distributed under the Creative Commons Attribution License, which permits unrestricted use, distribution, and reproduction in any medium, provided the original work is properly cited.

Objective. To investigate if 3D printed guides and preoperative planning can accurately control femoral stem anteversion. **Methods.** A prospective comparative study was carried out from 2018 to 2020, including 53 patients who underwent hip arthroplasty for femoral neck fracture. The target rotation center of the femoral head is determined by three-dimensional planning. In group A, planning was made by 2D templates. In group B, preoperative 3D planning and 3D printed osteotomy/positioning guides were performed. After the operation, 3D model registration was performed to calculate the accuracy of anteversion restoration. **Results.** We screened 60 patients and randomized a total of 53 to 2 parallel study arms: 30 patients to the group A (traditional operation) and 23 patients to the group B (3D preoperative planning and 3D printed guide). There were no significant differences in demographic or perioperative data between study groups. The restoration accuracy of group A was $5.42^\circ \pm 3.65^\circ$ and of group B was $2.32^\circ \pm 1.89^\circ$. The number and rate of abnormal cases was 15 (50%) and 2 (8.7%), respectively. Significant statistical differences were found in angle change, restoration accuracy, and number of abnormal cases. **Conclusion.** Three-dimensional preoperative planning and 3D printed guides can improve the accuracy of the restoration of femoral anteversion during hip arthroplasty.

1. Introduction

Hip arthroplasty is an extremely successful procedure, which help improving range of motion and decreasing pain and finally improving patients' quality of life [1, 2]. However, mispositioning of the implants can result in premature implant failure requiring revision [1–4]. Although the most common cause of revision surgery was due to cup mispositioning (33%), surgeons should be aware of the variability of the femoral anteversion of uncemented stems [5, 6]. The traditional methods of using preoperative anteroposterior pelvis radiographs for planning and standard surgical instrumentation have shown potential for inaccuracy which varies with surgeon experience. With the development of digital orthopedics, CT-based three-dimensional planning and navigation systems

have been introduced to improve the accuracy of prosthesis implantation [7–9]. However, the implantation of the femoral stem is affected by the surgical incision, visual field, and irregular medullary cavity shape of the proximal femur. It is difficult to accurately restore the anteversion, even based on preoperative CT measurement results [6, 10].

3D printed personalized guides have been used in orthopedic surgery in recent years and have achieved good results [11, 12]. Based on a patient's unique bony morphologic features is an improvement over generic instruments by minimizing sources of error from standard surgical instruments that depend on appropriate patient positioning, exposure, and surgeon experience [13–15]. However, there are rare reports in the previous literature about the use of guide to assist the femoral anteversion restoration [6]. Based on the

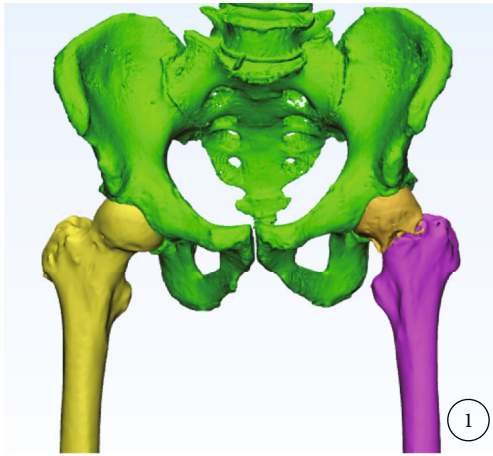


FIGURE 1: Fracture modeling build an independent three-dimensional model of fracture through CT.

preoperative three-dimensional planning, we developed a femoral osteotomy guide and a stem positioning guide. For hip arthroplasty, it is expected to accurately restore the femoral anteversion.

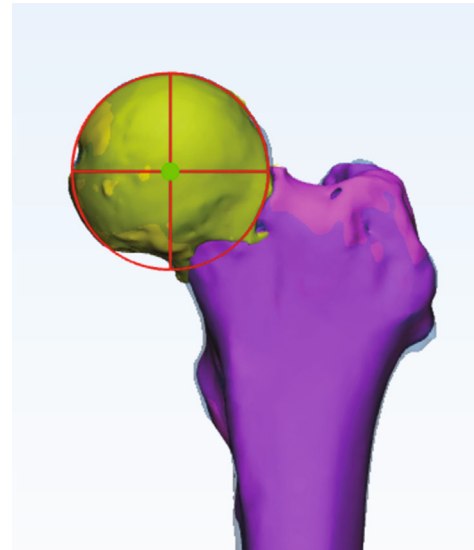
2. Materials and Methods

This prospective, controlled trial was performed from January of 2018 to January of 2020 at a single large academic institution. This study was approved by our institutional review board, and every patient gave written informed consent to participate.

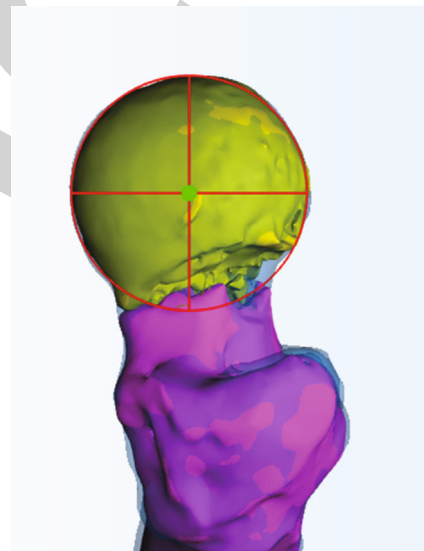
2.1. Patients. Patients scheduled for a primary arthroplasty were approached for the study. Inclusion criteria are as follows: (1) unilateral traumatic femoral neck fracture, (2) primary hip replacement, (3) age > 18 years old at time of surgery, (4) cementless straight stem (Johnson & Johnson/Zimmer Biomet, USA), and (5) able to get a preoperative and postoperative CT scans. Exclusion criteria are as follows: (1) hip joints had abnormalities before this injury and (2) condition deemed by physician to be nonconductive to patient's ability to complete the study. Demographic information collected on all patients was age, gender, and body mass index (BMI).

2.2. Three-Dimensional Planning. In all cases, the appropriate type of prosthesis was selected through the traditional two-dimensional template. Preoperative CT scans of the pelvis and proximal femur were obtained (Siemens, 120 kV, 350 mA, layer spacing < 1 mm). CT data was imported into the Mimics 20.0 software (Master, Belgium). Separate models of the pelvis, healthy femur, injured femoral head, and proximal shaft were established by threshold difference and manual segmentation (Figure 1). After virtual fracture reduction or mirror healthy model registration, the target femoral head center can be obtained by articular surface fitting (Figure 2).

Then, the femoral stem prosthesis model was imported into the software. Taking the center of the target femoral head as a reference, surgeon adjusted the posture of the prosthetic stem in the front view, lateral view, and top view. In the



(a)



(b)

FIGURE 2: Mirror/virtual fracture reduction, fitting articular surface to determine the target rotation center: front view (a); side view (b); the red circle is the fitting sphere, and the green dot is the planned center.

top view, the axis of the prosthesis's neck passes through the target center. In the front and lateral view, the axis of the prosthesis stem was coaxial with the centerline of the proximal medullary cavity (Figure 3). In group A, 3D process was performed after surgery. In group B, femoral neck osteotomy guide and stem positioning guide were designed (Figure 4). The guide models were output in STL format, printed with 0.1 mm precision photosensitive medical-grade resin. Guides were sterilized by low-temperature plasma.

2.3. Surgical Procedure. The operations were performed by the same group of surgeons. All femoral components were made with cementless devices. After receiving general anesthesia or nerve block anesthesia, patients were positioned in

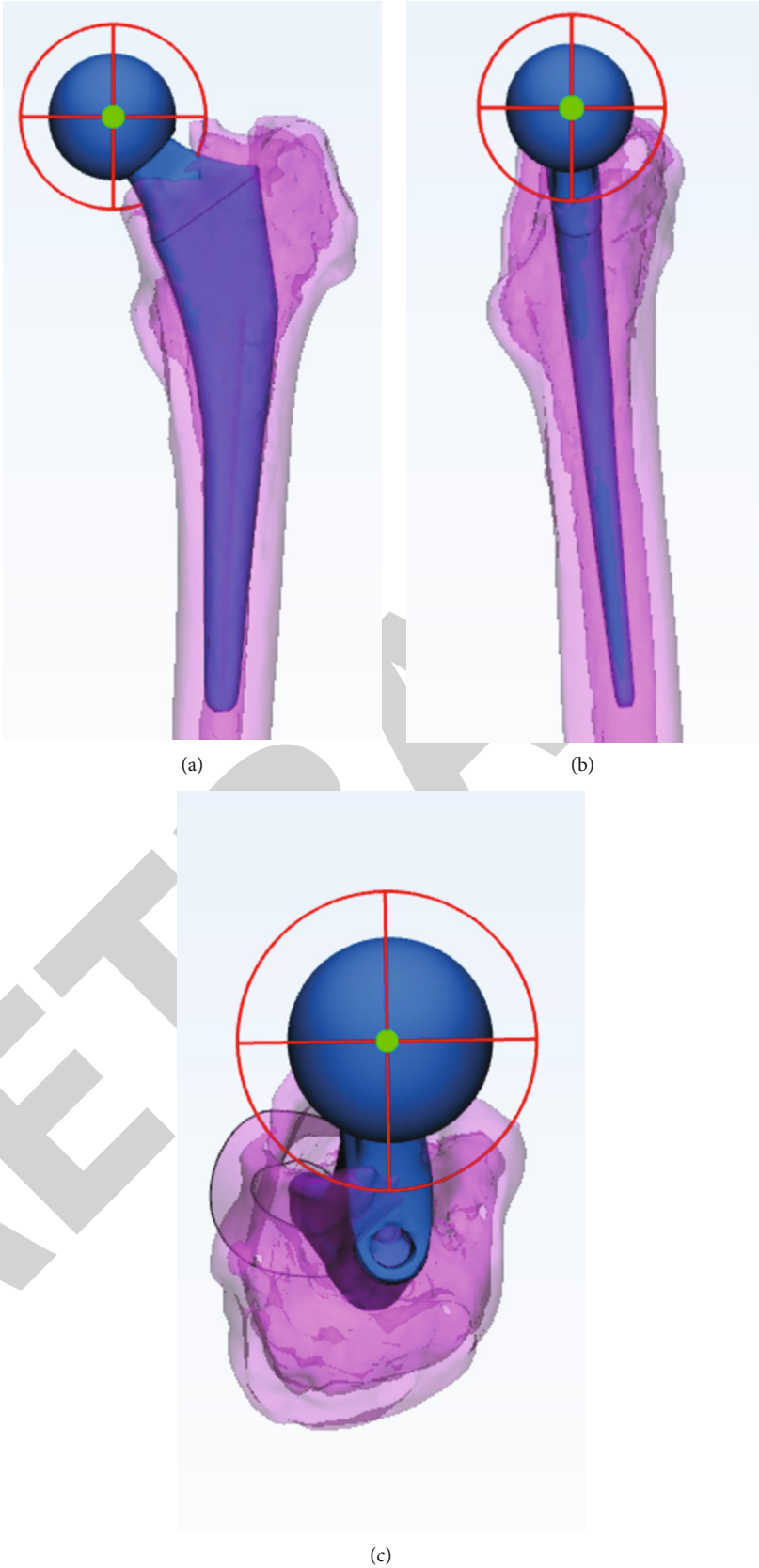


FIGURE 3: Simulated placement of femoral prosthesis: front view (a), lateral view (b), and top view (c).

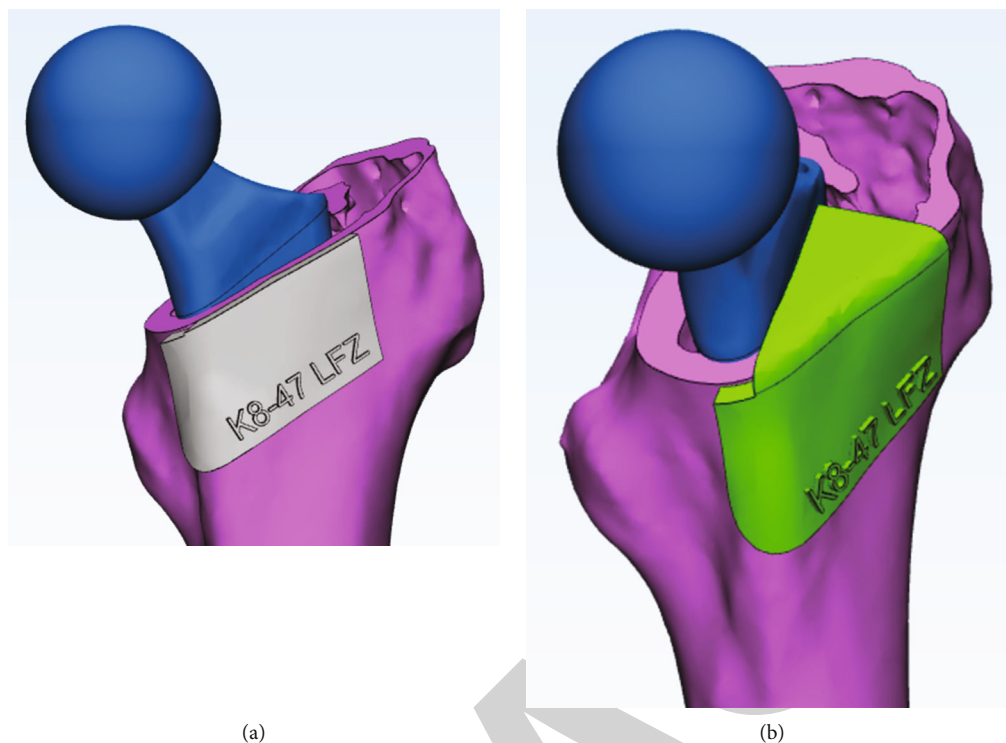


FIGURE 4: Design of femoral neck osteotomy guide (a) and prosthesis positioning guide (b).

the lateral decubitus position for all procedures. The operative technique for both groups was completed using anterolateral approaches. In the group A, surgeons performed operations based on two-dimensional planning and experience. In the group B, 3D preoperative planning was performed before surgery; after exposure of the femoral neck, the bone was cleaned to ensure a secure fit for the guides. Next, the guide was placed in a position to fit around bone in a “best fit” position. The femoral neck osteotomy was performed according to the edge of the guide (Figure 5(b)). After removing the femoral head, the acetabulum was cleaned. Then, the femoral medullary cavity was formed, and the position guide was placed on the osteotomy surface during the forming process (Figure 5(c)). After the stability testing, the femoral stem was implanted according to the guide (Figure 5(d)).

2.4. Postoperative Evaluation. All patients received a CT scan prior to discharge using the same technique as the preoperative scans. Evaluation of the final anteversion was determined by superimposing the previous planned stem position to the actual stem position and compared using Tsai’s definitions (Figure 6) [3]. From the top view, the planned and postoperative anteversion was measured. The angle difference between the postoperative femoral prosthesis neck axis and the preoperatively planned center was calculated as accuracy value (Figure 6(c)). Cases with the angle change more than 5° were counted as abnormal case.

2.5. Statistical Analysis. The data are reported using descriptive statistics, including mean, standard deviation, and range

values. The accuracy of the anteversion restoring was compared among groups. Chi-squared test and Mann–Whitney *U* test are used to test differences between groups. $P < 0.05$ was regarded as significant difference.

3. Results

We screened 60 patients and randomized a total of 53 to 2 parallel study arms: 30 patients to the group A (traditional operation) and 23 patients to the group B (3D preoperative planning and 3D printed guide). There were no significant differences in demographic or perioperative data between study groups (Tables 1 and 2).

The average planned anteversion for groups was $22.6^\circ \pm 11.4^\circ$ (group A) and $21.6^\circ \pm 9.9^\circ$ (group B), respectively. The average actual anteversion for groups was $21.8^\circ \pm 14.5^\circ$ and $21.8^\circ \pm 10.3^\circ$, respectively. The accuracy for groups was $5.42^\circ \pm 3.7^\circ$ (range 0.5° to 17.7°) and $2.32^\circ \pm 1.89^\circ$ (range 0.1° to 6.8°), respectively. The number and rate of abnormal cases was 15 (50%) and 2 (6.7%), respectively. Significant statistical differences were found in angle change, restoration accuracy, and number of abnormal cases.

4. Discussion

Component positioning in hip arthroplasty can have a major effect on both clinical outcome and complications rate. Previous studies have focused on the accuracy of acetabular implantation [3, 16–18]. With the introduction of concepts such as combined version, more and more attention has been paid to stem anteversion [19]. Substantial changes in femoral

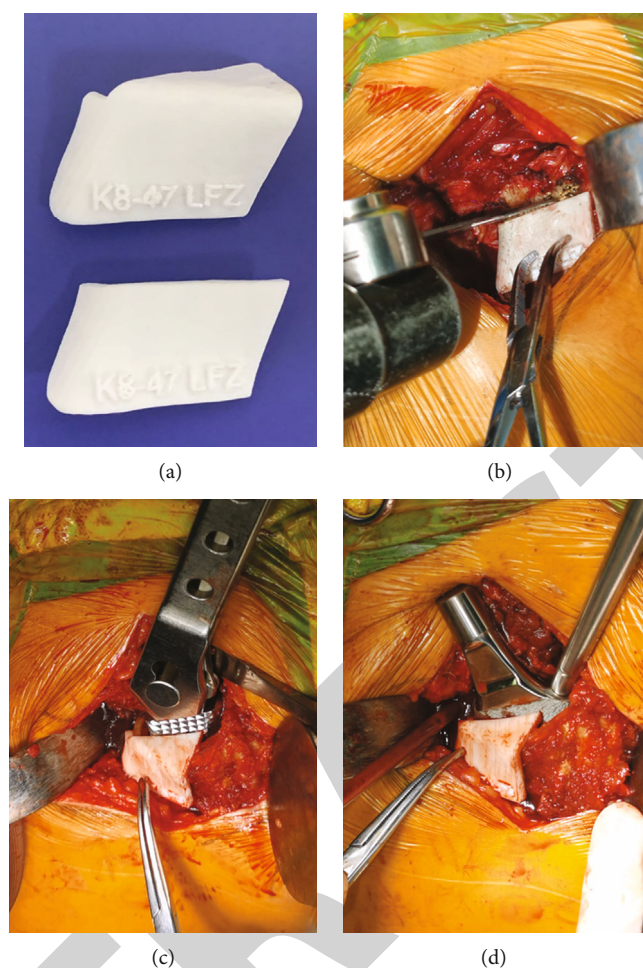


FIGURE 5: Guide plate printing (a), intraoperative osteotomy (b), intraoperative medullary cavity formation (c), and intraoperative implantation of femoral stem (d).

neck version with stem implantation create concurrent changes in anterior and lateral femoral offset, potentially resulting in decrements in abductor strength [20]. Surgical approaches also affect the anteversion change [21].

Traditionally, the recommended positioning for femoral stem is to restore natural offset and anteversion. Various works have in fact shown native femoral neck version that has a wide variation. Abe reported the mean preoperative femoral anteversion was $27.8^\circ \pm 10.6^\circ$ in Japanese population. Koerner reported average femoral version was $8.84^\circ \pm 9.66^\circ$, with no statistically significant differences between ethnicities [22]. Our study presented similar results that the standard deviation is about 10° . The variable anteversion may cause difficulty for the surgeon to implant correctly.

In order to accurately restore the femoral rotation center, surgeons usually control stem anteversion during the operation, based on experience and visual assessment. But the surgeon's estimation of the anteversion of the cementless femoral stem has poor precision [23]. Wines reported that the mean difference between the surgeons' intraoperative assessment of femoral component version and the CT measurement was an underestimation of 1.18° , with a standard deviation of 10.4° and a range of 25° underestimation to 30°

overestimation [24]. In a research of 65 patients, Woerner reported the mean difference between the 3D-CT results and intraoperative estimations by the eye was -7.3° (-34° to 15°) and an overestimation of $>5^\circ$ for stem torsion in 40 hips. Using 3D reconstruction and method, Tsai reported femoral anteversion of the implanted side was significantly increased by $11.4^\circ \pm 11.9^\circ$ [3]. In this study, date of group A also presented that even experienced surgeon's intraoperative estimation of stem position by the eye is not reliable.

Several studies have investigated the accuracy of measurements obtained using a goniometer or navigation systems [25–27]. Mitsutake developed an angle-measuring instrument; mean measurement accuracy was $0.9^\circ \pm 6.1^\circ$, and the absolute measurement accuracy was $4.9^\circ \pm 3.7^\circ$ [25]. Using stem-first technique with navigation system, Okada reported absolute discrepancy between intraoperative and postoperative assessment was $5.81^\circ \pm 4.42^\circ$ (range 0.01° – 17.4°) [28]. In a robotically assisted study, Marcovigi reported average difference between preoperative and actual stem anteversion was $1.6^\circ \pm 9.8^\circ$ (max 34° in anteversion, min -52° in retroversion). Previous literatures remind that the accurate restoration of femoral anteversion is still a concern for surgeons.

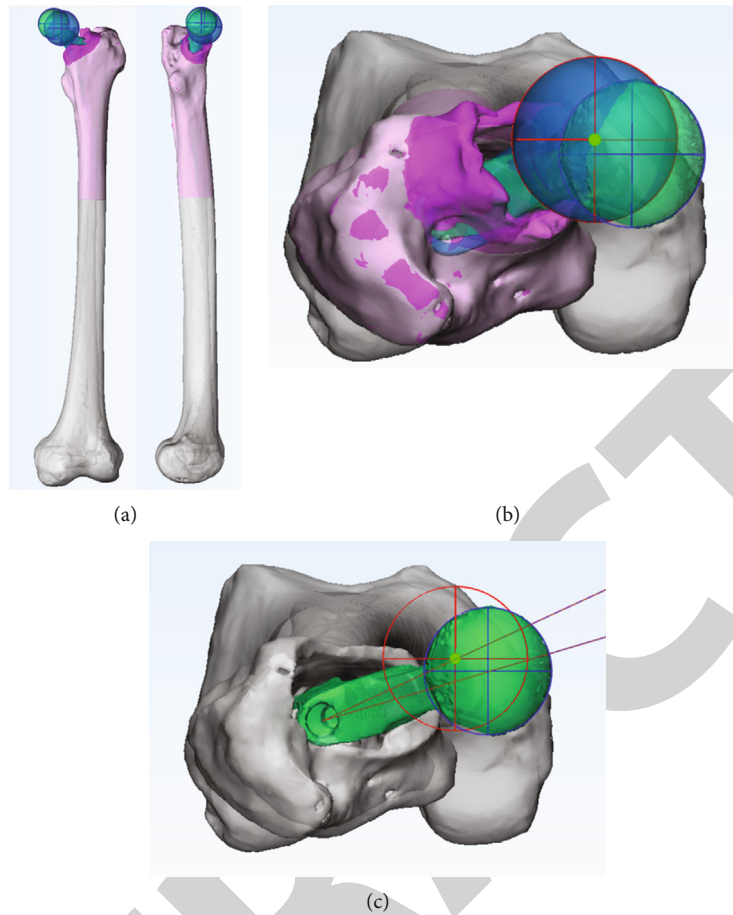


FIGURE 6: Postoperative modeling and registration (a). Fit the postoperative rotation center (b). Calculate the preoperative planning, the actual postoperative anteversion angle, and the difference (c). Red sphere indicates the planned center; blue sphere indicates the actual center.

TABLE 1: Patient characteristic data.

Variable	Group A	Group B	<i>P</i> value
Age at operation (years)	75.5 (54-89)	73.5 (52-86)	0.886 ^a
Sex distribution (M/F)	10/20	8/15	0.912 ^b
Height (m)	1.61 ± 0.08	1.61 ± 0.08	0.921 ^a
Weight (kg)	56.82 ± 10.26	60.48 ± 9.07	0.239 ^a
BMI (kg/m ²)	21.88 ± 3.23	23.34 ± 2.70	0.116 ^a
Location (L/R)	17/13	15/8	0.528 ^b
Operation type (T/H)	17/13	17/6	0.194 ^b

M: male; F: female; L: left hip; R: right hip; BMI: body mass index; T: total hip arthroplasty; H: hemiarthroplasty. ^aMann-Whitney *U* test. ^bChi-squared test, significance set at $P < 0.05$.

For joint arthroplasty, 3D printed instruments have already been successfully translated into large-scale clinical use for knee arthroplasty. Some studies introduced patient specific instruments that assist acetabular cup placement and femoral neck osteotomy in hip replacements [11, 14]. Lee combined 3D printed instrument and navigation system for an in vitro study with a sawbone model, and the absolute deviation between plan and actual anteversion was $1.41^\circ \pm 1.03^\circ$ (range 0.02° - 3.32°) [29]. However, Lee prepared the

TABLE 2: Comparison of preoperative and postoperative anteversion.

Variable	Group A	Group B	<i>P</i> value
Preoperative femoral anteversion (degrees)	22.61 ± 11.43	21.61 ± 9.96	0.816 ^a
Postoperative femoral anteversion (degrees)	21.77 ± 14.48	21.84 ± 10.25	0.971 ^a
Anteversion change (degrees)	5.42 ± 3.65	2.32 ± 1.89	0.000 ^a
Abnormal case (>5°)	15 (50%)	2 (8.7%)	0.002 ^b

^aMann-Whitney *U* test. ^bChi-squared test, significance set at $P < 0.05$.

proximal medullary canal using only a box chisel. Various authors have pointed out that, especially in cementless arthroplasty, the stem finds its way to an anteversion position, where it fits best to the rigid canal of the femur. It should be noted that the entry point of the medullary cavity will affect the anteversion angle and the center of rotation.

For the first time, this article compared the accuracy of anteversion restoration between 3D printed guide and traditional operation. The method of mirror model and virtual reduction was used to determine the target rotation center;

then, the personalized osteotomy/positioning guides were designed and manufactured. The results shown that the error of the traditional experience operation is relatively high. The number of abnormal cases is 15 (50%), which is like previous studies. The 3D printed guides improve the accuracy, even better than some navigation system in previous reports. The abnormal case was reduced from 50% to 6.7%. The reason may be that the positioning guide in this experiment is very close to the box chisel and stem, which helps the surgeon choose the appropriate entry point and be a reference during the medullary cavity formation process. The planned stem axis should be overlapped with the proximal medullary cavity axis, which can reduce the mismatch of medullary cavity. In this experiment, the guide does not need to be fixed on the bone and change the surgical procedure slightly.

5. Conclusions

We have proposed the method including 3D planning and 3D printed osteotomy/positioning guides for femoral anteversion restoration. The proposed method was more accurate and consistent than the conventional method. 3D printed guides can reduce the number of inappropriate anteversion. Paying attention to the relationship between the entry point of the box-chisel and the geometry of the osteotomy surface can improve the accuracy of the operation.

Data Availability

All the data could be provided if any qualified authors required.

Ethical Approval

This study was approved by the Medical Ethics Committee of Shanghai Tongji Hospital (No. 2018-054).

Disclosure

The project funding did not affect the opinions of article, the results data, and statistical analysis.

Conflicts of Interest

All authors declare no conflict of interest in the research.

Authors' Contributions

Yingqi Zhang and Zhitao Rao contributed equally. They were responsible for experimental design and operation, statistical analysis, and article writing. Yeqing Sun and Jincheng Zhang participated in the operation. Shijie Li collected the data. Yeqing Sun and Shimin Chang reviewed the content of the article. Yingqi Zhang and Zhitao Rao contributed equally to this work.

Acknowledgments

This work was granted by the Clinical Technology Innovation Project of Shanghai Shenkang Hospital Development

Center (No. SHDC12017X15) and the Shanghai Municipal Health Commission Clinical Research (No. 20184Y0279 and 201740078).

References

- [1] K. H. Widmer and B. Zurfluh, "Compliant positioning of total hip components for optimal range of motion," *Journal of Orthopaedic Research*, vol. 22, no. 4, pp. 815–821, 2004.
- [2] D. D. D'lima, A. G. Urquhart, K. O. Buehler, R. H. Walker, and C. W. Colwell JR., "The effect of the orientation of the acetabular and femoral components on the range of motion of the hip at different head-neck ratios," *The Journal of Bone and Joint Surgery. American Volume*, vol. 82, no. 3, pp. 315–321, 2000.
- [3] T. Y. Tsai, D. Dimitriou, G. Li, and Y. M. Kwon, "Does total hip arthroplasty restore native hip anatomy? Three-dimensional reconstruction analysis," *International Orthopaedics*, vol. 38, no. 8, pp. 1577–1583, 2014.
- [4] T. Y. Tsai, J. S. Li, D. Dimitriou, and Y. M. Kwon, "Does component alignment affect gait symmetry in unilateral total hip arthroplasty patients?," *Clinical Biomechanics*, vol. 30, no. 8, pp. 802–807, 2015.
- [5] G. D. Wera, N. T. Ting, M. Moric, W. G. Paprosky, S. M. Sporer, and C. J. Della Valle, "Classification and management of the unstable total hip arthroplasty," *The Journal of Arthroplasty*, vol. 27, no. 5, pp. 710–715, 2012.
- [6] M. A. Belzunce, J. Henckel, A. di Laura, and A. Hart, "Uncemented femoral stem orientation and position in total hip arthroplasty: a CT study," *Journal of Orthopaedic Research*, vol. 38, no. 7, pp. 1486–1496, 2020.
- [7] Y. Wako, J. Nakamura, M. Miura, Y. Kawarai, M. Sugano, and K. Nawata, "Interobserver and intraobserver reliability of three-dimensional preoperative planning software in total hip arthroplasty," *The Journal of Arthroplasty*, vol. 33, no. 2, pp. 601–607, 2018.
- [8] E. Sariali, R. Mauprivez, F. Khiami, H. Pascal-Moussellard, and Y. Catonné, "Accuracy of the preoperative planning for cementless total hip arthroplasty. A randomised comparison between three-dimensional computerised planning and conventional templating," *Orthopaedics & Traumatology, Surgery & Research*, vol. 98, no. 2, pp. 151–158, 2012.
- [9] L. Renner, V. Janz, C. Perka, and G. I. Wassilew, "What do we get from navigation in primary THA?," *EFORT open reviews*, vol. 1, no. 5, pp. 205–210, 2016.
- [10] D. Dimitriou, T. Y. Tsai, and Y. M. Kwon, "The effect of femoral neck osteotomy on femoral component position of a primary cementless total hip arthroplasty," *International Orthopaedics*, vol. 39, no. 12, pp. 2315–2321, 2015.
- [11] T. Small, V. Krebs, R. Molloy, J. Bryan, A. K. Klika, and W. K. Barsoum, "Comparison of acetabular shell position using patient specific instruments vs. standard surgical instruments: a randomized clinical trial," *The Journal of Arthroplasty*, vol. 29, no. 5, pp. 1030–1037, 2014.
- [12] M. Olsen, D. D. Naudie, M. R. Edwards, M. E. Sellan, R. W. McCalden, and E. H. Schemitsch, "Evaluation of a patient specific femoral alignment guide for hip resurfacing," *The Journal of Arthroplasty*, vol. 29, no. 3, pp. 590–595, 2014.
- [13] Q. Q. Xing, D. Zhong, Y. X. Pan et al., "A comparative study of patients' subjective feelings toward total hip arthroplasty with